2011

PHOTON FACTORY ACTIVITY REPORT

PART B : Users' Report #29

Photon Factory Activity Report 2011

PART B

Users' Report

Contents

Atomic and Molecular Science

[Top]

Chemistry

25	Study on Regeneration of Catalyst for Hydrotreating of High Boiling Point Oil using XAFS (Japanese)	IWANAMI Yoshimu	2009I005	NW10A
26	Local Structure Analysis of Positive Electrode Materials in Lithium Ion Battery (Japanese)	HIRANO Tatsumi	2009I007	9C, 12C, NW2A
27	In-situ XAFS Analysis of Automobile Exhaust Catalyst (Japanese)	MIURA Kazuya	2009I009	NW10A
28	EXAFS Analysis of the Rh-Te Alloy Nanoparticles Prepared by Liquid Phase Reduction Method	YAGIHASHI Noritoshi	2010G 593	NW10A
29	Precise Analysis of New Type Adhesives (Japanese)	MATSUBA Go	2010G006, 2010G007	10C, 6A
30	Shear-Induced Crystallization Process of Syndiotactic Polystyrene	ZHAO Yunfeng	2010G007	6A
31	XAFS Characterization of SiO_2-Supported Ru Complex for Sulfoxidation	MAITY Niladri	2010G020	NW10A
32	Mechanistic Insights into Photochromic Behavior of a Ruthenium(II)-Pterin Complex	ISHIZUKA Tomoya	2010G039	NW2A
33	Imaging XAFS Analysis of Cs in Soil and Minerals (Japanese)	OKAMOTO Yoshihiro	2010G047	27B
34	Behavior of Ru in High-Temperature Simulated High-Level Waste Glass Melt	OKAMOTO Yoshihiro	2010G048	NW10A
35	Formation Process of Surfactant Gel Network Structures (Japanese)	KAWABATA Yohei	2010G057	4A, 6A, 15A, 9C
36	Nanophase-Separated Supramolecular Assemblies of Functionalized Polymers via Ionic Hydrogen Bonding	NORO Atsushi	2010G059	6A, 15A
37	EXAFS Analysis for Structure of Active Site for Glycerol Hydrogenolysis	AMADA Yasushi	2010G069	NW10A
38	EXAFS Analysis for Supported Ru Catalyst Active for Syntheses of Quinoxaline Derivatives	ZAZYBIN Alexey	2010G109	NW10A
39	Structural Studies on Ni Phosphide Catalysts by Operando XAFS	TAKAGAKI Atsushi	2010G127, 2011A1972(SPring-8)	7C, BL14B2(SPring-8)
40	XAFS Study of Rhodium Cocatalyst Loaded on $K_2Ti_6O_{13}$ Photocatalyst	YOSHIDA Hisao	2010G149, 2011G575	NW10A
41	Fluoride Addition Effect on the EXAFS of Neodymium Cation in Molten Chlorides	FUJITA Kazuhiro	2010G165	7C
42	Thermal Changes of Structures and Properties of Pi-Backdonating Metal Complexes (in 2010)	AKITSU Takashiro	2010G510	19B
43	Anisotropy of Functions and Thermally Structural Changes for Cu(II) Complexes (in 2010)	AKITSU Takashiro	2010G511	8B
44	B1-to-B2 Structural Transitions in Rock Salt Intergrowth Structures	YAMAMOTO Takafumi	2010G560	NE1A
45	Characterization of Supported Ruthenium Catalysts for Hydrolysis of Cellulose (Japanese)	KOBAYASHI Hirokazu	2010G591	NW10A
46	Analysis of Stereo Complex Crystals in Poly(L-Lactic Acid)/Poly(D-Lactic Acid) Blends (Japanese)	HENMI Kouta	2010G626, 2011A1961(SPring-8)	6A, BL40B2(SPring-8)
47	Electronic and Local Structures of $Ce(PO_4)_{1-x}(VO_4)_x$-Based Proton-Electron Mixed Conductor	IDEMOTO Yasushi	2010G629, 2011A1974(SPring-8)	BL14B2(SPring-8)
48	Coordination Structure of Er-PTA Complex in Ethanol Solution	YAITA Tsuyoshi	2010G679	27B
49	Structural Analysis of 2,7-Diphenyl[1]Benzothieno[3,2-*b*][1]Benzothiophene (Japanese)	MIYAZAKI Eigo	2010G701	8B
50	Elucidation of the Mechanisms of Remineralization and Recrystallization of Early Caries Lesion with a Water-Soluble Calcium, POs-Ca by XAFS Analysis for Improving Caries Prevention Effect (Japanese)	KOBAYASHI Takatsugu	2010I001	9A, 11A
51	Analysis of Catalysts for Alkaline Membrane Fuel Cell (Japanese)	WATANABE Shin	2010I003	9C, 12C, NW10A
52	Characterization of Electronic States in Cyanide-Bridged Fe-Co Tetranuclear Complexes by X-Ray Absorption Spectroscopy (Japanese)	NIHEI Masayuki	2010G009	8A
53	Complex Formation of Starch and Surfactant in Aqueous Solution	YAMAMOTO Kyoko	2011G006	10C
54	Effect of the Supports on the Oxidative Esterification of Propionaldehyde on Supported Palladium Catalysts	SUGIYAMA Shigeru	2011G007	NW10A
55	Structure of Copper Hydroxy Anions in the Layered Double Hydroxides for the Photocatalytic Conversion of Carbon Dioxide to Methanol	AHMED Naveed	2011G033, 2011A1977(SPring-8)	7C, 9C, BL01B1(SPring-8)
56	Spectroelectrochemical Measurement of Uranium Ions in Nitric Acid and Sodium Carbonate Solutions	UEHARA Akihiro	2011G034	27B
57	Powder Diffraction Structure Analysis of Humidity and Temperature Dependent Structure Transition of Amino Acids and Oligopeptides (Japanese)	KIYOTANI Tamiko	2011G060, 2011A4805(SPring-8)	4B2, BL15XU(SPring-8)

58	Monitoring of Photocatalytic Reduction Sites of Preferential Oxidation of Carbon Monoxide in Hydrogen	YOSHIDA Yusuke	2011G083, 2011A1978(SPring-8)	7C, 9C, BL01B1(SPring-8)
59	Local Structure Analysis of Uranium Tetravalent Ions in LiCl-CsCl Mixtures by Synchrotron XAFS Measurement (Japanese)	NAGAI Takayuki	2011G111	27B
60	Study on Mechanisms of Electrochemical Reactivity in P2-$Na_x[Fe_{1/2}Mn_{1/2}]O_2$ as Positive Electrode Materials for Sodium-Ion Rechargeable Batteries	YABUUCHI Naoaki	2011G141	7C
61	XAFS Analysis of Local Structure of Active Sites for Asymmetric Cyclopropanation on Copper Ion-Planted Mesoporous Al-MCM-41	KATO Hiroki	2011G146	7C, 9C
62	XAFS Analysis of Pt Catalyst for Autothermal Reforming (Japanese)	TAKAGAKI Atsushi	2011G163	7C
63	Oxalate Metal Complexes in Aerosols: Implications for the Hygroscopicity of Oxalate-Containing Particles	TAKAHASHI Yoshio	2011G197	9A, 12C
64	Investigation on Oxygen Reduction Reaction Activity of Multi-Copper Complex Deposited on Electrodes by XAFS (Japanese)	YAGI Ichizo	2011G200, 2011A1981(SPring-8), 1105045PF(SAGA-LS)	9C, BL14B2(SPring-8), BL11(SAGA-LS)
65	Evaluation of Hypoxia in Tokyo Bay by Chemical States of Iron and Manganese in the Sediments (Japanese)	YAMAGATA Takehiro	2011G251	9A, 12C
66	Structural Studies on the Light-Harvesting Membrane Protein Complexes from Thermophilic Photosynthetic Bacteria	YU Long-Jiang	2011G514	17A, NE3
67	Effects of Diameter and Dimension of Ordered Mesoporous Metal Oxides as Templates on Formed Pt Nanoparticles and Pt–C Nanocomposites	OKA Kazuki	2011G523	9C
68	Anomalous Valence Change of Zinc Ion Exchanged in MFI-Type Zeolite Being Efficient for Dissociative Adsorption of Dihydrogen	ODA Akira	2011G538	7C, 9C
69	PXRD Structure Analysis of Dehydration of Cephalosporin Antibiotic Hydrate Crystal (Japanese)	UEKUSA Hidehiro	2011G551, 2011A1935(SPring-8)	4B2, BL02B2(SPring-8)
70	Design and Characterization of Visible Light-Responsive Ti-Based Metal-Organic Frameworks for the Application to Photocatalytic Hydrogen Evolution	HORIUCHI Yu	2011G556	7C
71	Attempt to Observe the Direct Interaction between Au-Au in the Luminescent	ASAKURA Kiyotaka	2011G558	9A
72	Structure of Supported Tantalum and Molybdenum Halide Clusters (Japanese)	KAMIGUCHI Satoshi	2011G559	7C, NW10A
73	Local Structure Analysis of Rh Catalysts Supported on Oxoacid Salts (Japanese)	IKEUE Keita	2011G619	NW10A
74	Absolute Asymmetric Polymerization with Synchrotron Light (Japanese)	GOTO Hiromasa	2011P101	3C
75	EXAFS Analysis of Pt-Core/Rh-Shell Bimetallic Nanoparticles Prepared by Multi-Step Reduction Processes	EINAGA Hisahiro	2012G069	NW10A, 7C

[Top]

Surface and Interface

Page	Title	First Author	Proposal No.	Beamline
76	Local Valence Electronic States of SiO_2 Ultrathin Films Grown on Si(111) Studied Using Auger Photoelectron Coincidence Spectroscopy (APECS): Observation of Upward Shift of Valence-Band Maximum Depending on the Interface Structure	KAKIUCHI Takuhiro	2006S2-002	1C
77	In situ Structural Studies on Ag/AgCl Reaction at the Underpotentially Deposited on the Au(111) Electrode Surface	KONDO Toshihiro	2008G124, 2009G038, 2010G051	4C
78	XANAM with Quartz Tuning Fork Cantilever	SUZUKI Shushi	2009G567	7C
79	Study on Magnetic Anisotropy of Fe/Co/Pd(111) Magnetic Thin Films Exhibiting Spin Reorientation Transitions (Japanese)	NAKAYAMA Takeshi	2009G629, 2011G664	7C, 11A
80	Mixed Valence State of TNAP on Bi(001)	NISHI Tatsuhiko	2009S2-007	13A
81	Isotope Effects on Thermal Dehydrogenation of Cyclohexane on Rh(111)	KOITAYA Takanori	2009S2-007	13A
82	High-Resolution X-Ray Photoelectron Spectroscopy Study on CH_3S/Au(111): Evidence for Formation of Au-Adatom-Dithiolate Complex	KONDOH Hiroshi	2009S2-007	13A
83	Acridine Orange Base as an Electron Donor on the ZnO Surfaces	OZAWA Kenichi	2009S2-007	3B, 13A
84	Interfacial Electronic Properties of Fullerene/Bathocuproine/Ag Heterostructures Studied by Ultraviolet Photoemission Spectroscopy	WANG Shenghao	2009S2007, 2011G026	3B, 13A

85	Local Structure of Pt(II) Pyridyl Complexes Anchored onto Mesoporous Silica as Photo-Induced H_2 Production Catalysts	MORI Kohsuke	2010G010	7C
86	Can Ion Pairs Adsorb on a Negatively Charged Mica Surface in Aqueous Solution?	SAKUMA Hiroshi	2010G119	4C
87	Local Structures of Hydrated Ions in Doped Ice (Japanese)	HARADA Makoto	2010G123	12C
88	Restricted Hydration Structure of Calcium Ion Formed in Slit-Shaped Carbon Micropore	KUSUDO Tomoko	2010G148	7C
89	Study of CO Oxidation Reaction on Ir(111) under near Atmosphere Pressure using Ambient Pressure XPS (AP-XPS)	SUZUKI Kazuma	2010G151	7A,13A
90	Phase Transition of Alkane Wetting Film on Surfactant Solution and Structural Change in Electrical Double Layer	OHTOMI Eisuke	2010G504	7C
91	Origin of Strong Adhesion between Rubber and Brass	OZAWA Kenichi	2010G550	3B, 13A
92	*In Situ* XAFS Observation of Platinum Nanoparticle Thin Layer Formed on HOPG Surface: A New Approach to the Carbon Electrode/Electrolyte Interface	UEHARA Hiromitsu	2010G601	12C, 9A
93	Relationship between Catalytic Property and NEXAFS of P-Doped Graphite	SHIMOYAMA Iwao	2010G634	27A
94	Immobilization of Alkyl Chain Molecules with Phosphonic Acid on Oxide Surface	NARITA Ayumi	2010G635	27A
95	Structure Analysis of Ag_2Pb Surface Alloy by KEK-RHEPD	FUKAYA Yuki	2010G652	SPF
96	Molecular Orientation of Regioregular Poly(3-Hexylthiophene) Film	IKEURA-SEKIGUCHI Hiromi	2010G653	27A
97	Depth Analysis of Organic Monolayers by C K-NEXAFS (Japanese)	ENDO Osamu	2010G657	7A
98	Determination of the Atomic Arrangement at the Graphene/α-Al_2O_3(0001) Interface by Normal Incident X-Ray Standing Wave Spectroscopy	ENTANI Shiro	2010G660	27A
99	Photo-Excited Carrier Transfer from Nb:$SrTiO_3$-Photoelectrode to Mn-Oxide-Cocatalyst Studied by In-Situ Electrochemical XAFS	YOSHIDA Masaaki	2010G677, 2011A1976(SPring-8)	12C, BL01B1(SPring-8)
100	Particle Size of Metal Salt Crystals in Doped Ice by Small-Angle X-Ray Scattering Technique (Japanese)	HARADA Makoto	2010P007	9C
101	Surface-Site-Selective Study of Valence Electronic States of Si(111)-7×7 Adsorbed with Water Using Si-$L_{23}VV$ Auger Electron Si-2*p* Photoelectron Coincidence Measurements	ARAE Sadanori	2011G013, 11-B-23(HiSOR)	BL13(HiSOR)
102	Analysis of Bonding Structure of Ultrathin Films of Oligothiophene Molecules Grown on Passivated Silicon Surfaces	TOYOSHIMA Hiroaki	2011G079	13A, 27A
103	Construction and Evaluation of Auger-Photoelectron Coincidence Apparatus at BL13 of HiSOR	KAKIUCHI Takuhiro	2011G099, 11-B-24(HiSOR)	BL13(HiSOR)
104	Core-Level Photoelectron Spectroscopy Study of the $TlBiSe_2$ Surface	HATTA Shinichiro	2011G576	18A
105	Molecular Chain Effect of Aromatic Self-Assembled Monolayers Measured in Soft X-Ray Stimulated Ion Desorption	WADA Shin-ichi	2011G626	7A
106	Measurement of Electronic Structure of Al_2O_3(0001) Surface	TOSAKA Aki	2011G671	18A
107	Study on Operando Synchrotron Radiation Photoemission Spectroscopy for Metal/Oxide/Semiconductor Interfaces under Bias Operaton (Japanese)	SHINOHARA Toshihiro	2011S2-003	2C
108	Chemical-State Resolved Depth Profile and Band Discontinuity in TiN/HfSiON Gate Stack Structure with an AlO_x Cap Layer	TOYODA Satoshi	2011S2-003	2C
109	Determining Factor of Effective Work Function in Metal/Bi-Layer High-*k* Gate Stack Structure Studied by Photoemission Spectroscopy	TOYODA Satoshi	2011S2-003	2C
110	Photoelectron Spectroscopic Study of CO Adsorption on Pd(100) Single Crystal Surface under Ambient-Pressure Conditions	TOYOSHIMA Ryo	2012G093	13A
111	High Thermal Stability of Au Clusters on a Nb-Doped TiO_2(110) Surface	TAKAKUSAGI Satoru	2012G094	9A
112	Temperature Dependence of Magnetization at the Surface and in the Inner Layers of Cu/Ni/Cu (Japanese)	AMEMIYA Kenta	2010S2-001	16A

[Top]

Electronic Structure of Condensed Matter

Page	Title	First Author	Proposal No.	Beamline
113	Soft X-Ray Resonant Photoemission Study of Filled Skutterudite Superconductor $PrPt_4Ge_{12}$	NAKAMURA Yoshiaki	2008S2-003, 2009G545	2C

114	In-Situ Photoelectron Spectroscopy of Mixed Metal Oxides for Selective Oxidation (Japanese)	MIYAZAKI Takafumi	2009G615, 1105038PF(SAGA-LS)	BL10(SAGA-LS)
115	Anisotropic Superconducting Gap in the Iron-Based Superconductor $BaFe_2(As_{1-x}P_x)_2$	YOSHIDA Teppei	2009S2-005	28A
116	Electronic Structure of $Ba(Fe_{0.96}Zn_{0.04})_2As_2$ with Antiferromagnetic Ordering	IDETA Shin-ichiro	2009S2-005	28A
117	Orbital Character of the Fermi Surfaces of the Iron-Based Superconductor $BaFe_2(As_{1-x}P_x)_2$	YOSHIDA Teppei	2009S2-005, ALS-05054	28A, BL10.0.1(ALS)
118	*R*-Site Randomness Effect on SpinOorbital Ordering in $SmVO_3$ (Japanese)	SASAKI Naoya	2009S2-008	4C, 8A
119	Structural Analyses of URu_2Si_2 by Synchrotron Radiation Single-Crystal X-Ray Diffraction (Japanese)	TABATA Chihiro	2009S2-008	8A, 8B
120	Ferroelectric Transition with Off-Center Magnetic Mn^{4+} Ions in $Sr_{1-x}Ba_xMnO_3$	SAKAI Hideaki	2009S2-008	8A
121	Resonant Soft X-Ray Scattering Study of Room Temperature Ferromagnet $Sr_3YCo_4O_{10.5}$ (Japanese)	OKAMOTO Jun	2009S2-008	16A
122	Resonant Soft X-Ray Scattering Study of Antiferromagnetic Ordering in $GeCo_2O_4$ (Japanese)	OKAMOTO Jun	2009S2-008	16A
123	Structure Analysis of (Nd,Sm)NiO_3 Electric Double Layer Transistors (Japanese)	ASANUMA Shutaro	2009S2-008	4C
124	Impurity Effects on Spinel-Type Vanadium Oxide MnV_2O_4 (Japanese)	HENMI Kazuhiro	2009S2-008, 2011S2-003	8A, 2C
125	Valence Band Structure of Fe_3O_4(100) (Japanese) Film Across Verwey Transition	RAN Fan-Yong	2010G095	18A
126	Peculiar Rashba Splitting on a Surface with Quasi 1D Structure (Japanese)	OHTAKA Minoru	2010G110	19A
127	Study of Magnetic Moments of Fe_3Pt by X-Ray Magnetic Diffraction	HIIRAGI Kenta	2010G147	3C
128	Metal-Insulator and Spin Structure Transition in $Ca_{1-x}Ce_xMnO_3$ Thin Film Studied by X-Ray Magnetic Circular Dichroism	HARANO Takayuki	2010G187	16A
129	X-Ray Magnetic Circular Dichroism Study of $FeCr_2S_4$	VERMA Kumar Virendra	2010G187, 2010S2-001	16A
130	Ru-Doped $La_{0.6}Sr_{0.4}MnO_3$ Thin Film as a Coercivity Tunable Material Studied by X-Ray Magnetic Circular Dichroism	HARANO Takayuki	2010G187, 2011A3840(JAEA)	16A, BL23SU(JAEA)
131	XMCD Study of Spin and Orbital States of FePt Nano-Particles Coated by SiO_2	KADONO Toshiharu	2010G187, 2011A3840(JAEA)	16A, BL23SU(JAEA)
132	X-Ray Magnetic Circular Dichroism of $SrRuO_3$(xML)/Nb:$SrTiO_3$ Thin Films	ISHIGAMI Keisuke	2010G187, 2011A3840(JAEA)	16A, BL23SU(JAEA)
133	Electronic Structure and Local Atomic Arrangement in 2-Dimensional Quasicrystals Al-Co-Ni	SODA Kazuo	2010G189	2C
134	Angle-Resolved Photoemission Study of Topological Insulator $Bi_{2-x}Sb_xTe_{3-y}Se_y$	ARAKANE Toshiyuki	2010G507	28A
135	Twin-to-Single Crystal Transformation in $La_{1-x}Sr_xCoO_3$ by Magnetic Fields	KYOMEN Toru	2010G544	3C
136	Electronic Structure of Delaffosite Oxides $CuCr_{1-x}Mg_xO_2$	YOKOBORI Takumi	2010G655, 2008G688	28A
137	Soft and Hard X-Ray Diffraction Studies of $DyMnO_3$ Thin Films	WADATI Hiroki	2010G678, 2011G062	3A
138	Electronic Structure of Anatase (TiO_2) by Means of X-Ray Raman Scattering	TEZUKA Yasuhisa	2010G697	7C, 15B1
139	Surface Electronic Structure and Selective Oxidation of Lithium Nickel Mixed Oxide（II）(Japanese)	MIYAZAKI Takafumi	2010G700	13A
140	Surface Electronic Structure and Selective Oxidation of Lithium Nickel Mixed Oxide (Japanese)	MIYAZAKI Takafumi	2010G700, 1105040PF(SAGA-LS)	BL10(SAGA-LS)
141	Thickness Dependent Metal-Insulator Transition in Ferromagnetic $La_{0.6}Sr_{0.4}MnO_3$ Thin Films Studied by X-Ray Magnetic Circular Dichroism	SHIBATA Goro	2010S2-001, 2010G187, 2011A3840(JAEA)	16A, BL23SU(JAEA)
142	Thickness Dependence of Electronic Band Structures of Ni Ultrathin Films on Cu(001)	KIM Sunghun	2011G084	18A, 19A
143	Giant Rashba Spin Splitting of Monolayer Pb Adsorbed Ge(111) Surface	YAJI Koichiro	2011G085	18A, 19A
144	Synchrotron Angle-Resolved Photoemission Spectroscopy Study of Iron-Based Superconductor $Ca(Fe_{1-x}Rh_x)_2As_2$ (Japanese)	TSUBOTA Koji	2011G086, 1105041PF(SAGA-LS)	BL10(SAGA-LS)
145	EXAFS Measurements Characterized Local Structure of Copper Complex Catalysts Encapsulated in Y-Zeolite Catalysts	INOUE Yoshiki	2011G111	7C
146	Electronic States of Infinite-Layer $Sr_{1-x}Eu_xFeO_{2-\delta}$ Thin Films Studied by X-Ray Photoemission and Absorption Spectroscopies	CHIKAMATSU Akira	2011G113, 2011S2-003	2C

147	ARPES Study of Rutile-Type Transition Metal Oxides (Japanese)	MURAOKA Yuji	2011G186, 1105044PF(SAGA-LS)	28A, BL10(SAGA-LS)
148	O 2p Partial Density of States and Local Structures in Oxide Glasses	HOSOKAWA Shinya	2011G520, 2009G605	2C
149	Substrate Dependence of Electronic Structure of $LaNiO_3$-Ultrathin Films (Japanese)	SAKAI Enju	2011S2-003	2C
150	Photoemission and X-Ray Absorption Spectroscopy Study of $Ba(Fe_{1-x}Mn_x)_2As_2$	SUZUKI Hakuto	2011S2-003, 2009S2-005	2C, 28A
151	X-Ray Absorption Spectra of Delaffosite Oxides $CuCr_{1-x}Mg_xO_2$	YOKOBORI Takumi	2011S2-003, 2011G061, 2010G655	2C

[Top]

Materials Science

Page	Title	First Author	Proposal No.	Beamline
152	Reconstruction of Calorimetric Curves from X-Ray Diffraction Data during the Melting-Recrystallization Process of Isotactic Poly(1-Butene) in Form III (Japanese)	TAKAHASHI Hiroshi	2004G265, 2005G301	9C
153	Micro-Structure Analysis of Heavy-Metal Ion Adsorbed PAAm Gels	YOSHIOKA Satoru	2008G191, 2007G053	10C
154	Resonant X-Ray Scattering Study of $Sr_{1/3}V_2O_5$ (Japanese)	OHWADA Kenji	2008G516	4C
155	Local Structure Analysis of Ga_2O_3 Polymorphs by XAFS	YOSHIOKA Satoru	2008G637	7C
156	Electronic Structure of the Cathode Material $Li_xFe_{0.5}Mn_{0.5}PO_4$ for Lithium-Ion Battery Analyzed by Resonant Photoemission Spectroscopy	HORIBA Koji	2008S2-003, 2011S2-003	2C
157	Magnetic-Field-Induced Transition in Mn_3O_4	NII Yoichi	2008S2-004	3A
158	Observation of Dilatant Fluid by X-Ray Talbot Interferometry with White Synchrotron Radiation (Japanese)	MOMOSE Atsushi	2009G031	14C1
159	Orientation of One-Dimensional Silicon Polymer Films Studied by Polarization-Dependent NEXAFS	Md. MANNAN Abdul	2009G553	27A
160	Free Volume in a Cold Worked $Zr_{55}Cu_{30}Ni_5Al_{10}$ Bulk Metallic Glass	HARUYAMA Osami	2009G575	7C
161	XAFS Studies for Al Dopants in Transparent Conductive ZnO Thin Films	OKUHARA Yoshiki	2009G619	11A, 7C, 9A
162	Coagulated Structure of NBR/SBR Blends by SAXS	JANG Junhyeok	2009G622	10C
163	Micro-Structural Analyses of UV-Irradiated AAm/SA Gels	YOSHIOKA Satoru	2009G651	10C
164	Nano-Structure Analysis of Poly(Acrylamide-Co-Maleic Acid) Gels by SAXS	YOSHIOKA Satoru	2009G651, 2011A1955(SPring-8)	10C, BL40B2(SPring-8)
165	B-Site Ordering State in Double-Perovskite La_2CrFeO_6 Films	OKUYAMA Daisuke	2009S2-003	3A
166	Molecular Displacement Directing Antiparallel to Macroscopic Polarization in TTF-CA	KOBAYASHI Kensuke	2009S2-003	8A
167	Investigation of Conditions and Materials for Emergence of Spin-State Polarons in Lightly Impurity Doped $LaCoO_3$ Systems (Japanese)	TOMIYASU Keisuke	2009S2-008	3A, 4C
168	The Structure-Magnetism Relationship in $LaCo_{1-x}Rh_xO_3$ (Japanese)	ASAI Shinichiro	2009S2-008	8A
169	Resonant Soft X-Ray Scattering Study of $[(LaMnO_3)_3/(SrMnO_3)_3]$ Thin Film (Japanese)	SUDAYAMA Takaaki	2009S2-008	16A
170	Multiferroicity in $NiBr_2$ with Long-Wavelength Cycloidal Spin Structure (Japanese)	OKUYAMA Daisuke	2009S2-008	3A
171	All-in-all-out Magnetic Order in the Insulating Phase of a Pyrochlore Iridate $Eu_2Ir_2O_7$	SAGAYAMA Hajime	2009S2-008	3A
172	Crystallization Behavior of Homopolymer/Block Chain Blends Confined in Nanocylinders with Different Diameters	NAKAGAWA Shintaro	2010G014	10C
173	Isothermal Crystallization of Double Crystalline Diblock Copolymers with Close Crystallizable Temperatures	LIANG Huang	2010G014	10C
174	Crystallization of Poly(ε-caprolactone) Blocks Confined in Crystallized Lamellar Morphology of Poly(ε-caprolactone)-*block*-Polyethylene Copolymers: Effects of Polyethylene Crystallinity and Confinement Size	SAKURAI Takuya	2010G014	10C
175	Photoluminescence Property of Magnetoplumbite-Type $LaAl_{12}O_{18}N:Eu^{2+}$ Phosphor and their XANES Spectra	MASUBUCHI Yuji	2010G024	9C
176	Observation of Rocking Curves from Polar Crystal for Phase Determination of Crystal Structure Factor	NEGISHI Riichirou	2010G026	15C
177	Edge-State in Nanographite, HNO_3-Doped Nanographite and its Residue Compounds	KIGUCHI Manabu	2010G036	7A
178	XAFS Analysis on the Supported Vanadium Carbide Catalysts	ICHIKUNI Nobuyuki	2010G064, CH-3497(ESRF)	7C, BM23(ESRF)
179	Depth-Resolved GISAXS of Block Copolymer Films on Si Substrates	OKUDA Hiroshi	2010G075	6A, 11B

180	XAFS Study on the Oxidation of Ni(0) Nanocluster into Ni(II) Nanocluster Catalyst	SAWADA Kazunari	2010G078	7C
181	Structure of Lyotropic Liquid Crystals of Amylose Alkylcarbamates in Ethyl Lactates (Japanese)	TERAO Ken	2010G080, 2011A1925(SPring-8)	10C, BL40B2(SPring-8)
182	Breaking Inversion Symmetry in $Pr_{0.5}Sr_{0.5}MnO_3$ Thin Film Detected by Resonant X-Ray Diffraction (Japanese)	YAMASAKI Yuichi	2010G086, 2011G597, 2009S2-008	4C
183	Nanocrystals and Small Clusters Investigated by Synchrotron Radiation and Microfluidics	OYANAGI Hiroyuki	2010G097	NW2A
184	EXAFS Investigation of Th(IV)-*N,N*-Di-Alkylamides Complexes	SUZUKI Shinichi	2010G143	27B
185	Crystallization Process of $SrZrO_3$ Thin Films by Pulsed Laser Deposition	SATA Noriko	2010G164	NW10A
186	Analysis of Dislocations in Single Crystalline Diamond by SR/X-Ray Topography (Japanese)	UMEZAWA Hitoshi	2010G168	15C
187	EXAFS Study on Phase Transition Phenomena of $BaTiO_3$ Using Ho as a Probe (Japanese)	MATSUSHIMA Yuta	2010G171	7C, 9A, 9C
188	Structure of Twisted Yarn of Carbon Nanotubes under Tensile Deformation	SHIOYA Masatoshi	2010G181	6A, 15A
189	XAFS Measurement of Am Oxides (Japanese)	NAKADA Masami	2010G196	27B
190	Thin Film Electrode of Prussian Blue Analogue for Li-Ion Battery	MORITOMO Yutaka	2010G502, 2011G501	7C,8A
191	Two-Electron Reaction in Nanoporous Cathode Material for Lithium Ion Secondary Battery	MATSUDA Tomoyuki	2010G502, 2011G501	7C, 8A
192	Third Polymorph of the $(BEDT\text{-}TTF)_2Ag(CF_3)_4(TCE)$ Organic Superconductor	KAWAMOTO Tadashi	2010G529	8A
193	Redox States of Shergottite Martian Meteorites as Inferred from Iron Micro-XANES Analysis of Maskelynite and Plagioclase	SATAKE Wataru	2010G534	4A
194	Observation of Strain Gradient of Weekly Bent Crystal using Mirage Fringes	JONGSUKSWAT Sukswat	2010G539	15C
195	In operando XAFS Studies of Polyoxometalate Molecular Cluster Batteries: Polyoxometalates as Electron Sponges	YOSHIKAWA Hirofumi	2010G557	NW10A
196	Lattice Distortions and Phase Transitions in Tl-Based Thermoelectric Materials	HOSOKAWA Shinya	2010G559	9C, NW10A
197	Synchrotron XRD Study of the $CuGaSe_2$ Thin Films Grown with Various Cu/III Ratio	ISLAM M. M.	2010G598	4C
198	Enhancement of Crystal Perfection for Tetragonal Hen-Egg White Lysozyme Crystals under Application of an External AC Electric Field	KOIZUMI Haruhiko	2010G605	15B1
199	Electronic Structure and Auto-Ionization Process of Ion-Electron Mixed-Conductor	YAMAGUCHI Shu	2010G613	19B
200	Photoreaction of TiO_2-Oraganic Hybrid Materials (Japanese)	SEGAWA Hiroyo	2010G614	7A, 9A, 12C
201	Structure Determination of Self-Assembled Monolayer on Oxide Surface by Soft-X-Ray Standing Wave	BABA Yuji	2010G635	27A
202	Local Structure Analysis of MgB_2 Thin Films by Polarized XAFS	SEO Mami	2010G646	11A
203	Surface Chemical States of $FeSi_2$ and Mg_2Si Crystals Studied by XPS and XAS	YAMAMOTO Hiroyuki	2010G658	27A
204	Strain Relaxation of GaAs Thin Layer Crystals Grown from Nano-Wires on Si Wafer (Japanese)	MIZUNO Kaoru	2010G672	15C
205	In Situ Evaluation of Ion-Beam Irradiation Induced Ferromagnetism at Ultra-Surface of FeRh Thin Films by XMCD	AIKOH Kazuma	2010G689	16A
206	Self-Assembled Structure and Sol-Gel Transition of Crystalline Organogels and Surfactant Organogels	TAKENO Hiroyuki	2010G699, 2010G134	10C, 15A
207	XAFS Studies of Metal Nanoparticles Prepared by Using Microwave Heating	HARADA Masafumi	2011G005	9C, NW10A
208	The Two-Dimensional Electronic Structures of Ultra-Thin Ti Oxide Films on Mo(100) (Japanese)	EDAMOTO Kazuyuki	2011G017	3B
209	Ferroelectic $KNbO_3$ in Orthorhombic Phase	SAKAKURA Terutoshi	2011G022	14A
210	Solvent Annealing Induced Highly Perpendicular Orientation of Cylindrical Microdomains in Block Copolymer Thin Film and Fabrication of Hexagonally Arrayed Nano-Channels	YAMAMOTO Katsuhiro	2011G029	6A, 9C, 15A
211	Transgranular Strain Distribution in Fe-Si Polycrystal Alloy with Plastic Deformation (Japanese)	SHOBU Takahisa	2011G064	4C
212	Dynamics of the Lamella-*Fddd* Transition in SI Diblock Copolymer Melts	CHIJIWA Takashi	2011G066	6A
213	XAFS Investigation of Chemical States and Formation Mechanism in Pt-Based Nano-Particle/Carbon Composites (Japanese)	NAKANISHI Makoto	2011G069	9A, NW10A

214	Analysis of Local Rocking Curves of Hen Egg-White Lysozyme Crystals by X-Ray Digital Topography with CCD Camera (Japanese)	FUJII Daiki	2011G073	15B1,15C
215	Study on Ion Beam Induced Non Thermal-Equilibrium Lattice Structures in FeRh Alloy by EXAFS Measurement	IWASE Akihiro	2011G103	27B
216	XANES Analysis of Layered Titanate Nanosheets with Lamellar Mesostructure	NAKAGAWA Keizo	2011G110	7C
217	XAFS Measurement of Sm-Doped TiO_2 Semiconductor Thin Films	HARAKO Susumu	2011G118	27B
218	SAXS and WAXS Studies on Guest Exchange Processes in Crystalline Complexes of Syndiotactic Polystyrene	KANEKO Fumitoshi	2011G123	6A, 9C
219	Photoresponse of Microphase Separation Structure for Liquid Crystalline Block Copolymers with Azobenzene Mesogens	TAKESHITA Hiroki	2011G130	6A
220	Temperature Variations of Lattice Constants for Trigonal Tellurium	IKEMOTO Hiroyuki	2011G140, 2011A1939(SPring-8)	BL19B2(SPring-8)
221	Study on the Crystal and Electronic Structures of the Layered Li_2MO_3-$LiMO_2$ Materials in Li De-Intercalation Process	KOBAYASHI Hironori	2011G151	7C
222	Evaluation of Phase Stresses and Phase Strains under Deformation in TRIP Steels (Japanese)	KIKUCHI Takuya	2011G157	6C
223	Widely-Dispersed Highly-Anisotropic Valence Band of Rubrene Single Crystals Observed by Photoelectron Spectroscopy (Japanese)	NAKAYAMA Yasuo	2011G161	13A, BL10(SAGA-LS)
224	Soft X-Ray ARPES of Superconducting Diamond Films with Systematically Controlled Carrier Concentration (Japanese)	MURAOKA Yuji	2011G162, 1105043PF(SAGA-LS)	2C, BL10(SAGA-LS)
225	XAFS Analysis of Ni-Zr Alloys after Thermal and Chemical Treatment	NOZAKI Ai	2011G182	7C
226	XAFS Analysis of Electro Luminescent Tb Doped Alumina Nanofiber Sol (Japanese)	BANDO Kyoko	2011G195	7C, 9C, 12C
227	Evolution of Threading Dislocation during SiC Solution Growth (Japanese)	HARADA Shunta	2011G247, 2011A1950(SPring-8)	15C, BL19B2(SPring-8)
228	Synthesis and Structural Analysis of Metal Particles in Ionic Liquids	HARADA Masafumi	2011G508	6A, 15A
229	Coordination Structures of Transition-Metal Ions in Ionic Liquids	IIDA Masayasu	2011G510	9C
230	Three-Dimensional Atomic Images of GeSbTe Phase-Change Materials	HOSOKAWA Shinya	2011G530	6C,15B
231	Middle Range Local Structure Analysis of Semiconductor $ZnSnAs_2$ Thin Film by X-Ray Fluorescence Holography	SUZUKI Akiko	2011G530, 2011G601	6C, 15B
232	NEXAFS Investigation of Order in Vertically Aligned Carbon Nanotubes Formed by Surface Decomposition of SiC	MARUYAMA Takahiro	2011G539	7A
233	*In Situ* NEXAFS Study on Carbon Nanotube Formation Process by Surface Decomposition of SiC	MARUYAMA Takahiro	2011G539	7A
234	Improvement of Physicochemical Character for Acyclovir by Co-Crystallization with Additives (Japanese)	YONEMOCHI Etsuo	2011G544	4B2
235	Postperovskite Transition in $NaCoF_3$ at Room Temperature under High Pressure (Japanese)	YUSA Hitoshi	2011G545	NE1A
236	Space Group Determination of the Magnetically Induced Ferroelectric Phase of Multiferroic YMn_2O_5	SAKAKURA Terutoshi	2011G549	14A
237	X-Ray Diffraction Study of CeT_2Al_{10} (T=Fe, Ru, Os) at High Pressures	KAWAMURA Yukihiro	2011G555	18C
238	Lamellar-to-Onion and Onion-to-Lamellar Transition Processes with Varying Temperature under Shear Flow in a Nonionic Surfactant/Water System	SATO Daijiro	2011G589	6A
239	X-Ray Photo-Induced Phase Transition in Fe-Doped Layered Manganite (Japanese)	YAMAKI Yuki	2011G610, 2010PF-17, 2010PF-31	3A
240	SAXS Studies on Deformation of the BCC Lattice for Spherical Microdomains Formed in an Elastomeric Block Copolymer Film along Several Cycles of Uniaxial Stretching (Loading and Unloading)	UOZUMI Madoka	2011G612	9C, 10C
241	Spontaneous Orientation of Crystalline Lamellae upon the Directional Crystallization of Poly(Ethyleneglycol) under a Temperature Gradient (Japanese)	KIMURA Go	2011G613	6A, 9C
242	Local Structure in Fast-Ionic Conductive AgI-As_2Te_3 Glasses	USUKI Takeshi	2011G617	NW10A
243	Swift Heavy Ion Irradiation Effect on Structural Properties for Epitaxial $Ba(Fe_{0.5}Mn_{0.5})O_{3-\delta}$ Thin Films	MATSUI Toshiyuki	2011G638	27A
244	Development of Pressure-Cell for Structure Analysis of Organic Compounds (Japanese)	KOBAYASHI Kensuke	2011G643, 2011PF-12	8A, 8B

245	Magnetic and Electronic Structures of Fe and Mn Co-Doped SnO_2	OKABAYASHI Jun	2011G657	7A
246	Local Structure Analysis on Functional Element Doped Hydroxyapatite for Use as a Drug Delivery System and Imaging Beads Materials	SATO Mitsutaka	2011G659	9A
247	X-Ray Absorption Study of $LaCo_{1-x}Rh_xO_3$ (Japanese)	SUDAYAMA Takaaki	2011G690, 2009S2-008	11B, 16A
248	Direct Evidence for Orientations in the Amorphous Functional Polymer Thin Films Deposited on Si Surface	ASAKURA Kiyotaka	2011P102	7A
249	Small Angle Resonant Soft X-Ray Magnetic Scattering in (Fe, Co)Si (Japanese)	YAMASAKI Yuichi	2011PF-02, 2011G597, 2009S2-008	11A, 16A
250	The Optimized Investigating Condition for Precise X-Ray Powder Diffraction Analysis in Functional Perovskite Ceramics (Japanese)	KAGOMIYA Isao	2011PF-17	4B2
251	High-Resolution Soft-X-Ray Photoemission Study on $SrTi_{0.99}Sc_{0.01}O_3$ Thin Film	OKUMURA Teppei	2011S2-003	2C
252	Shear-Induced Structural Transition of Triblock Copolymer Lamellar Phase (Japanese)	FUJII Shuji	2012G005	10C
253	Local Structure Analysis of $Fe_{83.3}Si_4B_8P_4Cu_{0.7}$ Alloy Studies by XAFS	OONO Akimi	2012G080	12C, 11B
254	Evaluation of Anti-Site Defects in Epitaxial Films of $CoFe_2O_4$ (Japanese)	YANAGIHARA Hideto	2012G128	4C
255	Ga^+-Induced Changes in Magnetic Anisotropy of Pt/Co/Pt Thin Films Studied by X-Ray Magnetic Circular Dichroism	AMEMIYA Kenta	2010S2-001	16A

[Top]

Crystallography

Page	Title	First Author	Proposal No.	Beamline
256	Crystal Structure Analysis of $Li_2MP_2O_7$ (M = Mn, Fe)	NISHIMURA Shinichi	2009G092, 2011G683	4B2
257	Crystal Structure of the C-Terminal Globular Domain of Oligosaccharyltransferase from *Archaeoglobus fulgidus*	MATSUMOTO Shunsuke	2009G208, 2011G020, 2011A1904(SPring-8)	5A, 17A, NW12A, NE3A, BL26B2(SPring-8)
258	Structural Approach to Inhibitor Design for African Trypanosome Glycerol Kinase	OLUWADARE Emmanuel Balogun	2009G524	1A, 5A, 17A, NW12A
259	A Superposed Kagome-Lattice Crystallization of a Keplerate-Type Polyoxometalate	SAITO Masaki	2009G636	NW2A
260	The Relation between Crystal Parameters and Tc in Iron Pnictide Superconductors (Japanese)	TAKEMORI Akira	2009S2-008	8A
261	The Effects of Pressure on Crystal Structure of δ-AlOOH up to 9.0 GPa	KURIBAYASHI Takahiro	2010G015	10A
262	The Structural Flexibility of the Shank1 PDZ Domain is Important for Its Binding to Different Ligands	EOM Hyun Soo	2010G062	NW12A
263	Crystallographic Studies of Extraterrestrial Materials (Japanese)	HAGIYA Kenji	2010G142	4B1
264	Crystal Structure and Electron Density Distributions of Hydroxyapatite and Carbonated Hydroxyapatite (Japanese)	KUBO Naoyuki	2010G144	4B2
265	Effect of SiO_2 Content and Local Structure Analysis of $CoMn_2O_4$ Nanoparticles (Japanese)	MIYASAKA Toshiki	2010G173	9C
266	A Look inside Epitaxial Cobalt Nanoparticles with a 3D Reciprocal Space Imaging	SUTURIN M. Sergey	2010G190	3A
267	Local Structure of Ti in Tektite by XAFS Spectroscopy	WANG Ling	2010G512	9A
268	Using InCl Vapor to Ion Exchange Indium into Zeolite Na-X. Single Crystal Structure of $\|In_{33}Na_{50}\|[Si_{100}Al_{92}O_{384}]$-FAU Containing In^+ and In_5^{7+}	SEN Dipak	2010G566	17A
269	EXAFS Analysis of Pt Doped SnO_2 Catalyst for Micro Gas Sensor	MURATA Naoyoshi	2010G592	12C, NW10A
270	Effective Potential for Ca-O Bonds in CaGeO3 Perovskite	YOSHIASA Akira	2010G608	10A
271	Association of a Novel Domain in the Active Site of the Archaic Hyperthermophilic Maltogenic Amylase from Staphylothermus Marinus	JUNG Tae-Yang	2010G711	17A, NW12A
272	Crystallographic Analysis of BphA4 Mutant	SENDA Miki	2011A1877(SPring-8), 2009G592	BL32XU(SPring-8)
273	Crystal Structure Analysis of $YBaCo_4O_7$-Based Materials at High Temperatures (Japanese)	HARATAKE Daiki	2011G185	4B2
274	Crystal Structure Analysis of $CaLnAlO_4$ (Ln = Rare Earth) by Synchrotron X-Ray Diffraction (Japanese)	OMOTO Kazuki	2011G185	4B2
275	Structure of TiO_2 Rutile Synthesized under Strong Gravity Field	YOSHIASA Akira	2011G528	10A
276	Local Structure of Ca in Natural Glasses and Tektite	TOBASE Tsubasa	2011G611	7C

277	Three-Dimensional Reconstruction of Defect Images Using Limited Projection Topographs (Japanese)	MIZUNO Kaoru	2011G675	15B
278	X-Ray Diffraction Analysis of Hayabusa-Returned Samples	NAKAMURA Tomoki	2011G691, 2011A1942(SPring-8)	3A, BL39XU(SPring-8)

[Top]

High Pressure Science

Page	Title	First Author	Proposal No.	Beamline
279	High-Pressure Reaction between Au and Na (Japanese)	TAKEMURA Kenichi	2008G534	13A, NE1A
280	High-Pressure X-Ray Diffraction Study of Mg_2Si Thermoelectric Material (Japanese)	MORI Yoshihisa	2009G070	NE1A
281	Structural Phase Transition in $CaGeO_3$	ONO Shigeaki	2009G507	NE7A
282	Anisotropic Strain Effects on $LaMnO_{3+\delta}$ Nanoparticles Embedded in Mesoporous Silica	TAJIRI Takayuki	2009G529, 2011G511	8B
283	In-Situ Synchrotron X-Ray Powder Diffraction of Antigorite at High Pressure and Temperature	WATANABE Tohru	2009G541	NE5C
284	Formation of The Perovskite Solid Solution in the System of $CaSiO_3$-$MnSiO_3$ at High Pressure and High Temperature	LI Lin	2010G060	NE1A
285	Influence of Water on Olivine Rheology under High-Pressure (Japanese)	OHUCHI Tomohiro	2010G136	NE7A
286	Reaction of Xenon with Metals and Silicates under High Pressure and Temperature (Japanese)	YAGI Takehiko	2010G141	NE1A
287	Viscosity of CO_2-Bearing Silicate Melts at High Pressure	SUZUKI Akio	2010G182	NE7A
288	A Stabilizing Mechanism of Carbon Dioxide Hydrate under Low-Temperature and High-Pressure	HIRAI Hisako	2010G508	18C
289	Pressure-Induced Phase Transitions of Complex-Hydride $LiNH_2$ (Japanese)	YAMAWAKI Hiroshi	2010G516	18C
290	High-Pressure/Low-Temperature X-Ray Diffraction Experiment for $Ba_{24}Ge_{100}$ under Quasi-Hydrostatic Pressure Condition (Japanese)	NAKANO Satoshi	2010G519, 2011A1943(SPring-8)	18C, BL10XU(SPring-8)
291	Pressure-Induced Changes in Hydrogen Bonds in Hydrous Materials	KAGI Hiroyuki	2010G609	18C
292	Crystal Structure of $FeSe_{1-x}S_x$ at Low Temperature under Pressure (Japanese)	TOMITA Takahiro	2010G620	18C
293	High-Temperature and High-Pressure X-Ray Diffraction Study of Ag-Doped Mg_2Si Thermoelectric Material (Japanese)	MORI Yoshihisa	2010G668	NE5C
294	High-Pressure Synthesis and Phase Transformation of $LiNbO_3$-Type Oxides	TANAKA Kei	2010P102, 2011G681	NE5C, 18C
295	Structure of Hydrous and Anhydrous $KAlSi_3O_8$ Melts under Pressures (Japanese)	YAMADA Akihiro	2011G065	5C, 7A
296	New Silicide Search at High Pressures and High Temperatures (Japanese)	IMAI Motoharu	2011G094	NE5C
297	PVT Data Collection for EoS Analyses of Antigorite and Phase A under High Pressure and High Temperature	INOUE Toru	2011G100	NE5C
298	High-Temperature and High-Pressure Phase Diagram of $RhSb_3$	MATSUI Kazuki	2011G139, 2011G095	NE5C, 18C
299	Structural Analysis of Zinc Orthophosphate under High Pressure by Synchrotron X-Ray Diffraction (Japanese)	HIRAYAMA Tomoko	2011G244	18C
300	Structural Analysis of Diamond-Like Carbon under High Pressure and High Temperature by Synchrotron X-Ray Diffraction (Japanese)	HIRAYAMA Tomoko	2011G245	NE5C
301	Synthesis and Phase-Boundary of a New Carbon-Nitride-Related Material (Japanese)	SOUGAWA Masaya	2011G580	NE1A
302	Pressure Induced Phase Transition of Type I and VIII Si Clathrates (Japanese)	KUME Tetsuji	2011G620	18C
303	Compressional Behavior of Hydrous SiO_2 Glass	URAKAWA Satoru	2011G652	NE5C

[Top]

Biological Science

Page	Title	First Author	Proposal No.	Beamline
304	Contribution of Asparagine Residues to the Stabilization of an Antigen-Antibody Complex, HyHEL-10-Hen Egg White Lysozyme	YOKOTA Akiko	2000G139	6A
305	Investigation of the Reaction Mechanism of Orotidine-5'-Monophosphate Decarboxylase	FUJIHASHI Masahiro	2006G164	5A, 17A, NW12A
306	Structural and Mutational Analyses of *Bacillus megaterium* Glucose 1-Dehydrogenase IV	NISHIOKA Taiki	2006G165, 2011G129	5A, NW12A, NE3A

307	Crystal Structures of the Inhibitor-Bound Quaternary Complexes of 1-Deoxy-D-Xylulose 5-Phosphate Reductoisomerase from *Plasmodium falciparum*	UMEDA Tomonobu	2007G025	17A, NW12A
308	Structural and Functional Studies of Assimilatory Nitrite Reductase	NAKANO Shougo	2007G080, 2009G100	17A, NW12A, NE3A
309	High Resolution X-Ray Structure Analysis of HIV-1 Protease in Complex with Potent Inhibitors	ADACHI Motoyasu	2007G212, 2008G524	5A, NW12A, NE3A
310	Crystal Structure of Actin Specific ADP-Ribosyltransferase Ia with β TAD and Actin	TSUGE Hideaki	2008G030, 2006G132	NW12A, 5A
311	Structure Determination of Enzymes Involved in the New Carbon Dioxide Fixation System	NAKAMURA Akira	2008G149	5A, 17A, NW12A
312	Distribution of the αC Region of Fibrinogen Molecule	KUBOTA Kenji	2008G520	10C
313	Structural Insights into the Peroxidase Activity and Inactivation of Human Peroxiredoxin 4	WANG Xi	2008G555	17A
314	Structural Insights into the Substrate Specificity of Human Granzyme H – the Functional Roles of a Novel RKR Motif	WANG Li	2008G555, 2008G556	6A, 17A, NE3A
315	Structural Mechanism of Juvenile Hormone Delivery in Silkworm (Japanese)	SUZUKI Rintaro	2008G581	17A, NE3A
316	Unexpected Substrate Recognition and Catalytic Reaction Mechanisms (Japanese)	ARIMORI Takao	2008G628	17A
317	Crystal Structure of Arl1 in Complex with Arfaptin-2 BAR Domain	NAKAMURA Kensuke	2008G690, 2009G637, 2008S2-001	5A, NW12A, BL41XU(SPring-8)
318	Crystal Structure Analysis of the Receptor Binding Domain of Botulinum D/C Mosaic Neurotoxin	TANAKA Yoshikazu	2009G032	5A
319	Structure Analyses of a Transcription Factor Involved in Fatty Acid Degradation (Japanese)	FUJIHASHI Masahiro	2009G186	5A
320	Binding and Selectivity of the Marine Toxin Neodysiherbaine A, and its Synthetic Analogues, to GluK1 and GluK2 Kainate Receptors	UNNO Masaki	2009G501	17A, 5A, NE3A, NW12A
321	X-Ray Structure of L-Ribose Isomerase from *Acinetobacter* sp.	YOSHIDA Hiromi	2009G512, 2011G504, 2011A1873(SPring-8)	5A, 17A, NW12A, NE3A, BL26B1(SPring-8)
322	Crystal Structures of *Burkholderia Thailandensis* Nucleoside Kinase: Insights into Catalytic Mechanism and Nucleoside Selectivity	YASUTAKE Yoshiaki	2009G517	5A, NW12A, NE3A
323	Quantitative Analysis of Lattice Like Structure of Smooth Muscles (Japanese)	WATANABE Masaru	2009G561, 2011A1920(SPring-8)	15A, BL45XU(SPring-8)
324	Sensing actin Dynamics: Structural Basis for G-Actin-Sensitive Nuclear Import of MAL	HIRANO Hidemi	2009G577, 2011A1875(SPring-8)	5A, 17A, BL41XU(SPring-8)
325	Structural Studies of Human Nuclear Receptor and their Ligand (Japanese)	TSUJI Eiichi	2009I010	NE3A
326	Crystal Structure of a Cellobiohydrolase, CcCel6A, from *Coprinopsis Cinerea* (Japanese)	TONOZUKA Takashi	2010G001	NW12A
327	The Structural Change in a Cellobiohydrolase, CcCel6C, from *Coprinopsis cinerea* (Japanese)	TONOZUKA Takashi	2010G001, 2011A1881(SPring-8)	NE3A, BL26B2 (SPring-8)
328	Structural Determination of GST of the Silkworm, *Bombyx mori*	YAMAMOTO Kohji	2010G085	5A, 13B1&13C1(NSRRC), BL44XU(SPring-8)
329	Specificity and Efficiency in Activity of Anti-HIV Actinohivin for Sugar Binding	TSUNODA Masaru	2010G088	5A, NW12A
330	Crystallography of Multi-Component Oxidoreductases from Archaea (Japanese)	FUSHINOBU Shinya	2010G107, 2011A1891	1A, 5A, 17A, NE3A, NW12A
331	Crystallographic Analysis of Prokaryotic V-Type ATPase	NUMOTO Nobutaka	2010G125	NE3A
332	Crystal Structure of Atg7 in Complex with Atg8	HONG Beom Seung	2010G518	NW12
333	Preliminary Crystallographic Analysis of Ser147Gln Mutant of Rv2613c Protein from *Mycobacterium tuberculosis* H37Rv (Japanese)	MORI Shigetarou	2010G520	NW12A
334	Structural Elucidation for the Metal Storage Function of *Helicobacter pylori* Neutrophil-Activating Protein	YOKOYAMA Hideshi	2010G530, 2008G587, 2007G052, 2011A1893(SPring-8)	5A, 6A, NW12A, NE3A, BL26B1(SPring-8)
335	Artificial Oxidation Treatment Induces Ca Accumulation in the Peripheral Part of Human Hair as Determined by X-Ray Imaging	ITO Atsushi	2010G542	11B, 4A
336	High-Pressure-Induced Water Penetration into IPMDH and Pressure Adaptation of Proteins of Deep-Sea Bacteria	NAGAE Takayuki	2010G543, 2011A1894	NW12A, BL41XU
337	Crimean Congo Hemorrhagic Fever Virus Nucleoprotein Reveals Endonuclease Activity in Bunyaviruses	YU Guo	2010G576	17A
338	X-Ray Structure of Hemagglutinin Subcomponent HA70 from *Clostridium botulinum* in Complexes with Sialylated Oligosaccharides	YAMASHITA Satoshi	2010G582, 2011A1873(SPring-8)	5A, 17A, NW12A, NE3A, BL26B1(SPring-8)
339	Crystal Structures of the Bacterial A1408G-Mutant A Site with and without Geneticin (Japanese)	KONDO Jiro	2010G585	NW12A, 5A, 17A

340	Structural Studies on Carbonyl Sulfide Hydrolase from *Thiobacillus thioparus* THI115 (Japanese)	NOGUCHI Keiichi	2010G597	5A, 6A, NW12A
341	Induction of Migration on Glioma Cells by Bystander Effect of Cells Exposed to X-Ray Microbeams (Japanese)	MAEZAWA Hiroshi	2010G602	27B
342	Crystal Structure Analysis of Mouse SMP30	HARADA Ayaka	2010G616	17A
343	Time Course of the Ordered Phase Formation in Lipid Bilayers Caused by Sphingomyelin Hydrolysis	KINOSHITA Masanao	2010G641	6A
344	Structural Basis of the Catalytic Cycle of Rieske Nonheme Iron Oxygenases (Japanese)	ASHIKAWA Yuji	2010G662	1A, 5A, NW12A
345	X-Ray Crystallographic Analysis of Inhibitor-Free Structure of L-(2*S*,3*S*)-Butanediol Dehydrogenase	SHIMEGI Tomohito	2010G698	NW12A
346	New Insight into the Substrate Binding of Dye-Linked L-Proline Dehydrogenase	SAKURABA Haruhiko	2011G002, 2011G502, 2011A1902(SPring-8)	5A, NW12A, BL26B1(SPring-8)
347	Structural Study of an Enzyme Catalyzing L-Glucose (Japanese)	FUKANO Kazuhiro	2011G023	1A, 5A, 17A, NW12A
348	The Structural Basis for the 2D Assembly of a β -Neurexin 1/Neuroligin 1 Complex	TANAKA Hiroki	2011G028	17A
349	Conformation of YB-1 Protein at Moderate and High Ionic Strength Studied by SAXS Technique	ALEXANDER Timchenko	2011G055	6A
350	Structure of Free $tRNA^{Gly}$(CCC) from *Pyrococcus horikoshii*	MIYAMOTO Yukari	2011G075	6A
351	Crystallography of Beta-Glucosidses Suitable for Biomass Degradation (Japanese)	FUSHINOBU Shinya	2011G080, 2011A1908	1A, 5A, 17A, NE3A, NW12A
352	Crystal Structure of Swi5-Sfr1C Complex from Fission Yeast	KUWABARA Naoyuki	2011G087	17A, NW12A
353	Crystal Structure of the GAPDH-CP12 Complex from Synechococcus elongatus (Japanese)	MATSUMURA Hiroyoshi	2011G097	1A, 17A
354	Structural Analysis of Temperature Stabilization Mechanisms using BPTI Variants	ISLAM Monirul Mohammad	2011G108	1A, 5A, 17A
355	Structural Analysis of Mammalian Xanthine Oxidoreductase (Japanese)	OKAMOTO Ken	2011G112, 2011G122, 2011G1561	5A, 17A, NW12A, NE3A
356	Local Structure of Random-Coiled Poly(*L*-Glutamic Acid) (Japanese) in Added Salt Solutions	SHIMIZU Shigeru	2011G114	10C
357	Crystal Structures of the A Variant of Human α_1-Acid Glycoprotein and Drug (Japanese)	NAKAMURA Teruya	2011G115	5A, 17A, NW12A, NE3A
358	Small-Angle X-Ray Scattering of Curdlan Gels Prepared by Diffusion Method (Japanese)	MAKI Yasuyuki	2011G118	6A
359	Crystal Structures of Beta-Glucan Recognition Protein from *Plodia interpunctella*	KANAGAWA Mayumi	2011G124, 2011G125	5A, NW12A, NE3A
360	Complex Formation by the 20S Proteasome and its Activators in an Aqueous Solution	SUGIYAMA Masaaki	2011G136, 2011A1928(SPring-8)	10C, BL45XU(SPring-8)
361	Oxidation States Change of Ce in the Mixtures of Manganese Oxides and *Pseudomonas fluorescens*	OHNUKI Toshihiko	2011G143, 2009G077, 優先枠(SSRF)	9A, 12C, 27B, BL-14W1, BL-15U(SSRF)
362	Elucidation of the Oligomerization of Leukocidin in the Presence of the MPD (Japanese)	GODA Shuichiro	2011G145	10C
363	Crystallographic Study of Innate Immune Receptor RP105/MD-1	OHTO Umeharu	2011G148	5A, NW12A, NE3A
364	Structural Analysis of a FMN-Binding Protein Homolog from Lactic Acid Bacteria (Japanese)	TAKAGI Rikako	2011G155	17A
365	Structural Study of hNck2 SH3 Domain Protein by X-Ray Solution Scattering III. Structure of hNck2 SH3 Domain at pH 2	MATSUMURA Yoshitaka	2011G188	15A
366	Structural Study of hNck2 SH3 Domain Protein by X-Ray Solution Scattering IV. Structural Analysis of hNck2 SH3 Domain at pH 2 and pH 6: Non-Native α-Helix-Rich Monomer and Native Dimer	SHINJO Masaji	2011G188	6A
367	Structural Study of hNck2 SH3 Domain Protein by X-Ray Solution Scattering II. pH-Dependent Structural Change	MATSUMURA Yoshitaka	2011G188	15A
368	Structural Study of hNck2 SH3 Domain Protein by X-Ray Solution Scattering I. Concentration Dependence at pH 6	MATSUMURA Yoshitaka	2011G188	15A
369	Crystal Structure Analysis of Bacilysin Biosynthesis Enzymes (Japanese)	TSUDA Takeo	2011G193	5A, 17A, NE3A, NW12A
370	Crystal Structures of MNV-1 RdRp-Complexes	ALAM Intekhab	2011G234, 2011G542	17A
371	Structure of mAG, a Monomeric Mutant of the Green Fluorescent Protein Azami-Green, Reveals the Structural Basis of its Stable Green Emission (Japanese)	NAGATA Koji	2011G248, 2011A1917(SPring-8)	5A, BL26B1(SPring-8)
372	Crystal Structure of UDP-Galactose 4-Epimerase-Like L-Threonine Dehydrogenase	YONEDA Kazunari	2011G502, 2011G002	5A, 17A, NW12A, NE3A
373	Refined Crystal Structures of Human Ca^{2+}/Zn^{2+}- Binding S100A3 Protein Characterized by Two Disulphide Bridges	UNNO Masaki	2011G518	NE3A, NW12A
374	Crystal Structures of Enzymes and Transporters Involved in Amino Acid Metabolism	TOMITA Takeo	2011G524	NW12, NE3A, 5A

375	Crystal Structures of the Enzymes Involved in Novel Lysine Biosynthetic Pathway using Amino Acid Carrier Protein	TOMITA Takeo	2011G525	NW12, NE3A, 5A
376	Structural Study of an Enzyme of Menaquinone Synthesis in Bacteria (Japanese)	FUKUOKA Daisuke	2011G529	1A, 5A, 17A, NW12A
377	Chromosomal Aberrations via Bystander Effect in Normal Human Fibroblasts Irradiated with Monochromatic X-Ray Microbeams	SUZUKI Masao	2011G572	27B
378	X-Ray Crystallographic Analysis of the (Runx1-CBFβ)$_2$-Ets1-DNA Complex Assembled on the Enhancer of T Cell Receptor α Chain Gene	SHIINA Masaaki	2011G600	1A, 5A, 17A
379	Effects of Sarcomere Length on the Intrinsic Distribution of Myosin Headsaround the Shaft of Thick Filament (Japanese)	TAKEMORI Shigeru	2011G602	6A
380	Colloidal Crystallization, Crystallization and Structure Analysis of Highly Concentrated Lysozyme Molecules in Very Dilute Electrolyte Solution (Japanese)	SUZUKI Yoshihisa	2011G606	5A
381	Open-Close Dynamics of Single Protein Molecule Observed by Diffracted X-Ray Tracking Synchronized with Pulse Laser	CHIYANAGI Kouhei	2011G608	NW14A
382	The Sructural Fluctuation of the Calmodulin Evaluated by Small-Angle X-Ray Scattering	SUGIMOTO Yasunobu	2011G668	6A, 15A
383	Preliminary X-Ray Crystallization of Psychrophilic Mutant of Uricase (Japanese)	HIBI Takao	2011G674, 2011A1882(SPring-8)	BL26B1(SPring-8)
384	Crystal Structure of the Superfamily 1 Helicase from *Tomato Mosaic Virus* (Japanese)	KATOH Etsuko	2011P005, 2011A2031(SPring-8)	17A, 5A, BL44XU(SPring-8)
385	Mechanism of Diterpene Cyclization in Cyclooctatine Biosynthesis	TOMITA Takeo	2012G019	NW12A, NE3A, 5A

[Top]

Medical Applications

Page	Title	First Author	Proposal No.	Beamline
386	Examination of the Specific Spatial Frequency of an Analog Image System for Diagnosis by Monochromatic X-Ray	KIMURA Chisato	2009P104	14C
387	XAFS Analysis of Co Contained in the Surrounding Tissues and Synovial Fluid of the Artificial Hip Joint (Japanese)	UO Motohiro	2010G022	9A , 12C
388	Preliminary Experimental Results with Transmission CT Imaging System for Fluorescent X-Ray CT	TAKEDA Toru	2010G055	NE7A
389	Quantitative Investigation on Density Resolution in X-Ray DEI (Japanese)	OKAMOTO Hiroyuki	2010G140	14B
390	Visualization of Renal Collecting Duct Using Synchrotron Radiation Micro-Angiography with Highly Sensitive Receiver	MATSUSHITA Shonosuke	2010G684	NE7A, 14C
391	Measurement of Pulmonary Arterial Flow Velocity in High Flow Pulmonary Hypertension Rat Model Using Synchrotron Radiation Pulmonary Micro-Angiography	TOKUNAGA Chiho	2010G695	NE7A
392	Preliminary Experiments on Characterization of an Image-Detector using Phantoms (Japanese)	MORI Koichi	2011R-27	14C1

[Top]

Applied Science

Page	Title	First Author	Proposal No.	Beamline
393	XAFS Analysis of Mn-Rich Layers in Fluvial Deposits in Active Volcano Area (Japanese)	KATSUTA Nagayoshi	2008G177	12C
394	Solution of the Destruction Mechanism using Imaging of the Defect or the Defective Part of the Construction Materials (Japanese)	HITOMI Takashi	2009I004	14B
395	XAFS Investigation for Structure Change of Ferrihydrite during As(V) Co-Precipitation Treatment in Wastewater (Japanese)	TOKORO Chiharu	2010G054	12C, 9A
396	Residual Order in the Thermally Oxidized Thin Film on Ge Substrates (Japanese)	SHIMURA Takayoshi	2010G070	4C
397	Analysis of Lattice Distortion in Multicrystalline Silicon for Photovoltaic Cells by Synchrotron X-Ray Diffraction	SHIMURA Takayoshi	2010G070	15C
398	Mesurement of Photolectron Emission Current from Satellite Surface Materials (Japanese)	NITTA Kumi	2010G093	20A
399	Investigation of Fixed-Sample Preparation Method for EUV Imaging of Bio-Cells (Japanese)	EJIMA Takeo	2010G522	11D
400	XAFS Analysis of Arsenic in Lake Baikal Sediment (Japanese)	MURAKAMI Takuma	2010G604	9A
401	Particle Statistics in Rotating-Specimen Powder Diffractometry	IDA Takashi	2011G015	4B2
402	Organochlorines in Surface Soil at Wire Burning and Metal Contribution by Means of Quantitative X-Ray Speciation	FUJIMORI Takashi	2011G174	11B

[Top]

Instrumentation and Technique

[Top]

20A/2010G083

Probing dissociative superexcited states of molecules by a detection of metastable atomic hydrogen in the 2s state

Takeshi Odagiri[1*†], Yoshiaki Kumagai[1], Takehiko Tanabe[1‡], Motoyoshi Nakano[1], Isao H Suzuki[2,3], and Noriyuki Kouchi[1]
[1] Department of Chemistry, Tokyo Inst. Tech., Meguro-ku, Tokyo 152-8551, Japan
[2] National Institute of Advanced Industrial Science and Technology, Tsukuba 305-8568, Japan
[3] Photon Factory, Tsukuba 305-0801, Japan

1 Introduction

Doubly excited states of molecules are short-lived resonance states and often play an important role as intermediates in a wide range of reactions such as dissociative recombination, associative ionization, Penning ionization, and so forth. The formation and decay of them provide a unified view for understanding the various dynamic processes [1].

Such doubly excited states embedded in the electronic continua are well observed in cross sections free from ionization such as dissociation cross sections. Recently, we have developed a new method for measuring the cross sections for production of metastable atomic hydrogen in the 2s state, the H(2s) atom, formed in photoexcitation of a hydrogen containing molecule [2, 3]. In the present study, the method was applied to CH_4 and NH_3 for identifying the dissociative doubly excited states leading to the formation of the metastable atomic hydrogen.

2 Experiment

The measurements were carried out at BL-20A. The metastable hydrogen atom in the 2s state was detected by the combination of a localized electric field created by a stack of parallel plate electrodes and a detector of photons that is composed of a microchannel plate (MCP) coated with CsI and an MgF_2 window in front of it. The 2s state of atomic hydrogen mixes with the 2p state by the Stark effect due to the electric field and the atom decays to the ground state by emitting a Lyman-α photon, which was detected by the photon detector. Other details of the experiment were described elsewhere [2, 3].

3 Results and Discussion

Figure 1 shows the cross sections for the production of the H(2s) atom from photoexcited CH_4 (a) and NH_3 (b) as a function of the incident photon energy. By a fitting based on a semi-classical analysis, superexcited states of CH_4 and NH_3 were found in the cross sections as shown by the dotted curves in the figure. Among them, the three peaks at 29.7, 35.0 and 39.3eV in figure 1 (a) and the peak at 31.6eV in figure 1 (b) were attributed to the doubly excited states. The doubly excited states of CH_4 seem to be the same that were observed in the cross sections to form H(2p) atoms in the photoexcitation of CH_4 [4] .

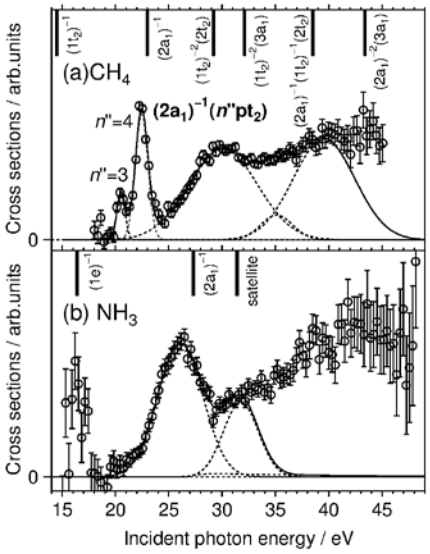

Figure 1. Cross sections for the production of the metastable hydrogen atom in the 2s state for (a) CH_4 and (b) NH_3 as a function of the incident photon energy. The vertical ionization potentials of CH_4 [5] and NH_3 [6] are displayed by thick vertical bars. The curves show the results of the fits by the semiclassical analysis.

References

[1] Nakamura H, *Int. Rev. Phys. Chem.* **10** 123–88 (1991)
[2] Odagiri T *et al*., *Rev. Sci. Instrum.* **81** 603108 (2010)
[3] Odagiri T *et al*., *Phys. Rev.* A **84** 053401 (2011)
[4] Fukuzawa H *et al., J. Phys.* B **38** 565 (2005)
[5] Potts A W *et al*., *Proc. R. Soc. Lond.* A **326** 165 (1972)
[6] Piancastelli M N *et al., J. Chem. Phys.* **87** 1982 (1987); Banna M S *et al., J. Chem.* 1 *Phys.* **63** 4759 (1975)

* E-mail address: odagiri.t@sophia.ac.jp
† Present address: Department of Materials and Life Sciences, Sophia University
‡ Present address: National Metrology Institute of Japan, AIST

7A/2010G541

Charge state distribution of ions resulting from the decay of the 2p→3d photoexcited states of atomic Fe

Ken KAWAJIRI[1], Norihiro SUZUKI[1], Galif KUTLUK[2], Tetsuo NAGATA[3], Yoshiro AZUMA[1] and Fumihiro KOIKE[4]

[1]Dept. of Materials and Life Sciences, Sophia Univ., Chiyoda-ku, Tokyo 102-8554, Japan
[2]Hiroshima Synchrotron Radiation Center, Hiroshima Univ., Hiroshima 739-0046, Japan
[3]Dept. of Physics, Tokyo Metropolitan University, Hachioji-shi, Tokyo 192-0397, Japan
[4]Dept. of Medicine, Kitasato Univ., Sagamihara-shi, Kanagawa 228-8555, Japan

1. Introduction

The photoprocess of the 3d metal atoms is of basic and practical importance. About two decades before, some of us had investigated a series of photoabsorption spectra in the 2p→3d excitation region of the 3d atoms Sc, Cr, Mn, Fe and Cu using the total photoion-yield technique [1]. From the viewpoint of atomic and plasma physics, it is very important to study the decay process of the 2p→3d excitation states. As a part of such studies, we have measured charge state distribution of final photoions for Fe atom.

2. Experimental

A monochromatized synchrotron radiation from beamline BL-7A was crossed with an atomic beam from a metallic oven of electron bombardment type. The photoions resulting from the photon-atom interaction were, with the aid of periodic positive pulses, pushed into the time-of-flight (TOF) tube and were detected by a detection system consisting of a microchannel plate (MCP) and subsequent electronics in counting mode [2]. After measurement of total photoion-yield spectrum, the TOF spectra were measured at selected photon energies.

3. Results and Discussion

Figure 1 shows the total photoion-yield spectrum of isolated Fe atom (bottom), which is almost the same as the absorption spectrum, and the charge-state distribution at selected energies (top). We can see some tendencies from these figures. First, the formation of Fe^+ ions at the excitation peaks B, C and E are quiet weak in comparison with those at off-peak energies. Second, the largest component in the charge state distribution changes from Fe^{2+} below the lowest excitation peak B to Fe^{4+} above the first 2p ionization limit (around 720 eV), and the average charge increases on the whole against the photon energy correspondingly. These experimental results are in course of analysis, including calculations of the excitation energies and oscillator strengths using the GRASP92 atomic code.

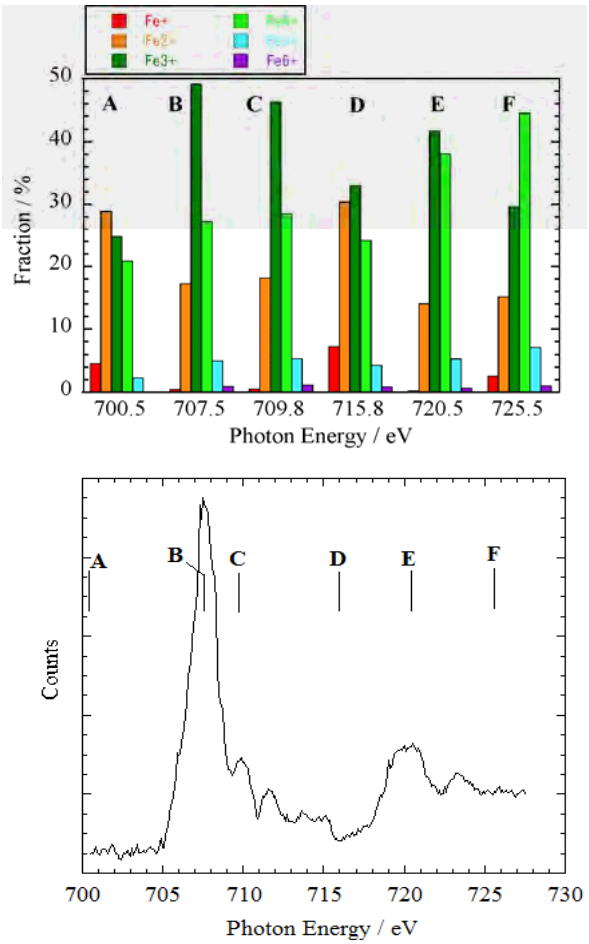

Figure 1. Top: Charge-state distribution at selected (A, B, ···) photon energies. Bottom: Total photoion-yield spectrum in the 2p→3d excitation region.

References

[1] Arp *et al* J. Phys. B: At. Mol. Opt. Phys. **27** (1994) 3389; *ibid.* **28** (1995) 225.
[2] Sato *et al* J. Phys. B: At. Mol. Phys. **18** (1985) 225.

20A/2010G-603

Ultra-low-energy electron scattering cross sections for He measured employing the threshold photoelectron source

Masashi Kitajima[*1], Keisuke Shigemura[1], Takeshi Odagiri[1], Kazutoshi Anzai[2], Atsushi Suga[2], Hidetoshi Kato[2], Masamitsu Hoshino[2], Hiroshi Tanaka[2], and Kenji Ito[3]
[1]Department of Chemistry, Tokyo Inst. Tech., Meguro-ku, Tokyo 152-8551, Japan
[2]Department of Physics, Sophia Univ., Chiyoda-ku, Tokyo 102-8554, Japan
[3]KEK-PF, Tsukuba, Ibaraki 305-0801, Japan

1 Introduction

The scattering of low-energy electrons by atoms and molecules has been the subject of extensive experimental and theoretical investigations. The cross-section data concerning electron-atom or -molecule scattering are of great importance in understanding fundamental physics of the electron collisions and applications such as electron-driven processes in the Earth and planets' phenomena, radiation chemistry, gaseous discharges, plasmas, and so on. When the collision energy becomes very low such as less than 100 meV, the de Broglie wavelength of electrons becomes very much greater than the typical size of an atom or molecule. In this area so called "cold electron collisions" [1], the interaction tend to be governed by asymptotic long range potentials and the scattering of cold electron is a subject closely related to the field of cold atom collision.

Recently, we developed a new method for producing an electron beam at very low energy for a cold electron collision experiment employing the threshold photoelectron source [2]. The technique enables one to perform high energy resolution experiments at very low electron energies by employing the penetrating field technique together with the threshold photoionizaion of atoms by the synchrotron radiation. The total cross sections for electron scattering from Ar, Kr and Xe in the energy range from around 10 meV to 20 eV were obtained at an electron energy width of 10 -12 meV with the apparatus employing the threshold photoelectron source [2-4]. In the present study, we measured the total cross sections for electron scattering from helium in the very low electron energy range.

2 Experiment

The experiment has been carried out at the beamline 20A of the Photon Factory, KEK, in Japan. An overview of the experimental setup is shown in Fig. 1. The setup consists of an electron scattering apparatus with a photoelectron source, an Au mesh monitor, and a microchannel plate (MCP). The electron scattering apparatus consists of a photoionization cell, three electrostatic lens systems, a collision cell, and a channel electron multiplier. The monochromatized SR tuned just at the first ionization threshold of Ar (15.760 eV) was focused on the center of the photoionization cell, filled with argon atoms. The threshold photoelectrons produced are extracted by a weak electrostatic field formed by the penetrating field technique and formed into a beam. The electron beam from the threshold photoelectron source is focused on the collision cell filled with target gas. The electrons passing through the cell without any collision with the target are detected by a channel electron multiplier (CEM). The counting rates of the detected electrons in the presence and absence of target gas are converted to the total cross section for electron scattering according to the attenuation law.

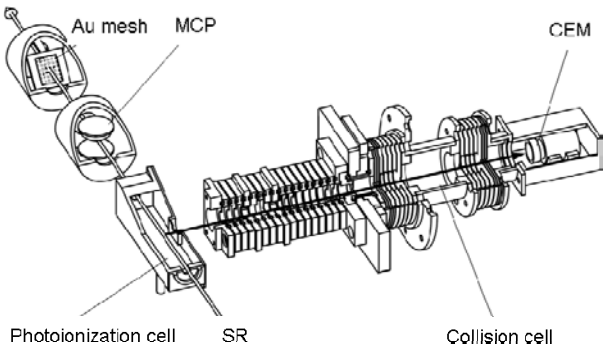

Fig. 1. Overview of the present experimental system.

3 Results and Discussion

Total cross sections for electron scattering from He at electron energies ranging from 7 meV to 20 eV were obtained using the threshold photoelectron source. The measured absolute values of the total cross sections agree with those obtained by other groups in the energy region above a few hundred meV where several experimental works have been reported. At very-low-energy region, where no experimental data exists, a reasonable agreement was obtained between our cross-section values and the theoretical prediction of Nesbet [5].

References

[1] D. Field *et al.*, Acc. Chem. Rev. **34**, 291 (2001)
[2] M. Kurokawa *et al.*, Phys. Rev. A **82**, 062707 (2010)
[2] M. Kurokawa *et al.*, Phys. Rev. A **84**, 062717 (2011)
[4] M. Kitajima *et al.*, Eur. Phys. J. D **66** 130 (2012)
[5] R. K. Nesbet, Phys. Rev. A **20**, 58 (1979)

* mkitajim@chem.titech.ac.jp

7A/2011G626

Site-Specific Ion Desorption of Methyl-Ester Terminated Biphenyl SAMs Induced by Core-Excitations

Ryosuke Koga[1], Shin-ichi Wada[1,2*], Mai Ogawa[1], Jumpei Kajikawa[1], Hironori Hayashita[1], Kenichiro Tanaka[3], and Atsunari Hiraya[1,2]
[1]Depertment of Physical Science, Hiroshima Univ., Higashi-Hiroshima 739-8526, Japan
[2]HSRC, Hiroshima Univ., Higashi-Hiroshima 739-0046, Japan
[3]XFEL Division, Japan Synchrotron Radiation Research Institute, Sayo, 679-5198, Japan

1 Introduction

Possibility of site-specific (site-selective) ionic dissociation induced by core-excitation has been focused on research in soft X-ray induced chemical reaction. The site-specific dissociation is obviously observed on solid surfaces than in gas phase. We focus on this difference, and propose a hypothesis as follows. Holes with excess energy created by core-excitations delocalize and redistribution of such high internal energy can cause a variety of chemical reactions. In such case, reactions lose the memory of the sites of the primary excitations, and the probabilities of such reactions can be determined by statistical considerations. In the case of isolated gaseous molecules, the excess energy that diffuses over a molecule can lead statistical chemical reactions dominantly, thus the site-specific reactions is strongly hidden. On the other hand, in the case of solid surfaces, the excess energy that diffuses over a molecule rapidly flows into the solid or neighboring molecules, which does not contribute to chemical reaction. As a result, statistical reactions are suppressed and therefore site-specific reactions are emphasized at the solid surfaces [1].

Recently, remarkable site-specific ion desorption was observed in methyl ester terminated self-assembled monolayer (MHDA SAM: Au-S$(CH_2)_{15}COOCH_3$). In this study, we focus on the role of spacers (molecular chains) between functional groups and metal substrates of SAMs. So, we investigated ion desorption of methyl ester-terminated biphenyl SAM (M2P SAM; Au-S$(C_6H_4)_2$-$COOCH_3$) which has conductive biphenyl spacer (Fig. 1), in order to clarify whether the difference of conductivity of spacers affects site-specific reactions.

2 Experiment

Experiments were performed at the BL7A of KEK-PF. Near edge X-ray absorption fine structure (NEXAFS) was recorded in total electron yield (TEY) mode by measuring a sample drain current. The measured TEY spectra are normalized to the incident photon flux monitored with a gold-coated mesh. Partial ion yield (PIY) spectra of M2P were measured by using TOF-MS in the single-bunch operation of the PF ring.

M2P SAMs were prepared by immersing Au coated Si substrates into 1.0mM methyl ethyl ketone solution during 24h. SAMs were rinsed in methyl ethyl ketone immediately after removal from the solution and quickly inserted into the UHV chamber for analysis..

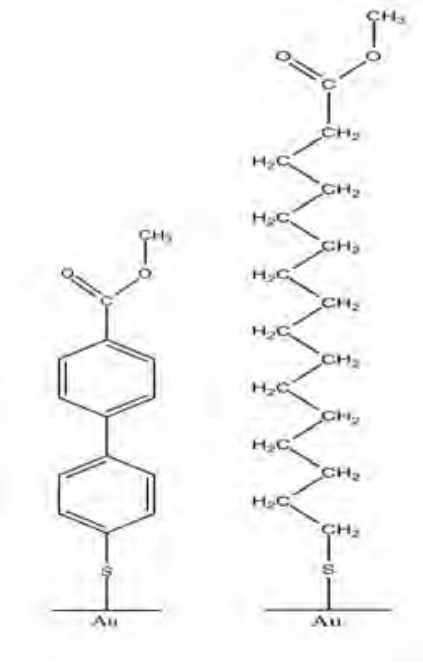

Fig. 1: Molecular structure of M2P (left) and MHDA (right) SAMs.

3 Results and Discussion

Fig. 2(a) shows TEY spectrum of M2P in the C K-edge region. The dotted lines are the peak element of each excitation state obtained from peak fitting analysis. The black-painted peak is the excitation of C1s(O-CH_3) to the σ^*(O-CH_3) antibonding orbital extracted from the conjugated and obscure NEXAFS spectrum by peak fitting procedure. Fig. 2(b) shows the PIY spectrum of CH_3^+. The site-specific ion desorption can be seen at this σ^* excitation as a pronounced desorption of CH_3^+ ion, as seen in other methyl ester terminated SAMs [1]. PIY spectra include site-specific component and non-specific one. In other words, ionic desorption induced by core-excitations is promoted by different two mechanisms, direct (specific) and indirect (non-specific) processes. The non-specific component in the PIY spectrum appear with intensity in proportion to the drain current, TEY. On the other hand, a specific desorption via a direct process should occur only at a specific resonant state. To estimate

the non-specific component, TEY and PIY spectra are normalized at the pre-edge (280 eV) and the ionization threshold (292 eV) where TEY includes less specific component. In this manner, the normalized TEY can be regarded as non-specific component. The thick line in Fig. 2(b) shows normalized TEY. At the σ^*(O-CH_3) excitation, the site-specific component of CH_3^+ is estimated to be more than 97% of CH_3^+ ion yield. This value is higher than that for MHDA SAM, where site-specific component at σ^*(O-CH_3) is estimated to be 90-95% in the previous study [1]. This result indicates that a conductive spacer, biphenyl, is more efficient to memorize a localization character of core-excitations than the insulating spacer, methylene long chain. This effect is also related to relaxation speed of holes created by Auger decay process. The holes diffused over the molecule after Auger decays would rapidly flow into the metal surface via its conductive spacer. This consideration supports our hypothesis mentioned above.

References

[1] S. Wada *et al.*, J. Phys.: Condens. Matter **18** (2006) S1629.

* swada@sci.hiroshima-u.ac.jp

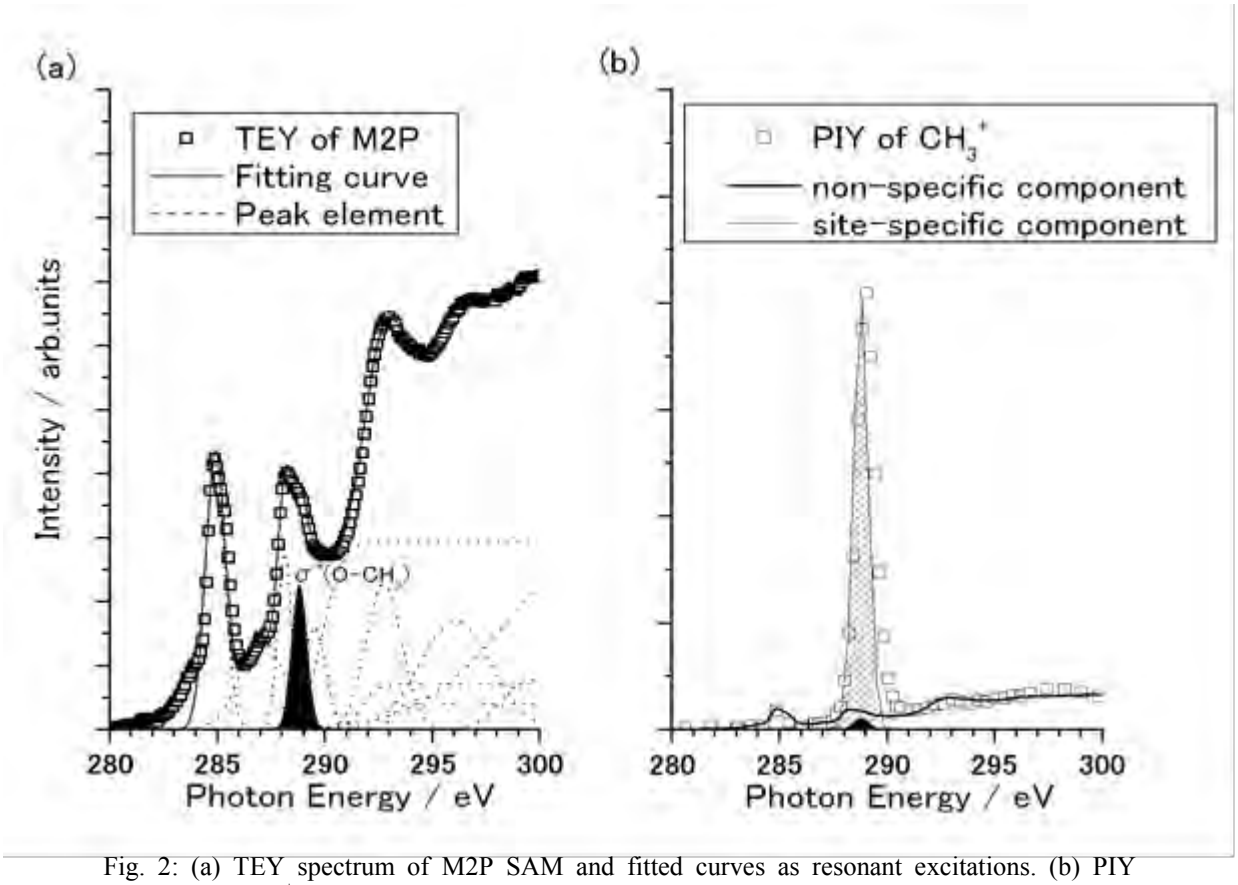

Fig. 2: (a) TEY spectrum of M2P SAM and fitted curves as resonant excitations. (b) PIY spectrum of CH_3^+ and normalized TEY. The black-painted peak shows non-specific component of σ^*(O-CH_3) excitation.

12C/2006G107, 2011G250

Reduction of hexavalent chromium in soils by X-ray irradiation

Atsuyuki OHTA*[1], Hiroshi TSUNO[2], Hiroyuki KAGI[3], Masaharu, NOMURA[4]

[1]Geological Survey of Japan, AIST, Ibaraki 305-8567, Japan
[2] Faculty of Education and Human Sciences, Yokohama National University, Kanagawa, 240-8501, Japan
[3] Geochemical Research Center, Graduate School of Science, The University of Tokyo, Tokyo 113-0033, Japan
[4] Photon Factory, Institute of Materials Structure Science, KEK, Ibaraki 305-0801, Japan

1 Introduction

A reduction of Cr(VI) by organic materials and Fe(II) in soils is a very interesting phenomenon for environmental problems because pollutant Cr(VI) disappears in a field system easily [1, 2]. We have focused on Cr(VI) stability in soils and Cr(III/VI) reacting with humic substances using the XAFS spectroscopy method [3, 4]. However, there is a serious problem that X-ray irradiation accelerates the reduction of Cr(VI) in such experimental systems during XAFS measurement. From this reason, the Cr K-edge XANES spectra of Cr(VI)-doped soils on the first measurement was used for analysis, although multiple scans were conducted for samples. We have not explained this problem in detail so far. In this study, we discuss how X-ray irradiation affects the Cr(VI) reduction in soil materials.

2. Experiment

A 13–15 mg of $K_2Cr_2O_7$ solid reagent was mixed with 4–5 g of JSO-1, which is a soil geochemical reference material provided by Geological Survey of Japan, AIST [5]. The sample contained approximately 1000 μg/g of Cr as Cr(VI) and 70 μg/g of Cr as Cr(III) [3]. We further added water to an aliquot of the sample (about 20 wt%). The JSO-1 samples mixed with $K_2Cr_2O_7$ powder kept under dry and wet condition are named as the dry sample and the wet sample, respectively. The XANES spectra of these samples were recorded on the second, 20th, 120th and 240th days after the preparation.

The Cr K-edge XAFS spectra were recorded in fluorescence mode at the BL-12C of KEK-PF. A Si(111) double-crystal monochromator was used to produce a monochromatic X-ray beam. The monochromator was calibrated at the sharp pre-edge peak of Cr(VI) at 5989 eV, which is sensitive to the presence of Cr(VI), using $K_2Cr_2O_7$ powder in the transmission mode. The fluorescence X-ray (Cr Kα: 5.4 keV) was measured using a 19 element pure-Ge solid-state detector. The XAFS spectra of all samples were measured at room temperature. The energy region around the Cr-Kα fluorescence was selected from elastic scattering using single-channel analyzers. Multiple scans (two–five times) were conducted for the samples. The $K_2Cr(VI)_2O_7$ and $Cr(III)(NO_3)_3$ 1000 μg/g standard solutions were also measured as reference substances. These materials are used for determining molar fractions of Cr(VI) and Cr(III) of samples.

4. Results and Discussion

Figure 1 shows the XANES spectra of JSO-1 reacting with $K_2Cr_2O_7$ in wet condition for 2 days. Because the x-ray beam was focused into an area smaller than 1 × 1 mm^2, the damaged area was very restricted. Figure 1 shows that the spectra dramatically changed with three repeat measurements. The sharp pre-edge peak at 5989 eV and the region around 6020–6040 eV decrease their intensities and the peak at 6003–6005eV increase its intensity during measurements. It takes 670 seconds for measuring the whole XANES region and 150 seconds for measuring within the pre-edge region including the pre-edge peak at 5989 eV. Those changes suggest that the X-ray irradiated to samples reduced Cr(VI) to Cr(III) remarkably within only 35 minutes.

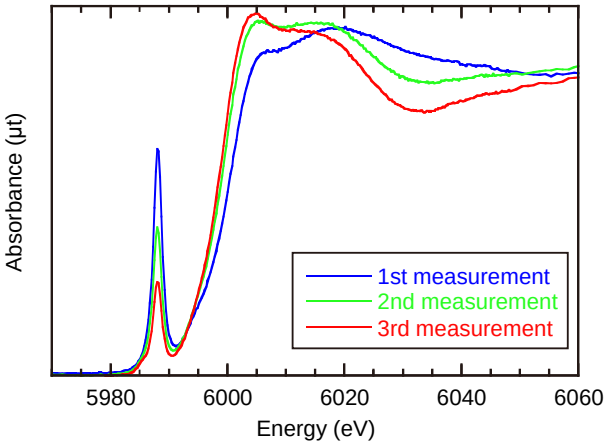

Fig. 1: XANES spectra of JSO-1 reacting with $K_2Cr_2O_7$ in wet condition for two days.

Figure 2 shows how the intensity of the pre-edge peak at 5989 eV in Cr K-edge XANES spectra changes during the repeated measurements. The intensity of the pre-edge peak (μt_{peak}) was subtracted off the pre-edge background absorption (μt_{BK}) and further normalized by the absorbance on the first measurement;

$$\mu t_{peak}' = (\mu t_{peak} - \mu t_{BK})/(\mu t_{peak} - \mu t_{BK})_{\text{the 1st measurement}}. \quad (1)$$

The Cr(VI)/Total Cr (Cr(VI)/T-Cr) ratios expressed on the legends in Fig. 2 are cited from Tsuno et al. [3]. The intensity of the sharp pre-edge peak in the samples under the wet condition decreases dramatically with repeated measurements (Fig. 2). The decrease of the intensity ($\mu t_{peak}'$) is same among all samples except for the samples

reacting for 20 days. The μt_{peak}' for the wet samples is reduced by half within three repeated measurements. The decrease of μt_{peak}' seems not to relate with Cr(VI) reduction properties. On the other hands, the changes at pre-edge peak for the dry samples are not pronouncedly. A decrease of 30% over time is found for μt_{peak}' at the highest different from wet samples. The decrease ratio of μt_{peak}' becomes small with increasing the reacting times (from 2 days to 240 days), although there is no significant difference between reactions times of 120 days and 240 days.

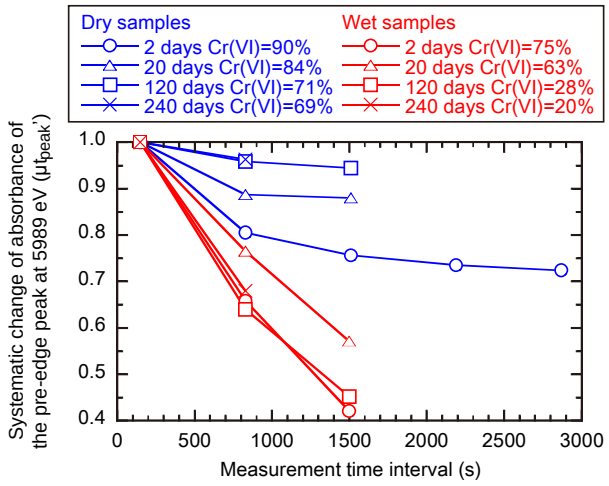

Fig. 2: The Systematic change of absorbance of the pre-edge peak at 5989 eV with the multi-scans. The measurement time interval for the pre-edge peak is calculated by 150s + 670s×(n−1), where n = 1–5.

Figure 3 shows that the Cr(VI)/T-Cr ratios determined using a linear combination fitting of standard Cr(III) and Cr(VI) materials. Because the whole XANES region was used for the fitting, the Cr(VI)/T-Cr data were plotted against the averaged time of the measurement (670s/2). The estimated ratio decreases gradually at each measurement. Especially, the percentages of Cr(VI) of the wet samples reacting with Cr(VI) for 2 days and 20 days decrease dramatically within three repeated measurements.

Table 1 summarizes the Cr(VI)/T-Cr ratios determined for samples. The "LCF" indicates a linear combination fitting result of XANES spectra measured on the first time using the spectra of Cr(VI/III) references. We fitted a linear regression line (y=a+bx) or a regression curve ($y=a+bx+cx^2$) to the data in Fig. 3. The estimated intercepts (a) indicate the Cr(VI)/T-Cr ratios that are free from reduction by X-ray irradiation. They are listed on Table 1 as "Regression". The re-evaluated Cr(VI)/T-Cr values for the dry samples do not differ from the LCF values significantly. The LCF values obtained for the wet samples reacting with Cr(VI) for 2 days and 20 days are 9–16% smaller than the re-evaluated Cr(VI)/T-Cr values. However, there are small differences for samples reacting with Cr(VI) over 120 days. The error in a linear combination fitting of XANES spectra is empirically ±5%. As long as the Cr(VI)/T-Cr ratio is determined using LCF, there seems not to be sever problem for the most samples. However, we must pay attention that the Cr(VI)/T-Cr ratios in soil samples determined using XAFS spectroscopy method are always lower than the real values because of the reduction process by X-ray irradiation.

Finally, it is reasonable that the reduction of Cr(VI) in the wet samples by X-ray irradiation is accelerated more than that in day samples. However, it is unclear why the Cr(VI) in dry samples is reduced by X-ray irradiation. The JSO-1 used for experiments was not dried under the high temperature. The amount of H_2O in JSO-1 is 8.36 wt. %, which is determined by drying at 110°C [5]. The hygroscopic minerals in JSO-1 would absorb variable amounts of moisture [5]. The Cr(VI) reduction of dry samples by X-ray irradiation would not be caused without such inherent waters.

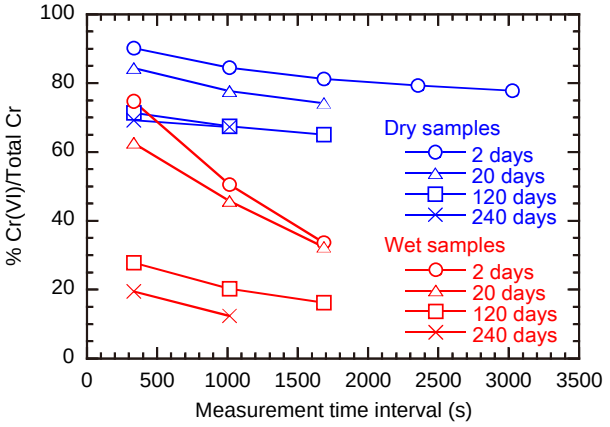

Fig. 3: The Cr(VI)/T-Cr ratios determined using a linear combination fitting of standard Cr(III) and Cr(VI) materials. The measurement time interval is calculated by 670s/2 + 670s×(n−1), where n = 1–5.

Table 1: Cr(VI)/T-Cr ratio determined for JSO-1 reacting with $K_2Cr_2O_7$

	Dry condition		Wet condition	
Reaction time	LCF	Regres-sion	LCF	Regres-sion
2 days	90%	93%	75%	89%
20 days	84%	89%	63%	72%
120 days	71%	74%	28%	33%
240 days	69%	70%	20%	23%

References

[1] P. R. Wittbrodt and C. D. Palmer, Environ. Sci. Technol. **30** (1996) 2470.
[2] N. Kožuh *et al*., Environ. Sci. Technol. **34** (2000) 112.
[3] H. Tsuno *et al*. Geostand Geoanalyt Res. **30** (2006) 55.
[4] A. Ohta *et al*. Bull. Geol. Surv. Japan **62** (2011) 347.
[5] A. Terashima *et al*. Geostand. Newsl. **26** (2002) 85.

* a.ohta@aist.go.jp

9A, 12C/2006G337, 2008G188

Ni-supported $Ce_2Zr_2O_x$ (x = 7-8) Catalysts for CH_4 Steam Reforming

Mizuki TADA*[1], Nozomu ISHIGURO[1,2], Jun-ichi SOGA[2], Shenghong ZHANG[1], Yasuhiro IWASAWA[2]

[1] Institute for Molecular Science, Myodaiji, Okazaki, Aichi 444-8585, Japan.
[2] Department of Chemistry, Graduate School of Science, The University of Tokyo, Hongo, Bunkyo-ku, Tokyo 113-0033, Japan.

Introduction

$Ce_2Zr_2O_x$ (x = 7-8) was prepared for a support for automobile exhausting catalyst[1], and we have found that Ni-supported $Ce_2Zr_2O_x$ was efficient for methane steam reforming reaction to produce H_2 and CO at H_2O/CH_4=1. The catalytic performance of $NiO_y/Ce_2Zr_2O_x$ (x=7-8) strongly depended on the phase and oxygen content (x) of $Ce_2Zr_2O_x$, showing a unique discontinuity in catalytic activity at x=7.5. The oxidation states and local coordination structures of Ni and Ce species on the catalysts were investigated by Ni K-edge and Ce L_{III}-edge XAFS analysis.

Experimental

Ordered $Ce_2Zr_2O_7$ solid solution (Ce/Zr=1/1 molar ratio) [1] was prepared by co-precipitation using an aqueous NH_3 solution of $Ce(NO_3)_3{\cdot}6H_2O$ and $ZrO(NO_3)_2{\cdot}2H_2O$, followed by reduction with CO at 1673 K. The sample was calcined at 773 K and impregnated with an aqueous solution of $Ni(NO_3)_2{\cdot}6H_2O$, followed by calcination. $Ni/Ce_2Zr_2O_7$ was prepared by the reduction of $NiO/Ce_2Zr_2O_8$ with H_2 at 773 K.

XAFS spectra were measured at 293 K at BL-9A (Ce L_{III}-edge) and BL-12C (Ni K-edge) with Si(111) channel-cut crystals monochrometer. Ni K-edge XAFS was measured in fluorescence mode, and fluorescent X-rays were detected by a Lytle detector filled with Ar, while incident X-rays were detected by an ionization chamber filled with N_2. Ce L_{III}-edge XANES was measured in transmission mode, and incident and transmitted X-rays were detected by ionization chambers filled with N_2 (30%) + He (70%) and N_2, respectively.

Results and Discussion

Methane steam reforming activity highly depended to the amount of oxygen (x) in $Ce_2Zr_2O_x$ and $NiO_y/Ce_2Zr_2O_x$ (x<7.5) showed significant activity for the reaction. Figure 1 (A) shows the Ce L_{III}-edge XANES spectra of $NiO_y/Ce_2Zr_2O_x$ samples. $Ni/Ce_2Zr_2O_7$, which was active for CH_4 steam reforming, showed no change in its XANES spectra before or after the CH_4 steam reforming at 923 K. Ce L_{III}-edge XANES data revealed that $NiO_y/Ce_2Zr_2O_{7.4}$ was reduced to $Ce_2Zr_2O_7$ after the CH_4 steam reforming. In contrast, there was no significant changes Ce L_{III}-edge XANES spectrum of $NiO_y/Ce_2Zr_2O_{7.6}$ and $NiO/Ce_2Zr_2O_8$ after CH_4 steam reforming. Thus, it was indicated that active $NiO_y/Ce_2Zr_2O_x$ (x<7.5) catalysts converted to $Ni/Ce_2Zr_2O_7$ under the CH_4 steam reforming conditions.

The oxidation states and local coordination structures of the supported Ni species were investigated by Ni K-edge XANES and EXAFS. Similar changes in the XANES spectra of $NiO_y/Ce_2Zr_2O_x$ (x<7.5) were observed at Ni K-edge before and after the CH_4 steam reforming (Figure 1 (B)). Ni species on the active phases converted to metallic Ni species, while oxidized Ni species on inactive phases did not change under the reaction conditions. The curve-fitting analysis of Ni K-edge EXAFS of $Ni/Ce_2Zr_2O_7$ suggested that the Ni nanoparticles were metallic Ni species, whose Ni-Ni coordination number was 11.1±1.3 at 0.249±0.001 nm.

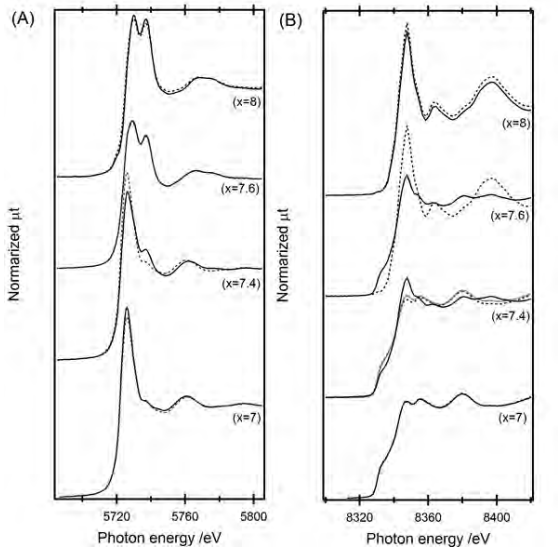

Figure 1. (A) Ce L_{III}-edge and (B) Ni K-edge XANES spectra of $NiO_y/Ce_2Zr_2O_x$ catalysts before and after the CH_4 steam reforming.

Reference

[1] A. Suda, Y. Ukyo, H. Sobukawa, M. Sugiura, *J. Ceram. Soc. Jpn.* **2002**, *110*, 126.

* mtada@ims.ac.jp

12C/2007G079 and 2009G014

In situ XAFS Study on Molecular Catalyst for Hydrogen Evolution Reaction Confined within Organic Molecular Layer on Si(111) Surface

Kohei Uosaki,[1,2,3,*] Takuya Masuda,[2] Hitoshi Fukumitsu,[2] Satoru Takakusagi,[4] Wang-Jae Chun,[5] Toshihiro Kondo,[6] and Kiyotaka Asakura[4]

[1]International Center for Materials Nanoarchitectonics (WPI-MANA), National Institute for Materials Science (NIMS), Tsukuba 305-0044, Japan

[2]Global Research Center for Environment and Energy based on Nanomaterials Science (GREEN), National Institute for Materials Science (NIMS), Tsukuba 305-0044, Japan

[3]Graduate School of Chemical Sciences and Engineering, Hokkaido University, Sapporo 060-0810, Japan

[4]Catalysis Research Center, Hokkaido University, Sapporo 001-0021, Japan

[5]Chemistry Department, International Christian University, Mitaka 181-8585, Tokyo, Japan

[6]Graduate School of Humanities and Sciences, Ochanomizu University, Ohtsuka, Bunkyo-ku, Tokyo 112-8610, Japan

1 Introduction

Catalysts play crucial roles in many chemical and energy conversion processes. Often precious metals and rare metals are the major components of active catalysts and many efforts have been made to maximize the utilization of these atoms such as increasing their dispersion in heterogeneous catalysts. Although 100% atom efficiency is expected at molecular and single atom catalysts, molecular catalysts are usually used in solution and have limited applications because of difficulty in separating the product and catalyst. It is very difficult to prepare single atoms and maintain them without their being converted into metal clusters or particles because they are more energetically stable. One would expect, however, that if the metal complexes are confined on or within a solid substrate at well isolated positions, they may act as molecular catalysts without aggregation. Recently, an organic molecular layer with viologen groups and Pt complexes was constructed on a Si(111) surface and very efficient photoelectrochemical hydrogen evolution current was achieved.[1] Here, we demonstrate that Pt complexes placed at precisely controlled position within the molecular layers act as molecular electrocatalysts for hydrogen evolution without being converted into metal clusters or particles.[2]

2 Experiment

Si(111) electrode was modified with five layers of viologen moiety with $PtCl_4^{2-}$ to yield a $(Pt\text{-}V^{++})_5$-Si(111) as previously reported.[1],[2]

XAFS measurements were performed at BL12C of the Photon Factory. Pt L_3–edge XAFS spectra were recorded under electrochemical conditions at room temperature. X-rays were monochromated using a Si(111) double-crystal monochromator. The fluorescence signals were detected using a 19-element pure Ge solid state detector (GL0110S; Canberra, USA). The EXAFS analyses and calculations were carried out using REX 2000 (Rigaku, Japan) and FEFF 8.0, respectively.

3 Results and Discussion

After $PtCl_4^{2-}$ was incorporated into the five layers of viologen moieties by ion exchange reaction, small fraction of Cl^- ligands were exchanged by oxygen species, e.g., OH^- and H_2O. As the potential was made more negative, the Cl^- ligands were gradually replaced by oxygen species and all the Cl^- was exchanged at –0.6 V. Hydrogen evolution reaction (HER) current started to flow from –0.8 V. Since this potential is 1.3 V more positive than the redox potential of $PtCl_4^{2-}$, e.g., +0.51 V, one would expect that the Pt complex is reduced to Pt particles which act as HER catalyst. However, EXAFS oscillation was still similar to that at –0.6 V and no Pt–Pt interactions were observed, indicating that Pt particles were not formed even when HER took place. Thus, it was proved that the Pt complexes act as molecular catalysts confined within organic molecular layers. It is considered that the formation of Pt particles was inhibited since the complexes were separated by the molecular layers. Once HER started, white line intensity of the XANES spectra decreased, suggesting the formation of a hydride complex as an intermediate of HER, although more detailed experimental and theoretical examinations are required to clarify the mechanism.

References

[1] T. Masuda, K. Shimazu, K. Uosaki, Journal of Physical Chemistry C, **112** (2008) 10923-10930.

[2] T. Masuda, H. Fukumitsu, S. Takakusagi, W.-J. Chun, T. Kondo, K. Asakura and K. Uosaki, Advanced Materials, **24** (2012) 268-272.

* uosaki.kohei@nims.go.jp

NW10A/2008G154, 2010G020

XAFS Characterization of Molecularly Imprinted Ru-Complex Catalysts for Asymmetric Transfer Hydrogenation Acting in Water Media

Zhihuan WENG[1], Satoshi MURATSUGU[1], Nozomu ISHIGURO[1], Mizuki TADA*[1]

[1] Institute for Molecular Science, Myodaiji, Okazaki, Aichi 444-8585, Japan.

Introduction

Molecularly imprinted Ru-complex catalysts acting in water were prepared on a SiO_2 surface by molecular imprinting of a SiO_2-supported Ru complex using organic polymers as surface matrix overlayers. The local coordination structures of the prepared molecularly imprinted Ru-complex catalysts, which exhibited fine shape selectivity for the asymmetric transfer hydrogenation of *o*-fluoroacetophenone and its derivatives in water media, were investigated by Ru K-edge EXAFS.

Experimental

A Ru precursor complex [(*p*-cymene)Ru{$NH_2CH(Ph)CH(Ph)NSO_2C_7H_7$}Cl] was attached on a SiO_2 surface via *p*-styryl moiety functionalized. A template alcohol molecule was coordinated to the supported Ru complex, and surface-matrix overlayers were stacked on the surface by the photopolymerization of Threebond 3026E polymer. Finally, the template was released from the supported Ru complex under appropriate reaction conditions, and a molecularly imprinted Ru complex was obtained on the SiO_2 surface.

Ru K-edge EXAFS was measured in a transmission mode at 20 K at the NW10A station with a Si(311) double-crystal monochromator. Ionization chambers filled with pure Ar and pure Kr were used to monitor incident and transmitted X-rays, respectively. EXAFS spectra were analyzed using Rigaku REX2000 package. Curve-fitting analysis was carried out in *k*-space and k^3-weighted EXAFS oscillations were Fourier transformed into *R*-space. Fitting parameters were coordination number (CN), interatomic distance (*R*), Debye-Waller factor (σ^2), and correction-of-edge energy (ΔE_0). Phase shifts and backscattering amplitudes for Ru-C, Ru-N, and Ru-Cl were calculated by the FEFF8 code.

Results and Discussion

The local coordination structures of the supported Ru complexes were examined by Ru K-edge EXAFS analysis, whose structural parameters are listed in Table 1. The supported Ru complex before the coordination of the template had Ru-N interaction at 2.11±0.01 Å, whose coordination number (CN) was estimated to be 2.0±0.4. After the coordination of the template, the average of bond distances of Ru-N (diamine ligand) and Ru-O (template) was estimated to be 2.14±0.01 Å (CN = 3.4±0.4).

The structural parameters of the local coordination of the molecularly imprinted Ru complexes after the stacking of polymer matrices were also investigated by Ru K-edge EXAFS. The CNs and bond distances of the template-coordinated Ru complex with surface matrix overlayers were similar to those of the template coordinated Ru complex without the matrix overlayers. Accompanied with the stoichiometric elimination of the template, the local coordination structure of the supported Ru complex recovered to the initial state as shown in Table 1.

Table 1 Structural parameters of the supported Ru complexes and molecularly imprinted Ru complexes with organic matrix overlayers obtained by curve-fitting analyses of Ru K-edge EXAFS measured at 20 K[a]

Shell	CN	*R* /Å	ΔE_0 /eV	σ /Å
Supported Ru complex R_f = 1.2 %				
Ru-C	5.5±0.9	2.22±0.01	10	0.07
Ru-N	2.0±0.4	2.11±0.01	6	0.03
Ru-Cl	1.5±0.2	2.44±0.01	17	0.08
Template-coordinated Ru complex R_f = 0.4 %				
Ru-C	6.4±0.7	2.33±0.01	24	0.10
Ru-N(O)	3.4±0.4	2.14±0.01	7	0.08
Template-coordinated Ru complex with surface matrix overlayers[b] R_f = 1.2 %				
Ru-C	6.0±0.7	2.30±0.01	20	0.10
Ru-N(O)	3.0±0.3	2.12±0.01	9	0.07
Molecularly imprinted Ru complex[b] R_f = 0.6 %				
Ru-C	5.6±0.7	2.21±0.02	8	0.07
Ru-N	1.8±0.5	2.10±0.01	14	0.04
Ru-Cl	1.6±0.4	2.42±0.02	13	0.12

[a] *k* range and *R* range were 3-14 $Å^{-1}$ and 1.0-2.4 Å, respectively.
[b] The height of the polymer matrices was 2 nm.

Reference

[1] M. Tada, S. Muratsugu, M. Kinoshita, T. Sasaki, Y. Iwasawa, *J. Am. Chem. Soc.* **2010**, *132*, 713.

* mtada@ims.ac.jp

BL9C, 12C/2008G188, 2011G176

XAFS Characterization of Ni/$NaCeTi_2O_6$ Catalysts for CH_4 Steam Reforming

Shenghong ZHANG[1], Satoshi MURATSUGU[1], Nozomu ISHIGURO[1], Mizuki TADA*[1]

[1] Institute for Molecular Science, Myodaiji, Okazaki, Aichi 444-8585, Japan.

Introduction

Enhancing the reducibility and basicity of support is one of the most promising methods to improve the resistance to coking on Ni catalysts for steam reforming of methane (SRM)[1]. We have succeeded in preparing Ni catalysts loaded on perovskite $NaCeTi_2O_6$ (NCT) oxide, which contains both reducible Ce^{3+} and basic Na^+ sites, and have investigated the oxidation states and local coordination structures of supported Ni/NCT catalysts before and after SRM reaction at 973 K[2].

Experimental

4 wt% Ni/NCT catalysts were prepared by a wet impregnation method, and SRM reactions were conducted at 973 K with a low H_2O/CH_4 ratio (1/1). Ni K-edge (fluorescence mode) and Ce L_{III}-edge XAFS (transmission mode) spectra were measured at 298 K at the BL-9C and BL-12C stations of KEK-PF with the monochromatized X-rays by Si(111) double crystals. XAFS data were analysed with IFEFFIT (Athena and Arthemis) ver. 1.2.11. Background subtraction was performed with Autobk and Spline smoothing algorithm in the Athena program. k^3-Weighted Ni K-edge EXAFS oscillations (k = 30-130 nm^{-1}) were Fourier transformed into R-space, and EXAFS curve-fitting analysis was carried out in R-space. Fitting parameters were coordination number (CN), interatomic distance (R), Debye-Waller factor (σ^2), and correction-of-edge energy (ΔE_0). Phase shifts and backscattering amplitudes were calculated from the crystal structure of Ni foil and NiO by using the FEFF8 code, and S_0^2 values were determined by the curve-fitting analysis of Ni foil and NiO [3].

Results and Discussion

The valence states of Ce and Ni were examined by Ce L_{III}-edge and Ni K-edge XANES, respectively. CeO_2 with Ce^{4+} showed two XANES peaks at 5731.1 and 5738.0 eV as shown in Figure 1 (A), while a sharp peak at 5726.6 eV was observed for $CeCl_3$ with Ce^{3+}. The Ce L_{III}-edge XANES spectra of NCT and Ni/NCT were very close to that of $CeCl_3$, with a sharp peak at 5726.3 eV, and remained unchanged after catalytic tests. These indicated that Ce^{3+} species predominated in the prepared catalysts and were quite stable under the SRM reaction conditions.

Ni K-edge EXAFS suggested the local coordination structure of the supported Ni species on Ni/NCT. Fresh Ni/NCT exhibited the similar Ni K-edge XANES to that of Ni foil, as shown in Figure 1 (B). The contribution of Ni-Ni at 0.248 ± 0.001 nm was observed on the fresh Ni/NCT, and the coordination number (CN) of the Ni-Ni bond was estimated to be 9.9 ± 1.1 (Table 1), indicating that the supported Ni species were metallic on NCT.

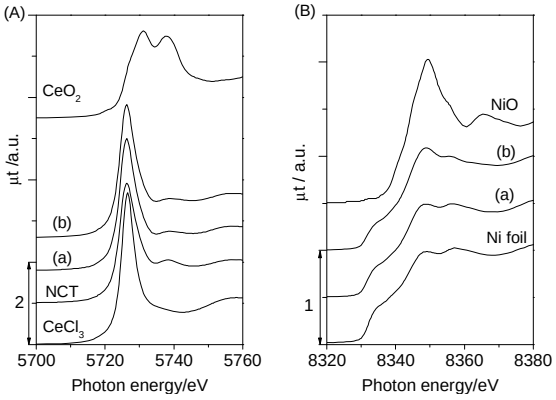

Figure 1 (A) Ce L_{III}-edge and (B) Ni K-edge XANES spectra of the Ni/NCT catalysts. (a) Fresh 4 wt% Ni/NCT and (b) used 4 wt% Ni/NCT.

After SRM reaction, the white-line intensity of the used Ni/NCT catalyst at the Ni K-edge XANES increased a little (Figure 1 (B)), implying the slight oxidation of Ni particles under the SRM reaction conditions. While Ni K-edge EXAFS Fourier transform was successfully fitted with Ni-Ni at 0.249 ± 0.001 nm (CN = 10.5 ± 0.5), and the contribution from NiO was negligible as shown in Table 1. These results suggested that metallic Ni dominated in the Ni/NCT catalysts with surface Ni species oxidized by steam under the reaction conditions.

Table 1: Curve fitting results of Ni K-edge EXAFS (R = 0.10- 0.30 nm)

Samples	Shell	CN	Distance /nm	σ^2 /× 10^{-5} nm^2
fresh	Ni-Ni	9.9 ± 1.1	0.248 ± 0.001	6 ± 1
used	Ni-Ni	10.5 ± 0.5	0.249 ± 0.001	5 ± 1

References

[1] D. L. Trimm, *Catal. Today*, **1999**, *49*, 3.
[2] S. Zhang, S. Muratsugu, N. Ishiguro, S. Ohkoshi, M. Tada, *ChemCatChem*, in press.
[3] Y. Chen, J. Shen, N. -X. Chen, *Solid State Commun.*, **2009**, *149*, 121-125; R. W. Cairns, E. Ott, *J. Am. Chem. Soc.* **1933**, *55*, 527-533.

* mtada@ims.ac.jp

7C/2008G621

Heat-Treatment Effect on Cathode Characteristics, and Average and Local Structures of $LiNi_{0.5}Mn_{0.5}O_2$ as a Cathode Active Material for Li-Ion Battery

Yasushi IDEMOTO*[1], Naoto KITAMURA[1], Yoshiharu UCHIMOTO[2]

[1]Department of Pure and Applied Chemistry, Faculty of Science and Technology, Tokyo University of Science, 2641 Yamazaki, Noda, Chiba 278-851, Japan
[2]Graduate School of Human & Environmental Studies, Kyoto University, Sakyo-ku, Kyoto 606-8501, Japan

1 Introduction

$LiCoO_2$-based materials with the layered rock-salt structure have been widely used as a cathode material for the lithium-ion battery, but they have some problems, such as high cost and high toxicity of Co. Therefore, developments of Co-free cathode active materials are highly expected. As one of the candidates, $LiNi_{0.5}Mn_{0.5}O_2$ with the similar crystal structure as the $LiCoO_2$ has drawn much attention, and it was already found that its cathode properties depended on the preparation process [1].

From such background, we focused on an effect of a post annealing on $LiNi_{0.5}Mn_{0.5}O_2$ in this work. As for the samples after the annealing, we investigated cathode properties, average crystal structures and local structures.

2 Experiment

$LiNi_{0.5}Mn_{0.5}O_2$ was synthesized by a conventional solid-state method. A mixture of starting materials was fired at 950 °C for 15 h in air. As a post annealing process, a high P_{O2} treatment was performed at 450 °C for 48 h in pure O_2 with a pressure of 2.0 MPa. In addition, the sample was heated at 600 °C for 48 h under the Ar condition. These obtained samples were characterized by X-ray diffraction measurements, inductively coupled plasma analyses (ICP), and charge-discharge cycle tests. In order to clarify the heat-treatments effects on the average structures, the Rietveld analysis was carried out using neutron diffraction data [HERMES(JRR-3)].

The annealing effects were also investigated from the viewpoint of local structures by using X-ray absorption fine structure (XAFS) techniques. XAFS spectra of the Ni and Mn *K*-edges were recorded with a transmission method by BL7C at Photon Factory in KEK, and then investigated with REX-2000 program. Theoretical parameters used in curve fittings of EXAFS data were calculated by FEFF8.

3 Results and Discussion

From X-ray diffraction patterns of a pristine $LiNi_{0.5}Mn_{0.5}O_2$ and the samples heat-treated in Ar reducing and high P_{O2} conditions, it was clarified that all the samples had a single phase of the layered rock-salt structure. It was also found by ICP that the metal compositions did not depend on the heat-treatment condition. Charge-discharge cycle tests clarified that the capacity retention was improved by these heat-treatments.

In order to clarify their crystal structures, we carried out the Rietveld analyses using the neutron diffraction patterns. From the results, it was suggested that the oxygen content was slightly lower than a stoichiometric composition of 2 in the pristine specimen. After the high P_{O2} annealing, the oxygen deficit became negligible by a gaseous oxygen uptake. On the other hand, the reducing heat-treatment increased the oxygen-deficit amount.

In addition, we discussed local structures based on EXAFS analyses. Figure 1 shows Fourier transformations of k^3-weighted EXAFS spectra of the pristine and heat-treated $LiNi_{0.5}Mn_{0.5}O_2$. For the purpose of local-distortion studies, curve fittings for the first coordination peaks (the TM-O shell) were performed, and the results are given in Table 1. In these analyses, the coordination numbers were fixed based on the oxygen contents refined by the Rietveld analyses. From the Debye-Waller factors, it was indicated that the distortion around Ni was relaxed by annealing under the reducing condition. Such a change in the local distortion is considered to have a positive influence on the cycle performance of $LiNi_{0.5}Mn_{0.5}O_2$.

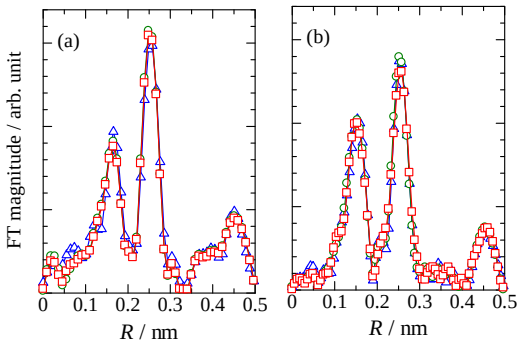

Fig. 1: Fourier transformations of EXAFS spectra of (a) Ni *K*- and (b) Mn *K*-edge of the prepared $LiNi_{0.5}Mn_{0.5}O_2$. (circle; pristine, triangle; reduced, square; oxidized)

Table 1: Interatomic distances (R) and Debye-Waller factors (σ) for Ni *K*- and Mn *K*-edge EXAFS spectra.

Sample	Ni-O		Mn-O	
	R / nm	σ / nm	R / nm	σ / nm
Pristine	0.2058	0.0130	0.1973	0.0128
Reduced	0.2066	0.0125	0.1973	0.0125
Oxidized	0.2057	0.0132	0.1975	0.0130

References

[1] Y. Idemoto, et. al., *Electrochemistry*, **79** (2011) 15.

* idemoto@rs.noda.tus.ac.jp

先端研究施設共用イノベーション創出事業【産業戦略利用】
フォトンファクトリーの戦略的産業利用

課 題 番 号： 2008I006
研究責任者： 山﨑紀子
利 用 施 設： 高エネルギー加速器研究機構　放射光科学研究施設　BL-9A
利 用 期 間： 2009 年 1 月～2009 年 12 月

ナノ構造多層膜の元素変換反応における Ca 添加効果の XAFS 解析

Local structure analysis of Ca in Pd complex in element transmutation reactions by XAFS

山﨑紀子 [1]、岩村康弘 [1]、伊藤岳彦 [1]
Noriko Yamazaki[1], Yasuhiro Iwamura[1] , Takehiko Ito[1]

[1] 三菱重工業株式会社　先進技術研究センター
Advanced technology research Center, Mitsubishi Heavy Industries, LTD

アブストラクト：　Pd 基板上に作成した Pd-CaO 多層膜の表面に特定の元素を添加して重水素ガスを透過すると添加した元素に換わって新たな元素が生成するという現象（元素変換反応）が確認されている。この現象のメカニズムを解明する手がかりを得るため、反応に重要な役割を果たしていると考えられる Ca について、Ca K-edge の XAFS 分析を実施した。得られた XANES スペクトルより、膜中の Ca は当初予想していた CaO とは著しく異なることが判明した。また、反応の前後で Ca の 1s から 3d への遷移を示す Pre-edge に違いが見られ、反応によって Ca 周りの原子の対称性が変化していることが示唆された。

Anomalous low energy nuclear transmutation reactions, for example transmutation of Cs into Pr, have been observed on the Pd complexes, which are composed of Pd and CaO thin film and Pd substrate, after subjecting the Pd complexes to D2 gas permeation. We assume that structure of Ca is important factor for this phenomenon. For clarification of this assumption, we analyzed XAFS of Ca K-edge. It turned out that structure of Ca in Pd complexes was remarkably different from CaO. We found pre-edge that meant the transition from Ca-1 to Ca-3d to be different before and after the reaction by XANES spectra. This suggests the change of the symmetry of the atom around Ca.

キーワード：
XANES, Ca K-edge, Pd, 重水素透過

１．はじめに：

Pd 基板上に作成した Pd-Ca 多層膜の表面に Cs 元素を添加して重水素ガスを透過すると、Cs が減少し新たに Pr が出現、増加してゆく現象が XPS により確認されている。[(1) (2) (3)]

これは、常温・常圧での重水素透過というシンプルな手法による元素変換を示しており学術的に新しい分野を創出する可能性が考えられるばかりでなく、昨今のエネルギー環境問題解決の視点からも、新エネルギー発生源、付加価値元素の生成、放射性元素の処理といった多くの応用が期待できるものである。

以上のような応用展開のためには、現時点で確認しているナノグラムオーダーという収量を大幅に増加させることが必須である。しかしながら、これまで主として、研究の重点を現象の確認（計測の信頼性向上）に向けてきたため、パラメーターサーベイ（材料条件・温度圧力条件等）が十分とは言えず、反応メカニズムについて解明が進んでいない状況である。そこで、生成量を増大させるためにも、早急に反応メカニズムを解明する必要があり、それには、反応場である Pd 多層膜の微細構造分析からのアプローチがキーになると考えた。

これまでの実験で、Pd 多層膜に CaO 層を挿入した場合にのみ元素変換反応が起こることがわかり、その再現性も確認されている。CaO が反応場である Pd の電子状態に何らかの変化を与えていると推測しているが、膜中の Ca が微量であること、また、多層膜が基板である Pd 表面の形状を反映して凹凸形状を持つことなどから分析が困難で、詳細は不明であった。

そこで、軽元素の分析に実績のある KEK-PF の光で XAFS 分析をすることにより、反応前後の膜で Ca の状態変化を捉え、元素変換反応における Ca の寄与を明らかにするところから、

反応メカニズム解明に繋がる手がかりを得る目的で本研究を実施した。

２．実験：

アニール処理及びエッチング処理を行ったPd基板（25ｍｍ×25ｍｍ×0.1ｍｍ）をイオンビームスパッタ装置のチャンバ内に設置し、膜厚をモニターしつつPdとCaOのターゲットの切り替えを行って積層膜を成膜している。得られた膜の積層構造はTEM（及びEDS）によりほぼ狙い通りであることが確認されている。（図1）

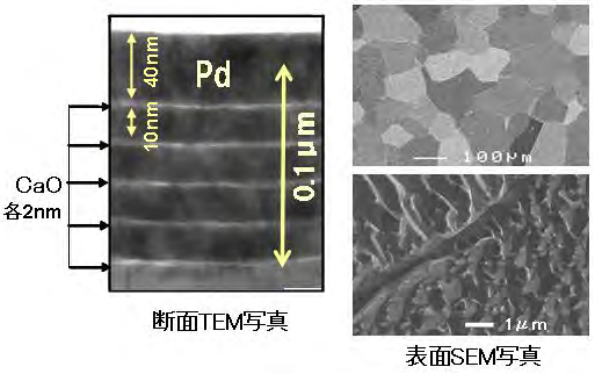

図１　Pd-CaO 多層構造観察結果

この膜の表面に電気化学的にCsを添加した後、図2のような実験装置にセットして重水素透過試験を行う。

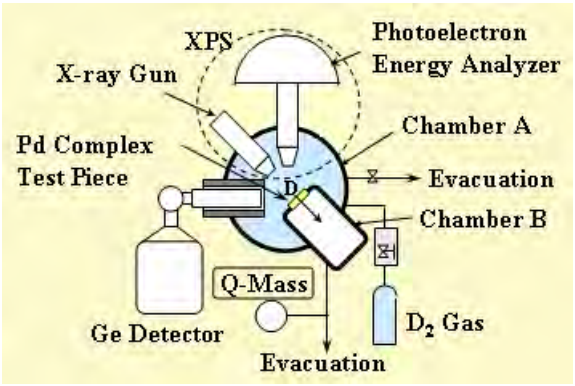

図2.　重水素透過実験装置

この試験の前後の試料についてCaK-edgeのXAFS分析を行い、Caの局所構造変化と元素変換量との相関を調べることにした。なお、比較のため数種のCa粉末試薬を用意し、同様にXAFSデータを取得した。

XAFS実験はKEK-PFのBL9Aにて行った。Ca K-edge（4038eV付近）を蛍光法（19素子SSD使用）により室温下で測定した。得られたﾃﾞｰﾀの積算を解析ｿﾌﾄREX2000で行い、詳細の解析にはAthena,Artemisを使用した。ｴﾈﾙｷﾞｰｷｬﾘﾌﾞﾚｰｼｮﾝはCa(OH)2試薬のWhite-Lineを4038.5eVとした。

膜中の Ca 濃度が微量であることから、Pd の影響を最小限に留め、かつ Ca の信号強度を確保するため、SSD の設定には詳細な調整を要した。また、Pd 基板に由来する回折線の影響を回避するためたびたび試料設置のやり直しを行うことになったが、最表層の Pd の影響を考慮して、斜入射試料台は使用せず、通常の 45 度入射よりやや浅い角度で測定を行った。

３．結果および考察：

まず、同じ成膜装置を使用して Pd-CaO の積層条件を変えた膜を作成し、（重水素透過試験はせず）XAFS 分析を行った。また、同時に CaO,Ca(OH)2,CaCO3,CaMoO4 の粉末試薬についても分析を行った。得られた XANES スペクトルを図 3 に示す。これより、膜中の Ca 構造は積層条件によらずほぼ一定であるものの、CaO 試薬に存在する 4031eV 付近のピークが見えておらず、CaO とは著しく異なるものであることが分かった。膜のスペクトルの特徴は 4028eV 付近に Pre-edge が存在していることにある。これは、Ca の 1s から 3d 電子への遷移を示しており、Ca の周囲の原子の何らかの対称性を持っていることを示している。（Ca1s から 3d の遷移は本来禁制だが、Ca 周囲の対称性によって許容遷移となるということで Ca の局所構造を知る目安とされている。）次に、このスペクトルより導いた $k^2\chi(k)$及び動径構造関数を図 4,5 に示した。積層条件を多少変えても、高エネルギー側の信号の S/N には向上が見られず、この試料での Ca-O の距離の議論は難しいと判断した。

我々が CaO に注目して膜中に挿入してきた目論見のひとつには、CaO の work function が小さく電子を放出しやすいことがあった。例えば Ca(OH)2 になると CaO に比べ work function が、大きくなることから、この分析によって初めて挿入した Ca が CaO と著しく異なるという結果を得たことは、反応メカニズムの仮説を検討する上で非常に重要と考えられた。

そこで、詳細を確認するため、スパッタ環境の異なる成膜装置（A : ｲｵﾝﾋﾞｰﾑｽﾊﾟｯﾀ装置従来使用機種、B : A と機種が異なるｲｵﾝｽﾊﾟｯﾀ装置、C : ﾏｸﾞﾈﾄﾛﾝｽﾊﾟｯﾀ装置）で膜を作成し、それらを用いて重水素透過試験を実施した試料についての XAFS 分析を行った。図 6 に XANES スペクトルを示す。試料の評価に先立ち、成膜に使用している CaO ターゲットの確認を行なったところ、4031eV 付近に CaO 構造に特徴的なピークが観とめられ、ほぼ変質がないことを確かめられた。

試料 A1,B1,C1 のスペクトルから、スパッタ装置を変えても作成される膜は同じ種類のものになり、CaO とは異なることがわかった。

ここで、A1 と A2,A3、B1 と B2、C1 と C2 を比較すると、重水素透過試験後に元素変換率の高かった膜のスペクトルは、試験前のスペクトルに存在する 4028eV 付近の Pre-edge ピークが消滅しており、元素変換反応の前後で Ca 周りの原子の対称性が変化していることがわかる。これは元素変換反応における Ca の何らかの寄与を示唆するものであると考えるが、詳細はまだ考察中である。図 3 で、この Pre-edge と同じものが CaMoO4 試薬のスペクトルで観測されていることから、CaMoO4 のクラスター計算も検討中で、こうした結果も含めて考察を深めていく。

４．まとめ：

元素変換反応で重要な役割を果たしている Ca について、XAFS 分析を行うことにより、反応前後の Ca の局所構造変化を初めて実分析データとして捉えることができた。本実験の結果は反応メカニズムの仮説を再検討する上で大きな手がかりとなる。

今後は計算的な検討も含め、収量増大につながる多層膜の構造適正化を目指したい。

参考文献

[1] “Elemental Analysis of Pd Complexes: Effects of D2 Gas Permeation” Y. Iwamura, M. Sakano and T. Itoh, *Japanese Journal of Applied Physics*, Vol. 41, pp. 4642-4650, 2002.

[2] 重水素透過による Pd 多層膜上での元素変換の観測”, 岩村康弘, 伊藤岳彦, 坂野充, 栗林志頭真, 固体物理 Vol. 39, pp. 203-210, 2004.

[3] Y. Iwamura, T. Itoh, M. Sakano, N. Yamazaki, S. Kuribayashi, Y. Terada and T. Ishikawa, “Observation of Surface Distribution of Products by X-ray Fluorescence Spectrometry during D2 gas permeation through Pd Complexes”, Proc of 12th Int. Conf. on Condensed Matter Nuclear Science, Nov. 27-Dec. 2, 2005, Yokohama, Japan, World Scientific, pp. 178-187, 2006.

成果発表状況：

未定

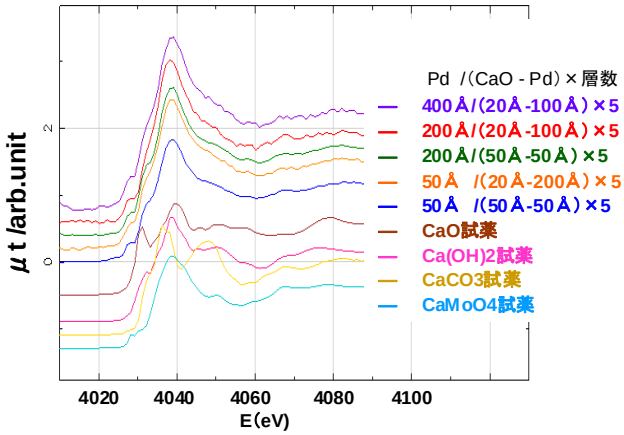

図 3　積層膜及び Ca 系試薬の Ca K-edge XANES

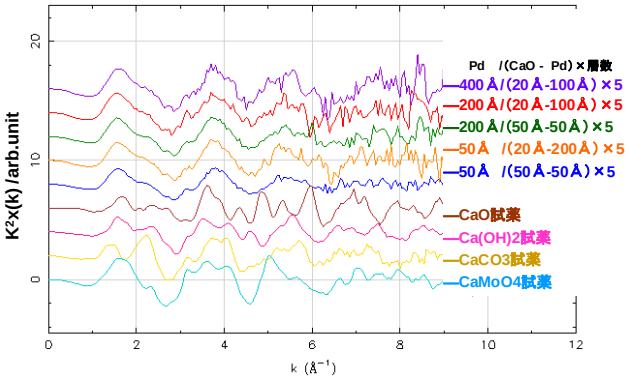

図 4　積層膜及び Ca 試薬の EXAFS 振動 $k^2\chi(k)$

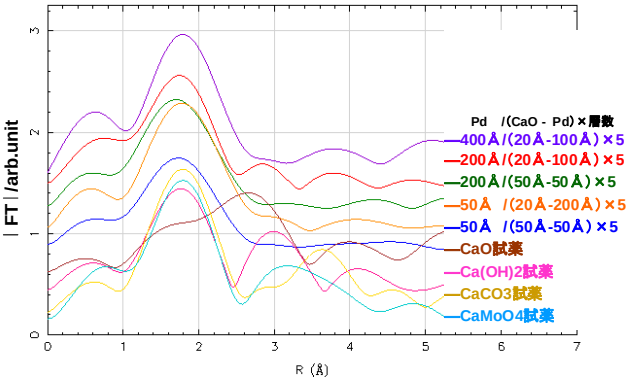

図 5　積層膜及び Ca 試薬の Ca 周りの動径構造関数

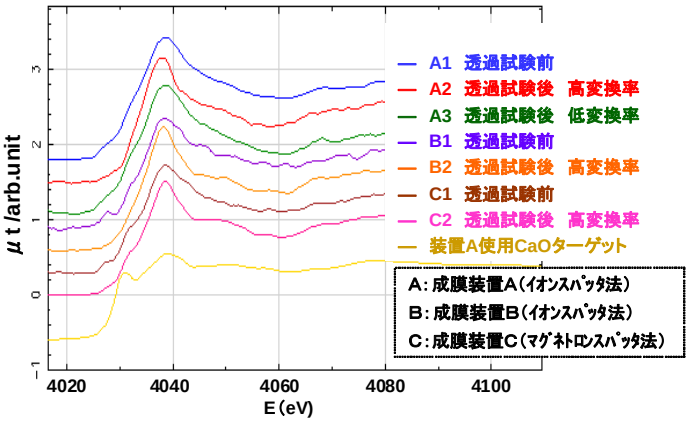

図 6　重水素透過試験前後の Ca K-edge XANES

先端研究施設共用イノベーション創出事業【産業戦略利用】

フォトンファクトリーの戦略的産業利用

課 題 番 号： 2008I007
研究責任者： 氏名　藤田孝、所属　東邦チタニウム株式会社
利 用 施 設： 高エネルギー加速器研究機構　放射光科学研究施設　BL-7C,12C
利 用 期 間： 2009 年３月～2010 年２月

チーグラー・ナッタ触媒の構造解明
Characterization of Ziegler-Natta Solid Catalyst

齋藤雅由 [1]、藤田孝 [1]、野村昌治 [2]、新田清文 [2]
Masayoshi Saito[1], Takashi Fujita[1],Masaharu Nomura[2],Kiyofumi Nitta

[1]東邦チタニウム株式会社、[2] 高エネルギー加速器研究機構
[1]TOHO TITANIUM Co., [2]KEK

アブストラクト：　マグネシウムーチタン型触媒中の活性点といわれているチタン元素の存在状態については不明であった。今回我々は、ＸＡＦＳを用いてチタンの存在状態を解明する目的で測定を試みたので報告する。

In this study, we investigated on the direct observation of Ti atom species in Ziegler-Natta solid catalysts with XAFS, which is owned by KEK, and tried to characterize the catalyst structure.

キーワード：　**Ziegler-Natta Solid Catalyst,XAFS,Ti atom**

１．はじめに：

チーグラー・ナッタ触媒から得られるポリエチレン（ＰＥ）およびポリプロピレン（ＰＰ）の世界的生産量は、現在では年間約１億トンにもおよび、５大汎用樹脂の中でも中核の位置づけとして捉えられており、今後も年１０％程度の成長があると報告がされている（図１）。

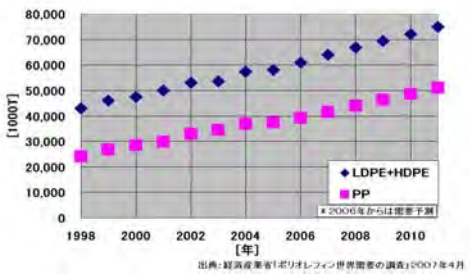

（上段：強磁場NMRと開発検出器、下段：従来NMR）

図１　　ＰＥ，ＰＰの世界的生産量

現在のＰＥおよびＰＰの研究開発の主要課題のひとつは、高強度や高剛性といった高性能ＰＥ，ＰＰの開発である。この開発を促進するためには精密な触媒設計とその設計を実現する触媒の開発が必要である。また、チーグラー・ナッタ触媒発見から６０年近くなり、種々の改良をなされているが、この触媒の主成分である塩化マグネシウム、四塩化チタンおよび電子供与体の相互作用については充分に判っていない。四塩化チタン中のチタン元素がＰＥ，ＰＰ重合の中心金属（活性点）と言われており、チタン元素、塩化マグネシウムおよび電子供与体との相互作用が正確に判れば、高機能ＰＥ，ＰＰ用触媒の設計に活用ができることを期待される。

２．実験：

ＸＡＦＳ測定については以下のようにして行った。

使用ビームライン：BL7C(3/18), BL12C(5/11)
測定吸収端：Ti K-edge(4.97keV)
測定法：透過法、蛍光法(Lytle)
サンプル調製：窒化ホウ素に混ぜて測定した。

エチレン重合は以下の条件で行った。
オートクレーブ=１．５リッターオートクレーブ
溶媒= ｎ－ヘプタン 700ｍｌ
Al/Ti=50
仕込み触媒量= 0.0176ｍｍｏｌ(Ti)
アルキルアルミニウム=トリエチルアルミニム
水素=３． ２liter
重合温度=８０℃-２時間-０． ８ＭＰａ

触媒合成は以下のように行った。
触媒合成（塩化マグネシウム／四塩化チタン・電子供与体錯体共粉砕触媒）
塩化マグネシウム 30g と四塩化チタン・電子供与体錯体 0.15mol を内容積１リッターのステンレス製振動ミルにて 0 時間、2 時間、5 時間および 20 時間共粉砕した。次にこれら粉砕物を、窒素置換されたフラスコ内に移し、遊離の四塩化チタンが無くなるまでヘプタンで洗浄・乾燥して触媒とした。試験番号と粉砕時間を図２に示す。

試験番号	粉砕時間（時間）
CP-11	0
CP-12	2
CP-13	5
CP-14	20

図２　塩化マグネシウム／四塩化チタン・電子供与体錯体共粉砕触媒の粉砕時間

比較として電子供与体を含まない触媒の合成を以下のように行った。
触媒合成（塩化マグネシウム／四塩化チタン共粉砕触媒）
塩化マグネシウム 30g と四塩化チタン 6.0ml を内容積１リッターのステンレス製振動ミルにて０時間、２時間、５時間および２０時間共粉砕した。次にこれら粉砕物を、窒素置換されたフラスコ内に移し、遊離の四塩化チタンが無くなるまでヘプタンで洗浄・乾燥して触媒とした。試験番号と粉砕時間を図３に示す。

試験番号	粉砕時間（時間）
CP-19	0
CP-20	2
CP-21	5
CP-22	20

図３　塩化マグネシウム／四塩化チタン共粉砕触媒の粉砕時間

高活性型触媒
電子供与体を添加しない方法で、JPN 特許 63310 の実施例 1 に準拠して触媒を合成した(CP-27)。

これらのチタン含有量を調べると、粉砕時間を長くすると、チタン含有量が増大していくことが判った（図４）。

試験番号	Ti 含有量（重量%）
CP-11	0.6
CP-12	3.5
CP-13	5.9
CP-14	8.6
CP-19	0.1
CP-20	1.2
CP-21	2.3
CP-22	4.3
CP-27	9.9

図４　　触媒中のチタン含有量

これらの触媒を用いてエチレン重合を行い活性の変化を調べた。結果を図５に示す。
結果、粉砕時間を長くするとエチレン重合活性が増大していくことが判った。

試験番号	エチレン重合活性 (g-PP/g-触媒)
CP-11	1500
CP-12	3300
CP-13	6200
CP-14	7400
CP-19	1100
CP-20	2200
CP-21	3000
CP-22	6700
CP-27	12000

図５　　エチレン重合結果

さらにより詳細な知見を得るためＸＡＦＳ測定を行いチタンの状態を確認することにした。

３．結果および考察：

結果

XANES を用いて測定を行った。Ziegler-Natta 触媒の吸収スペクトルと XANES 部分の拡大を図６に示す。

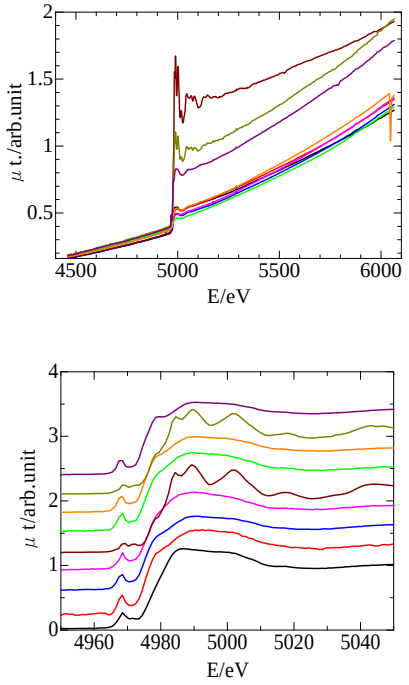

図　６　Ziegler-Natta 触媒の Ti K-edge 吸収スペクトル(上)と規格化吸収スペクトル(下)

おおよそ同程度の濃度に調整してある試料に対して edge-jump（吸収端前後の吸収係数の差、試料中の吸収原子の量と相関がある）が著しく異なっていた(図７)。

試料 (線色)	CP11 (黒)	CP12 (赤)	CP13 (青)	CP14 (桃)	
jump	0.14	0.12	0.11	0.08	
試料 (線色)	CP19 (茶)	CP20 (緑)	CP21 (橙)	CP22 (金)	CP27 (紫)
jump	0.95	0.05	0.13	0.51	0.37

図７　　edge-jump 結果

XANES の構造については pre-edge(4970eV 付近 1s→3d+Cl2p)、shoulder(4980eV 付近 1s→4s+Cl2p or 4p)、及び white line(1s→4p)の構造から試料の構造は 3 つのグループに分類できることが示唆される、すなわち

Group1、CP11

Group2、CP12,CP13, CP14,CP20,CP21,CP27

Group3、CP19,CP22

である。

それぞれの構造に対しての知見を得るために、参照物質の測定を行った。

【$TiCl_3$ 及び $TiCl_4$ のスペクトルの変化】

参照物質の内、$TiCl_3$ と $TiCl_4$ は測定中に XANES スペクトルに変化が見られた。過去の論文(例えば J.Phys.Chem.A,111(2007)5270、Phys.Rev. B 77(2008)235114)[1]を参照すると黒実線で描かれているスペクトルがそれぞれ $TiCl_3$ と $TiCl_4$ と予想される（図８）。

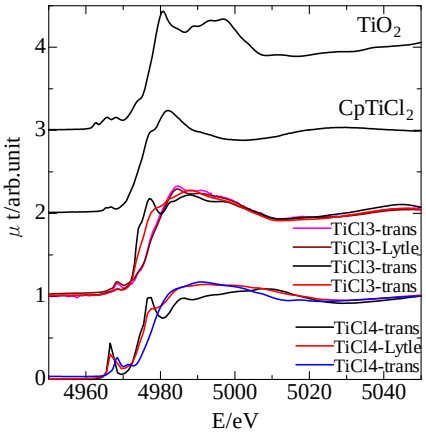

図 8　参照物質の Ti K-edge XANES

次に示す図９は実試料と Ti-Cl 結合を含む参照試料の XANES スペクトルである。

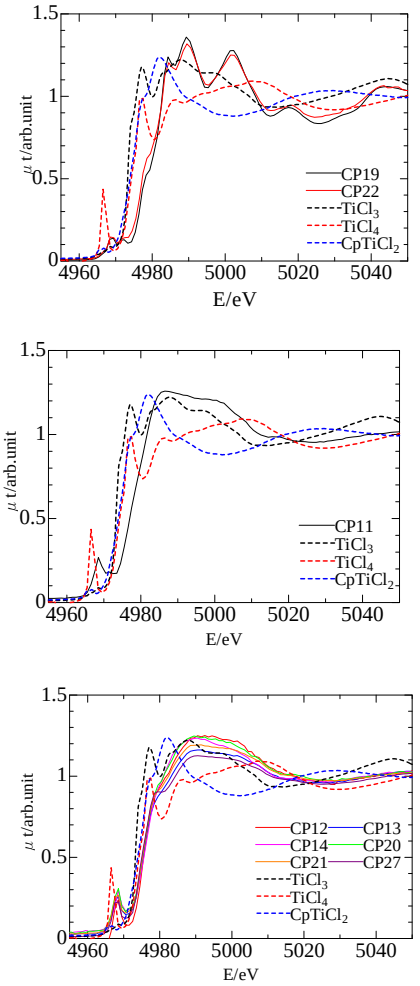

図 9　3 つの group の XANES と Ti-Cl 結合を含む参照試料の比較

これらの図から分かる通り、実試料のスペクトルは Ti-Cl 系の参照物質とは著しく形状が異なっており、実試料スペクトルの参照試料スペクトルによる最小自乗フィットからも、これらの参照試料がある割合で混合していない(スペクトルの再現ができない)ことが分かった。

考察

実試料のスペクトル(図６下)と $TiCl_4$ のスペクトル(図８)を見比べてみると、空気中の水と反応して変化していると予想される $TiCl_4$ のスペクトル(青線、赤線)と group1,group2 の実試料のスペクトルが非常によく似ているように見える。また group3 のスペクトルは
γ-TiO_2 と非常によく似ている（図１０）。

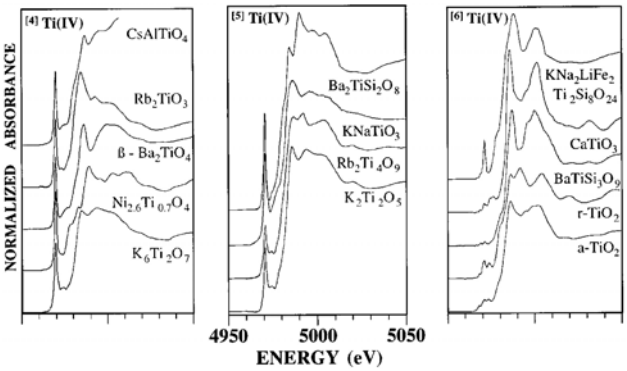

図 １０　Ti-O 配位の XANES スペクトル (Phys.Rev.B,56(1997)1809)

Ziegler-Natta 触媒の構造は Ti に Cl もしくは C が配位している構造という理解であったが、測定から得られたスペクトルは Ti-O の寄与が示唆されるスペクトルであった。

４．まとめ：

今回の測定結果、Ti-O 結合が生じたため測定が十分納得するものではなかった。Ti-O のる可能性としては、

① 触媒合成時触媒そのものが Ti-O 結合を含む

② PF 持ち込み時シールが不十分だった

③ XAFS 測定用試料成型時グローブボックスのガス置換、脱水が不十分だった
④ 測定中シールが不十分だった
ことが考えられる。
今後、上記の問題を解消すべく方法を考える必要がある。

参考文献

[1] J.Phys.Chem.A,111(2007)5270、Phys.Rev. B 77(2008)235114)

成果発表状況：
無し。

7C, NW10A/2009G001

XAFS Study of Charcoal-Supported Palladium and Nickel Bimetal Catalysts for Lignin Gasification in Supercritical Water

Aritomo Yamaguchi, Norihito Hiyoshi, Osamu Sato, and Masayuki Shirai*
Research Center for Compact Chemical System, National Institute of Advanced Industrial Science and Technology (AIST), Sendai 983-8551, Japan

1 Introduction

Lignin is a major fraction of woody biomass and a polymer having aromatic compounds as monomer units. The gasification of lignin to hydrogen and methane is needed for its efficient use as a high quality energy source. Supercritical water (T_c = 647.3 K, P_c = 22.1 MPa) gasification of lignin is a promising technique because of a decrease of lignin gasification temperature. We have reported that charcoal-supported ruthenium (III) salts were reduced to form highly-dispersed ruthenium metal particles during the lignin gasification, which were active for the lignin gasification [1]. We applied palladium and nickel salts to the lignin gasification in order to prepare highly-dispersed Pd-Ni alloy particles on charcoal support during the lignin gasification and to investigate activity of Pd-Ni alloy, compared with the individual monometals [2].

2 Experiment

The catalysts used in this work were prepared by an impregnation method using activated charcoal powder and aqueous solutions of tetraamminepalladiuum (II) nitrate or nickel (II) nitrate. The supported binary metal salt catalysts (denoted as Pd(II)-Ni(II)/C) were prepared by physically mixing two kinds of supported monometal salt catalysts (denoted as Pd(II)/C and Ni(II)/C).

Gasification of lignin was carried out in a batch reactor. A product yield (C%) was calculated based on the carbon amount of reactant lignin [1,2].

X-ray absorption near edge structure (XANES) and extended X-ray absorption fine structure (EXAFS) measurements were performed using a synchrotron radiation ring in transmission mode at AR-NW10A, PF-KEK. The EXAFS spectra were analyzed by the UWXAFS package. The backscattering amplitudes and phase shifts were calculated by the FEFF8 code.

3 Results and Discussion

The gas yields from the lignin gasification over the Pd(II)-Ni(II)/C catalysts were higher than the linear combination of gas yields over the individual monometals (Fig. 1), indicating that the Pd(II)-Ni(II)/C binary salts catalysts showed the synergetic effect of Pd-Ni. The main peaks in Fourier transforms of k^3-weighted EXAFS for Pd(II)-Ni(II)/C(3:1), Pd(II)-Ni(II)/C(1:1), and Pd(II)-Ni(II)/C(1:3) gradually decrease and shift to the shorter distance with the decrease of Pd/Ni ratio (Fig. 2), indicating the formation of Pd-Ni bond in addition to Pd-Pd bond. EXAFS and XRD analysis show the formation of small Pd-Ni alloy particles, which are the active sites for the lignin gasification.

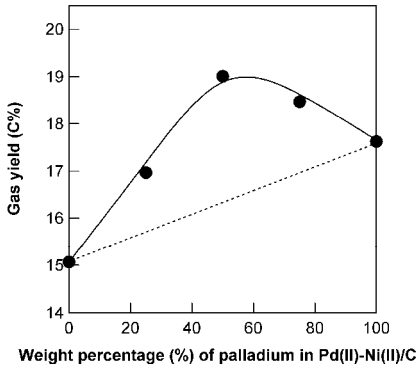

Fig. 1: Gas yield of lignin gasification in supercritical water at 673 K for 1 h over Ni(II)/C, Pd(II)-Ni(II)/C, and Pd(II)/C catalysts.

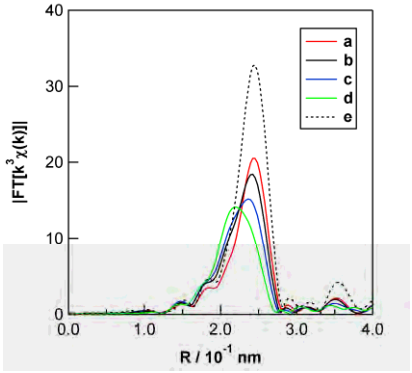

Fig. 2: Fourier transforms of k^3-weighted Pd K-edge EXAFS spectra of Pd(II)-Ni(II)/C and Pd(II)/C catalysts after lignin gasification in supercritical water at 673 K for 1 h (phase shift uncorrected). (a) Pd(II)/C, (b) Pd(II)-Ni(II)/C(3:1), (c) Pd(II)-Ni(II)/C(1:1), (d) Pd(II)-Ni(II)/C(1:3), and (e) reference Pd metal foil.

References

[1] (i) A. Yamaguchi and M. Shirai *et al.*, Energy Fuels **22** (2008) 1485; (ii) A. Yamaguchi and M. Shirai *et al.*, Catal. Lett. **122** (2008) 188; (iii) A. Yamaguchi and M. Shirai *et al.*, Catal. Today **146** (2009) 192.

[2] A. Yamaguchi and M. Shirai *et al.*, Chem. Lett. **39** (2010) 1251.

* m.shirai@aist.go.jp

7C, NW10A/2009G001

Structural Study of Charcoal Supported Noble Metal Salt Catalysts for Gasification of Organosolv-lignin in Supercritical Water

Aritomo Yamaguchi, Norihito Hiyoshi, Osamu Sato, and Masayuki Shirai*
Research Center for Compact Chemical System, National Institute of Advanced Industrial Science and Technology (AIST), Sendai 983-8551, Japan

1 Introduction

Biomass and organic wastes have attracted much attention as renewable energy sources because the green house effect of carbon dioxide from the combustion of fossil fuel has to be reduced. Lignin is a major fraction of woody biomass and the gasification of lignin to hydrogen and methane is needed for its efficient use. We have reported that charcoal-supported ruthenium (III) salts were reduced to form highly-dispersed ruthenium metal particles during the lignin gasification, which were active for the lignin gasification [1]. We investigated the catalytic activity for the lignin gasification of various charcoal supported metal salt catalysts and investigated the structural change for metal species by X-ray absorption near edge structure (XANES) and extended X-ray absorption fine structure (EXAFS) analyses [2].

2 Experiment

The various catalysts used in this work were prepared by an impregnation method using activated charcoal powder and solutions of metal salts. Gasification of lignin was carried out in a batch reactor [1,2].

XANES and EXAFS measurements were performed using a synchrotron radiation ring in transmission mode at AR-NW10A, PF-KEK. The EXAFS spectra were analyzed by the UWXAFS package. The backscattering amplitudes and phase shifts were calculated by the FEFF8 code.

3 Results and Discussion

Fig. 1 shows XANES spectra for supported rhodium salt catalysts before and after lignin gasification in supercritical water at 673 K. The XANES spectra of the $RhCl_3$/C, $Rh(NO_3)_3$/C, and $Rh(acac)_3$/C (Fig. 1 (a)) before the lignin gasification changed drastically after the gasification (Fig. 1 (b)) and the XANES spectra after the gasification were the same as the rhodium metal. These results indicate that rhodium salt species were reduced to metal states during the lignin gasification. The same phenomena were observed in ruthenium, platinum, and palladium catalysts. EXAFS analysis also showed that small metal particles were formed on the charcoal support after the gasification for the supported metal salt catalysts without chloride anion and showed higher activities for the lignin gasification. Lower activities and deactivation of supported metal chloride catalysts were caused by the smaller number of metal sites and surface poisoning by chloride anions.

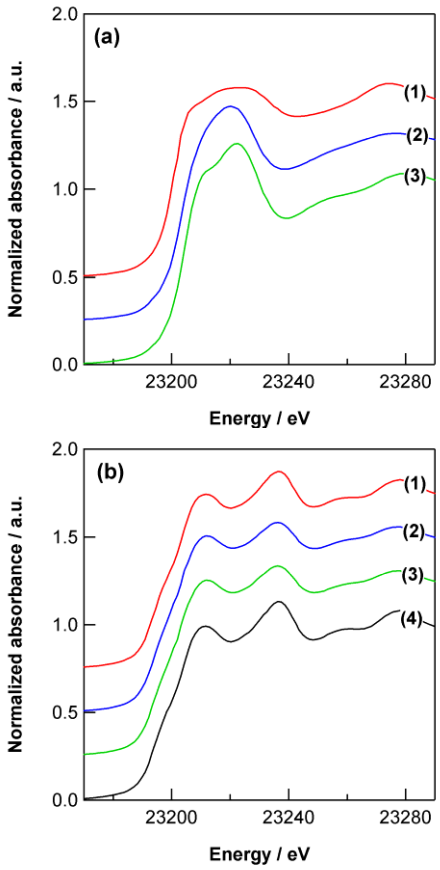

Fig. 1: XANES spectra for supported metal salt catalysts before and after lignin gasification in supercritical water at 673 K. (a) Rh K-edge: (1) $RhCl_3$/C, (2) $Rh(NO_3)_3$/C, and (3) $Rh(acac)_3$/C before the gasification, and (b) (1) $RhCl_3$/C, (2) $Rh(NO_3)_3$/C, and (3) $Rh(acac)_3$/C after the gasification (1 h), and (4) rhodium metal foil.

References

[1] (i) A. Yamaguchi and M. Shirai *et al.*, Energy Fuels **22** (2008) 1485; (ii) A. Yamaguchi and M. Shirai *et al.*, Catal. Lett. **122** (2008) 188; (iii) A. Yamaguchi and M. Shirai *et al.*, Catal. Today **146** (2009) 192; (iv) A. Yamaguchi and M. Shirai *et al.*, Chem. Lett. **39** (2010) 1251.

[2] A. Yamaguchi and M. Shirai *et al.*, Topics Catal. in press.

* m.shirai@aist.go.jp

9C, BL12C/2009G076

XAFS Characterization of Re-Pt Bimetallic Catalyst in ZSM-5 Zeolite for Selective Benzene Oxidation

Shin-ichi NAGAMATSU[1,2], Mizuki TADA[1], Takehiko SASAKI[3], Linsheng WANG[2], Yasuhiro IWASAWA*[2]

[1] Institute for Molecular Science, Myodaiji, Okazaki, Aichi 444-8585, Japan.
[2] University of Electro-Communications, Chofu, Tokyo 182-8585, Japan.
[3] The University of Tokyo, Kashiwanoha, Chiba 277-8561, Japan.

Introduction

Oxide-supported metal complexes are expected to show unique and tremendous catalysis and to possess the great advantages of both homogeneous and heterogeneous catalysts. We have found that ZSM-5-supported Re-Pt bimetallic catalysts are active for selective benzene oxidation to phenol with NH_3.[1] The oxidation states and local coordination structures of the supported Re-Pt bimetallic catalysts pretreated under different conditions were investigated by Re L_{III}-edge XANES and EXAFS, and the determined structural parameters were compared to catalytic performances for the phenol synthesis by benzene hydroxylation.

Experimental

ZSM-5-supported Re-Pt bimetallic catalysts were prepared by ion exchange with $[NH_3]_4Pt(NO_3)_2$ in water, followed by filtering and drying, and the subsequent impregnation of methyltrioxorhenium in ethanol solution. After calcination at 773 K, the samples were treated with a flow of NH_3 or a flow of an NH_3-O_2-bezene mixture to activate the catalyst for the selective oxidation of benzene.

Re L_{III}-edge XAFS spectra were measured at 20 K in a transmission mode with a Si(111) channel-cut double-crystal monochrometer at the BL-9C and BL-12C stations, using ion chambers with N_2(85%)/Ar(15%) and Ar(100%) for I_o and I_t, respectively. XAFS spectra were also measured in a fluorescence mode using a Lytle detector with Ar(100%) for I_f. Phase shifts and backscattering amplitudes were calculated by the FEFF8.0 code. EXAFS data were fitted with IFEFFIT in *R*-space.

Results and Discussion

Figure 1 (left) shows XANES spectra at Re L_{III}-edge for Re(2.5 wt%)-Pt(2.1 wt%)/ZSM-5 samples pretreated with O_2 at 773 K for 0.5 h, NH_3 at 553 K for 2 h, NH_3-O_2-benzene at 493 K for 1 h, and NH_3-O_2-benzene at 493 K for 1 h & H_2O-benzene at 493 K for 18 min. The catalysts pretreated with O_2 at 773 K for 0.5 h, with NH_3-O_2-benzene at 493 K for 1 h, and with NH_3-O_2-benzene at 493 K for 1 h & H_2O-benzene at 493 K for 18 min were similar to each other, which indicate an oxidized Re state.

Figure 1 (right) shows the Fourier transform of EXAFS data for the Re(2.5 wt%)-Pt(2.1 wt%)/ZSM-5 catalyst pretreated with O_2 at 773 K. The EXAFS Fourier transform was fitted by Re=O at 0.176 nm (CN: 3.3) and Re-O at 0.209 nm (CN: 0.6), which indicates a monomeric $[ReO_4]$ structure bonded to ZSM-5 pore wall.

Figure 2 shows the EXAFS Fourier transform and fitting result for the catalyst after NH_3 pretreatment at 553 K for 2 h, where a cluster formation was suggested by the presence of Re-Re (partially Pt) bonds at 0.270 nm (CN: 2.4) and 0.300 nm (CN: 0.7) besides Re=O at 0.174 nm and Re-O at 0.199 nm. It is suggested that the catalyst after NH_3 pretreatment possesses a cluster structure, but the catalyst in the steady state reaction for the phenol synthesis decomposes to distorted $[ReO_x]$ monomers.

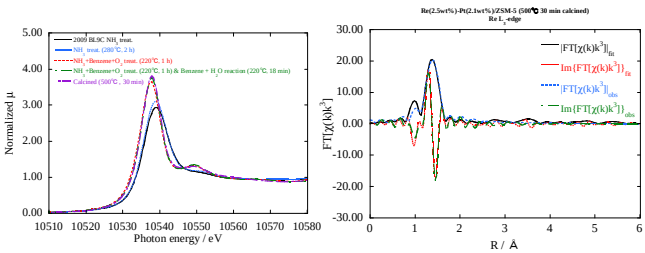

Fig.1 (left) Re L_{III}-edge XANES spectra and (right) EXAFS Fourier transforms for Re(2.5 wt%)-Pt(2.1 wt%)/ZSM-5.

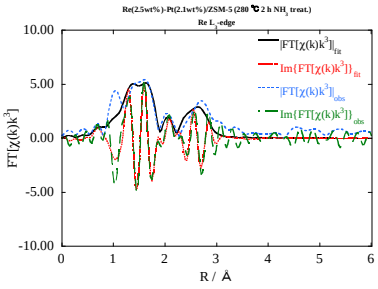

Fig.2
Re L_{III}-edge EXAFS Fourier Transforms for the NH_3-pretreated Re (2.5 wt%)-Pt(2.1 wt%) /ZSM-5 catalyst.

Reference

[1] 王林勝, 唯美津木, 永松伸一, 佐々木岳彦, 岩澤康裕, *触媒* **54**, 147-149, 2012.

* iwasawa@pc.uec.ac.jp

9C, 12C/2009G076, 2010G021

Local Coordination Structures of γ-Al_2O_3-Supported Ir Dimer for Surface-Assisted Transfer Hydrogenation Catalysis

Satoshi MURATSUGU*[1] and Mizuki TADA[1]
[1] Institute for Molecular Science, Myodaiji, Okazaki, Aichi 444-8585, Japan.

Introduction

A novel oxide-supported Ir dimer, which was found to be active for transfer hydrogenation of aromatic ketones, was prepared on a γ-Al_2O_3 surface. Detail characterization of the supported Ir dimer revealed the surface-assisted transfer hydrogenation catalysis on the supported Ir dimer catalyst. Local coordination structures of the supported Ir dimers were investigated by Ir L_{III}-edge XAFS.

Experimental

An Ir dimer $[Ir_2\{\eta^5\text{-}C_5(CH_3)_5\}_2(\mu\text{-}CH_2)_2]$ (**Ir_2**) was impregnated on several oxide supports (γ-Al_2O_3, SiO_2, and MgO) and reacted with surface hydroxyl groups on these surfaces at 473 K for 2 h (**Ir_2/γ-Al_2O_3**, **Ir_2/SiO_2**, and **Ir_2/MgO**). Hydride intermediate Ir dimer was prepared by the reaction of the supported Ir dimer on γ-Al_2O_3 and isopropanol at 343 K (**Ir_2-H_2/γ-Al_2O_3**), and subsequent reaction with acetopheone was performed in toluene at 343 K (**Ir_2-Rxn1/γ-Al_2O_3**).

Ru K-edge XAFS was measured at BL9C and BL12C stations with Si(111) double crystal monochrometer. Ionization chambers filled with pure N_2 and Ar gases were used to monitor the incident and transmitted X-rays, respectively. EXAFS spectra were analyzed using REX2000, Ver. 2.3.3, Rigaku. Curve-fitting analysis was carried out in *k*-space and k^3-weighted EXAFS oscillations were Fourier transformed into *R*-space. The fitting parameters were coordination number (CN), interatomic distance (*R*), Debye–Waller factor (σ^2; mean-square-displacement), and the correction-of-edge energy (ΔE_0). Phase shifts and backscattering amplitudes for Ir–Ir and Ir–C ($C_5(CH_3)_5$) were calculated by using FEFF8 code.

Results and Discussion

The local coordination structure of **Ir_2/γ-Al_2O_3** was investigated by the curve-fitting analysis of Ir L_{III}-edge EXAFS data using the results of quantitative analysis of the coordinating ligands (Table 1). The precursor **Ir_2**, whose coordination structure was determined by X-ray diffraction, was successfully fitted and the EXAFS oscillation of **Ir_2/γ-Al_2O_3** was fitted well with four contributions: Ir–Ir at 0.269 ± 0.001 nm (CN = 1.2 ± 0.2), Ir–C ($C_5(CH_3)_5$) at 0.245 ± 0.001 nm (CN = 5.0 ± 0.7), Ir–O at 0.212 ± 0.001 nm (CN = 3.2 ± 0.2), and Ir···Al at 0.319 ± 0.001 nm (CN = 1.9 ± 0.2). The Ir–Ir bond distance at 0.269 ± 0.001 nm indicates that the Ir=Ir bond of **Ir_2** was stretched to a single Ir–Ir bond on the γ-Al_2O_3 surface. The CN of Ir···Al (1.9 ± 0.2) at 0.319 ± 0.001 nm suggested that there were two O(Al) species coordinated to the Ir center. The CN of Ir–O/C was estimated to be 3.2 ± 0.2, where the oxygen and carbon contributions cannot be discriminated by EXAFS curve fitting. The quantitative analysis by GC indicated that one μ-CH_2 ligand remained on the Ir dimer (the CN of Ir–C (μ-CH_2) = 1), and hence the CN of Ir–O was estimated to be 2, which was similar to that of Ir···Al (1.9 ± 0.2).

Ir L_{III}-edge EXAFS revealed that **Ir_2-H_2/γ-Al_2O_3** maintained its original dimeric structure with the Ir–Ir bond at 0.267 ± 0.001 nm (CN = 0.9 ± 0.1). It is to be noted that the CN of Ir···Al dropped from 1.9 ± 0.2 at 0.319 ± 0.001 nm to 1.2 ± 0.2 at 0.321 ± 0.001 nm. The CN of Ir–O/C was also reduced from 3.2 ± 0.2 (0.212 ± 0.001 nm) to 2.3 ± 0.2 (0.212 ± 0.001 nm), indicating that the CN of Ir–O(Al) was reduced from 2 to 1 under the consideration of the Ir–C (μ-CH_2) contribution (CN = 1). These results suggest that the bridged Ir–$(OAl)_2$–Ir bonds in the **Ir_2/γ-Al_2O_3** became a monodentate Ir–O(Al) bond in each Ir center to form **Ir_2-H_2/γ-Al_2O_3**. It was proposed that the interfacial bond transformation between the Ir dimer (**Ir_2/γ-Al_2O_3**) and the γ-Al_2O_3 surface promoted the formation of the dihydride Ir complex on γ-Al_2O_3 as an intermediate in the transfer hydrogenation.

Table 1 Structural Parameters Determined by Curve-Fitting Analysis of Ir L_{III}-edge EXAFS for **Ir_2/γ-Al_2O_3**, **Ir_2-H_2/γ-Al_2O_3**, and **Ir_2-Rxn1/γ-Al_2O_3**

Shell	CN	Distance /nm	ΔE_0 /eV	σ^2 /10^{-5} nm^2
Ir_2/γ-Al_2O_3 (R_f =0.15%)				
Ir–Ir	1.2 ± 0.2	0.269 ± 0.001	-1	6
Ir–C ($C_5(CH_3)_5$)	5.0 ± 0.7	0.245 ± 0.001	-6	9
Ir–O	3.2 ± 0.2	0.212 ± 0.001	17	5
Ir···Al	1.9 ± 0.2	0.319 ± 0.001	20	3
Ir_2-H_2/γ-Al_2O_3 (R_f =0.51%)				
Ir–Ir	0.9 ± 0.1	0.267 ± 0.001	-2	4
Ir–C ($C_5(CH_3)_5$)	4.9 ± 0.7	0.246 ± 0.001	-10	8
Ir–O	2.3 ± 0.2	0.212 ± 0.001	17	4
Ir···Al	1.2 ± 0.2	0.321 ± 0.001	21	4
Ir_2-Rxn1/γ-Al_2O_3 (R_f =0.13%)				
Ir–Ir	1.1 ± 0.1	0.268 ± 0.001	0	5
Ir–C ($C_5(CH_3)_5$)	4.9 ± 0.7	0.242 ± 0.001	-9	8
Ir–O	3.2 ± 0.2	0.213 ± 0.001	16	6
Ir···Al	2.2 ± 0.3	0.319 ± 0.001	20	5

Measured at 20 K. k = 30 – 150 nm^{-1}, R = 0.14 – 0.31 nm.

Reference

[1] M. Tada, S. Muratsugu, M. Kinoshita, T. Sasaki, Y. Iwasawa, *J. Am. Chem. Soc.* **2010**, *132*, 713.

* smura@ims.ac.jp

7C/2009G177

Determination of the specific microstructure of iron titanate catalyst for NH_3-SCR of NO_x by XAFS method

Fudong Liu[1], Kiyotaka Asakura[2], Pengyang Xie[3], Jianguo Wang[3], Hong He*[1]
[1]Research Center for Eco-Environmental Sciences, Chinese Academy of Sciences, Beijing 100085, China
[2]Catalysis Research Center, Hokkaido University, Sapporo 001-0021, Japan
[3]College of Chemical Engineering and Materials Science, Zhejiang University of Technology, Hangzhou 310032, China

Introduction

In our previous study, we have successfully developed a novel and environmental-friendly iron titanate ($FeTiO_x$) catalyst prepared by conventional co-precipitation method, which showed high activity, N_2 selectivity and H_2O/SO_2 durability for the selective catalytic reduction of NO_x with NH_3 (NH_3-SCR) in the medium temperature range (200-400 ^oC).[1-4] This $FeTiO_x$ catalyst is promising to be used in the deNO_x process for flue gas and diesel engine exhaust for environmental protection. We deduced that the iron titanate crystallite with specific Fe-O-Ti structure, but not aggregated Fe_2O_3 oxide particles, was the real active phase in NH_3-SCR reaction. However, no direct evidence was obtained using XRD, UV-vis DRS, TEM and Raman spectroscopy *etc.* due to the poor crystallinity of this catalyst both in the bulk phase and on the surface. In order to understand in-depth the structural nature of the active phase in this $FeTiO_x$ catalyst for further catalyst redesign and activity improvement, more powerful characterization method for determining the local structure of catalytic materials should be applied, such as the XAFS method. In this study, using XANES and EXAFS combined with theoretical calculation, the specific microstructure of $FeTiO_x$ catalyst will be systematically determined.[5]

Experimental

The XAFS of Fe, Ti K-edges were recorded in a transmission mode on BL-7C beam line at PF, KEK, Japan. Data were analyzed using the REX2000 program. The geometry optimization of TiO_2, Fe_2O_3 and Fe_2TiO_5 crystals using DFT were carried out using Dmol3 module in Materials Studio software package.

Results and discussion

The NH_3-SCR activity at low temperatures over catalysts prepared by different precursors and methods decreased in the following sequence: $FeTiO_x$-$Ti(SO_4)_2$ >> Fe_2O_3/TiO_2 > $FeTiO_x$-$TiCl_4$. New highly active species with specific structure should be formed in the most active $FeTiO_x$-$Ti(SO_4)_2$. As confirmed by XANES, well crystallized Fe_2O_3 and TiO_2 exists in Fe_2O_3/TiO_2 catalyst, and $FeTiO_x$-$Ti(SO_4)_2$ catalyst possessed octahedrally coordinated Fe^{3+} and Ti^{4+} species with severe structure distortion which were mainly from iron titanate crystallite. As for $FeTiO_x$-$TiCl_4$ catalyst, only half of the Fe^{3+} species in this catalyst was in the form of active iron titanate crystallite, and accordingly the low temperature NH_3-SCR activity over $FeTiO_x$-$TiCl_4$ catalyst was much lower than that over $FeTiO_x$-$Ti(SO_4)_2$ catalyst but higher than that over Fe_2O_3/TiO_2 catalyst. The XANES results and DFT calculation also confirmed the presence of electronic inductive effect between Fe^{3+} and Ti^{4+} species, which effectively reduced the electron density around the Fe^{3+}, thus leading to the enhancement of NO adsorption, oxidation ability and finally the low temperature NH_3-SCR activity.

Fig. 1 depicts the Fourier transform of filtered k^3-weighted EXAFS oscillations of Fe-K and Ti-K edges into R space. Fe_2O_3/TiO_2 catalyst has similar coordination peaks of Fe-K and Ti-K edges as those of hematite Fe_2O_3 and anatase TiO_2, respectively. As suggested by XANES results, $FeTiO_x$-$TiCl_4$ catalyst shows peaks in the second coordination shells similar to those of Fe_2TiO_5, Fe_2O_3 and rutile TiO_2. However, these peaks are much smaller due to the coexistence of iron titanate crystallite. For $FeTiO_x$-$Ti(SO_4)_2$ catalyst, the intensity of the second coordination peaks of both Fe and Ti was rather low, implying a crystallite state of this sample again. It is noteworthy that only one single peak appeared for the second coordination shells of both Fe and Ti species in $FeTiO_x$-$Ti(SO_4)_2$ catalyst, which was totally different from those of reference samples and the other two catalysts.

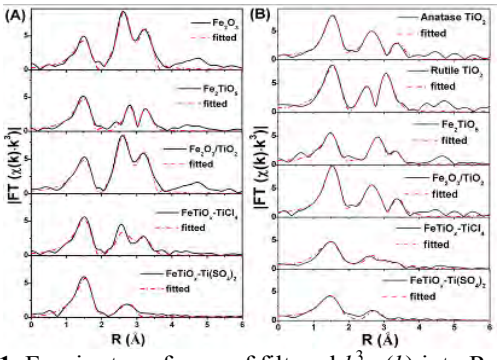

Fig. 1. Fourier transforms of filtered $k^3 \bullet \chi(k)$ into R space of (A) Fe-K and (B) Ti-K edges in different samples.

The single peak in the second coordination shells of $FeTiO_x$-$Ti(SO_4)_2$ catalyst can be assigned to Fe^{3+}-O-Ti^{4+} linkage suggested by the XANES results. The curve fitting results indicate the Fe^{3+}-O-Ti^{4+} distance as 3.09 ± 0.04 Å, which agrees well with the edge shared Fe-O-Ti and Ti-O-Fe structures. Compared to the edge shared Fe-O-Ti structure in well crystallized Fe_2TiO_5 reference sample, the bond distances of Fe-O-Ti and Ti-O-Fe in this catalyst is 0.09 Å shorter. This is also probably related with the nano effect of $FeTiO_x$-$Ti(SO_4)_2$ catalyst in poor crystallinity, of which the catalyst surface possessed a large proportion of unsaturated coordination atoms with shorter average bond distances. The stronger interaction between Fe^{3+} and Ti^{4+} species in this catalyst induces the shift of Fe-K absorption edge to higher energy than that of Fe_2TiO_5. Fe^{3+} species must be more positively charged on the catalyst surface and is probably responsible for its highest NH_3-SCR activity. After curve fitting, the coordination numbers of Fe-O-Ti and Ti-O-Fe bonds are 2.6 and 2.0, indicating again the small particle size or crystallite phase of iron titanate species in this catalyst.

In order to further confirm the size of the crystallite domains of iron titanate species in $FeTiO_x$-$Ti(SO_4)_2$ catalyst, the Fe-K EXAFS and Ti-K EXAFS were calculated by FEFF8.4 code using iron titanate crystallite with different atom numbers as models. Besides of the Fe-O and Ti-O coordination peaks in the first shell, only Fe-O-Ti and Ti-O-Fe coordination peaks in the second shell were observed when the atom numbers in the iron titanate crystallite were set to 15, which was mainly due to the inclusion of Fe^{3+}-O-Ti^{4+} linkages with edge shared oxygens in the adopted model. These results are consistent with the EXAFS data of $FeTiO_x$-$Ti(SO_4)_2$ catalyst, in which the only Fe-O-Ti and Ti-O-Fe coordination peaks in the second shell were also observed. However, further increasing the atom numbers to 27 resulted in the appearance of another two shoulder peaks in the second coordination shells of Fe and Ti species, which were mainly due to the inclusion of Fe^{3+}-O-M and Ti^{4+}-O-M (M = Fe or Ti) linkages with corner shared oxygens. These results clearly suggest that the crystallite domains of iron titanate species in $FeTiO_x$-$Ti(SO_4)_2$ catalyst were mainly composed by *ca.* 15 atoms, which is in well agreement with the very small particle size of iron titanate crystallite that was concluded from EXAFS curve fitting results.

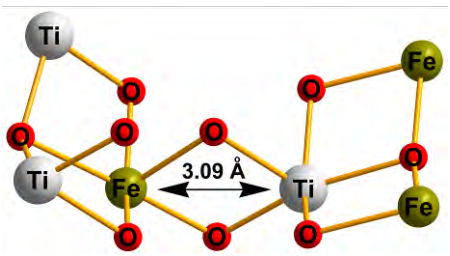

Fig. 2. Proposed model of homogeneous edge shared Fe^{3+}-$(O)_2$-Ti^{4+} structure in iron titanate catalyst.

Based on XANES and EXAFS results, a structure model of iron titanate catalyst $FeTiO_x$-$Ti(SO_4)_2$ derived from $Ti(SO_4)_2$ precursor is proposed, as shown in Fig. 2. In this model, the edge shared Fe-O-Ti structure can be denoted as Fe^{3+}-$(O)_2$-Ti^{4+}, where Fe^{3+} and Ti^{4+} species are connected with two edge shared oxygen atoms with shorter Fe-Ti bond distance than that in well crystallized Fe_2TiO_5. This special structure is in crystallite state, *i.e.* iron titanate with very small particle size. In other words, the active phase in $FeTiO_x$-$Ti(SO_4)_2$ catalyst is macroscopically disordered but microscopically ordered. In this active phase, Fe^{3+} and Ti^{4+} species was strongly linked through edge shared fashion, and the electron density around the Fe^{3+} species is effectively reduced by the surrounding Ti^{4+} ions, which is beneficial to the enhancement of NO adsorption, oxidation ability and thus the low temperature NH_3-SCR activity. The presence of Fe^{3+}-$(O)_2$-Ti^{4+} structure in $FeTiO_x$-$Ti(SO_4)_2$ catalyst may also be responsible for its high resistance to SO_2 poisoning due to the low decomposition temperature of sulfate species on Ti^{4+}. In the future study, we can stabilize this structure onto some catalyst supports with large surface areas for practical use, such as the deNO_x process for flue gas in coal-fired power plants and diesel engine exhaust for environmental protection.

References

[1] F. Liu et al., Chem. Comm. 17, 2043 (2008).
[2] F. Liu et al., Appl. Catal. B 96, 408 (2010).
[3] F. Liu et al., J. Phys. Chem. C 114, 16929 (2010).
[4] F. Liu et al., Appl. Catal. B 164, 488 (2011).
[5] F. Liu et al., Catal. Today, in press (2012).

* honghe@rcees.ac.cn

NE3A/2009G502

二重構造の球状錯体の合成
Synthesis of Sphere-in-Sphere Complex

佐藤宗太 [1*], 孫　慶福 [1], 村瀬隆史 [1], 藤田　誠 [1,2]
[1] 東京大学大学院工学系研究科、〒113-8656 文京区本郷 7-3-1
[2]JST-CREST

1　はじめに

二座の折れ曲がった配位子(L: ligand)と、平面四配位性のパラジウム(II)イオン(M: metal ion)とを混合して自己組織化すると、$M_{12}L_{24}$ 組成の球状錯体が得られる[1]。配位子の折れ曲がり角度が同一である大きな配位子と小さな配位子を、それぞれパラジウム(II)イオンと自己組織化させた場合は、それぞれ大きな球状錯体と小さな球状錯体が得られる。しかし、これらの配位子を連結した場合、同じ配位能力の配位子が混在する状態となるために、単一の生成物を得ることは一般に困難である。

今回、球状構造を作りやすい剛直な配位子構造を用い、適切な長さを持つ柔軟なリンカーをで大小 2 種類の配位子を連結することで、二重球構造の錯体合成をめざした。分子モデルシミュレーションを併用して、四座の配位子 **1** を設計した。

2　実験

大小 2 種類の配位子を共有結合性のリンカーで連結した配位子 **1** を合成し、Pd(II)イオンとの自己組織化を検討した（図 1）。NMR, MS による構造決定を行い、大きな配位子は大きな球状錯体を、小さな配位子は小さな球状錯体を形成し、リンカーによって大きな球に小さな球が閉じ込められた二重球構造の生成物 **2** であることがわかった。貧溶媒である酢酸エチルを蒸気拡散することで単結晶を得ることができ、放射光 X 線回折を検討した。種種のクライオプロテクタントの検討にもかかわらず、良好な反射点を得ることは困難を極めた。最終的に、NE3A においてキャピラリーに封入した結晶を室温で測定したところ、良好な反射像を得ることができ、結晶は *I*4/*m* の空間群であり、単位格子は $a = b = 46.3$, $c = 72.8$ Å と巨大であることがわかった。

3　結果および考察

解析の結果、おそらくパッキングによる影響で球状の錯体分子はやや歪んでいるが、大小 2 種類の球はそれぞれ $M_{12}L_{24}$ 球状錯体の立方八面体構造であることがわかった。リンカーとして用いたオリゴエチレングリコール鎖によって、小さな球は大きな球の中心部につり下げられている様子が明確に示された。錯体分子の長軸方向では、リンカーが伸びきった状態となるためにリンカー上の酸素原子をモデル化できたが、短軸方向ではリンカーがゆるんだ状態となってディスオーダーし、モデル化できなかった。

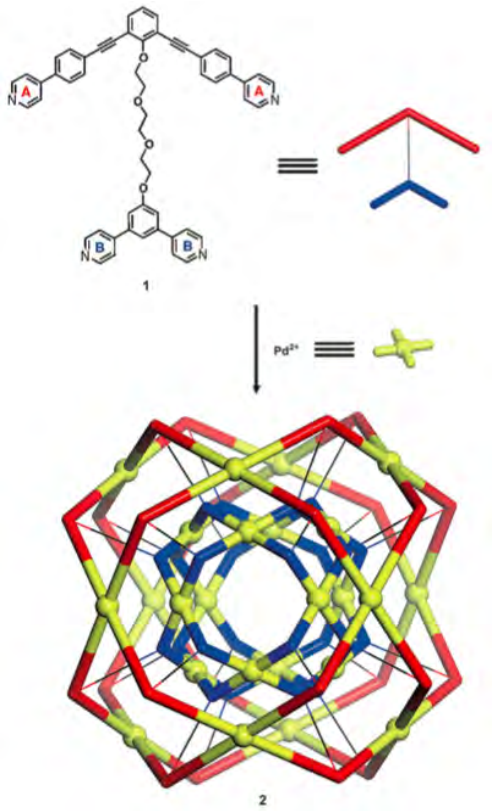

図 1 ：2 種類のピリジル基を有する配位子と Pd(II) イオンを用いた二重球の自己組織化

4　まとめ

大小二種類の二座配位子を連結した配位子には、同等の配位能を持つ二種類のピリジル基があるが、Pd(II)イオンとの自己組織化では、剛直な配位子構造により角度が規定されたそれぞれのピリジル基が球殻構造を形成することで、二重球構造の巨大錯体が得られた。その立体構造を放射光 X 線を用いた単結晶構造解析によって明らかにした[2]。

参考文献

[1] M. Tominaga, K. Suzuki, M. Kawano, T. Kusukawa, T. Ozeki, S. Sakamoto, K. Yamaguchi, and M. Fujita, Angew. Chem. Int. Ed. **43 (**2004) 5621.
[2] Q.-F. Sun, T. Murase, S. Sato, and M. Fujita, Angew. Chem. Int. Ed. **50** (2011) 10318.

* ssato@appchem.t.u-tokyo.ac.jp

NE3A/2009G502

白金(II)イオンと配位子の自己組織化による球状錯体の合成
Synthesis of Spherical Complexes Self-Assembled from Pt(II) ions and Ligands

佐藤宗太 [1*], 藤田大士 [1], 高橋麻奈 [1], 藤田　誠 [1,2]
[1] 東京大学大学院工学系研究科、〒113-8656 文京区本郷 7-3-1
[2] JST-CREST

1　はじめに

これまでに、折れ曲がった二座配位子(L: ligand)とパラジウム(II)イオンとの自己組織化によって、$Pd_{12}L_{24}$ 組成の中空球状錯体を合成し、内面を化学修することによって精密制御されたシリカナノ粒子合成[1]や、外表面を化学修飾することによって無機基板表面への錯体固定[2]といった機能化を達成してきた。この錯体は、48 本もの配位結合でつながれた 12 成分の M、24 成分の L、合計で 36 成分という非常に多くの成分によって構成されているが、ただ一つの立方八面体構造の錯体だけが収率 100%で得られる。その理由は、自己組織化による合成の過程において、成分同士をつなぐ配位結合が可逆的に生成と切断をくり返すことによって、熱力学的に最安定な 1 つの構造だけが最終的に得られるからである。

パラジウム(II)イオンと同様に、平面四配位性の配位様式である白金(II)イオンは、少成分数からなる錯体に対してはパラジウム(II)イオンの代わりに用いることができ、配位結合がパラジウム(II)イオンのそれよりも強いために安定な錯体が得られる。しかし、$Pt_{12}L_{24}$ 錯体を合成しようと試みた場合、成分数が多いために強い配位結合が協同的に作用し、十分な結合の切断がおこらず、生成物は混合物となってしまい $Pt_{12}L_{24}$ 錯体は得られなかった。

今回、合成の際に溶媒として水素結合供与体として知られるトリフルオロエタノール（TFE）を添加することで、配位結合と水素結合とを競合させると効率的に配位結合を弱めることができ、$Pt_{12}L_{24}$ 錯体を得られることを見いだした。また、この揮発性の TFE を減圧下で除去すると、$Pt_{12}L_{24}$ 錯体は耐酸性を示す安定な錯体であることがわかった。この新規 $Pt_{12}L_{24}$ 組成の球状錯体の立体構造を明らかにするために、放射光 X 線を用いた単結晶構造解析を行った。

2　実験

折れ曲がった二座配位子と硝酸白金の自己組織化を、TFE を添加した DMSO 溶媒中で行うことで $Pt_{12}L_{24}$ 錯体を合成し、NMR, MS による構造決定を行った。貧溶媒である酢酸イソプロピルを蒸気拡散することで単結晶を調製し、放射光 X 線による単結晶回折実験を行った。キャピラリーに封入した結晶を室温で測定することで良好な反射像が得られ、$Pm\bar{3}m$ の空間群、30.8 Å の単位格子であることがわかった。

3　結果および考察

構造解析の結果、硝酸(II)イオンを用いて合成した $Pd_{12}L_{24}$ 錯体と類似の立方八面体型の錯体であることがわかった（図 1）。白金(II)イオンと配位子間の強い配位結合が、TFE との水素結合と競合することで、合成条件における配位結合が実質的に弱められ、36 成分という多成分の系においても熱力学的に最安定な構造だけが得られたと考えられる。

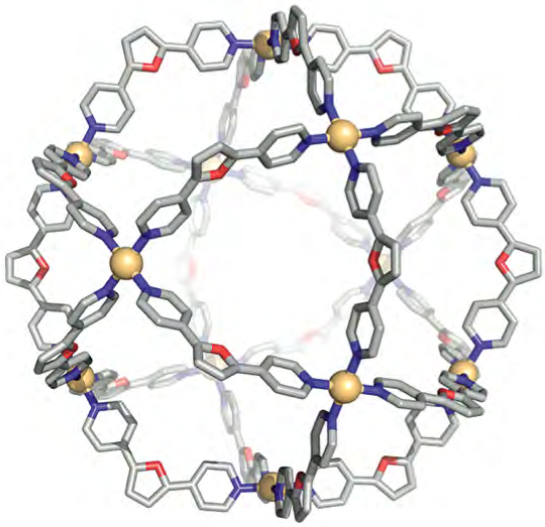

図 1 ：単結晶 X 線構造解析で明らかになった立方八面体型の $Pt_{12}L_{24}$ 錯体の構造

4　まとめ

安定な $Pt_{12}L_{24}$ 錯体の立体構造が、従来の $Pd_{12}L_{24}$ 錯体と類似の立方八面体型であると決定でき、トリフルオロエタノールを添加剤とする多成分白金錯体の自己組織化合成法の有用性を示すことができた[3]。

参考文献

[1] K. Suzuki, S. Sato, and M. Fujita, Nature Chem. **2** (2010) 25.
[2] M. Ikemi, T. Kikuchi, S. Matsumura, K. Shiba, S. Sato, and M. Fujita, Chem. Sci. **1**, (2010) 68.
[3] D. Fujita, A. Takahashi, S. Sato, and M. Fujita, J. Am. Chem. Soc. **133** (2011) 13317.

* ssato@appchem.t.u-tokyo.ac.jp

Australian Synchrotron MX1&MX2/4278a,b; 17A/2009G502

経験予測に基づく $M_{24}L_{48}$ 球状錯体の合成
Synthesis of $M_{24}L_{48}$ Spherical Complexes Based on Empirical Prediction

佐藤宗太[1*], Jens Bunzen[2], 岩佐淳司[1], Pia Bonakdarzadeh[2], 沼田恵里[1], Kari Rissanen[2], 藤田　誠[1,3]
[1]東京大学大学院工学系研究科、〒113-8656 文京区本郷 7-3-1
[2]Department of Chemistry, NanoScience Center University of Jyväskyla
[3]JST-CREST

1 はじめに

これまでに、様々な折れ曲がり角度の二座配位子(L: ligand)と、平面四配位性のパラジウム(II)イオン(M: metal ion)の自己組織化によって M_nL_{2n} (n = 6, 12, 24...)組成の球状錯体が得られることを見いだした。生成物の組成は、折れ曲がり角度に依存し、127 °（配位子 **1**）では $M_{12}L_{24}$ 錯体、149 °（配位子 **5**）では $M_{24}L_{48}$ 錯体が得られる（図 1）[1]。しかし、実際に錯形成反応を試さずに、配位子の構造だけから生成物の錯体構造を予測することはできない。そこで、配位子 **1** と **5** とを任意の比率で混合して錯形成を行い、平均角度と生成物との相関を調べたところ、131~134 °で $M_{12}L_{24}$ 錯体から $M_{24}L_{48}$ 錯体に構造が切り替わることがわかった。この経験的に求めた角度を使って実際の生成物の構造を予測できるか検討するために、配位子の中央のピロール環の置換様式をわずかに変化させ、135 ° ~ 147 °の角度の配位子 **2** から **4** を合成した。これらの単一の配位子をそれぞれパラジウム(II)イオンと自己組織化し、その生成物の構造を調べることで、経験的な予測に基づいて設計した多成分錯体の合成、という新しい合成手法の確立をめざした。

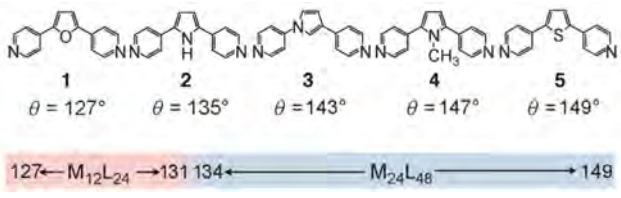

図 1 ：二座配位子の折れ曲がり角度

2 実験

新規配位子 **2** から **4** を合成し、それぞれパラジウム(II)イオンと自己組織化して球状錯体を合成した。いずれの配位子を用いた場合にも、反応は効率的に進行し、定量的に単一の生成物が得られた。DOSY NMR を使って分子の大きさを見積もり、また MS によって分子組成を決定することで、$M_{24}L_{48}$ 錯体が得られたことがわかった。経験的な予測が有用であることが示された。得られた新規錯体の立体構造を明らかにするために、単結晶構造解析を検討したところ、酢酸エチルを気相拡散させることで単結晶が得られ、放射光 X 線を用いて回折像を得ることができた。

3 結果および考察

解析の結果、斜方立方八面体の構造を有する $M_{24}L_{48}$ 球状錯体の立体構造が明らかになった（図 2）。NMR や MS などの他の解析手法では、分子の大きさや組成を決めることはできるが、立体構造は明らかにできず、X 線構造解析によって初めて確認できた。配位子 **3** は左右非対称な構造であるが、位置異性体の混合物として生成物が得られ、結晶構造においては中央のピロール環のピリジル基が置換している窒素原子と炭素原子は区別することができなかった。

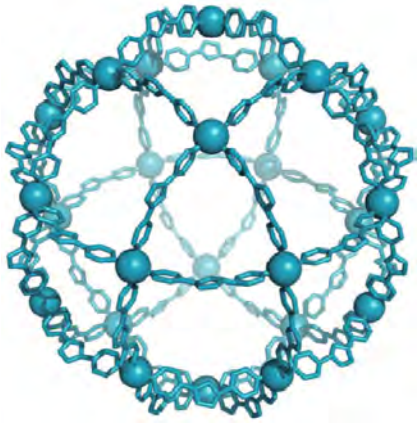

図 2：単結晶 X 線構造解析で明らかになった $M_{24}L_{48}$ 球状錯体の構造（配位子 **3** を用いて合成）

4 まとめ

異なる折れ曲がり角度を持つ 2 種類の配位子を混合し、その平均角度と錯体構造との相関から決定した経験的な予測角度の値を用いると、単一の新規配位子を用いた場合に得られる錯体の構造を予測できることを明らかにした[2]。

参考文献

[1] Q.-F. Sun, J. Iwasa, D. Ogawa, Y. Ishido, S. Sato, T. Ozeki, Y. Sei, K. Yamaguchi, and M. Fujita, Science **328** (2010) 1144.
[2] J. Bunzen, J. Iwasa, P. Bonakdarzadeh, E. Numata, K. Rissanen, S. Sato, and M. Fujita, Angew. Chem. Int. Ed. **51** (2012) 3161.

* ssato@appchem.t.u-tokyo.ac.jp

NE3A/2009G502

星型化した立方八面体型の錯体の合成
Synthesis of Stellated Cuboctahedral Complex

佐藤宗太[1*], 孫　慶福[1], 藤田　誠[1,2]
[1]東京大学大学院工学系研究科、〒113-8656 文京区本郷 7-3-1
[2]JST-CREST

1 はじめに

プラトンの立体（正多面体）やアルキメデスの立体（半正多面体）の形を持つ分子は、多くの化学者の興味を引き、その人工合成が達成されてきている。遷移金属イオンと配位子とを、それぞれ頂点と辺とする多面体型錯体もその一例であり、我々は立方体や正八面体、立方八面体、近年では、斜方立方八面体[1]、二重の立方八面体[2]など、多くの錯体分子の自己組織化による合成を報告してきている。

一方、凸型の表面を持つ「星形多面体」は、その複雑な構造ゆえに合成が難しく、合成例がない。本研究では、立方八面体型の分子（アルキメデスの立体の一種）を一度作り、この分子に突起部を付け加えることで星形化した立方八面体に変換する新しい合成法を使い、また、可逆的に突起部を除くことで元の立方八面体に戻すことを検討した。

折れ曲がった二座配位子(L: ligand)と、平面四配位性のパラジウム(II)イオン(M: metal ion)の自己組織化によって $M_{12}L_{24}$ 組成の球状錯体が得られる。この配位子は剛直な構造を持ち、配位部位である 2 つのピリジル基は、立方八面体の錯体骨格を形成するのに適した折れ曲がり角度を固く保っている。この配位子の頂点に、柔軟なリンカーを介して追加の配位部位としてピリジル基を導入すれば、この配位部位は錯体骨格形成に対してエントロピー的に不利であると考えた。骨格形成に必要な化学量論のパラジウム(II)イオンを作用させた場合は、$M_{12}L_{24}$ 組成の球状錯体が得られた。さらに、過剰量のパラジウム(II)イオンを作業させた場合は、追加した配位部位が配位結合を形成し、錯体表面上の 6 箇所で凸型部位を形成し、$M_{18}L_{24}$ 錯体が得られた。この星型化反応は可逆的であることも明らかにした。本研究では、このようにして合成した錯体の立体構造を決定するために、放射光を用いた単結晶 X 線構造解析を検討した。

2 実験

合成した錯体の単結晶化を検討したところ、貧溶媒の気相拡散によって回折実験に適した結晶を得られることがわかった。放射光 X 線を用いた結晶構造解析を検討した結果、キャピラリーに封入した結晶を室温で測定することで良好な反射像を得ることができた。$M_{12}L_{24}$ 錯体は $Im\bar{3}m$ の空間群、39.3 Å の単位格子、星型化された $M_{18}L_{24}$ 錯体は $F432$ の空間群、53.3 Å の単位格子であった。

3 結果および考察

解析の結果、母核として用いた立方八面体の構造を有する $M_{12}L_{24}$ 球状錯体の立体構造が明らかになった（図 1 左）。追加導入した配位部位は遊離しており、ディスオーダーして観測された。一方、星型化された立方八面体構造の $M_{18}L_{24}$ 球状錯体では、四方から集まった追加の配位部位がパラジウム(II)イオンに配位している様子が明らかになった（図 1 右）。金属イオンを頂点、配位子を辺として明確に定義される、初めての星型化された多面体の立体構造を、単結晶 X 線構造解析によって明瞭に決定できた。

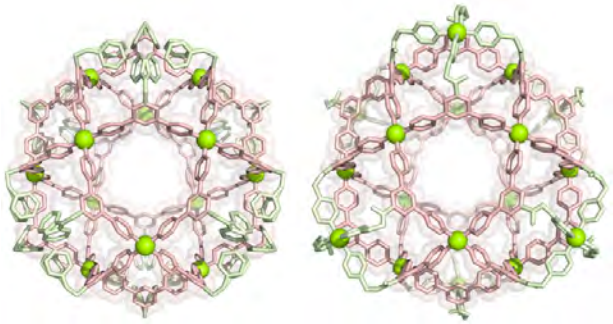

図 1 ：単結晶 X 線構造解析で明らかになった立方八面体型 $M_{12}L_{24}$ 錯体(左)と星型化 $M_{18}L_{24}$ 錯体(右)

4 まとめ

初めての星型化された多面体骨格を有する錯体分子の合成を達成した[3]。母核となる剛直な立方八面体型分子を基盤とし、柔軟なリンカーを介して金属配位部位を追加することで、段階的な錯形成反応を使って複雑な星型化構造を得ることができた。

謝辞

単結晶 X 線構造解析にあたり、有益なアドバイスをいただいた尾関智二先生に感謝いたします。

参考文献

[1] Q.-F. Sun, J. Iwasa, D. Ogawa, Y. Ishido, S. Sato, T. Ozeki, Y. Sei, K. Yamaguchi, and M. Fujita, Science **328** (2010) 1144.
[2] Q.-F. Sun, T. Murase, S. Sato, and M. Fujita, Angew. Chem. Int. Ed. **50** (2011) 10318.
[3] Q.-F. Sun, S. Sato, and M. Fujita, Nature Chem. **4** (2012) 330.

* ssato@appchem.t.u-tokyo.ac.jp

27B/2009G544

EXAFS on thorium fluoride in molten mono- and divalent cationic fluoride mixtures

Masahiko NUMAKURA[1], Yasuaki SHIMOHARA[1], Keisuke TAJIMA[1], Hirokazu KAWANO[1], Takeshi NAKAHAGI[1], Atsushi NEZU[1], Hiroshi AKATSUKA[1], Nobuaki SATO[2], Catherine BESSADA[3], Haruaki MATSUURA*[1]

[1]Res. Lab. for Nucl. Reactors, Tokyo Tech., Ookayama, Meguro-ku, Tokyo, 152-8550, Japan
[2]Inst. of Multidisc. Res. for Adv. Mater., Tohoku Univ., Katahira, Aoba-ku, Sendai, 980-8577, Japan
[3]CEMHTI, CNRS, 1D avenue de la recherche scientifique, 45071 Orléans cedex 2, France

Introduction

For the development of the on-line recycling process of molten salt reactor, it is important to establish the separation technique of actinides (An) and lanthanides (Ln) by electrochemical methods. To find better electrolysis conditions to improve the efficiency of the pyrochemical reprocessing, systematic clarification of the correlation between structures of molten An (Ln)F_n and their physico-chemical properties is useful. In this study, ThF_4-LiF-CaF_2 and ThF_4-LiF-MgF_2 mixtures are focused for the structural investigation by EXAFS.

Experimental

The Th L_{III}-edge EXAFS spectra have been collected with fixed time scan method by the X-ray from a double Si (111) crystals monochromator in transmission modes. ThF_4 was synthesized by ThO_2 under fluorine gas (40 ml/min) at 650 ^oC for 4 h. Mixtures made by ThF_4, LiF and CaF_2 or MgF_2 were melted once in a glassy carbon crucible at 1073 K in a quartz chamber filled with an argon atmosphere in high purity. Then, they were mixed with boron nitride powder, and pressed into pellets in 7 mm diameter and 1 mm thickness. The mixing weight ratio of ThF_4 to BN was ca. 1: 2.5. To prevent chemical reaction of sample and contamination of ThF_4 to outside during heating process in EXAFS measurements, these pellets were installed in a double barrier cell. The 1st barrier is made with pyrolytic boron nitride and the 2nd barrier is made with boron nitride (HIP). The electric furnace was filled with He gas at ca. 30 kPa. EXAFS data were analysed by using the WinXAS ver.3.1 and 3rd and 4th cumulants were introduced for the curve fitting analyses of EXAFS data at molten phase due to their large anharmonic effect in the spectra.

Results and discussion

The BF_2 (B = Ca, Mg) concentration dependence of local structural parameters derived from EXAFS of the constant concentration of x_{ThF4} = 0.25 are shown in Fig. 1. Although inter-ionic distance seems to be independent from the both concentration of CaF_2 and MgF_2, coordination number, Debye-Waller factor and C_3 cumulant parameter of MgF_2 mixture are larger than those of CaF_2 in general, and increasing rates depending on the concentration of MgF_2 are also larger than those of CaF_2. These facts imply that MgF_2 makes much un-stabilized local environment around Th^{4+} than CaF_2 does. The similar tendency is also confirmed at the TbF_3 – LiF - BF_2 (M=Ca, Mg) mixtures. This is caused by the difference between the coulombic interaction of Mg^{2+} - F^- and Ca^{2+} - F^-. Ionic radius of Mg^{2+} is smaller than that of Ca^{2+}, thus Mg^{2+} can easily approach to the coordinated F^- around Th^{4+}. Therefore, Mg^{2+} makes un-stabilised local structure around Th^{4+} more strongly.

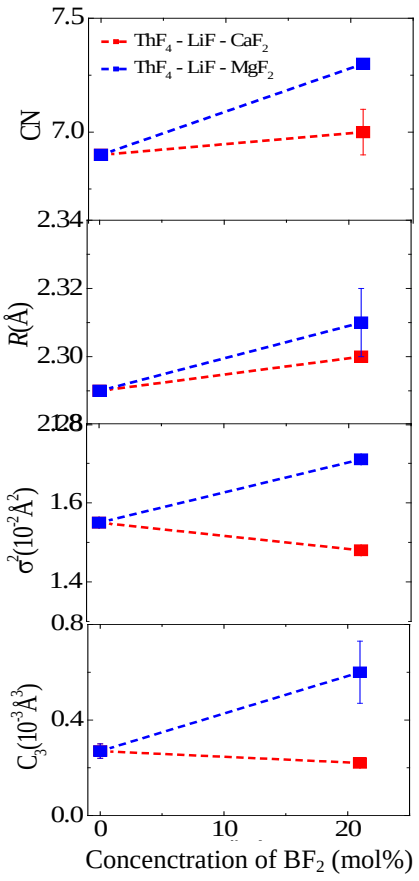

Fig. 1 Structural paramenters obtained by EXAFS of molten 0.25ThF_4 – (0.75-x)LiF - x CaF_2 or MgF_2 mixtures (0<x<1), from the top, coordination number, inter-ionic distance, Debye-Waller factor and C_3 cumulant.

*hmatsuur@nr.titech.ac.jp

9C/2009G591

Structural Analysis of the Adsorbed Dioxygen Species on Copper Ion-Exchanged MFI Zeolite at Room Temperature

Yuusuke Sogawa, Atsushi Itadani, Hiroe Torigoe, Akira Oda, Mitsuhiro Ushio, Masayasu Nishi, Takahiro Ohkubo, and Yasushige Kuroda*
Okayama University, Okayama 700-8530, Japan

1 Introduction

Copper ion-exchanged MFI zeolite (CuMFI) has been well-known to exhibit high levels of catalytic activity for the direct decomposition of NO [1]. This material also has surprising adsorption features for N_2, H_2, and Xe; CuMFI strongly interacts with these gases, even at room temperature [2]. The active center in CuMFI for such phenomena has been accepted to be the monovalent copper ion (Cu^+) which is formed by the evacuation at high temperatures [1,2]. Recently, Groothaert et al. have reported that CuMFI interacts with O_2 and consequently works as the oxidation catalyst for CH_4; the methanol synthesis through the reaction of CH_4 with the adsorbed O_2 is achieved [3]. However, the state of the adsorbed O_2 species on CuMFI and the reaction mechanism are not completely clarified, although some reports have so far been made on them [4]. We believe that the elucidation of the interaction between CuMFI and O_2 is essential to understand the above subject. In this work, we examined the interaction of CuMFI with O_2 at room temperature by the X-ray absorption fine structure (XAFS) measurement.

2 Experiment

CuMFI (Si/Al = 11.9; ion-exchange level = 131%) was prepared at room temperature in a mixed aqueous solution of $Cu(CH_3COO)_2$ and NH_4CH_3COO. The XAFS spectra were collected in transmission mode at the beamline PF-9C equipped with a double crystal monochromator of Si(111). The self-supporting disk was placed into an in situ sample cell which is capable of pre-treatment of sample and gas introduction in situ.

3 Results and Discussion

Fig. 1 shows the X-ray absorption near edge structure (XANES) spectra and the Fourier transform of the extended X-ray absorption fine structure (EXAFS) oscillations at the K-edge of the copper-ion exchanged in CuMFI under various atmospheres. For the 873 K-treated sample, two characteristic bands are observed at 8.983 and 8.993 keV, which are due to the $1s–4p_\pi$ and $1s–4p_\sigma$ electronic transitions of Cu^+ in the sample, respectively. Appearance of these bands is explained by considering that the Cu^+ ions are in a linear or a planar coordination state. When the CuMFI sample was exposed to O_2 gas at room temperature, the intensity of the band at 8.983 keV is considerably smaller than that of the band for the sample evacuated at 873 K, being interpreted that a linear or a planar coordination structure around Cu^+ in CuMFI was deformed by the interaction with O_2. The intensity of the 8.983 keV-band for the sample re-evacuated at room temperature hardly changes. The result clearly indicates the existence of the strong interaction between Cu^+ and O_2. In the EXAFS spectrum of the 873 K-treated sample, a band is observed at around 1.6 Å (no phase-shift correction), which is due to the backscattering from the nearest neighboring oxygen atoms. The analysis of the EXAFS data clarified that the Cu^+ ions are in the two- or three-coordination state with lattice oxygen atoms (Cu–O distance: 1.95 Å). In addition, in the case of the present CuMFI sample, a peculiar backscattering at around 2.2 Å (no phase-shift correction) attributed to the $Cu^+–Cu^+$ interaction is confirmed (analysis data: coordination number ($N_{Cu–Cu}$) = 0.8; distance ($r_{Cu–Cu}$) = 2.65 Å). For CuMFI adsorbing O_2 strongly, the band at 1.6 Å increases in its intensity and width, compared with that for the sample evacuated at 873 K. Simultaneously, an additional band clearly appears at around 2.5 Å (no phase-shift correction). For the band at 1.6 Å, the analysis values were evaluated to be $N_{Cu–O}$ = 4.2 and $r_{Cu–O}$ = 1.94 Å (including lattice oxygen). For the band at 2.5 Å, the fitting result of $Cu^+–Cu^+$ was better than that of Cu–O ($N_{Cu–Cu}$ = 0.8; $r_{Cu–Cu}$ = 2.90 Å). The distance of Cu–Cu was found to be longer after the interaction with O_2 than that before one. These results suggest the existence of the species composed of two Cu^+ ions bridging O_2. Taking into other experimental and calculational data consideration, further discussion will be necessary. The details are in progress.

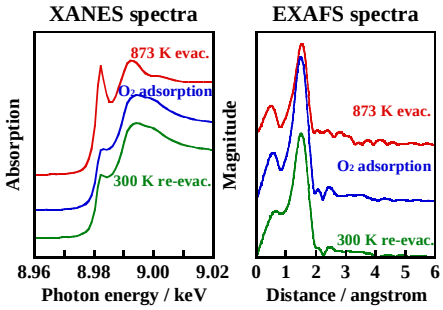

Fig. 1. XANES and EXAFS spectra for CuMFI.

References

[1] M. Iwamoto and H. Yahiro, Catal. Today **22** (1994) 5.
[2] Y. Kuroda *et al*., J. Phys. Chem. B **103** (1999) 2155; Y. Kuroda *et al*., Chem. Lett. **33** (2004) 1580; H. Torigoe *et al*., J. Phys.. Chem. Lett. **1** (2010) 2642.
[3] M. H. Groothaert *et al*., J. Catal. **220** (2003) 500; J. Am. Chem. Soc. **127** (2005) 1394.
[4] J. S. Woertink *et al*., PNAS **106** (2009) 18908; P. J. Smeets *et al*., J. Am. Chem. Soc. **132** (2010) 14736.

* kuroda@cc.okayama-u.ac.jp

先端研究施設共用促進事業
フォトンファクトリーにおける産業利用促進

課 題 番 号： 2009I003
研究責任者： 成行あかね、日揮ユニバーサル株式会社
利 用 施 設： 高エネルギー加速器研究機構　放射光科学研究施設　BL-9C,BL-12C
利 用 期 間： 平成 21 年 10 月～22 年 9 月

オゾン/アルデヒド脱臭触媒の構造解明

Structure elucidation of ozone/aldehyde exhaust gas deodorizing catalyst

成行あかね、竹内健太、相川亮二、辻一誠、橋本真治、櫻井孝信、伊藤浩文、中野美樹
Akane Nariyuki, Kenta Takenouchi, Ryouji Aikawa, Issei Tsuji, Shinji Hashimoto, Takanobu Sakurai, Hirofumi Ito, Yoshiki Nakano

日揮ユニバーサル株式会社
Nikki-Universal Co., Ltd.

アブストラクト：
Mn 系触媒は、環境汚染防止の観点から、長寿命化及び再利用化が要求されている。そこでその耐久性を左右する要因を解明した。NH_3 脱臭には、Mn-O は関与せず構造が変化しないことが分かった。一方、CH_3SH 脱臭では、Mn-O の配位数が耐久性向上の鍵であり、反応させると、Mn 触媒中の酸素を消費し Mn-O の配位数が減少（還元）する。この改良としての K/MnO_2 触媒は、K は Mn の骨格内部ではなく、表面に吸着することが分かった。

英文アブストラクト
Currently Mn catalysts are required to be improved performance of, especially, life and reusability in order to preserve environment. So we tried to clarify what are the factors effecting on catalyst's endurance, and then we have clarified some interesting facts concerning ammonia and methyl mercaptan deodorization. As ammonia deodorization, Mn-O does not concern on reaction. On the other hands, as methyl mercaptan deodorization, the coordination number of Mn-O has big impact to improve catalyst's endurance. In case that Mn catalyst is poisoned, methyl mercaptan consumes oxygen in Mn catalyst, and then the coordination number of Mn-O is reduced (redacted). As advanced catalysts, K/MnO_2 was prepared. Potassium was not make up of manganese framework , but adsorbed on the surface of manganese dioxide.

キーワード：　Mn 系触媒,　NH_3 脱臭、CH_3SH 脱臭、排気ガス

１．はじめに：

従来から、空気中の悪臭や有害成分を除去する方法として、活性炭やゼオライトによる物理吸着、反応性の化合物による反応分解、貴金属系触媒による燃焼、Mn系触媒による化学吸着と分解、光触媒による分解、オゾン利用による酸化分解触媒など、作用が異なる技術が知られている。中でもMnO_2系触媒は、多くの分野に採用されているが、その触媒耐久性を左右する要因が明らかにされていない。端緒として、劣化機構および高耐久触媒の構造解析を検討しているが、上記触媒はアモルファスであり、XRDで構造情報を得ることが出来ない。本研究の目的は，XRDでは捕捉出来なかった触媒活性種のNH_3及びCH_3SH脱臭による構造変化(劣化機構)を解明し、これをもとに耐久性向上の方向性を見いだすことを目標とする。

２．実験：

2.1　CH_3SH及びNH_3の脱臭調製

作成した各MnO_2触媒粉0.5gを挿入した試料ホルダーにファンを取り付け、30L容器の中へ入れた。CH_3SH及びNH_3の濃度を100 ~ 22000 ppmに調整し、ファンで攪拌を継続して、容器内の反応ガス濃度（残留濃度、ｐｐｍ）を光音響ガスモニタによって測定し、反応が行われていることを確認した。

2.2.　XAFS測定

XAFSスペクトルの測定は、高エネルギー加速

器研究機構、放射光科学研究施設BL-12C, BL-9Cにて Mn-K, K-K吸収端に対して透過法にて行った。解析には、得られたスペクトルⅠf／Ⅰ0の吸収端前領域にビクトリーンの計算式を用いて最小２乗フィッティングを行い、それを外挿することによってバックグラウンドを差し引いた。Mn-Oのカーブフィッティングは REX-2000(リガク)を用い MnO_2 を標準試料とした。

３．結果および考察：

3.1 NH_3 の脱臭前後の構造変化

NH_3 脱臭では、反応開始と共に NH_3 の吸収が現れ、加熱再生すると NH_3 が NO_2 へ変化しながら脱離していることを FT-IR 測定により確認した。

図 1 及び表 1 に Mn-K 吸収端の XANES と Mn-O のカーブフィッティング結果を示す。NH_3 脱臭では、被毒~再生加熱再生過程において XANES と Mn-O 配位数が変化しないことが分かった。即ち、Mn 上に NH_3 として弱く吸着し、加熱と共に Mn 上の酸素ではなく、空気中の酸素を取り込みながら NO_2 として脱離することが分かった。

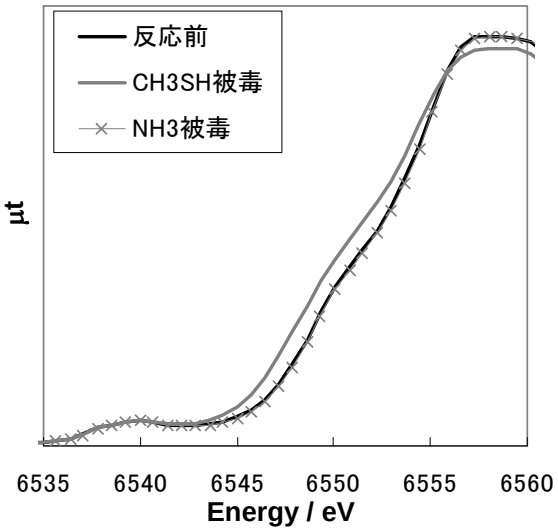

図 1. MnO_2 触媒の NH_3 (10000ppm)及び CH_3SH (10000ppm)脱臭前後における Mn–Kedge XANES スペクトル

3.2 CH_3SH の脱臭前後の構造変化

CH_3SH 脱臭では、反応ガス濃度増大に伴い、XANES スペクトルで吸収端が低エネルギー側にシフトし、Mn-O の配位数も減少、即ち還元することが分かった。また再生後も Mn-O は完全再生されないことが分かった。

表 1　MnO_2 触媒の NH_3 及び CH_3SH 脱臭前後における Mn-O カーブフィッテイング結果

触媒雰囲気条件	Mn-O		
	R/nm	CN	Rf/%
反応前	0.193	6.0	2.0
NH_3, 100 ppm	0.193	6.0	2.1
NH_3, 1000 ppm	0.193	6.1	2.2
NH_3, 10000 ppm	0.192	6.1	2.3
NH_3, 22000 ppm	0.193	5.9	1.9
NH_3, 加熱再生後	0.193	5.9	2.3
CH_3SH, 100 ppm	0.195	5.2	2.2
CH_3SH, 1000 ppm	0.197	4.0	2.5
CH_3SH, 10000 ppm	0.199	3.7	2.8
CH_3SH,加熱再生後	0.120	4.8	3.3

3.3　改良触媒-K 添加 Mn の構造

3.2 で CH_3SH 脱臭について、Mn 骨格増加よりも活性点数増加が有効であると判断した。Mn 上に第二活性点となる K を数%添加すると、予想通り CH_3SH 等 S 系やアルデヒド系は、脱臭が促進された。また、調製条件により性能を制御できる事が分かった。（活性の良い順に"K/$MnO_2$①" "K/$MnO_2$②"とする。）一方、O_3 や NH_3 は脱臭が阻害されることも確認した。表 2 に MnO_2 および K/ MnO_2 触媒の CH_3SH 脱臭前後における Mn-O カーブフィッテイング結果を示す。これより K を添加することにより Mn-O 配位数の減少が抑えられることが分かった。

図 2 に K 添加前後における Mn K 吸収端 EXAFS のフーリエ変換を示す。K 添加によって Mn 周囲の構造は変化していない。K は Mn 骨格内には存在せず、表面に吸着していると推定できる。MnO_2 上の活性点は温存されたまま、K によって部分的にキャップされる。CH_3SH やアルデヒドは、MnO_2 および K 上に吸着するため、脱臭は促進されるが、O_3 や NH_3 は K 上には吸着されないため、K によりキャップされた MnO_2 活性点分だけ、分脱臭が阻害されると考えられる。また、"K/$MnO_2$①" と"K/$MnO_2$②"は同構造であることが分かった。また K 添加により

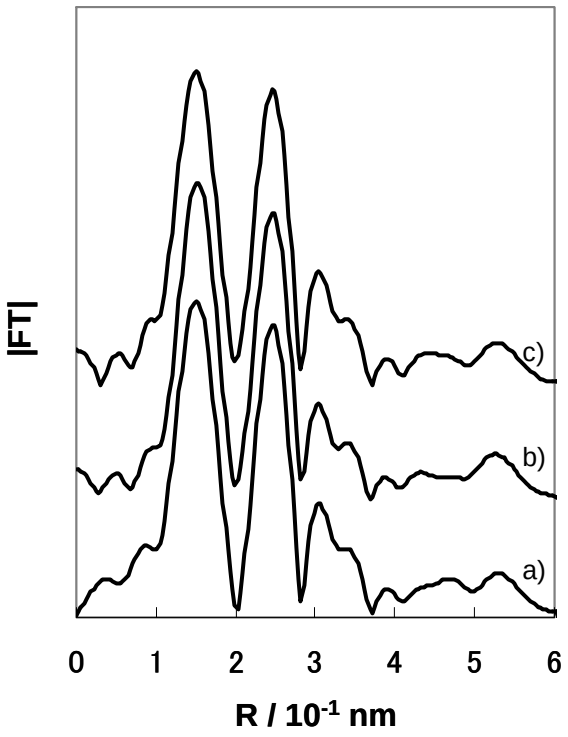

図 2　Mn-K 吸収端における MnO_2 のカリウム添加有無におけるフーリエ変換
(a): MnO_2, (b): $K/MnO_2$①, (c) $K/MnO_2$②.

図 3 に K 吸収端からみた XANES スペクトルを示す。a)は K の原料である、K_2CO_3、b)は K_2O を示す。K 添加し、良活性である $K/MnO_2$①は、K_2O と異なる構造を有しながら、分散しており、活性が低い程（$K/MnO_2$②）、K_2O に近似してくることが分かった。

表 2　MnO_2 および K/ MnO_2 触媒の CH_3SH 脱臭 (1000ppm) 前後における Mn-O カーブフィッテイング結果

触媒雰囲気条件	Mn-O		
	R/nm	CN	Rf/%
反応前	0.193	6.0	2.0
MnO_2	0.197	4.0	2.5
K/MnO_2	0.194	5.3	2.3

４．まとめ：

NH_3 脱臭では、Mn 構造が変化しないのに対し、CH_3SH 等 S 系は、マンガン上の酸素を消費し Mn-O の配位数が減少（還元）する。CH_3SH の脱臭性能向上は Mn-O の配位数が鍵となっていることが分かった。これより、改良触媒として、Mn 上に第 2 活性点となる K を添加し、性能が向上された。この K は Mn の骨格内部ではなく、表面に吸着し、K_2O とは異なる構造であることが分かった。

本発明の脱臭触媒により、従来の MnO_2 を成分とする脱臭触媒の脱臭性能を大幅に向上させることができた。とりわけ脱臭速度と吸着容量が飛躍的に高く、このため大量のガスを高速で処理できるため、小型化が可能であり、かつ再始動時に起こりやすい臭気成分の脱着がないため、高温の車内などでも快適に過ごすことができる。

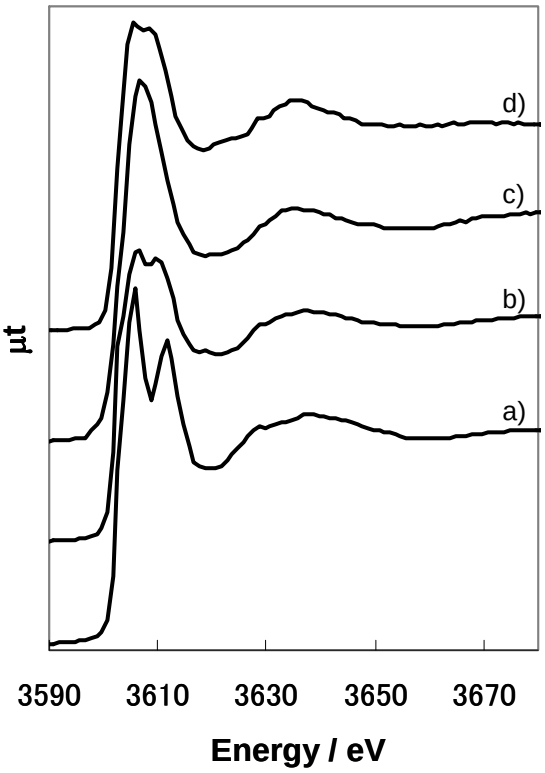

図 3　K-K 吸収端における XANES スペクトル
(a): K_2CO_3, (b): K_2O, (c): $K/MnO_2$①, (d) $K/MnO_2$②.

成果発表状況：

成行あかね、橋本真治、相川亮二、竹内健太、戸塚裕二, 脱臭触媒及びこれを用いた脱臭方法ならびに該触媒の再生方法、PCT/JP2009/062712、2009 年 7 月 14 日.

先端研究施設共用促進事業
フォトンファクトリーにおける産業利用促進

課 題 番 号： **2009I005**
研究責任者： 岩波睦修、JX 日鉱日石エネルギー　研究開発本部　中央技術研究所
利 用 施 設： 高エネルギー加速器研究機構　放射光科学研究施設　BL-NW10A
利 用 期 間： 2009 年 10 月～2010 年 9 月

XAFS 法を活用した高沸点油処理触媒の再生技術の研究

Study on regeneration of catalyst for hydrotreating of high boiling point oil using XAFS

岩波 睦修[1]、小西 友弘[1]、中村 誠[1]、今野 聡一郎[1]、佐野 孝[1]、石井 光男[1]、
新田 清文[2]、西野 潤一[2]、仁谷 浩明[2]、丹羽 尉博[2]、野村 昌治[2]
Yoshimu IWANAMI[1], Tomohiro KONISHI[1], Makoto NAKAMURA[1], Souichirou KONNO[1], Takashi SANO[1], Mitsuo ISHII[1], Kiyofumi NITTA[2], Junich NISHINO[2], Hiroaki NITANI[2], Yasuhiro NIWA[2], Masaharu NOMURA[2]

[1]JX 日鉱日石エネルギー、[2]高エネルギー加速器研究機構
[1] JX Nippon Oil ＆ Energy Corporation, [2] KEK

アブストラクト：使用済みの CoMo 系および NiCoMo 系水素化脱硫触媒を再生すると、再生触媒の活性は再生温度に大きく依存し、ある温度で最大となった。Mo K 吸収端 EXAFS 測定の結果、触媒を低温で再生するほど、活性を低下させると考えられる大きな Mo 硫化物クラスターが残存することがわかった。一方 XRD 測定の結果、触媒を高温で再生するほど、活性を低下させると考えられる $CoMoO_4$ 結晶の生成・成長が促進されることがわかった。したがって、Mo 硫化物クラスターの残存も $CoMoO_4$ 結晶の生成・成長もない温度で使用済み触媒を再生すると、活性は最大になると推定された。さらに *In-situ* Mo K 吸収端 EXAFS 測定により、再生温度と Mo 硫化物クラスターを除去するために必要な最短の再生時間の関係を明らかにした。再生温度が低いほど、再生に必要な最短時間は長くなることがわかった。

The hydrodesulfurization activities of regenerated CoMo and NiCoMo catalysts varied greatly depending on the regeneration temperature. Specifically, the activities of the regenerated catalysts were maximized by regenerating at certain temperatures. Mo K-edge EXAFS showed that larger Mo sulfide clusters remained when the spent catalysts were regenerated at lower temperatures, and this may cause reduced activity. On the other hand, XRD showed that there was increased formation and growth of $CoMoO_4$ crystals when the spent catalysts were regenerated at higher temperatures, which may also cause reduced activity. If the spent catalyst is regenerated at a temperature at which no larger Mo sulfide clusters remain and no formation and growth of $CoMoO_4$ crystals occurs, the loss of activity by regeneration may be minimized.
Further, *in-situ* Mo K-edge EXAFS allowed us to determine the relationship between the regeneration temperature and the minimum regeneration time required to eliminate the larger Mo sulfide clusters. The EXAFS analysis suggested that the minimum time required for regeneration increases as the regeneration temperature decreases.

キーワード：水素化脱硫、触媒再生、活性、担持金属、EXAFS

１．はじめに：

（背景）高沸点油（沸点600℃以下）を処理する水素化脱硫装置に用いられる触媒は使用時間が増加するにつれて活性が低下するが、再生処理を行うことにより活性が回復する。しかし、触媒は1回再生すると活性が新触媒に比べて約10%、2回再生するとさらに約10%低下するため、1回再生品は使用されるが、2回再生以後は活性低下が大きく製油所での生産ロスとなるため、全量抜き出し、廃触媒として製油所から産廃業者へ搬出されている。なお廃触媒量は日本国内の製油所で年間約10,000トンと推定される。

触媒の2回再生使用が可能となれば、日本全体では年間約4,000トンの廃触媒削減が期待される。したがって、従来に比べて活性低下の小さい触媒再生技術を開発し、触媒を有効活用することは環境負荷の低減のために必須である。

（目的）使用済み触媒は付着した炭素分などを

加熱により酸化除去することで再生される。従来は、再生温度、再生時間、空気量など再生条件を触媒に付着した堆積物が一定量以下にするよう決定されており、触媒の構造変化には着目していなかった。そこで、本研究は触媒活性を支配していると考えられる触媒に担持されている金属に着目して、XAFS 法などにより触媒再生条件と金属の状態・構造との関係を明らかにすることにより、最適な再生方法の指針を見出し、従来に比べて活性低下の小さい触媒再生技術の開発を目的とする。

（目標）水素化脱硫装置に用いられる高沸点油（沸点 600℃以下）の処理触媒について、XAFS 法などにより得られた活性低下が小さい触媒再生方法の指針を活用して、再生 1 回毎の活性低下が 5%以下となる触媒再生技術を開発することを目標とする。これにより、2 回再生触媒の使用が可能となると考えられる。

・1 回再生触媒:
　新触媒に対する相対活性 0.95 以上
・2 回再生触媒:
　1 回再生触媒に対する相対活性 0.95 以上

２．実験：

製油所において高沸点油（沸点 600℃以下）を処理する水素化脱硫装置で使用された触媒について実験室スケールで温度を変化させて再生する。再生した触媒の担持金属の XAFS 測定などを行い金属の状態・構造を推定し、再生温度と活性の関係を明らかにし、活性低下の小さい触媒再生方法（温度）の指針を得る。さらに、上記実験に用いた使用済み触媒について一定温度、一定空気量下における担持金属の状態・構造の時間的変化を推定するために XAFS 測定を行い、触媒再生方法（時間）の指針を得る。

XAFS 法などにより得られた「活性低下の小さい触媒再生方法の指針」に基づいた条件を触媒再生メーカーに提示して商業スケールの装置で触媒再生テストを行い、製油所装置へ再生触媒を充填して触媒活性低下挙動を調べることを目指す。

検討試料、実験方法は以下のとおりである。

①試料：
(a)CoMo 系水素化脱硫触媒
　ⅰ)新触媒を製油所で使用した後の触媒
　ⅱ)新触媒を製油所で使用した後、商業装置で再生し再び製油所で使用した後の触媒
(b)NiCoMo 系水素化脱硫触媒
　ⅰ)新触媒を製油所で使用した後の触媒

②実験室スケール再生方法：
電気炉を使用して上記使用済み触媒を一定時間、空気流通下で温度を変化させて加熱

③活性評価：
実験室スケールで再生した触媒の水素化脱硫活性をベンチスケールプラントで評価

④EXAFS 測定：
Mo K 吸収端（透過法）
(a)実験室スケールで再生した触媒を室温で測定
(b)使用済み触媒を一定温度、空気流通下で測定（*In-situ* セルを使用（図 1））

⑤XRD 測定：
X 線源：CuKα

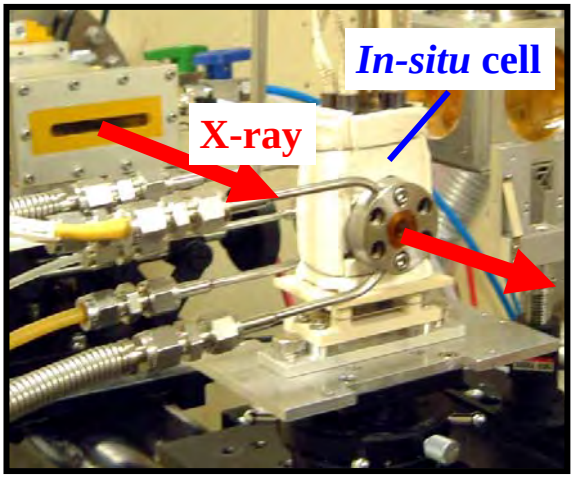

図 1　In-situ セルの概観

３．結果および考察：

３－１　再生温度と触媒活性、触媒担持金属の状態・構造との関係

(a)CoMo 系水素化脱硫触媒
ⅰ)1 回再生の検討
（新触媒を製油所で使用した後の触媒を実験室スケールで再生）

温度を変えて実験室スケールで再生した触媒について活性評価を行った。その結果、触媒再生後の活性低下が小さい温度領域（新触媒比の相対活性 0.95 以上）があることがわかった（図

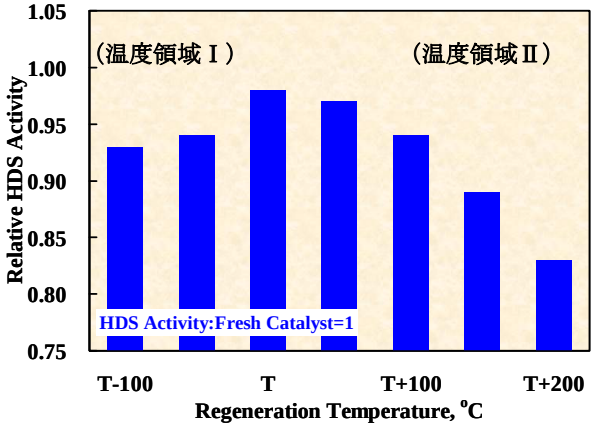

図 2　再生触媒の活性評価結果

2)。そこで、活性低下の小さい触媒再生方法（温度）の指針を得るために、再生触媒の担持金属（Mo）の状態・構造を EXAFS および XRD により調べた。

Mo K 吸収端 EXAFS 測定結果から、再生温度により動径構造関数の形状が異なることわかった（図 3 左）。そこで、活性種 Mo 硫化物に由来する Mo-S ピークに着目し、再生温度とそのピーク強度との関係を調べた。その結果、活性低下の大きい低温側の「温度領域 I 」で再生した触媒は（図 2）、Mo-S ピーク強度が高いことから（図 3 右）、大きな Mo 硫化物クラスターが残存していると推定される。再生触媒を活性化処理（硫化処理）すると、残存する大きな Mo 硫化物クラスターが凝集して硫化物表面にある活性点が減少するため、活性が低下すると推定される。

また、XRD 測定より、再生温度により XRD パターンが異なることがわかった（図 4 左）。解析の結果、活性低下の大きい高温側の「温度領域Ⅱ」で再生した触媒は（図 2）、$CoMoO_4$ 結晶が生成・成長することがわかった（図 4 右）。再生触媒を活性化処理すると、$CoMoO_4$ 結晶が硫化されるため生成する Mo 硫化物は大きく、硫化物表面にある活性点が減少するため、活性が低下すると推定される。

以上の結果から、大きな Mo 硫化物クラスターの残存がなく、かつ $CoMoO_4$ 結晶の生成、成長がない温度領域で再生すると、再生触媒の活性低下が抑制されると推定されるため、これを「活性低下の小さい触媒再生方法の指針」とした。

ⅱ)2 回再生の検討

（新触媒を製油所で使用した後、商業装置で再生し再び製油所で使用した後の触媒を実験室スケールで再生）

前記ⅰ)の触媒再生方法の指針を検証するために、新触媒を製油所で使用した後商業装置で再生し再び製油所で使用した後の触媒について温度を変えて実験室スケールで再生して、再生触媒の担持金属（Mo）の状態・構造を EXAFS および XRD により調べた。その結果、大きな Mo 硫化物クラスターの残存がなく、かつ $CoMoO_4$ 結晶の生成、成長がない温度領域、すなわち活性低下の小さい再生温度領域は T'～T'+50℃であることがわかった。再生触媒の活性を評価したところ、上記温度領域で再生した触媒は他の温度で再生した触媒に比べて活性低下が小さいことがわかった（図 5、1 回再生触媒比の相対活性 0.95 以上）。

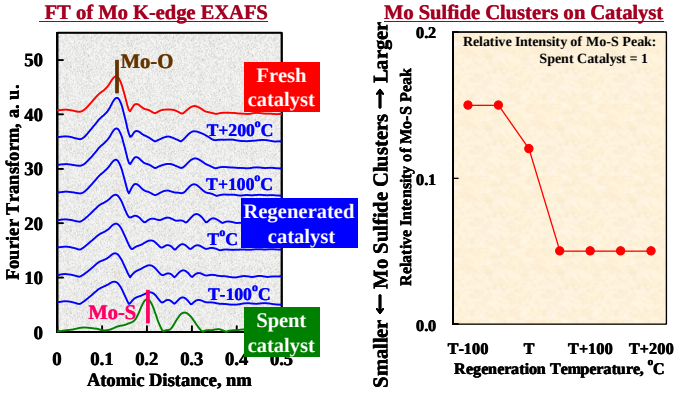

図 3 再生触媒の Mo K 吸収端 EXAFS 測定結果

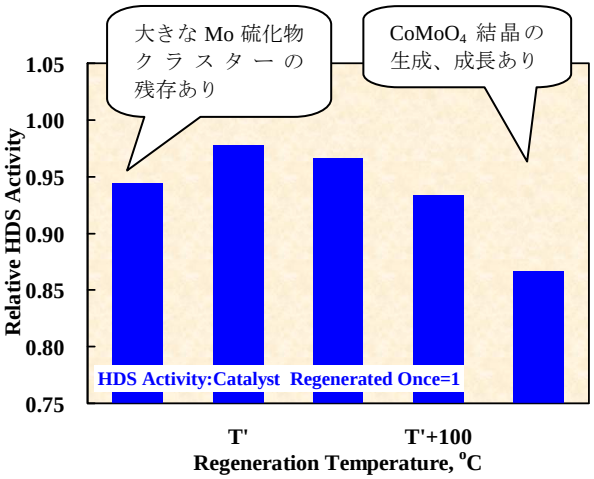

図 5　再生触媒の活性評価結果

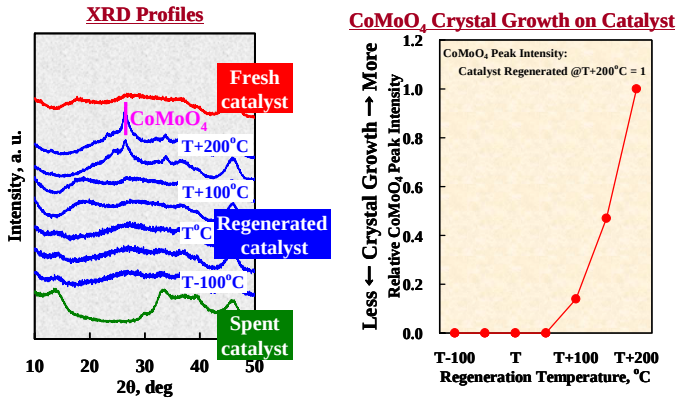

図 4　再生触媒の XRD 測定結果

(b) NiCoMo 系水素化脱硫触媒

ⅰ)1 回再生の検討

(a)-ⅰ)と同様に実験室スケールで再生した触媒の EXAFS 測定、XRD 測定を行った結果、活性低下の小さい再生温度領域が T"～T"+50℃であることがわかり、活性評価結果と一致した（図 6、新触媒比の相対活性 0.95 以上）。

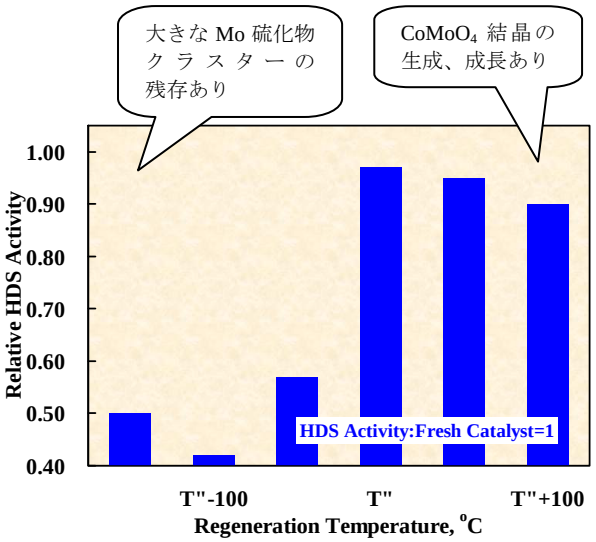

図 6　再生触媒の活性評価結果

３－２再生時間と触媒担持金属の状態・構造との関係（CoMo系水素化脱硫触媒）

前記３－１の検討結果から、大きなMo硫化物クラスターが残存すると再生触媒の活性が低いことがわかった。そこで、再生触媒の活性低下を抑制するために、触媒再生工程においてMo硫化物クラスターを消失（Mo硫化物をMo酸化物に変化）させるために必要な時間を見積もった。製油所で使用した触媒を*in-situ*セルに入れて空気流通下、一定温度で加熱（再生）しながらMo K吸収端EXAFS測定を行い、Moの状態・構造の経時変化を追跡した。時間経過とともに動径構造関数の形状は変化し、Mo硫化物由来のMo-Sピークの強度が低下し、Mo酸化物由来のMo-Oピークの強度が高くなる、すなわちMo硫化物がMo酸化物に変化する様子を観測することができた（図7）。再生時間とMo-Sピークの強度との関係をプロットした（図8）。ピーク強度が一定となる時間はMo硫化物クラスターが消失する時間なので、その時間は再生に必要な最短時間

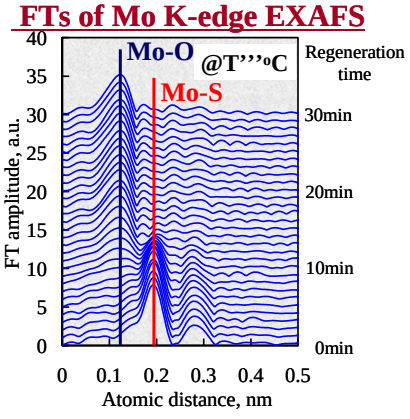

図 7　使用済み触媒の Mo K 吸収端 in-situ EXAFS 測定結果

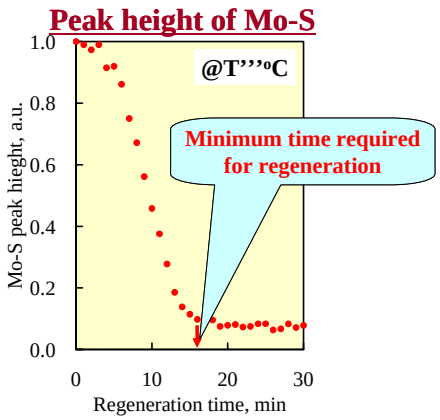

図 8　再生時間と Mo-S ピーク強度との関係

と考えられる。

次に再生温度を変えて同様な実験を行い、再生温度と最短再生時間との関係を得た（図 9）。その結果、再生温度が低いほど最短再生時間は長くなることがわかった。このことから、再生温度が低くても時間を長くすることにより Mo 硫化物クラスターを消失させることができるとわかった。また、低温で再生する際に Mo 硫化物クラスター消失に必要な時間は高温再生時の 3 倍以内であることもわかった。

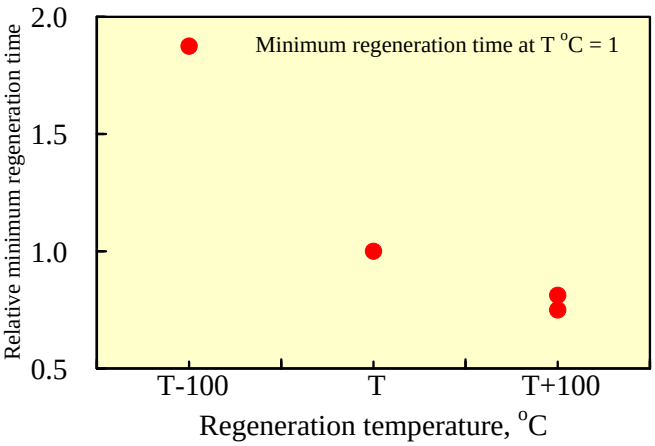

図 9　再生温度と最短再生時間との関係

４．まとめ：

製油所で使用した触媒について温度を変えて実験室スケールで再生して、再生触媒の担持金属（Mo）の状態・構造を EXAFS および XRD により調べ、活性評価結果と比較することで、当初の計画どおり活性低下の小さい触媒再生方法の指針を得ることができた。また、得られた指針を活用して、1 回の触媒再生につき活性低下が 5%以下とする目標も達成できた。さらに、再生時の担持金属（Mo）の状態・構造の時間的変化を EXAFS により追跡することで前記指針を補強する知見も得ることができた。

なお、NiCoMo 系水素化脱硫触媒については 2 回再生の検討および再生時間と触媒担持金属の状態・構造との関係の検討については今回実施できなかったので、今後の課題である。

今後、XAFS 法により得られた「活性低下の小さい触媒再生方法の指針」に基づいた条件を触媒再生メーカーに提示して商業スケールの装置を使用して触媒再生テストを行い、製油所装置へ再生触媒を充填して触媒活性低下挙動を調べる予定である。

参考文献

[1] A. Nishijima *et al.*, Catalyst Deactivation, 39 (1987).

成果発表状況：

学会・論文発表

(1)Yoshimu IWANAMI, Tomohiro KONISHI, Makoto NAKAMURA, Souichirou KONNO, Wataru SAHARA, Kiyofumi NITTA, Junich NISHINO, Hiroaki NITANI, Yasuhiro NIWA, Masaharu NOMURA、*In-situ* EXAFS study on a spent CoMo hydrodesulfurization catalyst during regeneration at various temperatures、The 6th International Workshop on Nano-Scale Spectroscopy and Nanotechnology（2010）

(2)Yoshimu IWANAMI, Tomohiro KONISHI, Makoto NAKAMURA, Souichirou KONNO, Masaharu NOMURA, *In-situ* EXAFS study on a spent CoMo HDS catalyst during regeneration at various temperatures**,** Photon Factory Activity Report 2009 (2010)

特許

(1)水素化処理用触媒の再生条件の選別方法、再生水素化処理用触媒の製造方法、岩波睦修、佐野孝、小西友弘、中村誠、今野聡一郎、新日本石油株式会社、特願2010-070553号、2010年3月25日、国内

(2)再生水素化処理用触媒の製造方法、岩波睦修、佐野孝、小西友弘、中村誠、今野聡一郎、ＪＸ日鉱日石エネルギー株式会社、特願2010-237538号、2010年10月22日、国内

先端研究施設共用促進事業
フォトンファクトリーにおける産業利用促進

課 題 番 号： **2009I007**
研究責任者： 平野辰巳、㈱日立製作所　日立研究所
利 用 施 設： 高エネルギー加速器研究機構　放射光科学研究施設　BL-9C,12C,NW2A
利 用 期 間： 2009 年 10 月～2010 年 9 月

リチウム二次電池用正極材料の局所構造解析
Local Structure Analysis of Positive Electrode Materials in Lithium Ion Battery

平野　辰巳、湯浅　豊隆、寺田　尚平、高松　大郊、日高　貴志夫
Tatsumi Hirano, Toyotaka Yuasa, Shohei Terada, Daikou Takamatsu, Kishio Hidaka

(株)日立製作所　日立研究所
Htachi Research Laboratory, Hitachi Ltd.

リチウムイオン電池におけるリチウムイオンの移動に伴う正極材内部の現象解明を目的として、XAFS により充放電における電極表面と内部の遷移金属元素の価数差異を評価した。$LiNi_{1/3}Mn_{1/3}Co_{1/3}O_2$、$LiFePO_4$における表面と内部の遷移金属元素の価数差異は、一相系と二相系の反応差異に起因する電極内部での電位勾配のモデルで説明できることがわかった。

We analyzed the valence of transition metals in the surface and inner regions of positive electrode materials of Lithium ion battery during the charge-discharge process using XAFS. It was found that the voltage gradient model in the positive electrode is a reasonable explanation for the valency difference between the surface and inner regions of $LiNi_{1/3}Mn_{1/3}Co_{1/3}O_2$ (one phase reaction) and $LiFePO_4$ (two phase reaction).

キーワード：リチウムイオン二次電池、正極材、XAFS、価数

１．はじめに

【背景】リチウムイオン二次電池(LIB)はラップトップ PC や携帯電話の民生用から車両搭載用に利用されつつある。特に、代替エネルギー、環境問題などから、高容量、長寿命、安全な産業用二次電池の開発が急務となっている。LIB の開発課題は、高容量化、長寿命化、高安全化、低コスト化であり、これらを兼ね備えた正極材料は開発されていない。本電池システムはリチウムイオンが電荷移動担体として機能していることから、正負極内のリチウムの状態及び量が重要な因子となる。

【目的】従来用いられている層状系（R-3m、$LiCoO_2$ 等）に比べて、オリビン系（Pnma、$LiFePO_4$ 等）は LIB の熱暴走時の酸素脱離が抑制され、熱的に安定とされている[1]。一方、リチウムイオンの伝導パスは、一次元方向（層状系：二次元）のため、低レート特性や高抵抗化などが問題となっている。このため、充放電における正極材粒子中のリチウム分布の評価が重要となる。更に、Ni 組成が多い層状系正極材では、粒子表面に形成される Ni 酸化物が劣化要因の一つ[2]と考えられており、オリビン系における劣化要因の評価も重要となる。そこで、リチウムイオンの移動に伴う正極材内部の現象解明を目的として、XAFS により充電中における遷移金属元素の価数や、電極表面と内部の価数差異を評価した。

【目標】１）オリビン系正極材の各充電状態における表面および内部の価数差異の明確化と層状系正極材との比較。２）高温貯蔵やサイクル試験により劣化したリチウム電池正極材の表面および内部の局所構造差異の明確化と各材料系との比較。

２．実験

【研究計画】１）モデル電池セルを用い、各充電状態（SOC：State of Charge）における遷移金属元素の価数評価、２）各SOCにおける遷移金属元素の表面および内部の価数差異評価。

【実験の方法】モデル電池セルとして、X線透過窓（カプトン膜）を設けた簡易電池セルを作製した。正極／セパレータ／Li金属（負極側）の構成でセルを組立、1/3Cの電流で初期化した。1/3Cの定電流定電圧モードで所定のSOCに設定し、電圧が安定した後に回路状態で透過のQuick-XAFSを測定した。表面および内部の価数評価については、所定のSOCに設定した正極試料をArグローブボックス内でアルミラミネートで封止した。透過法での測定後に、アルミラミ

ネートから試料を取り出し、He転換電子収量法（CEY法）で測定した。透過法（CEY法）は、試料内部（表面~100nm）の評価に対応する。価数が既知である標準試料を用い、測定試料の吸収スペクトルのエネルギー位置から各遷移金属元素の価数を算出した。

【試料】層状系正極材は$LiNi_{1/3}Mn_{1/3}Co_{1/3}O_2$（LNMCO）、オリビン系正極材は$LiFePO_4$（LFPO）を用いた。SOCは充電方向で設定した。オリビン系正極試料は、放電方向でもSOCを設定し、充電および放電方向での価数差異を評価した。

３．結果および考察

層状系およびオリビン系の充電反応は、

$$LiMO_2 \leftrightarrow Li_{1-x}MO_2 + xLi^+ + xe^- \text{ (層状系)}$$

$$LiMPO_4 \leftrightarrow MPO_4 + Li^+ + e^- \text{（オリビン系）}$$

で表され、M は遷移金属元素（Mn、Fe、Co、Ni など）である。また右方向の反応が充電である。図１にモデル電池セルによる初期化時の充電曲線（(a)、(b)）と各遷移金属元素の価数の SOC 依存性（(c)、(d)）を示す。LNMCO の充電曲線（図１(a)）の電圧は、徐々に増加しており一相系反応であることが分かる。SOC が高くなると正極から負極に Li が移動し、正極にある遷移金属元素の価数は大きくなる。LNMCO の各遷移金属元素の価数変化は、Mn＜Co＜Ni の順で大きく、Ni の価数変化が一番大きい（図１(c)）。即ち、正極からの Li 脱離による電荷補償として、Ni が主に担っていることになる。図１(b)に示したオリビン系の充電曲線では、電圧が一定となる領域が存在し、二相系反応であることがわかる。LFPO では、SOC の増加とともに、Fe の価数も増加し、Fe が Li 脱離による電荷を補償している。これから、充電曲線における電圧変化と各遷移金属元素の価数変化の対応が明らかになった。また、モデル電池セルを用いて充放電による価数のその場評価が実現できた。

図２にアルミラミネートした正極シートにおける表面および内部の各遷移金属元素の価数の SOC 依存性を示す。塗りつぶし（●）は透過法による結果で試料内部の価数である。白抜き（○）は CEY 法による結果でセパレータ側の試料表面の価数である。充電方向で SOC を調整した LNMCO では、Mn、Co、Ni の各遷移金属元素とも内部と表面で価数の差異はない（図２(a)）。一方、LFPO では、表面と内部で Fe の価数が異なっている（図２(b)）。SOC を充電方向で調整した場合（赤色）、表面の価数は内部に比べて 0.2 程度大きく、表面には内部に比べて高価数の FePO4 が多く存在する。一方、SOC を放電方向で調整した場合（青色）、SOC：50%以上で表面の価数は内部に比べて 0.1 程度小さく、表面には低価数の $LiFePO_4$ が存在する。

充電による正極シート内での Li 分布のモデルを図３に示す。充電により正極から負極に Li イオンが移動するが、正極内での非一様な電位勾配によりセパレータ側である表面の方が内部に比べて Li 脱離量が多いと考えられる。LNMCO の層状系は一相系反応のため、表面側の Li 組成を 1-x、アルミ集電体側の Li 組成を 1-y とすると、x>y となる。層状系では、充電曲線が徐々に変化する（図１(a)参照）。SOC 調整後に電流を切断すると、Li 組成分布に起因して電極内部には電位勾配が存在する。この電位勾配により Li イオンが拡散し、電位勾配が平坦になる。このため電極表面と内部における Li 組成の差異はなくなると考えられる。一方、LFPO のオリビン系は二相系反応のため、充電中の正極内での非一様な電位勾配により表面側の $FePO_4$ の量が内部に比べて多くなる。オリビン系では、図１(b)に示すように充電曲線は一定であるため、SOC 調整後に電流を切断しても電極内部の電位勾配がない。このため、Li イオンは移動せず、表面側の $FePO_4$ 量は内部に比べて多い状態で維持される。この結果、表面側の Fe 価数は内部に比べて高くなると考えられる。放電は、この現象の逆で、負極から正極に Li イオンが移動する。放電中の非一様な電位勾配により表面の $LiFePO_4$ の量が内部に比べて多くなる。充電と同様に SOC 調整後に電流を遮断しても Li イオンの移動がないので、この状態が維持され、表面側の Fe 価数は内部に比べて低くなる。

以上、LNMCO、LFPO における表面と内部の遷移金属元素の価数差異は、一相系と二相系の反応差異に起因する電極内部での電位勾配によるものと考えられる。

４．まとめ

モデル電池セルを用いて、各 SOC における遷移金属元素の価数が評価できることがわかった。更に、オリビン系正極材では、放電および充電で表面と内部で価数差異が存在する。これは、二相系反応に起因する電極内部での平坦な電位によるモデルで説明できる。以上の結果から、当初の目標１）を達成した。一方、充電および放電で、表面と内部で価数差異が存在するため、目標２）の高温貯蔵やサイクルの劣化による表面と内部の価数差異の評価が困難となることが判明した。LIB の実用化には、この劣化機構の解明と対策が必要となるが、本手法を適用するには、より詳細な基礎データの取得を必要とすることがわかった。

オリビン系正極は、熱的安定性に優れた材料系であるが、層状系に比べて導電率が数桁低い。これは、車載用で要望される高速充放電の障害となると予想される。この解決には、１）高抵抗化要因の解明、２）粒子内での Li イオンの挿入脱離挙動の解明、３）充放電における Li 緩和現象の解明、４）正極粒子の粒径最適化、添加元素の最適化などが必要となる。３）については、１秒以下で測定できる DXAFS が有効であり、今後の検討課題である。

参考文献

[1] 山田淳夫他、日本結晶学会誌、**51** (2009) 175.
[2] 野中敬正、放射光、**21** (2008) 313.

成果発表状況

（本課題で実施した実験結果に関わる発表）

(1) 小西宏明他、"Ni-Mn-Co 三元系正極材料の熱安定性の検討"、第 50 回電池討論会（2009）。
(2) 平野辰巳他、"XAFS による Li 正極材料の熱安定性の検討"、第 27 回 PF シンポジウム（2009）。

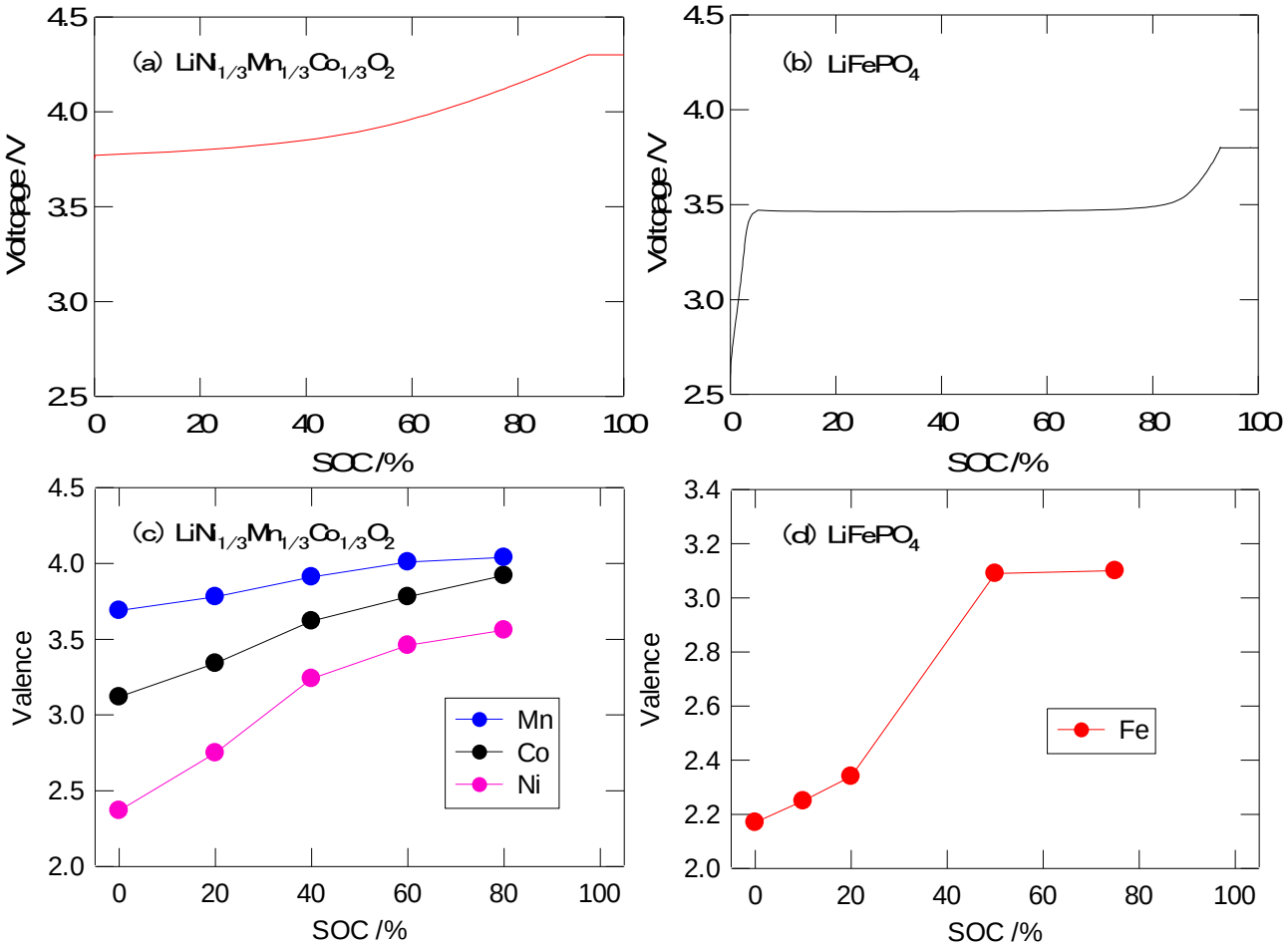

図1　モデル電池セルによる初期化時の充電カーブ((a)、(b))と遷移金属元素の価数のSOC（充電深度）依存性((c)、(d))。

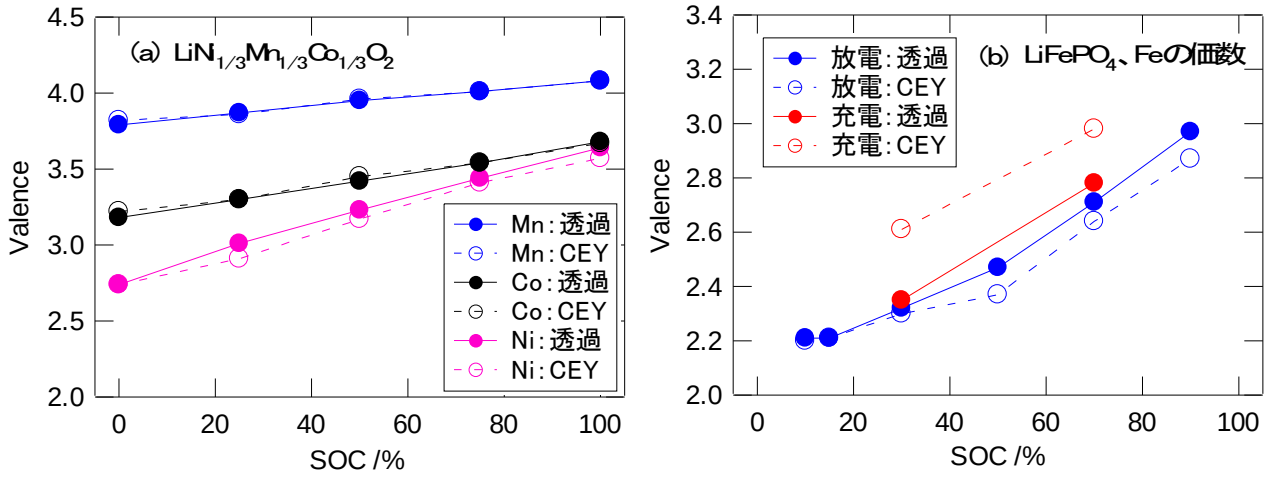

図2 アルミラミネートした正極シートにおける遷移金属元素の価数のSOC依存性。(a)：$LiNi_{1/3}Mn_{1/3}Co_{1/3}O_2$、充電でSOCを調整、(b)：$LiFePO_4$、充電および放電でSOCを調整。塗りつぶし(●)は透過法で試料内部の価数。白抜き(○)はCEY法でセパレータ側試料表面の価数。

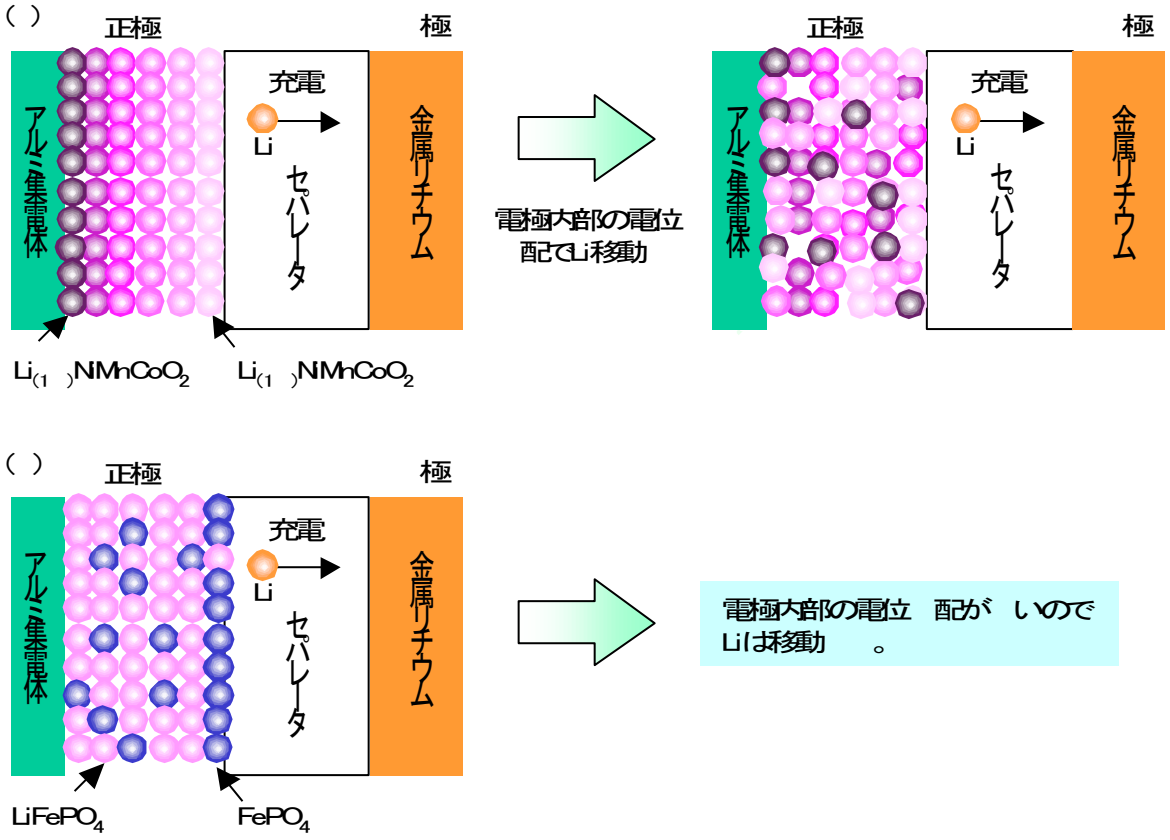

図　充電による正極内でのLi分布のモデル。( )：$LiNi_{1/3}Mn_{1/3}Co_{1/3}O2$。( )：$LiFePO_4$。

先端研究施設共用促進事業
フォトンファクトリーにおける産業利用促進
利用報告書

課 題 番 号： **2009I009**
研究責任者： 加藤 英純 スズキ株式会社
利 用 施 設： 高エネルギー加速器研究機構　放射光科学研究施設　PF-AR NW10A
利 用 期 間： 2010 年 1 月～2010 年 12 月

自動車排気ガス浄化触媒の in-situ XAFS 測定

In-situ XAFS analysis of automobile exhaust catalyst

三浦 和也[1]、西野 潤一[2]、津田 豊史[1]、木俣 文和[1]、村上 春彦[1]、新田 清文[2]、丹羽 尉博[2]、仁谷 浩明[2]、阿部 仁[2]、上村 洋平[2]、野村 昌治[2]
Kazuya Miura[1], Junichi Nishino[2], Toyofumi Tsuda[1], Fumikazu Kimata[1], Haruhiko Murakami[1], Kiyofumi Nitta[2], Yasuhiro Niwa[2], Hiroaki Nitani[2], Hitoshi Abe[2], Youhei Uemura[2] and Masaharu Nomura[2]

[1] スズキ株式会社、[2] 高エネルギー加速器研究機構
[1]Suzuki Motor Corporation, [2]KEK

アブストラクト：実用の自動車排気ガス浄化触媒の Pd に注目して in-situ XAFS 測定を実施し、さらにモデルガス浄化率と比較した。その結果、NOx 浄化率が上昇する条件では Pd が還元し、逆に NOx 浄化率が低下する条件では Pd が酸化した。この結果は金属状態の Pd 表面が NOx 浄化の活性点であると示唆する。

Pd K-edge in-situ XAFS measurements were carried out for the automobile catalyst, to investigate the correlation between the chemical states of Pd and the model-gas conversion activity. The chemical state of Pd becomes metallic state under the condition that the NOx conversion rate becomes rising. Oppositely, the Pd becomes oxidized state when the NOx conversion rate decreases. It is suggested that the metallic Pd surface is efficient catalyst for the NOx conversion reaction.

キーワード：自動車排気ガス浄化触媒, in-situ XAFS, Pd K-edge, Ce K-edge

１．はじめに：ガソリン車には白金族元素（Pt, Pd, Rh）を担持した三元触媒が搭載されており、商品価値の高い車を造るために浄化性能を満足しつつ白金族元素の使用量を低減することが求められている。XAFS（X 線吸収微細構造）法により白金族元素の挙動を解明することで、その使用量低減につながるアイデアが得られると期待されている[1, 2]。

本研究の目的は実用環境を模擬した雰囲気（モデルガス）にて実用触媒をXAFS測定し、白金族元素の化学状態と触媒の浄化率の間に対応関係を見出すことである。白金族元素のうち最も担持濃度の高いPdについて解析した。

２．実験：Pd K-edgeおよびCe K-edge XAFS測定はPF-AR NW10A(分光結晶 Si(311))にて透過法で実施した。量産車に搭載されている触媒（コージェライト製ハニカムに厚さ数μmの触媒層をコートしたもの。触媒層はPd 3.2 wt%を担持したCe-Zr系酸化物とγ-アルミナの混合物）を空気中で950℃ 10時間熱劣化した後、還元雰囲気(CO 2%, C_3H_6 9000ppm, 窒素希釈)で500℃ 1時間、さらに酸化雰囲気(O_2 2%, NO 3000ppm, 窒素希釈)で500℃ 1時間処理し、それぞれ以下の実験に用いた。

[浄化率測定] XAFS 測定と独立し、浄化率を測定した。φ30mm×30mm のハニカム触媒に酸素過剰率(λ)＝0.9 または 1.3 のモデルガスをフローした。表 1 にガス条件を示す。ガスを加熱することで触媒温度を制御し、さらに触媒前後のガス組成をモニターすることで、CO, HC および NOx の浄化率を求めた。

表 1. 浄化率測定用モデルガス.

	λ=1.3	λ=0.9
C_3H_6 [ppm]	180	
CO [vol%]	0.21	
NO [ppm]	400	
O_2 [vol%]	0.22	0.15
N_2	Balance	
全流量 [L/min.]	20	

[Pd K-edge ex-situ 測定] in-situ 測定に先立ち、ex-situ 測定を実施した。λ＝0.9 又は 1.3 雰囲気（表 1）のモデルガスをハニカム触媒へフローし、モデルガスを加熱することで触媒をそれぞれ 160, 300 または 500℃とした。約 5 分保持した後、雰囲気を保って触媒を冷却し、触媒層のみ採取してペレット（φ7mm×1mm, 120mg）成型した。この試料の Pd K-edge を大気中で測定した。

[Pd K-edge in-situ 測定] ペレット成型した触媒試料を PF 所有の in-situ 測定装置に設置し、もう一度 500℃, 1 時間の酸化処理を行った。その後 λ＝0.9 または 1.3 のモデルガスをフローして 150℃に加熱し、3℃/min.で 500℃へ昇温しつつ 1min. の quick scan で Pd K-edge を測定した。

浄化率測定実験や ex-situ 測定実験と比較し、in-situ 測定実験の条件には以下の変更点がある。第一に、ハニカム触媒を透過法で XAFS 測定することはできないため、ペレット状態の触媒にモデルガスを作用した。第二に、利用した in-situ 測定装置の仕様上、モデルガスを加熱せず、触媒試料を直接加熱した。第三に、ペレットが飛散する恐れがあったためモデルガス流量を 0.1L/min.へ落とした。触媒重量あたりの C_3H_6, CO, NO 及び O_2 分子供給量を全ての実験で同等に調整するため、各成分の濃度を表 1 の 4 倍とした。

[Ce K-edge in-situ 測定] ペレット成型した触媒試料に還元ガス(CO 11%, C_3H_6 14000ppm, 窒素希釈)をフローして 120℃に加熱し、10℃/min.で 500℃へ昇温した。500℃で約 1 時間保持した後、120℃に冷却し酸化ガス(O_2 24%, NO 18000ppm, 窒素希釈)をフローした。この間の Ce K-edge を 1min.の quick scan で in-situ 測定した。

３．結果および考察：

[Pd K-edge ex-situ 測定の結果] λ＝0.9 および 1.3 の結果をそれぞれ図 1, 2 に示す。XAFS は全て μ_0 で規格化して示す。

いずれも 160℃条件では、初期状態（酸化処理後の状態, 図には示さない）と同等の XAFS が得られた。Pd の化学状態は金属 Pd と酸化 Pd の混合状態であり、完全には酸化していない。

λ=0.9 雰囲気では、Pd は昇温により還元した。

λ=1.3 雰囲気では、酸素過剰雰囲気であるにもかかわらず、300℃条件で Pd が還元した。しかしながら 500℃まで昇温すると Pd が酸化し初期状態と類似した XAFS を示した。

後ほど図 7 で例を示すとおり、動径構造関数の詳しい解析はできなかった。

[Pd K-edge in-situ 測定の結果] λ＝0.9 および 1.3 の結果のうち、特徴的な 3 点をそれぞれ図 3, 4 に示す。

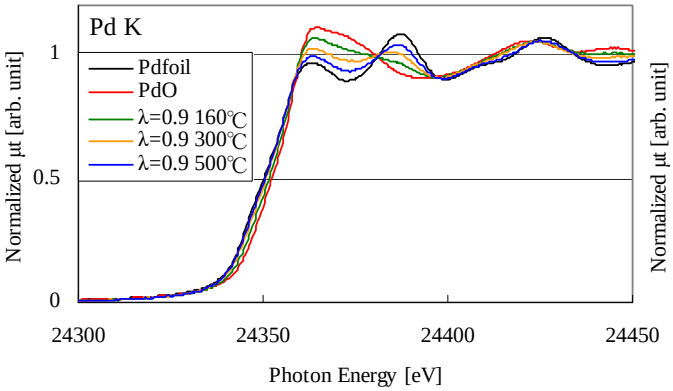

図 1. ex-situ XAFS 測定結果 (酸素過剰率 λ＝0.9).

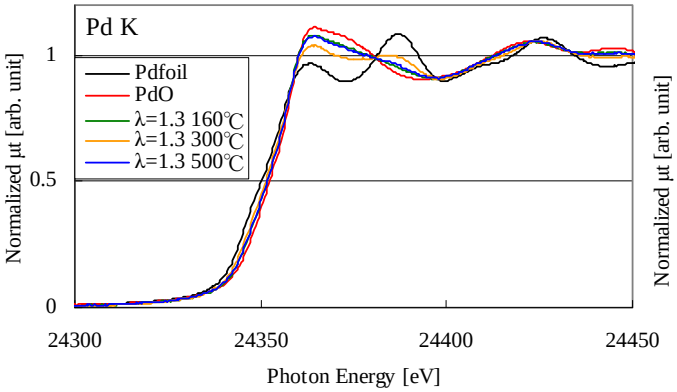

図 2. ex-situ XAFS 測定結果 (酸素過剰率 λ=1.3).

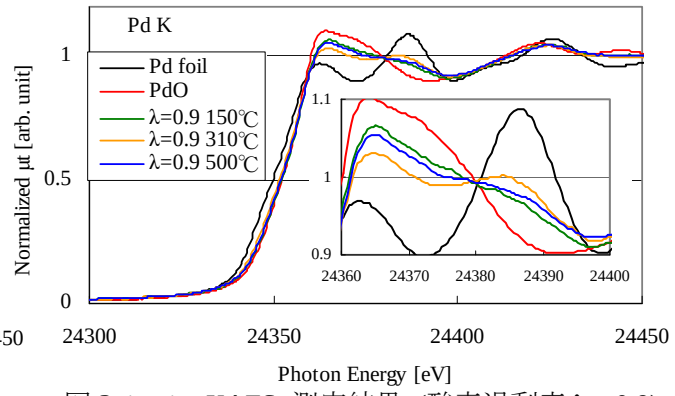

図 3. in-situ XAFS 測定結果 (酸素過剰率 λ＝0.9).

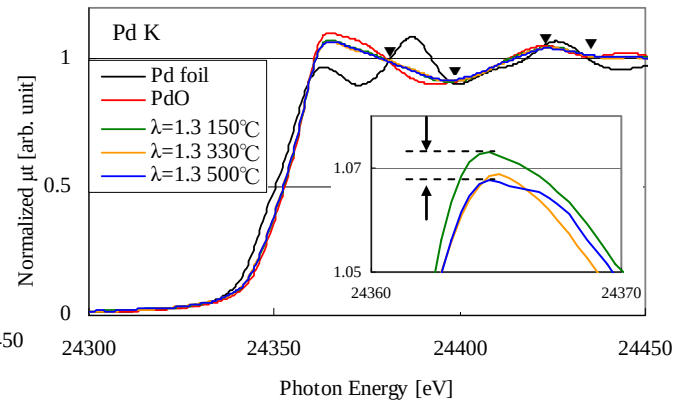

図 4. in-situ XAFS 測定結果 (酸素過剰率 λ=1.3). マーカーは等吸収点.

まずλ＝0.9 の結果に注目する。Pd は 150℃条件で最も酸化しており、310℃条件で最も還元していた。そこでこれら 2 条件の XAFS を基準に用いて Linear Combination Fitting (LCF)解析した。結果を図 5 に示す。約 210℃を超えると Pd の還元が始まり(図 5 挿入図)、300℃前後で急激に還元が進んだ。これは ex-situ 測定結果に対応する。しかしながら約 360℃以上では Pd が酸化しており、ex-situ 測定結果と対応しなかった。

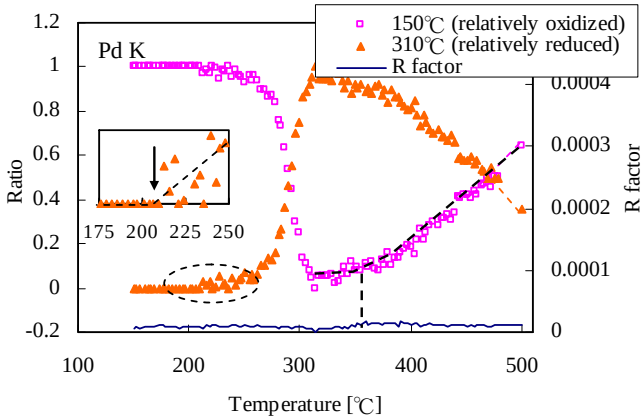

図 5. LCF 解析結果 (λ=0.9 条件).
480℃と 500℃の間は入射により未測定.

λ＝1.3 の結果(図 4)に注目する。ex-situ 測定（図 2）と比べて XAFS の変化は小さかった。いずれの XAFS も 2 個の標準試料（Pd foil, PdO）と等吸収点で交差したため、標準試料を基準に用いて LCF 解析した。図 6 は LCF 解析結果のうち、Pd foil の寄与を示す。約 210℃を超えると Pd が還元して金属 Pd が形成した。しかしながら約 320℃を超えると Pd は酸化し始めた。この結果は ex-situ 測定の結果と対応する。

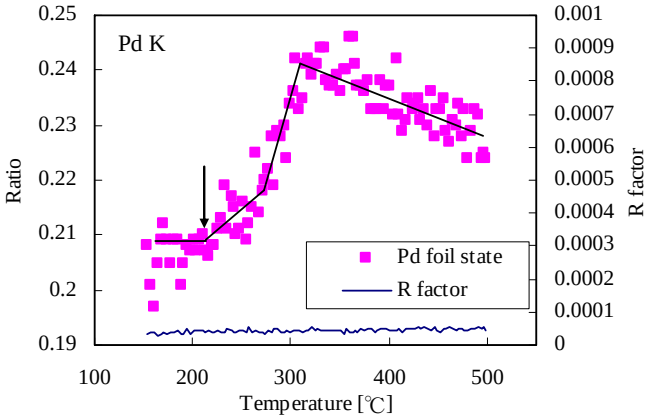

図 6. LCF 解析結果 (λ=1.3 条件).

[動径構造関数] λ=0.9 または 1.3 雰囲気の in-situ または ex-situ 測定において、得られた動径構造関数はいずれも Pd foil と PdO の中間的な形状であった。例として図 7 にλ=1.3 条件 ex-situ 測定結果の動径構造関数を示す。

1.5Å近辺の Pd-O 結合を除き、2Å～4Åのピークは複数の散乱パスが重複しており適切なカーブフィッティングが困難であった。3Å付近のピークは Pd と担体元素（Ce 又は Zr）の配位を示す可能性がある[1]。構造決定には別途 TEM･STEM 観察が必要である。

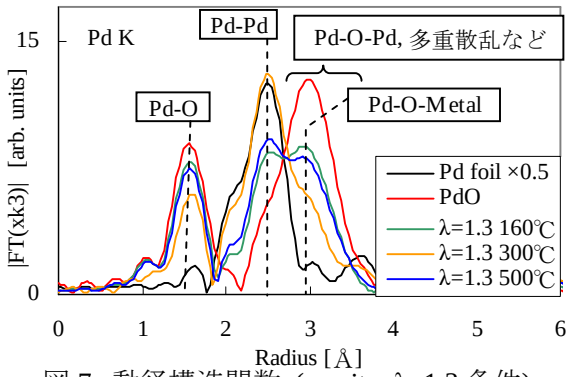

図 7. 動径構造関数 (ex-situ, λ=1.3 条件).

[Ce K-edge in-situ 測定の結果] 触媒試料の Ce K-edge について、吸収端エネルギーの解析結果を図 8, 9 に示す。触媒試料の Ce-Zr 系酸化物は CeO_2 標準試料より吸収端が高エネルギー側であった。Ce_2O_3 標準試料は空気中で自然酸化し、適切に測定できなかった。

図 8 は還元雰囲気の結果である。約 350℃以上で Ce が還元した。これは Ce-Zr 系酸化物が酸素を放出したことを示す[1, 3]。

図 9 は還元処理した触媒試料を 120℃に冷却し、酸化ガスを導入した際の結果である。酸化ガスを導入後、ただちに Ce が酸化し、酸素を吸蔵したことが示された。

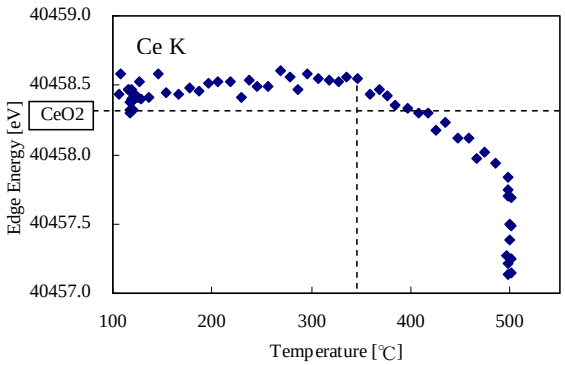

図 8. 吸収端エネルギー (還元雰囲気).

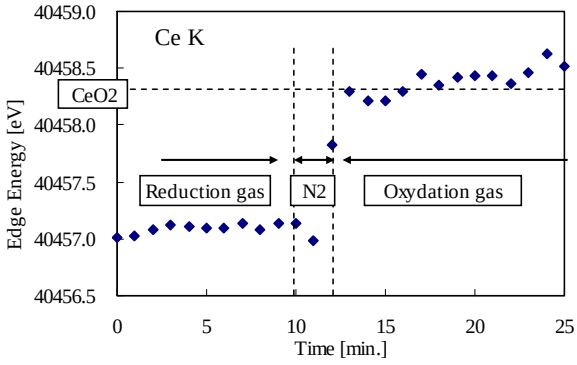

図 9. 吸収端エネルギー (酸化雰囲気 120℃).

[XAFS とモデルガス浄化率の比較] λ=0.9 または 1.3 雰囲気にて触媒試料を昇温すると、Pd が①初期状態（前処理により酸化した状態）を保つ、②還元する、③再び酸化する、と振舞うことが in-situ 測定で明らかになった。図 10 は Pd がそれぞれ①～③の挙動を示した温度を、モデルガス浄化率曲線上にプロットして示す。母材の Ce-Zr 系酸化物が酸素を放出する（Ce^{4+}が還元する）温度もあわせて示す。

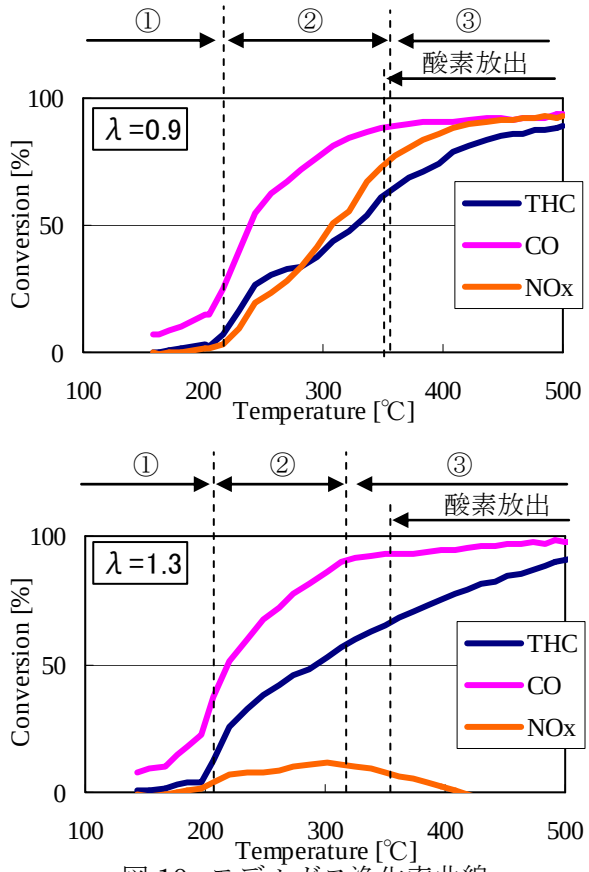

図 10. モデルガス浄化率曲線.

[考察：ライトオフ温度] λ=0.9 および 1.3 条件ともに、約 210℃を超えると Pd が還元し始めた。200℃以上で各成分の浄化率が立ち上がる（ライトオフ）ことから、ライトオフ温度以上では CO や HC の酸化反応に Pd 表面の酸素が消費され、Pd が還元したと解釈できる。

[考察：NOx 浄化率] λ＝1.3 条件の NOx 浄化率に注目する。NOx 浄化率が上昇する 200~300℃にかけて Pd は還元し、NOx 浄化率が低下する約 300℃以上で Pd は酸化した。この結果は、金属的な Pd 表面が優れた NOx 浄化触媒であり、酸化した Pd は NOx を浄化し難いことを示唆する。この件については更なる知見の蓄積が必要である。なお Pt については、金属状態の Pt 表面が NO 浄化に効果的に働くと提案されている[4]。

[考察：in-situ 測定の問題点] 断言はできないが、本研究の in-situ 測定では試料をペレット成型したために、ex-situ 測定と結果の一部が対応しなかったと予想する。λ=0.9 条件 in-situ 実験（図 3）の高温時には Ce-Zr 系酸化物の酸素放出に伴う Pd の酸化が、還元ガスによる Pd の還元より優位となり ex-situ 実験（図 1）と結果が異なったと予想する。ペレット成型によりガス拡散性が悪くなることが原因と疑われる。λ=1.3 条件の in-situ 測定（図 4）では CO, C_3H_6 がペレット表面近傍で消費され内部まで拡散せず、ex-situ 測定（図 2）ほど Pd の還元が顕著でなかったと想像する。

４．まとめ：金属状態の Pd が NOx 浄化反応の活性種であると示唆された。
ライトオフ温度で酸化 Pd が還元した。

今後の課題

試料をペレット成型せずに in-situ XAFS 測定したいと考えている。具体的には
① ハニカム状態の触媒を蛍光法で in-situ 測定
② さらに浄化率を同時計測
できることが、強く望まれる。

このようなシステムを用いて、Pd が酸化または還元する活性化温度のミクロ構造依存性を解明することで、触媒貴金属の低減につながる具体的なアイデアが得られると期待している。

謝辞：本研究は PF スタッフの支援によって実施できました。

参考文献

[1] Yasutaka Nagai *et. al., Catal. Today* 145 (2009) 279.
[2] Anna Kubacka *et. al., J. Catal.* 270 (2010) 275.
[3] M. Ozawa *et. al., J. Alloys Compd.* 193 (1993) 73.
[4] A. Eichler *et. al., Chem. Phys. Lett.* 343 (2001) 383.

成果発表状況

(1) 西野潤一 他、自動車排気ガス浄化触媒中の金属微粒子の in-situ XAFS 測定、第 13 回 XAFS 討論会 (2010) 立命館大学.
(2) 三浦和也、 自動車排ガス浄化触媒の XAFS 解析、平成 22 年度シンクロトロン光利用者研究会 第 2 回 XAFS グループ (2010) 名古屋.
(3) 三浦和也 他、自動車排気ガス浄化触媒の in-situ XAFS 測定、第 28 回 PF シンポジウム (2011) つくば.

参考

はじめに：予備実験として、酸化または還元雰囲気における Pd の状態変化を in-situ 測定した。

実験：ハニカム触媒を空気中で 950℃ 10 時間熱劣化し、触媒層のみ収集してペレット成型した。試料を 500℃に加熱し、還元雰囲気(CO 11%, C_3H_6 14000ppm, 窒素希釈)で 1 時間、次いで酸化雰囲気(O_2 24%, NO 18000ppm, 窒素希釈)で 1 時間処理した。この前処理を複数回行ない、以下の実験に用いた。

[in-situ 測定] 試料を 120℃に加熱して還元ガスをフローし、10℃/min で 500℃へ昇温、1 時間保持した後 120℃へ冷却した。次いで酸化ガスをフローし 10℃/min で 500℃へ昇温した。この間、1min.の quick scan で Pd K-edge を測定した。

[ex-situ 測定] 試料をそれぞれ①1%H_2, ②3%CO, ③1000ppm C_3H_6 または④3%CO, 1000ppm C_3H_6 混合（全て窒素希釈）雰囲気の 500℃で 1 時間還元した。そして Pd K-edge を大気中で測定した。

結果と考察：**[in-situ 測定]** 図 11 は還元雰囲気 120, 380 または 500℃で測定した XAFS を示す。これらは等吸収点を通らない（挿入図）。したがって Pd の状態は 3 成分以上存在する。対応する動径構造関数を図 12 に示す。120℃の結果は金属 Pd と酸化 Pd の混合状態を示す。380℃の結果は金属 Pd に帰属される。500℃の結果は金属 Pd と似ているが、Pd-Pd 結合距離が長い構造である。これを金属 Pd 類似構造と呼ぶ。

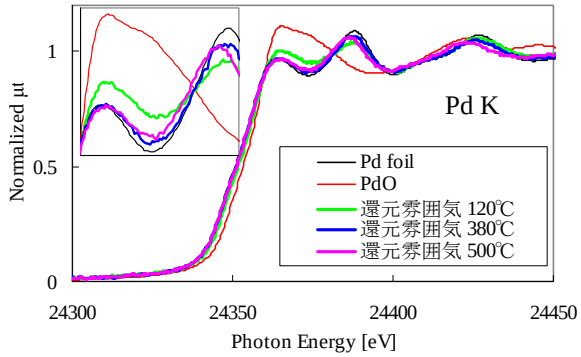

図 11. in-situ XAFS (還元雰囲気).

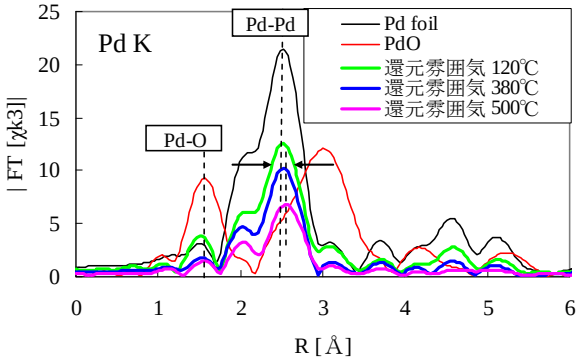

図 12. 動径構造関数（還元雰囲気).

酸化雰囲気の結果を図 13, 14 に示す。120℃で金属 Pd 類似構造、360℃で金属 Pd、500℃で金属 Pd と酸化 Pd の混合状態の存在が示唆された。

本論（図 7）と異なり、図 12, 14 では Pd-Pd 結合を明確に判別できた。これは大きな Pd ナノ粒子の存在を意味する。雰囲気に依存した可逆変化を解明するため、実験前に酸化, 還元処理を複数回行なった。これにより Pd が熱力学安定な状態になると期待した。その結果 Pd ナノ粒子が粗大化したと考えている。

図 15, 16 は得た各 XAFS の吸収端エネルギー, Pd-Pd 結合のフィッティング解析結果および LCF 解析結果を温度に対して示す。LCF は金属 Pd, 金属 Pd 類似構造, 金属 Pd と酸化 Pd の混合状態の 3 成分で実施した。酸化雰囲気で Pd は酸化しながら Pd-Pd 配位数を減少し、逆に還元雰囲気で Pd は還元しながら Pd-Pd 配位数を増大した。これは Pd ナノ粒子が酸化雰囲気で分散・微細化し、還元雰囲気で凝集・粗大化したことを示す[1, 2]。LCF 結果より、約 200℃（ライトオフ温度）を超えると Pd の化学状態が変化した（矢印）。Pd が活性状態になり、周囲の分子と相互作用して化学状態が変化したと考えられる。

[ex-situ 測定] ex-situ 測定によって得た動径構造関数を図 17、Pd-Pd 結合の解析結果を表 2 に示す。炭素を含むガスで還元した触媒にて、金属 Pd 類似構造が認められた。その正体を炭素原子が固溶した Pd [2]と予想する。

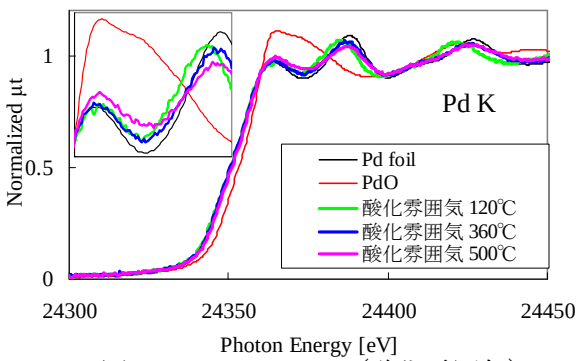

図 13. in-situ XAFS (酸化雰囲気).

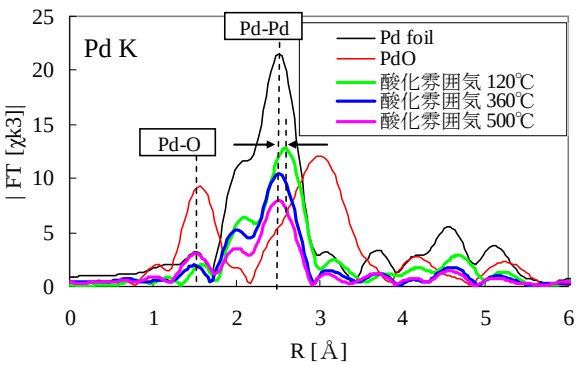

図 14. 動径構造関数（酸化雰囲気).

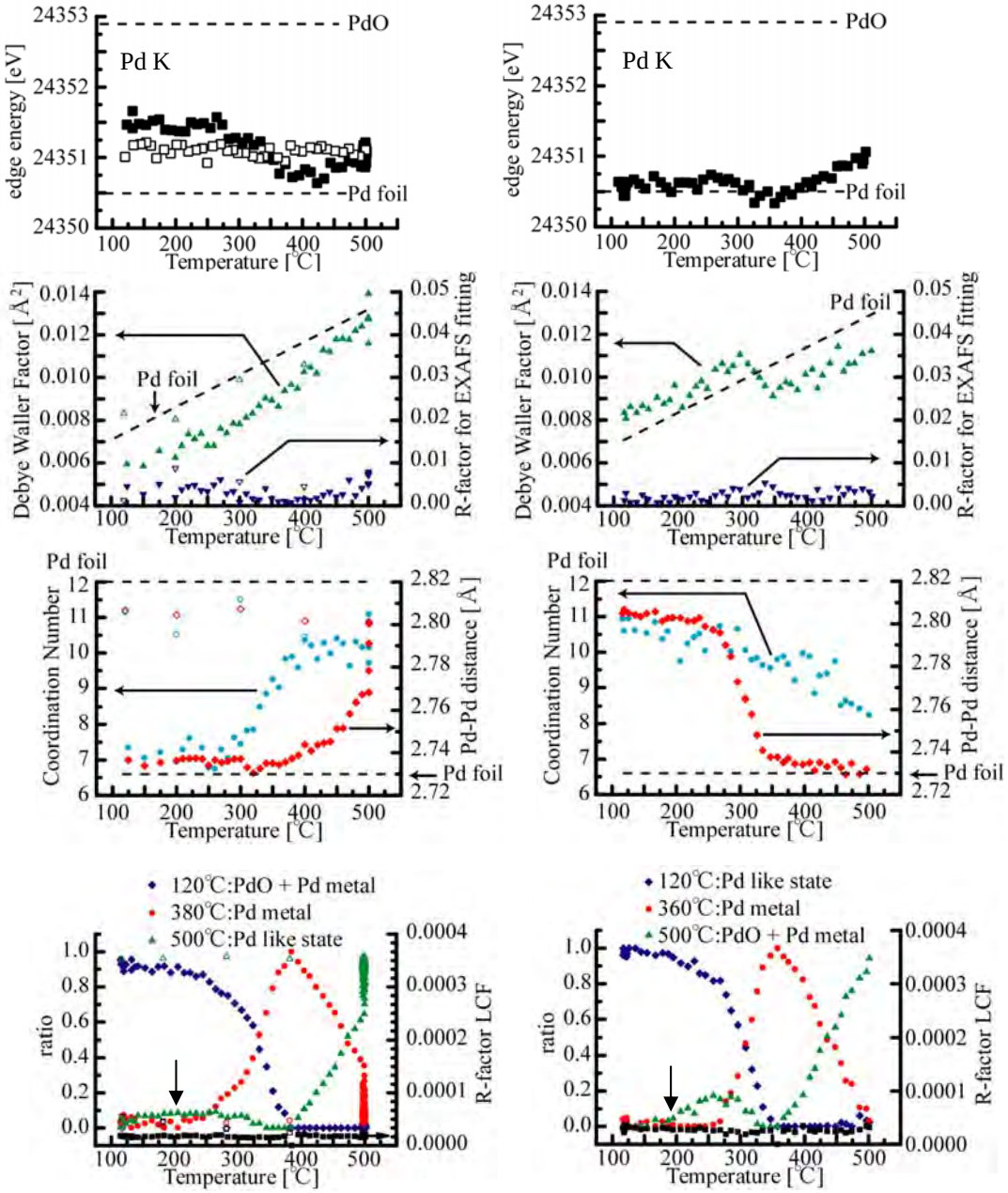

図 15. in-situ XAFS 解析結果 (還元雰囲気). 白のマーカーは冷却時の結果

図 16. in-situ XAFS 解析結果 (酸化雰囲気). 時間の都合上 500℃到達後は測定できなかった

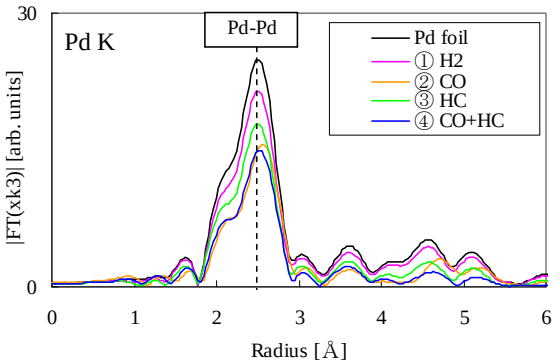

図 17. 動径構造関数 (還元した触媒試料).

表 2. Pd-Pd 結合構造パラメータ (還元した触媒試料).

	配位数	結合距離 [Å]	デバイワラー因子[Å²]	R factor
Pd foil	12±0.4	2.741±0.001	0.0057±0.0001	0.00018
①H_2	10.7±0.3	2.741±0.002	0.0060±0.0002	0.00020
②CO	10.5±0.5	2.801±0.002	0.0075±0.0002	0.00034
③HC	10.4±0.5	2.744±0.002	0.0069±0.0003	0.00058
④CO+HC	10.1±1.0	2.764±0.004	0.0078±0.0005	0.00207

NW10A / 2010G 593

EXAFS analysis of the Rh-Te alloy nanoparticles prepared by liquid phase reduction method

Noritoshi YAGIHASHI[1], Masafumi NAKAYA[2] , Atsushi MURAMATSU[2], Kiyotaka ASAKURA[3]*,
[1]Graduate School of Engineering, Tohoku University, Aoba-ku, Sendai, Miyagi 980-8579, Japan
[2] Institute of Multidisciplinary Research for Advanced Materials, Tohoku University, Sendai, Miyagi 980-8577, Japan
[3]Catalysis Research Center, Hokkaido University, Sapporo, Hokkaido 001-0021, Japan

Introduction

The rhodium tellurium (RhTe) bimetallic nanoparticle works as the catalyst of oxidative diacetoxylation reaction of butadiene. In our previous study, RhTe nanoparticles were prepared by liquid-phase reduction in the presence of chelating agents. In this study, we have applied the liquid phase reduction method to prepare RhTe nanoparticles in organic solvent. In this paper, we have studied the structure of prepared Rh-Te nanoparticles by using EXAFS analysis to figure out preparation mechanism.

Experimental

The EXAFS measurements were carried out at BL14B2 of SPring-8 with 8 GeV - 99.5 mA (Proposal No. 2011A1973) and at NW10A of PF-AR with 6.5 GeV – 60 mA. The X-rays at BL14B2 passed through a Si(311) double-crystal monochromator and focused onto the sample. The Rh K-edge EXAFS data was collected in a transmission mode using I_0 and I ionization counters filled with 100% Ar and 30% Kr/Ar, respectively. The Te K-edge EXAFS data was collected in a transmission mode using I_0 and I ionization counters filled 20% Kr/Ar and 100% Kr for Te K-edge, respectively. The X-rays at NW10A were monochromatized with a Si(311) double crystal monochromator. The monochromatized X-ray was focused to the sample by a Pt-Coated bent cylindrical mirror. The critical energy for the total reflection of the mirror was set at 42 keV. The I_0 and I signals were measured by Ar and Kr filled ionization counters, respectively. The RhTe nanoparticles were prepared by the liquid-phase reduction method using ethylene glycol.

Results and discussion

Figure 1 shows the Rh K-edge FT-EXAFS spectra of RhTe alloy nanoparticles on SiO_2 support, RhTe alloy nanoparticles powder without support, reference of RhTe alloy bulk and Rh foil. The peak around 0.2 - 0.3 nm corresponds to the Rh-Rh or Rh-Te distance and the peak of the reference of Rh_3Te_2 ingot. Rh metal might not be formed, since there was not peak at 0.4 - 0.5 nm corresponding to Rh-Rh bond derived from fcc Rh.

Figure 2 shows the Te K-edge FT-EXAFS spectra of RhTe alloy nanoparticles on SiO_2 support, RhTe alloy nanoparticles powder without support, the reference of RhTe alloy bulk and Te powder. The peak around 0.2 - 0.3 nm corresponded to the Te-Rh distance. In the case of RhTe without support, the peak around 0.3 - 0.4 nm corresponding to the peak of Rh_3Te_2 was observed.

These results show that the resulting nanoparticles might be composed of Rh-Te without Rh-Rh phase. In addition, Rh_3Te_2 alloy nanoparticles were synthesized when the nanoparticles were prepared without SiO_2 support. The preparation method might affect the formation of Rh-Te bond by uniform exist of Rh and Te precursors in reaction solution.

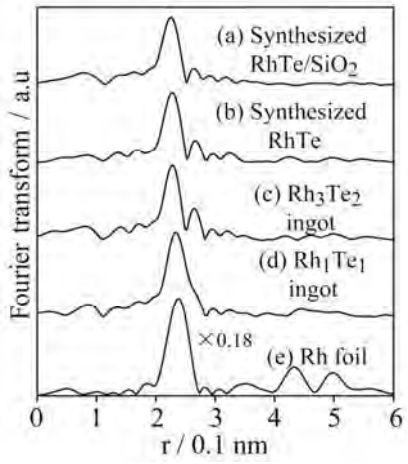

Figure 1. Rh K-edge FT-EXAFS spectra of (a) RhTe nanoparticles on SiO_2, (b) RhTe nanoparticles, (c) Rh_3Te_2 ingot, (d) Rh_1Te_1 ingot and (e) Rh foil

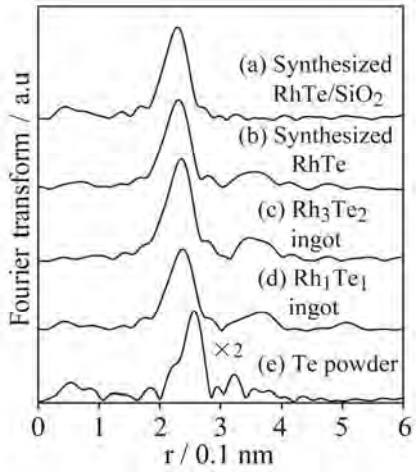

Figure 2. Te K-edge FT-EXAFS spectra of (a) RhTe nanoparticles on SiO_2, (b) RhTe nanoparticles, (c) Rh_3Te_2 ingot, (d) Rh_1Te_1 ingot and (e) Te powder

10C, 6A/2010G006, 2010G007

新規粘着剤の表面精密構造解析
Precise Analysis of New Type Adhesives

松葉　豪 [1*], 山下幸志 [2], 仲野真一 [2], 河原伸一郎 [2]
[1] 山形大学工学部、〒992-8510 米沢市城南 4-3-16
[2] ニッタ（株）　〒639-1085 大和郡山市池沢町 172

1 はじめに

接着や粘着の技術は、現代の産業において欠かすことの出来ないものである。粘着剤は、被着体に固着し、完全に固定させることのできる接着剤とは異なり、条件によって力学的に剥離することの出来るものをさす。しかしながら、粘着およびその剥離機構に関しては、ほとんど構造についての議論があまりなされていないため、これまで不明な点も多いことから、現在においても数多く研究されている。粘着や剥離の機構を解明するためには、粘着剤そのものの性質を明らかにすることはもちろんのこと、粘着材と被着材の界面の挙動が非常に重要になるのは言うまでもない。

そこで、本研究では、温度によって粘着特性が変化する新規粘着剤「インテリマー®」に着目した。インテリマー®は結晶性の側鎖を持ったアクリル酸系の粘着剤であり、本研究で用いる試料は高温(50 °C 以上)で粘着性を発揮し、室温に冷却すると粘着性を失い容易に剥離することができる機能性材料である。まず、インテリマー®の材料としての性質を明らかにするために、結晶成長および融解挙動を X 線散乱測定により観測した。さらに、インテリマー®の薄膜の表面構造を精密に観測することで粘着性と界面との相関を明らかにすることを試みた。

2 実験

試料として、ニッタ（株）から提供していただいたアクリル酸系粘着剤であるインテリマー®を用いた。結晶成長・融解機構の解明には、示差走査型熱量測定（DSC）および、茨城県つくば市にある高エネルギー加速器研究機構のフォトンファクトリー・ビームライン 6A および 10C を用いた。温度調整装置として Metler 社製の FP-90 システムをそれぞれのビームラインのサンプルに取り付けて、in-situ 測定を行った。

3 結果および考察

インテリマー®試料をフィルム上に成形した試料を溶融後、再結晶化のプロセスを DSC で観測した。粘着性が出現する温度である 50 °C 付近に融点があることがわかった。これによってインテリマー®の粘着性発現には結晶融解および結晶化が重要な役割を果たすことがわかった。広角 X 線回折測定を用いて結晶構造の温度依存性を評価した。その結果、昇温時に確かに結晶由来の回折ピークが減少し融解していることが示された。さらに、(a)30 °C および(b) 150 °C での小角X線散乱測プロファイルを示す。30 °C において密度揺らぎの大きさは約 5.7 nm であり、密度揺らぎは昇温させる事で 150 °C では 5nm と徐々に小さくなるが消えないことがわかった。これは、側鎖のオレフィン部分と主鎖のアクリル酸が混合せず、高温においても成分揺らぎが存在しているためである。また、揺らぎサイズが変化することについては、側鎖の融解によって分子運動が活発になった為であると考えられる。

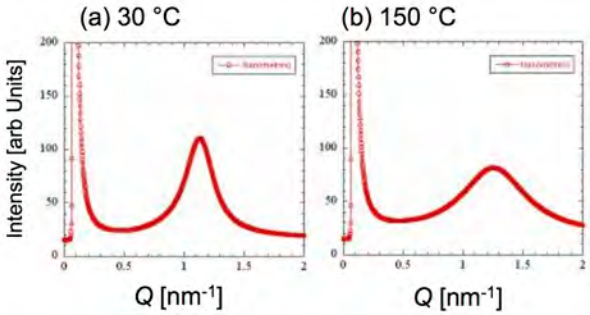

Fig. 1 SAXS profiles of Intelimer annealing at 30 °C (a) and 150 °C.

4 まとめ

放射光 X 線を用いたその場小角および広角 X 戦乱測定を用いて粘着剤の成分揺らぎおよび結晶構造を評価した。粘着挙動には結晶融解が非常に重要な役割を果たしていることがわかった。また、成分揺らぎは高温でも消失していないことが示された。

謝辞

本研究は、2011 年 3 月卒業の井上弘樹君、八巻龍一君、および 2012 年 3 月卒業の板垣祐樹君、西村達朗君の卒業研究の一環として行われ、いい成果がでました。心より感謝いたします。

* gmatsuba@yz.yamagata-u.ac.jp

6A/2010G007

Shear-Induced Crystallization Process of Syndiotactic Polystyrene

Yunfeng ZHAO, Go MATSUBA* and Hiroshi ITO
Yamagata University, Yonezawa 992-8510, Japan

1 Introduction

It is well known that when semi-crystalline polymers are crystallized under shear or elongational flow, crystallization rate is enhanced and the so-called "shish-kebab" structure is formed. It is considered that shish-kebabs consist of extended chain crystals (shish) and fold chain lamellar crystals (kebab) grow periodically around shish in the simplest case. The formation mechanism of shish-kebabs is still an unsolved problem about polymer physics and properties regardless the considerable works. Especially, it is very significant to understand shear-induced crystallization and to control polymer properties. In this study, we have focused on shear-induced crystallization process of a crystalline polymer with x-ray scattering measurements.

2 Experiment

We used syndiotactic polystyrene (sPS) with molecular weight M_w = 300,000 and polydispersity of M_w/M_n = 3.9 purchased from Scientific Polymer Products Inc. The nominal melting temperature T_m of sPS determined in DSC measurements with a heating rate of 5 °C /min is 270 °C. A Linkam CSS-450 high temperature shear cell was used to control the temperature of the sample and the shear conditions. Time-resolved small-angle X-ray scattering (SAXS) measurements were carried out by using an apparatus installed at a beam BL15A/6A in a synchrotron radiation X-ray scattering facility, Photon Factory, KEK, in Tsukuba, Japan. A two dimension (2D) CCD camera (C7300: Hamamatsu Photonics K.K.) with an image intensifier was used as the X-Ray detector. The wavelength λ of the X-ray beam was 1.54 Å, and the camera length was 2.3 m for SAXS measurements. The q range in the SAXS measurements was 8 x 10^{-3} - 1.5 x10^{-1} Å^{-1} where q is the scattering vector, $q=4\pi\sin\theta/n\lambda$ (2θ and n are the scattering angle and the refractive index, respectively).

3 Results and Discussion

We observed isothermal crystallization process sPS after applying a steady shear flow with a constant shear rate and various shear strains below the nominal melting temperature T_m by using time-resolved SAXS. The shear temperature T_{shear} was 260 °C and the isothermal crystallization temperature T_c was 250 °C. The shear rate was 60 s^{-1} and the shear stain was 0 to 360,000 %. Fig 1 showed crystallization time evolution of SAXS profiles in various shear strains. It was found that crystallization was accelerated after cessation of shear flow (b, c, d) compared with the quiescent state (a). Especially, it is obvious that crystallization had been progressed in the case of (c, d) at the onset of measurements (t = 0) while no crystalline scattering feature was observed in (a) at the same time.

On increasing shear strain, the meridian scattering features respect to the flow direction became stronger and the 2D scattering patterns became more heterogeneous. Meanwhile, only homogeneous 2D scattering patterns were observed in the quiescent state, which indicated the spherulitic morphology. The anisotropic scattering features can be attributed to the scattering features of oriented (stacked) lamella crystals in size dimension in the case of flow-induced crystallization. Usually, the equatorial streaks with respect to flow direction are thought to be the scattering features of shishs while the meridian spots are thought to be the scattering features of kebabs. The meridian scattering features were found during isothermal crystallization but the equatorial streaks were absent at these shear conditions. As the intensity scattered by SAXS measurements is insensitive to low concentration or low electron density contrast, we cannot deny the existence of shish entity at above shear conditions.

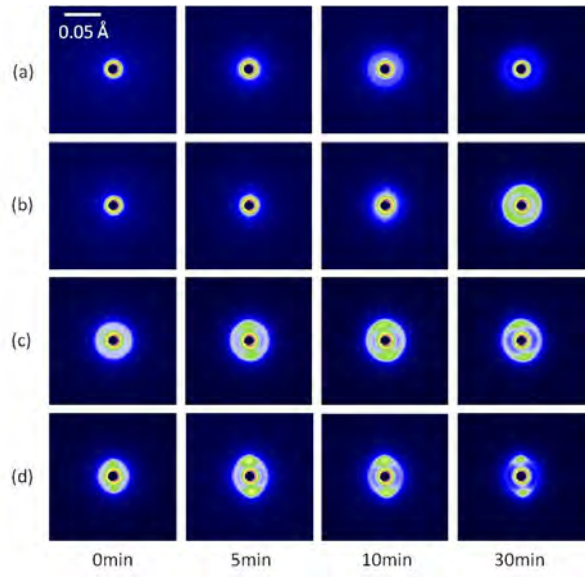

Fig. 1: Crystallization time evolutions of 2D SAXS patterns of sPS at 250 °C. (a): at quiescent state; (b), (c), (d): after applying a steady shear flow with a constant shear rate = 60 s^{-1} and various shear strains ε at 260 °C. (b): ε = 48,000 %; (c): ε = 180,000 %; (d): ε= 360,000 %.

*gmatsuba@yz.yamagata-u.ac.jp

NW10A/2010G020

XAFS Characterization of SiO_2-Supported Ru Complex for Sulfoxidation

Niladri MAITY[1], Chularat WATTANAKIT[1], Satoshi MURATSUGU[1], Nozomu ISHIGURO[1], and Mizuki TADA[1*]

[1] Institute for Molecular Science, Myodaiji, Okazaki, Aichi 444-8585, Japan.

Introduction

Advantage of a supported metal-complex catalyst is not only simpler separation between catalyst and reaction medium but also their unique activity and higher stability of the catalyst. In particular, the site-isolation of a supported metal complex often provides unique catalytic performance on a surface. We have succeeded in preparing site-isolated Ru complex supported on a SiO_2 surface and found that the supported Ru complex was active for sulfoxidation using O_2/aldehyde system.[1] The local coordination structures of the SiO_2-supported Ru complexes were investigated by Ru K-edge EXAFS.

Experimental

A SiO_2-supported Ru complex (**B**) was prepared by reacting a Ru precursor complex [(*p*-cymene)Ru{$H_2NCH_2CH_2NSO_2C_8H_7$}Cl] (**A**) with a *p*-styryl moiety on SiO_2. The supported Ru complex was converted to an active structure (**C**) with unsaturated coordination by a reaction with isobutyraldehyde (IBA) and O_2 on **B**. Ru K-edge EXAFS spectra were measured in transmitted mode at 20 K at the NW10A station of the KEK PF-AR ring with Si(311) channel-cut crystals. Ionization chambers filled with pure Ar and Kr gases were used to monitor the incident and transmitted X-rays, respectively. Ru K-edge EXAFS spectra were analyzed with IFEFFIT (Athena and Arthemis) and k^3-weighted EXAFS oscillations (30-170 nm^{-1}) were Fourier transformed into *R*-space and curve-fitting analysis was carried out in *R*-space.

Results and Discussion

Structural parameters (CNs (coordination numbers) and bond distances) of the local coordination of **A**, **B**, and **C** were estimated by the curve-fitting analysis of Ru K-edge EXAFS Fourier transforms. The CNs and bond distances of Ru-N, Ru-C, and Ru-Cl in **B** were found to maintain those of **A** as shown in Table 1, indicating the supported Ru complex **B** had a similar local coordination structure to precursor complex **A**, whose coordination structure was determined by X-ray diffraction.

The reaction with **B** and IBA/O_2 released the coordinating *p*-cymene ligand from Ru in **B**, which was detected by GC, and local coordination structure of **C** was determined by Ru K-edge EXAFS (Ru-N at 0.206 ± 0.002 nm: CN = 3.0 ± 1.1; Ru-Cl at 0.236 ± 0.005 nm: CN = 1.3 ± 1.2). No Ru-Ru interaction was found, suggesting that the elimination of the *p*-cymene ligand did not produce the aggregation of Ru particles and **C** had a Ru monomer structure on the SiO_2 surface. There were no significant differences between the local coordination structures of **B** and **C** with Ru loadings of 0.4 and 1.6 wt%.

We found that the supported Ru complexes (**B** and **C**) were active for the sulfoxidation of sulfides using IBA/O_2 systems, in which sulfoxide was selectively formed at the beginning of reaction and the formation of sulfone proceeded by the further oxidation of produced sulfoxide, not directly from sulphide. After the sulfoxidation, the monomer structure of **C** was found to be maintained on the SiO_2 surface (Table 1) and there was no Ru-Ru bond observed by Ru K-edge EXAFS.

Table 1: Curve-fitting results of Ru K-edge EXAFS Fourier transforms of **A**, **B**, and **C** (before and after the sulfoxidation)

Shell	CN	Distance /nm	σ^2 /nm^2
Ru precursor (**A**) [a]			
Ru-N	2.0	0.208±0.002	$(0.7\pm2.3)\times10^{-6}$
Ru-C	6.0	0.219±0.002	$(1\pm1)\times10^{-5}$
Ru-Cl	1.0	0.242 ± 0.003	$(2\pm1)\times10^{-5}$
Supported complex (**B**) [b]	Ru 0.4 wt%		
Ru-N	1.9±0.7	0.210±0.002	0.7×10^{-6}
Ru-C	4.8±1.7	0.221±0.002	1×10^{-5}
Ru-Cl	1.1±0.2	0.244±0.002	2×10^{-5}
Supported complex (**C**) [c]	Ru 0.4 wt%		
Ru-N	3.0±1.1	0.206±0.002	$(2\pm2)\times10^{-5}$
Ru-Cl	1.3±1.2	0.236±0.005	$(7\pm8)\times10^{-5}$
(**C**) after sulfide oxidation [d]	Ru 0.4 wt%		
Ru-N	3.7±0.7	0.208±0.001	$(3\pm1)\times10^{-5}$
Ru-Cl	1.4±1.2	0.238±0.007	$(13\pm8)\times10^{-5}$

[a] k = 30-170 nm^{-1}, R = 0.115-0.25 nm, R_f = 1.0%. CNs were fixed.
[b] k =30-140 nm^{-1}, R = 0.115-0.25 nm, R_f = 0.6%.
[c] k = 30-140 nm^{-1}, R = 0.13-0.24 nm, R_f = 1.2%.
[d] k = 30-140 nm^{-1}, R = 0.13-0.24 nm, R_f = 0.3%.

References

[1] N. Maity, C. Wattanakit, S. Muratsugu, N. Ishiguro, Y. Yang, S. -I. Ohkoshi, M. Tada, *Dalton Trans.* **2012**, *132*, 713.

* mtada@ims.ac.jp

AR NW2A/2010G039

Mechanistic Insights into Photochromic Behavior of a Ruthenium(II)–Pterin Complex

Tomoya Ishizuka,[1] Takuya Sawaki,[1] Soushi Miyazaki,[2] Masaki Kawano,[3] Yoshihito Shiota,[4] Kazunari Yoshizawa,[4] Shunichi Fukuzumi,*[2, 5] and Takahiko Kojima*[1]

[1]Department of Chemistry, Graduate School of Pure and Applied Sciences, University of Tsukuba, 1-1-1 Tennoudai, Tsukuba, Ibaraki 305-8571 (Japan)

[2]Department of Material and Life Science, Graduate School of Engineering, Osaka University 2-1 Yamada-oka, Suita, Osaka 565-0871 (Japan)

[3]Division of Advanced Materials Science (WCU Project), POSTECH, Hyojadong, Pohang 790-784, South Korea

[4]Institute for Materials Chemistry and Engineering, Kyushu University, Motooka, Nishi-Ku, Fukuoka 819-0395 (Japan)

[5]Department of Bioinsipired Science (WCU Project), Ewha Womans University, Seoul 120-750 (South Korea)

Introduction

Molecular bistability is an essential factor to control molecular structures and functionality toward the development of molecular devices. Among a variety of molecular bistability, photochromism of coordination compounds has been reported, however, the number of the examples of photochromic metal complexes is so limited in comparison with that of organic molecules. As a metal center, ruthenium has been useful to exhibit the photochromic structural change due to the formation of metal-centered triplet excited states (^{3}MC) derived from triplet metal-to-ligand charge transfer (^{3}MLCT) excited states. Ru(II) complexes in the ^{3}MC state undergoes thermal ligand dissociation to result in drastic structural change.

Ru(II) complexes having heteroaromatic compounds as ligands have been known to show strong MLCT absorption that is essential for photo-excitation. As heteroaromatic ligands, diimine compounds such as 2,2'-bipyridine have been used to photochemical structural change, however, the structural change inevitably reaches to photostationary state to afford mixtures of photoproducts and starting materials.

In this report, we describe a complete photochromic structural change of a Ru(II) complex bearing a pterin derivative, which is a redox-active heteroaromatic co-enzyme, as a bidentate ligand, together with tris(2-pyridylmethyl)amine (TPA) as an ancillary ligand, as shown in Scheme 1.

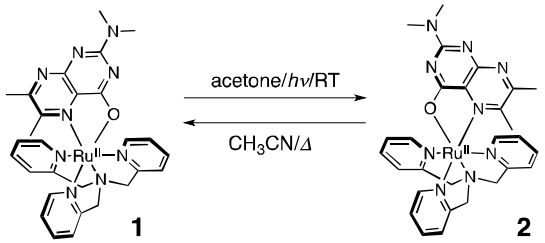

Scheme 1.
Photochromic structural change between **1** and **2**.

Results

Photoirradiation of a Ru(II)-TPA complex with a deprotonated pterin derivative, dmdmp$^-$ (Hdmdmp = *N*,*N*-dimethyl-6,7-dimethylpterin), [Ru(dmdmp)(TPA)]ClO_4 (**1**), at 460 nm in acetone afforded complete conversion to the isomer of **1**, in which the pterin ligand underwent an apparent 180-degree pseudo-rotation relative to the original orientation in **1**. The structure of the isomeric complex **2** was by X-ray crystallography. Diffraction data of the crystal of **2** was collected at Photon Factory-Advanced Ring for Pulse X-rays (PF-AR NW2A) of KEK. The crystal structure is presented in Figure 1.

Thermal recovery of **1** from **2** was completely achieved by heating **1** in CH_3CN. The thermodynamics of the reverse structural change was established by kinetic analysis.

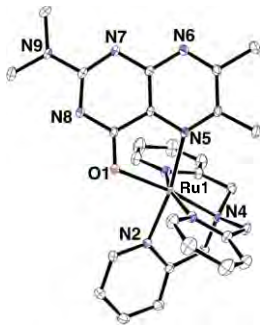

Figure 1.
Synchrotron X-ray structure of **2**. Hydrogen atoms and ClO_4^- are omitted.

References

[1] T. Ishizuka *et al.*, Chem.–Eur. J. 2011, 17, 6652 – 6662.

* kojima@chem.tsukuba.ac.jp

27B/2010G047

イメージング XAFS 法による土壌および鉱物試料中のセシウム観察
Imaging XAFS analysis of Cs in soil and clay minerals

岡本芳浩 [1*], 中田正美、赤堀光雄、大杉武史、中塩信行
[1] 日本原子力研究開発機構、〒319-1195 茨城県那珂郡東海村白方白根 2-4

1 はじめに

福島第一原子力発電所の事故以来、環境中の放射性セシウムの除去が大きな課題になっている。中でも、土壌などに強く固着したセシウムは、その効果的な除染法の確立が急がれている。土壌のように複雑な多成分系試料中のセシウムの化学状態を把握するために、元素選択性に優れた放射光 XAFS 分析法を用いる意義は大きい。

本研究では、土壌中の粘土鉱物に吸着したセシウムの分布と化学状態を調べるために、イメージング XAFS 分析法の適用を試みた。

2 実験

イメージング XAFS 測定は、BL-27B ステーションにおいて、セシウムの L_3 吸収端（E_0=5.012keV）を使用して実施した。図 1 に示すように、通常の透過法 XAFS 測定のレイアウトから、下流のイオンチェンバーをイメージング測定機器に置き換えただけである[1]。

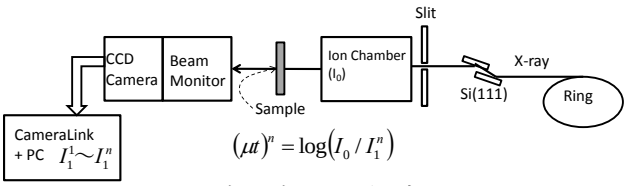

図 1　イメージング XAFS 測定のレイアウト

試料は、土壌に非放射性のセシウムを吸着させたものを用いた。硝酸セシウム水溶液中に浸漬した土壌を、洗浄・乾燥した上で測定試料とした。

3 結果および考察

イメージング XAFS 試験に先立って、通常の XAFS 測定を実施した。土壌試料中のセシウムの含有量は、酸化物換算で 0.5~1.0%程度であり、蛍光法による測定が最適である。しかし、実際には鉱物中にわずかながら含まれるチタンの Kα線による影響で、有意な XAFS スペクトルの取得はできなかったで。一方、透過法によりセシウムの L_3吸収端 XAFS スペクトルが取得できたが、チタンの K 吸収端（E_0=4.966keV）が近くにあり、その影響が無視できない。つまり、チタンによる EXAFS 振動が、セシウムの XAFS 領域に重なる。

図 2 に、土壌試料中のイメージング XAFS 試験の結果から得られたセシウムの分布を示す。試料中の特定の領域に集中して分布している。これは、同時に調べたチタンの分布とは異なっていた。

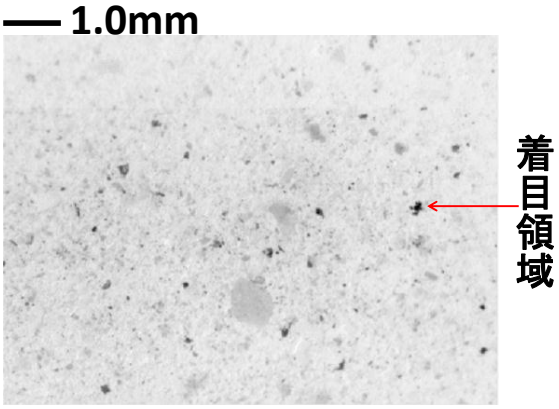

図 2　土壌試料中のセシウム分布

そこで、図 2 の中のセシウム濃度の高い微小領域（図中の着目領域で、約 50 μm 四方が対象）について XAFS スペクトルを導出した。その結果を図 3 に示す。

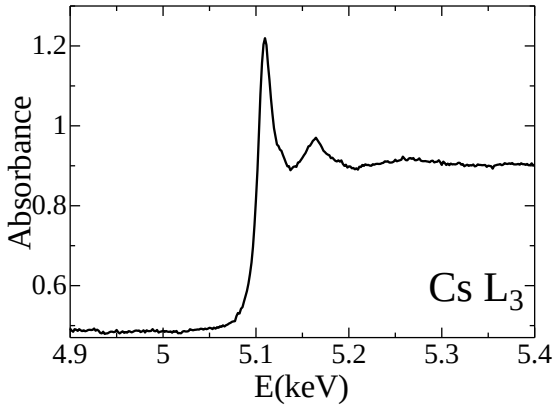

図 3　着目領域のイメージング XAFS スペクトル

4 まとめ

土壌試料中のセシウムのイメージング XAFS 試験を行い、セシウムの分布を明らかにするとともに、微小領域の XAFS スペクトルを導出した。

参考文献

[1] Y.Okamoto et al., Adv. X-ray Chem. Anal. 42, 183 (2011).

* okamoto.yoshihiro@jaea.go.jp

NW10A/2010G048

Behavior of Ru in high-temperature simulated high-level waste glass melt

Yoshihiro Okamoto*[1], Masami Nakada[1], Mitsuo Akabori[1], Satoshi Komamine[2], Toshiki Fukui[2], Eiji Ochi[2], Hiroaki Nitani[3], Masaharu Nomura[3]
[1]JAEA, Tokai, Ibaraki 319-1195, Japan
[2]JNFL, Rokkasho, Aomori 039-3212, Japan
[3]KEK-PF, Tsukuba, Ibaraki 305-0801, Japan

1 Introduction

High-level radioactive liquid waste(HLLW) generated in reprocessing of spent nuclear fuels is solidified with borosilicate glass in stainless canisters. They are cooled and stored in the storage facility. Understanding behavior of fission product elements in a glass melting furnace is important for safe and efficient management. In the present work, behavior of ruthenium in the simulated glass melt was examined by using an imaging XAFS technique at high temperature..

2 Experiment

Imaging XAFS measurement was carried out at the NW10A beamline. The imaging system (Hamamatsu Photonics,K.K.) which consists of the beam monitor AA40 and the high-sensitive CCD camera C9300-221 is used in place of an ion chamber[1] as shown in Fig.1. The image from the CCD camera was stored as 12bit TIFF files. The resolution of this imaging system is 10μm.

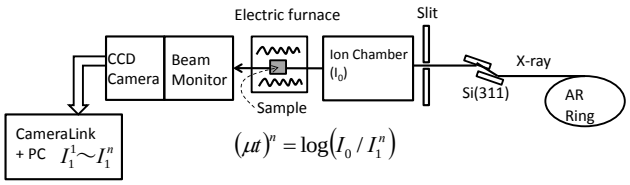

Fi.1 Layout of the X-ray imaging measurement

X-ray absorption images of the simulated glass sample melt containing fission product elements like Ru were recorded at 22.20keV of X-ray energy (just after (Ru K-absorption edge E_0=22.117keV). Position sensitive X-ray absorption spectra were also obtained by scanning energetic range from 21.8 to 22.6keV.

3 Results and Discussion

X-ray imaging measurement including imaging XAFS was performed several times to observe behavior of the ruthenium element. In most cases, condensation and sedimentation of the ruthenium element were observed in the glass melt above 1200℃. The imaging XAFS result of the frozen glass after the heating is shown in Fig.1 The condensation of the ruthenium can be confirmed by the gray-scale change between the two CCD images at 22.05keV and 22.20keV. From the imaging XAFS analysis shown in the Fig.1, it can be seen that the chemical character of the condensation object is RuO_2.

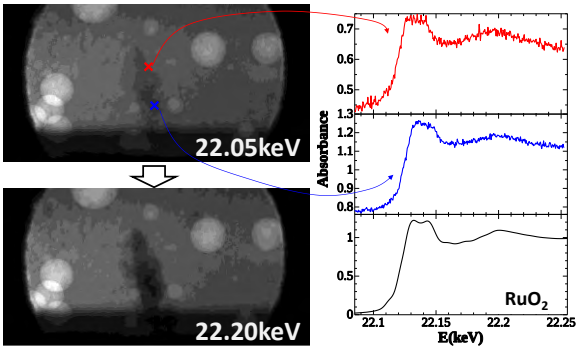

Fig.2 Imaging XAFS result of the frozen sample

In the next step, we tried to obtain imaging XAFS spectrum of high-temperature glass met by a quick scan of the X-ray energy. Fig.3 shows the imaging XAFS result obtained at 1300℃. The imaging XAFS spectrum at the bottom of the cell is close to the XAFS of RuO_2.

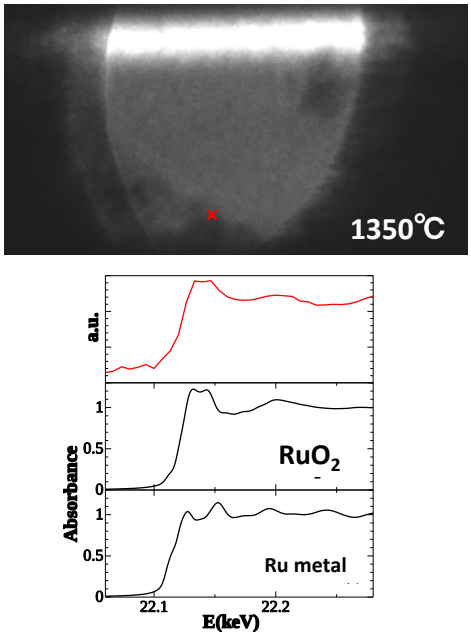

Fig.3 Imaging XAFS result of the molten sample

References

[1] Y. Okamoto *et al.*, Trans. Atom. Energ. Soc. Jpn. **11** (2012) 127.

* okamoto.yoshihiro@jaea.go.jp

4A,6A,15A,9C/2010G057

界面活性剤ゲルにおけるネットワーク構造の形成過程
Formation process of surfactant gel network structures

川端庸平*, 山内陽介, 永井翔, 林賢利, 加藤直
首都大学東京、〒192-0397　八王子市南大沢 1-1

1 はじめに

界面活性剤水溶液におけるクラフト転移は界面活性剤分子疎水基の結晶化現象として知られており、転移に伴って界面活性剤の結晶が析出する。一方、界面活性剤の種類によっては結晶が析出せずに系全体がミクロンスケールで均一となり、ゲル状態を示すこともある。非イオン界面活性剤もそのうちの一つであり、我々のグループではポリオキシエチレン鎖を親水基にもつ長鎖アルキル基の界面活性剤水溶液系（$C_{16}E_m$: $C_{16}H_{33}(OC_2H_4)_mOH$）において、クラフト温度以下でベシクルやラメラドメインが乱雑に配置したネットワーク型のゲル状構造となることを見出してきている[1-3]。これらの構造形態は親水性の微妙な差異で劇的に変化し、ネットワーク型構造を形成する $C_{16}E_6$ およびベシクルを形成する $C_{16}E_7$ の混合水溶液において、$C_{16}E_7$ モル分率 0.8 付近で不連続的にベシクルへと形状を変え、膜形状の転移と捉えることができる。

本研究では親水性の変化に伴うミクロンスケールの構造形態変化の起源を探るべく、小角 X 線散乱測定（SAXS）を行った。

2 実験

試料には $C_{16}E_6$/ $C_{16}E_7$ 混合水溶液を $C_{16}E_7$ の混合モル分率を変えた試料を数種類作成した。全界面活性剤濃度は 10wt%とした。試料は厚さ 1mm の銅板に穴を開け、カプトンで挟み込む形で保持した。試料温度は Instec 社の mk1000-TS62 により制御し、それぞれの試料のクラフト温度以下にクエンチ幅を 2℃程度変化させながら時分割測定を行った。SAXS 測定はビームライン 4A、15A (6A)、9C で行った。また震災による救済措置により SPring-8 BL45XU での実験も行った。検出器は 4A、15A (6A)では CCD カメラと Image Intensifier を、9C では PSPC、BL45XU では PILATUS を用いた。測定波数レンジは $0.3 < q < 3$ nm^{-1} である（$q=4\pi\sin\theta/\lambda$, 2θ:散乱角）。

3 結果および考察

図 1 左図は $C_{16}E_7$ の混合モル分率γ_{E7}=0.8 近傍および $C_{16}E_6$、$C_{16}E_7$ 単独系の SAXS プロファイルである。γ_{E7} の増加とともにブラッグピークが低 q 側に移り繰り返し距離が増大している。γ_{E7}=0.8,0.83 近傍では 2 種類の繰り返し距離に相当するブラッグピークが出現しており、ラメラーラメラ相分離の状態となっている。このモル分率近傍では図 2 の共焦点顕微鏡

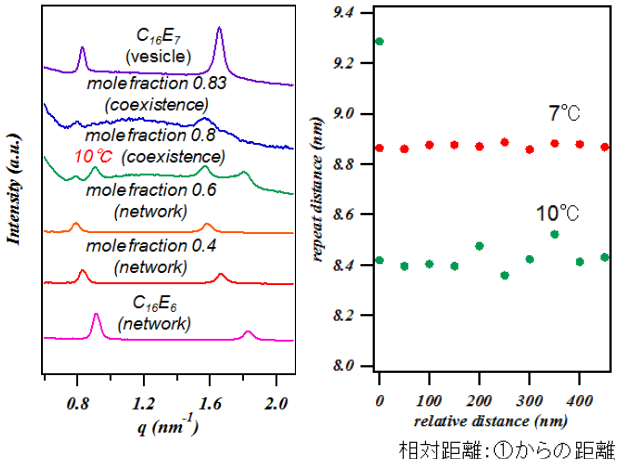

図 1　左図：$C_{16}E_7$ の混合モル分率γ_{E7}=0.8 近傍および $C_{16}E_6$、$C_{16}E_7$ 単独系の SAXS プロファイル。右図：マイクロビーム（ビームサイズ 5×5 mm）のサンプル内照射位置を相対的に移動させた場合の繰り返し距離の分布。

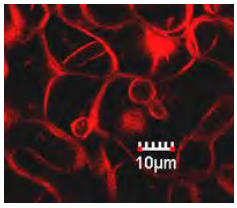

図 2　$C_{16}E_7$ の混合モル分率 gE7=0.8 における共焦点顕微鏡画像。

画像で示すように、ベシクルとネットワーク様の形態が共存しており、この 2 種類の構造形態に相当するラメラ構造が 2 種類の繰り返し構造として現れたのではないかと考えられる。また、図 1 右図は、マイクロビーム（ビームサイズ 5×5 μm^2）のサンプル内照射位置を相対的に移動させた場合の繰り返し距離の分布を示したものであり、ベシクルのみが存在する 7℃では繰り返し距離の分布幅は小さいが、共存状態である 10℃では不均一性があることが明らかである。この結果からもベシクルとネットワーク様構造が共存する場合、nm スケールの膜構造にも不均一性が現れ、構造形態特有の膜構造があるのではないかと考えられる。

参考文献

[1] Y. Kawabata et al., J. Phys. Chem. B, 17, 5686 (2009).
[2] Y. Kawabata et al., Phys. Chem. Chem. Phys., 13, 3484 (2011).
[3] Y. Kawabata et al., J. Phys. Chem. B, 116, 1593 (2012).

* youheik@tmu.ac.jp

6A/2010G-059

Nanophase-Separated Supramolecular Assemblies of Functionalized Polymers via Ionic Hydrogen Bonding

Atsushi Noro,* Koji Ishihara, and Yushu Matsushita
Department of Applied Chemistry, Graduate School of Engineering, Nagoya University, Furo-cho, Chikusa-ku, Nagoya 464-8603, Japan

1 Introduction

Nanophase separation is the phase separation phenomenon at the nanoscopic scale for multicomponent soft materials, especially block or graft copolymers. Recently, "block or graft supramacromolecules", including nanophase-separated supramolecular assemblies of two or more polymers through non-covalent bonding, have attracted more attention because non-covalent bonding provide smart materials with stimuli responsiveness by temperature or shear stress. Block or graft-type supramolecular assemblies, however, usually require precise synthesis of end-modified polymers as building blocks. Here in this study[1], we present simple preparation and morphology observation of graft-type supramolecular assemblies via ionic hydrogen bonding by mixing two commodity polymers.

2 Experiment

ω-Carboxyl-terminated poly(dimethyl siloxane) (PDMS-COOH, M_n ~ 1450, *PDI* ~ 1.6, T_g ~ -125 °C, purchased from Shin-Etsu Chemical Co. Ltd.) and polyethylenimine (PEI, M_n ~ 1200, M_w ~ 1300, T_g ~ -56 °C, purchased from Aldrich) were blended in a mixed solvent of tetrahydrofuran/methanol (5/5=v/v). Then, the solvent was slowly evaporated for 24h, and the blend sample was further dried *in vauo* for 48h at 35 °C. The weight ratio of PDMS-COOH:PEI in the blends were varied as 25:X (X = 1~5), where five blend samples were prepared. The blends were coded as DE-25:X. To investigate the morphological behavior of the blends at the nanoscopic scale, small angle X-ray scattering (SAXS) were carried out at room temperature at the beamline 15A in the Photon Factory, Tsukuba, Japan.

3 Results and Discussion

SAXS profiles of all DE-25:X samples were shown in Figure 1. The profiles of neat PDMS-COOH (DE-25:0) and neat PEI were also shown at the bottom and the top in the figure, respectively. There are no peaks on the profiles of DE-25:0 and neat PEI, indicating no notable electron density difference at the nanoscopic level in the neat samples. However, once both neat samples are mixed, the shapes of profiles became totally different. The blends even with the small amount of PEI such as DE-25:1 show broad peaks at around 1.0 nm^{-1} on their profiles, representing a correlation hole peak which might be originated from electron density difference between PDMS and PEI with the length scale of several nanometers. On the profile of DE-25:2, there are three sharp peaks at 0.85, 1.7, and 2.55 nm^{-1}, relative q values of 1, 2, and 3, indicating a lamellar nanophase-separated structure with domain spacing of 7.4 nm in the blend. Other profiles of DE-25:X (X ≥ 3) have also sharp peaks at relative q values of 1, 2, and 3, but the location of peaks shifted to lower q values as the X value increases, representing domain spacing expansion probably due to the increase in the thickness of a COOH/PEI phase in nanophase separated structures.

In conclusion, we have demonstrated facile building-up of nanophase-separated supramolecular assemblies composed of two functionalized polymers such as a pair of PDMS-COOH and PEI via ionic hydrogen bonding. The lamellar nanophase separated structures between a PDMS phase and a PEI/COOH phase were also observed in the blends by SAXS measurements.

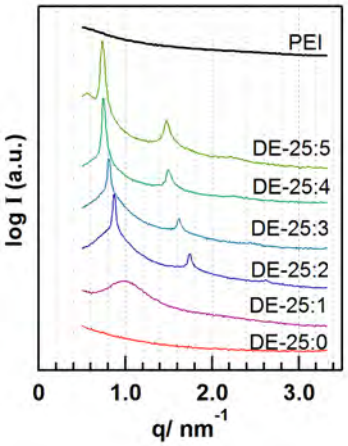

Figure 1. SAXS profiles of DE-25:X (X = 0~5) and PEI. SAXS was measured at room temperature.

Acknowledgements

Use of synchrotron X-ray source was supported by Photon Factory, KEK in Tsukuba, Japan (No. 2010G059 for A.N.). This work was also supported through Grants-in-Aid (No. 21750217 (AN,), No. 23655213 (A.N.), No. 18068008 (Y.M.), and No. 22245038 (Y.M.)) by JSPS and MEXT, Japan. This work was also partially supported by the Global COE Program in Chemistry at Nagoya University.

References

[1] A. Noro, K. Ishihara, Y. Matsushita, *Macromolecules* **44** (2011) 6241-6244.

* noro@apchem.nagoya-u.ac.jp

NW10A, 2010G069

EXAFS analysis for structure of active site for glycerol hydrogenolysis

Yasushi AMADA*[1], Shuichi KOSO[1]
Kazu OKUMURA[2], Yoshinao NAKAGAWA[1] and Keiichi TOMISHIGE[1,3]
[1]Department of Applied Chemistry, Tohoku University, Sendai, Miyagi 980-8579, Japan
[2]Department of Materials Science, Tottori University, Minami, Tottori 680-8552, Japan
[3]Institute of Materials Science, University of Tsukuba, Tsukuba, Ibaraki 305-8573, Japan

Introduction

The grouping importance in the production of non-petroleum chemicals for a substitute for petroleum and sustainability has led to the development for the transformation of non food biomass. A target of the non-petroleum chemicals is oxygenates such as terminal-diols. Terminal-diols will be used as monomers for the production of polyesters and polyurethanes. It has been recently reported that modification of Rh/SiO_2 with Re species is effective for the hydrogenolysis of glycerol, although the selectivity to 1,3-propanediol is not so high. In this research, we carried out the characterization of modification of Ir/SiO_2 with Re species which shows high activity in the hydrogenolysis of glycerol to 1,3-propanediol. The maximum yield of 1,3-propanediol over $Ir\text{-}ReO_x/SiO_2$ catalyst is 38% at 36 h.

Experimental

Supported $Ir–ReO_x$ catalyst was prepared using the sequential impregnation method. First, H_2IrCl_6 aq was impregnated to SiO_2 and dried catalyst at 383 K for 12 h. Secondary, NH_4ReO_4 aq was impregnated Ir/SiO_2 catalyst and then after dried at 383 K for 12 h, calcined at 773 K in air for 3 h and reduced at 473 K in H_2 for 1 h. The reference compounds such NH_4ReO_4 and Re powder were pressed into self-supporting 7 mm-diameter wafers under atmosphere. The EXAFS analysis of $Ir\text{-}ReO_x/SiO_2$ catalysts was used after the reaction of glycerol. The glycerol hydrogenolysis reaction was performed using the autoclave. Therefore, after the reaction, H_2 pressure was decreased to some extent and the autoclave was opened in a glove box filled with nitrogen. The used catalysts, after separation, were transferred again to the measurement cell. Re L_3-edge EXAFS spectra were measured by transmission mode at room temperature. After back ground subtraction, k^3 weighted EXAFS functions were Fourier transformed into R space and the one or two-shell fitting were analyzed by curve fitting.

Results and Discussion

Fig. 1 shows the Fourier transform (FT) of Re L_3-edge EXAFS oscillations of $Ir\text{-}ReO_x/SiO_2$ after the glycerol hydrogenolysis reaction. The FT of NH_4ReO_4 and Re powder are shown as a reference for Re-O bond and Re-Re bond, respectively. Theoretical functions for the Re-Ir bond were calculated using the FEFF8.2 program. For $Ir\text{-}ReO_x/SiO_2$, a peak between 0.14 and 0.32 nm was observed in the FT; they are assignable to the Re–O and Re–Ir (or –Re) bond. In the EXAFS analysis, it is impossible to distinguish between Ir and Re as a backscattering atom theoretically. Table 1 lists their curve fitting results. The curve fitting analysis indicates the presence of the Re–O and Re–Ir (or –Re) bonds with bond distance of 0.202–0.203 and 0.268 nm, respectively.

The presence of the Re–O bond indicates that Re species is not fully reduced to the metallic state The CN of the Re–Ir (or –Re) bond was almost constant among the $Ir–ReO_x/SiO_2$ catalysts with various Re contents. This suggests that local structures of Re were not dependent on the added Re amount.

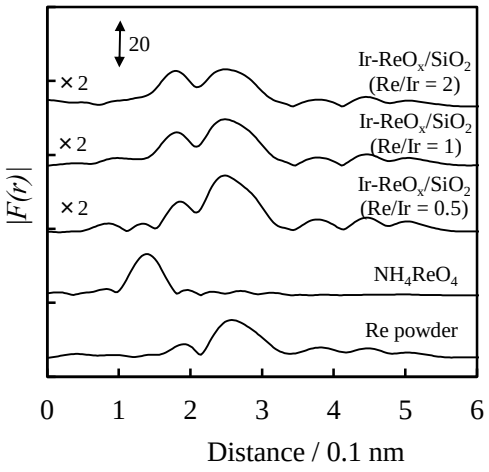

Fig. 1 Results of Fourier transform of k^3-weighted Re L_3-edge EXAFS oscillation of $Ir\text{-}ReO_x/SiO_2$ after the glycerol hydrogenolysis reaction, NH_4ReO_4 and Re powder. The results of NH_4ReO_4 and Re powder are also shown as a reference.

Table 1 Curve fitting of Re L_3-edge EXAFS of $Ir\text{-}ReO_x/SiO_2$.

Catalyst	Re/Ir	Shells	CN[a]	R / 10^{-1} nm
$Ir\text{-}ReO_x/SiO_2$	0.5	Re-O	1.1±0.8	2.03±0.07
		Re-Ir (or -Re)	5.9±0.8	2.68±0.01
$Ir\text{-}ReO_x/SiO_2$	1	Re-O	1.4±0.5	2.02±0.03
		Re-Ir (or -Re)	6.2±0.9	2.68±0.01
$Ir\text{-}ReO_x/SiO_2$	2	Re-O	1.7±0.5	2.03±0.03
		Re-Ir (or -Re)	6.1±1.1	2.68±0.01
NH_4ReO_4	-	Re=O	4.0	1.74
Re powder	-	Re-Re	12.0	2.74

[a]Coordination number. [b]Bond distance. Ir: 4 wt%, Re/Ir = 0.5–2. Fourier filtering range: 0.129–0.316 nm.

* yasushi.amada@gmail.com

NW10A/2010G109

EXAFS Analysis for Supported Ru Catalyst Active for Syntheses of Quinoxaline Derivatives

Alexey ZAZYBIN[1], Murugulla Adharvana Chari[1], Donthabakthuni Shobha[1], Takehiko SASAKI*[1],
[1]Department of Complexity Science and Engineering, School of Frontier Sciences, The University of Tokyo, 5-1-5, Kashiwanoha, Kashiwa, Chiba 277-8561, Japan.

1 Introduction

Many Heterocyclic compounds are acting as various drugs. Here we synthesized various biologically active substituted heterocyclic compounds such as quinoxalines, benzimidazoles, benzoxazoles and benzothiazoles using novel recyclable silica supported ruthenium catalyst. For the purpose of obtaining reactive and selective catalysts, the selection of metal element and the ligand whch promotes catalytic function of metal atom are very important. In this study we tried to develop multinuclei Ru catalyst using $Ru_3(CO)_{12}$ and 1,3,5-trimethyl-hexahydro- 1,3,5-triazine, which will be referred to as N3 ligand hereafter, as a ligand for stabilization and promotion of complex. N3 ligand possesses the three nitrogen atoms which can interact with mutinucleic Ru catalytic species. Catalytic performance and EXAFS characterization exhibited that the present catalyst was active for syntheses of quinoxaline derivatives.

2 Experimental

For the preparation of the catalyst, N3 ligand was reacted with $Ru_3(CO)_{12}$ where reaction was done at 65^0C in toluene. The product was removed from the unreacted starting material with Soxhlet extraction with hexane and subsequent redissolving in methanol with filtration. The resulting dark-brown microcrystalline product was characterized with elemental analysis, IR and NMR ^{1}H and ^{13}C spectroscopy, and EXAFS. In order to prepare solid catalyst for recycles and easy separation of products from the catalyst, the compound was impregnated on silica support from methanol solution. This silica supported Ru catalyst (containing 0.186 mmol/g as Ru) was used for catalytic reactions.

Measurements of extended X-ray absorption fine structure (Ru K-edge EXAFS of each element) were carried out at the Photon Factory in the Institute of Materials Structure Science, High Energy Accelerator Research Organization (KEK－IMSS－PF). The EXAFS spectra were analyzed with the UWXAFS package. The curve-fitting analysis was carried out using the FEFFIT program in the R-space.

3 Results and Discussion

We observed the silica supported Ru catalyst with N3 ligand is highly reactive in the synthesis of various biologically active heterocyclic compounds.

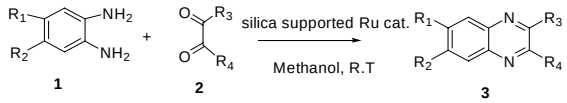

R_1 = H,Cl, CH_3
R_2 = H,Cl, NO_2
CH_3
$R_3 = R_4$ = Ph,Furyl, CH_3

Several substituted OPDAs such as chloro, nitro, methyl, dichloro, dimethyl, cyclohexyl and EDA, bisOPDA, were used to get the products in excellent yields as shown in the above scheme. Substituted diamines and various aromatic and aliphatic substituted diketones like benzyl, furyl and 2,3-butadione or diacetal were used to synthesize multifunctionalised quinoxalines and 2,3-dihydropyrazines using the silica supported Ru catalyst. Similarly, the above diamines treated with various substituted aromatic aldehydes to get excellent yields of benzimidazoles. The catalyst was reusable up to 4 times without significant drop of reactivity.

Ru-K edge EXAFS measurements were conducted to characterize the local structure of the supported Ru catalyst. Fig. 1 shows the k^3-weighted Ru K-edge EXAFS Fourier transforms and curve fitting results for $RuN3/SiO_2$ catalyst. Three shells were observed in the spectrum. The first shell corresponds to the overlapped paths of Ru-N and Ru-C. The second shell corresponds to the Ru-(C)-O and the third shell corresponds to the Ru-Ru path. It was found that the multinucleic character of Ru was retained in the present supported Ru catalyst.

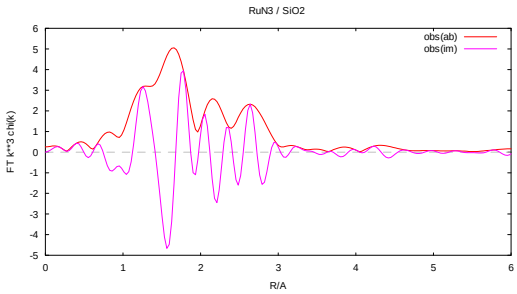

Fig. 1 : k^3-weighted Ru K-edge EXAFS Fourier transforms and curve fitting results for $RuN3/SiO_2$ catalyst.

* takehiko@k.u-tokyo.ac.jp

7C/2010G127
(SPring-8) BL14B2/2011A1972

Structural studies on Ni phosphide catalysts by Operando XAFS

Atsushi Takagaki[1], Ara Cho[1], S. Ted Oyama[1,2,*], and Kiyotaka Asakura[3,*]
[1]School of Engineering, The University of Tokyo, Tokyo 113-8656, Japan
[2]Virginia Polytech Institute and State University, Blacksburg, Virginia 24061-0211, USA
[3]Catalysis Research Center, Hokkaido University, Sapporo 001-0021, Japan

1 Introduction

The thermal treatment of biomass yields a liquid product that is known as biooil, which is a promising substitute for petroleum derived fuels, but which contains high levels of oxygen which reduce the heating value and make the oil unstable [1]. The purpose of this study is to investigate a new catalyst for oxygen removal, nickel phosphide. These materials were shown to have high activity in sulfur and nitrogen removal, so are promising candidates. As a model for biooil, use is made of the compound 2-methyltetrahydrofuran (2MTHF).

2 Experiment

The Ni_2P/SiO_2 catalyst was prepared by a temperature-programed reduction method from supported phosphate precursors. Reactivity studies were carried out in a flow reactor at 0.4 MPa using a mixture of 95 vol% of 2-MTHF and 5 vol% of *n*-heptane as an internal standard mixed with a H_2 gas to give a reactant stream of 3 or 5 mol% 2-MTHF in H_2. X-ray absorption spectra at the Ni K-edge of reference and catalyst samples were recorded in the energy range 8.233 keV. Measurements were carried out by standard transmission mode using a Si (111) monochrometer double crystal at room temperature on BL7C beam line at KEK-PF and BL14B2 at SPring-8.

3 Results and Discussion

The reactivity of the Ni_2P/SiO_2 is shown in Fig.1. The results show that the major products were the deoxygenated products *n*-pentane and *n*-butane. As intermediates, 2-pentanone, 2-pentanol and 1-pentanol were observed. These suggest that the HDO proceeds as shown in Fig 2.

Fig. 3 shows the Fourier transformed Ni K-edge EXAFS spectra for Ni_2P/SiO_2 and bulk Ni_2P. The peak which corresponds to Ni-Ni bond was weakened in the Ni_2P/SiO_2, indicating that small particles of Ni_2P were formed on silica. Each parameter in Ni_2P/SiO_2 was as follows. Ni-P (CN:2.0, R: 2.22Å, σ^2: 0.0024 Å^2); Ni-Ni (CN: 2.6, R: 2.66Å, σ^2: 0.0092 Å^2).

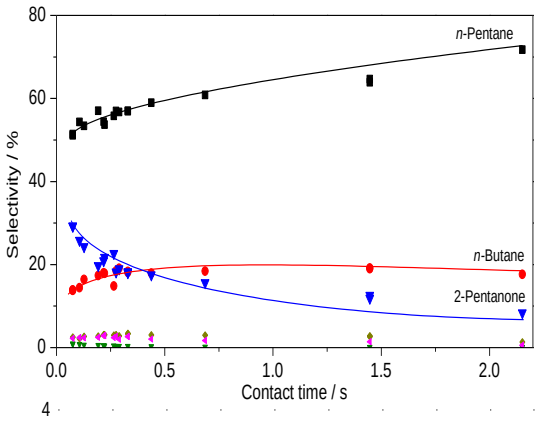

Fig 1: Contact time study of 2-MTHF HDO over Ni_2P/SiO_2.

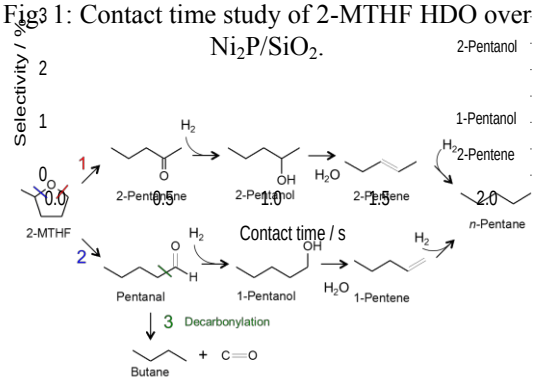

Fig. 2: A proposed reaction network for 2-MTHF HDO

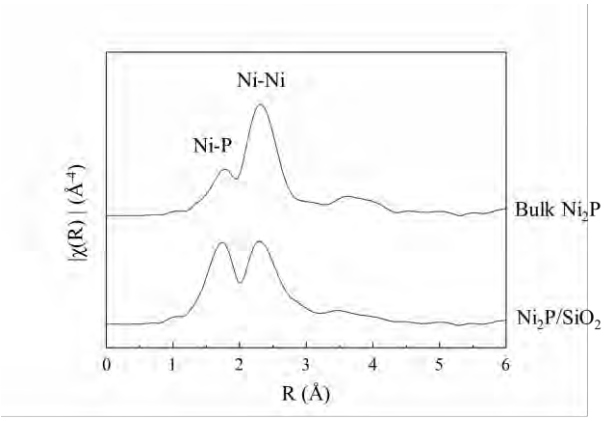

Fig. 3: Fourier transformed Ni K-edge EXAFS for bulk Ni_2P and Ni_2P/SiO_2.

References

[1] A.V. Bridgwater, Biomass & Bioenergy **38** (2012) 68-94.

* ted_oyama@chemsys.t.u-tokyo.ac.jp; askr@cat.hokudai.ac.jp

NW10A/2010G149, 2011G575

XAFS Study of Rhodium Cocatalyst Loaded on $K_2Ti_6O_{13}$ Photocatalyst

Hisao Yoshida* and Katsuya Shimura
Nagoya University, Nagoya 464-8603, Japan

1 Introduction

Some photocatalysts have been found to promote the photocatalytic steam reforming of methane (PSRM; 2 $H_2O_{(g)}$ + CH_4 → 4 H_2 + CO_2) around room temperature [1-5]. The activity was much influenced by not only the properties of semiconductor but also the metal cocatalyst loaded on the surface. Although the platinum loaded $K_2Ti_6O_{13}$ photocatalyst show high activity, unfavorable formation of carbon monoxide and gradual deactivation were observed. On the other hand, a rhodium-loaded $K_2Ti_6O_{13}$ photocatalyst showed two times higher activity than the platinum-loaded one did, and promoted the PSRM selectively without deactivation for many hours [6]. Further, the activity strongly depended on the loading method for the cocatalyst. In this study, we investigated the local structure of rhodium cocatalysts on the $K_2Ti_6O_{13}$ photocatalyst by using XAFS spectroscopy.

2 Experiment

A $K_2Ti_6O_{13}$ photocatalyst was prepared by the solid-state reaction method. Four rhodium-loaded samples were prepared: three Rh(0.03 wt%)/$K_2Ti_6O_{13}$ samples were prepared by impregnation and successive different thermal treatments, i.e., reduction at 473 K (*sample a*), calcination at 773 K before reduction at 473 K (*sample b*), and calcination at 773 K (*sample c*). The other sample was prepared by the photodeposition method in the presence of dissolved oxygen (*sample d*).

Rh K-edge XAFS spectra were recorded at the NW-10A station [7] of KEK-PF at room temperature with a Si(311) double crystal monochromator in a transmission mode and in a fluorescence mode by using the Lytle-detector (100 mm ion chamber filled with krypton) with a ruthenium filter (μt=6). The spectra were analyzed with a REX 2000 software (Rigaku).

3 Results and Discussion

Among these four samples, the catalyst prepared by the photodeposition method (*sample d*) showed the highest activity. The activity of the four samples was in the following order, *sample d* > *sample a* > *sample b* > *sample c*.

The Rh K-edge XANES spectra (Fig. 1A) revealed that the Rh cocatalyst would be almost metallic on both the *sample a* and the *sample b*. On the other hand, large edge shifts to higher energy suggested that the Rh cocatalyst would be almost oxidized on both the *sample c* and the *sample d*.

Fig. 1B shows the Rh K-edge EXAFS spectra of them. The curve-fitting analysis of EXAFS clarified that the peaks observed at 1.6 and 2.8 Å were assignable to the Rh–O and Rh–Rh shells in rhodium oxide, respectively. The atomic distance of the Rh–O shell was 2.06 Å, which is close to the Rh–O distance in Rh_2O_3 (2.03–2.05 Å, ICSD #108941) but different from that in RhO_2 (1.93–2.02 Å, ICSD #28498). The curve-fitting analysis also provided that the peak observed at 2.4 Å was assignable to the Rh–Rh shell with atomic distance of 2.70 Å, which is consistent with the Rh–Rh distance in rhodium metal (2.69 Å, #650218). For the *sample a*, a very small peak and a large peak were observed at 1.6 and 2.4 Å, respectively, although the intensity of the latter peak (the Rh–Rh shell) was not so large as compared with that for the rhodium foil. These results indicate that the Rh species on the *sample a* would dominantly exist as relatively large metal nanoparticles. For the *sample b*, two peaks at 1.6 and 2.4 Å were observed, suggesting that both small metal and oxide moieties would coexist on it. For the *sample c*, a large peak at 1.6 Å and a small peak at 2.8 Å were observed, while the peak at 2.4 Å was hardly observed, showing that the Rh species would mainly exist as relatively large oxide particles. For the *sample d*, a clear peak at 1.6 Å, a relatively small peak at 2.4 Å and a shoulder at 2.8 Å were observed, showing that there were small metal and large oxide moieties.

From this result and other evidences, it is suggested that this coexistence of the rhodium metal and oxide particles as cocatalyst would enhance the photocatalytic activity.

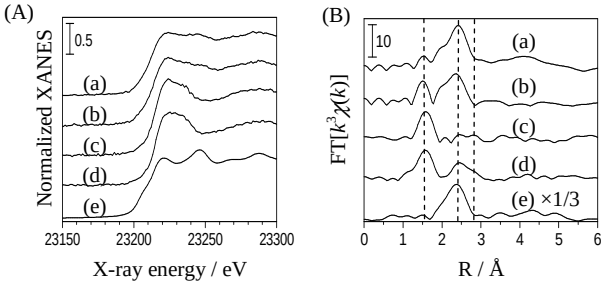

Fig. 1 (A) Rh K-edge XANES, and (B) Fourier transforms of Rh K-edge EXAFS spectra for the Rh(0.1)/$K_2Ti_6O_{13}$ photocatalysts, *samples a*−*d* in the text (a)−(d), and rhodium foil (e).

References

[1] H. Yoshida, *et al.*, Chem. Lett., **36** (2007) 430.
[2] H. Yoshida, *et al.*, J. Phys. Chem. C, **112** (2008) 5542.
[3] K. Shimura, *et al.*, J. Phys. Chem. C, **114** (2010) 3493.
[4] K. Shimura, and H. Yoshida, Energy Environ. Sci., 3 (2010) 615.
[5] K. Shimura *et al.*, J. Phys. Chem. C **144** (2010) 11466.
[6] K. Shimura, *et* al., Chem. Commun., **47** (2011) 8958.
[7] M. Nomura *et al.*, AIP Conf. Proc. **882** (2007) 896.

* yoshidah@apchem.nagoya-u.ac.jp

7C/2010G165

Fluoride addition effect on the EXAFS of neodymium cation in molten chlorides

Kazuhiro FUJITA[1], Atsushi NEZU[1], Yasuaki SHIMOHARA[1],
Hiroshi AKATSUKA[1], Haruaki MATSUURA*[1]
[1]Res. Lab. for Nucl. Reactors, Tokyo Tech., Ookayama, Meguro-ku, Tokyo, 152-8550, Japan

Introduction

Neodymium magnet has the strongest magnetism among the magnets currently industrialized, thus it has been used as motors in hybrid cars, electric vehicles, wind farms and medical instruments which are required with strong magnetism. However, over 97 % of the first resource of rare earths including neodymium is now produced in China. If the demand of the electric vehicles and wind farms rapidly increases in the world, it leads to special concern about the lacking of rare earth resource. Therefore, we have focused on nickel misch metal hydride batteries as a secondary resource of rare earths, and investigated applicability of molten salt electrolysis to extract neodymium from them. To find out the much efficient electrochemical condition for the separation of neodymium, the electrochemical behaviour of neodymium in molten LiCl – KCl and LiCl – $CaCl_2$ eutectic coexisting various amount of LiF has been examined. To elucidate the relationship between the variation of electro-reduction potential and local structure around neodymium cation depending on fluoride concentration in molten chloride, EXAFS experiments of neodymium cation in molten LiCl – KCl – LiF and LiCl – $CaCl_2$ – LiF have been performed.

Experimental

EXAFS spectra of Nd L_{III}-edge (6.209 keV) were collected with a fixed time scan method by using Si (111) double crystal monochromator in transmission mode. Mixtures of $NdCl_3$ (x = 5mol%) in eutectic LiCl – KCl or LiCl – $CaCl_2$ with LiF in the amount of various times to the concentration of $NdCl_3$ (0 to 10), were melted once in a glassy carbon crucible at 873 K in a glove box filled with an argon atmosphere in high purity. Then, they were mixed with boron nitride powder, and pressed into pellets. To prevent from the chemical reaction during heating process in EXAFS measurements, these pellets were installed in a cell made with pyrolytic boron nitride and the electric furnace was filled with He gas under 30 kPa. EXAFS data were analysed by using the WinXAS ver.3.1.

Results and discussion

The structural functions of molten $NdCl_3$ – LiCl – KCl – LiF (0 and 6 times of concentration of Nd) and $NdCl_3$ – LiCl – $CaCl_2$ – LiF (0, 6 and 10 times of concentration of Nd) at 873 K are shown in Fig. 1. In both systems, with increasing fluoride concentration, interionic distance between Nd^{3+} and anion decreases, that is corresponding to the fact that chloride anions in the 1st coordinated sphere around Nd^{3+} are exchanged by fluoride anions. The most striking feature derived from these figures is the local structure of Nd^{3+} is more affected by fluoride addtion in LiCl - KCl eutectic than in LiCl – $CaCl_2$ eutectic. This is due to the difference of coulombic interaction, i.e., Ca^{2+} much strongly coodinates F^- than K^+ does, thus it prevents fluoride coordination around Nd^{3+} in the first coordination sphere. It has been found that the tendency of the variation of electro-deposition potential depending on fluoride concentation is different, thus profound discussion on the relationship between electrochemical behaviour and local structure is now expected.

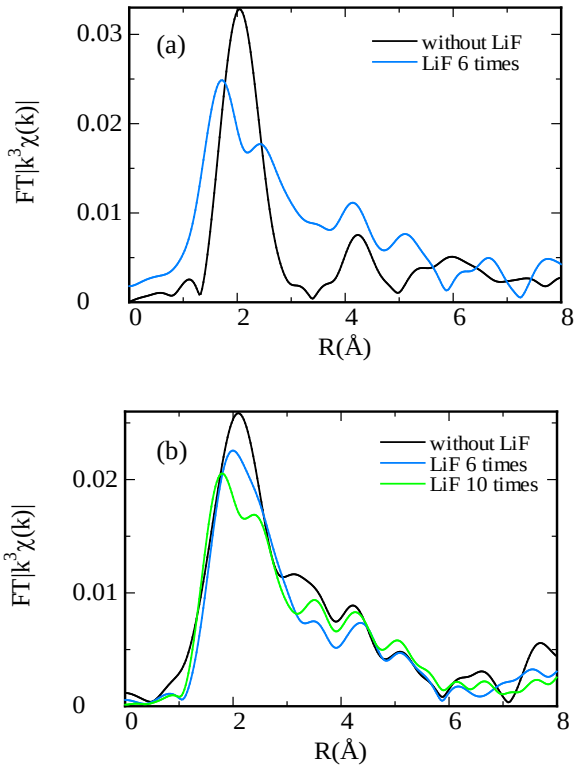

Fig. 1 The structural functions of molten (a) $NdCl_3$ – LiCl – KCl – LiF (0 and 6 times of concentration of Nd) and (b) $NdCl_3$ – LiCl – $CaCl_2$ – LiF (0, 6 and 10 times of concentration of Nd) at 873 K.

*hmatsuur@nr.titech.ac.jp

19B/2010G510

Thermal changes of structures and properties of pi-backdonating metal complexes (in 2010)

Takashiro AKITSU*[1]
[1] Department of Chemistry, Faculty of Science, Tokyo University of Science,
1-3 Kagurazaka, Shinjuku-ku, Toyo 162-8601, Japan

Introduction

Recently, (magnetic) cyanide-bridged bimetallic assemblies, which is typical systems of pi-backdonation, and the related precursor chiral, achiral or racemic Cu(II) complexes have been investigated by means of variable temperature XRD or XAS [1-4]. Additionally, we prepared $[M_2O_7]^-$-bridged (M = Cr, Mo, and W) bimetallic assemblies [5] for comparison of valences via bridging ligands indicating pi-backdonation ($[A(CN)_n]^{m-}$) or non-pi-backdonation ($[M_2O_7]^-$-). Moreover, we have developed new preparations for bimetallic oxides $[Cu_aM_bO_c]$ from these bimetallic assemblies of bridged complexes by burning. However, oxidation of metal ions must be expected and detailed measurements of valences should be carried out before and after preparations besides electronic states inner shell at low temperature. Herein, we have investigated valence states of Cu(II) ions as a standard some bimetallic assemblies and the resulting bimetallic oxides by means of soft X-ray spectroscopy.

Experimental section

Preparations

Bimetallic oxides have been prepared from the corresponding precursors of chiral or racemic bimetallic complexes as follows: $[CuL'_2][CrO_4]$ L' = (*1R,2R*)-*N,N*'-dimethyldiaminocyclohexane, $[CuL'_2][Cr_2O_7]$, $[CuL_2][CrO_4]$ L = (*1R,2R*)-diaminocyclohexane,, $[CuL_2][Cr_2O_7]$, $[CuL_2]$[reduced Mn12-SMM], $[CuL''_2]$[reduced Mn12-SMM] L'' = *N*-ethylethylenediamine, $[CuL_2][Mo_2O_7]$, $[CuL''_2][Mo_2O_7]$, and $[CuL''_2][PtCl_4]$. Characterization was carried out by means of IR spectra, magnetic measurements, and XRD.

The powder XRD patterns of the precursor complexes and resulting were also measured at KEK-PF BL-8B (2010G511; 8 keV, λ = 1.54 Å) at 100 and 300 K.

Mearurements

The $Cu2p_{3/2}$ and $Cu2p_{1/2}$ peaks of XAS (soft X-ray absorption spectra) for these samples were measured at KEK PF BL-19B (at a constant ring current) under variable temperature (room temperature – about 60 K). The spectra were corrected by the standard Au sample.

Results and discussion

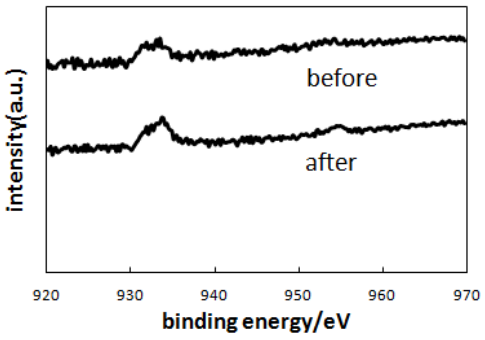

Figure 1: The XAS of $Cu2p_{1/2}$ and $Cu2p_{3/2}$ peaks for and $[CuL_2]$[reduced Mn12-SMM] (before) and $[Cu_aMn_bO_c]$ (after).

For example, we mention the results for chiral $[CuL_2]$[reduced Mn12-SMM] and its oxide, $[Cu_aMn_bO_c]$. At room temperature, the precursor shows $Cu2p_{1/2}$ and $Cu2p_{3/2}$ peaks around 955 and 945 eV, respectively. The resulting oxides also shows $Cu2p_{1/2}$ and $Cu2p_{3/2}$ peaks around 955 and 945 eV, respectively. The results suggest that Cu(II) ion is not oxidized during preparation, while only Mn(III) or Mn(IV) ions may be oxidized up to higher valence states.

However, more stable ions such as Pt(II) in $[CuL''_2][PtCl_4]$ or metal ions at the highest valence states, namely Cr(VI) in $[CuL_2][Cr_2O_7]$, could not be oxidized furthermore.

Of course, substitution of coordination atoms, for example $[CuN_4O_2]$ environment for the precursor and $[CuO_6]$ environment for the resulting oxides may be a factor of changing XAS peaks.

References

[1] T. Akitsu et al., Open. Cryst. J. 4, 8 (2011).
[2] T. Akitsu et al., Open. Cryst. J. 4, 21 (2011).
[3] T. Akitsu et al., Open. Cryst. J. 4, 2 (2011).
[4] T. Akitsu et al., Open. Cryst. J. 4, 25 (2011).
[5] N. Hayashi and T. Akitsu, Polymers, 3, 1029 (2011).

* akitsu@rs.kagu.tus.ac.jp

8B/2010G511

Anisotropy of functions and thermally structural changes for Cu(II) complexes (in 2010)

Takashiro AKITSU*[1]
[1] Department of Chemistry, Faculty of Science, Tokyo University of Science,
1-3 Kagurazaka, Shinjuku-ku, Toyo 162-8601, Japan

Introduction

Recently, we have widely investigated metal-organic frameworks or transition metal complexes [1-4] by means of powder X-ray diffraction (XRD) in view of thermally-accessible structural changes of Jahn-Teller distortion (local distortion around coordination environment) and global strain of crystal lattice. Last year we have prepared several chiral or racemic bimetallic assemblies composed of Cu(II) complexes and Cr(VI), Mo(VI), or W(VI) complexes [5]. Furthermore, these types of bimetallic assemblies may be appropriate precursor for preparing bimetallic metal oxides because of highly homogeneous structures. Herein we have attempted to prepare bimetallic metal oxides from bimetallic assemblies of metal complexes by burning and measured their XRD patterns by changing temperature.

Experimental section

Preparation

For example, slow diffusion of aqueous solution of a precursor complex $[Cu(chxn)_2(H_2O)_2](NO_3)_2$ (chxn = (*1R, 2R*)-diaminocyclohexane) onto methanol solution of reduced Mn12-cluster (a typical single molecule magnet) as counter anions allowed to stand at 298 K for several days to gave rise to resulting precipitates. The bimetallic assemblies were burned to give rise to bimetallic metal oxides. The products were characterized by means of IR spectra, soft X-ray absorption spectra, magnetic measurements, and XRD.

X-ray Crystallography

Powder XRD patterns of the precursor complexes and resulting were measured at BL-8B (8 keV, λ = 1.54 Å) at 100 and 300 K.

Results and discussion

For example, we mention the results for chiral $[Cu(chxn)_2][Mn12]$ and its oxide. At 100 K, the precursor shows some intense peaks around 25 degrees, while the resulting oxide shows some predominant peaks around 35 degrees (Figure 1). Temperature dependence of shift of XRD peaks was commonly expected behavior. Because both XRD patterns differs completely, preparation of oxide can be confirmed. The corresponding IR spectra (organic ligands' moieties vs M-O bonds) also support the results. Interestingly, the precursor $[Cu(chxn)_2][Mn12]$ indicates paramagnetism merely besides characteristic behavior of single molecule magnets, while the resulting bimetallic oxide indicates ferromagnetism clearly. In this context, this is a good method for preparing bimetallic oxides as magnetic materials.

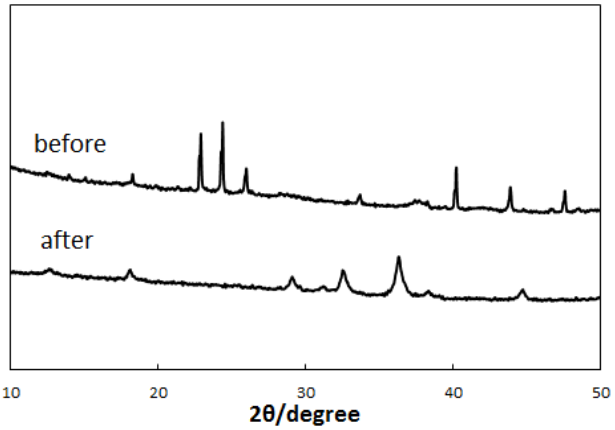

Figure 1: Temperature dependence of XRD patterns of a precursor, $[Cu(chxn)_2][Mn12]$ (before), and its oxides (after) at 100K.

Moreover, we have prepared other bimetallic oxides from the following precursors of chiral or racemic bimetallic complexes: $[CuL'_2][CrO_4]$ L' = (*1R,2R*)-*N,N'*-dimethyldiaminocyclohexane, $[CuL'_2][Cr_2O_7]$, $[CuL_2][CrO_4]$, $[CuL_2][Cr_2O_7]$, $[CuL''_2]$[reduced Mn12-SMM] L'' = *N*-ethylethylenediamine, $[CuL_2][Mo_2O_7]$, $[CuL''_2][Mo_2O_7]$, and $[CuL''_2][PtCl_4]$.

References

[1] T. Akitsu et al., Open. Cryst. J. 4, 8 (2011).
[2] T. Akitsu et al., Open. Cryst. J. 4, 21 (2011).
[3] T. Akitsu et al., Open. Cryst. J. 4, 2 (2011).
[4] T. Akitsu et al., Open. Cryst. J. 4, 25 (2011).
[5] N. Hayashi and T. Akitsu, Polymers, 3, 1029 (2011).

* akitsu@rs.kagu.tus.ac.jp

NE1A/2010G560

B1-to-B2 Structural Transitions in Rock Salt Intergrowth Structures

Takafumi Yamamoto[1,*], Taku Okada[2], Takehiko Yagi[2], Takumi Kikegawa[3], and Hiroshi Kageyama[1]
[1]Kyoto University, Kyoto 615-8510, Japan
[2]University of Tokyo, 5-1-5 Kashiwanoha, Kashiwa, Chiba 277-8581, Japan
[3]KEK, 1-1 Oho, Tsukuba, Ibaraki 305-0801, Japan

1 Introduction

It is known that the rock salt (*B*1) structure of binary compounds transforms to the CsCl (*B*2) structure under high pressure. Recently, the *B*1-to-*B*2 transition have been reported in the two-legged spin ladder structure $Sr_3Fe_2O_5$, an intergrowth compound composed of alternate stacking of the SrO rock salt block and the $(SrFeO_2)_2$ ladder block along the *c* axis [1]. Notably, this is a first compound that exhibits the *B*1-to-*B*2 transition in intergrowth compound.

In this study, we investigated the presence of pressure-induced structural transitions in one-dimensional (1D) compounds A_2MO_3 (A = Sr, Ca; M = Cu, Pd). The crystal structure is shown in Figure 1a. A_2MO_3 is an intergrowth structure of the AO rock salt blocks and the 1D chains of corner-shared MO_2 squares (or one-legged ladders), and adopt the *Immm* space group. All examined A_2MO_3 compounds exhibit the same type of structural transitions as $Sr_3Fe_2O_5$, which provides a unique opportunity to discuss the intrinsic nature of this transition and quantitative comparison with the well-studied binary systems.

2 Experiment

A powder sample of A_2MO_3 was synthesized by the high temperature ceramic method [2,3].

High resolution powder synchrotron XRD experiments under high pressures were performed at room temperature up to 37 GPa for Sr_2CuO_3, 51 GPa for Ca_2CuO_3 and 35 GPa for Sr_2PdO_3 using the NE1A synchrotron beam line of PF-AR. A powder sample of A_2MO_3 was loaded into a 180 μm diameter hole of a pre-indented rhenium gasket of the diamond-anvil cell. Helium was used as a pressure transmitting medium for Sr_2CuO_3 and Sr_2PdO_3, while a 4:1 methanol:ethanol mixture was used for Ca_2CuO_3. The pressure gradients within the samples were not more than 8 GPa for Sr_2CuO_3, 4 GPa for Ca_2CuO_3 and 1 GPa for Sr_2PdO_3 at maximum pressures applied in this study. The incident X-ray beam was monochromatized to a wavelength of 0.4115 Å for Sr_2CuO_3 and 0.4114 Å for Ca_2CuO_3. For Sr_2PdO_3, the first batch was measured with a wavelength of 0.4115 Å, until the used DAC was broken at 24GPa. The second batch was measured with a wavelength of 0.4114 Å in a pressure range from 19 GPa to 35GPa. The obtained synchrotron XRD data were analyzed by the Rietveld method using RIETAN-FP program [4].

3 Results and Discussion

The diffraction patterns of these compounds in the low pressure regime could be assigned to the orthorhombic *I*-centered unit cell, consistent with the reported data at ambient pressure. As is expected, the 2θ angles of the reflection peaks gradually increase with increasing pressure, resulting from contraction of the lattice. For all the compounds examined, the further application of pressure finally results in drastic change in the diffraction patterns featured by a discontinuous change in the cell constants and by modified reflection conditions compatible with the orthorhombic *A*-centered lattice. The P_s values are 29 GPa for Sr_2PdO_3, 30 GPa for Sr_2CuO_3, and 41GPa for Ca_2CuO_3. We assumed that this is the same *B*1-to-*B*2 transition as observed in $Sr_3Fe_2O_5$.

The high pressure A_2MO_3 structure was refined using the synchrotron XRD data at 34.7 GPa for Sr_2PdO_3, at 37.4 GPa for Sr_2CuO_3, and at 51.3 GPa for Ca_2CuO_3, assuming the space group *Ammm* (as in $Sr_3Fe_2O_5$ [1]). The atoms are placed at 4*j* (0.5, 0, *z*) for A = Sr or Ca, 2*a* (0, 0, 0) for M = Cu or Pd, 4*i* (0, 0, *z*) for O(1), and 2*b* (0, 0.5, 0) for O(2). During the refinements, the occupancy factors were constrained to unity. All the refinements converged well, yielding R_p = 0.75%, R_{wp} = 1.21%, χ^2 = 2.83 for Sr_2PdO_3, R_p = 0.90%, R_{wp} = 1.20%, χ^2 =2.49 for Sr_2CuO_3, and R_p = 0.69%, R_{wp} = 1.24%, χ^2 = 1.59 for Ca_2CuO_3.

Now that the proposed high pressure structure of A_2MO_3 is confirmed, we can say that the pressure-induced *B*1-to-*B*2 transition generally occurs in the rock salt/spin-ladder intergrowth compounds and is not restricted to iron oxides and/or two-legged ladder structure . Namely, we can propose that $(AO)(AMO_2)_n$ (n = 1, 2, 3…) with the AO rock salt unit and the $(AMO_2)_n$ n-legged spin ladder unit, if synthesized, would exhibit the same type of transition.

Let us now quantitatively compare the *B*1-to-*B*2 structural transition between binary systems and the intergrowth systems. Figure 2 shows the empirical relation, where the logarithm of transition pressure P_s shows a linear dependence on ratio of the cation/anion radius, R_A/R_O. It is remarkable that the critical pressures for the binary compounds AO, the intergrowth compounds A_2MO_3 and $Sr_3Fe_2O_5$ are located just on the line. This means that P_s is determined solely by R_A/R_O in the AO block. Insensitivity of the ladder block to P_s in turn implies that the ladder subunit at ambient pressure is a favorable form at high pressure. The structural stability

of the ladder subunit under high pressure is understandable because it should have high compressibility along the out-of-plane direction as a result from the complete absence of apical oxygen.

In summary, we demonstrated that the pressure-induced *B*1-to-*B*2 transition generally occurs in the rock salt/spin-ladder intergrowth compounds. It is remarkable that the critical pressures P_s for the intergrowth compounds are determined solely by R_A/R_O, showing quantitatively the same trend as the binary AO compounds, which make it possible to predict P_s of other related compounds.. For more details of the study, see the reference [5].

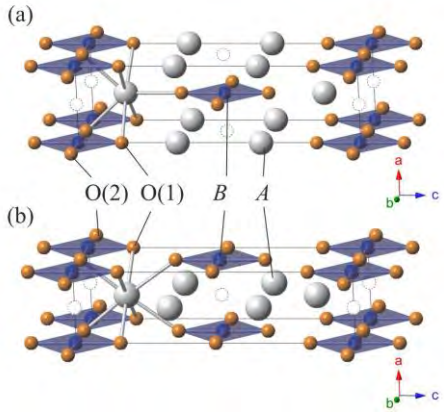

Fig. 1: The A_2MO_3 structures (a) at low pressure ($P < P_s$) and (b) at high pressure ($P_s < P$). White, blue, and orange spheres represent A, M and O atoms, respectively.

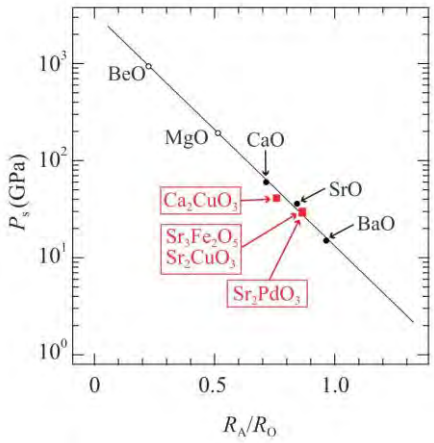

Fig. 2: P_s vs the A-site ion radius (R_A) to the oxide ion radius (R_O). R_A in 6- and 7-fold coordination is used [6], respectively, for the low pressure structure of AO, and A_2MO_3 ($Sr_3Fe_2O_5$). Experimental (black closed circles) and theoretical (black open circles) values for binary systems AO (A = Ca, Sr, Ba) are from the references [7-9]. Red Closed squares represent the data obtained in this study.

Acknowledgement

This work was supported by the Japan Society for the Promotion of Science (JSPS) through its "Funding Program for World-Leading Innovative R&D on Science and Technology (FIRST) Program", T.Y. was supported by the Japan Society for the Promotion of Science for Young Scientists.

References

[1] T. Yamamoto *et al*., J. Am. Chem. Soc. 133 (2011) 6036.
[2] M. T. Weller and D. R. Lines, J. Solid State Chem. 82 (1989) 21.
[3] Y. Nagata *et al*., J. Alloys Compounds 346 (2002) 50.
[4] F. Izumi et al., Solid State Phenom. 130, 15(2007).
[5] T. Yamamoto *et al*., J. Inorg. Chem. 50 (2011) 11787.
[6] R. Shannon, J. Acta Crystallogr. 32 (1976) 751.
[7] L. Liu and W. A. Bassett, J. Geophys. Res. 77 (1972), 4934.
[8] R. Jeanloz *et al*., Science 206 (1979) 829.
[9] Y. Sato and R. J. Jeanloz, Geophys. Res. 86 (1981) 11773.

* yamamoto.takafumi.55u@st.kyoto-u.ac.jp

NW10A/2010G591

セルロース加水分解活性を有する担持ルテニウム触媒の分析
Characterization of Supported Ruthenium Catalysts for Hydrolysis of Cellulose

小林広和 [1*], 駒野谷将 [1,2], 原賢二 [1], 田旺帝 [3], 福岡淳 [1]
[1] 北海道大学触媒化学研究センター、〒001-0021 札幌市北区北 21 条西 10 丁目
[2] 北海道大学大学院総合化学院、〒060-8628 札幌市北区北 13 条西 8 丁目
[3] 国際基督教大学大学院アーツ・サイエンス研究科、〒181-8585 三鷹市大沢 3-10-2

1 はじめに

再生可能な資源としてバイオマスが注目されている。特に、最も豊富に存在し、かつ非可食であり食料と競合しないセルロースを化学資源として有効利用できれば意義深いと考えられる。

セルロースはグルコースがグリコシド結合により多数繋がった分子であり、加水分解すればグルコースを合成できる(図 1)。我々はメソポーラス炭素 CMK-3 に Ru を担持した触媒 Ru/CMK-3 が本反応に高い活性を示すことを見出した[1]。Ru が加水分解を促進することは興味深く、Ru 種の化学状態を XAFS により検討した [2, 3]。

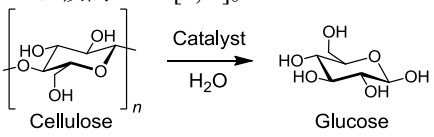

図 1：セルロースの加水分解反応

2 実験

触媒は、$RuCl_3$ を CMK-3 に含浸担持し、400 °C で水素還元後、室温で空気暴露して調製した。

Ex-situ Ru K-edge XAFS 測定は、He クライオスタットにより 30 K に冷却した後、透過法で測定した。触媒調製の in-situ QXAFS 測定は、Bando らの方法[4]を参考にして作製した SUS316 製の常圧固定床流通式反応装置を用いて、透過法で測定した。反応の in-situ QXAFS 測定は、PEEK 製の耐圧セルに触媒、基質、水を入れた後、120 °C まで徐々に昇温し、加熱中ならびに恒温中に透過法で測定した。カーブフィッティングには RuO_2 の結晶構造データを用いた。

3 結果および考察

Ru/CMK-3 触媒ならびに各種標準試料の XAFS スペクトルを測定した(図 2)。本 Ru 触媒と $RuO_2{\cdot}2H_2O$ のスペクトル形状ならびにカーブフィッティング結果(表 1)はよく一致した。R_f 値が比較的高いのは、2.2 Å のピークをアサインできていないためである。

$RuO_2{\cdot}2H_2O$ の生成過程を明らかにするため、触媒調製中の in-situ QXAFS を測定した。結果、水素還元後は Ru 金属ナノ粒子であるが、室温の酸素暴露により酸化され、さらに水を吸着させることにより、本化学種が生成することが明らかになった。TEM から見積もった Ru 種の粒子径は 1 nm であり、極めて小さいために容易に再酸化されたと考えられる。

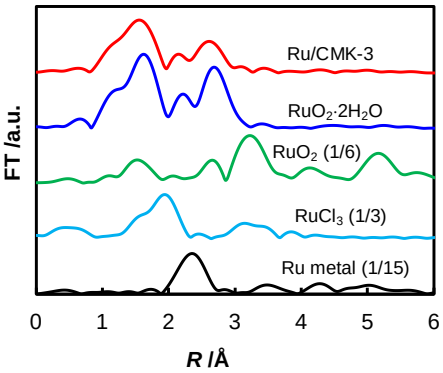

図 2：Ru K 殻 EXAFS フーリエ変換スペクトル

表 1：Ru 種のカーブフィッティング結果

sample	shell	CN	*R* (Å)	R_f (%)
Ru/CMK-3	Ru–O	6.9 ± 1.4	1.98 ± 0.02	9.7
	Ru–Ru	1.0 ± 0.4	3.06 ± 0.02	
$RuO_2{\cdot}2H_2O$	Ru–O	6.4 ± 1.3	2.01 ± 0.02	13
	Ru–Ru	1.4 ± 0.4	3.10 ± 0.01	

さらに、セロビオースをモデル基質に用いて加水分解中の in-situ QXAFS 測定を行ったところ、120 °C で Ru 種の還元が徐々に進行し、Ru 金属と類似のスペクトルになった。しかし、Ru の K 殻吸収端は依然として金属よりも 2 eV 高く、酸化されていることが示唆された。この $Ru^{\delta+}$種が酸触媒として機能する活性種である可能性がある。

4 まとめ

CMK-3 上の Ru 種は水和した RuO_2 であり、加水分解中に部分的に還元されて金属の構造に近い $Ru^{\delta+}$種になることが示唆された。

謝辞

XAFS の解析でお世話になった朝倉清高教授ならびに in-situ 測定セルを作製された向井慎吾氏に感謝申し上げる。

参考文献

[1] H. Kobayashi et al., ChemSusChem, **3** (2010) 440.
[2] T. Komanoya et al., Appl. Catal. A, **407** (2011) 188.
[3] H. Kobayashi et al., Catal. Sci. Technol., 2 (2012) 869.
[4] K.K. Bando et al., J. Synchrotron Rad., **8** (2001) 581.

* kobayashi.hi@cat.hokudai.ac.jp

6A/2010G626, BL40B2,SPring-8/2011A1961

ポリ乳酸ステレオコンプレックスの結晶構造形成の解明
Analysis of Stereo Complex Crystals in Poly(L-lactic Acid)/Poly(D-Lactic Acid) Blends

辺見幸大[1], 松葉　豪[1*], 辻秀人[2], 河井貴彦[3], 金谷利治[4],
小田顕通[5], 豊原清綱[5]
[1]山形大学　〒992-8510 米沢市城南 4-3-16
[2]豊橋技術科学大学　〒441-8580 愛知県豊橋市天伯町雲雀ケ丘 1-1
[3]群馬大学　〒373-0057 群馬県太田市本町 29-1
[4]京都大学　〒611-0011 京都府宇治市五ヶ庄
[5]帝人（株）　〒740-8511 山口県岩国市日の出町 2-1

1 はじめに

ポリ乳酸(PLA)は非石油由来の高分子であり、カーボンニュートラルな材料として注目されている。しかし、PLA は高分子材料に必要な力学特性や、耐熱性の点で既存の汎用高分子に比べ劣っていることから、改善するため多くの研究が行われている。その中で、高分子材料は熱処理条件によってその特性、性質、物性は大きく変化する特性に着目した。例えば、溶融状態からの結晶化過程やガラス状態からのアニール処理などによって、球晶の密度や大きさが大きく変化することが知られている。

そこで、本研究では、鏡像異性体であるポリ(L-乳酸)とポリ(D-乳酸)をブレンドさせた試料で形成されるポリ乳酸ステレオコンプレックス結晶(Sc 結晶)に着目した。Sc 結晶はポリ(L-乳酸)やポリ(D-乳酸)の単体から形成される Homo 結晶より融点が 50 °C 以上も高く、耐熱性に優れ、結晶成長速度も大きくなることが知られている。そこで、アニール処理プロセスによる Sc 結晶の結晶構造およびラメラ構造の変化について時分割小角および広角 X 線散乱測定を用いて明らかにすることを試みた。温度処理による構造の変化を議論するため、高強度・高輝度の放射光 X 線を用いた。

2 実験

試料として、帝人株式会社製のポリ(L-乳酸)（M_w = 166,000, M_w/ M_n = 2.0）とポリ(D-乳酸) （M_w = 179,000, M_w/ M_n = 2.0）を重量比 50:50 で混合させたポリ乳酸ブレンドを用いた。溶融結晶化過程は 240 °C で 5 分溶融後、5 °C/min で冷却し 190 °C で等温結晶化プロセスを観察した。ガラス結晶化過程は、溶融サンプルを 0 °C に冷却した真空プレス内に移すことで得られたガラス試料（ガラスサンプル）を室温より 190 °C まで 5 °C /min で昇温、その後等温結晶化させたときの結晶成長過程を観察した。上記の試料の温度条件は、メトラー社製 FP90 システムを用いて制御した。それぞれの過程の降温/昇温プロセスの高分子のモルホロジーの変化を、小角 X 線散乱測定、広角 X 線散乱測定を用いて追跡した。なお、兵庫県佐用町の SPring-8 の BL40B2 で時分割同時測定を行った。

3 結果および考察

図 1 に昇温、降温過程における SAXS プロファイルの温度依存性を示す。縦軸は IQ^2、横軸は散乱ベクトル Q （= $4\pi\sin\theta/\lambda$: 2θ 散乱角、λ：波長）である。溶融結晶化過程(a)においては、温度が低くなるに従って、0.12 nm^{-1} 付近にピークが 205 °C 付近で観測され始め、降温するに従って徐々にピーク位置が広角側に移動し、190 °C では 0.15 nm^{-1} に観測された。このピークは長周期に起因する。このように、降温するに従って徐々に長周期が小さくなる傾向はポリエチレンやポリプロピレンなどでも観測されている傾向と一致している。一方、ガラス結晶化過程(b)では、昇温すると、PLA のガラス転移温度（63 °C）を超えると Q = 0.4 nm^{-1} 付近にピークが観測される。このピークは昇温に伴って、徐々に小角側に移動し、Homo 結晶の融点（160 °C）付近で一度消失することがわかった。よって、小角側に移動しているピークは Homo 結晶からなるラメラ構造によるものであると考えられる。Homo 結晶の融解後、さらに昇温させ 170 °C を超えると Q = 0.12 nm^{-1} 付近にピークが現れ、さらに小角側に移動していることがわかった。一方、170 °C 以上ではさらに広角側に新たにピークが出現し、同様に徐々に小角側に移動していた。190 °C まで昇温させると Q = 0.09 および 0.3 nm^{-1} 付近の二つのピークとなった。190°C は、Homo 結晶の融点よりも十分に高いことから、これらの構造は Sc 結晶に起因していると考えられる。ガラス結晶化過程で観察される Sc 結晶からなる長周期構造は、

溶融結晶化過程で観察される Sc 結晶からなる長周期構造とは大きく異なっていることがわかった。ガラス結晶化過程においては、試料をガラス状態から徐々に昇温させるため、ガラス転移温度以上で出現する Homo 結晶からなるラメラ構造が昇温により融解することで、Sc 結晶からなるより大きな長周期構造が出現すると考えられる。さらに、ガラス結晶化過程および溶融結晶過程で作製した試料に対して、透過型電子顕微鏡観察を行った。その結果、ガラス結晶化試料からは二種類の相関を持つ長周期構造が発見された。この結果は、ラメラのモルホロジーが結晶成長の際の熱処理プロセスに大きく依存していることを示している。

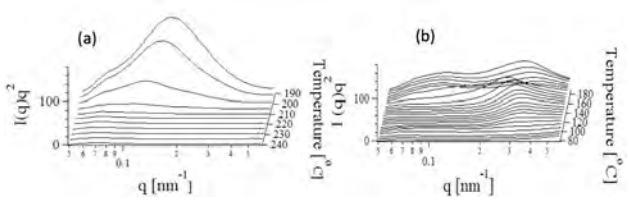

Fig. 1: SAXS profiles of Poly(L-lactic acid)/Poly(D-lactic acid) blends in the case of cooling down from the molten state (a) and of heating up from glassy state (b).

さらに WAXS 測定の結果について議論する。ガラス結晶化過程では Sc 結晶が PLA の Homo 結晶と同時に 80 °C から出現していることがわかった。また、さらに昇温させると、Homo 結晶は、160 °C 付近から融解していることがわかった。この結果は DSC 測定で観測される結果と一致している。融解させたと同時に Sc 結晶のピークが増大し始めることがわかった。これは、すなわち Sc 結晶が成長を開始することを示唆している。小角 X 線散乱測定で得られた結果である、160℃近傍で Homo 結晶が融解し、190 °C では、Homo 結晶融解に起因した大きい相関と、Sc 結晶由来の小さな相関の二つの相関距離を持つ構造を持つと言う傾向とガラス結晶化過程の広角 X 線散乱測定の結果とよく一致していた。一方、溶融体を降温させた溶融結晶化過程では、190 °C の結晶成長プロセスでは、Sc 結晶由来の結晶格子のみが観察されていた。すなわち Sc 結晶の成長プロセスのみが観測されており、Homo 結晶は全く観測されなかった。また、ガラス結晶化および溶融結晶化過程において、結晶格子についてはほぼ同じであることがわかった。すなわち、アニール処理によって、ラメラの成長過程が変化するため長周期構造が非常に大きな影響を受けるが、結晶格子についてはほとんど影響を受けていないことが示された。

謝辞

本研究は、東日本大震災による PF 共同利用実験が停止したことに伴って、震災優先枠を利用して BL40B2/SPring-8 にて実験させていただいたものです。(2011 年 5 月 10 日実施)。SPring-8 での実験の際にご尽力してくださった、JASRI の太田昇様、小川紘樹様および震災優先枠の利用の際にさまざまな形でお世話になりました KEK/PF の伊藤健二様、清水伸隆様には心より感謝申し上げます。また、震災直後で、実験や研究の進行が非常に困難な時期に、さまざまな形でご尽力していただきました SPring-8 および PF の多くのスタッフの方々に心より感謝いたします。

* gmatsuba@yz.yamagata-u.ac.jp

2011A1974/2010G629

Electronic and Local Structures of $Ce(PO_4)_{1-x}(VO_4)_x$-Based Proton-Electron Mixed Conductor

Yasushi IDEMOTO*[1], Naoto KITAMURA[1], Yoshiharu UCHIMOTO[2]

[1]Department of Pure and Applied Chemistry, Faculty of Science and Technology, Tokyo University of Science, 2641 Yamazaki, Noda, Chiba 278-851, Japan

[2]Graduate School of Human & Environmental Studies, Kyoto University, Sakyo-ku, Kyoto 606-8501, Japan

1 Introduction

In recent years, the monazite-type $CePO_4$-based materials have drawn much attention because the materials exhibited proton-electron mixed conduction at elevated temperature under a wide range of oxygen partial pressure, and thus are expected to be applied for a hydrogen-permeable membrane, an electrode of a solid oxide fuel cell (SOFC) and so on [1, 2]. Among the materials, $Ce(PO_4)_{1-x}(VO_4)_x$ can be regarded as promising because of its high electronic conduction, but it is ambiguous how the composition affects the electronic and local structures at this moment.

From such background, we prepared the monazite-type $Ce(PO_4)_{1-x}(VO_4)_x$, and then investigated their electrical conductivities. In order to clarify the electronic and local structures, we also carried out X-ray absorption fine structure (XAFS) measurements, and then discussed a relationship among the structures and conduction properties.

2 Experiment

$Ce(PO_4)_{1-x}(VO_4)_x$ (x=0~0.3) was prepared by means of a hydrothermal process using $Ce(NO_3)_3$, $(NH_4)_2HPO_4$ and NH_4VO_3 as starting materials. Phases of the obtained samples were identified by X-ray diffraction measurements. We also measured electrical conductivities of the sintered $Ce(PO_4)_{1-x}(VO_4)_x$ at the temperature range from 300 to 900 °C under various partial pressures of water vapour and oxygen.

As for these samples, XAFS measurements of Ce *K*- and L_{III}-edges were performed with a transmission mode at BL14B2 installed at SPring-8. Some of the samples were heat-treated under Ar condition, in order to investigate an effect of oxygen partial pressure on electronic and local structures. The obtained spectra were analyzed with the REX-2000 program.

3 Results and Discussion

X-ray diffraction techniques demonstrated that all the prepared $Ce(PO_4)_{1-x}(VO_4)_x$ had a single phase of the monazite structure (S. G.: $P2_1/n$) and the structure was kept even after the heat-treatment in Ar. Based on a change in the lattice constants, it could be considered that the VO_4^{3-} replaced PO_4^{3-} successfully. It was also clarified that the conductivity became higher as the VO_4^{3-} content, *x*, increased, regardless of the measurement condition.

As for all the samples, XAFS measurements were carried out in order to clarify effects of the partial replacement of VO_4^{3-} for PO_4^{3-} on the electronic and local structures. Fig. 1 shows XANES spectra of Ce L_{III}-edge for the $Ce(PO_4)_{1-x}(VO_4)_x$ in air. As shown in this figure, it was demonstrated that the substitution of the orthovanadate affected the electronic state of Ce. In addition, the similar tendency was also observed in the case of the samples after heating in the Ar condition. According to previous works [1], it is supposed that such a change of the electronic state of Ce is one of the reasons why the VO_4^{3-} replacement improved the conductivity.

Fig. 2 shows Fourier transformations of k^3-weighted EXAFS spectra of Ce *K*-edges. This result implied that a local distortion around Ce became higher with increasing VO_4^{3-} content, maybe due to a large difference in the ionic radii between P and V.

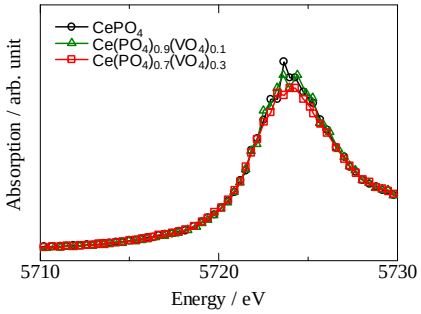

Fig. 1: XANES spectra of Ce L_{III}-edge of the $Ce(PO_4)_{1-x}(VO_4)_x$ in air.

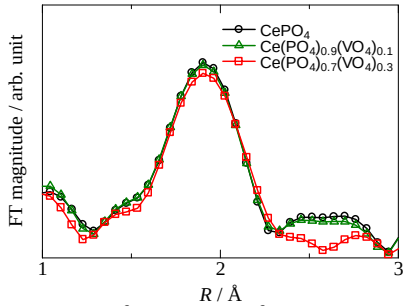

Fig. 2: Fourier transformations of EXAFS spectra of Ce *K*-edge of the prepared samples.

References

[1] N. Kitamura, et al., *J. Electrochem. Soc.*, **152** (2005) A658.

[2] N. Kitamura, et al., *J. Mater. Sci.*, **47** (2012) 6220.

* idemoto@rs.noda.tus.ac.jp

27B/2010G-679

Coordination Structure of Er-PTA complex in Ethanol Solution

Tsuyoshi Yaita[1,*] Toru Kobayashi[1], Yuji Miyazaki[1]
[1]JAEA, QuBS, SPring-8, 1-1-1 Kouto, Sayo-cho, Sayo-gun, Hyogo 678-5148, Japan

1 Introduction

Soft donor ligands are promising for separation of the minor actinides (MA), i.e., Am, Cm, from trivalent lanthanides in high level radioactive wastes (HLW)[1]. Since lanthanides in HLW, which are included 30 times as MA, show large neutron cross section, this separation process would be very important for improvement of transmutation efficiency toward MA. On these background, we developed a new type of soft donor ligand, *N*-methyl-*N*-phenyl-1,10-phenanthroline-2-carboxamide (PTA) which coordinates to a trivalent lanthanide or actinide ion with two nitrogens and one oxygen, and showed the sufficient separation factor between Am and Eu from the acidic media less than pH 2 on biphasic extraction system. [2] In this study, coordination structure of PTA with lanthanide, in particular Er in this study, was studied as preliminary investigation of coordination structure of MA for elucidation of discrimination mechanism between lanthanide and actinides.

2 Experiment

Structural determinations were carried out by x-ray crystallography for solid state and synchrotron radiation based EXAFS for solution state, respectively. EXAFS spectrum was measured at BL27B in transmission mode. The sample for EXAFS was prepared by dissolution of 1:4 ratio mixture in metal to ligand ratio into methanol. EXAFS analysis was done by WinXAS ver.3.2 [3] software and FEFF8 [4].

3 Results and Discussion

The crystal structure of $[Er(NO_3)_2(PTA)_2]$ complex, isolated from the unit cell, in Fig. 1 shows that two PTA and nitrates coordinates directly to Er. Especially, oxygen of PTA ligates more strongly than the other donor atoms due to evaluation from bond distances. The radial structural function based on the Fourier transformed EXAFS oscillation in Fig.2 dominantly consists of three peaks, and the first peak would probably include the three interactions with oxygen from carbonyl group of PTA, oxygen from nitrate ion, and nitrogen from PTA of phenanthroline (phen) moiety. Although EXAFS fitting for first shell should be carried out one or two shell model based on averaging, FEFF simulation spectrum estimated from the crystal coordinate really agreed with real spectrum, demonstrating that the coordination structure shows quite similar to the crystal. The bond distances by EXAFS fitting done by 3 shell model are 2.31(1) Å for carbonyl oxygen of PTA, 2.46(5) Å for nitrogen from phen moiety, 2.58(3) Å for oxygen of nitrate ion. Accordingly, PTA works as efficient ligand toward trivalent lanthanides and actinides with the same size of erbium.

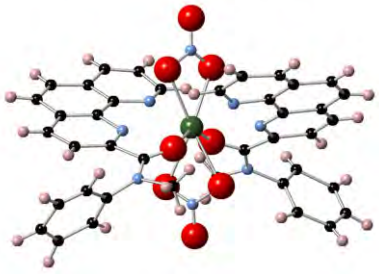

Fig. 1: The single crystal structure of $[Er(NO_3)_2(PTA)_2]$ complex. *The symbols denote Green: erbium, Red: oxygen, Blue: nitrogen, Black: carbon, Pink: hydrogen. Space group: Cc, Crystal system: monoclinic, a=19.200(3), b=17.841(3), c=13.091(2), α=114.5650(14), β= γ=90.0000, Z=4.

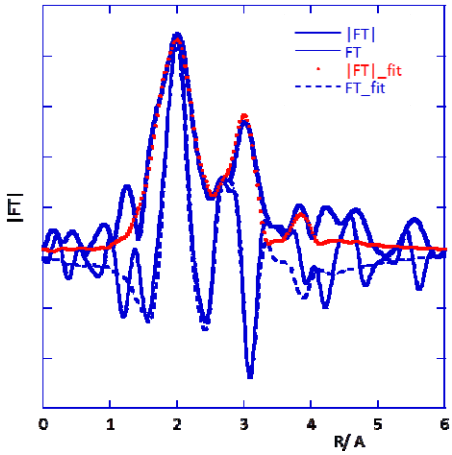

Fig. 2: The radial structural functions based on the Fourier transformed Er-L_{III} EXAFS oscillation of Er-PTA complex in ethanol. *This function consists of three dominant peaks arising from 1) O&N of PTA and O of nitrate ion, 2) C around donor atoms of PTA, 3) multiple scattering contribution of Er-N-O of nitrate ion. The phase shifts was not corrected.

Acknowledgement

We thank the Drs. Kobayashi and Usami and the other PF staff for the useful help.

References

[1] Z. Kolarik, *Chem. Rev.*, 108, 4208 (2008).
[2]T. Kobayashi et al, *SST*, 45, 2431 (2010).
[3]T. Ressler, J. Syn. Rad., 5, 118 (1998).
[4] A. L. Ankudinov et al., Phys. Rev. B, 58, 7565 (1998).

* yaita@spring8.or.jp

8B/2010G701

Structural analysis of 2,7-diphenyl[1]benzothieno[3,2-*b*][1]benzothiophene

宮碕栄吾 [1], 品村祥司 [1], 尾坂格 [1], 中尾朗子 [2], 山岸正和 [3], 竹谷純 [3], 瀧宮和男 [1*]
[1] 広島大学大学院工学研究院、〒739-8527 東広島市鏡山 1-4-1
[2] 放射光科学研究施設、〒305-0801 つくば市大穂 1-1
[3] 大阪大学産業科学研究所、〒567-0047 茨木市美穂ヶ丘 8-1

1 はじめに

ヘテロアレン化合物は有機半導体として近年活発に研究されており、有機電界効果トランジスタ (OFET) 等の有機薄膜デバイスの活性層として注目されている。我々は新規ヘテロアレン化合物として 2,7-diphenyl[1]benzothieno[3,2-*b*][1]benzothiophene (DPh-BTBT) および 2,7-diphenylnaphtho[2,3-*b*:6,7-*b*']dithiophene (DPh-NDT) を開発し、これら二種の化合物が OFET において 1 $cm^2 V^{-1} s^{-1}$ 以上の高移動度を示す材料であることを明らかにした (図 1) [1,2]。

DPh-BTBT, DPh-NDT の基本骨格である BTBT および NDT は、ベンゼン環とチオフェン環の縮合様式の異なる構造異性体の関係にあり、構造と半導体特性の相関関係に興味が持たれる。DPh-NDT はヘリングボーン様式の結晶構造を取ることを明らかにしたが、DPh-BTBT は微結晶しか得られず結晶構造は未解明であった。今回放射光を利用することにより DPh-BTBT の単結晶構造解析に成功した。

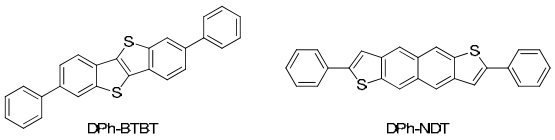

図 1 : DPh-BTBT および DPh-NDT の化学構造

2 実験

試料の調製

DPh-BTBT は我々が報告している方法に従って合成した[1]。DPh-BTBT の単結晶は窒素雰囲気下、温度勾配昇華結晶化法により作製し、単結晶X線構造解析に用いた。

単結晶X線構造解析

測定にはリガク社製 DSC イメージングプレートシステムを用い、シリコンで単色化した放射光 (λ = 1.000 Å) を使用した。測定は 200 K で行った。初期構造は SHELXL-97 を用いた直接法により解析した [3]。水素原子を除く全ての原子に異方性温度因子を適用し、Texsan を用いて構造精密化を行った[4]。また、水素原子は計算により理想的な位置に配置した。

DPh-BTBTの結晶学的データ: $C_{26}H_{16}S_2$ (392.53), colorless plate, 0.10 x 0.10 x 0.01 mm^3, monoclinic, space group, $P2_1/c$ (#14), a = 6.334(2), b = 7.462(5), c = 19.516(2) Å, β = 93.06(3)º, V = 921.1(7) $Å^3$, Z = 2, R = 0.0843 for 1284 observed reflections ($I > 2\sigma(I)$) and 152 variable parameters, wR_2 = 0.2377 for all data.

3 結果および考察

単結晶X線構造解析により得られた DPh-BTBT の分子構造を図 2 に示す。フェニル基と BTBT 骨格との２面角は約 26 º であり DPh-NDT における２面角 (~0 º) より大きくなっていた。これは DPh-BTBT では縮環ベンゼンにフェニル基が結合しているため、*o* 位の水素原子との立体反発が生じたためと考えられる。DPh-BTBT の結晶構造は、DPh-NDT と同様のヘリングボーン様式であった (図 2)。

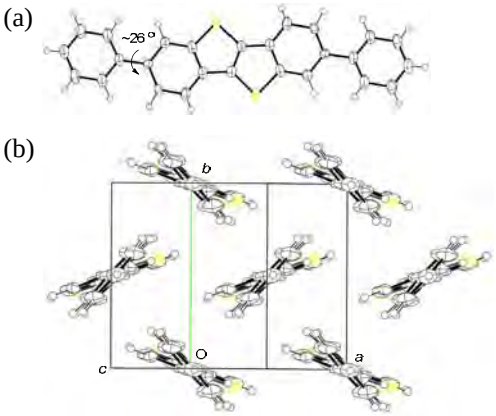

図 2: DPh-BTBT の分子構造 (a) ならびに結晶構造 (b)

OFET における高移動度と結晶構造の相関を明らかにするために、得られた結晶構造を基にして分子間の移動積分を計算した [2]。その結果、DPh-BTBT では DPh-NDT と同様に二次元性の強い分子間移動積分となっていることが分かった。本成果は、高性能 OFET 材料にはヘリングボーン様式の構造を持つだけでなく、高次のキャリア移動が可能な分子配向を取ることが重要である事を示唆する結果である。

参考文献

[1] K. Takimiya, et al, J. Am. Chem. Soc. **128**, 12604 (2006).
[2] S. Shinamura, et al, J. Am. Chem. Soc. **133**, 5035 (2011).
[3] Sheldrick, G. M. SHELXL (SHELX97). Programs for the refinement of crystal structures. University of Goettingen: Germany, 1997.
[4] teXsan: Single Crystal Structure Analysis Software, Version 1.19; Molecular Structure Corporation and Rigaku Corporation: 2000.

* ktakimi@hiroshima-u.ac.jp

先端研究施設共用促進事業
フォトンファクトリーにおける産業利用促進
利用報告書

課 題 番 号： **2010I001**
研究責任者： 小林 隆嗣 (江崎グリコ株式会社)
利 用 施 設： 高エネルギー加速器研究機構　放射光科学研究施設　BL-9A, 11A
利 用 期 間： 2010 年 4 月～2011 年 3 月

XAFS 解析を用いた水溶性カルシウム素材 POs-Ca の初期う蝕の再石灰化・再結晶化メカニズムの解明とう蝕予防効果の改善

Elucidation of the mechanisms of remineralization and recrystallization of early caries lesion with a water-soluble calcium, POs-Ca by XAFS analysis for improving caries prevention effect

小林 隆嗣 [1]、田中 智子 [1]、滝井 寛 [1]、釜阪 寛 [1]
Takatsugu Kobayashi[1], Tomoko Tanaka[1], Hiroshi Takii[1], Hiroshi Kamasaka [1]

[1] 江崎グリコ株式会社
[1]Ezaki Glico Co., Ltd.

アブストラクト：　POs-Ca は水溶性の高いカルシウム素材である。POs-Ca とフッ化物は初期う蝕の再石灰化を促進することでう蝕予防に寄与する。まずわれわれは POs-Ca 水溶液の Ca-K XAFS を測定し、POs のリン酸基とカルシウムイオンが会合していることを見出した。POs とカルシウムの間の大まかな会合の比率を水和したカルシウムイオンとリン酸と会合したカルシウムイオンの XANES の線形フィッティングより見積もった。次に POs-Ca+フッ化物により再石灰化したエナメル質の表面領域の F-K XANES を測定し、フッ化物がエナメル質表面に CaF_2 として堆積すること、さらに 10–20 μm の深さで歯エナメル質に取り込まれ、ハイドロキシアパタイトがフッ化アパタイトとなっていることが示された。

POs-Ca is a highly soluble calcium material. POs-Ca and fluorides contribute to caries prevention by enhancing the remineralization of early caries lesions. First, we measured Ca-K XAFS of POs-Ca solutions, and found the association of the phosphate group in POs and a calcium ion. A rough association ratio between POs and Ca was estimated by the linear combination fitting between the XANES from hydrated calcium ions and phosphate-bound calcium ion. Next, F-K XANES of the surface area of enamel remineralized with POs-Ca+fluoride was measured, and showed that fluorides were deposited as CaF_2 on the surface of enamel, and then incorporated into tooth enamel and converted hydorxyapatite to fluorapatite at the depth of 10–20 μm.

キーワード：　エナメル質 再石灰化 フッ素 カルシウム XAFS

１．はじめに：

う蝕 (いわゆるむし歯) は歯周病と並んで大きな歯の喪失要因であるにもかかわらず、未だに多くの人々が患っている疾病である。う蝕予防のためには、穴の開く前の初期むし歯 (初期う蝕) という可逆的に回復しうる段階で進行を抑え、対処することが望ましい。初期う蝕は歯エナメル質の表面は残ったまま、表層下からエナメル質を構成するハイドロキシアパタイト (HAp, $Ca_{10}(PO_4)_6(OH)_2$) がう蝕原性細菌の産生する酸により溶出 (脱灰) して生じる。表層が残っていれば初期むし歯の脱灰部分は唾液からのカルシウムとリン酸の供給により回復 (再石灰化) する。

江崎グリコでは、水溶性のカルシウムを唾液に補う素材としてリン酸化オリゴ糖カルシウム (phosphoryl oligosaccharides of calcium, POs-Ca) を開発し[1]、POs-Ca の再石灰化促進効果と HAp の結晶構造回復 (再結晶化) 促進効果を X 線透過法および X 線回折法により示した[2–4]。そして、現在 POs-Ca を配合したガムを特定保健用食品として販売している。

さらに POs-Ca 配合ガムの有効性を高めるた

めに、歯科で広く再石灰化促進があると認められているフッ化物を加えたときの効果を調べている。フッ化物からのフッ素はエナメル質中のハイドロキシアパタイトの水酸基と置換してフルオロアパタイト (FAp, $Ca_{10}(PO_4)_6F_2$) に変え、化学的安定性が高める。しかし、一般にフッ化物とカルシウムの共存は、速やかに水に不要なフッ化カルシウム (CaF2) の形成を引き起こすため、互いの再石灰化促進効果を打ち消しあってしまう。POs-Ca のカルシウムと低濃度のフッ化物イオンは共存することができ、効率よく歯の再石灰化を促進することがわかっている。

しかし、実際にフッ素がエナメル質の HAp に取り込まれているかどうかは分かっていなかった。特に、低濃度のフッ化物により歯のエナメル質がどのような化合物を経てフッ素置換されるかは、国内外を含めて知見が得られていなかった。

本研究では、POs-Ca とその再石灰化作用に関連し、以下の 2 つを目的として研究を行った。
① POs-Ca の溶液中におけるカルシウム安定化の基盤を溶液の Ca-K XAFS の解析により解明し、POs-Ca のカルシウム素材の利用性を明らかにすることで、新しい産業価値の創出につなげる。
② POs-Ca+フッ化物処理でフッ素がどのような化学形態で、どの程度浸透しているかをCa-K XAFSおよびF-K XANES解析により明らかにする。そしてカルシウム素材とフッ化物を併用することで、フッ化物のもつ耐酸性などの特性を歯に付加できるか検証する。

２．実験：

【POs-Ca溶液の測定】

実際の使用を想定した1% POs-Ca溶液 (Ca換算で13 mM) をpH 3.0–8.0に調整した。対照として、単純に水和したカルシウムイオン、リン酸が会合したカルシウムイオンを含む溶液を得るため、0.1 M 塩化カルシウム溶液、カルシウム:リン酸 = 1:5から1:20までの塩化カルシウム (1.5 mM) –リン酸二水素カリウム溶液を調製した。後者の溶液は水酸化カリウムでpH 7.0に調整した。Ca-K XAFSは以上の溶液を厚さ5 mmのカプトン窓を持つセルに満たしたものをサンプルとしてBL-9Aで 19素子SSD による蛍光法で EXAFS領域まで (3133–5138 eV) 測定した。

【再石灰化エナメルの測定】

人工的に酸により脱灰状態を作り出した歯を人工唾液 (1.5 mMカルシウムと3.6 mMリン酸を含む中性溶液) にPOs-CaもしくはPOs-Ca + 低濃度フッ化物を添加した溶液に浸して再石灰化処理した。処理後のエナメル質から表層100 µm を切り出してBL-9Aにおいて透過法によりCa-K XAFSを測定した。また、表層から10 µmずつ研磨紙を替えながら粉末化し、それぞれの研磨紙上の粉をカーボンテープに固定してサンプルとし、真空下 (< 10^{-6} Torr) でSDDを用いた蛍光法によりF-K XANESを測定した。

３．結果および考察：

【POs-Ca 溶液の測定】

pH を pH 3.0 から 8.0 まで 1 刻みで変化させて POs-Ca 溶液を調製し、Ca-K XAFS を測定した結果、図 1A に示すように pH によらず同一の XANES が得られた。塩化カルシウム溶液およびリン酸水素カリウムを加えた溶液 (Ca+P 溶液) の Ca-K XANES では塩化カルシウム溶液と比較して 4053.7 eV の位置に新しいピークが現れる。POs-Ca でも同一のエネルギーでピークが得られている (図 1A)。また、EXAFS より得られる同系分布関数では、カルシウムとリン酸のリンとの結合距離に近い位置にピークが現れる (図

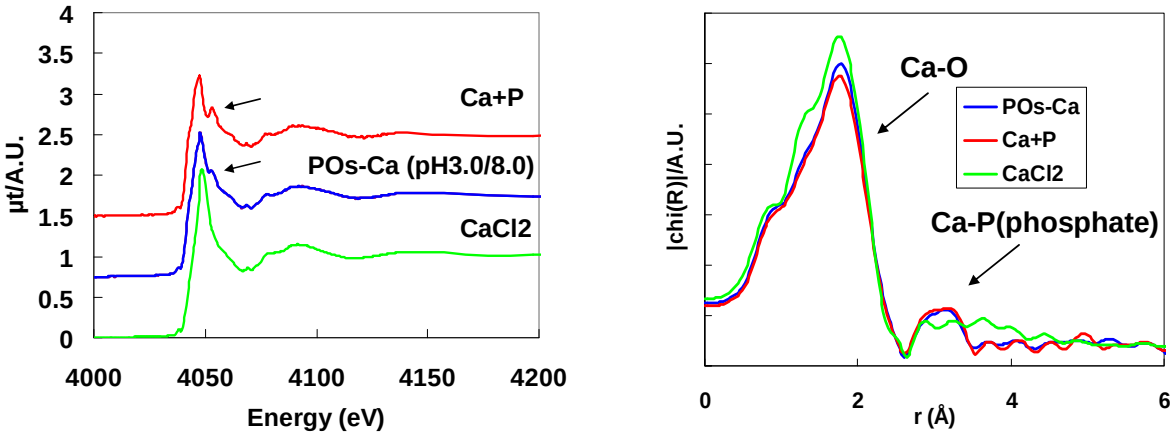

図 1 溶液の Ca-K XAFS 比較。(A) XANES 領域の比較。リン酸と相互作用した矢印で示すピークがリン酸と会合したカルシウム由来のピークと考えられる。 (B) XAFS から導き出される動径分布関数のプロット。
Ca+P:リン酸二水素カリウムを添加した塩化カルシウム水溶液 (Ca/PO_4 = 0.4)

1B)。以上から、POs-Ca のリン酸基とカルシウムイオンが相互作用している様子が観察されたと考えられる。

POs-Ca の XANES は塩化カルシウム水溶液と Ca+P 溶液の XANES の中間にあたる形状であった。リン酸をカルシウムに対して 5 倍、10 倍、20 倍と過剰に供給したとき、Ca/PO_4 = 0.1 以下では XANES の変化がなくなることから、Ca/PO_4 = 20 では水溶性を保った状態でカルシウムに対してリン酸が十分に会合した状態とみなすこととした。そこで、塩化カルシウム水溶液および Ca/PO_4 = 20 の Ca+P 溶液の XANES について、POs-Ca 溶液の XANES に対して線形フィッティングを行い比較すると、図 2 のようにカルシウムに対するリン酸の会合割合を計算することができた。POs-Ca のリン酸化オリゴ糖部分はカルシウムと緩やかに会合していることが示された。

【再石灰化エナメルの測定】

POs-Ca もしくは POs-Ca とフッ素の併用により再石灰化した歯のエナメル質表層 100 μm の Ca-K XAFS を測定したが、HAp 由来のピークしか見出されなかった。再石灰化により析出すると考えられるカルシウム-リン酸化合物の標準物の XANES 比較でも HAp の XANES との間に微小な差異しか観察されないことから、HAp 以外の生成物の検出は困難と判断した。

次に、POs-Ca+低濃度フッ化物で再石灰化したエナメル質の F-K XANES を測定した結果、図 3 のような結果が得られた。未処理のエナメル質からはフッ素由来のピークは検出されなかった。一方、POs-Ca+フッ化物処理した歯では、表層から深さ 0–10 μm のサンプルからは CaF_2 が主成分で FAp が混合していると思われる XANES が得られた。一方、表層から深さ 10–20 μm の部分では、FAp と思われる XANES が得られた。それより深い層では、フッ素は XANES 検出限界以下であった。これらより、POs-Ca とフッ化物の併用による再石灰化では、表層にフッ化カルシウムが堆積しつつ、歯の表面付近のエナメル質にフッ化アパタイトとしてフッ素が取り込まれることが明らかとなった。

４．まとめ： 本研究では、当初予定していた歯の再石灰化に伴って蓄積するカルシウムの種類を区別することはできなかった。今後 F-K XAFS の測定で利用したサンプル調製法を利用することで、健全なハイドロキシアパタイトの混入を防ぐことができれば、歯の微小領域の組成を解析できる可能性はある。その他に、歯の微小 X-PEEM と組み合わせた XAFS 測定の例も報告されている[5]。

一方、POs-Ca の溶液中での状態の知見と、歯へのフッ素の浸透についての知見は得ることができた。POs-Ca のリン酸化オリゴ糖が溶液中で緩やかにカルシウムと会合し安定化することが実証されたことで、キレート剤よりも徐放性に優れたカルシウム安定化剤であることが実証できた。リン原子の側からの XAFS 解析により、さらなる詳細な解析ができると期待される。また、低濃度のフッ化物の利用により、フッ素のコーティング効果やフッ化アパタイトが形成されるかどうかはこれまで歯科領域でも未知であったが、本研究によりそれらの効果が実証された。今後、POs-Ca とフッ化物の併用により、歯の質を高める製品の開発・販売への利用が期待される。

参考文献

[1] Kamasaka H. et al. *Biosci. Biotechnol. Biochem.* **59**, 1412–1416 (1995).
[2] Yagi N. et al. *J. Synchrotron Rad.* **16**, 398–404 (2009).
[3] Tanaka T. et al. *Caries Res.* **44**, 253–259 (2010).
[4] 田中美由紀ら. 日本歯科保存学雑誌 **52**,

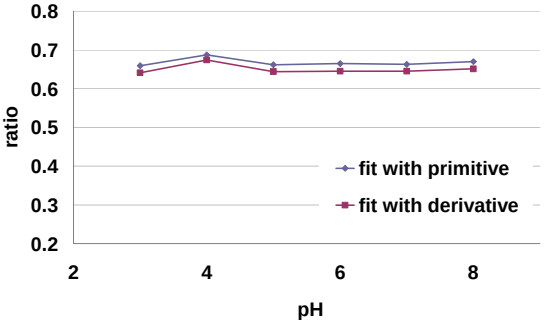

図 2 各 pH における POs-Ca の溶液中で会合しているカルシウムの割合 (XANES 領域の原始関数及びその微分についてフィッティングした結果を示す)

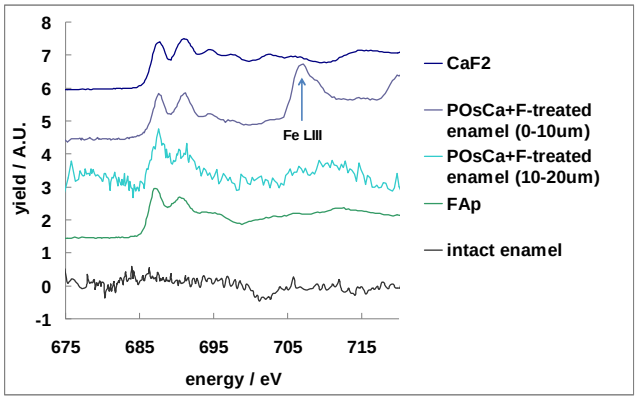

図 3 POs-Ca とフッ化物で処理をした歯の F-K XANES 一部のサンプルに、再石灰化成分として加えている物質の夾雑物由来と思われる鉄のピークが見えている。

534–542 (2009).
[5] Beriash E. et al. *J. Struct. Biol.* **166**, 133–143 (2009).

成果発表状況： 再石灰化エナメルの解析の成果について投稿準備中。

先端研究施設共用促進事業
フォトンファクトリーにおける産業利用促進
利用報告書

課 題 番 号： **2010I003**
研究責任者： 氏名 渡辺 伸、所属　株式会社トクヤマ　開発センター
利 用 施 設： 高エネルギー加速器研究機構　放射光科学研究施設　BL-9C, 12C, NW-10A
利 用 期 間： 2010 年 4 月～2011 年 3 月

アルカリ膜型燃料電池用触媒の解析
Analysis of catalysts for Alkaline Membrane Fuel Cell

渡辺　伸[1]、三嶋　祐[2]、根岸　貴幸[1]、織田　健吾[1]、和間　良太郎[1]、
大越　秀樹[1]、飯田　伸仁[2]、福田憲二[1]
Shin Watanabe[1], Yu Mishima[2], Takayuki Negishi[1], Kengo Oda[1], Ryotaro Wama, [1]
Hideki Okoshi[1], Nobuhito Iida[2], Kenji Fukuta[1]

[1]株式会社トクヤマ　開発センター、[2]株式会社トクヤマ　RC 研究所
[1]Tokuyama Corporation Research and Development Division, [2]Tokuyama Corporation RC Laboratories

アブストラクト：
燃料電池は再生可能な代替エネルギーとして近い将来の大変有望な技術である。現在、我々は、アルカリ膜型燃料電池の開発を進めている。この電池は、非 Pt 系金属を触媒として利用可能であるという特徴を有する。しかし、アルカリ膜型燃料電池用触媒として高活性を示す非 Pt 系触媒は見つかっておらず、また、研究例も非常に少ない。そこで、アルカリ膜型燃料電池用のナノ金属触媒の活性向上に関与する因子を探ることを目的とし、XAFS 測定を行った。

カソード用触媒として、Cu/ Fe の二元系触媒を検討した。Cu や Fe は、単独では触媒活性を示さないが、合金化することで活性を示すようになることを期待した。金属組成や量を変更したものを測定したが、Cu, Fe ともに合金は形成せず、単独で酸化物を形成していることが分かった。同時に、期待していた触媒活性は見られなかった。

また、アノード用触媒として、Pd/ Ni の二元系触媒を検討した。Pd は組成に関わらず、Pd metal として存在していた。一方、Ni は、合金もしくは NiO として存在していることが分かった。さらに、NiO が存在する系は合金を形成したものに比べ、触媒活性が高いことが明らかとなった。

英文アブストラクト
Fuel cell is very promising technology as the alternative energy. We are developing Alkali Membrane Fuel Cell (AMFC). It has the feature that non-Pt metal can be used as a catalyst. However, the catalytic activity of non-Pt metals is low. Furthermore, there are few studies of them for the application to AMFC. Therefore we tried to understand the factor which can control the activity with XAFS.

Cu/ Fe nano-particles were examined as the cathode catalyst. Each of Cu and Fe did not show catalytic activity, but we expected that they come to show activity by becoming as alloy. The result of XAFS measurement showed that they did not form alloy, and existed respectively as each oxide. At the same time, they did not show enough activity for the practical use.

Pd/ Ni nano-particles were examined as the anode catalyst. In this case, Pd existed as Pd metal regardless of the composition of the catalyst. On the other hand, Ni formed an alloy with Pd, or NiO. Furthermore, the catalysts with NiO showed higher activity.

キーワード：　アルカリ膜型燃料電池、非 Pt 系触媒、アルコール酸化、触媒活性、合金化

１．はじめに：

燃料電池はリン酸形や固体酸化物形など、各種の方式が検討されている。その中でも、固体高分子形燃料電池は、比較的低温で作動可能であるため、携帯機器用、家庭用定置型、自動車用などの電源として活発に研究開発が進められている。従来一般に検討されてきた、プロトン交換膜形燃料電池では、触媒電極層が酸性雰囲気となるため使用可能な触媒が Pt などの貴金属に限られるという問題がある。貴金属は高価である上に埋蔵量も限られているため、燃料電池を世界的に普及させることは不可能である。一方、水酸化物イオン（OH^-）が伝導するアルカリ膜形燃料電池では、安価な非貴金属触媒を用いることができるため、製造コストの削減と市場の拡大が期待できる。しかしながら、未だに Pt 触媒に優る非貴金属触媒の開発には至っていない。アルカリ膜形燃料電池の実用化に向けて、より高活性な非貴金属触媒の開発が切望されているのが現状である。

我々は、Pt と同等以上の高活性な非貴金属触媒を開発することを目標とし、アルカリ膜形燃料電池用の電極触媒の開発を進めている。中でも、非貴金属を中心とした多元系金属（または合金系）ナノ触媒に注目し、導電性のあるカーボンを担体とした担持触媒について検討を行っている。

その中で、触媒活性は金属の電子状態に深く関わっているため、製造条件の最適化には電子状態を正しく理解することが不可欠である。そこで、評価手法の一つとして XAFS 測定を取り入れ、XAFS による解析結果と、触媒活性や製造条件の違いなどを関連付けることで新規の高活性電極触媒の開発を行なう。

２．実験：

燃料電池の作動には、カソード用触媒及びアノード用触媒がそれぞれ必要である。そのため、カソード用触媒として、Cu/ Feの二元系触媒を選択した。ナノ金属粒子がカーボン担体に担持された以下の試料をスパッタ法により作製した。値は全て合成後の測定値である。

試料	Fe/wt%	Cu/wt%
No.1	0.29	-
No.2	0.68	-
No.3	1.09	-
No.4	-	0.92
No.5	-	1.75
No.6	-	3.57
No.7	0.31	0.73
No.8	0.60	1.54
No.9	1.32	3.20
No.10	0.95	1.15
No.11	1.47	0.88

アノード用触媒としてPd/ Niの二元系触媒を選択した。1-1~1-3は蒸発乾固法、2-1~2-3は液相還元法にて合成した。

試料	Pd /wt%	Ni /wt%
1-1	19.5	21.4
1-2	25.0	15.1
1-3	28.6	8.5
2-1	11.1	14.4
2-2	14.6	6.4
2-3	14.5	3.4

触媒金属は、粒径数十nmのカーボン担体に担持した。合成した試料は、SAMPLEM4Mによって試料量を計算したところ、ほとんどの試料が、透過測定が可能であった。そこで、30分程度メノウ乳鉢を用いて均一化させた後、内径7mmΦ×10mmtのAl製リングに入れ、SUS製の棒で押し固めたものを測定試料とした。

XAFS測定は透過法によって、全てK端に対して行った。測定後、スペクトルの解析には

ATHENA, ARTEMISを用いた。

３．結果および考察：

Fig.1 にカソード用触媒である Cu/Fe 系触媒中の Cu の測定結果を示す。まず、共存元素である Fe の量や存在比に関わらず、XANES スペクトルは全てほぼ一致した。フーリエ関数では、No.5, 6 は、他の試料に比べ高強度となっており、Fe が存在すると、配位数が増加することが示唆された。Fig.1 より、Cu は、CuO として存在していることが分かった。

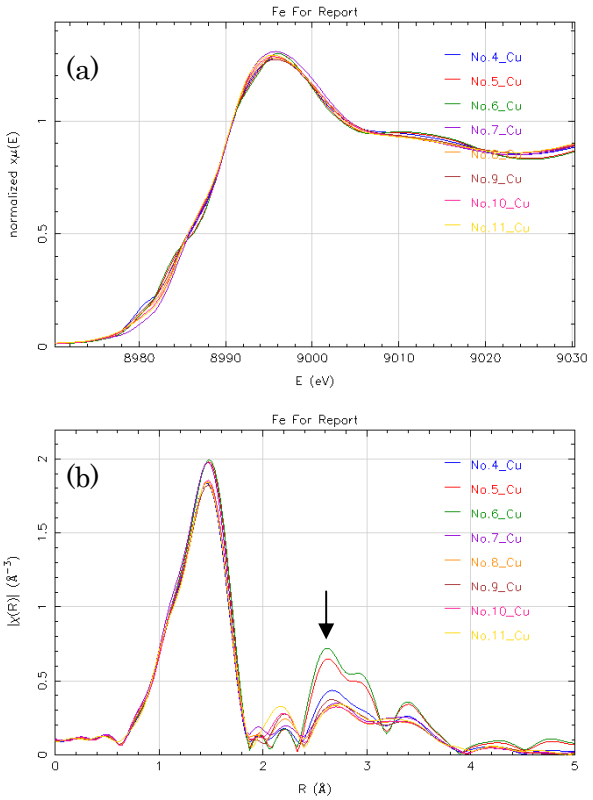

Fig.1 Cu/Fe 系触媒中の Cu の測定結果

(a) XANES スペクトル (b) フーリエ関数

Fig.2 に示す Fe の測定結果においては、Cu の共存による大きな変化は見られず、Fe_2O_3 として存在していることが分かった。従って、Cu, Fe 共に、空気中での自然酸化によって、酸化物として存在していることが明らかとなった。

詳細にフーリエ関数を観察すると、矢印で示すピークに若干のシフトが見られ、このシフトの方向は、組成に従っている。つまり、Fig.1 では、Fe が増えるほど長距離側へ、Fig.2 では Cu が増えるほど短距離側へのシフトが見られた。このシフトが Cu と Fe の間での相互作用を示しているかどうかは不明であるが、真空中での合成直後には、合金形成を起こしており、それが空気酸化及び粗大化を起こすことで、酸化物として分離した過程も考えられる。合成後、大気開放せずに保管した試料にて確認が必要であると思われる。

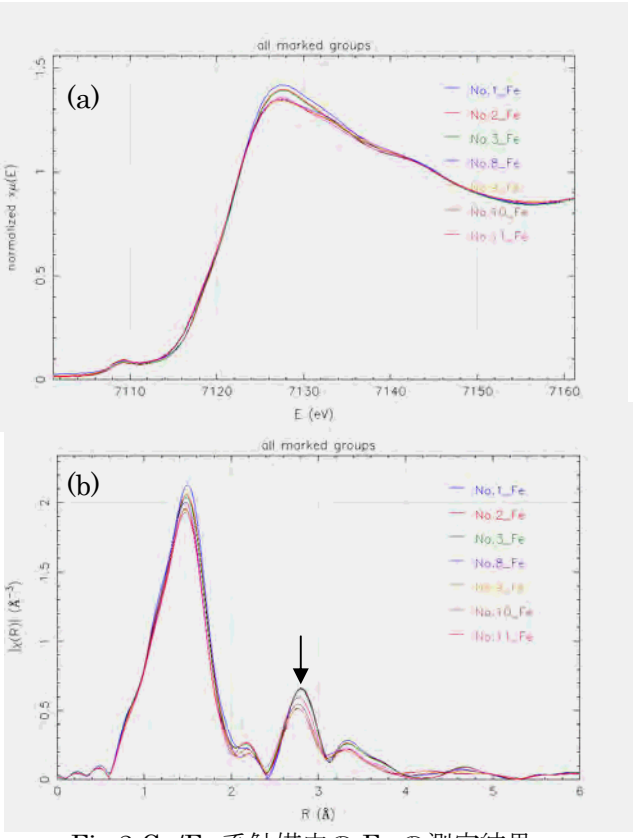

Fig.2 Cu/Fe 系触媒中の Fe の測定結果

(a)XANES スペクトル (b)フーリエ関数

また、本測定で対象としたカソード用触媒では、還元活性はほとんど示さず、量や組成による差は確認されなかった。これは、たとえピークシフトが合金形成を示唆したとしても、大部分が単独の酸化物として存在したためと考えられる。

ここで、本来であれば、カソード用触媒の開発を続けるところであるが、高活性な非貴金属系カソード用触媒の市販が始まり入手可能となったため、その開発の優先度は低くなった。そこで我々は方針の変更を行い、より優先度が高まったアノード用触媒の開発に着手した。

次に、アノード用触媒の測定結果について述べる。まず、Fig.3 に Pd/Ni 系触媒の触媒活性評価の結果を示す。本研究では、蒸発乾固法と液相還元法の、２通りの合成方法によって触媒を合成したが、その手法によって、触媒活性に大きな違いが見られた。低電圧・高電流であることが高活性である指標となるた

め、液相還元法で作成したものの方が、高活性であると言える。また、この活性の大きさは、単独の Pd を超えるほどのものである。前述の通り、蒸発乾固法は、焼成過程を含むため、液相還元に比べ、粗大化を起こしやすい。そのため、平均粒径によって電流量の規格化を行ったが、相対的な関係は変化しなかった。

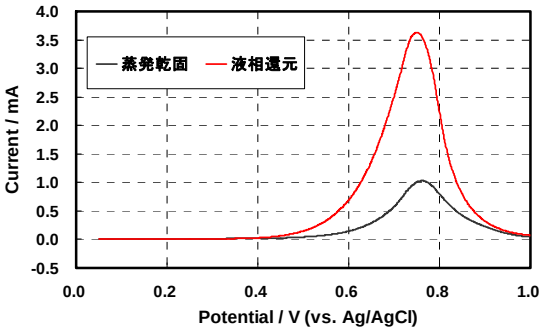

Fig.3 Pd/Ni 系触媒の触媒活性評価の結果

次に、合成方法による活性の違いが、合金形成の有無にあると考え、XRD 測定を行った。Fig.4 に回折パターンを示す。

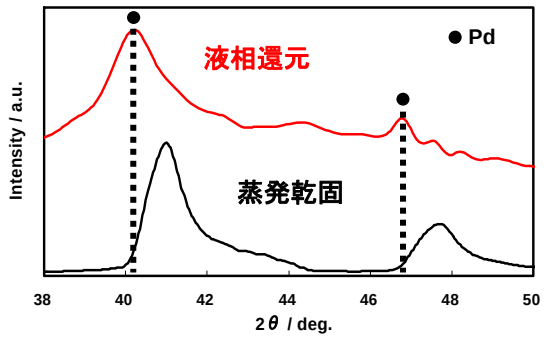

Fig.4 Pd/Ni 系触媒の XRD パターン

液相還元法で合成した Pd/Ni では、Pd のピークのみが検出され、Ni のピークは得られなかった。また、蒸発乾固法で合成した Pd/Ni では、Pd, Ni いずれのピーク位置からもずれた位置で回折ピークが検出され、合金化を示唆する結果が得られた。

以上の結果から、蒸発乾固法にて合成すると、Pd と Ni は合金化し、触媒活性が低いこと、また液相還元法で合成すると Pd が存在することが確認され、単独の Pd よりも触媒活性が高いことが分かった。しかし、触媒活性の向上の理由については、XRD 測定からは明らかにならず、Ni の存在状態に鍵があると予想された。そこで、液相還元法で合成した Pd/Ni 中の Ni の状態を明らかにするために、XAFS 測定を行った。

Fig.5 に、Pd 及び Ni の XANES スペクトルを示す。

Pd の XANES スペクトルでは、合成法や組成に関わらず、全て Pd foil とよい一致が見られた。一方、Ni の XANES スペクトルにおいて、蒸発乾固法は Ni foil とほぼ一致したが、液相還元法では、NiO に近いことが分かった。液相還元法では、Pd, Ni ともに還元剤によって瞬時に還元されるため、それぞれが独立で粒子となり、Ni は空気酸化によって NiO となったと考えられる。

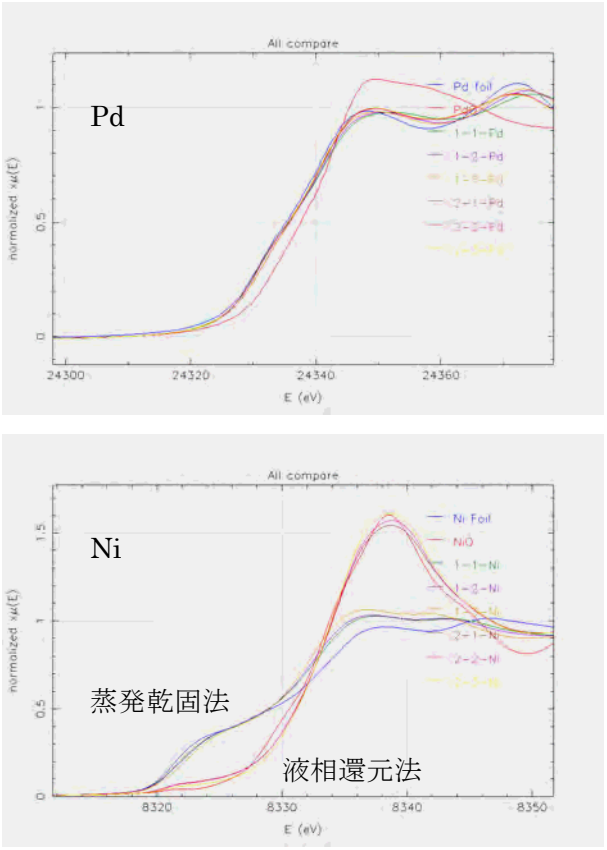

Fig.5 Pd/Ni 系触媒の XANES スペクトル

次に、Fig.6 に Pd/Ni 系触媒のフーリエ関数を示す。まず、蒸発乾固法で調整した触媒(Sample 1-1~1-3)から考えると、Pd, Ni 共に、組成によりピーク位置に大きな変化が見られる。この挙動は、Pd と Ni の合金形成を示唆していると考えられる。Pd-Pd と Pd-Ni の 2 シェルを用い、Pd のデバイワーラー因子（σ^2）は Pd 箔の測定結果をフィッティングした結果得られた値（0.0062）に固定してフィッティングを行った。配位数（N）は Pd 箔の測定値を 12 として算出した S_0^2 パラメータを用いて決定した。結果は、末頁の Table.1 に示した。また、Ni についても Ni-Pd と Ni-Ni の 2 シェルを用い、Ni のデバイワーラー因子（σ^2）は Ni 箔の測定結果をフィッティングした結果得られた値（0.0062）に固定してフィッティングを行った。配位数（N）は Ni 箔の測定値を 12

として算出した S_0^2 パラメータを用いて決定した。結果は、Table.2 にまとめた。Table.1,2 では、Ni-Pd 結合距離はどちらの元素から見ても、ほぼ同じ値を示し、それらは Pd metal と Ni metal の中間の値を示したことから、これらの試料は Pd-Ni の合金となっていると考えられる。また、配位数の Pd/Ni 比は、Pd と Ni の存在比に近いことも、ランダム合金相の存在を示唆している。

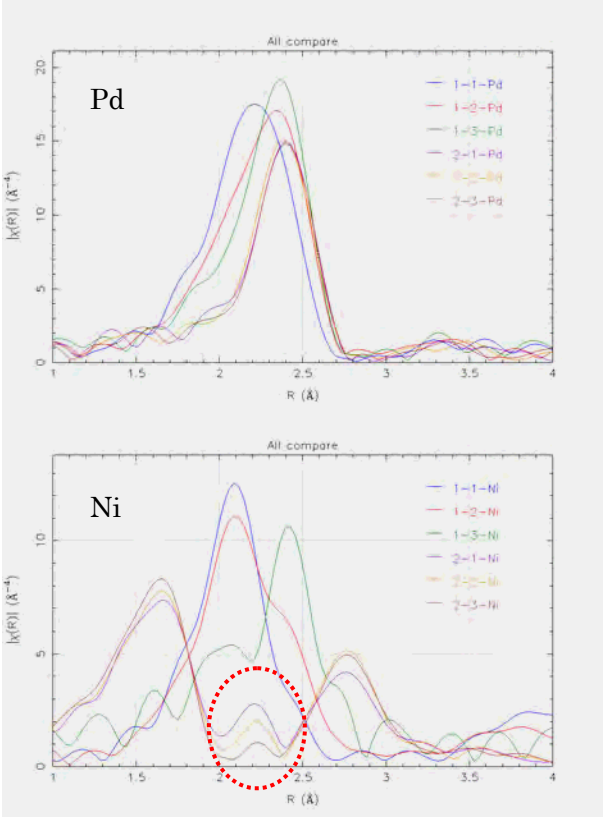

Fig.6 Pd/Ni 系触媒のフーリエ関数

次に、Fig.6 において、液相還元法(Sample 2-1~2-3)で合成した Pd では、組成によるピーク位置の変化は見られなかった。Pd metal の第一近接の 1 シェルを用いフィッティングを行った結果を Table.3 に示す。フィッティング結果は十分に収束しており、Pd/Ni の組成にかかわらず、Pd はほぼ同じ構造であることから、Pd 単独の粒子になっていると考えられる。また、配位数が 7 程度と小さいのは触媒の粒径が小さいためと考えられる。fcc の場合、約 1 nm の粒径で平均的な配位数は 7 程度となる。一方、Ni では、液相還元法では、1.6Å付近と、2.7Å付近にピークが見られており、これは NiO の存在を示唆していると考えられる。そこで、酸化ニッケル（NiO）の第一近接（Ni-O）と第二近接（Ni-Ni）の 2 シェルでフィッティングを行った。各々のシェルを単独に q 空間でフィッティングし、それで得られた r の値を固定して 2 シェルでの R 空間でのフィッティングを行った。配位数（N）は NiO の第一近接（Ni-O）の測定値を 6、第二近接（Ni-Ni）の測定値を 12 として算出した S_0^2 パラメータを用いて決定した。結果を Table.4 に示す。フィッティング結果より、Ni は酸化物になっていると考えられる。第一近接の Ni-O は酸化ニッケルとほぼ同じ結合距離と配位数を持っているが、第二近接の Ni-Ni は結合距離が長く配位数も少ないため、第二近接以遠の構造には乱れが生じていると考えられる。また Ni 組成が少なくなるにつれて R-factor は小さくなり、フィッティングの収束が良くなっているが、これは試料 2-1 と 2-2 で第一近接と第二近接の間の 2.2 Åあたりにある小さなピーク（赤点線内）が 2 シェルではうまく再現されないためと考える。そこで、第一近接ピークと第二近接ピークの間に小さなピークは Ni メタルの第一近接の距離（2.48 Å）に近く、Ni 組成比が増えるに従って大きくなっているように見えるため、Ni メタルの第一近接も含めた 3 シェルでフィッティングを試みた。Ni メタル成分の配位数（N）は Ni 箔の測定値を 12 として算出した S_0^2 パラメータを用いて決定した。結果を Table.5 に示す。2 シェルフィッティングよりも R-factor が小さくなり、フィッティングの収束は良くなった。これより、試料中に Ni Metal が存在する可能性はあるが、EXAFS の結果だけからは、その存在状態（単独粒子で存在するか、酸化物粒子中に混在しているか等）を断言することはできない。結果、Ni は酸化物ではあるものの、Ni-Ni の距離が NiO のそれ（2.96 Å）よりも長く配位数が少ないことより、NiO の結晶構造（NaCl 型）からは乱れが生じた酸化物と考えられる。また、Ni の仕込み比が増えると構造の乱れが大きくなる。

4．まとめ：

本検討では、カソード用触媒として Cu/Fe 系触媒、アノード用触媒として Pd/Ni 系触媒の XAFS 測定を行った。カソード用触媒では、組成や含有量による構造の差や触媒活性の差がほとんど見られなかったため、本検討の結果から、開発にフィードバックすることはできなかった。一方、アノード用触媒では、合成方法によって状態の差があり、以下の知見が得られた。(1)蒸発乾固法の試料では Pd-Ni の合金となっていると考えられる。また、Pd/Ni の配位数比は試料作製時の Pd と Ni の仕込み比に近いため、ランダム合金相の存在を

示唆している。（２）液相還元法の試料は、Pd は単独のメタル粒子として、Ni は酸化物として存在していると考えられる。Pd/Ni の仕込み比にかかわらず、Pd はメタル粒子のままで構造や粒径に変化はない。しかし Ni は構造の乱れた酸化物と推定され、Ni の仕込み比が増えると構造の乱れが大きくなった。

これらの知見は、我々の行った他の分析方法では得られなかったものであり、今回の測定によりＸＡＦＳ測定の有用性を確認することができた。

今後、上記 Ni 酸化物が、どのような機構で触媒活性を向上させたかを明らかにすれば、貴金属触媒の使用量の低減、さらには非貴金属触媒の開発に有用だと考えられる。

謝辞

カソード用ナノ金属触媒のバレルスパッタ法による調製は富山大学教授　阿部孝之先生に御指導をいただきました。ここに深謝の意を表します。

Table.1 蒸発乾固法 PdK 端のフィッティングより得られた構造パラメータ

Sample	Pd/Ni	配位数比	N_{Pd-Ni}	N_{Pd-Pd}	r_{Pd-Ni}(Å)	r_{Pd-Pd}(Å)	σ^2_{Pd-Ni}(Å^2)	σ^2_{Pd-Pd}(Å^2)	E_0 (eV)	R-factor
1-1	34/66	41/59	5.5±0.6	3.9±0.4	2.57±0.006	2.68±0.003	0.0074±0.0008	0.0062	-3.3±1.0	0.0012
1-2	48/52	56/44	4.7±2.2	5.9±0.8	2.60±0.015	2.70±0.005	0.0103±0.0045	0.0062	-2.4±1.9	0.0083
1-3	65/35	67/33	3.5±2.1	7.0±0.5	2.63±0.017	2.71±0.004	0.0110±0.0058	0.0062	-2.3±1.2	0.0062

Table.2 蒸発乾固法 NiK 端のフィッティングより得られた構造パラメータ

Sample	Pd/Ni	配位数比	N_{Ni-Pd}	N_{Ni-Ni}	r_{Ni-Pd}(Å)	r_{Ni-Ni}(Å)	σ^2_{Ni-Pd}(Å^2)	σ^2_{Ni-Ni}(Å^2)	E_0 (eV)	R-factor
1-1	34/66	38/62	2.8±0.3	4.6±0.1	2.54±0.007	2.49±0.006	0.0081±0.0010	0.0062	-10.0±0.8	0.0008
1-2	48/52	56/44	4.9±0.5	3.8±0.1	2.58±0.005	2.50±0.004	0.0113±0.0010	0.0062	-9.5±0.6	0.0012
1-3	65/35	80/20	7.7±0.6	1.9±0.2	2.62±0.005	2.56±0.009	0.0102±0.0007	0.0062	-7.9±0.6	0.0028

Table.3 液相還元法試料 PdK 端の測定結果より得られた構造パラメータ

Sample	Pd/Ni	N_{Ni-Pd}	r_{Ni-Pd}(Å)	σ^2_{Ni-Ni}(Å^2)	E_0 (eV)	R-factor
2-1	30/70	7.7±0.6	2.73±0.004	0.0079±0.0004	-3.6±0.9	0.0059
2-2	56/44	7.5±0.7	2.73±0.004	0.0078±0.0005	-4.1±1.0	0.0070
2-3	70/30	7.5±0.4	2.73±0.002	0.0079±0.0003	-3.4±0.6	0.0026
Pd foil		12	2.74±0.002	0.0062±0.0002	-2.6±0.5	0.0015

Table.4 液相還元法試料 Ni*K*端の測定結果を 2 シェルでフィットした構造パラメータ

Sample	Pd/Ni	N_{Ni-O}	r_{Ni-O}(Å)	σ^2_{Ni-O}(Å^2)	N_{Ni-Ni}	r_{Ni-Ni}(Å)	σ^2_{Ni-Ni}(Å^2)	E_0 (eV)	R-factor
2-1	30/70	4.8±0.3	2.06	0.0064±0.0024	5.2±3.5	3.11	0.0148±0.0061	2.2±1.3	0.0984
2-2	56/44	5.0±0.9	2.06	0.0064±0.0018	3.3±1.4	3.11	0.0094±0.0032	1.8±0.9	0.0532
2-3	70/30	5.5±0.8	2.06	0.0068±0.0015	3.1±1.2	3.12	0.0093±0.0029	0.8±0.8	0.0380
NiO		6	2.08	0.0050±0.0017	12	2.96	0.0067±0.0007	-1.4±0.9	0.0065

Table.5 液相還元法試料 Ni*K*端の測定結果を 3 シェルでフィットした構造パラメータ

		NiO							
Sample	Pd/Ni	N_{Ni-O}	r_{Ni-O}(Å)	σ^2_{Ni-O}(Å^2)	N_{Ni-Ni}	r_{Ni-Ni}(Å)	σ^2_{Ni-Ni}(Å^2)	E_0 (eV)	R-factor
2-1	30/70	4.9±1.0	2.06	0.0067±0.0023	5.0±2.8	3.11	0.0140±0.0061	1.8±1.1	0.0308
2-2	56/44	4.9±0.8	2.06	0.0063±0.0019	4.2±1.5	3.11	0.0111±0.0032	1.7±0.8	0.0207
NiO		6	2.08	0.0050±0.0017	12	2.96	0.0067±0.0007	-1.4±0.9	0.0065

		Ni Metal		
Sample	Pd/Ni	N_{Ni-Ni}	r_{Ni-Ni}(Å)	σ^2_{Ni-Ni}(Å^2)
2-1	30/70	0.7±0.9	2.50±0.02	0.0060±0.0084
2-2	56/44	0.4±0.5	2.50±0.02	0.0035±0.0087
NiO		12	2.48±0.003	0.0062±0.0004

8A/2010G009

Characterization of Electronic States in Cyanide-bridged Fe-Co Tetranuclear Complexes by X-ray Absorption Spectroscopy

二瓶雅之 [1], 関根良博 [1], 熊井玲児 [2], 中尾裕則 [2], 村上洋一 [2], 大塩寛紀 [1*]
[1] 筑波大学数理物質系、〒305-8571 つくば市天王台 1-1-1
[2] 高エネルギー加速器研究機構物質構造科学研究所、〒305-0801 つくば市大穂 1-1

1 はじめに

鉄イオンとコバルトイオンがシアン化物イオンで架橋されたバルク化合物であるプルシアンブルー類似体は、シアン化物イオンを介した電子的・磁気的相互作用により興味深い物性を示す。中でも、低温における光誘起磁化は、光による磁性スイッチの観点から注目を集めている。一方、シアン化物イオン架橋 Fe-Co 多核錯体は、プルシアンブルー類似体のユニット構造をもつ孤立分子であり、その柔軟な構造と電子状態に基づき、多様な物性を示す。我々は、鉄イオンとコバルトイオンからなる環状四核錯体 $[Co_2Fe_2(CN)_6(L1)_2(L2)_4](PF_6)_2$ (**1**: L1 = tris(dimethylpyrazolyl)borohydride, L2 = bipyridine; **2**: L1 = tris(pyrazolyl)borohydride, L2 = di-*t*-Bu-bipyridine; **3**: L1 = tris(dimethylpyrazolyl)borohydride, L2 = di-*t*-Bu-bipyridine) が、置換基のわずかな違いにより全く異なる電子状態を示すことを明らかにしてきた[1]-[3]。特に、錯体 **3** は、温度により常磁性 HS 状態 ($[Fe^{II}_{LS2}Co^{III}_{LS2}]$)と反磁性 LS 状態($[Fe^{III}_{LS2}Co^{II}_{HS2}]$)を可逆に示すと共に、低温における 808 nm 光照射により LS 状態から HS 状態への光磁性変換を示す事を見出した。本研究では、錯体 **1-3** の電子状態をより詳細に明らかにすることを目的とし、X 線吸収スペクトル測定を行った。

2 実験

錯体 **1-3** の単結晶をすりつぶし、キャピラリーに封入したものを X 線吸収スペクトル測定試料として用いた。測定はビームライン 8A にて行い、測定法としては、透過法をもちいた。また、測定エネルギー範囲は Co K 端の前後(7.70-7.75 keV)、測定温度は 10-330 K の範囲で行った。

3 結果および考察

錯体 **1-3** の X 線吸収スペクトルを図 2 に示す。錯体 **1** は、全ての測定温度範囲で Co^{II}_{HS} 状態に特徴的なスペクトルを示した。これは、**1** が常磁性 HS 状態 ($[Fe^{II}_{LS2}Co^{III}_{LS2}]$)を示すことに対応する。錯体 **2** においては、Co^{III}_{LS} 状態に帰属されるスペクトルを示し、温度依存性を示さなかった。すなわち、錯体 **2** は、全ての温度範囲で反磁性 LS 状態 ($[Fe^{III}_{LS2}Co^{II}_{HS2}]$)を示すと考えられる。一方、錯体 **3** のスペクトルは、顕著な温度依存性を示した。100 K においては錯体 **1** と同様の Co^{III}_{LS} 状態に帰属されるスペクトルを示すのに対し、330 K においては Co^{II}_{HS} 状態に対応するスペクトルを示した。これは、錯体 **3** における熱誘起電子移動共役スピン転移による、LS 状態から HS 状態への変換を示していると考えられる。

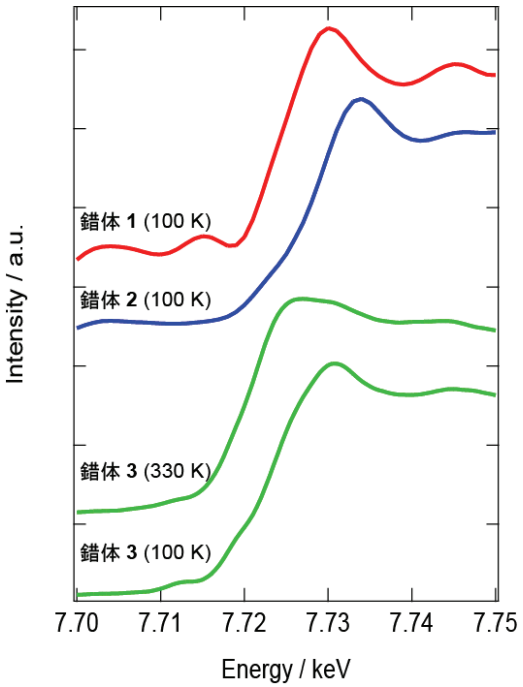

図 1 ：錯体 **1-3** の X 線吸収スペクトル.

4 まとめ

以上より、本研究では、X 線吸収スペクトル測定により、Fe-Co 四核錯体の電子状態について明らかにした。その結果、錯体 **3** が反磁性 LS 状態と常磁性 HS 状態を熱により可逆に示すことを明らかにした。

参考文献

[1] M. Nihei, Y. Sekine, N. Suganami, H. Oshio, Chem. Lett. 39, 978 (2010).
[2] M. Nihei, Y. Sekine, N. Suganami, K. Nakazawa, A. Nakao, H. Nakao, Y. Murakami, H. Oshio, J. Am. Chem. Soc. 133, 3592 (2011).
[3] G. N. Newton, M. Nihei, H. Oshio, Eur. J. Inorg. Chem. 2011, 3031-3042.

* oshio@chem.tsukuba.ac.jp

10C/ 2011G006

Complex Formation of Starch and Surfactant in Aqueous Solution

Kyoko Yamamoto[1] and Yoshiaki Yuguchi[1,*]
[1] Osaka Electro-Communication University, 18-8 Hatsu-cho, Neyagawa-shi, Osaka, 572-8530, Japan

1 Introduction

Starch is a mixture of amylose, linear chain, and amylopectin, branched chain. The saccharide chain is composed of α-1,4 linked glucose, so its chain tends to have helical conformation. This property reveals the inclusion of various molecules into amylose helix. In this study we prepared the complex of starch and surfactant by mixing at solution state, then analyzed by means of small angle X-ray scattering (SAXS).

2 Experiment

Amylopectin sample (Lintner's soluble waxy corn starch) was purchased from Hayashibara Co., Ltd. Sodium dodecyl sulphate (SDS) was used as surfactant sample. Their aqueous solutions were prepared by heating to make homogeneous transparent solution. Then they were mixed. SAXS experiments were carried out with SAXES optics installed at BL-10C in Photon Factory. The scattering intensity was detected with position sensitive proportional counter (PSPC).

3 Results and Discussion

Figure 1 shows the SAXS from the amylopectin samples (C_p=17%) in aqueous solutions without and with different concentrations of SDS. The scattering profile of amylopectin by addition of SDS gave clear peak around 0.04 as *q* value, the magnitude of scattering vector. Simultaneously in the figure the scatterings from SDS are also shown. At the comparison of them, the intensity from mixture is higher and the peak is clearer. The peak is due to the correlation hole from the electrostatic repulsive interaction. The SDS molecule has anionic charge of sulfate group, while the starch is neutral polysaccharide. So this scattering behavior suggests that the amylose chains distributed in the surface or inside of branched amylopectin makes the complex by including SDS with helical structure. Consequently it is thought that the interaction between charged complex domains is observed as clear peak.

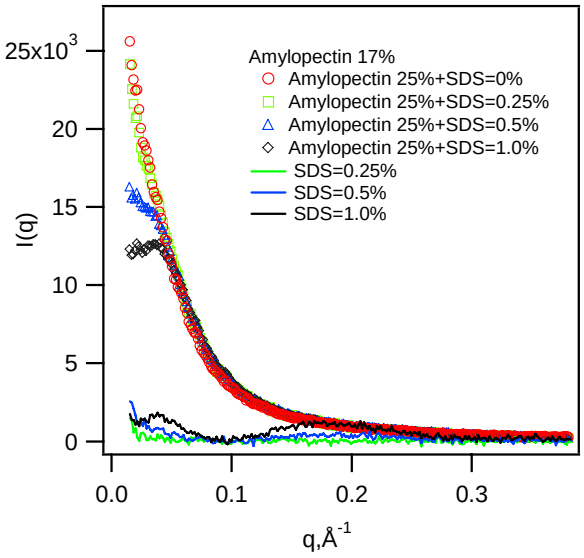

Figure 1. Small angle X-ray scattering (SAXS) from mixture of amylopectin (Lintner's soluble waxy corn starch) and Sodium dodecyl sulphate (SDS) in aqueous solution.

* yuguchi@isc.osakac.ac.jp

References

[1] O. Glatter and O. Kratky, *Small-angle X-ray Scattering*, Academic press, London (1982)
[2] A. Buleon, P. Colona, V. Planchot, S. Ball, *Int. J. Bio . Macro.*, 23, 85-112 (1998)

NW10A/2011G007

Effect of the Supports on the Oxidative Esterification of Propionaldehyde on Supported Palladium Catalysts

Shigeru Sugiyama,[1,2*] Yukimi Furukawa,[2] Keizo Nakagawa,[1,2] Toshihiro Moriga,[1,2] and Yuuki Katou[3]
[1]Department of Advanced Materials, Institute of Technology and Science, The University of Tokushima, Minamijosanjima, Tokushima 770-8506, Japan
[2]Department of Chemical Science and Technology, The University of Tokushima 770-8506, Japan
[3]Mitshubishi Rayon Co. Ltd., 20-1, Miyuki-cho, Otake-shi, Hiroshima 739-0693, Japan

1 Introduction

Recently, Pd catalysts doped with a heavy metal supported on various oxides and active carbon have attracted attention, particularly for industrial application. However, recent reports state that the use of pressurized O_2 resulted in great activity for the reaction of sodium lactate to sodium pyruvate using heavy-metal-free Pd/C, indicating that loading by heavy metals is not needed for the catalytic reaction, which is important for green chemistry and suggests the potential use of heavy-metal-free Pd catalysts for other catalytic reactions [1]. The direct oxidative esterification of propionaldehyde (PA) to methyl propionate (MP) in the liquid phase attracts attention in our laboratory [2]. Earlier studies have established that the oxidative esterification of PA to MP in the liquid phase occurs readily using Pd/Al_2O_3 doped with Pb [3]. In the present study, Pd/C and Pd/Al_2O_3 without heavy-metal doping were used for the direct oxidative esterification of PA to MP in the liquid phase under at 0.1 MPa of O_2 to examine the unnecessary of heavy-metal doping and the effect of the supports.

2 Experiment

Pd/C and Pd/Al_2O_3 (both with Pd of 5% by weight) were used as supplied. The BET surface areas of Pd/C and Pd/Al_2O_3 were 946 and 94.0 m^2/g, respectively. Catalytic activity was tested in a magnetically-stirred stainless steel autoclave (85 ml) reactor. The catalyst (0.5 g, Pd/C or Pd/Al_2O_3) was added into a 25 mL methanol solution containing 75 mmol of propionaldehyde in the reactor. Then, 25 μL of aqueous 5M NaOH and 0.025 g of $Mg(OH)_2$ were added to keep the solution pH at 6–8. Reactions were carried out at 333 K and oxygen pressure of 0.1 MPa. Analysis of EXAFS near the Pd-K edge was carried out at the High Energy Accelerator Research Organization with a storage ring current of 400 mA (6.5 GeV). The X-rays were monochromatized with Si(311) at an NW-10A station. The absorption spectra were observed using ionization chambers in the transmission mode. Since it was impossible to compress Pd/C and Te/Pd/C into a disk with diluents, the catalysts were carefully placed into a hand-made sample holder with two polypropylene windows. The photon energy was scanned in the range of 24,080–25,600 eV for the Pd-K edge.

3 Results and Discussion

At first, the oxidative esterification of PA with methanol was examined at 333 K and oxygen pressure of 0.1 MPa. After 2 h, the conversion of PA and the yield of to MP using Pd/C were 1.5 and 0.5% while 12.8 and 1.9 using Pd/Al_2O_3, indicating that Al_2O_3 support seems to be suitable support for the present system. Although the situation of Pd in both supported catalyst was checked using XRD, any evident differences of Pd species on those supported catalyst did not obtained. Therefore EXAFS analyses were employed to this catalyst system. Figure 1 shows the Pd-K edge EXAFS spectra of Pd/C (A) and Pd/Al_2O_3 (B), indicating that Pd nature on Pd/C was evidently different from that on Pd/Al_2O_3.

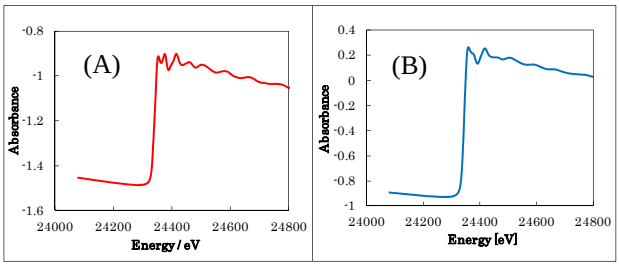

Figure 1. Pd-K edge EXAFS spectra of (A) Pd/C and (B) Pd/Al_2O_3.

Figure 2 shows the Fourier transformation of EXAFS of both supported catalysts. Single signal due to metallic Pd was detected from Pd/C while complex signals due to metallic and oxidized Pd species was detected from Pd/Al_2O_3. Therefore it may be concluded that the ease redox nature of PD species in Pd/Al2O3 results in the better activity that that using Pd/C

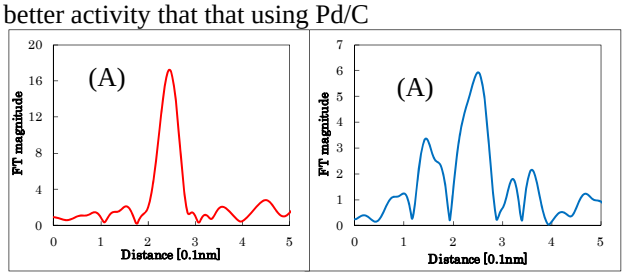

Figure 2. Fourier transformation of Pd-K edge EXAFS spectra of (A) Pd/C and (B) Pd/Al_2O_3.

References

[1] S. Sugiyama *et al.*, J. Chem. Eng. Jpn., **43** (2010) 514.
[2] S. Sugiyama *et al.*, J. Jpn. Petrol. Inst., **54** (2011) 380.
[3] Y. Diao *et al.*, J. Mol. Catal. A, 303 (2009) 35.

* sugiyama@chem.tokushima-u.ac.jp ()

KEK-PF 7C, 9C, SPring-8 01B1/2011G033, 2011A1977

Structure of Copper Hydroxy Anions in the Layered Double Hydroxides for the Photocatalytic Conversion of Carbon Dioxide to Methanol

Ahmed Naveed, Motoharu Morikawa, and Yasuo Izumi*

Department of Chemistry, Graduate School of Science, Chiba University, Inage-ku, Chiba 263–8522

1. Introduction

The number of reports of CO_2 photoreduction has been dramatically increased in a couple of years [1] in expectations of reducing the atmospheric CO_2 concentration and also obtaining useful chemicals, *e.g.* formic acid and methanol. Layered double hydroxides (LDHs) of $[Zn_3Ga(OH)_8]^+_2[Cu(OH)_4]^{2-}\cdot mH_2O$ and $[Zn_{1.5}Cu_{1.5}Ga(OH)_8]^+_2[Cu(OH)_4]^{2-}\cdot mH_2O$ photocatalytically converted CO_2 to methanol using hydrogen as a reducing agent [2,3]. The photocatalytic role of $[Cu(OH)_4]^{2-}$ sites should be essential and the structure was investigated using Cu K-edge XANES.

2. Methods

The synthesis of LDH samples starting from $[CuCl_4]^{2-}$ was described in literature [3]. Cu K-edge XAFS spectra were measured on a beamline 9C and 7C in KEK-PF and also on a beamline 01B1 at SPring-8. The sample disk was set in an in-situ cell equipped with PEN/Kapton film windows.

3. Results and Discussion

Cu K-edge EXAFS spectrum is shown in Figure 1A for $[Zn_3Ga(OH)_8]^+_2[Cu(OH)_4]^{2-}\cdot mH_2O$. Two intense peaks in the Fourier transform (FT) at 0.16 and 0.27 nm (phase shift uncorrected) derived from Cu–O and Cu···Zn (or Cu···Ga) pairs, respectively, appeared in Figure 1B. But a peak derived from Cu–Cl bond(s) at ~0.195 nm (phase shift uncorrected) was not present. No Cu–Cl peaks were found in the FT for this LDH photocatalyst, demonstrating the complete hydrolysis of $[CuCl_4]^{2-}$ into $[Cu(OH)_4]^{2-}$ during the synthesis.

$$[CuCl_4]^{2-} + 4NaOH \rightarrow [Cu(OH)_4]^{2-} + 4NaCl \cdots(1)$$

$$2[Zn_3Ga(OH)_8]^+ + [Cu(OH)_4]^{2-} + mH_2O \rightleftarrows [Zn_3Ga(OH)_8]^+_2[Cu(OH)_4]^{2-}\cdot mH_2O \cdots(2)$$

Based on the Cu K-edge X-ray absorption near-edge structure (XANES) spectra and the theoretical simulation, complex formation between cationic layer and $[Cu(OH)_4]^{2-}$ anion was suggested (Figure 2).

$$[Zn_3Ga(OH)_8]^+_2[Cu(OH)_4]^{2-}\cdot mH_2O \rightleftarrows Zn_6Ga_2(OH)_{13}\{(\mu\text{–}O)_3Cu(OH)\}\cdot mH_2O + 3H_2O \cdots(3)$$

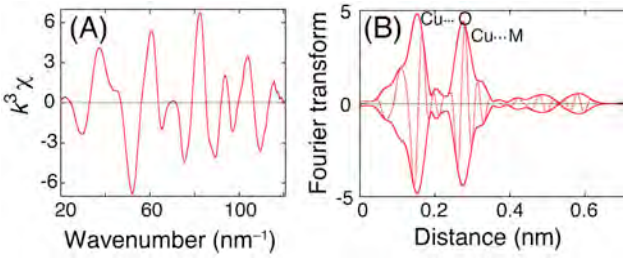

Figure 1. Cu K-edge EXAFS spectra for $[Zn_3Ga(OH)_8]^+_2[Cu(OH)_4]^{2-}\cdot mH_2O$. (A) k^3-weighted EXAFS χ-function and (B) its associated FT. The solid and dotted lines represent the magnitude and the imaginary part in (B).

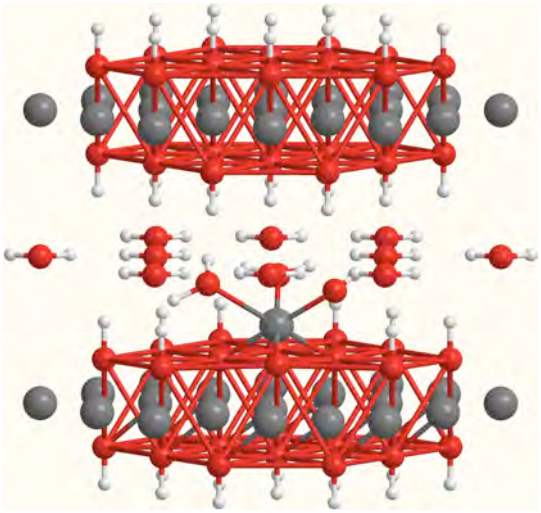

Figure 2. Proposed structure of $[Zn_3Ga(OH)_8]^+_2[Cu(OH)_4]^{2-}\cdot mH_2O$.

The interlayer $(\mu\text{–}O)_3Cu(OH)$ site was 5.9 times more active than the octahedral Cu sites in the octahedralCu sites in the cationic layers of $[Zn_{1.5}Cu_{1.5}Ga(OH)_8]^+$ for the photocatalytic conversion of CO_2 to methanol.

References

[1] Y. Izumi, *Coord. Chem. Rev.*, http://dx.doi.org/10.1016/j.ccr.2012.04.018.

[2] N. Ahmed, Y. Shibata, T. Taniguchi, Y. Izumi, *J. Catal.* **279**, 123–135 (2011).

[3] N. Ahmed, M. Morikawa, Y. Izumi, *Catal. Today* **185**, 263–269 (2012).

*yizumi@faculty.chiba-u.jp

BL27B/2011G034

Spectroelectrochemical Measurement of Uranium Ions in Nitric Acid and Sodium Carbonate Solutions

Akihiro UEHARA[1,*], Toshiyuki FUJII[1],
Hajimu YAMANA[1] and Yoshihiro OKAMOTO[3]
[1]Division of Nuclear Engineering Science, Research Reactor Institute, Kyoto University,
2-1010, Asashiro Nishi, Kumatori, Sennan, Osaka, 590-0494, Japan
[2]Quantum Beam Science Directorate, Japan Atomic Energy Agency,
2-4, Shirakatashirane, Tokai, Ibaraki 319-1195, Japan

Introduction

Understanding the uncertainty of the complexation mechanism and stability of uranium(IV) ions in acidic and basic solutions is important in the assessment of environmental impact on the disposal nuclear waste as well as the development of chemical separation of actinide ions. In the present study, coordination circumstance of uranium ions of which oxidation state in nitric acid and sodium carbonate solutions is controlled electrochemically, was analysed by XAS measurement.

Experimental

Sample preparation

Uranyl nitrate hydrate was dissolved into 0.1 M HNO_3 and 1 M $NaCO_3$ solutions. The uranium concentration used in the EXAFS measurements was 0.05 M (mol dm^{-3}) for HNO_3 and 0.02M for $NaCO_3$ solutions. In order to avoid oxidation by O_2 in air, sample preparation was carried out under the Ar atmosphere.

Electrochemical cell

Three electrodes consist of reference, working, and counter electrode, respectively Reference electrode is Ag|AgCl containing 1 M LiCl, working electrode is Pt wire. Counter electrode is Ag wire containing 1M LiCl separated from sample solution by porous film to avoid gas evolution. The cell is stored in containment vessel served as double confinement against radionuclide release. IVIUM compact stat was used for electrochemical measurements.

EXAFS data acquisition and analysis

EXAFS measurements were carried out at BL27B beam-line of the Photon Factory in High Energy Accelerator Research Organization (KEK), Tsukuba, Japan. EXAFS measurements based on the U L_{III}-absorption edge were performed. All the solutions were measured in fluorescence mode using a Ge solid state detector.

Results

Figure 1 (a) shows the XANES spectra of 0.05 M uranium (UO_2^{2+}) in 0.1 M HNO_3 solutions. During the electrolysis applying constant current (-1 mA) to reduce from UO_2^{2+} to uranium(IV)(U^{4+}) as following equation (1);

$$UO_2^{2+} + 2e^- + 4H^+ \rightarrow U^{4+} + 2H_2O \quad (1)$$

By continuing electrolysis, it was found that UO_2^{2+} was quantitatively reduced to form U^{4+}. The peak shift of absorption edge in HNO_3 solutions was similar to that in $HClO_4$ reported previously [1]. On the other hand, when 0.1 M $NaCO_3$ was used, the following reaction proceeded by applying constant potential (-0.95 V).

$$UO_2^{2+} + e^- \rightarrow UO_2^{+} \quad (2)$$

One electron reduction of UO_2^{2+} to UO_2^{+} causes a shift in the U L_{III}-edge position from 17.172 to 17.170 keV as shown in Fig. 1 (b), consistent with the shift reported [2].

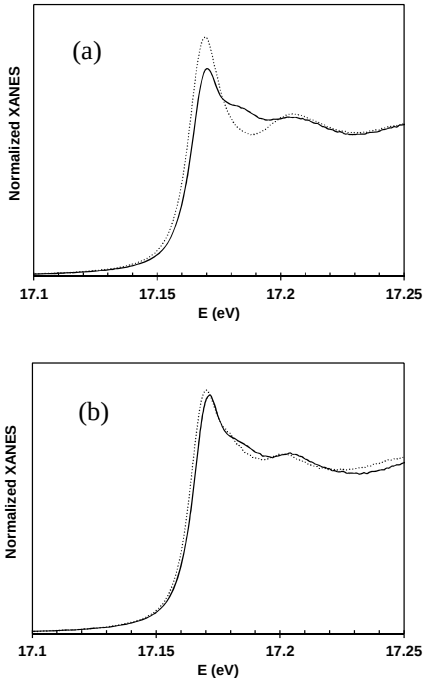

Fig. 1. U L_{III}-edge EXAFS data for (a) 0.05 M UO_2Cl_2 in 0.1 M HNO_3 and (b) 0.02 M UO_2Cl_2 in 1 M $NaCO_3$: solid line, before, dotted line, after electrolysis.

References

[1] A. Uehara, et al., KEK activity report 2011.
[2] TI Docrat, et al., Inorg. Chem., 38 (1999) 1879.

*auehara@rri.kyoto-u.ac.jp

4B2/2011G060
SPring-8/15XU/2011A4805 注

粉末回折法によるアミノ酸およびオリゴペプチドの環境変化に伴う構造変化の解析
Powder diffraction structure analysis of humidity and temperature dependent structure transition of amino acids and oligopeptides

清谷多美子 [1*], 菅原洋子 [2]
[1] 昭和薬科大学、〒194-8543 町田市東玉川学園 3-3165
[2] 北里大学理学部　〒252-0373 相模原市南区北里 1-15-1

1 はじめに

温度や湿度条件などの環境変化に伴う医薬品（特に水和物）の結晶構造の変化は、薬効に影響を及ぼす可能性が高いことが知られている。また、品質保持の観点からも、医薬品の製造、流通から投薬、服薬に至るまでの各段階での構造変化の有無と、その特性を明らかにすることは重要である。

医薬品は、主として有機物であり、合成物、天然物、アミノ酸、ペプチドなどが挙げられる。アミノ酸は生物の生命を維持するために不可欠な物質であり、ヒトの体を構成する膨大なタンパク質はわずか 20 種類のアミノ酸が構成単位である。2 個以上のアミノ酸がペプチド結合により繋がってできた物質であるオリゴペプチドは、生理活性を持つものが多く、医薬品や甘味料、食品添加物などとして広く用いられている。

脱水による構造転移においては、一般的に単結晶性が劣化するため、粉末結晶構造解析に期待が持たれる。本研究は、アミノ酸およびオリゴペプチドの水和物結晶を対象に、粉末回折法により脱水和状態の構造決定法を確立することを目指している。その第一歩として、アミノ酸 2 個から構成されるジペプチドであるグリシル－L－チロシン（以降、Gly-Tyr）の水和物を対象とした実験を行った。

Gly-Tyr は、水 - メタノール混合溶液から二水和物が得られ、その結晶構造が報告されていたが[1]、我々は水溶液から新たに三水和物を得て、単結晶構造解析により構造決定を行った[2]。また、この三水和物結晶は、24℃、相対湿度 0%で一水和物に変化し、更に、相対湿度 0%下で昇温すると 50℃で無水物に転移することを明らかにした。

この様な背景の元に、Gly-Tyr 三水和物の脱水和により得られる一水和物および無水物について、BL4B2 の多連装粉末回折計および SPring-8/BL15XU（物質・材料研究機構 高輝度放射光ステーション）の高分解能粉末回折装置（東日本大震災優先枠課題）を用いて粉末回折強度測定を行い、両結晶について粉末結晶構造解析に成功した。

2 実験および解析

Gly-Tyr 一水和物は PF/BL4B2 の多連装粉末回折計を用いて、無水物については SPring-8/BL15XU（物質・材料研究機構 高輝度放射光ステーション）の高分解能粉末回折装置を用いて粉末 X 線回折強度測定を行った。両測定とも、あらかじめ脱水処理を施した試料をガラスキャピラリに封入し、配向の影響を軽減するために回転試料台を用いて、ω軸を回転しながら透過法により測定を行った。

粉末結晶構造解析プログラムとしては、DASH（Cambridge Crystallographic Data Center）および PDXL（（株）リガク）を用いた。三水和物の結晶構造解析より得られている Gly-Tyr の分子構造を用いて、実空間法により一水和物および無水物の構造モデルを得て、リートベルト法により構造精密化を行った。現時点での一水和物の R_{wp} は 0.061、R_e は 0.031、S は 1.93、χ^2 は 3.72、無水物の R_{wp} は 0.035、R_e は 0.001、S は 35.60、χ^2 は 1267 である。Gly-Tyr 一水和物および無水物のリートベルト解析の結果をそれぞれ図 1 および図 2 に示す。

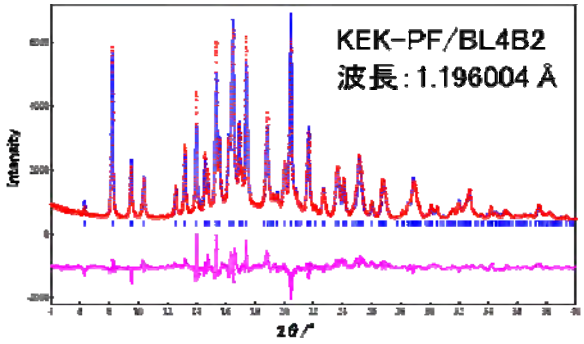

図 1：Gly-Tyr 一水和物のリートベルト解析結果

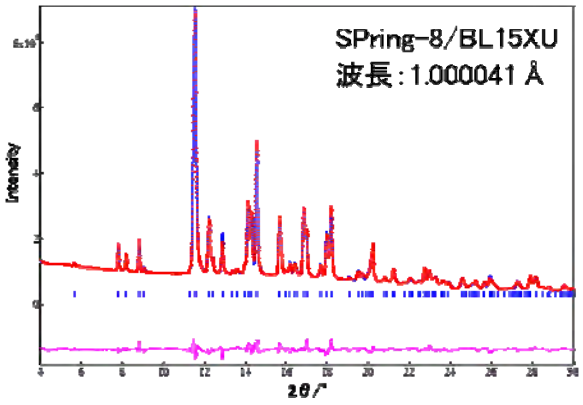

図 2：Gly-Tyr 無水物のリートベルト解析結果

3 結果および考察

粉末 X 線回折データを用いて決定した Gly-Tyr 一水和物および無水物の結晶学的パラメータを三水和物と対比させて表 1 に示す。三水和物から一水和物への変化では、*a* および *b* 軸がそれぞれ約 10%縮み、*c* 軸には僅かではあるが伸長がみられた。一方、一水和物から無水物への変化では、空間群が $P2_12_12$ から $P2_12_12_1$ 変化し、*a* 軸は約 10%、*b* 軸は 3%縮んでいるのに対して、*c* 軸には 7%の伸長がみられた。

表 1：Gly-Tyr 三水和物の構造変化に伴う
結晶学的パラメータの変化

	三水和物	一水和物	無水物
解析方法	単結晶法	粉末法	粉末法
測定温度	298K	298K	300K
晶系	斜方晶系	斜方晶系	斜方晶系
空間群	$P2_12_12$	$P2_12_12$	$P2_12_12_1$
a/Å	18.598 (3)	16.787 (−10%)	14.688 (−13%)
b/Å	15.728 (2)	14.447 (−8%)	14.012 (−3%)
c/Å	4.814 (1)	4.925 (+2%)	5.289 (+7%)

Gly-Tyr 三水和物の脱水に伴う構造変化を図 3 に示す。三水和物から一水和物への脱水に伴い、結晶水領域（青枠内）が減少するとともに、*c* 軸投影図における Gly-Tyr 分子の主鎖($NH_3C\alpha CONHC\alpha COO^-$)（赤紫楕円内）の傾きが変わっており、これが、*a* および *b* 軸長の縮小と相関している。一水和物から無水物に移行する際には、主鎖の傾きはあまり変化していないが、水分子が抜けるとともに、Gly-Tyr 分子が *c* 軸に沿ってスライドしており、空間群の変化と、*c* 軸長の伸長をもたらすことが明らかになった。

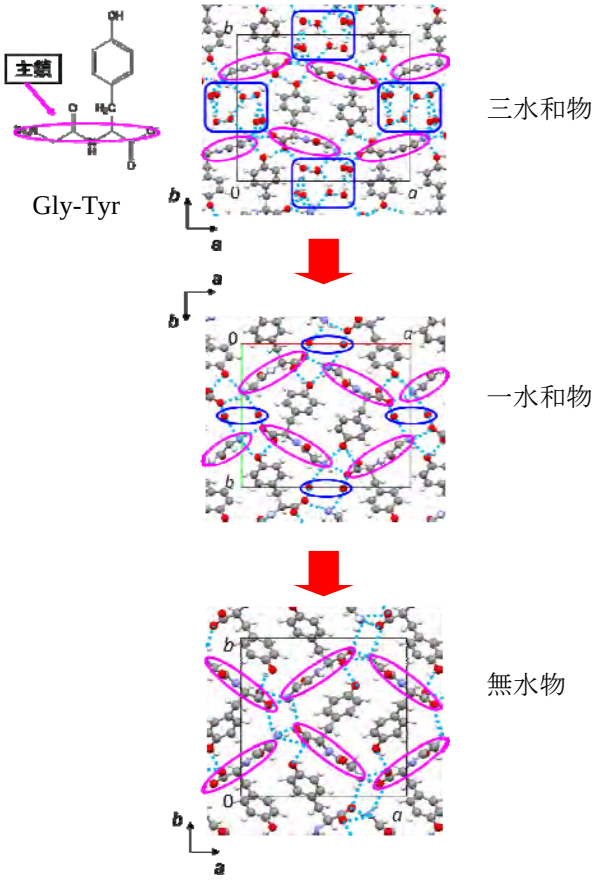

図 3：Gly-Tyr 三水和物の脱水に伴う構造変化
（*c* 軸投影図）

4 まとめ

放射光測定データを用いることにより、ジペプチド水和物について乾燥および加温により生じる脱水和物の粉末結晶構造解析に成功し、この様な系における粉末結晶構造解析法の有用性を立証するとともに、構造転移の概要を明らかにすることができた。

謝辞

本実験の一部は、東日本大震災優先枠課題として、SPring-8 の物質・材料研究機構 高輝度放射光ステーション（BL15XU）で実施しました。実験の実施にあたり、多大なるご支援を賜りましたステーションのスタッフである坂田修身博士、田中雅彦博士、松下能孝博士、勝矢良雄博士に深く感謝いたします。

参考文献

[1] M.Cotrait, J.-P.Bideau, *Acta Cryst.*, **B30**, 1024 (1974).
[2] T. Kiyotani, et al., *CrSJ Annual Meeting* 2011, **2011**, OB-II-02.

* kiyotani@ac.shoyaku.ac.jp

注：2011 年 東日本大震災優先枠により実施

KEK-PF 7C, 9C, SPring-8 01B1/2011G083, 2011A1978

Monitoring of Photocatalytic Reduction Sites of Preferential Oxidation of Carbon Monoxide in Hydrogen

Yusuke Yoshida and Yasuo Izumi*

Department of Chemistry, Graduate School of Science, Chiba University, Inage-ku, Chiba 263–8522

1. Introduction

Hydrogen energy is advantageous because it does not produce CO_2 when the chemical energy is transformed to electricity. In this study, the reduction sites of inexpensive preferential oxidation (PROX) photocatalyst of CO [1] for purification of hydrogen were investigated using Cu K-edge XANES.

2. Methods

Cu K-edge XAFS spectra were measured on a beamline 9C and 7C in KEK-PF and also on a beamline 01B1 at SPring-8. The sample disk was set in a cell equipped with polyethylene naphthalate windows. The sample was illuminated with an Xe arc lamp placed perpendicular to the X-ray beam path with the CO, O_2, and H_2.

3. Results and Discussion

The Cu K-edge XANES spectrum for the fresh Cu–spheroidal ZnO catalyst is shown in Figure 1A-a. The Cu valence state was II in fresh Cu–spheroidal ZnO. After illumination for 1 min under UV–visible light, a weak shoulder peak began to appear at 8983.1 eV (Figure 1A-b). The shoulder peak intensity grew gradually to 0.0727 under the illumination for 3 h (Figure 1A-d). One minute after the UV–visible light was removed, the peak intensity at 8983.1 eV reduced by 0.0035 (Figure 1A-e).

The shoulder peak at 8983.1 eV originated from Cu^{I} sites. The Cu K-absorption edge energy negligibly changed when the Cu^{II} sites were reduced to Cu^{I} sites. Therefore, the Cu^{I}-site ratio in the sample was approximated using the following equation:

$$\frac{\text{Peak intensity@8983.1 eV} - 0.048\ (\text{for } Cu^{II}\ 100\%)}{0.21\ (\text{for } Cu^{I}\ 100\%) - 0.048\ (\text{for } Cu^{II}\ 100\%)}$$

Based on this approximation, 3.9% of Cu^{I} sites were formed in the initial 1 min, and this population gradually increased to 15.6% after 3 h of illumination. When the illumination was removed, the Cu^{I} population dropped to 13.4%. Cu^{II} and Cu^{I} sites were in a dynamic equilibrium in a steady-state population of transmitted electrons that were photogenerated and did not recombine with holes during the diffusion to surface. The Cu ions were active for CO reduction in the PROX reaction.

$$K = \frac{[Cu^{I}]}{[Cu^{II}][e^{-}_{\text{diffused to surface}}]}.$$

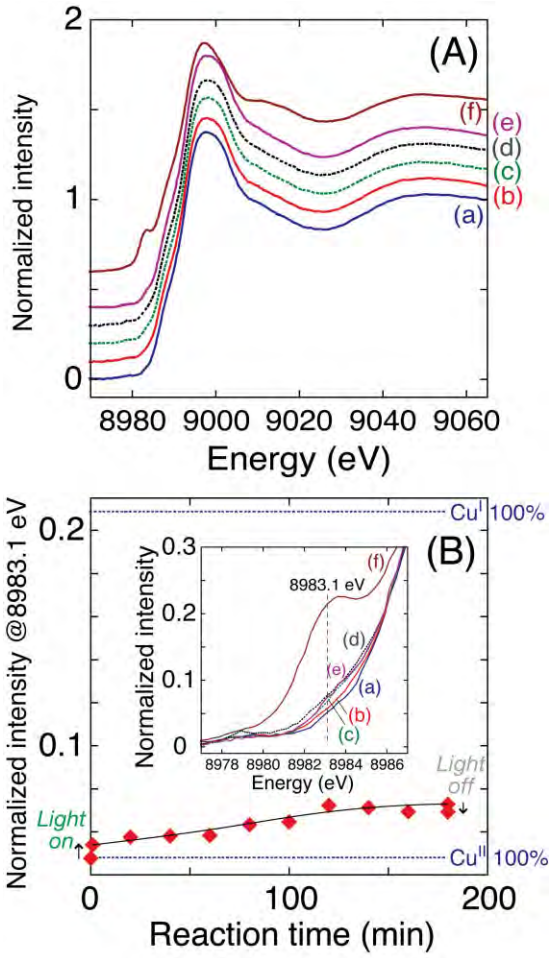

Figure 1. (A) Normalized Cu K-edge XANES spectra for Cu–spheroidal ZnO before illumination (a), at 1 (b), 80 (c), and 180 min (d) of illumination in CO (135 Pa), O_2 (270 Pa), and H_2 (13 100 Pa), and at 1 min after the illumination (e) for Cu–spheroidal ZnO-reduced (f). (B) The intensity change of a shoulder peak at 8983.1 eV during the illumination of UV–visible light.

Reference

[1] Y. Yoshida, Y. Mitani, T. Itoi, Y. Izumi, *J. Catal.* **287**, 190–202 (2012).

*yizumi@faculty.chiba-u.jp

27B/2011G111

放射光XAFS測定による各種アルカリ溶融塩中のウラン錯イオンの局所構造解析

永井崇之[1*], 上原章寛[2], 藤井俊行[2], 北脇慎一[3], 小藤博英[3], 岡本芳浩[4]
[1]日本原子力研究開発機構核燃料サイクル工学研究所 〒319-1194 東海村村松 4-33
[2]京都大学原子炉実験所 〒590-0494 大阪府泉南郡熊取町朝代西 2-1010
[3]日本原子力研究開発機構次世代原子力システム研究開発部門 〒319-1194 東海村村松 4-33
[4]日本原子力研究開発機構量子ビーム応用研究部門 〒319-1195 東海村白方白根 2-4

1 はじめに

塩化物溶融塩を用いた乾式再処理プロセス研究の一環として、筆者らは溶融アルカリ塩化物中におけるウランイオンの酸化還元反応やウラン錯イオンの構造を電気化学測定や吸光分光測定により評価[1,2]している。本研究では、溶媒であるアルカリ塩化物のカチオン半径によるウラン 4 価イオン（U^{4+}）の局所構造を評価するため、LiCl と CsCl の割合を変えた混合アルカリ塩化物中に UCl_4 を溶存させた試料を調製し、放射光 XAFS 測定を行った。

2 実験

XAFS 試料は、京都大学原子炉実験所の乾燥 Ar ガス雰囲気の電気炉付グローブボックスにおいて、以下の手順で調製し、KEK-PF へ送付した。AAPL 製無水試薬（純度 99.99%）の LiCl 及び CsCl を CsCl モル比 0, 0.2, 0.4, 0.6, 0.8, 1.0 に秤量して石英丸底管内で 700 ºC まで加熱して LiCl-CsCl 混合塩を調製した後、一旦冷却凝固させた。別の石英管に UCl_4 と凝固 LiCl-CsCl 混合塩を 5 mol% UCl_4 となるように装荷して 700 ºC で溶融し、この状態で乾燥 Cl_2 ガスを塩中に供給し、その後 Ar ガスで残留 Cl_2 を掃気してから冷却凝固させた。凝固させた UCl_4 を含む塩を乳鉢で粉砕して、試料毎に 1 g の粉末を分取してポリエチレン袋にシール封入し、ポリエチレン袋三重密封の状態で、XAFS 測定に供した。また、比較として UCl_4 顆粒を同様に封入して測定に供した。

XAFS 測定は、BL-27B の XAFS 測定装置を用いて、U L_{III}-edge を対象に 16.9～18.2 KeV の範囲を蛍光法で 5 回繰り返した。

3 結果

図 1 に、蛍光法で測定した規格化 XANES スペクトルを示す。17.2 keV 付近のスペクトル形状を比較すると、LiCl 単体に UCl_4 を溶存させたスペクトル(b)は UCl_4 顆粒のスペクトル(a)と類似していた。これに対し、LiCl-CsCl 混合塩及び CsCl 単体のスペクトル(c)～(g)は UCl_4 顆粒スペクトル(a)と異なり、また CsCl モル比に関係なく同様なパターンを示した。現在スペクトル解析を行っており、今後詳細な検討を行う予定であるが、溶融状態でない凝固塩の状態においても、LiCl 中における U^{4+} の局所構造が CsCl の添加によって変化すると考えられる。

この LiCl 単体と CsCl が含まれる混合塩組成との相異は、溶融 LiCl 中でのウランイオンの酸化還元電位や吸光スペクトルが LiCl-CsCl 混合塩中と異なる傾向を示すことと共通している。今後、得られた XAFS 測定結果と酸化還元電位や吸光スペクトル[1,2]等のデータを比較し、塩化物組成によるウランイオンの局所構造への影響を解明する予定である。

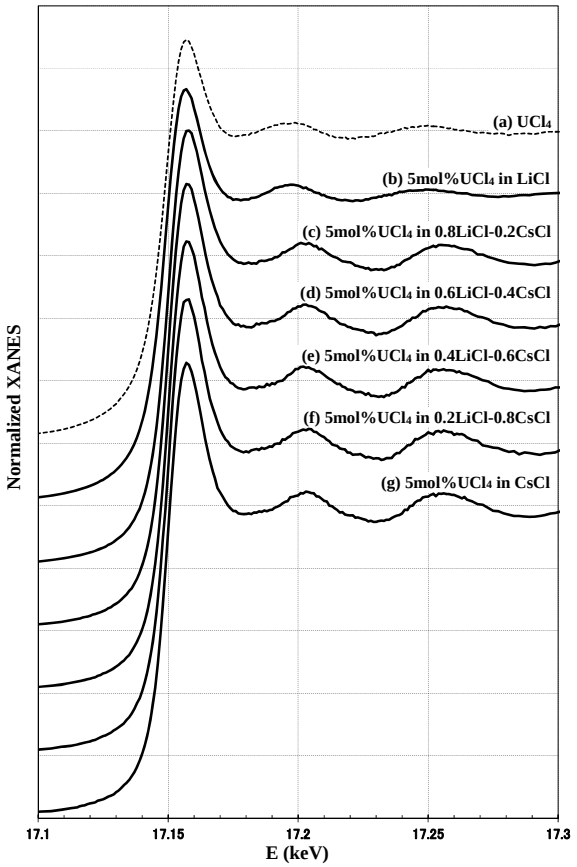

図 1　蛍光法による 5mol%UCl_4 含有 LiCl-CsCl 混合塩（凝固塩）中 U L_{III}-edge の規格化 XANES スペクトル

参考文献
[1] T. Nagai *et al.*, J. Nucl. Mater. **414** (2011) 226.
[2] K. Fukasawa *et al.*, J. Nucl. Mater. **424** (2012) 17.

* nagai.takayuki00@jaea.go.jp

7C/2011G141

Study on Mechanisms of Electrochemical Reactivity in P2-$Na_x[Fe_{1/2}Mn_{1/2}]O_2$ as Positive Electrode Materials for Sodium-ion Rechargeable Batteries

Naoaki Yabuuchi, Masataka Kajiyama, Junichi Iwatate, and Shinichi Komaba*
Department of Applied Chemistry, Tokyo University of Science,
1-3 Kagurazaka, Shinjuku, Tokyo 162-8601 Japan

1 Introduction

Li-ion batteries have risen to prominence as key devices for green and sustainable energy development. Lithium batteries have potential applications for energy storage within electrical grid systems to effectively use electricity from power plants, solar cells and wind turbines. Manganese- and iron-based positive-electrode materials, such as $LiMn_2O_4$ and $LiFePO_4$, could be used in the large-scale batteries. Manganese and iron are abundant elements in the earth's crust, but lithium is not. In contrast to lithium, sodium is an attractive charge carrier on the basis of elemental abundance. We have therefore interested to realize the Na-ion batteries[1]. Recently, we have reported sodium iron manganese oxides, $Na_x[Fe_yMn_{1-y}]O_2$, as the promising positive electrode materials for the rechargeable sodium batteries. P2-type $Na_{2/3}[Fe_{1/2}Mn_{1/2}]O_2$, consisting of only abundant elements in the earth's crust, delivers large reversible capacity (more than 180 mAh g^{-1}) with relatively good capacity retention at room temperature[1]. In this study, We examine the charge compensation mechanisms of P2-type $Na_x[Fe_{1/2}Mn_{1/2}]O_2$ during sodium extraction process by X-ray absorption spectroscopy (XAS) .

2 Experiment

Composite positive electrodes consisted of 80 wt % $Na_x[Fe_{1/2}Mn_{1/2}]O_2$, 10wt % acetylene black, and 10wt % polyvinylidene fluoride (PVdF), pasted on aluminum foil as a current collector. The electrolyte solution used was 1 mol dm^{-3} $NaClO_4$ dissolved propylene carbonate (Kishida Chemical Co. Ltd., Japan) with 2 vol.% fluorinated ethylene carbonate as an electrolyte additive. Electrochemical testing was conducted using R2032-type coin cells with Na metals as negative electrodes. The coin cells were assembled in an Ar-filled glovebox and cycled at a rate of 13 mA g^{-1}. After the electrochemical tests, composite electrodes were taken out from the cell, and the electrodes were rinsed with DMC and sealed in a water-resistant polymer film in the Ar-filled glovebox.

3 Results and Discussion

X-ray absorption near edge structure (XANES) spectra of P2-$Na_x[Fe_{1/2}Mn_{1/2}]O_2$ at Fe K-edge are shown in Figure 1(a). The spectrum is slightly shifted after charge to 3.8 V, but much more clear shift towards higher energy region is found at the Mn K-edge (Fig.1(c), indicating that the charge compensation is mainly achieved by oxidation of Mn. When the $Na_x[Fe_{1/2}Mn_{1/2}]O_2$ is charged to 4.2 V, the clear shift of Fe K-edge absorption spectrum is observed to the higher energy region. The shift could be contributed from the complicated situations, including the changes in the local structures, e.g., sodium extraction from the Fe face-shared sites and P2/OP4 transition. Therefore, extended X-ray absorption fine structure (EXAFS) spectra during charge were further analyzed. The change in radial distribution around Fe during charge to 4.2 V is shown in Fig. 1(b). The radial distribution around Fe is not affected by charge to 3.8 V, and the interatomic distance of Fe-O remains unchanged (2.00 Å for as-prepared and 1.99 Å for 3.8 V charge). The Fe-O local environment is drastically changed after charge to 4.2 V. The intensity of the peaks for both first and second coordination shells, Fe-O and Fe-Fe(Mn), is reduced, suggesting that the distortion around Fe. The distortion also influences the neighboring Mn ions (Fig(1d).Thus, the Fe^{3+}/Fe^{4+} redox in P2-$Na_x[Fe_{1/2}Mn_{1/2}]O_2$ could be accessible. Note that this observation was further supported by Mössbauer spectroscopy.[2]

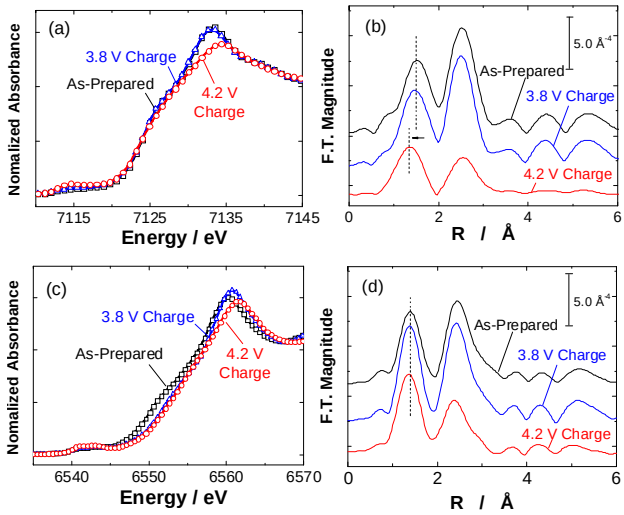

Fig. 1 XAS spectra of the P2-type $Na_x[Fe_{1/2}Mn_{1/2}]O_2$ samples charged to 3.8 and 4.2 V; Fe K-edge XANES (a) and EXAFS (b) spectra, and Mn K-edge spectra are also shown in (c) and (d).

References
[1] S. Komaba *et al*., *Adv. Funct. Mater.*, 21, 3859 (2011).
[2] N. Yabuuchi *et al*., *Nature Mater.*, **11**, 512 (2012).

* komaba@rs.kagu.tus.ac.jp

9C/2011G146

XAFS Analysis of Local Structure of Active Sites for Asymmetric Cyclopropanation on Copper Ion-planted Mesoporous Al-MCM-41

Hiroki KATO, Masashi TANAKA, Insuhk SUH, Haruro ISHITANI, Masakazu IWAMOTO*
Chemical Resources Laboratory, Tokyo Institute of Technology, Nagatsuta, Midori-ku, Yokohama 226-8503, Japan

1 Introduction

Copper ion-planted mesoporous Al-MCM-41 (Cu-AlM41) has been found to show high catalytic activity for asymmetric cyclopropanation of styrene derivatives and diazo compounds [1]. In this reaction, the Cu-AlM41 catalysts should be evacuated at elevated temperatures, such as 873 K, for the appearance of the catalytic activity. This result indicated that some specialized states of copper ion would be the active species. However, the states have little been clarified. In this study, the local structure of copper species on the Cu-AlM41 sample activated by the heat-treatment and subsequently modified by the addition of indane-derived bis(oxazoline) (IndaBOX) as chiral ligand were examined by using XAFS spectroscopy.

2 Experimental

AlM41 was synthesized by using high-purity colloidal silica (PL-3), aluminium nitrate, and $C_{12}H_{25}N(CH_3)_3Br$. The copper ion was planted in the as-synthesized AlM41 before organic template removal, according to the template-ion-exchange method [2]. The resulting powder was calcined at 873 K in air to remove the templates. The Si/Cu and Si/Al atomic ratios of the Cu-AlM41 sample obtained were 161 and 26, respectively. In the XAFS experiments, the Cu-AlM41 sample was evacuated at 873 K and was subsequently modified by adding CH_2Cl_2 solution of IndaBOX under an N_2 atmosphere. The dried sample at each process was pressed into self-supporting disk under an N_2 atmosphere. The XAFS spectra of Cu K-edge were recorded on beam line 9C of PF-KEK. The spectrum was treated by the REX2000 program. The curve-fitting analyses for Cu-O and Cu-N contributions were performed by using the FEFF6 code.

3 Results and Discussion

The XANES spectrum and Fourier transforms of k^3-weighted EXAFS spectrum of Cu-AlM41 evacuated at 873 K are shown in Fig. 1. The XANES bands at 8.983 and 8.994 keV were observed. These bands were assignable to the 1s–4p electronic transitions of Cu^+. Thus, it was clear that Cu^+ species are formed on Cu-AlM41 by the heat-treatment. In the EXAFS spectrum, a band due to back-scattering from the nearest neighboring oxygen atoms was observed at around 1.5 Å (no phase-shift correction). The structure parameters calculated from the EXAFS data using the least-square method are summarized in Table 1. The coordination number (CN) of Cu-O is 2.1 and the interatomic distance was 1.90 Å. It was found that Cu^+ species are coordinated with two lattice oxygen atoms in the AlM41.

When IndaBOX was added to the sample (Fig. 1a), the XANES band at 8.983 keV decreased in intensity. The band at around 1.5 Å (no phase shift correction) in the EXAFS spectra increased its intensity in comparison with the band obtained for the 873 K-treated sample. These results suggested that IndaBOX was coordinated to Cu^+ on AlM41. The curve-fitting analysis resulted in no changing CN of Cu-O but the elongation of Cu-O distance and the appearance of the contribution due to Cu-N. The CN of Cu-N was 2.1. Therefore, it was suggested the formation of the four-coordinate Cu^+ structure with two lattice oxygen atoms in the AlM41 and bidentate nitrogen atoms of IndaBOX. On the basis of the results, we propose that such four-coordinate Cu^+ species would act as active sites for asymmetric cyclopropanation.

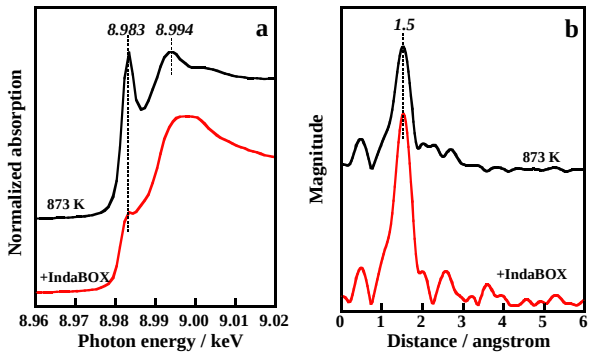

Fig. 1: (a) XANES spectra and (b) Fourier transforms of k^3-weighted EXAFS spectra of Cu-AlM41 evacuated at 873 K and subsequently modified by adding IndaBOX.

Table 1: Structure parameters of Cu-AlM41 evacuated at 873 K and subsequently modified by the addition of IndaBOX

	shell	CN[a]	R (Å)[b]	σ^2 (Å^2)[c]
evac. at 873 K	Cu-O	2.1	1.90	0.0083
addition of IndaBOX	Cu-O	2.1	1.96	0.0104
	Cu-N	2.1	1.91	0.0058

[a] Coordination number. [b] Interatomic distance. [c] Debye-Waller factor.

References

[1] M. Iwamoto et al., Shokubai **49** (2007) 426: **52** (2010), 453.

[2] M. Iwamoto, Y. Tanaka, Catal. Surv. Jpn. **5** (2001) 25.

* iwamoto@res.titech.ac.jp

7C/2011G163

オートサーマル改質 Pt 触媒の XAFS 解析
XAFS Analysis of Pt Catalyst for Autothermal Reforming

高垣敦 [1*]
[1] 東京大学大学院工学系研究科、〒113-8656 東京都文京区本郷 7-3-1

1 はじめに

天然ガスや液体炭化水素から水素や合成ガスを製造するプロセスは、来るべき水素社会の普及期には欠かすことのできないキーテクノロジーである。メタン等からの合成ガスの製造方法のうち、オートサーマル改質(ATR)は、水蒸気改質と部分酸化の両方の利点を合わせた反応であり、現在、精力的に触媒開発が進められている。

ATR において触媒には Rh や Ni が用いられており、これらの担体によっても大きくその触媒活性が影響することが示されている。近年、担体としてセリア・ジルコニア固溶体を用いた、$Pt/Ce_{0.75}Zr_{0.25}O_2$ 触媒が ATR において高活性、高寿命を有することが報告されている[1]。

本研究では、Pt について XAFS 測定を行うことで、本触媒の反応メカニズムを理解することを目的とした。本年度は、Ce/Zr の異なるセリア・ジルコニア固溶体を用いた $Ce\text{-}Zr\text{-}Ox/Al_2O_3$ を担体とし、還元した Pt 試料の EXAFS を測定した。

2 実験

各種 $Pt/Ce_xZr_{1-x}/Al_2O_3$ 触媒(x = 0.25, 0.50, 0.75, 1)は、含浸法にて調製した[2]。まず、アルミナに硝酸セリウム(IV)アンモニウムと硝酸ジルコニウムからなる水溶液を含浸し、$20wt\%Ce_xZr_{1-x}/Al_2O_3$ を調製した。その後 1.5wt%の Pt を含浸担持した。得られた $Pt/Ce_xZr_{1-x}/Al_2O_3$ を所定量ペレットにしたのち、773 K にて 1 時間水素雰囲気にて還元処理した。

このようにして調製した $Pt/Ce_xZr_{1-x}/Al_2O_3$ の Pt L_{III}-edge XAFS を透過法にて測定した。測定は室温にて行い、ビームラインは BL-7C を利用した。

3 結果および考察

昇温還元(TPR)測定では、453 K 付近に大きなピークが観測されたことから、773K の水素還元処理では十分に Pt が還元されていることが示唆された。

図 1 に各種 $Pt/Ce_xZr_{1-x}/Al_2O_3$ 触媒のフーリエ変換後の Pt L_{III} edge EXAFS を示す。担体により、そのスペクトルの形状は大きく異なった。Zr 導入量の多い試料($Pt/Ce_{0.50}Zr_{0.50}/Al_2O_3$および $Pt/Ce_{0.25}Zr_{0.75}/Al_2O_3$)では、Pt-Pt に Pt-O を加えてカーブフィッテイングを行った。Ce_xZr_{1-x} 担体では全体として、Pt-Pt 配位数が比較的低いことがわかった。Pt-O の原因については、種々の可能性が想定されるため今後さらに検討する。

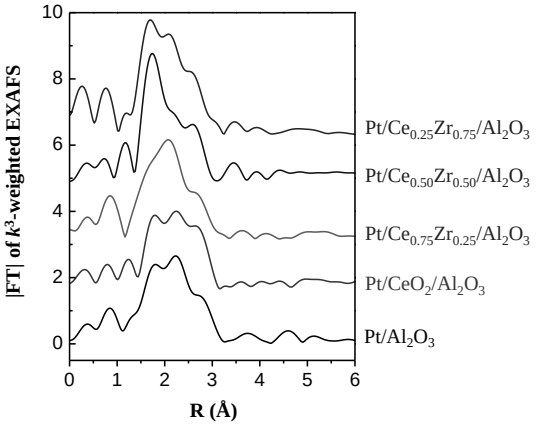

図 1 ：Pt L_{III}-edge EXAFS of $Pt/Ce_xZr_{1-x}/Al_2O_3$catalysts.

表 1: EXAFS parameters for $Pt/Ce_xZr_{1-x}/Al_2O_3$

Sample		CN	R /Å
$Pt/Ce_{0.25}Zr_{0.75}/Al_2O_3$	Pt-Pt	5.1	2.57
	Pt-O	1.4	2.03
$Pt/Ce_{0.50}Zr_{0.50}/Al_2O_3$	Pt-Pt	5.4	2.60
	Pt-O	1.6	2.07
$Pt/Ce_{0.75}Zr_{0.25}/Al_2O_3$	Pt-Pt	5.9	2.57
$Pt/CeO_2/Al_2O_3$	Pt-Pt	3.9	2.61
Pt/Al_2O_3	Pt-Pt	6.8	2.66

4 まとめ

$Pt/Ce_xZr_{1-x}/Al_2O_3$ の Pt L_{III}-edge EXAFS 測定を行った。いずれも Pt-Pt の配位数は小さく、Ce/Zr 比率によりスペクトルの形状が大きく異なった。

参考文献

[1] J.A.C. Ruiz, F.B. Passos, J.M.C. Bueno, E.F. Souza-Aguiar, L.V. Mattos, F.B. Noronha, Appl. Catal. A, **334** (2008) 259.
[2] F.A. Silva, K.A. Resende, A.M. de Silva, K.R. de Souza, L.V. Mattos, M. Montes, E.F. Souza-Aguiar, F.B. Noronha, C.E. Hori, Catal. Today, **180** (2012) 111.

* atakagak@chemsys.t.u-tokyo.ac.jp

9A、12C/2011G197

Oxalate metal complexes in aerosols: implications for the hygroscopicity of oxalate-containing particles

Yoshio Takahashi[1]
[1]Department of Earth and Planetary Systems Science, Graduate School of Science, Hiroshima University, Higashi-Hiroshima, Hiroshima 739-8526, Japan

Some anthropogenic aerosols, such as organic aerosols and sulfate aerosols, have a direct cooling effect by scattering solar radiation, and an indirect cooling effect by acting as cloud condensation nuclei (CCN) because of their hygroscopic properties. The global average contribution of the indirect cooling effect (i.e., the cloud albedo effect) is estimated to be −0.3 to −1.8 W/m^2 [1]. In the report of the Intergovernmental Panel on Climate Change (IPCC), the sum of the direct and indirect cooling effect of aerosols is almost equivalent to the warming effect of carbon dioxide [1]. However, a large uncertainty exists because of the indirect effect discussed in the IPCC report [1], which must be evaluated more precisely for a better understanding of the Earth's climate. Thus, a number of studies have been performed on sulfate aerosols and on organic aerosols because of their complex nature in terms of composition and chemical transformation in the atmosphere, and also because of their importance in the global CCN budget. Among the various organic aerosols studied, water-soluble organic compounds (WSOCs) in aerosols influence the heat budget at earth surface as they act as CCN activator because of their hygroscopic properties. We can assume that dicarboxylic acids (DCA) contribute to the CCN activity, considering that DCA, which are major constituents of WSOCs, have hygroscopic nature.

Oxalic acid is a major component of DCA and also an important component of identified secondary organic aerosols. In this study, we focused on oxalic acid as a representative component of low molecular weight DCA in the atmosphere, and our results can be extended to other DCA, such as malonic and succinic acids. We expect that oxalic acid can form metal oxalate complexes in aerosols by reacting with metal ions due to several reasons: (i) aerosols contain various metal ions originating from sea salts, desert dusts, continental soils, and anthropogenic sources; (ii) oxalic acid is formed in the aqueous phase at aerosol surfaces in the atmosphere or cloud droplet, where the aqueous phase can be a reaction field for metal complexation; (iii) polyvalent metal ions can form stable complexes with oxalate ion. However, metal oxalate complexes are not detected using conventional methods, such as gas chromatography and ion chromatography (IC). In the latter analysis, a large volume of water sufficient to dissolve metal oxalate complexes in aerosols is usually employed during the water extraction procedure. In this case, metal oxalate complexes can be readily dissolved, despite the low solubility of some metal oxalate complexes, and it is difficult to distinguish between noncomplexed and metal-complexed oxalate species in aerosols. Hence, only a few studies have suggested that DCA can react with metal ions and mineral aerosols. However, these studies employed indirect methods that cannot show direct evidence of the formation of metal oxalate complexes in aerosols.

In our study [2], we applied X-ray absorption fine structure (XAFS) spectroscopy to show the presence of metal oxalate complexes in aerosols, coupled with IC and inductively coupled plasma atomic emission spectrometry (ICP-AES) analyses to determine the ratio of metal oxalate and noncomplexed oxalate species. In this study, Ca K-edge XANES and Zn K-edge XANES and EXAFS were performed at BL-9A and BL-12C, respectively, which allows us to demonstrate the presence of metal oxalate complexes.

As a result, it was revealed that 10–60% and 20–100% of the total Ca and Zn in the finer particles (<2.1 μm) were present as Ca and Zn oxalate complexes, respectively. Considering the presence of other metal ions, such as Mg^{2+}, Pb^{2+}, and Cu^{2+}, the concentration of free oxalic acid can be much lower than that expected. Therefore, the contribution of oxalic acid to hygroscopicity of aerosol particles must have been overestimated. Thus, the present study may claim reevaluation of the contribution of oxalic acid to CCN activity of aerosols, because most of the oxalic acid can exist as non-hygroscopic metal oxalate complexes. Similar to oxalic acid, other WSOCs, such as malonic and succinic acids, can transform to metal complexes in aerosols. Therefore, in discussing the hygroscopicity and related effects of organic aerosols, it is necessary to evaluate the contribution of the complexation of dicarboxylic acids with metal ions.

References

[1] IPCC Climate Change 2007, Synthesis Report, the Intergovernmental Panel on Climate Change, Cambridge University Press, UK (2007).
[2] T. Furukawa and Y. Takahashi, Atmos. Chem. Phys., **11** (2011) 4289.

* ytakaha@hiroshima-u.ac.jp

1A/2011G200
SPring-8 BL14B2&SAGA-LS BL11

電極上に担持した多核銅錯体における酸素還元機能の XAFS による解明
Investigation on Oxygen Reduction Reaction Activity of Multi-Copper Complex Deposited on Electrodes by XAFS

八木一三 [1,2*], 君島堅一 [2], 太田鳴海 [2], 野津英男 [2], 上原広充 [1], 高草木 達 [1], 朝倉清高 [1]
[1] 北海道大学 〒001-0021 札幌市北区北 21 条西 8 丁目
[2] 技術研究組合ＦＣ−Ｃｕｂｉｃ　〒135-0064 江東区青海 2-3-26

1 はじめに

酸素還元反応（ORR）を利用するカソード（空気極）は、電池外部の空気を直接利用することでエネルギー密度を飛躍的に向上できるため、各種燃料電池の他、金属-空気電池などに利用されている。また、得られる電流密度もまた空気極の性能により制限され、空気極の性能向上はエネルギーデバイスのさらなる高効率化に欠かせない。近年、生体内で酸素の活性化に用いられている金属酵素（多核銅酵素）を電極表面に固定すると、一般に燃料電池で使用されている白金触媒よりも過電圧が低い（ca. 1.2 V vs. RHE からの）ORR を実現できることが示唆され、バイオカソードの研究の活性化に繋がっている。金属酵素自体の耐久性や精製過程を含めた材料コストの問題があるため、反応中心部を模倣した銅錯体触媒の電極応用に関する研究が行われている。その結果、単核銅錯体については最近、Chidsey らの研究グループによって様々な官能基を有するフェナントロリン銅錯体の ORR 活性が研究され、0.68 V vs, RHE（可逆水素電極、pH 4.8）という結果が得られている[1]。また、最近、Gewirth らは、カーボンブラック（CB）粉体の表面に複核銅錯体を固定するだけで極めて高い ORR 性能を示すことを報告している[2]。

我々もごく最近、非白金系ではほぼ最高の ORR 性能（アルカリ性溶液中）をもつ複数のトリアゾール系配位子を用いた複核銅錯体（CuII2[3,5-diamino-1,2,4-triazole]2 錯体）の調製に成功した。この試料は、きわめて、調製条件に対して敏感にその性能が変化する。X 線光電子分光（XPS）による表面分析や FE-SEM による形態観測によってもその違いを明らかにできなかった。すなわち、炭素表面との相互作用で生じるわずかな複核銅錯体の局所構造の変化が ORR 性能に影響を及ぼしていると考えられる。そこで本研究では、Cu^{II}_2[3,5-diamino-1,2,4-triazole]$_2$ 錯体の Cu K 端の XANES ならびに XAFS を測定することでカーボン担体表面上での構造や電子状態を調べ、その調製条件による構造の差違と ORR 活性の関係を明らかにすることを試みた。

2 実験

本研究では基本的にカーボンブラック（CB）担体に複核銅錯体を固定した試料を透過 XAFS で測定した。既報[2]に従い、CB 担体と Cu^{2+}イオンを混合した状態で配位子（3,5-diamino-1,2,4-triazole: Hdatrz）を添加することで複核銅錯体担持 CB を調製した。CB 担体の種類としても、既報で用いられている Vulcan XC-72 を標準とし、ケッチェンブラック（KB）を用いた試料も調製した。Cu と CB の比あるいは Cu と配位子の比を変えて調製を行うことで ORR における触媒性能の変化が期待され、触媒活性変化と XAFS で得られる結果の対比を行うことで相関が得られることを想定し、実験を進めた。また、複核銅錯体 $Cu_2(Hdatrz)_2$ の結晶も既報[3-5]に従って調製し、参照試料の１つとして使用した。また、調製時の錯体形成・担持の過程で意図的に遅延をはさみ、錯体担持濃度を高めた試料も調製した。その他の参照試料として、Cu 箔、CuO、Cu_2O、$Cu(NH_3)_4(SO_4)$-H_2O 等を用意した。試料・参照試料ともに粉末であるため、samplem を用いてエッジジャンプが 1 程度になるように計算して得られた量を秤りとり、窒化ホウ素（BN）粉末と混合・粉砕し、錠剤成形器を用いて直径 10 mm のペレットとした。試料測定時には、ポリ袋に試料を入れ、試料枠にそのポリ袋ごと貼り付けた状態で保持した。

透過 XAFS 実験は、震災優先枠として SPring-8 BL14B2 ならびに SAGA-LS BL11 で行った他、復旧後の KEK-PF BL9C にて Cu K 端の透過 XAFS 測定を実施した。SPring-8 では Cu-Cu 間に存在する可能性のある水を脱離させるために、真空下加熱による変化の計測に取り組んだほか、KEK-PF では EXAFS 振動の精密解析のため、クライオスタットを用いて低温での透過 XAFS 測定を実施した。SAGA-LS では事前に実施した SPring-8 における透過 XAFS 測定結果を参照し、比較可能なレベルでスペクトルが測定できるよう、エネルギー範囲で積算時間を長くした。XAFS スペクトルは（株）リガク製の REX2000 を用いてバックグラウンド処理し、EXAFS 振動の抽出、k2 の重み付けをし、フーリエ変換することで動径構造関数を導出した。

3 結果および考察

図 1 は、SPring-8 BL14B2 ならびに SAGA-LS BL11 にて測定した参照試料 CuO の EXAFS 振動を比較したものである。前者はクイック XAFS で若干

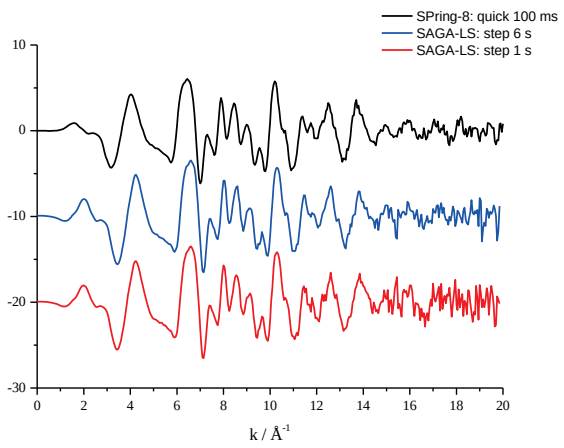

図 1　CuO 参照試料で得られた EXAFS 振動の比較（SPring-8 クイック 100 ms，SAGA-LS でそれぞれ 1step あたりの積算を 1s, 6s でそれぞれ測定した結果。

チャンネル毎の積算時間を増やし、測定時間 8 分で取得したものであり、後者は比較可能な S/N 比になるよう、高エネルギー側の積算時間を長くすることで取得した。このため、1 スペクトルあたりの測定時間は 35 分程度になった。クイック XAFS で積算することも試したが、S/N は図 1 の真ん中の振動より向上することはなかった。

図 2 は、$Cu_2(Hdatrz)_2$ 錯体を $[Cu^{2+}]$:[Hdatrz]比を変えて KB に担持した一連の試料の動径構造関数を示している。$[Cu^{2+}]$/[Hdatrz]が 0.25 の場合は他の試料と比較して大きな変化が認められるが、この値が 0.5 以上になるとほぼ同じ構造であることが推察される。$Cu_2(Hdatrz)_2$ 錯体の形成のためには $[Cu^{2+}]$/[Hdatrz] = 1 である必要があるが、実際には Cu 量が少なくともほぼ同じ構造の複核錯体が形成されている可能性がある。文献[2]でも、高性能触媒のレシピとして$[Cu^{2+}]$/[Hdatrz] = 0.5 を報告しており、カーボンブラックを担体として用いることが、表面に形成される錯体の構造自体に影響することを示唆している。

今回調製した触媒の Cu 源として硫酸銅を、溶媒

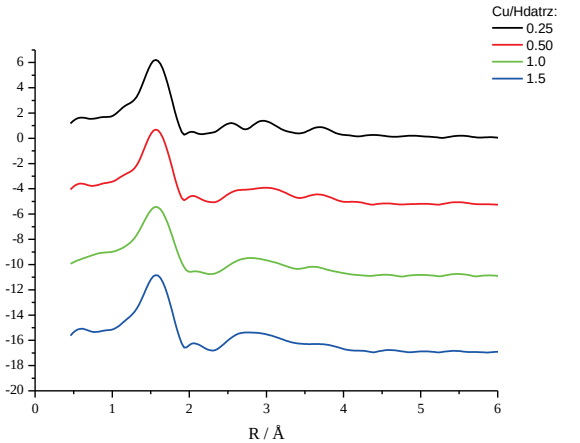

図 2　$Cu_2(Hdatrz)_2$ 錯体の$[Cu^{2+}]$/[Hdatrz]比を変えて KB に担持した一連の触媒の EXAFS 振動から求めた動径構造関数

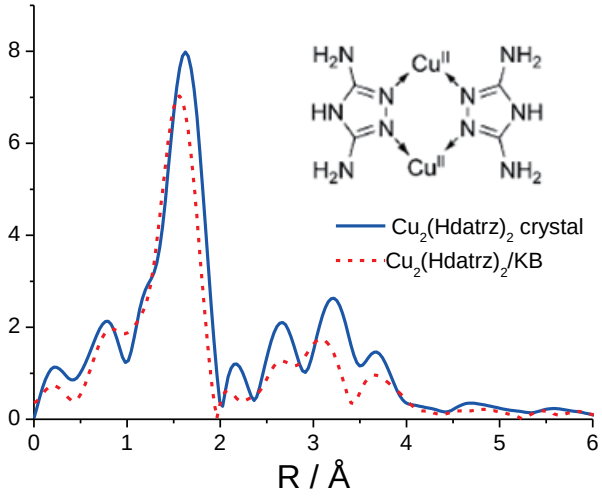

図 3　70 K で測定した $Cu_2(Hdatrz)_2$ 錯体結晶（実線）と KB 担持触媒（破線）の透過 EXAFS 振動から求めた動径構造関数と錯体の分子構造。

として水を利用しているため、Cu にはトリアゾール環の窒素の配位以外にも硫酸根や水が配位していることが予想される。EXAFS では O と N を分離することが難しいため、動径構造関数において 1.85～1.99 Å に現れるピークが Cu-O/N であると考えられるが、2～4 Å に複数のピークが観測され、構造評価のため、低温での測定を実施した。

70 K での測定により、図 3 のようによりシャープなピークが観測され、結晶では 3.2～3.4 Å に Cu-Cu に同定されるピークが観測されている。また、担持触媒では明らかにピーク位置のシフトが観測され、結晶とは異なる構造でカーボン表面に固定されていることも示唆される。しかし予想に反して低温でもピークが多く観測され、第一配位、第二配位を含めて FEFF による構造推定を進めている。

4　まとめ

空気極触媒として高活性な Cu 複核錯体担持触媒を調製し、その結晶ならびに担持状態の構造解析のため、XAFS 測定を実施した。結晶と担持状態では錯体分子構造が異なることが明らかになったが、詳細は依然解析中である。現在、蛍光 XAFS による in situ 測定を実施している。

謝辞

本研究の実施において、特に震災優先枠のビームタイムを利用させていただき、かつ測定時のサポートをいただいた方々に深く感謝致します。

参考文献

[1] McCrory et al., J. Phys. Chem. A, **111** (2007) 12641
[2] M.S. Thorum, J. Yadav, A. A. Gewirth, Angew. Chem. Int. Ed., **48** (2009) 165
[3] E. Aznar et al., Euro. J. Inorg. Chem. (2006) 5115
[4] R.B. Zhang et al., Cryst. Growth Des., **8** (2008) 3735
[5] A. Ray, S. Mitra, G.M. Rosair, Inorg. Chem. Comm., **11** (2008) 1256

* i-yagi@aist.go.jp

9A,12C/2011G251

東京湾における底質中の鉄およびマンガンの化学状態を用いた貧酸素水塊の評価
Evaluation of hypoxia in Tokyo Bay by chemical states of iron and manganese in the sediments

山形武広[1*],起孝志[1],小豆川勝見[1],松尾基之[1]
[1]東京大学大学院総合文化研究科、〒153-8902 東京都目黒区駒場 3-8-1

1 はじめに

貧酸素水塊は溶存酸素量(DO)が欠乏している水塊を指し(DO<2.0mg/L)[1]、内湾部のような閉鎖系水域においてしばしば発生する。東京湾においては 1960～1970 年代に大規模な浚渫が行われ、周囲に比べ水深が顕著に深い場所が存在するが（浚渫窪地）、これらの浚渫窪地においては海水の循環が起こりづらいため、酸素が欠乏し、貧酸素水塊の発生源になっているといわれている。しかしながら、貧酸素水塊の原因や挙動はいまだ明確になっていないため、底質を用いて浚渫工事の行われた時期からの酸化還元状態を把握することが重要である。

底質から過去の水質の酸化還元状態を知る上では、堆積物中に含まれる元素の価数が指標となる。我々は東京湾の浚渫窪地の環境評価を行うために、有機物の分解過程に関与する底質中の Fe および Mn の化学状態に着目し[2][3]、XANES スペクトルの測定を行ったので以下に報告する。

2 実験

サンプリングは 2009 年 9 月 4 日、2010 年 7 月 20 日、2011 年 2 月 16 日に実施した。底質の採取は、東京湾奥部における最大の窪地である幕張沖浚渫窪地内（調査点）および対照点である窪地外（平場）で行った。サンプリングデータを表 1 に示す。HR 型不攪乱柱状採泥器で採取したサンプルは、鉛直方向に 3cm ごとに切り分け、化学状態の変化を防ぐため窒素とともにパウチ袋に封入し、約-80℃で保存した。

また、堆積した Fe と Mn の堆積後の変化について検討するために、底質試料を取り巻く酸化還元状態を人為的に変化させた試料も調製した。具体的には 2010 年に採取した浚渫窪地中層部(15-18cm)の底質試料に海水を加え、そこに酸化剤(H_2O_2)と還元剤(Na_2S)を加えることで海水の Eh を変化させた。酸化剤を加えた試料の Eh はおよそ+550 mV、還元剤を加えた試料はおよそ-250 mV となった。この状態で試料を 96h 静置させ、その後約-80℃で保存した。

冷凍保存した湿試料をポリエチレンフィルムに封入し、Fe および Mn の K 吸収端の XANES スペクトルを室温で測定した。実験ラインは BL-12C を用い、蛍光法（Lytle 型検出器）で測定を行った。

表 1：底質のサンプリングデータ

	緯度(N) 経度(E)	水深 (m)	コア長 (cm)	試料数
2009 年 窪地	35°37.699′N 140°01.099′E	26	39	13
2009 年 平場	35°36.820′N 140°00.980′E	8.6	10	3
2010 年 窪地	35°37.699′N 140°01.099′E	24.9	35	11
2010 年 平場	35°36.403′N 140°04.044′E	17.5	50	16
2011 年 窪地	35°37.550′N 140°01.187′E	23.4	45	15
2011 年 平場	35°36.833′N 140°01.081′E	9.8	30	8

3 結果および考察

図 1-1、1-2 に Fe と Mn の XANES スペクトルを示す。すべてのコアの表層(0-3cm)、およびコア長が短かった 2009 年平場以外のコアの最深層のスペクトルを同時に示す。

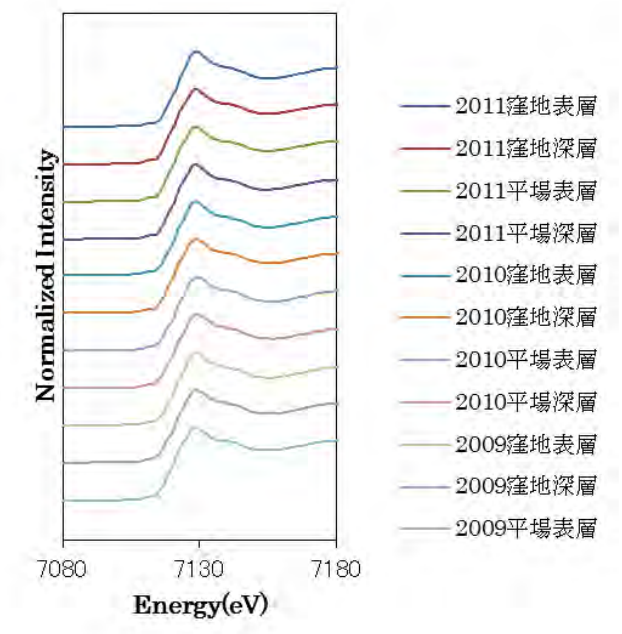

図 1-1：Fe の XANES スペクトル

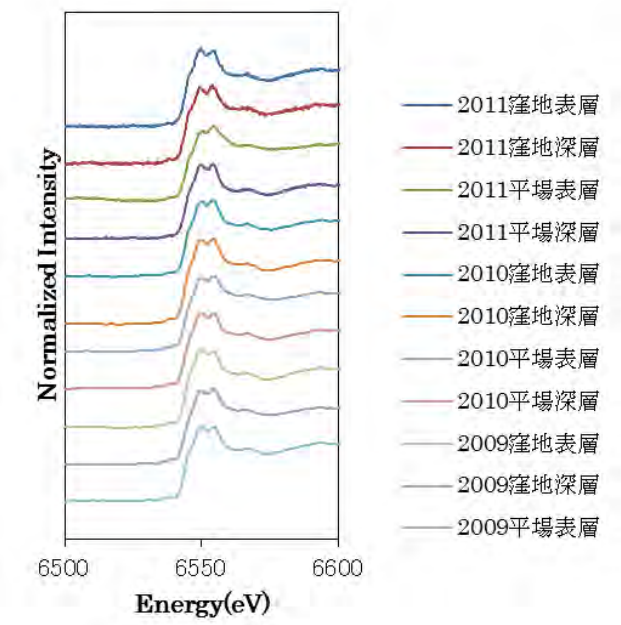

図 1-2：Mn の XANES スペクトル

いずれの底質試料でも、Fe では 7128eV 付近にピークが見られ、Mn では 6550eV、6555eV 付近にピークが見られた。標準試薬と比較したところ、Fe のピークは FeOOH に近く、Fe(Ⅲ)に由来するものと考えられる。Mn についてみると、6550eV のピークは $MnSO_4$ に近く、6555eV のピークは Mn_2O_3 に近いことから、それぞれ Mn(Ⅱ)、Mn(Ⅲ)に由来するものと考えられる。すべての試料についてスペクトルにほとんど差異が見られなかったので、昨年報告した S の場合[4]と異なり、Fe および Mn ではサンプルの採取時期や採取地点によって化学状態の変化がほとんど見られないことが判明した。

化学状態が変化しにくいことは『過去の』環境評価には必要な条件であるが、これらの元素を指標として用いるには、環境が変化した時の元素の挙動を知る必要があると考えられる。そこで、2010 年に採取した浚渫窪地中層部(15-18cm)の底質試料に酸化剤(H_2O_2)と還元剤(Na_2S)を加え、人為的に Eh を変化させた試料の化学状態を分析した。実験の部で述べたように、酸化剤を加えた試料の Eh はおよそ+550 mV、還元剤を加えた試料はおよそ-250 mV となったが、これらの Eh は Eh-pH ダイアグラム[5]からみても、通常は Fe、Mn の状態を変化させるには十分なものであるといえる。これらの Eh を変化させた試料の XANES スペクトルを図 2-1、2-2 に示す。しかし、酸化剤、還元剤を加えたもの双方で未処理のものと比較して変化がみられなかった。このことから、これらの元素は、堆積した後に大きな酸化還元環境の変化があったとしても、化学状態が変化せず堆積した当時の状態を維持すると考えられる。

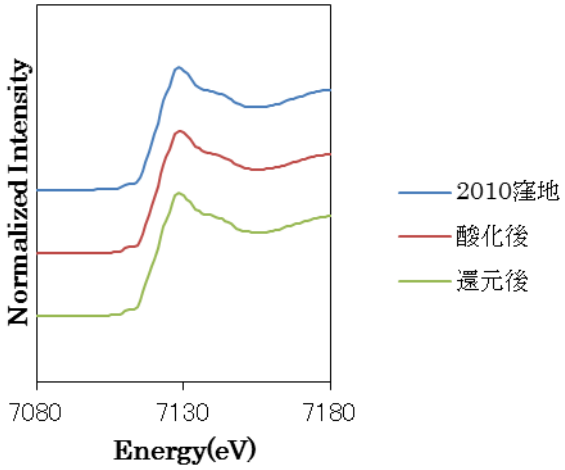

図 2-1：Eh を変化させた試料における Fe の XANES スペクトル

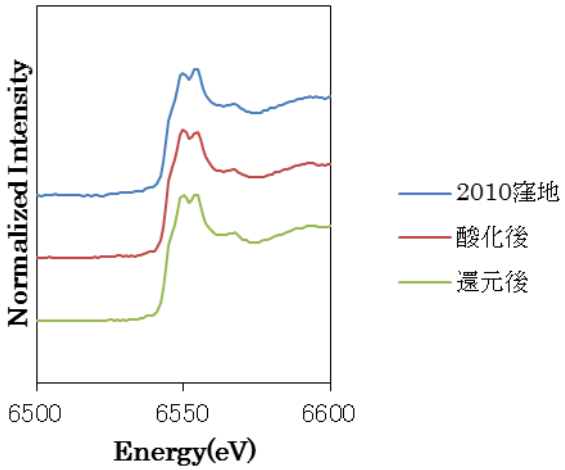

図 2-2：Eh を変化させた試料における Mn の XANES スペクトル

以上の結果から、Fe および Mn は、一度堆積したら安定な物質として存在し、堆積後に環境変化があっても化学状態が保存されていることが示唆された。そのため、過去数十年間の環境を評価するための指標として有用であるものと考えられる。

参考文献

[1] R. J. Diaz et al., Science, 321, 926-929(2008).
[2] J. Thomson et al., Geochimica et Cosmochimica Acta, 57, 579-595(1993).
[3] P. N. Froelich et al., Geochimica et Cosmochimica Acta, 43, 1075-1090(1979).
[4] T. Okoshi et al., PF Activity Report, 28B, 14(2011).
[5] D. G. Brookins, “Eh-pH diagrams for geochemistry”, Springer-Verlag(1988).

* 0084385768@mail.ecc.u-tokyo.ac.jp

17A, NE3/2011G514

Structural studies on the light-harvesting membrane protein complexes from thermophilic photosynthetic bacteria

Long-Jiang YU[1], Yu HIRANO[2], Yukihiro KIMURA[3], Kunio MIKI[2] and Seiu OTOMO*[1]

[1]Faculty of Science, Ibaraki University, Mito 310-8512, Japan; [2] Department of Chemistry, Graduate School of Science, Kyoto University, Kyoto, Japan; [3] Organization of Advanced Science and Technology, Kobe University, Nada, Kobe 657-8501, Japan

Introduction

In purple photosynthetic bacteria, the light energy is absorbed by two types of light-harvesting complexes (LH1, LH2), and then is transferred efficiently to the reaction center (RC) where the primary charge separation takes place across the membrane and a cyclic electron transport chain occurs. The LH1 complex is located intimately around the RC with a fixed stoichiometric ratio to form the so-called core complex (LH1-RC). LH1 is a large oligomer of a basic structural unit composed of a heterodimer of two small integral membrane polypeptides (α and β, ca. 6 kDa) associated with bacteriochlorophyll (BChl) and carotenoid molecules. *Thermochromatium* (*Tch.*) *tepidum* is a thermophilic purple sulfur photosynthetic bacterium originally isolated from a hot spring in Yellowstone National Park. It grows anaerobically at optimum temperatures of 48 – 50 ºC with an upper limit of 58 ºC, and contains an unusual LH1 complex that absorbs maximally around 917 nm (Q_y transition). In a series of investigations, we found that the *Tch. tepidum* LH1 is highly stable at room temperature when copurified with RC in a LH1-RC form, and calcium ions are involved in both the enhanced thermal stability and the large red shift of the LH1 Q_y transition[1, 2].

We further explore the putative Ca^{2+}-binding sites in *Tch. tepidum* LH1 complex by using both native and biosynthetically Sr-substituted LH1-RC complexes. Preliminary results on crystallization of the native LH1-RC complex are reported towards future X-ray crystal structure determination.

Materials and Methods

Crystallization of the native *Tch. tepidum* LH1-RC complex was performed using sitting-drop vapor-diffusion method at 20 ˚C. The protein solution was mixed with the same volume of precipitant solution (20 mM Tris-HCl, pH 7.5, 3 mM DPC, 50 mM $CaCl_2$, 16% w/v PEG3000).

Sr-substituted LH1-RC complex was obtained by cultivating the *Tch. tepidum* cells in a medium containing Sr^{2+} instead of Ca^{2+}, followed by the purification procedure described previously[1]. Spectroscopic and thermodynamic characterizations were carried out on the Sr-LH1-RC complex.

Results and Discussion

Crystals of the native *Tch. tepidum* LH1-RC complex were obtained using PEG as a precipitant. The crystals showed a rhombic shape with typical size of 0.4 mm × 0.2 mm × 0.2 mm. We have being trying to improve the crystal quality by screening the optimum condition of buffer pH, detergents, small molecule additives, cryoprotectants and soaking with heavy metals in order to get higher-resolution diffraction and finally to identify the Ca^{2+}-binding sites.

The LH1-RC complex purified from Sr-substituted cells exhibited a Q_y transition at 888 nm, 27 nm shorter than that of native LH1-RC. Removal of Sr^{2+} resulted in a spectral change of the LH1 Q_y transition to around 870 nm[3]. Reconstitutions of Sr^{2+} and Ca^{2+} into the Sr-depleted complex resulted in a red-shift of the Q_y peak back to 888 nm and 908 nm, respectively, although the latter was distinctively different from the native Q_y peak position. Thermal stability of the Sr-LH1-RC was slightly lower than that of its native counterpart as revealed by differential scanning calorimetry measurement[3]. These results indicate that the Ca^{2+} ions in the native LH1-RC complex were replaced with the Sr^{2+} ions at the same or similar binding sites although the coordination states are somewhat different between each other. The differences are reflected on the absorption spectra and thermodynamic property. This study reveals evidence for the LH1 complex to have ability of adaptation to the environmental changes *in vivo* by utilizing the exogenous metal cations, and provides an alternative means to identify the metal-binding sites in this complex.

References

[1] Y. Kimura, Y. Hirano, L.-J. Yu, H. Suzuki, M. Kobayashi and Z.-Y. Wang(Otomo), *J. Biol. Chem.*, **283**, 13867(2008)

[2] Y. Kimura, L.-J. Yu, Y. Hirano, H. Suzuki and Z.-Y. Wang(Otomo), *J. Biol. Chem.*, **284**, 93(2009)

[3] Y. Kimura, Y. Inada, L.-J. Yu, Z.-Y. Wang(Otomo) and T. Ohno, *Biochemistry* **50**, 3638(2011)

*otomo@mx.ibaraki.ac.jp

KEK-PF 9C/2011G523

Effects of Diameter and Dimension of Ordered Mesoporous Metal Oxides as Templates on Formed Pt Nanoparticles and Pt–C Nanocomposites

Kazuki Oka,[1] Teruaki Koizumi,[2] Takashi Kawase,[2] Hideaki Yoshitake,[2] and Yasuo Izumi[1,*]

[1] *Department of Chemistry, Graduate School of Science, Chiba University, Inage-ku, Chiba 263–8522*

[2] *Division of Materials Science and Chemical Engineering, Faculty of Engineering, Yokohama National University, Hodogaya-ku, Yokohama 240–8501*

1. Introduction

Significant part of catalysts to make fossil fuel and to convert chemical energy to electricity depends on platinum [1]. It is essential to study the minimum size of Pt particles to perform the decomposition of hydrocarbons and electro-redox reactions of H_2 and O_2 and to maximize available surface Pt atoms in the catalytic reaction space.

In this proposal, effects of diameter and dimension of ordered mesoporous aluminum–silicon oxides on formed Pt nanoparticles and Pt–carbon nanocomposites were investigated using Pt L_3-edge XANES and EXAFS.

2. Methods

One-dimensional mesoporous ordered Al–SiO_2 Al–MCM-41 (1.1 wt% Al) was purchased from Aldrich. Three-dimensional mesoporous order Al–SiO_2 Al–MCM-48 (1.1 wt% Al) and Al–KIT-6 (1.1 wt% Al) were synthesized. The uniform pore size of Al–MCM-41, Al–MCM-48, and Al–KIT-6 was 3, 3, and 8 nm, respectively. $Pt^{II}(NH_3)_4(OH)_2{\cdot}mH_2O$ was ion-exchanged with Al–MCM-41, Al–MCM-48, or Al–KIT-6 from aqueous solution [1]. The Pt–exchanged samples were heated in hydrogen at 573 K. The samples were further reacted with acetylene diluted with nitrogen at 973 K. Then, the Al–SiO_2 part was removed by washing with hydrofluoric acid solution. Obtained replica samples were denoted as Pt–C-M41, Pt–C-M48, and Pt–C-K6, respectively.

Pt L_3-edge XAFS spectra were measured on a beamline 9C. H_2–treated samples were measured in H_2 atmosphere, but acetylene- or HF–treated samples were measured as exposed to air. The data were analyzed using the package XDAP, XAFS Services International.

3. Results and Discussion

The best-fit results of Pt L_3-edge EXAFS data are listed in Table 1. For Pt–Al–MCM-41, only a Pt–Pt peak appeared. In contrast, coordination numbers (*N*) of Pt–O bond for Pt–Al–MCM-48 and Pt–Al–KIT-6 were 2.5–2.6, suggesting that three-dimensional ordered mesoporous Al–MCM-48 and Al–KIT-6 were susceptible to interact strongly with Pt nanoparticles.

The *N* values of Pt–Pt bonds for Pt–C–M41 and Pt–C-M48 decreased to 2.5–1.2 compared to that for samples before acetylene and/or HF treatments. In contrast, the *N* values of Pt–Pt bonds for Pt–C–K6 did not decrease (3.1–4.2). It was suggested that ordered three-dimensional pores of 8 nm were most suitable to synthesize stable Pt–C nanocomposite for polymer electrolyte fuel cells and other related electro/photocatalysis.

Table 1. Best-fit Results of Pt L_3-edge EXAFS for Pt–Ordered Mesoporous Metal Oxides (Al–MCM-41, Al–MCM-48, and Al–KIT-6), Acetylene-treated Samples, and HF-treated Samples

Sample	Pt–O (or Pt–C)		Pt–Pt	
	N	*R* (nm)	*N*	*R* (nm)
Pt–Al–MCM-41	—	—	4.2	2.74
Pt–C–Al–MCM-41	1.9	2.16	4.3	2.67
Pt–C-M41	3.6	1.96	2.5	2.81
Pt–Al–MCM-48	2.5	2.15	4.4	2.72
Pt–C-M48	3.6	1.99	1.2	2.80
Pt–Al–KIT-6	2.6	2.15	3.3	2.93
Pt–C–Al–KIT-6	2.2	2.06	3.1	2.59
Pt–C-K6	2.6	2.02	4.2	2.78

Reference

[1] K. Oka, Y. Shibata, T. Itoi, Y. Izumi, *J. Phys. Chem. C*, **114**, 1260–1267 (2010).

*yizumi@faculty.chiba-u.jp

7C,9C/2011G538

Anomalous Valence Change of Zinc Ion Exchanged in MFI-Type Zeolite Being Efficient for Dissociative Adsorption of Dihydrogen

Akira Oda, Atsushi Itadani, Hiroe Torigoe, Yuusuke Sogawa, Mitsuhiro Ushio, Masayasu Nishi, Takahiro Ohkubo, and Yasushige Kuroda*
Okayama University, Okayama 700-8530, Japan

1 Introduction

Zinc ion-exchanged zeolites have been well-known to exhibit high levels of catalytic activity for dehydrogenation and aromatization of light alkanes [1,2]. In addition, the dissociative adsorption of dihydrogen (H_2) molecule has so far been recognized to occur on the zinc ion-exchanged samples at relatively low temperature [3]. Therefore, it is important to clarify the state of active centers in the samples for these phenomena from the viewpoint of the development of efficient activation catalysts for alkanes and H_2. However, the kind of exchangeable sites for zinc ions in zeolites and the state of zinc ions exchanged are not completely elucidated, although some reports have so far been made on the subject [4,5]. In this contribution, the state of zinc ions exchanged in MFI-type zeolite and/or the change in the state of zinc ions exchanged by heat-treatment in vacuo and/or heat-treatment under an atmosphere of H_2 were studied by means of X-ray absorption fine structure (XAFS) method. Through this work, we found the unprecedented redox behavior of zinc ions in MFI which work as the real activation sites for H_2 [6].

2 Experiment

Zinc ion-exchanged MFI zeolite (ZnMFI) (Si/Al ratio of 11.9; zinc ion-exchange level = 95%) was prepared at room temperature in a $Zn(NO_3)_2$ solution. The XAFS spectra were collected in transmission mode at the beamlines PF-7C and 9C equipped with a double crystal monochromator of Si(111). The self-supporting disk was placed into an in situ sample cell which is capable of pre-treatment of sample and gas introduction in situ.

3 Results and Discussion

Fig. 1 shows the Fourier transform of the extended X-ray absorption fine structure (EXAFS) oscillations at the K-edge of the zinc-ion exchanged for ZnMFI evacuated at 873 K. The analysis of the EXAFS data clarified that the zinc ion situated at the neighbourhood of three zeolite-lattice oxygen atoms with bond distance of about 2.05 Å. Taking accounts of the results of the density functional theory (DFT) calculations and other experiments, the EXAFS data indicated that the zinc ion is present at the M7 site in MFI with a certain environment and acts as the active center for H_2 dissociation: the formation of –ZnH and –OH species.

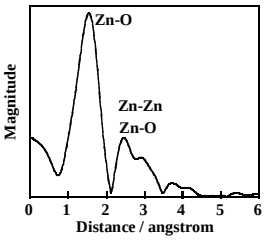

Fig. 1. EXAFS spectrum for ZnMFI.

In next, we chased the change of the state of zinc ions in ZnMFI by heat-treatment under an atmosphere of H_2. Fig. 2 represents the first derivative spectra of the X-ray absorption near edge structure (XANES) spectra (DXANES) for ZnMFI treated at various conditions. In this study, we look more closely at the change of the state of zinc ion in ZnMFI from the DXANES spectra since the distinct difference was hardly confirmed from the XANES spectra. The DXANES spectra exhibited clear difference in the changes in the respective XANES spectra; the characteristic shoulder band appears at around 9.658 keV in the DXANES spectrum for the H_2-treated sample at 573 K, together with the 9.660 keV- and 9.668 keV-bands observed for every sample. The latter two bands are assigned to the 1s–4p electronic transitions of Zn^{2+}. The Zn metal (Zn^0), which was measured as the reference material, also shows the band at 9.659 keV in the DXANES spectrum. Therefore, we can consider that the 9.658 keV-band observed for the H_2-treated sample at 573 K (in DXANES) is due to the Zn^0 formed in ZnMFI, which is well supported by DFT calculations. It is interesting that a stable Zn^0 species is nevertheless formed in MFI by the reaction of Zn^{2+} with H_2, also the order in the ionization tendency series is situated in the position between Zn^{2+} (E^0 = – 0.762 V) and H^+. The Zn^0 species formed were completely converted into the Zn^{2+} by re-evacuation at 873 K, which is accompanied by the disappearance of the characteristic band at 9.658 keV. From these results, we found the reversible redox cycle of zinc ions in ZnMFI being efficient for the dissociative adsorption of H_2: $Zn^{2+} \rightarrow ZnH \rightarrow Zn^0 \rightarrow Zn^{2+}$.

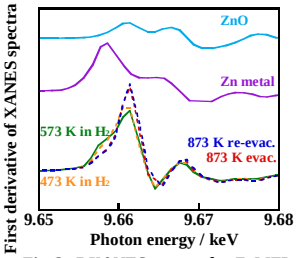

Fig. 2. DXANES spectra for ZnMFI and reference materials.

References

[1] T. Mole *et al*., Appl. Catal. **17** (1985) 141.
[2] Y. Ono, Catal. Rev.–Sci. Eng. **34** (1992) 179.
[3] V. B. Kazansky *et al*., Catal. Lett. **66** (2000) 39.
[4] El-M. El-Malki *et al*., J. Phys. Chem. B **103** (1999) 4611.
[5] L. A. M. M. Barbosa and R. van Santen, J. Phys. Chem. B **107** (2003) 14342.
[6] A. Oda *et al*., Angew. Chem. Int. Ed. Accepted.

* kuroda@cc.okayama-u.ac.jp

4B2/2011G551, 2011A1935

粉末未知結晶構造解析によるセファロスポリン系抗生物質結晶の脱水相転移の解明

PXRD Structure Analysis of Dehydration of Cephalosporin Antibiotic Hydrate Crystal

植草秀裕[1*]、藤井孝太郎[1]

[1]東京工業大学大学院理工学研究科、〒152-8551 目黒区大岡山 2-12-1

1 はじめに

水和物結晶は安定な擬似多形として理解され、医薬品原薬として多用されるが、湿度や温度などの外部環境により水和数が変化し、それに伴って結晶構造および物性が変化する。よって水和結晶の溶解性・安定性などの物性変化を解明するためには、結晶構造解析から分子間相互作用を調べる必要がある。しかし、脱水転移により単結晶が粉末結晶へと変化することが多く、単結晶構造解析により転移後の構造を調べることは困難だが、最近では粉末結晶X線回折データを直接解析することで分子・結晶構造を決定する、粉末未知結晶解析の手法が実用化段階に入りつつあり、このような相転移現象の構造的解明に威力を発揮している。

セファロスポリン系抗生物質であるエリスロマイシン（下図）は二水和物結晶として用いられるが、加熱により無水和物結晶 I へ、さらに熔解・再結晶により無水和物結晶 II に転移する事が分かった。そこで本研究では、これらの結晶構造について高分解能高精度放射光粉末 X 線回折データを測定し、粉末未知結晶構造解析を行った。

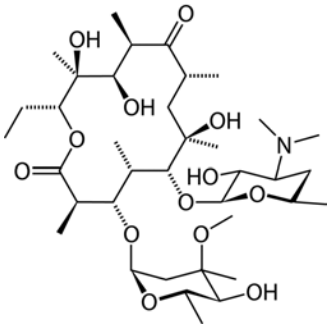

2 実験

無水和物結晶 I の粉末回折データは、SPring-8 BL02B2 の IP カメラで測定を行った（被災量子ビーム施設ユーザー支援課題として実施）。試料はキャピラリに封じ、装置上で 100℃に加熱して脱水転移を行った。無水和物結晶 II は物質構造科学研究所・放射光科学研究施設（Photon Factory）4B2 の多連装型回折計 MDS を用いて行った。予め加熱により相転移した試料粉末をキャピラリに封じて常温で測定を行った。粉末構造解析は既知の二水和物結晶中の分子構造をモデルとして実空間法（DICVOL04, DASH, GSAS）により行い、それぞれの結晶構造を得た。

3 結果および考察

最終 Rietveld 構造精密化の結果を下に示す。無水和物結晶 II は独立分子数が 2 であり、26 のパラメータを使った大規模な構造解析となったが、最終 R_{wp} が 0.0528 と良好な解析結果となった。

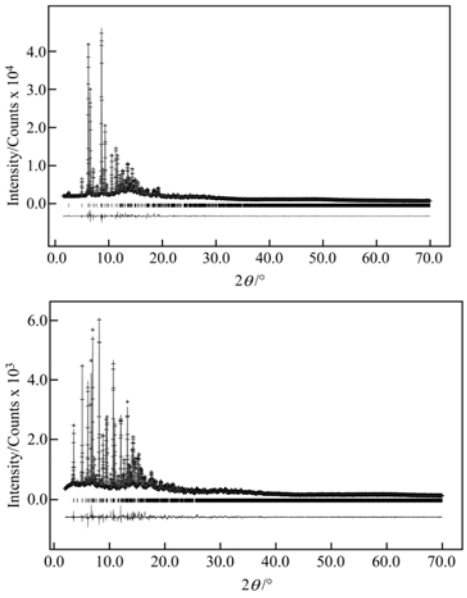

最終 Rietveld fitting (上) I): a = 9.5162 (3), b =9.5449(3), c= 46.255(1)Å, V=4201.4(3)Å^3, $P2_12_12_1$, Z=4, R_{wp}=0.0374, (下) II): a=32.6162(9), b=23.8539(7), c=10.7657(2)Å, V=8350.3(5)Å^3, $P2_12_12$, Z= 8, R_{wp}=0.0528

無水和物結晶 I の結晶中では結晶水に相当する空間が void として残っており、水和物結晶の構造と近い事が分かった。これは脱水により PXRD パターンの変化が少ない同形脱溶媒現象を示す事、また低湿度でも吸湿して水和転移しやすい事をよく説明している。一方無水和物結晶 II は、全く異なる結晶構造を持ち、分子の周りに多数の疎水性 void を持つ特異な構造を持っていた。非化学量論的な水和が起こる事はこの結晶構造に起因すると考えられる。

* uekusa@cms.titech.ac.jp

7C/2011G556

Design and Characterization of Visible Light-Responsive Ti-Based Metal–Organic Frameworks for the Application to Photocatalytic Hydrogen Evolution

Yu HORIUCHI*
Department of Applied Chemistry, Graduate School of Engineering
Osaka Prefecture University, Osaka 599-8531, Japan

1 Introduction

There has been much attention to H_2 evolution from water under sunlight in the context of clean energy production. H_2 is a promising energy source because it does not emit greenhouse gases upon combustion. In order to utilize solar light effectively the development of photocatalysts efficiently operating under visible light is urgently needed. Metal–organic frameworks (MOFs) referred to as porous coordination polymers (PCPs) are favorable candidate materials because of their diversity of chemical and structure features. The various combinations of organic linkers and metal-oxo clusters allow for accurate material design. The present study focuses on the development of an amino-functionalized Ti-based MOF (Ti-MOF-NH_2) that can absorb visible light due to the chromophore in their organic linkers and its application to visible-light-promoted H_2 evolution from aqueous media.

2 Experiment

Ti-MOF-NH_2 was prepared based on previously reported method [1]. A mixture of tetrapropyl orthotitanate, 2-amino-terephthalic acid acid, N'N-dimetylformamide (DMF), and methanol was subject to solvothermal conditions in a Teflon-lined stainless steel autoclave for 48 h at 423 K under autogenous pressure. The formed precipitate was separated by filtration, washed repeatedly with DMF and dried at room temperature overnight, followed by drying under vacuum for 1 h, yielding Ti-MOF-NH_2 as yellow powder.

Characterizations were conducted by using UV–vis, XRD, and XAFS measurements. Ti K-edge XAFS spectra were measured in the fluorescence mode at the BL-7C facilities of the Photon Factory at the National Laboratory for High-Energy Physics, Tsukuba.

Photocatalytic H_2 evolution was performed under visible-light irradiation (λ > 420 nm) from 500 W Xe lamp fitted with an appropriate cut-off filter. Ti-MOF-NH_2 was dispersed in an aqueous solution containing 0.01 M triethanolamine (TEOA) as a sacrificial electron donor. The reactant solution was degassed to remove air prior to irradiation. The evolved H_2 was analyzed by GC.

3 Results and Discussion

The UV–vis spectrum of Ti-MOF-NH_2 showed an observable band in the visible-light region up to around 500 nm. XRD measurements revealed that the synthesized Ti-MOF-NH_2 possesses a 3-D network structure coincident with conventional Ti-MOF prepared using terephthalic acid [1]. To elucidate the local structure around Ti center in Ti-MOF-NH_2 Ti K-edge XAFS analyses were performed. Fig. 1 shows Ti K-edge XANES spectra of Ti-MOF-NH_2 and titanium dioxides (anatase and rutile). Ti-MOF-NH_2 exhibited completely different spectrum from titanium dioxides, indicating that bulky titanium dioxide does not form in Ti-MOF-NH_2. Moreover the Ti-MOF-NH_2 spectrum resembles that of an intermediate titanium cluster formed during the formation of titanium dioxide nanoparticles, reported by J. Stötzel *et al* [2].

Following the confirmation of the formation of a visible light-responsive Ti-MOF, the H_2 evolution reaction from aqueous solution containing TEOA as a sacrificial electron donor was performed by using the Ti-MOF-NH_2 photocatalyst under visible-light irradiation (λ > 420 nm). Continuous H_2 evolution occurs from the beginning of the irradiation period, and the total evolution of H_2 after 3 h irradiation reaches 5.0 μmol. Thus the Ti-MOF-NH_2 was found to act as an efficient visible light-responsive photocatalyst.

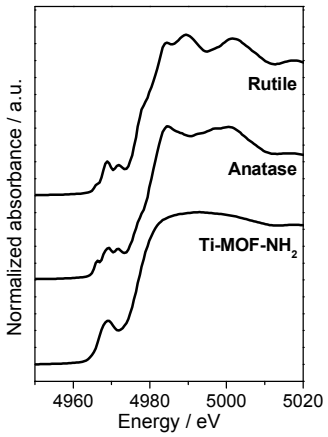

Fig. 1: Ti K-edge XANES spectra of Ti-MOF-NH_2, anatase, and rutile.

Acknowledgement

XAFS spectra were recorded at the beamline BL-7C facility of the Photon Factory at the National Laboratory for High-Energy Physics, Tsukuba, Japan (2011G556).

References

[1] M. Dan-Hardi *et al*., J. Am. Chem. Soc. **131** (2009) 10857.
[2] J. Stötzel *et al.*, J. Phys. Chem. C 114 (2010) 6228.

* horiuchi@chem.osakafu-u.ac.jp

9A/ 2011G558

Attempt to observe the direct interaction between Au-Au in the luminescent

Kiyotaka Asakura[1*], Hiromitsu Uehara[1], Hiroko Ariga[1], Satoru Takakusagi[1], Sayaka Kurenuma[2], Mai Muromoto[2], and Hajime Ito[2]

[1]Catalysis Research Center, Hokkaido University, Sapporo 001-0021, Japan.
[2]Division of Chemical Process Engineering, Graduate School of Engineering, Hokkaido University, Sapporo, 060-8628, Japan

1 Introduction

Reversible mechanochromism is the phenomenon of color change induced by mechanical grinding or pressing of a solid sample, and the subsequent reversion to its original color reversibly through treatment such as heating or recrystallization. Photoluminescent compounds that possess mechanochromic properties in their solid-state emissions can provide unique recording or sensing materials that involve luminescence detection. The mechanochromic luminescence behavior of $[(C_6F_5Au)_2(\mu$-1,4-diisocyanobenzene)](**1**), has been reported as the photoluminescence of the solid, upon grinding, to undergo a drastic change and, upon exposure to solvent or its vapor, being restored to its original color.[1]

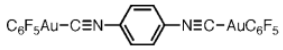

(1)

It was assumed that intermolecular aurophilic interactions were responsible for the altered emission of the ground samples. But direct evidence was hardly obtained because of its amorphous structure after the grinding. In this work we tried to elucidate the Au-Au interaction directly by the difference EXAFS method.

2 Experiment

The sample was prepared in a previously reported way.[1] The experiments were carried out in BL9A of Photon Factory. Au L_3 edge was measured at 15 K in order to reduce the thermal vibration of Au-Au bonding.

3 Results and Discussion

Figure 1 shows the EXAFS oscillations before and after the grinding process. There was no big difference, indicating the Au molecular structure was unchanged.

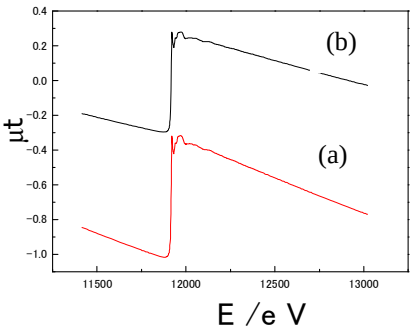

Fig.1 XAFS spectra of (**1**) before (a) and after (b) grinding.

We carried out the difference spectrum analysis between the two. Figs. 2 and 3 show the difference EXAFS spectrum and its Fourier transform, respectively. A small oscillation appeared in Fig.2 which was Fourier transformed to give a peak at 2.5 Å. We performed the curve fitting analysis assuming the peak might appear with the Au-Au interaction and found 0.36 Au was present at 3.17 Å. However, the peak was very small and more careful investigations such as checking the reproducibility and measuring the other similar samples which show mechanochromism are necessary as well as the measurement of the sample at much lower temperature (around 4 K).

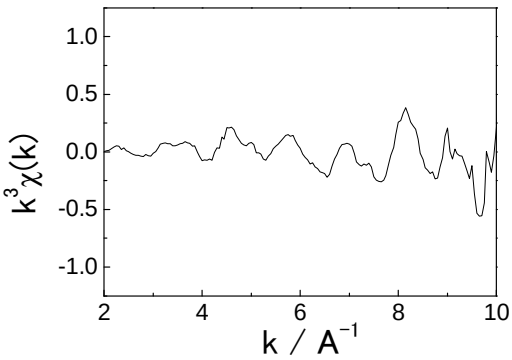

Fig.2 A difference spectrum between the ones after and before the grinding sample measured at 15 K.

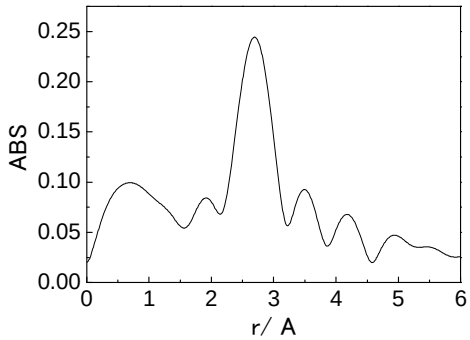

Fig.3 Fourier transform of the difference spectrum in Fig.2.

[1] H. Ito, T. Saito, N. Oshima, N. Kitamura, S. Ishizaka, Y. Hinatsu, M. Wakeshima, M. Kato, K. Tsuge, M. Sawamura, *J. Am. Chem. Soc.* 2008, **130**, 10044.

*askr@cat.hokudai.ac.jp

7C, NW10A/2011G559

タンタルおよびモリブデンハライドクラスター触媒の担持構造
Structure of supported tantalum and molybdenum halide clusters

上口賢 [1*], 長島佐代子 [2], 白井誠之 [3], 山口有朋 [3]
[1] 理化学研究所　〒351-0198 和光市広沢 2-1
[2] 埼玉大学　〒338-8570 さいたま市桜区下大久保 255
[3] 産業技術総合研究所　〒983-8551 仙台市宮城野区苦竹 4-2-1

1 はじめに

直接結合した 3 個以上の金属原子を有する金属クラスター化合物は複数の金属原子サイトが協奏的に働くことにより新たな反応性や選択性を発現する触媒として期待されている。しかし、これまで主として用いられてきた、炭素が配位した有機金属クラスターは金属–金属結合が弱いため、高々200 ℃程度で分解し生じた単核錯体などの断片が真の触媒活性種であることがほとんどである。そこで我々は 650–1700 ℃で合成され熱的に安定と考えられる、ハロゲンを配位子とするクラスター（ハライドクラスター）を触媒として利用する研究を行っている。これまでは主に結晶性のクラスターを担体等に担持せずそのまま用い、ヘリウムなどのガス気流下で加熱活性化を行うことにより様々な反応の触媒となることを報告してきた[1]。また、触媒が結晶性であるため加熱による構造の変化を単結晶または粉末 X 線回折により追跡でき、例えばモリブデンクロライドクラスターでは 500 ℃程度まで金属クラスター骨格が保持されることを見いだしている[2]。一方、クラスターを担体に担持すれば触媒の活性が著しく向上すると予測されるが、担持クラスターは非晶質であるため上記 X 線回折を用いた構造変化の追跡は困難である。そこで本研究では EXAFS によるハライドクラスターの構造分析の可能性を検討した。第一段階として活性化処理を行っていない種々の無担持モリブデンクラスターについて EXAFS の測定および解析を行い単結晶 X 線構造解析の結果と比較した。

2 実験

モリブデンクラスター $[Mo_6Cl_8]Cl_2Cl_{4/2}$ (**1**) および $[(Mo_6Cl_8)Cl_4(CH_3CN)_2]$ (**2**)（図 1 ）を文献記載の方法により合成した[3, 4]。クラスター（15 mg）を窒化ホウ素（200 mg）と均一になるまで混合した後、カプトンフィルムを窓材に用いたアルミ製のセルに封じこめた。測定は AR-NW10A にて行った。Mo *K*-edge に対し透過法を用い、X 線の単色化にシリコン二重結晶モノクロメータを用いて室温で測定を行った。標準試料にはモリブデン箔を用いた。解析にはプログラム UWXAFS を用いた。

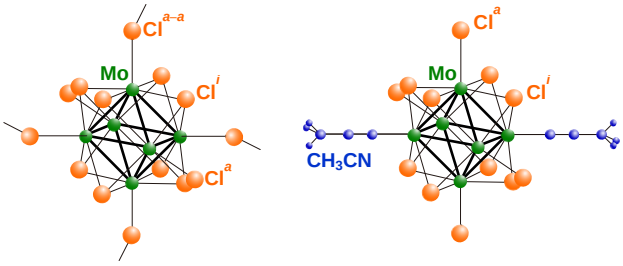

図 1 ：$[Mo_6Cl^i_8]Cl^a_2Cl^{a-a}_{4/2}$ (**1**) および $[(Mo_6Cl^i_8)Cl^a_4(CH_3CN)_2]$ (**2**)

3 結果および考察

カーブフィッティングにより求めた構造パラメーターを表 1 に示す。**1** における最適値での結合長は単結晶 X 線構造解析により決定した Mo–Mo（2.60 Å）および Mo–Cl（2.47 Å）の結合長とよく一致し[5]、配位数も図 1 の構造（Mo–Mo では 4, Mo–Cl では 5）と概ね一致した。**2** についても同様である。以上から EXAFS の利用によりハライドクラスターの構造分析が可能であることが明らかになった。

表 1: Mo K 吸収端の EXAFS ﾌｨｯﾃｨﾝｸﾞﾊﾟﾗﾒｰﾀｰ

クラスター	結合	結合長/Å	配位数
1	Mo–Mo	2.61(1)	4.0(8)
	Mo–Cl	2.49(2)	5.8(10)
2	Mo–Mo	2.62(2)	4.0(15)
	Mo–Cl	2.49(3)	6.0(16)

参考文献

[1] 上口賢ら, 触媒 **49** (2007) 554.
[2] S. Kamiguchi *et al.*, J. Mol. Catal. A **253** (2006) 176.
[3] J. C. Sheldon, J. Chem. Soc., (1960) 1007.
[4] W. M. Carmichael et al., J. Inorg. Nucl. Chem., **29** (1967) 1535.
[5] H. G. Von Schnering *et al.*, Z. Kristallogr., **208** (1993) 368.

* kamigu@riken.jp

NW10A/2011G619

オキソ酸塩に担持した Rh 触媒の局所構造解析
Local structure analysis of Rh catalysts supported on oxoacid salts

池上啓太*, 日隈聡士, 町田正人
熊本大学大学院自然科学研究科、〒860-8555 熊本市中央区黒髪 2-39-1

1 はじめに

自動車触媒用の貴金属の需要は、2000 年以降急激に増加している。そのため、貴金属使用量削減を目指した触媒開発が求められている。貴金属触媒微粒子は、高温で粒成長を起こし比表面積が激減するために劣化する。この熱劣化を防ぎ、調製時の高分散状態を保持できれば貴金属使用量を削減できる。これに対してわれわれは、貴金属触媒微粒子の高分散化を実現する新規担体物質として耐熱性オキソ酸塩が有望であることを見出した[1]。本研究では、各種オキソ酸塩（リン酸塩、硫酸塩、ホウ酸塩）と Rh との間の相互作用に寄与する局所構造を解析し、リン酸塩上の Rh が高活性を示す要因を解明した。

2 実験

種々の担体($AlPO_4$, ZrP_2O_7, $LaBO_3$, $La_2O_2SO_4$, SiO_2, La-Al_2O_3, ZrO_2 and MgO)に $Rh(NO_3)_3$ を含浸し、空気中 600 ˚C, 3 h の加熱により担持 Rh 触媒を得た。Rh 吸収端の XAFS は、NW10A にて透過法で測定した。検出器ガスは入射側 Ar 100%、出射側 Kr 100%を用いた。

3 結果および考察

Fig. 1 にオキソ酸塩担体上に担持した Rh 触媒の K 吸収端 EXAFS を示す。酸化物担体を用いた場合、Rh-O-M(M:金属)に帰属されるピークが認められ、Rh 酸化物は酸素を介した結合によって担体上に固定化されている。これに対して、リン酸、ケイ酸塩、硫酸塩では、それぞれ Rh-O-P, Rh-O-Si, Rh-O-S に帰属される結合を形成しており、オキソ酸ユニットを介した Rh との相互作用を示唆している。また、ホウ酸塩($LaBO_3$)では第 2 配位圏に Rh-O-La に帰属できるピークを示さず、ホウ酸ユニットを介した結合(Rh-O-B)の可能性がある。

Rh-O-M に代わって Rh とオキソ酸ユニットとの結合が形成する原因として、金属オキソ酸塩の化学結合様式があげられる。DFT 計算によると、例えば、リン酸塩 $AlPO_4$(tridymite 相)の場合、結晶構造は共有結合した PO_4 四面体と Al^{3+}とから構成されるが、Al^{3+}と PO_4 との間はイオン結合的である。このように共有結合とイオン結合が共有するオキソ酸塩の構造的特徴が、Rh との相互作用に反映されると推定される。

種々の担体の O1s XPS を測定したところ、オキソ酸塩の O1s の束縛エネルギー(B.E.)は表面酸素が SiO_2 と同様に共有結合性の強い状態であることを示した。酸化状態にある担持 Rh 触媒の H_2-TPR 測定より RhO_x の還元温度(T_R)を測定した。T_R は表面酸素がイオン結合性を示す担体ほど上昇する傾向を示した。これは担体との相互作用による RhO_x の安定化効果を示唆している。これに対して担体表面酸素が共有結合性になるほど RhO_x は易還元性になった。担持 Rh 触媒を用いた NO-CO-C_3H_6-O_2 反応の結果をもとに、NO 転化率が 50%に達する温度 T_{50} と RhO_x の還元性との関係を調べた。RhO_x が易還元性であるほど低温で触媒反応が開始する傾向が確認され、NO-CO-C_3H_6-O_2 反応における担持 Rh 触媒の活性種が金属 Rh であることに一致する。

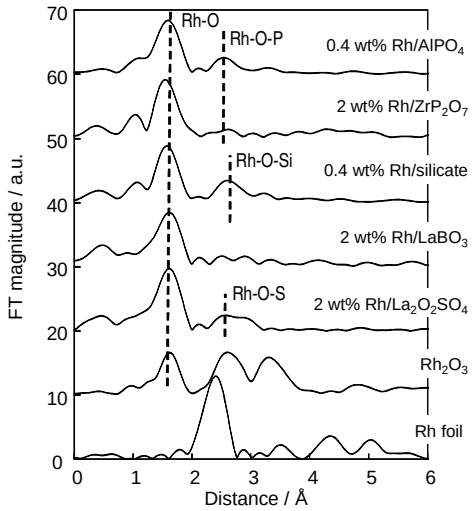

Fig. 1 Fourier transformed Rh K-edge EXAFS for Rh loaded on different oxoacid salts.

4 まとめ

本研究では、$AlPO_4$ 担持 Rh 触媒の高い熱安定性と高活性に寄与する因子を局所構造の観点から明らかにした。リン酸塩をはじめとするオキソ酸塩担体上の Rh 触媒が低温触媒活性を示す理由は、Rh−担体間の相互作用が RhO_x の易還元性を損なわないためと考えられる。

5 参考文献

[1] M. Machida et al., Chem. Mater., **21** (2009) 1796.

* ikeue@kumamoto-u.ac.jp

2011P101

放射光による絶対不斉重合
Absolute asymmetric polymerization with synchrotron light

後藤 博正 [1,2], 川畑 公輔 [2,] 新田佑介 [2], 川島裕嗣 [2],
中尾裕則 [3], 張小威 [3], 平野馨一 [3], 村上洋一 [3], 伊藤正久 [4]

[1] 筑波大学数理物質系、〒305-08573 つくば市天王台 1-1-1
[2] 筑波大学大学院数理物質科学研究科 物性・分子工学専攻、
〒305-08573 つくば市天王台 1-1-1
[3] 高エネルギー加速器研究機構 物質構造科学研究所 放射光科学研究施設、
〒305-0801 つくば市大穂 1-1
[4] 群馬大学大学院工学研究科電気電子工学専攻 〒371-8515 群馬県桐生市天神町 1-5-1

1 はじめに

本研究では放射光用いて、不斉ポリマーを合成することを目的とする。ポリマーへの放射光の照射あるいは重合中における放射光の照射により、右巻きあるいは左巻きのらせん体が分解することにより対称性がなくなり、光学活性を示すことが予想される。

現在までに我々はカイラリティー制御の観点から液晶を用いてカイラリティーをもたない原材料から、光学活性触媒を用いることなく、光学回転をもち、さらにこれを電場で駆動させることのできる導電性高分子の合成を行った。本研究では、液晶を用いることなく放射光を用いてカイラリティーを制御することを試みた。

2 実験

2.1. 放射光照射下での電解重合

実験は放射光（KEK, BL-3C）を、モノマーを含む電解液に照射しながら電解重合を行い、この酸化-還元の様子をサイクリックボルタンメトリーで観測した。

2.2. 光硬化樹脂に光異性体をブレンドしたポリマーの放射光照射下での光硬化

光重合性の液状モノマーにアゾベンゼンを溶解させ、これを放射光照射によって光硬化させた。

3 結果および考察

放射光照射下での電解重合におけるサイクリックボルタモグラムでは良好な酸化-還元サイクルを示しながら電流密度が上昇したことより、良好な電解重合が行われたことを示した。また光硬化反応においてアゾベンゼンドープしたフィルムは400－500 nmに強い吸収を示した(Fig.1)。通常n-π*遷移に由来するこの吸収体の強度は低いが、今回のように強い吸収を示したのは、エネルギーの高い放射光によって、高い効率で*cis*に異性化したアゾベンゼンが、そのままの形で光硬化性樹脂により固められたためであると思われる。

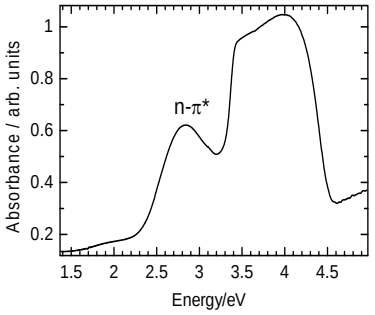

Fig. 1. 放射光下で光硬化反応を行ったアゾベンゼンを含むポリマーの紫外－可視吸収スペクトル

4 これから

円偏光白色放射光下でのπ−共役系ポリマーの合成に関しては今までほとんど報告例がない。また電解重合を放射光下で行ったことや、光異性色素を分散した系での光誘起硬化反応を行った例は、今回のレポートが初めてであると思われる。今後は得られたポリマーの円偏光二色性や直線偏光二色性を評価する。また別途、アミノ酸残基をもつポリマーの合成にも成功しているため、このサンプルに放射光を照射しその性質の変化を調べて行く。放射光は外部摂動となり、特殊な反応場を形成する。ここでの化学合成、特に有機ポリマーの合成は今までにない試みである。

NW-10A, 7C/2012G069

EXAFS analysis of Pt-core/Rh-shell bimetallic nanoparticles prepared by multi-step reduction processes

Hisahiro Einaga*, Kana Kimura and Yasutake Teraoka
Department of Energy and Material Sciences, Faculty of Engineering Sciences, Kyushu University, 6-1, Kasuga-koen, Kasuga, Fukuoka, 816-8580 Japan

1 Introduction

Preparation of supported metal nanoparticles with high dispersion is one of the important topics in the research field of catalysis science and technology. Our preparation methods involve the formation of colloidal nanoparticles by the reduction of metal ions in alcohol-ethanol solution in the presence of protecting polymers. We have reported that highly-dispersed Pt/TiO2 catalysts were obtained by this method [1]. This method is also effective for obtaining bimetallic nanoparticles composed of two kinds of noble metals, such as Pt and Rh [2]. We herein report the EXAFS studies of Pt-core/Rh-shell bimetallic nanoparticles prepared by multi-step reduction processes using photoirradiation and refluxing in aqueous ethanol solution.

2 Experimental

Pt nanoparticles were prepared by photoreduction of $PtCl_4^{2-}$ to Pt in EtOH-H_2O solution in the presence of poly-N-vinylpyrrolidone (PVP). An aqueous ethanol solution containing $RhCl_3$ and PVP was added to the Pt-containing colloidal dispersion and the mixed solution was refluxed for 1h. EXAFS measurements were performed in transmission mode and fluorescence mode at room temperature, using BL-NW10A and BL-7C at KEK-PF.

3 Results and Discussion

Pt-Rh bimetallic nanoparticles prepared by the photoirradiation-refluxing steps have the average particle sizes with ca. 3.0 nm. Fig. 1 shows the EXAFS spectra of the samples where the atomic ratio of Pt-Rh was 4:1, 1:1, 1:4, along with reference alloy foils. The Pt L3-edge spectra show that the bands due to Pt-Pt bonds were mainly present in the sample with the Pt-Rh ratio of 1:1 and 4:1. On the other hand, no obvious Rh-Rh bonds were observed for these samples, as shown in the Rh-K edge spectra, indicating that Pt-Rh bonds were formed in these samples.

When the Pt-Rh ratio was changed to 1:4, the bands due to Rh-Rh bonds appeared for the Rh-K spectra and the bands were split to two peaks due to the phase shift caused by the formation of Pt-Rh bonds.

On the basis of the findings described above, we proposed the models for Pt-Rh bimetallic nanoparticles. For the particles with lower Rh/Pt ratio than that corresponding to monolayer coverage, Rh metals were highly dispersed on Pt nanoparticles, whereas Pt nanoparticles were fully covered with Rh metals for high Rh/Pt ratio. Thus, Pt-core/Rh-shell bimetallic nanoparticles were obtained by our preparation methods. In addition, the particles were deposited on TiO_2 by liquid phase adsorption processes. FTIR studies for the samples after CO adsorption revealed that the particles retained Pt-core/Rh-shell structures.

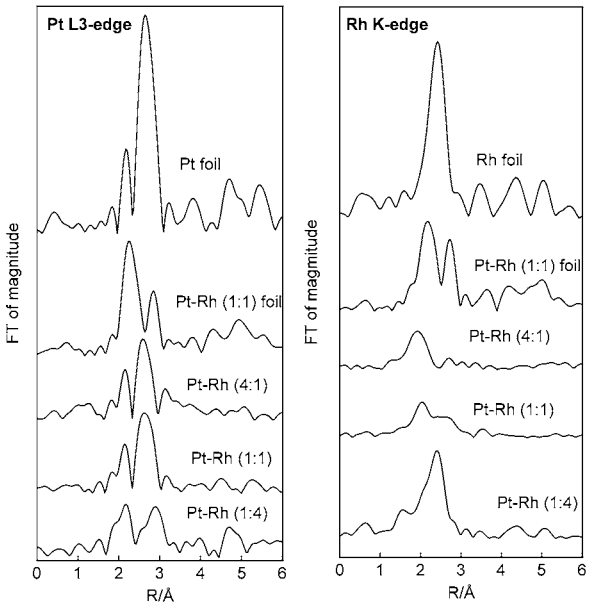

Fig. 1: EXAFS spectra of Pt-Rh bimetallic nanoparticles and reference foils.

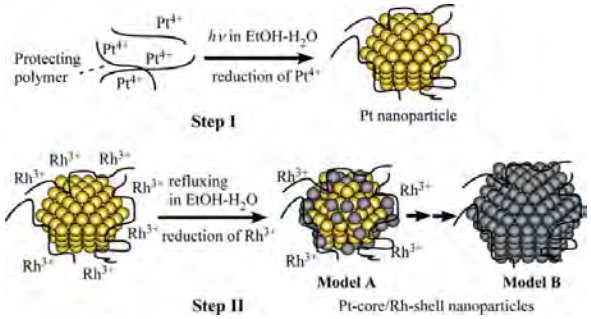

Fig. 2: Proposed models for Pt-core/Rh-shell bimetallic nanoparticles.

References

[1] H. Einaga, H. Harada, Langmuir, **21** (2005) 2578.
[2] H. Harada, H. Einaga, J. Colloid. Interf. Sci., **308,** (2007) 568.

* einaga.hisahiro.399@m.kyushu-u.ac.jp

1C/2006S2-002

Local Valence Electronic States of SiO_2 Ultrathin Films Grown on Si(111) Studied Using Auger Photoelectron Coincidence Spectroscopy (APECS): Observation of Upward Shift of Valence-Band Maximum Depending on the Interface Structure

Takuhiro KAKIUCHI[*1], Narihiko FUJITA[2], Kazuhiko Mase[3, 4], and Masatoshi TANAKA[2]
[1]Department of Chemistry, Faculty of Science, Ehime University, 2-5 Bunkyocho, Matsuyama, Ehime 790-8577, Japan
[2]Department of Physics, Faculty of Engineering, Yokohama National University, 79-5 Tokiwadai, Hodogaya-ku, Yokohama 240-8501, Japan
[3]KEK-PF, Tsukuba, Ibaraki 305-0801, Japan
[4]Department of Materials Structure Science, School of High Energy Accelerator Science, the Graduate University for Advanced Studies, 1-1 Oho, Tsukuba 305-0801, Japan

Introduction

The local valence electronic states of SiO_2 ultrathin films grown on Si single crystal (SiO_2/Si) have been studied extensively because (1) in-depth understanding of the electronic properties of surfaces and interfaces from an atomic point of view is of fundamental importance in science, and (2) these films play dominant roles in metal-oxide-semiconductor field-effect transistors (MOS-FETs). Recently, We found that the valence electronic states in the vicinity of the Si^{n+} site of SiO_2/Si(100) ultrathin films shift to deeper binding energies as n increases and that the valence-band maximum (VBM) of the SiO_2 ultrathin films shifts toward the Fermi level by about 1.6 eV as the SiO_2 thickness decreases to 1.2–1.1 ML (1.7–1.5 Å) [1]. In this study, we investigate the local valence electronic states of the surface of the SiO_2/Si(111) ultra-thin films by using Si-$L_{23}VV$ Auger electron – Si^{4+}-2p photoelectron coincidence spectroscopy (Si-$L_{23}VV$-Si^{4+}-2p APECS, the oxidation number represents the number of oxygen bonding to Si) [2].

Results and Discussions

Figure 1 shows the Si-2p photoelectron spectrum of a SiO_2/Si(111) with a thickness of 3.4 Å (≈2.2 ML, 3.4-Å SiO_2/Si(111)). The Si-2p peaks are decomposed into the Si^{n+}-2p photoelectron components (n = 0, 1, 2, 3, 4). The

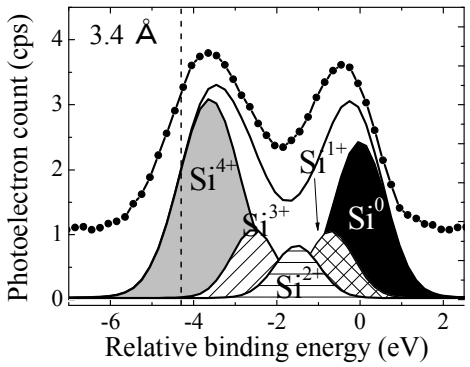

Fig. 1. Si-2p photoelectron spectrum of SiO_2 thermally grown on Si(111)-7×7 surface.

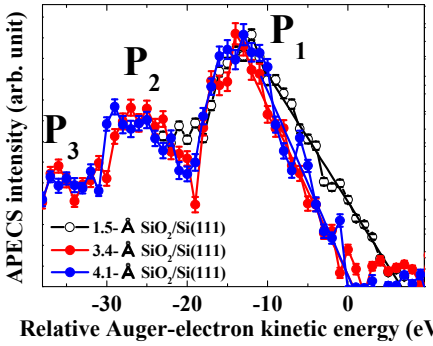

Fig. 2. Si-$L_{23}VV$-Si-2p APECS of SiO_2/Si(111) with the various thickness.

straight dashed line at +4.2 eV represents the Si^{4+}-2p photoelectron kinetic energy (*PeKE*) position taken as the trigger signals for APECS measurements.

Figure 2 shows a series of Si-$L_{23}VV$-Si^{4+}-2p APECS spectra for 4.1-, 3.4-, and 1.5-Å SiO_2/Si(111). The Si^{4+}-2p *PeKE* positions taken as trigger signals of these APECS were set to the same value. Every Si-$L_{23}VV$-Si^{4+}-2p APECS spectrum shows clear three peaks (P_1–P_3). The P_1 peaks shift by ≈1 eV to the higher-*AeKE* side, while the cut-offs shift by ≈6 eV to the higher-*AeKE* side as the SiO_2 thickness decreases. These results indicate that the binding energies of valence band maximum of 1.5-Å SiO_2/Si(111) are shifted upwards by ~2.7 eV (toward the Fermi level) in comparison with that of 4.1-Å SiO_2/Si(100). This upward shift is much larger than that of SiO_2/Si(100)-2×1. We attribute the large shift of the VBM of SiO_2/Si(111) to the formation of SiO_2 islands on the 7×7 structure and to the presence of Si^{1+} atoms adjacent to the SiO_2 sites [2].

References

[1] T. Kakiuchi and K. Mase *et al.*, J. Phys. Soc. Jpn. **80**, 084703 (2011).
[2] T. Kakiuchi and K. Mase *et al.*, J. Phys. Soc. Jpn. **81**, 074706 (2011).
* kakiuchi.takuhiro.mc@ehime-u.ac.jp

4C/2008G124, 2009G038, 2010G051

In situ Structural Studies on Ag/AgCl Reaction at the Underpotentially Deposited on the Au(111) Electrode Surface

Toshihiro KONDO[*1], Jun MORITA[2], Tomoko KATSUZAKI[2], Satoru TAKAKUSAGI[2], Kazuhisa TAMURA[3], Masamitu TAKAHASI[3], Jun'ichiro MIZUKI[3], Takuya MASUDA[2], and Kohei UOSAKI[2,4]

[1]Ochanomizu University, Ohtsuka, Bunkyo-ku, Tokyo 112-8610, Japan

[2]Hokkaido University, Sapporo 060-0810, Japan

[3]Japan Atomic Energy Agency, Koto, Sayo-cho, Hyogo 679-5148, Japan

[4]MANA, National Institute for Materials Science (NIMS), Tsukuba, Ibaraki 305-0044, Japan

Introduction

To fully understand the mechanisms of electrochemical reactions and to apply these reactions to modern nanotechnoloty such as fuel cells, sensors, and molecular devices, it is very important to know the structures at the electrode/electrolyte interfaces in situ in real time with an atomic resolution. It is also well-known that physical and chemical properties of an ultrathin metal layer on a foreign substrate are different from those of the bulk metal [1,2]. The establishment of preparation methods of ultrathin metal films with ordered structures and understanding of the origin of their unique physical and chemical properties are very important for both fundamental science and industrial applications. For example, we have studied the structure of an underpotentially deposited (UPD) Ag ultrathin layer on a Au(111) surface using in situ surface X-ray scattering (SXS) technique and proved that the UPD Ag layer on Au(111) is pseudomorphic mono- and bi-layers at 50 and 10 mV (vs. Ag/Ag^+), respectively [3], and the structure of the Ag bilayer is intact even after the circuit was disconnected and the surface exposed to ambient atmosphere [4].

Ag/AgCl reaction (Eq. (1)) is one of the most fundamental reactions in electrochemistry and is a basis for a Ag/AgCl reference electrode.

$$Ag + Cl^- \rightleftarrows AgCl + e^- \quad (1)$$

Moreover, the silver halides have been playing an important role in photography. There are, however, no reports about Ag/AgCl reaction at an atomic level, although several structural studies on a Cl monolayer on a Ag single crystal surface with an atomic dimension are available. This is because when potential is made positive so that the chlorination reaction (forward reaction of Eq. (1)) proceeds at the Ag single crystal electrode, the reaction takes place not only at the surface but also at the bulk, and the aggregates of AgCl clusters, in which atomic arrangements should be random, are formed. Furthermore, the electrochemical reduction of AgCl does not result in an atomically flat single crystalline Ag surface.

Here, we were able to investigate the Ag/AgCl reaction at an atomic level for the first time by using the Ag bilayer prepared by UPD on Au(111) (Ag(2ML)/Au(111)) as a substrate. Electrochemical quartz crystal microbalance (EQCM), scanning tunneling microscopy (STM), SXS, and electrochemical techniques were used [5].

Experimentals

Prior to Ag UPD, the Au(111) disk electrode was annealed using a Bunsen burner and quenched in ultrapure water. Only the (111) face was contacted to a deaerated 50 mM H_2SO_4 containing 1 mM Ag_2SO_4 while keeping the potential at +700 mV (vs. Ag/Ag^+). The Ag UPD bilayer on the Au(111) electrode was electrochemically prepared by scanning the potential from +700 to +10 mV with a scan rate of 5 mV s^{-1}. After that, the surface was rinsed and set to the SXS cell. In situ SXS measurements were carried out in 50 mM H_2SO_4 containing a given amount of NaCl at a several electrode potentials in BL4C at Photon Factory.

Results and Discussion

From the results of EQCM, STM, and SXS, we concluded as follows; Ag bilayer was anordically converted to AgCl when the potential more positive than +230 mV (vs. Ag/AgCl), at which the anodic current peak due to the chlorination was observed, was applied. The formation of AgCl clusters and the AgCl monolayer of (√13×√13)*R13.9*° structure, although the former and the latter were formed slowly and very slowly, respectively. The AgCl monolayer of (√13×√13)*R13.9*° structure was transformed to the AgCl monolayer of (4×4) structure when the potential more positive than +480 mV, at which a very broad anodic current peak was observed, was applied for prolonged time. The AgCl monolayer of (4×4) structure was returned to the AgCl monolayer of (√13×√13)*R13.9*° structure when the potential became more negative than +330 mV, at which a sharp cathodic current peak was observed. Both AgCl clusters and the AgCl monolayer of the (√13×√13)*R13.9*° structure disappeared, and the Ag monolayer, not bilayer, was formed on the Au(111) surface when the potential became more negative than +180 mV, where a very large cathodic peak was observed.

In the sequent potential cycling between 0 and +600 mV, the conversion of Ag monolayer ⇄ AgCl cluster + AgCl monolayer of (√13×√13)*R13.9*° ⇄ AgCl cluster + AgCl monolayer of (4×4) took place repeatedly.

References

[1] G. A. Somorjai, "Surface Chemistry and Catalysis", Wiley, New York (1994).

[2] H. Naohara et al., J. Electroanal. Chem., 500, 435 (2001).

[3] T. Kondo et al., J. Electroanal. Chem., 532, 201 (2002).

[4] T. Kondo et al., Electrochem. Commun., 11, 804 (2009).

[5] K. Uosaki et al., J. Phys. Chem. C, 115, 12471 (2011).

* kondo.toshihiro@ocha.ac.jp

7C/2009G567

XANAM with Quartz tuning fork cantilever

Shushi SUZUKI*[1], Shingo MUKAI[2], Wang Jae CHUN[4], Masaharu NOMURA[3], and Kiyotaka ASAKURA[2]
[1]Nagoya University, Nagoya, Aichi 464-8603, Japan
[2]Hokkaido University, Sapporo, Hokkaido 001-0021, Japan
[3]KEK-PF, Tsukuba, Ibaraki 305-0801, Japan
[4]International Christian University, Mitaka, Tokyo 181-8585, Japan

Scanning tunnelling microscopy (STM) and noncontact atomic force microscopy (NC-AFM) provide information of physical and chemical properties of substrate surfaces at the atomic level. However, elemental analysis by those methodologies is still a difficult issue. Previously, we have proposed the X-ray aided noncontact atomic force microscopy (XANAM), a new SPM technique for chemical analysis in combination with Synchrotron X-ray. Previously, we found interaction between X-rays and the attractive force in NC-AFM measurements on Au [1-3] as two characteristic features; one is a peak occurred near the absorption edge energy of sample's element, and another is a gradual change across the absorption edge energy. We expect that the former is useful for nano-chemical analysis and imaging as our final goal. However, our AFM instrument equipped a cantilever of a Piezo-thin film type, which was not easy to high resolution measurements of XANAM. Thus, we adopted quartz tuning fork (QTF) cantilever as a new force detection system to improve signal to noise ratio and stability of measurements, for detecting the former force component preferentially.

The QTF is normally used as a high quality factor resonator for use as a stable frequency reference for a wrist watch. Previously, Giessibl reported first that the QTF could be applied to NC-AFM measurement as a cantilever with attaching a tiny sharpened metal wire tip like a STM tip, which provided a highly resolved NC-AFM image of Si(111)-(7x7) at the atomic level[4]. The QTF cantilever has three merits compared to the Si-based cantilever fabricated by semiconductor processes. First, a substance of the tip is selectable among any solid materials. It requires X-ray absorption edge energy of the tip material should be distinctively different from the one of target atoms on sample surfaces. For the XANAM measurements, this is advantageous to avoid the influence of X-ray absorption at the tip. Second, the QTF cantilever is a self-sensing and self-actuating probe. It means additional resonators and optics to measure tip deflection are not required. Thus, the instruments can be simplified and downsized to be a compact design. The second feature is also advantageous to ensure keeping the X-ray beam position between a tip and a sample surface for a long experimental time at the beam line. Then, we fabricated a home made the QTF cantilever, and examined its performance for the XANAM measurement.

In order to fabricate the QTF cantilever, we used a QTF device which is normally used for a wrist watch with resonance frequency of ~32.7 kHz. The size of QTF is 2 mm x φ1 mm without a wiring part. A small tiny metal wire was attached with adhesive glue onto a prong of the QTF by micromanipulator (Suruga Seiki Co., Ltd.). An exclusive cantilever holder was fabricated to set the QTF cantilever on the AFM stage. We used Au deposited on a Si wafers to evaluate the performance of QTF cantilever for the XANAM measurement.

Figure 1 shows a picture of QTF cantilever and a sample in our UHV chamber at the beam line. Figure 2 shows Au coated surface. We confirmed resolution of AFM images was improved. Although stability of QTF cantilever for scanning was improved under X-ray irradiation, the stability of the QTF cantilever was not sufficient to get several image frames. Thus, further improvement of the QTF cantilever is required to establish the XANAM imaging. This work is supported by a Grant-in-Aid for Scientific Research for young scientist promotion (A) (No. 20686004), from the JSPS.

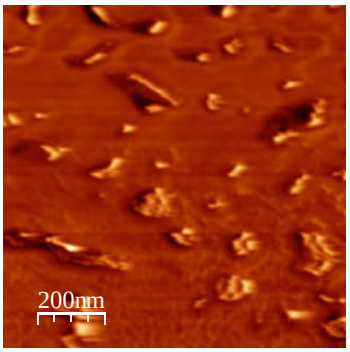

Fig.1 AFM image of Aui deposited surface on Si surface

References

[1] S. Suzuki et al., Chem.Lett. 33, 636-637 (2004).
[2] S. Suzuki et al., Catal. Today 117, 80 (2006).
[3] S. Suzuki et al., J. Phys. Conf. Ser., 61, 1171 (2007).
[4] F.J. Giessibl, Appl. Phys. Lett., 73, 3956 (1998).

*shushi@apchem.nagoya-u.ac.jp

7C, 11A/2009G629, 2011G664

スピン再配列転移を起こす Fe/Co/Pd(111)磁性薄膜における磁気異方性の研究
Study on magnetic anisotropy of Fe/Co/Pd(111) magnetic thin films exhibiting spin reorientation transitions

中山丈嗣[1]，香西将吾[1]，酒巻真粧子[2]，阿部仁[2]，雨宮健太[2]，近藤寛[1]，
[1]慶應義塾大学　大学院理工学研究科
[2]高エネルギー加速器研究機構　物質構造科学研究所

１．序

ハードディスク等の薄膜磁気記録媒体では近年垂直磁気記録方式が採られており、膜表面に対し磁化を垂直(面直)方向へ向けて情報を記録している。しかし、この垂直磁気異方性(Perpendicular Magnetic Anisotropy, PMA)は古典的な磁気双極子相互作用のみでは説明することができず、ミクロな視点から起源が未だよく分かっていないのが現状である。

磁性薄膜の磁化容易軸が面内・面直どちらに傾くかということは以下の(1)式で現象論的に理解される。

$$\Delta E = -2\pi M_s^{\,2} + K_{cr} + K_{me} + (K_s + K_i)/d \qquad (1)$$

(1)式の左辺 $\Delta E < 0$ のとき薄膜は面内磁化を示し、$\Delta E > 0$ ならば薄膜は面直磁化を示す。右辺第１項は形状磁気異方性、続いて結晶磁気異方性、磁気弾性異方性、表面・界面磁気異方性をそれぞれ表す。また d は膜厚を表す。これらの磁気異方性の微視的起源を明らかにする為、多くの研究者が様々な系を用いて検討を重ねてきた。

Fe/Co/Pd(111)磁性薄膜は図１に引用して示すように Fe 蒸着によって 2 度のスピン再配列転移(Spin Reorientation Transitions, SRT)を起こす。図１より

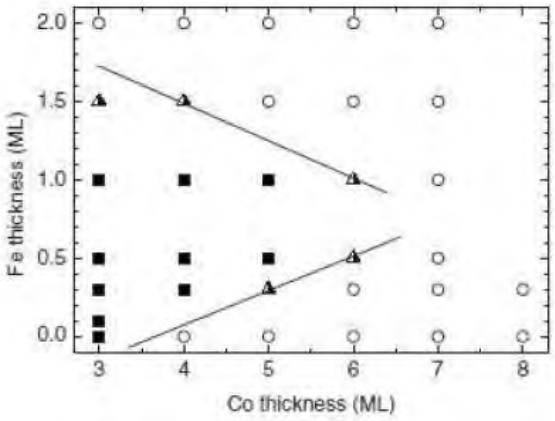

図１．Fe/Co/Pd(111)磁化容易軸方向相図[1]
(■：面直磁化　○：面内磁化)

例えば Fe(1 ML)/Co(5 ML)/Pd(111)では PMA を示す。また、転移膜厚では(1)式において $\Delta E = 0$ となる。

本研究ではこの Fe/Co/Pd(111)磁性薄膜に於いて、SRT の前後における磁性の変化と構造変化を XAFS を用いて対応付けることを目的とした。

２．実験

実験は KEK-PF BL-7C および 11A にて行った。7C では Fe および Co の K-EXAFS、XANES 測定、11A では XMCD および L-EXAFS の測定を行った。いずれの実験もビームライン末端に MCD 実験用真空槽を設置し、*in situ* で測定を行った。

３．結果および考察

SRT が 2 度観測される Fe/Co(5 ML)/Pd(111)に対して XANES 測定を行った結果の一部を図２に示す。また比較の為に Co の hcp 構造と fcc 構造を仮定した計算スペクトルを図２中に示した。

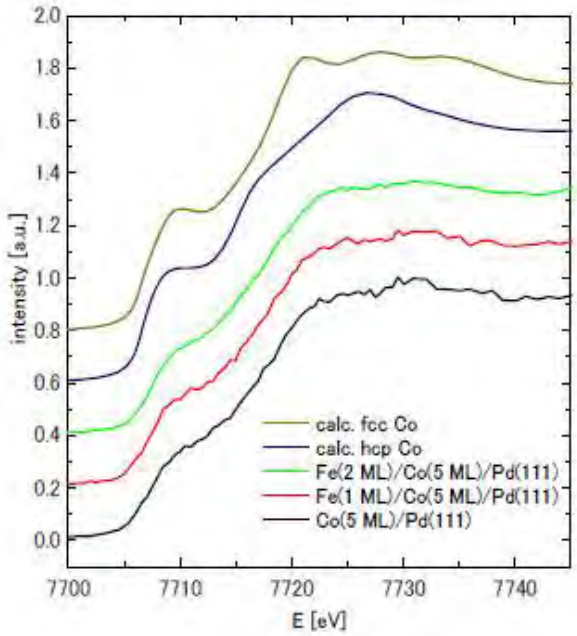

図２．Fe/Co(5 ML)/Pd(111)の Co-K edge XANES スペクトルと FEFF を用いた理論計算の比較

図２より、SRT を 2 度引き起こす Fe 蒸着過程において Co 層は fcc 構造を保ったまま変化していないことがわかる。また Co の EXAFS 解析からも、Fe の蒸着によって Co の構造が変わってないことを確認した。これらの結果は SRT の起源が、Co 層の構造変化ではなく、上にのった Fe 層の磁気構造に起因することを示唆すると考えられる。

参考文献
[1] H. Abe, et al, Phys. Rev. B 78, (2008) 014424.

* nakayama@chem.keio.ac.jp

13A/2009S2-007

Mixed valence state of TNAP on Bi(001)

Tatsuhiko Nishi[1*], Takuya Kuzumaki[2], Masayuki Yamamoto[2] and Kazuyuki Sakamoto[2]
[1]Center for Frontier Science, Chiba University, Chiba 263-8522, Japan
[2]Graduate school of Advanced Integration Science, Chiba University, Chiba 263-8522, Japan

1 Introduction

Charge transfer complexes, which are known to show various properties depending on the amount of charge transfer [1], are one of the most notable systems regarding the mixed valence states of organic materials. In the case of organic thin film, charge transfer is a key point to determine the strength of the organic molecule-substrate interaction [2].

11,11,12,12, -tetracyanonaphtho-2,6-quinodimethane (TNAP, Fig.1) is a strong acceptor type molecule and is known to show interesting phenomena [3]. For example, different molecule-substrate interactions were reported for TNAP on noble metals, such as weak interaction on Au, an ionic interaction with charge transfer on Ag, and diffusion of atoms on Cu. The difference in interactions was proposed to have a correlation with the work functions of the substrates (Au: 5.3eV, Ag: 4.7eV, Cu: 4.9eV) [3]. That is, a substrate with smaller work function was supposed to have a stronger interaction. However, despite of its small work function (4.22 eV), Bismuth (001) was considered to be inert against organic molecule [4].

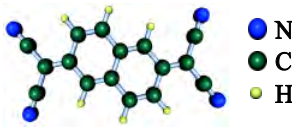

Fig. 1: TNAP

Here, we report the electronic structure of TNAP/Bi(001) obtained with X-ray photoemission spectroscopy (XPS). Mixed valence state of neutral and anionic TNAP was observed for the first monomolecular layer (ML).

2 Experimental

Samples were prepared by depositing TNAP (Tokyo Chemical Co., Ltd.) on a Bi (001) film grown on Si(111) in an ultra high vacuum (UHV) chamber. XPS measurement was performed in the UHV chamber (2.8×10^{-10} Torr) in normal emission at BL-13A. The reliability of the spectra was checked by the time dependence of the beam damage and reproducibility. All measurements were carried out at ~295 K.

3 Results and Discussion

Figure 2 shows the N1s spectra obtained at different TNAP thickness. At a thickness of 0.075 nm, whose value corresponds to a coverage of approximately 1/4 ML, a peak is clearly observed at a binding energy of 397.7eV. At 0.3 nm (1ML), two more peaks appear at binding energies of 400.0eV and 398.8 eV. Taking the previous report of tetrafluoro- tetracyanoquinodimethane (F4-TCNQ) adsorbed on graphene [5] into account, we assign the origins of the two peaks at 397.7 eV and 400.0 eV to the anionic and neutral nitrogen, respectively. This indicates that TNAP is anionic at 1/4 ML and mixed valence state of anionic and neutral nitrogen is present at 1ML. Furthermore, the peak of anion shifts slightly to higher binding energy by increasing the thickness. This indicates that anionic TNAP is not strongly hybridized to Bi(001). The result about the hybridization has been confirmed by the Metastable atom electron spectroscopy (MAES) spectra, in which a density of states (DOS) is observed just below the Fermi energy (in the case of strong hybridization, the DOS of the single occupied molecular orbital would not appear just below the E_F like the case of TNAP/Ag or Cu). In order to obtain information about the film growth mode, we have measured the cut-off of secondary electron in ultraviolet photoelectron spectroscopy (UPS) that showed a large shift up to 1 ML and a small shift at higher coverage. This change in cut-off indicates that the film does not grow as islands. Regarding the peak at 398.8 eV, its origin might be anionic TNAP affected by the surrounding neutral TNAP. The present results suggest that the molecule–substrate interaction is comparable to the intermolecular one, and that Bi(001) plays as a donor, which is different from the cases of other organic molecule systems.

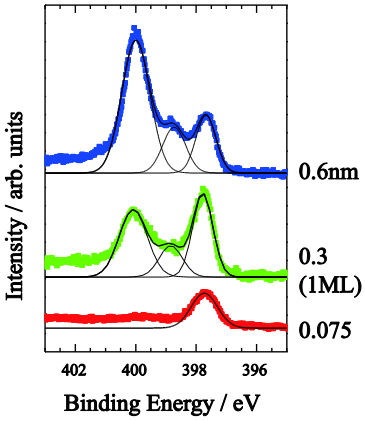

Fig. 2: N1s spectra

References
[1] G. Saito and Y. Yoshida, Bull. Chem. Soc. Jpn. 80 (2007) 1.
[2] H. Ishii *et al.*, Adv. Mater. 11 (1999) 605.
[3] K. Kanai *et al.*, J. Appl. Phys. **105** (2009) 023703; K. Kanai and K. Seki, J. Vac. Soc. Jpn. **50** (2007) 722.
[4] H. Kakuta *et al.*, Phys. Rev. Lett. **98**, 247601 (2007).
[5] C. Coletti *et al.*, Phys. Rev. B **81** (2010) 235401.

* Tatsuhiko. Nishi@jp.sony.com

13A/2009S2-007

Isotope effects on thermal dehydrogenation of cyclohexane on Rh(111)

Takanori Koitaya, Sumera Shimizu, Kozo Mukai, Shinya Yoshimoto, and Jun Yoshinobu*
The Institute for Solid State Physics, The University of Tokyo, Chiba, 277-8581, Japan

1 Introduction

Activation of C-H bonds of saturated hydrocarbons by metals is a key step in conversion to more valuable functionalized molecules as well as in dehydrogenation to produce hydrogen [1]. In the case of cyclohexane adsorbed on metal surfaces, softened C-H stretching modes have been observed between 2400 and 2800 cm^{-1} [2-4]. The significant red-shift is a consequence of the electronic interaction between unoccupied C-H orbitals and occupied metal states (C-H···M interaction) [5, 6]. The C-H···M interaction is similar to the typical hydrogen bond. It has been revealed that the hydrogen bond shows an isotope effect; the A-D···B bond is weaker than the A-H···B bond due to the quantum nature of hydrogen [7]. Hence, we expect that adsorbed cyclohexane on the Rh(111) surface exhibits a similar isotope effect, which affects reactivity of cyclohexane. In this study, the isotope effect on thermal dehydrogenation of cyclohexane on the Rh(111) surface was investigated by high-resolution X-ray photoelectron spectroscopy (HR-XPS).

2 Experiment

The HR-XPS measurements were carried out at the soft X-ray undulator beam line 13A. The base pressure of the chamber was $<1\times10^{-8}$ Pa. HR-XPS spectra were obtained using a hemispherical electron analyzer (SPECS, phoibos 100) with photon energy of 410 eV at a normal emission angle. After cleaning of the Rh(111) surface by several sputtering-annealing cycles, the cyclohexane monolayer was prepared by exposure of an excess amount of cyclohexane molecules on the surface at 150 K, followed by the measurement at 90 K. Then, the sample was heated to 240 K at which all adsorbed molecules were desorbed or dehydrogenated.

3 Results and Discussion

Figure 1 shows C 1s spectra of monolayer cyclohexane, and residual species after heating to 240 K. The desorption and the dehydrogenation are competing processes. The main path was intact desorption. There is an isotopic difference in the reactivity of cyclohexane; a 10.6% of monolayer C_6H_{12} molecules are dehydrogenated by heating, whereas only 5.9% of C_6D_{12} go on the dehydrogenation path. In addition, stability of reaction products is also different between C_6H_{12} and C_6D_{12}. The spectra of the thermal reaction products are clearly different between two isotopes; the C 1s spectrum of the reaction products of C_6H_{12} consists of at least two components between 284 – 283.2 eV, whereas that of C_6D_{12} has a single peak at 283.9 eV. The observed peak of C_6D_{12} can be assigned to benzene. Thus, all reacted

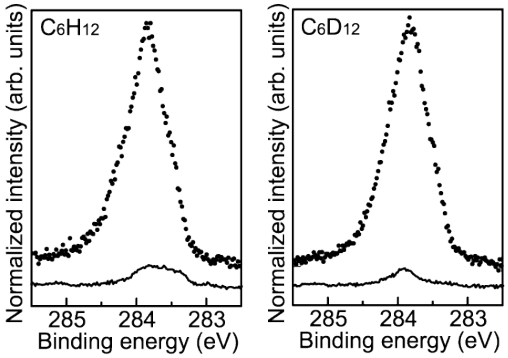

Fig. 1. C 1s photoelectron spectra (hν = 410 eV) of adsorbed cyclohexane at monolayer coverage (dots), and reaction products after heating to 240 K (solid lines).

C_6D_{12} molecules are dehydrogenated to C_6D_6 at 240 K. In the case of C_6H_{12}, the other components at lower binding energy (Fig. 1; left) are tentatively attributed to the π-allyl C_6H_9 based on results of vibrational spectroscopy [8]. Hence, the C_6H_6 and π-allyl species can coexist at 240 K.

The isotope effect in the reactivity of cyclohexane on the Rh(111) surface is caused by the weaker C-D···M interaction compared to the C-H···M interaction. The weaker C-D···M interaction leads to faster desorption and slower dehydrogenation of C_6D_{12}. This affects the branching ratio between desorption and dehydrogenation processes. Based on the similarity to the typical hydrogen bond, we attribute the origin of the isotope effects to the quantum nature of hydrogen in the C-H···M interaction [8].

Acknowledgement

The authors thank the staff members of the BL-13A for their technical support.

References

[1] J. A. Labinger and J. E. Bercaw, Nature **417**, 507 (2002).
[2] J. E. Demuth et al., Phys. Rev. Lett. **40**, 1044 (1978).
[3] R. Raval and M. A. Chesters, Surf. Sci. **219**, L505 (1989).
[4] T. Koitaya et al., Phys. Rev. B **80**, 193409 (2009).
[5] K. A. Fosser et al., Angew. Chem. Int. Ed. **41**, 1735 (2002).
[6] Y. Morikawa et al., Phys. Rev. B **69**, 041403 (2004).
[7] Y. Ikabata et al., J. Phys. Chem. A **115**, 1433 (2011).
[8] T. Koitaya et al., J. Chem. Phys. **136**, 214705 (2012).

* yoshinobu@issp.u-tokyo.ac.jp

13A/2009S2-007

High-Resolution X-ray Photoelectron Spectroscopy Study on CH_3S/Au(111): Evidence for Formation of Au-Adatom-Dithiolate Complex

Hiroshi Kondoh[1],* Koichiro Nakaya[1], Kozo Mukai[2], Kazuhiko Mase[3], and Jun Yoshinobu[2]
[1]Department of Chemistry, Keio University, Yokohama 223-8522, Japan
[2]ISSP, The University of Tokyo, Kashiwa 277-8581, Japan
[3]Photon Factory, Tsukuba 305-0801, Japan

1 Introduction

The methylthiolate (CH_3S) monolayers adsorbed on Au(111) surfaces can be considered as prototypical self-assembled monolayers and have been extensively studied from the structural and electronic points of view. Although its structure has been long under controversy, a scanning tunneling microscopy (STM) study revealed that Au adatoms ejected from the surface contribute to stabilization of the methylthiolate monolayers via formation of a CH_3S-Au-SCH_3 complex as illustrated in Fig. 1 [1]. However, this Au-dithiolate complex model was not fully supported by a later high-resolution x-ray photoelectron spectroscopy (XPS) study, where a Au-monothiolate complex (CH_3S-Au) model was proposed based on the relative Au4f XPS intensity of the Au atoms with different chemical environments [2]. In this study, we conducted high-resolution XPS measurements for the CH_3S/Au(111) system to check the both models.

2 Experiment

The experiments were carried out at the high-resolution XPS station of BL-13A, which was equipped with a hemispherical electrostatic electron-energy analyser (PHOIBOS 100). A Au(111) single-crystal surface was cleaned by repeated cycles of Ar ion sputtering and annealing. The cleanliness and ordering were checked by XPS and LEED. A saturated methylthiolate monolayer was prepared by exposing the clean Au(111) surface to gaseous dimethyldisulfide at room temperature.

3 Results and Discussion

Fig. 2 shows Au4f XP spectra taken for clean and CH_3S-adsorbed Au(111) surfaces. The XP spectra were deconvoluted into several components by curve-fitting with the Doniach-Sunjic line shape convoluted by Gaussian functions. The clean surface spectrum exhibits two components from the bulk (B) and the surface layer (S), latter of which is significantly enhanced due to the high surface sensitivity of the Au 4f photoelectrons detected here ($E_{kin} \approx 50$ eV). The CH_3S-adsorbed Au(111) surface gives a higher-energy component (T_a) which is associated with the Au adatom [2] and instead the surface-layer component (S) is reduced in intensity. A part of the surface-layer Au atoms should be bound to the thiolate (T_s) and appear at the same binding energy as that of the bulk (B). The integrated intensity ratio T_a/S is obtained as 0.25. This ratio is in agreement with the Au-dithiolate model (0.25) but not with the Au-monothiolate model (0.33). This provides evidence for that the Au-dithiolate complexes cover the Au(111) surface, which is consistent with a recent STM study on CH_3S-sturated Au(111) surfaces [3].

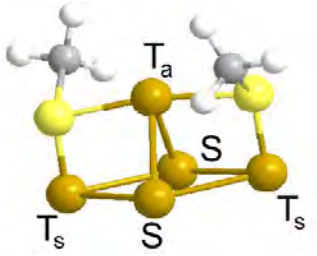

Fig. 1: Structure model for the CH_3S-(Au adatom)-SCH_3 dimer complex adsorbed on Au(111). T_a and T_s denote Au adatoms and surface Au atoms bound to the sulphur atom of the thiolate, respectively. S denotes surface Au atoms that are not bound to the thiolate.

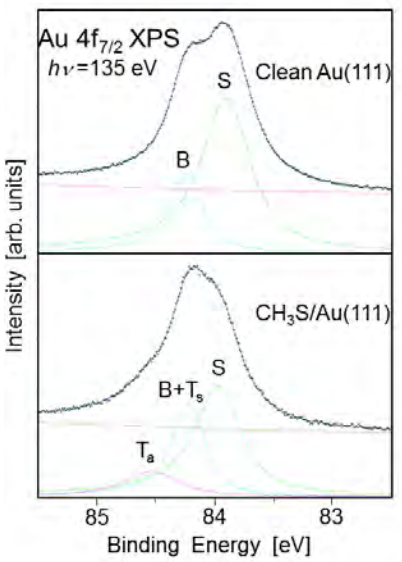

Fig. 2: High-resolution Au $4f_{7/2}$ XP spectra taken for clean and CH_3S-adsorbed Au(111) surfaces. T_a, T_s and S denote components corresponding to Au atoms shown in Fig. 1.

References

[1] P. Maksymovych et al, *PRL* **97,** 146103 (2006).
[2] A. Chaudhuri et al. *PRL* **102,** 126101 (2009).
[3] O. Voznny et al. *JACS* **131,** 12989 (2009).

* kondoh@chem.keio.ac.jp

3B, 13A/2009S2-007

Acridine Orange Base as an Electron Donor on the ZnO Surfaces

K. Ozawa[1,*], M. Suzuki[2], R. Tochikubo[2], H. Kato[2], and K. Mase[3]
[1]Tokyo Institute of Technology, Tokyo 152-8551, Japan
[2]Hirosaki University, Hirosaki 036-8560, Japan
[3]Institute of Materials Structure Science, Tsukuba 305-0801, Japan

1 Introduction

ZnO is a wide-band-gap n-type semiconductor with the Fermi level (E_F) lying just below the conduction band minimum (CBM). Electron-doping of the surface by hydrogen (H) adsorption leads to significant downward band bending so that the CBM is lowered below E_F, and surface metallization by forming two-dimensional electron gas is realized [1-3]. Metallization of the ZnO surfaces is also achieved by adsorption of water and methanol, both of which adsorb dissociatively to form adsorbed H which acts as an electron donor [1]. In search of organic molecules that bring oxide surfaces the metallic nature, we first examined tetrathiafulvalene (TTF) [4], a prototype of an electron donor molecule in organic charge-transfer salts. However, TTF is found not to donate electrons to ZnO but to withdraw them from ZnO [4]. In the present study, we have investigated the interaction between ZnO and acridine orange base (AOB, Fig. 1) by photoelectron spectroscopy (PES).

2 Experiment

AOB was purified once by vacuum sublimation by heating the sample at 120°C. Deposition of AOB on the ZnO surfaces was done at 120°C by using a home-build evaporator in the ultrahigh vacuum chamber. The PES measurements were carried out at beamlines 3B and 13A.

3 Results and Discussion

The measurements of the valence band spectra reveal that AOB induces downward bending of the ZnO band on both the Zn-terminated (0001) and O-terminated (000-1) surfaces, while the position of the band is almost intact on the (10-10) surface (Fig. 2). This means that AOB acts as an electron donor on the (0001) and (000-1) surfaces, whereas charge transfer between AOB and the (10-10) surface is not operative. The valence band maximum (VBM) positions on the clean surfaces are 3.0 eV, 2.9 eV, and 2.4 eV on the (0001), (10-10) and (000-1) surfaces, respectively, and they are shifted to 3.5 eV and 3.0 eV on the (0001) and (000-1) surfaces, respectively, by AOB adsorption. Considering the band gap of ZnO is 3.37 eV, the CBM on the (0001) surface covered with AOB should be located at 0.1 eV below E_F, whereas those on the other two surfaces remain above E_F.

One of the criteria for metallization is that the CBM of the substrate surface should be lowered below E_F. Therefore, the AOB-adsorbed ZnO(0001) surface is possibly in a metallic nature. Although a direct evidence for surface metallization is still unavailable, AOB is the first organic molecule which may induce metallization of the oxide surface.

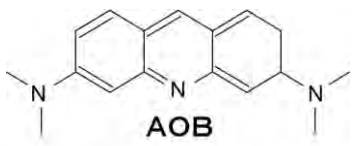

Fig. 1 Molecular formula of acridine orange base (AOB).

References

[1] K. Ozawa and K. Mase, Phys. Status Solidi A **207** (2010) 277.
[2] K. Ozawa and K. Mase, Phys. Rev. B **81** (2010) 205322.
[3] K. Ozawa and K. Mase, Phys. Rev. B **83** (2011) 125406.
[4] K. Ozawa, S. Munakata, K. Edamoto, K. Mase, J. Phys. Chem. C **115** (2011) 21843.

* ozawa.k.ab@m.titech.ac.jp

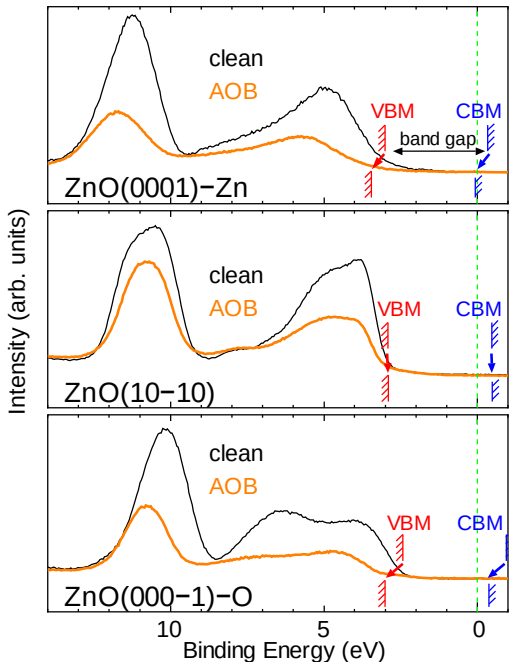

Fig. 2 Normal-emission valence band spectra of AOB-covered ZnO surfaces. Positions of the VBM and CBM before and after AOB adsorption are indicated.

3B, 13A/2009S2-007, 2011G026

Interfacial electronic properties of fullerene/bathocuproine/Ag heterostructures studied by ultraviolet photoemission spectroscopy

Shenghao Wang[1], Takeaki Sakurai[*1,2], Ryusuke Kuroda[1] and Katsuhiro Akimoto[1]

1. Institute of Applied Physics, University of Tsukuba, Tsukuba, Ibaraki 305-8573, Japan
2. PRESTO, Japan Sceience and Technology Agency (JST), Kawaguchi, Saitama 332-0012, Japan

1 Introduction

Organic solar cells (OSCs) have great potential in the photovoltaic market due to the advantages of low cost, easy fabrication, and compatibility with large-scale and flexible substrates. It is a key issue for organic electronic devices to understand the electronic properties of interfaces, because they strongly affect the charge transfer and collection. Bathocuproine (BCP), as a buffer layer inserted between fullerene (C_{60}) layer and the cathode layer, can improve the power efficiency of OSCs. However, the role of BCP buffer layer still remains unclear. Gaining insight into the interfacial properties of C_{60}/BCP/metal heterostructures is necessary for understanding the role of BCP and further improving the performance of OSCs. It has been demonstrated that the performance of OSC was dependent on the thickness of BCP. In present work, we studied the influence of BCP thickness on the energy level alignment of C_{60}/BCP/Ag heterostructures using synchrotron-based in situ ultraviolet photoemission spectroscopy (UPS)[1]. We found that relatively thin BCP layer has favourable energy level alignment for the OSCs.

2 Experiment

The UPS experiments were carried out at beamline 3B of the Photon Factory. *Ex* situ cleaned Si(100) wafers were used as substrates. The C_{60}/BCP/Ag heterostructures were formed by depositing BCP on Ag and subsequently depositing C_{60} with increasing thickness from 0.4 to 5 nm onto BCP/Ag stack layers in the UHV chamber. BCP layers with thicknesses of 0.8 and 5 nm were formed in two samples; these represent thin and thick layers, respectively. Prior to deposition, BCP (Wako Corp., sublimated grade) and C_{60} (Sigma-Aldrich, 99.5 %) were purified three times by vacuum gradient sublimation. The deposition rates for both materials were 0.01 nm/s and the thicknesses were monitored by a quartz-crystal microbalance. UPS spectra were measured in an analysis chamber (< 9.0×10^{-10} Torr) using the photon energy of 30 eV.

3 Results and Discussion

Fig. 1 shows UPS spectra of C_{60} layers with various thicknesses deposited on BCP/Ag stack layers with 0.8 and 5 nm for BCP layer thickness. The abscissa is the electron binding energy (*BE*) relative to the Fermi level (E_F) of Ag. From Fig. 1(a), small peaks at about 1.8 eV can be clearly observed near the E_F, indicating the generation of gap states. Apart from the gap states, there is hardly any other change and shift for the spectrum after depositing 0.4 nm C_{60}. The peak of the highest occupied molecular orbital (HOMO) for C_{60} exhibits no shift as the thickness is increased up to 5 nm, indicating the pinning of E_F.

To the contrary, no small peak can be observed near the E_F and obvious peak shifts for the BCP features can be seen upon the deposition of C_{60}, implying that the molecular orbitals of BCP change. After depositing 0.8 nm C_{60}, the HOMO peak of BCP abruptly shifts to lower *BE* by 0.6 eV. When the C_{60} layer thickness is increased from 1.6 to 5 nm, the HOMO peak of C_{60} shifts to lower *BE* by 0.2 eV. The change of the HOMO peak indicates that band bending occurs for both BCP and C_{60} at the interface of C_{60}/BCP heterojunction. This band bending will enlarge the offset of the lowest unoccupied molecular orbital (LUMO) levels of C_{60} and BCP at the interface, and therefore generate a Schottky barrier for electrons transport, which is undesirable for the device performance.

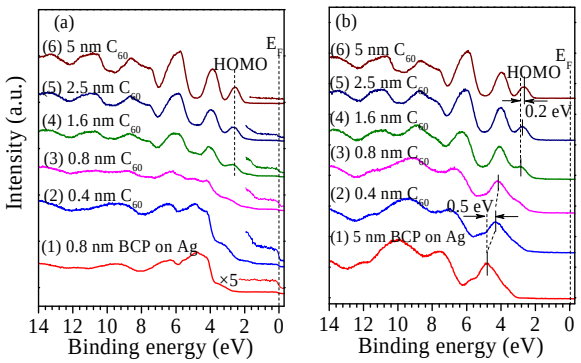

Fig. 1 UPS spectra of C_{60} layers with various thicknesses deposited on (a) BCP (0.8 nm)/Ag stack layers and (b) BCP (5 nm)/Ag stack layers

References

[1] S. Wang, T. Sakurai, R. Kuroda, and K. Akimoto. Appl. Phys. Lett. **100**, 243301 (2012).

* sakurai@bk.tsukuba.ac.jp

7C/2010G010

Local Structure of Pt(II) Pyridyl Complexes Anchored onto Mesoporous Silica as Photo-induced H_2 Production Catalysts

Kohsuke Mori* and Hiromi Yamashita
Divisions of Materials and Manufacturing Science, Graduate School of Engineering,
Osaka University, 2-1 Yamada-oka, Suita, Osaka, Japan.

1 Introduction

Recently, investigations into emissive square-planar d^8 Pt(II) pyridyl complexes have been numerous owing to their potential capacity for application in chemical sensing, solar energy conversion, and photocatalysis. The photoluminescence from such complexes originates from a variety of lowest triplet excited states, including ligand-centered (LC), metal-to-ligand charge-transfer (MLCT) and metal-metal-to-ligand charge-transfer (MMLCT) excited states. A low-lying ^{3}MMLCT excited state occurs in dimers and aggregates with short Pt···Pt separation, and the resulting emission is observed at longer wavelengths than those of unimolecular ^{3}LC and ^{3}MLCT emissions. These unique characteristics provide with the new photocatalyst systems allowing H_2 production as well as selective photooxidation using molecular oxygen.

Bering this in mind, we developed an inorganic-organic hybrid photocatalyst by anchoring the chloro(2,2':6',2''-terpyridine)platinum(II) ([Pt(tpy)Cl]Cl) complex to mesoporous silica modified with (3-aminopropyl)trimethoxysilane (APTMS). It was proven that the anchored Pt complex creates new bifunctional heterogeneous photocatalyt enabling both visible-light photosensitization associated with the ^{3}MMLCT excited states and H_2-evolution in aqueous media without an electron relay (**Scheme 1**). In this paper, the relationship between the local structure and photocatalytic activities was examined by XAFS analysis [1].

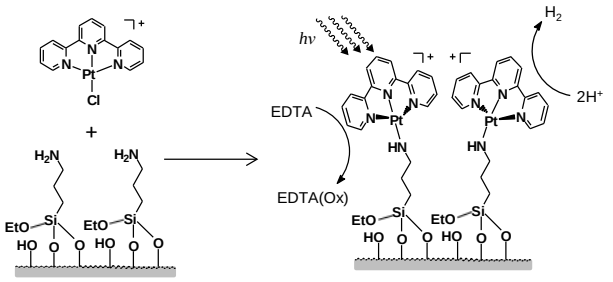

Scheme 1. Anchoring of $[Pt(tpy)Cl]^+$ complex onto the modified silica surface and schematic illustration of bifunctional heterogeneous photocatalyt for H_2-evolution in aqueous media without an electron relay.

2 Experiment

Anchoring of Pt complex on to MCM-48: Mesoporous silica MCM-48 and [Pt(tpy)Cl]Cl complex were synthesized according to the literature procedures, respectively. 200 ml of chloroform solution of [Pt(tpy)Cl]Cl was stirred with 1.0 g of APTMS-modified MCM-48 sample at room temperature for 24 h. The product was recovered by vacuum filtration, washed with chloroform, and dried under vacuum overnight to give Pt(tpy)/MCM-48 samples with different Pt loadings (Pt: 0.2, 0.4 0.8, 1.2 and 2.4 wt%), respectively. The Pt loadings were determined by inductively coupled plasma (ICP) analysis.

XAFS analysis: Pt L_{III}-edge XAFS spectra were recorded at room temperature in fluorescence mode at the BL-7C facilities of the Photon Factory at the National Laboratory for High-Energy Physics, Tsukuba (2009G221). A Si(111) double crystal was used to monochromatize the X-rays from the 2.5 GeV electron storage ring. In a typical experiment, the sample was loaded into the *in situ* cell with plastic windows. EXAFS data were examined using the EXAFS analysis program, Rigaku EXAFS. The pre-edge peaks in the XANES regions were normalized for atomic absorption, based on the average absorption coefficient of the spectral region. Fourier transformation (FT) of k^3-weighted normalized EXAFS data was performed over 3.5 Å < k/Å^{-1} < 12 Å range to obtain the radial structure function. CN (coordination number of scatters), R (distance between the absorbing atom and the scatterer), and Debye-Waller factor were estimated by curve-fitting analysis with the inverse FT in the 0.8 < R/Å < 2.8 range assuming single scattering.

3 Results and Discussion

Figure 1A shows XANES spectra at the Pt L_{III}-edge of the [Pt(tpy)Cl]Cl complex and anchored samples with different Pt loadings. The white line at around 11565 eV is an absorption threshold resonance, which is known to be intensified as a result of oxidation. The results show that all anchored samples afforded higher intensity peaks compared to free [Pt(tpy)Cl]Cl, suggesting that the surface anchored Pt species appear to be in a slightly electron-deficient state, because of the decrease in the σ-donor electron by replacement of the fourth coordinated ligand from chloride to a nitrogen atom.

In the FT-EXAFS spectra, all samples show a strong peak at around 1.5 Å attributable to a Pt–N bond and a small second shell at ca. 2.4 Å assignable to neighboring carbon atoms (**Figure 1B**). This corroborates a tridentate binding structure for Pt(II). In the case of the [Pt(tpy)Cl]Cl complex, an additional peak due to the Pd–Cl bond was observed at around 1.8 Å, which completely disappeared after reaction with APTMS-modified MCM-48 to generate the new Pt–N bond accompanied by elimination of the Pt–Cl bond. It is notable that the samples with high Pt loadings exhibit the additional peak

at around 3.5 Å, which may be ascribed to the short Pt···Pt interactions as discussed later. Moreover, the first peaks of Pt(tpy)/MCM-48 were slightly shifted toward shorter interatomic distances with increasing Pt content. The average Pt–N distances determined by curve-fitting analysis decreased from 2.06 to 2.02 Å as the Pt loading amount increased, which suggests that the anchored Pt complexes may undergo slight distortion within the channel, due to the steric constraints at high Pt loading.

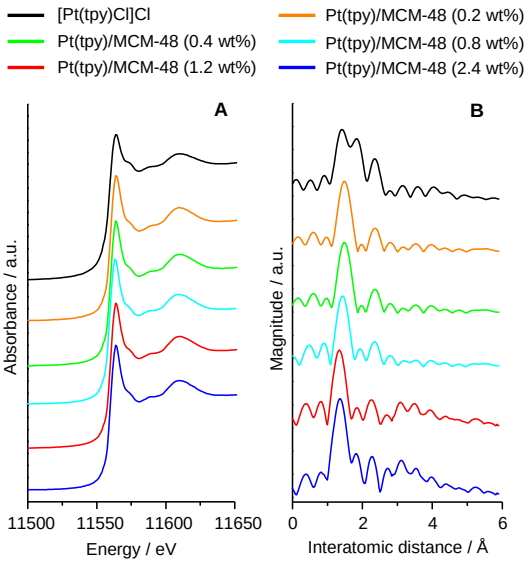

Figure 1. (**A**) Pt L_{III}-edge XANES spectra and (B) FT-EXAFS spectra.

Anchoring of the [Pt(tpy)Cl]Cl complex to mesoporous silica results in photocatalysts which allows H_2-evolution in aqueous media in the presence of EDTA under visible-light irradiation (λ > 420 nm). Time course of H_2 production normalized based on Pt amount are shown in **Figure 2**. No significant reaction is observed under either dark condition in the presence of the photocatalyst or without EDTA under light irradiation. It should be noted that the photocatalytic activity significantly varies according to the amount of Pt loadings; no H_2-evolution occur to any significant extent at less than 0.4 wt% Pt loadings, while photocatalytic activity gradually increased at more than 0.8 wt% Pt loadings. This behavior is in good accordance with the increasing intensity of the luminescence emission due to the ^{3}MMLCT states. Significantly, the maximum activity obtained by 2.4 wt% Pt loading is higher than that of the homogeneous counterparts under identical conditions.

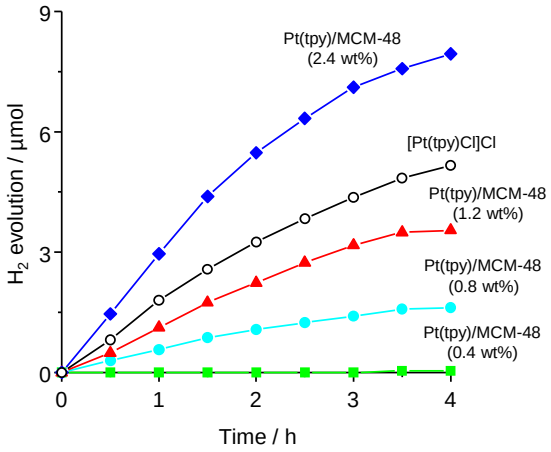

Figure 2. Photocatalytic H_2 production from an aqueous acetate buffer solution (pH = 5.0) and 30 mM EDTA in the presence of Pt catalyst (Pt: 4 µmol).

References

[1] K. Mori, K. Watanabe, K. Fuku, H. Yamashita, *Chem. Eur. J.*, **18** (2012) 415.

* mori@mat.eng.osaka-u.ac.jp

4C/2010G119

Can Ion Pairs Adsorb on a Negatively Charged Mica Surface in Aqueous Solution?

Hiroshi Sakuma[1,*], Hironori Nakao[2], and Yuichi Yamasaki[2]
[1]Tokyo Institute of Technology, 2-12-1 Ookayama, Meguro 152-8551, Japan
[2]Photon Factory, Tsukuba 305-0801, Japan

1 Introduction

Ion adsorptions on a mineral surface are important to develop an interfacial double layer theory. The phenomena are also critical to remove toxic elements in water. A comparison of molecular dynamics (MD) simulations and x-ray crystal truncation rods (CTR) scattering measurements implied an excess adsorption of Cs^+ on a muscovite surface more than the number to compensate the negatively charged muscovite surface in water [1]. This could be explained by the co-adsorption of Cs^+ and Cl^- in the aqueous solution. Such an ion-pair adsorption enhances the maximum number of cations adsorption on a mineral surface and therefore it is important to know the mechanism of the ion-pair adsorption. Here we investigated the interfacial structures of aqueous KCl and KI solutions on muscovite surfaces using the x-ray CTR scattering measurements and discussed the possibility of potassium-monovalent anion pair adsorption on a negatively charged mineral surface.

2 Experiment

Mica (Muscovite:$KAl_2(OH)_2(AlSi_3)O_{10}$) belongs to the group of 2:1 layer silicates and consists of an octahedral [AlO_6] sheet sandwiched between two tetrahedral [$(Si,Al)O_4$] sheets. One of the four Si atoms in the tetrahedron is replaced by an Al atom because of which there exists an overall negative charge on the layers. This charge is compensated for and the layers are bonded together by an interlayer of K^+ ions. The mica crystals were cut into 1×1 cm^2 squares and glued on flat silica glass lenses. A peeling procedure was employed to prepare fresh and clean (001) mica planes. The surface was immediately immersed in a 0.5 M KCl or KI solution and kept in it for at least a few hours. Just prior to the CTR measurements, the mica was mounted on a thin-flim liquid cell and the liquid cell was covered using a polyester film 6 μm thick to prevent the solution from evaporating. The x-ray CTR scattering intensities were corrected by the scattering area, Lorentz, polarization, attenuation factors, and rod interception. The experiments were carried out at Photon Factory, KEK, Japan (BL-4C) by using monochromatic x-rays of 11.0 keV. The CTR refers to scattering with a momentum transfer vector perpendicular to the interface Q. The CTR profile was obtained in the range Q = 1.3–4.4 Å^{-1} with individual rocking scans at given Q values. The resolution of the data was approximately equal to π/Q_{max}, where Q_{max} is the highest Q value at which data were obtained. In these measurements, the resolution was 0.72 Å.

3 Results and Discussion

The x-ray CTR scattering profiles of KCl and KI solutions on mica surfaces were shown in Fig. 1. The Bragg reflection points (00l) (l = 4, 6, 8, 10, 12, and 14) of the mica surface were at $Q \approx$ 1.2, 1.9, 2.5, 3.2, 3.8, and 4.4 Å^{-1}, respectively. The intensities between the Bragg reflection points reflect the scattering from the aqueous salt solution/mica interfaces. There was no distinct difference between the scattering profiles of the KCl and KI solutions on mica surfaces, indicating that these interfacial electron densities should be similar between them. Since the number of electron of an iodide is much larger than a chloride, no difference of the CTR scattering profiles implied that ion-pair (K-Cl or K-I) adsorption was minor on a mica surface.

The ion-pair adsorption would depend on the energy balance among the hydration energies of ions, attractive interaction between cations and anions, and interactions of ions with a negatively charged mica surface. Low hydration energy of cations would be most important factor to realize the ion-pair adsorption on a mica surface. The adsorption behaviour of Cs^+ ions with various monovalent anions should be investigated in the future works.

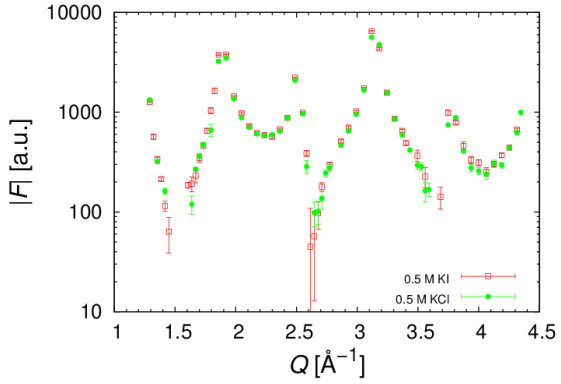

Fig. 1: X-ray CTR scattering profiles of 0.5 M KI and KCl solutions on muscovite surfaces. The normal axis is absolute value of the structure factor F of the interfaces.

Acknowledgement

This work was partly supported by JSPS KAKENHI 23740390.

References

[1] H. Sakuma and K. Kawamura, Geochim. Cosmochim. Acta **75** (2011) 63.

* sakuma.h.aa@m.titech.ac.jp

12C/2010G-123

ドープ氷中に存在するイオンの局所構造
Local Structures of Hydrated ions in doped ice

原田誠 [1*], 社本泰樹 [1], 荒井雄太 [1], 岡田哲男 [1]
[1] 東京工業大学大学院理工学研究科、〒152-8551 東京都目黒区大岡山 2-12-1

1 はじめに

氷は非常に身近な物質であるが、まだ不明な点も多く、その解明が期待されている。水溶液を凍結させると、溶存している塩を含むドープ氷となる。ドープ氷中の塩の状態は例えば急速凍結かどうかによっても影響を受ける。非常にゆっくりと時間を掛けて凍結させると、海氷のように塩濃度が高くても氷になるときに塩が押し出され、氷自体には塩は含まれない。ドープ氷の場合、水溶液を比較的急速に凍結するので氷中に塩が取り残される。しかしながら、ドープ氷中であっても塩は氷のネットワークに取り込まれているわけではない。氷は氷微結晶が凝集して構成されている。塩はその微結晶の隙間であるグレインバウンダリーに存在している。グレインバウンダリーに存在する塩の状態は主にその共晶点温度に依存している。小角X線散乱の結果から、液体窒素を使って急速に凍結させたドープ氷中の塩は、共晶点以下で塩が臭化ルビジウムの場合には直径 3～4nm 程度の塩結晶微粒子として氷中に存在することがわかった（2010P007）。一方、共晶点以上では氷中であっても水和したイオンとなり、氷中に存在した結晶微粒子は観測されなかった。

本研究では SSD を使ってドープ氷の蛍光 XAFS 測定を行い、含まれるイオンの局所構造解析を行い、水溶液の塩の種類や濃度によってドープ氷中の塩の状態がどのように変化するのかを検討した。

2 実験

実験装置の概略を図 1 に示す。-5～-20℃の氷温を維持するためにペルチェ素子を用い、Pt100 を温度センサとして常に試料氷の温度を測定しながら温調した。X 線が氷表面に照射するようにゴニオメータを用いて試料氷を傾けた。蛍光測定は 19ch SSD を用いた。入射光強度測定には 4cm イオンチャンバを用いた。利用したビームラインは BL12C および BL9C である。

測定試料は KCl、RbBr であり、濃度を 0.5、1、3、5、10、50mM とした。これらの水溶液をペルチェ上もしくは液体窒素を用いて凍結して調製したドープ氷を用いた。

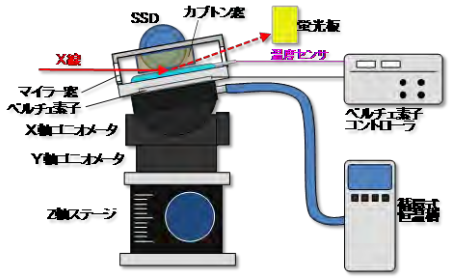

図 1 氷蛍光 XAFS 測定装置図。

3 結果および考察

図 2 に測定した XAFS スペクトルを示す。測定温度を-20～-5℃まで昇温させて測定した。RbBr の共晶点は-11.8℃である。共晶点より温度が低い場合には RbBr 固体のスペクトルとほとんど変わらなかったが、温度上昇につれて徐々に水溶液中でのスペクトルに近づいて、共晶点以上になるとほぼ水中のスペクトルと一致した。このスペクトルを固体と水和の寄与を見積もるためにそれぞれのスペクトルを用いてフィッティングしたところ（図 3）、共晶点でイオンの構造が大きく変化していることが明らかとなった。

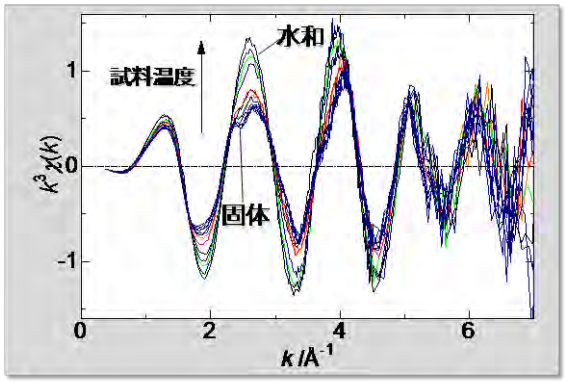

図 2 種々の温度による 10mM RbBr ドープ氷の Br-K 端での XAFS スペクトル。

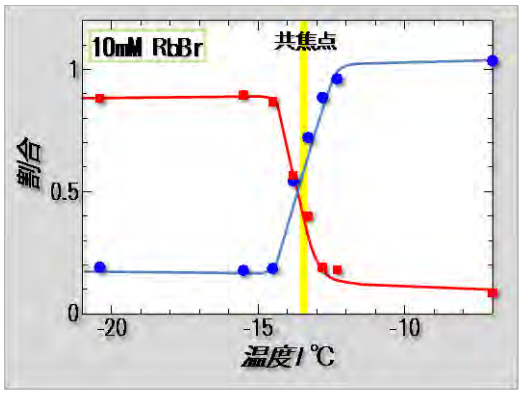

図 3 固体と水溶液のスペクトルを用いて図 2 のスペクトルをフィッティングした結果。

4 参照論文

M. Harada , Y. Tasaki , H. Qu, T. Okada *RSC Adv.*, **2012**, *2*, 461-466

7C/2010G148

Restricted Hydration Structure of Calcium Ion Formed in Slit-Shaped Carbon Micropore

Tomoko Kusudo, Masayasu Nishi, Hiroe Torigoe, Mitsuhiro Ushio, Akira Oda, Yuusuke Sogawa, Atsushi Itadani, Takahiro Ohkubo*, and Yasushige Kuroda
Faculty of Science, Okayama University, Okayama 700-8530, Japan

1 Introduction

We have studied the specific structure of hydrated ions such as Rb^+ confined in solid nanospaces of activated carbons [1, 2] and single-wall carbon nanohorn [3] with the X-ray absorption fine structure (XAFS) technique. The structural information of nano-confined solution (nanosolution; NSN) of metal ions is indispensable for the development of a lot of devices such as electric double layer capacitor. We also understand that a lot of ions such as Ca^{2+}, Cu^{2+}, and Zn^{2+} are playing important roles in our body, and the almost of them can be worked under nano-restricted conditions. Recently, we reported the dehydrated structure around a zinc ion of dissolved zinc acetate [4] and specific structure of dinuclear complex of copper acetate [5] restricted in slit-shaped micropore of activated carbon fiber (ACF). In this report, we will discuss the specific hydration structure around a calcium ion restricted in the micropore of ACF with the data of XAFS spectra and other experimental results.

2 Experiment

In the present study, calcium nitrate ($Ca(NO_3)_2$) was impregnated into the micropore of ACF (P7; average pore width = 0.63 nm). The calcium-deposited sample (denoted by P7-Ca) was evacuated at 423 K before the saturated adsorption of water vapor to provide nanosolution formed in the micropore. *In-situ* XAFS measurements were performed at KEK-PF (BL-7C) on the *K*-edge of Ca (4038 eV).

3 Results and Discussion

Fig. 1 shows the Fourier-transformed spectra of Ca *K*-edge EXAFS of P7-Ca in evacuated (P7-Ca-evac) and saturated water-vapor adsorbed states (P7-Ca-H_2O), respectively. The figure also shows the spectra of crystal ($Ca(NO_3)_2$-crystal) and aqueous solution of $Ca(NO_3)_2$ ($Ca(NO_3)_2$ aq.) for comparison. The first shell for each sample can be ascribed to the Ca-O shell. The peak intensity of the first shell for P7-Ca-H_2O is smaller than that of bulk aqueous solution of $Ca(NO_3)_2$ even at the saturated adsorption state of water. Also, the ordered structure over 3.1 Å was vanished in the micropore of P7 although the higher shells can be formed around 3.5 Å for both $Ca(NO_3)_2$-crystal and $Ca(NO_3)_2$ aq. This result indicates that even if water molecules adsorb and fill the micropore deposited by the electrolyte, water molecules are hard to hydrate to the nearest neighboring of the ion and to form the ordered structure at the higher shell in the micropore of P7.

Table 1 summarizes the structural parameters obtained by curve fitting of reverse Fourier transforms of 1st neighboring shell of each sample. Coordination number ($N_{Ca\text{-}O}$) of the 1st neighbor around a calcium ion for P7-Ca-H_2O is smaller than that in bulk aqueous solution, indicating the formation of dehydrated structure in the micropore of P7. Also, coordination distance between a calcium ion and nearest oxygen atoms ($r_{Ca\text{-}O}$) is obviously decreased compared with that of both $Ca(NO_3)_2$-crystal and $Ca(NO_3)_2$ aq. Generally, ionic radii are smaller if the coordination numbers are decreased. Therefore, the smaller distance for P7-Ca-H_2O strongly indicates a high compression effect in the micropore because the distance is still smaller than that of $Ca(NO_3)_2$-crystal even if the coordination numbers are similar to each other.

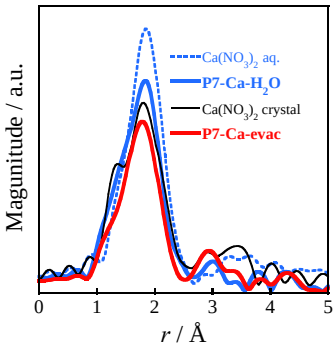

Fig. 1: Fourier-transformed spectra of Ca *K*-edge EXAFS.

Table 1: Structural parameters obtained by curve fitting.

Sample	$N_{Ca\text{-}O}$	$r_{Ca\text{-}O}$/Å	σ^2/ 10^{-2} Å^2	ΔE/eV
P7-Ca-evac	5.6	2.38	0.720	-8.5
P7-Ca-H_2O	7.5	2.40	1.05	-6.4
$Ca(NO_3)_2$-crystal	7.1	2.44	1.18	-5.2
$Ca(NO_3)_2$ aq.	8.0	2.45	1.14	0.5

References

[1] T. Ohkubo *et al.*, J. Am. Chem. Soc. **124** (2002) 11860.
[2] T. Ohkubo *et al.*, J. Phys. Chem. B **107** (2003) 13616.
[3] T. Ohkubo *et al.*, Physica Scr. **T115** (2005) 685.
[4] T. Ohkubo *et al.*, J. Phys. Chem. C **115** (2011) 14954.
[5] T. Ohkubo *et al.*, Micropor. Mesopor. Mater. **154** (2012) 82.

* ohkubo@okayama-u.ac.jp

7A, 13A/2010G151

Study of CO oxidation Reaction on Ir(111) under near Atmosphere Pressure using Ambient Pressure XPS (AP-XPS)

Kazuma SUZUKI[1]*, Masaaki YOSHIDA[1], Yuji MONYA[1], Ryo TOYOSIMA[1],
Kazuhiro MASE[2], Kenta AMEMIYA[2], Hiroshi KONDOH[1]
[1]Keio University, Hiyoshi, Kanagawa 222-8522, Japan
[2]KEK-PF, Tshukuba, Ibaraki 305-0801, Japan

Introduction

In this decade, destruction of environment by automotive exhaust is becoming a more and more serious problem. Study of CO oxidation reaction is potentially useful for giving a solution to this problem since this reaction is one of the elementary steps of the complex reaction occurring at exhaust gas catalysts. The CO oxidation has been studied mostly under ultrahigh vacuum (UHV) conditions so far. Differences in reaction mechanism between UHV and high-pressure conditions have been paid much attention recently. In this work, we studied CO oxidation reaction on Ir(111) under near ambient pressure using AP-XPS.

Experimental section

Clean Ir(111) surfaces were exposed to O_2 and CO gases up to near 1 Torr at 400 K. The partial pressure of gases was monitored by the quadrupole mass spectroscopy (QMS). During the gas exposure, XP spectra were obtained.

Results and Discussion

Fig. 1 shows mass monitoring and fig. 2 shows O1s XP spectra taken under a reaction condition. Each mass measurement (A, B) corresponds to each XP spectrum with the same label. From Fig.1, we could find decreasing of CO production with time. Under condition A (more active), three peaks are observed in the XP spectra.

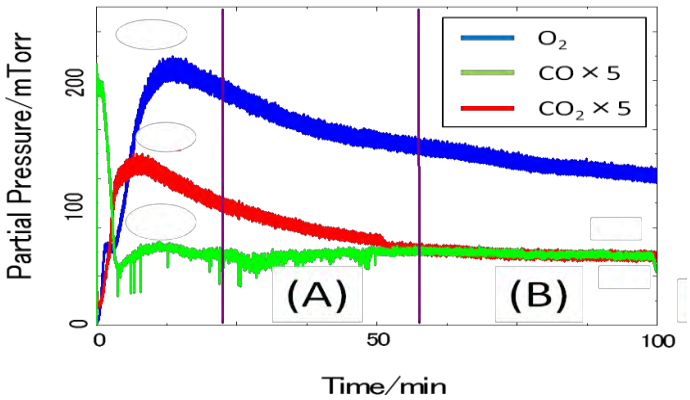

Figure 1: Mass monitoring under a reaction condition.

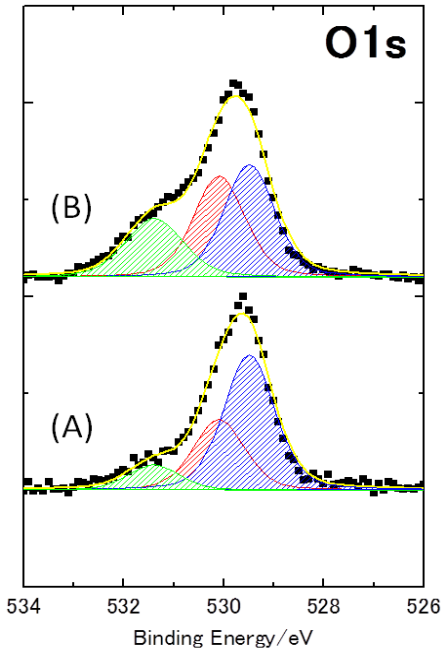

Figure 2: O1s XP spectra taken under a reaction condition.

A peak at 530.1 eV (red) is attributed to chemisorbed O. Another peaks at 529.5 eV and 531.1 eV are associated with the O-Ir-O tril-ayer surface oxide[1] which contains two oxygen species. Under condition B (less active), the same three peaks are observed but the intensity ratio was changed. The drastic increase of the green peak suggests growth of the O-Ir-O tri-layer surface oxide. Therefore, we suppose that the presence of the O-Ir-O tri-layer surface oxide suppresses the CO oxidation reaction on the Ir(111) surface. The chemisorbed O species seems to be mainly contributing to the CO oxidation.

Reference
[1] He, Y. B.; Stierle, A.; Li, W. X.; Farkas, A.; Kasper, N.; Over, H. J. Phys. Chem. C 2008, **112,** 11946.

*k.suzuki@chem.keio.ac.jp

1A/2010G-504

Phase Transition of Alkane Wetting Film on Surfactant Solution and Structural Change in Electrical Double Layer

Eisuke Ohtomi and Hiroki Matsubara*
Department of Chemistry, Kyushu University, Fukuoka 812-8581, Japan

1 Introduction

Electrical double layer is generally composed of the Stern layer and diffusion double layer. In the Stern layer, the counterions bound to the oppositely charged surface, while those distributed in the diffusion double layer more loosely interacting with the charged surface. The adsorbed film formed by ionic surfactants necessarily associates with the electrical double layer, however, the detail structure of them has never determined due to a lack of proper experimental techniques.

Recently, we have utilized total-reflection XAFS to investigate the local chemical environment of surfactant counterions (Br^-) and found that the ratio of Br^- ions in the diffused double layer (free-Br) and in the Stern layer (bound-Br) can be deduced from EXAFS analysis [1,2].

We report here the application of TR-XAFS to the hexadecane wetting film on hexadecyltrimethylammonium bromide (HTAB) aqueous solution surface. In this case, hexadecane molecules penetrate into the surfactant adsorbed film then gives rise to the surface phase transition between liquid- and solid-monolayers upon cooling [3]. Therefore, the effect of surface phase transition to the structure of electrical double layer can be discussed.

2 Experiment

The XAFS experiments were performed by using the synchrotron radiation at beamline 7C of the Photon Factory of the National Laboratory for High Energy Accelerator Research Organization (Tsukuba, Japan). The XAFS method was applied to the air/water surface under the total-reflection condition. The X-ray beam monochromatized by a double-crystal monochromator [Si-(111)] hits the solution surface at about 1 mrad. The incident beam intensity I_0 was measured by a gas ionization chamber filled with nitrogen, the signal intensity I was detected by the total-conversion helium ion yield method, and I/I_0 versus photon energy plots were obtained. In the present study, the photon energy was scanned from 13 391 to 13 633 eV, which was enough to obtain the jump values at the K absorption edge and to extract the solvation structure because the oscillation of the spectra was greatly diminished at photon energies above 13 560 eV. The depth of the evanescent wave was estimated to be around 7 nm; therefore, TRXAFS is surface-selective. Details of the principle, procedures, and schematic views of the methods were fully described in our previous papers [1, 2].

3 Results and Discussion

The surfactant concentration was fixed at m = 0.1 mmol kg^{-1}. Hexadecane dissolved in chloroform was placed onto the HTAB solution surface to spread hexadecane molecules in the adsorbed film. The EXAFS spectrum obtained can be expressed as follows,

$$k^3\chi = \alpha_1 k^3\chi_1 + \alpha_2 k^3\chi_2 \quad (1)$$

where k is the photo electron wave vector. χ_1 and χ_2 indicate the specific EXAFS spectra for free-Br and bound-Br, and α_1 and α_2 the weight of each spectrum. The α_2 determined by least-square fitting of the measured EXAFS spectrum is summarized in Table. 1 as a function of temperature. The surface phase transition temperature determined by ellipsometry is around 21.0 ^oC. From these data, we have concluded that the ratio of Br^- ion in the Stern layer increases accompanied with the liquid-solid phase transition of the mixed adsorbed film of surfactant and oil. In other words, the compression of electrical double layer occurs by the surface phase transition. This idea would be potentially of relevance to a wide range of industrial processes, including foaming and emulsification. Our latest paper concerning thin-thick transition of foam film induced by surface phase transition is one of such examples [4].

Table 1: Ratio of bound Br^- in the adsorbed film

Liquid monolayer		Solid monolayer	
T / °C	α_2	T / °C	α_2
25.0	0.54	20.0	0.75
24.0	0.64	19.0	0 86
23.0	0.68	18.0	0.83
22.0	0.59	17.0	0 73
	0.62		0.79

Acknowledgement

We thank Prof. Iwao Watanabe and Dr. Hajime Tanida for the support of TR-XAFS experiment.

References

[1] M. Aratono *et al*., Analitical Sciences **24** (2008) 1279.
[2] K. Shimamoto *et al*., Langmuir **25** (2008) 1279.
[3] E. Ohtomi *et al*., Colloid Polym. Sci. **288** (2010) 1333.
[4] E. Ohtomi et al., submitted to Chem. Lett.

* h.matsubara@chem.kyushu-univ.jp

3B, 13A/2010G550

Origin of Strong Adhesion Between Rubber and Brass

K. Ozawa[1,*], T. Kakubo[2], K. Shimizu[2], N. Amino[2], K. Mase[3], and T. Komatsu[1]
[1]Tokyo Institute of Technology, Tokyo 152-8551, Japan
[2]The Yokohama Rubber Co., Ltd., Hiratsuka 254-8601, Japan
[3]Institute of Materials Structure Science, Tsukuba 305-0801, Japan

1 Introduction

Steel-cord reinforced rubber products are used as automotive tires, conveyor belts, etc. In these products, steel cords are embedded to give rubber a structural strength while maintaining flexibility. Strong adhesion between rubber and the steel cords is crucial for a good performance of these rubber products. In automotive tires, brass-plated steel cords are exclusively used to realize stiff rubber-cord adhesion. It has already been recognized in the early 1970's that copper sulfides are formed at the rubber-brass interface and speculated that these sulfides should be responsible for the interface adhesion [1,2]. However, details of chemical composition of copper sulfides and its formation process have not been understood yet. One of the reason is that, because of strong adhesion between rubber and brass, it is difficult to expose the interface nondestructively for chemical analysis by means of electron spectroscopy. In the present study, high-resolution photoelectron spectroscopy (PES) is utilized to investigate the chemical composition at the rubber-brass interface to elucidate the origin of strong adhesion and the degradation between robber and brass.

2 Experiment

The PES measurements were done at beamlines 3B and 13A. As a model sample of brass-plated steel cords, we employed brass plates (5 × 5 × 0.5 mm^3, $Cu_{66}Zn_{34}$), which were sandwiched by filtered papers, embedded in uncured pads of rubber compounds. The sample-containing rubber was vulcanized at 170°C. The sample plates were retrieved from rubber and subjected to the PES measurements.

3 Results and Discussion

In the present study, special attention has been given to copper sulfides formed on the brass surface. Fig. 1 shows the S 2p spectra of the brass samples subjected to different vulcanization time from 2 to 50 min. The photon energy of 260 eV was used so that the sampling depth was at least 0.4-to-0.55 nm. By analyzing the S 2p core-level spectra, at least five sulfur-containing species are resolved at the interface. Among them, crystalline CuS and amorphous Cu_2S are identified as copper sulfide species. These species are not uniformly distributed within the layer, but there exists the concentration gradation; the concentration of Cu_2S is high in the shallow region from the surface and is diminished in the deeper region, while vice versa for that of CuS.

The relative intensities of Cu_2S and CuS to the total S 2p peak intensity are monotonically decreased from 2 min to 50 min. This indicates that a large amount of copper sulfides is formed within 2 min, and that prolonged vulcanization leads to decomposition of these species. The decomposition rate is faster for Cu_2S than CuS so that the Cu_2S/CuS ratio of 0.52 at 2 min is diminished to 0.25 at 40 min (Fig. 2).

It is empirically known that a longer vulcanization time results in degradation of rubber-brass adhesion. Therefore, the present results imply that Cu_2S is more crucial than CuS to realize strong rubber-to-brass interaction.

References

[1] W.J. Ooij, Rubber Chem. Technol. **52** (1979) 605.
[2] W.J. Ooij, Rubber Chem. Technol. **57** (1984) 421.

* ozawa.k.ab@m.titech.ac.jp

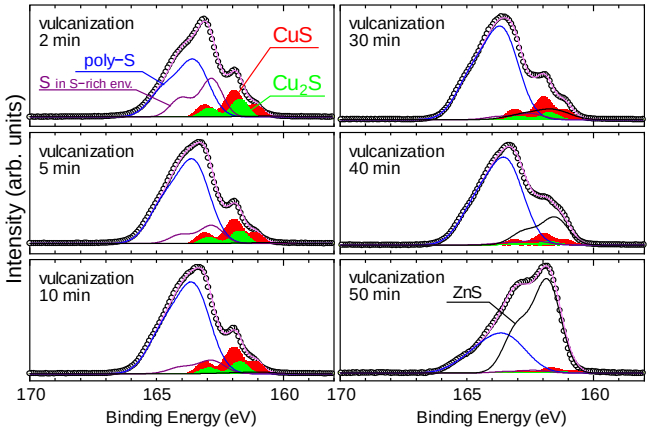

Fig. 1 S 2p spectra from the brass surfaces at various vulcanization time.

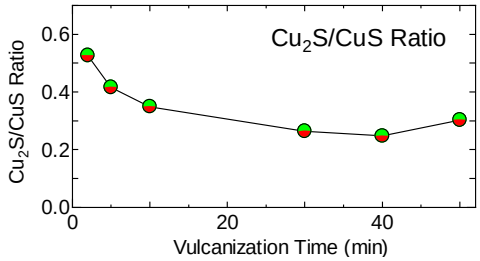

Fig. 2 Change in the Cu_2S/CuS ratio (the S 2p peak intensity ratio) as a function of the vulcanization time.

12C&9A/ 2010G601

In Situ XAFS Observation of Platinum Nanoparticle Thin Layer Formed on HOPG surface: A New approach to the Carbon Electrode/Electrolyte Interface

Hiromitsu Uehara[1], Takafumi Ogawa[1], Kentaro Kono[1], Hua Huang[1], Satoru Takakusagi[1], Kiyotaka Asakura[*]
Yasuhiro Niwa[2], Hiroaki Nitani[2], Hitoshi Abe[2] and Masaharu Nomura[2]
[1]Catalysis Research Center, Hokkaido University, Sapporo 001-0021, Japan
[2]Photon Factory, Institute of Materials Structure Science, KEK, Tsukuba 305-0801, Japan

1 Introduction

Platinum nanoparticles (PtNPs) are widely used as the fuel cell catalyst because of their high electrocatalytic activity such as hydrogen evolution reaction (HER), oxygen reduction reaction (ORR) or methanol oxidation reaction (MOR). However its degradation process and the interaction among carbon substrate, PtNPs and polymer electrolyte are still unclear.

Polarization dependent total reflection fluorescence X-ray absorption fine structure (PTRF-XAFS) shown in Figure 1a is the most appropriate technique for the investigation of interface structure and the local interaction between metal and support. However, the thin electrolyte layer prevents the effective mass transport to the electrode surface and also decreases the incident X-ray intensity. In this study, we carried out a new XAFS set-up where X-ray irradiates the PtNPs from the back side of the highly oriented pyrolytic graphite (HOPG) substrate and XAFS was detected in the fluorescence X-ray mode at the same side (Figure 1b) in order to minimize the X-ray absorption by electrolyte and enhance interface effect.

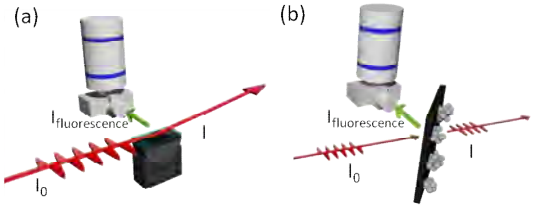

Figure 1 Schematic illustration of (a) PTRF-XAFS configuration and (b) backside irradiation in this study.

2 Experiment

Well-defined dodecanethiol-protected PtNPs were prepared according to the literature [1] and deposited on the atomically flat HOPG (S = 1.44 cm^2) by spin coating. After spin coating, dodecanethiol layers were removed by electrochemical oxidation-reduction cycles (ORC) treatment in 0.1 M $HClO_4$ aqueous solution. For XAFS experiment, freshly cleaved HOPG sheet was used as an X-ray window (Figure 2a). The fluorescence signal was extracted from scattering X-ray using a BCLA (Bent Crystal Laue Analyzer designed for 8.4 keV) and detected by a 19 elements Ge-detector (Figure 2b).

3 Results and Discussion

According to the electrochemical measurement, the electrocatalytic activity of PtNPs for HER was increased with increasing the number of potential cycles (Figure 3a) because of desorption of dodecanethiol layer coated on PtNPs surface. From the cyclic voltamogram (CV), platinum active surface area was calculated as 0.074 cm^2. XANES spectra of Pt L_3-edge were obtained at various electrode potential although background signal caused by scattering from the electrolyte was increased (Figure 3b). However, BCLA reduced the most of the undesired scattering X-ray and we could get good S/B ratio spectra. The result indicated that the thin HOPG sheet could be used for an X-ray window and polarization technique was applicable to the studies of PtNPs on HOPG.

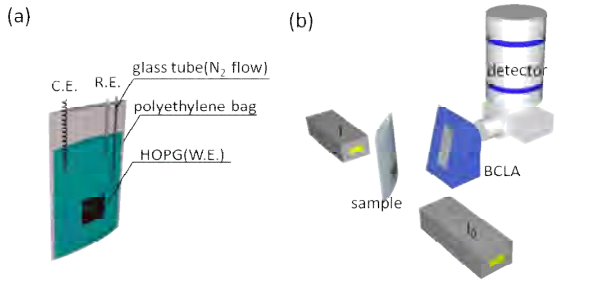

Figure 2 Schematic illustration of (a) sample for *in situ* XAFS measurement and (b) optical configuration with BCLA. C.E and R.E. are a counter electrode and a reference electrode, respectively.

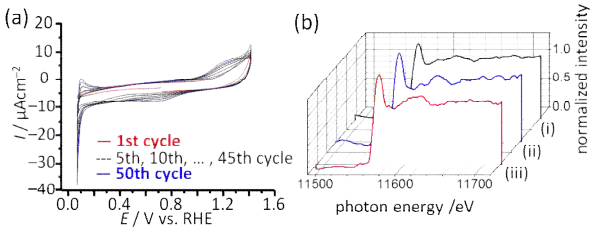

Figure 3. (a) CVs of PtNPs on HOPG in 0.1 M $HClO_4$. (b) XANES spectra recorded at various electrode potential; (i) E = 0.2 V (before ORC treatment), (ii) E = 0.2 V (after ORC treatment), (iii) E = 0.05 V (after ORC treatment).

Acknowledgement

The work is supported by NEDO project of PEFC project.

References

[1] C. Dablemont, P. Lang, C. Mangeney, J.-Y. Piquemal, V. Petkov, F. Herbst, and G. Viau, *Langmuir* **24** (2008) 5832.

* askr@cat.hokudai.ac.jp

27A/2010G634

Relationship between catalytic property and NEXAFS of P-doped graphite

Iwao SHIMOYAMA*, Teruyuki HAKODA, Yuji BABA, Tetsuhiro SEKIGUCHI,
Norie HIRAO, Kaveenga Rasika KOSWATTAGE
Japan Atomic Energy Agency, Tokai-mura, Ibaraki 319-1195, Japan

1. Introduction

Recently, it has been reported B- and/or N-doped carbon electrodes and nanotubes have high catalytic property on oxygen reduction reaction [1,2]. Therefore, hetero-atom doping in π-conjugated carbon materials attracts much attention to design "carbon alloys" which are expected to have many functionalities. So far, study of carbon alloys with other dopants is behind those prepared with typical B and N dopants. Since P is one of the group V elements as well as N, we focused on P doping in graphite as a standard material of π-conjugated carbon, and investigated electronic structures at the dopant sites by NEXAFS in this work. Furthermore we studied catalytic property of P-doped graphite using electrochemical experiments, and found a relationship between catalytic property and NEXAFS.

2. Experimental

Experiments were performed at the BL27A. PCl_3 was used for P doping. Fragment ions of PCl_3 were formed by a cold cathode ion gun and irradiated on a highly oriented pyrolytic graphite (HOPG) with an acceleration energy of 3 keV. Three samples were compared. Sample A was prepared by ion doping at 700 °C with YAG laser heating. The fluences of the total fragment ions was 3.5×10^{16} ions/cm^2. After doping, this sample was annealed at 800 °C. Samples B and C were prepared at room temperature with ion fluences of 2.0×10^{16} and 2.6×10^{15} ions/cm^2, respectively, and then annealed at 800 ºC. Contents of P were estimated by P2s/C1s photoelectron-peak intensity-ratios in XPS spectra measured with an MgKα source. Polarization dependence of NEXAFS was obtained by measuring total electron yield at various incidence angles θ that is defined by the angle between the electric field vector of the linearly polarized X-ray and the surface normal of the HOPG. Electrochemical experiments were performed by rotatable disc electrode (RDE) system [3] in 0.5 M H_2SO_4 solutions. P-doped HOPG samples were equipped on the RDE as the working electrode and cyclic voltammograms (CV) were measured in both O_2 and N_2 saturated solutions. The reference and counter electrodes were Ag/AgCl with a saturated KCl solution and a Pt wire, respectively. The RDE was operated at 1500 rpm.

3. Results and Discussion

Figure 1 shows P K-edge NEXAFS spectra of the P-doped HOPG measured at magic angle. Red, black, and blue curves show the results for samples A, B, and C, respectively. Since the most intense peak around 2147 eV almost coincides with the P1s → σ* peak of PCl_3 [4], it was difficult to distinguish carbon phosphide (CP_x) compounds from phosphorous chloride without annealing. However, another peak appeared around 2144 eV for sample A, and samples B and C after the annealing. Since content of Cl drastically decreased by the heating procedures, this peak is attributed to some CP_x prepared by the ion doping.

Figure 2 shows polarization dependences of the P K-edge NEXAFS spectra. The top, middle, and bottom show results for samples A, B, and C, respectively. Solid, broken, and dotted curves correspond to the spectra measured at θ = 20, 50, and 90°, respectively. Sample A showed clear graphite-like polarization dependence. This suggests that P atoms were incorporated in the *c*-plane of graphite and formed two-dimensional structure. Therefore, the peak at 2144.1 eV is assigned to P1s → π* out-of-plane transition of planar CP_x compounds. Since the peak around 2148 eV showed opposite polarization dependence, this peak can be assigned to P1s → σ* in-plane transition of same compounds.

Polarization dependences of samples B and C were smaller than that of sample A. We first supposed that the decrease of polarization dependence was caused by damage induced by ion beam irradiation. Polarization dependence can decrease when two-dimensional orientation of HOPG is disordered by ion beam irradiation. However, we noticed that the magnitude of polarization dependence was similar for samples B and C. Since the ion fluence of sample B was larger by almost

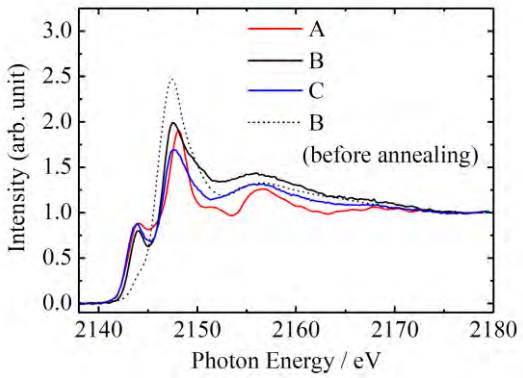

Figure 1. P K-edge NEXAFS spectra of P-doped HOPG. Red, black, and blue curves correspond to the results of samples A, B, and C, respectively. Dotted curve shows the result of sample B before annealing. (see text).

eight times than that of sample C, different magnitude of polarization dependences would be observed between these samples if degradation of polarization dependence was caused by damage effect. This implies that small polarization dependence was caused by the change of local configuration at P sites. We think distorted π-conjugated structures may be formed at P sites in samples B and C because some theoretical works indicated that substitution of P for C in π-conjugated carbon matrix can cause distortion of planar structure due to formation of "fullerene-like (FL) structure" [5,6].

Figure 3 shows reduction parts of CV for samples A, B, and C. Black and red curves correspond to the results obtained in N_2 and O_2 saturated solutions, respectively. P contents estimated from XPS spectra are also shown in the figure. Sample A shows almost identical CV for N_2 and O_2 saturated solutions. This means that the electrochemical reduction related to oxygen scarcely occurred on the surface of sample A. On the other hand, sample B and C showed different CV between N_2 and O_2 saturated solutions. For sample B, some electrochemical reduction related to oxygen was observed that around 0.1 V. This potential increased up to about 0.3 V (vs. Ag/AgCl) for sample C which showed the highest catalytic property among the samples. Since sample C had the smallest P content among them, we think amount of P was not the reason of the different catalytic properties. We consider that defects produced by ion beam were not the main cause of the catalytic property because the ion fluence of sample B was higher than that of sample C. Up to now, the reason why sample C had higher catalytic property than sample B is not clear. However, we noticed that both the samples B and C showed smaller polarization dependence of NEXAFS than sample A. This indicates that catalytic property was influenced by the local configuration at P sites, and distorted configuration can give better catalytic property to carbon alloys than planar configuration.

While the structure of the distorted configuration at P sites has not been clarified, our results indicate that P doping can also provide catalytic property for π-conjugated carbon materials. We also found that the catalytic property is related to the polarization dependence of NEXAFS. This suggests catalytic property can be designed by local configuration at dopant sites.

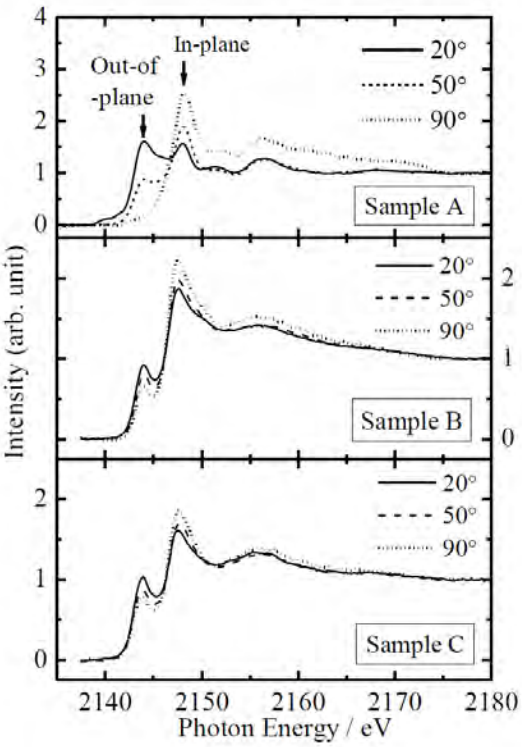

Figure 2. Polarization dependence of P K-edge NEXAFS spectra of samples A(top), B(middle), and C(bottom). Solid, broken, and dotted curves correspond to the spectra measured at θ = 20, 50, and 90°, respectively.

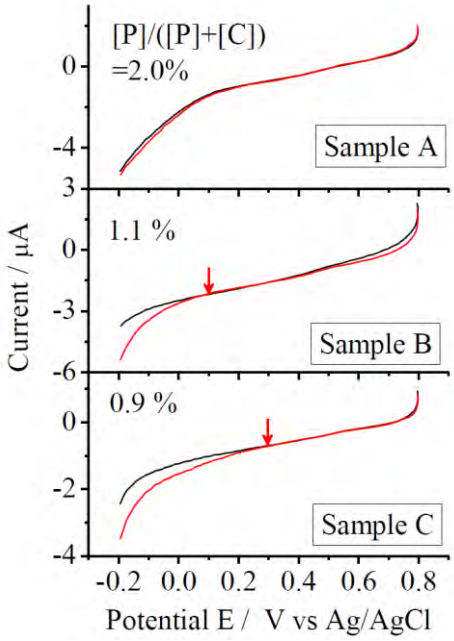

Figure 3. Cyclic voltammograms (CV) of P-doped HOPG in N_2 (black) and O_2 saturated H_2SO_4 solutions. Top, middle, and bottom show results of sample A, B, and C, respectively. P contents were estimated from XPS measurements.

References

[1] J. Ozaki *et al.*, Carbon 45, 1847 (2007).
[2] K. Gong *et al.*, Science 323, 760 (2009).
[3] T. Hakoda *et al.*, Appl. Surf. Sci. 257, 1556 (2010).
[4] Y. Baba *et al.*, Surf. Sci. 377-379, 699 (1997).
[5] A. Furlan *et al.*, Thin Solid Films 515, 1028 (2006).
[6] G. K. Gueorguiev *et al.*, Chem. Phys. Lett. 426, 374 (2006).

shimoyama.iwao@jaea.gp.jp

27A/2010G-635

Immobilization of alkyl chain molecules with phosphonic acid on oxide surface

Ayumi NARITA[*1,2], Yuji BABA[1], Tetsuhiro SEKIGUCHI[1], Iwao SHIMOYAMA[1], Norie HIRAO[1], Tsuyoshi YAITA[1,2]

[1]Quamtum Beam Science Directorate, Japan Atomic Energy Agency, Tokai-mura, Naka-gun, Ibaraki 319-1195, Japan

[2]Graduate School of Science and Engineering, Ibaraki Univ., Mito-shi, Ibaraki 310-8512, Japan

1 Introduction

In order to apply organic thin films as optical or electronic device materials, it is important to form uniform and stable films on solid surfaces. However, the immobilization of organic molecules on oxide surfaces is difficult because oxides are chemically inert. Phosphoric acid is one of functional groups which have high affinity for oxides. In this study, we have investigated the immobilization of alkyl chain molecules on the oxide surface through phosphonic acid as an anchor.

2 Experiment

All experiments were performed at the BL-27A station. C(0001) face of sapphire plates were used as substrates. We chose decylphosphonic acid (DPA) molecules as an adsorbate. The DPA film was formed by immersing the substrate in 0.01 Mol/dm^3 of DPA ethanol solution, and the substrate was rinsed by supersonic waves in ethanol. The chemical states of the interface were measured by X-ray photoelectron spectroscopy (XPS) and near-edge X-ray fine structure (NEXAFS). The sample was heated up to 250°C in vacuum by YAG laser from the outside of the vacuum.

3 Results and Discussion

The XPS spectra were measured at two incident angles; one was 35° and the other was 0.5° (total reflection condition). The C 1s peak intensity for the total reflection condition is enhanced compared with that for 35°. The XPS measured for the total reflection condition is surface sensitive, so the results suggest that the carbon atoms are located at the topmost surface. It indicates that the alkyl chain of the DPA molecules is located at the upper side, while the phosphonic acid is the lower side on the surface.

Fig.1 shows P K-edge NEXAFS and P 1s XPS spectra of the DPA film before and after heating. For the NEXAFS spectra, the main peak at 2152.8 eV is the resonance from P 1s to unoccupied orbital localized at the P atom [1]. The intensity of the peak decreased after heating. The detection depth of the NEXAFS measured by total electron yield is deeper than 10 nm, so the peak intensity is proportional to the total amount of the DPA molecules. Therefore, the NEXAFS results indicate that a part of DPA molecules were desorbed from the surface.

For the XPS spectra, on the other hand, the peak intensity of photoelectrons increased after heating. The P 1s photoelectron was excited by 3000 eV photons, so the kinetic energy of the P 1s photoelectrons is 850 eV. The inelastic mean free path (IMFP) of P 1s photoelectrons is 1.7 nm [2]. Therefore, it is suggested that the DPA molecules forming island structures at room temperature changed to thin uniform layer by heating. Thus, the increase of the photoelectron intensity of the P 1s in spite of the decrease of the DPA molecule quantity indicates that the surface was homogeneously covered by DPA molecules and the film became uniform by heating.

In summary, we succeeded in forming uniform and thermally stable films of alkyl chain molecules on the oxide surfaces using phosphonic acid as an anchor.

References

[1] G. Küper *et al.,* Chem. Phys. 165, 405 (1992).

[2] R. F. Egerton, Electron energy-loss spectroscopy in the electron microscope (Plenum Press, New York, 1996).

* narita.ayumi@jaea.go.jp

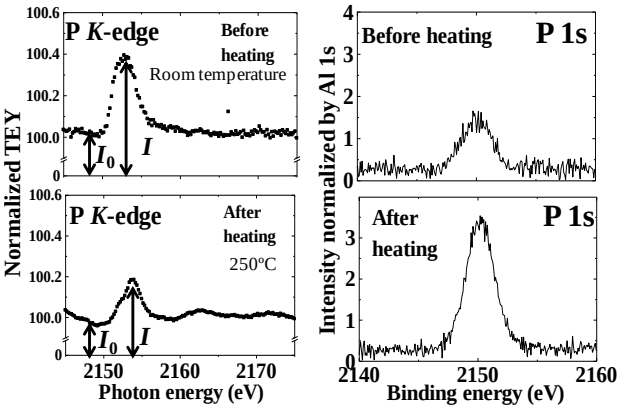

Fig.1 Left : P *K*-edge NEXAFS spectra for DPA films on sapphire C-plane before and after heating. I_0 is the normalized TEY at the off resonance energy and I is the normalized TEY at the resonance peak energy. Right : P 1s XPS spectra excited by 3000 eV photons for DPA film on sapphire C-plane before and after heating. The Intensity was normalized by that of Al 1s originated from substrates.

SPF/2010G652

Structure analysis of Ag_2Pb surface alloy by KEK-RHEPD

Yuki Fukaya[1,*], Iwao Matsuda[2], Masaki Maekawa[1], Izumi Mochizuki[1], Ken Wada[3], Toshio Hyodo[3], and Atsuo Kawasuso[1],
[1]JAEA, Takasaki 370-1292, Japan
[2]University of Tokyo, Chiba 277-8581, Japan
[3]KEK-IMSS, Tsukuba 305-0801, Japan

1 Introduction

By the deposition of a 1/3 monolayer (ML, 1 ML = 1.38×10^{15} cm^{-2}) of Bi or Pb atoms on the Ag(111) surface, the surface alloy phase with a $\sqrt{3}\times\sqrt{3}$ structure is formed. This surface alloy is known as a giant Rashba surface [1]. The Rashba energy for the Ag_2Bi surface alloy is estimated to be 200 meV [1], which is much larger than that for two-dimensional hetero-semiconductors (~1 meV). First-principles calculations suggested that the magnitude of the Rashba energy is closely related to the outward displacement of the topmost heavy element [2]. However, the relationship between them still remains unresolved.

Reflection high-energy positron diffraction (RHEPD) is a surface-sensitive tool to determine the topmost atomic structure and property owing to the total reflection. Recently, a new RHEPD apparatus was developed using an intense position beam from a linac at the Slow Positron Facility at the Institute of Materials Structure Science, KEK [3]. The fractional spots for the Si(111)-7×7 surface were clearly observable. In this report, measurements of the RHEPD rocking curves from the Ag_2Pb alloy surfaces with changing the film thickness of the underlying Ag layers are described. The surface structure was analyzed using the dynamical diffraction theory.

2 Experiment

To make crystalline Ag(111) thin films, Ag atoms were deposited onto the Si(111)-7×7 surface at 130 K. The substrates were cut from a mirror-polished Si(111) wafer. After gradually annealing up to room temperature, well-ordered Ag(111) thin films were formed. Subsequently, 1/3 ML Pb atoms were deposited on the Ag(111)-1×1 surface at 400 K.

The RHEPD experiments were carried out at the slow positron beam line SPF-B1 at the Slow Positron Facility, KEK [3]. The positron beam energy was 10 keV. To measure the rocking curves, the glancing angle was varied up to 6° by rotating the sample.

3 Results and Discussion

Figure 1 displays the RHEPD rocking curves of the specular spots measured for the Ag_2Pb surface alloys with Ag film thicknesses (t_{Ag}) of 6, 11, 22 ML under the one-beam condition. In this condition, the rocking curve depends mainly on the vertical displacement of the atomic positions. Although the change in the rocking curves with t_{Ag} is small, the intensitiy in the glancing angle range of 2.0°-4.5° gradually decreases as t_{Ag} increases. This indicates that the Pb atoms are shifted upward with increasing t_{Ag}.

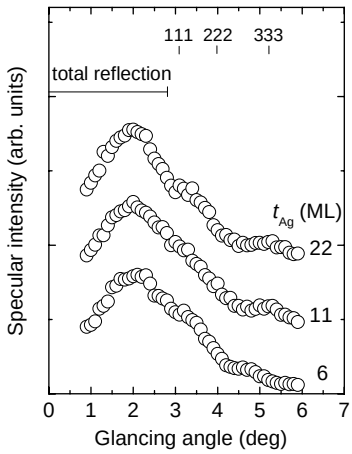

Fig. 1 (a) RHEPD rocking curves of the specular spots measured for the $\sqrt{3}\times\sqrt{3}$ of Ag_2Pb surface alloys with t_{Ag} = 6, 11, and 22 ML. The critical angle for total reflection is estimated to be 2.7°. The index of the Bragg reflection is shown at the top of figure.

To determine the outward displacement of the Pb atoms, the RHEPD intensities were calculated based on the dynamical diffraction theory. It was found that the outward displacement of the Pb atoms increases with increasing t_{Ag}. In order to confirm the displacement with t_{Ag}, the measurements of the rocking curves for the Ag_2Pb surface alloy with various t_{Ag} are needed. Further, to verify the relationship between the atomic displacement and the Rashba energy, the surface electronic band structures will be measured by using angle-resolved photoemission spectroscopy (ARPES).

References

[1] C. R. Ast *et al*., Phys. Rev. Lett. **98** (2007) 186807.
[2] G. Bihlmayer, S. Blügel, and E. V. Chulkov, B **75** (2007) 195414.
[3] K. Wada *et al*., Eur. Phys. J. D **66** (2012) 37.

* fukaya.yuki99@jaea.go.jp

27A/2010G653

Molecular orientation of regioregular poly(3-hexylthiophene) film

Hiromi Ikeura-SEKIGUCHI*[1], Tetsuhiro SEKIGUCHI[2]
[1]National Institute of Advanced Industrial Science and Technology (AIST), Tsukuba, Ibaraki 305-8568, Japan
[2]Japan Atomic Energy Agency (JAEA), Tokai-mura, Naka-gun, Ibaraki 319-1195, Japan

Introduction

Intermolecular - stacking interactions through its aromatic rings play a dominant role in the performance of organic semiconductor devices. Regioregular (RR)-P3HT has been used as the active material in OFETs in which the preferential - stacking of the polymer chains perpendicular to the substrate produces charge transport between the source and the drain occurs parallel to the substrate. On the contrary, in bulk heterojunction (BHJ) solar cells, the charges have to be transported perpendicular to the substrate to reach each electrode. The - stacking oriented perpendicular to the substrate takes advantage of high mobility pathways to the electrodes. The degree of regioregularity of P3HT backbone strongly influence on structural order which is related to solar cell performance.

Experimental

Experiments were performed at beamline BL-27A with energy resolution of 0.9 eV around the S *K*-edge using X-ray absorption spectroscopy (XAS). The XAS spectra were measured using monitoring sample drain current near the S *K*-edge (2465–2500 eV). Such energies were chosen to excite the S 1*s* core electron to unoccupied orbitals of regioregular poly(3-hexylthiophene) RR-P3HT. Angle dependent XAS data were obtained by changing the angle between the incoming x-ray beam and the sample surface.

Results and discussion

Figure 1 shows the S *K*-edge XAS spectra of RR-P3HT film at various angles of X-ray incidence , between the direction of propagation of incident synchrotron light X-ray and the surface plane. The XAS of RR-P3HT film changes in intensity at Peak 1 and Peak 2, which indicates that a well-ordered morphology is produced. In contrast, the XAS of polycrystalline RR-P3HT powder shows no polarization dependence and is reasonably similar to that of the film at =55° (magic angle). Peak 1 can be assigned to S 1*s* • * (C=C) and *(S–C) unoccupied states on the previous XAS studies of thiophene[1] and polythiophene[2]. The S 1*s* • * (C=C) excitation is lower in energy by ~ 1 eV than the S 1*s* • *(S–C). On the analogy of polythiophene spectra[3] as probed by XAS combined with Resonant Auger Spectroscopy[3], Peak 1 is suggested to be dominated by S 1*s* • *(S–C) excitation. Peak 1 is enhanced at normal incidence of X-ray, while peak 2 is enhanced at grazing incidence and almost absent at normal incidence. Peak 1 and peak 2 clearly show opposite polarization dependence with changing incidence angles. Thus, peak 2 can be assigned to S 1*s* • * excitation. It is therefore considered that most RR-P3HT chains are well-aligned and oriented *face-on* with respect to the Si substrate.

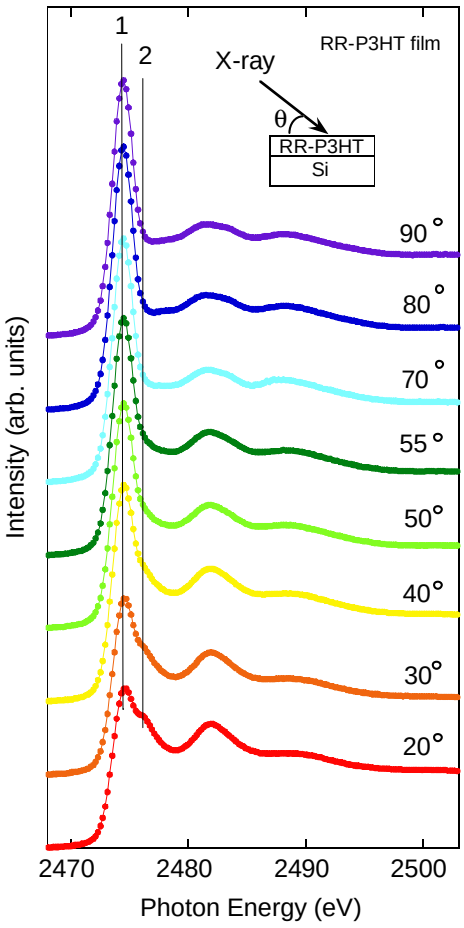

Fig.1 XAS spectra of RR-P3HT - stacking film as a function of angle of X-ray incidence near the S *K*-edge together with RR-P3HT polycrystalline powder.

References

[1] A.P. Hitchcock, J.A. Horsley, J. Stöhr, *J. Chem. Phys.* **85**, 4835 (1986).
[2] H. Ikeura-Sekiguchi, T. Sekiguchi, *Surf. Int. Anal.* **40**, 673 (2008).
[3] H. Ikeura-Sekiguchi, T. Sekiguchi. *Phys. Rev. Lett*. **99**, 228102 (2007).

*ikeura-sekiguchi@aist.go.jp

7A/2010G657

有機単分子層の深さ分解 C K-NEXAFS による解析
Depth Analysis of Organic Monolayers by C K-NEXAFS

遠藤　理[1*]、中村　将志[2]、雨宮　健太[3]
[1]東京農工大、〒184-8588 小金井市中町 2-24-16
[2]千葉大工、〒263-8522 千葉市稲毛区弥生町 1-33
[3]KEK-PF、〒305-0801 つくば市大穂 1-1

1 はじめに

X 線吸収端近傍微細構造分光法(NEXAFS)は、内殻励起過程を利用し、空軌道のエネルギー・空間分布から薄膜や表面での分子配向を決定する有力な手法である。有機化合物の主成分である炭素のスペクトルでは総和が得られるので、詳細な解析には内殻エネルギー以外の手段を用いたスペクトル分離が望まれる。吸収に伴って放出されるオージェ電子を計数する際、平均自由行程 λ の電子が深さ d から出射角 θ で検出された場合の強度が $\exp(-d/\lambda\sin\theta)$に比例することを利用し、$d$ に依存したスペクトルに分離できることが、磁性材料の XMCD 測定で示されている[1]。本研究では、Au(111)面における芳香族チオール単分子層の測定を行い、 C K-NEXAFS のスペクトル分離について検討した。

2 実験

実験は軟 X 線分光ステーション BL-7A で 1×10^{-7} Torr 以下の高真空下で行った。Au(111)面を大気中でアニール後、チオールのアルコール溶液に 2 時間浸すことで単分子層を作成した。深さ分解 C K-NEXAFS 測定は MCP 背面の蛍光スクリーン像を CCD カメラで画像検出することにより行った。阻止電位 200 V を印加し低速の電子をカットした。

3 結果および考察

Au(111)面における p-トルエンチオール単分子層の C K-NEXAFS スペクトルの偏光依存から分子配向を解析した結果、ベンゼン環を基板表面から 30°程傾けた配向の試料 a と、ほぼ垂直に立てた配向の試料 b が得られたため、両者について深さ分解解析を行った。各励起エネルギーに対し、図 1 内挿図の様に表面に平行にスライスしたチャンネル毎の収量をプロットすることにより図 1 のような深さ分解曲線が得られる。全ての曲線を、特定のエネルギーの二曲線の成分に分解して得られた分離スペクトルが図 2 である。図 2a では 2 種類の π^*_{CC}軌道への遷移と、287 eV 付近の連続状態のステップが分離されているのに対し、図 2b では σ^*_{CS} 軌道への遷移を主成分にもつスペクトルとそれ以外に分離されている様子が分かる。この結果は、試料 b では σ^*_{CS} 軌道への遷移が強調されている場合、CS 結合に寄与する炭素原子が直立配向の分子において他の炭素原子よりも深い位置にあることを、より顕著に反映したことを示していると考えられる。一方寝た配向の試料 a では、ベンゼン環とメチル基とが分離されているか、π^*_{CC} 軌道への遷移で生じる共鳴オージェ過程において、異なるエネルギーや出射角分布を持つ電子が、特異な深さ分解曲線を与えているものと考えられる。

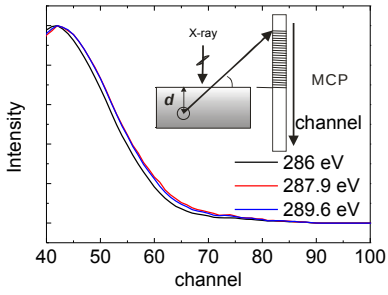

図 1：深さ分解曲線。

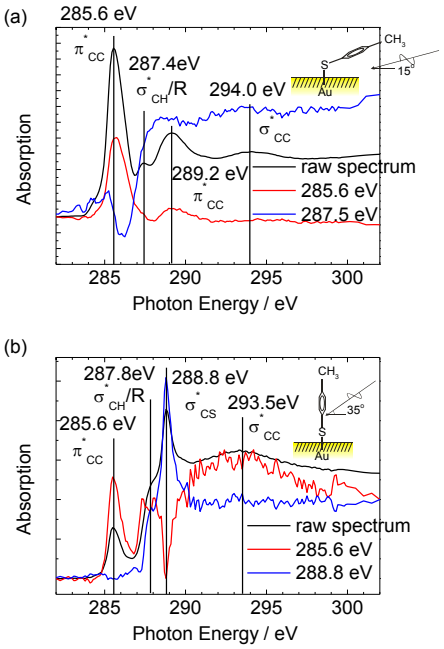

図 2：p-トルエンチオール/Au(111)単分子層の分離した C K-NEXAFS スペクトル。(a)30°、(b)直立配向。

謝辞

本研究は科研費若手(B)(No. 22760027)の助成を受けたものである。

参考文献

[1] K. Amemiya *et al.*, Phys. Rev. B **71** (2005) 214420.

* oendo@cc.tuat.ac.jp

27A/2010G660

Determination of the atomic arrangement at the graphene/α-Al_2O_3(0001) interface by normal incident X-ray standing wave spectroscopy

Shiro Entani[1,*], Manabu Ohtomo[1], Yoshihiro Matsumoto[1], Yuji Baba[2], Ayumi Narita[2], Norie Hirao[2], Iwao Shimoyama[2], Tetsuhiro Sekiguchi[2], Pavel V. Avramov[1], Naramoto Hiroshi[1] and Seiji Sakai[1]
[1]Advanced Science Research Center, Japan Atomic Energy Agency, Tokai 319-1195, Japan
[2]Quantum Beam Science Directorate, Japan Atomic Energy Agency, Tokai 319-1195, Japan

1 Introduction

Direct growth of graphene films on insulator substrates is currently one of the most important subjects for graphene-based nanoelectronics and spintronics. Despite the critical role of substrate on the electronic property of graphene, the atomic structure of the graphene/insulator substrate interface is still not clear. Normal incidence X-ray standing wave (NIXSW) spectroscopy is a powerful tool for investigating the interface atomic structure, because the positions of atoms relative to the scattering plane in the substrate can be determined precisely and element-specifically [1]. In this study, the atomic arrangement of single-layer graphene (SLG) directly grown on c-plane sapphire (α-Al_2O_3(0001)) has been studies by NIXSW spectroscopy.

2 Experiment

The graphene growth on α-Al_2O_3(0001) was performed in a vacuum quartz tube furnace with a base pressure of 2 × 10^{-6} Pa. The α-Al_2O_3(0001) substrate was annealed at 1173 K for 60 min in an open air to prepare atomically flat surface. The SLG film was grown by exposing the α-Al_2O_3(0001) surface to methanol vapour in a pressure of ~1000 Pa at the substrate temperature of 1273 K [2]. The NIXSW measurements were conducted at the BL-27A station by scanned-energy technique [3]. The NIXSW profiles were obtained by recording the intensities of the Al 1*s*, O 1*s* and C 1*s* photoelectrons as a function of the photon energy.

3 Results and Discussion

Figures 1 (a), (b) and (c) show SW profiles for the Al, O and C atoms in SLG/α-Al_2O_3(0001). Clear SW profiles are seen in Fig.1, and the Bragg energy can be determined as 2938.5 eV. This energy nearly corresponds to the Bragg diffraction peak from the one-sixth of the c-axis of α-Al_2O_3 unit cell (d = 2.17 Å). The SW profile is written as

$$I(E)/I_0 = 1+R(E)+2F[R(E)]^{1/2}\cdot\cos[2\pi d_H-\delta(E)] \quad (1)$$

where E is the photon energy, $R(E)$ is the reflectivity of the substrate, $\delta(E)$ is the energy-dependent phase modulation caused by the X-ray standing wave, F is the structure factor, and d_H is the coherent position of the atoms measured from the X-ray scatter plane [4]. The d_H of Al, O and C is calculated as -0.1 ± 0.1, 0.5 ± 0.3 and 1.7 ± 0.3, respectively. Thus, the Al, O and C atoms respectively are located at -0.2, 1.1 and 3.7 Å above the scatter plane. From these results, we propose the vertical structure of SLG/α-Al_2O_3(0001) as schematically illustrated in Fig.2. The SLG layer is ~2.6 Å above the α-Al_2O_3(0001) surface, which is comparable with the distance between the SLG layer and the Ni(111) surface (2.14 Å) [5]. This suggests rather strong interaction at the SLG/α-Al_2O_3(0001) interface.

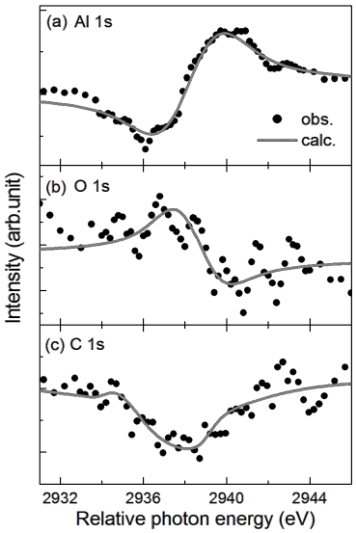

Fig. 1: NIXSW profiles from (a) Al 1*s*, (b) O 1*s* and (c) C 1*s* core level emission. The calculated SW profiles (solid line) are also included in the figure.

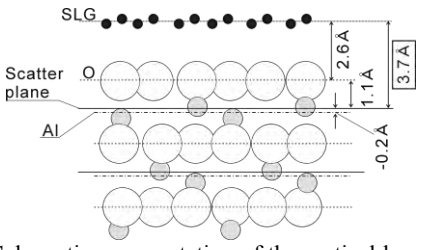

Fig. 2: Schematic representation of the vertical locations of the Al, C and O atoms in SLG/α-Al_2O_3(0001).

References
[1] D.P. Woodruff *et al*., Phys. Rev. Lett. **58** (1987) 1460. D.P. Woodruff *et al.*, Prof. Surf. Sci., **57** (1998) 1.
[2] S. Entani *et al.*, *unpublished*.
[3] Y. Baba *et al.*, e-J. Surf. Sci. Nanotech., **10** (2012) 69.
[4] P. Fenter *et al.*, Surf. Sci. **412**/**413** (1998) 213.
[5] Y. Gamo *et al.*, Surf. Sci. **374** (1997) 61.

* entani.shiro@jaea.go.jp

PF 12C/2010G677, SPring-8 01B1/2011A1976

Photo-excited carrier transfer from Nb:$SrTiO_3$-photoelectrode to Mn-oxide-cocatalyst studied by in-situ electrochemical XAFS

Masaaki YOSHIDA[1,*], Takumi YOMOGIDA[1], Takahisa HATA[1], Ryo TOYOSHIMA[1], Kiyohumi NITTA[2], Kazuo KATO[2], Takuya MASUDA[3], Hiroaki NITANI[4], Hitoshi ABE[4], Satoru TAKAKUSAGI[5], Tomoya URUGA[2], Kiyotaka ASAKURA[5], Kohei UOSAKI[3], and Hiroshi KONDOH[1]

[1]Keio University, [2]Japan Synchrotron Radiation Research Institute, [3]National Institute for Materials Science, [4]Photon Factory, KEK, [5]Hokkaido University

1 Introduction

Photoelectrochemical water splitting is an attractive candidate for the sustainable production of hydrogen gas by solar energy [1]. The surface modification of Mn-oxide particles to semiconductor photoelectrodes greatly enhances the overall efficiency for water splitting, because Mn-oxide species work as an efficient cocatalyst for oxygen evolution reaction. However, the immigration processes of photo-excited carriers from photoelectrode to cocatalyst have not yet been enough realized. In this study, the electronic structure of Mn-oxide cocatalyst on the Nb:$SrTiO_3$ photoelectrode under UV irradiation was investigated by the in-situ electrochemical X-ray absorption fine structure (XAFS) spectroscopy.

2 Experiment

The in-situ electrochemical XAFS measurements were performed at BL-12C of Photon Factory and BL01B1 of SPring-8. An n-type Nb:$SrTiO_3$ substrate was used as a photoelectrode after deposition of Mn-oxide particle cocatalyst. The Teflon-made electrochemical cell was used with a Pt wire counter electrode and a Ag/AgCl (saturated KCl) reference electrode in an 0.1 M Na_2SO_4 aqueous solution with Ar bubbling. A Xenon lamp was used for photoelectrochemical reaction under UV irradiation.

3 Results and Discussion

Fig. 1 shows the Mn K-edge XAFS spectra taken for Mn-oxide cocatalysts on the Nb:$SrTiO_3$ photoelectrode were observed under potential control between -1.0 V and 1.0 V vs. Ag/AgCl. At the potential of -1.0 V, the peak of Mn species was observed at 6551 eV. The edge position corresponded with that of the MnO reference sample, indicating that the electronic structure of Mn-oxide particles is likely to be the same with that of Mn^{2+}. With changing the potential from -1.0 V to 1.0 V, the higher energy peak was gradually observed at 6557 eV. The edge position was coincident with that of the Mn_2O_3 reference sample, implying that the structure of Mn-oxide particles can change between Mn^{2+} and Mn^{3+} species. The Mn-K edge XAFS spectra were taken at the potential of 1.0 V under UV irradiation. The edge position at 6557 eV was gradually shifted to lower energy at 6551 eV under irradiation, suggesting that some Mn^{3+} species changed to Mn^{2+} due to the immigration of photo-excited electrons, although the Mn-oxide particles apparently work as oxygen evolution cocatalyst via the photo-excited hole transfer. This result indicates that a part of Mn-oxide particles was positioned at the lower potential by the photo-excited electron transfer and does not function as oxygen evolution sites. Thus, the efficient transfer of photo-excited carriers to cocatalyst particles is likely to be an essential key for improvement of water splitting capability.

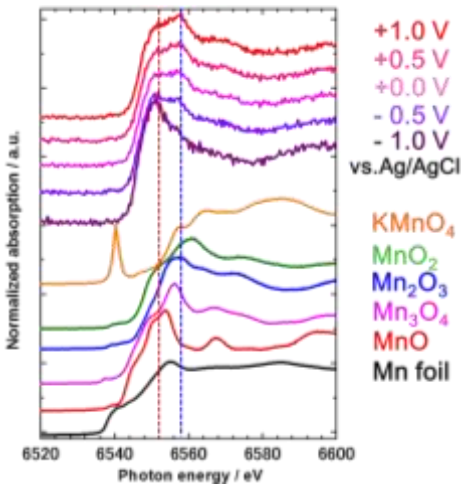

Fig. 1: Mn K-edge XAFS spectra taken for the Mn-oxide on Nb:$SrTiO_3$ electrode at various applied potenstials in Ar saturated 0.1 M Na_2SO_4 aqueous solution.

Acknowledgement

The present work has been performed at Photon Factory (2010G677) and SPring-8 (2011A1976(Priority Program for Disaster-Affected Quantum Beam Facilities), 2011B1080, 2012A1623). This work was supported by MEXT/JSPS KAKENHI (22850015, 24750134).

References

[1] G. W. Michael, L. W. Emily, R. M. James, W. B. Shannon, M. Qixi, A. S. Elizabeth and S. L. Nathan, Chem. Rev. **110** (2010) 6446.

* yoshida@chem.keio.ac.jp

12C/2010P-007

小角X線散乱法によるドープ氷中の金属塩結晶の粒径解析

Particle size of metal salt crystals in doped ice by small-angle X-ray scattering technique

原田誠 [1*], 橋本拓也 [1], 社本泰樹 [1], 岡田哲男 [1]
[1] 東京工業大学大学院理工学研究科、〒152-8551 東京都目黒区大岡山 2-12-1

1 はじめに

最も身近な溶媒である水の固体である氷は、水溶液を凍結させると、溶解していた塩は氷の中に閉じこめられることがある。ゆっくりと時間を掛けて凍結させると、氷は溶解しているイオン等を水分子のネットワークから排除しながら結晶成長するために純粋氷となるが、急速に冷却することで、塩は氷中に残り、いわゆるドープ氷となる。しかしながら、溶質は氷のネットワーク中に取り込まれるわけではなく、グレインバウンダリーという氷微結晶の狭い隙間に濃縮される。グレインバウンダリーの塩は共晶点に依存し、共晶点以下では塩結晶となり、共晶点以上では水和状態となっていると考えられている。本研究では、水溶液を凍結した際にグレインバウンダリーに析出する金属塩の結晶の大きさを小角X線散乱法によって解析し、用いる水溶液の塩濃度や金属塩の種類、凍結からの時間経過などで、結晶の粒子経がどのように依存するのかを検討した。

2 実験

測定は BL-10C に備え付けられている酵素回折計を使い、検出器として PSPC を用いた。-5～-20℃の低温下で小角X線散乱測定を行うために、試料ホルダとして図 1 に示すようなセルを用いた。セルの温度を調整するためにペルチェ素子を用い、Pt100 を温度センサとして常に試料の温度を測定した。図 1 上のような銅製サンプルホルダに試料水溶液を入れ、ホルダ毎液体窒素中に沈めて急速に冷凍し、試料溶液を凍結した。凍結後、ペルチェ素子上に設置したセルホルダに差し込み、全体をアクリルカバーで覆い、X線が空気によって減衰しないように内部をヘリウムで置換した。X 線はカバーのカプトン窓から試料に照射した。試料によって散乱したX線は後方のカプトン窓から酵素計を通過して PSPC へ透過するようにした。

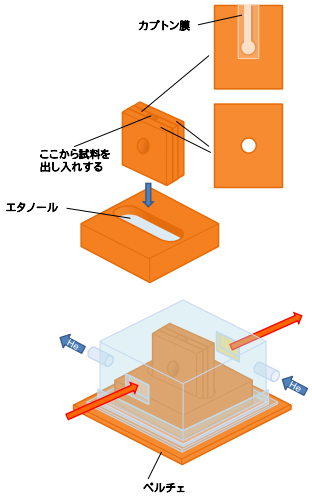

図 1 氷小角X線散乱測定セル。

3 結果および考察

図 2、3 に測定したスペクトルを Guinier 解析した結果を示す。時間経過によってグレインバウンダリーの結晶成長が見られることを期待したが、粒径の経時変化は見られなかった。ドープ氷を作成してから測定スタートするまでに 5 分程度を要するため、この時間にグレインバウンダリーを通って塩の凝集が起こったか、もしくは氷の微結晶が生じる際に同時に塩が結晶化したかのどちらかが考えられる。図 2、3 からも明らかなように、多少の差は見られるが濃度が違っても粒径には大きな違いはなく、ほぼ一定しており、これは濃度が塩結晶微粒子の大きさではなく、粒子数に依存することがわかった。

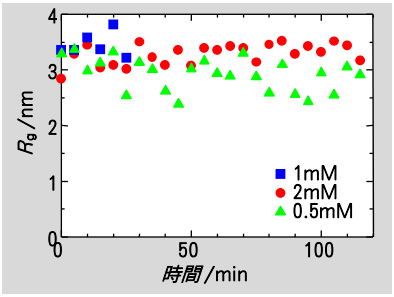

図 2 -15℃での RbBr ドープ氷の Guinier Plot の結果。

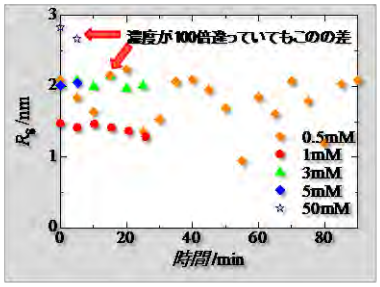

図 3 -15℃での KCl ドープ氷の Guinier Plot の結果。

金属塩の種類が変わるといくらか大きさが異なり、結晶を構成するイオンの結晶での半径（結合距離）が異なるためではないかと考えている。

4 謝辞

本実験を進めるに当たり、さまざまな助言・ご指導をいただいた東京工業大学・野島修一先生に深く感謝いたします。

5 参照論文

M. Harada , Y. Tasaki , H. Qu, T. Okada *RSC Adv.*, **2012**, *2*, 461-466

HiSOR BL-13/ HiSOR-PAC 11-B-23, PF-PAC 2011G013

Surface-Site-Selective Study of Valence Electronic States of Si(111)-7×7 Adsorbed with Water Using Si-$L_{23}VV$ Auger Electron Si-2*p* Photoelectron Coincidence Measurements

S. Arae,[1] S. Kajikawa,[2] H. Hayashita,[2] M. Ogawa,[2] S. Ohno,[1] S. Wada,[2]
T. Sekitani,[2] Y. Sato,[3] S. Hanaoka,[3] T. Kakiuchi,[3] K. Mase,[4,5] M. Okusawa,[6] and M. Tanaka[2]
[1]Yokohama National University, Yokohama 240-8501, Japan
[2]Hiroshima University, Higashi-Hiroshima 739-8526, Japan
[3]Ehime University, Matsuyama 790-8577, Japan
[4]Institute of Materials Structure Science, Tsukuba 305-0801, Japan
[5]The Graduate University for Advanced Studies, Tsukuba 305-0801, Japan
[6]Gunma University, Maebashi 371-8510, Japan

1 Introduction

Interaction of water and a clean silicon surface has been investigated extensively because it is a typical system for understanding of chemisorptions, and because oxidation of silicon by water is important for semiconductor industry [1,2]. The unit cell of a clean Si(111)-7×7 surface includes 12 adatoms, 6 rest atoms, 36 pedestal atoms (atoms directly bonded to the adatoms), 18 dimer atoms, and 1 corner-hole atom [3]. *Ab initio* theoretical studies show that a clean Si(111)-7×7 is metallic owing to the midgap states at the adatoms [4]. Water is reported to be chemisorbed dissociatively on Si(111)-7×7 at room temperature (RT), forming Si–H and Si–OH species [5,6]. In a study using a scanning-tunneling microscope (STM) and high resolution electron energy-loss spectroscopy T. Yamada *et al.* reported that the OH and H fragments bond to the adatom and adjacent rest atom, respectively, and that half of the adatoms remain intact in the half unit cell at room temperature (RT) [7].

In the present study we investigated the change of valence electronic states in the vicinity of the adatom site of Si(111)-7×7 induced by water chemisorption at RT using high-resolution coincidence measurements of Si-$L_{23}VV$ Auger electrons and Si-2*p* photoelectrons. Si-$L_{23}VV$-Si-2*p* Auger photoelectron coincidence spectroscopy (APECS) is a unique technique to investigate valence electron states at a specific surface Si site that exhibits a specific surface core-level shift [8,9]. APECS is more surface-sensitive than the conventional photoemission and Auger electron spectroscopy (PES and AES) [10], because the escape depth (*ED*) of electrons detected by APECS is given by

$$\frac{1}{ED_{\mathrm{APECS}}} = \frac{1}{\mu_{\mathrm{Pe}}} + \frac{1}{\mu_{\mathrm{Ae}}},\ \mu_{\mathrm{Pe}} = \lambda_{\mathrm{Pe}}\cos\theta_{\mathrm{Pe}}, \mu_{\mathrm{Ae}} = \lambda_{\mathrm{Ae}}\cos\theta_{\mathrm{Ae}},$$

where λ and θ denote the inelastic mean free path and the emission angles of the detected electrons, respectively. The subscripts APECS, Pe and Ae denote electrons detected by APECS, PES, and AES, respectively. By using synchrotron radiation (SR) with a photon energy ($h\nu$) of 130 eV and a house-made APECS analyzer [11], ED_{APECS} for Si-$L_{23}VV$-Si-2*p* APECS can be shortened as small as about 1.3 Å [9]. This value is shorter than the averaged thickness of a monolayer of Si(111) (~1.57 Å). Thus, Si-$L_{23}VV$-Si-2*p* APECS is an ideal tool to monitor the change of valence electronic states in the vicinity of Si adatoms induced by water adsorption.

2 Experiment

Experiments were carried out in an ultrahigh vacuum chamber (base pressure: 1~2×10^{-7} Pa) at a soft X-ray beamline, BL-13 at HiSOR. A clean reconstructed Si(111)-7×7 surface was prepared by direct-current heating at > 1400 K for several seconds followed by slow cooling to RT. Then the clean Si(111)-7×7 was exposed to water of ~10 L (1 L = 1×10^{-6} Torr s) at RT. The sample was irradiated with *p*-polarized SR with an incidence angle of 84˚ from the surface normal.

3 Results and Discussion

Figure 1 shows an enlarged Si 2*p* photoelectron spectrum of Si(111)-7×7 measured with the double-pass cylindrical mirror analyzer (DP-CMA) of the APECS analyzer at a photon energy of 130 eV. This spectrum was decomposed into surface, bulk, and Si^{1+} components by a fitting procedure [9]. The presence of the small Si^{1+} 2*p* component indicates that this surface is partly contaminated with residual water. Figure 2 shows the Si-$L_{23}VV$-Si-2*p* APECS spectrum of adatom sites of Si (111)7×7 at $h\nu$ of 130 eV. The shape of the APECS spectrum in the high kinetic energy region of 90–93 eV is almost the same to that of the Si-$L_{23}VV$ AES spectrum. This result indicates that the density of states just below the Fermi level is localized in the vicinity of adatoms. This result is consistent with a previous study using current-imaging tunneling spectroscopy [12]. The kinetic energy of the highest peak of the APECS spectrum (about 87.5eV), on the other hand, is about 0.5 eV smaller than that of the Si-$L_{23}VV$ AES spectrum. This result indicates that the adatom site is positively charged. These conclusions are consistent with a previous a theoretical study [4]. After exposure to water of 10 L at RT the kinetic energy of the highest peak of the APECS spectrum

remained unchanged but the intensities in the high kinetic energy region of 90–93 eV were decreased. This result is consistent with a previous STM study which reported that half of the adatoms remain intact at RT [7].

Acknowledgement

This work was approved by the Photon Factory Program Advisory Committee (PF PAC, No. 2011G013) but performed at the HiSOR in July, 2011 with the approval of the HiSOR Program Advisory Committee (11-B-23) because PF was damaged by the Great East Japan Earthquake on March 11, 2011. We express our sincere thanks to the staff of the HiSOR, Hiroshima University, and PF for their valuable help during the course of the experiments.

References

[1] P. A. Thiel and T. E. Madey, Surf. Sci. Rep. **7** (1987) 211.
[2] M. A. Henderson, Surf. Sci. Rep. **46** (2001) 1.
[3] K. Takayanagi, Y. Tanishiro, M. Takahashi, and S. Takahashi, J. Vac. Sci. Technol. A **3** (1985) 1502.
[4] J. E. Northrup, Phys. Rev. Lett. **57** (1986) 154.
[5] H. Kobayashi, T. Kubota, M. Onchi, M. Nishijima, Phys. Lett. A **95** (1983) 345.
[6] H. Ibach, H. Wagner, and D. Bruchman, Solid State Commun. **42** (1982) 457.
[7] T. Yamada, Y. Ohtsuka, H. Okuyama, T. Aruga, Phys. Rev. B **72** (2005) 1.
[8] T. Kakiuchi, S. Hashimoto, N. Fujita, M. Tanaka, K. Mase, and S. Nagaoka, J. Phys. Soc. Jpn. **79** (2010) 064714.
[9] T. Kakiuchi, M. Tahara, S. Hashimoto, N. Fujita, M. Tanaka, K. Mase, and S. Nagaoka, Phys. Rev. B **83** (2011) 035320.
[10] W. S. M. Werner, W. Smekal, H. Störi, H. Winter, G. Stefani, A. Ruocco, F. Offi, R. Gotter, A. Morgante, and F. Tommasini, Phys. Rev. Lett. **94** (2005) 038302.
[11] T. Kakiuchi, S. Hashimoto, N. Fujita, K. Mase, M. Tanaka, and M. Okusawa, J. Vac. Soc. Jpn. **51** (2008) 749. [in Japanese]
[12] R. J. Hamers, R. M. Tromp, and J. E. Demuth, Phys. Rev. Lett. **56** (1986) 1972.

* mase@post.kek.jp

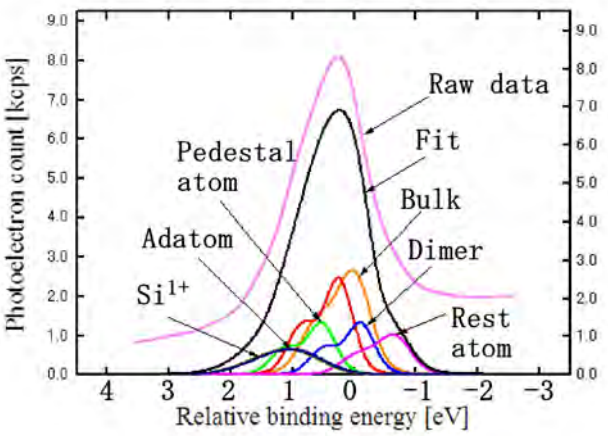

Figure 1: Enlarged Si 2*p* photoelectron spectrum of Si(111)-7×7 measured with the DP-CMA of the APECS analyzer at $h\nu$ = 130 eV.

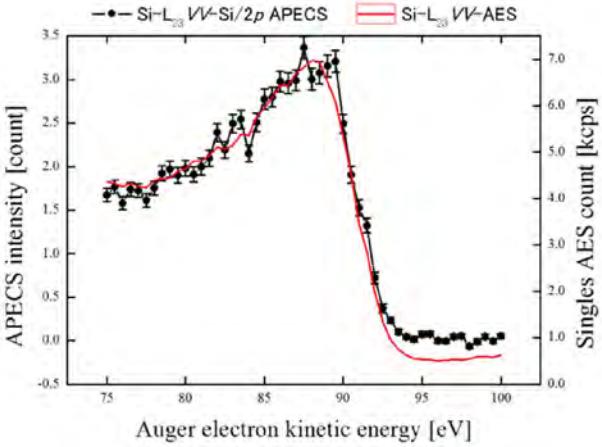

Figure 2: APECS spectrum (filled circles) of adatom sites of Si (111)7×7 at $h\nu$ = 130 eV.

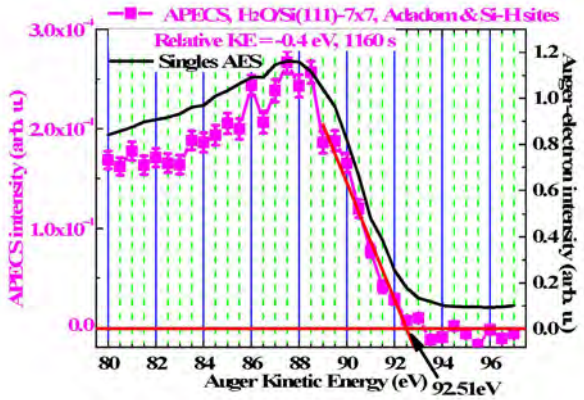

Figure 3: APECS spectrum (filled circles) of adatom sites of Si (111)7×7 exposed to water of 10 L at RT. $h\nu$ = 130 eV.

13A, 27A/2011G079

Analysis of bonding structure of ultrathin films of oligothiophene molecules grown on passivated silicon surfaces

H. Toyoshima[1], K. Hiraga[1], S. Ohno[1], M. Tanaka[1*], K. Ozawa[2], K. Mase[3], N. Hirao[4], T. Sekiguchi[4], I. Shimoyama[4], Y. Baba[4]

[1]Department of Physics, Yokohama National University, Hodogaya-ku, Yokohama 240-8501, Japan
[2]Department of Chemistry and Materials Science, Tokyo Institute of Technology, Ookayama, Meguro-ku, Tokyo 152-8551, Japan
[3]KEK-PF, Tsukuba, Ibaraki 305-0801, Japan
[4]Japan Atomic Energy Agency, Tokai-mura, Naka-gun, Ibaraki 319-1195, Japan

1 Introduction

The knowledge of the interaction between organic molecules and semiconductor surfaces is important to adapt organic semiconductors into the semiconductor technology [1]. In this study, the processes of α-sexithiophene (α-6T) thin layer formation on passivated Si surfaces have been investigated in situ by means of PES, NEXAFS, surface differential reflectance spectroscopy (SDRS) and reflectance difference spectroscopy (RDS).

2 Experiment

Si(001)-(2x1) surface was exposed independently to H_2O, O_2, atomic H, and C_2H_4 gas in an ultrahigh vacuum chamber. α-6T molecules were deposited on these passivated surfaces at room temperature to the nominal thickness of 5 nm at most.

3 Results and Discussion

Figure 1 shows normalized S-2p photoelectron spectra of α-6T thin films on water-adsorbed Si(001). A feature related to the interface is found only in the film with a thickness of 1 nm, which means sulfur atoms are combined with the substrate atoms. On the other hand, The C-1s photoelectron spectra indicate that carbon atoms are also combined with the substrate atoms.

Figure 2 shows S-1s NEXAFS spectra of α-6T film on water-adsorbed Si(001) measured at three incident angles. The thickness was 0.6 nm. The spectrum is dominated by an electronic transition to π* states at normal incidence,

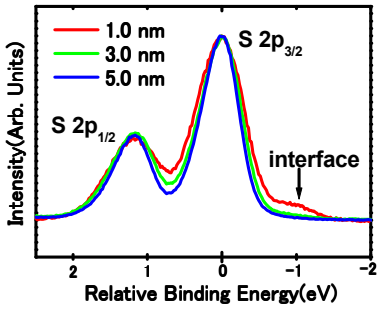

Fig. 1. Normalized S-2p PES spectra of α-6T thin films on water-adsorbed Si(001).

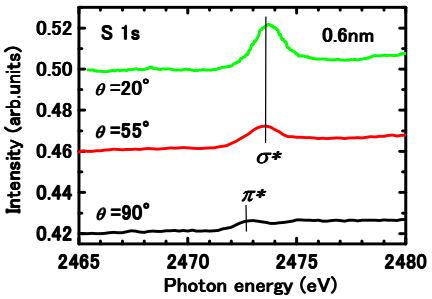

Fig. 2. S-1s NEXAFS spectra of a α-6T thin film on water-adsorbed Si(001).

while it is dominated by that to σ* states at grazing incidence. This means that majority of α-6T molecules are standing on the substrate.

The main findings obtained from the experimental results including SDRS and RDS as well as PES and NEXAFS are as follows. α-6T molecules are upright-standing to form bulk-like islands or films from the first layer on oxidized Si(001) and monohydride Si(001). Carbon atoms of the standing molecules are combined with the substrate atoms. On water-adsorbed Si(001), isolated α-6T molecules are flat-lying and align parallel to the dimer row until the thickness becomes 3 nm. Sulfur atoms of the lying molecules are combined with -OH of the surface. Above 3 nm, most of molecules are standing and constitute well ordered islands or films. On ethylene-adsorbed Si(001), the majority of α-6T molecules are flat-lying, and isolated molecules and those in the islands or films tend to align parallel and perpendicular to the dimer row, respectively. Thus, the orientation and electronic states of the molecules depend on the method of passivation, which raises the possibility of controlling the molecular orientation by the surface modification.

References

[1] R.J. Hamers, Annu. Rev. Anal. Chem. **1**, 707 (2008).

* mtanaka@ynu.ac.jp

HiSOR BL-13 / HiSOR-PAC 11-B-24, PA-PAC 2011G099

Construction and Evaluation of Auger-Photoelectron Coincidence Apparatus at BL13 of HiSOR

T. Kakiuchi[1,*], Y. Sato[1], S. Hanaoka[1], S. Kajikawa[2], H. Hayashita[2], M. Ogawa[2], S. Arai[3], S. Wada[2], T. Sekitani[2], S. Nagaoka[1], M. Tanaka[3], and K. Mase[4, 5]

[1]Department of Chemistry, Faculty of Science, Ehime University, 2-5 Bunkyo-cho, Matsuyama 790-8577, Japan.

[2]Department of Physical Science, Hiroshima University, Kagamiyama, Higashi-Hiroshima 739-8526, Japan

[3]Department of Physics, Faculty of Engineering, Yokohama National University, 79-5 Tokiwadai, Hodogaya-ku, Yokohama 240-8501, Japan

[4]Institute of Materials Structure Science, KEK, 1-1 Oho, Tsukuba 305-0801, Japan

[5]Department of Materials Structure Science, School of High Energy Accelerator Science, the Graduate University for Advanced Studies, 1-1 Oho, Tsukuba 305-0801, Japan

1 Introduction

Auger-photoelectron coincidence spectroscopy (APECS) combined with synchrotron radiation (SR) is the most surface-sensitive technique because the escape depth of Auger-electron detected by APECS is given by

$$\frac{1}{ED_{APECS}} = \frac{1}{\lambda_{PE}\cos\theta_{PE}} + \frac{1}{\lambda_{AE}\cos\theta_{AE}}$$

where λ_{PE} and λ_{AE} denote the inelastic mean free pass of photoelectron and Auger-electron, and θ_{PE} and θ_{AE} denote the emission angles of the detected photoelectron and Auger-electron, respectively [1]. In addition, the core-valence-valence (*CVV*) APECS spectra reflect the local valence electronic states at specific surface sites if the energy-resolution of the analyzer for the photoelectron is higher than the surface core level shift [2, 3]. For these APECS measurements we have installed an electron-electron-ion (EEICO) analyzer to an ultrahigh vacuum chamber at BL13 of HiSOR.

2 Experiment

The EEICO analyzer mainly consists of a coaxially symmetric mirror electron energy analyzer (ASMA), a double-pass cylindrical mirror electron energy analyzer (DP-CMA), etc [4]. The performance of the apparatus was evaluated by measuring APECS spectra of a Si(111) surface in an ultra-high vacuum chamber with a base pressure of 4.5×10^{-9} Torr at BL13 of HiSOR. The photon energy was fixed at 130 eV. The incident angle was 86º from the surface normal. The Si(111) was cleaned by direct-current heating.

3 Results and Discussion

Figure 1 shows a wide scan Si photoelectron spectrum (PES) of Si(111) measured with the ASMA.

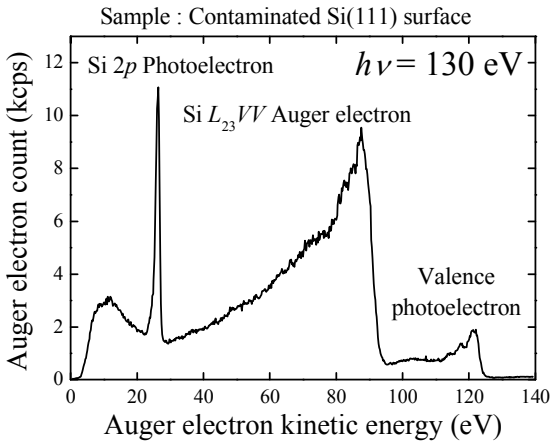

Fig. 1: Wide scan Si photoelectron spectrum of a partly contaminated Si(111) measured with the ASMA at $h\nu$ = 130 eV.

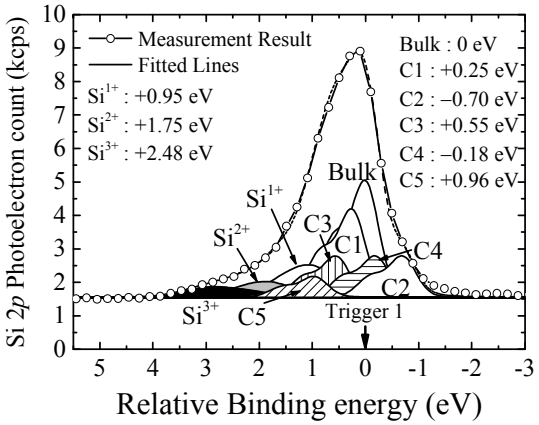

Fig. 2: Enlarged Si 2*p* photoelectron spectrum of a partly contaminated Si(111) measured with the DP-CMA at $h\nu$ = 130 eV.

Figure 2 shows the enlarged Si 2*p* PES measured with the DP-CMA drown on relative binding energy scale where the Si $2p_{3/2}$ peak of Si bulk is taken as the origin. This Si 2*p* PES is decomposed into five surface components (C1: pedestal atoms, C2: rest atoms, C3: adatoms, C4: dimers, and C5: unknown surface components), partly oxidized Si (Si^{n+} (n = 1, 2, 3)), and the bulk one using a well-known curve-fitting procedure [1-4]. The presence of partly oxidized Si sites suggests that the surface was partly contaminated with residual water. The Lorentzian width of 0.08 eV and Gaussian width of 0.55 eV for C1–C5 and 1.0 eV for Si^{n+} (n = 1, 2, 3) are used for the Si-2*p* PES peak fitting. The spin-orbit coupling between Si $2p_{1/2}$ and Si $2p_{3/2}$ and the intensity ratio of Si $2p_{1/2}$ to Si $2p_{3/2}$ are taken as 0.6 eV and 0.5, respectively. The same procedure is applied to the Si 2*p* PES measured with the ASMA. From the fitting results, the overall energy resolution ($E/\Delta E$) of both the ASMA and the DP-CMA combined with BL13 of HiSOR is estimated to be ~50. These values are nearly equal to those of the APECS apparatus at PF ($E/\Delta E$ = ~55) [4].

Figure 3 shows a TOF spectrum of Si $L_{23}VV$ Auger electron with a kinetic energy (*KE*) of 88 eV measured by a multichannel-scaler by taking the bulk Si 2*p* photoelectron signal as the trigger (APECS TOF spectrum). A clear coincidence peak appears at 74.5 ± 11 ns. A series of APECS TOF spectra were measured by changing the *KE* of the Si-$L_{23}VV$ Auger electron. Figure 4 shows a Si-$L_{23}VV$-Si^{bulk}-2*p* APECS spectrum obtained by plotting the integrated coincidence counts of these APECS TOF spectra as a function of Si $L_{23}VV$ Auger electron *KE* (filled circles with solid line). The highest peak of Si-$L_{23}VV$-Si^{bulk}-2*p* APECS is shifted by ~1.0 eV to higher *KE* side than normal Si $L_{23}VV$ Auger electron spectrum (singles AES, solid line). This result indicates that the Si-$L_{23}VV$-Si^{bulk}-2*p* APECS spectrum mainly reflects the Si $L_{23}VV$ AES of bulk Si.

In conclusion, we constructed an APECS apparatus at BL13 of HiSOR. The performance of this apparatus

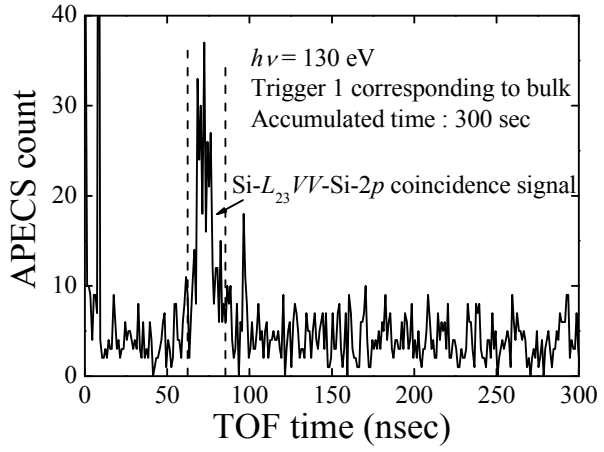

Fig. 3: APECS TOF spectrum of a partly contaminated Si(111) surface at $h\nu$ = 130 eV.

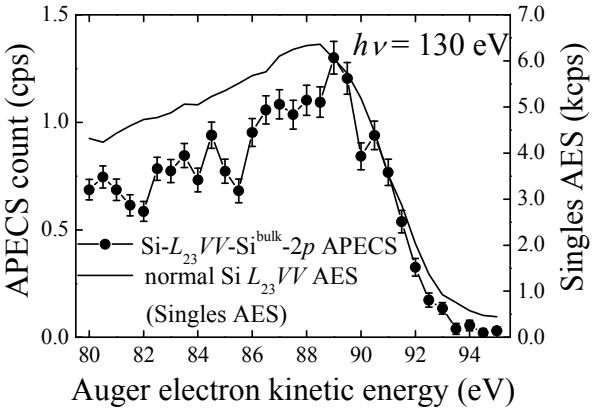

Fig. 4: PECS spectrum (filled circles) of a partly contaminated clean Si (111)7×7 at $h\nu$ = 130 eV.

such as $E/\Delta E$, the ratio of the APECS signal to the background, coincidence count rates are comparable to that of previous one developed in PF.

Acknowledgement

This work was approved by the Photon Factory Program Advisory Committee (PF PAC, No. 2011G099) but performed at the HiSOR in July, 2011 with the approval of the HiSOR Program Advisory Committee (11-B-24) because PF was damaged by the Great East Japan Earthquake on March 11, 2011. We express our sincere thanks to the staff of the HiSOR, Hiroshima University, and PF for their valuable help during the course of the experiments.

References

[1] T. Kakiuchi, K. Mase *et al.*, Surf. Sci. **604** (2010) L27.
[2] T. Kakiuchi, K. Mase *et al.*, Phys. Rev. B **83** (2011) 035320.
[3] T. Kakiuchi, K. Mase *et al.*, J. Phys. Soc. Jpn. **80** (2011) 084703.
[4] T. Kakiuchi, K. Mase *et al.*, J. Vac. Soc. Jpn. **51** (2008) 749 [in Japanese].

*kakiuchi.takuhiro.mc@ehime-u.ac.jp

18A/2011G576

Core-level photoelectron spectroscopy study of the $TlBiSe_2$ surface

Shinichiro HATTA[1,2*], Yoshiyuki OHTSUBO[1,2], Yukihiro HAYASHI[1],
Kazuki NAKATSUJI[1], Tetsuya ARUGA[1,2]
[1]Department of Chemistry, Graduate School of Science, Kyoto Univ., Kyoto 606-8502, Japan
[2]JST CREST, Saitama 330-0012, Japan

Introduction

We have studied the (111) surface of $TlBiSe_2$ with core-level photoelectron spectroscopy (PES). The material is known to be one of three-dimensional topological insulators. Angle-resolved PES measurements of $TlBiSe_2$ demonstrated the Dirac-cone surface state in the bulk band gap of ~0.3 eV [1, 2]. Such electronic structure is expected to open the application of topological insulators to practicable devices operating at room temperature. On the other hand, a recent theoretical study by ab initio calculation showed that the surface-state band dispersion depends crucially on surface termination, relaxation and reconstruction, and is not reproduced by the simple models with terminations of Tl, Bi and Se [3]. Until now, the atomic structure of the cleaved $TlBiSe_2$ surface was not experimentally revealed.

Experimental

The core-level PES measurements of Tl 5d, Bi 5d and Se 4d were performed at beam line 18A. A $TlBiSe_2$ crystal was grown by the Bridgeman method. The (111) orientation of the sample was confirmed by X-ray diffraction. The sample was cleaved at pressure below 1×10^{-7} Torr in the preparation chamber and immediately transferred to the analyzer chamber at 2×10^{-10} Torr. Low-energy electron diffraction (LEED) showed a sharp (1×1) pattern with low background intensity. We confirmed the Dirac-cone surface state with valence PES by a SES100 spectrometer. We used an ADES-500 spectrometer to measure the emission-angle and photon-energy dependence of the core levels with a fixed incident angle of 45˚. The used photon energy ranges from 50 to 130 eV. All PES measurements were performed at room temperature.

Results and discussion

Figure 1(a) shows the normal-emission core-level spectra with 90-eV photons. It is found that a shoulder appears on the high binding-energy side of each main peak of Tl 5d, in contrast to the Bi and Se peaks with a single component. The relative intensity of the lower-binding-energy component (labeled α) decreases for lower photon energies. With 70-eV photons, the two components of Tl 5d have comparable intensity in normal emission as shown in Fig. 1(b). With increasing the emission angle, it is found that the peak intensity of the component α rapidly decreases.

The $TlBiSe_2$ crystal has a rhombohedral structure, which is characterized by the stacking sequence of -Se-Bi-Se-Tl-Se- along the [111] direction. Each layer consists of hexagonally-closed-packed layers of Tl, Bi and Se. The larger interlayer distance of Tl-Se indicates cleavage between the Tl and Se layers. If no surface reconstruction is assumed, Tl or Se terminated surface is likely to appear on the cleaved surface.

Taking into accounts the emission-angle dependence of Tl 5d and the single component peak of Se 4d, it is proposed that the higher-binding-energy component (β) is attributed to the surface Tl atoms. The observed binding energy shift of ~0.4 eV indicates that the state of the surface Tl atom is significantly different from that in the bulk. We are proceeding with further analysis of the surface atomic structure in combination with the core-level PES data, dynamical LEED *I-V* curve analysis and scanning tunneling microscopy observation.

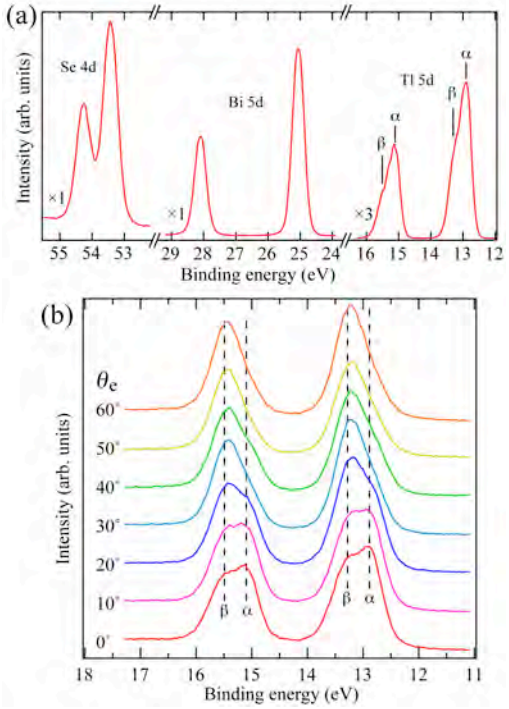

Fig. 1. (a) Normal-emission core-level spectra of the cleaved $TlBiSe_2$ surface with $h\nu$=90 eV. (b) The emission angle dependence of Tl 5d with $h\nu$=70 eV.

References

[1] T. Sato *et al.*, Phys. Rev. Lett. 105, 136802 (2010).
[2] K. Kuroda *et al.*, Phys. Rev. Lett. 105, 146801 (2010).
[3] S.V. Eremeev *et al.*, Phys. Rev. B 83, 205129 (2011).

* hatta@kuchem.kyoto-u.ac.jp

7A/2011G626

Molecular Chain Effect of Aromatic Self-Assembled Monolayers Measured in Soft X-Ray Stimulated Ion Desorption

Shin-ichi Wada[1,2*], Mai Ogawa[1], Ryosuke Koga[1], Jumpei Kajikawa[1], Hironori Hayashita[1], Kenichiro Tanaka[3], and Atsunari Hiraya[1,2]
[1]Depertment of Physical Science, Hiroshima Univ., Higashi-Hiroshima 739-8526, Japan
[2]HSRC, Hiroshima Univ., Higashi-Hiroshima 739-0046, Japan
[3]XFEL Division, Japan Synchrotron Radiation Research Institute, Sayo, 679-5198, Japan

1 Introduction

Inner shell excitation of a specific atom in a molecule by soft X-ray irradiation can induce site-selective chemical bond breaking due to spatial localization of core electrons. Self-assembled monolayers (SAMs) consist of end functional groups, molecular chains and thiol groups, and so far, we have investigated site-selective photostimulated ion desorption (PSID) in the end functional group of methyl-ester terminated aliphatic thiol SAM (MHDA : Au-S$(CH_2)_{15}$-$COOCH_3$) [1]. Differently from insulating aliphatic chain, it is known that aromatic thiols show high conductivity due to its delocalized π conjugation [2]. Furthermore, from previous studies, it is considered that site-selectivity and yield in PSID strongly depend on molecular environment [1]. In this study, we have studied two types of methyl ester terminated aromatic thiols, MP0 (Au-$SC_6H_4COOCH_3$) and MP1 (Au-$SCH_2C_6H_4COOCH_3$), in order to discuss how molecular chains affect PSID in their end functional groups. Chemicals used in this study are illustrated in Fig. 1. Both of MP0 and MP1 have a phenyl groups as molecular chains and additional insulating methylene group (-CH_2-) is absent for MP0, while it is inserted between phenyl and thiol groups of MP1.

2 Experiment

The experiment was performed at the beamline BL7A of KEK-PF. During measurements, the experimental chamber had a base pressure of 1×10^{-9} Torr. Near edge X-ray absorption fine structure (NEXAFS) was recorded in TEY mode by measuring a sample drain current. The TEY spectra were measured at 20° incident angle from the sample surface. Partial ion yield (PIY) spectra were measured using TOF mass spectrometer system. All spectra were normalized to the incident photon flux monitored with a gold-coated mesh. SAMs used in this study were prepared by immersing Au coated Si substrates in 1mM ethanol solution of target molecules at room temperature during one day.

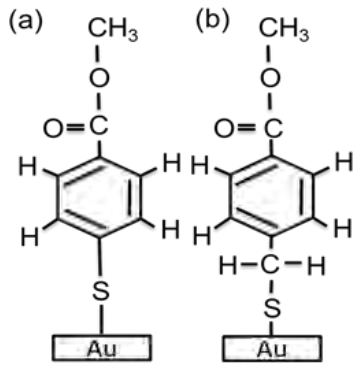

Fig. 1: Chemical structure of target molecules: (a) MP0 and (b) MP1 SAMs.

3 Results and Discussion

Fig. 2 shows the TEY and PIY spectra for MP0 in C 1s region. All peaks in the spectrum can be assigned based on a building-block method using Refs. 1 and 3. The C 1s → σ^*(O-CH_3) excitation located on the shoulder around the photon energy of 289 eV overlaps $2\pi^*$(C=C):C-H excitation. Obvious desorption of CH_n^+ (n = 0~3) ions, however, indicates that the site-selective ion desorption of CH_n^+ is promoted by the resonant excitation to the σ^*(O-CH_3) unoccupied orbital.

Fig. 3 shows the fragmentation patterns of CH_n^+ ions desorbed from MP0 and MP1 at the C 1s → σ^*(O-CH_3)

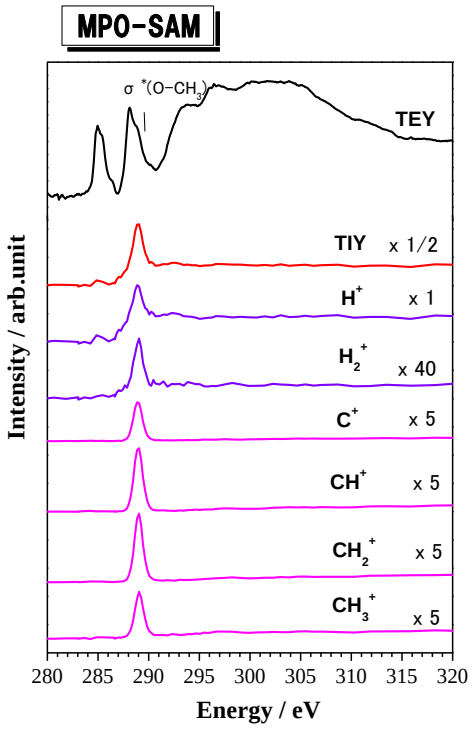

Fig. 2: TEY and PIY spectra measured for MP0 in C 1s region.

excitations, together with the result of MHDA for easy comparison. Here is noted that CH_n^+ ions come from the fragmentation of CH_3^+ ions after leaving substrate molecules (SAM molecules). The more internal energy for CH_3^+ ions in desorbing becomes high, the more C-H bonds would break. The internal energy of desorbed CH_3^+ ions from aromatic thiol SAMs (MP0 and MP1) becomes higher than that from the aliphatic thiol SAM (MHDA). Moreover, MP0 indicates more pronounced production of fragment ions in comparing with MP1. Based on these results, it can be considered that ion yield and site-selectivity of desorbed ions from different conductivity environments are strongly attributed to charge transfer rates between SAM molecules and metal surfaces.

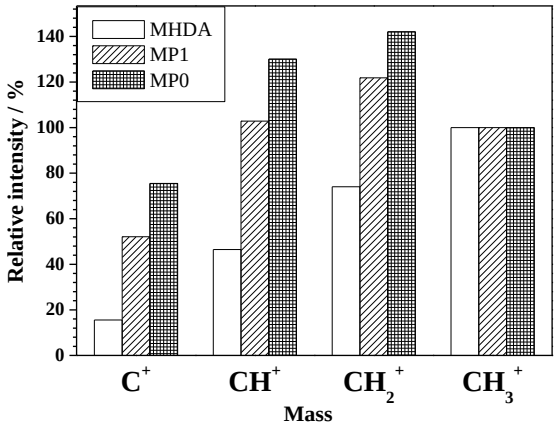

Fig. 3: Fragmentation ratio of desorbed CH_n^+ (n = 0~3) ions by the C 1s → σ^*(O-CH_3) excitations of MP0 and MP1 aromatic SAMs and MHDA aliphatic SAM.

References

[1] S. Wada *et al.*, J. Phys.: Condens. Matter **18** (2006) S1629.
[2] T. Dadosh *et al.*, Appl. Phys. Lett. **89** (2006) 213104.
[3] A. P. Hitchcock *et al.*, J. Phys. Chem. **91** (1987) 531.

* swada@sci.hiroshima-u.ac.jp

18A/2011G671

Measurement of Electronic Structure of Al_2O_3(0001) Surface

Aki TOSAKA, Takuhiro SUGIYAMA, Yukichi SHIGETA*
Graduate School of Nanobio-Sciences,
Yokohama City University.

Al_2O_3 has been widely used as a substrate for GaN thin film. When the GaN film is deposited, the substrate temperature should be raised above 1000 °C. Therefore, the detailed investigation of the Al_2O_3 surface at high temperature is key to improve the quality of GaN and other semiconductor films. The stable surface structure of Al_2O_3(0001) is the 1×1 structure. However the surface structure is reconstructed to the √31×√31±R9° structure (hereafter √31 structure) by annealing at about 1000 °C in the vacuum [1-3]. It is theoretically predicted that the√31 reconstruction occurs by removing oxygen layers from the surface and forming Al layers[4]. Therefore the change of the electronic structure from the 1×1 structure to the √31 structure is very interesting.

We use well-oriented Al_2O_3 (0001) samples, which were supplied by Namiki Precision Jewel Co. Ltd. The samples were cut parallel to the (0001) plane with off angle being 0.15° ±0.02° off for <10T0> direction and annealed at 1000°C or 1400°C annealing in air. The air-annealed surface shows a clear 1×1 Reflection High Energy Electron Diffraction (RHEED) pattern without any treatment in the vacuum.

We tried to measure the photoelectron spectra (PES) from the Al_2O_3 (0001) surface. Figure 1 shows a typical example of the PES, where the photo-electrons emitted to the normal direction are measured at photon energies (E_p) from 22 eV to 35 eV. The PES at E_p below 25 eV show two clear states originate from the *Al-O* bonding state and the O-*2p* state [5]. On the other hand, the PES at E_p over 28 eV become noisy and each peak is shifted to unsystematic directions. The random shifts will be caused by a charging up on the insulator surface.

Therefore, PES have measured at E_p below 25 eV. From the PES from 1x1 and √31 structures, we have obtained some experimental evidences that the √31 structure is formed by Al layers by leaving O layer on top of the Al_2O_3 (0001) surface from the results of the PES and RHEED. Detailed structure model will be published in elsewhere in the near future.

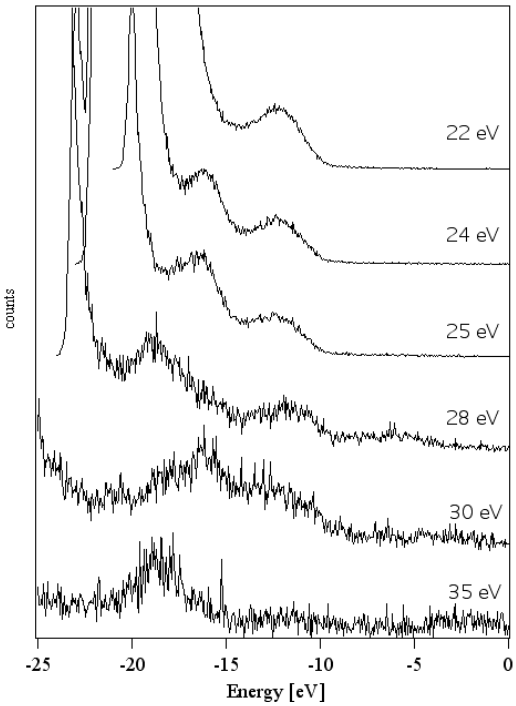

Fig. 1. PES from Al_2O_3 (0001) surface at photon energies (E_p) from 22 eV to 35 eV

We thank Kouji Koyama (Namiki Precision Jewel Co., Ltd.) for suppling of well-oriented Al_2O_3 (0001) samples.

References

[1] J.M. Charig, Appl. Phys. Lett. 10 (1967) 139.
[2] C. C. Chang, J. App. Phys. 39 (1968) 5570.
[3] T. M. French and G. A. Somorjai, J. Phys. Chem. 74 (1970)2489.
[4] G. Renaud et al., Phys. Rev. Lett. 73 (1994)1825.
[5] R. H. French, J. Am. Ceram. Soc. 73 (1990)477.

* e-mail address: shigeta@yokohama-cu.ac.jp

2C/2011S2-003

バイアス印加放射光光電子分光による金属/高誘電率酸化物ゲートスタック構造の界面準位密度解析

篠原稔宏 [1], 豊田智史 [1-3*], 組頭広志 [1-3], 尾嶋正治 [1-3], 片山俊治 [4], 助川孝江 [4], 劉紫園 [4]
[1]Department of Applied Chemistry, The University of Tokyo, Tokyo 113-8656, Japan
[2]JST-CREST, Tokyo 113-8656, Japan
[3]The University of Tokyo, Synchrotron Radiation Research Organization, Tokyo 113-8656, Japan
[4]STARC, Kohoku-ku, Kanagawa 222-0033, Japan

はじめに

界面トラップ準位は金属/高誘電率酸化物ゲートスタック構造のデバイス特性に閾値電圧シフトなどの影響を与えるが、その起源やエネルギー準位について未だ不明な点が多い。我々はこれまで、金属/高誘電率酸化物ゲートスタック構造試料において、内殻準位光電子スペクトルの放射光照射時間依存性を解析することによって、ゲート絶縁膜中のトラップ密度を決定し、これらが N-Hf 結合に起因していることを明らかにしてきた [1)]。本研究では、そのエネルギー分布を特定するため、金属/高誘電率酸化物/半導体構造に対して、外場電圧を印加しながら放射光光電子分光測定を行った。

実験

試料はシリコン基板上に原子層堆積法(ALD)によって作製した Hf 濃度および N 濃度の異なる HfSiON/SiON ゲートスタック構造を用いた。上部電極として Ag を薄く堆積し、図 1 の挿入図に示す試料ホルダーを用いて試料ステージから外場電圧を印加した。Ta 板を用いて上部から試料を固定し、コンタクト部分に Au 厚膜を蒸着し、絶縁部分にカプトンシートを用いた。電圧は上部電極側をアースに落として基板側へ印加し、-2V から+2V まで、0.01V 刻みで走査しながら内殻準位スペクトルを測定した。アースの安定性は、上部電極側 Au 厚膜からの Au 4*f* 内殻準位スペクトルが電圧印加によってほとんどシフトしなかったことから確認できた。

結果と考察

金属/高誘電率酸化物/半導体デバイス構造に外場電圧を印加すると、シリコン基板からのピークのシフトが観測され、そのシフト量は界面準位密度に依存する。図 1 に Si 2*p* (基板成分)内殻光電子ピークシフトを外場電圧に対してプロットした。どの試料においても負バイアス側ではほとんど線形なシフトが観測されるが、正バイアス側において明確な違いが見て取れる。これは HfSiON/Si 界面におけるトラップ準位に関係していると考えられる。これらを元に界面準位密度分布 [2)]を決定した結果を図 2 に示す。N 濃度あるいは Hf 濃度の高い試料において界面準位密度が増大する傾向があり、これらは膜中 N-Hf 結合に起因するトラップの実験的な証拠であることを示唆していると考えられる。

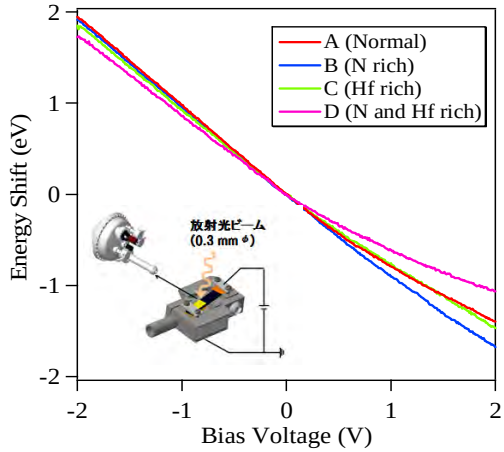

図 1 外場電圧に対する Si 2*p* 光電子ピークのエネルギーシフトプロット

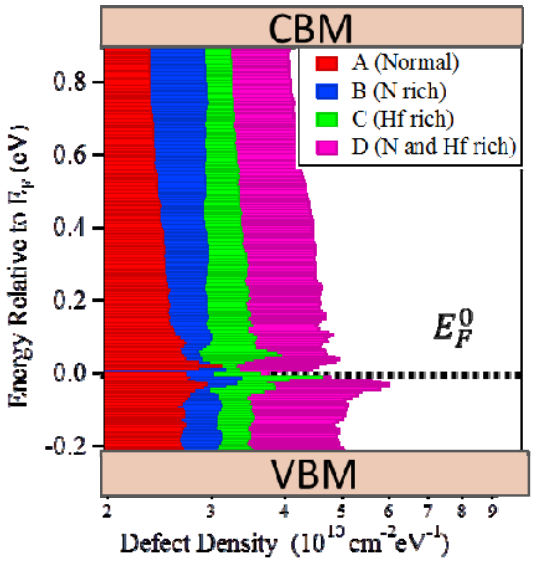

図 2 界面準位密度のエネルギー分布

参考文献

[1)] T. Tanimura *et al.*, Appl. Phys. Lett. **96**, 162902 (2010).
[2)] H. Kobayashi *et al.*, J. Appl. Phys. **34**, 959 (1995).
*toyoda@sr.t.u-tokyo.ac.j

2C/2011S2-003

Chemical-state resolved depth profile and band discontinuity in TiN/HfSiON gate stack structure with an AlO_x cap layer

Satoshi TOYODA[1-3*], Hiroyuki KAMADA[1], Hiroshi KUMIGASHIRA[1-3], Masaharu OSHIMA[1-3]
[1]Department of Applied Chemistry, The University of Tokyo, Tokyo 113-8656, Japan
[2]JST-CREST, Tokyo 113-8656, Japan
[3]The University of Tokyo, Synchrotron Radiation Research Organization, Tokyo 113-8656, Japan

Introduction

For sub 32 nm complementary metal-oxide-semiconductor (CMOS) devices, metal/high-dielectric metal oxide (high-*k*)/Si gate stacked structures with LaO_x and AlO_x cap layers have been widely studied in order to fine-tune threshold voltages for NMOS and PMOS, respectively. One of the most critical issues to be solved in metal/high-*k* systems is to control the flat-band voltage (V_{fb}) after the high-temperature thermal annealing for dopant activation. It is necessary to develop the guidelines for control of the V_{fb} shift in overall stacked structures with a cap layer and to reveal their complicated mechanisms such as Fermi-level pinning and interface-dipole effects. Although the physical origin of the V_{fb} shift has recently been considered to be due to interface dipole at high-*k*/SiO_2 interfaces, there are few reports on effects of N bonding state and their changes in depth profiles upon annealing. In this study, we have investigated chemical-state-resolved depth profiles and band discontinuity for TiN/HfSiON gate stack structure with the AlO_x cap layer on a Si substrate using backside angle-resolved photoemission spectroscopy.

Experimental

The HfSiON dielectric layers were grown by atomic layer deposition (ALD) on SiO_2 interface layers. AlO_x capping layers and TiN gate electrodes were also deposited by ALD processes. Rapid thermal annealing was performed. Photoemission measurements were carried out at BL-2C of the Photon Factory in the High Energy Accelerator Research Organization (KEK), which is equipped with a high performance photoelectron analyzer (VG-SCIENTA SES2002). Angle-resolved core-level photoemission spectra from the backside of the gate-stacked structures were measured using synchrotron radiation focused beam of 0.1 x 0.5 mm^2. Photoelectron emission angles (θ_e) were changed from the surface normal to 75° for enhancement of surface sensitivity.

Results and Discussion

Figure 1 shows atomic concentration depth profiles in the SiO_2/high-*k*/TiN stacked structures without (a) and with (b) the AlO_x cap layer. Depth profile for each sample shows the anticipated stacked structure except for the position of AlO_x compounds and the distribution of N atoms. In other words, depth profiles related to Al and N atoms are significantly changed upon annealing. Although the AlO_x layer is deposited on the HfSiO layer in the as-grown stage, Al atoms diffuse into the interface between the HfSiON and SiO_2 layers during rapid thermal annealing and AlO_x compounds have broad distribution around the HfSiON layer. Core-level intensity ratio of Al 2*p* to Hf 4*f* increases for enhancing surface sensitivity by changing emission angle as shown in the inset of Fig. 1(b), which suggests that AlO_x compounds are highly distributed at the high-*k*/SiO_2 interface rather than throughout the high-*k* layer. Such concentration of Al atoms at the high-*k*/SiO_2 interface may control the effective work function for PMOS devices. We note that inserting the AlO_x layer also changes distribution of nitrogen atoms in the HfSiON layer. The total amount of nitrogen atoms decreases by AlO_x layers. High nitrogen concentration in the high-*k* layer may be originated from the TiN gate electrode, so the insertion of AlO_x layer prevents excess nitrogen diffusion from the electrode. Thus, it is found that effect of the AlO_x capping layer at the interface of high-*k*/TiN strongly influences depth profile of nitrogen atoms [1].

References

[1] S. Toyoda *et al.*, J. Appl. Phys. **110**, 104107 (2011).

*toyoda@sr.t.u-tokyo.ac.jp

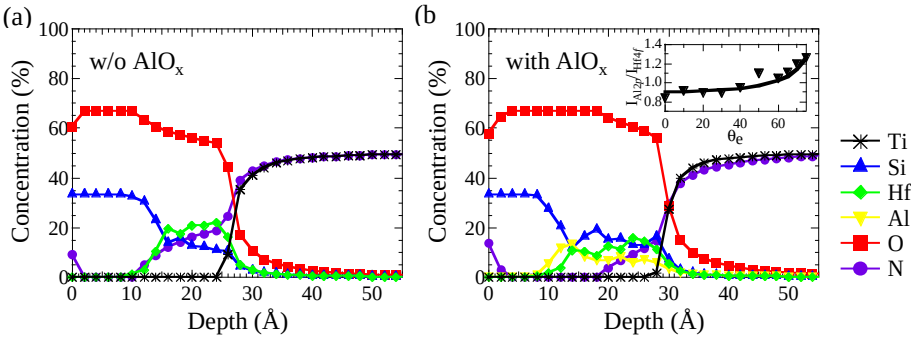

Fig. 1; Depth profiles are analyzed using the angle-resolved core-level intensity with (a) and without (b) AlO_x cap layer. Core-level intensity ratio of Al 2*p* to Hf 4*f* as a function of θ_e are also shown in the inset of Fig. 1(b).

2C/2011S2-003

Determining factor of effective work function in metal/bi-layer high-*k* gate stack structure studied by photoemission spectroscopy

Satoshi TOYODA[1-3*], Hiroshi KUMIGASHIRA[1-3], Masaharu OSHIMA[1-3], Hidetaka SUGAYA[4], Hiromi MORITA[4]

[1]Department of Applied Chemistry, The University of Tokyo, Tokyo 113-8656, Japan
[2]JST-CREST, Tokyo 113-8656, Japan
[3]The University of Tokyo, Synchrotron Radiation Research Organization, Tokyo 113-8656, Japan
[4]JST-PRESTO, Tokyo 113-8656, Japan
[5]Panasonic Corporation, Moriguchi, Osaka 570-8501, Japan

Introduction

Recently, metal/high-dielectric oxide (high-*k*)/Si gate stack structures with LaO_x and AlO_x cap layers have been studied due to excellent controllability of effective work function (EWF) in complementary metal-oxide-semiconductor devices, after high-temperature thermal annealing for dopant activation. The physical origin of change in the EWF is considered to be due to magnitude of microscopic dipoles at the high-*k*/SiO_2 interface, which is readily modulated by diffusion of La or Al atoms from the cap layer. Investigation of the determining factor of EWF only by electrical measurements involves some difficulties, because there are few methods to reveal chemically and electronically resolved depth distribution of metal/high-*k* gate stack structures. We have previously analyzed depth profiles of atomic concentration and contribution of the interface dipoles in TiN/LaO_x/HfSiO/SiO_2 stack structures by angle-resolved core-level photoemission spectroscopy, which is expected to be one of the promising candidate techniques to experimentally elucidate the determining factor of EWF in metal/high-*k* gate stack structures [1]. In this study, we have focused on bi-layer HfO_2/Al_2O_3 high-*k* materials on SiO_2/Si substrates, and investigated the effects of a Si interlayer among the bi-layer high-*k* materials.

Experimental

1.0 nm HfO_2 and 1.0 nm Al_2O_3 dielectric layers were grown on 1.0 nm SiO_2 interface layers on Si substrates. Si layers are inserted at the HfO_2/Al_2O_3 (Sample A) and Al_2O_3/SiO_2 (Sample B) interfaces as interface passivation layers. The EWFs are determined to be 4.93 and 4.96 eV for samples A and B by *C-V* characteristics, respectively. Finally, 15 nm TiN and thick poly-Si for gate electrodes were also deposited. Photoemission measurements were performed at BL-2C of the Photon Factory in the High Energy Accelerator Research Organization (KEK), which is equipped with a high performance photoelectron analyzer (VG-SCIENTA SES2002). Photoelectron emission angles were changed from the surface normal to 75° for enhancement of surface sensitivity.

Results and Discussion

Figure 1 shows depth profiles of atomic concentration in the SiO_2/bi-layer high-*k*/TiN stacked structures for (a) Sample A and (b) Sample B. Inset for each panel indicates the as-grown sample structures. It is found that inserting a Si passivation layer at the HfO_2/Al_2O_3 interface effectively modulates depth profiles of cations such as Al and Hf atoms. The inserted Si layer is completely oxidized during film growth or annealing processes, and outward diffusion of Al atoms into the top HfO_2 layer is suppressed. It is well known that EWF of the Al_2O_3/SiO_2 stack is larger than that of the HfO_2/SiO_2 stack, which is based on the interface dipole model. Since high concentration of Al atoms at the SiO_2 and high-*k* layers should increase EWF by enhancing magnitude of the interface dipole between the SiO_2 and high-*k* layers, the fact that EWF of Sample A is larger than that of Sample B cannot be interpreted only by variation in dipole at the SiO_2/high-*k* interface. Although effect of the interface dipole is suppressed by inserting the Si layer at the HfO_2/Al_2O_3 interface, the Si layer effectively prevents oxygen diffusion from the HfO_2 layer into the TiN metal electrode, resulting in a decrease in the EWF of the TiN metal electrode [2]. Thus, the guideline for high EWF is promotion of TiN metal electrode oxidation at the high-*k*/TiN interface without weakening the magnitude of interface dipole. This can be utilized in fabrication processes of metal/high-*k* gate stack structures.

References

[1] S. Toyoda *et al.*, Appl. Phys. Lett. **96**, 042905 (2010).
[2] S. Toyoda *et al.*, Appl. Phys. Lett. **100**, 112906 (2012).

*toyoda@sr.t.u-tokyo.ac.jp

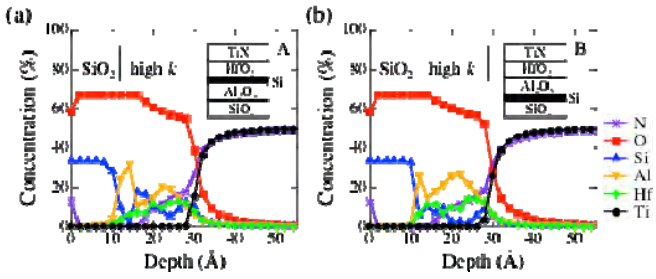

Fig. 1; Depth profiles of atomic concentration in the SiO_2/bi-layer high-*k*/TiN stacked structures. Passivation layers of Si are inserted at the HfO_2/Al_2O_3 (a) and Al_2O_3/SiO_2 (b) interfaces for Sample A and Sample B.

13A/2012G093

Photoelectron spectroscopic study of CO adsorption on Pd(100) single crystal surface under ambient-pressure conditions

Ryo TOYOSHIMA[1*], Masaaki YOSHIDA[1], Yuji MONYA[1], Kazuma, SUZUKI[1], Kenta AMEMIYA[2], Kazuhiko MASE[2], and Hiroshi KONDOH[1]

[1]Keio University, Hiyoshi, Kanagawa 222-8522, Japan

[2]KEK-PF, Tsukuba, Ibaraki 305-0801, Japan

INTRODUCTION

The adsorption structure of carbon monooxide (CO) on late-transition metal surfaces under atmospheric conditions is an issue of technological and scientific interest. In this study, we conducted a work on CO adsorption on a Pd(100) single crystal, because the Pd has been used as a catalyst of CO oxidation (i.e. three-way catalyst). Under UHV conditions, the adsorption structure has been widely investigated.[1-2] Ambient-Pressure X-ray Photoelectron Spectroscopy (AP-XPS) enables to measure the XP spectrum even under 1 Torr pressure condition using a differential pumping system.

EXPERIMENTAL SECTION

A Pd(100) single crystal was cleaned using well-established procedures in a preparation chamber, the base pressure was < 2×10^{-10} Torr. Then it was transferred to a high-pressure experimental chamber. The CO gas (99.99% purity) was introduced to the chamber up to 0.5 Torr at room temperature. The photon energy of 435 eV was used for $Pd3d_{5/2}$ and C1s XPS.

RESULTS and DISCUSSION

Fig. 1 shows a series of $Pd3d_{5/2}$ XP spectrum of CO adsorption up to 0.5 Torr. At 1×10^{-7} Torr, the bulk and an additional peak component at higher binding energy CO(I) are observed. This is associated with the $(2\sqrt{2}\times\sqrt{2})R45°$ structure. With increasing CO gas pressure, a new component CO(II) appears at about 336 eV, and the $(3\sqrt{2}\times\sqrt{2})R45°$, (II)/(I)=0.5 and $(4\sqrt{2}\times\sqrt{2})R45°$, (II)/(I)=1 is formed. These structures have been found at low temperatures under UHV conditions.

However, a new structure, (II)/(I)>1, is reversibly observed at 0.5 Torr. This is interpreted as a (1×1) structure predicted by theoretical calculations.[3]

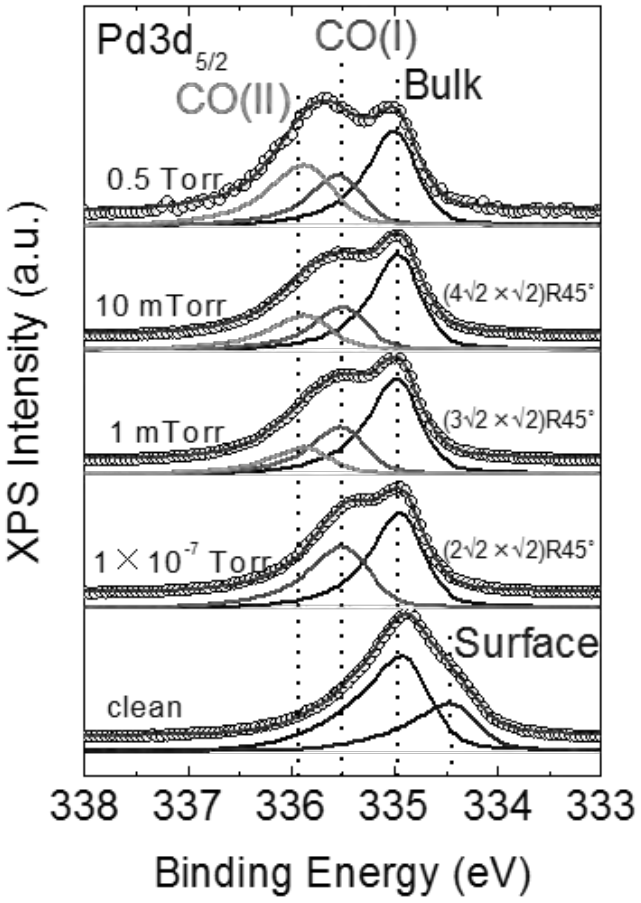

Figure1 a series of $Pd3d_{5/2}$ XP spectrum up to 0.5 Torr CO pressure at room temperature.

References

1. Berndt et al., *Surf. Sci. Lett.* **1988,** *279,* L165.
2 .Andersen et al., *Phys. Rev. Lett.* **1991,** *67,* 2822.
3. Rogal et al., *Phys. Rev. Lett.* **2007,** *98,* 046101.

9A/ 2012G094

High thermal stability of Au clusters on a Nb-doped TiO_2(110) Surface

Satoru TAKAKUSAGI[1], Hiromitsu UEHARA[1], Takafumi OGAWA[1], Kentaro KONO[1], Wang-Jae CHUN[2], Masaharu NOMURA[3], Yasuhiro IWASAWA[4], Kiyotaka ASAKURA[1]*
[1]Catalysis Research Center, Hokkaido University, Sapporo 001-0021, Japan, [2]International Christian Univ., Mitaka 181-8585, Tokyo, Japan, [3]PF IMSS, KEK, Tsukuba 305-0801, Japan, [4]The Univ. of Electro-Communications, Tokyo 182-8585, Japan

Introduction

It is a common sense that Gold is inert and noble metal with no catalytic applications. Haruta et al. have reported pioneering works on the nanoscale Au clusters showing CO oxidation reaction below zero degree.[1] "Nano" makes gold active and variable. However, why "Nano" performs the miracle is one of the biggest mystery in the catalyst field. To obtain the further insight of Au-TiO_2 interaction at an atomic level, preparation and characterization of well-defined model catalysts using single crystal surfaces are indispensable.

In this work, small Au clusters were deposited on a Nb-doped TiO_2(110) surface by vacuum deposition, and the structure of the deposited Au clusters on the TiO_2(110) surface was investigated by using the polarization-dependent total reflection XAFS (PTRF-XAFS) technique.[2] The effect of high temperature treatment on the structure of the Au clusters on the TiO_2(110) surface was also examined to see thermal stability of them.

Experimental

Nb-doped (0.05 wt%) TiO_2(110) surface was cleaned by immersing 10% HF solution and annealing at 650°C in air for 1h according to the previous reports.[3] The TiO_2 sample was transferred into the ultra-high vacuum (UHV) PTRF-XAFS chamber and annealed at 700°C for 1 h to remove residual adsorbed water and reduce carbon contaminant. Then Au was vacuum-deposited on the sample surface and the Au coverage was estimated to be ca. 0.2 ML by XPS (1 ML was defined as 1.4×10^{15} atoms/cm^2). PTRF-XAFS was carried out with the UHV PTRF-XAFS chamber. XAFS analysis was carried out using REX 2000 and FEFF9.0.

Results and Discussion

Fig. 1(a)-(c) shows the observed Au L_3-edge PTRF-EXAFS spectra of the vacuum-deposited Au on a Nb-doped TiO_2(110) surface. There was no significant difference in all three orientations, indicating that the structure of the Au species should be a symmetric one. The characteristic oscillation due to Au-Au interaction was observed for all spectra, but the periodicity was longer than that of Au foil while the amplitude was smaller. These results indicated that Au-Au bond length was shorter than that of Au foil and coordination number was smaller, which suggested the formation of small Au clusters.

The sample was then annealed at 500°C for 1 h in UHV and the PTRF-EXAFS measurement of the annealed sample was done at RT as shown in Fig. 1(d)-(f). No significant change was observed before and after the high temperature treatment, showing that no significant aggregation of the Au clusters occurred even at 500°C and they were thermally stable.

Previous results reported that Au was easily aggregated on undoped TiO_2(110) surfaces, which were prepared by cycles of ion sputtering and high temperature annealing in UHV.[4] The high thermal stability of the Au clusters, which were observed in this study, might be related to the difference of electronic states of the substrate TiO_2 between Nb doipng and undoping.[5] We are now planning to perform similar experiments using an undoped TiO_2(110) substrate.

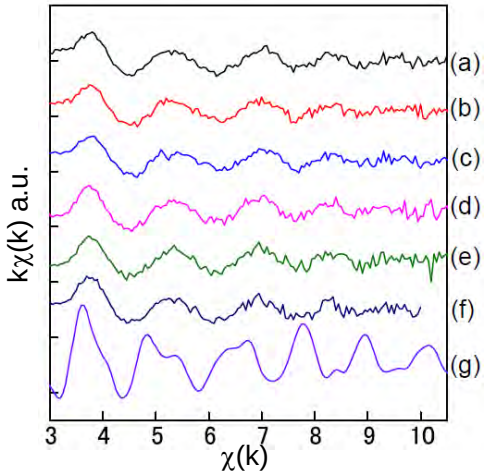

Figure 1 (a)-(c) PTRF-EXAFS spectra of the vacuum-deposited Au on a Nb-doped TiO_2(110) surface. (d)-(f) were the PTRF-EXAFS spectra obtained after annealing at 500°C for 1 h. (a) and (d) E//[001], (b) and (e) E//[1-10], (c) and (f) E//[110]. (g) EXAFS spectrum of Au foil.

References

[1] M. Haruta et al., *Gold Bulletain,* **37** (2004) 27.
[2] W.-J. Chun et al., *J. Synchrotron Rad.,* **8** (2001) 168.
[3] Yamamoto et al., *Jpn. J. Appl. Phys., 44* (2005) L511, Nakamura et al., *J. Phys. Chem. B,* **109** (2005) 1648.
[4] C.E.J. Mitchell et al., *Surf. Sci.*, **490** (2001) 196.
[5] D. Morris et al., *Phys. Rev. B,* **6** (2000) 13445.
* askr@cat.hokudai.ac.jp

16A/2010S2-001

Cu/Ni/Cu の界面および内部層における磁化の温度依存性
Temperature dependence of magnetization at the surface and in the inner layers of Cu/Ni/Cu

雨宮健太*, 酒巻真粧子
放射光科学研究施設＆構造物性研究センター，〒305-0801 つくば市大穂 1-1

1 はじめに

磁性体を薄膜にすると，その磁化がバルクとは異なった温度依存性を示すのは衆知の事実である。例えば，バルク Ni のキュリー温度は 630 K 程度なのに対し，Cu(100)単結晶上に成長させた 5 ML(原子層)の Ni 薄膜のキュリー温度は室温程度である。また，7 ML 以下の Ni/Cu(100)薄膜では磁化の温度依存性において 2 次元的なふるまいが報告されている[1]。それでは，同じ薄膜の中で，表面と内部層における磁化の温度依存性はどのように異なる(あるいは異ならない)のであろうか。

この極めて基本的な疑問を明らかにするために我々は，ここ数年開発してきた深さ分解 XMCD (X-ray Magnetic Circular Dichroism) 法 [2] を用いて，Cu/Ni/Cu(100)薄膜において Cu との界面にある Ni と内部層 Ni の磁化を分離し，それぞれの温度変化を観察した。

2 実験

実験はアンジュレータビームライン BL-16A において行った。試料は超高真空チェンバー中で，Ni および Cu を電子衝撃加熱法によって Cu(100)基板上に順次蒸着することで作製した。この際，基板温度は室温とし，RHEED (Reflection High-Energy Electron Diffraction)のその場観察によって Ni と Cu の膜厚を制御した。このようにして作製した試料に対して，同じ超高真空チャンバー内で 80 K から 450 K の間で Ni L 吸収端の深さ分解 XMCD 測定を行った。

3 結果および考察

図 1 に，異なる検出深度に対する Ni L 吸収端 XMCD スペクトルの温度依存性を示す。試料は表面側から Cu/Ni/Cu(100)という構造になっているので，表面感度が高いほど上の Cu/Ni 界面の寄与が大きいことになる。このデータからは検出深度による温度依存性の違いは明瞭には観測されず，例えば表面のみが極端に低い温度で磁化を失うというようなことは起こっていないことが見て取れる。

こうした一連のスペクトル(実験では 15 種類の検出深度に対するデータ群が一度に得られる)を解析して磁化の界面および内部層成分を見積もった結果を図 2 に示す。全体的に界面の方が磁化の値が小さいが，最終的に磁化がゼロになる温度は界面と内部層で一致している。今後，磁化の温度変化についてのシミュレーションを含めた考察を行う予定である。

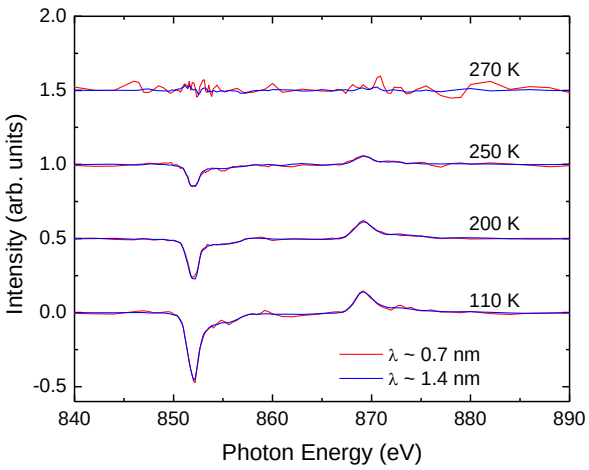

図 1 ：異なる検出深度(λ)に対する Ni L 吸収端 XMCD スペクトルの温度依存性。

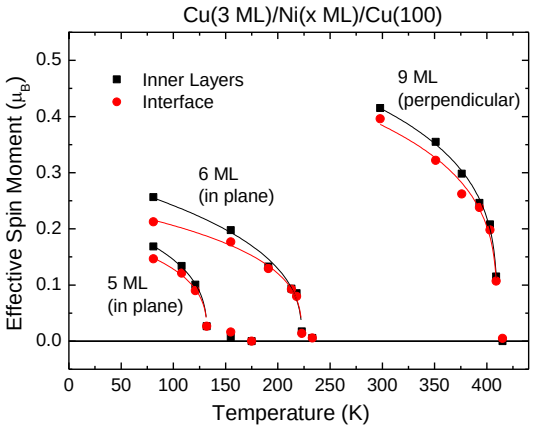

図 2 ：界面と内部層を分離した XMCD スペクトルから見積もった，界面および内部層における磁化の温度依存性。

参考文献

[1] F. Huang et al., Phys. Rev. B **49** (1994) 3962.
[2] K. Amemiya et al., Appl. Phys. Lett. **84** (2004) 936.

* kenta.amemiya@kek.jp

2C/08S2-003 and 09G545

Soft x-ray resonant photoemission study of filled skutterudite superconductor $PrPt_4Ge_{12}$

Y. Nakamura[1], H. Okazaki[1,2], R. Yoshida[1], T. Wakita[1,2], M. Hirai[1], Y. Muraoka[1,2], H. Takeya[3], K. Hirata[3], H. Kumigashira[2,4], M. Oshima[2,4], and T. Yokoya[1,2,*]

[1]The Graduate School of Science and Technology, Okayama University, Okayama 700-8530

[2]CREST, Japan Science and Technology Corporation (JST), Okayama 700-8530

[3]National Institute for Materials Science, Tsukuba 305-0047

[4]Department of Applied Chemistry, The University of Tokyo, Bunkyo-ku, Tokyo 113-8656

1 Introduction

$PrPt_4Ge_{12}$ is a novel filled skutterudite superconductor reported in 2008 [1]. This compound exhibits a superconducting transition temperature (T_c) of 7.9K, being unexpectedly high among the filled skutterudite superconductors containing Pr 4*f* electrons. The reduced gap value ($2\Delta/k_BT_c$) estimated from a specific heat jump was 4.7, which classifies $PrPt_4Ge_{12}$ into a strong coupling superconductor. More recently, muon-spin rotation and specific heat measurements down to very low temperature suggest point-like node in the superconducting gap [2]. In contrast, NMR studies of $LaPt_4Ge_{12}$, its non 4*f* counterpart, suggests a conventional BCS-type superconductivity [3]. In order to understand the exotic superconducting properties in $PrPt_4Ge_{12}$, it is important to investigate the role of 4*f* electrons in $PrPt_4Ge_{12}$.

2 Experiment

Polycrystalline samples of $PrPt_4Ge_{12}$ and $LaPt_4Ge_{12}$ were prepared by a conventional arc-melting method. It was confirmed that they consisted of a single phase of $PrPt_4Ge_{12}$ or $LaPt_4Ge_{12}$ by analyses using an X-ray diffractometer. T_c of $PrPt_4Ge_{12}$ and $LaPt_4Ge_{12}$ samples determined from magnetic susceptibility measurements were 7.9 and 8.2 K, respectively.

Soft x-ray resonant photoemission spectroscopy (SXRPES) and soft x-ray absorption spectroscopy (XAS) were carried out at BL2C, KEK-PF, measured at 20 K and under an ultrahigh vacuum of better than 1 x 10^{-10} Torr. PES measurements were done with a SES2000 analyzer with total energy resolutions setting to 200-300 meV depending on the photon energies. XAS measurements with a total electron yield mode were also performed for the same samples. Clean sample surfaces for SXRPES and XAS measurements were obtained with *in-situ* fracturing of samples at 20 K.

3 Results and Discussion

The results of the bulk sensitive Pr 3*d*→4*f* SXRPES performed at BL2C, KEK-PF shown in Fig. 1 [4]. We found that the spectral shape of the off-resonance spectrum (A in Fig. 1(b)) can be explained by band structure calculations. In the on-resonance spectrum (E), the peak at the binding energy of 4.5 eV can be a Pr $4f^1$ final state, and another enhanced peak near the Fermi level (E_F) indicated with a thick bar possibly corresponds to intermediate states. Absence of a strong peak at E_F in the on-resonance spectrum confirms the localized-like nature of Pr 4*f* electrons. These results from SXRPES studies support the fully localized treatment of Pr 4*f* and the dominant Ge 4*p* character of the states at E_F.

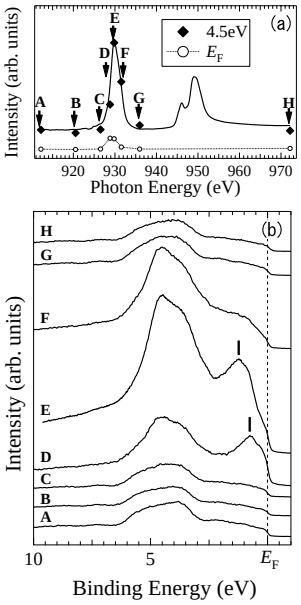

Fig. 1: (a) Pr 3*d*→4*f* XAS and (b) SXRPES spectra of $PrPt_4Ge_{12}$ across Pr 3*d*→4*f*. SXRPES spectra denoted with A-H are measured at photon energies indicated by arrows A to H on the XAS spectrum, respectively. Open circles and filled diamonds are the intensities at E_F and 4.5eV binding energy of the SXRPES spectra.

Acknowledgement

This work was partly supported by a Grant-in-Aid for Scientific Research on Innovative Areas "Heavy Electron" (No. 20102003) from the Ministry of Education, Culture, Sports, Science and Technology, Japan. SXRPES measurements were performed under the project 08S2-003 and 09G545 at the Institute of Materials Structure Science in KEK.

References

[1] R. Gumeniuk *et al.*, Phys. Rev. Lett. **100** (2008) 017002.

[2] A. Maisuradze *et al.*, Phys. Rev. Lett. **103** (2008) 147002.

[3] M. Toda *et al.*, J. Phys. Soc. Jpn. **77** (2008) 124702.

[4] Y. Nakamura *et al.*, J. Phys. Soc. Jpn. **79** (2010) 124701.

* yokoya@cc.okayama-u.ac.jp

SAGA-LS BL10/2009G615

複合金属酸化物の選択酸化機能に関する in-situ 光電子分光

In-situ photoelectron spectroscopy of mixed metal oxides for selective oxidation

宮崎隆文[1]*, 白方宏幸[1], 吉村大介[2], 瀬戸山寛之[2], 隅井良平[3], 雨宮健太[3]
[1]愛媛大院・理工　〒790-8577 松山市文京町 3 番
[2]九州シンクロトロン光研究センター　〒841-0005 鳥栖市弥生が丘 8-7
[3]KEK-PF　〒305-0801 つくば市大穂 1-1

1. はじめに

今回、メタン酸化カップリング（OCM）反応に活性を有する AB_2O_4 型複合酸化物の触媒機能解析を目的とした。この酸化物では A サイトと B サイトの金属元素の組み合わせにより C_2 収率が増減するという報告がある。そこで、AB_2O_4 型複合酸化物である $CaFe_2O_4$、$ZnLa_2O_4$、$ZnFe_2O_4$、$NiFe_2O_4$ を調製して、活性温度域まで加熱処理した各試料の紫外光電子スペクトル（UPS）および X 線光電子スペクトル（XPS）を測定した。内殻準位および価電子帯上部の電子構造から選択酸化機能と表面電子構造の基礎データを収集する。XPS では構成元素である Fe2p, Zn2p, O1s, C1s の各内殻準位と UPS では 40eV の光励起による価電子帯上部の詳細な電子構造を調べた。

2. 実験

AB_2O_4 型複合酸化物の光電子スペクトルを測定して表面電子構造を調べるため、$CaFe_2O_4$、$ZnLa_2O_4$、$ZnFe_2O_4$、$NiFe_2O_4$ を調製した。図 1 にはこれらの試料の XRD パターンを示す。調製した試料の XRD パターンには目的生成物とは異なる、帰属不能な不純物と思われる回折ピークも観測されているが、これらの試料を用いた OCM 活性には差異が認められた。C_2 選択性から見ると $ZnLa_2O_4$(42%)＞$NiFe_2O_4$(14%) ≈ $ZnFe_2O_4$(13%)＞$CaFe_2O_4$(0%)の順であった。そこで、今回のマシンタイムでは $CaFe_2O_4$ と $ZnLa_2O_4$ の光電子スペクトルの測定実験を行った。実験では表面清浄化のために 600℃の加熱処理後および OCM 反応活性温度である 750℃の加熱処理後の光電子スペクトルを測定して表面の電子状態の比較を行った。

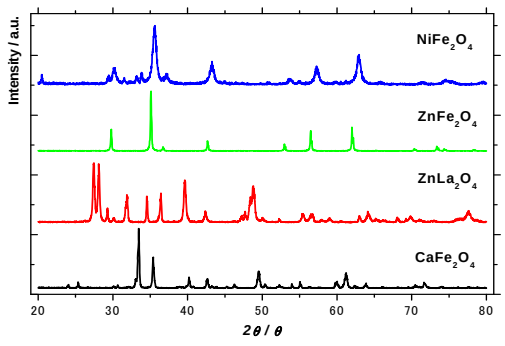

図 1. AB_2O_4 型試料の XRD パターン

3. 結果および考察

今回のマシンタイムでは $CaFe_2O_4$ と $ZnLa_2O_4$ の UPS および XPS の測定実験を行った。$CaFe_2O_4$ と $ZnLa_2O_4$ の 600℃および 750℃に加熱した後の O1s スペクトルを図 3～6 に示す。600℃で加熱処理された $CaFe_2O_4$ では O1s はブロードなピークとして観測された。また、750℃の熱処理後では高エネルギー側に僅かにピーク幅は増大していることが分かる。一方、600℃で加熱処理した $ZnLa_2O_4$ には 2 本の O1s ピークが認められ、750℃まで加熱処理した試料では、それらのピーク形状が増大して明瞭になった。特に、高エネルギー側のピーク強度が相対的に増大している事が分かる。これらの結果は OCM 反応に対して高選択性の $LiNiO_2$ においても 2 本の O1s ピークがあり、AB_2O_4 型複合酸化物の中で比較的に活性の高い $ZnLa_2O_4$ でも結合エネルギーの異なる 2 種類の表面格子酸素種が共存している事が分かった。特に、高結合エネルギー側の格子酸素種の生成が OCM 活性に関連していることが推察される。

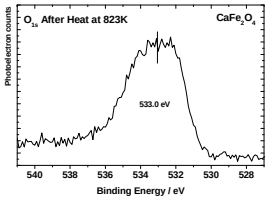

図 3. $CaFe_2O_4$ の O1s (600℃処理)

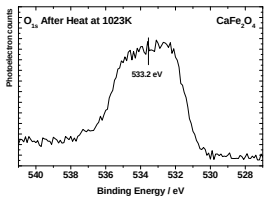

図 4. $CaFe_2O_4$ の O1s (750℃処理)

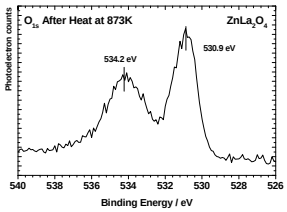

図 5. $ZnLa_2O_4$ の O1s (600℃処理)

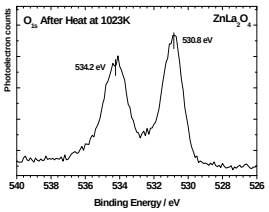

図 6. $ZnLa_2O_4$ の O1s (750℃処理)

謝辞

この実験研究を実施するに当たり、九州シンクロトロン光研究センターのスタッフにはマシンタイム調整、受入準備、実験のサポートなど、大変お世話になりました。心より感謝申し上げます。

* miyazaki@eng.ehime-u.ac.jp

28A/2009S2-005

Anisotropic superconducting gap in the iron-based superconductor $BaFe_2(As_{1-x}P_x)_2$

Teppei YOSHIDA[1,2], Shin-ichiro IDETA[1], Takahiro SHIMOJIMA[3], Walid MALAEB[4], Hakuto SUZUKI[1], Ichiro NISHI[1], Kei SHINADA[3], Atsushi FUJIMORI[1,2], Kyoko ISHIZAKA[3], Shik SHIN[4], Yosuke NAKASHIMA[5], Hiroaki ANZAI[5], Masashi ARITA[5], Akihiro INO[5], Hirofumi NAMATAME[6], Masaki TANIGICHI[6], Hiroshi KUMIGASHIRA[7], Kanta ONO[7], Shigeru. KASAHARA[8,9], Takasada SHIBAUCHI[9], Takahito TERASHIMA[8], Yuji MATSIDA[9], Masamichi NAKAJIMA[1], Shinichi UCHIDA[1,2], Yasuhide TOMIOKA[2,10], Toshimitsu ITO[2,10], Kunihiro KIHOU[2,10], Chul-Ho LEE[2,10], Akira IYO[2,10], Hiroshi EISAKI[2,10], Hiroaki IKEDA[2,9] and Ryotaro ARITA[2,3]

[1]Department of Physics, University of Tokyo, Bunkyo-ku, Tokyo 113-0033, Japan
[2]JST, Transformative Research-Project on Iron Pnictides (TRIP), Chiyoda, Tokyo 102-0075, Japan
[3]Department of Applied Physics, University of Tokyo, Tokyo 113-8656, Japan
[4]Institute of Solid State Physics, University of Tokyo, Kashiwa 277-8581, Japan
[5]Graduate School of Science, Hiroshima University, Higashi-Hiroshima 739-8526, Japan
[6]Hiroshima Synchrotron Center, Hiroshima University, Higashi-Hiroshima 739-0046, Japan
[7]KEK, Photon Factory, Tsukuba, Ibaraki 305-0801, Japan
[8]Research Center for Low Temperature and Materials Sciences, Kyoto University, Kyoto 606-8502, Japan
[9]Department of Physics, Kyoto University, Kyoto 606-8502, Japan and
[10]National Institute of Advanced Industrial Science and Technology, Tsukuba 305-8568, Japan

Introduction

In the iron-based superconductors, most of the experimental studies have so far indicated that the superconducting (SC) gap is nodeless and opens on the entire Fermi surfaces (FSs) in contrast to the *d*-wave SC gap in the high-T_c cuprate superconductors. However, some systems such as $BaFe_2(As_{1-x}P_x)_2$ [1] show signatures of line nodes in the SC gap. Experimental determination of the presence or absence of line nodes in momentum space is a crucial test of the order parameter symmetry and, hence, of the pairing mechanism. In a laser angle-resolved photoemission (ARPES) study of $BaFe_2(As_{1-x}P_x)_2$ by Shimojima *et al.* [2], nearly anisotropic, FS-independent superconducting gaps around the Z point have been identified. However, a recent study by Zhang *et al.* [3] has reported the observation of a horizontal line node on the outer hole Fermi surface around the Z point. In order to resolve the controversy, in this work, we have performed a systematic ARPES study of $BaFe_2(As_{1-x}P_x)_2$.

Experimental condition

High-quality single crystals of $BaFe_2(As_{1-x}P_x)_2$ with x=0.3 (T_c= 30 K) were grown using the self-flux method. Angle-resolved photoemission (ARPES) experiments were carried out at BL 28A of Photon Factory (PF). A Scienta SES-2002 analyzer and a circularly-polarized light were used with the total energy resolution of ~8-10 meV. The crystals were cleaved *in situ* at T=8-13 K in an ultra-high vacuum of ~5 x10^{-11} Torr.

Results and Discussion

In order to investigate the possible existence of line nodes on the electron FSs, a photon energy of hν =40 eV with a circularly polarized light was used as shown in Fig. 1. Energy distribution curves (EDCs) at Fermi momentum k_F below (T=13K) and above (T=35K) Tc for the inner electron FSs are plotted in Fig. 1(a). The energy shifts of the crossing point between the EDCs below and above T_c. are plotted in Figs. 3(c). These plots indicate that the inner FS has a gap minimum at the edge of the FS (θ_{FS}~0 or 180°). Although the minimum gap value appears to be finite, it should be remembered that ARPES has finite k_z resolution (inverse of the photoelectron meanfree-path ~0.5 nm) and, therefore, that a finite gap may appear even at a nodal k_F point unless the line node is directed in the vertical (k_z) direction. Therefore, the deep gap minima in the inner electron FSs are suggestive of line nodes.

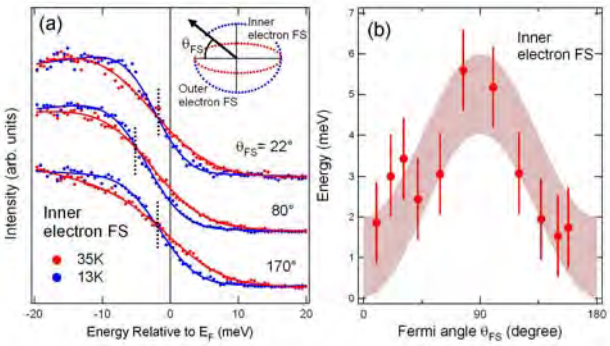

Fig.1: Superconducting gap anisotropy observed on the electron FSs around the X point in $BaFe_2(As_{1-x}P_x)_2$ (x=0.30, T_c=30K). (a) EDCs at k_F taken below (T=13K) and above (T=35 K) Tc for the inner FS. The Fermi angle is defined so that the direction from X to Γ is θ_{FS}=0°. Vertical bars indicate the crossing energy between the spectra below and above T_c. (b) Energy of the crossing point for the inner FSs are plotted as a function of Fermi surface angle θ_{FS}.

References

[1] K. Hashimoto *et al.*, Phys. Rev. B **81**, 220501 (2010).
[2] T. Shimojima *et al.*, Science **332**, 564 (2011).
[3] Y. Zhang *et al.*, Nature Phys. 8, 371 (2012).

*yoshida@wyvern.phys.s.u-tokyo.ac.jp

28A/2009S2-005

Electronic structure of $Ba(Fe_{0.96}Zn_{0.04})_2As_2$ with antiferromagnetic ordering

Shin-ichiro Ideta[1,*], Teppei. Yoshida[1,2], Ichiro Nishi[1], Atsushi Fujimori[1,2], Yoshinori Kotani[3], Kanta Ono[3], Masamichi Nakajima[1,2,4], Kunihiro Kihou[2,4], Yasuhide Tomioka[2,4], Chul Ho Lee[2,4], Akira Iyo[2,4], Hiroshi Eisaki[2,4], Toshimitsu Ito[2,4], Shin-ichi Uchida[1,2], and Ryotaro Arita[2,5]

[1] Department of Physics, University of Tokyo, Tokyo, Japan
[2] JST, Transformative Research-Project on Iron Pnictides (TRIP), Japan
[3] KEK, Photon Factory, Tsukuba, Japan
[4] National Institute of Advanced Industrial Science and Technology, Tsukuba, Japan
[5] Department of Applied Physics, University of Tokyo, Tokyo, Japan

1 Introduction

One of the parent compounds in iron-based superconductors $BaFe_2As_2$ (Ba122) is an antiferromagnetic metal below the Néel temperature (T_N), and becomes superconducting (SC) by the substitution of transition-metal atoms such as Co, Ni, and Cu for Fe [1, 2, 3, 4]. This is a remarkable phenomenon given the fact that the substitution of transition-metal atoms in the CuO_2 plane of the cuprate superconductors quickly kill the superconductivity [5]. According to the rigid-band model, the substitution leads to electron doping and the doped electron number in $Ba(Fe_{1-x}Co_x)_2As_2$ (Co-Ba122), $Ba(Fe_{1-x}Ni_x)_2As_2$ (Ni-Ba122), and $Ba(Fe_{1-x}Cu_x)_2As_2$ (Cu-Ba122) is expected to be x, $2x$, and $3x$, respectively. Experimental studies have shown that the electrons are indeed doped by substitution of Co, Ni, and Cu for Fe, and the electronic structure may show the rigid-band model [2, 4]. However, according to a recent calculation on supercells [7, 8], the extra electronic charges are largely distributed on the substituted Co, Ni, Cu or Zn atoms, apparently contradicting with the rigid-band model.

Recently, our angle-resolved photoemission spectroscopy (ARPES) study has revealed that the electronic structure of the transition-metal doped Ba122 is deviated from the rigid-band model in going from Co-, Ni-, to Cu-Ba122 due to the increasing strength of the impurity potential, and hence part of the doped electrons may not participate in the formation for the Fermi surfaces [6]. This also indicates that the impurity potential is one of the key factors to determine the T_c of the electron-doped iron-based superconductors. However, an interesting question still remains: Zn doped $Ba(Fe_{1-x}Co_x)_2As_2$ and $LaFeAsO_{1-x}F_x$ still show a relatively high T_c [9, 10], although Zn is one of the strong scatteres and this compound is expected to be heavily electron doped. It is an intriguing issue to elucidate why the Zn atom does not destroy the superconductivity.

We have performed an ARPES measurement to investigate the electronic structure on $Ba(Fe_{0.96}Zn_{0.04})_2As_2$ (Zn-Ba122). We find that hole and electron Fermi surfaces (FSs) show a band folding due to the antiferromagnetic ordering below T_N with little indication of carrier doping, and the electronic structure of Zn-Ba122 does not agree with the rigid-band model.

2 Experiment

High-quality single crystals of Zn-Ba122 with x = 0.04 were grown by the self-flux method. ARPES measurements were carried out at beamline 28A of Photon Factory (PF) using linearly-polarized light. The crystals were cleaved *in situ* at T = 20 K in an ultra-high vacuum of 5×10^{-11} Torr.

3 Results and Discussion

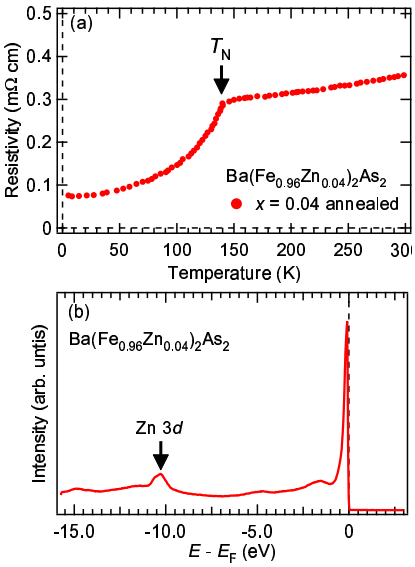

Fig. 1: (a): *ab*-plane resistivity as a function of temperature for annealed Zn-Ba122. (b): Valence-band spectrum taken at $h\nu$ = 60 eV and T = 20 K.

Figures 1(a) and 1(b) show respectively the resistivity and the valence-band spectrum observed by angle-integrated photoemission spectroscopy of Zn-Ba122 with x = 0.04. One can see that the resistivity shows a kink around T~ 140 K, which corresponds to the magnetic phase transition like the parent compound

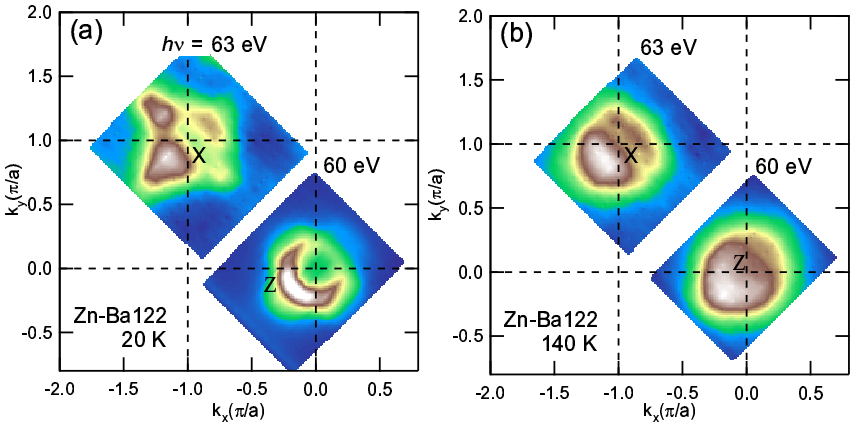

Fig. 2: ARPES intensity map in the two-dimensional k_x-k_y plane for $Ba(Fe_{0.96}Zn_{0.04})_2As_2$ (Zn-Ba122) taken at T = 20 and 140 K.

$BaFe_2As_2$. The valence-band spectrum is shown in Fig. 1(b), and the Zn 3*d* band appears around 10 eV below Fermi level as shown by a black arrow. The binding energy of the Zn 3*d* band is consistent with the band-structure calculation [7]. From analogy to the previous ARPES study [6], one can expect that Zn-Ba122 does not follow the rigid-band model due to the strong impurity potential.

We show an ARPES intensity plot of Zn-Ba122 taken at T = 20 and 140 K in Figs. 2(a) and 2(b), respectively. One finds that the shapes of the hole and electron FSs are similar to those of parent compound, namely, small pockets are observed as expected for zone folding after the spin density wave formation. One may expect that the doped Zn atoms donate four times as large number of electrons as that in the case of Co atom. However, the hole FSs are clearly observed. Therefore, in the case of Zn doping, the doped electrons do not supply carriers into the Fe 3*d* band. Hence, we can conclude that the rigid-band model fails in Zn-Ba122.

In conclusion, we have performed an ARPES study to investigate the electronic structure of the electron-doped $Ba(Fe_{0.96}Zn_{0.04})_2As_2$. We have found that the shape and the area of the hole and electron FSs does not change apparently from the parent compound $BaFe_2As_2$. This is due to the strong impurity potential of the Zn atom which localizes all the doped electrons at the Zn site.

Acknowledgement

This work was supported by an A3 Foresight Program from Japan Society for the Promotion of Science, a Grant-in-Aid for Scientific Research on Innovative Area “ Materials Design through Computics: Complex Correlation and Non-Equilibrium Dynamics ”, and a Global COE Program “ Physical Sciences Frontier ”, MEXT, Japan. S.I. acknowledges support from the Japan Society for the Promotion of Science for Young Scientists.

References

[1] A. S. Sefat, R. Jin, M. A. McGuire, B. C. Sales, D. J. Singh, and D. Mandrus, Phys. Rev. Lett. **101** (2008), 117004 .
[2] P. C. Canfield, S. L. Bud’ko, Ni Ni, J. Q. Yan, and A. Kracher, Phys. Rev. B **80** (2009), 060501(R).
[3] L. J. Li, Y. K. Luo, Q. B. Wang, H. Chen, Z. Ren, Q. Tao, Y. K. Li,X. Lin, M. He, Z. W. Zhu, G. H. Cao, and Z. A. Xu, New J. Phys. **11** (2009), 025008.
[4] N. Ni, A. Thaler, J. Q. Yan, A. Kracher, E. Colombier, S. L. Bud’ko, P. C. Canfield, and S.T. Hannahs, Phys. Rev. B **82** (2010), 024519.
[5] Y. Fukuzumi, K. Mizuhashi, K. Takenaka, and S. Uchida, Phys. Rev. Lett. **76** (1996), 684.
[6] S. Ideta, T. Yoshida, I. Nishi, A. Fujimori, Y. Kotani, K. Ono, Y. Nakashima, M. Matsuo, T. Sasagawa, M. Nakajima, K. Kihou, Y. Tomioka, C. H. Lee, A. Iyo, H. Eisaki, T. Ito, S. Uchida and R. Arita, arXiv:1205.1889.
[7] H. Wadati, I. Elfimov, and G. A. Sawatzky, Phys. Rev. Lett. **105**, 157004 (2010).
[8] K. Nakamura, R. Arita, and H. Ikeda, Phys. Rev. B **83**, (2011) 144512.
[9] Y. Li, J. Tong, Q. Tao, C. Feng, G. Cao, W. Chen, F.-C. Zhang, and Z.-A. Xu, New J. Phys. **12**, (2010) 083008.
[10] J. Li, Y. Guo, S. Zhang, S. Yu, Y. Tsujimoto, H. Kontani, K. Yamaura, and E. Takayama-Muromachi, Phys. Rev. B **84**, (2011) 020513(R).

* ideta@ap.t.u-tokyo.ac.jp

28A/2009S2-005; ALS BL10.0.1/ ALS-05054

Orbital character of Fermi surfaces of the iron-based superconductor $BaFe_2(As_{1-x}P_x)_2$

Teppei YOSHIDA[1,2], Shin-ichiro. IDETA[1], Takahiro SHIMOJIMA[3], Walid MALAEB[4], Hakuto SUZUKI[1], Ichiro NISHIi[1], Kei SHINADA[3], Atsushi FUJIMORI[1,2], Kyoko ISHIZAKA[3], Shik SHIN[4], Sung-Kwan MO[5], Zahid HUSSAIN[5], Zhi-Xun SHEN[6], Yosuke NAKASHIMA[7], Hiroaki ANZAI[8], Masashi ARITA[8], Akihiro INO[7],Hirofumi NAMATAME[8], Masaki TANIGUCHI[7,8], Hiroshi KUMIGASHIRA[9], Kanta ONO[9], Shigeru KASAHARA[10,11], Takasada SHIBAUCHI[11], Takahito TERASHIMA[10], Yuji MATSUDA[11], Masamichi NAKAJIMA[1], Shinichi UCHIDA[1,2], Yasuhide TOMIOKA[2,12], Toshimitsu ITO[2,12], Kunihiro KIHOU[2,12], Chul-Ho LEE[2,12], Akira IYO[2,12], Hiroshi EISAKI[2,12], Hiroaki IKEDA[2,11] and Ryotaro ARITA[2,3]

[1]Department of Physics, University of Tokyo, Bunkyo-ku, Tokyo 113-0033, Japan
[2]JST, Transformative Research-Project on Iron Pnictides (TRIP), Chiyoda, Tokyo 102-0075, Japan
[3]Department of Applied Physics, University of Tokyo, Tokyo 113-8656, Japan
[4]Institute of Solid State Physics, University of Tokyo, Kashiwa 277-8581, Japan
[5]Advanced Light Source, Lawrence Berkeley National Lab, Berkeley, California 94720, USA
[6]Department of Applied Physics and Stanford Synchrotron Radiation Laboratory, Stanford University, Stanford, California 94305, USA
[7]Graduate School of Science, Hiroshima University, Higashi-Hiroshima 739-8526, Japan
[8]Hiroshima Synchrotron Center, Hiroshima University, Higashi-Hiroshima 739-0046, Japan
[9]KEK, Photon Factory, Tsukuba, Ibaraki 305-0801, Japan
[10]Research Center for Low Temperature and Materials Sciences, Kyoto University, Kyoto 606-8502, Japan
[11]Department of Physics, Kyoto University, Kyoto 606-8502, Japan and
[12]National Institute of Advanced Industrial Science and Technology, Tsukuba 305-8568, Japan

Introduction

Most of experimental results on the iron-pnictide superconductors have so far indicated that the superconducting gap opens on the entire Fermi surfaces (FSs), most likely a s_{+-}-wave gap, in contrast to the *d*-wave superconducting gap in the high-T_c cuprate superconductors. While majority of the iron-based superconductors possess nodeless gaps, some systems such as $BaFe_2(As_{1-x}P_x)_2$ [1], show signatures of line nodes in the superconducting gap. According to the spin-fluctuation-mediated mechanism, when the three-dimensionality of the FSs is taken into account, "horizontal" line nodes may appear in the strongly warped part of the hole FS [2] which has $3z^2$-r^2 orbital character. Thus, determination of the orbital character in the FSs is important to understand the Cooper pairing in this system. In order to clarify the orbital character of the FSs of $BaFe_2(As_{1-x}P_x)_2$, we have performed a polarization-dependent ARPES study.

Experimental condition

High-quality single crystals of $BaFe_2(As_{1-x}P_x)_2$ with x=0.34 (T_c=30 K) were grown using the self-flux method. Angle-resolved photoemission (ARPES) experiments were carried out at BL 10.0.1 of Advanced Light Source (ALS). A Scienta SES-R4000 analyzer and a linearly-polarized light were used with the total energy resolution of ~15 meV. The crystals were cleaved *in situ* at T=10 K in an ultra-high vacuum of ~2 x10^{-11} Torr.

Results and discussion

We have performed FS mapping in k_x-k_z plane with different polarization vector by changing the photon energy as shown in Fig. 1. The electric polarization vectors are parallel and perpendicular to the sample surface in Figs. 1(a) and 1(b), respectively. The observed shapes of the FSs are consistent with our previous ARPES study [3]. Considering the matrix element effect in these geometries, while the signal from the *xy* and *yz* orbital character are enhanced in Fig1.(a), that from the *xz* and $3z^2$–r^2 orbital character is enhanced in Fig1.(b). Therefore, the present result clearly indicates that the three-dimensional outer hole FS around the Z point has *xz* and $3z^2$–r^2 orbital character, consistent with the band calculation result [3].

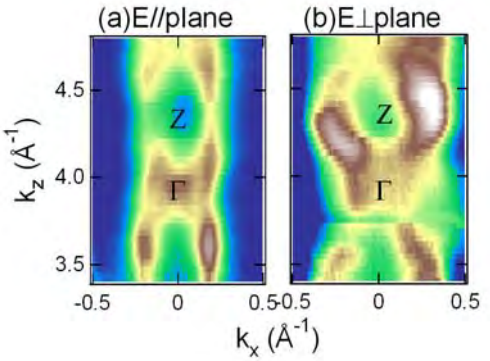

Fig.1: Fermi surface mapping in k_x-k_z plane for $BaFe_2(As_{1-x}P_x)_2$ (x=0.34, T_c=30K) obtained by changing the photon energy. Hole Fermi surfaces around the center of the Brillouin zone (BZ) are mapped with in-plane (a) and out-of-plane (b) vector.

References

[1] K. Hashimoto *et al.*, Phys. Rev. B **81**, 220501 (2010).
[2] K. Suzuki, H. Usui, and K. Kuroki, J. Phys. Soc. Jpn. **80**, 013710 (2011).
[3] T. Yoshida *et al.*, Phys. Rev. Lett. **106**, 117001 (2011).

*yoshida@wyvern.phys.s.u-tokyo.ac.jp

4C,8A/2009S2-008

$SmVO_3$ の磁気軌道秩序に対する *R* サイトランダムネス効果
R-site randomness effect on spin/orbital ordering in $SmVO_3$

佐々木直哉 [1*],逸見和宏 [1*], 福田龍一郎 [1*], 宮坂茂樹 [1*], 田島節子 [1*],山崎裕一 [2*], 中尾朗子 [2*], 中尾裕則 [2*],熊井玲児 [2*], 村上洋一 [2*],
[1] 阪大院理、〒560-0043 豊中市待兼山町 1-1
[2] 高エネ機構物構研 PF/CMRC、〒305-0801 つくば市大穂 1-1

1 はじめに

ペロブスカイト型 RVO_3(*R*:希土類または Y)は、*R* サイトのイオン半径を変化させることにより、*G* 型軌道・*C* 型磁気秩序(以下 *G*-OO/*C*-SO)、または *C* 型軌道・*G* 型磁気秩序(以下 *C*-OO/*G*-SO)という 2 種類の磁気軌道秩序が現れる [1]。その中で、*R* サイトイオン半径のミスマッチによるランダムネスは、*G*-OO/*C*-SO を不安定化させ、*C*-OO/*G*-SO を安定化させる[2]。そこでその異常現象を調べるために、*R* サイトのイオン半径を固定したランダムネスの導入を $Sm_{1-x}(La_{0.322}Y_{0.678})_xVO_3$ により行った。イオン半径の分散であるランダムネスの大きさはイオン半径の分散で表され、これは *x* に比例して大きくなる。*x* = 0 の $SmVO_3$ においては、*G*-OO/*C*-SO しか現れない。しかしながら、ランダムネスを大きくしていくと別の秩序状態(*C*-OO/*G*-SO)が現れる。この新たに現れる秩序状態を解明するために、粉末 X 回折による測定と共鳴 X 線散乱による測定を行った。

2 実験

試料は Floating Zone(FZ)法により単結晶化したものを使用した。格子定数の温度依存性を調べるために、BL-8A において粉末 X 線回折測定を行った。粉末化した試料を φ=0.2 または 0.3mm のリンデマンガラス製キャピラリに詰め、He 吹付式冷却装置を用いて冷却しながらエネルギー15keV の X 線を用いて測定をした。

また、軌道秩序の存在確認と秩序パターンの決定のために、共鳴 X 線散乱実験を行った。入射 X 線は σ (散乱面に対して垂直)偏光であり、エネルギーは V の K 吸収端近くの 5.48keV を用いた。散乱 X 線の偏光依存性を見るためにパイログラファイトの(004)面を用いて π'(散乱面に対し平行)偏光と σ'(散乱面に対し垂直)偏光に分解した。

3 結果および考察

$Sm_{1-x}(La_{0.322}Y_{0.678})_xVO_3$ において、磁化の温度依存性から決定した磁気軌道秩序相図を図 1 に示す。*x* = 0(variance ; $\sigma^2 = 0$)においては、低温で *G*-OO/*C*-SO のみが出現し、*C*-OO/*G*-SO は出現しない。しかし、*x* (variance) の増加とともに *G*-OO、*C*-SO の相転移温度 T_{OO1}、T_{SO1} は減少傾向を示し *x* = 0.8 において消失している。一方で、*x* = 0 では存在しなかった新しい秩序相(*C*-OO/*G*-SO)が *x* = 0.5 より出現し、*x* の増加とともに相転移温度が上昇していく傾向が見られた。

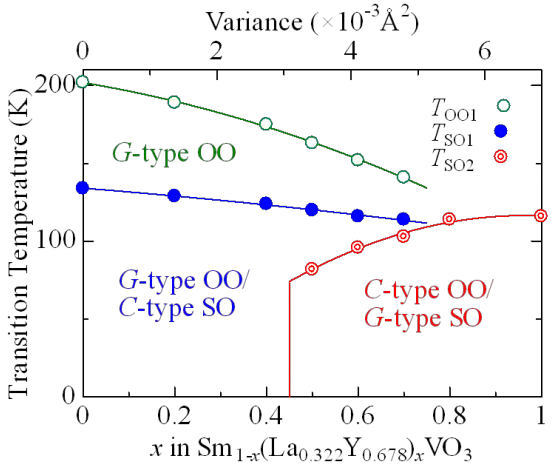

図 1：$Sm_{1-x}(La_{0.322}Y_{0.678})_xVO_3$ における磁気軌道秩序相図。緑丸[○]、青丸[●]、赤二重丸[◎]はそれぞれ *G*-OO、*C*-SO、*C*-OO/*G*-SO 相転移温度 T_{OO1}、T_{SO1}、T_{SO2} を示す。

図 2 に BL-8A にて行った粉末 X 線回折から得られた格子定数の温度依存性と SQUID による磁化の測定結果を示す。*x* = 0($SmVO_3$)は相転移温度 T_{OO1} で、*G*-OO の出現と同時に室温 orthorhombic *Pbnm* から低温 monoclinic $P2_1/b$ へ構造相転移を起こす。この構造相転移に対応して格子定数に折れ曲がりが生じる。さらに温度を下げると相転移温度 T_{SO1} で *C*-SO が生じ、磁化が大きく変化する。しかし、この点において構造は変化しないので格子定数に大きな変化はない。*x* = 0.6 は低温側の磁化において新しい秩序が現れた試料である。先ほどと同様に相転移温度 T_{OO1}、T_{SO1} において *G*-OO、*C*-SO に対応した格子定数、磁化の振る舞いを示している。さらに低温部の相転移温度 T_{SO2} においては、磁化、格子定数ともに先ほどと違う不連続な変化をしており新しい秩序相の存在が示唆される。*x* = 1.0 は磁化の異常が 1 点しか見られなかった試料である。この試料においても相転移温度 T_{SO2} において磁化、格子定数ともに不連続な変化を生じており、*x* = 0.6 の低温部で見られた新たな秩序相と同じものであることが確認できる。また、同様の実験が $Eu_{1-x}(La_{0.254}Y_{0.746})_xVO_3$ においても行われており[3]、その類似性と次に示す共鳴 X 線散乱

の実験結果からこの相転移温度以下において *C*-OO/*G*-SO の出現が示唆される。

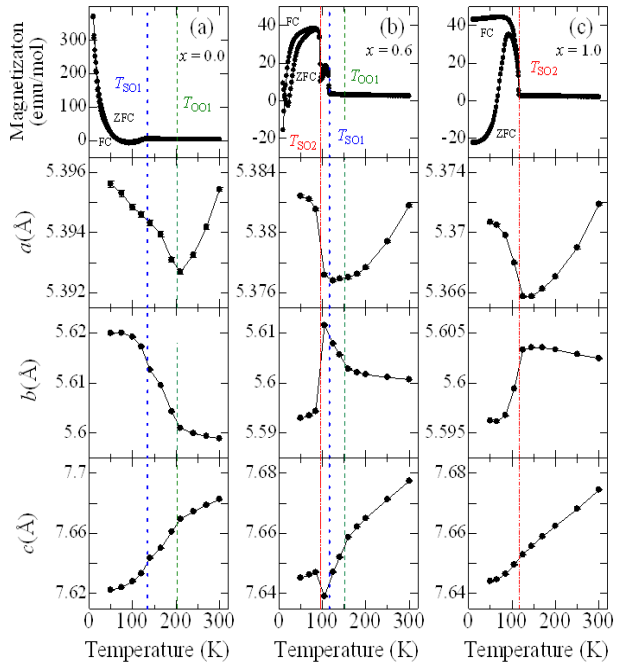

図 2：$Sm_{1-x}(La_{0.322}Y_{0.678})_xVO_3$ において、SQUID による磁化測定結果と粉末 X 線回折測定(BL-8A)による格子定数の温度依存性。(a) x = 0、(b) x = 0.6 (c) x = 1.0 の各組成の結果。

図 3 に共鳴 X 線散乱実験による測定結果を示す。図 3(a) に $Sm_{1-x}(La_{0.322}Y_{0.678})_xVO_3$ x = 1.0 における(100)反射のエネルギースペクトルを示す。この(100)反射は通常禁制反射となり強度はゼロであるが、*C*-OO が存在する場合は V の K 吸収端のみで強度が有限となる。V の K 吸収端(～5.48keV)において、最低温度 20K での(100)反射が有限値を取っていることから *C*-OO の存在が示唆される。また、その温度変化をみると相転移温度 T_{SO2} をまたいで強度が大きく変化しているので、この相転移で *C*-OO が出現していると言える。

また図 3(b)に $Sm_{1-x}(La_{0.322}Y_{0.678})_xVO_3$ x = 1.0 の(100)反射のアジマス角依存性を示した。軌道秩序パターンを決定するために、入射 X 線のエネルギーを V の K 吸収端に固定してアジマス角依存性を測定した。試料の表面形状による強度変化を考慮するために、許容反射である(200)反射強度で規格化を行った。入射 X 線はσ偏光であり、散乱 X 線の偏光をσ'とπ'に分解して測定した。入射 X 線の電場ベクトル E_i が orthorhombic *Pbnm* における *b* 軸に平行な方向をアジマス角ゼロとした。測定は 20K で行っている。σ'偏光の場合、(100)反射強度は非常に弱くほぼゼロである。一方でπ'偏光の場合、(100)反射強度は $E_i \parallel b$ で最大値を取り、$E_i \parallel c$ でほぼゼロになる。*C*-OO を仮定したモデル計算の結果を黒実線(π'偏光)、赤点線(σ'偏光)で示した。それぞれの偏光における アジマス角依存性は *C*-OO におけるモデル計算とよく一致している。この事から $Sm_{1-x}(La_{0.322}Y_{0.678})_xVO_3$ x = 1.0 の 20K においては、x = 0 において存在しなかった *C*-OO が存在していることが示された。

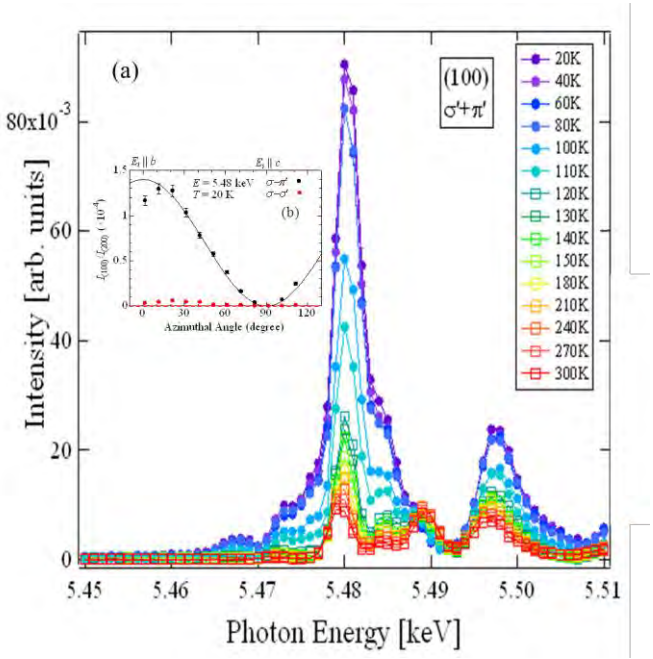

図 3：(a) $Sm_{1-x}(La_{0.322}Y_{0.678})_xVO_3$ x = 1.0 における(100)反射のエネルギースペクトル。中塗り丸印[●]は磁化により決定した相転移温度以下での測定結果であり、白抜き四角[□]は相転移温度以上での測定結果である。(b)$Sm_{1-x}(La_{0.322}Y_{0.678})_xVO_3$ x = 1.0 の K 吸収端における(100)反射強度のアジマス角依存性。(100)反射強度は同じアジマス角における(200)反射強度を用いて規格化されている。

4 まとめ

$SmVO_3$ において、*R* サイトにランダムネスを導入する事により元々安定していた *G*-OO/*C*-SO が不安定化していくとともに、新たに *C*-OO/*G*-SO が出現する。さらに、ランダムネスの導入とともに *C*-OO/*G*-SO は安定化するという事が示された。

参考文献

[1] S.Miyasaka *et al.* ,Phys.Rev.B,**68**,R100406(2003)
[2] J.-Q.Yan *et al.* ,Phys.Rev.Lett,**99**,197201(2007)
[3]R.Fukuta *et al* . , Phys.Rev.B,**84**,140409(2011)

*sasaki@tsurugi.phys.sci.osaka-u.ac.jp

8A/2009S2-008

放射光単結晶 X 線回折による URu_2Si_2 の構造解析
Structural Analyses of URu_2Si_2 by Synchrotron Radiation Single-Crystal X-Ray Diffraction

田端千紘，三浦植幸，安孫子和弘，日髙宏之，柳澤達也，横山淳 [A]，網塚浩，
小林賢介 [B]，熊井玲児 [B]，中尾裕則 [B]，村上洋一 [B]
北大理，茨城大理 [A]，高エ研 [B]

1 はじめに

URu_2Si_2（$ThCr_2Si_2$ 型体心正方晶，空間群 *I4/mmm*）は、T_o = 17.5 K で起こる相転移の秩序変数が不明であることから、25 年以上の間多くの関心を集めてきた物質である[1~3]。この相転移は「隠れた秩序」と呼ばれ、この謎を解明するために様々な理論的・実験的研究が行われてきた。その中でも X 線や中性子を用いた回折実験および熱膨張測定の実験において、隠れた秩序に伴う格子の歪みの有無や格子定数の温度変化などが精密に調べられており[4~6]、*I4/mmm* からの対称性の低下が実験の精度内で無いことが報告されている。その一方で、結晶構造の内部パラメータの変化の有無についてはこれまでほとんど報告されていない。

$ThCr_2Si_2$ 型の結晶構造においては、4(e)サイトの Si 原子の *z* 位置パラメータがフリーパラメータであり、先行研究では室温で *z* = 0.371 と報告されている[7]。4(e)サイトの Si 原子は *c* 軸上で U 原子の上下の最隣接位置にあるため、隠れた秩序相における Si の s, p 軌道と U の 5f 軌道の混成効果やバンド構造などを考える上で、z パラメータを正確に決めることは重要であると考えられる。

我々は放射光 X 線を用いて、URu_2Si_2 の単結晶試料に対して X 線構造解析を行い、Si の z パラメータおよび原子変位パラメータの温度変化を調べた。

2 実験

測定は直径約 20μm の単結晶試料を 0.1ϕの銅線の先にワニスで固定したものを使用し、PF の BL-8B でイメージングプレート型回折計を用いて行った。17.01keV の X 線を用い、振動写真法で回折強度データを収集した。測定温度範囲は 6 K～26 K で、冷却には GM 冷凍機を用いた。

以上の測定から得られた回折強度データに対して、最小自乗フィッティングプログラム Shelx[8]を用い、各温度での構造パラメータ（原子変位パラメータ及び Si の z パラメータ）の精密化を行った。

3 結果および考察

構造パラメータの精密化の結果、Si の z パラメータと各原子の原子変位パラメータの温度変化に T_o = 17.5 K 付近で階段状の異常がみられた（図）。しかし Si の z パラメータが回折強度に与える寄与は小さく、z パラメータを固定して最小二乗フィットを行ってもフィッティング結果にほとんど影響を及ぼさないことが分かった。これに対して U 原子の原子変位パラメータが回折強度に対して支配的であり、隠れた秩序に伴って U 原子の周りの電子密度分布に何らかの変化が起こっている可能性が考えられる。

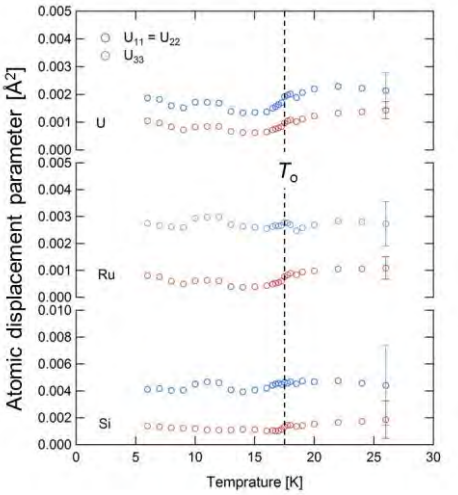

図：原子変位パラメータの温度変化

4 まとめ

PF の BL-8B で URu_2Si_2 における放射光 X 線回折実験を行い、結晶の構造パラメータの温度変化を調べた。その結果、20μm 程度の小さな単結晶において、Si の z パラメータ及び原子変位パラメータに相転移温度付近で異常を示すことが分かった。これらのパラメータのうち、U の原子変位パラメータが回折強度の変化に特に大きく寄与することから、U 原子の電子密度分布が相転移に伴って変化している可能性がある。

参考文献

[1] T.T.M. Palstra *et al.*, Phys. Rev. Lett. 55, 2727 (1985).
[2] M.B. Maple *et al.*, Phys. Rev. Lett. 56, 185 (1986).
[3] W. Schlabitz *et al.*, Z. Phys. B 62, 171 (1986).
[4] N. Kernavanois *et al.*, Physica B 259-261, 648 (1999).
[5] P.G. Niklowitz *et al.*, Phys. Rev. Lett. 104, 106406 (2010).
[6] A. de Visser *et al.*, Phys. Rev. B 34, 8168 (1986).
[7] G. Cordier *et al.*, J. Less-Common Met. 110, 327 (1985).
[8] Sheldrick, G.M, Acta Cryst. A64, 112-122 (2008).

c.tabata@phys.sci.hokudai.ac.jp

2009S2-008

Ferroelectric transition with off-center magnetic Mn^{4+} ions in $Sr_{1-x}Ba_xMnO_3$

H. Sakai[1,2*], J. Fujioka[3], T. Fukuda[4], D. Okuyama[2], D. Hashizume[5], F. Kagawa[3], H. Nakao[6], Y. Murakami[6], T. Arima[7], A.Q.R. Baron[3], Y. Taguchi[2], and Y. Tokura[2,3,8]

[1] *School of Physics & Astronomy, Univ. of St Andrews, North Haugh, St Andrews KY16 9SS, UK*
[2] *CMRG&CERG, RIKEN Advanced Science Institute, Wako, Saitama 351-0198, Japan*
[3] *Department of Applied Physics, Univ. of Tokyo, Tokyo 113-8656, Japan*
[4] *Materials Dynamics Laboratory, SPring-8/RIKEN, Sayo, Hyogo 679-5148, Japan*
[5] *Advanced Technology Support Division, RIKEN, Wako, Saitama, 351-0198, Japan*
[6] *CMRC-PF, IMSS, KEK, Tsukuba, 305-0801, Japan*
[7] *Department of Advanced Materials Science, Univ. of Tokyo, Kashiwa 277-8561, Japan*
[8] *Multiferroics Project, ERATO, JST, Tokyo 113-8656, Japan*

1 Introduction

Most ferroelectric perovskites discovered so far are non-magnetic without *d* electrons on off-center transition metal ions, as exemplified by $BaTiO_3$ and $Pb(Zr,Ti)O_3$. This empirical "d^0-ness" rule can be explained in terms of the stabilization of the ferroelectric distortion by forming a covalent bond between empty *d* orbitals of transition metal and filled 2*p* orbitals of oxygen. In contrast, magnetism requires d^n states in transition metal ions with $n\neq0$. Such incompatibility between ferroelectric and magnetic properties has been one of the most important challenges in designing new multiferroic materials. Recently, however, several first-principles calculations predicted the ferroelectric ground states in perovskite $AMnO_3$ (*A*=Ca, Sr, and Ba), where the magnetic (d^3) Mn^{4+} ions move off-center due to strong Mn-O bond covalency. Experimentally, these manganites with a cubic perovskite structure have not been explored, since the hexagonal polymorphs become more stable with increasing the *A*-site ionic radius. In this study, we have developed a two-step crystal growth technique, consisting of a floating-zone method and high-pressure oxygen annealing (~6 GPa) [1]. This enabled the synthesis of single crystals with the perovskite structure up to 50% Ba substitution.

2 Results and Discussion

Figure 1(a) shows the dependence of lattice constant *a* on Ba concentration (*x*) for $Sr_{1-x}Ba_xMnO_3$ ($0\leq x\leq0.5$). As *x* increases from 0 to 0.4, the lattice constant at 300 K monotonically increases from 3.807 to 3.856Å with keeping the cubic symmetry. Around x=0.45, the crystal structure changes from cubic to tetragonal, indicating ferroelectric distortion with an elongation of the *c*-axis. Figure 1(b) shows a magnetoelectric phase diagram for $Sr_{1-x}Ba_xMnO_3$ as a function of *x*. The ferroelectric transition temperatures T_C were determined as the temperatures where the tetragonal distortion vanishes. The G-type antiferromagnetic phase is stable for the entire doping range ($0\leq x\leq0.5$), although the transition temperature T_N gradually decreases from 230 K (x=0) to 185 K (x=0.5). For $x \geq 0.45$, a novel multiferroic phase thus appears below T_N ($<T_C$), associated with the antiferromagnetic ordering of off-center Mn^{4+} ions.

To further investigate the atomic displacements in the ferroelectric lattice for x=0.5, we have performed the single-crystal structural analysis by using synchrotron x-ray diffraction at BL8A. Figures 1(c) and (d) show the detailed crystal structures at 225 K (above T_N) and at 50 K (below T_N), respectively. All the reflection points are well assigned based on the non-centrosymmetric tetragonal *P*4*mm* space group at both temperatures. Noteworthy is that the magnitude of shift of Mn^{4+} ion from the center of the surrounding oxygens is dramatically suppressed below T_N. In particular, the Mn-O-Mn bond significantly deviates from 180° above T_N [~175.4(5)°], but becomes close to 180° below T_N [~179.1(5)°]. This may correspond to the spontaneous polarization change by several μC/cm^2, indicating huge magnetoelectric coupling in the present system.

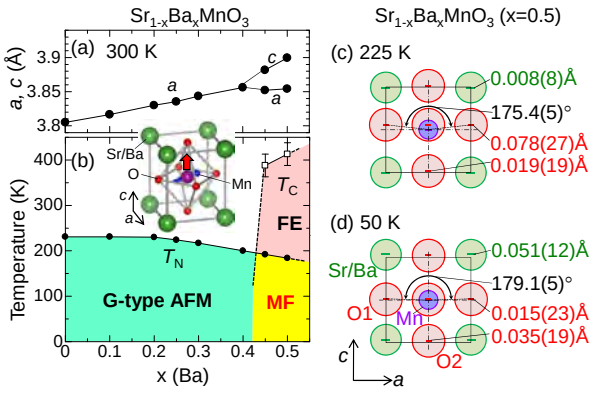

Fig. 1: (a) Lattice constant and (b) phase diagram for $Sr_{1-x}Ba_xMnO_3$ as a function of *x*. PM, AFM, PE, FE, and MF denote paramagnetic, antiferromagnetic, paraelectric, ferroelectric and multiferroic phases, respectively. Detailed crystal structures at (c) 225 K and (c) 50 K are deduced from the single-crystal x-ray diffraction.

References

[1] H. Sakai *et al.*, Phys. Rev. Lett. **107**, 137601 (2011).

* hs36@st-andrews.ac.uk

16A/2009S2-008

室温強磁性 $Sr_3YCo_4O_{10.5}$ の共鳴軟 X 線散乱研究
Resonant soft X-ray scattering study of room temperature ferromagnet $Sr_3YCo_4O_{10.5}$

岡本淳 [1*], 中尾裕則 [1], 小林航 [2], 石渡晋太郎 [3], 山崎裕一 [1], 須田山貴亮 [1], 寺崎一郎 [4], 村上洋一 [1]
[1] 構造物性研究センター、放射光科学研究施設、〒305-0801 つくば市大穂 1-1
[2] 筑波大学数理物質科学研究科物理学専攻、〒305-8571 つくば市天王台 1-1-1
[3] 東京大学大学院工学系研究科付属 QPEC、〒113-8656 文京区本郷 7-3-1
[4] 名古屋大学大学院理学研究科物質理学専攻、〒464-8602 名古屋市千種区不老町

1 はじめに

ペロブスカイト型 Co 酸化物 $Sr_3YCo_4O_{10.5}$(以下 SYCO)は、Co 酸化物中ではもっとも高い強磁性転移点(T_C ~ 340 K)を示す物質として知られている。その強磁性の発現機構について、Co *K* 端共鳴 X 線散乱で磁気転移と同時に *a* 軸方向に x^2-z^2/y^2-z^2 と揃う e_g 軌道秩序が観測されたことから、中間スピン(IS)状態が、高スピン(HS)状態と反強磁性的に揃うことでフェリ的に磁性を発現させるモデルが考えられている[1]。このモデルを確認するには、e_g 軌道秩序構造、磁気秩序構造を形成する電子状態を知ることが必要である。Co $L_{2,3}$端、O *K* 端での共鳴軟 X 線散乱(RSXS)を測定し、e_g 軌道秩序[*q* = (1, 0, 0)]と磁気秩序構造[*q* = (2, 0 ,0)]を作る Co *3d* 軌道や O *2p* 軌道の情報を直接得ることを試みた。

2 実験

SYCO の Co $L_{2,3}$端、O *K* 端 RSXS 実験は、KEK-PF の軟 X 線アンジュレータビームライン BL-16A で行った。SYCO 単結晶試料は(100)面を切り出し、表面を鏡面研磨した。試料は超高真空二軸回折計に、*ac* 面を散乱面とし、入射光の偏光ベクトルがσ偏光(π偏光)で // *b*(⊥ *b*)になるように配置した。測定時の真空は 1x10^{-5} Pa である。検出器には MCP を用いた。入射光のエネルギー分解能は~ 0.1 eV である。

3 結果および考察

Co $L_{2,3}$端の RSXS では(1, 0, 0)は MCP の検出感度では明確な構造が見つからなかった。(2, 0, 0)は明確な構造が観測された。図 1 に(2, 0, 0)の RSXS 強度のエネルギー依存性を示す。XAS と比較して、XAS ピークと Co^{3+}のスピン状態の変化が見られる肩構造の準位(点線)で緩やかな構造が見られた。また、Co L_3 端の XAS ピークと肩構造間のエネルギー(一点鎖線)で顕著な構造が見られた。O *K* 端の RSXS では(1, 0, 0)の測定を行った。図 2 の RSXS スペクトルに見られるように、531 eV 付近に構造が見られた。この領域は、Co^{3+}の LS-HS 状態変化で、Co *3d* 軌道と混成した O *2p* 非占有状態密度の変化が明確に現れる領域である。このことは、室温強磁性と e_g 軌道秩序に関係する HS/IS 状態を直接観測し、電子状態に O *2p* 軌道が大きく寄与していることを示したと言える。

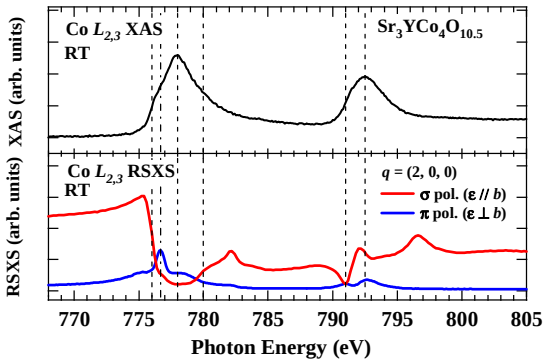

図 1 ：SYCO の Co $L_{2,3}$端 XAS(上)と(2, 0,.0)構造の RSXS スペクトル(下)。

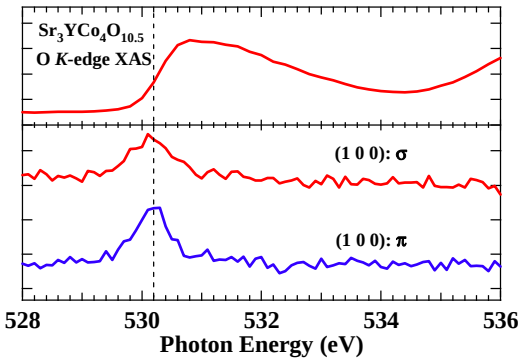

図 2 ：SYCO の O *K* 端 XAS(上)と(1, 0, 0)構造の RSXS スペクトル(下)。

4 まとめ

$Sr_3YCo_4O_{10.5}$ の e_g 軌道秩序構造及び磁気秩序構造について Co $L_{2,3}$端と O *K* 端での共鳴軟 X 線散乱を測定した。構造がスピン状態変化に敏感な準位で見られたことから、中間/高スピン状態が軌道・磁気秩序を作り $Sr_3YCo_4O_{10.5}$ の磁性を担うというモデルを指示する結果が得られた。

参考文献

[1] H. Nakao *et al.*, J. Phys. Soc. Jpn. **80** (2011) 023711.

* jun.okamoto@kek.jp

16A/2009S2-008

$GeCo_2O_4$の反強磁性秩序の共鳴軟X線散乱研究
Resonant soft X-ray scattering study of antiferromagnetic ordering in $GeCo_2O_4$

岡本淳[1*], 中尾裕則[1], 富安啓輔[2], 池田伸一[3], 原茂生[4], 山崎裕一[1], 須田山貴亮[1], 村上洋一[1]
[1]構造物性研究センター、放射光科学研究施設、〒305-0801 つくば市大穂 1-1
[2]東北大学大学院理学系研究科物理学専攻、〒980-8578 仙台市青葉区荒巻青葉 6-3
[3]産業技術総合研究所、〒305-8569 つくば市梅園 1-1-1
[4]中央大学理工学部物理学科　結晶物理学教室、〒112-8551 文京区春日 1-13-27

1 はじめに

スピネル型酸化物 AB_2O_4 は、酸素に八面体配位されている B サイトが、頂点共有した四面体がつながるパイロクロア格子を組み、幾何的にフラストレートした系をとる。幾何的フラストレーションはスピンや軌道の自由度と組み合わせることで多様な物性を示すことで知られている。

スピネル型 Co 酸化物 $GeCo_2O_4$(Co^{2+} : d^7)も幾何的にフラストレートした、t_{2g} 軌道に自由度のある系である。三方晶的な伝搬ベクトル(1/2,1/2,1/2)を持つ反強磁性秩序(T_N ~ 21 K)に転移するが、同時に立方晶から正方晶への構造転移を起こす[1]。これだけではスピンと格子の対称性が一致していないが、同時に正方晶的な伝搬ベクトル(1, 0, 0)を持つ反強磁性秩序が最近中性子散乱で確認され[2]、対称性を満たしていることが分かっている。

$GeCo_2O_4$ で Co サイトの幾何的フラストレーションが反強磁性にどのような影響を及ぼしているか知るには、反強磁性秩序構造を担う電子状態が、どのようなスピン・軌道状態をとるのかが重要な情報となる。フラストレーション系 $GeCo_2O_4$ の磁気秩序構造(1/2, 1/2, 1/2)をとる Co^{2+}のスピン、軌道モーメントについて知るために、Co $L_{2,3}$端での共鳴軟 X 線散乱測定を行った。

2 実験

$GeCo_2O_4$ の Co $L_{2,3}$端 RSXS 実験を、KEK-PF の軟 X 線アンジュレータビームライン BL-16A で行った。$GeCo_2O_4$ 単結晶試料は(111)面を切り出し、表面を鏡面研磨した。試料は超高真空二軸回折計に、[111]と[1-10]で散乱面を構成するように配置した。測定時の真空は 1x10^{-5} Pa である。検出器には MCP を用いた。入射光のエネルギー分解能は~ 0.1 eV である。

3 結果および考察

図 1 に、$GeCo_2O_4$ の Co $L_{2,3}$端 XAS スペクトルと、(1/2, 1/2, 1/2)の RSXS スペクトルを示す。$LaCoO_3$ の XAS に見られる Co^{3+}の XAS 構造と $GeCo_2O_4$ に見られる XAS 構造を比較して、$GeCo_2O_4$ の構造が低エネルギー側にあることと L_3 端のスペクトル形状が CoO のそれに近いことから、$GeCo_2O_4$ の Co は Co^{2+} HS 状態であることが分かる。

Co $L_{2,3}$端 RSXS スペクトルでは、Co L_3端構造に比べて、Co L_2 端構造が非常に弱い。磁気散乱は大まかに磁気円二色性(XMCD)の自乗に比例することから、XMCD 総和則を元に、磁気秩序している Co^{2+}は大きな軌道モーメントを持つことが分かる。RSXS の L_3端、L_2端エネルギー積分強度比が 11.8 ± 0.5 であることから、Co^{2+} の L/S 比は~ 0.6 ± 0.1 と見積もられる。

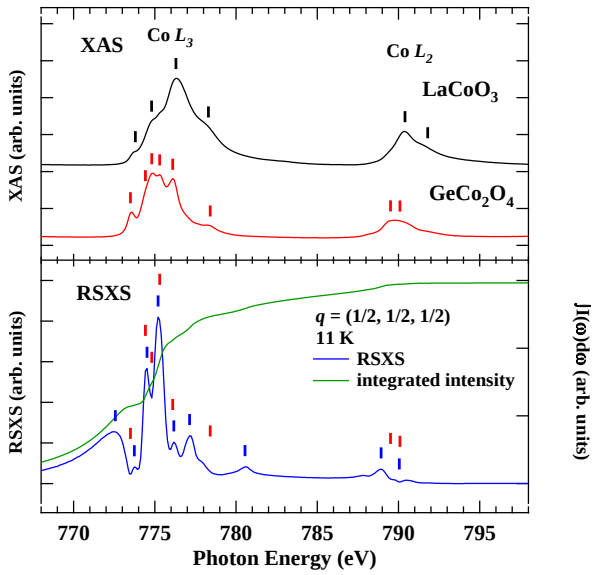

図 1 ： $GeCo_2O_4$ の Co $L_{2,3}$端(上)XAS と (下) RSXS スペクトル(1/2, 1/2, 1/2)とその積分強度。縦棒は Co^{2+} XAS(赤), Co^{3+} XAS(黒), RSXS(青)の構造の位置

4 まとめ

Co $L_{2,3}$端 XAS と RSXS から、$GeCo_2O_4$ の反強磁性秩序構造(1/2, 1/2, 1/2)をとる Co は、大きな軌道モーメントを持つ Co^{2+} 高スピン状態をとっていることが分かった。

参考文献

[1] T. Hosoi *et al.*, J. Magn. Magn. Mat. **310** (2007) 448.
[2] K. Tomiyasu *et al.*, J. Phys.: Conf. Ser. **320** (2011) 012038.

* jun.okamoto@kek.jp

4C/2009S2-008

$(Nd,Sm)NiO_3$ 電気二重層トランジスタの構造解析
Structure analysis of $(Nd,Sm)NiO_3$ electric double layer transistors

浅沼周太郎*, 山田浩之、澤彰仁
産業技術総合研究所　〒305-8562 つくば市東 1-1-1

1 はじめに

近年、半導体の微細化は限界に近付いており、微細化限界の問題を解決し、高性能化を持続するために新規材料を導入したデバイス、いわゆる Beyond CMOS が検討されている。その一つの候補として、強相関酸化物の金属絶縁体相転移（Mott 相転移）に伴う抵抗の変化を利用した Mott transistor が研究されている。Mott transistor は大量の電子が関与する電子相転移である Mott 相転移を利用することから 10nm 以下に加工しても微細化による諸問題が顕在化しないと予想されている。これまでの Mott transistor の研究開発では、おもに銅酸化物超伝導体や巨大磁気抵抗マンガン酸化物などがチャンネルに用いられてきたが、金属相を誘起するのに高密度の電荷ドープが必要もしくは 200K以下の低温でしか動作しないなどの問題があった。

そのような問題の解決法として、われわれは、チャンネル材料にペロブスカイト型ニッケル酸化物 $(Nd,Sm)NiO_3$(NSNO)、ゲート絶縁層に高密度キャリアを誘起出来るイオン液体を用いた電気二重層トランジスタ(EDLT)法を採用した Mott Transistor を作製し、ホールドープを行うことで電子相を制御することに成功した[1]。一方、始めに正のゲート電圧を印可してホールを空乏させたところ（または電子をドープさせると）、室温におけるドレイン電流 I_D が 6 桁程度減少し、V_G を 0 に戻してもその値が保持される現象が観測された（図 1）。その後、負の V_G を印加すると I_D はもとの値へと戻ることが確認され、この I_D の変化は可逆な不揮発スイッチング現象であることが分かった。これに似た不揮発スイッチング現象として酸化還元反応を利用した ReRAM がある。もし NSNO EDLT の抵抗変化にも酸化還元反応が関係しているとすると、抵抗変化に伴い大きな格子定数の変化が起きると予想される。

2 実験

5 mm × 5 mm の $NdGaO_3$(110)基板上に膜厚 12 nm の NSNO 膜を製膜した後に、ソース・ドレイン・ゲート電極(Au 90 nm/Pt 10 nm)を蒸着し、図 2 の形状に加工した。このサンプルの表面にイオン液体 DEME-TFSI を厚さ 500 μm 程度塗布し、ゲートとチャンネルが同一平面上にあるプレナー型の EDLT を作製した。SD 間電圧を 1V に固定しゲート電圧 V_G を変化させたときの SD 間電流 I_{SD} を測定するのと並行して 8.38 keV の放射光を用いて NSNO の(220)ピークの in-situ 観測を行った。

3 結果および考察

図 3 に I_{SD} の V_G 依存性を示す。この実験に用いた単純な構造の EDLT でも SD 間の電流が 3 桁以上変化していることが分かる。図 3 の 1 は初期状態、2 は正の電圧を印加し高抵抗になった状態、3 は負の電圧を印加し再び低抵抗になった状態を示している。図 4 に図 3 の 1、2、3 の状態における(220)ピークの回折パターンを示す。1 と 2 の状態では I_{SD} の値は 3 桁以上変化しているが、構造の変化は観測されなかった。また 2 と 3 の状態でも、僅かに X 線回折の強度が落ちているが、構造はほとんど変化していない。酸化還元反応により 3 桁以上 I_{SD} が変化したと仮定すると、大きな構造の変化が起きると予想されることから、実験結果は NSNO EDLT に正の電界を印加したときに起こる I_{SD} の大きな変化には、酸化還元反応以外のメカニズムが関わっていることを示唆している。

4 まとめ

放射光 X 線回折を使い、NSNO EDLT の初期状態、高抵抗状態、低抵抗状態における NSNO チャンネルの(220)ピークを観測した。その結果、抵抗状態の違いによる大きな格子定数の変化は見られなかった。この結果は、巨大な抵抗変化の由来が単純な酸化還元反応ではないことを示唆している。

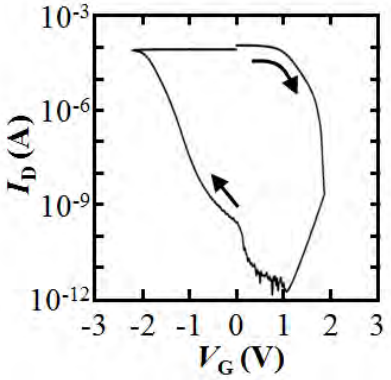

図 1　微細加工を行って作製した NSNO EDLT のゲートに電界を印加してときのドレイン電流 ID の変化

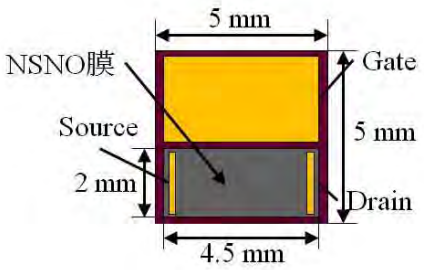

図 2　放射光 X 線回折実験に用いたサンプルの模式図

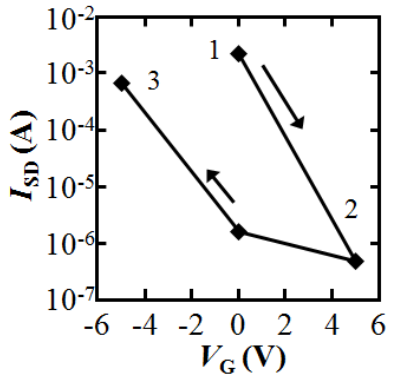

図 3　構造解析に用いた NSNO EDLT のゲートに電界を印加したときの SD 間電流 I_{SD} の変化

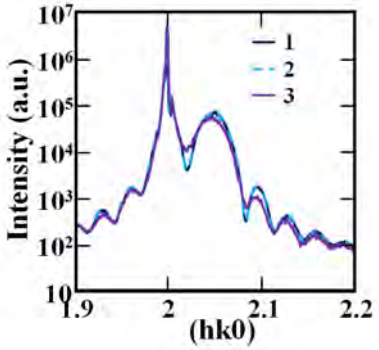

図 4　図 3 の 1、2、3 の状態における NSNO チャンネルの(220)回折ピーク

謝辞
本研究の一部は、科研費（22360280）、日本学術振興会の最先端研究開発支援プログラムにより、助成を受けたものである。

参考文献

[1] S. Asanuma *et al.*, Appl. Phys. Lett. 97, 142110 (2010).

*shutaro-asanuma@aist.go.jp

8A, 2C/2009S2-008, 2011S2-003

スピネル型バナジウム酸化物 MnV_2O_4 における不純物置換効果
Impurity effects on spinel-type vanadium oxide MnV_2O_4

逸見和宏[1*], 佐々木直哉[1], 福田龍一郎[1], 小林達也[1], 田中清尚[1], 宮坂茂樹[1], 田島節子[1], 中尾朗子[2], 中尾裕則[2], 熊井玲児[2], 組頭広志[2], 村上洋一[2]

[1]阪大院理　〒560-0043 大阪府豊中市待兼山町 1-1

[2]KEK 物構研 PF/CMRC　〒305-0801 つくば市大穂 1-1

1 はじめに

MnV_2O_4は、磁場中で冷却することで、Mn^{2+} ($3d^5$) S=5/2とV^{3+} ($3d^2$) S=1によるコリニアフェリ磁性が生じる。またV^{3+}がt_{2g}軌道に軌道の自由度を持つため、より低温で構造相転移を伴った軌道秩序が生じる。同時にVのスピンが傾くことでノンコリニアフェリ磁性が生じる[1]。本研究では、MnV_2O_4のVサイトに軌道の自由度を持たない遷移金属元素Cr^{3+}($3d^3$)とMo^{3+}($4d^3$)を置換した試料$Mn(V_{1-x}M_x)_2O_4$ (M=Cr, Mo)において、軌道秩序が抑制される効果を観測した。また、それに伴う電子状態の変化を観測し、軌道秩序抑制効果との相関を明らかにすることを目的とした。

2 実験

磁化測定、電気抵抗率測定、光学反射率測定、高エネルギー加速器研究機構 Photon Factory BL-8A での X 線回折実験、BL-2C での共鳴光電子分光実験を行った。

3 結果および考察

磁化測定・粉末X線回折実験から、不純物置換によって磁気相転移温度はほとんど変化しないことが分かった。一方、軌道秩序転移温度は低温側にシフトし、あるところで軌道秩序相が完全に消失することが分かった。このことから軌道の自由度を持たない不純物置換により、軌道秩序が抑制されたといえる。また、軌道秩序が消失する置換量から、Cr置換に比べてMo置換は軌道秩序抑制効果が強いことが分かった。

次に電気抵抗率測定・光学反射率測定から、Cr置換した試料はMnV_2O_4と同じくモット絶縁体的な振る舞いを示すのに対して、Mo置換した試料は抵抗率の低下やドルーデピークの出現など、金属的な振る舞いに近づいていることが分かった。このような違いは、局在性が強いCrの3*d*電子と遍歴性が強いMoの4*d*電子の性質が現れた結果だと言える。またその遍歴性の違いが軌道秩序抑制効果の強さの違いとも相関している可能性も考えられる。

これらの結果を踏まえて、共鳴光電子分光実験によって、不純物置換による電子構造の変化を観測した。Mn、V、Cr 各遷移金属元素の 2*p*-3*d* 共鳴条件を満たす時と共鳴条件を満たさないときのスペクトルを比較することで、Cr、Mo の *d* 電子の電子状態を観測した。その結果、Cr の 3*d* 電子は V の t_{2g}バンドのエネルギーの直下にバンドを作るのに対し、Mo は V の t_{2g} バンドとほぼ同じエネルギーに電子状態を作っていることが明らかになった。

以上のことから、伝導度の上昇は Mo の 4*d* 電子のインコヒーレントな電子状態に起因しており、Cr と Mo の *d* 電子の局在性、遍歴性の違いの結果と言える。

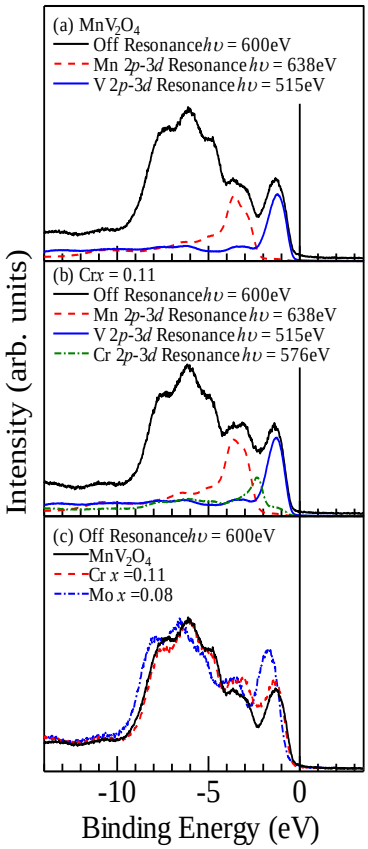

図 1 ：MnV_2O_4, $Mn(V_{0.89}Cr_{0.11})_2O_4$, $Mn(V_{0.92}Mo_{0.08})_2O_4$, の電子分光スペクトル
(a)MnV_2O_4, (b) $Mn(V_{0.89}Cr_{0.11})_2O_4$, (c) Off Resonance の比較

参考文献

[1] R. Plumier and M. Sougi, Physica (Amsterdam) **155B**, 315 (1989).

* khenmi@tsurugi.phys.sci.osaka-u.ac.jp

18A/2010G095

Valence Band Structure of Fe_3O_4(100) Film Across Verwey Transition

Fan-Yong Ran*, Yasushi Tsunemaru, Yasuo Takeichi, Ayumi Harasawa, Koichiro Yaji, Sung-Hun Kim, and Akito Kakizaki

Synchrotron Radiation Laboratory, Institute for Solid State Physics, The University of Tokyo, 5-1-5 Kashiwanoha, Kashiwa-shi, Chiba 277-8581, Japan

1 Introduction

Magnetite undergoes Verwey transition on cooling through ~122 K (*T*v), which is characterized by an abrupt decrease in the electrical conductivity by two orders of magnitude and accompanied by a structure distortion from cubic to monoclinic [1]. It is found that low temperature phase exhibits a monoclinic superstructure with *Cc* space group symmetry [2]. However, the origin of Verwey transition is still under highly debate. Verwey interpreted the transition as an electron delocalization-localization transition accompanied by a long-range charge ordering (CO) of Fe^{3+} and Fe^{2+} ions (CO model) [3]. Recently, a t_{2g} orbital ordering (OO) on the Fe^{2+} sublattice is also revealed [4]. To clearly understand the Verwey transition, systematic work on the electronic band structures of Fe_3O_4 below and above *T*v is required.

2 Experiment

The experiments were carried out at the Photon Factory beamline 18A. Fe_3O_4 (001) films were deposited on MgO(001) surface in a preparation chamber with a base pressure of < 2×10^{-10} mbar. During the growth, the O_2 pressure was maintained at 2×10^{-6} mbar, and a substrate temperature of about 250 °C was used. After preparation, the films were *in situ* transferred into an analysis chamber (base pressure, < 8×10^{-11} mbar). Then, the structural properties and chemical composition were investigated by low-energy electron diffraction (LEED) and x-ray photoelectron spectroscopy (XPS), respectively. Using a photon energy of *h*v=48 eV, valence band structure along $\bar{\Gamma}$-$\bar{M}$ direction in the surface Brillouin zone of Fe_3O_4 films were measured at RT and 90 K using angle-resolved photoemission spectroscopy (ARPES).

3 Results and Discussion

Figure 1(a) shows LEED pattern of surface of pure Fe_3O_4 films. Clear $(\sqrt{2}\times\sqrt{2})R45^o$ reconstruction (white solid square) and (1×1) unit cell (white dashed square) are visible, indicating well-ordered surface. The Brillouin zone and $\bar{\Gamma}$-$\bar{M}$ direction of Fe_3O_4(100) surface are schematically represented in Fig. 1(a) (black solid line). Zero field cooled curve suggests that the Verwey transition occurs at about 115 K for the Fe_3O_4 (001) film.

Figure 1(b) exhibits normal emission measured at RT and 90 K. The spectral feature crosses the E_F at RT, indicating metallic feature of the film. On cooling to 90 K, a band gap of about 70 meV below E_F can be observed. ARPES spectra along the $\bar{\Gamma}$-$\bar{M}$ direction in the surface Brillouin zone measured at RT and 90 K are indicated in

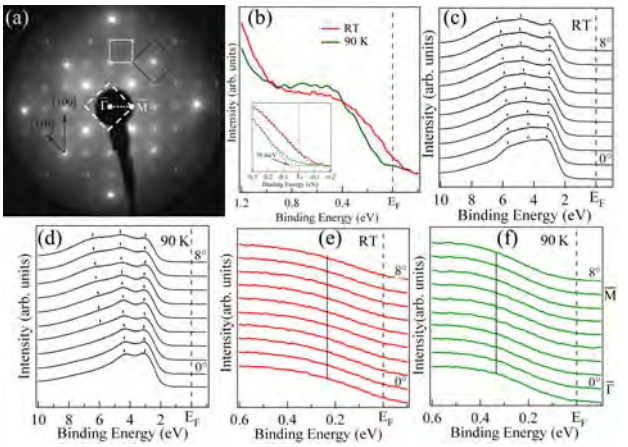

Fig. 1: (a) LEED pattern of Fe_3O_4 (001) film; (b)-(f) ARPES spectra of Fe_3O_4 (001) film measured at RT and 90 K.

Fig. 1(c)-(f). The major dispersions are marked in the figures. In Fig. 1(c), there are three O 2*p*-derived features, which locate near 5.9 eV, 4.6 eV and 3 eV of the binding energy can be observed. With temperature reduces from RT to 90 K (Fig. 1(d)), the feature at about 3 eV is nearly not changed through 0^o - 8^o, while the other two features are varied a lot. The feature at about 4.6 eV shifts about 0.15 eV to E_F side near 7^o, however no obvious change can be observed for the feature around 0^o ($\bar{\Gamma}$). Feature at about 5.5 eV disappears near 0^o ($\bar{\Gamma}$), whereas it is almost the same to that of RT spectra in the range of 5^o - 8^o. ARPES spectra near E_F (< 0.6 eV) at RT and 90 K are shown in Fig. 1(e)-(f). No regular band dispersion can be observed, suggesting that the Fe *d* states are non-dispersive or the dispersions are hard to track due to the broad Fe *d* states. It can be seen that the feature near E_F of Fe_3O_4(001) films at 90 K locates at about 0.34±0.05 eV, about 0.1 eV deeper than that at RT. These results are reasonably in agreement with recent band calculations.

References

[1] E. J. Verwey, Nature (London) **144**(1939) 327.
[2] M. S. Senn, J. P. Wright, and J. P. Attfield, Nature **481(**2012)173.
[3] Y. Fujii, G. Shirane, and Y. Yamada, Phys. Rev. B **11(**1975) 2036.
[4] H.-T. Jeng, G.Y. Guo, and D. J. Huang, Phys. Rev. Lett. **93** (2004)156403.

* fyran80@gmail.com

19A/2010G110

擬一次元構造表面における特異な Rashba 分裂
Peculiar Rashba splitting on a surface with quasi 1D structure

大高実[1], 青木嵩[1]、石川裕隆[1]、武市泰男[2]、原沢あゆみ[2]、矢治光一郎[2]、坂本一之[1]
[1]千葉大学大学院融合科学研究科、〒263-8522 千葉市稲毛区弥生町 1-33
[2]東京大学物性研究所　〒277-8581 千葉県柏市柏の葉 5-1-5

1 はじめに

スピン軌道相互作用と空間反転対称性の破れにより非磁性体でもスピン偏極した電子バンドが生じる。これは Rashba 効果[1,2]として知られ、半導体スピントロニクスデバイスの動作と関連することから応用的に興味が持たれる研究対象である。初期の研究において貴金属の単結晶表面[3]で観測された小さな Rashba 分裂であるが、近年、重元素原子を軽元素金属基板に 1ML 以下吸着させることによって巨大な Rashba 分裂が発現することが報告された[4]。また、重元素吸着半導体表面においては巨大な Rashba 効果の発現のみでなく、表面の対称性に起因した特異な Rashba 効果の存在も報告された[5,6]。そこで、本研究ではこれまで報告のない(擬)一次元構造での特異な Rashba 効果の観測とその起源の解明を目的に、C_{1h} 対称性を有する Si(110)表面に Tl を吸着させて形成される Tl/Si(110)-(1×1)表面のスピン偏極電子構造をもとめることを目的とした。

2 試料作成と SARPES 測定

試料はまず、超高真空下で 1520 K のアニーリングによって Si(110)表面を清浄化し、その上に Tl を 1ML 蒸着した後 420 K のアニーリングを 2 分間行うことによって得た。試料の構造と質は低速電子線回析(LEED)によって確認した。また、スピン・角度分解光電子分光法測定は KEK-PF の BL-19A で行った。BL-19A は独自のスピン検出器、very low-energy Electron diffraction(VLEED)装置[7]を備えており、通常のスピン分解光電子分光法で用いられる Mott 検出器よりも高効率での測定が可能である。測定はエネルギー分解能・角度分解能をそれぞれ 50meV と 1°、試料温度 40K で行った。

3 結果および考察

図 1 は光エネルギー(hν) 35eV で測定した Tl/Si(110)-(1×1)表面の束縛エネルギー170meV でのマッピングと表面ブリルアンゾーンの $\bar{\Gamma}-\bar{X}'$ 方向の電子バンド構造を示している。これより、束縛エネネルギー170meV においては $\bar{\Gamma}-\bar{X}'$ 方向のみに電子状態があり、それと垂直な $\bar{\Gamma}-\bar{X}$ にはないことから原子構造だけでなく、電子構造も擬一次元的であることがわかる。また、$\bar{\Gamma}-\bar{X}'$ の電子バンドが分裂していることも見て取れる。図 1 中の(a)-(c) の点と線は VLEED を用いてスピン分解光電子分光を行った場所を示している。

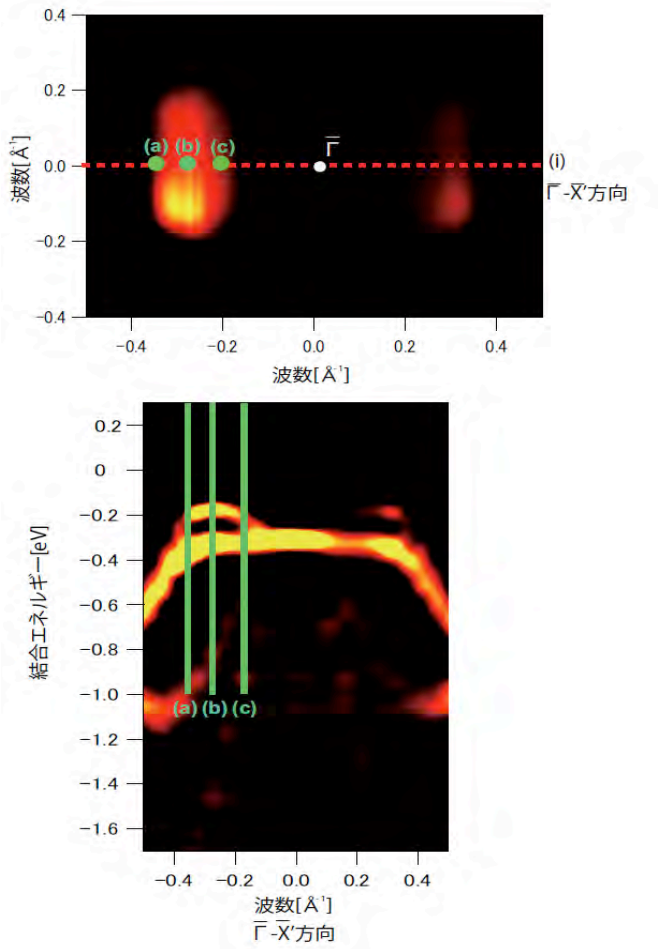

図 1: Tl/Si(110)-(1×1) 表面の電子状態。E_B = 170 meV でのマッピングと $\bar{\Gamma}-\bar{X}'$ 方向の電子バンド構造。

図 1 中の各点で測定した、表面平行方向、波数垂直方向のスピンに関するスピン分解光電子スペクトルを図 2 に示す。この結果から、図 1 で観測された $\bar{\Gamma}-\bar{X}'$ 方向の分裂がスピン分裂であり、スピンの向きが Rashba スピンと同じであることがわかった。また、$\bar{\Gamma}$ 点の反対側の分裂バンドではスピンが逆転していたことから、時間反転対称性を有する Rashba 効果によるスピン分裂であると結論づけた。

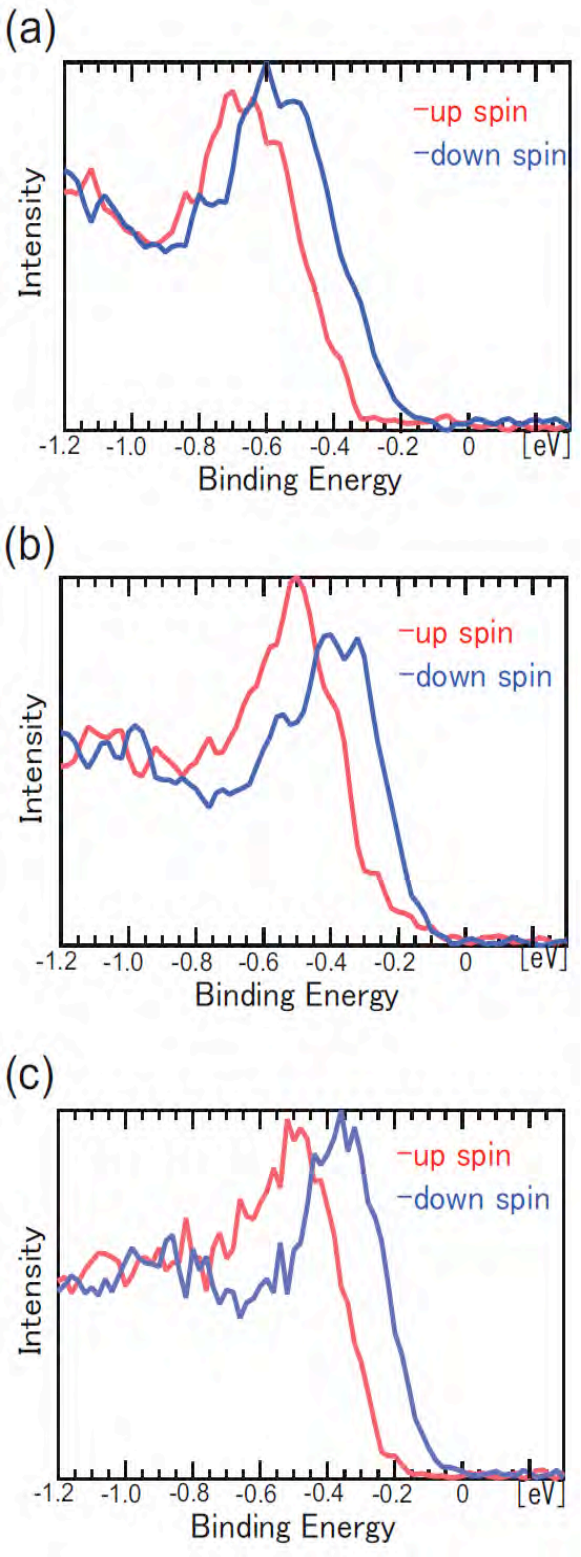

図 2: 図 1 の(a)-(c) で測定したスピン分解光電子分光スペクトル。スピンの向きは表面平行方向、波数に対して垂直方向である。

4 まとめ

本実験では、Tl/Si(110)-(1×1) 表面におけるスピン偏極した電子状態をスピン分解光電子分光によって測定した。その結果、この表面の C_{1h} 対称性に由来すると考えられる擬一次元的な電子構造と擬一次元的な Rashba 効果を観測した。

謝辞

本研究は科研費 JSPS (20244045) と G-COE MEXT(G-03) の助成を受けたものである。

参考文献

[1] E.I. Rashba, Sov. Phys. Solid State **2**, 1109 (1960).
[2] Y. A. Bychkov and E. I. Rashba, JETP lett. **39**, 78 (1984).
[3] S. LaShell, B. A. McDougall, and E. Jensen, Phys. Rev. Lett. **77**, 3419 (1996).
[4] C. R. Ast *et al.*, Phys. Rev. Lett. **98**, 186807 (2007).
[5] K. Sakamoto *et al.*, Phys. Rev. Lett. **102**, 156801 (2009).
[6] K. Sakamoto *et al.*, Phys. Rev. Lett. **103**, 096805 (2009).
[7] T. Okuda *et al.*, Rev Sci Instrum. **89**, 123117 (2008).

3C/2010G147

Study of magnetic moments of Fe_3Pt by X-ray magnetic diffraction

Kenta HIIRAGI[1], Masahiro NAITO[1], Hiromi WATANABE[1],
Hiroshi MARUYAMA[2], and Masa-hisa ITO[1],
[1]Graduate school of Eng., Gunma Univ., Tenjin-cho 1-5-1, Kiryu, Gunma 376-8515,Japan
[2]Graduate school of Sci., Hiroshima Univ.,
Kagamiyama 1-3-2, Higashi-Hiroshima, Hiroshima 739-8516, Japan

Introduction

A ferromagnetic alloy Fe_3Pt shows the invar property that is thought to be related with magnetism. In this research we have measured spin and orbital magnetic form factor of Fe_3Pt separately by the X-ray magnetic diffraction (XMD) experiment and have obtained the spin and orbital magnetic moment by using atomic-model theoretical values for the form factors.

Experiment

The sample was a single crystal and was a sphere with a diameter 5mm. The crystalline structure is Cu_3Au-type in the order phase.

The XMD experiment has been performed on BL3C where the dedicated XMD experimental system is installed. We measured the spin and orbital magnetic form factor separately by utilizing the LS separation method. Here the spin and orbital magnetic form factor are denoted as $\mu_S(K)$ and $\mu_L(K)$ respectively, where $K=\sin\theta/\lambda$ (θ is Bragg angle, λ is X-ray wavelength).

Result and discussion

We have measured $\mu_S(K)$ and $\mu_L(K)$ for 26 and 21 reciprocal lattice points, respectively. The observed $\mu_S(K)$ and $\mu_L(K)$ are shown in Fig. 1 and Fig. 2. In these figures solid circles denotes the fundamental reflections the Miller indices (*hkl*) of which are all even or all odd, and open circles denote the superlattice reflections the Miller indices of which are mixed with even and odd integers.

In Fig. 1 it is noted that $\mu_S(K)$ and $\mu_L(K)$ of the superlattice reflections show different trends from those of the fundamental reflections due to the difference in the crystal structure factors for these reflections. In Fig. 2 it is shown that all $\mu_L(K)$ values are close to zero which suggests that the orbital moment is almost quenched.

We estimated the spin and orbital magnetic moment of Fe and Pt by using atomic-model theoretical values for $\mu_S(K)$ and $\mu_L(K)$ under the dipole approximation. In this model $\mu_S(K)$ is presented as $\mu_S(K)=3m_{S,Fe}\langle j_{0,Fe}(K)\rangle+m_{S,Pt}\langle j_{0,Pt}(K)\rangle$ for fundamental reflections and $\mu_S(K)=m_{S,Pt}\langle j_{0,Pt}(K)\rangle-m_{S,Fe}\langle j_{0,Fe}(K)\rangle$ for superlattice reflections where $m_{S,Z}$ is spin magnetic moment of Z atom and $\langle j_{n,Z}(K)\rangle$ is integral of radial wavefunction of Z atom multiplied by the n-th order spherical Bessel function. For $\mu_L(K)$ the above equations hold but $m_{S,Z}$ and $\langle j_{0,Z}(K)\rangle$ are replaced with $m_{L,Z}$ and $\langle j_{0,Z}(K)\rangle+\langle j_{2,Z}(K)\rangle$. We used $\langle j_{n,Z}(K)\rangle$ values for Fe and Pt in reference [1] and [2], respectively.

The least squares fitting analysis gave us the spin magnetic moment $1.99\pm0.01\mu_B$ for Fe, $0.61\pm0.24\mu_B$ for Pt, and the orbital magnetic moment $-0.01\pm0.01\mu_B$ for Fe, $-0.10\pm0.10\mu_B$ for Pt. Calculated spin and orbital magnetic form factor are shown as solid lines in Figs. 1 and 2 respectively, where the theoretical curves reproduce the observed value. In conclusion we have succeeded in estimating the spin and orbital magnetic moment of Fe and Pt in Fe_3Pt by the XMD experiment.

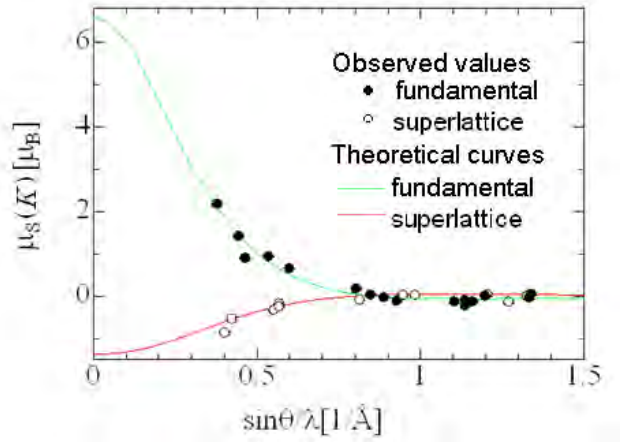

Fig. 1 Spin magnetic form factor.

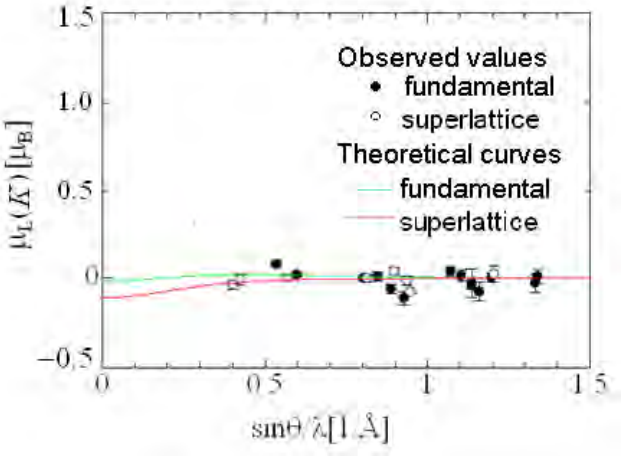

Fig. 2 Orbital magnetic form factor.

[1] International Tables for X-ray Crystallography Vol. IV (1974).
[2] K. Kobayashi, T. Nagao and M. Ito, Acta Cryst. A **67** (2011) 473.

16A2/2010G187

Metal-insulator and spin structure transition in $Ca_{1-x}Ce_xMnO_3$ thin film studied by x-ray magnetic circular dichroism

T. Harano[1]*, G. Shibata[1], K. Ishigami[2], V.K.Verma[1], F. Takahashi[1], K. Yoshimatsu[1]
T. Kadono[1], T. Yoshida[1], A. Fujimori[1], T. Koide[3], P. Xiang[4], H. Yamada[4], A. Sawa[4]

[1] *Department of Physics, Graduate School of Science, The University of Tokyo*,
7-3-1 Hongo, Bunkyo-ku, Tokyo 113-0033, Japan
[2] *Department of Complexity Science and Engineering, Graduate School of Frontier Sciences, The University of Tokyo*,
5-1-5 Kashiwanoha, Kashiwa, Chiba 277- 8561, Japan
[3]*High Energy Accelerator Research Organization* (*KEK*) *Photon Factory*,
1-1 Oho, Tsukuba, Ibaraki 305-0801, Japan
[4] *Correlated Electron Heterointerfaces Group, Nano electronics Research Institute, National Institute of Advanced Industrial Science and Technology* (*AIST*), 1-1-1 Umezono, Tsukuba, Ibaraki 305-8561, Japan

1 Introduction

Perovskite manganite has the chemical formula $R_{1-x}A_xMnO_3$, where R and A are a rare earth element and an alkali earth element, respectively. One can control the spin, orbital and charge ordering by changing the R, A and *x*. Manganite also attracted attention as a material showing giant magnetroresistance. In the case of thin films, one can also control the physical properties by changing their substrates through lattice distortion caused by the epitaxial strain [1].

Electron-doped systems such as $Ca_{1-x}Ce_xMnO_3$ (CCMO) have been extensively studied in addition to the hole-doped systems such as $La_{1-x}Sr_xMnO_3$ (LSMO). In CCMO, one can control the resistivity and the spin structure by substituting Ce for Ca. Xiang *et al.* [2] reported that the resistivity and the spin structure can be controlled by changing the substrates such as $YAlO_3$ (YAO), $NdAlO_3$ (NAO), and $LaSrAlO_4$ (LSAO). The phase diagram of CCMO with different substrates is shown in Fig. 1. Unfortunately, one cannot detect the magnetization of CCMO thin film on NAO substrate by SQUID measurements because of the strong paramagnetic signal from the substrate. X-ray magnetic circular dichroism (XMCD) measurements are useful to obtain the information about the magnetism of Mn in samples grown on NAO substrates. In the present work, we have obtained the information about the magnetic anisotropy of Mn in CCMO thin films grown on NAO substrates.

2 Experimental

Thin films of CCMO were fabricated by the pulsed laser deposition (PLD) method. The thickness of these samples was 40nm (100ML) and their surfaces are capped by $LaAlO_3$ layer (1nm). XMCD measurements were performed at BL-16A2 of KEK-PF with the total electron yield (TEY) method. Substitution ratio *x* of the samples with NAO substrates are *x*=0.01, 0.04 and 0.07. Measurements were performed at temperature *T*=30K with a magnetic field *H*=1T.

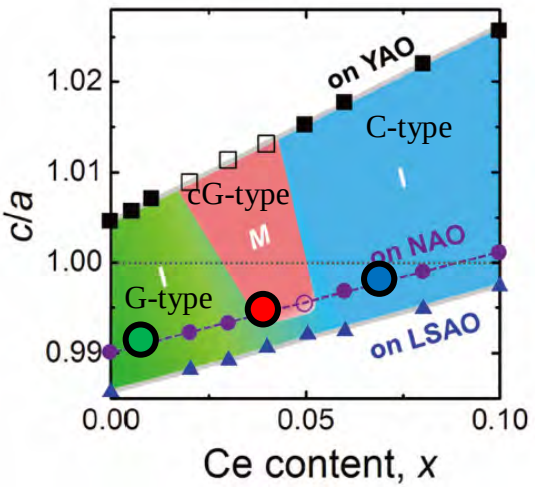

Fig. 1: Phase diagram of $Ca_{1-x}Ce_xMnO_3$ thin films grown on different substrates [1]. Green, red, and blue regions indicate G-type antiferromagnetic insulator, canted G-type antiferromagnetic metal, and C-type antiferromagnetic insulator, respectively. Samples studied here are marked by large circles.

3 Results & Discussion

Figure 2 shows the Mn 2*p*-3*d* XMCD spectra for CCMO with various doping concentrations grown on NAO. For *x*=0.01, the L_3 peak of θ = 60° is larger than that of θ = 0°. θ is defined by the angel between the vector of incident light and the normal vector of the sample surface. On the other hand, the trend is opposite for *x*=0.04 and 0.07. Therefore, the *x*=0.01 sample has in-plane magnetic anisotropy, while those of *x*=0.04 and 0.07 samples have out-of-plane magnetic anisotropy.

From this result, we conclude that the magnetic anisotropy of *x*=0.04 (canted G-type AFM), is similar to that of *x*=0.07 (C-type AFI). This result is different from LSMO thin film in which the magnetic anisotropy depends on whether the ratio between the lattice constants *a* and *c* (*c*/*a*) is larger than one or not.

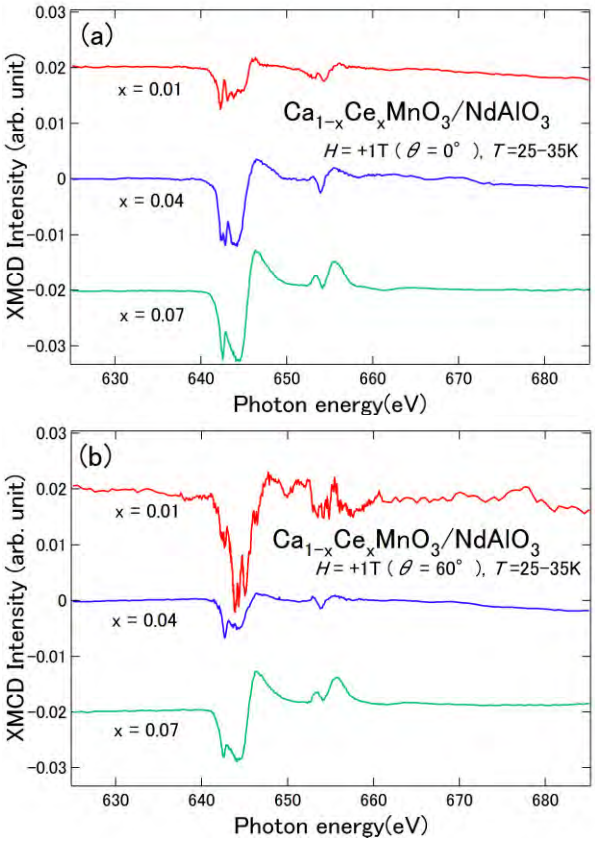

Fig. 2: Mn 2*p*-3*d* XMCD spectra for CCMO on NAO for various doping concentrations. Panels (a) and (b) show the spectra for θ=0° and 60°, respectively.

Reference

[1] Y. Konishi *et al* , J. Phys. Soc. Jpn. **68**, 3790 (1999).
[2] P. Xiang *et al* , Adv. Mater. **23**, 48 (2011).

* harano@wyvern.phys.s.u-tokyo.ac.jp

16A/2010G187 & 2010S2-001

X-ray magnetic circular dichroism study of $FeCr_2S_4$

Virendra Kumar VERMA[*1], Vijay Raj SINGH[1], Keisuke ISHIGAMI[1], Goro SHIBATA[1], Takayuki HARANO[1], Toshiharu KADONO[1], Atsushi FUJIMORI[1], Tsuneharu KOIDE[2], Kenya OHGUSHI[3], Yoshinori TOKURA[3]

[1]Department of Physics, University of Tokyo, Bunkyo-ku, Tokyo 113-0033, Japan
[2]Photon Factory, IMSS, High Energy Accelerator Research Organization, Tsukuba, Ibaraki 305-0801, Japan
[3]Dept. of Applied Physics, University of Tokyo, Tokyo 113-8656, Japan

Introduction

Transition metal-based spinel compounds (AB_2X_4), have been a hot topic of experimental and theoretical studies for researchers [1]. $FeCr_2S_4$ is a ferromagnetic semiconductor with T_C ~ 170 K. This material shows large negative magnetoresistance near the Curie temperature [2]. Park *et al*. [3] reported a band-structure calculation for $FeCr_2S_4$ in which each sublattice of the Fe and Cr transition metals orders ferromagnetically, while the two sublattices are coupled antiferromagnetically to each other. Recently, the electronic structure of $FeCr_2S_4$ has been studied by density functional calculation. [4]. Here, we report on Fe and Cr $L_{2,3}$ x-ray absorption and x-ray magnetic circular dichroism (XMCD) measurements of $FeCr_2S_4$ single crystal in order to study the electronic structure and magnetic properties of Fe and Cr ions in single crystal and we find that the Fe ions show large orbital magnetic moment at 80K.

Experiment

The sample studied here is a single crystal of $FeCr_2S_4$. The $FeCr_2S_4$ single crystal was grown by a chemical vapor transport method with $CrCl_3$ as a transport agent. The sample is cleaved *in-situ* to obtain a clean surface. The XAS and XMCD measurements were done at BL-16 of KEK-Photon Factory (PF), Japan. The XAS spectra were taken in the total electron yield (TEY) mode.

Results and Discussion

The XAS spectra were taken in a magnetic field of 1T at temperature of 80K and are denoted by μ_- and μ_+ for left and right circularly polarized light, respectively. The XMCD spectrum was obtained by taking a difference between the XAS spectra with negative and positive helicity of the circular polarized light. Figures 1 (a) and (b) show the Fe and Cr 2*p*-3*d* XAS and the XMCD spectra, respectively. The main two groups of the peaks shown in the XAS spectra are due to the $2p_{3/2}$ (L_3 edge) and $2p_{1/2}$ (L_2 edge) spin-orbit components. The Fe and Cr ions were in the 2+ and 3+ states, respectively, and both sublattices were found to be antiferromagnetically coupled to each other, finding from the opposite signs of the XMCD signals. From the sum rule analysis, the orbital magnetic moments of Fe and Cr ions are found to be 0.14 and 0.006 μ_B/ion, respectively. In the Fe ions, the spin and orbital moments have the same sign, whereas opposite sign is found in the Cr ions. This is because the *d* states of Fe^{2+} are more than half filled while those Cr^{3+} is less than half filled of *d* states. The orbital moment of the Cr ions is found to be small due to the d^3 configuration of Cr. However, the large orbital moment of the Fe ions is remarkable since the spin-orbit interaction within *e* levels of Fe should be small. A possible reason of large orbital magnetic moment of Fe ions is that the crystal-field splitting is small in $FeCr_2S_4$.

References

[1] P. G. Radaelli, New J. Phys. **7**, 53 (2005).
[2] A. P. Ramirez *et al.*, Nature **386**, 156, (1996).
[3] M. S. Park *et al.*, Phys. Rev. B **59**, 10018 (1999).
[4] S.Sarkar *et al.*, Phys. Rev. B **80**, 201101(R) (2009).

* vkverma@wyvern.phys.s.u-tokyo.ac.jp

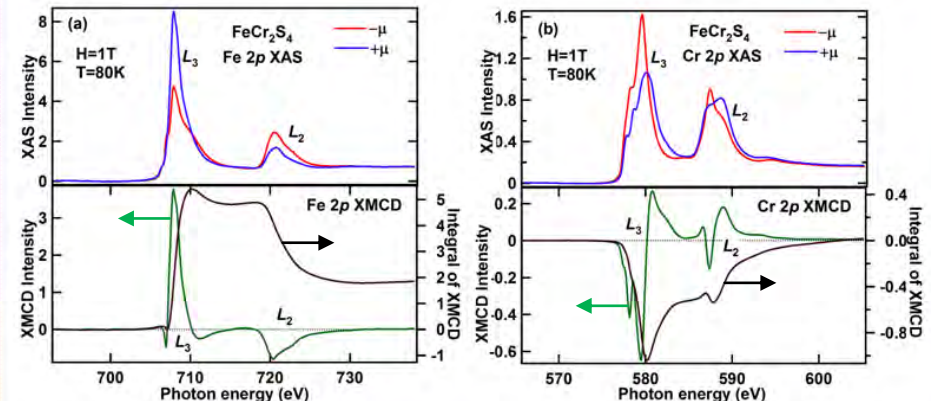

Figure 1: Fe and Cr $L_{2,3}$-edge XAS and XMCD of $FeCr_2S_4$ single crystal.

16A2/2010G187; SPring-8 BL23SU/2011A3840

Ru-doped $La_{0.6}Sr_{0.4}MnO_3$ thin film as a coercivity tunable material studied by x-ray magnetic circular dichroism

Takayuki Harano[1, *], Goro Shibata[1], Keisuke Ishigami[2], Verma Kumar Verma[1], Toshiharu Kadono[1], Atsushi Fujimori[1, 3], Yukiharu Takeda[3], Tetsuo Okane[3], Yuji Saito[3], Hiroshi Yamagami[4], Hiroyuki Yamada[5], Akihito Sawa[5], Masashi Kawasaki[6], Yoshinori Tokura[6], Arata Tanaka[7]

[1]Department of Physics, University of Tokyo, Bunkyo, Tokyo 113-0033, Japan
[2]Department of Complexity Science and Engineering, University of Tokyo, Kashiwa, Chiba 277- 8561, Japan
[3]Quantum Beam Science Directorate, Japan Atomic Energy Agency (JAEA), Sayo, Hyogo 679-5148, Japan
[4]Department of Physics, Kyoto Sangyo University, Kyoto, Kyoto 603-8555, Japan
[5]National Institute of Advanced Industrial Science and Technology (AIST), Tsukuba, Ibaraki 305-8561, Japan
[6]Department of Applied Physics, University of Tokyo, Bunkyo, Tokyo 113-8656, Japan
[7]Department of Quantum Matter, ADSM, Hiroshima University, Higashi-Hiroshima, Hiroshima 739-8530, Japan

Introduction

$La_{1-x}Sr_xMnO_3$ (LSMO) is a typical half-metallic compound. Although LSMO is attracting attention for possible applications to magnetic tunnel junctions, there is a serious problem that the coercivity (H_C) is too small. Yamada *et al.*[1] reported that one can enhance the coercivity by substituting Ru for Mn, and attributed this effect to antiferromagnetic coupling between Mn and Ru and charge transfer from Mn^{4+} to Ru^{4+} ($Mn^{4+}+Ru^{4+}\rightarrow Mn^{3+}+Ru^{5+}$).

In order to obtain information about the electric and magnetic states of each element in this system and to elucidate the mechanism of the coersivity enhancement, we performed x-ray magnetic circular dichroism (XMCD) measurements.

Experimental

We fabricated the thin films by plused laser deposition (PLD) method. The thickness of these samples was 50nm. The substitution ratio y of Ru was 0.05. XMCD measurements were performed at BL23SU of SPring-8. The measurement was performed in the total electron yield (TEY) mode with T=30K and H=1T (out of plane). We used 1Hz helicity-switching mode. [2]

Results and Discussion

The XMCD spectra of Mn L-edge and Ru M-edge are shown in Fig. 1 and Fig. 2, respectively. One can conclude that the spin direction of Mn is opposite to that of Ru consistent with Yamada *et al.* [1] . By applying the XMCD sum rules, we found that the orbital moment of Ru is finite and is parallel to the spin moment. This suggests that Ru 4*d* orbitals are occupied by more than 5 electrons and that the valence of Ru is 3+.

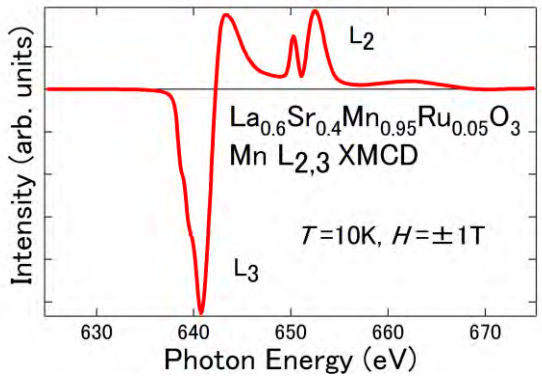

Fig. 1 XMCD spectrum at the Mn L-edge

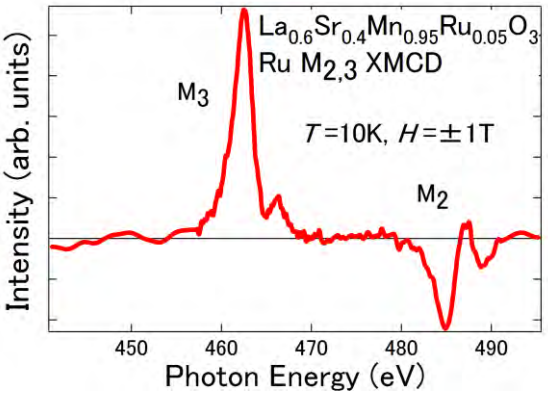

Fig. 2 XMCD spectrum at the Ru M-edge

Reference
[1] H. Yamada *et al*., Appl. Phys. Lett. **86**, 192505 (2005).
[2] Y. Saitoh *et al*., J. Synchrotron Radiation. **19**, 3, 388 (2012).

*harano@wyvern.phys.s.u-tokyo.ac.jp

16A/2010G187; SPring-8 BL23SU/2011A3840

XMCD study of spin and orbital states of FePt nano-particles coated by SiO_2

Toshiharu KADONO[1*], Vijay Raj SINGH[1], Virendra Kumar VERMA[1], Keisuke ISHIGAMI[1], Goro SHIBATA[1], Takayuki HARANO[1], Atsushi FUJIMORI[1], Tsuneharu KOIDE[2],
[1]Department of Physics, University of Tokyo, Bunkyo-ku, Tokyo 113-0033, Japan
[2]KEK-PF, Tsukuba, Ibaraki 305-0801, Japan

1 Introduction

$L1_0$ ordered FePt nano-particles coated by SiO_2 have a great attention as a material to be used in high density magnetic storage memory devices because this particles possesses a high magneto-crystalline anisotropy. The FePt nano-particles made by gas phase preparation method [1] have some problems to apply manufacturing process. Recently, on the other hand, FePt nano-particles coated with SiO_2 were found for practical realization and were investigated. FePt nanoparticles prepared by this method have a gigantic magnetic coercive force much larger than gas phase preparation. Since the orbital magnetic moment determines magneto-crystalline anisotropy, to obtain information about the orbital magnetic moment is important. In the present work, we have applied the XMCD technique to the SiO_2-coated FePt nanoparticles to characterize their magnetic properties.

2 Experimental conditions

FePt nano-particle samples were prepared by the wet chemical preparation method [2]. For the XMCD measurements, the nanoparticle samples were mounted on a sample holder using silver paste. After the preparation of the samples, they were kept in an Ar atmosphere in order to prevent oxidation until the XMCD measurements.

XAS and XMCD measurements were performed at the helical undulator beam line BL23SU of SPring-8. The highest applied magnetic field was 9 T. The measurements were performed under an ultra-high vacuum of ~4.8×10^{-9} Pa at room temperature (~300 K) with the total electron-yield (TEY) mode. The magnetic field dependence of the XMCD intensity at the peak of the Fe L_3 edge was measured in the range of -9 T ≤ H ≤ 9 T.

3 Results and discussion

Figures 1 (a) and (b) show the Fe 2p-3d XAS and XMCD spectra of FePt nano-particles, respectively. One can see Fe-oxide spectra overlapping on the high energy side of the main L_2 and L_3 XAS peaks. In XMCD spectrum in applied 9 T magnetic field, we have observed Fe^{3+} signal which is absent in the XMCD with 0 T magnetic field. This means that this peak is a paramagnetic component derived from Fe_2O_3. Since the samples were kept in Ar atmosphere to prevent oxidization just before the measurements, oxidization may have occurred between the SiO_2-coat and the Fe component. By applying optical sum rules [3, 4] to the measured XMCD spectrum, the ratio μ_L/μ_S is found to be 0.08, where μ_S and μ_L are the spin and orbital magnetic moments of Fe 3d electrons, respectively. Figure 2 shows hysteresis loops of the XMCD intensities at the Fe L_3 edge of the SiO_2-coated FePt nano-particle sample at room temperature. The magnetization measured by Fe L_3-edge XMCD was saturated around 6 T and the coercive force was as large as 1.7 T, consistent with the result of SQUID measurement [5].

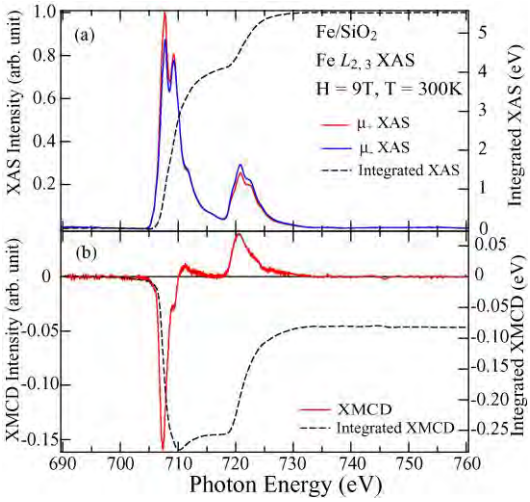

Figure 1 : (a) XAS spectra of Fe component in FePt nano-particles, (b) XMCD spectrum of Fe component at applied magnetic field 9 T.

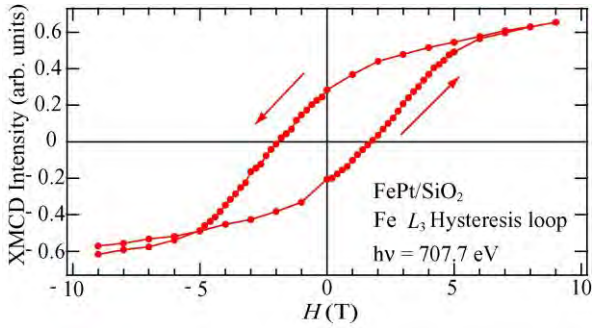

Figure 2 : Hysteresis loop of the XMCD intensities at the Fe L_3 edge of the SiO_2-coated FePt nano-particles.

References

[1] O. Dmitrieva *et al.*, J. Phys. D: Appl. Phys. **39**, 4741 (2006).
[2] S. Yamamoto *et al.*, Chem. Matter. **18**, 5385 (2006).
[3] B. T. Thole, *et al.*, Phys. Rev. Lett. **68**, 1943 (1992).
[4] P. Carra, *et al.*, Phys. Rev. Lett. **70**, 694 (1993).
[5] Y. Tamada, *et al.*, Appl. Phys. Lett. **90**, 162509 (2007).

* kadono@wyvern.phys.s.u-tokyo.ac.jp

16A/2010G187, 2011A3840

X-ray Magnetic Circular Dichroism of $SrRuO_3$(xML)/Nb:SrTiO3 Thin Films

Keisuke ISHIGAMI[*1], Kouhei YOSHIMATSU[1], V. K. Verma[1], Goro SHIBATA[1], Takayuki HARANO[1], Toshiharu KADONO[1], Tsuneharu KOIDE[2], Yukiharu TAKEDA[3], Tetsuo OKANE[3], Yuji SAITO[3], Hiroshie YAMAGAMI[3], Hiroshi KUMIGASHIRA[2], Masaharu OSHIMA[1], Teppei YOSHIDA[1], Atsushi FUJIMORI[1]

[1]Univ. of Tokyo, Bunkyo-ku, Tokyo 113-0033, Japan

[2]Photon Factory, Tsukuba, Ibaraki 305-0801, Japan

[2] Japan Atomic Energy Agency, Synchrotron Radiation Research Center, Hyogo 679-5148, Japan

1 Introduction

Ferromagnetic metal $SrRuO_3$ (SRO) is a promising material for oxide electronic devices in terms of chemical stabilization and perovskite-type crystal structure. It is commonly known that electronic and magnetic properties of epitaxial gown thin films are sensitive to thickness, which show larger resistivity compared with bulk state by making film thickness thinner. This phenomenon is considered that interface between substrate and film and/or structural defect influence with state of films.

In these days, Toyota et al. reported conductance and X-ray photoemission result of epitaxial grown SRO on Nb dopped $SrTiO_3$ (Nb:$SrTiO_3$), saying that 4-5ML thickness SRO films shows transition from insulator to metal with increasing film thickness [1]. While, Mahadevan et al. reported density functional theory's (with generalized gradient approximation) calculation result, saying that 8ML thickness SRO shows transition from antiferromagnetic insulator to ferromagnetic metal with increasing thickness [2]. Xia et al. explained the inconsistency of transition thickness according to an antiferromagnetic layer between SRO and Nb:$SrTiO_3$ (an antiferromagnetic surface and a ferromagnetic bulk (AFMS-FMB)) suggested with Magneto-optical Kerr effect measurement[3]. With there works, it was found that SRO thin films shows antiferromagnetic insulator under 4ML, AFMS-FMB metal state upper 4ML and metal-insulator transition occur together with ferromagnetic-antiferromagnetic transition.

However, transition of magnetic state cause by the antiferromagnetic layer (variation of hybridization between ruthenium and oxygen) has never been measured directly yet. The goal of this study is directly measure the magnetic transition of SRO thin films with the antiferromagnetic layer by X-ray Magnetic Circular Dichroism (XMCD) and comparison magnetic structure with electronic one.

2 Experiment

SRO thin film ware fabricated epitaxially on TiO_2-terminated Nb:$SrTiO_3$ substrate by laser Molecular Beam Epitaxy (MBE) method. The thickness of thin films (xML = 4,2ML) examined by Reflection High Energy Electron Diffraction (RHEED) oscillation. Crystallographic properties examination by Atomic Force Microscope shows a step-and-terrace structure and well-ordered surface. Total electron yield XMCD spectra taken at 20.0K under vertically applied 0.1-8.0T external magnetic field with thin film surface. XMCD measurement performed on BL16A at PF and on BL23SU at SPring-8.

3 Results and Discussion

We have measured behaviour of magnetization with changing the thickness of SRO on Nb:$SrTiO_3$. In 4ML case, it shows Ru 3p 1/2 XMCD peak. On the other hands, 2ML thickness SRO doesn't (Fig. 1 (left)). By plotting XMCD ratio for each magnetic field, 2ML won't react with any external magnetic field even 8.0T, on the other hands 4ML shows ferromagnetic behaviour. In critical thickness 4ML case, ferromagnetic and antiferromagnetic states coexist. The coexistence is consistent with the results from first principle calculation.

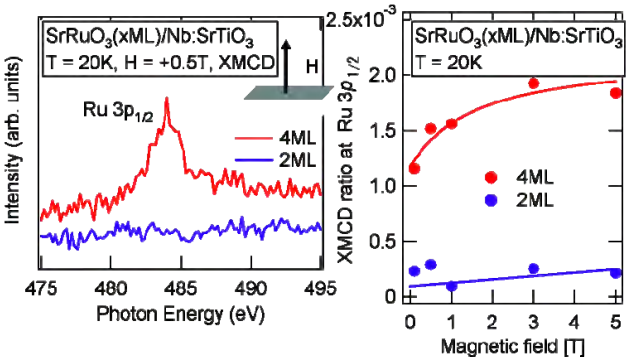

Figure 1: (left) variety of Ru 3p 1/2 XMCD spectra with 2 and 4 ML thickness SRO. (right) XMCD ratio as a function of magnetic field.

References

[1] D. Toyota *et al.*, Appl. Phys. Lett. **87**, 162508 (2005)

[2] Priya Mahadevan *et al.*, Phys. Rev. B **80**, 035106 (2009)

[3] Jing Xia *et al.*, Phys. Rev. B **79**, 140407 (2009)

* ishigami@wyvern.phys.s.u-tokyo.ac.jp

2C/2010G189

Electronic Structure and Local Atomic Arrangement in 2-dimensional Quasicrystals Al-Co-Ni

Kazuo Soda[1,*], Manabu Inukai[2,1], Yeong-Gi So[3], Kei-ichi Edagawa[3], Yoshihiko Yokoyama[4], Yasuhisa Tezuka[5] and Osamu Morimoto[6]
[1]Graduate School of Engineering, Nagoya University, Nagoya 464-8603, Japan
[2]Toyota Technical Institute, Nagoya 468-8511, Japan
[3]Institute of Industrial Science, the University of Tokyo, Tokyo 153-8505, Japan
[4]Institute for Materials Research, Tohoku University, Tsukuba 980-8577, Japan
[5]Faculty of Science and Technology, Hirosaki University, Hirosaki 036-8560, Japan
[6]Hiroshima University, Hiroshima 739-8511, Japan

1 Introduction

Decagonal quasicrystals (d-QC), where quasiperiodic atomic layers are periodically stacked along a direction, are viewed as consisting of quasiperiodically arranged decagonal columnar structures. In particular, Al-Co-Ni alloys form d-QC in a wide concentration range with different structural modifications depending on a Co/Ni ratio [1]. According to a theoretical study [2], because of strong Al-Co and Ni-Ni interactions, a decagonal (pentagonal) ring of Al and transition metals (TM) are formed in the center of the column in Co-rich $Al_{72}Co_{20}Ni_8$, while Ni-rich $Al_{72}Co_8Ni_{20}$ shows an atomic arrangement in a hexagon-boat-star tiling with Ni-Ni pairs. However, it is difficult to distinguish these TM's by transition electron microscope. Thus we have investigated the electronic structures of Al-Co-Ni d-QC by the TM $L\alpha$ soft X-ray emission spectroscopy (XES) as well as the X-ray photoelectron one (XPS) and a cluster calculation in order to clarify the atomic arrangement from spectroscopic points of view.

2 Experiment

XES measurements were performed at BL2C of Photon Factory. The synchrotron light from the beamline was employed as the excitation source and its photon energy was calibrated by measuring XPS spectra of an Au plate. The energy of emitted photon was calibrated with the already calibrated and elastically scattered excitation photons. The energy resolution was estimated with the elastically scattered photons as ~1eV. Specimens were prepared by Ar arc-melting and subsequent quenching for Ni-rich d-QC $Al_{72}Co_8Ni_{20}$ and by the Czochralski method for Co-rich one $Al_{72}Co_{16}Ni_{12}$. They were mechanically polished before the XES measurement.

3 Results and Discussion

Figure 1 compares XES spectra of $Al_{72}Co_8Ni_{20}$ with those of $Al_{72}Co_{16}Ni_{12}$. In the figure, these XES spectra are plotted so that the integrated intensity is proportional to the TM concentration. While the 3*d* band in the XPS spectra, which represent the total electronic density of states (DOS), is shifted from the binding energy E_B of 2.3 eV in the Ni-rich d-QC to 1.8 eV in the Co-rich one, the spectral shape and peak position of the Co and Ni $L\alpha$ XES spectra, which stand for the partial DOS of the respective 3*d* states, in the Ni-rich d-QC are not so much different from those in the Co-rich one. In particular, a double peak feature predicted as a bonding and anti-bonding bands of the Ni-Ni pair in the Ni-rich d-QC by the electronic structure calculation for a model cluster (shown in the bottom panel of the figure) [3], is not recognized in the Ni $L\alpha$ XES spectrum. This is partly due to the emphasized Ni-Ni pairs in the model calculation and suggests the predominance of Ni-Al pairs or a strong Ni-Al interaction. This might also imply that the d-QC form as a TM atom is surrounded by Al atoms.

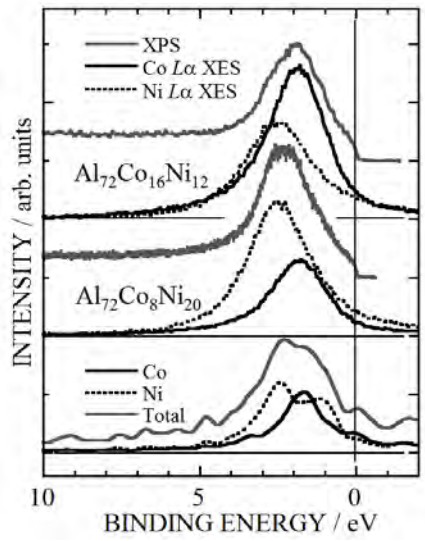

Fig. 1: XES and XPS spectra of Al-Co-Ni quasicrystals.

References
[1] S. Ritsch *et al.*, Phil. Mag. A **71** (1995) 671.
[2] S. Hiramatsu and Y. Ishii, J. Phys. Soc. Jpn. **75** (2006) 054602.
[3] K. Soda et al., Phil. Mag. **91** (2010) 2510.

* j45880a@cc.nagoya-u.ac.jp

28A/2010G507

Angle-resolved photoemission study of topological insulator $Bi_{2-x}Sb_xTe_{3-y}Se_y$

T. Arakane[1], T. Sato[2], S. Souma[1], K. Kosaka[2], K. Nakayama[2], M. Komatsu[2], T. Takahashi[1,2,*], Zhi Ren[3], Kouji Segawa[3] and Yoichi Ando[3]

[1]WPI Research Center, Advanced Institute for Materials Research, Tohoku University, Sendai 980-8577, Japan

[2]Department of Physics, Tohoku University, Sendai 980-8578, Japan

[3]Institute of Scientific and Industrial Research, Osaka University, Ibaraki, Osaka 567-0047, Japan

1 Introduction

The three-dimensional topological insulator is a novel quantum state of matter where the insulating bulk hosts gapless topological surface states (SS) characterized by the Dirac-cone energy dispersion [1]. The realization of topological-insulator devices to utilize the peculiar surface-transport properties requires a highly insulating bulk property and the tunability of Dirac carriers. To achieve the latter, it is desirable to control the energy position of the Dirac cone in the band gap, because the chemical potential of bulk insulators is difficult to tune [2]. Here we show that the tetradymite solid-solution $Bi_{2-x}Sb_xTe_{3-y}Se_y$ is the first topological-insulator system that simultaneously satisfies the above requirements, by directly measuring the electronic structure with angle-resolved photoemission spectroscopy [3]. Upon increasing the Sb content x with tuning the Se content y so as to maintain the bulk-insulating nature, we observed that the chemical potential is always located in the bulk gap and the surface Dirac point, which separates the hole- and electron-like regimes and is buried in the bulk band in Bi_2Te_2Se (x = 0; y = 1), starts to be isolated from the bulk band above $x \sim 0.25$. Furthermore, a sign change of the Dirac carriers was observed at $x \sim 0.9$. Such a tunable Dirac cone in the bulk-insulating platform opens a promising pathway to the development of novel topological-insulator devices.

2 Experiments

High-quality single crystals of $Bi_{2-x}Sb_xTe_{3-y}Se_y$ were grown by melting high purity elements with the stoichiometric ratio at 850□ in an evacuated quartz tube, followed by gradual cooling and annealing [2]. ARPES measurements were performed with a VG-Scienta SES2002 electron analyzer with a tunable synchrotron light at the beamline BL28A at Photon Factory (KEK). We used circularly polarized light of 36-116 eV. The energy and angular resolutions were set at 15-30 meV and 0.2°, respectively.

3 Results and Discussion

Figure 1 shows comparison of the Fermi surface and the near-E_F band structure for different compositions in the bulk insulating phase. The bulk insulating nature is confirmed by the present ARPES result (Fig. 1) showing that only the SS is seen at E_F for all the samples. Interestingly, the SS Fermi surface systematically shrinks upon increasing x (Fig. 1a) accompanied with an overall upward shift of the SS (Fig. 1b), demonstrating that the increase of x (and the simultaneous increase of y) provides more acceptors likely because of the slight change in the carrier compensation. We find that the Dirac band is systematically shifted in a rigid-band manner as a function of x, since the bands for different x values essentially overlap with each other when they are plotted with respect to the Dirac-point energy (E_{DP}) despite the total chemical potential (μ) shift of as large as 0.3 eV. Intriguingly, the SS band dispersion below E_F for x = 1.0 suggests that the Dirac point is located slightly above E_F, pointing to the sign change of Dirac carriers from n- to p-type at some x between 0.5 and 1.0. Another important indication in Fig. 1 is that the bulk VB does not show a rigid-band shift relative to the SS, as evident from the experimental result that the lower hole-like branch of the Dirac cone for x = 1.0 is more clearly visible than in x = 0. The present result provides an important step to establish the means to control of surface Dirac fermions in TIs and to explore a variety of exotic physical properties proposed for this exciting class of materials.

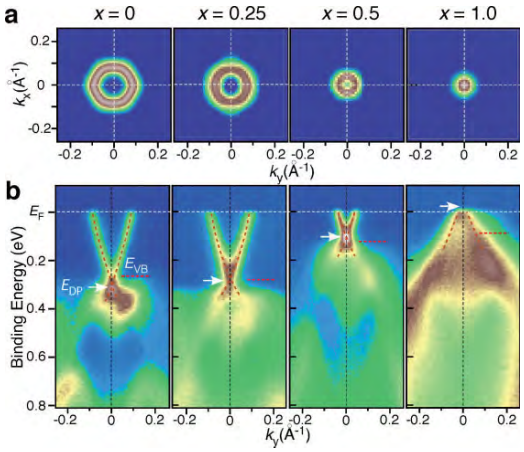

Fig. 1: (a) Fermi surface and (b) band structure of $Bi_{2-x}Sb_xTe_{3-y}Se_y$ for various compositions.

References

[1] M. Z. Hasan and C. L. Kane, Rev. Mod. Phys. **82** (2010) 3045.

[2] Z. Ren *et al.*, Phys. Rev. B **84** (2011) 165311.

[3] T. Arakane *et al.*, Nat. Commun. **3** (2012) 636.

* t.takahashi@arpes.phys.tohoku.ac.jp

3C/2010G544

Twin-to-single crystal transformation in $La_{1-x}Sr_xCoO_3$ by magnetic fields

Tôru KYÔMEN*, Minoru HANAYA, Masahiro Naito, Kenta Hiiragi, Kosuke SUZUKI and Masahisa ITO
Graduate School of Engineering, Gunma University, Kiryu, Gunma 376-8515, Japan

Introduction

Electronic and spin states of a metallic ferromagnet $La_{1-x}Sr_xCoO_3$ have attracted many researchers since suggestion of intermediate-spin state [1]. However, difficulty of the single crystal preparation disturbs the progress in the research of the compounds.

$La_{1-x}Sr_xCoO_3$ ($0 \leq x \leq 0.7$) crystals have a cubic perovskite-type structure at high temperatures and transform to a rhombohedral structure by contraction in a [111] direction of the cubic unit cell at a low temperature. There are thus four variants in the rhombohedral phase. In actual, any crystal we have grown was not a single crystal but a twin crystal [2].

In our previous studies [3], we have observed that the variants of $La_{1-x}Sr_xCoO_3$ twin crystal were reoriented by magnetic fields and suggested the origin is strong magnetocrystalline anisotropy with a plane of easy magnetization. In the present study, we tried and succeeded to change a $La_{0.57}Sr_{0.44}CoO_{3.01}$ twin crystal a single crystal by applying magnetic fields.

Experimental

$La_{0.57}Sr_{0.44}CoO_{3.01}$ twin crystals were grown by a flux method [2]. The Curie temperature was about 240 K. 100 Laue spot was measured at 60 K in order to investigate the change in the twin structure by magnetic fields. The *c* axis of one variant (variant 1) was aligned to the vertical line and the *ab* plane was set parallel to the horizontal plane. An imaging plate was set for the normal line to be perpendicular to the incident X-ray direction.

Results and Discussion

Figure 1(a) shows 100 (indexed by hexagonal setting of rhombohedral lattice) Laue spot of a $La_{0.57}Sr_{0.44}CoO_{3.01}$ twin crystal measured at 60 K before applying magnetic fields. Because of the twin structure, the 100 Laue spot split into a few spots. After this measurement, 20 kOe magnetic field was applied along a direction parallel to the *ab* plane (plane of easy magnetization) of variant 1 and the crystal was rotated by 120° about the *c* axis under the fields. During the rotation, the magnetic field was always parallel to the plane of easy magnetization. Then, the magnetic field was changed to zero, and 100 Laue spot was measured again as shown in Fig. 1(b). It is found that the splitting disappeared.

The result was understood as follows. There are four variants in the crystal. The variant 1 has the lowest magnetic energy among the four variants when the magnetic field was applied parallel to the plane of easy magnetization. The other variants have higher energy. The energy of the other variants changes by rotating the crystal about the *c* axis of variant 1. The variants would transform to variant 1 when the magnetic energy is highest.

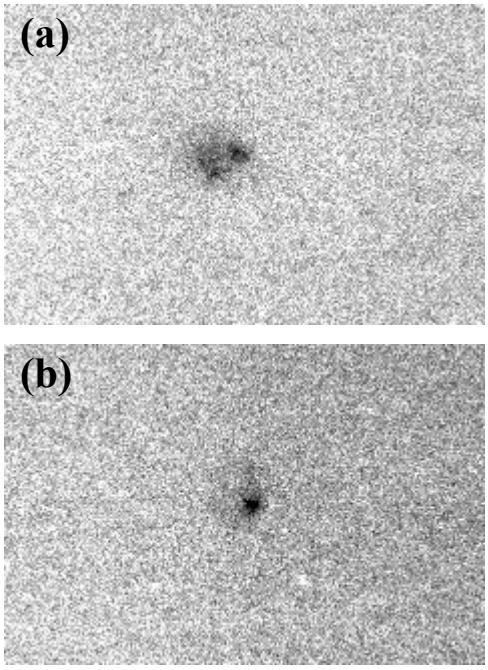

Figure 1 100 Laue spot before (a) and after (b) applying magnetic fields parallel to an easy-plane of magnetization of a $La_{0.57}Sr_{0.44}CoO_{3.01}$ twin crystal.

Conclusions

It was succeeded to change a $La_{0.57}Sr_{0.44}CoO_{3.01}$ twin crystal a single crystal by applying magnetic fields along all directions parallel to an easy-plane of magnetization.

References

[1] M. A. Senaris-Rodriguez et al., J. Solid State Chem. **118**, 323 (1995).
[2] T. Kyômen et al., Chem. Mater. **20**, 5114 (2008).
[3] 2008G560; T. Kyômen et al., Phys. Rev. B **82**, 64402 (2010).

*tkyomen@ gunma-u.ac.jp

28A/2010G655, 2008G688

Electronic Structure of Delaffosite Oxides $CuCr_{1-x}Mg_xO_2$

Takumi Yokobori,[1] Mario Okawa,[1] Kouta Konishi,[1] Ryota Takei,[1] Kazuya Katayama,[1] Satoshi Oozono,[2] Takashi Shinmura,[2] Tetsuji Okuda,[2] Kanta Ono,[3] Noriaki Hamada,[4] and Tomohiko Saitoh[1,*]

[1]Department of Applied Physics, Tokyo University of Science, Shinjuku, Tokyo 162-8601, Japan
[2]Department of Electrical and Electronics Engineering, Kagoshima University, Korimoto, Kagoshima 890-0065, Japan
[3]Photon Factory, Tsukuba, Ibaraki 305-0801, Japan
[4]Department of Physics, Tokyo University of Science, Chiba 278-8510, Japan

1 Introduction

Delaffosite oxides $CuMO_2$ (M = metal element) have various interesting physical properties both in fundamental and applicational terms; $CuAlO_2$ is the first p-type transparent oxide semiconductor [1], for example, and $CuFeO_2$ is a typical multiferroic compound [2]. The delaffosite oxides have also considerable potential for thermoelectric materials [3] because of its layered structure of edge-shared MO_6 octahedrons, which is the same as thermoelectric $NaCoO_2$ [4]. Hole-doped $CuCr_{1-x}Mg_xO_2$ is one of such candidates; in $CuCrO_2$, $3d^3$ electrons of the Cr^{3+} ions under the O_h local symmetry fill up the narrow Cr 3d t_{2g} band and thus steep density of states (DOS) at the Fermi level (E_F) may be realized near the t_{2g} band edge in the hole-doped system $CuCr_{1-x}Mg_xO_2$ with one of the highest conductivity among delaffosite oxides [3]. In this paper, we briefly report our research on the valence-band electronic structure of this system.

2 Experiment

Polycrystalline samples of $CuCr_{1-x}Mg_xO_2$ (x=0, 0.02, 0.03) were prepared by the standard solid-state reaction [3]. Photoemission measurements were performed at BL-28A of Photon Factory in KEK. The samples were fractured *in situ* in the main chamber right before measurements in ultrahigh vaccum (better than 1.2×10^{-7} Pa) at 300 K. The intensity of the spectra was normalized using photon current of the exit mirror. The energy resolution of about 30 meV and the E_F location were both determined by Gold Fermi edge.

3 Results and Discussion

Figure 1 shows the valence-band spectra of the x=0.02 sample taken with the photon energies around the Cr 3p-3d (Panel (a)) and the Cu 3p-3d (Panel (b)) resonance energies. The intensity of the near-E_F leading structures (the 1.4-eV shoulder and the 2.3-eV peak) systematically changes with increasing photon energy, as displayed in Fig. 1 (c) and (d). In Panel (c), the 1.4-eV shoulder shows a clear resonance-type behavior with the maximum at 50.0 eV, the Cr 3p-3d resonance energy, whereas the 2.3-eV peak shows a typical weak anti-resonance-type behavior with a dip at the Cu 3p-3d resonance energy of

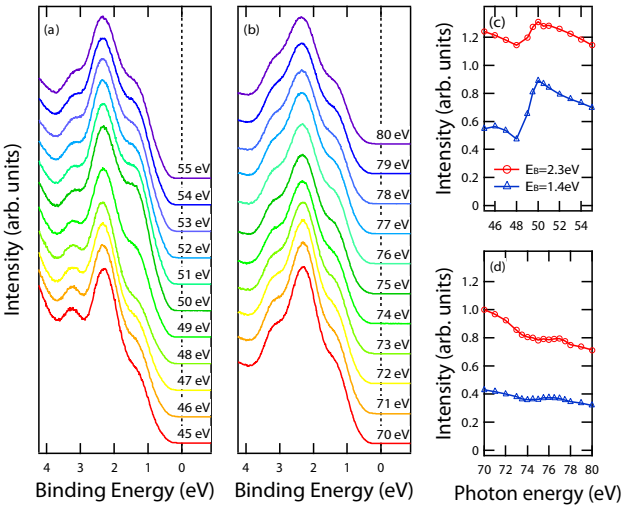

Fig. 1: Valence-band spectra of $CuCr_{0.98}Mg_{0.02}O_2$ taken with the photon energy around (a) the Cr 3p-3d resonance region and (b) the Cu 3p-3d resonance region. (c) and (d) show CIS spectra of the 1.4-eV and 2.3-eV structures.

74.0 eV in Panel (d). Therefore, the Cr 3d character is dominant in the 1.4-eV shoulder and the Cu 3d character is dominant in the 2.3-eV peak. However, one can also notice that a weak resonance of the 2.3-eV peak exists at 50.0 eV and a tiny anti resonance of the 1.4 eV at 74.0 eV does. This is demonstrating that there exists sizeable hybridization between the Cr 3d and Cu 3d states via O 2p states. Although the obtained energy diagram is somewhat different from previous works [5,6], it is in agreement with another previous work [7] and our band-structure calculations. It is also reasonable in terms of the difference between the O 2p-to-Cr 3d charge-transfer energy and the O 2p-to-Cu 3d charge-transfer energy [8].

Acknowledgement

We would like to thank Prof. T. Mizokawa for useful discussions.

References
[1] H. Kawazoe, M. Yasukawa, H. Hyodo, M. Kurita, H. Yanagi, and H. Hosono, Nature **389** (1997) 939.
[2] T. Kimura, J. C. Lashley, and A. P. Ramirez, Phys. Rev. B **73** (2006) 220401(R).
[3] T. Okuda, N. Jufuku, S. Hidaka, and N. Terada, Phys. Rev. B **72** (2005) 144403.
[4] I. Terasaki, Y. Sasago, and K. Uchinokura, Phys. Rev. B **56** (1997) R12685.
[5] H. Hiraga, T. Makino, T. Fukumura, H. Weng, and M. Kawasaki, Phys. Rev. B **84** (2011) 041411(R).
[6] T. Arnold, D. J. Payne, A. Bourlange, J. P. Hu, R. G. Egdell, L. F. J. Piper, L. Colakerol, A. De Masi, P.-A. Glans, T. Learmonth, K. E. Smith, J. Guo, D. O. Scanlon, A. Walsh, B. J. Morgan, and G. W. Watson, Phys. Rev. B **79** (2009) 075102.
[7] A. Maignan, C. Martin, R. Fresard, V. Evert, E. Guilmeau, S. Hebert, M. Poienar, and D. Pelloquin, Solid State Commun. **149** (2009) 962.
[8] H. Iwasawa, K. Yamakawa, T. Saitoh, J. Inaba, T. Katsufuji, M. Higashiguchi, K. Shimada, H. Namatame, and M. Taniguchi, Phys. Rev. Lett. **96** (2006) 067203.

* t-saitoh@rs.kagu.tus.ac.jp

3A/2010G678, 2011G062

Soft and hard x-ray diffraction studies of $DyMnO_3$ thin films

Hiroki Wadati[1,*], Valerio Scagnoli[2], Shih-Wen Huang[2], Urs Staub[2], Takaaki Sudayama[3], Jun Okamoto[3], Yuichi Yamasaki[3], Hironori Nakao[3], Yoichi Murakami[3], Masao Nakamura[4], Masashi Kawasaki[1,4], and Yoshinori Tokura[1,4]

[1]Department of Applied Physics and Quantum-Phase Electronics Center (QPEC), University of Tokyo, Hongo, Tokyo 113-8656, Japan

[2]Swiss Light Source, Paul Scherrer Institut, 5232 Villigen PSI, Switzerland

[3]Photon Factory and Condensed Matter Research Center, Tsukuba, Ibaraki 305-0801, Japan

[4]Cross-Correlated Materilas Reserach Group, RIKEN Advanced Science Institute, Wako 351-0198, Japan

Introduction

Recently, there has been a lot of interest in multiferroic materials displaying both ferroelectric and magnetic orders. Orthorhombic (*o*) RMnO$_3$ (R denotes rare earth metal) with perovskite structure belongs to this category and can be viewed as prototypical multiferroic materials. The fabrication of the *o*-RMnO$_3$ thin films has been especially important for device application of the multiferroic materials. Nakamura *et al*. reported the fabrication of *o*-YMnO$_3$ thin films onto the YAlO$_3$ (010) substrate [1]. By combining soft and hard x-ray diffraction, it was revealed that the magnetic structure of the YMnO$_3$ thin film is the coexistence of the E-type and the cycloidal states [2]. They also succeeded in fabricating *o*-DyMnO$_3$ thin films onto the YAlO$_3$ (010) substrate. In this study we performed soft x-ray diffraction at Mn 2p→3d edges to obtain the information of magnetic ordering and hard x-ray diffraction to investigate lattice distortions in the DyMnO$_3$ thin film. Our results reveal that the ground state of the DyMnO$_3$ thin film is very similar to that of the YMnO$_3$ thin film, that is, the coexistence of the E-type and the cycloidal states.

Experiment

The thin film (40 nm) of DyMnO$_3$ was grown on a YAlO$_3$ (010) substrate by pulsed-laser deposition. Hard x-ray diffraction experiments were performed on beamlines 3A at the Photon Factory, KEK, Japan. The photon energy of the incident x-rays was 12 keV.

Results and Discussion

In order to investigate the lattice distortions associated with magnetic order and electric polarization, we performed hard x-ray diffraction measurements of the DyMnO$_3$ thin film. The commensurate (0 3 0) reflection appears below 35 K as shown in Fig. 1. This reflection is structurally forbidden in the chemical high-temperature structure (Pbnm) and caused by the lattice distortion accompanying ferroelectricity. Interestingly, no incommensurability of this reflection is observed by hard x-ray diffraction, in clear contrast to the observed magnetic reflection. This reflection does appear below 35 K as can be seen from the temperature-dependent integrated intensity shown in Fig. 1(b). This temperature is lower than the onset of the magnetic reflection of 40 K.

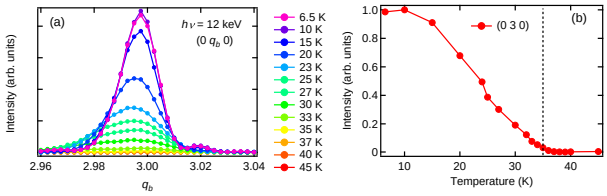

Fig. 1: Temperature dependence of the (0 3 0) peak taken at $h\nu$ = 12 keV. Peak intensities are plotted as a function of temperature in panel (b).

Our results indicate that the magnetic states of the epitaxial DyMnO$_3$ thin film is similar to those of the YMnO$_3$ thin film [2], that is, the coexistence of the E-type and the cycloidal states. In this coexistence region, magnetic reflection is incommensurate and lattice peaks are commensurate because the E-type phase has a much larger lattice distortion than the cycloidal phase. Further studies such as the measurements of electric polarization will be necessary for supporting this scenario.

Acknowledgment

This research is granted by the Japan Society for the Promotion of Science (JSPS) through the “Funding Program for World-Leading Innovative R&D on Science and Technology (FIRST Program),” initiated by the Council for Science and Technology Policy (CSTP).

References

[1] M. Nakamura *et al.*, Appl. Phys. Lett. **98**, 082902 (2011).
[2] H. Wadati *et al.*, Phys. Rev. Lett. **108**, 047203 (2012).

* wadati@ap.t.u-tokyo.ac.jp

7C,15B1/2010G697

Electronic Structure of Anatase (TiO_2) by means of X-ray Raman Scattering.

Yasuhisa Tezuka,[1*] Shota Jin,[1] Ryusuke Oura,[1] Yusuke Sasaki,[1] Shunsuke Nozawa,[2] Toshiaki Iwazumi,[3] Yasuhito Isozumi,[4] Kenichi Ozawa,[5] Masato Emori,[6] and Hiroshi Sasama[6]

[1]Grad. Sch. of Sci. and Tech., Hirosaki Univ., 3 Bunkyo-cho, Hirosaki, 036-8561, Japan
[2]Photon Factory, Inst. of Mats. Struct. Sci., 1-1 Oho, Tsukuba 305-0801, Japan
[3]Grad. Sch. of Eng., Osaka Pref. Univ., Sakai 599-8531, Japan
[4]RI Research Center, Kyoto Univ., Kyoto 606-8501, Japan
[5]Dept. of Chem. and Mats. Sci., Tokyo Inst. of Tech., Ookayama, Tokyo 152-8551, Japan
[6]Dept. of Phys., Sophia Univ., Kioi-cho, Chiyoda-ku, Tokyo 102-8554, Japan

1 Introduction

Titanium dioxide (TiO_2) occurs in nature as three different polymorphs. Other than most common rutile structure, it forms anatase and brookite structures. Among them, anatase shows strong photocatalytic activity. Though the anatase has been studied extensively, the electronic properties are not made clear enough, because TiO_2 is an insulator and thus photoemission, most general method, cannot be applied basically.

We have reported X-ray emission spectra (XES) of some Ti-compounds, which include X-ray Raman scattering (XRS) and fluorescence.[1] The XRS spectra, excited by the photon energy just below the absorption edge, can observe electronic structures of unoccupied state of materials, regardless of its conductivity. In the case of TiO_2, Ti 3*d* state can be observed clearly.

2 Experiment

The XRS and Ti *K* XAS experiments were performed at beamlines BL7C and BL15B1. X-ray emission spectra having an energy centered at the Ti *Kα* fluorescence lines ($K\alpha_1$=4510.84 and $K\alpha_2$=4504.86 eV) were observed. The spectrum changes continuously from *Kα* fluorescence to XRS when the excitation energies are changed from above to below the absorption edge. The fluorescence peaks have constant emission energies, while each XRS peak has each constant loss-energy from the excitation energy (Raman shift). The energy resolution for both the Ti *K* XAS and XRS measurements was about 1 eV for 5 keV photon.

Commercially obtained powder sample (Furuuchi Chemical Co.) and epitaxially grown single crystal were used in this experiment. The single-crystal anatase TiO_2(001) thin films were grown using PLD on $LaAlO_3$(100) and has 500 nm thickness.[2] The crystallinity of the sample was checked by XRD measurement.

3 Results and Discussion

Figure 1 shows XRS spectra of rutile and anatase, excited by same energy (4964.9 eV). Though only the spectra of powder samples are shown in the figure, single crystal anatase showed similar spectrum. Both of the XRS spectra show seven peaks which are originated from excitation including pairs of Ti 2*p* core-hole and excited electron in unoccupied state. The three peaks at high energy correspond to the electrons in Ti 4*p* state, while the four peaks at low energy correspond to those in Ti 3*d* state. The Ti 3*d* peaks consist of two pairs, because of the spin-orbit interaction of Ti 2*p* state (L_{III} and L_{II}), and each pair is split into t_{2g} and e_g by ligand field (in O_h approximation).

As can be seen in the figure, the e_g peaks in anatase are weaker than that of rutile, suggesting that the e_g state in anatase is more occupied. Since the e_g orbital is oriented to O-ions and is hybridized with O 2*p* state, the result means that the hybridized Ti 3*d* electrons in anatase are more localized. On the other hand, the lowest energy peak of Ti 4*p* spectrum of anatase shows lower intensity. Since the peak corresponds to Ti 4*p*<u>*L*</u> state in XAFS spectrum, where <u>*L*</u> denote ligand hole, dynamical charge transfer from ligand oxygen to titanium is weak in anatase. This result is consistent with the localization of Ti 3*d* electron in ground state. Such localization of 3*d* electrons would result high efficient photo-excitation on Ti site under UV irradiation; i.e. high efficient photocatalyst.

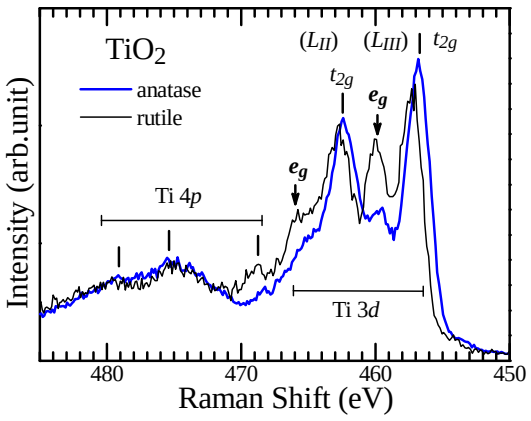

Fig. 1: XRS spectra of TiO_2. Comparison between the spectra of rutile and anatase.

References

[1] Y. Tezuka, et al., Photon Factory Activity Report, #24, 69 (2007); *ibid.* #25, 76 (2008)
[2] M. Emori, M. Sugita, K. Ozawa, and H. Sakama, Phys. Rev. B **85**, 035129 (2012).

* tezuka@cc.hirosaki-u.ac.jp

BL13A/2010G700

リチウム-ニッケル複合酸化物の表面電子状態と選択酸化機能（II）

Surface Electronic Structure and Selective Oxidation of Lithium Nickel Mixed Oxide（II）

宮崎隆文 [1]*, 紋谷祐爾 [2], 近藤 寛 [2], 隅井良平 [3], 間瀬一彦 [3]
[1]愛媛大院・理工　〒790-8577 松山市文京町 3 番
[2]慶応大・理工　〒 223-0061 横浜市港北区日吉 3-14-1
[3]KEK-PF　〒305-0801 つくば市大穂 1-1

1. はじめに

メタンの酸化カップリング（OCM：メタンをエタンやエチレンの C_2 炭化水素へ直接転換）反応に活性を有する Li-Ni 系層状複合酸化物の選択酸化触媒機能の起源を解明するために、OCM 反応進行時における電子状態の変化を調べた。$LiNiO_2$ は 700℃以上で OCM 反応が活性となる。本実験では準大気圧下、600℃以上での in-situ 光電子スペクトル測定を行った。また、Ni の一部を Al に置換した C_2 選択性が低い $Li_{0.9}NiAl_{0.1}O_2$ の電子状態変化と比較した。

2. 実 験

実験は BL13A に付設した AP（Ambient Pressure）-XPS 装置を使用して、in-situ 光電子スペクトルを測定した。最高到達温度 665℃での Li-Ni 系層状複合酸化物 $LiNiO_2$、$Li_{0.7}Ni_{1.3}O_2$、$Li_{0.5}Ni_{1.5}O_2$、$LiNi_{0.95}Al_{0.05}O_2$ について、励起光エネルギー100eV および 650eV における光電子スペクトルを測定した。また、室温～665℃までの加熱を行い、1.5×10^{-2} torr の CH_4 や O_2 のガス雰囲気下での光電子スペクトルの経時変化を測定した。

3. 結果および考察

図 1（a～c）には室温～600℃までの C1s, O1s, Li1s を示している。室温～500℃までの試料表面には水酸化リチウムや炭酸リチウムなどの不純物が残留されているが、600℃以上の加熱処理後には、それらのピークが消失している。それに代わって、600℃以上では結合エネルギー（BE）の異なる Li1s ピークが認められる。また、400 ℃以上の試料表面には 2 種類の O1s が確認でき、600℃以上では高結合エネルギー側の O1s ピークの相対強度が増大している。これらのことから試料表面には[Li-O]種が生成していることが分かる。hv=100eV（表層）と hv=640eV（バルク）の励起光による価電子帯上部の光電子スペクトルには BE=1.5eV 付近の Ni3d、BE=5.3eV と 7.8eV には O2p に帰属され、試料表層には BE の異なる 2 つの酸素種が共存している。図 1(d)には $LiNiO_2$ を 660℃まで加熱したまま、メタンガスを導入開始後から約 40 分間の価電子帯上部の電子構造の経時変化を示している。660℃の $LiNiO_2$ と $Li_{0.9}NiAl_{0.1}O_2$ の UPS を比較すると、$LiNiO_2$ では Ni3d（A:e_g と B:t_{2g}）と O2p（C と D）のピーク強度は同等であるが、$Li_{0.9}NiAl_{0.1}O_2$ では低結合エネルギー側の O2p の相対的なピーク強度が異なる。また、$Li_{0.9}NiAl_{0.1}O_2$ の Ni3d の A と B の BE 間隔は $LiNiO_2$ の場合と異なる。メタン導入直後から $LiNiO_2$ の O2p の強度が減少し、2 つの Ni3d の相対強度比（B/A）が顕著に変化していることが観測された。一方、$Li_{0.9}NiAl_{0.1}O_2$ の経時変化には特徴的な変化は認められなかった。これらの電子構造の変化の違いが選択酸化機能の違いとして反映されていると考えられる。

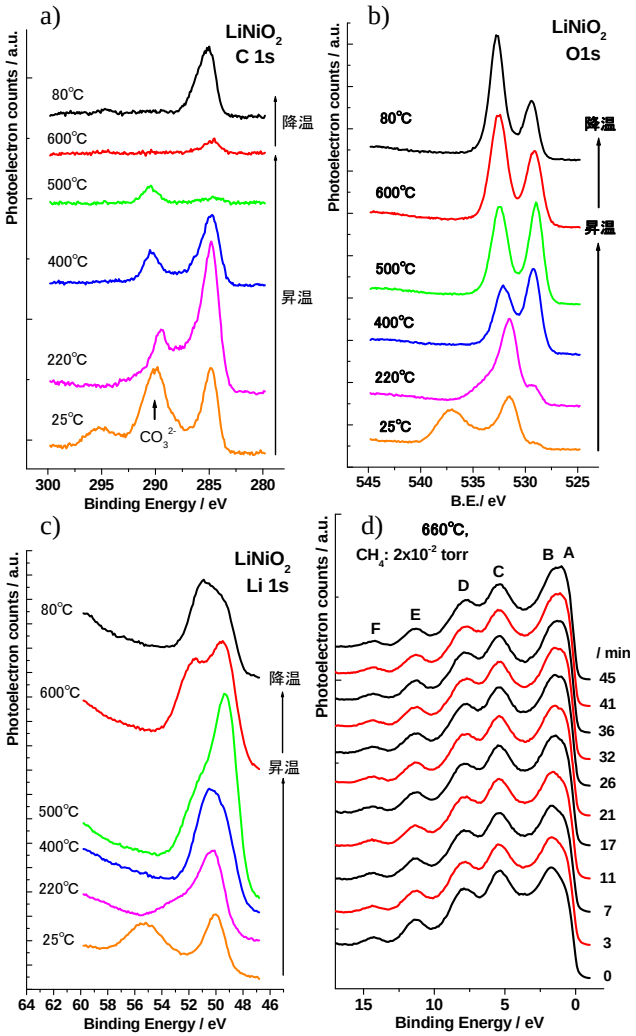

図 1. $LiNiO_2$ の XPS と UPS およびその温度依存性

* miyazaki@eng.ehime-u.ac.jp

SAGA-LS BL10/2010G700

リチウム–ニッケル複合酸化物の表面電子状態と選択酸化機能

Surface Electronic Structure and Selective Oxidation of Lithium Nickel Mixed Oxide

宮崎隆文 [1]*, 吉村大介 [2], 瀬戸山寛之 [2], 隅井良平 [3], 間瀬一彦 [3]

[1] 愛媛大院・理工　〒790-8577 松山市文京町 3 番

[2] 九州シンクロトロン光研究センター　〒841-0005 鳥栖市弥生が丘 8-7

[3] KEK-PF　〒305-0801 つくば市大穂 1-1

1. はじめに

今回、メタン酸化カップリング（OCM）反応に活性をもつ Li-Ni 複合酸化物触媒の選択的な酸化反応機能の解析を目的としている。この反応では触媒上の表面格子酸素がメタンの活性化と生成したメチルラジカルを選択的にカップリングする重要な役割を担っていることが示唆されている。しかし、OCM 反応の選択酸化機構を解明するには酷しい反応条件のために従来の表面解析手法の適用が難しく、その詳細は分かっていない。今回の利用実験では加熱前後のリチウムニッケル複合酸化物 $Li_xNi_{2-x}O_2(0<x\leqq 1.0)$の表面状態を調べるために、紫外光電子スペクトル（UPS）および X 線光電子スペクトル（XPS）を測定して、表面電子構造の基礎データを収集する。

2. 実験

リチウムニッケル複合酸化物 $Li_xNi_{2-x}O_2(0<x\leqq 1.0)$ の表面電子構造の変化を調べるために、図 1 には調製した各試料の XRD パターンを示す。$Li_{0.1}Ni_{1.9}O_2$、$Li_{0.3}Ni_{1.7}O_2$、$Li_{0.5}Ni_{1.5}O_2$ は立方晶、$Li_{0.7}Ni_{1.3}O_2$ と $LiNiO_2$ は六方晶に帰属され、目的物以外の不純物のピークは認められなかった。図 2 には、これらの試料を使った OCM 反応の C_2 選択性の経時変化を示す。$Li_{0.7}Ni_{1.3}O_2$ と $LiNiO_2$ の反応開始直後の C_2 選択性は約 90%であるのに対し、$Li_{0.3}Ni_{1.7}O_2$ と $Li_{0.5}Ni_{1.5}O_2$ は約 40%、$Li_{0.1}Ni_{1.9}O_2$ では OCM 初期活性は確認できなかった。これらの試料の OCM 活性と表面電子構造の相関を見るために紫外光電子スペクトル（UPS）および X 線光電子スペクトル（XPS）を測定した。光電子スペクトルの測定は、九州シンクロトロン BL10 の角度分解光電子分光装置を使用した。予備真空槽にて 600℃と 750℃の加熱処理した後、室温で光電子スペクトルの測定を行った。

3. 結果および考察

立方晶 $Li_{0.3}Ni_{1.7}O_2$ と六方晶 $LiNiO_2$ の UPS および XPS の測定実験を行った。$Li_{0.3}Ni_{1.7}O_2$ と $LiNiO_2$ の 600℃および 750℃に加熱した後の O1s スペクトルを図 3～6 に示す。$Li_{0.3}Ni_{1.7}O_2$ の場合、O1s ピークは 1 本しか見られず、加熱前後でも O1s の結合エネルギーはほとんど変化していない。一方、$LiNiO_2$ では 2 本の O1s ピークが認められ、加熱処理により $LiNiO_2$ の場合には O1s ピークが高結合エネルギー側にシフトしている。また、750℃の加熱後の試料では、高エネルギー側のピークの相対強度が増大しており、O1s ピークの相対強度比が変化している事がわかる。750℃加熱後の $Li_{0.3}Ni_{1.7}O_2$ と $LiNiO_2$ の試料の Li1s スペクトルを比べると、$Li_{0.3}Ni_{1.7}O_2$ の Li1s は明瞭に観測されなかったが、$LiNiO_2$ では 65eV のショルダーを伴った強いピークとして観測された。OCM 反応に対する低い選択性の立方晶 $Li_{0.3}Ni_{1.7}O_2$ では、完全酸化反応に寄与する低結合エネルギーの酸素種がメタン分子の酸化過程に関与している。一方、OCM 反応に対する高い選択性のある六方晶 $LiNiO_2$ では、完全酸化反応に寄与する低結合エネルギーの酸素種は認められるが、より高結合エネルギーの酸素種が触媒表面に出現しており、この酸素種が OCM 反応に深く関わっていると推察される。

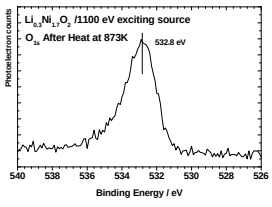

図3. $Li_{0.3}Ni_{1.7}O_2$のO1s (600℃処理)

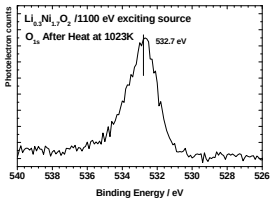

図4. $Li_{0.3}Ni_{1.7}O_2$のO1s (750℃処理)

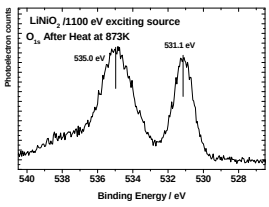

図5. $LiNiO_2$のO1s (600℃処理)

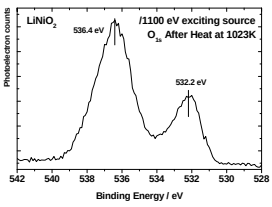

図6. $LiNiO_2$のO1s (750℃処理)

[謝辞]

この実験を実施するに当たり、九州シンクロトロン光研究センターのスタッフの皆様にはマシンタイム調整、受入準備、実験サポートなど、大変お世話になりました。心より御礼申し上げます。

* miyazaki@eng.ehime-u.ac.jp

16A2/2010S2-001, 2010G187; SPring-8 BL23SU/2011A3840

Thickness dependent metal-insulator transition in ferromagnetic $La_{0.6}Sr_{0.4}MnO_3$ thin films studied by x-ray magnetic circular dichroism

Goro SHIBATA[*1], Keisuke ISHIGAMI[2], Vijay Raj SINGH[1], Virendra Kumar VERMA[1], Takayuki HARANO[1], Toshiharu KADONO[1], Atsushi FUJIMORI[1, 2, 3], Tsuneharu KOIDE[4], Yukiharu TAKEDA[3], Tetsuo OKANE[3], Yuji SAITOH[3], Hiroshi YAMAGAMI[3, 5], Akihito SAWA[6], Kohei YOSHIMATSU[1, 7], Enju SAKAI[4, 7], Hiroshi KUMIGASHIRA[4, 7], and Masaharu OSHIMA[7]

[1]Department of Physics, University of Tokyo, Bunkyo-ku, Tokyo 113-0033, Japan
[2]Department of Complexity Science and Engineering, University of Tokyo, Bunkyo-ku, Tokyo 113-0033, Japan
[3]Condensed Matter Science Division, Japan Atomic Energy Agency, Sayo-cho, Sayo-gun, Hyogo 679-5148, Japan
[4]Photon Factory, Institute of Materials Structure Science, High Energy Accelerator Research Organization (KEK), Tsukuba, Ibaraki 305-0801, Japan
[5]Department of Physics, Faculty of Science, Kyoto Sangyo University, Kyoto 603-8555, Japan
[6]Nanoelectronic Research Institute, National Institute of Advanced Industrial Science and Technology (AIST), Tsukuba, Ibaraki 305-8562, Japan
[7]Department of Applied Chemistry, University of Tokyo, Bunkyo-ku, Tokyo 113-0033, Japan

Introduction

Perovskite-type transition-metal oxides (TMO) have been widely investigated due to their variety of physical properties. Recently, the physical properties of TMO ultrathin films have been intensively studied. A number of studies have shown that metal-insulator transitions (MITs) are widely observed in TMO thin films as a function of film thickness [1-5]. $La_{0.6}Sr_{0.4}MnO_3$ (LSMO) is a ferromagnetic metal which shows half metallicity. It has been found that the metallicity and ferromagnetism are lost below a critical thickness around 6-8 ML [1, 2]. We have performed x-ray absorption spectroscopy (XAS) and x-ray magnetic circular dichroism (XMCD) measurements of the LSMO thin films grown on $SrTiO_3$ (STO) substrates to clarify the microscopic electronic and magnetic states of the LSMO ultrathin films across the thickness-dependent MIT.

Experimental condition

LSMO thin films with thicknesses ranging from 2 to 15 monolayer (ML) were grown on STO substrates by the laser molecular beam epitaxy. The films were capped with 1 ML of $La_{0.6}Sr_{0.4}TiO_3$ (LSTO) and 2 ML of STO. The LSTO layer was deposited to avoid excess hole doping into the topmost MnO_2 plane of LSMO [1]. After deposition, the samples were annealed in an O_2 atmosphere of 1 atm for 45 minutes to remove oxygen deficiencies. This procedure was repeated several hours before the measurements. Detailed sample growth conditions and characterizations are described in Ref. 1.

The XAS and XMCD spectra were taken at BL-16A2 at Photon Factory (PF) and BL23SU at Spring-8 in the total electron yield (TEY) mode. The magnetic field was applied perpendicular to the sample surface.

Results and discussion

Figure 1 shows the Mn 2*p*-3*d* XAS and XMCD spectra of LSMO films with various thicknesses. As shown in Fig. 1(b), the XMCD intensity decreases as the film thickness decreases, reflecting the loss of magnetization observed below the critical thickness [1, 2]. In the XAS spectra [Fig. 1(a)], with decreasing LSMO thickness, the intensities of shoulder structures a and d increase and peaks c and e are shifted towards lower photon energies. The reference spectra in Refs. 6 and 7 show that structures a and d originate from the Mn^{3+} and that peaks

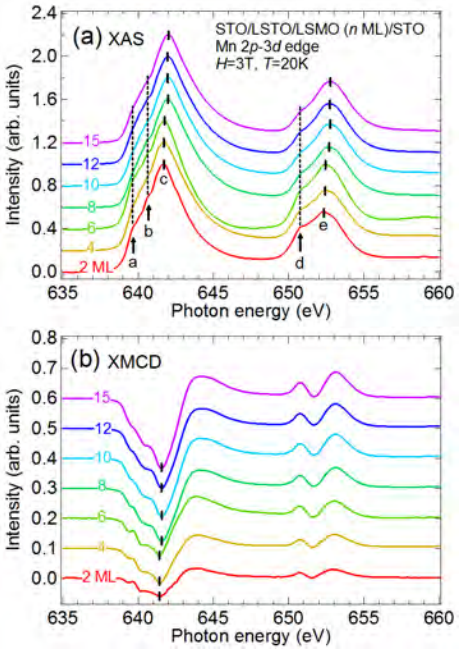

Fig. 1: Mn 2*p*-3*d* XAS (a) and XMCD (b) spectra for various LSMO thicknesses.

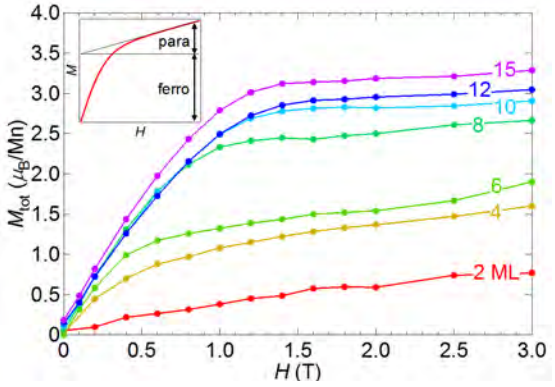

Fig. 2: Magnetic-field (H) dependence of the total magnetic moment (M_{tot}) of Mn estimated from the XMCD sum rules [8, 9]. M_{tot} is defined as the sum of the spin (M_{spin}) and orbital (M_{orb}) magnetic moments. Inset shows the definition of the ferromagnetic and paramagnetic components.

c and e are located at lower photon energies for Mn^{3+} than Mn^{4+}. The present results indicate that the valence of the Mn ions is shifted from Mn^{4+} to Mn^{3+} as the LSMO thickness is decreased. Similar peak shifts are also observed in the XMCD spectra in Fig. 1(b).

Using XMCD sum rules [8, 9], we have estimated the spin and orbital magnetic moments of Mn ions. The orbital magnetic moment M_{orb} was found to be negligibly small compared to the spin magnetic moment M_{spin} ($M_{orb}/M_{spin} \sim 0.01$). In Fig. 2 we show the magnetic field (H) dependence of the total magnetic moment M_{tot}. We have decomposed the M_{tot}-H curves into two components: the ferromagnetic component which saturates around $H \sim 1.5$ T and the paramagnetic component which increases linearly with H up to higher magnetic fields. We have estimated the saturation magnetization and the paramagnetic susceptibility, defined as the intercept and the slope of the M_{tot}-H curves at higher magnetic fields, respectively, and plotted them in Fig. 3 as functions of the LSMO thickness. It can be clearly seen that the ferromagnetic component gradually decreases and the paramagnetic component increases.

In order to test the validity of the 'dead layer' model [1], we have simulated the expected intensity of the ferromagnetic component for a model depicted in the inset of Fig. 3(a). In this model, one assumes that at the LSMO/STO interfaces there are layers with thickness $d \sim$ 4ML (half of the critical thickness) where ferromagnetism is lost. The result of the simulation is shown in Fig. 3(a). The observed ferromagnetic component is quite larger than the simulation. Even if we varied the thicknesses of the top and bottom dead layers independently, we could not reproduce the experimental ferromagnetic moment. This suggests that the loss of ferromagnetism in ultrathin LSMO films cannot be explained by the dead layer model. Alternatively the ferromagnetism may be rather uniformly lost in the entire film.

We have also simulated the paramagnetic susceptibility assuming that all the Mn ions which do not participate in

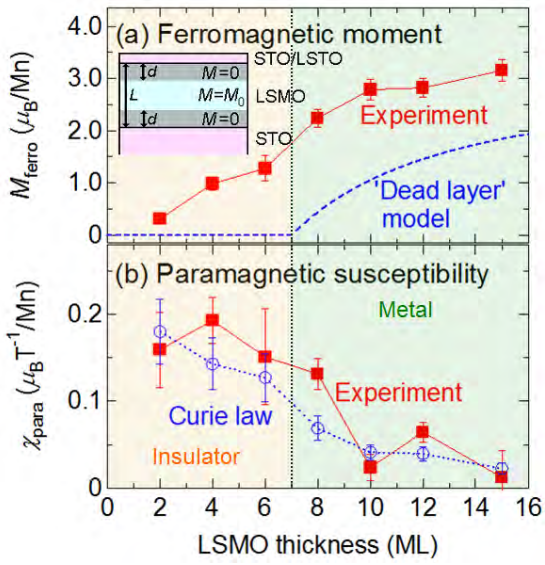

Fig. 3: Thickness dependence of the magnetic properties of the LSMO thin films. (a) Ferromagnetic moment of the experiment (red solid curve) and the simulation (blue dotted curve). Inset shows the 'dead layer' model used for the simulation. (b) Paramagnetic susceptibility estimated from the experiment (red solid curve) and the simulation (blue dotted curve).

the ferromagnetism are in the paramagnetic state of Curie-type. The result of the simulation is shown in Fig. 3(b). The experimental susceptibility is comparable to the simulation at 2 ML and above 10 ML, or slightly larger between 4 ML and 8 ML. This indicates that the magnetic state of the Mn ions can be explained as a mixture of the ferromagnetic insulating (FM-I) phase and the Curie-Weiss-type paramagnetic insulating phase with small Curie temperature (that is, there is weak ferromagnetic spin correlation between the paramagnetic Mn ions). According to the bulk phase diagram of $La_{1-x}Sr_xMnO_3$ [10], a FM-I phase appears around $0.1<x<0.15$. The emergence of the FM-I phase may be related to the valence shift towards Mn^{3+} inferred from the XAS spectra.

References

[1] K. Yoshimatsu *et al.*, Appl. Phys. Lett. **94**, 071901 (2009).
[2] X. Hong *et al.*, Appl. Phys. Lett. **86**, 142501 (2005).
[3] D. Toyota *et al.*, Appl. Phys. Lett. **87**, 162508 (2005).
[4] J. Xia *et al.*, Phys. Rev. B **79**, 140407 (2009).
[5] K. Yoshimatsu *et al.*, Phys. Rev. Lett. **104**, 147601 (2010).
[6] T. Burnus *et al.*, Phys. Rev. B **77**, 125124 (2008).
[7] R. K. Sahu *et al.* Phys. Rev. B **66**, 144415 (2002).
[8] P. Carra *et al.*, Phys. Rev. Lett. **70**, 694 (1993).
[9] B. T. Thole *et al.*, Phys. Rev. Lett. **68**, 1943 (1992).
[10] A. Urushibara *et al.*, Phys. Rev. B **51**, 14103 (1995).
* shibata@wyvern.phys.s.u-tokyo.ac.jp

18A, 19A/2011G084

Thickness dependence of electronic band structures of Ni ultrathin films on Cu(001)

Sunghun Kim[1,*], Koichiro Yaji[1,**], Yasuo Takeichi[1], Ayumi Harasawa[1], and Akito Kakizaki[1]
[1]*Institute for Solid State Physics, University of Tokyo, Kashiwa, 277-8581, Japan*

1 Introduction

Ultrathin nickel (Ni) film on Cu(001) single crystal is one of the most famous systems which represents peculiar magnetic property as perpendicular magnetic anisotropy (PMA). The Ni films show PMA in a thickness range between 10 and 40 atomic monolayers (ML), while the easy axis of magnetization becomes the in-plane direction with respect to the film surface below and above this range [1, 2]. We note that not only the magnetic property but also the electronic structures of Ni/Cu(001) should be investigated in order to clarify the physical origin of the magnetic anisotropy transition (MAT). Former theoretical studies show that the electronic structure of Ni single layer is very different from that of bulk Ni [3, 4]. On the other hand, three-dimensional like Fermi surface was reported at 1.2 ML of Ni/Cu(001) [5]. Also different result at a single monolayer has been traced by using angle-resolved photoelectron spectroscopy (ARPES) [6]. This motivates to clarify thickness dependence of electronic structure near the Fermi level, furthermore to find the evidence for MAT on Ni/Cu(001).

2 Experiment

A disk-shaped (t = 1 mm) Cu single crystal with [001] direction normal to the surface has been used for growing the Ni films. The mechanically and electrochemically polished Cu(001) substrate was cleaned by several cycles of Ar^+ ion sputtering at 1 keV and annealing up to 830 K for 10 minutes in ultra-high vacuum (UHV) chamber. The clean surface of Cu(001) was checked by low-energy electron diffraction (LEED), Auger electron spectroscopy (AES) and ARPES. Ni was deposited on Cu(001) *in situ* at room temperature. The pressure in the UHV chamber was kept below 8×10^{-10} mbar during the deposition. The thickness of the film was controlled by observing the intensity oscillation of reflection high-energy electron diffraction (RHEED) as shown in Fig. 1. The ARPES spectra were measured with a hemispherical electron energy analyzer (VG SCIENTA SES-100) and synchrotron radiation provided at the BL-18A in Photon Factory. Sample temperature was set to 60 K during the ARPES measurements.

3 Results and Discussion

Figure 2(a) shows photoelectron spectra of each Ni film taken with normal emission. Ni *d*-states are appeared around 0.8 eV on 2.5 ML-Ni film. These states clearly split into two with increasing the thickness, where the peak positions are marked with A and B. The peak positions of A and B were plotted as a function of film thickness as shown in Fig. 2(b). Binding energy shift can be found with increasing the thickness up to 7 ML. This behavior agrees the result reported by Pampuch *et al*. [6].

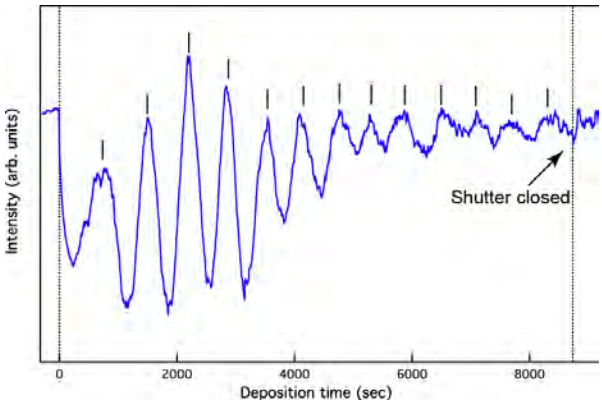

Fig. 1: RHEED intensity oscillation with Ni deposition.

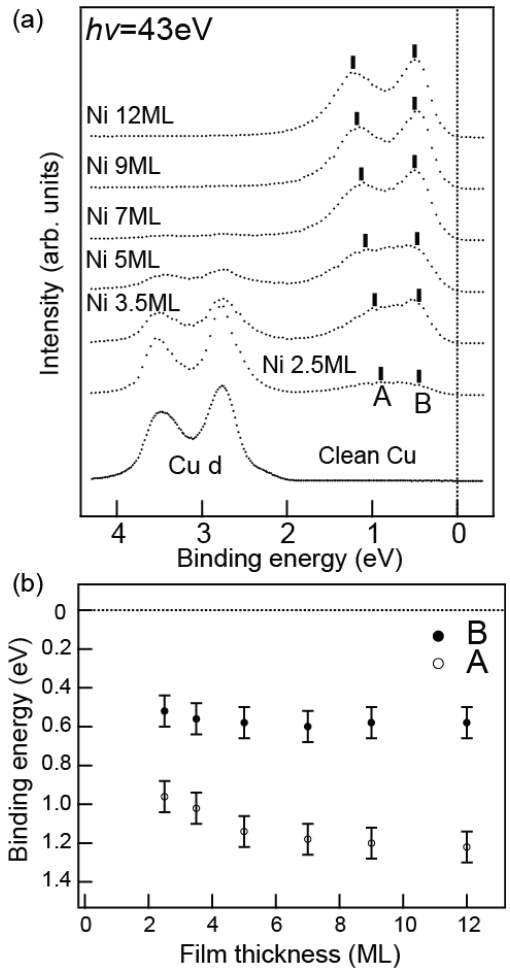

Fig. 2: (a) Photoelectron spectra in normal emission. (b) Peak positions of A and B as a function of thickness.

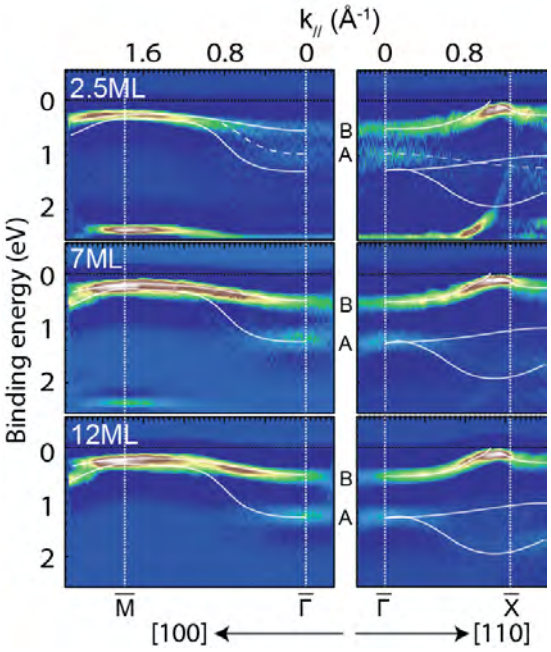

Fig. 3: In-plane band structure of 2.5, 7 and 12 ML Ni/Cu(001)

Figure 3 shows the band structures of 2.5, 7 and 12 ML Ni/Cu(001) taken with the in-plane directions i.e. Γ-M and Γ-X. White solid curves represent the typical band structures of 12 ML Ni, and dashed curves follow that of 2.5 ML Ni, for guides to see. It is found that the shape of the upper band, named B, for 2.5 ML is similar to those for 7 and 12 ML. On the other hand, the shape of the lower band (A) for 2.5 ML is obviously different from those of the other two films along both Γ-M and Γ-X. The band structure of 7 ML Ni is similar to that of 12 ML Ni that exhibits the bulk-like band structure. Note that the 7ML- and 12 ML-Ni show the in-plane magnetic anisotropy and PMA, respectively. However we found no critical change of the band structures.

It is generally known that the PMA appears with decreasing the thickness of films, in which magneto-elastic anisotropy caused by lattice mismatch is considered for the reason. However, the Ni/Cu(001) system shows again the in-plane magnetic anisotropy with decreasing the thickness (less than 6~8 ML-Ni). Although the present results show no direct hints for MAT in this system, magneto-crystalline anisotropy is still convincing for the reason that causes MAT, because this is a direct consequence of spin-orbit coupling reflecting electronic structure.

In summary, we have investigated the band structures of Ni/Cu(001) ultrathin films by ARPES. We found the thickness dependence of the band structures between the 2.5 ML- and 7 ML. On the other hand, no difference of the band structures was found at the critical thickness of MAT. In the future, we would investigate the spin-dependent band structures of Ni/Cu(001) in order to clarify the physical origin of MAT, where spin- and angle-resolved photoelectron spectroscopy can be good technique.

Acknowledgement

This work was supported by KEK-PF (Proposal No. 2011G084).

References

[1] W. L. O'Brien and B. P. Tonner, Phys. Rev. B **49** (1994) 15370.
[2] B. Schulz and K. Baberschke, Phys. Rev. B **50** (1994) 13467
[3] D. –S. Wang, A. J. Freeman and H. Krakauer, Phys. Rev. B **24** (1981) 1126.
[4] J. Tersoff and L. M. Falicov, Phys. Rev. B **26** (1982) 6186.
[5] G. J. Mankey *et al*., Phys. Rev. Lett. **78** (1997) 1146.
[6] C. Pampuch *et al*., Phys. Rev. B **63** (2001) 153409.

* kimsh@issp.u-tokyo.ac.jp
** yaji@issp.u-tokyo.ac.jp

18A, 19A/2011G085

Giant Rashba spin splitting of monolayer Pb adsorbed Ge(111) surface

Koichiro Yaji[*1,2], Akito Kakizaki[1], and Tetsuya Aruga[2,3]
[1]*Institute for Solid State Physics, University of Tokyo, Kashiwashi, Chiba 277-8581, Japan.*
[2]*JST CREST, Saitama 332-0012, Japan.*
[3]*Graduate School of Science, Kyoto University, Kyoto, 606-8502, Japan.*

Introduction

Rashba spin splitting of a surface state band on a semiconductor surface allows us to open a novel physics such as a spin transport at the surface. The Rashba spin-split bands on the semiconductor surfaces have been identified on Si(111) and Ge(111) surfaces so far [1-4]. Among them, monolayer lead (Pb) adsorbed Ge(111) surface (Pb/Ge(111)-β) is remarkable because one of the surface state bands crosses Fermi level with the Rashba spin splitting. In the present study, we report on the giant Rashba spin-split band of Pb/Ge(111)-β studied by spin- and angle-resolved photoelectron spectroscopy (SARPES).

Experiment

Experiments were performed at KEK-PF BL18A and 19A. A Ge(111) substrate was prepared by several cycles of Ar^+ bombardment with 0.5 kV and annealing up to 900 K for a few seconds. Pb was deposited onto the surface at room temperature, which was then annealed at 570 K for three minutes to prepare a well-ordered wide terrace of Pb/Ge(111)-($\sqrt{3}\times\sqrt{3}$)*R*30°.

Results and discussion

Figure (b) shows the ARPES image taken along $\bar{\Gamma}\bar{M}\bar{\Gamma}$ of ($\sqrt{3}\times\sqrt{3}$)*R*30° surface Brillouin zone (SBZ) shown in Fig. (a). We found three Pb-induced bands named S_1, S_2 and S_3. The spin structures were investigated by SARPES. Hereafter, we focus on the S_2 band. First, it is found that the spin-up and spin-down branches of S_2 are degenerate at the $\bar{M}$ point. Also, the peaks of S_2 show clear energy splitting and the peak positions of the spin-up and spin-down branches are inverted around $\bar{M}$. We therefore concluded that the S_2 band splits into two due to the surface Rashba effect. The Rashba parameter is roughly evaluated to be 1.9 eV Å, which is comparable with the other giant Rashba systems [1-3].

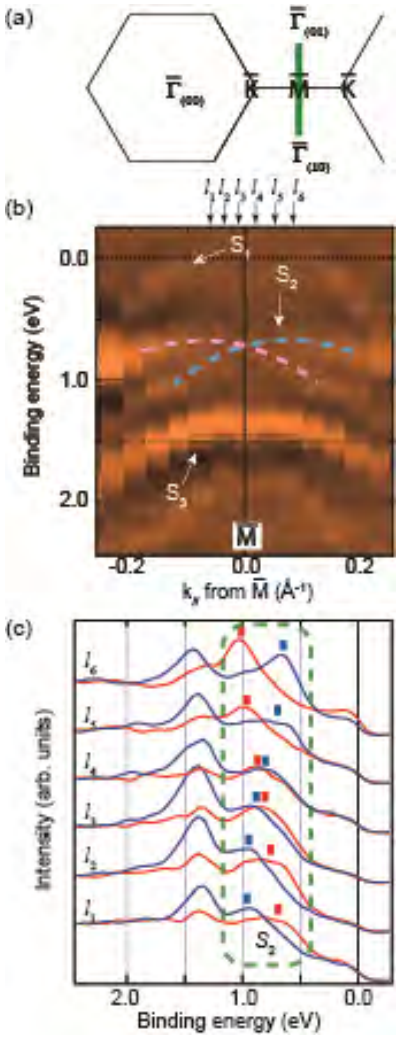

Figure (a) SBZ of Pb/Ge(111)-β. (b) ARPES image taken along green line in the SBZ shown in (a). Dashed curves represent two branches of S_2. (c) SARPES spectra taken with the arrows shown in (b). Red and blue lines represent the up and down spin states, respectively.

References

[1] I. Gierz *et al*., PRL **103**, 046803 (2009).
[2] S. Hatta *et al*., PRB **80**, 113309 (2009).
[3] K. Sakamoto *et al*., PRL **103**, 156801 (2009).
[4] K. Yaji *et al*., Nature. Commun. 1:17 (2010).
* yaji@issp.u-tokyo.ac.jp

SAGA Light Source BL10/2011G086

鉄系超伝導体 $Ca(Fe_{1-x}Rh_x)_2As_2$ の放射光角度分解光電子分光
Synchrotron angle-resolved photoemission spectroscopy study of iron-based superconductor $Ca(Fe_{1-x}Rh_x)_2As_2$

坪田幸士[1*], 脇田高徳[1], 長尾浩樹[1], 吉村大介[2], 瀬戸山寛之[2], 岡島敏浩[2], 村岡祐治[1], 横谷尚睦[1]
[1]岡山大学大学院自然、〒700-8530 岡山市北区津島中 1-1-1
[2]佐賀シンクロトロン光研究センター 841-0005 佐賀県鳥栖市弥生が丘 8-7

1 はじめに

122 系の鉄系超伝導体の母物質 $CaFe_2As_2$ は、圧力を加えることにより、一旦超伝導を示すが、さらに圧力を増加すると、超伝導が突如消失する。結晶構造から見ると、超伝導-非超伝導の転移は Tetragonal(T)相から collapsed Tetragonal(cT)相への相転移に対応する[1]。T-cT 相転移は、c 軸の減少を伴う。理論的には、電子構造の次元性が二次元的から三次元的に変化することが予測されている[2]。電子構造の次元性の低下はフェルミ面形状のネスティングの傾向を減少させる。鉄系超伝導体においては、フェルミ面間のネスティングが超伝導の発現と密接に関係していると考えられている。そのため、T-cT 相転移による電子構造の次元性の変化の観測を行うことで、鉄系超伝導の超伝導転移のメカニズムに電子構造の次元性が関与しているかどうかを検証できる。しかし、$CaFe_2As_2$ は高圧下においてのみ T-cT 相転移を示すので、実験的な検証は難しく、直接的にフェルミ面形状の変化を観測した実験はなかった。

今回測定を行った $Ca(Fe_{1-x}Rh_x)_2As_2$ [3]は、Rh をドープすることにより、低温において Orthorhombic(O)相から T 相、更には cT 相へと変化させることができる (図 1)。バルク超伝導は T 相でのみ観測されている。この変化は、$CaFe_2As_2$ に圧力を加えた時と似た変化であり、Rh 置換が正の化学圧力効果を与えていることを示す。このことは、常圧下においても温度を変化させることによって T-cT 相転移の観測が可能となった。

本研究では、T-cT 構造相転移に伴うフェルミ面形状の変化を直接観測することを目的として、$Ca(Fe_{1-x}Rh_x)_2As_2$ の放射光角度分解光電子分光を行った。

2 実験

測定試料は$Ca(Fe_{1-x}Rh_x)_2As_2$(x=3.4%)の単結晶試料を用いた。この試料は、温度50K付近でT-cT相転移を示す。清浄試料表面は超高真空下において劈開で得た。

角度分解光電子分光は九州シンクロトロン光研究センター（SAGA-LS）県有ビームラインBL 10を用いた。入射光の偏光は円偏光、エネルギーはhv = 90−200 eVとした。測定時の全エネルギー分解能は70−100 meVに設定した。試料温度は 20 K (cT相) および 200 K (T相)である。

3 結果および考察

図 1、2 はそれぞれ x=3.4%の試料の T 相、cT 相におけるフェルミ準位近傍（-15meV<結合エネルギー(E_B)<15meV）の光電子強度マップである。光電子強度の規格化はフェルミ準位(E_F)より高 E_B の強度で行っている。白線で描かれている枠は格子定数から

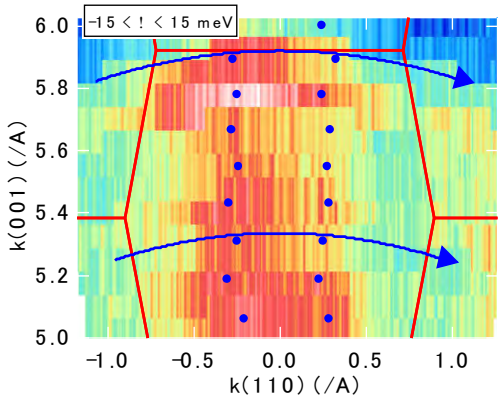

図 1：T 相における $Ca(Fe_{1-x}Rh_x)_2As_2$ の E_F 近傍の光電子強度マップ

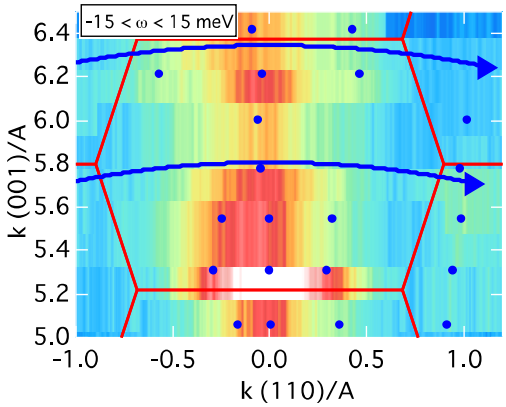

図 2：c T 相における $Ca(Fe_{1-x}Rh_x)_2As_2$ の E_F 近傍の光電子強度マップ

求めた $Ca(Fe_{1-x}Rh_x)_2As_2$ のブリルアンゾーンである。黒点は、E_F 近傍の運動量分布関数(Momentum Distribution Curve, MDC)におけるピーク位置であり、バンドがフェルミ準位を横切る位置（フェルミ運動量 k_F）またはバンドがフェルミ準位極近傍に存在する位置に対応する。

T 相と cT 相の強度分布の傾向を比較すると、T 相では強度分布の k_z 依存性が少ないように見えるのに対して、cT 相においては強度分布に k_z 依存性があり、Γ 点近傍の強度が低く Z 点近傍で強度が強くなっているように見える。強度分布の違いは、MDC 解析の結果に顕著な違いとなって現れる。T 相では MDC の構造は Z-Γ-Z 線の両脇に存在し k_z 依存性はほとんどないように見える。その一方で cT 相では、MDC の構造の位置は Z-Γ-Z 線付近にプロットされとともに、Z 点近傍ではその両側にも構造が存在する。外側の構造が顕著な k_z 依存性を持つことを示唆している。これらの結果は、T 相においてはフェルミ面形状が二次元的であるのに対して、cT 相においては 3 次元的なフェルミ面が存在することを示唆している。超伝導の消失と電子構造の次元性の変化が関連していることを示唆している。

4 まとめ

今回の実験で、T-cT 相転移においてフェルミ面の次元性の変化を示唆するデータを得ることに成功した。しかしながら、測定時間の関係で S/N および測定点において粗いデータとなってしまった。今後は k_z 分散において、より詳細な実験を行い転移前後の電子構造変化をより明瞭に観測するとともに、面内マッピングも行うことにより 3 次元運動量空間において具体的にフェルミ面の形状変化、より具体的にはネスティングの度合いがどうのように変化するかを観測したいと考えている。

謝辞

本研究は、岡山大学大学院自然科学研究科、壇浦 匡隆氏、工藤一貴助教、野原 実教授との共同研究です。ここに感謝いたします。

参考文献

1) A. Kreyssig, et al., Phys. Rev. B 78, 184517 (2008).
2) D. A. Tompsett and G. G. Lonzarich, Physica B 405, 2440-2443 (2010).
3) M. Danura, et al., J. Phys. Soc. Jpn. 80, 103701 (2011).

* sc19221@s.okayama-u.ac.jp

7C/2011G111

EXAFS Measurements Characterized Local Structure of Copper Complex Catalysts Encapsulated in Y-Zeolite Catalysts

Yoshiki INOUE, Yuichi ICHIHASHI, Satoru NISHIYAMA*
Kobe Univ., Rokkodai, Nada, Kobe, 657-8501, Japan

Introduction

The synthesis of phenol through a direct oxidation of benzene in an aqueous solution of acetic acid was studied by using copper supported catalysts. It was recognized that the high yield of phenol was obtained as a main product in this reaction. Though the reusability of used catalysts is quite low due to the elution of copper species into the reaction solution. Then, we prepared copper complex catalysts encapsulated in Y-zeolite. The effect of the steric hindrance between several ligands and pore size was investigated on the elution of vanadium species.

In this study, EXAFS measurements characterized local structure of these catalysts.

Experimental

Catalyst preparation

Copper complex catalysts encapsulated in Y-zeolite were prepared by following method. Cooper was supported on Y-zeolite by ion exchange method, and the product named Cu-Y. Cu-Y was mixed with solution of ligand such as picolinic acid ,quinaldic acid, and pyrazine carboxylic acid, and Cu complex catalysts encapsulated in Y-zeolite were got. Encapsulated catalyst used picolinic acid was named CuPA-Y, quinaldic acid was named CuQA-Y, pyrazine carboxylic acid was named CuPCA-Y.

EXAFS measurements

EXAFS region of the X-ray absorption coefficient was analyzed to have information about the local environment of copper ions, in term of interatomic distances and coordination numbers. X-ray absorption spectroscopy was performed for the Cu K-edge. As a standard reference, X-ray absorption spectra in transmission mode were recorded for CuO crystalline powder. EXAFS data processing was carried out by REX2000.

Result and discussion

EXAFS measurements of Cu K-edge of Cu complex encapsulated catalysts were carried out in order to obtain the information of the local structures. Table1 shows the results of curve fitting of Cu K-edge EXAFS data. The interatomic distances of the neighboring oxygen in the every catalyst are the almost same, ca. 1.94-1.95Å. It is indicated that the four neighboring oxygen in CuQA-Y catalyst is two. Hence the structure of Cu species in the CuQA-Y catalyst seems to be different from other catalysts. We previously reported that the activity of CuQA-Y for the benzene oxidation to phenol was higher than the other two catalysts. It is speculated that these difference of coordination structures affects the catalytic activity. The models of these Cu complexes are described in Fig.1. The size of ligands of CuQA-Y is larger than the others. Therefore, the coordination structure of only CuQA-Y may be different from the CuPA-Y and CuPCA-Y due to the steric hindrance between ligands and pore size of Y-zeolite.

Table1 Results of the Curve Fitting of Cu-Kedge EXFAS Data for Cu Catalyst

Catalysts	Shell	R(Å)	N	dE	DW
CuPA-Y	Cu-O	1.94	3.2	-2.76	0.048
CuQA-Y	Cu-O	1.95	2.4	-4.56	0.068
CuPCA-Y	Cu-O	1.95	3.7	-0.953	0.061

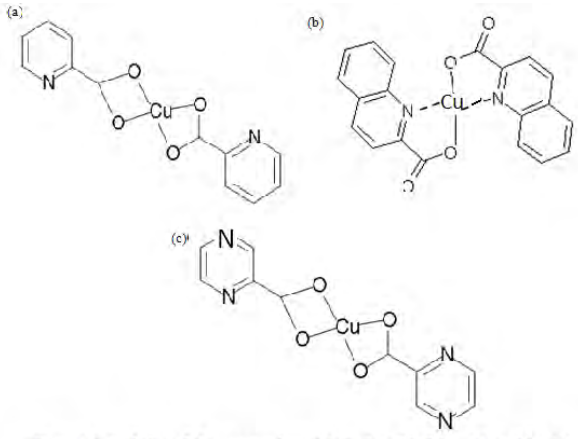

Fig. 1 Models of Cu complex (a)CuPA-Y (b)CuQA-Y (c)CuPCA-Y

Conclusion

The interatomic distances between Cu atom and neighboring oxygen was 1.94-1.95Å. Cu atoms were coordinated by four neighboring oxygen in CuPA-Y and CuPCA-Y, though the coordination number of neighboring oxygen in CuQA-Y was two due to the steric hindrance between ligands and pore size of Y-zeolite.

2C/2011G113, 2011S2-003

Electronic states of infinite-layer $Sr_{1-x}Eu_xFeO_{2+\delta}$ thin films studied by X-ray photoemission and absorption spectroscopies

Akira CHIKAMATSU*[1,2], Toshiya MATSUYAMA[1], Tsukasa KATAYAMA[1], Yasushi HIROSE[1,2,3], Hiroshi KUMIGASHIRA[4], Masaharu OSHIMA[5], Tomoteru FUKUMURA[1,2], Tetsuya HASEGAWA[1,2,3]

[1]Department of Chemistry, The University of Tokyo, Tokyo 113-0033, Japan
[2]CREST, Japan Science and Technology Agency (JST), Tokyo 113-0033, Japan
[3]Kanagawa Academy of Science and Technology (KAST), Kawasaki 213-0012, Japan
[4]Institute of Materials Structure Science, KEK, Tsukuba 305-0801, Japan
[5]Department of Applied Chemistry, The University of Tokyo, Tokyo 113-8656, Japan

1 Introduction

$SrFeO_2$ has attracted much attention because it is an isostructural analog of an infinite-layer cuprate, $SrCuO_2$, which exhibits high transition-temperature superconductivity by carrier doping [1]. $SrFeO_2$ shows an antiferromagnetic insulator with a high Néel temperature of T_N = 473 K, and has tetragonal unit cells with a lattice constant of a = 0.3991 nm and c = 0.3475 nm [1]. We recently demonstrated that electron carriers can be doped into $SrFeO_2$ by Eu substituting for Sr sites in the form of epitaxial thin film [2]. The $Sr_{0.9}Eu_{0.1}FeO_{2+\delta}$ film exhibited as low as ~0.15 Ωcm at room temperature, which was approximately four orders of magnitude lower than that of undoped $SrFeO_2$, and showed semiconducting behavior [2]. In this study, we measured the core-level spectra of $Sr_{1-x}Eu_xFeO_{2+\delta}$ films by X-ray photoemission (XPS) and absorption (XAS) spectroscopies to investigate the valences of the Fe and Eu ions in them.

2 Experiment

Epitaxial thin films of $Sr_{1-x}Eu_xFeO_{2+\delta}$ with x = 0, 0.05, 0.10, 0.15, and 0.20 were fabricated on $SrTiO_3$ (001) substrates by combining pulsed laser deposition method with solid-phase reduction using CaH_2 at 280 °C for 24 hours. The typical thickness of the films was ~150 nm. The valences of the Fe and Eu ions were evaluated by Fe 2*p* core-level XPS spectra and XAS spectra near the Eu *M*-edge at beamline 2C of the Photon Factory, KEK. The Fermi levels of the samples were referred to that of Au foil in electrical contact with the samples. The XAS spectra were measured by the total-electron-yield method.

3 Results and Discussion

Figure 1(a) shows the Fe 2*p* core-level XPS spectra of the $Sr_{1-x}Eu_xFeO_{2+\delta}$ films. Each spectrum is characterized by a Fe $2p^{1/2}$–Fe $2p^{3/2}$ doublet and a weak satellite located at a binding energy of ~715 eV between the doublet peaks. It is known that the position of the Fe 2*p* satellite is very sensitive to the oxidation state of Fe. By comparing Fig. 1(a) with the Fe 2*p* XPS spectra of the $SrFeO_2$ and $SrFeO_{2.5}$ films [3], we determined the valences of the Fe ions in all compositions of the $Sr_{1-x}Eu_xFeO_{2+\delta}$ films to be divalent, irrespective of Eu contents. Figure 1(b) shows the XAS spectra near the Eu *M*-edge in the $Sr_{1-x}Eu_xFeO_{2+\delta}$ films. As seen in Fig. 1(b), each spectrum has peaks at photon energies of ~1127 eV, ~1132 eV, and ~1136 eV in the Eu M_5-edge. It also has peaks at ~1160 eV and ~1163 eV, and a shoulder at ~1158 eV in the Eu M_4-edge. These spectra are completely similar to the calculated 3*d*-4*f* XAS spectra for Eu^{3+} ions as reported previously [4]. Therefore, the valences of Eu in the $Sr_{1-x}Eu_xFeO_{2+\delta}$ films are essentially trivalent, irrespective of Eu contents. These results imply that the electron carriers in $Sr_{1-x}Eu_xFeO_{2+\delta}$ are supplied by Eu^{3+} ions substituting for Sr^{2+} sites, corresponding to the negative Hall coefficients of the $Sr_{1-x}Eu_xFeO_{2+\delta}$ films [2]. Considering charge neutrality of $Sr_{1-x}Eu_xFeO_{2+\delta}$, it is suggested that excess oxygen atoms δ are incorporated between FeO_2 sheets with increasing Eu contents.

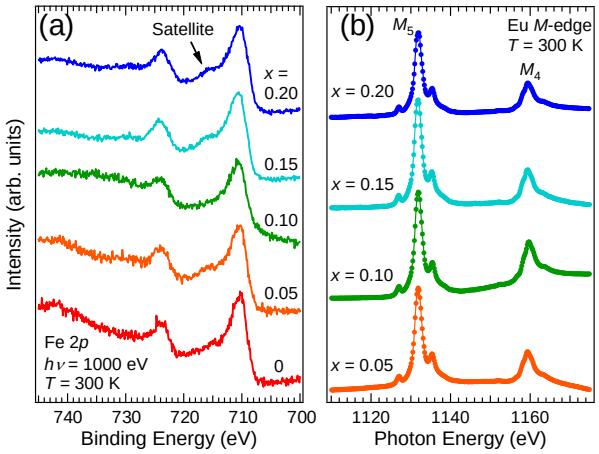

Fig. 1. (a) Fe 2*p* XPS spectra and (b) XAS spectra near the Eu *M*-edge in the $Sr_{1-x}Eu_xFeO_{2+\delta}$ thin films.

References

[1] Y. Tsujimoto, et al., Nature **450**, 1062 (2007).
[2] T. Matsuyama, et al., Appl. Phys. Express **4**, 013001 (2011).
[3] A. Chikamatsu, et al., J. Electron Spectrosc. Relat. Phenom., **184**, 547 (2012).
[4] T. Kinoshita, et al., J. Phys. Soc. Jpn. **71**, 148 (2002).

* chikamatsu@chem.s.u-tokyo.ac.jp

PF: 28A/2011G186, SLS: 1105044PF

ルチル型遷移金属酸化物の角度分解光電子分光測定
ARPES study of rutile-type transition metal oxides

村岡祐治*、長尾浩樹、坪田幸士
岡山大学大学院自然科学研究科、〒700-8530 岡山市北区津島中 3-1-1

1 はじめに

VO_2は 340Kで結晶構造の変化を伴う金属絶縁体転移を示す。この転移の起源を電子状態の立場から解明しようと、古くから角度分解光電子分光(ARPES)実験に興味が持たれている。しかし 3 次元物質であるVO_2はへき開面が化学的に安定ではなく、また、転移の際に体積が大きく変化し結晶が割れやすい問題も加わり、これまでこの物質でのARPES測定は困難であった。ところが最近、パルスレーザー堆積法によりTiO_2基板上に堆積したVO_2エピタキシャル成長膜を用いると上記のような単結晶での問題が生じず、光電子分光（PES）測定ができることが報告された。VO_2エピタキシャル成長薄膜が光電子分光測定に有効であることを示している。そこで我々はVO_2エピタキシャル成長膜を用いてARPES測定を行うことによりVO_2のバンド分散の観測を目指した。本研究では金属相Γ-X方向に注目した。この方向には、フェルミ準位を横切る複数のバンドの存在が理論計算より予想されている。また、この方向を含む金属相ΓXRZフェルミ面にはネスティングベクトルの存在が予想されている。金属相Γ-Xにおけるバンド分散の観測は、パイエルス転移説の検証につながる。

2 実験

VO_2薄膜はTiO_2基板(001)面上にKrFエキシマレーザー（波長248 nm）を用いたパルスレーザー堆積法(PLD法)により作製した。作製したVO_2薄膜の物性評価は低速電子線回折観測(LEED)と光電子分光測定により行った。

金属相Γ-Z方向のARPES測定は、佐賀Light SourceのBL10軟X線角度分解光電子分光装置により行った。測定時の試料温度は380K(金属相)で、入射光のエネルギーは100eV～160eVまで変化させながら測定した。

3 結果および考察

図 1 に入射光エネルギー155 eVにおける光電子スペクトルの、フェルミ準位近傍の強度変化とその 2 階微分を示した。入射光エネルギー155eVは、フェルミ面における第 4 ブリルアンゾーンのΓ点を与える。E_B = 0.2 ～ 0.4 eVの構造はV 3*d*バンド、E_B = 0.5 eV以上の構造はO 2pバンドによるものである。2 階微分の図より、Γ-X方向にΓ点を中心とした下に凸の、フェルミ準位E_Fを横切るバンドが存在していることが分かる。現在、E_F近傍のバンド構造を詳しく会席している最中である。

今後解析をすすめてバンドの本数やバンド幅などを明らかにし、Γ-X 方向のバンド構造を示したい。また、得られた結果をもとに定量的な解析を行い、有効質量やフェルミ波数等の物理パラメータを導出したい。

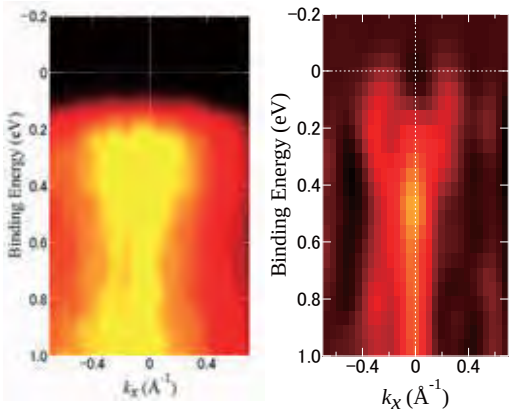

図 1： Γ-X 方向の E-k マップ（左）とその 2 階微分(右)

4 まとめ

実験により観測したΓ-X 方向のバンド構造を解析することが当面の課題である。バンド構造を明らかにすること、さらにどのバンドがどの軌道由来であるかを明らかにすることがポイントである。課題の解決にはこれまでに方向のある理論計算の結果と実験結果を比較することが有効である。実験より求めたバンドの本数、バンド幅、フェルミ波数や有効質量を用いれば、理論との相違について定量的な議論ができる。比較により得られた知見はこれまでに報告されている理論の妥当性を検証する上でも、あるいは新たな理論モデルを作る上でも有用であり、金属絶縁体転移の起源解明に重要な役割を果たす。

謝辞

SLS で実験を進めるにあたり、PF スタッフに手続きでお世話になりました。また、実験では SLS の吉村氏、瀬戸山氏、岡島氏に多大なる技術支援を受けました。ここに感謝致します。

*ymuraoka@cc.okayama-u.ac.jp

2C/2011G520,2009G605

O 2p partial density of states and local structures in oxide glasses

Shinya Hosokawa[1,*], Hitoshi Sato[2], Kojiro Mimura[3], and Yasuhisa Tezuka[4]
[1]Kumamoto University, Kumamoto 860-8555, Japan
[2]Hiroshima University, Higashi-Hiroshima 739-0046, Japan
[3]Osaka Prefecture University, Sakai 599-8531 Japan
[4]Hirosaki University, Hirosaki 036-8561 Japan

1 Introduction

Oxide glasses have been widely used for human life for more than three thousands years, which are a group of non-crystalline materials of chemically stable. One of the typical oxide glasses is silica (SiO_2), in which SiO_4 tetrahedra are connected with each other by corner sharing of O atoms, and form continuous networks similar to the crystal quartz. From previous structural studies [1], the Si-O-Si bond angle is about 150°, almost rectilinear. On the other hand, the structure of another typical oxide glass, B_2O_3, is based on the B_3O_3 hexagonal rings (boroxol ring), where the B-O-B bond angle is about 120° [1, 2], much smaller the that in SiO_2 glass.

It is no doubt that the bond angles around the O atoms in the oxide glasses strongly affect the electronic structures. However, the experimental investigations, such as by photoemission spectroscopy, are very difficult because these glasses are highly insulating. Soft x-ray emission spectroscopy (SXES) can provide information on valence-band density of states (DOS) of such insulating materials. However, some SXES experiments of these oxide glasses were limited to be carried out for the kation (Si [3] or B [4]) partial DOSs so far. In this paper, we report results of O 2p partial valence-band DOS of SiO_2 and B_2O_3 glasses obtained by O 1s SXES.

2 Experiment

The SXES measurements were performed at BL2C of PF-KEK at room temperature on SiO_2 and B_2O_3 glasses. In the experiments, core absorption spectra were carefully measured firstly by total emission yield method around the O *K* absorption edge of about 537 eV in order to obtain information on the O 2p partial conduction-band DOS. After then, O 1s SXES spectra were measured at various incident photon energies from about 530 to 560 eV.

3 Results and Discussion

The SXES spectra of glassy SiO_2 and B_2O_3 are shown by dashed and solid curves, respectively, at $h\nu$ = 550 eV. The intensities are reduced with respect to the peak intensities at about $h\nu$ = 525 eV. As clearly seen in the figure, the SXES spectrum of B_2O_3 glass are very different from that of SiO_2 glass. In particular, (1) the first peak emission energy is shifted towards the higher energy by about 1 eV, and (2) the sub-band structures in the lower emission energy region are much simpler. Theoretical analyses of these experimental results using an *ab initio* molecular dynamics simulation are now in progress.

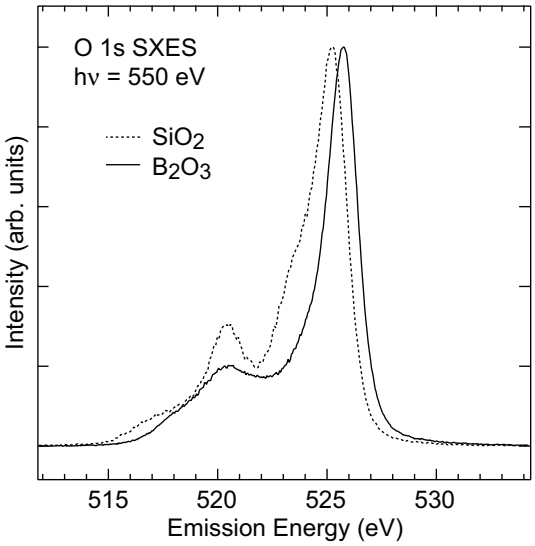

Fig. 1: O 1s soft x-ray emission spectra of SiO_2 (dashed curve) and B_2O_3 (solid curve) glasses at $h\nu$ = 550 eV.

Acknowledgement

We acknowledge Professor Y. Ishiwata of Saga University for the help of the SXES experiments.

References

[1] For example, S. Kohara and K. Suzuya, Phys. Chem. Glasses **43**C (2002) 51.
[2] F. L. Galeener *et al.*, Phys. Rev. B **22** (1980) 3983.
[3] V. J. Nithianandam and S. E. Schnatterly, Phys. Rev. B **38** (1988) 5547.
[4] Y. Muramatsu *et al.*, Phys. Rev. Lett. **71** (1993) 448.

* hosokawa@sci.kumamoto-u.ac.jp

2C/2011S2-003

二次元化された $LaNiO_3$ 薄膜の電子状態の基板依存性
Substrate dependence of electronic structure of $LaNiO_3$ ultrathin films

坂井延寿[1*]、玉光雅智[2]、吉松公平[2]、堀場弘司[2]、尾嶋正治[2]、組頭広志[1,2,3]

[1]放射光科学研究施設　物質構造科学研究所、〒305-0801 茨城県つくば市大穂 1-1
[2]東京大学工学系研究科応用化学専攻、〒113-8656東京都文京区本郷7-3-1
[3]JST さきがけ、〒332-0012、埼玉県川口市本町4-1-8

1 はじめに

酸化物ヘテロ構造を利用して強相関酸化物を擬二次元化することで、新奇な物性を発現させようという試みが数多くなされている。常磁性伝導性酸化物である $LaNiO_3$（LNO）においても、数原子層レベルの薄膜で新奇な絶縁相が生じることが報告されている[1]。この絶縁化では基板の違いによる臨界膜厚の違いも報告されており、基板応力による格子定数の違いや基板−薄膜界面における電荷移動が重要な役割を果たしている可能性がある。そこで、本研究では LNO の低次元化による絶縁化の起源を明らかにするために *in situ* 光電子分光、X線吸収分光により、LNO 薄膜の電子状態の膜厚依存性と基板依存性を調べた。

2 実験

LaserMBE 法により LNO を 1 ML から 100 ML の範囲で $SrTiO_3$（STO）および $LaAlO_3$（LAO）基板上に堆積させた。膜厚制御は反射高速電子線回折の強度振動の観察により行った。試料は超高真空中を保ったまま測定槽に搬送し、*in situ* で光電子分光（PES）、X線吸収分光（XAS）測定を行った。

3 結果および考察

図1にLAO、STO基板上にそれぞれ作製したLNO薄膜のフェルミ準位（E_F）近傍における光電子分光スペクトルを示す。どちらの基板上においても10 ML以上ではスペクトル形状にほとんど変化が見られていない。それに対して、10 ML以下では、Ni e_g 軌道由来のピーク強度が膜厚と共に徐々に減少していき、フェルミ準位上の状態密度が減少していることが見てとれる。

その結果、LNO薄膜はSTO上、LAO上共にそれぞれ臨界膜厚3 ML、2 MLで絶縁化する。しかしながら、その挙動は基板により大きく異なっている。LAO基板上の薄膜では、Valence band maximum（VBM）の位置をほぼ保ったまま、膜厚の減少と共に徐々に E_F 上の状態密度が減少していき、2MLで絶縁化する。これに対して、STO基板上の薄膜では3から4 MLにかけて、VBMが不連続に〜1.2 eVシフトすることで絶縁化する。

この観測された基板による絶縁化の違いが界面における電荷移動の有無に由来するか調べるために、X線吸収分光によって界面価数の評価を行った。LNO/LAO界面ではNiの価数は3価を保っているのに対して、LNO/STO界面では界面電荷移動によりNiの価数が2価へと変化していることが明らかになった。

以上の結果は、LNO薄膜の極薄膜領域の電子状態では界面電荷移動が重要な役割を担っていることを示している。

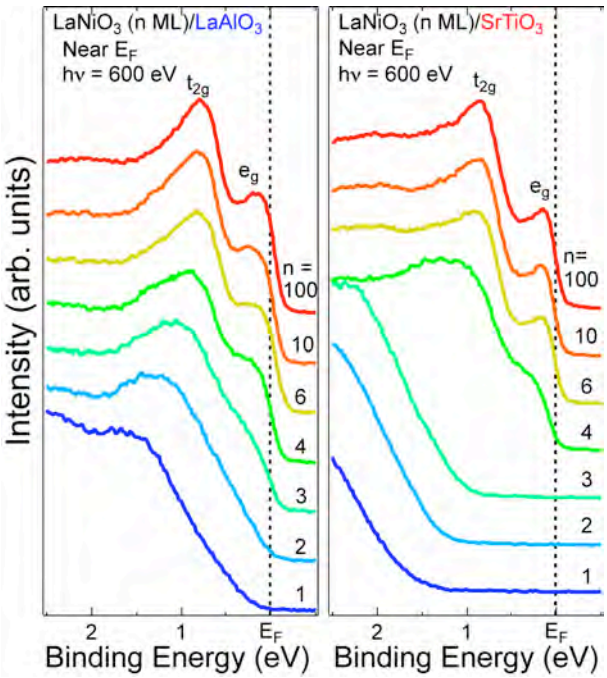

図 1：STO、LAO 基板上に作製した LNO 薄膜のフェルミ準位近傍光電子分光スペクトル

参考文献

[1] R. Scherwitzl, *et al.*, Phys. Rev. Lett. **106**, 246403 (2011).

*enju@post.kek.jp

28A,2C/2009S2-005, 2011S2-003

Photoemission and X-ray absorption spectroscopy study of $Ba(Fe_{1-x}Mn_x)_2As_2$

H. Suzuki[1*], T. Yoshida[1], S. Ideta[1], A. Fujimori[1], K. Ono[2], E. Sakai[2], H. Kumigashira[2], M. Matsuo[3] and T. Sasagawa[3]

[1]University of Tokyo, Hongo, Tokyo 113-0033, Japan
[2]KEK, Photon Factory, Tsukuba, Ibaraki 305-0801, Japan
[3]Tokyo Institute of Technology, Kanagawa 226-8503, Japan

Introduction

Superconductivity in iron-based materials is induced either by hole or electron doping into the parent antiferromagnetic metal. For example, electron doping can be achieved by Co substitution for Fe in $BaFe_2As_2$. Hole doping in $BaFe_2As_2$ by Mn, however, does not induce superconductivity. In addition, the remaining antiferromagnetic metallic phase is reported to be quite peculiar [1]. In order to elucidate the pairing mechanism in iron-pnictide systems, the absence of superconductivity for Mn doping could give useful insight. We have performed a photoemission and X-ray absorption spectroscopy (XAS) study of the iron-pnictide material $Ba(Fe_{1-x}Mn_x)_2As_2$ (Mn-Ba122, x=0.08) at beamlines 28A and 2C, respectively. XAS spectra have made clear that the dopant Mn atoms take a strongly hybridized ground state. We have also deduced the partial density of states (PDOS) of Mn *3d* orbitals by resonant photoemission spectroscopy. The data indicate that the Mn *3d* PDOS is distributed at E_B~1-10eV but not near E_F.

X-ray absorption spectroscopy

Figure 1 shows X-ray absorption spectra at the Mn and Fe *L*-edges. The line shapes of the Mn $L_{2,3}$-edges of $Ba(Fe_{0.92}Mn_{0.08})_2As_2$ resemble those of Mn metal and to some extent $Ga_{1-x}Mn_xAs$. The dopant Mn is tetrahedrally coordinated by As atoms both in Mn-Ba122 and $Ga_{1-x}Mn_xAs$, and, therefore the lineshapes resemble each other in that there is no multiplet structure unlike MnO. The L_3 line shape of $LaMnO_3$ has its weight at higher photon energies (~642eV) than that of Mn-Ba122. These results suggest that the doped Mn atoms take Mn^{2+} state and are strongly hybridized with As *4p* orbitals.

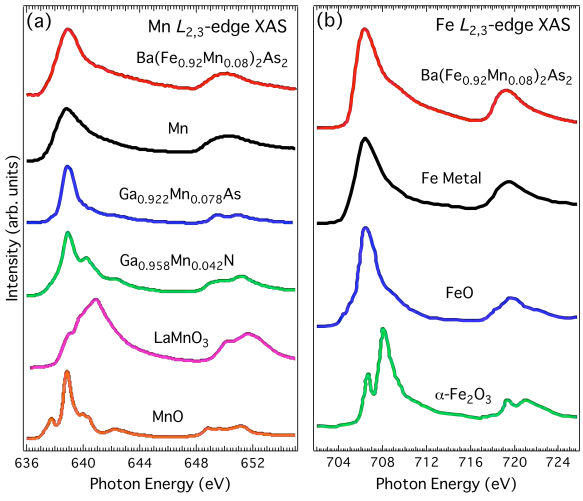

Figure 1: XAS spectra of Mn (left) and Fe (right) *L*-edges.

The peak positions of Fe $L_{2,3}$-edges in $Ba(Fe_{0.92}Mn_{0.08})_2As_2$ are also close to those of FeO. The line shapes those of Fe metal. These results confirm that Fe atoms in the parent compound have the valence 2+ and are in the strongly hybridized ground state.

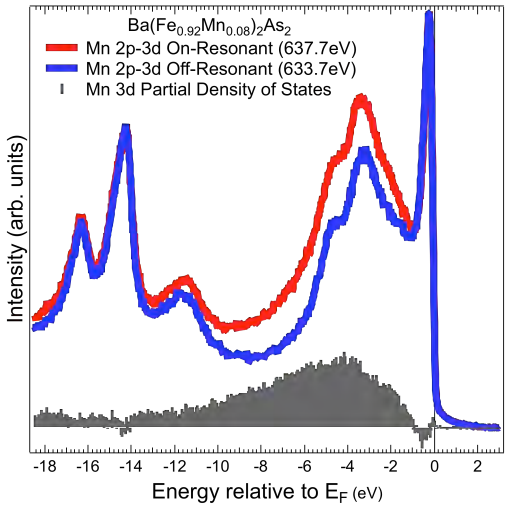

Figure 2: Valence-band spectra taken with Mn *2p-3d* on-resonant (637.7eV, red) and off-resonant (633.7eV, blue) photons. The bottom curve shows the Mn *3d* PDOS.

Resonant photoemission spectroscopy

Resonant photoemission spectroscopy is a useful tool to investigate the partial density of states of a specific element in solids. Figure 1 shows the valence-band spectra taken with Mn *2p-3d* on-resonant and off-resonant photons. The difference in the spectral weight corresponds to the partial density of states of the dopant Mn. This result show that the Mn *3d* PDOS is located at 1-10eV below the Fermi level and that there is little Mn *3d* PDOS at. EF, suggesting that the Mn *3d* electrons are localized at the dopant site.

References

[1] J. S. Kim et al., Phys. Rev. B. **82**, 024510 (2010).
[2] M. G. Kim et al., Phys. Rev. B **82**, 220503 (2010)

* hakuto@wyvern.phys.s.u-tokyo.ac.jp

2C/2011S2-003, 2011G061, 2010G655

X-ray Absorption Spectra of Delaffosite Oxides $CuCr_{1-x}Mg_xO_2$

Takumi Yokobori,[1] Mario Okawa,[1] Kouta Konishi,[1] Satoshi Oozono,[2] Takashi Shinmura,[2] Tetsuji Okuda,[2] Hiroki Wadati,[3] Hiroshi Kumigashira,[4] Masaharu Oshima,[5] and Tomohiko Saitoh[1,*]

[1]Department of Applied Physics, Tokyo University of Science, Shinjuku, Tokyo 162-8601, Japan
[2]Department of Electrical and Electronics Engineering, Kagoshima University, Korimoto, Kagoshima 890-0065, Japan
[3]Department of Applied Physics and Quantum-Phase Electronics Center, University of Tokyo, Bunkyo, Tokyo 113-0032, Japan
[4]Photon Factory, KEK, Tsukuba, Ibaraki 305-0801, Japan
[5]Department of Applied Chemistry, University of Tokyo, Bunkyo, Tokyo 113-8656, Japan

1 Introduction

Delaffosite oxides $CuMO_2$ (M = metal element) have various important physical properties both in fundamental and applicational terms. For example, $CuAlO_2$ is the first p-type transparent oxide semiconductor [1], and $CuFeO_2$ is a typical multiferroic compound [2]. This family have also potential for thermoelectric materials [3] because of its layered structure of edge-shared MO_6 octahedrons, being the same as thermoelectric $NaCoO_2$ [4]. Hole-doped $CuCr_{1-x}Mg_xO_2$ is one of such candidates; in $CuCrO_2$, $3d^3$ electrons of the Cr^{3+} ions under the O_h local symmetry fill up the narrow Cr $3d$ t_{2g} band and thus a rapid change of density of states at the Fermi level (E_F) may be realized near the t_{2g} band edge in the hole-doped system $CuCr_{1-x}Mg_xO_2$, a high conductivity delaffosite [3]. However, whether the doped hole will go into the Cr $3d$ states or not is unknown. In order to observe valence changes of the Cu and Cr ion in this system, we performed x-ray absorption spectroscopic measurements.

2 Experiment

Polycrystalline samples of $CuCr_{1-x}Mg_xO_2$ (x=0, 0.02, 0.03) were prepared by the standard solid-state reaction [3]. Soft x-ray absorption spectroscopy (XAS) measurements were performed at BL-2C of Photon Factory in KEK. The samples were fractured *in situ* right before measurements in ultrahigh vacuum (better than 1.2×10^{-7} Pa) at 300 K.

3 Results and Discussion

Figure 1 shows XAS spectra of $CuCr_{1-x}Mg_xO_2$ (x=0, 0.02, 0.03) at the Cr $L_{2,3}$ and Cu L_3 edges. The Cr $L_{2,3}$ spectra in Panel (a) are of the typical Cr^{3+} one [5] and show no observable change with x. By contrast, the Cu L_3 edge at x=0 is the typical Cu^+ spectrum and the prepeak at 926.5 eV, which is associated with the Cu^{2+} signal [6], systematically increases wih x. These facts are indicating that the hole is not doped into the Cr states but into the Cu states.

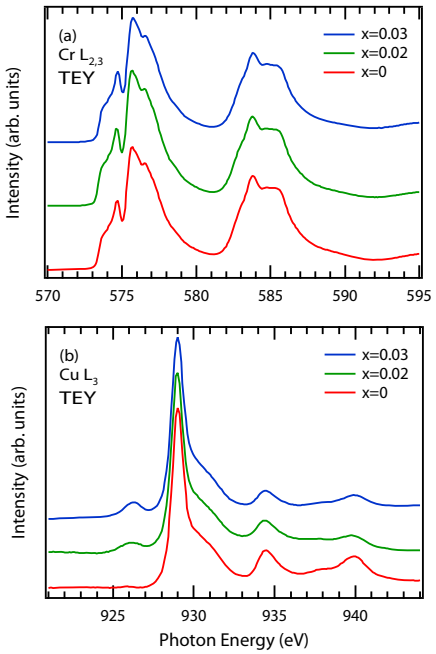

Fig. 1: XAS spectra of $CuCr_{1-x}Mg_xO_2$ (x=0, 0.02, 0.03) at (a) the Cr $L_{2,3}$ edge and (b) the Cu L_3 edge.

Acknowledgement

We would like to thank Prof. T. Mizokawa for useful discussions.

References

[1] H. Kawazoe *et al.*, Nature **389** (1997) 939.
[2] T. Kimura *et al.*, Phys. Rev. B **73** (2006) 220401(R).
[3] T. Okuda *et al.*, Phys. Rev. B **72** (2005) 144403.
[4] I. Terasaki *et al.*, Phys. Rev. B **56** (1997) R12685.
[5] M. Matsubara *et al.*, J. Phys. Soc. Jpn. **71** (2002) 347.
[6] T. Arnold *et al.*, Phys. Rev. B **79** (2009) 075102.

* t-saitoh@rs.kagu.tus.ac.jp

9C/2004G265,2005G301

結晶性高分子ポリブテン-1 の融解再結晶過程における吸発熱曲線の X 線回折データからの再構成
Reconstruction of Calorimetric Curves from X-ray Diffraction Data during the Melting-Recrystallization Process of Isotactic Poly(1-butene) in Form III

高橋　浩 [1*], 島田健一郎 [2], 山本雄三 [2], 上原宏樹 [2]
[1]群馬大学工学研究科（荒牧）　〒371-8510 前橋市荒牧 4-2
[2]群馬大学工学研究科（桐生）　〒376-8515 桐生市天神町 1-5-1

1 はじめに

ある種の結晶性高分子の融解挙動を示差走査熱量計（DSC）で調べると、２つ（それ以上の）吸熱ピークの出現が観察される。このような高分子の複雑な熱挙動の理解には、熱の出入りに伴って起こる構造変化と熱的変化の相関を明らかにすることが不可欠である。本研究[1]では、昇温時に 2 つの異なる結晶相を経て融解に至る過程の構造変化と熱の関係を明らかにするために、X 線データから DSC 曲線を再構成する解析方法を確立することを目的とした。

試料には、温水パイプをはじめとして、広く工業材料として利用されているポリブテン-1(PB-1)を選んだ。PB-１は、結晶化条件に応じて幾つかの種類（I、II、III 型）の結晶を形成する。

2 実験

シクロヘキサン溶液から結晶化した III 型結晶のみを含む PB-１を加熱すると、吸熱・発熱・吸熱プロセスを経て融解する。この融解過程の X 線回折・熱量同時測定を KEK-BL9C において行った。

3 結果および考察

図１に、同時測定で得られた DSC 曲線、小角 X 線回折像、広角 X 線回折像を左から順に横に並べて示した。この図から、小角領域に観察されるラメラ周期の温度依存性は、発熱が観察される温度を境に変化していることが分かる。広角領域では、はじめ III 型に対応する反射が観察され、温度上昇に伴い、

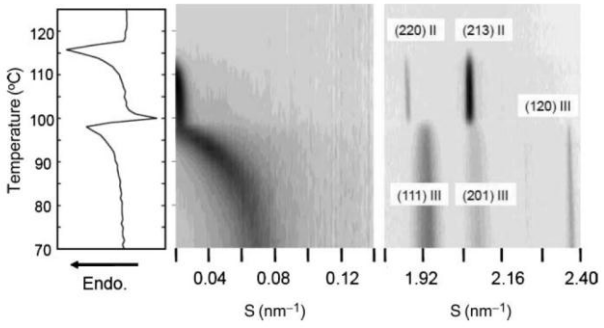

図１　同時測定で得られた PB-1 の DSC 曲線(左)、小角 X 線回折像(中)、および、広角 X 線回折像(右)。

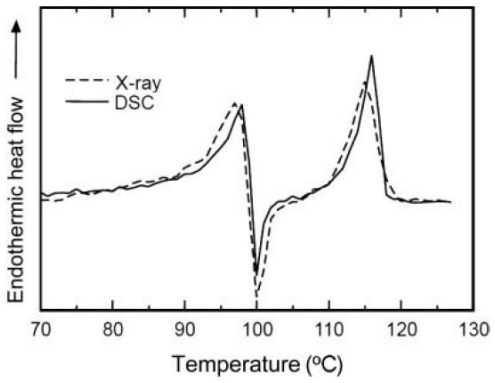

図２　PB-1 の実測 DSC 曲線（実線）と X 線回折データから再構成した曲線（破線）の比較。

その反射強度は減少し、代わりに II 型の結晶反射が出現した。X 線回折の結果から、以下の手順で DSC 曲線を再構築した。まず、広角の III 型、II 型、それぞれの X 線反射強度の温度依存性を温度で微分し、２つの曲線を求めた。この２つの曲線を、それぞれの結晶の融解エンタルピーの値を使って規格化し、足し合わせることで、X 線回折データからの再構成 DSC 曲線を得た。この曲線を、実測の DSC 曲線と比較したところ、1 度以内の範囲で良い一致を示した（図２）。この解析から、III 型結晶の PB-1 は、昇温時、融解・再結晶を経て、II 型を形成した後に最終的な融解を起こすが、III 型が完全に融解した後に II 型が再結晶するのでなく、２つの現象は、ある程度同時進行することが明らかになった。

謝辞

PF の BL9C 担当スタッフの野村昌治教授、小山篤先任技師のサポートに感謝する。本研究の一部は NEDO 産業技術研究助成事業の助成によってなされた。

参考文献

[1] H. Takahashi *et al*., J. Macromol.Sci.Phys.B **51** (2012) 338.

* hirotakahashi@gunma-u.ac.jp

10C/2008G191, 2007G053

Micro-structure Analysis of Heavy-metal ion Adsorbed PAAm Gels

Satoru Yoshioka*[1], Naohiro Ueno[1], Kohtaro Terayama[1], Toshihiro Okajima[2], and Kazuhiro Hara[1]
[1]Faculty of Engineering Kyushu University, Fukuoka, 819-0395, Japan
[2]SAGA-LS, Tosu, 841-0005, Japan

1 Introduction

Some polymer gels with ionic groups can capture harmful heavy-metal ions; therefore they have a possibility of being utilized for the purification of waste water contaminated with hazardous heavy metals. Properties of the gels are considerably influenced with environmental conditions due to the interaction between solvent and polymer network. By adsorbing heavy-metal ion, gels shrink dramatically. In addition to this macroscopic feature, there also occur micro-structural changes by introducing the ionized group in the gel. The adsorbing ability is naturally considered to be higher if more carboxyl groups are introduced in the polymer network; and, in this sense, introduced sodium malate or sodium fumarate containing plural carboxyl groups as the complexing agent instead of sodium acrylate. However, the change of polymer network before/after heavy-metal adsorbed is not understood clearly. It is important to get the sufficient information on the nano-structures of the heavy-metal-adsorbed polymer gels and on the local structures around the captured heavy metals for the improvement of their heavy-metal-capturing efficiency. In the present study, the authors have investigated these structural properties of Poly Acryl Amide (PAAm) gels by Small Angle X-ray Scattering (SAXS).

2 Experiment

PAAm gels were synthesized by a free-radical polymerization. Sodium acrylate (SA), sodium fumarate (SF) and sodium malate (SM) were selected as the complexing agent. We choose cupper as heavy-metal ions capturing by gels. In the adsorbing process, these gels were soaked in 0.1 M $CuCl_2$ control solution for 2 days.

SAXS measurements were carried out at the BL10C in KEK-PF. Scattering Patterns were measured at room temperature by using Position Sensitive Proportional Counter. The camera length was settled about 2 m with the X-ray wavelength λ of 1.5 Å.

3 Results and Discussion

Figure 1 shows the SAXS patterns of PAAm gels before and after adsorbed cupper ions. The SAXS profiles before adsorbed cupper ions have no peak and the intensities are decrease sharply in the low scattering-vector region. On the other hands, after cupper ions adsorbing process, the SAXS profile of AAm/SA gel shows a distinct peak around 0.018 $Å^{-1}$ indicating a regular nano-structure. Other samples show no sharply peak in the measured range. Besides, demonstrating the different nanostructures with the respective ionic groups, the gyration radii estimated by the Guinier plots are 75 Å in the AAm/SA gel, 114 Å in the AAm/SF gel and 194 Å in the AAm/SM gel, which are consistent with them derived from the pair-distance distribution functions calculated by an indirect Fourier transform GNOM software[1)].

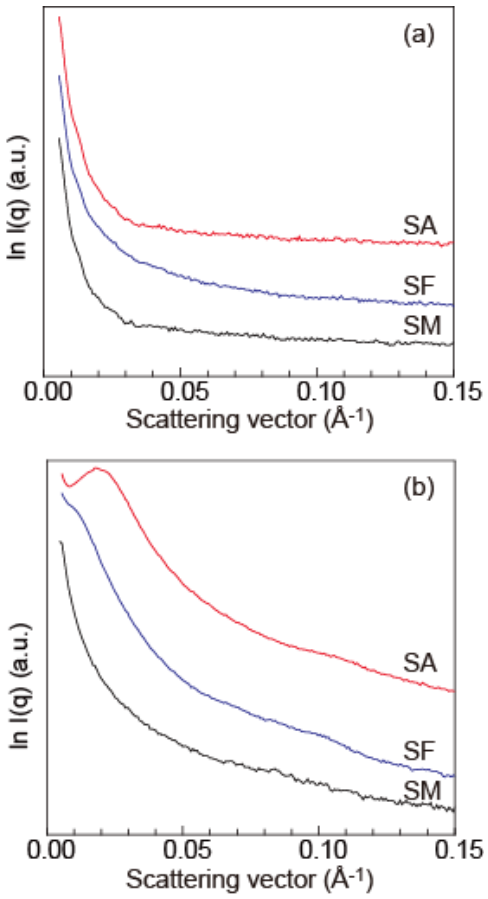

Fig. 1: SAXS profiles of PAAm gels synthesized with the the complexing agent SA, SF and SM respectively. (a) as synthesized and (b) after adsorbed cupper ions.

Reference

[1] D. Svergun, J. Appl. Crystallogr. 25 (1992) 495-503

* syoshioka@nucl.kyushu-u.ac.jp

4C/2008G516

$Sr_{1/3}V_2O_5$の共鳴X線散乱実験
Resonant X-ray Scattering Study of $Sr_{1/3}V_2O_5$

大和田謙二[1*], 藤井保彦[2], 山内徹[3], 上田寛[3]
[1]日本原子力研究開発機構　〒679-5148 兵庫県佐用郡佐用町光都 1-1-1
[2]CROSS　〒319-1106 茨城県東海村 162-1
[3]東京大学物性研究所　〒277-8581 千葉県柏市柏の葉 5-1-5

1 はじめに

ベータバナジウムブロンズと呼ばれる一次元伝導体 $A_{1/3}V_2O_5$（A = アルカリ、アルカリ土類金属）は共通して、室温付近の高温側で A サイトカチオンの秩序化を示し、続いて低温側で金属絶縁体相転移を示す。また、これらの系が示すもっとも興味深い性質の一つに圧力誘起超伝導転移がある。

A サイトが一価のイオンの場合（*A* = Na+, Li+）10 GPa 程度の超高圧下で超電導相転移（*Tc* = 5-10 K 程度）を示すが、一方で二価のイオンの場合（A = Sr^{2+}, Ca^{2+}）は超伝導相転移を示さないことが知られている[1]。これらの違いが何に由来するのかは分かっていないが、超伝導転移よりも高温側の絶縁体相における「電荷配列」の状態が深くかかわっているであろうことが推測される。

金属絶縁体相転移は電荷の自由度が凍結することにより発生し、低温相では ***b*** 軸方向に 6 倍周期の電荷配列が発生する。例えば、*A* = Na^+のケースでは中性子散乱実験[2]や NMR[3]により電荷配列パターンが良く調べられており、それらの結果によれば驚くべきことに、各バナジウムサイトの電荷は非整数であることが示唆されている。臨界指数の議論からもそのようなことが示唆される[4]。つまり電荷密度波のような状態が実現されている。それでは二価の Sr^{2+}などではどうであろうか。そこで我々は Sr^{2+}における共鳴X線散乱実験を行い、Sr^{2+}における電荷配列パターンが Na^+と比べてどのように異なるのかを議論することにした。

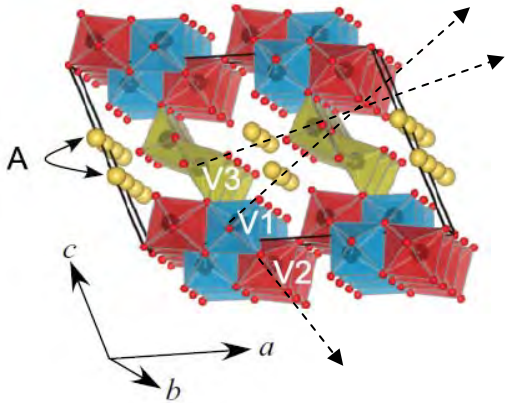

図 1：$A_{1/3}V_2O_5$ の結晶構造。矢印方向と偏光方向が一致した時に強い pre-edge ピークが観測される。VESTA により描画[5]。

2 実験

実験は放射光実験施設 PF の BL-4C を用いて行った。金属絶縁体相転移に伴って現れる超格子反射(0, 10/6, 0)のエネルギー依存性をバナジウム吸収端近傍で測定することにより電荷秩序の情報を取り出した。今回はさらに、大きく分けて 3 種類のバナジウムサイトにどのように電荷が入っているかを議論するために、(0, 10/6, 0)反射強度のアジマス角度依存性を測定した。結晶中には大別して 3 種のバナジウムサイト（V1、V2、V3（図 1 参照））があるが、それらは周りの酸素とピラミッド構造を形成している。一般にピラミッド構造を持つ場合、バナジウムー頂点酸素を結ぶ軸と偏光が一致した時非常に大きな pre-edge ピークが観測される。今回はこの現象を利用する。V1 サイトにおける V1-O^{頂点}軸を 0 度としたとき V2、V3 サイトにおける頂点酸素の方向はそれぞれ 25 度、110 度離れており（図 1 における点線矢印を参照）、アジマス角依存性――つまり、散乱ベクトルを固定しながら結晶の方位と入射X線の偏光方向との相対関係を変化させることによる X 線散乱強度の変化――を観測することにより、各サイトを分離することが可能となる。

実測試料は Sr^{2+}であるが、リファレンスとして Na^+も測定して比較した。

3 結果および考察

図 2 に *A* = Sr^{2+}の結果を、図 3 に *A* = Na^+の結果を示す。一見して明らかなように、Sr^{2+}と Na^+では、そのアジマス角度依存性が大きく異なることが分かった。*A* = Sr^{2+}の場合アジマス角度依存性が明確に観測されるのに対し、*A* = Na^+の場合、アジマス角度依存性は非常に小さい。これは次のようにして解釈される。*A* = Na^+の場合、***b*** 軸方向に起きる電荷密度波のようなものの節（電荷密度が小さい領域）が 3 つのバナジウムサイトにおいて同位相で存在するのに対し（図 4）、*A* = Sr^{2+}の場合は一致していないことが示唆される。

これらを説明可能な電荷配列パターンのうちの一つは図 5 のようなものである。ただし今回の解析からは厳密な荷数までは求まらなかった。V1、V2 に

おける電荷密度の節がそれぞれ位相を違えて存在していることが分かる。以上は、電荷配列のみを考慮して結果を説明したが、現在、歪を考慮した他の電荷配列モデルでも説明が可能かどうか検討中である。

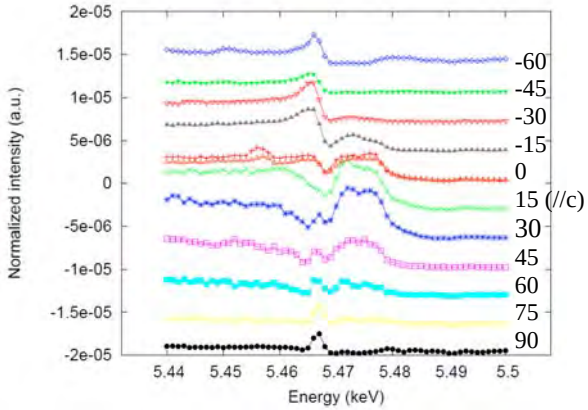

図 2：A = Sr^{2+}における(0, 10/6, 0) 反射強度のエネルギー依存性と、そのアジマス角依存性。数値はアジマス角度に相当。15 度の時 c 軸と平行になる。

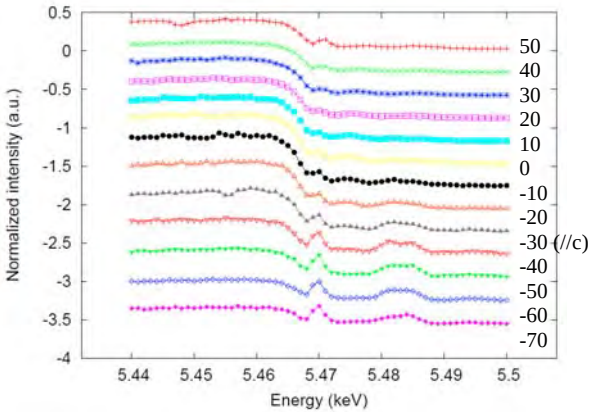

図 3：A = Na^{+}における(0, 10/6, 0) 反射強度のエネルギー依存性と、そのアジマス角依存性。数値はアジマス角度に相当。-30 度の時 c 軸と平行になる。

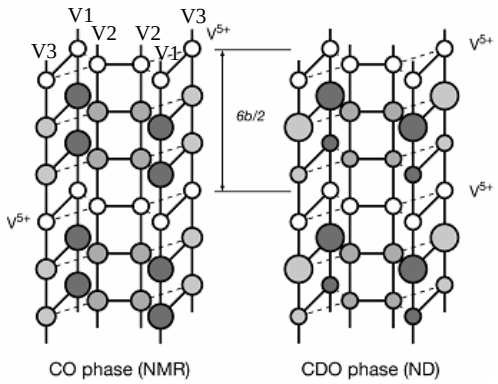

図 4：A = Na^{+}における電荷配列パターン。（左）NMR[3]、（右）中性子線回折実験[2]から求められた。ともに、サイト毎は非整数電荷であり、かつ、電荷の存在しないレイヤー「節（白丸）」が存在する。

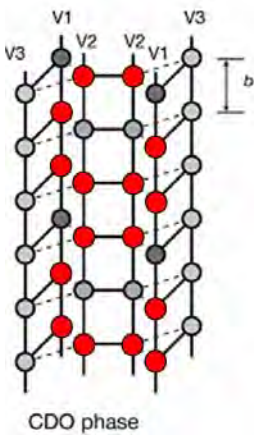

図 5：A = Sr^{2+}における可能な電荷配列パターンの一つ。赤で示したサイトに（非整数）電荷が集中し、その他のサイトには比較的電荷が存在しない。節がサイト毎に異なっている。

4 まとめ

結晶構造が局所的な異方性を持つことを逆手にとって、超格子反射のエネルギー依存性のアジマス角依存性を測定した。その結果、明らかに A = Sr^{2+}と A = Na^{+}においては、その電荷配列パターンに大きな違いが存在することが示唆された。実際に解析を行うことで、A = Sr^{2+}においては各 V1、V2 サイトにおいて、その電荷密度の薄い「節」が位相を違えて存在することが分かった。

ただし、以上の解析結果は電荷配列のみを考慮したものであるが、電荷配列に伴う歪を考慮した他の電荷配列モデルでも説明が可能かどうかも検討する必要があるだろう。

参考文献

[1] 山内徹, 博士学位論文（東京大学）2009 年.
[2] S. Nagai *et al.*, J. Phys. Soc. Jpn. **74** (2005) 1297.
[3] M. Itoh *et al.*, Phys. Rev. B **74** (2006) 054434.
[4] K. Ohwada *et al.*, Phys. Rev. B **85** (2012) 134102.
[5] K. Momma and F. Izumi., J. Appl. Crystallogr. **41** (2008) 653.
* ohwada@spring8.or.jp

7C/2008G637

Local structure analysis of Ga_2O_3 polymorphs by XAFS

Satoru Yoshioka[1,*], Naohiro Ueno[1], Toshihiro Okajima[2] and Kazuhiro Hara[1]
[1]Faculty of Engineering, Kyushu University, Fukuoka 802-3488, Japan
[2]SAGA-LS, Saga 841-0005, Japan

1 Introduction

Gallium oxide (Ga_2O_3) has many of functionalities, such as wide-gap semiconductor for transparent conductive thin film and catalysis for dehydrogenation of paraffin to olefin. Ga_2O_3 appears a polymorphism similar to aluminum oxide. Roy *et al.* reported five polymorphs of Ga_2O_3[1]. Among them, β phase which has a monoclinic structure is commonly formed under ordinary conditions. We have already reported the stability of these five phases by first principles lattice dynamics calculations[2]. Recently, many works related to metastable phases of Ga_2O_3 were reported through chemical or physical deposition and sol-gel routes. In this study, we prepare Ga_2O_3 polymorphs by sol-gel method and investigate the local structure of them by XAFS.

2 Experiment

A total amount of 1 g gallium nitrate hydrate was solved in 50 ml water. A aqueous ammonia solution which was diluted in water (50 vol.%), was slowly added to this solution until no further precipitate was observed. The resulting gels were separated from the solutions with filter papers and were immediately washed with water. The obtained solids were calcined on a platinum foil in electric furnace at each temperature, 500, 600 and 700 ºC for 1 hour. Ceramic specimens were powdered before structure analysis.

Ga *K*-edge XAFS spectra were obtained at BL-7C of Photon Factory (PF) in High Energy Accelerator Research Organization (KEK). All of the spectra were recorded in transmission mode at room temperature with Si(111) double crystal monochromator. Specimens are diluted by high purity hexagonal type boron nitride powder before measurement.

3 Results and Discussion

The XRD measurements of samples were performed with versatile Cu-tube type instruments. The diffraction patterns of the sample calcined at 500 ºC and 700 ºC are indexed as α-Ga_2O_3 with corundum structure and β-Ga_2O_3, respectively. The profile of the sample calcined at 600 ºC is mixed with α-Ga_2O_3 and β-Ga_2O_3. Ga *K*-edge XANES spectra of these samples are showed in Fig. 1, together with standard sample of β-Ga_2O_3. The spectrum of α-Ga_2O_3 (calcined at 500 ºC) shows single peak at 10376 eV. Alpha phase of Ga_2O_3 has only one Ga site, which is octahedral. On the other hands, β-Ga_2O_3 spectrum has a peak with a shoulder at which is located at 10372 eV (indicated with an arrow in Fig. 1). Beta phase has equal numbers of two kind Ga sites, tetrahedral and octahedral ones. Theoretical XANES spectrum of β-Ga_2O_3 performed by first principles calculation shows that the rising edge of spectra is mainly composed by tetrahedral site and strong main peak is composed by octahedral site[3]. In comparison to the standard sample β-Ga_2O_3, the ration of intensity between the main peak and shoulder in the spectra of the sample calcinated at 700 ºC which is assigned as β phase by XRD, is slightly different. It shows that atom arrangement in long range is composed, but local structure is not conclusively laid out as β-Ga_2O_3.

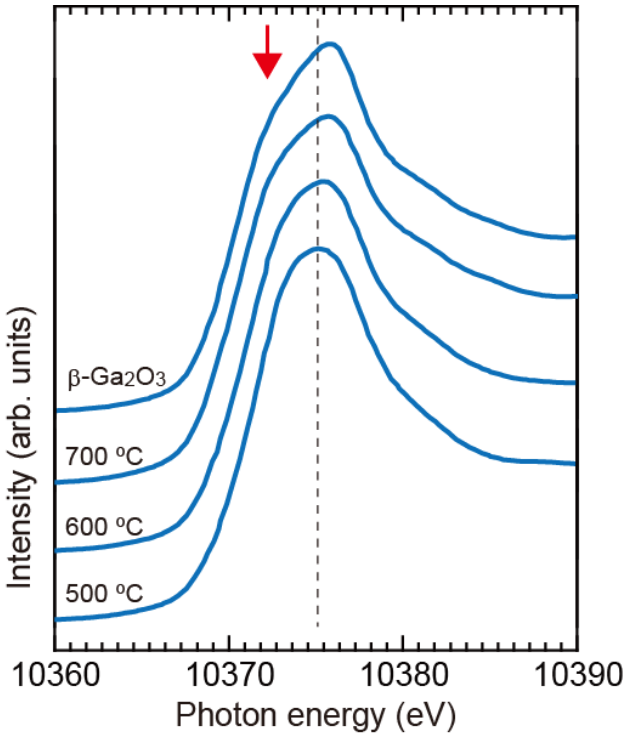

Fig. 1: Ga *K*-edge XANES spectra of samples prepared with water and calcined at each temperature for 1 h, together with that of β-Ga_2O_3 as a reference.

References

[1] R. Roy et al., J. Chem. Soc. 74 [3], 719-22 (1952)
[2] S. Yoshioka et al., J. Phys.: Cond. Mat. 19, 346211 (2007)
[3] I. Tanaka et al., Nature Mat. 2, 541-545 (2003)

* syoshioka@nucl.kyushu-u.ac.jp

2C/2008S2-003, 2011S2-003

Electronic Structure of the Cathode Material $Li_xFe_{0.5}Mn_{0.5}PO_4$ for Lithium-Ion Battery analyzed by Resonant Photoemission Spectroscopy

Koji Horiba[1,2,*], Shodai Kurosumi[1], Naoka Nagamura[1,2], Satoshi Toyoda[1,2], Hiroshi Kumigashira[3,4], Masaharu Oshima[1,2], Sho Furutsuki[5], Shin-ichi Nishimura[5], Atsuo Yamada[5], and Noritaka Mizuno[1]

[1] Department of Applied Chemistry, The University of Tokyo, Tokyo 113-8656, Japan
[2] Synchrotron Radiation Research Organization, The University of Tokyo, Tokyo 113-8656, Japan
[3] Photon Factory, Institute of Materials Structure Science, High Energy Accelerator Research Organization, Tsukuba 305-0801, Japan
[4] Precursory Research for Embryonic Science and Technology, Japan Science and Technology Agency, Kawaguchi 332-0012 Japan
[5] Department of Chemical System Engineering, The University of Tokyo, Tokyo 113-8656 Japan

1 Introduction

Olivine-type compounds Li*M*PO_4 [*M* = Fe, Mn, Co, Ni] is one of the most promising candidates for cathode materials of the lithium-ion battery, because of its prominent properties such as low cost, high level of safety and huge power generation. Especially, the solid solution $LiMn_yFe_{1-y}PO_4$ has attracted much attention due to relative high potential of Mn^{3+} / Mn^{2+} redox couple at 4.1 V vs. Li /Li^+, which generates the higher energy density. Although the change in the valence states of the transition metals accompanied with the delithiation has been reported so far, the detailed electronic structure of $LiMn_yFe_{1-y}PO_4$ has not been understood yet. Therefore, in this work, we focus on revealing experimentally the change in the electronic structure of $LiMn_{0.5}Fe_{0.5}PO_4$, especially in the transition metal 3*d* states through the charge process by resonant photoemission spectroscopy (PES).

2 Experimental

Pristine $LiMn_{0.5}Fe_{0.5}PO_4$ powders were synthesized by solid state reactions. Starting materials and 10 wt% carbon were mixed and sintered at 600 ^oC for 6 h under Ar gas flow. The characterization was performed by X-ray diffraction measurements. In order to obtain $Li_xMn_{0.5}Fe_{0.5}PO_4$ (x = 0, 0.5, 1), electrochemical delithiation process was carried out.

To investigate the electronic structure of Fe and Mn 3*d* states in $Li_xMn_{0.5}Fe_{0.5}PO_4$, we have performed Fe and Mn *L*-edge X-ray absorption spectroscopy (XAS) and the resonant photoemission spectroscopy (PES) at BL-2C of Photon Factory. In order to avoid moisture air exposure, we transferred the samples to a load lock chamber using a grove bag filled with dry-N_2 gas.

3 Results and Discussion

Figure 1 (a) shows Fe 2*p* – 3*d* resonant PES spectra of $Li_xMn_{0.5}Fe_{0.5}PO_4$ measured at the photon energy of Fe 2*p* – 3*d* absorption edges corresponding to the Fe^{2+} (R1) and Fe^{3+} (R2) states. The maximum intensity in the resonant PES spectra was observed at the excitation energy R1 for $LiMn_{0.5}Fe_{0.5}PO_4$, whereas that was observed at the excitation energy R2 for $Li_{0.5}Mn_{0.5}Fe_{0.5}PO_4$ and $Mn_{0.5}Fe_{0.5}PO_4$. Figure 1 (b) shows the resonant PES spectra of $LiFePO_4$ and $LiMn_{0.5}Fe_{0.5}PO_4$ measured at the excitation energy of R1, whereas Fig. 3 (c) shows those of $FePO_4$ and $Li_{0.5}Mn_{0.5}Fe_{0.5}PO_4$ measured at the excitation energy of R2. Comparing both resonant PES spectra at each excitation energy, we can find that both spectral-line shapes are almost identical, suggesting that the partial substitution of Fe by Mn does not influence the Fe 3*d* states significantly, which may be due to the strong localization of the Fe 3*d* states.

Acknowledgments

This research is supported by the Japan Society for the Promotion of Science (JSPS) through its "Funding Program for World-Leading Innovative R&D on Science and Technology (FIRST Program)."

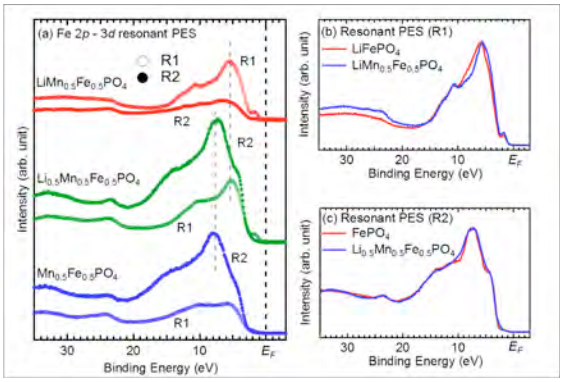

Figure 1. (a) Fe 2*p* – 3*d* resonant PES spectra of $Li_xMn_{0.5}Fe_{0.5}PO_4$. (b), (c) Comparison of Fe 2*p* – 3*d* resonant PES spectra between $LiMn_{0.5}Fe_{0.5}PO_4$ and $LiFePO_4$ measured at R1, and $Li_{0.5}Mn_{0.5}Fe_{0.5}PO_4$ and $FePO_4$ measured at R2, respectively.

3A/2008S2-004

Mn_3O_4 における磁場誘起相転移
Magnetic-field-induced Transition in Mn_3O_4

新居陽一 [1*], 佐賀山基 [1], 有馬孝尚 [1]
[1] 東京大学新領域創成科学研究科、〒277-8561 柏市柏の葉 5-1-5

1 はじめに

スピネル構造における八面体配位の B サイトはパイロクロア格子状に配列するため、磁性を持つイオンが B サイトに入ると、多くの場合、幾何学的フラストレーションが生じる。さらに、A サイトにも磁性イオンが入ると、B サイトの磁気モーメントは A サイトとの間に働く反強磁性的な超交換相互作用の影響を受ける。結果として、スピネル構造を有する磁性化合物では温度変化に伴う逐次磁気転移[1]、非共線的磁気秩序[2]、磁場誘起相転移[3]、磁気強誘電性[4]など興味深い現象が生じやすい。

Mn_3O_4 は、スピネル型磁性酸化物の一種である。B サイトを占有する Mn^{3+}イオン($3d^4$)の軌道占有が強的な秩序配列を取り、その結果、室温では、大変大きな共同ヤーンテラー歪みを伴う正方晶となっている[5]。一方、四面体配位の A サイトに入る Mn は二価($3d^5$)であり、軌道自由度は持たないが大きな磁気モーメント S=5/2 をもつ。冷却に伴う逐次磁気相転移は以前から知られていた[6]が、近年、磁場印加に伴う別の相転移が新たに発見された。図 1 が磁化や歪みの測定から得られている相図である。本研究では、低温の磁場誘起相の本質を知るために、Mn_3O_4 の交換歪の測定を行い、他の測定手法で得られた結果と比較した。

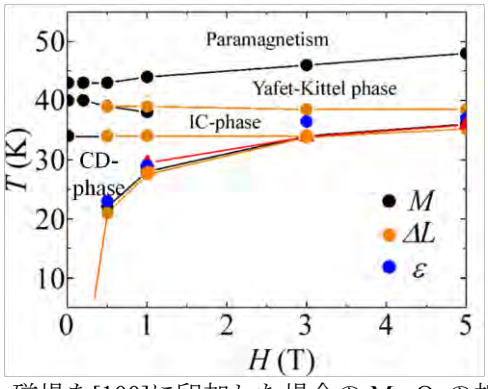

図 1 ：磁場を[100]に印加した場合の Mn_3O_4 の相図。

2 実験

試料には、フローティングゾーン法で育成した Mn_3O_4 の単結晶を用いた。面心正方晶[7]の単位胞で、(100)面を切り出した試料を BL-3A に設置されている超伝導磁石つきのクライオスタットの中に入れ、低温・強磁場下での回折実験を行った。磁場が[010]軸に平行に印加できる配置とした。回折計は横振りタイプであり、入射 X 線としては 14keV で散乱面に平行な偏光(π)のビームを用いた。

3 結果および考察

図 2 (a)に、ゼロ磁場下で (8+q q 0)に沿って測定したプロファイルの温度変化を示す。低温では q=1/2 の位置に超格子反射が観測される。34 K と 35 K の間で整合不整合転移が起きて、波数 q が 0.45 付近に飛ぶことが分かる。さらに昇温を続けると、q が小さくなるとともに反射強度が減少し、41 K で超格子反射は消滅する。図 2 (c)には、今回観測した変調波数 q と、中性子回折で観測した磁気超格子反射の波数との比較を示している。磁気変調と同じ波数で格子も変調を受けていることが分かる。

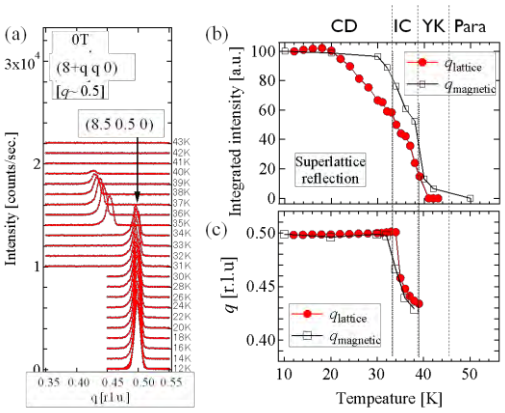

図 2 ：ゼロ磁場下での超格子反射の温度変化。(a) (8+q q 0)プロファイル。(b)超格子反射強度。(c)変調波数。(b),(c)には、中性子回折で測定した磁気超格子に関する情報も同時に載せてある。

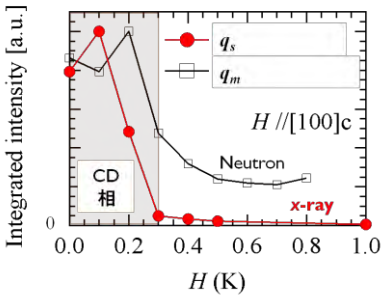

図 3 ：超格子反射強度の磁場変化。

次に、10 K で測定した超格子反射の磁場変化を図３に示す。0.3T 以上の磁場誘起相では超格子反射が消失することが分かった。同時に、磁場誘起相に入るとともに、8 0 0 反射の 2θ位置が一次転移的に 0.4%程度高角側へ飛ぶことも確認できた。すなわち、磁場方位方向と垂直な方向が縮んだ構造を取っている。

これらの結果を巨視的な磁歪や中性子回折のデータを比較することにより、次のような描像を得た。磁場を[010]軸に平行に印加すると、４つの Mn^{3+}で形成される四面体の辺の中で、[011]あるいは[01-1]軸に平行な Mn 対の間隔が伸びてフラストレーションを緩和し、そのスピン対が強磁性的に配列する。磁場印加に伴うスピン配列の変化を図４に示す。

この磁場誘起相転移の発現機構として、次のようなものを考えている。磁場印加前は、Mn^{2+}のスピンは<110>軸方向を向いており、巨視的な斜方晶歪みが小さくなるようにスピンが配列している。磁場を b 軸方向に印加すると、Mn^{3+}の磁気モーメントの ab 面内成分が磁場と反平行な向きに変わる。このとき、原子内のスピン軌道相互作用のため、3d 軌道に面内異方性が生じ、MnO_6 八面体を b 軸方向に伸ばそうとする。この歪みと同期するように、Mn^{3+}の磁気モーメントの c 軸成分の配列パターンが変化し、結果として、大きな磁歪が生じると考えられる。すなわち、この磁場誘起相転移は、原子内のスピン軌道相互作用とスピンの幾何学的フラストレーションの緩和のための交換歪の協力現象として捉えられる。

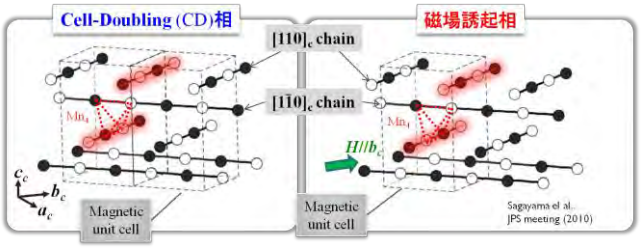

図４：[010]に磁場を印加した場合の磁気構造変化。Mn^{2+}の磁気モーメントは磁場と平行であり、簡単のため、省いてある。Mn^{3+}のモーメントは磁場と反平行な方向から±50 度ほど c 軸方向に傾く。図の黒丸と白丸は正負のどちらに傾くかを示している。

謝辞

単結晶試料の成長は阿部氏および梅津氏（当時東北大）によって行われました。また、超伝導磁石は、中尾氏、山崎氏ら 3A の担当者の皆様によって管理・運用されています。ここに謝意を表します。

参考文献

[1] 例えば、T. Katsufuji *et al.*, J. Phys. Soc. Jpn. **77**, 053708 (2008).
[2] Y. Yafet and C. Kittel, Phys. Rev. **87**, 290 (1952).
[3] 例えば、H. Ueda *et al.*, Phys. Rev. B **73,** 094415 (2006).
[4] Y. Yamasaki *et al.*, Phys. Rev. Lett. **96,** 207204 (2006).
[5] G. Aminoff, Z. Krist. **64**, 475 (1926).
[6] G. B. Jensen and O. V. Nielsen, J. Phys. C **7**, 409 (1974).
[7] 面心立方格子が c 軸に伸びた場合、本来ならば、正方晶相では体心正方晶になるように a,b 軸の方向を 45 度回転させて定義しなおすべきだが、相転移に伴う変化を議論するために、本報告では面心正方の単位胞を用いる。

* nii@cor.k.u-tokyo.ac.jp

14C1/2009G031

X 線 Talbot 干渉計と白色放射光によるダイラタント流体観察
Observation of Dilatant Fluid by X-ray Talbot Interferometry with White Synchrotron Radiation

百生敦 [1*], 山﨑岳 [2], 矢代航 [2], 桑原宏萌 [2]
[1] 東北大学多元研　〒980-8577 仙台市青葉区片平 2-1-1
[2] 東京大学新領域　〒277-8561 千葉県柏市柏の葉 5-1-5

1 はじめに

透過格子を用いる X 線 Talbot 干渉計は、柔軟で様々な形態の X 線位相ｲﾒｰｼﾞﾝｸﾞに使えるﾃﾞﾊﾞｲｽとして、近年注目が増している。ひとつの使い方として、白色放射光で動作させ、高速位相撮影がある[1]。もうひとつの興味深い特徴として、吸収画像、微分位相画像に加えて、散乱画像と呼べる新たな画像が得られるという事実がある。これは、試料による極小角散乱によって X 線の空間的干渉性が損なわれ、ﾓｱﾚ画像の鮮明度が低下することを捉えるものである。すなわち、試料内においてある範囲の散乱角に対応する極小角散乱が強いか弱いかでｺﾝﾄﾗｽﾄが付けられる。

以上の特徴を生かして、本研究ではﾀﾞｲﾗﾀﾝﾄ流体（ｺｰﾝｽﾀｰﾁの水の混合体）を散乱動画像で観察した。ﾀﾞｲﾗﾀﾝﾄ流体は急激な応力が加えられると固体のように振舞いを変える。その際、試料中の粒子の分散具合の変化に依存し、散乱画像ひ変化が現れることが期待される。そこで、試料ｾﾙに入れたﾀﾞｲﾗﾀﾝﾄ流体に棒を落下させ、そのときの散乱画像の変化を 1ms の時間分解能で観察した。

2 実験

BL-14Cにおいて得られる白色放射光に対して、28.8keVのX線に最適となる配置でX線Talbot干渉計を構築した。これは、π/2位相格子（G1）と振幅格子（G2）から成り、共に5.3μmの周期を持つL&Sﾊﾟﾀｰﾝを持つ。被写体の背後にG1を配置し、その下流326mmの位置にG2を置き、さらにその背後に画像検出器を設置した。高速撮影を可能とするために、この画像検出器は、CMOSｶﾒﾗ(pco.dimax, PCO AG)と20μm厚のP46蛍光ｽｸﾘｰﾝをﾚﾝｽﾞｶｯﾌﾟﾙしたものである。画素サイズ11.2μmを持つ。ﾌﾚｰﾑﾚｰﾄは1.7kf/sとした。

散乱画像を得るためには、位相計測で使っている縞走査法やﾌｰﾘｴ変換法で得られるﾃﾞｰﾀが使える。演算公式が異なるだけである。多くの場合、縞走査法が使われるが、格子を並進させて複数（例えば５枚）のﾓｱﾚ画像を撮影する必要があるため、高速撮影を目的とする本実験には望ましくない。そこで、ﾌｰﾘｴ変換法を採用した。これは、格子を傾けることにより生じる回転ﾓｱﾚをｷｬﾘｱﾌﾘﾝｼﾞとして使い、ﾌｰﾘｴﾌｨﾙﾀﾘﾝｸﾞにより微分位相像を得る方法である。一枚のﾓｱﾚ画像から一枚の微分位相像が得られるため、高速撮影に向いている。ただし、空間分解能はｷｬﾘｱﾌﾘﾝｼﾞの間隔によって決まるため、縞走査法に比べて空間分解能が劣るが、本実験では問題とはならない。

試料（ｺｰﾝｽﾀｰﾁの水の混合体）は底面10mm角の角柱ｾﾙに入れ、上部よりｱｸﾘﾙ棒を落下させた。

3 結果および考察

ｱｸﾘﾙ棒は、試料に入ると、そこに到達する前に上方に跳ね返った。すなわち、棒からの力により、棒の下部でﾀﾞｲﾗﾀﾝﾄ現象が起こったと考えられる。図１は棒が跳ね返る直前(a)および直後(b)の画像である。後者において、棒の下部でｺﾝﾄﾗｽﾄが発生している。

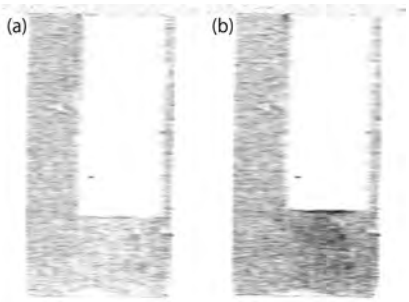

図１：散乱動画像によるﾀﾞｲﾗﾀﾝﾄ流体の観察。落下する重りにより流体が固くなった直後、ｺﾝﾄﾗｽﾄの変化が検出された。

4 まとめ

動的観察を可能とすることで、ms ｵｰﾀﾞｰのﾀﾞｲﾗﾀﾝﾄ現象によるｺﾝﾄﾗｽﾄを検出することに成功した。今後定量的実験を重ね、本結果の物理的理解と、さらには、ﾀﾞｲﾗﾀﾝｼｰの物理的理解に貢献したい。

謝辞

本研究は、JST 先端計測のｻﾎﾟｰﾄにより推進した。

参考文献

[1] A. Momose *et al*., Opt. Express **17** (2009) 12540.

* momose@tagen.tohoku.ac.jp

27A/2009G553

Orientation of one-dimensional silicon polymer films studied by polarization-dependent NEXAFS

Md. Abdul MANNAN[1,2], Yuji BABA[*1], Tetsuhiro SEKIGUCHI[1], Iwao SHIMOYAMA[1], Norie HIRAO[1], Masamitsu NAGANO[2], Hideyuki NOGUCHI[2]
[1]Japan Atomic Energy Agency, Tokai-mura, Naka-gun, Ibaraki 319-1195, Japan
[2]Department of Chemistry and Applied Chemistry, Saga University, Saga 840-8502, Japan

Introduction

Polysilanes composed of silicon-silicon backbone are considered to be ideal one-dimensional (1D) molecular wires with high electric conductivity. It has also been predicted that the polysilanes possess electronic structure similar to direct band-gap semiconductor. Since the electric and optical properties in thin films of 1D polymer strongly depend on the configuration of the molecular skeleton, it is much important to determine the precise molecular orientation of polymers on solid surfaces. In the previous paper, we have reported that the Si-Si skeleton of polydimethylsinane (PDMS) deposited on indium tin oxide (ITO) surface is perpendicularly oriented, and the polymer has a helical conformation rather than zig-zag structure with polar angle around 40° [1]. In this report, we present the results for the orientation of PDMS films grown on highly oriented pyrolytic graphite (HOPG) substrate and the results are compared with the previously obtained ones.

Experimental

All the experiments were performed *in situ* at the BL-27A station. The PDMS powder was evaporated by electron-bombardment heating. The evaporation rate was precisely controlled by monitoring the positive current of the shutter. The molecular orientations were investigated by Si *K*-edge NEXAFS measurements. The NEXAFS spectra were taken with the total electron yield mode.

Results and discussion

Fig.1(a) shows the Si *K*-edge NEXAFS spectra taken at different incident angles for 1.25 nm layer. The spectra show at least four resonance peaks of which two peaks are found to be strongly polarization dependent. The peak A is due to the resonance excitation from Si 1s to σ^* p_{yz} orbitals (plane type) localized at the Si–C bond, and the peak B corresponds to the resonance from Si 1s to σ^* p_x orbitals (vector type) localized at the Si–Si bond [2]. Fig.1(b) displays the normalized intensities of the peaks A and B as functions of the incident angle θ [3]. The filled circles are the experimental values. It is observed that the experimental values of the polar angles for both the vector and plane type orbitals follow the theoretical lines around 65°.

If the structure is flat-lying helical, α=48.5°, and γ=41.5°. For the flat-lying zig-zag configuration, there are two cases. One is that the Si–C plane is perpendicular to the surface. In this configuration, α=54.5° and γ=0°. The second case is that the Si–Si bond is parallel to the surface. In this configuration, α=90°and γ=0°. The experimental data show that α=65°, and γ=65°. The values are not exactly the same as those of the flat-lying helical structure. But if the configuration is flat-lying zig-zag, at least γ -value should be nearly 0 for both cases. Thus we tentatively assign that the configuration is flat-lying helical with the polar angle of around 65°.

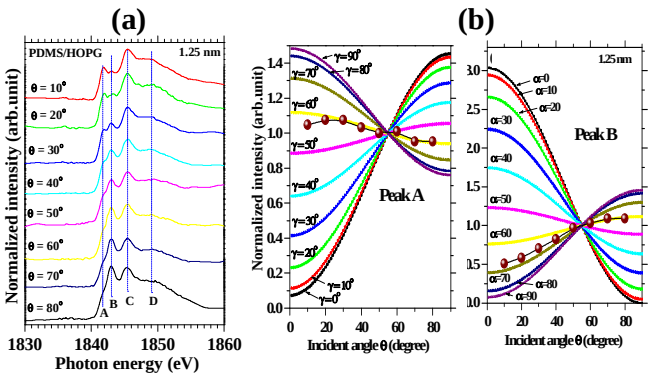

Fig.1 (a) Si *K*-edge NEXAFS spectra taken at different incident angles for multilayered PDMS film on HOPG. (b) Normalized intensity ***I*** of the peaks A and B in the NEXAFS spectra as a function of the incident angle θ. The filled circles are the experimental values.

As to the question why the orientations of the PDMS molecules are opposite between HOPG and ITO surfaces, we consider as follows. PDMS molecules lie down along the surface morphology through van-der-Waals force. The ITO surface is vertically undulated in the order of 10 nm. Therefore, the first layer of PDMS on ITO cannot lie down due to the stress, so PDMS molecules stand-up. On the other hand, HOPG has perfectly flat surface without defects and steps, so the first layer of PDMS can lie flat along the surface. It is considered that the succeeding over layers follow the orientation of the first layer.

References

[1] M.A. Mannan *et al.*, J. Electron Spectrosc. Relat. Phenom. **181,** 242 (2010).
[2] V.R. McCrary *et al.*, J. Chem. Phys. **88**, 5925 (1988).
[3] J. Stöhr, XEXAFS spectroscopy, Springer (1996).

* baba.yuji@jaea.go.jp

7C/2009G575

Free Volume in a cold-worked $Zr_{55}Cu_{30}Ni_5Al_{10}$ Bulk Metallic Glass

Osami Haruyama[1,*], Kazumasa Kogure[1], Toru Kawamata[2] and Kazumasa Sugiyama[2]
[1]Tokyo University of Science, Noda 278-8510, Japan
[2]Institute for Materials Research, Tohoku University, Sendai 980-8577, Japan

1 Introduction

It was reported that the volume fluctuation called the free volume is introduced into a plastically deformed amorphous alloy and metallic glass [1, 2]. However, the change in the glass structure of a deformed metallic glass has been insufficiently studied for recent years. The discovery of bulk metallic glasses (BMGs) gives us much opportunity to elucidate the structural properties in a deformed metallic glass. The high intensity x-ray of PF enables us to obtain new information of the details of plastically deformed BMGs.

2 Experiment

The $Zr_{55}Cu_{30}Ni_5Al_{10}$ BMG was prepared by the tilted cupper mold-casting technique [3] with a size of 14 mm in diameter and 30 mm in length. Two disks with a thickness of about 2 mm were cut from the rod shape BMG. One piece was thinned down into a fraction of about 90% by cold working at room temperature and another was regarded as the standard sample. The structure of both samples was investigated by a normal scattering technique with x-ray energy of selected 15.000 keV at BL7C station. The scattering experiment was performed with a vertical type two-axis goniometer and a SSD (Ge) detector. Then the scattering angle (2θ) was changed from 4 to 140 degrees. The coherent intensity of scattered photons was estimated from the diffracted beam and the structure factor, $S(Q)$, was derived, where Q is the magnitude of the scattering vector.

3 Results and Discussion

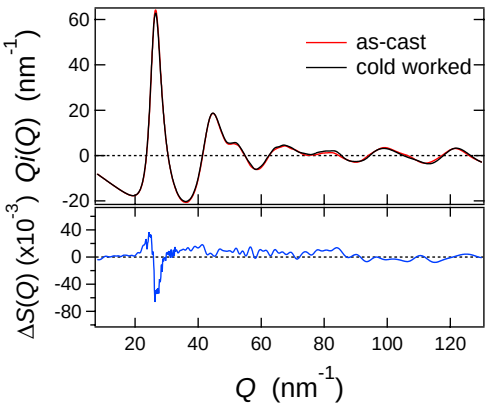

Fig. 1: $Qi(Q)$'s of as-cast, deformed BMGs and the difference of $S(Q)$.

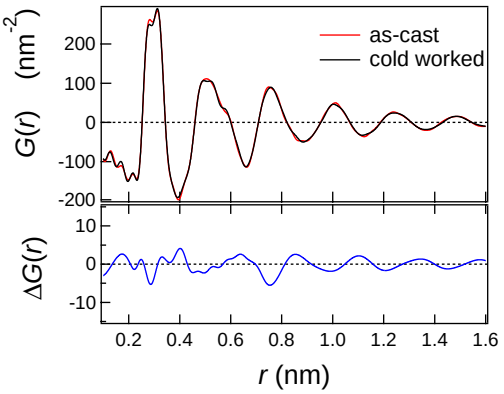

Fig. 2: $G(r)$'s of as-cast, deformed BMGs and the difference of $G(r)$.

The reduced radial distribution function, $G(r)$, was calculated by Fourier transformation of $S(Q)$. Figure 1 exhibits, $Qi(Q)=Q(S(Q)-1)$, of standard as-cast and 10% cold-worked BMGs and the difference of $S(Q)$, $\Delta S(Q) = S_{cw}(Q)-S_{as}(Q)$. The change in $S(Q)$ representatively appears around its first peak, i.e. a peak shift to lower side and a small broadening of peak. The corresponding $G(r)$'s are shown in Fig. 2 together with the difference, $\Delta G(r)=G_{cw}(r)-G_{as}(r)$. The overall behavior in $\Delta G(r)$ is definitely in anti-phase to both $G_{as}(r)$ and $G_{cw}(r)$, meaning that the amplitude of $G_{cw}(r)$ became smaller than the $G_{as}(r)$. The result suggests that the topological disorder of the as-cast BMG increased by cold working. The change in the glass structure by the structural relaxation was quantitatively investigated by the atomic level stress model [4]. Following this model, the $\Delta G(r)$ for structural relaxation was expressed as,

$$\Delta G(r) \approx -\tfrac{1}{2}\gamma^2 \partial^2 G_0 / \partial r^2 \left(\left\langle p^2 \right\rangle_{as} - \left\langle p^2 \right\rangle_{relax} \right),$$

where $\langle p^2 \rangle$ is the fluctuation of the atomic level hydrostatic pressure, and γ^2 is the r-dependent parameter approximately equivalent to a constant over first peak of $G(r)$. The G0(r) is the reduced radial distribution function from the region with almost 0 pressure, and it is actually approximated by the $G(r)$ in as-cast state. In case of structural relaxation, the $\Delta G(r)$ changed in phase to a minus second derivative of $G_{as}(r)$, $-\partial^2 G_0/\partial r^2$, and consequently a positive change in $\langle p^2 \rangle_{as} - \langle p^2 \rangle_{relax}$ was obtained. The result was interpreted as the decrease of topological disorder, i.e. the fluctuation of atomic level stress. Figure 3 plots $-\partial^2 G_0/\partial r^2$ against the distance, r,

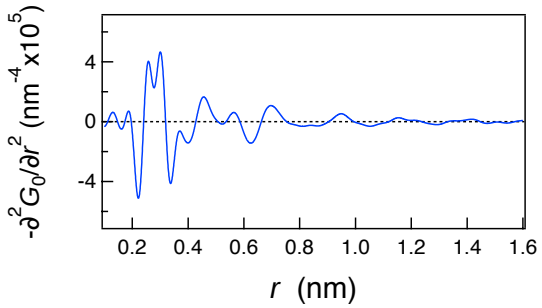

Fig. 3: $-\partial^2 G_0/\partial r^2$ of as-cast $G(r)$

where the curve was smoothed by cubic spline functions after the subtractive calculation. We can easily see an anti-phase behavior of $-\partial^2 G_0/\partial r^2$ against $\Delta G(r)$, meaning that $\langle p^2\rangle_{as}$-$\langle p^2\rangle_{cw}$ becomes a negative value, and it is an opposite sign to the structural relaxation. Thus we conclude that the volume fluctuation, which is characterized by the atomic-level stress, increases after plastically deforming BMG. The result consists with the volume and enthalpy change of cold-worked $Zr_{55}Cu_{30}Ni_5Al_{10}$ BMG [5].

References

[1] Y. Waseda and T. Egami, J. Mater. Sci., **14** (1979) 1249.
[2] D. Deng and B. Lu, Scr. Met., **17** (1983) 515.
[3] Y. Yokoyama, K. Yamano, K. Fukaura, H. Sunada and A. Inoue, Mater. Trans., **42** (2001) 623.
[4] D. Srolovitz, T. Egami and V. Vitek, Phys. Rev. B, **24** (1981) 6936.
[5] O. Haruyama *et al*., Acta mater. to be submitted.

* haruyama@ph.noda.tus.ac.jp

11A, 7C, 9A /2009G619

XAFS studies for Al dopants in transparent conductive ZnO thin films

Yoshiki Okuhara*[1], Yasutoshi Mizuta[1], Yoshihiro Kato[2], Norifumi Isu[2], Chiya Numako[3]
[1] JFCC, 2-4-1 Mutsuno, Atsuta-ku, Nagoya, Aichi 456-8587, Japan
[2] LIXIL Corporation, 3-77 Minatomachi, Tokoname, Aichi 479-8588, Japan
[3] Chiba University, 1-33 Yayo-cho, Inage-ku, Chiba 263-8522, Japan

Introduction

Transparent conductive oxide films have been widely utilized as transparent electrodes for flat panel displays, photo-voltaic solar cells and so on. The authors have developed aluminum-doped zinc oxide (ZnO:Al) films as solar heat shielding coatings [1, 2]. Suitable substitution of doped-Al^{3+} for Zn^{2+} sites generates free electrons, which make the films conductive and near-infrared reflective. This study aimed to investigate the influence of the local structure of Al dopants on carrier generation efficiency.

Experimental

Thin films of ZnO:Al were prepared on SiO_2 substrates by reactive sputtering process using metallic Zn and Al targets under Ar+O_2 atmosphere. The sputtering voltage of the Al target and the oxygen flow rate during sputtering affected not only the Al content but also the carrier generation efficiency.

Zn K-edge XAFS spectra for the ZnO:Al films were measured at the BL-9A and 7C station of the KEK PF rings in fluorescence yield mode using a Lytle detector. Al and oxygen K-edge XANES spectra were acquired at the BL-11A station in total electron yield mode in vacuum ambient (<10^{-5} Pa).

Results and Discussions

Under suitable doping of Al at Al sputtering voltage of 250 V, lowering O_2 flow rate to 1.70 sccm enhanced carrier generation efficiency and near-infrared reflectance.

Despite the small amount of Al dopants in the ZnO films less than 2 at.%, the XANES spectra for the Al K-edge were able to be observed as shown in Fig.1. The ZnO:Al film prepared under high O_2 flow rate of 2.15 sccm had the carrier generation efficiency of 4%, while low O_2 flow rate of 1.70 sccm caused drastic enhancement of the efficiency to 66%. Therefore, this result indicated that the Al dopants with higher carrier generation efficiency were found to have the Al K-edge absorption at higher energy level resulting from low electron density around the doped-Al. The shift in absorption energy is not due to a band gap widening because there was no shift in absorption energy for the oxygen K-edge XANES spectra. The spectral profiles preserved similar shape, implying that the low electron density around the doped-Al is attributed to more effective generation of free electrons rather than oxidization of Al.

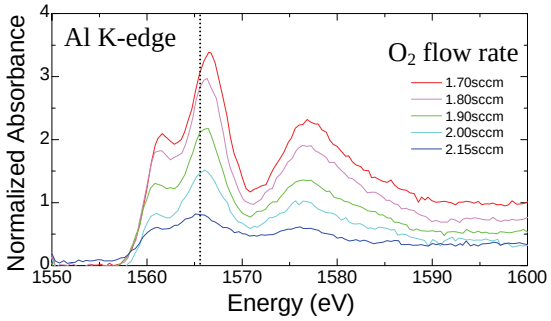

Fig.1 XANES spectra of the Al K-edge for the ZnO:Al films. These films were prepared by applying Zn sputtering power of 60W and Al sputtering voltage of 250V under various O_2 flow rates.

The Al K-edge features broadened with increasing O_2 flow rate. This behavior is attributed to deterioration of local structure around the Al dopants. In contrast, XANES spectrum of Zn K-edge had no broadening even at high O_2 flow rate, suggesting that the deterioration of local structure occurred only around the Al dopants.

In summary, optimization of ambient oxygen content to the lower limit provided successful substitution of Al for Zn sites. The efficient generation of electrons and the conservation of local structure around the appropriately doped Al were revealed by the XANES spectra in Fig.1.

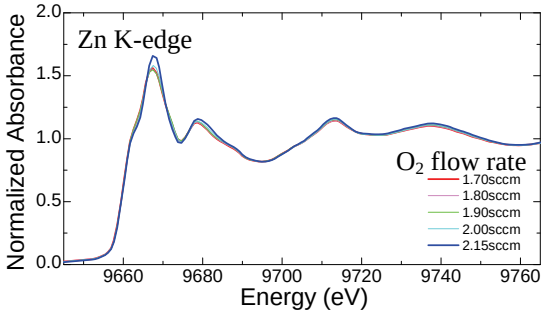

Fig.2 XANES spectra of the Zn K-edge for the same ZnO:Al films.

Acknowledgements

This work was supported by NEDO as “The Project of Development of Multi-ceramic Films for New Thermal Insulators”.

References

[1] Y. Okuhara et al., Thin Solid Films, 519, 2280 (2010).
[2] Y. Okuhara et al., Mater. Sci. Eng., accepted.

* okuhara@jfcc.or.jp

10C/2009G622

Coagulated structure of NBR/SBR blends by SAXS

Junhyeok JANG, Hirohisa YOSHIDA*
Department of Applied Chemistry, Graduate School of Environmental Science, Tokyo Metropolitan University, Hachiouji, Tokyo 192-0397, Japan

Introduction

Acrylonitrile-co-butadiene rubber (NBR) and styrene-co-butadiene rubber (SBR) are key amorphous components in the rubber industry. NBR/SBR blend are immiscible blend, the mixing state in NBR/SBR blend solution influences the phase separation structure and the mixing state of NBR/SBR blend solid film [1]. In this study, NBR/SBR blend films with various fractions and temperature were investigated by SAXS.

Experiments

SBR (Zeon Co., Nipol 1502, styrene composition 23.5 %) and NBR (Zeon Co., Nipol 1042, acrylonitrile composition 33.5 %) were mixed in THF and toluene solutions with 3 wt%. NBR/SBR blend film was prepared by casting from each solution. THF was good solvent for NBR and toluene was good solvent for SBR. Blend fraction was indicated by SBR weight fraction as ϕ_{SBR}.

Small-angle X-ray scattering (SAXS) experiments of PMMA and PMMA-SiO_2 composites were performed at 25 °C using the SAXS optics at the beam line 10C, Photon Factory, High Energy Accelerator Research Organization, Tsukuba, Japan. The wavelength of X-ray (λ) used was 0.15 nm. The accumulation time of SAXS measurement was 300 sec. The scattering vector ($q = (4\pi \sin\theta)/\lambda$) covered from 0.02 to 5 nm^{-1}, 2θ was the scattering angle. The simultaneous DSC [2] was setting on the optics.

Results

SAXS profiles of NBR on heating were shown in Fig.1. SAXS profiles were obtained at 70, 80, 90, 100, 110, 120, 130, 140, 150 and room temperature after cooling form 150 °C from the top. SAXS profile of NBR at room temperature indicated single scattering peak at q = 2.24 nm^{-1}, and the peak shifted to the low q side with the increase of temperature up to 70 °C. The peak shift stopped above 70 °C, and the small peak appeared at 2.05 nm^{-1}. The new peak shifted to the low q side and the peak intensity decreased with the increase of temperature and varnished at 120 °C. After cooling the scattering peak scarcely observed at room temperature.

SAXS profiles of NBR/SBR blends prepared by solvent casting from THF solution were shown in Fig.2. NBR and NBR/SBR blends had the scattering peak at 2.24 nm^{-1} and the scattering peak at around 2 nm^{-1}, the peak position depended on ϕ_{SBR}, in the ϕ_{SBR} range from 0.1 to 0.6. SAXS profiles for NBR/SBR blends prepared from toluene showed one broad scattering peak at 2.4 nm^{-1} in the ϕ_{SBR} range from 0.1 to 0.6. From these results suggested that the scattering peak was due to the coagulation of acrylonitrile sequences.

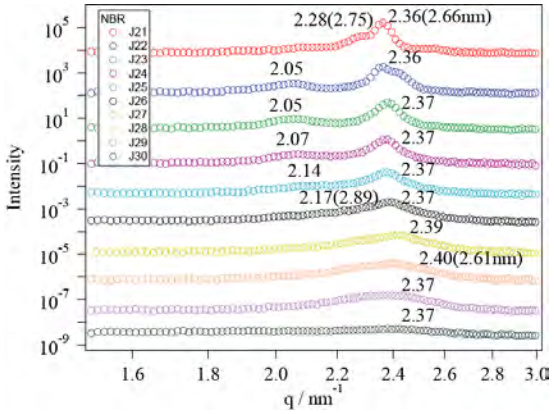

Fig1. SAXS profiles of NBR at various temperature from 70 to 150°C.

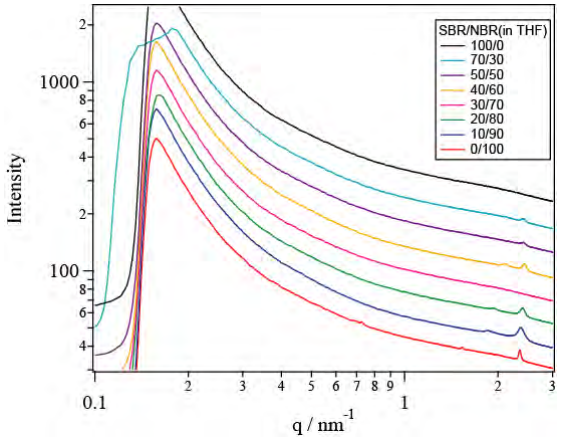

Fig2. SAXS profiles of NBR/SBR blend with various blend fraction prepared from THF solution.

References

[1] J. Jang, H. Yoshida, M. Kawazoe, *Netsu Sokutei*, **W39**, 33-39 (2012)
[2] H. Yoshida, R. Kinoshita, Y. Teramoto, *Thermochimica Acta*, **264**, 173-183 (1995)

* yoshida-hirohisa@tmu.ac.jp

10C/2009G651

Micro-structural Analyses of UV-Irradiated AAm/SA Gels

Satoru Yoshioka*[1], Yoshio Uemoto[1], Masaaki Sugiyama[2], and Kazuhiro Hara[1]
[1]Faculty of Engineering, Kyushu University, Fukuoka 802-3488, Japan
[2] Kyoto University Research Reactor Institute, Kyoto University, Sennan, 590-0494, Japan

1 Introduction

Some polymer gels with ionic groups can adsorb harmful heavy-metal ions and can be usable as a kind of purifying materials of the waste-water. The authors have conceived the idea of photolysis of the gel's surface with ultraviolet (UV) irradiation for effective heavy-metal ion swelling. It is because the gel's network gets contracted on adsorbing heavy-metal ions and the follow-on ions cannot easily permeate into the gel's inside. After UV-irradiating process, on the macroscopic observation, the gels turn opaque the by adsorbing copper ion, unlike with the sample not UV-irradiated. The nano-structures of gels were expected to change by the UV-irradiation judging from occurrence of the considerable turbidity, which can be reflected in the adsorbed-Cu distribution. In this study, the authors have investigated the UV-irradiation effect on the microstructure of poly-acrylamide/sodium acrylate (AAm/SA) gel by Small Angle X-ray Scattering (SAXS), using a synchrotron light source.

2 Experiment

The AAm gels were synthesized by a free-radical polymerization. The wet gels were irradiated to UV light with a versatile lamp. The intensity of UV light is 170 mW/cm^2 and exposure times are from 0 to 900 sec. We choose cupper as heavy-metal ions capturing by gels. In the adsorbing process, these gels were soaked in 0.1 M $CuCl_2$ control solution for 96 hours. SAXS measurements were carried out at the BL10C in KEK-PF. Scattering Patterns were measured at room temperature by using Position Sensitive Proportional Counter. The camera length was settled about 2 m with the X-ray wavelength λ of 1.5 Å.

3 Results and Discussion

Figure 1 is the SAXS profiles of the gels adsorbing copper ions after UV-irradiation. As can be seen from this figure, distinct peaks indicating a regular nano-structure are different in the position and the shape. As UV-irradiation time is longer, the peak-positions in transverse shit to lower: for as-prepared gel, the position of peak is around 0.020 Å^{-1} while 0.015 Å^{-1} for UV-irradiated one (900 seconds). This change is corresponding to an increase by 33 % in periodic length of a regular nano-structure. Besides, the breadths of the peaks get narrower by UV-irradiation. From these results, there are possibilities that the gel's network structure changes by UV-irradiation and the distribution of copper ions is influenced.The gyration radii estimated by the Guinier plots are listed on Table I together with the results from Small Angle Neutron Scattering (SANS). It is indicated that the size of gyration radii from SAXS have a negative correlation with those from SANS.

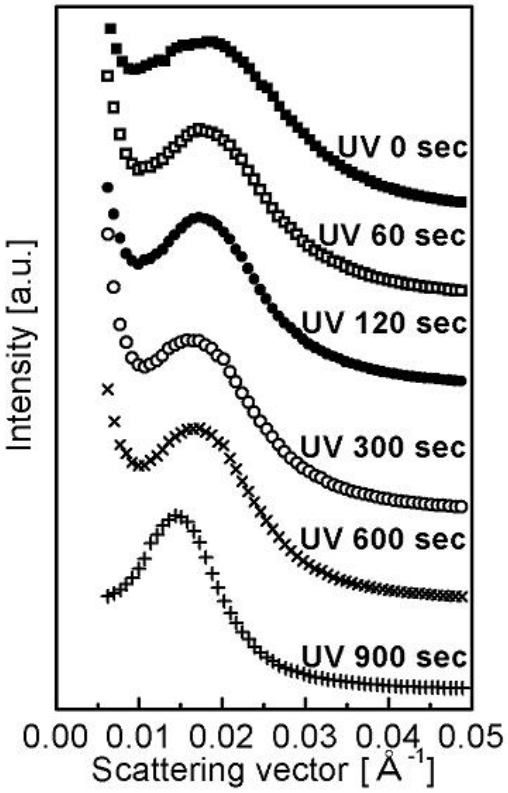

Fig. 1: SAXS profiles of AAm/SA gels with different exposure times of UV light.

Table I: The gyration radii estimated by the Guinier plots.

exposure time [sec.]	Gyration radius [Å]	
	SAXS	SANS
0	330	75
300	370	69

* syoshioka@nucl.kyushu-u.ac.jp

10C/2009G651, 2011A1955

Nano-structure Analysis of Poly(acrylamide-co-maleic acid) Gels by SAXS

Satoru Yoshioka[1,*], Ahamad Hassan[1], Toshio Ishioka [2], Toshihiro Okajima[3], and Kazuhiro Hara[1]
[1]Faculty of Engineering, Kyushu University, Fukuoka 802-3488, Japan
[2]Interdisciplinary Graduate School of Engineering Sciences, Kyushu University, Fukuoka 816-8580, Japan
[3]SAGA-LS, Saga 841-0005, Japan

1 Introduction

Polymer gels have been paid many attentions in various industrial and technological fields. Composed of cross-linked polymer chain (known as polymer network) and solvent, they were proven as a promising candidate for heavy- and rare-metal ion adsorbents: it has been demonstrated that acrylamide-co-sodium acrylate (AAm/SA) gels show considerably high weight ratio of captured metal to absorbent; and, in the ion-capturing process, it was understood that the carboxyl group of sodium acrylate acts as a complexing agent for the metal ions. The absorbing ability is naturally considered to be higher if more carboxyl groups are introduced in the polymer network; and, in this sense, introduced maleic acid (MA) containing plural carboxyl groups as the complexing agent instead of sodium acrylate. However, under certain synthesis conditions, the AAm/MA gels were found to be turbid indicating existence of inhomogeneity in the gels, which has been known to be undesirable for metal ion adsorption. Therefore, it was necessary to elucidate the synthesis conditions that cause the cloudiness in the AAm/MA gel and the corresponding inhomogeneous structure in order to develop the high-performance metal ion capturing gels. The objects of this study is to quantify the opaqueness of the AAm/MA gels, to make clear the conditions where to opaqueness occurs and to investigate the nanostructures of the turbid AAm/MA gels.

2 Experiment

Synthesized were the AAm/MA gels with various ingredients composition, 0.7, 1.4, 2.1 M in (AAm + MA) concentration, 6:1, 5:2, 4:3 in AAm/MA molar ratio and 12, 25, 37 mM in BIS (N, N'-methelynebisacryamide; cross-linker) concentration.

Nano-structures of the gels were investigated by the small angel X-ray Scattering (SAXS) performed at the BL40B2 in SPring-8. Scattering Patterns were measured at room temperature by using Imaging plate (Rigaku R-AXIS VII). The camera length was settled about 2 m with the X-ray wavelength λ of 1.5 Å.

3 Results and Discussion

Figure 1 shows the SAXS profiles of the AAm/MA gels, in which one can observe the scattered X-ray intensities in the low scattering-vector region are stronger as is the concentration of cross-linker increased. The gyration radii estimated by the Guinier plots are listed on Table I, The turbidities of the AAm/MA gels were found to increase (namely, the transmissivity decrease) with the cross-linker concentrations by utilizing a spectrophotometer at 600 nm. It is indicated that the gyration radii have a positive correlation with the turbidities of the gels.

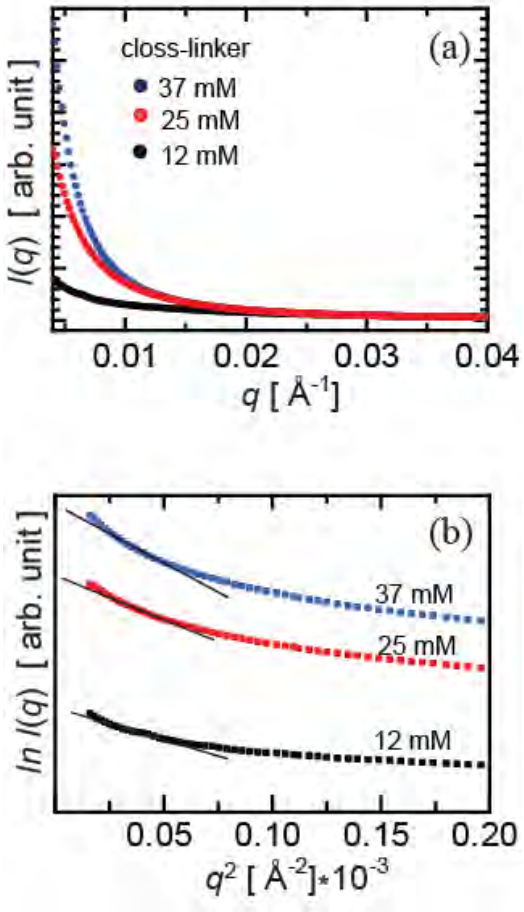

Fig. 1: SAXS profiles of AAm/MA gels at different cross-linker concentration. Total monomer concentrations and MA molar ratios were 1.4 M and AAm : MA = 5:2, respectively.

Table I: The gyration radii estimated by the Guinier plots.

Concentration of cross-linker [mM]	12	25	37
Gyration radii [Å]	130	160	190

* syoshioka@nucl.kyushu-u.ac.jp

3A/2009S2-003

B-site ordering state in double-perovskite La_2CrFeO_6 films

Daisuke OKUYAMA*[1], Suvankar CHAKRAVERTY[1,2], Akira OHTOMO[2,3], Mitsuhiro SAITO[4], Masaki OKUDE[2], Reiji KUMAI[5], Taka-hisa ARIMA[6], Yoshinori TOKURA[1,7], Susumu TSUKIMOTO[4], Yuichi IKUHARA[4,8], Masashi KAWASAKI[1,2,4,7]

[1]CMRG/CERG, ASI, RIKEN, Wako 351-0198, Japan
[2]Institute for Materials Research, Tohoku University, Sendai 980-8577, Japan
[3]Department of Applied Chemistry, Tokyo Institute of Technology, Tokyo 152-8552, Japan
[4]WPI-Advanced Institute for Materials Research, Tohoku University, Sendai 980-8577, Japan
[5] CMRC, Institute of Materials Structure Science, KEK, Tsukuba 305-0801, Japan
[6]Department of Advanced Materials Science, University of Tokyo, Kashiwa 277-8561, Japan
[7]Department of Applied Physics, University of Tokyo, Tokyo 113-8656, Japan
[8]IEI, University of Tokyo, Tokyo 113-8656, Japan and Nanostructures Research Laboratory, JFCC, Nagoya 456-8587, Japan

Introduction

Double-perovskite La_2CrFeO_6 has been intensively studied because there is a possibility to have a ferri-magnetic ground state with a net spin moment $2\mu_B$/f.u. through the $3d^3$(Cr)-$3d^5$(Fe) superexchange interaction [1]. In contrast, the (111)-oriented $LaCrO_3/LaFeO_3$ super-lattice shows ferromagnetism, though the measured saturation magnetic moment is much less than the expected value [2]. To clarify this inconsistency, we fabricated La_2CrFeO_6 films on (111)-oriented $SrTiO_3$ substrates using pulsed-laser deposition method under the various conditions and examined the degree of order of Cr and Fe by using synchrotron x-ray diffraction.

Experimental results and Discussions

Fig. 1(a) shows a schematic crystal-structure model of (111)-oriented La_2CrFeO_6 film. From the model with the antiside disorder (*AS*) fraction, which is defined as the percentage of misplaced Cr at Fe site and vice versa, and atomic displacement of La and O ions towards Fe-rich transition-metal-site plane (δ_{La} and δ_O), we calculated the structure factor at each reciprocal lattice point as follows:

$F_{(1/21/21/2)}=(1\text{-}2AS)(f_{Cr}\text{-}f_{Fe})+2f_{La}\sin(3\pi\delta_{La})+6f_O\sin(3\pi\delta_O)$
$F_{(111)}=f_{Cr}+f_{Fe}\text{-}2f_{La}\cos(6\pi\delta_{La})\text{-}6f_O\cos(6\pi\delta_O)$
$F_{(3/23/23/2)}=(1\text{-}2AS)(f_{Cr}\text{-}f_{Fe})\text{-}2f_{La}\sin(9\pi\delta_{La})\text{-}6f_O\sin(9\pi\delta_O)$
$F_{(222)}=f_{Cr}+f_{Fe}+2f_{La}\cos(12\pi\delta_{La})+6f_O\cos(12\pi\delta_O)$
$F_{(5/25/25/2)}=(1\text{-}2AS)(f_{Cr}\text{-}f_{Fe})+2f_{La}\sin(15\pi\delta_{La})+6f_O\sin(15\pi\delta_O)$
$F_{(333)}=f_{Cr}+f_{Fe}\text{-}f_{La}\cos(18\pi\delta_{La})+f_{La}\cos[9\delta(1+2\delta_{La})]$
$\text{-}3f_O\cos(18\pi\delta_O)+3f_O\cos[9\pi(1+2\delta_O)]$

Here, f_{Cr}, f_{Fe}, f_{La}, f_O, and $F_{(hhh)}$ represent atomic form factors of Cr, Fe, La, O, and structure factor of (*h h h*) reflection, respectively. The calculated intensity *I* was obtained from $I=FF^*\times L\times p\times N$. *L*, *p*, and *N* are Lorentz factor, polarization factor, and scale factor, respectively.

From the analyses of experimental data, the *AS* ratio of the condition A, B, D samples are estimated as 0.051, 0.145, 0.34, respectively (Fig. 1(b-d)). By using these samples, the magnetic field and temperature dependences of the magnetization are measured (Fig.1 (e, f)). The samples with the high degree of order (A and B) show ferromagnetic orders with $2\mu_B$/f.u. magnetic moment, which is consistent with previous theoretical prediction [1]. In contrast, the sample of the low degree of order (C) shows a ferromagnetism with a small magnetic moment. Detailed information are reported in ref. [3].

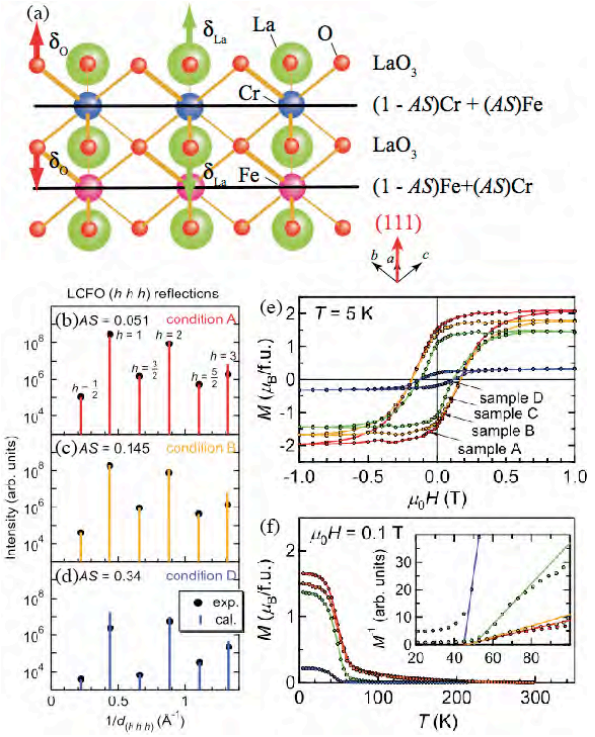

Fig. 1: (a) The schematic model of La_2CrFeO_6 thin film. (b-d) X-ray diffraction results of the samples grown under conditions A, B, and D. The observed intensity and calculated one are indicated by circles and bars, respectively. (e,f) Magnetic field and temeratpure dependences of the magnetization.

References

[1] W. E. Pickett, Phys. Rev. B **57** (1998) 10613.
[2] K. Ueda *et al.*, Science **280** (1998) 1064.
[3] S. Chakraverty *et al.*, Phys. Rev. B **84** (2011) 064436.
* okuyama@riken.jp

8A/2009S2-003

Molecular Displacement Directing Antiparallel to Macroscopic Polarization in TTF-CA

Kensuke Kobayashi,[1*] Sachio Horiuchi,[2,3] Reiji Kumai,[1,2,3] Fumitaka Kagawa,[3,4] Youichi Murakami,[1] and Yoshinori Tokura[2,4,5]

[1]Condensed Matter Research Center (CMRC) and Photon Factory, Institute of Materials Structure Science, High Energy Accelerator Research Organization (KEK), Tsukuba, 305-0801, Japan.
[2]National Institute of Advanced Industrial Science and Technology (AIST), Tsukuba, 305-8562, Japan.
[3]CREST, Japan Science and Technology Agency (JST), Tokyo 102-0076, Japan.
[4]Department of Applied Physics, University of Tokyo, Tokyo 113-8656, Japan.
[5]Correlated Electron Research Group (CERG) and Cross-correlated Materials Research Group (CMRG), ASI-RIKEN, Wako 351-0198, Japan

Introduction

The organic charge-transfer complex TTF-CA comprised of an electron donor, tetrathiafulvalene (TTF) and an acceptor, *p*-chloranil (CA) have been attracting much attention because of novel ferroelectric neutral-to-ionic phase transition [1]. Recently, in contrast to conventional point-charge picture, the first-principles calculations invoked a much larger spontaneous polarization (3~10 μCcm^{-2} along the *a*-direction) with two contrasting candidates of electronic states [2]. The total polarization is predicted to direct either parallel or antiparallel to the ionic polarization, depending on the antiferromagnetic or nonmagnetic state. Such predictions strongly motivated us to experimentally determine both the magnitude and the direction of spontaneous polarization.

Experimental Results and Discussions

The symmetry-breaking of TTF-CA crystal structure under electric field was probed by the intensity difference between Bijvoet pair (*hkl* versus $\bar{h}\bar{k}\bar{l}$) reflections, which arises from the anomalous x-ray scattering effect. The simulation based on the crystal structures at T = 15 and 40 K [3] predicts that the Bijvoet pair reflections 101 and $\bar{1}0\bar{1}$ have sufficient intensities and are the most susceptible to the anomalous x-ray scattering for x-ray wavelength λ = 1.55 Å used. Figure 1 depicts the temperature dependence of their normalized integrated intensity $I_+ \equiv I(101)/\{I(101) + I(\bar{1}\bar{0}\bar{1})\}$ and $I_- \equiv I(\bar{1}\bar{0}\bar{1})/\{I(101) + I(\bar{1}\bar{0}\bar{1})\}$. Just below T_c, the observed I_+ and I_- readily approach 0.705 or 0.295 (horizontal broken lines in Fig. 1), which corresponds to the full polarization into either polarity according to the simulation. Therefore, the poling field of 4 kVcm^{-1} is regarded as sufficient for developing a single-domain state. By comparing the observed intensity of Bijvoet pair (I_+ and I_-) with the simulation, we found that the positively charged TTF molecules shift toward the positive electrode and the negatively charged CA toward the negative electrode. These experimental observations confirm recent first-principles calculations predicting an extreme contribution of the electronic polarization, which directs antiparallel to the ionic displacement and governs the magnitude of polarization. The electronic ferroelectricity itself is currently one of the key issues for multiferroelectrics. The electronic response with less energetic cost of lattice deformations will promise both high-performance and high-frequency operations as well as new functionalities.

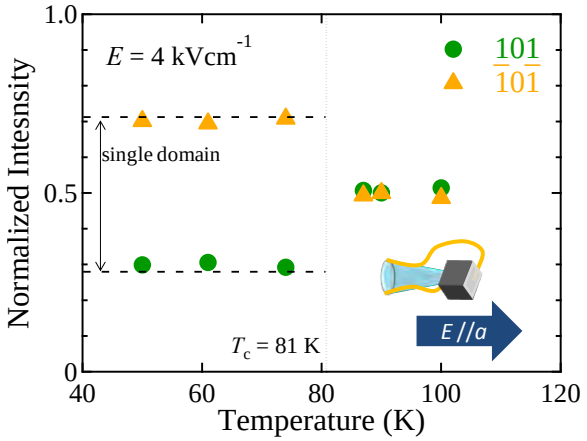

Fig. 1: Temperature dependence of normalized integrated intensities of Bijvoet pair reflections 101 and $\bar{1}0\bar{1}$ at constant E = +4 kVcm^{-1}. Inset shows a schematic drawing of diffraction experiment. Broken lines indicate calculated values of single domain model.

References

[1] J. B. Torrance *et al*., Phys. Rev. Lett. **46** (1981) 253.
[2] G. Giovannetti *et al*., Phys. Rev. Lett. **103** (2009) 266401, S. Ishibashi *et al*., Physica B **405** (2010) S338.
[3] M. Le Cointe *et al*., Phys. Rev. B **51** (1995) 3374, P. García *et al*., Faraday Discuss. **135** (2007) 217.

* kensuke.kobayashi@kek.jp

3A & 4C/2009S2-008

希薄不純物置換 $LaCoO_3$ 系におけるスピン状態ポーラロン発現の条件と物質の探査
Investigation of Conditions and Materials for Emergence of Spin-State Polarons in lightly impurity doped $LaCoO_3$ systems

富安啓輔 [1*], 久保田祐貴 [1], 下村紗耶 [2], 中尾裕則 [3]
[1] 東北大学 大学院理学研究科、〒980-8578 宮城県仙台市青葉区荒巻字青葉 6-3
[2] 東北大学 理学部、〒980-8578 宮城県仙台市青葉区荒巻字青葉 6-3
[3] 高エネルギー加速器研究機構 放射光科学研究施設、〒305-0801 茨城県つくば市大穂 1-1

ペロフスカイト型酸化物 $LaCoO_3$ (Co^{3+}: d^6) は、高・中間・低スピン状態という自由度を示す珍しい物質である。La サイトに Sr を 0.2 %ドープすると（ホールドープ）、10 μ_B/hole 以上もの巨大磁気モーメントが発現する[1]。Sr をさらにドープしていくと、巨大磁気抵抗、異常ホール効果、絶縁体金属転移などを示す[2]。これらの現象の共通の起源は、スピン状態自由度に由来する「スピン状態ポーラロン」にあると考えられている[3]。スピン状態ポーラロンという概念は比較的新しく、発現機構も未だ解明されていないが、Co^{4+}を核として周囲の Co^{3+}を非磁性の低スピン状態から磁性の中間／高スピン状態へ変化させることにより生成するスピンクラスターと提案されている（スピン分子 7 量体モデル）[3]。極低ホール濃度領域においては、互いに孤立したスピン状態ポーラロンが巨大磁気モーメントを伴う超常磁性を発現し、より高濃度領域においては輸送特性のキャリアを担うと期待される。

本研究では、スピン状態ポーラロンの発現機構の解明と、ホールドープとは異なる新種のスピン状態ポーラロンの創出を目指し、希薄不純物置換系 $La(Co_{0.99}M_{0.01})O_3$ (M = Cr, Mn, Fe, Ni) における磁化測定、放射光による蛍光 X 線測定、中性子散乱を行った。ここでは放射光実験の部分を紹介する。

PF の BL-3A と 4C にて、室温の K 吸収端近傍の吸収スペクトルを測定した。入射光のエネルギーを各ドープ元素の K 吸収端前後で変化させ、1%という低濃度ドープ元素の価数を評価するため、各ドープ元素の K_α線または K_α線と K_β線のみの散乱光を検出した。測定には、$La(Co_{0.99}M_{0.01})O_3$ (M = Cr, Mn, Fe, Ni) の単結晶、M^{3+}の参照物質として $LaMO_3$ (M = Cr, Mn, Fe) と $(LaSr)NiO_4$ の多結晶ペレットを用いた。

図 1 は測定結果を示す。Cr ドープ系のスペクトルは $LaCrO_3$ と良く一致し、これは Cr が 3 価であることを示す。Mn と Fe ドープ系のスペクトルは $LaMnO_3$ と $LaFeO_3$ より約 2 eV 高エネルギー側にシフトし、これは Mn と Fe が 3 価から 4 価側にずれていることを示す。Ni ドープ系のスペクトルの吸収端エネルギー位置は$(LaSr)NiO_4$ とおよそ一致し、これは Ni が 3 価であることを示唆する。

これらの価数評価の結果は、各ドープ元素の化学ポテンシャル（軌道／フェルミエネルギー）の大小と一致する。現在、スピン状態ポーラロンと化学ポテンシャルの関係を考察中である。

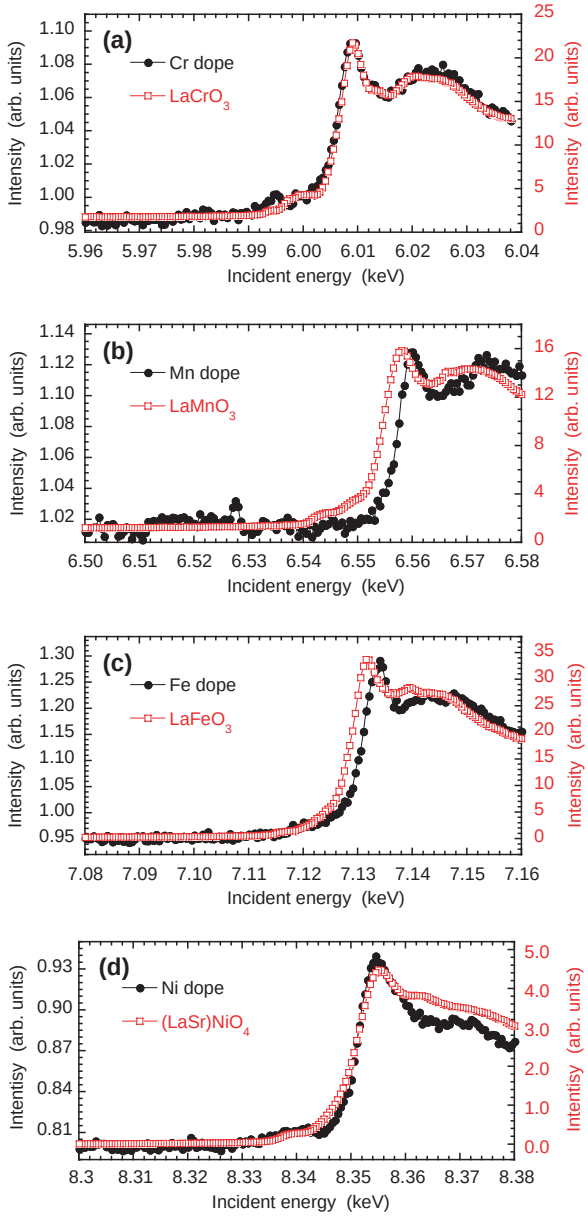

図 1 ：K 吸収端近傍のエネルギースペクトル

参考文献
[1] S. Yamaguchi *et al.*, PRB **53**, 6 (1996).
[2] 例えば Y. Onose *et al.*, PRB **73**, 174421 (2006).
[3] A. Podlesnyak *et al.*, PRL **101**, 247603 (2008).

* tomiyasu@m.tohoku.ac.jp

8A/2009S2-008

$LaCo_{1-x}Rh_xO_3$ における磁性と構造の相関

The structure-magnetism relationship in $LaCo_{1-x}Rh_xO_3$

浅井晋一郎 *[1]、古田倫靖 [1]、五十嵐太一 [1]、岡崎竜二 [1]、安井幸夫 [1]、寺崎一郎 [1]、
小林航 [2]、中尾朗子 [3]、須田山貴亮 [4]、小林賢介 [4]、熊井玲児 [4]、中尾裕則 [4]、村上洋一 [4]
[1] 名古屋大学理学研究科、〒 464-8602 愛知県名古屋市千種区不老町
[2] 筑波大学数理物理科学研究科、〒 305-8571 茨城県つくば市天王台 1-1-1
[3] 総合科学研究機構東海事業センター、〒 319-1106 茨城県那珂郡東海村白方 162-1
[4] 高エネルギー加速器研究機構物質構造科学研究所、〒 305-0801 茨城県つくば市大穂 1-1

1 はじめに

ペロブスカイト酸化物 $LaCoO_3$ では Co^{3+} のスピン状態が温度によって変化し、温度上昇に伴い、非磁性の基底状態から磁性をもつ励起状態に変化する [1]。Co^{3+} の基底状態は低スピン状態と呼ばれる非磁性状態であることが知られているが、励起状態はまだよく分かっていない。$LaCoO_3$ では、Co^{3+} を Rh^{3+} ($4d^6$:低スピン状態) と置換すると低温で非磁性にならずに磁化が発達する一方で、Ga^{3+}($3d^{10}$) と置換すると低温の非磁性状態が保たれたまま室温付近の磁化が大きく減少することが報告されている [2]。我々はこれまでの研究から、Rh^{3+} を置換すると低温まで磁化をもった励起状態が安定に保たれ、さらに強磁性が誘起されることを見出した [3]。さらに室温付近の磁化と格子体積の解析結果は、Rh^{3+} は低スピン状態の Co^{3+} を、Ga^{3+} は高スピン状態の Co^{3+} を優先的に置き換えるように振る舞うことを示唆する [3, 4]。この実験結果は $LaCoO_3$ の励起状態が少なくとも 2 種類以上のスピン状態をもつ Co^{3+} が混ざり合った状態であることを支持する。今回、より詳細に Co^{3+} のスピン状態の温度変化に対する Rh^{3+} 置換効果を調べるため、多結晶試料 $LaCo_{1-x}Rh_xO_3$ ($x = 0.1, 0.2$) の放射光 X 線回折実験を行ったので、その結果を報告する。

2 実験

多結晶試料 $LaCo_{1-x}Rh_xO_3$ ($x = 0.1, 0.2$) は固相反応法で作製した。放射光 X 線回折実験は高エネルギー加速器研究機構のフォトンファクトリーのビームライン 8A で行い、30 K から 300 K までの回折パターンのプロファイルの温度変化を測定した。温度変化には He ガスの吹き付けを用いた。得られた回折パターンはリートベルト解析用プログラムの RIETAN-FP [5] を用いて解析した。

3 結果および考察

図 1 に、$LaCo_{0.9}Rh_{0.1}O_3$ の回折パターンの温度変化を示す。T = 300 K の回折パターンでは 2 本のピークが現れている。これらは $LaCoO_3$ と同じ空間群 R-3c の結晶構造から期待されるピークである。温度が減少すると、2 本のピークの間に新しいピークが発達するが、これは R-3c では説明できない。$LaCo_{1-x}Rh_xO_3$ の相図 [3] からこのピークが $LaRhO_3$ と同じ空間群 Pnma の結晶構造から期待されるものであると考えると、このピークは説明できる。この時、この回折パターンの温度変化は $LaCo_{0.9}Rh_{0.1}O_3$ では結晶構造が異なる 2 つの相が混在し、温度変化によってそれらの体積分率が変化していることを明確に示している。そこで我々は、異なる 2 つの相の体積分率が温度変化すると考えて解析を行い、格子体積の温度変化を見積もった。$LaCoO_3$ では 100 K 付近から急激に格子体積が減少するが、これは Co^{3+} のスピン状態の温度変化によるものであると考えられている [6]。Rh^{3+} を置換した試料では、100 K 付近からの格子体積の急激な減少はどちらの相においても抑えられた。これは Rh^{3+} が置換された試料では Co^{3+} のスピン状態の温度変化が抑えられ、低温まで励起状態が安定になることを示唆する。これは磁化の温度変化に対する Rh^{3+} の置換効果と矛盾しない結果である。

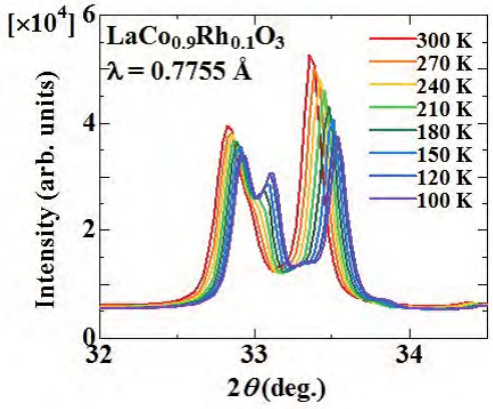

図 1: $LaCo_{0.9}Rh_{0.1}O_3$ の X 線回折パターンの温度変化

参考文献

[1] K. Asai *et al.*, Phys. Rev. B **40** (1989) 10982.
[2] T. Kyomen *et al.*, Phys. Rev. B **67** (2003) 144424.
[3] S. Asai *et al.*, J. Phys. Soc. Jpn. **80** (2011) 104705.
[4] S. Asai *et al.*, arXiv:1206.4472v1 (2012).
[5] F. Izumi and K. Momma, Solid State Phenom., **130** (2007) 15.
[6] P. G. Radaelli and S. -W. Cheong, Phys. Rev. B **66** (2002) 094408.

* asai.shinichiro@h.mbox.nagoya-u.ac.jp

16A/2009S2-008

共鳴軟 X 線散乱実験による人工超格子薄膜[$(LaMnO_3)_3/(SrMnO_3)_3$]の研究
Resonant soft x-ray scattering study of [$(LaMnO_3)_3/(SrMnO_3)_3$] thin film

須田山貴亮 [1*], 岡本淳 [1], 山崎裕一 [1], 中尾裕則 [1], 村上洋一 [1], 久保田正人 [2], 山田浩之 [3], 澤彰仁 [3]
[1]KEK 物構研 PF/CMRC、〒305-0801 茨城県つくば市大穂 1-1
[2]原子力機構、〒319-1195 茨城県那珂郡東海村白方白根 2-4
[3]産総研、〒305-8562 茨城県つくば市東 1-1-1

1 はじめに

$LaMnO_3$(LMO)と $SrMnO_3$(SMO)で作製される超格子薄膜[$(LMO)_m/(SMO)_n$]において積層枚数である m と n を変化させることで興味深い物性を示すことが報告されている。特に m = n = 2 (L2S2)では反強磁性絶縁体(AFI)と強磁性金属(FM)との境界に位置し、外場を加えることにより巨大な磁気抵抗効果を示すことが報告されている[1]。これは m = n = 3 (L3S3)でも観測されており、AFI と FM の相競合が原因であると考えられている。また、この現象は $La_{1-x}Sr_xMnO_3$ バルク試料やその薄膜では観測されておらず超格子の界面が重要であると考えられている。

加えて、我々は以前、m = n = 5 (L5S5)の積層枚数の強磁性絶縁体における共鳴軟 X 線散乱実験結果を報告した。Mn の L 吸収端 ($2p \rightarrow 3d$) を用い、[$(LaMnO_3)_5/(SrMnO_3)_5$]をユニットセルとした場合に散乱ベクトル Q = (0 0 L)の超格子反射のスペクトルを調べた。その結果、L = 1 が強磁性シグナルに対応した温度変化を示し、L = 2 は顕著な温度変化をしないことを示した[2]。本研究では、電気抵抗でクロスオーバー的な振る舞いを示す m = n = 3 (L3S3)の積層枚数を持つ薄膜について共鳴軟 X 線散乱実験を行い磁性についての研究を行った。

2 実験

高エネルギー加速器研究機構のフォトンファクトリーBL-16Aで人工超格子Mn薄膜[$(LMO_3)_3/(SMO_3)_3$]について共鳴軟X線散乱実験を行った。およそ30 Kから260 Kまでの温度変化を測定した。

3 結果および考察

図 1 (a)は[$(LaMnO_3)_3/(SrMnO_3)_3$]をユニットセルとした場合に Q = (0 0 L)における Mn の L 吸収端付近の共鳴散乱スペクトルである。測定温度は 40K で行った。図 1(b)は 1(a)で得られたエネルギースペクトルから特徴的なピークである L = 1 で見られる peak A と L = 2 で見られる peak B の強度の温度変化である。Mn の吸収端で Q = (0 0 L)における L = 1、L = 2 においてそれぞれ異なる温度変化を示す反射のシグナルを検出することが出来た。L = 1 では L5S5 と同様に磁化測定で得られる強磁性転移を示す温度付近(約 200 K)からシグナルが低温に向けて増大するのに対して、界面の情報を含む L = 2 の反射ではおよそ 150 K 付近から低温になるにつれてシグナルが増大する振る舞いを観測した。L = 2 でのこの振る舞いは L5S5 のときでは見られないものであり、L3S3 の電気抵抗率測定で見られる特徴的なクロスオーバーに関連した磁気成分の振る舞いではないかと考えられる。

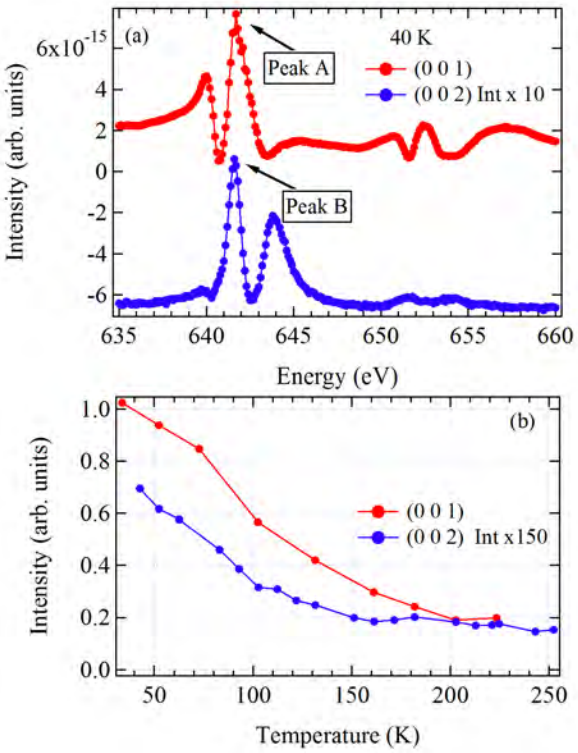

図 1 ：(a) Q = (0 0 L)における L = 1, 2 の Mn 吸収端での共鳴散乱スペクトル、(b) Q = (0 0 1)で見られる Peak A と(0 0 2)で見られる peak B の強度の温度変化

今後の研究課題として、磁気抵抗効果を解明する上で、磁場下での共鳴軟 X 散乱実験を行うことが必要である。

参考文献

[1] H. Yamada *et al.*, PRB **81** (2010) 014410.
[2] M. Kubota *et al.*, 日本物理学会　第 67 回年次大会 25aPS-42

* Takaaki.sudayama@kek.jp

3A/2009S2-008

長周期螺旋磁気構造を持つ $NiBr_2$ のマルチフェロイックス特性
Multiferroicity in $NiBr_2$ with long-wavelength cycloidal spin structure

奥山大輔 [1*], 徳永祐介 [1], 車地崇 [2], 有馬孝尚 [3], 中尾裕則 [4], 村上洋一 [4], 田口康二郎 [1], 十倉好紀 [1,2]
[1] 理研-CMRG/CERG　〒351-0198 和光市広沢 2-1
[2] 東大物工　〒113-8656 文京区本郷 7-3-1
[3] 東大新領域　〒277-8561 柏市柏の葉 5-1-5
[4] 物質構造科学研究所-CMRC　〒305-0801 つくば市大穂 1-1

1 はじめに

(反)強磁性と強誘電性が強く結合しているマルチフェロイックス物質は、本来電場でしか制御できない強誘電分極の符号や方向を磁場でコントロール出来きることから、その発現機構や応用に向けての研究が盛んに行われている。本研究の対象物質である $NiBr_2$ は、T_{N1}=44 K 以下で共線的な反強磁性秩序を形成し、更に T_{N2}=22.8 K 以下では(δ δ 3/2)方向へ伝播する非常に周期の長いサイクロイド磁気秩序が起きる事が報告されている(4.2 K ではδ=0.027) [1]。我々は、最低温相でサイクロイド磁気秩序が形成されている事より、磁気秩序由来の強誘電性が発現している可能性があると考え研究を始めた [2] 。

2 実験結果および考察

図 1(a)と(b)は、それぞれ磁化の温度変化と焦電流測定より求めた強誘電分極の温度変化である。磁化に異常が観測されている T=23 K 以下より、主に[1 -1 0]方向に強誘電分極の発生が観測されている。また、[0 0 1]方向にも[1 -1 0]方向に比べて 1/20 程度の分極値が観測されている。サイクロイド磁気転移と同じ温度で発生した強誘電分極が、磁気弾性効果により生ずる格子歪みに起因しているかどうかを確かめるため、放射光 X 線を用いた回折実験を行った。

実験は、PF-BL3A に設置されている 4 軸回折計と He 循環型冷凍機を用いて行った。図 1(d)は実際に T=5.3 K で観測された磁気弾性効果由来の格子歪みによる等価な(-1-q 2-q 12)と(-1+q 2+q 12)の超格子反射である。(-1+q 2+q 12)反射の温度変化を詳細に観測したところ、図 1(e)のように温度に対して大きく伝播波数を変化させている事が分かった。各温度の超格子反射のプロファイルをガウス関数でフィッティングして得られた伝播波数δ_s の温度変化と、中性子回折で観測されている磁気反射の伝播波数δ_m[1]の温度変化を比較すると、ほぼδ_s=2×δ_m の関係が成り立っていた。これは放射光回折で観測されている超格子反射が、磁気弾性効果由来の格子歪みを観測している事を意味していると考えられる。以上より、$NiBr_2$ のサイクロイド磁気秩序相では、磁気秩序が起因となって格子が歪み強誘電分極が発生しているマルチフェロイックス特性が実現している事を示す結果を得た。詳細な議論及び実験データは、論文[3]を参照していただきたい。

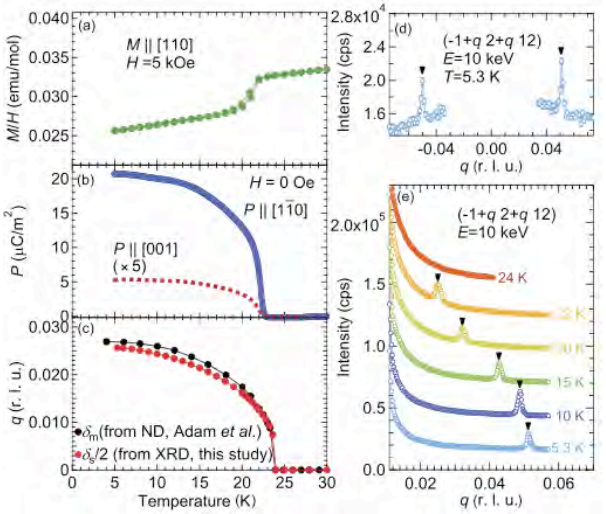

図 1: (a)磁化の温度変化。T=23 K 付近にサイクロイド磁気秩序による異常が観測されている。(b)焦電流測定から求めた強誘電分極値の温度変化。主に[1 -1 0]方向に電気双極子モーメントを持つ強誘電分極が発生している。(c-e)X 線回折より観測された (-1±q 2±q 12)超格子反射。それぞれ、観測された伝播波数の温度変化と中性子回折で得られた磁気伝播波数[1]との比較(c)、等価な(-1-q 2-q 12)反射と(-1+q 2+q 12) 反射のプロファイル(d)、(-1+q 2+q 12) 反射の温度変化(e)、を示している [3]。

3 まとめ

低温でサイクロイド磁気秩序を示す $NiBr_2$ で、磁気転移と同じ温度で強誘電分極が発生している事を示した。更に、放射光回折実験より、磁気弾性効果に伴う格子歪みが発生している事を発見した。これらの実験結果より、$NiBr_2$ がマルチフェロイックス特性を有している事を示した。

参考文献

[1] A. Adam *et al.*, Solid State Commun. **35** (1980) 1.
[2] T. Arima *et al.*, J. Phys. Soc. Jpn. **76** (2007) 023602.
[3] Y. Tokunaga *et al.*, Phys. Rev. B **84** (2011) 060406(R).
* okuyama@riken.jp

3A/2009S2-008

All-in-all-out Magnetic Order in the Insulating Phase of a Pyrochlore Iridate $Eu_2Ir_2O_7$

Hajime Sagayama[1,*], Daisuke Uematsu[1], Taka-hisa Arima[1,2]
[1]Department of Advanced Materials Science, Univ. Tokyo, Kashiwa 277-8561, Japan
[2]RIKEN Spring-8 Center, Hyogo 679-5148, Japan

1 Introduction

Ir oxide compounds can exhibit a novel J_{eff}=1/2 state with unquenched orbital momentum due to strong spin-orbit coupling.[1-3] For example, there is an intense debate about the role of the J_{eff}=1/2 state in a metal-insulator transition, which several Ir oxide compounds undergo. Rare-earth (R) iridium oxide compounds $R_2Ir_2O_7$ with the geometrically frustrated pyrochlore lattice exhibit a metal-insulator transition accompanying an anomaly in magnetic susceptibility except R=Pr.[4-6] The origin of the transition is yet unclear partly because of a lack of information on the magnetic structure in the insulating phase.

Here we study magnetic order in the low-temperature insulating phase of $Eu_2Ir_2O_7$, which undergoes this metal-insulator transition at T_{MI}~120 K.[5,6] Large neutron absorption coefficients of Eu and Ir make a neutron study on the compound difficult. On the other hand, resonant x-ray diffraction is a useful tool for studying magnetic order in iridium compounds, because the $L_{2,3}$ absorption includes the excitation of an electron from 2p core states to partially filled 5d valence states, which are directly associated to the magnetism.[2] The wavelength of $L_{2,3}$ absorption edge is near 0.1 nm, which is suitable for diffraction.

2 Experimental

A single crystal was grown from a flux and characterized by J. J. Ishikawa and S. Nakatsuji, ISSP, Univ. Tokyo.[6] The crystal has shiny triangle surfaces of a dimension of about 0.5 mm. The resonant x-ray diffraction measurement was carried out by using a multi-circle diffractometer at BL-3A. The sample was mounted in a ^{4}He closed-cycle refrigerator. The incident beam was polarized perpendicular to the scattering plane (σ). Mo (200) reflection was used to analyze the polarization of scattered beam.

3 Results and Discussions

A previous muon spin rotation study suggests that Ir moments should be arranged with some commensurate propagation vector.[7] Several line scans along (*qkl*), (*qql*), and (*qqq*), where *k* and *l* are integers, at 10 K indicate the absence of extra reflection at incommensurate positions with relatively high symmetries. Hereafter, we discuss resonant x-ray reflections at (4*n*+2, 0, 0), which are ordinarily forbidden in pyrochlore systems. Figure 1 shows temperature dependence of the integrated intensity of (10 0 0) reflection at 11.23 keV (Ir L_3 edge) at 10 K. Here the scattering plane is set perpendicular to the [0 1 -1] axis, and σ' (π') denotes the scattered beam polarized perpendicular (parallel) to the scattering plane. In the σ-π' channel, the reflection emerges only below T_{MI}, while the reflection in the σ-σ' channel remains above T_{MI}. It is well known that the reflection condition originating from a screw axis or glide plane can be relaxed for anomalous scattering terms in general. In the pyrochlore iridate, each IrO_6 octahedron has trigonal distortion of compressed type. The distortion induces an anisotropy in Ir atomic anomalous scattering factor, and makes the (4*n*+2 0 0) reflections allowed. In the present configuration, the anomalous-tensor-susceptibility (ATS) scattering of (4*n*+2 0 0) may appear only with the σ' polarization. The π' component is hence assigned to the magnetic scattering. Spectra of the intensity for (10 0 0) and (6 0 0) reflections shown in Fig. 2 also confirm the magnetic origin of the π' component. The scattering in the σ-π' channel shows a resonant peak at 11.230 keV. On the other hand, the spectrum in the σ-σ' channel is characterized by a resonant peak at 11.238 keV as well as a shoulder at around 11.23 keV. The difference in spectrum is well explained in terms of ligand-field splitting of 5d state. The octahedral ligand field splits the Ir 5d orbitals into e_g and t_{2g} states. The L_3-edge $2p_{3/2}$-5d absorption is hence composed of two bands. Five 5d electrons in the lower-lying t_{2g} state are the source of a magnetic moment of each Ir^{4+} ion, while the empty e_g band is irrelevant to the magnetism. As a consequence, it is predicted that the magnetic scattering should be resonant only with the lower-lying $2p_{3/2}$-t_{2g} excitation, whilst the anomalous tensor susceptibility of Ir atom should be enhanced at both the absorption energies.

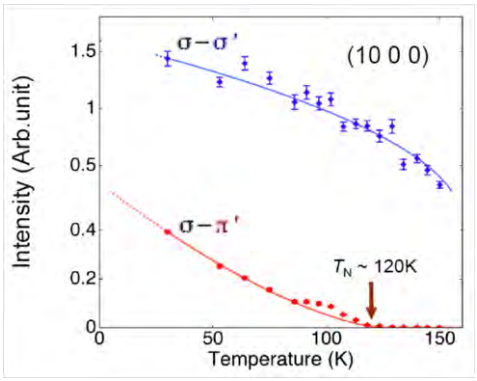

Fig. 1: Integrated intensity of (10 0 0) reflection as a function of temperature. The x-ray photon energy is 11.230 keV. Blue and red dots show intensities in the s-s' and s-p' channels, respectively.

The emergence of (4*n*+2 0 0) magnetic reflections clearly indicates that a magnetic unit cell should contain four Ir^{4+} moments. Here we propose the most probable arrangement of the magnetic moments among several candidates of four-sublattice magnetic order. The moments on four vertices of each Ir tetrahedron point to the center of the tetrahedron (inwards) or in the opposite direction (outwards), which can be termed 'all-in-all-out' structure. Only this magnetic structure can retain the cubic symmetry[8], which is in accord with a detail x-ray analysis of the crystal structure at low temperatures.

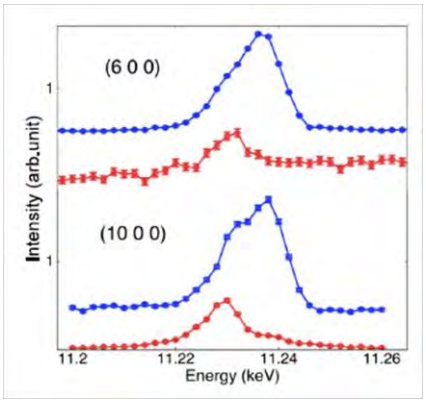

Fig. 2: Spectra of the peak intensity for (6 0 0) and (10 0 0) reflections near Ir L_3 absorption edge. Blue and red dots show intensities in the σ-σ' and σ-π' channels, respectively.

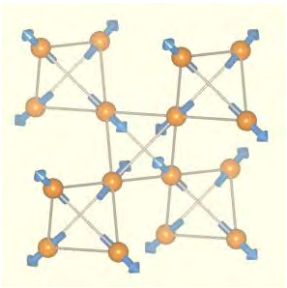

Fig. 3: All-in-all-out magnetic structure in the pyrochlore lattice.

Acknowledgment

The sample crystal was provided by J. J. Ishikawa and S. Nakatsuji.

References

[1] B. J. Kim *et al*., Phys. Rev. Lett. **101**, 076402 (2008).
[2] B. J. Kim *et al*., Science **323**, 1329 (2009).
[3] G. Jackeli and G. Khaliullin, Phys. Rev. Lett. **102**, 017205 (2009).
[4] K. Matsuhira *et al.,* J. Phys. Soc. Jpn. **76**, 043706 (2007).
[5] K. Matsuhira *et al.*, J. Phys. Soc. Jpn. **80,** 094701 (2011).
[6] J. J. Ishikawa *et al.*, cond-matt 1203.4182v1.
[7] Songrui Zhao *et al.*, Phys. Rev. B **83**, 180402(R) (2011).
[8] J. Yamaura *et al.*, Phys. Rev. Lett. **104**, 247205 (2012).

* sagayama@k.u-tokyo.ac.jp

10C/2010G014

Crystallization Behavior of Homopolymer/Block Chain Blends Confined in Nanocylinders with Different Diameters

Shintaro Nakagawa, Takumi Tanaka, and Shuichi Nojima*
Department of Organic and Polymeric Materials, Graduate School of Science and Engineering, Tokyo Institute of Technology, H-125, 2-12-1, Ookayama, Meguro-ku, Tokyo 152-8552, Japan

1 Introduction

Crystalline blocks in crystalline-amorphous diblock copolymers crystallize within nanodomains formed by microphase separation if the amorphous block is vitrified. Our previous investigation on crystallization of homopolymers and block chains confined in nanodomains suggested that the chain-end tethering accelerated nucleation upon crystallization [1]. It was also revealed that the effect of chain-end tethering depended significantly on nanodomain size and crystallization temperature [2].

In the present study, we investigate the isothermal crystallization behavior of binary blends consisting of homopolymers and block chains confined in cylindrical nanodomains (nanocylinders) as a function of both blend composition and nanocylinder size to understand how the confinement diameter affects the crystallization behavior of crystalline chains through the chain-end tethering.

2 Experiment

Samples Two Poly(ε-caprolactone)-*block*-polystyrene (PCL-*b*-PS) diblock copolymers, PCL-PS2 and PCL-PS5, with different molecular weights and similar compositions were synthesized. These PCL-*b*-PS copolymers have a photocleavable *o*-nitrobenzyl group between PCL and PS blocks that allows them to separate into PCL and PS homopolymers when irradiated with ultraviolet light (UV). The binary blends of PCL homopolymers and PCL blocks were prepared using controlled UV irradiation after the formation of cylindrical microphase-separated structure. Here we define f_h as the weight fraction of PCL homopolymers against all PCL chains (i.e., PCL homopolymers + PCL blocks) existing in the system.

Measurements The diameter of nanocylinders was evaluated from the volume fraction of each block and the primary peak position in synchrotron small-angle X-ray scattering (SR-SAXS) curves, which were obtained at beam line BL-10C in KEK-PF. Differential scanning calorimetry (DSC) was utilized to observe the isothermal crystallization behavior of the blends.

3 Results and Discussion

Fig. 1(a) shows the SAXS profiles of crystallized PCL-PS2 and PCL-PS5 with f_h = 0 (neat PCL blocks) and maximum f_h (almost PCL homopolymers). All crystallized samples have a couple of scattering peaks, the positions of which exactly correspond to a ratio of $1:3^{1/2}:2(:7^{1/2})$, indicating the formation of well-ordered nanocylinders. The diameters of nanocylinders existing in PCL-PS2 and PCL-PS5 were evaluated from Fig. 1(a) to be 14.9 nm and 17.2 nm, respectively.

Crystallization kinetics of both systems was analyzed using crystallization halftime $t_{1/2}$, where $t_{1/2}^{-1}$ is a measure for the crystallization rate of PCL chains. Fig. 1(b) shows the plot of $t_{1/2}^{-1}$ against f_h for each sample at the same crystallization temperature T_c (= -40 ℃). $t_{1/2}^{-1}$ increases monotonously with increasing f_h in PCL-PS2 whereas it decreases with increasing f_h in PCL-PS5. From Fig. 1(b), we suppose two distinct effects of chain-end tethering on the crystallization behavior. One is the acceleration of nucleation rates at the tethering points and the other the deceleration of nucleus growth rates by reduced chain mobility. The relative magnitudes of these two opposite effects vary with the confinement size to yield the marked difference in the f_h dependence of crystallization rates between PCL-PS2 and PCL-PS5.

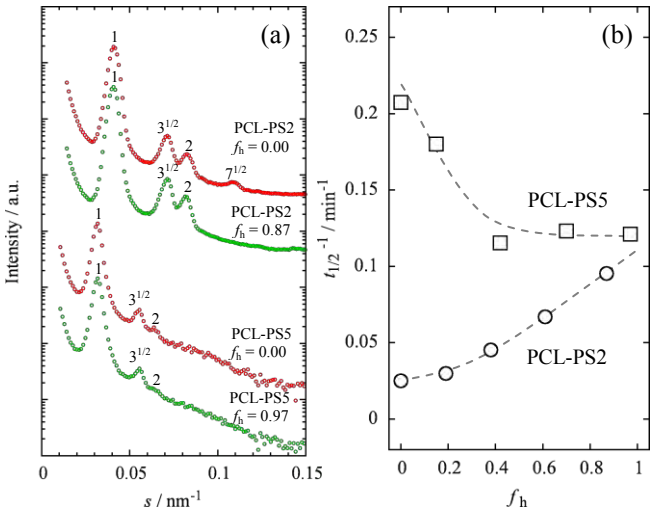

Fig. 1: (a) SR-SAXS curves of crystallized PCL-PS2 and PCL-PS5 with different f_h indicated. (b) $t_{1/2}^{-1}$ plotted against f_h for PCL-PS2 and PCL-PS5 crystallized at T_c = -40 ℃.

References

[1] Nojima, S. *et al*., *Macromolecules* **41**, 1915 (2008).
[2] Nakagawa, S. *et al.*, *Macromolecules* **45**, 1892 (2012).

* snojima@polymer.titech.ac.jp

BL-10C/2010G014

Isothermal Crystallization of Double Crystalline Diblock Copolymers with Close Crystallizable Temperatures

Liang Huang, Gaito Kiyofuji, and Shuichi Nojima*
Department of Organic and Polymeric Materials, Graduate School of Science and Engineering, Tokyo Institute of Technology, H125, 2-12-1 Ookayama, Meguro-ku Tokyo 152-8552, Japan

1 Introduction

Morphology formation in double crystalline diblock copolymers is extremely complicated due to the interplay between two kinds of crystallization starting from the molten microdomain structure. The relative position of crystallizable temperatures of two blocks is an important factor to control the crystallization behavior. In our previous work[1], we investigated the non-isothermal crystallization behavior of crystalline-crystalline diblock copolymers with close crystallizable temperatures, poly (β-propiolactone)-*block*-polyethylene (PPL-*b*-PE), and found that when the crystallization rate of one block was large, that of the other block was small, suggesting simultaneous crystallization. In this study, we investigate the isothermal crystallization behavior of PPL-*b*-PE.

2 Experimental

Samples Four PPL-*b*-PE copolymers were synthesized using anion polymerization. The samples were named as PL-PE10, PL-PE15, PL-PE20, and PL-PE51, where the numeral in the sample code represents the mole% of 1,2-addition for ethylene monomers in PE blocks. The volume fraction of PPL blocks was around 0.5.

Measurements The microdomain structure was investigated using small-angle X-ray scattering with synchrotron radiation (SR-SAXS), which was performed at beam line BL-10C in KEK-PF. The isothermal crystallization behavior was also observed using time-resolved SR-SAXS, and independently using Fourier transform infrared spectroscopy (FT-IR).

3 Results and Discussion

The SR-SAXS curves from molten and crystallized samples have several scattering peaks, the angular positions of which exactly correspond to a ratio of 1: 2: 3. This indicates that the lamellar morphology is formed in all samples at both amorphous and crystallized states. Fig. 1 shows the time-resolved SR-SAXS curves for PL-PE10 and PL-PE51 isothermally crystallized at 55℃. The SR-SAXS curves for PL-PE10 show the monotonous increase in the primary peak intensity with increasing crystallization time *t* except at the initial period (< 50 s). It is successfully explained by considering that the PE blocks crystallize promptly during quenching to form the crystallized lamellar microdomains, which are rigid and stable against subsequent crystallization of PPL blocks. Therefore, the crystallization of PPL blocks occurs within this crystallized microdomain. The SR-SAXS curves for PL-PE51 have the minimum of the primary peak intensity (indicated by an arrow) during isothermal crystallization, suggesting the morphological transition from the molten lamellar microdomain structure into crystallized lamellar morphology. That is, the scattering peak intensity arising from the microdomain structure steadily decreases and simultaneously that from the crystallized lamellar morphology increases with increasing *t* to yield the peak intensity minimum during the course of crystallization.

The results of isothermal crystallization behavior for PL-PE10 and PL-PE51 obtained using FT-IR are consistent with those obtained by SR-SAXS measurements. In addition, we found from FT-IR results that PE blocks in PL-PE51 do not crystallize during isothermal crystallization. On the contrary, the PE blocks in PL-PE10 crystallize. We conclude that the difference in crystallization behavior between PL-PE10 and PL-PE51 mainly arises from the rigidity of the lamellar microdomain structure existing just before the crystallization of PPL blocks.

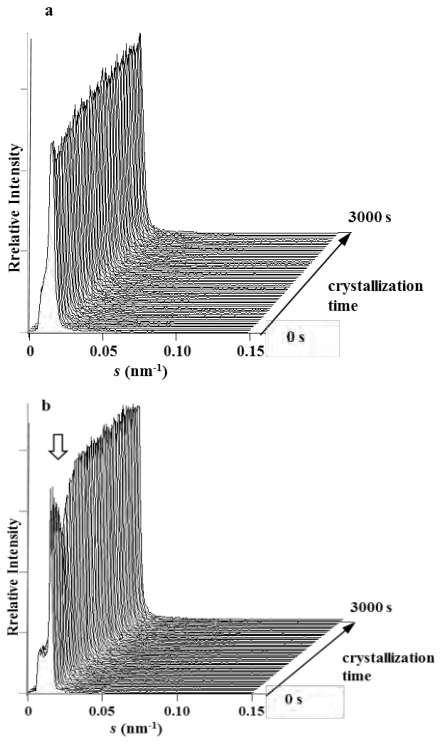

Fig. 1: Time-resolved SR-SAXS curves of PL-PE10 (a) and PL-PE51 (b) isothermally crystallized at 55 ℃.

1 J. Matsumoto *et al*., *Photon Factory Activity Report* 2010, **28**, 162 (2011).

* snojima@polymer.titech.ac.jp

BL-10C/2010G014

Crystallization of Poly(ε-caprolactone) Blocks Confined in Crystallized Lamellar Morphology of Poly(ε-caprolactone)-*block*-Polyethylene Copolymers: Effects of Polyethylene Crystallinity and Confinement Size

Takuya Sakurai, Hikaru Nagakura, Satoru Gondo, and Shuichi Nojima*
Department of Organic and Polymeric Materials, Graduate School of Science and Engineering, Tokyo Institute of Technology, H-125, 2-12-1 Ookayama, Meguro-ku Tokyo 152-8552, Japan

1 Introduction

In crystalline-crystalline diblock copolymers with separate melting temperatures, poly(ε-caprolactone)-*block*-polyethylene (PCL-*b*-PE), crystal orientation of PCL blocks depended significantly on the size of spatial confinement provided by the crystallized lamellar morphology of PE blocks (PE lamellar morphology) [1]. In this study, we investigated the crystal orientation of PCL blocks spatially confined in the PE lamellar morphology with different crystallinities of PE blocks χ_{PE} and layer thicknesses of PCL blocks d_{PCL}, and elucidated the combined effects of χ_{PE} and d_{PCL} on the subsequent crystallization of PCL blocks.

2 Experiment

Samples PCL-*b*-PE copolymers with several χ_{PE} were synthesized using anionic polymerization. PE blocks crystallize first on quenching to form the crystallized lamellar morphology (PE lamellar morphology), followed by the crystallization of PCL blocks spatially confined in the PE lamellar morphology. E07 and E23 are PCL-*b*-PE copolymers with similar and smaller d_{PCL} (8.3 ~ 8.8 nm) and different χ_{PE} (χ_{PE} ~ 7 % for E07 and χ_{PE} ~ 23 % for E23). The uniaxial orientation of the PE lamellar morphology was carried out at 70 °C by applying the rotational shear to the samples in order to investigate the internal crystal orientation of PCL blocks.

Measurements The morphology formed in the system was investigated using two-dimensional synchrotron small-angle X-ray scattering (2D-SAXS), which was performed at beam line BL-10C in KEK-PF. The crystal orientation of PCL blocks was observed using two-dimensional conventional wide-angle X-ray diffraction (2D-WAXD).

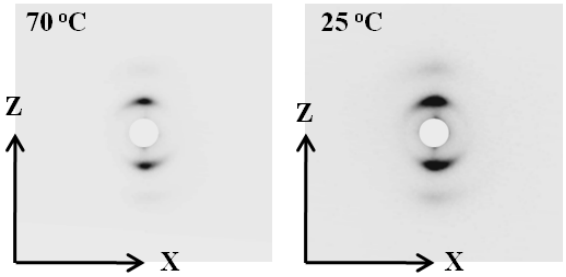

Fig. 1. 2D-SAXS patterns of uniaxially oriented E07 when viewed from the Y direction, which is perpendicular to the shear direction (X).

3 Results and Discussion

Fig. 1 shows the 2D-SAXS patterns of sheared PCL-*b*-PE at selected temperatures indicated. We find a couple of scattering spots on the meridian arising from parallel stacking of PE lamellae at 70 °C, showing that the PE lamllar morphology is preferentially oriented parallel to the shear direction. It is also found that these scattering patterns are maintained at 25 °C, where PCL blocks have already crystallized, indicating that PCL blocks crystallize within the oriented PE lamellar morphplogy.

Fig. 2 shows the diffraction intensity from the (110) plane of PCL crystals plotted against azimuthal angle φ evaluated from 2D-WAXD patterns at selected temperatures. At 0 °C, E07 has two distinct peaks at φ ~ 90 ° and 270 °, and E23 seems to have no peaks. At 45 °C, on the other hand, E07 still has two peaks similar to those at 0 °C, but E23 has four peaks at φ ~ 65 °, 115 °, 245 °, and 295 °. Fig. 2 indicates that the c-axis of PCL crystals in E23 changes almost random to perpendicular to the lamellar surface normal with increasing crystallization temperature T_c. The c-axis of PCL crystals in E07, however, is independent on T_c. These results suggest that when d_{PCL} is smaller, the PE lamellar morphology with higher χ_{PE} plays as hard confinement similar to glassy microdomains and that with lower χ_{PE} does as soft confinement similar to rubbery microdomains.

References

[1] T. Higa *et al.*, *Polymer* **51**, 5576-84, 2010.

* snojima@polymer.titech.ac.jp

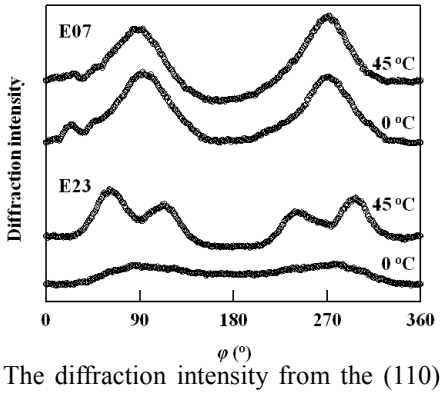

Fig. 2. The diffraction intensity from the (110) plane of PCL crystals plotted against azimuthal angle φ at T_c = 0 °C and 45 °C. φ = 0 ° and 180 ° correspond to the meridian.

9C/2010G024

Photoluminescence property of magnetoplumbite-type $LaAl_{12}O_{18}N:Eu^{2+}$ phosphor and their XANES spectra

Yuji MASUBUCHI*[1], Shinichi KIKKAWA[1], Teruki MOTOHASHI[1], Takashi TAKEDA[2], Kei-ichiro MURAI[3], and Akira YOSHIASA[4]
[1]Hokkaido Univ., Sapporo 060-8628, Japan
[2]NIMS, Tsukuba 305-0044, Japan
[3]Tokushima Univ., Tokushima 770-8506, Japan
[4]Kumamoto Univ., Kumamoto 860-8555, Japan

1 Introduction

White light emitting diodes (LEDs) have received much attention as high efficiency, safe and environmental friendly devices. In white LED applications, blue LED light is combined with yellow light emitted from a phosphor to obtain white light. To improve the color rendering properties of white LEDs, both green and red light emitting phosphors have been used with yellow phosphor. Such phosphorous materials have been developed among silicon oxynitride and alumino-silicon oxynitrides. However, study on aluminum (oxy)nitrides is limited.

Three emission peaks for Eu^{2+} doped AlON with an impurity phase of magnetoplumbite(MP)-type $EuAl_{12}O_{19}$ has been reported by Kikkawa et al. [1]. They attributed the multiple emissions to the presence of the different coordination environments around Eu^{2+} with different O/N ratios in the MP structure. The MP-type oxynitride has been reported only in lanthanum aluminum oxynitride, $LaAl_{12}O_{18}N$. However, the crystal structure and photoluminescence properties of Eu^{2+} doped MP-type lanthanum aluminum oxynitride have not yet been reported.

In this study, Eu^{2+} doped MP-type $LaAl_{12}O_{18}N$ was prepared using aluminum glycine gel precursors followed by post-annealing of the calcined precursor. The luminescence property was discussed in relation to the crystal structure and Eu valency.

2 Experiment

The calcined precursors were prepared through ammonolysis of oxide powders obtained from aluminium glycine gel as described in Ref [1]. The calcined precursors were post-annealed at 1700 °C for 3 h under a nitrogen gas pressure of 0.2 MPa in a gas pressure furnace.

Crystalline phases were characterized using powder x-ray diffraction (XRD). Luminescence property was measured by a spectrofluorometer. X-ray absorption of Eu L_{III}-edge was measured in transmission mode at the beam line 9C in Photon Factory. Neutron diffraction measurements were performed using HERMES installed at JRR-3 in JAEA. The Rietveld program RIETAN-2000 [2] was used for structural refinement.

3 Results and Discussion

After post annealing at 1700 °C for 3 h under a nitrogen gas pressure of 0.2 MPa, pure MP-type $LaAl_{12}O_{18}N$ doped with Eu were obtained from 0% to 30% of Eu doping. Eu doped products exhibited broad blue emission at 440 nm with a shoulder peak at 464 nm under excitation at 254 nm. No characteristic sharp peaks due to Eu^{3+} ion were observed, which confirms the presence of only Eu^{2+} ions in the oxynitride phosphor. The Eu^{2+} was supported by a single absorption peak at 6972 eV in the XANES spectra for the Eu L_{III}-edge as shown in Fig. 1. Eu doped $CaAl_{12}O_{19}$ had a single emission at 415 nm.

Structural refinement using neutron diffraction showed the lanthanum site occupied by Eu^{2+} is split into 2*d* and 6*h* sites at the intermediate layer in the MP-type aluminium oxynitride. The shoulder emission peak in the emission spectrum of the oxynitride is related to the Eu^{2+} site splitting induced by the two kinds of anions.

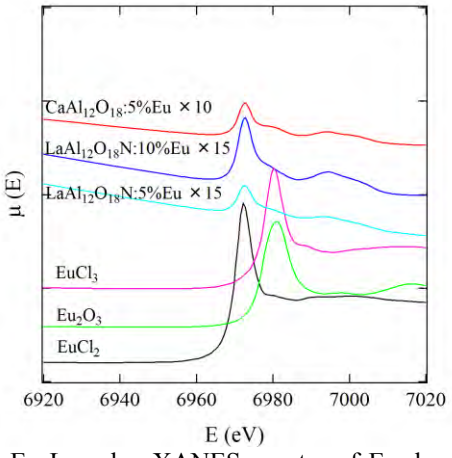

Fig. 1 Eu L_{III}-edge XANES spectra of Eu doped MP-type $LaAl_{12}O_{18}N$ and $CaAl_{12}O_{19}$.

References

[1] S. Kikkawa, et al., J. Am. Ceram. Soc., **91** (2008) 924.
[2] F. Izumi, et al., Mater. Sci. Forum, **321-324** (2000) 198.

* yuji-mas@eng.hokudai.ac.jp

15C/2010G026

Observation of Rocking Curves from Polar Crystal for Phase Determination of Crystal Structure Factor

R. Negishi[1,*], T. Fukamachi[1], S. Jongsukswat[1], Ken. Hirano[1], Kei. Hirano[2], and T. Kawamura[3]

[1]Saitama Institute of Technology, Fukaya, Saitama, 369-0293, Japan
[2] Photon Factory, Tsukuba, Ibaraki, 305-0801, Japan
[3]University of Yamanashi, Kofu, Yamanashi, 400-8510, Japan

We have previously reported phase determination of crystal structure factor by using the phase difference between the diffracted and transmitted rocking curves in Laue case [1]. In this paper, we propose another phase determination approach by using FWHM (full width at half maximum) and intensities of measured rocking curves from the front and bottom surfaces of a polar crystal. We assume that only one atom in a unit cell suffers anomalous scattering and the atomic site is known. Then the crystal structure factor is given by

$$F_h = |F_{hr}| \exp(i\alpha_{hr}) + i|F_{hi}| \exp(i\alpha_{hi}) \quad . \qquad (1)$$

The first term is the real part to be determined, and the second one the imaginary part assumed to be known. If FWHM's of rocking curves from the front and bottom surfaces in Bragg case are written as $\Delta\Theta$ and the refractive index is equal to one, the crystal structure factor is given by

$$|F_{\pm h}| = \frac{\omega^2 V \sin 2\theta_B}{8\pi} \Delta\Theta \quad . \qquad (2)$$

Here ω is the X-ray energy, V the volume of a unit cell and θ_B the Bragg angle. The crystal structure factor is also expressed as,

$$F_{\pm h} = |F_{hr}| (1 \mp 2k|\sin\delta|)^{1/2} \exp[i(\pm\alpha_{hr} + \theta)], \qquad (3)$$

with $k = |F_{hi}| / |F_{hr}|$ being assumed to be much less than one. In eq. (3), the relation

$$\alpha_{hr} = \alpha_{hi} - \delta \qquad (4)$$

holds and

$$\theta = \tan^{-1}[k\cos\delta / (1 \mp k|\sin\delta|)]. \qquad (5)$$

If the intensity ratio r between from the top and the bottom side of the surface is written as

$$r = |F_{-h|}| / |F_{+h}| \quad , \qquad (6)$$

then the phase δ is given by

$$\sin\delta = \frac{1}{2k} \cdot \frac{r-1}{r+1} \qquad (7)$$

The phase δ can be determined by measuring intensities from the top and bottom surfaces. If $\Delta\Theta$ and r are given by measuring rocking curves, α_{hr} is to be determined.

We measured $\Delta\Theta$ and r from a GaAs crystal by using X-rays from synchrotron radiation at KEK-PF, Tsukuba, Japan. We tuned the energy at 10.3770 keV by using two Ge 333 asymmetric monochromators. Fig. 1 shows the measuring optical system and Fig. 2 shows the measured ±333 rocking curves near the K-absorption of Ga in a GaAs crystal.

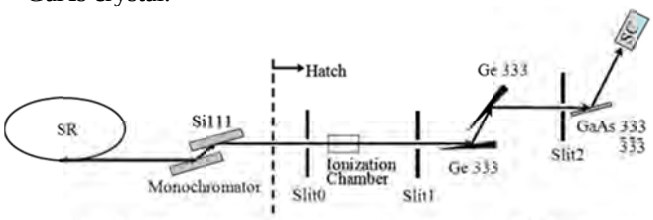

Fig. 1: The measuring optical system at KEK-PF. The asymmetry α of the two asymmetric monochromators at the K-absorption edge of Ga is approximately 12.

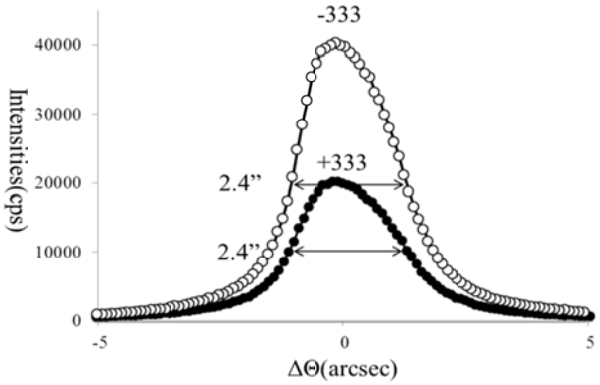

Fig. 2: The measured rocking curves of ±333 reflections from a GaAs crystal at 9.0 eV above the K-absorption edge of Ga.

The measured FWHM and intensity ratio r for GaAs $\pm$ 333 were $\Delta\Theta = 2.4"$ and $r = 2.0$, respectively. The phase $a_{\pm hr}$ was determined to be $\mp$ 40°. Because many protein crystals have polar faces, the current approach should be very useful for phase determination of a nearly perfect protein crystal [2], as it becomes available today.

References

1. R. Negishi, et al.; *Phys. Status Solidi A*, (2011) **208**, p2567.
2. T. Sawaura, et al.: *J. Cryst. Growth*, (2011) **318**, p1071.

* negishi@sit.ac.jp

7A/2010G036

Edge-state in Nanographite, HNO_3-Doped Nanographite and Its Residue Compounds

Manabu Kiguchi*, Si-Jia Hao, Satoshi Kaneko, Jun-ichi Takashiro, Kazuyuki Takai, V. L. Joseph Joly, Toshiaki Enoki

[1]Tokyo Institute of Technology, Ookayama, Meguro-ku, Tokyo 152-8551, Japan

Introduction

Graphene, the 2D one-atom-thick monolayer of carbon atoms arranged in a honeycomb lattice, has recently attracted tremendous interests from the scientific community for both fundamental and applied researches owing to its unconventional electronic structure of massless Dirac fermions which gives rise to unprecedented physical properties such as the room-temperature half-integer quantum Hall effect, the extremely high mobility of its charge carriers, the tunable band gap of graphene nanoribbons, and the potential for realizing ballistic conduction. In investigating the properties of the nanographene, it is particularly important to confirm the presence of edge-states. Here, we pay attention to the activated carbon fibers (ACFs). ACFs are nanoporous carbon consisting of a three dimensional disordered network of nanographite domains, each of which is a stack of 3-4 nanographene sheets with the mean in-plane size of about 2-3nm. ACFs have a high density of edge carbon atoms (the number ratio of edge carbon atoms to the interior carbon atoms is ca. 30/200) due to the small size of nanographene sheets. To understand more comprehensively behavior of edge-state in the nanographite system, in the present research we investigated the electronic structure of the edge-state for ACFs, HNO_3 doped ACFs, and its residue compounds

Experiment

Pristine ACFs were commercially available samples (Kurary Chemicals, FR-20; specific surface areas of 2000 m^2/g) prepared by the activation of phenol-based precursor materials. The nitric acid adsorbed samples (HNO_3-ACFs) were prepared by placing the ACFs in the HNO_3 gas shower at room temperature and the duration of the adsorption was at least 2 h which was enough to reach the equilibrium. In addition, the residue compounds (RC) were made by evacuating these as-prepared HNO_3-ACFs samples to ~ 10^{-6} Torr again at room temperature (RC-RT), 100 ^oC (RC-100), 200 ^oC (RC-200), 300 ^oC (RC-300), 400 ^oC (RC-400), 500 ^oC (RC-500), 600 ^oC (RC-600) and 800 ^oC (RC-800) for 12 hours. The carbon K-edge NEXAFS was measured at the soft x-ray beam line BL-7A in the Photon Factory in the Institute of Materials Structure Science. The ground powder sample was mounted on a Ta plate and loaded into the chamber maintained in ultrahigh-vacuum (10^{-7} Pa). NEXAFS spectra were then obtained by measuring the sample photocurrent.

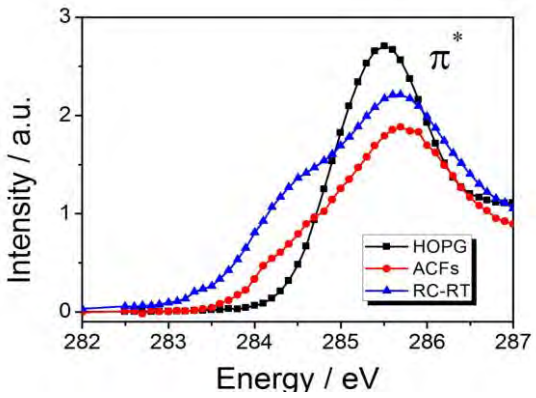

Fig. C K-edge NEXAFS for the ACFs-RT, RC-RT and HOPG.

Results

Figure shows the C K-edge NEXAFS for the ACFs-RT, RC-RT and HOPG, with the photon energy between 282 eV and 287 eV. It is clear to see that compared to the HOPG, a shoulder located at the low-energy side of the π*-state peak of the ACFs is presented. Moreover as shown in the Figure, the feature of such unoccupied state is enhanced for the evacuated HNO_3-ACFs sample at room temperature (RC-RT). The feature decreased with heating temperature.

The existence of the additional peak originates from the edge state of the nano graphene [1,2]. The edge state peak becomes enhanced in the HNO_3-ACFs since Fermi energy is shifted down through the charge transfer process. The heat-treatment under evacuation to the HNO_3-ACFs recovers the electronic structure to that of non-adsorbed ACFs, indicating the disappearance of the charge transfer interaction through desorption of the HNO_3 molecules.

References

[1] J. Joly et al., *Phys. Rev. B* 81, 245428 (2010).
[2] M. Kiguchi et al., *Phys. Rev. B* 84, 045421 (2011).

* kiguti@chem.titech.ac.jp

7C/2010G064, BM23/CH3497

XAFS analysis on the supported vanadium carbide catalysts

Nobuyuki Ichikuni*, Ryohei Ohashi, Takayoshi Hara, Shogo Shimazu
Chiba University, Inage-ku, Chiba 263-8522, Japan

1 Introduction

Early transition metal carbides (ETMC) are one of the potential materials to substitute the Pt group metals, since they have the resemblance in catalysis to those of group 8-10 metals [1]. However, high temperature is required to prepare the ETMC, and hence, the aggregation of active site is inevitable. To prevent the aggregation of ETMC, we succeeded to fix the niobium oxide on SiO_2 support and converted into NbC/SiO_2 [2].

It is reported that bulk vanadium oxide is carburized into vanadium carbide at 1253 K [3]. In this report, SiO_2 supported VC catalyst was prepared by carburization of vanadium oxide on SiO_2 (VO_x/SiO_2) as a precursor oxide. The effect of retention time on the carburization degree of vanadium was studied by XAFS.

2 Experimental

Precursor oxide (VO_x/SiO_2) was prepared from peroxovanadic acid and SiO_2 support (Aerosil, #200) by conventional impregnation method. Vanadium loading was regulated as 3 wt%. VO_x/SiO_2 was carburized in a flow reactor under CH_4-H_2 mixed gas stream to produce VC/SiO_2 catalyst. Carburizing process is consisted from two steps; one is temperature-elevating step at a linear rate of 10 K·min^{-1} to 1073 K, and the second is temperature-retaining step at a 1073 K for a certain period (0 to 90 min).

V *K*-edge XAFS were collected at BL-7C (KEK-PF) and BM23 (ESRF) in a fluorescence mode. Catalyst was transferred into aluminium cell with Kapton windows at the X-ray path. EXAFS analysis was carried out by EXAFS analysis program REX2000 (Rigaku Co.).

3 Results and Discussion

FT spectra of V *K*-edge EXAFS are presented in Fig. 1. Although small peak at around 0.24 nm, which can be assigned to V-(C)-V coordination, was observed for VC/SiO_2-1073K(0min), overall FT profile was resembled to V_2O_5. The vanadium oxide on SiO_2 support was not carburized but reduced partly as only elevating the temperature up to 1073 K under CH_4-H_2 mixed gas stream.

The peak corresponding to V-(C)-V coordination was clearly observed as lengthening the temperature-maintaining time (Fig. 1(b)-(d)). As extended the time of 90 min, FT profile showed the similarity to bulk VC except for the intensity (Fig. 1(d) and (f)). Gas composition analysis revealed that 90 min at 1073 K is enough for carburization of 3 wt% VO_x/SiO_2 into VC/SiO_2. The coordination numbers of V-(C)-V for bulk VC and VC/SiO_2-1073K(90min) were 12.0 and 8.7±0.6, respectively. It is concluded that the carburization temperature can be lowered down to 1073 K by supporting vanadium species on SiO_2 and the small vanadium carbide cluster can be obtained without visible aggregation by using VO_x/SiO_2 as a carbide precursor.

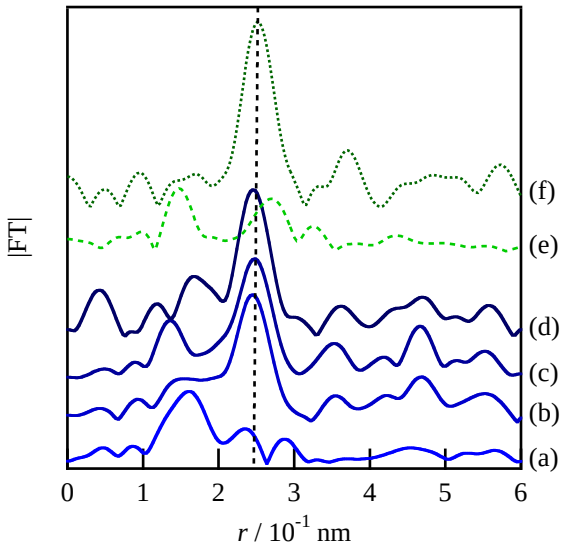

Fig. 1: FT of k^3-weighted V *K*-edge EXAFS for carburized V catalysts and reference compounds; (a) VC/SiO_2-1073K(0min), (b) VC/SiO_2-1073K(30min), (c) VC/SiO_2-1073K(60min), (d) VC/SiO_2-1073K(90min), (e) V_2O_5 and (f) bulk VC.

Acknowledgement

XAFS experiments for this report were performed on the BM23 beamline at the European Synchrotron Radiation Facility (ESRF), Grenoble, France (CH-3497, Priority Program for Disaster-Affected Quantum Beam Facilities) and BL-7C beamline at KEK-PF, Tsukuba, Japan (2010G064). We are grateful to Dr. Santiago Figueroa at ESRF for providing assistance in using beamline BM23

References

[1] R. B. Levy and M. Boudart, Science **181** (1973) 547.
[2] N. Ichikuni, et al., Top. Catal. **18** (2002) 101.
[3] S. Ramanathan and S. T. Oyama, J. Catal. **112** (1995) 16365.

* ichikuni@faculty.chiba-u.jp

6A-11B/2010G075

Depth-resolved GISAXS of Block Copolymer Films on Si substrates

Hiroshi OKUDA[1,*] Kohki TAKESHITA[1] Masayuki KATO[1] Shojiro OCHIAI[1] Shinichi SAKURAI[2]
Hiroki OGAWA[3], and Yoshinori KITAJIMA[4]
[1]Kyoto University, Kyoto 606-8501, Japan
[2]Kyoto Inst. Tech., Kyoto 606-8585, Japan
[3]JASRI, SPring8 Sayo, 679-5198, Japan
[4]Photon Factory, Tsukuba 305-0801, Japan

1 Introduction

Grazing-Incidence Small-angle X-ray scattering is a useful approach to examine three dimensional nanostructures of thin soft-matter films without destroying them. In principle, it is known that depth-sensitive measurements are possible by controlling penetration depth, which may be realized by controlling angle of incidence. However, soft matter films contain light elements, resulting in smaller critical angles. This sometimes makes a problem is controlling penetration depth by chosing appropriate incident angle because surface undulation is sometimes larger than the required angular resolution.

By using a softer X-ray photon energy, it is easier to control the depth owing to larger refractive indices, both in real and imaginary parts. We examined the change in GISAXS pattern with the incident angle at the Si K absorption edge.

2 Experiment

Toluene solution of the sample was spin-cast on a spinner with a rotation speed of 3000 rpm and then annealed at 413 K to form microphase separated structure.

The film thicknesses used in the present measurements were 400 nm for thick one and 50 nm for thin one. GISAS measurements were performed at BL11B. The photon energy was chosen as 1770 eV and 1830 eV in the present measurements. The GISAXS intensities were measured with Image Plates.

3 Results and Discussion

Figure 1 shows the change of the peak width (FWHM) of the 110 diffraction peak of microphase- separated structure that was reported to have bcc structures. Calculated penetration depth of the SEBS films are shown in the figure as a function of grazing angle, assuming densities taken from some references on bulk materials and the one obtained from reflectivity measurements. The penetration depth of the incident X-ray becomes smaller with decreasing nominal angle of incidence, and the resolution may have about a couple of ten nanometers. A simple kinematical calculation of FWHM which is determined by the penetration depth qualitatively agreed with the experimental results after correction concerning refractive indices.

The Bragg peaks observed in the GISAXS profile have two components, which have different FWHM, one with relatively wide and the other relatively small in the direction perpendicular to the substrate. For the smaller angle of incidence, the former becomes dominant, and very weak diffuse scattering from surface remains for large angle of incidence, which is eventually negligible at the larger angle of incidence above 0.8 degree. In contrast, the width of the peak is almost constant for the in-plane direction, suggesting that the degree of ordering does not change much in the in-plane direction. At present, the absolute value of FWHM in the in-plane direction is strongly affected by the beam shape which makes difficult to discuss the domain size in detail.

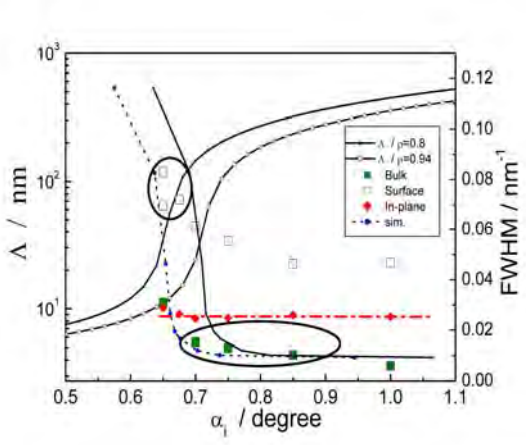

Fig. 1: FWHM of a diffraction peak for .

References

[1] H. Okuda *et al.*, J.Appl.Cryst.,44 (2011)380.

* okuda.hiroshi.5a@kyoto-u.ac.jp

7C/2010G078

XAFS study on the oxidation of Ni(0) nanocluster into Ni(II) nanocluster catalyst

Kazunari SAWADA[1], Nobuyuki ICHIKUNI*[1], Haruno MURAYAMA[2],
Takayoshi HARA[1], Shogo SHIMAZU[1]
[1]Chiba University, Inage-ku, Chiba 263-8522, Japan
[2]Chuo University, Kasuga, Bunkyo-ku, Tokyo 112-8551, Japan

Introduction

Metal nanoclusters are currently attracting much attention because of their unique characteristics. Supported NiO are used for various catalysis, such as oxidative dehydrogenation of hydrocarbons. However, conventional preparation methods of supported NiO catalysts give metal particle size usually lager than 10 nm, and hence, the development of the NiO nanocluster preparation method is expected.

In this study, we demonstrate a synthesis of SiO_2 supported Ni(II) nanocluster catalyst by oxidizing polyvinylpyrrolidone (PVP) stabilized Ni(0) colloid on SiO_2. Ni(0) colloid is sensitive toward oxygen and is easily oxidized by exposing to air. The effect of oxidation time and method on the Ni(II) nanocluster was investigated by XAFS analysis.

Experimental

Ni(0) colloid was synthesized by reduction of $NiCl_2$ using $NaBH_4$ in refluxing MeOH at 338 K in the presence of PVP [1]. PVP/Ni molar ratio was varied from 1 to 5.

Supported Ni(0) catalysts were prepared by impregnating SiO_2 (Aerosil, #200) with the colloidal Ni(0) solution, followed by solvent removal *in vacuo*. Then, catalysts were exposed to air and were washed with distilled water. Catalysts are designated with PVP/Ni ratio in the parentheses as Ni/SiO_2 (*PVP1*). The catalyst exposed to air at room temperature for 12 h before washing was denoted as Ni/SiO_2 (*PVP1*)-ox. The Ni loadings were regulated to 3 wt%.

Ni K-edge EXAFS were collected at PF BL-7C with Si(111) double crystal monochromator in a transmission mode. Samples were pressed into self-supporting disc and sealed in polyethylene bag. Curve-fitting analysis of k^3-weighted EXAFS oscillations in *k*-space were performed by REX2000 (Rigaku Co.). Model parameters for curvefitting analysis were extracted from bulk NiO.

Results and Discussion

It was expected that Ni(0) catalysts were changed into NiO by exposing to air. However, Ni(0) catalysts may react with water as well as oxygen. Thus, $Ni(OH)_2$ generation will be also expected by washing treatment.

FT of Ni K-edge EXAFS for catalysts were shown in Fig.1. The peak at around 0.27 nm can be well reproduced by using Ni-(O)-Ni. It is revealed that these supported Ni(0) catalysts were oxidized by exposing to air or washing treatment, and is suggested that the catalyst is composed of both NiO and $Ni(OH)_2$.

The curve-fitting results are listed in Table. The coordination numbers (CN) of Ni-(O)-Ni for Ni/SiO_2 (*PVP1*), Ni/SiO_2 (*PVP3*) and Ni/SiO_2 (*PVP5*) catalysts were almost the same as 6.7. PVP amount did not affect the Ni nanocluster size in these molar ratios. On the other hand, CN for catalysts exposed to air for 12 h became larger as 7.5 to 8.0. Cluster size growth is not expected by exposing to air for long time. This increment of CN can be explained by changing the ratio of NiO to $Ni(OH)_2$ because CN for $Ni(OH)_2$ is small as 6. It can be said that to increase purity of NiO, it is necessary to expose catalysts to air for a long time before washing treatment.

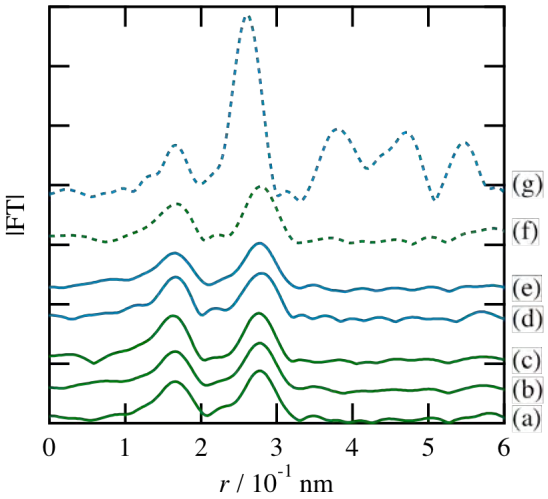

Fig.1: FT of k^3-weighted Ni K-edge EXAFS oscillations for Ni catalysts and reference compounds; (a) Ni/SiO_2 (*PVP1*), (b) Ni/SiO_2 (*PVP3*), (c) Ni/SiO_2 (*PVP5*), (d) Ni/SiO_2 (*PVP1*)-ox, (e) Ni/SiO_2 (*PVP5*)-ox, (f) $Ni(OH)_2$ and (g) NiO.

Table: Curve fitting results for Ni-(O)-Ni coordination

catalyst	CN	*r* / nm	d*E* / eV	DW / nm
Ni/SiO_2 (*PVP1*)	6.7	0.308	0.7	0.008
Ni/SiO_2 (*PVP3*)	6.8	0.308	2.3	0.008
Ni/SiO_2 (*PVP5*)	6.7	0.309	2.3	0.009
Ni/SiO_2 (*PVP1*)-ox	7.5	0.310	-0.9	0.009
Ni/SiO_2 (*PVP5*)-ox	8.0	0.309	3.8	0.009
NiO (model)	12	0.295	0.0	0.006

FT *k*-range: 35-150 nm^{-1}.

Reference

[1] Ö. Metin and S. Özkar, *J. Mol. Catal. A.* **295**, 39 (2008).

* ichikuni@faculty.chiba-u.jp

10C/2010G080
SPring-8/BL40B2/2011A1925

アミロースアルキルカルバメート－乳酸エチル系のリオトロピック液晶構造
Structure of Lyotropic Liquid Crystals of Amylose Alkylcarbamates in Ethyl Lactates

寺尾憲, 小山田景子, 佐藤尚弘
大阪大学大学院理学研究科、〒560-0043 豊中市待兼山町 1-1

1 はじめに

アミロースは水溶液中で比較的高い屈曲性を持つことが知られており、その誘導体についても液晶性の研究はみられない。最近、我々は図 1 に示すアミロースストリス（*n*-ブチルカルバメート）（ATBC）が、分子内水素結合によって安定化された剛直な形態を溶液中でも保持すること[1-3]、テトラヒドロフラン（THF）中でコレステリック液晶相が発現することを見出した[1]。同様の剛直らせん構造および液晶性は類似の化学構造を持つアミロースストリス（エチルカルバメート）（ATEC）やアミロースストリス（*n*-ヘキシルカルバメート）（ATHC）についてもみられた。これらの高分子が剛直鎖として振る舞う THF 中と乳酸エチル中において液晶性を詳細に調べた結果、THF 中ではコレステリック液晶を形成するのに対し、乳酸エチル溶液はより低濃度で白濁した液晶相を形成すること、THF 溶液とは異なり、選択反射がみられなかった。この乳酸エチル中の液晶相の構造を調べるため、本研究では放射光を用いた小角 X 線散乱（SAXS）測定を行った。

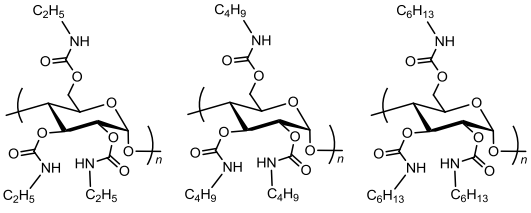

図 1 ：ATEC, ATBC, ATHC の化学構造式

2 実験

ATEC、ATBC、ATHC 試料の乳酸エチルおよび THF 濃厚溶液について PF の BL-10C および SPring-8 の BL40B2 で SAXS 測定を行った。イメージングプレート（Rigaku R-AXIS VII）を検出器とし、太さ 1.5 mm または 2 mm の石英キャピラリーに詰めた溶液の散乱像を得た。10 T の磁場を 50 時間印加した溶液の SAXS 測定も行った。

3 結果および考察

図 2 に ATBC 2 試料の乳酸エチル濃厚溶液の SAXS プロファイル（散乱強度 $I(q)$対散乱ベクトルの絶対値 q のプロット）を示す。小角側にいくつかのピークが見られる。最小角のピークが希薄溶液中の測定より決められた分子鎖長よりも少し長く、また高次のピークが 1 次のピークの整数倍の位置にあることから、スメクチック液晶の形成が明らかになった。また、磁場配向試料のデータより、これらの分子は磁場方向に配列することがわかった。またコレステリック液晶を形成する THF 中ではこのような小角側のピークはみられない。これら 2 つの溶媒の希薄溶液中において ATBC の分子形態はそれほど変わらないことから、異なる液晶相の出現は高分子―溶媒間のなんらかの相互作用の違いに起因すると考えられる。

また、広角側には鋭い 2 本のピークが観測された。これらの内、小角側のピークは分子鎖軸に垂直に配向したため分子鎖間の距離に由来するものであることがわかった。これに対し、広角側のピークは小さく、試料によっては観測できないこともあり、また、明確な磁場配向を示さなかったことから、キャピラリーの壁付近に異なる液晶構造が存在することが示唆される。ATEC や ATHC の乳酸エチル系についても同様の結果が得られた。

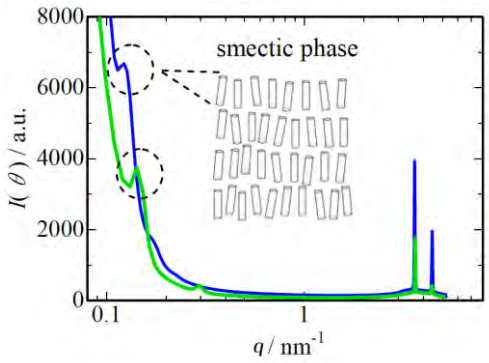

図 2：分子量の異なる 2 つの ATBC 試料の乳酸エチル濃厚溶液の小角 X 線回折プロファイル
緑：分子量 6 万、青：分子量 13 万

謝辞

測定法等を指導いただいた大阪大学の猪子洋二博士に感謝する。液晶の磁場配向に関する議論・実験でお世話になった京都大学の木村恒久教授、木村史子博士、大阪大学の諏訪雅頼博士、アミロース試料をご提供頂いた大阪府立大学の北村進一教授に感謝する。

参考文献

[1] K. Terao, *et al.* Macromolecules **43** (2010) 1061-1068.
[2] Y. Sano, *et al.* Polymer **51** (2010) 4243-4248.
[3] S. Arakawa *et al.* Polym. Chem. **3** (2012) 472-478.

4C/2010G086、2011G597、2009S2-008

共鳴 X 線散乱法を用いた $Pr_{0.5}Sr_{0.5}MnO_3$ 薄膜の空間反転対称性破れの検出
Breaking Inversion Symmetry in $Pr_{0.5}Sr_{0.5}MnO_3$ Thin Film Detected by Resonant X-ray Diffraction

山崎裕一、須田山貴亮、中尾裕則、村上洋一、
小川直毅[A]、荻本泰史[A,B]、宮野健次郎[C,D]
KEK 物構研 PF/CMRC、理研 CERG[A]、富士電機[B]、物材機構[C]、東大先端研[D]

1 はじめに

従来、強誘電性を示すペロブスカイト型酸化物は B サイトイオンが反転中心位置から変位することによって、電気分極が発現する。変位によって配位子の酸素イオンとの共有結合によるエネルギーの利得が得られるので強誘電性が安定になると考えられている。そのため、B サイトイオンに 3d 電子が入っていない d^0-ness が強誘電性発現に重要であると考えられてきた。しかし、近年になって d 電子が 3.5 個持つ Mn イオンを含む $Pr_{0.5}Sr_{0.5}MnO_3$ 薄膜において、軌道秩序による shear 歪みに伴って空間反転対称性が破れることが SHG の実験から明らかになった。第一原理計算から Mn イオンが変位している可能性が示唆されているが、実験的に確認されていない。本研究では、空間反転対称性の破れに敏感な Mn の K 吸収端プリエッジ領域における共鳴 X 線散乱実験により、Mn サイトの空間反転対称性破れを検出することを目的とした。

2 実験

本実験では LSAT(110)基板上に $Pr_{0.5}Sr_{0.5}MnO_3$ を 20 nm 成膜した薄膜試料を用いた。共鳴 X 線散乱実験は BL-4C に設置されている HUBER の 6 軸回折計を用いて行った。

3 結果および考察

$Pr_{0.5}Sr_{0.5}MnO_3$ 薄膜は 170 K で shear 歪みにより正方晶から単斜晶に構造相転移し、単斜晶ドメイン（ここでは m1 と m2 と呼ぶ）が形成される（図 a, b）。図 c には構造相転移温度以上の 200 K で(300)反射の Mn K 吸収端における共鳴 X 線散乱を測定した結果を示しているが、プリエッジ領域に異常は見られない。また、蛍光法によって測定した X 線吸収スペクトルは、構造相転移では変化しないことがわかる。図 d には単斜晶相において、m1 と m2 のそれぞれのドメインで測定した共鳴 X 線散乱スペクトルを示している。それぞれのスペクトルは、入射 X 線の偏光が異なっており、m1 ドメインは c 軸に、m2 ドメインでは a 軸に電場ベクトルが向いている。メインエッジ領域の 6.56 keV 近傍とプリエッジ領域の 6.54 keV 近傍においてドメイン間でスペクトルに差異が生じていることがわかる。メインエッジの差異は、3d 電子 x^2-y^2 軌道の秩序によるものである。一方で、プリエッジ領域の信号は空間反転対称性の破れを反映したものと考えられる。プリエッジ領域は 1s→3d の遷移に対応するが、双極子遷移は禁制であり、四極子遷移のみとなるため共鳴効果は弱い。しかし、空間反転対称性が破れると 4p 状態と 3d 状態の混成が生じ、双極子遷移が許容になるため共鳴が起きたと考えられる。スペクトルのシミュレーション計算から、電気分極に対して平行に偏光が入った時に、共鳴が現れることがわかった。この結果は、電気分極が c 軸方向に発現していること示唆している。

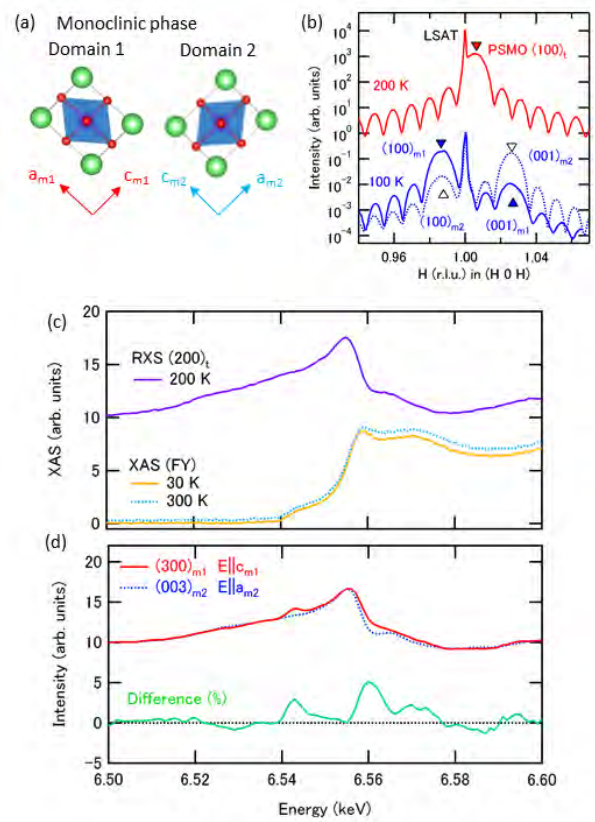

参考文献

[1] N. Ogawa et al, Phys. Rev. Lett. 108 , 157603 (2012).

* yuichi.yamasaki@kek.jp

NW2A/2010G097

Nanocrystals and small clusters investigated by synchrotron radiation and microfluidics

H. Oyanagi[1,2*], Z. H. Sun[1,2], Y. Jiang[1,2], M. Uehara[3], H. Nakamura[3], K. Yamashita[3], Y. Orimoto[3], L. Zhang[3], C. Lee[3], A. Fukano[1], and H. Maeda[3,4,5]

[1]*AIST, 1-1-1 Umezono, Tsukuba, Ibaraki 305-8568, Japan*

[2]*NSRL, University of Science and Technology of China, Hefei, Anhui 230029, People's Republic of China*

1 Introduction

Recently, small clusters (SCs) formed by N atoms where N<50 attract keen attention, associated with recent demands on understanding microscopic mechanisms of initial growth (nucleation) of nano particles (NP's) and state of "monomers". Combining synchrotron radiation and x-ray absorption spectroscopy (XAS) with microfluidics allows us to study the initial process within a limited volume (<1 mm^3) *in-situ*. Microfluidic cell[1] is a microchannel device along which a chemical reaction occurs in a laminar flow.[2] For investigating time-dependent structures of NPs, "monomers" or SCs, a high-sensitivity is needed which is realized by high brilliance x-ray beam available from insertion devices at the 3rd generation facilities (*ca.* 10^{12} photons per sec) and modern x-ray detectors.

2 Experiment

Here, we describe *in-situ* XAS studies using microfluidics to illustrate the capability described above, demonstrated by a couple of applications, *i.e.*, i) the structural and kinetics studies during the initial stage of CdSe NPs[3] and ii) copper SCs (N=13-19) photo-induced by intense x-ray beam. Colloidal semiconductor NPs, sometimes called quantum dots, became popular due to their size-tunable optical properties and a variety of industrial applications. We demonstrated that time-dependent EXAS (conventionally used as an average local probe) is informative on higher order structures, *i.e.*, NP size and density if bond formation kinetics is analyzed.[4] The second application is copper SCs formed by a reducing reaction in organic solvent under photo-irradiation. The local structure of SCs prepared in organic solution by reducing Cu(II) hexafluoroacetylacetonate [$Cu(hfac)_2$] was studied by XANES and EXAFS. The Cu K-XANES spectra indicated the formation of copper SCs by ligand-exchange with oleylamine and a subsequent reducing by diphenylsilane.

3 Results and Discussion

Our *in-situ* EXAFS study on CdSe NPs found discrepancy with the optical spectroscopy that implies that at the initial stage of the nucleation and growth, most of the particles are in the amorphous state, contrary to hypothesis of the classical nucleation theory. These amorphous nuclei would crystallize rapidly over time, with the rate depending on the reaction conditions such as growth temperature, reaction time, surface ligand, and so on. The effect of surfactant (amine) was also studied through a comparison of the growth and crystallization processes in the presence of DDA with different concentrations. The results show a strong non-linear effect in surfactant concentration. The results indicate that surfactants play two competitive roles: accelerating the formation of amorphous nuclei, and hindering the subsequent crystallization and growth when the ligand concentration exceeds a critical limit. The multiple-scattering (MS) XANES calculation for various model SCs suggests that the SCs consist of 13-19 atoms that are characterized by a similar fcc-like local structure although the SCs are expected to be insulating based on the electronic state calculated by DFT on possible models.

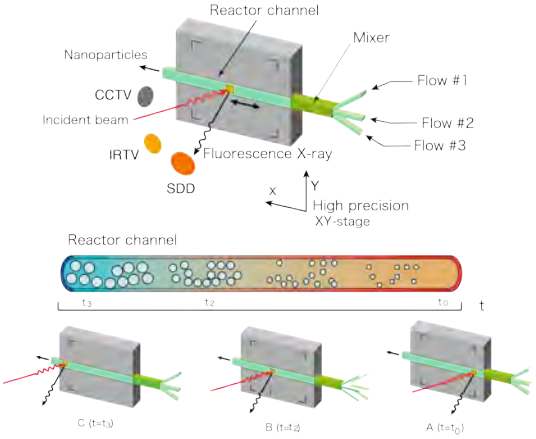

Fig. 1: Schematic representation of in-situ XAS using a microfluidic cell

Acknowledgement

The authors express their thanks to the PF staff for their kind support during the experiment.

References

[1] H. Nakamura *et al.*, *Chem. Commun*. 2844 (2002).
[2] H. Holman *et al.*, *Anal. Chem*. 81, 8564 (2009)
[3] M. Uehara *et al.*, *Appl. Phys. Lett*. 94, 063104 (2009).
[4] Z. Sun *et al.*, *J. Phys. Chem.* C 113, 18608 (2009).
[4] H. Oyanagi *et al.*, *J. Appl. Phys.* 111, 084315 (2012).
*h.oyanagi@aist.go.jp

27B/2010G143

EXAFS Investigation of Th(IV)-*N*,*N*-Di-alkylamides Complexes

Shinichi SUZUKI, Yoshihiro OKAMOTO, Tsuyoshi YAITA, and Hideaki SHIWAKU
Quantum Beam Science Directorate, Japan Atomic Energy Agency, Tokai-mura, Naka-gun, Ibaraki 319-1195

Introduction

In our previous research work, the obtained bond distance between uranium(VI) and oxygen of *N*,*N*-dialkylamides are 2.40 Å for *N*,*N*-dioctylbutanamide (DOBA) and 2.31 Å for *N*,*N*-di(2-ethyl)hexyl(2,2-dimethyl)propanamide (D2EHDMPA) [1]. The bond distance of U(VI)-O=C(amide) depended on amides structure, especially carbonyl alkyl branching on α-position. In this study, we investigated Th(IV) complexes with these *N*,*N*-dialkylamides in the organic solution by extended X-ray absorption fine structure(EXAFS).

Experimental

N,*N*-dialkylamides: DOBA and D2EHDMPA were synthesized in our laboratory (Fig.1). The thorium samples were made as following procedures. 1) 1.0 ml of 1 M DOBA-n-dodecane as an organic solvent was shaken with the same volume of 5.0 M nitric acids containing 40 mM of Th^{4+}. Equal volumes (0.5 mL) of aqueous and pre-equilibrated organic phases containing Th(IV) were shaken for 10 minutes in a thermostatic atmosphere at 298 K within ±0.1 K. After the equilibration, the system was centrifuged at 5000 rpm for 5 minutes. After centrifugation, 0.45 mL organic solution was separated and used as sample. 2) 0.5 mL of ethanol as an organic solvent containing 0.8 M DEH2DMPA was added to the same volume of ethanol solution containing 40 mM of Th^{4+}. After mixture these solution, 0.45 mL ethanol solution was used as samples.

The EXAFS measurement was carried out at beam line BL27B station using the fluorescence and the transition methods. The measurement was carried out Th-L_{III} (16.30 keV) absorption edge. The extraction data of EXAFS oscillation from absorption spectra were carried out by WinXAS Ver. 3.1**[2]**. The theoretical parameters for curve fittings of the EXAFS spectra were calculated using FEFF 8.20 **[3]**.

Results and Discussion

Figure 1a shows the raw k^3-weghted Th L_{III}-edge EXAFS spectra and the corresponding fourier transforms (FT) of Th(IV)-DOBA complex in n-dodecane prepared by the solvent extraction methods. The first peak of the RSF is based on two carbonyl oxygen atoms of DOBA and 4 oxygen atoms of the nitrate ions which coordinated to Th by bidentate fashion and 2 nitrogen atoms of nitrate ions. The obtained bond distance between Th(IV) and carbonyl oxygen of DOBA is 2.32 Å which is shorter than that of U(VI)-DOBA complex (2.40 Å ; which showed at introduction). This result shows that DOBA coordinates to Th(IV) more strongly than U(VI).

Figure 1b shows the raw k^3-weghted Th L_{III}-edge EXAFS spectra and the corresponding fourier transforms (FT) of Th(IV)-D2EHDMPA complex in ethanol (Th : amide = 1 : 20). The first peak of the RSF is based on two oxygen atoms of water molecules and 4 oxygen atoms of the nitrate ions which coordinated to Th by bidentate fashion and 2 nitrogen atoms of nitrate ions. The obtained bond distance between thorium(IV) and oxygen of water molecule is 2.35 Å. This result means that Th(IV) does not combine with D2EHDMPA in ethanol solution, even if D2EHDMPA exists superfluously because the steric hindrance around carbonyl oxygen of D2EHDMPA increased with introducing tert-butyl group to carbonyl carbon atom.

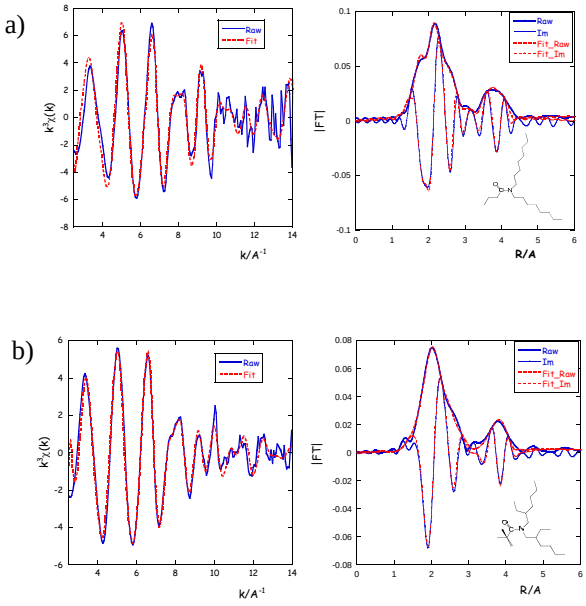

Fig.1 The raw k^3-weghted Th L_{III}-edge EXAFS spectra (left) and the corresponding FTs (right) ; a) Th(IV)-DOBA complex in n-dodecane solution, b) Th(IV)-D2EHDMPA complex in ethanol solution (Th : amide= 1 : 20). The phase shifts are not corrected. Experimental data (Blue line), theoretical fit (Red line).

References

[1]S.Suzuki et al., *OECD-NEA/NSC/DOC*, **15**, 13 (2009)
[2]T.Ressler, J. Synch. Rad., **5**, 118 (1998).
[3]A.L.Ankudinov et al., Phys. Rev. B **58**, 7565(1998).

* suzuki.shinichi@jaea.go.jp

NW10A/2010G164

Crystallization Process of $SrZrO_3$ Thin Films by Pulsed Laser Deposition

Noriko SATA*[1], Yuta FUJIWARA[1], Yoshikazu SHIBATA[1],
Katsuhiro NOMURA[2], Hiroyuki KAGEYAMA[2], Fumitada IGUCHI[1], Hiroo YUGAMI[1]
[1]Graduate School of Engineering, Tohoku University, Sendai 980-8579, Japan
[2]AIST-Kansai, Ikeda, Osaka 563-8577, Japan

Introduction

Pulsed Laser Deposition (PLD) is well known to provide highly epitaxial thin films of perovskite type oxides when they are grown on single crystal substrates at high temperatures. We have reported that room-temperature PLD and the following post-annealing process can be another route for epitaxial crystallization, however, their properties may be different due to different routes of crystallization [1]. *In-situ* XRD analyses of crystallization process have revealed that the as-deposited amorphous phase can easily be rearranged into a periodical structure above 520°C along with the ionic arrangements of the single crystal substrate, while polycrystalline phases of a few hundred-nm sized grains are obtained on amorphous substrates at the same temperature. Furthermore, a zirconia phase is obtained above 620°C on the amorphous substrate.

In this report, the results of XANES analyses of $SrZr_{0.95}Y_{0.05}O_3$ (SZY) and $Zr_{0.84}Y_{0.16}O_{2-\delta}$ (YSZ) thin films are presented to observe the change in the local structures around Zr ions in amorphous and the crystalline phases.

Experimental

Thin films have been deposited on optically-polished fused silica wafers (15×15×0.5 mm^3) by PLD at room temperature using ceramic targets. As-deposited and post-annealed thin films have been investigated by XRD and XANES measurements. Fluorescence XANES spectra of the Zr K-edges have been obtained by a Lytle-type ionization chamber at PF-AR NW10A.

Results and discussion

It is found that the zirconia secondary phase, in the form of nano-sized crystals around the a few hundred nm-sized SZY grains, precipitates only on amorphous substrates and the volume ratio of zirconia phase depends on the PLD condition. In our previous reports [1], it has been shown that configuration (CN, bond length) of the oxygen ions around Sr in as-deposited thin film is clearly different from that of the crystalline phase both in powder and the post-annealed SZO thin films, while almost no difference is found around Zr. It is found that YSZ thin films prepared by the same process crystalize easily below 500°C. These facts suggest that very similar local environment around Zr ion is formed already in the as-deposited amorphous phase as in the perovskite structure, that is, the coordination number of Zr cation in the SZY thin films is 6 to form ZrO_6 molecule both in as-deposited and post-annealed specimens. The formation of ZrO_6 in the as-deposited amorphous phase by PLD from SZY target might enable easy crystallization at relatively low temperatures.

As reported in zirconium oxides with different structures [2], XANES spectrum reflects the coordinating environment of the absorbing atom. Difference in the peak profiles in Zr K XANES spectra observed between YSZ and SZY thin films both in as-deposited and post-annealed thin films in the figure suggests the formation of the similar short range order by PLD at room temperature with each target material.

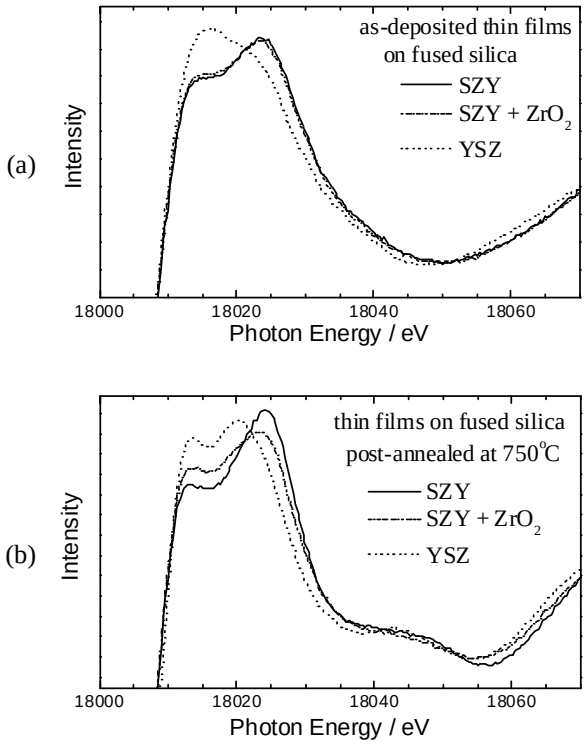

Fig. Zr-K XANES spectra of SZY and YSZ thin films.
(a) as-deposited, (b) post-annealed (750C, 10 hrs).
($SZY+ZrO_2$: with higher volume ratio of zirconia phase).

References

[1] N.Sata *et al.*, Photon Factory Activity Report, Part B, 2008 #26 (2009) 132/ 2010 #28 (2011) 173

[2] D.Komyoji *et al.*, Solid State Ionics 50 (1992) 291

* Noriko.Sata@dlr.de (present address: DLR-Stuttgart, 70569 Stuttgart, Germany)

15C/ 2010G168

SR/X 線トポグラフィによるダイヤモンド単結晶の転位解析
Analysis of Dislocations in Single Crystalline Diamond by SR/X-ray Topography

梅沢 仁*, 加藤 有香子
産業技術総合研究所 ダイヤモンド研究ラボ、〒305-8568 つくば市梅園 1-1-1

1 はじめに

半導体ダイヤモンドは、優れた材料物性から次々世代パワーデバイス材料として期待されている。これまで高温高圧合成ダイヤモンド上にデバイスが試作され、高温・高電流密度・高耐圧動作が可能であることが示された[1,2]。しかし、その特性は材料限界には及んでおらず、特に素子サイズの大型化にともなう素子特性の劣化が指摘されている[3]。これは、デバイス電極下にエピを貫通する欠陥(転位)が混入していることが原因と考えられる。

この問題を解決する為、①欠陥解析手法の確立、②電流リーク源となる欠陥の特定　②低欠陥基板の合成技術開発、に取り組む必要がある。今回、我々は大型単結晶ウェハの種結晶に用いられる IIa 型ダイヤモンド基板中に存在する転位のバーガースベクトルと転位ベクトルを評価、解析した。

2 実験

転位観察として HPHT 法で合成した住友電工製単結晶ダイヤモンド(IIa 型)を用いて X 線トポグラフィ評価を行った。X 線トポグラフィには、フォトンファクトリーの BL15C の単色 X 線を用いている。簡単な配置図を図 1 に示す。回折ベクトル(g)として、反射 Bragg 配置[044]、[404]、[113]、[1-13]、および透過 Laue 配置[111]、[220]を用いた。回折ベクトル(g)とバーガースベクトル(b)と像のコントラストの間には次のような関係があるため、X 線トポグラフィ像から転位のバーガースベクトルと転位ベクトルを知る事ができる。

g・b = 0 : 像コントラスト消滅

反射 Bragg 条件では、表面感度を増すための低角入射(ω_{inc}<0.5°)から、深さ方向の評価が可能な条件(1°<ω_{inc}<4°)まで X 線波長を変えることによって転位評価を行った。転位像の取得には、まず X 線イメージングプレートにて各 g ベクトルにおける回折条件(ω、2θ、ϕ)を確認し、続いて Ilford 社製 Type L4 原子核乾板(25μm)で回折像を取得した。取得した X 線トポグラフィ像を図 2 に示す。

3 結果および考察

図 2 の X 線トポグラフィ像が示すように、IIa 型 HPHT ダイヤモンドには主な転位種として積層欠陥と貫通転位が見られている。欠陥密度は 10^2~10^4/cm^2 程度であった。これは HPHT/Ib 型結晶と比べて低い密度である。貫通転位は、バーガースベクトルと転位ベクトルが垂直な刃状転位と 45°、60°の複合転位が確認できている。これら転位の種類と発生場所に規則性はなかった。HPHT/Ib 型ダイヤモンドと比べて積層欠陥が多く観察されており[4]、合成条件や Ib 結晶中に含まれる不純物窒素が積層欠陥の生成に影響を与えている可能性がある。今後は、エピ膜を合成した際の転位の引き継ぎ、I-V 特性について評価を行う。

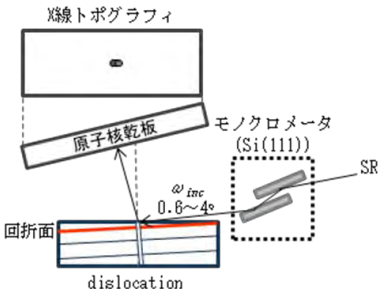

図１　X 線トポグラフィ実験配置図

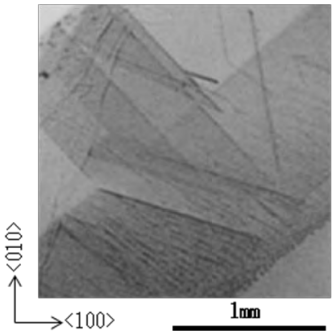

図２　X 線トポグラフィ g=[111]

4 まとめ

HPHT 合成 IIa 単結晶ダイヤモンドを X 線トポグラフィ法によって転位評価した。IIa 型に含まれる転位は積層欠陥の他、刃状転位および 45°、60°複合転位が存在することが分かった。Ib 型と比べ転位密度は低いものの積層欠陥が多数存在しており、合成条件もしくは不純物が転位生成に影響を与えている可能性があることが分かった。

参考文献

[1] H.Umezawa et al, Diamond Relat. Mater., 24 (2012) 201.
[2] P.N.Volpe et al., Appl. Phys. Lett., 97 (2010) 223501.
[3] R.Kumaresan et al., Diamond Relat. Mater., 19 (2010) 1324.
[4] H.Umezawa et al., Diamond Relat. Mater., 20 (2011) 523.

* hitoshi.umezawa@aist.go.jp

7C, 9A, 9C/2010G171

希土類元素をプローブに用いたチタン酸バリウムの相転移現象の EXAFS 解析
EXAFS study on phase transition phenomena of $BaTiO_3$ using Ho as a probe

松嶋雄太*, 春日慎之介, 岩瀬勝彦
山形大学大学院理工学研究科 〒992-8510 山形県米沢市城南 4-3-16

1 はじめに

チタン酸バリウム($BaTiO_3$)は代表的な電子セラミックスであり、積層セラミックコンデンサの主成分として用いられている。チタン酸バリウムの結晶は、室温では強誘電体相である正方晶系に属し、130℃付近で常誘電体相である立方晶系に相転移する。また、誘電率は相転移付近で極大を示す。この相転移現象について、X 線回折法で調べた例はあるが、局所構造という観点で XAFS を用いて相転移現象を調べた例はない。その理由の一つとして、Ti K 吸収端(4965 eV)と Ba L 吸収端(L_I: 5951, L_{II}: 5630, L_{III}: 5249 eV)が近接しているため、構成元素に対する XAFS 法が適用できないということが挙げられる。

一方、筆者らは近年、新しい水溶性のチタン酸バリウム前駆体の開発に成功し、水系ディップコート法による透明チタン酸バリウム薄膜の作製に成功した[1]。この前駆体では、各成分が原料状態において、水溶液というイオン・分子レベルで均一な状態で分散されるため、ドープチタン酸バリウム系作製の際に有利であることが分かってきた。希土類元素の一つである Ho を添加したチタン酸バリウム系に対する筆者らの一連の研究で、仕込み組成により容易に Ho の置換サイトを制御できる可能性が明らかになった。

本研究では、局所構造の観点から相転移挙動を調べるために Ho^{3+}をプローブとして Ti^{4+}サイトに置換し、温度とともに Ho 周囲の局所構造がどのように変化するかを調べることを目的とした。具体的には、筆者らの開発した置換サイト制御技術を用いて Ho^{3+}を Ti^{4+}に置換した $BaTi_{0.95}Ho_{0.05}O_{3-\delta}$を作製し、温度を変化させながら Ho L_{III} EXAFS 解析を実施した。

2 実験

測定用の試料は、筆者らが開発してきた水溶液前駆体法を使用した[2]。$BaTiO_3$ を基本組成とし、Ho^{3+}を Ti^{4+}に置換した $BaTi_{0.95}Ho_{0.05}O_{3-\delta}$ (Bサイト置換)を作製した。なお、Ti^{4+}が酸化数の異なる Ho^{3+}に置換される際の電荷補償メカニズムについては不明な点もあるが、ここでは便宜上酸素空孔によるものと仮定した。測定は XAFS 測定ステーション BL-7C, 9A, 9C で行った。測定はライトル検出器による蛍光法とし、Ho L_{III} 端にて測定を行った。作製したドープチタン酸バリウムペレットを小型のセラミックヒータ上に固定し、温度を室温、50℃、80℃、110℃、140℃、180℃と変化させながら XAFS スペクトルを測定した。なお、解析には FEFF6 を使用し、第一近接の酸素に対しシングルシェルモデルを使用してフィッティングを行った。

3 結果および考察

図 1 に、Ho^{3+}をプローブに用いた局所構造の変化を示す。図 1(a)は Ho-O の原子間距離の温度変化、図 1(b)は第一近接の酸素シェルの Debye-Waller 因子の温度変化である。

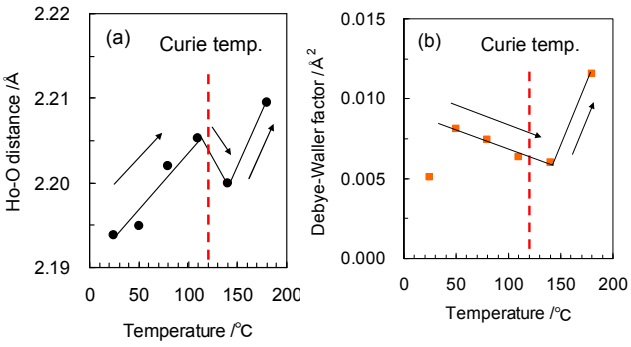

Fig. 1 Temperature dependency of Ho-O distance and Debye-Waller factor of Ho LIII EXAFS for $BaTi_{0.95}Ho_{0.05}O_{3-\delta}$. (a) Ho-O distance and (b) Debye-Waller factor of the first O shell.

Ho-O 酸素の原子間距離に注目すると、大変興味深いことに、温度の上昇とともに Ho-O 間距離が増大し、強誘電体相－常誘電体相間の相転移点であるキュリー点付近で一旦原子間距離が減少することが分かった。そして、キュリー点後に再び増加に転じることが分かった。また、Ho に配位する酸素シェルの Debye-Waller 因子に注目する(図 1(b))と、温度の上昇とともに減少し、やはりキュリー点付近で特異な現象を示すことが分かった。

この結果を完全に解釈できているわけではないが、局所構造的な観点から見て相転移付近で構造緩和などの特異な現象が起こっていることを示唆していると考えられる。ただし、測定温度の間隔が広いことは課題として残っており、また、現象の再現性などを慎重に調査している。今後更に解析の精度を挙げて検討していく予定である。

参考文献

[1] 岩瀬勝彦ら, 日本セラミックス協会 2010 年年会講演予稿集 P.94 (2010).
[2] S.Kasuga et al., 12th ECerS – in Stockholm, Abstract #1066 (2011).

* ymatsush@yz.yamagata-u.ac.jp

6A, 15A/2010G181

Structure of Twisted Yarn of Carbon Nanotubes under Tensile Deformation

Masatoshi SHIOYA[1,*], Yoshiki SUGIMOTO[1], Shinichi SAKURAI[2], Katsuhiro YAMAMOTO[3]
[1]Tokyo Institute of Technology, 2-12-1-S8-34 Ookayama, Meguro-ku, Tokyo 152-8552, Japan
[2]Kyoto Institute of Technology, Matsugasaki, Sakyo-ku, Kyoto 606-8585, Japan
[3]Nagoya Institute of Technology, Gokiso-cho, Showa-ku, Nagoya 466-8555, Japan

1. Introduction

A twisted yarn of carbon nanotubes (CNT) has the possibility to show very high strength, while more detailed studies are needed to optimize the processing method and the structure of the yarn. The change in the structure of the yarn under tensile deformation is one of the subjects to be studied. In this study, time-resolved small-angle X-ray scattering (SAXS) of the twisted yarn of CNT has been carried out and the results have been analyzed in more detail as compared with the previous study.

2. Experimental

The twisted yarn used in this study was 8 μm in diameter and consisted of multi-walled CNT having a diameter of 10 to 15 nm and a length of 200 μm. The single yarn with a length of 6 mm was stretched stepwise with an increment of 20 μm. At each step of stretching, SAXS was measured for 100 s. The SAXS patterns were detected using an image intensifier and a CCD camera.

3. Results and Discussion

The distribution of the CNT in the yarn varies depending on the processing method of the yarn and two typical distribution patterns are shown in Fig. 1. The pattern of Fig. 1(a) is developed when unidirectionally aligned CNT mat is wound and all the CNT have a constant inclination angle around the yarn axis. In this case, the azimuthal SAXS intensity distribution shows two maxima around the equator. On the other hand, the patterns of Fig. 1(b) is developed when unidirectionally aligned CNT yarn is twisted and the inclination angle of CNT varies in the radial direction. In this case, the azimuthal SAXS intensity distribution shows a maxima on the equator.

The measured azimuthal SAXS intensity distribution could be decomposed into two peaks as shown in Fig. 2. This indicates that the distribution pattern of CNT for the yarn used in this study is close to that of Fig. 1(a) whereas inclination angle is not constant but has some distribution around the average inclination angle. The changes of the average inclination angle with the displacement of the chucks during tensile deformation is shown in Fig. 3. It is known that the inclination angle decreases during tensile deformation of the twisted yarn. This result will be used for the simulation of the tensile properties of the twisted yarn of CNT.

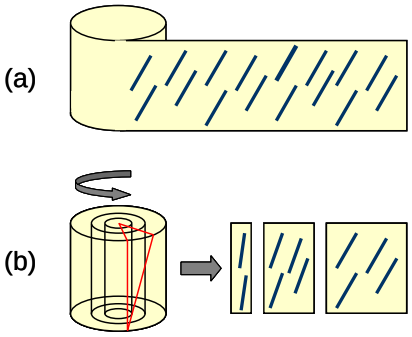

Fig. 1 Distribution patterns of CNT in twisted yarns where inclination angle is constant (a) and varies with radial distance (b).

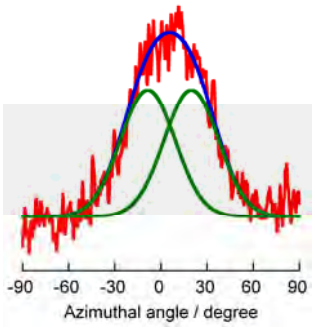

Fig. 2 Azimuthal SAXS intensity distribution of twisted yarn of CNT. Measured curve (red) could be decomposed into two peaks (green) and their sum (blue) reproduced the measured curve.

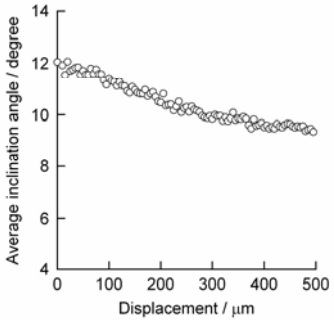

Fig. 3 Variation of average inclination angle of CNT with displacement of chucks.

* shioya.m.aa@m.titech.ac.jp

27B/2010G196

アメリシウム酸化物の XAFS 測定
XAFS measurement of Am oxides

中田正美*, 西剛史, 赤堀光雄, 鈴木知史
日本原子力研究開発機構、〒319-1195 那珂郡東海村白方白根２−４

1 はじめに

アメリシウムなどの放射性物質、特にα放射体は、取り扱いが可能な施設が限られており、研究手段もそれほど多くないのが現状である。その中で、物質構造科学研究所・放射光科学研究施設（Photon Factory:PF）の BL-27 は、アメリシウムの XAFS 測定が出来、物性研究が可能な数少ない施設である。

本報告では、AmO_2 及び Am_2O_3 の XAFS 測定した結果を報告する。

2 実験

Am 核種として、同じ Bq 数でも試料量が多く使用できる半減期が長い ^{243}Am を用いた。$^{243}AmO_2$ 及び $^{243}Am_2O_3$ は、グローブボックス中で合成し、グローブボックス中に設置してある X 線回折測定により確認をおこなった[1,2]。図１に Am_2O_3 のスペクトルを示した。ZrN は、内部標準試料である。これらの試料から BL-27 の許可量である 37MBq を分取し、グラファイト粉末と良く混合し、ペレットを作成し、容器に封入し、密封線源を作製した。この密封線源を A 型輸送容器に入れ PF へ輸送し、XAFS 測定用試料とした。XAFS 測定は、試料を専用のチェンバーに入れ、Am-L_3 吸収端（約 18.5keV）で測定した。

3 結果および考察

測定した EXAFS スペクトルを図２（上）、XANES スペクトルを図２（下）に示した。EXAFS スペクトルを解析した結果、X 線回折の結果と一致した。また、XANES スペクトルでは、図２（下）に示したように AmO_2 と Am_2O_3 のでは差が見られた。XANES スペクトルと第一原理計算をおこなった結果を比較し、電子構造について検討した[1-4]。

4 まとめ

試料量を多く使用できない Am でも、輝度が高く許可がある PF で Am 酸化物の XAFS スペクトルを測定することが出来た。

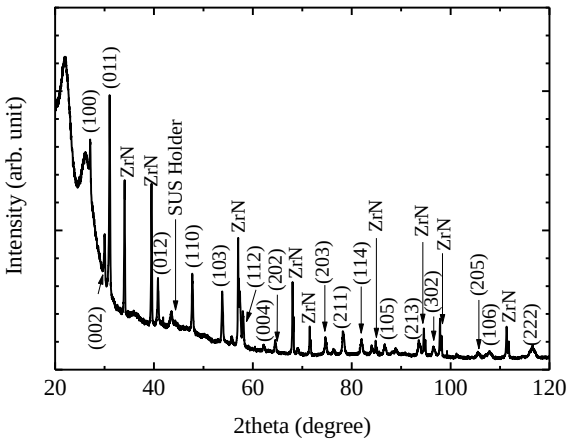

図１：Am_2O_3 の X 線回折測定

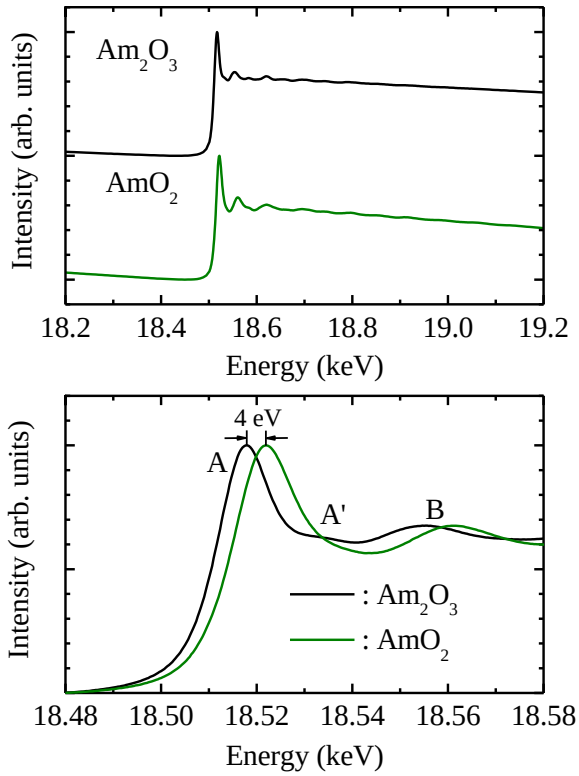

図２：AmO_2 及び Am_2O_3 の EXAFS（上）、XANES（下）スペクトル

参考文献
[1] T. Nishi *et al.*, J. Nucl. Mater. **374** (2008) 339.
[2] T. Nishi *et al.*, J. Nucl. Mater. **401** (2010) 138.
[3] C. Suzuki *et al.*, J. Quantum. Chem. **109** (2009) 2744.
[4] C. Suzuki *et al.*, J. Phys. Chem. Sol. **73** (2012) 209.

*nakada.masami@jaea.go.jp

7C/2010G502
8A/2011G501

Thin Film Electrode of Prussian Blue Analogue for Li-ion Battery

Yutaka Moritomo[1,2,3], Masamitsu Takachi[2], Yutaro Kurihara[3], and Tomoyuki Matsuda[3]
[1]TIMS, University of Tsukuba, Tsukuba305-8571, Japan
[2]School of Science and Engineering, University of Tsukuba, Tsukuba, Ibaraki 305-8571, Japan
[3]Graduated School of Pure and Applied Science, University of Tsukuba, Tsukuba 305-8571, Japan

1 Introduction

Next-generation electrode materials that provide rapid and reversible Li_+ insertion/extraction have been intensively explored in order to achieve a low-cost Li^+ secondary battery (LIB) with a high charge/discharge rate. Recently, Matsuda and Moritomo[1] reported that a thin film of the Prussian blue analogue, $Na_{1.32}Mn[Fe(CN)_6]_{0.83}3.5H_2O$ exhibits a large capacity (= 128 mAh/g) and good cyclability (= 87\% of the initial value at 100 cycles).

In this study, we investigated the Li^+ intercalation speed in thin film electrodes of the Prussian blue analogues $(Li,Na)_{4y-2}M[Fe(CN)_6]_yzH_2O$ (M = Ni, Co, Mn and Cd).X-ray powder diffraction (XRD) measurements revealed that the Li-substituted compounds are face-centered cubic ($Fm\underline{3}m$; Z = 4).The X-ray absorption fine structure (XAFS) near the Fe K-edge revealed the reduction of Fe (Fe^{3+} ➔ Fe^{2+}) with the Li^+ intercalation. The reduction of Fe causes a significant color change of the thin film electrodes.

2 Experiment

Thin films of $Na_{0.72}Ni[Fe(CN)_6]_{0.68}5.1H_2O$ (denoted as NNF68), $Na_{0.84}Co[Fe(CN)_6]_{0.71}3.8H_2O$ (NCF71), $Na_{1.24}Mn[Fe(CN)_6]_{0.81}3.0H_2O$ (NMF81), and $Na_{1.84}Cd[Fe(CN)_6]_{0.96}4.8H_2O$ (NCdF96) were electrochemically synthesized on an indium tin oxide (ITO) transparent electrode under potentiostatic conditions at - 0.50 V vs a Ag/AgCl electrode in an aqueous solution. The thicknesses of the films were 1 μm, which were measured with a profilometer (Dektak3030). The mass of each film was measured with a conventional electronic weighing machine after the film was carefully removed from the ITO glass with a microspatula. The experimental error of the mass is 10%. Chemical compositions of the films were determined by the inductively coupled plasma (ICP) method and CHN organic elementary analysis (Perkin-Elmer 2400 CHN Elemental Analyzer). Rietveld analysis of the XRD pattern revealed that the compounds are face-centered cubic with lattice constant a = 10.200(3) Å for NNF68, 10.296(2) Å for NCF71, 10.544(2) Å for NMF81, and 10.7001(4) Å for NCdF96. The Li^+ was substituted for Na^+ by performing charge/discharge cycles of the thin films against Li. The electrolyte was ethylene carbonate (EC)/diethyl carbonate (DEC) solution containing 1 mol/L $LiClO_4$. The charge/discharge current is 10 μA (= 0.5 - 1.0 C), and the cutoff voltage was from 2.0 to 4.2 V. Thus, we obtained thin film electrodes, i.e., $Li_xNa_{0.04}Ni[Fe(CN)_6]_{0.68}5.1H_2O$ (M = Ni), $Li_xNa_{0.13}Co[Fe(CN)_6]_{0.71}3.8H_2O$ (M = Co), $Li_xMn[Fe(CN)_6]_{0.81}3.0H_2O$ (M = Mn), and $Li_xNa_{0.88}Cd[Fe(CN)_6]_{0.96}4.8H_2O$ (M = Cd). In the XRD and XAFS experiments, the Li concentration (x) was controlled by the cutoff voltage.

The valence states of the Fe, Mn, Ni, Co, and Cd sites were determined by the *ex-situ* X-ray absorption spectra (XAS) around the K-edge and L_I -edge spectra. The XAS measurements were conducted at the beamline 7C of the Photon Factory, KEK. The XAS spectra were recorded by a Lytle detector in a fluorescent yield mode with a Si(111) double-crystal monochromator at 300 K. The background subtraction and normalization were done using ATHENA program[2].

The *ex-situ* powder X-ray diffraction (XRD) patterns were measured at the beamline 8A of KEK-PF equipped with an imaging plate detector. The charged/discharged samples were washed with DEC, and were carefully removed from the ITO glasses. The obtained powders were sealed in 300 μm glass capillaries. XRD patterns were measured at 300 K and the exposure time was 10 min. Wavelength of the X-ray was 0.77474 Å. The lattice constants of each compounds were refined by the RIETAN-FP program [3].

3 Results and Discussion

Figure 1 shows the XAFS spectra of the thin film electrodes against x.The measurements were carried out at the 7C beamline of Photon Factory (PF), KEK. The XAFS spectra near the Fe K-edge, Ni K-edge, Co K-edge, Mn K-edge, and Cd L_I-edge were recorded by a Lytle detector in fluorescent yield mode with a Si(111) double-crystal monochromator and were normalized by the intensities at 7140, 8360, 7740, 6560, and 4060 eV, respectively. In all the compounds, the absorption peaks in the Fe K-edge spectra [Figs. 2(a), 2(c), 2(e) and 2(g)] show a redshift with increasing in x. The redshift is ascribed to the reduction of Fe (low-spin Fe^{3+} ➔ low-spin Fe^{2+}. The reduction of Fe causes a significant color change, as shown in Fig.2, which can be utilized as a battery power monitor. On the other hand, the absorption peaks in the Ni K-edge [(b)], Co K-edge [(d)], Mn K-edge [(f)], and Cd L_I-edge [(h)] spectra show no shift, indicating that the valence states of M remain unchanged.

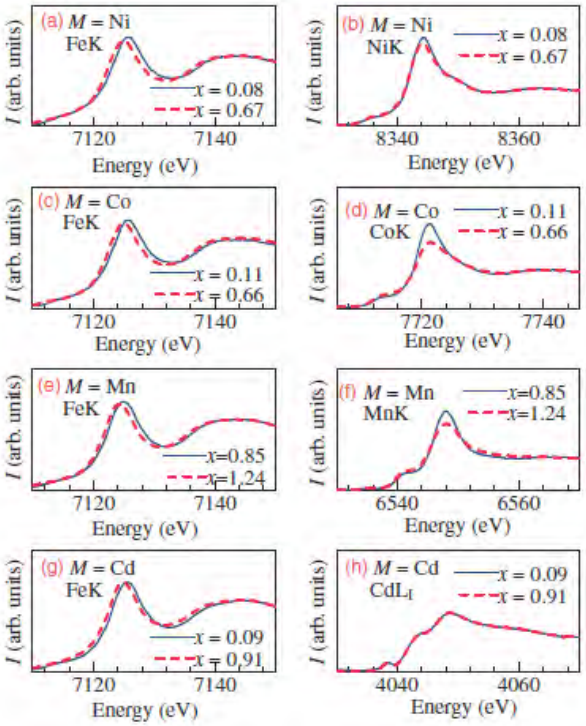

Fig. 1: X-ray absorption spectra of $Li_xNa_{0.04}Ni[Fe(CN)_6]_{0.68}5.1H_2O$ [(a) and (b)], $Li_xNa_{0.13}Co[Fe(CN)_6]_{0.71}3.8H_2O$ (c) and (d)], $Li_xMn[Fe(CN)_6]_{0.81}3.0H_2O$ [(e) and (f)], and $Li_xNa_{0.88}Cd[Fe(CN)_6]_{0.96}4.8H_2O$ [(g) and (h)] against x. The two spectra completely overlap each other in (h)

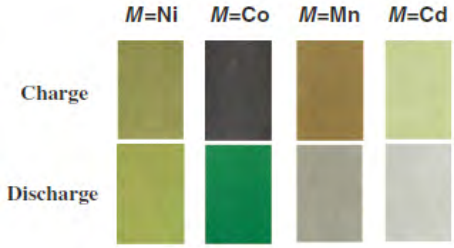

Fig. 2: Color of thin-film electrodes of the Prussian blue analogues, $Li_xNa_{0.04}Ni[Fe(CN)_6]_{0.68}5.1H_2O$ (M = Ni), $Li_xNa_{0.13}Co[Fe(CN)_6]_{0.71}3.8H_2O$ (M = Co), $Li_xMn[Fe(CN)_6]_{0.81}3.0H_2O$ (M = Mn), and $Li_xNa_{0.88}Cd[Fe(CN)_6]_{0.96}4.8H_2O$ (M = Cd), in the charge and discharge states

Figure 3 shows examples of the XRD patterns of $Li_xNa_{0.13}Co[Fe(CN)_6]_{0.71}3.8H_2O$. We confirmed that the XRD patterns of all the compounds can be indexed with the face-centered cubic ($Fm\underline{3}m$: Z = 4) setting, as shown in Fig. 3. The lattice constants (a) are plotted in Fig. 4 against x. Except for the Cd compound, a slightly decreases with increasing in x. The decrease in a is probably due to the smaller size of $[Fe^{II}(CN)_6]^{4-}$ than that of $[Fe^{III}(CN)_6]^{3-}$. Actually, the Fe^{II} - N bond length (= 3.00 - 3.01 Å) is shorter than the Fe^{III} - N bond length (= 3.10 Å) in $RbMn[Fe(CN)_6]$. In the Mn compound, a decreases in the Mn redox region (x < 0.24).

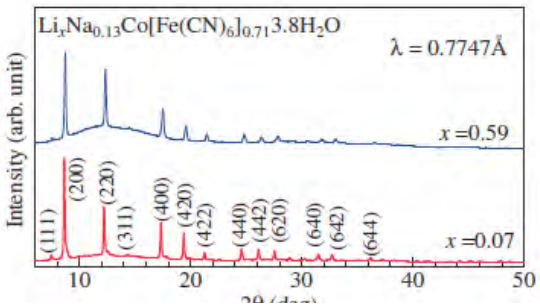

Fig. 3: X-ray diffraction patterns of $Li_xNa_{0.04}Ni[Fe(CN)_6]_{0.68}5.1H_2O$ against x. Parentheses represent indexes in the face-centered cubic setting.

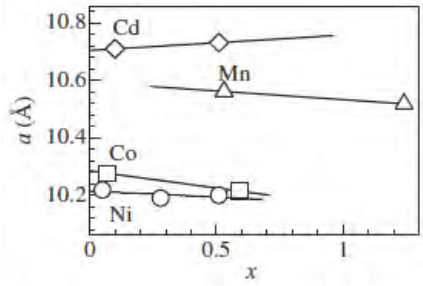

Fig. 4: Lattice constant (a) of $Li_xNa_{0.04}Ni[Fe(CN)_6]_{0.68}5.1H_2O$ (circles), $Li_xNa_{0.13}Co[Fe(CN)_6]_{0.71}3.8H_2O$ (squares), $Li_xMn[Fe(CN)_6]_{0.81}3.0H_2O$ (triangles), and $Li_xNa_{0.88}Cd[Fe(CN)_6]_{0.96}4.8H_2O$ (diamonds) against x. Straight lines are results of the least-squares fitting, and also represent the Fe redox region

Acknowledgement

This work was supported by a Grant-in-Aid (21244052) for Scientific Research from the Ministry of Education, Culture, Sports, Science and Technology. Elementary analysis was performed at Chemical Analysis Division, Research Facility Center for Science and Engineering, University of Tsukuba. The X-ray powder diffraction and X-ray absorption experiments were performed under the approval of the Photon Factory Program Advisory Committee (Proposal No. 2010G502 and 2011G501).

References

[1] T. Matsuda, and Y. Moritomo, Appl. Phys. Express, **4** (2012) 047101.
[2] B. Ravel, and M. Newville, J. Synchrotron Radiation, **12** (2005) 537-541.
[3] F. Izumi, and K. Momma, Solid State Phenomena, **130** (2007) 15-20.

* pf-acr2011@kek.jp

7C/2010G502
8A/2011G501

Two-electron reaction in nanoporous cathode material for Lithium ion secondary battery

Tomoyuki Matsuda[1] and Yutaka Moritomo[1,2]
[1]Graduated School of Pure and Applied Science, University of Tsukuba, Tsukuba 305-8571, Japan
[2] TIMS, University of Tsukuba, Tsukuba305-8571, Japan

1 Introduction

Lithium ion batteries have aided the portable electronics revolution during the past two decades, and are now being intensively pursued for transportation applications and the efficient storage and utilization of intermittent renewable energies like solar and wind. Therefore, next-generation electrode materials have been intensively explored in order to achieve a highly-capacious, safe, environmentally-friendly, and low cost Li-ion secondary battery.

Prussian blue analogues, represented as $A_xM[M'(CN)_6]_y \cdot zH_2O$ (A is an alkali metal ion, and M and M' are transition metal ions), have nanoporous three-dimensional network structures. Recently, we realized a good cyclability with a high charge capacity in the film-type electrode of $Li_xMn[Fe(CN)_6]_{0.83} \cdot 3.5H_2O$ [1,2]. The film-type electrode does not contain a conductive material nor a binder polymer. Here, we present structure and valence states of $Li_xMn[Fe(CN)_6]_{0.83} \cdot 3.5H_2O$ against Li concentration (x). The data clearly indicates that the compound exhibits two-electron reaction without structural phase transition.[3]

2 Experiment

Thin film of $Na_{1.32}Mn[Fe(CN)_6]_{0.83} \cdot 3.5H_2O$ was electrochemically synthesized on an indium tin oxide (ITO) transparent electrode under potentiostatic conditions at −0.50 V vs a standard Ag/AgCl electrode in an aqueous solution containing 1.0 mmol dm^{-3} $K_3[Fe(CN)_6]$, 1.5 mmol dm^{-3} $MnCl_2 \cdot 6H_2O$, and 1.0 mol dm^{-3} NaCl. The obtained film was transparent with a thickness of around 1 μm. Chemical compositions of the films were determined by the inductively coupled plasma (ICP) method and CHN organic elementary analysis (Perkin-Elmer 2400 CHN Elemental Analyzer). The Li^+ was substituted for Na^+ by performing the charge/discharge cycles of the thin film against Li. Thus, we obtained thin films of $Li_xMn[Fe(CN)_6]_{0.83} \cdot 3.5H_2O$.The thin film was used as prepared (film-type electrode). The lithium metal was used as the reference and counter electrode, and the cut-off voltage was from 2.0 to 4.3 V. The electrolyte was ethylene carbonate (EC) / diethyl carbonate (DEC) solution containing 1 mol dm^{-1} $LiClO_4$.

The valence states of the Fe and Mn sites were determined by the *ex-situ* X-ray absorption spectra (XAS) around the Mn and Fe K-edge. The XAS measurements were conducted at the beamline 7C of the Photon Factory, KEK. The XAS spectra were recorded by a Lytle detector in a fluorescent yield mode with a Si(111) double-crystal monochromator at 300 K. The background subtraction and normalization were done using ATHENA program[4].

The *ex-situ* powder X-ray diffraction (XRD) patterns were measured at the beamline 8A of KEK-PF equipped with an imaging plate detector. The charged/discharged samples were washed with DEC, and were carefully removed from the ITO glasses. The obtained powders were sealed in 300 μm glass capillaries. XRD patterns were measured at 300 K and the exposure time was 5 min. Wavelength of the X-ray was 0.77516 Å. The lattice constants of each compounds were refined by the RIETAN-FP program [5].

3 Results and Discussion

Figure 1 shows the charge/discharge curve of the film-type electrode of $Li_{1.32}Mn[Fe(CN)_6]_{0.83} \cdot 3.5H_2O$ at the 2nd cycle. We electrochemically controlled the Li ion concentration (x) as indicated by the arrows.

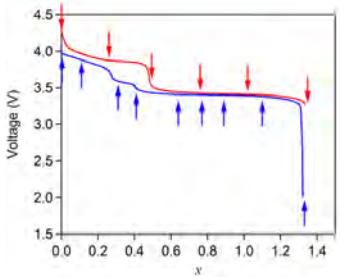

Fig. 1: Voltage vs composition curves for charge (red) and discharge (blue) process of film-type electrode of $Li_xMn[Fe(CN)_6]_{0.83} \cdot 3.5H_2O$ thin film at the 2nd cycle. The arrows indicate the compositions for the XAS and XRD measurements.

Figure 2a shows the Fe K-edge XAS spectra of charge/discharge process. The absorption peak energies (E) in the Fe K-edge spectra show clear blue shift with

decrease in x (Figure 2b). The blue shift is ascribed to the oxidization of Fe (low spin Fe^{II} → low-spin Fe^{III}). We emphasize that the blue shift saturates below x = 0.46 (0.41) in the charging (discharging) process. Figure 3a shows the Mn K-edge XAS spectra of charge/discharge process. The shoulder peak appeared around 6553 eV in the small-x region. This new peak is ascribed to the oxidization of Mn (high spin Mn^{II} → high-spin Mn^{III}) [10]. These data indicated that the oxidization of Fe takes place in the large-x region, while the oxidization of Mn takes place in the small-x region.

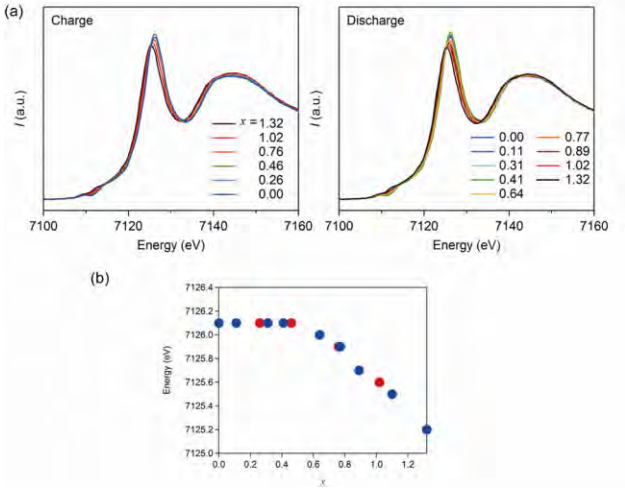

Fig. 2: (a) Fe K-edge XAS spectra for the charging (left), discharging (right) processes of film-type electrode of $Li_xMn[Fe(CN)_6]_{0.83}\cdot 3.5H_2O$. (b) Peak energy ($E(x)$) against x for the charging (red) and discharging (blue) processes.

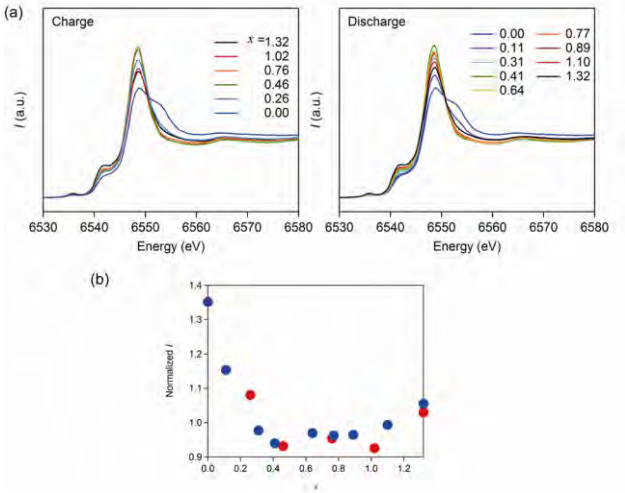

Fig. 3: (a) Mn K-edge XAS spectra for the charging (left), discharging (right) processes of film-type electrode of $Li_xMn[Fe(CN)_6]_{0.83}\cdot 3.5H_2O$. (b) Normalized intensity ($I(x)$) against x for the charging (red) and discharging (blue) processes.

Figure 4 shows the magnified XRD patterns during charge/discharge process. The lattice structure remains the face-centered cubic ($Fm-3m$; Z = 4) throughout the charge/discharge process. In the charging process, the reflection shifts to the lower-angle side above x = 0.76 while shifts to the lower-angle side below x = 0.46. In the discharging process, the reflection shifts to the lower-angle side below x = 0.41 while shifts to the higher-angle side above x = 0.64.

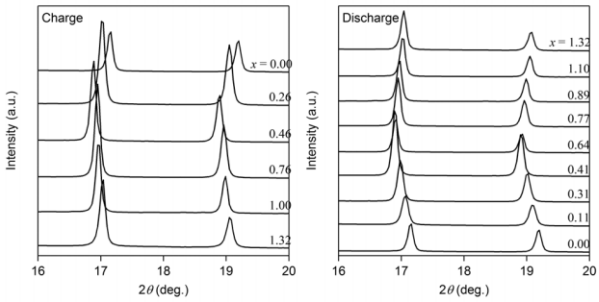

Fig. 4: XRD patterns for the charging (left) and discharging (right) processes of film-type electrode of $Li_xMn[Fe(CN)_6]_{0.83}\cdot 3.5H_2O$.

Figures 5a and 5b show the molar ratios of the Fe^{III} and Mn^{III} against x, respectively. These data clearly indicate the charge/discharge process of the film-type electrode consists of the two reactions, i.e., Mn^{II}/Mn^{III} and Fe^{II}/Fe^{III} reactions. The Mn^{II}/Mn^{III} reaction takes place in the small-x region (x < 0.46: indicated by vertical broken line in Fig.5), while the Fe^{II}/Fe^{III} reaction takes place in the large-x region (x > 0.46). The first and second plateaus in the charging process (see Fig.1) are ascribed to the oxidization of Mn^{II} and $[Fe^{II}(CN)_6]^{4-}$, respectively. On the contrary, the first, second and third plateaus in the discharge process is due to the reduction of Mn^{III}, Mn^{III}, and $[Fe^{III}(CN)_6]^{3-}$, respectively.

Figure 5c shows the lattice constant against x. The lattice constants were refined by the Rietveld analysis. In the Mn^{II}/Mn^{III} redox region, the lattice constant increases with x. The increase is ascribed to the larger ionic radius of Mn^{II}. In the Fe^{II}/Fe^{III} region, the lattice constant decreases with x. The decrease is ascribed to the smaller size of $[Fe^{II}(CN)_6]^{4-}$ as compared with that of $[Fe^{III}(CN)_6]^{3-}$.

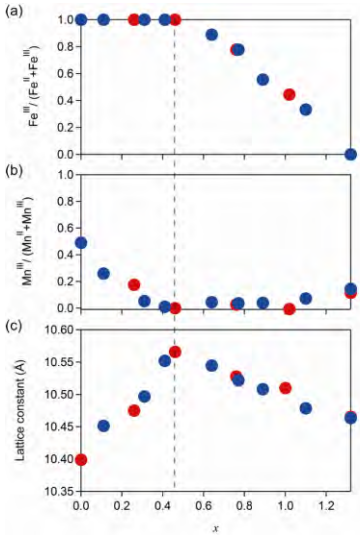

Fig. 4: (a) Molar ratios of the Fe^{III}, (b) molar ratios of the Mn^{III} (b), and (c) lattice constants for the charging (red) and discharging (blue) processes of $Li_xMn[Fe(CN)_6]_{0.83}\cdot 3.5H_2O$.

Acknowledgement

This work was supported by a Grant-in-Aid (21244052) for Scientific Research from the Ministry of Education, Culture, Sports, Science and Technology. Elementary analysis was performed at Chemical Analysis Division, Research Facility Center for Science and Engineering, University of Tsukuba. The X-ray powder diffraction and X-ray absorption experiments were performed under the approval of the Photon Factory Program Advisory Committee (Proposal No. 2010G502 and 2011G501).

References

[1] T. Matsuda, and Y. Moritomo, Appl. Phys. Express, **4** (2012) 047101.
[2] Y. Moritomo, M. Takachi, Y. Kurihara, and T. Matsuda, Appl. Phys. Express, **5** (2012) 041801.
[3] T. Matuda and Y. Moritomo, J. Nanotech, (2012) 568147.
[4] B. Ravel, and M. Newville, J. Synchrotron Radiation, **12** (2005) 537-541.
[5] F. Izumi, and K. Momma, Solid State Phenomena, **130** (2007) 15-20.

* pf-acr2011@kek.jp

8A/2010G529

Third polymorph of the (BEDT-TTF)$_2$Ag(CF$_3$)$_4$(TCE) organic superconductor

Tadashi KAWAMOTO*[1], Takehiko MORI[1], Akiko NAKAO[2], Youichi MURAKAMI[2], and John A. SCHLUETER[3]

[1]Department of Organic and Polymeric Materials, Graduate School of Science and Engineering, Tokyo Institute of Technology, O-okayama, Meguro-ku, Tokyo 152-8552, Japan

[2]Institute of Materials Structure Science, High Energy of Accelerator Research Organization, Tsukuba, Ibaraki 305-0801, Japan

[3]Materials Science Division, Argonne National Laboratory, Argonne, Illinois 60439, USA

Introduction

In 1994, Argonne National Laboratory group discovered new organic superconductors based on BEDT-TTF [bis(ethylenedithio)tetrathiafulvalene] using the anion of $[M(CF_3)_4]^-$ (M = Cu, Ag, Au) [1,2]. They found that there were low- and high-T_c phases. Although the low-T_c phase was the usual κ-type structure, the structure of the high-T_c phase was unknown. The lattice parameters of the high-T_c phase were presented in 1995, and suggested that the large unit cell contained four κ-type conducting layers [2]. We report that the high-T_c phase of the Ag(CF$_3$)$_4$ salts has the unusual crystal structure, the dual layered structure (κ- and α'-types), among the organic superconductors. Recently, another research group has succeeded independently the crystal structure analysis for the high-T_c phase of (BEDT-TTF)$_2$Ag(CF$_3$)$_4$(TCE) [3]. However, their result differs from ours; the crystal system is triclinic and the unit cell contains two donor layers, so-called κα'$_1$-phase. Several results show that there are two kinds of high-T_c phases for the Ag(CF$_3$)$_4$ salts (T_c = 9.4 K and 11.1 K) [1]. This means that our solved structure (κα'$_2$-phase) is the third polymorph in the superconducting Ag(CF$_3$)$_4$ salts. The magnetic torque measurements show that the superconducting critical temperatures are approximately 9.5 K and 11.0 K for the two-layered (κα'$_1$-phase) and four-layered (κα'$_2$-phase) phases, respectively.

Results and Discussion

The structure was solved using the direct method (SIR2004) and was refined using the full-matrix least-squares procedure (SHELXL) [4,5]. Figure 1(a) shows the crystal structure of the high-T_c phase [6]. The chemical composition is (BEDT-TTF)$_2$Ag(CF$_3$)$_4$(TCE), and all molecules are ordered. There are two kinds of donor arrangements, κ- and α'-types, and the unit cell contains four crystallographically independent donors, two independent anions, and two independent solvent molecules. The crystal structure is similar to that of the κα'$_1$-phase. The charge transfer degrees estimated from the bond lengths of two crystallographically independent molecules in the α'-layer are 0.97(9) and 0.18(10), respectively; the α'-layer is in a charge-ordered state [7]. This indicates that the κ-layer shows superconductivity. To determine the T_c values of the κα'$_1$- and κα'$_2$-phases, the magnetic torque has been measured after examining the lattice parameters using x-ray oscillation photographs. The magnetic torque clearly shows that the κα'$_1$-phase has a lower T_c than the κα'$_2$-phase.

In summary, we have found the third polymorph of the title compound with the charge ordered layers. The present structure is similar to the κα'$_1$-phase recently found in high-T_c Ag(CF$_3$)$_4$ salts. The onset superconducting transition temperatures determined from the magnetic torque are approximately 9.5 and 11.0 K for the κα'$_1$- and κα'$_2$-phases, respectively.

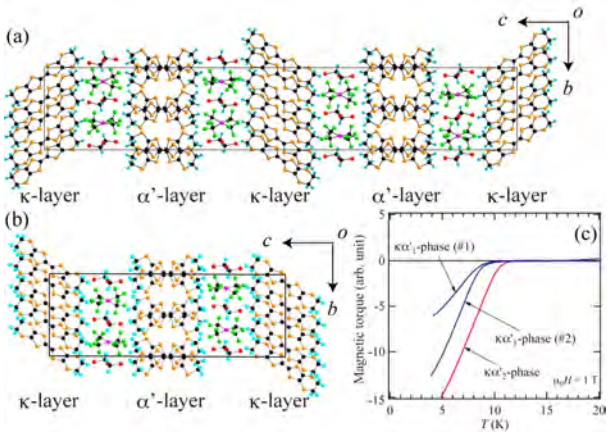

Figure 1: Crystal structure of the κα'$_2$-phase (a) and the κα'$_1$-phase from Ref.3 (b). (c) Temperature dependence of the magnetic torque.

References

[1] J. A. Schlueter et al., Physica C **233**, 379 (1994).
[2] J. A. Schlueter et al., Adv. Mater. **7**, 634 (1995).
[3] J. A. Schlueter et al., J. Am. Chem. Soc. **132**, 16308 (2010).
[4] M. C. Burla et al., J. Appl. Cryst. **38**, 381 (2005).
[5] G. M. Sheldrick et al., Acta Cryst. A **64**, 112 (2008).
[6] Crystal data of κα'$_2$-(BEDT-TTF)$_2$Ag(CF$_3$)$_4$(TCE) at 66 K: monoclinic, space group $P2_1/n$, a = 8.4013(2) Å, b = 13.1846(2) Å, c = 75.3636(7) Å, β = 90.1090(13)°, V = 8347.8(2) Å^3, Z = 8, R = 0.1151 for all observed reflections (14775 reflections). The lattice parameters are qualitatively the same as those in Ref. 2.
[7] P. Guionneau et al., Synth. Met. **86**, 1973 (1997).

* kawamoto@o.cc.titech.ac.jp

4A/2010G-534

Redox States of Shergottite Martian meteorites as Inferred from Iron Micro-XANES Analysis of Maskelynite and Plagioclase

Wataru Satake and Takashi Mikouchi*
Dept. of Earth and Planetary Science, University of Tokyo,
7-3-1 Hongo, Bunkyo-ku, Tokyo 113-0033, Japan

1 Introduction

Shergottite is the largest group of Martian meteorites that crystallized at 160-550 Ma near the Martian surface as shallow intrusions or thick lava flows [e.g., 1]. Recent petrological and isotopic studies have revealed that shergottites show obvious correlations between oxidation state and geochemical characteristics, and such correlation must have important information about their mantle sources and are directly relevant to Martian evolution [e.g., 2]. The difference in such geochemical characteristics can divide them into three subgroups: depleted, enriched and intermediate shergottites [e.g., 3]. Enriched shergottites show high La/Yb, low Sm/Nd, and high $^{87}Sr/^{86}Sr$ ratios. Enriched shergottites crystallized under the oxidized environment at the oxygen fugacity (fO_2) of log fO_2=QFM-1.0 by Fe-Ti oxide oxybarometer [e.g., 2].

From such studies, there are two models regarding the two geochemical source reservoirs for the shergottites. One model proposes assimilation of oxidized crust by mantle-derived, reduced magmas [2, 4]. In this model, the assimilated enriched reservoir occurs as domains in the crust, which must be traversed by ascending mantle magmas. Herd et al. [2] proposed that the assimilated material may be the product of early and extensive hydrothermal alteration of the Martian crust, or it may be amphibole- or phlogopite-bearing basaltic rock within the crust. The other model proposes mixing of two distinct mantle reservoirs during melting as stated above [3, 5-6]. In this model both geochemical reservoirs reside in the mantle and were formed as a result of either crystallization of a magma ocean to produce geochemically-depleted and enriched domains [5], or fluid-induced metasomatism that produced mantle heterogeneity [6].

However, redox states of many shergottites have not been estimated. Typically, iron titanium oxide oxybarometer and/or orthopyroxene-olivine-spinel oxybarometer are used to estimate redox states of shergottites. However, sometimes these minerals are not in equilibrium because most shergottites are rapidly cooled lava, and therefore, this method cannot be used to estimate redox states of all shergottites.

Therefore, we focused on iron valence of plagioclase and maskelynite (shocked plagioclase glass) which can be a good indicator of redox condition, because all shergottites contain plagioclase and/or maskelynite. In this study, we estimated $Fe^{3+}/\Sigma Fe$ ratios of plagioclase and maskelynite in 14 shergottites by using the synchrotron micro-XANES (X-ray Absorption Near Edge Structure) analysis to discuss the redox states and the origin of shergottites.

2 Samples

We analyzed thin sections of two geochemically-depleted (Dar al Gani 476 and Dhofar 019), four geochemically-intermediate (EETA 79001 lithology A., ALH 77005, LEW 88516 and NWA5029) and eight geochemically-enriched (NWA 856, Dhofar 378, Zagami, Shergotty, RBT 04262, NWA 4468, NWA 1068 and LAR 06319) shergottites.

3 Experiment

$Fe^{3+}/\Sigma Fe$ ratios of minerals can be estimated from the energy shift of a pre-edge peak in XANES spectra obtained using the synchrotron X-ray fluorescence because the pre-edge peak is independent of influence of self-absorption effects [7]. Pre-edge peak is always observed on the low-energy side of K-absorption edges (main-edge) of first-row transition elements. The region below the absorption edge typically contains a pre-edge peak due to electronic transition from 1*s* to 3*d*. This pre-edge position shifts to higher energy with increasing the $Fe^{3+}/\Sigma Fe$ ratios of the minerals. Bajt et al. [7] observed a linear relationship between pre-edge peak position and the $Fe^{3+}/\Sigma Fe$ ratio in silicate and oxide minerals by using the shift of pre-edge position.

We performed XANES experiment at the BL-4A, PF. The transmitted and fluorescent X-rays were measured by an ionization chamber and a Si (Li) detector, respectively. The angle between the incident beam and the detector was fixed at 90^o. Kirkpatrick-Baez geometry mirrors were used to focus the beam to about a 5 x 5 μm square on the specimen. Spectra were recorded from 7087 to 7183 eV using a 0.11 eV step for the pre-edge and main-edge regions. The energy was calibrated by defining the first derivative peak of Fe foil to be 7111 eV and standard kaersutites ($NaCa_2(Mg,Fe^{2+})_4TiSi_6Al_2O_{22}(OH)_2$) were measured at regular intervals to determine the energy reproducibility [8].

4 Results and Discussion

From all samples, sharp pre edge spectra of Fe XANES analysis were obtained. The $Fe^{3+}/\Sigma Fe$ ratios of maskelynite and plagioclase in depleted, intermediate, and enriched shergottites are about 0.24-0.49 (0.42-0.49 in Dar al Gani 476 and 0.24-0.28 in Dhofar 019), 0.13-0.66 (0.13-0.29 in ALH77005, 0.47-0.60 in EETA 79001 lithology A., 0.65-0.66 in LEW 88516 and 0.32-0.41 in NWA 5029,) and 0.41- 0.74 (0.55-0.69 Dhofar 378, 0.54-

0.56 in LAR 06319, 0.44-0.59 in NWA 856, 0.58-0.62 in NWA 1068, 0.65-0.71 in NWA 4468, 0.52-0.58 in Zagami, 0.74-0.75 in RBT 04262, and 0.41-54 in Shergotty), respectively. (Table1). Thus, the $Fe^{3+}/\Sigma Fe$ ratio of all shergottites that we analyzed shows a wide range from about 0.13 to 0.75.

DaG 476 crystallized under depleted environment (log fO_2=QFM-2.5), EETA 79001 lithology A crystallized under intermediate redox state (log fO_2=QFM-1.7) and two enriched shergottites (Zagami and Shergotty) crystallized under similar oxidized environment (log fO_2=QFM-1.0) [2]. The $Fe^{3+}/\Sigma Fe$ ratios of enriched shergottites are clearly higher than those of the depleted shergottites. Therefore, we conclude that all eight enriched shergottites (Dhofar 378, LAR 06319, NWA 856, NWA 1068, NWA 4468, Zagami, RBT 04262 and Shergotty) may have crystallized under oxidized environment with similar fO_2 (fO_2=QFM-1.0) although Fe-Ti oxide oxybarometer has not been performed on Dhofar 378, NWA 856, NWA 4468 and RBT 04262 some samples.

The εNd of enriched shergottites shows negative value, on the other hand, the εNd of depleted shergottites shows positive value [e.g., 3]. It showed that the $Fe^{3+}/\Sigma Fe$ ratio of shergottites is consistent with geochemical characteristic εNd. Furthermore, the similar young crystallization ages of enriched shergottites ~190 Ma [1] suggest that all of enriched shergottites may have been formed by related magmatic events because these shergottites are similar in many ways.

In the case of depleted shergottites, Dhofar 019 which has not been performed by Fe-Ti oxide oxybarometer has the $Fe^{3+}/\Sigma Fe$ ratios lower than the Dag 476. Thus, we also conclude that Dhofar 019 depleted shergottite may have crystallized under oxidized environment with even lower fO_2 than Dag476 (fO_2=QFM-2.5). Because these two depleted shergottites have the similar values of εNd [e.g., 3] (crystallization ages are slightly different), these two meteorites (Dhofar 019 and Dag 476) have the same origin.

The $Fe^{3+}/\Sigma Fe$ ratios of intermediate shergottites have very wide range (0.13-0.66) covering both depleted and enriched shergottites (Table1). The εNd value of intermediate shergottites is intermediate between those of depleted and enriched shergottites [3]. In contrast, the crystallization age of intermediate shergottites is similar to those of enriched shergottites [1]. It is indicated that intermediate and enriched shergottites crystallized at almost the same age, but they were of different origin. If enriched shergottites were produced from the mantle-derived reduced magmas that were affected by early and extensive hydrothermal alteration of the Martian crust [2], intermediate shergottites sources were also affected, because intermediate and enriched shergottites have similar crystallization ages [1]. It can be explained that the model proposes mixing of two distinct mantle reservoirs during melting as stated above [3, 5-6]. Based on these considerations, we conclude that the wide ranges of $Fe^{3+}/\Sigma Fe$ ratios obtained from intermediate shergottites show the evidence for mixing of two distinct mantle reservoirs during melting.

Recently, LAR06139 was reported to show the redox change during crystallization [9]. Because plagioclase crystallizes in a wide temperature range, Fe-XANES analysis of shergottite maskelynite with core-rim zoning allows tracking the possible redox change during plagioclase crystallization, which we plan to work on to further compare different shergottite samples.

Table 1 The $Fe^{3+}/\Sigma Fe$ ratios of all analyzed shergottites.

Sample	Group	The $Fe^{3+}/\Sigma Fe$ ratio (%)
DAG476	Depleted	42-49
Dhofar019	Depleted	24-28
ALH77005	Intermediate	13-29
EETA79001 lithology A	Intermediate	47-60
LEW88516	Intermediate	65-66
NWA5029	Intermediate	32-41
Dhofar378	Enriched	55-69
LAR06319	Enriched	54-56
NWA856	Enriched	44-59
NWA1068	Enriched	58-62
NWA4468	Enriched	65-71
Zagami	Enriched	52-58
RBT04262	Enriched	74-75
Shergotty	Enriched	41-54

Acknowledgement

We express very much gratitude to Prof. A. Iida for supports during micro-XANES analysis.

References

[1] Nyquist L. E. et al. (2001) *Space Sci. Rev.*, **96**, 105-164.
[2] Herd C. D. K. et al. (2002) *Geochim. Cosmochim. Acta*, **66**, 2025-2036.
[3] Symes S. J. K. et al. (2008) *Geochim. Cosmochim. Acta*, **72**, 1696-1710.
[4] Wadhwa M. et al. (2001) *Scienc*e, **291**, 1527-1530.
[5] Borg L. E. and Draper D. S. (2003) *Meteorit. Planet. Sci*., **38**, 1713-1731.
[6] Treiman, A. H. et al. (2003) *Meteorit. Planet. Sci*., **38**, 1849-1864.
[7] Bajt S. et al. (1994) *Geochim. Cosmochim. Acta*, **58**, 5209-5214.
[8] Monkawa A. et al. (2006) *Meteorit. Planet. Sci*., **41**, 1321-1329.
[9] Peslier A. H. et al. (2010) *Geochim. Cosmochim. Acta*, **74**, 4543-4576.

*Corresponding: mikouchi@eps.s.u-tokyo.ac.jp

15C/2010G539

Observation of Strain Gradient of Weekly Bent Crystal Using Mirage Fringes

Sukswat JONGSUKSWAT,[*1] Tomoe FUKAMACHI, [1] Kenji HIRANO, [1] Dongying JU, [1]
Riichirou NEGISHI, [1] Keiichi HIRANO, [2] and Takaaki KAWAMURA[3]
[1]Saitama Institute of Technology, 1690 Fusaiji, Fukaya, Saitama 369-0293, Japan
[2]Institute of Material Structure Science, KEK-PF, High Energy Accelerator Research Organization, Oho, Tsukuba, Ibaraki 305-0801, Japan
[3]University of Yamanashi, Kofu,Yamanashi 400-8510, Japan

We report on the observation of strain gradient of a uniformly deformed crystal by using X-ray mirage fringes.

Under an anomalous transmission condition in the Bragg mode, the refracted beam propagates along a hyperbolic trajectory and it returns to the incident surface (mirage diffraction). The beam corresponding to the Poynting vector is called the refracted beam here. Since the refracted beam is regarded as a quasi-spherical wave, it produces several types of interference fringes such as mirage fringes [1] and IFMRB [2]. These fringe spacing decreases as the strain increases. It is possible to know the strain gradient of a bent crystal by observing interference fringes in X-ray section topographies.

The X-ray topographies of Si 220 were observed at the beam line BL-15C, KEK-PF. The X-rays were σ-polarized and monochromated using a Si 111 double-crystal monochromator. The X-ray energy was 11100 eV. The geometry of X-rays and the sample are shown in Fig. 1. Fig. 2 shows the topographies observed between the free edge and the clamped side of the sample. We can see the curved mirage fringes in the center of the sample and IFMRB near the free edge. According to the rod theory, the strain gradient is maximum at the clamped end and zero at the free edge under uniformly distributed load due to gravity. The observed spacing of mirage fringes becomes narrower around the center of the sample and IFMRB is observed even at the free edge. The former should be explained by the effect of buckling induced by the force holding the sample. The latter should be explained by the residual strain after manufacturing the sample. There still remains large discrepancy between the theoretically calculated strain and the observed one. More precise analysis should be needed to determine the strain by using the mirage fringes or IFMRB.

This work was partly supported by the Open Research Project for Private Universities: 2007-2011, matching fund subsidy from MEXT.

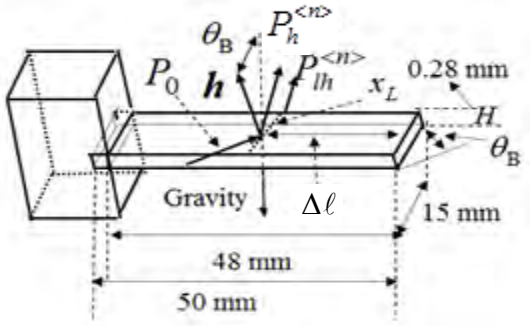

Fig.1. Geometry of X-rays and sample.

References

[1] T. Fukamachi *et al.*, Acta Cryst. A**66**, 421, (2010).
[2] T. Fukamachi *et al.*, J. Phys. Soc. Jpn. **80** 083002, (2011).

*e1001kyb@sit.ac.jp

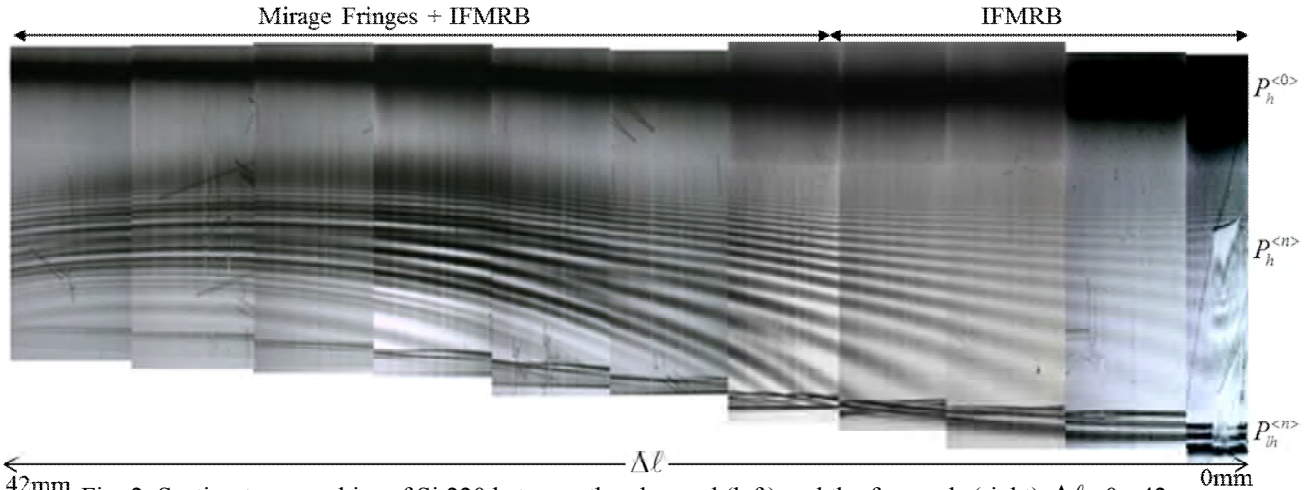

Fig. 2. Section topographies of Si 220 between the clamped (left) and the free ends (right). $\Delta\ell$ =0 - 42 mm.

NW10A/2010G557

In operando XAFS Studies of Polyoxometalate Molecular Cluster Batteries: Polyoxometalates as Electron Sponges

Hirofumi Yoshikawa[1,*], Heng Wang[1], Toshihiko Yokoyama[2], and Kunio Awaga[1]
[1]Nagoya University, Furo-cho, Chikusa, Nagoya 464-8602, Japan
[2]Institute for Molecular Science, Myodaiji, Okazaki 444-8585, Japan

1 Introduction

Recently, we have proposed a novel rechargeable battery, "molecular cluster battery (MCB)", in which the cathode comprises polynuclear metal complexes (molecular clusters), and the anode is lithium metal. It is expected that MCBs would show a high capacity and a rapid charging/discharging due to multi-electron redox reactions of the molecular clusters and quick lithium-ion diffusion, respectively. Among of molecular clusters, polyoxometalates (POMs) have attracted much attention due to their various properties, such as photoluminescence, catalytic activity, and single-molecule magnetism. They are also reported to operate as a cathode-active material of high-capacity lithium batteries, though the valence and structural changes of the POMs in the battery reaction has not yet been investigated. In the present study, we performed in operando Mo K-edge XAFS measurements on the MCBs of a representative Keggin-type POM, (tetrabutyl ammonium)$_3$[$PMo_{12}O_{40}$].

2 Experiment

For in operando XAFS measurements, the battery was fabricated in a similar way using a special battery cell with an X-ray window in the center, which we developed previously.[1] During the charging/discharging tests at a constant current of 1.0 mA, in operando Mo K-edge XAFS spectra were recorded in the energy range from 19498.9 to 20003.9 eV with a transmission mode at room temperature, using the beam line BL-NW10A of the Photon Factory Advanced Ring (PF-AR) in KEK, Tsukuba, Japan.

3 Results and Discussion

The XANES analysis indicates that the reduction from Mo^{6+} to Mo^{4+} takes place at the twelve Mo^{6+} sites in one molecule, forming the super-reduced species, $[PMo_{12}O_{40}]^{27-}$, after the twenty-four-electron reduction. In contrast, it is known that the usual solution electrochemistry can produce only two- or three-electron reduction species of $[PMo_{12}O_{40}]^{3-}$ in the typical electrochemical windows of solvents. The $[PMo_{12}O_{40}]^{3-}$ can be regarded as a molecular "electron-sponge" in solid-state electrochemistry.

As shown in Fig. 1(a), the EXAFS analyses exhibited four main peaks at 1.1, 1.6, 2.3, and 3.2 Å in the initial and charged state. They were assigned to an Mo=O double bond (1.7 Å), two kinds of Mo−O single bonds (1.9 and 2.4 Å), and an Mo−Mo distance (3.4 Å) in

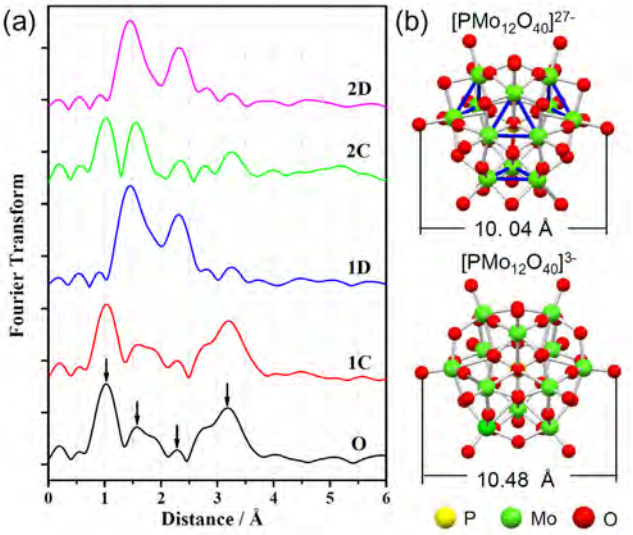

Fig. 1 (a) EXAFS spectra of the initial (**O**), 1st charge/discharge (**1C**, **1D**), and 2nd charge/discharge (**2C**, **2D**), (b) Structures of $[PMo_{12}O_{40}]^{27-}$ and $[PMo_{12}O_{40}]^{3-}$.

$[PMo_{12}O_{40}]^{3-}$, respectively. However, after the discharging, the peaks at 1.1 and 3.2 Å become very small, and those at 1.6 and 2.3 Å are significantly enhanced (Fig. 1(a)). The curve-fitting for the EXAFS spectra suggested that the distances of Mo−O and Mo−Mo become ca. 2.0 and 2.6 Å, respectively, after discharging. By taking account of these changes from the original $[PMo_{12}O_{40}]^{3-}$ structure, we estimated a molecular structure of the super-reduced species, $[PMo_{12}O_{40}]^{27-}$. This structure is slightly reduced in size from the original one; the maximum dimension of the $[PMo_{12}O_{40}]^{3-}$ decreases from 10.5 to 10.0 Å (Fig. 1(b)). In addition, this structure involves a characteristic triangular structure formed by Mo^{4+} metal-metal bonding (blue line in Fig. 1(b)), which stabilizes the structure of the super-reduced one.

This electron sponge behavior is a newly revealed characteristic of POMs, and indicates that they are promising cathode active materials for high-performance rechargeable batteries.

References

[1] H. Yoshikawa *et al.*, Chem. Asian J. **6** (2011) 1074.
[2] H. Yoshikawa *et al.*, J. Am. Chem. Soc. **134**, (2012) 4918.

* yoshikawah@mbox.chem.nagoya-u.ac.jp

9C,NW10A/2010G559

Lattice distortions and phase transitions in Tl-based thermoelectric materials

Shinya Hosokawa,[1,*] Hiroyuki Ikemoto,[2] Naohisa Happo,[3] Kojiro Mimura,[4] Kouichi Hayashi,[5] Kazuki Wakita,[6] and Nazim Mamedov[7]

[1]Kumamoto University, Kumamoto 860-8555, Japan
[2]University of Toyama, Toyama 930-8555, Japan
[3]Hiroshima City University, Hiroshima 731-3194, Japan
[4]Osaka Prefecture University, Sakai 599-8531, Japan
[5]Tohoku University, Sendai 980-8577, Japan
[6]Chiba Institute of Technology, Narashino 275-0016, Japan
[7]Azerbaijan National Academy of Sciences, 1143 Baku, Azerbaijan

1 Introduction

Ternary Tl-compounds with TlSe-type structure attract much attention because of their extremely large thermoelectric power, small thermal conductivity, and relatively large electrical conductivity. Thus, these materials, such as $TlInSe_2$ and $TlGaTe_2$, are foreseen as a member of a new class of thermoelectric materials [1].

$TlGaTe_2$ has a rather complex tetragonal chain structure at room temperature, which can be described as a set of $GaTe_4$ chains extended along the *c*-axis and connected with each other through one dimensional chains of Tl atoms (normal (N) phase). At temperatures lower than 290K, the positions of Tl atoms are believed to deviate from the periodicity of the $GaTe_4$ frameworks, indicating an incommensurate (IC) phase [2]. With the further decrease of temperature, another phase transition from IC to commensurate (C) phases is expected to occur at about 100 K. These phase transitions cause the degree of positional order of the Tl atoms and strongly affects thermoelectric properties of this material.

In this study, we have started a series of structural measurements on $TlGaTe_2$ by means of x-ray diffraction, XAFS, and x-ray fluorescence holography at low temperatures down to 30K, where the N-IC-C phase transition takes place.

2 Experiment

Single crystal $TlGaTe_2$ was grown by a modified Bridgeman method [1]. The well-ground powder of the sample was mixed with BN and pressed into a pellet with a diameter of 13 mm.

The Ga *K* edge (10.367 keV) and Tl L_{III} edge (12.657 keV) XAFS spectra were measured at BL9C of the PF, and the Te *K* edge (31.811 keV) spectra at NW10A of the PF-AR.

3 Results and Discussion

Figure 1 shows the Ga *K* XAFS signal (upper) and its Fourier transform (lower) of $TlGaTe_2$ at 30 K. As seen in the figure, good quality of the XAFS signal was obtained in the C phase. The similar qualities of the data were obtained in all of the edges at low temperatures.

With increasing temperature beyond 100K, the quality of the Tl L_{III} edge XAFS data gets worse, which is not due to the temperature effect only, but spatial fluctuations of the Tl atoms may set in at about 100K, which may be related to the C-IC phase transition. Detailed analyses of the present XAFS results are now in progress.

Acknowledgement

We acknowledge Professor T. Miyanaga of Hirosaki University for the help of the XAFS experiments and for discussion.

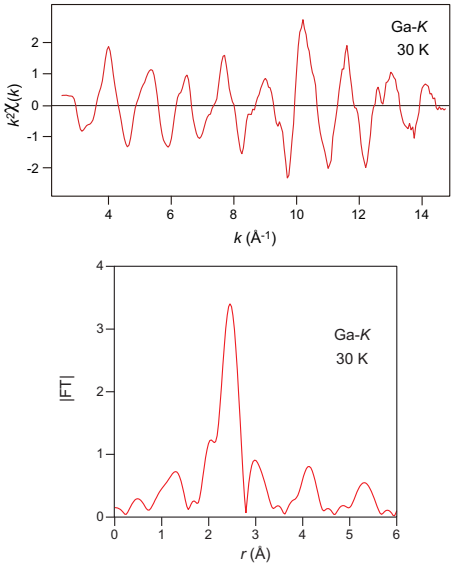

Fig. 1: Ga *K* XAFS signal (upper) and its Fourier transform (lower) of $TlGaTe_2$ at 30 K.

References

[1] N. Mamedov *et al.*, Thin Solid Films **499** (2006) 275.
[2] V. A. Aliev *et al.*, JETP Lett. **45** (1987) 534.

* hosokawa@sci.kumamoto-u.ac.jp

4C/2010G598

Synchrotron XRD study of the $CuGaSe_2$ thin films grown with various Cu/III ratio

M.M.Islam[1], A.Yamada[2], T.Sakurai[1], M.Kubota[3], S.Ishizuka[2], K.Matsubara[2], S.Niki[2], and K.Akimoto[1]

[1]University of Tsukuba, Tsukuba 305-8573, Japan

[2]Advanced Industrial Science and Technology (AIST), Tsukuba 305-8568, Japan

[3]Japan Atomic Energy Agency (JAEA), Tokai 319-1195, Japan

1 Introduction

Chalcopyrite $Cu(In,Ga)Se_2$ (CIGS), is one of the most promising materials to realize high-efficiency, low cost thin film solar cell. Efficiency of 19.9% has already been achieved for the CIGS-based solar cell [1]. Deviation from the ideal stoichiometry (i.e. 1:1:2) of this material is reported to form some secondary phases e.g. $Cu(In,Ga)_3Se_5$ (1:3:5), $Cu(In,Ga)_2Se_{3.5}$ (1:2:3.5) etc. which are commonly named as ordered defects compounds (ODC) preferably segregated on the surface of the film and affect electrical, optical and microstructural properties of the films.Therefore, intensive study is indispensable to understand the proper physics and growth condition for the ODC phase formation in this material. In this study we have performed synchrotron XRD of the $CuGaSe_2$ thin film to investigate the formation of ODC phase in our samples.

2 Experiment

Polycrystalline $CuGaSe_2$ thin films with the typical thickness of 2 μm were grown over Mo-coated soda lime glass (SLG) substrates through a three-stage co-evaporation process using molecular beam epitaxy system [8]. All the samples were grown at the constant flux rate of Cu, Ga and Se. Several $CuGaSe_2$ films with various Cu/III(= Cu/(Cu+Ga) ratio have been fabricated by changing the third stage growth time. Synchrotron XRD was performed using Beam Line-4C at E= 8.017 keV in KEK, Japan.

3 Results and Discussion

Figure 1 shows synchrotron XRD of the several $CuGaSe_2$ thin films having different Cu/III ratio in the film. As seen from the XRD profile, the (112) peak shifts from $2\theta = 27.6^o$ for Cu-rich sample with Cu/III = 1.12 to $2\theta = 27.95^o$ for the Cu-deficient sample with Cu/III = 0.37. The systematic right shifting of (112) peak with increasing Cu-deficiency in the film indicates the phase transition from the stoichiometric (1:1:2) phase to the ordered defect chalcopyrite (ODC) related phases. The right shift of the peak can be attributed to the reduction of the lattice parameter in (1:2.3.5), (1:3:5) etc. ODC phases comparing to that of (1:1:2) chalcopyrite structure [2]. No peak related to the formation of $Cu_{2-x}Se$ phases was found in the investigated range of XRD pattern for the Cu-excess film with Cu/III = 1.12.

For the film with composition near stoichiometry (Cu/III ~ 1.0), XRD pattern reflect only (1:1:2) chalcopyrite structure without any additional phase formation. However, an additional peak appeared at $2\theta \approx 22.8^o$ for the film with Cu/III ~ 0.7 and 0.37, which can be attributed to the formation of ODC related phase. This additional reflection originates from the different cation ordering and the presence of Cu-vacancies in the ODC related structures. Fitting of the (112) peak shows the co-existing of both chalcopyrite (i.e. 1:1:2) and ODC (i.e. 1:3:5) phase in this film. Further reduction of Cu/III ratio increases the contribution of ODC phase as can be seen for the film with Cu/III ~ 0.37 where, the XRD patterns could attributed to (1:3:5) phase only with no evidence of (1:1:2) chalcopyrite phase. These results suggest that reduction of Cu/III ratio in the $CuGaSe_2$ films introduce phase transition from the stoichiometric to the ODC phases that affect the solar cell performances fabricated based on this material and the optimization of this phase transition is necessary to realize the best efficiency.

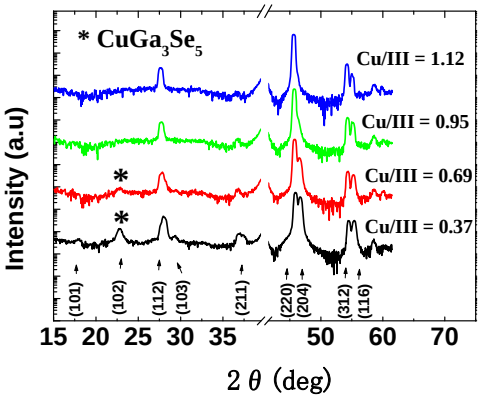

Fig. 1 Synchrotron X-ray diffraction pattern at θ-2θ mode of several $CuGaSe_2$ thin films grown with different Cu/III ratio in the film.

Acknowledgement

This work was partly supported by the Ministry of Education, Culture, Sports, Science and Technology (MEXT), Japan.

References

[1] I. Repins *et al.*, Progress in Photovoltaics: Research and Application **16** (2008) 235.

[2] G. Marin et al., Materials Research Bulletin **33** (1998) 1057.

15B1/2010G605

Enhancement of Crystal Perfection for Tetragonal Hen-egg White Lysozyme Crystals under Application of an External AC Electric Field

Haruhiko Koizumi[1,*], Satoshi Uda[1], Kozo Fujiwara[1], Masaru Tachibana[2], Kenichi Kojima[3] and Jun Nozawa[1]

[1]Institute for Materials Research, Tohoku University, Sendai 980-8577, Japan

[2]Graduate School of Nanobioscience, Yokohama City University, Yokohama 236-0027, Japan

[3]Yokohama Soei University, Yokohama 226-0015, Japan

1 Introduction

High quality single crystals of proteins are required to achieve structure-guided drug design and controlled drug delivery, because the crystal quality governs the distinctness of the 3D structure of protein molecules obtained from X-ray structure analysis. The distinctness of a 3D protein structure is defined by the resolution, and a resolution of less than 1.5 Å is desirable to achieve structure-guided drug design and controlled drug delivery, which enables each carbon atom on a protein molecule to be distinguished. However, it is quite difficult to obtain high quality single crystals of proteins with a resolution of less than 1.5 Å. Therefore, the establishment of a crystallization technique that can obtain high quality single crystals of proteins is required.

Recently, we have successfully achieved both an increase and decrease in the nucleation rate of HEWL crystals by changing the frequency of an applied electrostatic field [1, 2, 3, 4] by focusing on the electrostatic term added to the chemical potentials of the liquid and solid phases. Furthermore, we have revealed that this crystallization technique is also adaptable to porcine insulin [5]. If crystal quality could also be improved by application of an external AC electric field, then this crystallization technique could be an excellent tool, because the nucleation rate can also be controlled. In this paper, we report on improvement of the crystal quality of HEWL crystals by application of the external AC electric field, as verified by X-ray diffraction rocking-curve measurements.

2 Experiment

HEWL was purchased from Wako Pure Chemical Industries, Ltd., and was used without further purification. Solutions of 57 mg/mL HEWL and 0.5 M NaCl at pH 4.3, were used for the crystallization experiments. Under these conditions, the obtained crystals were tetragonal with the $P4_32_12$ space group, and lattice constants of a = 79.1 Å and c = 37.9 Å.

Crystallization experiments were conducted at 21±0.2 °C using the batch method. HEWL crystals grown on the sides of electrodes were used to obtain X-ray diffraction rocking-curve profiles. The distance between the electrodes was 12 mm, and the solution volume was 2.9 mL. An external AC electric field of 400 V/cm was applied at 1 MHz. Crystals were grown with and without application of the external electric field for 9 days.

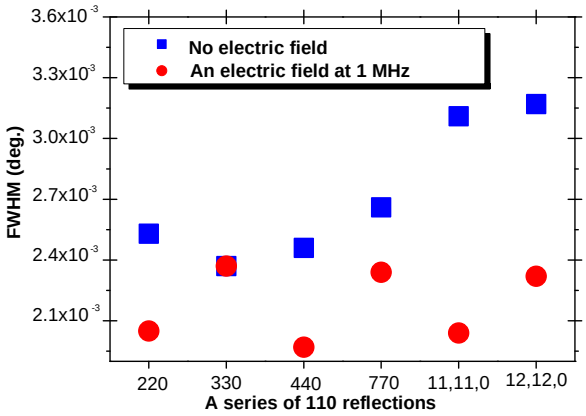

Fig. 1: Dependence of FWHM on a series of 110 reflections for HEWL crystals grown with and without application of an external electric field.

X-ray diffraction rocking-curve measurements were conducted in BL15B1 at the Photon Factory (PF) of the High Energy Accelerator Research Organization (KEK). A two-crystal monochromator consisting of a Si(111) crystal was located 24 m from the source and was used to select an X-ray wavelength of λ = 1.2 Å. Samples were measured with a high-resolution step by mounting on a precision goniometer (minimum angular step width: 5.3×10^{-5} °). Under such a condition, the reflected images of entire crystals for a series of 110 reflections were detected using a high spatial resolution, two-dimensional digital CCD camera (effective pixel: 6.45 μm × 6.45 μm). X-ray rocking-curve profiles for a series of 110 reflections were reconstructed from the reflected intensities using the same region of the crystal with a beam spot size of 212.85 μm (33 pixels). Therefore, the beam divergence was 1.7×10^{-5} rad (0.9×10^{-3} °). The full width at half maximum (FWHM) of each rocking-curve profile measured for samples prepared with and without an external electric field was evaluated using a Gaussian

function.

3 Results and Discussion

Figure 1 shows the dependence of the FWHMs on a series of 110 reflections from crystals prepared with and without an external electric field. The FWHMs obtained from crystals prepared without an external electric field increased for diffraction peaks with higher-order than the 440 reflection, as shown in Fig. 1. In particular, the FWHMs were larger for the 11,11,0 and 12,12,0 higher-order reflections. This is due to the sensitivity of the higher-order reflection to strain in the crystals; therefore, the FWHMs of the higher-order reflections are suitable for assessment of the crystal quality. In contrast, for crystal growth with an external electric field at 1 MHz, the FWHMs were almost constant for all order diffraction peaks, as shown in Fig. 1. Furthermore, the FWHMs of crystals grown with an external electric field were smaller than those without, except for the 330 reflection. It should be noted that the FWHMs for the 11,11,0 and 12,12,0 reflections of crystals grown with an external electric field were significantly smaller than those without. This indicates that the crystal quality of HEWL crystals was significantly improved by application of an external AC electric field.

With respect to improvement of the crystal quality, Taleb *et al*. have suggested that the crystal quality of HEWL crystals was slightly improved by application of an external DC electric field [6], and they reported a 17% improvement of the crystal quality for crystals grown under application of an external DC electric field, although the diffraction vector of the measured X-ray rocking-curve profiles was not described in Ref. [6]. The present enhancement of 26% for the crystal quality was observed for the 440 reflection by application an external AC electric field, and an enhancement of 34% was achieved for the 11,11,0 higher-order reflection. Therefore, the results suggest that application of an external AC electric field can be employed to improve the quality of protein crystals.

The higher-order reflection cannot often be observed for X-ray structure analysis of protein molecules, which results in a lowering of the resolution for the structure of protein molecules. This phenomenon is attributed to deterioration in the crystal quality of the protein crystals. However, we have observed that the FWHM for the higher-order reflection was improved when an external AC electric field was applied during crystal growth, which suggests that it may be possible to distinctly observe the higher-order reflections of crystals grown under application of an external AC electric field. Thus, enhancement of the resolution for the structural analysis of protein molecules could be expected by application of an external AC electric field during crystal growth.

In summary, we have observed that the FWHMs of X-ray rocking-curve profiles for crystals grown with an external electric field were smaller than those without. The FWHMs for the higher-order reflections were significantly smaller for those crystals grown with an external electric field than those grown without. These results indicate that the crystal quality of HEWL crystals could be improved by application of an external AC electric field during growth. This is a novel crystallization technique for proteins, which can be employed to not only enhance the nucleation rate [1, 2, 3, 4, 5], but also improve the crystal quality.

Acknowledgement

X-ray diffraction rocking-curve measurements were performed at the Photon Factory (PF) under the auspices of the Photon Factory Program Advisory Committee of KEK (Proposal No. 2010G605, 2011G073) and at SPring-8 with approval of the Priority Program for Disaster-Affected Quantum Beam Facilities (Proposal No. 2011A1947).

References

[1] H. Koizumi, K. Fujiwara and S. Uda, Cryst. Growth Des. **9** (2009) 2420.
[2] H. Koizumi, K. Fujiwara and S. Uda, Cryst. Growth Des. **10** (2010) 2591.
[3] H. Koizumi, S. Uda, K. Fujiwara and J. Nozawa, J. Crystal Growth **312** (2010) 3503.
[4] H. Koizumi, S. Uda, K. Fujiwara and J. Nozawa, Langmuir **27** (2011) 8333.
[5] H. Koizumi, S. Uda, K. Fujiwara and J. Nozawa, J. Crystal Growth **352** (2012) 155.
[6] M. Taleb, C. Didierjean, C. Jelsch, J. Mangeot, B. Capelle and A. Aubry, J. Crystal Growth **200** (1999) 575.

* h_koizumi@imr.tohoku.ac.jp

19B/2010G613

Electronic structure and auto-ionization process of ion-electron mixed-conductor

Shu Yamaguchi [1], Tohru Higuchi [2], Yukiko Oyama [1], Shogo Miyoshi [1], Mao Tamaru [1]
[1] The University of Tokyo Bunkyo-ku, Tokyo 113-8656, Japan
[2] Tokyo University of Science, Shinjuku-ku, Tokyo 162-8601, Japan

1 Introduction

Solid Oxide Fuel Cell (SOFC) is one of the most promising devices for efficient energy conversion. In order to lower the operating temperature, proton-conducting oxides have attracted much attention as electrolyte of SOFCs. $BaZrO_3$-based perovskite oxides are most promising materials for the electrolytes due to their good chemical stability and high proton conductivity. On the other hand, the electrode materials for such proton-conducting SOFCs have not been well studied. In order to provide larger effective electrode reaction area and high electrode performance, it is required to develop materials with proton-electronic mixed conduction.

For developing such mixed-conducting materials, the electrochemical properties have been investigated on $BaZrO_3$ doped with Pr, which takes a mixed valence sate of $Pr^{3+/4+}$. It was found that the electric conduction in oxidizing atmosphere is dominated by electron hole, while in reducing atmosphere, protonic conduction prevails in addition to hole conduction. Both of the hole and proton conductivity increase with the Pr concentration in the perovskites. However, the dependence of the both conductivity on the Pr concentration is nonlinear, showing a cubic dependency.

In this study, soft X-ray Absorption Spectroscopy (XAS) has been employed to observe the unoccupied density of states around the Fermi level, which is crucial to the hole conduction.

2 Experiment

The powders of $BaZr_{1-x}Pr_xO_3$ ($0 \leq x \leq 0.6$) have been prepared via a citrate method, and then sintered at 1873K. Prior to the XAS measurements, the samples have been equilibrated at 873K in dry O_2 atmosphere. Soft X-ray absorption spectra have been collected by a total fluorescence method at BL-19B of Photon Factory, KEK.

3 Results and Discussion

Figure 1 shows the O1*s*-2*p* XAS spectra of $BaZr_{1-x}Pr_xO_3$. The spectrum of $BaZrO_3$ shows a main absorption edge peak (B) at 533eV with no pre-edge peaks. The feature (D) significantly attenuates upon increase in the Pr concentration, *x*, which indicates the origin being Zr4*d* orbital. On the other hand, the features (C) and (E) grow due to the contribution from Pr 4*f* orbital.

More importantly, a pre-edge peak (A) appears upon Pr-doping, and the intensity increases with *x*. Undoped $BaPrO_3$, which is essentially a p-type conductor [1], shows the identical pre-edge peak as found in Fig. 1 and previously reported [2]. As previously discussed [2], this pre-edge peak is considered to originate from the unoccupied state in O2*p* orbital, that is, holes localized at oxide ions. Therefore, the hole conductivity in $BaZr_{1-x}Pr_xO_3$, which increases with *x*, is regarded as closely related to the unoccupied density of states (A).

The intensity of the pre-edge peak (A) linearly increases with *x*. On the other hand, the hole conductivity, σ_h, has been found in a cubic correlation with *x* as previously mentioned; $\sigma_h \propto x^3$. The difference in the dependence on *x* between the density of the hole state (A) and the hole conductivity indicates that the apparent mobility of the holes is strongly dependent on the Pr concentration. This behaviour suggests that the electron holes, which are located on the oxide ion, are strongly correlated with the negative electronic defects, i.e., Pr^{3+}, via the auto-ionization reaction: $Pr^{4+} + O^{2-} \rightarrow Pr^{3+} + O^{-}$.

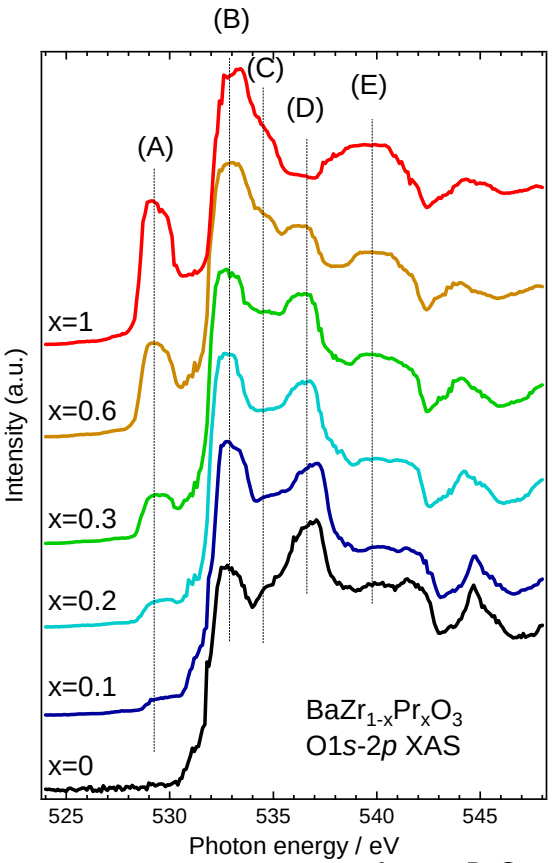

Fig. 1: O1*s*-2*p* XAS spectra of $BaZr_{1-x}Pr_xO_3$.

References

[1] S. Mimuro et al., Solid State Ionics 178, 641 (2007).
[2] S. Yamaguchi et al., PF Activity Report 2008 (2009).

* yamaguchi@material.t.u-tokyo.ac.jp

BL7A,9A,12C/2010G614

TiO_2-有機ハイブリッド材料のパターン形成メカニズムの解明
Photoreaction of TiO_2-Oraganic hybrid materials

瀬川浩代 [1*]
[1]物質・材料研究機構、〒305-0044 つくば市並木 1-1

1 はじめに

TiO_2 を含む化合物は高屈折率であり、レンズなどの光学材料として様々な分野へ応用されている。しかしながら、化学的安定性が高く、微細な加工を行うためには強い化学薬品を必要とする。有機物とハイブリッド化することよって簡便に数百 nm 程度の大きさの微細パターンを作製でき、それを焼結することによって TiO_2 の微細加工が可能であることをこれまでに明らかにしてきた[1]。このようなパターニングにおいては、Ti を含む金属アルコキシドとβ-ジケトンをゾル-ゲル法によって反応させたゾル溶液を用いて有機-無機ハイブリッド膜の作製を行う。Ti アルコキシドとβ-ジケトンはゾル溶液中でキレート構造を有していることが知られている。このキレート構造は紫外～可視光域においてπ–π*遷移に帰属される吸収を有しており、対応する紫外光あるいはレーザー光を露光することによってこれらのキレート構造は分解される。このような光による結合状態の変化によって、露光部と未露光部のアルコールに対する溶解度に違いが生じ、その溶解度差を利用してパターン形成が可能であると考えられている。しかしながら、光を当てた際に Ti の配位環境がどのように変化し、アルコールに対する溶解度差が生じるかに関する詳細な検討は行われていない。本研究では、TiO_2-有機ハイブリッド材料を対象として、露光前後によるキレート化合物の変化を明らかにすることで光によるパターン形成メカニズムの解明を目的とした。

2 実験

測定用の膜は $Ti(OBu)_4$、ジベンゾイルメタン、メタクリル酸、2-エトキシエタノールを用いてゾルゲル法によって作製した。作製したゾルをポリプロピレンフィルムに塗布した。異なる時間紫外線を露光したサンプルを二十枚程度重ね、XAFS 測定を行った。標準試料として Ti 配位数の異なる TiO_2(2 種類), $CaTiO_3$, $FeTiO_3$, $Na_2Ti_3O_7$, $K_2Ti_4O_9$, $SrTiSi_2O_8$ 粉末サンプルを準備し、ペレットを作製した。

透過法によって Ti の *K* 吸収端(4964.5eV)の測定を行った。まずは、光感応性を有するサンプルが X 線により変化しないことを QuickScan 法によって確認した。特に影響が確認されなかったので、通常の透過法によって測定した。

3 結果および考察

粉末サンプル及び膜サンプルについて得られた XANES スペクトルを図 1 に示す。XANES 領域の高さとエネルギー値が Ti の配位数と相関があることが知られており、作製した膜サンプルがほぼ 6 配位をとっていることがわかった。また紫外線の照射時間が異なるサンプルにおいてもほぼ XANES 領域の変化が確認されず、紫外線の露光前後に Ti の配位数変化がほとんど起こらないことが確認された。また、XANES スペクトルの形状を比較すると $FeTiO_3$ と最もよく似ていたので、フィッティングによってそのデバイワラー因子を求め、それを用いてサンプルの EXANES 領域の解析を行った。求められた Ti 配位数及び Ti-O 距離は紫外線照射でほとんど変化しないことが明らかになった。これより、紫外線露光によってキレートの分解が起こっているにもかかわらず、サンプル中の Ti の配位環境はほとんど変わらないことが明らかになった。

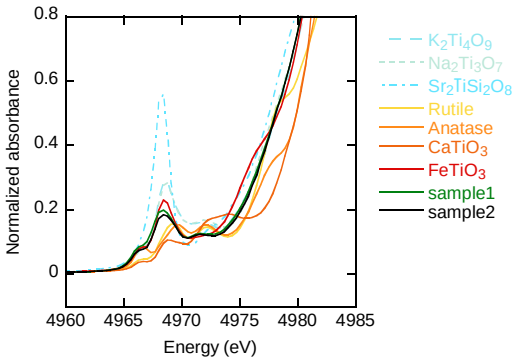

図 1 ：XANES スペクトル

4 まとめ

TiO_2-有機ハイブリッド材料中の Ti の局所構造は紫外線露光によってほとんど変わらないことを明らかにした。

謝辞

仁谷さんをはじめとする PF スタッフの方々に大変お世話になりました。ここに感謝致します。

参考文献

[1] H. Segawa, *J. Ceram. Soc. Jpn.*, **116** (2008) 251-259.

* SEGAWA.Hiroyo@nims.go.jp

27A/2010G635

Structure determination of self-assembled monolayer on oxide surface by soft-X-ray standing wave

Yuji BABA[*1], Ayumi NARITA[1], Tetsuhiro SEKIGUCHI[1], Iwao SHIMOYAMA[1], Norie HIRAO[1], Shiro ENTANI[2], Seiji SAKAI[2]

[1]Quantum Beam Science Directorate, Japan Atomic Energy Agency, Tokai-mura, Naka-gun, Ibaraki 319-1195, Japan

[2]Advanced Science Research Center, Japan Atomic Energy Agency, Tokai-mura, Naka-gun, Ibaraki 319-1195, Japan

Introduction

Determination of geometrical location of adsorbed atoms and molecules on a surface is one of the key factors to be elucidated in surface science. A normal incidence X-ray standing wave (NIXSW) using soft X-rays has excellent characteristic, in which the distance between adsorbed atoms and surface can be precisely determined [1]. In this work, we present the first results for the geometrical determination of atoms and molecules adsorbed on a surface of insulating oxide with wide band-gap. The system investigated is decyl-phosphonic acid (DPA, C_{10}-alkyl phosphonic acid) adsorbed on a sapphire surface, which is one of the candidate systems for self-assembled monolayers (SAM) of organic molecules on oxide surface.

Experimental

The experiments were performed at the BL-27A station. A C(0001) face of a sapphire plate was used as a substrate. The substrate was immersed in 0.01 Mol/dm^3 of DPA-ethanol liquid for 20 hours, and then rinsed by supersonic waves in ethanol. For the NIXSW measurements, the sample surface was irradiated by soft X-rays from the surface normal. The intensities of the total electrons, P 1s and C 1s photoelectrons were plotted as a function of the photon energy.

Results and discussion

Fig.1 shows the total electron yield for clean surface of sapphire as a function of the photon energy. The most intense peak was observed around 3050 eV, which is due to the standing wave originating from the sapphire substrate. This energy nearly corresponds to one of the Bragg diffraction peaks from α-Al_2O_3 with corundum structure.

Fig.2 displays the intensities of the P 1s photoelectrons, as a function of the photon energy around 3050 eV. The normalized intensity of the photoelectron ($I(E)/I_0$) being concerned is described as

$$I(E)/I_0=1+R(E)+2F[R(E)]^{1/2}\cdot\cos[2\pi d_H-\delta(E)] \qquad (1)$$

where $R(E)$ is the reflectivity of the substrate, $\delta(E)$ is the energy-dependent phase modulation caused by the X-ray standing wave, F is the structure factor, and d_H is the coherent position of the atoms measured from the surface [2]. The photon energy, E, is normalized by the "W parameter" that stands for the deviation from the Bragg

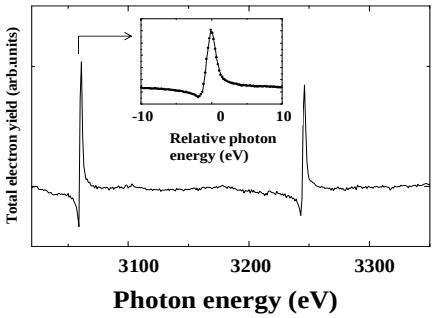

Fig.1 Total electron yield for clean sapphire substrate as a function of photon energy. The incidence angle of X-rays was surface normal.

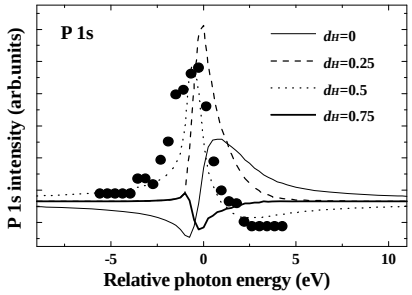

Fig.2 Intensity of P 1s for DPA/Sapphire as a function of photon energy. The theoretical curves calculated by eq.(1) for four different locations of phosphorus atoms are also shown.

diffraction condition [3]. The intensity of the P 1s follows the theoretical curve for d_H=0.5. This means that the phosphorus atoms in DPA molecules are located at the half of the coherent position, i.e., d=0.21 nm, deduced from the Bragg energy. Therefore, it is concluded that phosphorus atoms are located at 0.11 nm from the surface and DPA molecules form SAM through phosphonic acids. The results shed light on the further applications of NIXSW to the structure analysis of atoms and molecules on insulating materials like oxides.

References

[1] D.P. Woodruff *et al.*, Phys. Rev. Lett. **58**, 1460 (1987).
[2] P. Fenter, *et al.*, Surf. Sci. **412/413**, 213 (1998).
[3] H. Hashizume *et al.*, Jpn. J. Appl. Phys. **27**, L1568 (1988).

* baba.yuji@jaea.go.jp

11A/2010G646

Local structure analysis of MgB_2 thin films by polarized XAFS

Mami Seo[1], Takafumi Miyanaga[1], Tomoe Kanno[1], Kouki Takeda[2], Daichi Hatanaka[2], Masahito Yoshizawa[2]
[1]Department of Advanced Physics, Hirosaki University, Hirosaki, Aomori, 036-8561, Japan
[2]Graduate School of Engineering, Iwate University, Morioka, Iwate, 020-8551, Japan

1 Introduction

MgB_2 discovered in 2001 shows the super-conducting transition temperature of 39K, which is the highest among metallic ones. The superconducting mechanism and applications as a device are attracting great interest. An important issue for the application to a device is the production of high-quality MgB_2 thin films. Although MgB_2 thin film grown-up on ZnO forms a reactive region in the interface, its crystallinity and superconductivity performance have been improved. The lattice distance of ZnO is close to that of MgB_2 (the lattice mismatch is about 5%). For studying the local structure of such thin films, EXAFS (extended X-ray absorption fine structure) is a powerful tool and the polarized EXAFS analyses are available, using a synchrotron radiation source. We analyzed the local structure of 50nm and 150nm MgB_2 thin films until now [1]. In this paper we present the results for the local structure of 10nm, 20nm and 30nm MgB_2 thin films.

2 Experiment

10nm, 20nm and 30nm MgB_2 films were prepared by co-evaporation MBE (molecular beam epitaxy) method [2]. Mg *K*-edge (1309eV) X-ray absorption spectra measured on BL11A at Photon Factory, KEK, Tsukuba, using fluorescence mode with silicon drift detector (SDD). Polarization-dependent XAFS measurement was applied to two directions: (a) The horizontal direction of the sample in which the electric vector of X-ray, ***E***, is perpendicular to the *c*-axis of MgB_2 thin film: (b) The vertical direction in which ***E*** is parallel to the *c*-axis. The EXAFS analyses were performed by XANADU code and FEFF 8.10 code. We applied the non-liner least square fitting (curve fitting) method to EXAFS data and obtained the structural parameters.

3 Results and Discussion

Fig. 1 and Fig. 2 show Fourier transform (FT) of $\chi(k)$ for the horizontal direction and for the vertical direction for MgB_2 thin films. Peaks around 2.0 Å, 2.8 Å and 3.5 Å correspond to 1NN (1st nearest neighbor) Mg-B, 2NN Mg-Mg and 3NN Mg-Mg, respectively. FT for 30nm MgB_2 film is similar to that for 50nm. On the other hand, FT for10nm and 20nm films have different structure from 30 and 50 nm films. Peak for 1NN Mg-B shifts to shorter distance and FT of 10nm film shows no clear polarization dependence.

Fig. 3 is atomic distance value, which is obtained by curve fitting as a function of film thickness.

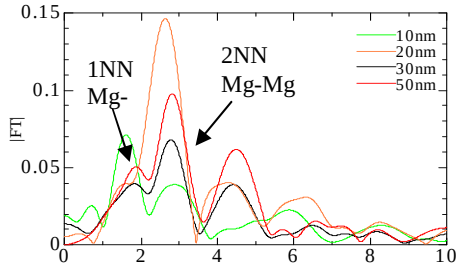

Fig. 1 FT of $\chi(k)$ for the horizontal direction MgB_2 films

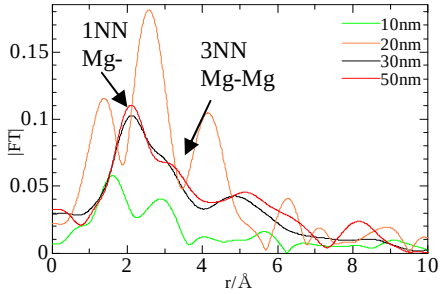

Fig. 2 FT of $\chi(k)$ for the vertical direction MgB_2 films

1NN distance becomes shorter as the film thickness is thinner. On the other hand, 2NN distance shows no clear dependence on the film thickness. Furthermore, the distance of 3NN for 10nm and 20nm are close to that of 2NN. It suggests the possibility of the structural change from the hexagonal form to tetragonal one. This is considered to be the effect of magnesium oxide.

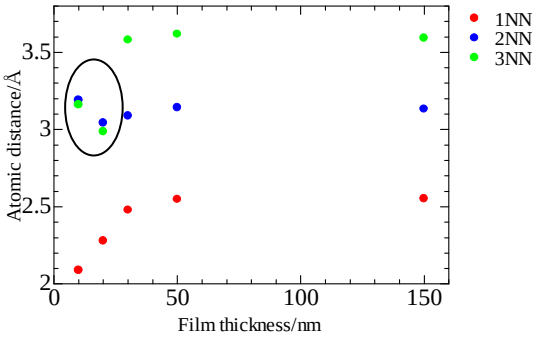

Fig. 3 Atomic distance vs film thickness

4 Reference

[1]T. Miyanaga, T. Kanno, Y. Fujine, J. Araaki, M. Yoshizawa, J. Elec. Spec. Rel. Phen., 184 254 (2011).
[2]Y. Harada, T. Takahashi, Y. Nakanishi, M. Yoshizawa, Physica C426-431 (part2) 011921 (2005).

27A/2010G658

Surface chemical states of $FeSi_2$ and Mg_2Si crystals studied by XPS and XAS

Hiroyuki YAMAMOTO, Fumitaka ESAKA*
Japan Atomic Energy Agency, Tokai, Naka, Ibaraki 319-1195, Japan

Introduction

Semi-conducting silicides are extensively investigated for using as silicon-based electronic devices. Among silicides, β-$FeSi_2$ and Mg_2Si are candidates as high performance thermo-electronic devices. Recently, large crystalline β-$FeSi_2$ and Mg_2Si have been synthesized [1,2]. Since then, it is expected to use crystalline β-$FeSi_2$ and Mg_2Si as the substrate for homoepitaxial growth of films. In order to fabricate homoepitaxial films with excellent quality, well-controlled surface of the substrate as well as optimized growth conditions are necessary.

In the present study, a combination of X-ray photoelectron spectroscopy (XPS) and X-ray absorption spectroscopy (XAS) is applied to clarify surface chemical states of β-$FeSi_2$, and Mg_2Si crystals.

Experimental

The β-$FeSi_2$ and Mg_2Si crystals with several millimeters in width were used in this work. The fabrication procedures were described in previous papers [1,2].

The XPS and XAS measurements were performed at the beam line 27A [3]. In the XPS measurement, excitation X-ray energies were set at 2700, 3000 and 3300 eV. The Si K-edge XAS spectra were obtained using total electron and partial electron yield (TEY and PEY) modes.

Results and Discussion

The XPS measurement showed the formation of SiO_2 in the β-$FeSi_2$ and that of SiO_2 and MgO in the Mg_2Si crystals. With decreasing excitation X-ray energy, the peak area ratio of oxide to silicide increased significantly. This implies that these oxide layers were formed on the surface of the β-$FeSi_2$ and Mg_2Si crystals.

Figure 1 shows the Si K-edge XAS spectra of the β-$FeSi_2$ crystal measured with TEY and PEY modes. The spectrum obtained with the TEY mode is in good agreement with that shown in a previous paper [3]. The peaks at about 1845 and 1848 are assigned to SiO and SiO_2, respectively. No significant changes were observed in the spectrum obtained with the PEY mode.

The Si K-edge XAS spectra of the Mg_2Si crystal were shown in Fig. 2. Four peaks at 1841 and 1843, 1845 and 1848 eV are observed in the spectrum obtained with the TEY mode. In the spectrum obtained with the PEY mode, a dominant peak assigned to SiO was observed. This is presumably due to the formation of SiO on the top of the surface of the Mg_2Si crystal. The formation of SiO on the Mg_2Si crystal was not observed in the Si 1s XPS spectra, which would be due to the lack of surface sensitivity.

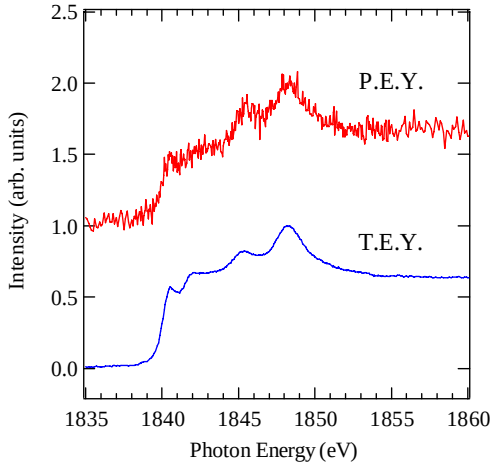

Fig.1. Si K-edge XAS spectra of a β-$FeSi_2$ crystal measured with PEY and TEY modes.

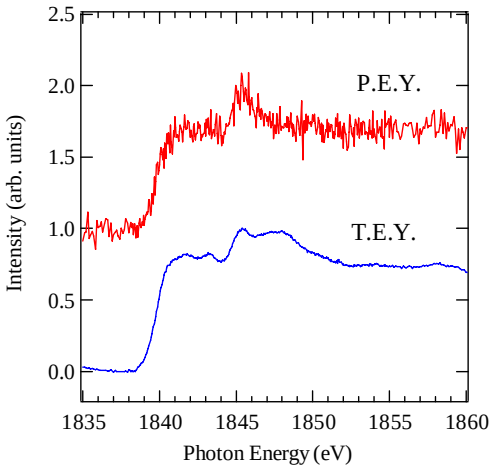

Fig.2. Si K-edge XAS spectra of a Mg_2Si crystal measured with PEY and TEY modes.

References

[1] H. Udono et al., Jpn. J. Appl. Phys. **39**, L225 (2000).
[2] D. Tamura et al., Thin Solid Films **515**, 8272 (2007).
[3] F. Esaka et al., Appl. Surf. Sci. **257**, 2950 (2011).
* esaka.fumitaka@jaea.go.jp

15C/2010G672
1105039PF

ナノワイヤーから成長した GaAs/Si 薄膜結晶のひずみ緩和機構の研究

Strain relaxation of GaAs thin layer crystals grown from nano-wires on Si wafer

水野　薫 [1*], 岡本博之 [2]
[1] 島根大学総合理工学部　〒690-8504 松江市西川津町 1060
[2] 金沢大学医薬保健研究域　〒920-0942 金沢市小立野 5-11-80

1 はじめに

ヘテロエピタキシャル半導体薄膜は基板と薄膜の物質が異なるにも関わらず，同じ方位を有する。そのため，格子定数の違いによる歪みの発生が避けられない。膜厚が薄いうちは弾性的な変形により，歪みの緩和が行われるが，ある厚さを越えると塑性変形を起こして緩和する。その時に導入される転位が不整合転位，はじめて不整合転位の発生する厚さが臨界膜厚とよばれている。この転位はデバイスの性能を悪化させたり寿命を短くすることが知られている。そのため，バッファー層を基板と薄膜の間に挟むなど，不整合転位を発生させない工夫が試みられている。他の方法として針状のナノ結晶を基板上に多数成長させたのち，成長温度を変化させて主として結晶の上部を太らせて隣接する結晶同士を合体させ，薄膜を成長させる方法が提案されている。[1] この薄膜結晶は基板と針状のナノ結晶で結合しているため，通常のヘテロエピタキシャル半導体薄膜とは異なる歪み緩和が生じていると期待できる。そのため，不整合転位が存在しない可能性もあり，もしそのような薄膜結晶であるならば，前述の不整合転位により引き起こされる弊害を取り除くことが可能である。

そこで本研究では，臨界膜厚よりも厚い薄膜結晶の表面反射トポグラフを撮影することにより，歪み緩和の結果として生じる格子欠陥の有無を観察する。さらに格子欠陥が観察された場合，欠陥の同定を行うため，異なる回折面によるトポグラフも撮影する。このことにより格子欠陥の歪み場を決定し，最終的には格子欠陥の種類を明らかにする。以上の研究により、最終的にナノ結晶より成長したヘテロエピタキシャル半導体薄膜の歪み緩和機構を明らかにすることを目的とする。

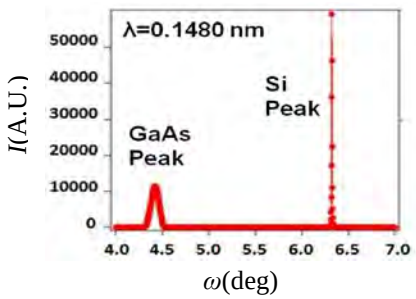

図１．ロッキングカーブ

2 実験

無転位 Si（111）基板上に MOVPE 法により GaAs ナノワイヤー結晶を多数成長させる。その後成長温度を下げ，径方向に成長させナノワイヤー同士を合体させ単結晶薄膜試料とした。次に（044）を回折面として波長 1.478Åの単色Ｘ線を用いて Si 基板結晶からの回折線を検出して X 線トポグラフを撮影した。さらに同じ波長で，GaAs からの回折線を検出して，この条件でもトポグラフの撮影を行った。この条件で，入射Ｘ線と試料表面のなす角（入射角）は約３°であるので，Ｘ線は数百μｍ まで侵入している。そこで X 線の侵入の深さを数十 nm 以下にするため，ブラッグ条件を満たしながら X 線のエネルギーを徐々に高くして，入射角を 0.1°にした。この条件での波長は 1.335Åであった。この微小角入射条件下で上記と同様にトポグラフを撮影した。逆格子マップの測定はトポグラフの撮影後に行った。また，本実験のトポグラフの撮影には分解能の高い画像を得るために原子核乾板を用いた。

3 結果および考察

図１に1.478Åの単色Ｘ線を用いて(440)を回折面として測定したロッキングカーブを示す。この図にはSi基板からのシャープで高い回折ピークとGaAs薄膜によるブロードで弱いピークがみられた。このうち基板(Si)の回折ピークで撮影されたトポグラフを図２(a), (b)に示す。厚い薄膜を付けたことにより，試料が反っているため，回折角をわずかにずらして3または4回に分けて２枚のトポグラフを撮影した。この２枚を合成した写真を図２(c)に示す。また，同じ波長を用いて，薄膜(GaAs)の回折ピークで撮影したトポグラフを図３に示す。この写真に局所的に回折条件を満たさず，白く抜けている微少領域は観察

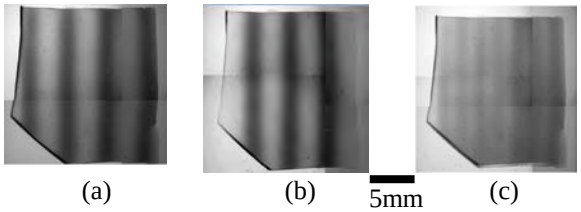

図２．Si基板のトポグラフ

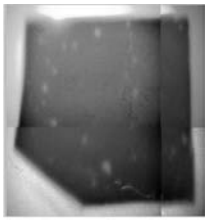

図３．GaAs薄膜のトポグラフ

されない。このことはGaAs薄膜が単結晶として基板の上に成長していることを示している。

さらに，図２，３に示す写真いずれにも転位線は見られなかった。つまり臨界の膜厚(4 nm)を大幅に越えた膜厚(約1μm)を有する薄膜試料にもかかわらず不整合転位は観察されなかった。そこで光学顕微鏡により，写真を拡大して観察した。図４(a)に拡大した写真を示す。拡大すると多数の斑点が観察できた。この斑点の大きさは原子核乾板の乳剤粒子の大きさよりも，数倍から数十倍大きい。写真乳剤の粒子の写真を図４(b)に示す。このことから乾板に見られた斑点に対応する歪みは基板から生えているナノワイヤー結晶の基部に存在する可能性がある。

次に，同じエネルギーのX線と回折面を用いて測定した逆格子マップの結果を図 5 に示す。図 5(a)は図 1 に示すロッキングカーブの Si の回折ピーク付近で，5(b)は GaAs の回折ピーク付近で測定した結果である。逆格子マップの測定はωおよび 2θ軸を回転して測定するため，結果は通常ωと 2θのグラフであるが，図 5 では座標軸を変換して試料表面に平行な軸 q_y と垂直な軸 q_h で示しており，回折ピークの断面を表している。そのため，グラフ上での広がりは格子定数の分布を示している。この図から，GaAs 薄膜の格子定数の広がりは水平方向では Si 基板と同程度であるが，垂直方向は 10 倍程度広がっていることが分かる。以上の結果から，ナノワイヤーから成長した GaAs 薄膜の歪み緩和は不整合転位を発生させるのではなく，Si 基板からナノワイヤーが生えているところで弾性的に緩和していると考えられる。

4 まとめ

Si 基板上に GaAs ナノワイヤーを密生させ，さらに横方向に成長させ薄膜化させたヘテロエピタキシャル半導体薄膜の界面における歪みは基板からナノワイヤーの生えている場所で弾性的に緩和されている可能性が高い。

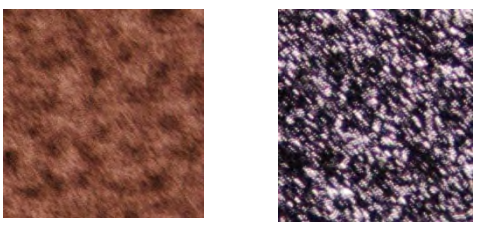

(a) (b)

図４．拡大したトポグラフ

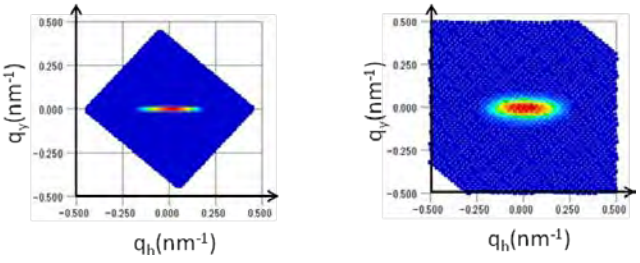

(a) (b)

図５．逆格子マップ

謝辞

試料はイタリアの国立結晶学研究所(IMM-CNR)の Paola Prete 博士らに作製・提供していただいた。さらに九州シンクロトロン光研究センターにおける実験に際して石地耕太朗博士および川戸清爾博士にご協力いただいた。ここに感謝致します。

参考文献

[1] Paola Prete and Nicola Lovergine : Nanowires (InTech, New York, 2010) pp51.

* mizuno@riko.shimane-u.ac.jp

16A1/2010G689

In Situ Evaluation of Ion-Beam Irradiation Induced Ferromagnetism at Ultra-Surface of FeRh Thin Films by XMCD

K. Aikoh[1], A. Tohki[1], M. Sakamaki[2], K. Amemiya[2], A. Iwase*[1] and T. Matsui[1]

[1] Osaka Prefecture University, Sakai, Osaka 599-8531, Japan
[2] High Energy Accelerator Research Organization (KEK), Tsukuba, Ibaraki 305-0801, Japan.

1 Introduction

FeRh alloys have several potential technological advantages for device applications, such as thermally assisted magnetic recording media, mainly due to their first order antiferromagnetic (AF) - ferromagnetic (FM) phase transition. Our previous studies have shown that energetic ion beam irradiation induces FM spin order in Fe-50at.%Rh even in low temperature regions at which they are originally AF state. [1-3] In the present studies, we tried to modify the magnetic state at the ultra-surface of the FeRh thin films by 1 keV Ar ion-beam irradiation. According to its small penetration depth less than 5 nm, the modified magnetic state was evaluated by means of soft x-ray Magnetic Circular Dichroism (XMCD)

2 Experiment

FeRh thin films 30 nm thick were prepared by ion-beam sputtering of $Fe_{50}Rh_{50}$ target at 700 ºC on MgO(100) single crystal. The crystal structure of the samples was characterized by X-ray diffraction. Irradiations with 1 keV Ar ions and XMCD measurements near Fe $L_{2,3}$-edge were carried out without exposing ambient atmosphere at the BL-16A of KEK-PF. First, the Fe $L_{2,3}$-edge XMCD spectrum for the unirradiated sample was measured under the magnetic field of 0.6 T. Then, the sample was irradiated with 1 keV Ar ions for 5 minutes and we measured again the XMCD spectrum at the same condition. The same experiments were performed also at the total irradiation time of 7.5, 12.5, 17.5 and 122.5 minutes.

3 Results and Discussion

Fig. 1 shows the dependence of XMCD spectrum on the Ar ion irradiation time. The intensity of the spectrum increases with increasing the irradiation time, reaches the maximum value at the irradiation time of 7.5 min., and then the intensity decreases. This fact indicates that the magnetic moment of Fe atoms increases by the small fluence of 1 keV Ar ion-beam irradiation. However, it also reveals that the irradiation with higher Ar ion fluences decreases the spin ordering. This trend of the change in magnetic properties is similar to our previous result for FeRh irradiated with several MeV ions..

The present XMCD result shows that the keV ion-beam irradiation systematically changes the magnetic moments of Fe atom at the ultra-surface of the FeRh thin film. The combination of the magnetic modification by keV ion beam with the original magnetic nature of the FeRh has some potential to make new magnetic devices.

To evaluate the present result more quantitatively, the analysis by using the well-established XMCD sum rule for the L edge is now in progress.

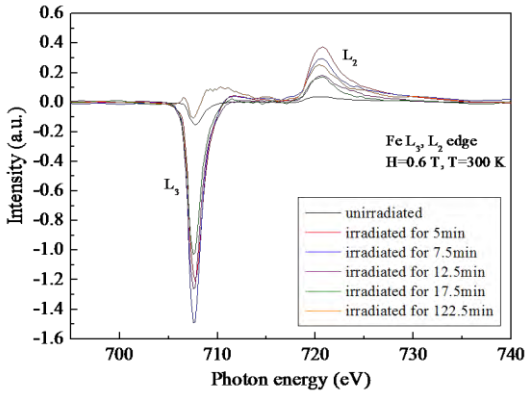

Fig. 1 The Fe $L_{2,3}$-edge XMCD spectra at 300 K for unirradiated sample and those irradiated with 1 keV Ar ion with various irradiation times.

References

[1]M. Fukuzumi et al., Nucl. Instr. and Meth. B **245**, 161 (2006).
[2]A. Iwase et al., Nucl. Instr. and Meth. B **256**, 429 (2007).
[3]Y. Zushi et al., Nucl. Instr. and Meth. B **256**, 434 (2007).

*iwase@mtr.osakafu-u.ac.jp

10C/2010G699, 15A/2010G134

Self-Assembled Structure and Sol-Gel Transition of Crystalline Organogels and Surfactant Organogels

*Hiroyuki TAKENO and Toshiro MOCHIZUKI
Department of Chemistry and Chemical Biology, Faculty of Engineering, Gunma University, Kiryu, Gunma 376-8515, Japan

1 Introduction

There has been an enormous increase of interest in the properties and structures of low-molecular mass organogels because of their potential applications. Self-assembled fibrillar network is formed in the gel.[1, 2] Usually the network is formed at low temperatures, while it melts at high temperatures, i.e., the gels are thermally reversible.

Recently Raghavan reported that there exist two types of low-molecular mass gels, crystalline gels and surfactant gels.[3] In the former gel, it has been ascertained by X-ray measurements that arrangement of the gelator molecules in the gel is similar to that in the crystalline powder. We showed that the composition and temperature did not affect the fiber structure using small-angle neutron scattering and synchrotron small-angle X-ray scattering (SAXS) for the gel of 12-hydroxystearic acid (12-HSA), which is known as one of the crystalline organogelators,, although they affected the fiber density.[4] On the other hand, the surfactant gel is produced by adding an additive into a surfactant micellar solution. In the case of this type of gel, temperature and concentration dependencies on structures of the gels is not fully understood at the present stage. In this study, we investigated structures and the sol-gel transition behavior for both types of gels using synchrotron SAXS measurements in order to clarify their gelation mechanism.

2 Experiment

In this study we used Lauroyl-L-glutamic-α-γ-dibutylamide (LGBA) and an anionic surfactant (AOT) as a gelator for preparation of the crystalline gels and the surfactant gels, respectively. Various kinds of additives were used for production of the latter type of gel. The synchrotron SAXS measurements were performed at the beam line 15A and 10C. The scattered intensity was detected with an image intensifier coupled to a CCD camera in the former, while it was detected using a imaging plate (RIGAKU R-AXIS) in the latter. The two dimensional scattered images were circularly averaged to obtain the scattering profiles as a function of the scattering vector q defined by $q = 4\pi\sin(\theta/2)/\lambda$, where θ and λ are the scattering angle and the wavelength of X-ray, respectively. The scattering data were corrected for the background scattering, the incident beam and the exposure time of the measurement.

3 Results and Discussion

The scattering profiles for LGBA gels in toluene at various concentrations and various temperatures showed almost the same shape in the log-log plot, while the scattering intensity gradually decreased with increasing temperature in the gel state, indicating that the fibers gradually melted with increase of temperature (not shown here). Further increase in temperature caused drastic decrease of the scattering intensity, which suggests that the sol-gel transition took place. These behaviors are very similar to that of 12-HSA gels.[4] On the other hand, the SAXS behavior for surfactant gels strongly depended upon composition and temperature. Figure 1 shows scattering profiles for a surfactant gel in toluene at various concentrations. The profiles for 5 wt% and 10 wt% surfactant gels monotonously decreased with increase of q. The profile for the gel with a higher concentration (15 wt%) had a sharp peak and a broad peak at q = 0. 32 Å^{-1} and $q \cong$ 0. 15 Å^{-1}, respectively. Appearance of the sharp peak suggests that an ordered structure was formed at the high concentration.

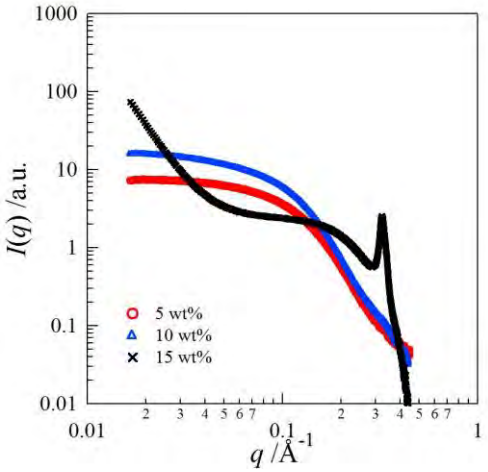

Figure 1 SAXS profiles for a surfactant gel at various concentrations.

References

[1] H. Takeno, N. Kikuchi, S. Kondo, T. Dobashi, Trans. MRS-J, 32 (2007) 835-838.
[2] H. Takeno, T. Mochizuki, K. Yoshiba, S. Kondo, T. Dobashi, Prog. Colloid Poly. Sci., 136 (2009) 47-53.
[3] S.R. Raghavan, Langmuir, 25 (2009) 8382-8385.
[4] H. Takeno, A. Maehara, D. Yamaguchi, S. Koizumi, J. Phys. Chem. B, **DOI:** 10.1021/jp3008514.

* takeno@gunma-u.ac.jp

9C, NW10A/2011G005

XAFS Studies of Metal Nanoparticles Prepared by Using Microwave Heating

Masafumi HARADA*, Cong CONG, and Tomoko SADA
Department of Clothing Environmental Science, Faculty of Human Life and Environment,
Nara Women's University, Nara 630-8506, Japan

Introduction

Microwave (MW) irradiation is one of the most promising techniques for the preparation of nanomaterials with controlled size and shape. In the past decade, there has been increasing interest in the use of MW irradiation instead of conventional heating in various kinds of metallic nano-sized particle syntheses [1, 2]. Recently we have developed an efficient preparation method of the size-regulated monometallic and bimetallic nanoparticles by means of MW irradiation. Here we demonstrate the structural analysis of monometallic Pd, Rh, Ru, Pt and Au nanoparticles by the use of EXAFS measurements.

Experimental

In a typical experiment for the preparation of monometallic Pd nanoparticles (Pd_EG) in ethylene glycol (EG), 555.7 mg PVP was dissolved in 50 ml of ethylene glycol as a solvent to make the polymer solution (PVP/EG) with a concentration of PVP equal to 100 mM. 0.2 ml of HCl was added to 88.66 mg of $PdCl_2$ powder to dissolve it into aqueous solutions. After the addition of HCl, 50 ml of PVP/EG solution was poured to prepare the metallic solution with the concentration of [Pd] = 10 mM. In the case of the preparation of Pd nanoparticles (Pd_gly.) in glycerol, glycerol was used as a solvent instead of EG to make PVP/glycerol solutions.

MW irradiation was carried out using an MW apparatus (MICROSYNTH PLUS, Milestone General K.K.) in a continuous wave mode at 700 W (2.45 GHz). For the preparation of Pd nanoparticles in EG, the solution temperature was raised to 471 K by heating the solution for about 2 min, and it was maintained at this temperature for about 10 min. After naturally cooling down to room temperature, the colloidal solutions were collected for the EXAFS measurements. For the preparation of Pd nanoparticles in glycerol, the solution temperature was raised to 523 K for about 3 min, and it was kept at this temperature for about 10 min. In the case of the other monometallic nanoparticles, the same experimental conditions (concentration of metal and PVP, reaction temperature, and MW heating time) were applied as in the case of Pd nanoparticles. The EXAFS measurements were carried out in a transmission mode at BL-9C and NW10A. Data analysis was performed by REX2000 (Rigaku Co.).

Results and Discussion

Table 1 shows the structural parameters such as coordination numbers (C.N.) and bond distances (r) of the monometallic Pd, Rh, Ru, Pt and Au nanoparticles prepared in EG or glycerol by using MW irradiation. In the Fourier transforms of all the colloidal samples (not shown in this report), only the peak attributed to metal-metal bond was observed between 0.2 and 0.3 nm, indicating that the starting ionic compounds were completely reduced to form metallic nanoparticles. In the case of Pd, Pt and Au nanoparticles, the C.N. obtained from the curve-fitting is nearly the same (ranging from 10.3 to 11.3). This suggests that the particle size of these nanoparticles is not strongly affected by the metal concentration and reaction temperature. However, in the case of Rh and Ru nanoparticles, the C.N. becomes larger when the metal concentration becomes higher. Moreover, C.N. of Rh-Rh bond is 9.1 (or 10.3) for EG solvent and 7.0 (or 9.3) for glycerol, suggesting that the size of Rh nanoparticles prepared in glycerol is relatively smaller. The same trend is also seen in the C.N. of Ru-Ru bond. The detailed analysis of monometallic and bimetallic Pd/Pt, Rh/Pt and Pd/Au nanoparticles is in progress.

Table 1. Structural parameters from EXAFS analysis for the colloidal dispersions of metal nanoparticles prepared by means of MW irradiation.

Sample	C.N.[a]	r / Å	dE / eV	DW / Å
Pd_EG ([Pd]=5mM)	10.7	2.74	-0.846	0.068
Pd_EG ([Pd]=10mM)	10.7	2.74	-0.757	0.065
Pd_gly. ([Pd]=5mM)	11.0	2.81	-0.750	0.077
Pd_gly. ([Pd]=10mM)	11.3	2.81	-0.836	0.073
Rh_EG ([Rh]=5mM)	9.1	2.67	-2.186	0.059
Rh_EG ([Rh]=10mM)	10.3	2.68	-0.659	0.064
Rh_gly. ([Rh]=5mM)	7.0	2.66	-4.613	0.052
Rh_gly. ([Rh]=10mM)	9.3	2.68	-1.611	0.066
Ru_EG ([Ru]=5mM)	10.5	2.66	-0.631	0.073
Ru_EG ([Ru]=10mM)	11.0	2.66	-1.32	0.075
Ru_gly. ([Ru]=5mM)	8.3	2.66	-3.009	0.071
Ru_gly. ([Ru]=10mM)	9.3	2.66	-4.00	0.076
Pt_EG ([Pt]=5mM)	10.3	2.76	-1.523	0.068
Pt_EG ([Pt]=10mM)	10.4	2.76	-1.020	0.066
Pt_gly. ([Pt]=5mM)	10.7	2.76	-1.276	0.070
Pt_gly. ([Pt]=10mM)	10.5	2.76	-1.187	0.068
Au_gly. ([Au]=5mM)	12.6	2.89	2.039	0.061
Au_gly. ([Au]=10mM)	12.1	2.88	0.678	0.060

[a] Coordination numbers of the corresponding metallic bond.

References

[1] T. Nakamura et al., *Bull. Chem. Soc. Jpn.* **2007**, *80*, 224. [2] M. Tsuji et al., *Chem. Eur. J.* **2005**, *11*, 440.

*harada@cc.nara-wu.ac.jp

3B/2011G017

Mo(100)上に作成した Ti 酸化物超薄膜の二次元電子状態
The two-dimensional electronic structures of ultra-thin Ti oxide films on Mo(100)

枝元一之 [1*], 長谷川智 [1]，宗像紫織 [1]，今西沙織 [1]，掛札洋平 [1]，小澤健一 [2]
[1] 立教大学理学部、〒171-8501 東京都豊島区西池袋 3-34-1
[2] 東京工業大学大学院物質科学専攻　〒152-8550 東京都目黒区大岡山 2-12-1

1 はじめに

金属表面における酸化物超薄膜の作成は、金属 - 酸化物界面の電子状態の解明のために重要であるのみならず、三次元結晶では見られない特異な構造の薄膜が得られる場合があり、近年注目を集めている。我々は、これまでに Ag(100)上に酸素雰囲気下で Ti を蒸着した場合、酸素圧を制御することにより、(1×1)TiO 超薄膜と(5×1)TiO_2超薄膜を選択的に合成することを見出した[1]。さらに、放射光を用いた角度分解光電子分光(ARPES)により、これらの薄膜の二次元電子状態の解明に成功している(2007G025)[2,3]。しかし、これらの薄膜を相互に変換することはできなかった。これは、Ag を基板に用いた場合、高温での酸化還元処理ができないためと考えられる。薄膜の酸化状態の自在制御を目指す観点からは、高温処理可能な高融点基板を用いる必要がある。今回、我々は Mo(100)上に Ti 酸化物薄膜を作成し、ARPES によりその二次元電子状態の解明を目指す研究を行った。

2 実験

Mo(100)は、超高真空下で 1800℃以上での加熱を繰り返すことにより清浄化した。Ti 酸化物薄膜は、通常の reactive deposition では下地 Mo が激しく酸化されるため、まず Ti を蒸着し、その後 Ti 薄膜を酸化(O_2 12L)することにより作成した。Ti の蒸着は、電子ビーム蒸着源(Omicron EFM3)を用いて行った。

実験は、BL3B において ARPES2 装置を用いて行った。今回作成した薄膜は、超薄膜であるため、スペクトルには下地 Mo の 4d バンドが重なって観測され、下地の二次元電子状態を選択的に観測することが難しい。そこで、今回は Mo4d のクーパー極小の光エネルギーを実験的に決定し(100 eV)、そのエネルギーにおいて下地のエミッションを抑えて測定を行った[4]。

3 結果および考察

今回、我々はまず Mo(100)上に Ti を蒸着し、これを酸化することにより、単結晶薄膜を合成することに成功した。Ti 3p スペクトルの解析により、Ti 酸化物薄膜を加熱すると 1000℃以下では Ti_2O_3 薄膜が生成し、それ以上の温度で加熱すると TiO 薄膜に転移することが分かった。TiO 薄膜は作成条件によりさまざまな周期性を示すが、その中で 1300℃で 10 秒間加熱することにより得られる(2×2)LEED パターンを示す相について ARPES 測定を行った。得られた ARPES スペクトルを二次微分し、その強度をプロットすることにより得られた二次元バンド構造を図 1 に示す。意外なことに、(2×2)相における TiO の電子状態は(1×1)周期性を示す。酸素のみを吸着して 1300℃で 10 秒間加熱しても(2×2)LEED パターンが得られることから、今回作成した(2×2)相においては、Mo(100)上に(1×1)TiO 薄膜で覆われた領域と、(2×2)酸素吸着面で覆われた領域が共存していると考えられる[4]。

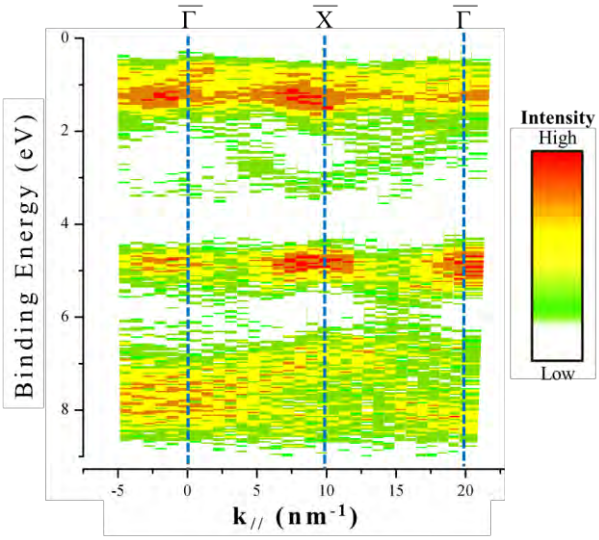

図 1 ：(2×2)TiO/Mo(100)の二次元バンド構造。

謝辞

この研究は、科学研究費補助金(No.22550127)の補助の下に行われた。ここに感謝致します。

参考文献

[1] H. Kaneko *et al*., Solid State Commun. **142** (2007) 32.
[2] H. Kaneko *et al*., Surf. Sci. **602** (2008) 2295.
[3] K. Edamoto *et al*., e-J. Surf. Sci. Nanotech. To be published.
[4] T. Hasegawa *et al*., Surf. Sci. **606** (2012) 414.

14A/2011G022

Ferroelectric $KNbO_3$ in Orthorhombic Phase

Terutoshi Sakakura[1*], Nobuo Ishizawa[2]
[1]Institute of Multidisciplinary Research for Advanced Materials, Tohoku University, 2-1-1 Katahira, Aoba-ku, Sendai 980-8577
[2]Ceramics Research Laboratory, Nagoya Institute of Technology, Asahigaoka, Tajimi, Gifu 507-0071

1 Introduction

From the environmental reasons, lead-free piezoelectric ceramics $KNbO_3$ and associated compounds are attracting attention as alternative candidates for lead zirconate titanate (PZT). $KNbO_3$ shows a similar phase transition sequence with $BaTiO_3$ and belongs to several space groups; cubic (*Pm3m*), tetragonal (*P4mm*), orthorhombic (*Bmm2*), and hexagonal (*R3m*) in decreasing order of temperature. Except for paraelectric cubic phase, several types of domain structures are known. Since these domains make diffraction spots split, single crystal X-ray diffraction measurements in ferroelectric phases are quite difficult [1]. However, recently we have noticed that only a few crystals in orthorhombic phase, that we have tested, exhibit no split of the diffraction spots due to domains, even for crystals more than several micrometers in size, although, in orthorhombic phase, 180-degrees, 90-degrees, and 60-degrees domains are typical. Since we are curious about the charge densities in ferroelectric phase of $KNbO_3$, we have started the investigation. From the preliminary studies using laboratory X-ray source MoKα and three circle diffractometer installing CCD detector (Bruker Smart APEX2), assumption of *Bmm2* space group does not converged to reasonable structure. To investigate the more details, we performed single-crystal X-ray diffraction measurement using synchrotron radiation.

2 Experimental

Single crystals of $KNbO_3$ were grown by the flux method and mounted on the borosilicate glass capillary by two-component epoxy adhesive. The crystals are tested using four-circle diffractometer (MAC Science MXC18XHF22, MoKα). Among more than 30 specimens, only one crystal about 10x10x10 micrometer in size was judged to have single diffraction peaks and suitable for single-crystal X-ray diffraction measurement at BL14A. X-ray of 0.7521Å was selected and lead to the four circle diffractometer installing an avalanche photodiode (APD) detector, whose count loss is less than 1% up to 10^7 cps. To minimize the contaminations due to simultaneous reflections, psi-scan simulation software MDC [2] was used and optimum four-circle angle settings were calculated for each reflection and all the diffraction intensities were collected at the calculated angles.

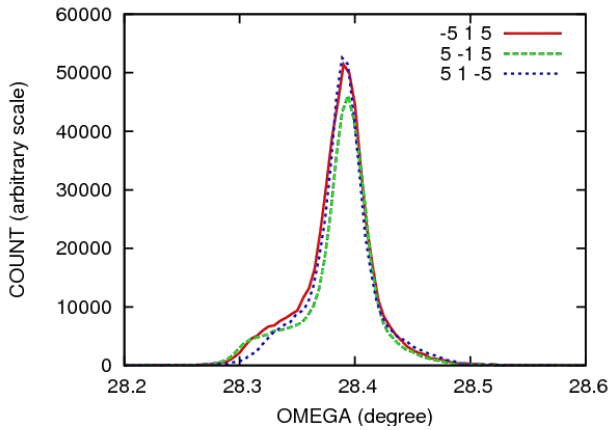

Figure 1: Peak profiles of some equivalent reflections.

3 Results and Discussions

All the peak profiles are asymmetric and have a tail towards lower angles suggesting the existence of slightly larger cells in some extent and this is ascribed to the surface relaxation. Figure 2 shows the intensity statistics of equivalent reflections assuming the space group *Bmm2*. Since intensities vary about 20% among the equivalents, *Bmm2* is not suitable for this crystal macroscopically. More details are under examination.

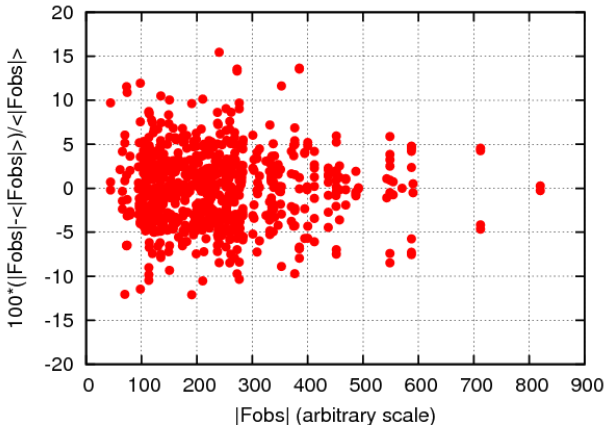

Figure 2: Deviation of intensities among the equivalents; reflections with $|F_{obs}|>50*\sigma(|F_{obs}|)$ are plotted .

References

[1] N. Ishizawa *et al.*, Solid State Chem. **183** (2010) 2731-2738.
[2] K. Tanaka *et al.*, Acta Cryst. **A50** (1994) 246-252.

* sakakura@tagen.tohoku.ac.jp

6A, 9C/2011G029

Solvent Annealing Induced Highly Perpendicular Orientation of Cylindrical Microdomains in Block Copolymer Thin Film and Fabrication of Hexagonally Arrayed Nano-channels

Katsuhiro Yamamoto[1,*] Satoshi Ohya[1], Shinichi Sakurai[2]
[1]Graduate School of Engin., Nagoya Inst. of Tech. Gokiso-cho, Showa-ku, Nagoya 466-8555, Japan
[2]Graduate School of Engin., Kyoto Inst. of Tech. Matsugasaki, Sakyo-ku, Nagoya 606-8585, Japan

1 Introduction

Microphase separated structures of block copolymer (BCP) thin films were extensively investigated by grazing incidence small angle X-ray scattering technique (GISAXS). Controlling the morphology and particularly the orientation behaviour of phase-separated structures in both thin and thick films has received considerable attention because of their potential nanofabrication application. In the thin film, surface-polymer interaction, confinement effect, and the film thickness are really important factor to give a morphology that is different from those in the bulk. In this report, solvent annealing method was applied to the thin film of ~ 500 nm in thickness (relatively thicker than usual film) and effect of initial morphology after spin-casting from common and selective solvents on equilibrium structure in the film will be reported.

2 Experiment

BCP Polystyrene (PS)-*b*-poly(4-hydroxy styrene) (PHS) was synthesized by anionic polymerization. Toluene and trahydrofuran (THF) were used for solvent of PS-*b*-PHS and annealing, respectively. Poly(ethyleneglycol) monometyl ether (PEG, M_n = 550) was blended in the solution. The mixture PS-*b*-PHS, PEG in toluene solution was spin-cast on a silicon wafer. After fully drying the thin film, the film was put in a chamber filled with THF vapor for solvent annealing. The structure in the thin film was analysed by GISAXS.

3 Results and Discussion

The microphase separated structure of PS-*b*-PHS / PEG blend thin film with thickness of 500 ~ 600 nm and solvent annealing effect on orientation behaviour of the structure in the thin film were investigated by grazing incidence small angle X-ray scattering (GISAXS). The toluene was selective solvent for PS and poor-solvent for PHS and PEG. In the toluene solution, the spherical microdomain was formed because of shrinking of the PHS/PEG domains. The equilibrium morphology of the block copolymer itself and the blend sample was confirmed to be a hexagonally packed cylinder in the bulk and thin film. After THF vapour annealing of the film for several minutes, the highly ordered and perpendicular oriented cylindrical structure was attained. Atomic force microscopic measurement revealed a hexagonal array in top of the surface. The perpendicular nano-channels were fabricated after removing PEG oligomer from the PHS/PEG cylindrical domains by washing with water. These were revealed by GISAXS (as shown in Figure 1) and AFM measurements. After removing PEG, the scattering intensity became considerably high. The increase in the GISAXS intensity was ascribed to removing PEG from cylinders and nano-holes were created in the film. One-dimensional profiles in the GISAXS patterns indicated *in-plane* scatterings at q_z ~ 0.35. These profiles are slightly different except for peak positions. The paracrysltalline distortion theory (hexagonally packed cylinder) revealed the detailed structure of cylinders. The structural parameters are summarized in Table 1. Before removing PEG, the contrast between PS matrix and PHS/PEG domain was seen. After removing PEG, the contrast between hole and the others was enhanced.

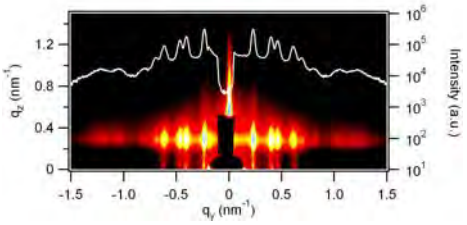

Fig. 1. GISAXS pattern of PS-*b*-PHS thin film having the hexagonally arrayed nano holes.

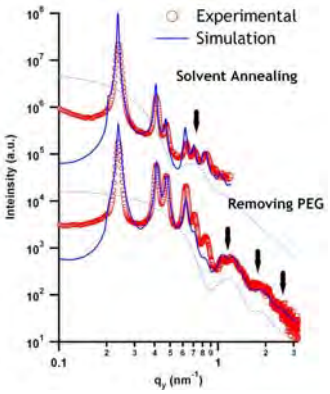

Fig. 2. *In-plane* GISAXS profiles before and after removing blended PEG components from the cylinders. Thick arrows indicate the form factor of cylinders (thin lines). The blue lines were simulated profiles.

Table 1: Structural Parameters of Cylinders

	d-spacing	Radius	$\phi_{cylinder}$
Solvent Ann.	26.7 nm	7.5 nm	21.5 %
Remv. PEG	26.7 nm	4.5 nm	7.5%

* yamamoto.katsuhiro@nitech.ac.jp

2011G064

塑性変形を受けた Fe-Si 合金多結晶体の粒内ひずみ分布
Transgranular strain distribution in Fe-Si polycrystal alloy with plastic deformation

菖蒲敬久 [1*], 城鮎美 [1,2], 新垣優 [3], 内藤大幹 [3], 羅紅岩 [3], 大工原森 [3], 友田陽 [3]
[1]（独）日本原子力研究開発機構、〒679-5148 兵庫県佐用郡佐用町光都 1-1-1
[2]徳島大学、〒770-8501 徳島県徳島市新蔵町 2-24
[3]茨城大学、〒316-8511 茨城県日立市中成沢町 4-12-1

1 はじめに

多結晶金属材料の塑性変形はほとんどの場合に転位の運動によって生じる。塑性変形が進むに伴って転位組織が形成され、内部応力分布が生じる。単結晶においても生じる転位セル壁とセル内部では転位密度が異なり応力が分配する（セル応力）。多結晶では結晶方位の相違によって塑性ひずみ量が異なり結晶粒単位で応力が分配する（粒応力）。さらに硬質粒子等があると、母相との間で塑性ひずみ差に起因して相応力が発生する。このような応力分配が重なりあってマクロな変形応力が決まっている。

本研究では、塑性変形に伴う局所内部応力分布の導出を目指し、多結晶体中の 1 結晶粒内ひずみ分布計測を行い、塑性変形前後でどのようなデータ差が生じるかを検討した。

2 実験

実験は BL4C で、ごく表面のみからの回折 X 線を計測するために Fe の吸収端より少し上のエネルギーである 8keV の高輝度な単色 X 線を使用した。

供試材は、Fe に Si を 0.75%添加した合金であり、熱処理したアニール材（無ひずみ）と 4%塑性変形させた 2 つを試験片とした。試験片のサイズは 10×10×1mm 程度であり、その試験片を回折計の φ ステージに取り付けた自動 xyz ステージに設置した。

Fig.1 にアニール材の写真と、電子線後方散乱回折法（EBSD）で測定した方位マッピングを示す。色は結晶方位を表しており、本試験片には mm オーダーの結晶粒が複数存在していることがわかる。測定は、アニール材については図 1 の四角い枠内のオレンジ部からの α Fe200 回折、4%塑性変形材については図では示していないが、同様に材料中のある結晶粒内からの α Fe200 回折を複数計測した。

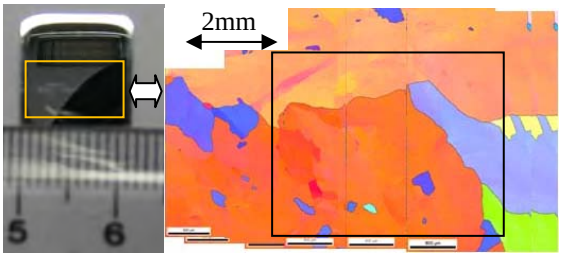

図 1 ：アニール材写真と EBSD.

3 結果

図 2 に、結晶粒内のいくつかの場所で測定したロッキングカーブを示す。どちらの図についても観測場所により角度、強度が異なっている。これは粒界はもたないが、局所的に結晶方位がわずかに異なっている、いわゆる亜粒界が存在しているためである。一方、2 つの図を比較すると、アニール材はロッキングカーブの幅が狭く、4%塑性変形材では幅が広いばかりでなく、その形も左右非対称でショルダーが存在している。これは塑性変形に伴う転位密度の増加やすべりにより、亜粒界よりもさらに小さいセル組織が発生し、各セルの結晶方位が細かく異なっているためであると考えられる。

図 3 に、2 つの材料の 1 結晶粒内の回折角分布を示す。黒い部分は観測できなかったところであり隣の結晶粒を表している。アニール材は緑一色であるのに対して、4%塑性変形材は粒界側に青色の領域が広がっている。これは隣り合う粒との粒間ひずみが発生しているためであると考えられる。

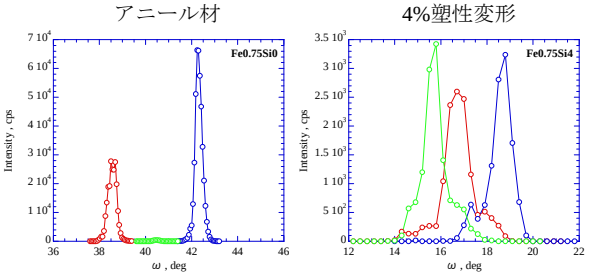

図 2 ：ロッキングカーブ.

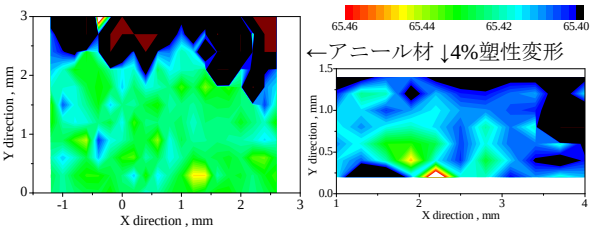

図 3 ：回折角分布

4 まとめ

本研究では、多結晶体中の 1 結晶粒内ひずみ分布計測を行い、塑性変形前後でロッキングカーブに大きな違い、および結晶粒内のひずみ分布に変化が現れることを明らかにした。今後、1 つの試験片で逐次変形させながら計測し、塑性変形と応力、転位などとの相関について検討していく予定である。

* shobu@spring8.or.jp

06A/2011G066

Dynamics of the Lamella-*Fddd* transition in SI diblock copolymer melts

Takashi Chijiwa[1], Myung Im KIM [1], Tsutomu WAKADA[1], Mikihito TAKENAKA[1*]
[1] Department of Polymer Chemistry, Graduate School of Engineering,
Kyoto University, Kyoto 615-8510 JAPAN

Introduction

Block copolymers that are composed of chemically different polymers connected by a covalent bond can self-assemble into various microstructures via microphase separation. Typically, the microstructures of block copolymer depend on several parameters such as the copolymer composition (f), the Flory-Huggins interaction parameter (χ), and the total number of the statistical segments (N). The phase behavior in block copolymers has also been studied extensively, both theoretically and experimentally [1]. Recently we reported a new bicontinuous microdomain morphology with the symmetry of *Fddd* space group found in a polystyrene-*block*-polyisoprene (SI) diblock copolymer with number–average molecular weight M_n = 2.67 x 10^4 g/mol, polydispersity index M_w/M_n =1.02, and volume fraction of polyisoprene f_{PI} = 0.629 [2]. In this study, we performed time-resolved SAXS experiments on the order-order transition (lamella-*Fddd*-gyroid) induced by temperature jump in SI diblock copolymer to investigate the ordering mechanism.

Experimental

We synthesized SI diblock copolymer with M_n = 2.68 x 10^4 g/mol, M_w/M_n=1.02 and f_{PI} = 0.641 via living anionic polymerization in benzene at 50˚C using *sec*-butyl lithium (Kanto Chemical Co.) as initiator. SI diblock copolymer were prepared by casting 5wt% toluene solution with 0.2 wt% Irganox and obtained by solvent casting at room temperature. Figure 1 shows the phase diagram of the IS diblock copolymer. Time-resolved SAXS experiments were performed at BL-06A in KEK, Japan by temperature jump of the sample. The X-ray wavelength and the sample-to-detector distance were, respectively, 0.154nm and 2000mm. Imaging plate was used as the detector.

Experimental

The temperature jump measurements were conducted by rapid heating SI diblock copolymer from 120˚C where we observed lamellar structure to 155˚C where we observed gyroid structures. Figure 2 shows the time-evolution of SAXS profiles after the T-jump from 140˚C to 150˚C. Before the T-jump to 150˚C, we found the peaks at q/q_m = 1, 2, and 3, where q_m is q at the first order peak, indicating that lamellar structure was formed. After the T-jump in 2000sec we found the peak at q/q_m =1, 1.22, thus, SI diblock copolymer transformed into *Fddd* structure. The time change in the peaks at 1.22 indicates that the L to *Fddd* transition may occurs via spinodal decomposition. Since there is no incubation time after temperature jump.

References

[1] A. K. Khandpur, et al. *Macromolecules* **1995**, *28*, 8796.
[2] M. Takenaka, et al. *Macromolecules* **2007**, *40*, 4399.
* takenaka@alloy.polym.kyoto-u.ac.jp

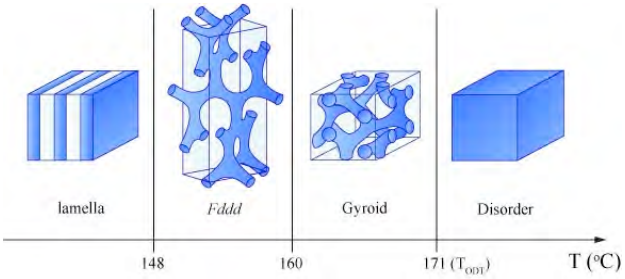

Figure 1. Phase diagram of the SI diblock copolymer.

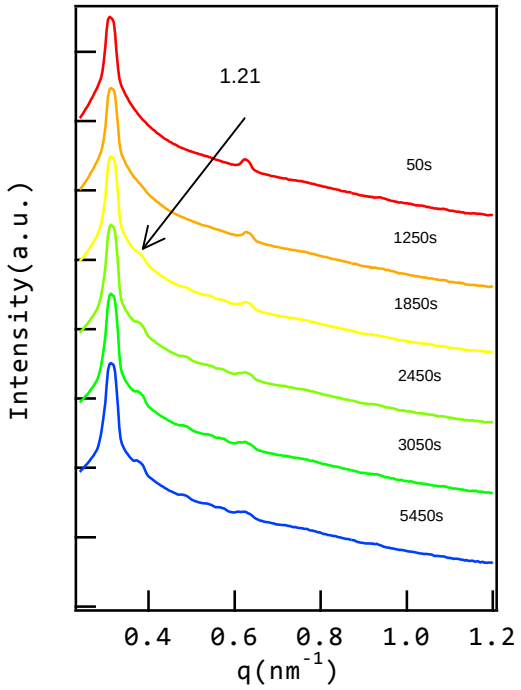

Figure 2 Time changes in the scattered intensity plotted as a function of q_m after T-jump from 140℃ to 150℃.

9A, NW10A/2011G069

XAFS による白金系ナノ粒子/炭素複合材料の化学状態評価と生成機構の解明
XAFS investigation of chemical states and formation mechanism in Pt-based nano-particle/carbon composites

中西真, 山下翔, 島本一弘, 藤井達生, 高田潤
岡山大学大学院自然科学研究科、〒700-8530 岡山市北区津島中 3-1-1

1 はじめに

固体高分子形燃料電池のアノード用触媒として Pt-Ru 合金ナノ粒子を炭素に担持させた複合材料（Pt-Ru/C）が用いられている。本研究グループにおいては、金属錯体高分子を経由して、直接炭素マトリックスの形成と合金ナノ粒子の生成を連続的に行う新規プロセス[1,2]の本系への適用を検討してきた。これまでに、作製した Pt-Ru/C の結晶構造、微細構造等を検討した結果、このプロセスで作製した Pt-Ru/C は熱分解後の時点では炭素マトリックスに Ru が高分散した Pt/C の状態であり、炭化処理を行うことによって Pt に炭素中の Ru が固溶していることが推測された。しかし、化学状態を含めた生成機構の全体像を把握することは困難であり、特にその合金化機構の詳細は明らかとなっていない。そこで、本研究では種々の炭化処理後の Pt-Ru/C において、Pt と Ru のそれぞれの化学状態を XAFS によって明らかにすることで、合金化機構に関する知見を得ることを目的とした。

2 実験

ジニトロジアンミン白金(II)（Pt-DNDA）、酢酸ルテニウム(III)、クエン酸、アンモニア水を出発原料として、混合後 80℃で 24 時間加熱撹拌を行い均一な錯体溶液を得た。続いてエチレングリコールを添加し、180℃で 20 時間の重縮合を行い、金属錯体高分子を得た。得られた金属錯体高分子を窒素気流中 300℃で 3 時間熱分解を行い、Pt-Ru/C 前駆体を得た。さらに、前駆体を窒素気流中 500～1000℃で 1 時間炭化を行い合金化を進行させ、Pt-Ru/C を得た。

種々の炭化条件で得られた Pt-Ru/C 粉末を BN と混合しペレット成型したものを試験片とし、9A および NW10A において、透過法により Pt-L_{III} および Ru-*K* 端の XAFS 測定を行った。

3 結果および考察

図 1 に標準試料、Pt-Ru/C 前駆体および種々の温度で炭化処理をして得られた Pt-Ru/C の Pt-L_{III} 端および Ru-K 端の XANES スペクトルを示す。Pt では炭化温度 800℃以上で吸収端が高エネルギー側にシフトし、Ru では同じ炭化温度 800℃以上で低エネルギー側へとシフトする振る舞いが確認できた。

吸収端エネルギーが価数と直線関係にあると仮定して、標準試料の吸収端を基に吸収端エネルギーから平均価数を見積もった。その結果、炭化温度が 800℃以上になると、Pt の平均価数は 0 価に近い状態から 2 価側へと増加し、一方 Ru の平均価数は 3 価側から 0 価側へと減少することが明らかとなった。

これまでの知見と合わせると、前駆体および低温側では炭素マトリックスに Ru がイオン化した状態で高分散した Pt/C の状態であり、温度を上げることで炭素中の Ru の還元と Pt への合金化が進行することを示唆している。また、高温では一部の Pt が炭素マトリックスへ拡散していることが確認されていたが、これが Pt のイオン化によって起こっていることも示唆された。

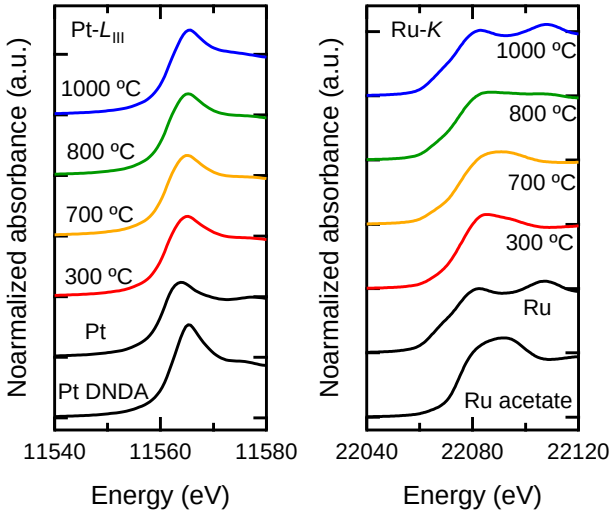

図 1 ：標準試料と種々の温度で炭化した Pt-Ru/C の Pt-L_{III} 端および Ru-*K* 端 XANES スペクトル

4 まとめ

Pt-Ru/C の Pt-LIII 端および Ru-K 端の XAFS 測定により、プロセス中の Pt および Ru の化学状態変化が明らかとなり、本系での Pt-Ru 合金ナノ粒子の合金化機構に関するモデルが得られた。

参考文献

[1] 中西 他, 炭素 **228** (2007) 158.
[2] 内田 他, 粉体および粉末冶金 **52** (2005) 640.

* mnaka@okayama-u.ac.jp

15B1, 15C/2011G073

X線デジタルトポグラフィによる 鶏卵白リゾチーム結晶の局所的ロッキングカーブの解析 Analysis of Local Rocking Curves of Hen Egg-white Lysozyme Crystals by X-ray Digital Topography with CCD Camera

藤居大毅[1]、若生啓[2]、塚島史朗[1]、
小島謙一[1,2]、橘勝[1※]
[1]横浜市立大学　〒236-0027　神奈川県横浜市瀬戸 22－2
[2]横浜創英大学　〒226-0015　神奈川県横浜市緑区 三保町 1 番地

Introduction

これまでタンパク質結晶の完全性の評価は、ロッキングカーブの測定や X 線トポグラフィによって行われてきた。我々はこれまで X 線トポグラフィによる結晶欠陥、特に転位の観察およびキャラクタリゼーションを行ってきた[1]。より詳細な完全性や結晶欠陥の評価を行うためには、同じ結晶にて X 線トポグラフィとロッキングカーブ測定の両方を行う必要がある。

最近では高分解能 X 線 CCD カメラを用いることにより解像度の高いデジタルトポグラフ図の取得に成功している。CCD カメラを用いることにより角度情報を含んだロッキングカーブ測定を行なうことができる。加えて、CCD カメラで撮影するための露光時間は短く、放射損傷を受けやすいタンパク質結晶において CCD カメラによるトポグラフ図の取得は効果的な方法である。この報告書では X 線デジタルトポグラフィによるタンパク質結晶の完全性の評価を報告する。

Experiments

塩化ニッケル濃度勾配法で育成した正方晶卵白リゾチーム結晶がサンプルに用いられた。

X 線デジタルトポグラフィは BL15B1 と BL15C で行なわれた。また、ビームにはモノクロメーターで単色化された波長 1.2Åの単色 X 線を用いた。サンプルである正方晶リゾチーム結晶は、単色 X 線がサンプルの(001)面にほぼ垂直に入射するよう設置した。トポグラフ図は高解像度 X 線 CCD カメラ(Photonic Science XFDJ)によって取得した。また CCD カメラ - サンプル間距離は 25cm であった。

100 枚程度の連続したデジタルトポグラフ像は当グループのプログラムによってロッキングカーブのピーク解析が行われた[2]。

Result＆Discussion

結晶における完全領域と転位領域でのロッキングカーブの形状に大きな違いがあらわれた。

一般に無機結晶では、転位領域のロッキングカーブの形状は完全領域に比べて、その強度が増加するだけでなく、その半値幅も増加する（Fig.1 参照）。したがって、結晶の完全性や欠陥の評価には半値幅を利用することもできる。一方、タンパク質結晶では、転位領域のロッキングカーブの形状が無機結晶の場合とは大きく異なることがわかった。

タンパク質結晶では、その強度や半値幅が完全領域とほぼ同じ 1.8×10^{-3} degree の値を示した。ところが、10 分の 1 幅に注目してみると、完全領域が 2.7×10^{-3} degree、転位領域は 5.1×10^{-3} degree の値を示し、その差に大きな違いがみられた。つまり、タンパク質結晶では、10 分の 1 幅にのみで転位領域と完全領域の違いが観察されるのである。これはタンパク質結晶の大きな格子定数あるいは分子形状による転位周辺の歪み場が無機結晶よりも大きく、緩やかに歪んだ結果であると考えられる。

タンパク質結晶の完全性評価においては半値幅に加えて、10 分の 1 幅による評価が行われている。この 10 分の 1 幅は、転位の分布状態の評価にも有効であることが提案される。

Reference

[1] T. Sawaura *et al.*, J. Crystal Growth **318**, 1071 (2011).
[2] K. Wako *et al.* (to be submitted).

※ tachiban@yokohama-cu.ac.jp

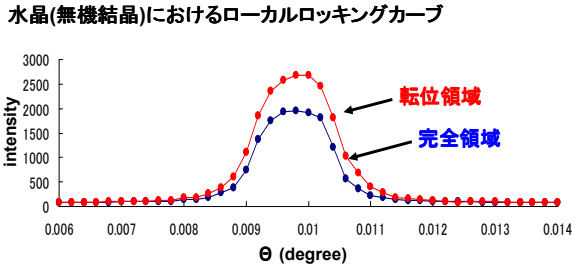

Fig.1　水晶におけるローカルロッキングカーブ

27B/2011G103

Study on Ion Beam Induced Non Thermal-Equilibrium Lattice Structures in FeRh Alloy by EXAFS Measurement

Akihiro Iwase[1,*] Shinya Kosugi[1], Nao. Fujita[1], Toshiyuki Matsui[1] , Yuichi Saitoh[2] and Yoshihiro Okamoto[3]

[1]Osaka Prefecture University, Sakai, Osaka, 599-8531, Japan

[2]Japan Atomic Energy Agency, Takasaki, Gunma, 370-1207, Japan

3 Japan Atomic Energy Agency, Tokai, Ibaraki, 319-1195, Japan

1 Introduction

Fe-Rh intermetallic compound shows the B2 (CsCl type) lattice structure at room temperature. Above 1300K, its lattice structure changes from B2 to A1 structure (the FCC structure with randomly distributed Fe and Rh atoms). Recently, we have found from the EXAFS and x ray diffraction (XRD) measurements that energetic ion irradiation induces A1 structure in FeRh alloy even at room temperature. In this report, we show the EXAFS spectrum for ion-irradiated FeRh, which clearly shows the A1 structure.

2 Experiment

Specimens used in the experiment were bulk Fe-50%Rh alloy specimens and thin films of Fe-53%Rh. The former specimens were cut into sheets of 5x5x0.2mm^3 from an ingot and the latter ones were synthesized by using an ion sputtering method. The thickness of the thin films was about 100 nm. These specimens were irradiated with 10 MeV iodine ions at Japan Atomic Energy Agency-Takasaki. Before and after the irradiation, the lattice structure of the specimens was estimated by means of XRD. The local atomic arrangement around Fe ions were studied by means of the extended x-ray absorption fine structure (EXAFS) at BL27B of KEK synchrotron radiation facility.

3 Results and Discussion

Figure 1 shows the FT-EXAFS spectra for unirradiated and irradiated FeRh thin films. The x-ray energy was near 7.1 keV (Fe K-absorption edge). Before the irradiation, a large peak is observed, which corresponds to nearest Rh atoms around Fe atom. The spectrum fitting by the computer code, FEFF shows that the lattice structure of the FeRh specimen is definitely the B2 structure, which is the thermal-equilibrium state at room temperature. After the irradiation with 10MeV iodine ions to the fluence of 1x10^{14}/cm^2, the main peak splits into two peaks. This result suggests that Fe and Rh atoms are randomly located around Fe atoms. The FEFF simulation shows that this FT-EXAFS spectrum corresponds to the A1 lattice structure. Under the thermal equilibrium condition, the A1 structure appears only above 1300C. The present experimental result shows that non thermal-equilibrium lattice structure is induced by energetic ion irradiation. Such a structure can hardly be realized by a conventional rapid–quenching procedure. We have also shown that the ion irradiation induced structural change is accompanied by the change in magnetic properties. The details have been published elsewhere[1,2].

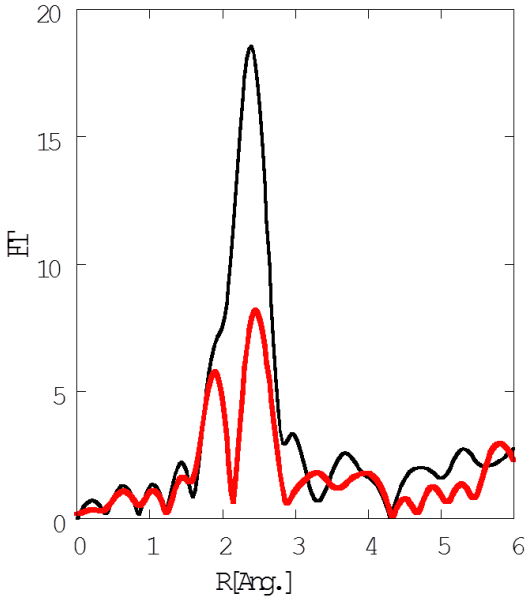

Fig. 1: EXAFS –FT spectra for unirradiated FeRh film (black) and that for FeRh film irradiated with 10 MeV iodine ions(red).

Acknowledgement

This research has been performed under the collaboration program between Osaka Prefecture University and Japan Atomic Energy Agency.

References

[1] S. Kosugi *et al.*, Nucl. Instr. Meth. **B269** (2011) 869-872

[2] Nao. Fujita *et al.*, J. Appl. Phys. 107(2010) 09E302.

* iwase@mtr.osakafu-u.ac.jp

7C /2011G110

XANES Analysis of Layered Titanate Nanosheets with lamellar mesostructure

Keizo NAKAGAWA*[1,2], Kazuki YAMAGUCHI[2], Keiji YAMADA[2],
Shigeru SUGIYAMA[1,2], Toshihiro MORIGA[1,2]
[1]Department of Advanced Materials, Institute of Technology and Science, The University of Tokushima, 2-1 Minamijosanjimacho, Tokushima 770-8506, Japan
[2]Department of Chemical Science and Technology, The University of Tokushima, 2-1 Minamijosanjimacho, Tokushima 770-8506, Japan

1 Introduction

Two-dimensional metal oxide nanosheets have attracted much attention because of their unique physical and chemical properties. We have developed layered titanate nanosheets with lamellar mesostructure using the lamellar phase of 1,12-dodecanediamine (DDA) self-assembly as a template and these nanosheets were applied to visible light photocatalysts [1]. However, it is difficult to investigate their structure because of the two dimensional nanostructure. Some research groups have reported the effective structural analysis using XAFS spectra toward the TiO_2-derived nanostructures [2]. In this study, XANES measurements were performed to investigate the local structure of layered titanate nanosheets with lamellar mesostructure.

2 Experiment

The synthesis process of layered titanate nanosheets have been reported in literature [1]. Tetraisopropyl orthotitanate (TIPT) was mixed with triethanolamine (TEOA) to form a Ti(IV) compound. A DDA aqueous solution was added to the Ti(IV) stock solution and aged at 373 K for 24 h and kept at 413 K for 96 h. The obtained products were washed with distilled water and ethanol and then dried at 333 K in air. The obtained sample was denoted Ti+DDA+TEOA. TIPT mixed with DDA or TEOA were synthesized to examine the role of DDA or TEOA molecules for the nanosheets formation and they were denoted Ti+DDA and Ti+TEOA, respectively. X-ray absorption spectra were measured at the Photon Factory for High Energy Accelerator Research Organization. Ti K-edge XANES measurements were performed at the beam line BL-7C equipped with Si(111) in a transmission mode at room temperature.

3 Results and Discussion

Layered titanate nanosheets with a lamellar mesostructure were obtained for the synthesis condition of Ti+DDA+TEOA. The XANES spectra of the obtained samples, anatase-type TiO_2 and Na_2TiO_3 are compared as shown in Fig.1. All the spectra exhibit a pre-edge feature consisting of multiple peaks (4964-4974 eV) (Fig.1b), which was followed by white line peaks (4983-5003 eV) (inset in Fig.1a). The pre-edge multiple peaks can be assigned to forbidden transitions from the core 1s level to unoccupied 3d state of a Ti(IV). According to the position of edge energy and the presence of pre-edge, it was considered that Ti ions in the layered nanosheets were mainly present as Ti(IV). In the pre-edge of the Ti K XANES for Ti+DDA+TEOA and Ti+DDA, relative intensity of peak B was higher compared with anatase and Ti+TEOA, and the peak feature was similar to titanate such as $Na_2Ti_3O_7$. However, the intensity profiles of peak C were notably different for Ti+DDA+TEOA and $Na_2Ti_3O_7$ (Fig.1b). The white line region in the XANES features arises from dipole-allowed transitions from the core 1s to unoccupied 4p states (inset in Fig.1a). Two excitation peaks (E and F) were observed for $Na_2Ti_3O_7$. In contrast, the peak feature of Ti+DDA+TEOA was different from that of $Na_2Ti_3O_7$ and was very similar to that of lepidocrocite shown in the previous paper [2]. Thus, XAFS spectra imply that the local structure of Ti+DDA+TEOA might be closer to that of lepidocrocite titanate than $Na_2Ti_3O_7$.

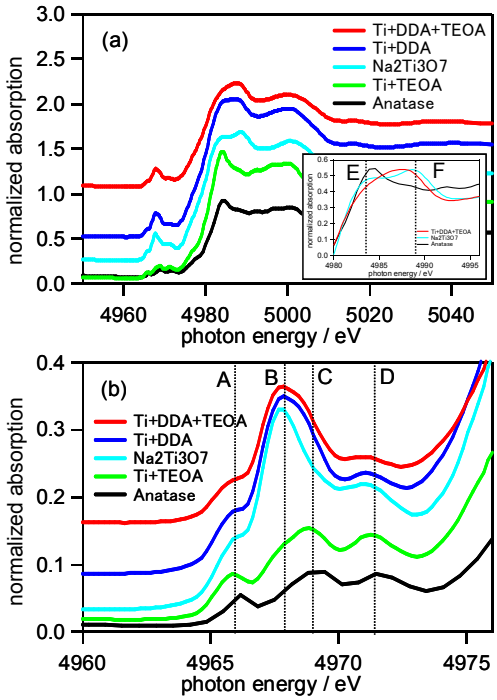

Fig. 1. (a) Ti K edge XANES spectra, inset: enlarged white line regions, (b) enlarged pre-edge regions of layered titanate nanosheets in comparison with other samples.

References

[1] K. Nakagawa *et al*., Eur. J. Inorg. Chem. 2012 (2012) 2741.
[2] R. Ma *et al*., J. Phys. Chem. B 109 (2005) 6210, T. Kubo *et al*., J. Phys. Chem. C 112 (2008) 1658.

* knakagaw@chem.tokushima-u.ac.jp

27B/2010G118

XAFS measurement of Sm-doped TiO_2 semiconductor thin films

S. Harako[1)], J. Sakurai[1)], T. Otsuki[1)], N.Hirao[2)] and X. Zhao[1)]
[1)] Advanced Device Laboratories and Department of Physics, Tokyo University of Science, 1-3 Kagurazaka, Shinjuku-ku, Tokyo 162-8601, Japan,
[2)] Japan Atomic Energy Agency, Naka, Ibaraki 319 1195, Japan

Introduction

Host semiconductors with wide band gap are generally known to excite the rare earth (RE) ion effectively, resulting in intense luminescence. TiO_2 is an attractive semiconductor for RE activation with a direct wide band gap (3.0-3.2eV). Furthermore, as described in this study, a TiO_2 crystal phase can be changed by post annealing temperature condition. In this work, we report the association between the photoluminescence property and local structure of Sm^{3+} ion in TiO_2. It was demonstrated by X-ray absorption fine structure (XAFS) measurements that the local structure of the Sm^{3+} ions played an important role in forming effective luminescent centers.

Experimental

The Sm-doped TiO_2 (TiO_2:Sm) thin films were deposited by laser ablating a TiO_2 ceramic target including 1.0 wt% Sm_2O_3. A Q-switched YAG laser ($4\omega_0$=266 nm, 1 J/cm^2) was used to ablate the target in a vacuum chamber in the O_2 pressure of 1 x 10 $^{-2}$ Torr. The TiO_2:Sm thin films of 300 nm thick was formed on the Si(100) surface at room temperature. After the deposition, the samples were annealed at 700 ^{o}C, 900 ^{o}C, 1000 ^{o}C, and 1100 ^{o}C for 2 min in the O_2 atmosphere for optical activation of Sm. Detailed microstructure characterization was performed by X-ray absorption fine structure (XAFS) in the fluorescence yield mode at the BL-27B beamline of the Photon Factory synchrotron facility (KEK, Tsukuba, Japan) at the total ion beam current amounted to 400 mA, was monochromatic using a Si(111) double-crystal monochromator. Each sample was placed at a 45° angle to the incident X-ray beam and fluorescence yield was monitored using a 7-element Ge SSD.

Result and Discussion

Figure 1 shows the PL spectra of the Sm^{3+} ions in TiO_2 thin films at room temperature, indicating the optical activation of Sm in TiO_2. Four emission bands peaking at 582, 611, 662 and 725 nm originating from the $^4G_{5/2}\rightarrow{}^6H_{J/2}$ (J = 5, 7, 9 and 11) transitions in Sm^{3+} ions were observed. The PL spectra for the sample annealed at 1100^{o}C, which showed Rutile-TiO_2 crystal phase, did not exhibit detectable Sm^{3+}-related emission. Figure 2 shows the radial structural function (RSF) around Sm, derived from the Fourier transform of XAFS spectra. The data window was chosen as the radius range from 1.1Å to 3.0Å, as shown by the slash lines in Fig.2. In this RSF, these small radii indicated the first nearest-neighbor atoms from Sm are O, and Sm-O distance of the sample annealed at 700^{o}C is the shortest one within these samples.

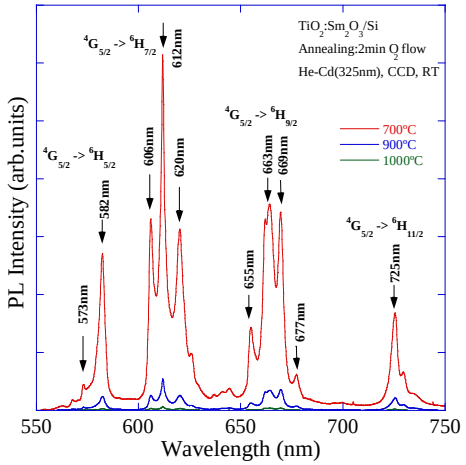

Fig1. PL spectra of Sm^{3+} ions in Anatase-TiO_2 thin films at room temperature.

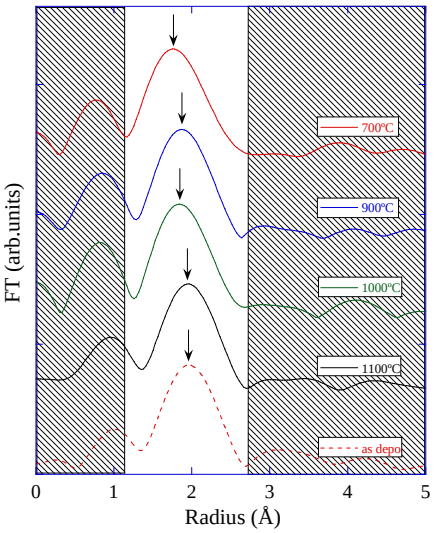

Fig2. Radial structural function around Sm of Sm-doped TiO_2 thin films.

References

[1] F.Jing, S.Harako, S.Komuro, X.Zhao. J. Phys. D: Appl. Phys. 42 (2009) 085109 (7pp)
[2] M.Ishii, S.Komuro, T.Morikawa. J. Appl. Phys. **94** (2003) 3823
* atom@rs.kagu.tus.ac.jp

6A & 9C /2011G-123

SAXS and WAXS Studies on Guest Exchange Processes in Crystalline Complexes of Syndiotactic Polystyrene

Fumitoshi Kaneko[1,*] and Keita Sasaki
[1]Graduate School of Science, Osaka University, Toyonaka, 560-0041, Japan

1 Introduction

Syndiotactic polystyrene (sPS) is a relatively new commodity polymer, which exhibits a variety of solid states. One of the important properties of sPS is the formation of co-crystal structures, where organic compounds are stored as guests in the cavities formed between polymer sheets consisting of sPS helices with TTGG conformation, as shown in Figure 1. It has been clarified that a wide range of chemical compounds including functional molecules can be incorporated into sPS lattice, for examples, crown ethers, organic radicals, fluorescent and dye molecules, and even polymeric molecules. The orientation of the guest compound can be adjusted by controlling the arrangement of the crystallites of the clathrate phase. Now sPS crystalline complexes are regarded as of high potential for polymer based composite materials.

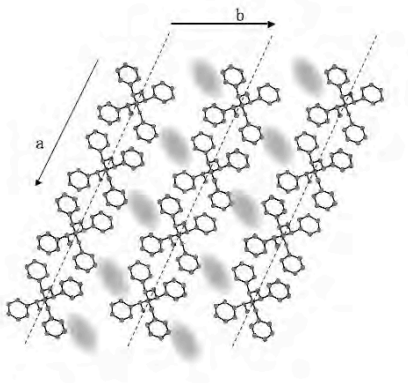

Fig. 1. Crystal structure of sPS complex.

The guest molecules in the sPS complexes can be replaced smoothly by exposing to a vapor or a liquid of another kind of molecule. The guest exchange method has an advantage that enables sPS to form crystalline complexes even with chemical compounds that are difficult to incorporate into the crystalline region by usual solution-cast and solvent-induced crystallization methods.

In order to obtain information how old guests are replaced with new ones, we tried to follow the guest exchange process from chloroform to triethyleneglycol dimethyl ether (TEGDME) by simultaneous WAXS and SAXS measurements.

2 Experiment

sPS was provided by Idemitsu Bussan Corp. In order to measure clear lamellar reflections in a well defined area, 4-5 times uniaxially drawn films about 50 μm thick were prepared. sPS/chloroform complex samples were prepared by exposing the films to Chloroform vapor.

Time resolved SAXS and WAXS measurements were carried out at BL-6A and BL 9C by using an imaging plate for WAXS and a CCD camera system for SAXS measurements.

The guest exchange process was initiated by injecting TEGDME into a glass capillary containing several pieces of sPS/chloroform complex film.

3 Results and Discussion

Figure 2 shows the changes in SAXS profile during guest exchange. The reflection corresponding to the lamellar repeat distance clearly shifts to a lower angle after a 3-hour latent period from the inception of the guest exchange, which indicates that the lamellar spacings are expanded during the course of the guest exchange.

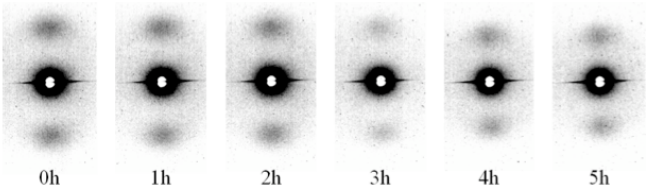

Fig. 2. Changes in SAXS profiles during sPS guest exchange process.

It has been found that the length of the latent period significantly depends on the sample condition as shown in Figure 3. Sample A, which was well dried after the complexation by chloroform, exhibits a long latent time, whereas Sample B, which was subjected to the guest exchange procedure just after the complexation with chloroform, immediately starts the lamellar expansion.

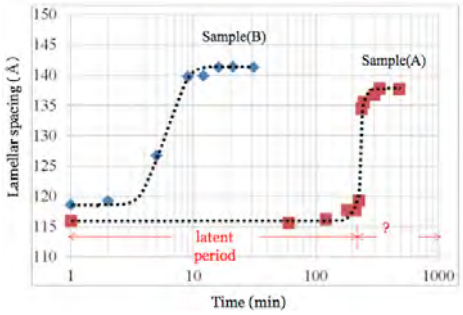

Figure 3. Time dependence of lamellar spacing.

* toshi@chem.sci.osaka-u.ac.jp

6A/2011G130

Photoresponse of Microphase Separation Structure for Liquid Crystalline Block Copolymers with Azobenzene Mesogens

Hiroki Takeshita[1,*], Tomoya Fujise[1], Kazuhiro Haginoya[1], Masamitsu Miya[1], Katsuhiko Takenaka[1] and Tomoo Shiomi[1]
[1]Nagaoka University of Technology, Nagaoka, Niigata 940-2188, Japan

1 Introduction

Liquid crystalline polymers having an azobenzene moiety in the side chain show a liquid crystalline/isotropic (LC/Iso) phase transition caused by tran-cis photoisomerization triggered by UV irradiation. Therefore LC block copolymers with azobenzene mesogens can change reversibly the spacing or morphology of the microphase separation (MS) by the UV-induced LC/Iso transition. In this paper, we will present responsiveness of the MS structure to the LC/Iso transition induced by photoisomerization for the block copolymer composed of azobenzene-type liquid crystalline (PAzo) and rubbery poly(*n*-butyl acrylate) (PBA) blocks.

2 Experiment

Block copolymers shown in Fig. 1 were synthesized by atomic transfer radical polymerization. The molecular weights of PBA(xx)-P06Azo(yy) are xx and yy thousands, respectively. SAXS experiments were carried out at BL-6A and BL40B2 (Priority Program for Disaster-Affected Quantum Beam Facilities) at Spring8. DSC and polarized optical microscopy (POM) were also used.

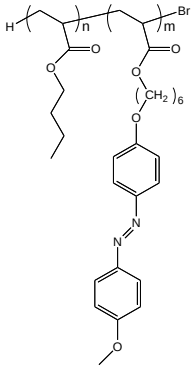

Fig. 1 Chemical Structure of the Block copolymer.

3 Results and Discussion

As shown in Fig. 2, the SAXS peak due to the smectic (Sm) LC structure appears and disappears at UV-off and –on, respectively, for the PAzo homopolymer. This LC transition is reversible in the repeat of UV-on/off. An LC texture observed by POM also disappears at UV-on.

Fig. 3 shows SAXS profiles for block copolymers at 80°C. The MS structures can be assigned from the ratio of the position of the peaks to be lamellar for Azo07, PAzo-cylindrical for Azo05 and PBA-cylindrical for Azo17. As shown in Fig. 4, the peak position q_m responds reversibly to UV-on/off. Fig. 4 also shows the required time for the change is 20-30 sec. The spacing of the MS structure is larger at UV-off, i.e., in the liquid crystalline state, as we reported previously in the thermotropic liquid crystallization [1-2]. This may be caused by the expansion of the main chain toward the microdomain interface.

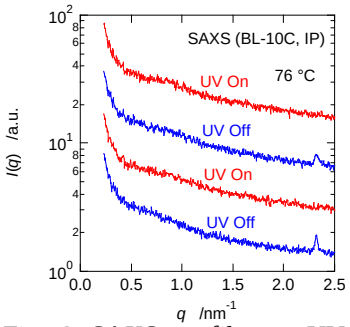

Fig. 2 SAXS profiles at UV-on/off for LC homopolymer.

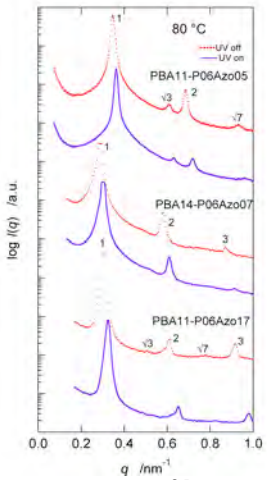

Fig. 3 SAXS profiles at UV-on/off for block copolymers.

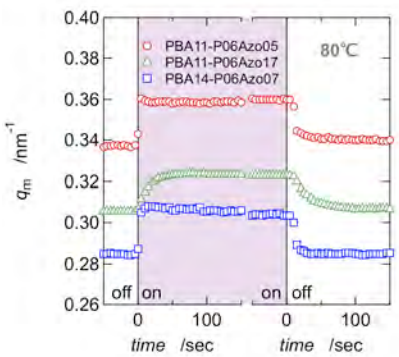

Fig. 4 The change of the MS peak position in UV-on/off for block copolymers.

Acknowledgment

The SAXS experiments were partially performed under the Priority Program for Disaster-Affected Quantum Beam Facilities (2011A1962).

References

[1] H. Takeshita et al., Polymer **50** (2009) 271.
[2] S. Taniguchi et al., Polymer **49** (2008) 4889.

* takeshita@mst.nagaokaut.ac.jp

SPring-8 BL19B2/2011G140(2011A1939)

Temperature Variations of Lattice Constants for Trigonal Tellurium

H. Ikemoto, and R. Sugibayashi
Faculty of Science, University of Toyama, Gofuku 3190, Toyama 930-8555, Japan

1 Introduction

Trigonal tellurium (t-Te) has a chain structure with two-fold coordinated covalent bonds. The lone-pair orbitals overlap with the antibonding orbitals in adjacent chain. The overlapping between lone-pair and antibonding orbitals in adjacent chain brings about interchain interactions and forms the trigonal structure. The overlapping weakens the covalent bonds and elongates the length of covalent bonds. Tellurium is a characteristic element, because it has a hierarchic structure.

Selenium which is congener element with tellurium has a unique temperature variations of lattice constants[1]. While the lattice constant of a-axis increases with temperature, the lattice constant of c-axis is nearly constant. We report the temperature variations of the lattice constants of t-Te in this report.

2 Experiment

A bulk of t-Te was crashed in argon gas circumstance for preventing oxidization. The powder was filled in the glass capillary with a diameter of 0.3 mm. The X-ray diffraction (XRD) measurements were done at BL19B2 of SPring-8 as Priority Program for Disaster-Affected Quantum Beam Facilities. The X-ray energy used for the XRD measurements was 12.40keV. The lattice parameters were obtained by using CellCalc[2].

3 Results and Discussion

Figure 1 shows the temperature variations of the lattice constant of a-axis. The length monotonically increases with the temperature as other materials. Figure 2 shows the temperature variations of the lattice constant of c-axis. The length of c-axis slightly decreases with temperature, which is different from other materials. In the case of t-Se the lattice constant of c-axis is nearly constant.

These results implies that the thermal expansion of t-Te is attributed to the elongation of a-axis. The length of a-axis is close relation with the interchain interactions, while that of c-axis is related to the chain which is a primary structure. The interchain interactions are influenced more than that of the intrachain interactions by the temperature. The expansion of the distance of the inter chains brings about the decreasing of the overlapping between the LP and anti bonding orbitals. The decrease induces the strengthening of the covalent bond, which causes the shortening of the lattice parameter of c-axis.

Compared to the case of Se, tendency of the value of a-axis is similar while that of c-axis is different. The interchain interactions of t-Te is stronger than that of t-Se, so the expansion of a-axis induces the strengthening of the covalent bond, which brings about the shortening of c-axis.

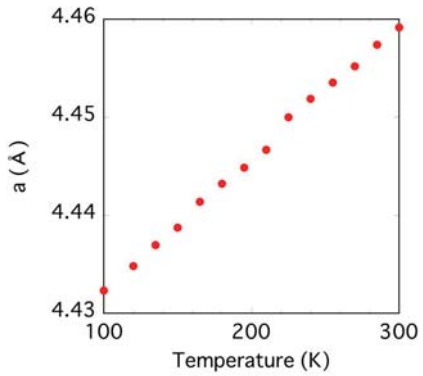

Fig. 1: The lattice constants of a-axis for the trigonal tellurium.

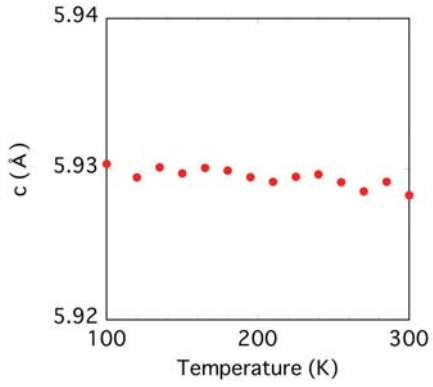

Fig. 2: The lattice constants of c-axis for the trigonal tellurium.

References

[1] Y, H, Zhao, K. Zhang, and K. Lu, Phys. Rev. B, 56 (1997) 14322
[2] http://homepage2.nifty.com/ hsc/soft/cellcalc.html

* ikemoto@sci.u-toyama.ac.jp

7C/2011G151

Study on the Crystal and Electronic Structures of the Layered Li_2MO_3-$LiMO_2$ Materials in Li de-intercalation process

Hironori Kobayashi[1,2], Masahiro Shikano[1], Hiroyuki Kageyama[1], Yuki Takenaka[2], Yoshinori Arachi[2], and Hiroaki Nitani[3]

[1] Research Institute for Ubiquitous Energy Devices, AIST, Ikeda, Osaka, 563-8577 Japan

[2] Department of Chemistry and Materials Engineering, Faculty of Chemistry, Materials and Bioengineering, Kansai University, Suita, Osaka, 564-8680 Japan

[3]Institute of Materials Structure Science, KEK, Tsukuba, 305-0801 Japan

1 Introduction

The layered Li_2MO_3-$LiMO_2$ materials are one of the promising positive electrode materials of lithium secondary battery because of their large capacity when operated above 4.6 V [1]. In this system, especially, $Li[Ni_{0.17}Li_{0.2}Co_{0.07}Mn_{0.56}]O_2$ displays a initial discharge capacity of c.a. 280 mAh/g in the voltage range of 2.5 to 4.8 V and keep a reversible capacity of c.a. 250 mAh/g after 50 cycles [2]. Several papers have reported on the mechanism why these materials show large reversible capacity. However, the initial charge and discharge process are still ambiguous. We have reported on the characteristic structural change during Li de-intercalation for $LiNi_{1/2}Mn_{1/2}O_2$ [3-4] using synchrotron radiation. Detailed information on the crystal and electronic structures above 4.6 V is very important in order to improve the calendar life and thermal stability of these materials and, therefore, the structural and electronic changes of $Li_{1.20}Ni_{0.17}Co_{0.10}Mn_{0.53}O_2$ (sample A) and $Li_{1.01}Ni_{0.49}Co_{0.21}Mn_{0.29}O_2$ (sample B) in Li de-intercalation process were studied in this paper.

2 Experiment

The de-lithiated $Li_{1.20-y}Ni_{0.17}Co_{0.10}Mn_{0.53}O_2$ (samples A-series) and $Li_{1.01-y}Ni_{0.49}Co_{0.21}Mn_{0.29}O_2$ (samples B-series) were electrochemically prepared using coin-type cells with Li/1M $LiPF_6$ in EC:DMC(1:2)/samples. Crystal and electronic structures were investigated by synchrotron XAFS (BL7C at PF) measurements. The bondlength were determined using the analysis programs REX2000.

3 Results and Discussion

Figure 1 shows the 1st charge and discharge curves of samples A and B in the voltage range of 2.0 and 4.8 V. The Li/sample A cell showed the 1st charge capacity of 282 mAh/g and gave the characteristic plateau region around 4.5 V. Figure 2 shows the Ni K-edge XANES Spectra of samples A-series and B-series with Li de-intercalation. For samples A-series, Ni K-edge XANES spectra shift to higher energy up to y=0.4-0.6 and then shift to lower energy up to y=0.93. This means that the valence state of Ni increased to 4+ and then decreased with Li de-intercalation. For samples B-series, Ni K-edge XANES spectra display continuous shifts to y=0.88. This means that the valence state of Ni increased to 4+ with Li de-intercalation. These results indicated that Li de-intercalated mechanism is different between samples A and B.

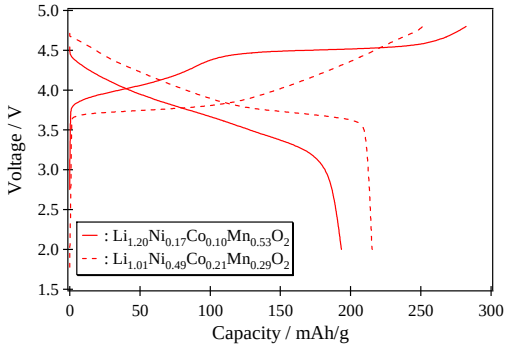

Fig. 1:1st charge and discharge curves for samples A and B.

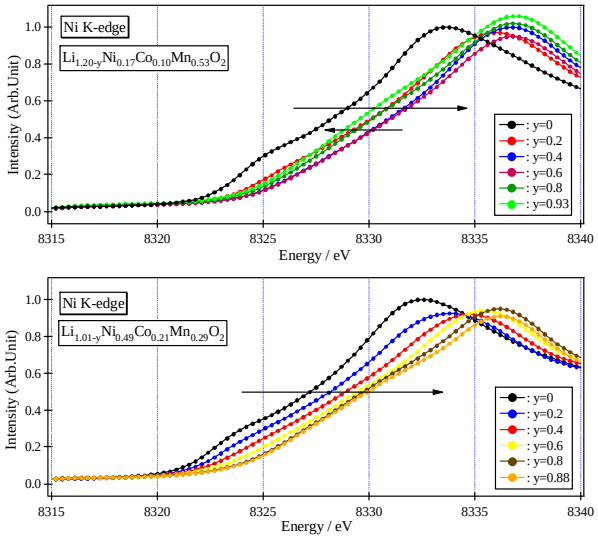

Fig. 2:Ni K-edge XANES Spectra of samples A-series and B-series.

References

[1] A. Ito *et al*, *J. Power Sources*, **183** (2008) 344.
[2] A. Ito *et al*, *J. Power Sources*, **195** (2010) 567.
[3] Y. Arachi *et al*, *Solid State Ionics*, **176** (2005) 895.
[4] H. Kobayashi *et al*, *J. Power Sources*, **146** (2005) 640.

BL-6C / 2011G157

TRIP 鋼の変形下での相応力・ひずみ解析
Evaluation of phase stresses and phase strains under deformation in TRIP steels

菊地　拓哉、熊谷　正芳、今福　宗行
東京都市大学工学部、〒158-8557 東京都世田谷区玉堤 1-28-1

1. はじめに

近年，環境問題に関する意識向上と安全性の観点から，自動車用鋼材の軽量化や高強度化が求められている．従来の鉄鋼材料は，優れた材料特性，経済性，リサイクル性などの理由により広く使用されてきたが，現在では，車体軽量化を目的として，アルミ合金や樹脂材料を使用することが多くなっている．しかし，鉄鋼材料にも材料特性の向上と経済性の面で注目されている高張力鋼板（ハイテン：High Tensile Strength Steel Sheets）がある．その中でも特に変態誘起塑性を利用した TRIP 鋼(Transformation Induced Plasticity Steels)は，高い加工性を持つだけでなく，衝突時の衝撃吸収性が大きいという特徴があり，車体のフロントサイドメンバなどに使用されている．

TRIP 鋼は，ベイナイトあるいはフェライトーベイナイト母相中に，変形によりマルテンサイトに変態するオーステナイトを残留させた鋼である．残留させたオーステナイトに塑性変形を与えると，変形とともにマルテンサイトが生成するというひずみ誘起変態を引き起こす変態誘起塑性を備えている．本研究では変態誘起塑性における力学的特性を評価するために放射光、ラボ X 線回折を用いて各相の引張変形に伴う残留応力の変化を測定する。

2. 実験・解析方法

試験片は、Fe-0.2C-1.5Mn-1.5Si の高強度低合金 TRIP 鋼板である。これに引張試験により公称ひずみを 0、3、6、10 %を与えた。放射光実験は、高エネルギー加速器研究機構 BL-6C を利用し、エネルギーは 6.5keV で測定を行った。ラボ X 線の実験は、自作の X 線応力測定装置を用いた。X 線管球は Cr を使用し、Cr-kα 特性 X 線を利用した。回折面は放射光、ラボ X 線ともにαFe-211 面である。また、ラボ X 線の実験では、こうしょうひずみ 0、3 %試料についてγFe-220 面の測定も行った。

3. 結果および考察

（1） 放射光、ラボ X 線でのα相とγ相の残留応力測定結果を図 1 に示す。放射光、ラボ X 線の実験結果ともに傾向は一致している。また、引張変形に伴いα相では圧縮残留応力が、γ相では引張残留応力が増大していることがわかる。

（2） 放射光、ラボ X 線でのα、γ相の半価幅を図 2 に示す。これらの図より、α相では圧縮残留応力の増大に伴い半価幅が増大しており、γ相では引張残留応力の増大に伴い半価幅が増大していることがわかる。

（3） 公称ひずみ 0 から 3 %では、マルテンサイト変態に伴い、オーステナイト相の残留応力値が引張側にシフトしており、半価幅が増大していることから、オーステナイト相が応力を負担していると考えられる。

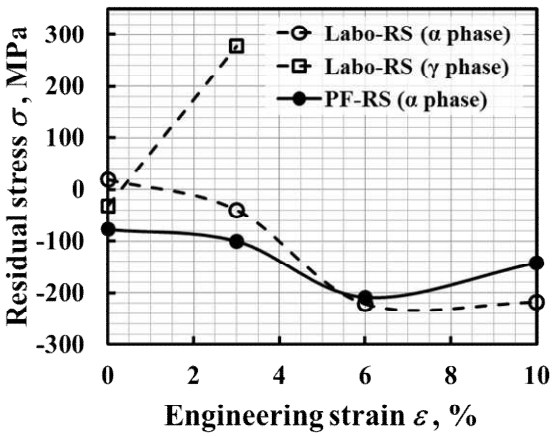

図１．　α相およびγ相の応力変化

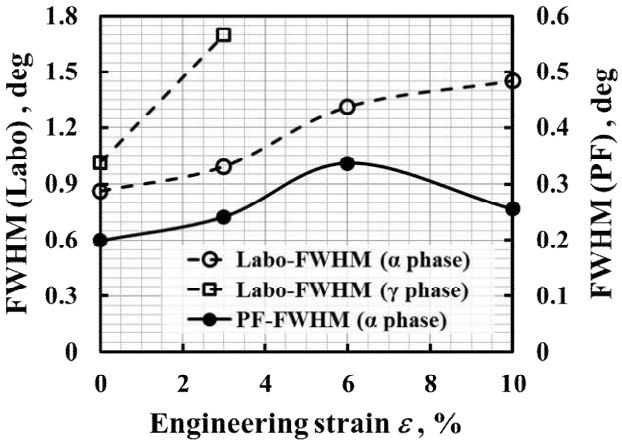

図２．　α相およびγ相の半価幅変化

(Corresponding Author: imafukum@tcu.ac.jp)

13A/2011G161; SAGA-LS BL10/1105042PF

ルブレン単結晶の異方的な価電子バンド分散の光電子分光法による実測
Widely-Dispersed Highly-Anisotropic Valence Band of Rubrene Single Crystals Observed by Photoelectron Spectroscopy

中山泰生[1*], 町田真一[2], 浦上裕希[2], Koswattage Rasika Kaveenga[1],
吉村大介[3], 瀬戸山寛之[3], 岡島敏浩[3], 間瀬一彦[4], 石井久夫[1,2]
[1]千葉大学先進科学センター、〒263-8522 千葉市稲毛区弥生町 1-33
[2]千葉大学大学院融合科学研究科、〒263-8522 千葉市稲毛区弥生町 1-33
[3]九州シンクロトロン光研究センター、〒841-0005 佐賀県鳥栖市弥生が丘 8-7
[4]高エネルギー加速器研究機構物質構造科学研究所、〒305-0801 つくば市大穂 1-1

1 はじめに

ルブレン(5,6,11,12-tetraphenyltetracene)の単結晶は，現在までのところ有機半導体としては最も高いキャリア移動度が報告されている材料であり[1]，また強い異方性など興味深い伝導特性を示すことから[2]，有機半導体内でのキャリアの振舞いを研究するためのベンチマーク材料として，応用面のみならず基礎科学的観点からも関心を集めてきた。移動度の温度依存性やホール効果，電子スピン共鳴の結果から，こうした高い移動度は数分子にわたるキャリアの非局在化や「バンド伝導」がルブレンのようなファン＝デル＝ワールス固体においても実現していることが提起されていたが[3]，ルブレン単結晶の最高占有準位(HOMO)が最も移動度の高い方位については有機半導体としては非常に広い 0.4 eV というエネルギー幅で分散した「価電子バンド」を形成していることを，筆者らは角度分解光電子分光法(ARPES)により実証した[4]。本研究では，ルブレン単結晶の示すキャリア移動度の強い異方性の電子論的な起源を解明するため，面内の３つの対称軸方位について，ARPES により価電子バンド構造を決定した。

2 実験

試料として用いたルブレン単結晶は，高純度窒素気流内での昇華・再結晶（物理気相成長法）により作製した。得られた矩形の薄片状結晶を，Au で被覆した Si 基板上に導電性銀ペーストにより固定したもの（図２(d)参照）を測定試料とした。ルブレン単結晶の結晶構造は ***a*** = 1.441 nm, ***b*** = 0.719 nm, ***c*** = 2.690 nm の斜方晶であり[5]，薄片状結晶の表面法線方向が結晶 ***c*** 軸，結晶が矩形の場合は長軸が ***b*** 軸と平行になることが知られている。本研究では，筆者らの過去の研究と同様[4]，こうした結晶形状の異方性から ARPES 計測における方位を決定した。

ARPES 計測は，高エネルギー加速器研究機構放射光施設(KEK, PF)BL-13A，および九州シンクロトロン光研究センター(SAGA-LS)BL10 において２次元光電子アナライザを用いて行った。試料のチャージアップ回避するため，測定時の試料電流は 10 pA 以下に抑え，かつ帯電電荷を光伝導によって相殺するため，測定時に波長 405 nm のレーザー光を試料に照射している。測定は全て室温で行った。

3 結果および考察

図１に SAGA-LS, BL10 にて計測されたルブレン単結晶のΓ-Y 方位の ARPES スペクトルを示す。励起エネルギーは 40 eV であり，この計測条件では Brillouin 帯ほぼ２つ分の領域が１枚のスペクトルイメージとして同時に計測されている。運動エネルギー35 eV 前後がルブレン単結晶の HOMO に帰属され，光電子放出量が極大値をとるエネルギーが放出角度に依存して周期的に変化することから，価電子バンドが形成していることが見て取れる。

図２に KEK, PF, BL-13A にて計測されたルブレン単結晶の面内３方位についての ARPES スペクトルを示す。励起エネルギーは 30 eV であり，ここに示した２次元スペクトルイメージは，試料に対するアナライザの仰角を 3º ごとに変化させて計測したスペクトルを積算している。隣接分子間のπ軌道の重なりが最も大きい ***b*** 軸方向(Γ-Y 方位)へは大きなエネルギー分散が見られているのに対し，試料を面内方向に 90º 回転させ ***a*** 軸方向(Γ-X 方位)への ARPES を計測すると，エネルギー分散はほぼ消失する。一方，Brillouin 帯の対角線にあたるΓ-M 方位ではΓ-Y 方位と殆ど等しい広いエネルギー幅で分散した価電子バンドが観察された。ただし，分散の周期はΓ点から

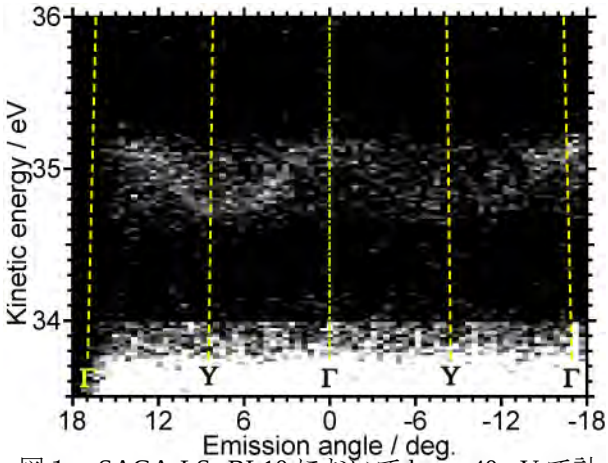

図１：SAGA-LS, BL10 において hν = 40 eV で計測されたルブレン単結晶のΓ-Y 方位の ARPES スペクトル。破線は結晶構造より計算される各対称点の位置。

Brillouin 帯境界までの距離の差を反映し，Γ-Y 方位より広くなっている。

図１・２に示した ARPES スペクトルを，図１については±1.1º，図２については±0.5º の範囲で積算し，それぞれ強度が最大になるエネルギーを各方位への波数に対してプロットすると，図３に示したようなバンド分散図が得られる。１次元の強結合近似(1D-TB)を仮定し，得られたエネルギー・波数の分散関係をから分子間の跳び移り積分 t および正孔有効質量 m_h^*をフィッティングにより 求めると，それぞれ表１のようになる。SAGA-LS での結果では PF での結果と比べ，t が 20%ほど低く見積もられているが，解析にあたり積算角度を広くとったためバンド端付近が鈍り，バンド幅を過小評価している可能性がある。PF での結果より見積もられたΓ-Y 方位での m_h^*は文献 4 と一致する。一方，Γ-M 方位への m_h^*は Brillouin 帯の拡張を反映して 30%以上重くなっており，殆ど分散のないΓ-X 方位と併せ，ルブレン単結晶の示す正孔移動度の強い異方性に対して，価電子バンド構造の観点からの根拠を与えている。

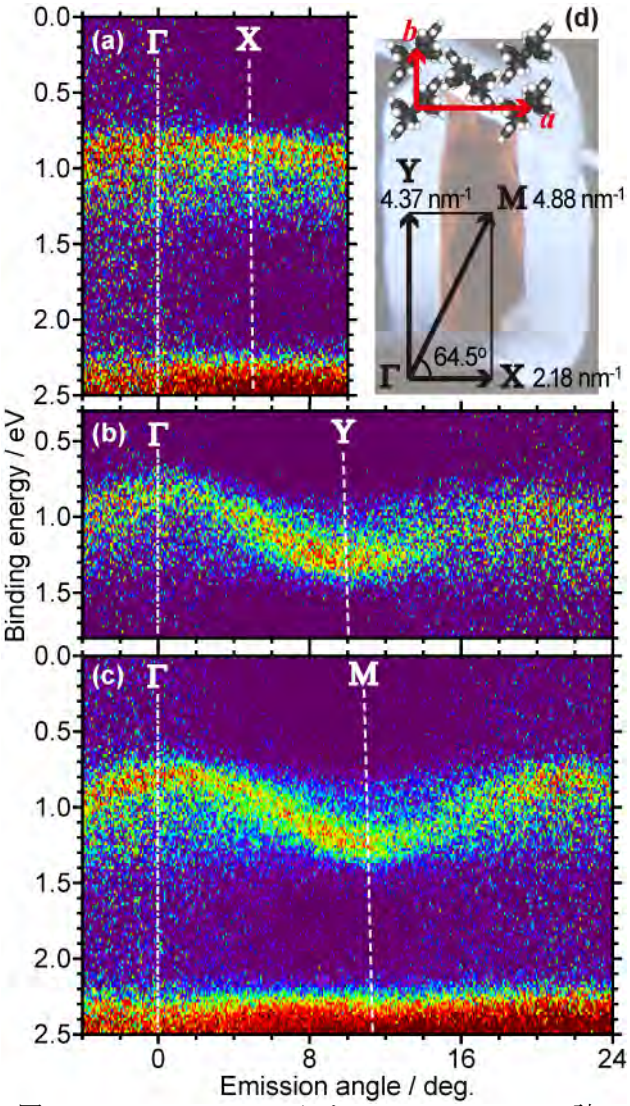

図２：KEK, PF, BL13A において hν = 30 eV で計測されたルブレン単結晶の(a) Γ-X, (b) Γ-Y, (c) Γ-M 方位の ARPES スペクトル。破線は結晶構造より計算される各対称点の位置。(d) ルブレン単結晶の表面面内方向の結晶格子，および Brillouin 帯構造の模式図。背景図は測定に用いたルブレン単結晶試料の写真。

表１：ルブレン単結晶の各方位への t および m_h^*

Γ–	X	Y(SAGA)	Y (PF)	M
t / meV	0	85	111	105
m_h^* / m_0	N/A	0.86	0.66	0.88

4 まとめ

ルブレン単結晶の面内３方位への価電子バンド分散構造を ARPES により実測し，分子間跳び移り積分および正孔有効質量の異方性を定量的に決定した。

謝辞

本研究の一部は，九州シンクロトロン光研究センターの「ＰＦ協力利用」としてビームタイム配分を，また高エネルギー加速器研究機構からは旅費の援助を頂き，実施した。また，本研究は，科学研究費補助金(23750209)，東電記念財団，および矢崎科学技術振興記念財団の研究助成の下で行われたものであり，日本科学協会の笹川科学研究助成金からも部分的に援助いただいている。ここに感謝申し上げます。

参考文献

[1] J. Takeya, *et al.*, Appl. Phys. Lett. **90** (2007) 102120.
[2] V. C. Sunder, *et al.*, Science **303** (2004) 1644.
[3] T. Hasegawa, *et al.*, Sci. Tech. Adv. Mat. **10** (2010) 024314.
[4] S. Machida, *et al.*, Phys. Rev. Lett. **104** (2010) 156401.
[5] B.D.Chapman, *et al.*, J. Cryst. Growth **290** (2007) 476.
* nkym@restaff.chiba-u.jp

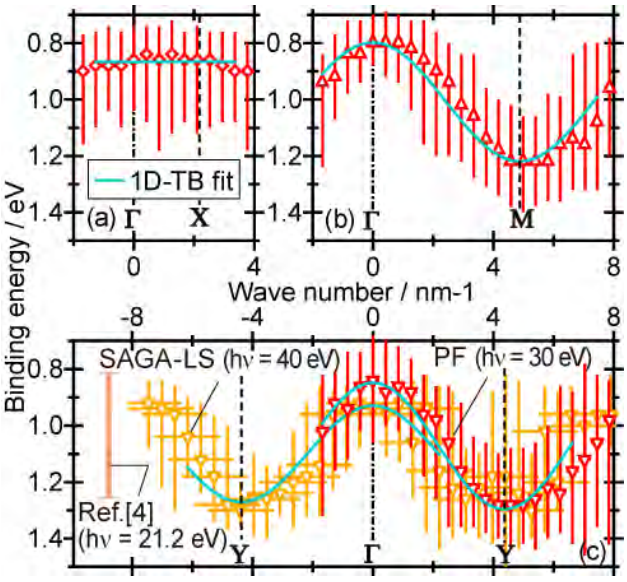

図３：HOMO ピーク領域の光電子強度が最大となるエネルギーを波数に対してプロットした価電子バンド分散図，および 1D-TB 近似によるフィッティング曲線。筆者らが過去に報告したΓ-Y 方位でのエネルギー分散幅も(c)に示した。

PF: 2C/2011G162, SLS: 1105043PF

キャリア濃度が系統的に制御された超伝導ダイヤモンド膜の軟Ｘ線角度分解光電子分光

Soft x-ray ARPES of superconducting diamond films with systematically controlled carrier concentration

村岡祐治*、平松千明、長尾浩樹
岡山大学大学院自然科学研究科、〒700-8530 岡山市北区津島中 3-1-1

1 はじめに

高濃度ホウ素ドープダイヤモンド超伝導体の高品質・高特性化は、基礎応用両側面で重要な課題である。高温高圧法により作製された最初のバルク試料では、超伝導転移温度はT_c =4 Kであった[1]。その後、マイクロ波プラズマ化学気相成長(MPCVD)法によって薄膜化に成功し、T_c は 10 Kまで上昇した[2]。極最近になって、ホットフィラメント化学気相成長(HFCVD)法でもダイヤモンド超伝導膜が作製できることが報告された。この膜では、MPCVD法膜よりも 1 桁少ない 10^{20} cm^{-3}オーダーでT_c = 10 Kが現れる[3]。その品質とT_cとの関係に興味が持たれている。

本実験では、独自に建設した HFCVD 装置を活用して作製したホウ素ドープダイヤモンド膜の品質を、光電子分光を用いて行った。

2 実験

ホウ素ドープダイヤモンド膜は、HFCVD法を用いて、Si（100）基板上に作製した。光電子分光測定はSAGA-LSのビームラインBL10で行った。測定前には試料の表面洗浄のため準備槽において700 °Cで15分間加熱を行った。測定には光のエネルギー1000eVを用いた。バルク敏感な測定が可能となり、表面の汚れなどの影響が抑えられる。測定は室温で行い、価電子帯とホウ素1*s*内殻準位を観測した。

3 結果および考察

図 1 に HFCVD 法で作製したホウ素ドープダイヤモンド膜の価電子帯スペクトルを示す。ダイヤモンドができていれば、0-25 eV に C 2*p*, C 2*p* と 1*s* の混合、C 1*s* に由来する状態が見えるはずだが、その構造ははっきりしない。構造が見分けにくいのは、スペクトルの S/N が良くないことが一因である。1000eV のエネルギーでは光のフラックス量が極端に少ないので、これはやむをえない。代わりに 28eV 付近の 2 つのピークが観測された。このピークは Ta に由来する。装置のフィラメントからの混入と考えられる。高品質膜を作る上で Ta の混入は抑えたい。対処すべき課題がみつかった。

HFCVD 法で作製した膜ではホウ素に由来するピークを観測することができなかった。これは、成膜時のホウ素量が少なかったためと考えられる。

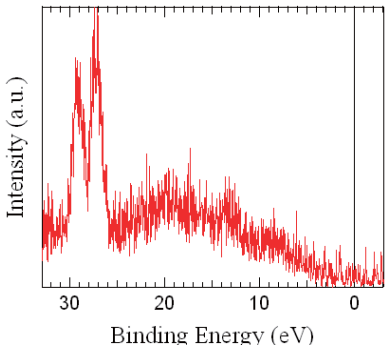

図 1： HFCVD 法で作製した試料の価電子帯スペクトル

4 まとめ

HFCVD 法膜にはタンタルが混入している。フィラメントからの飛散が原因である。高品質な HFCVD 法膜を得るには、フィラメント材料のタンタルの混入を抑えることが課題である。そのためには混入の原因を明らかにすることが大事である。フィラメントの状態を詳しく調べることが原因究明につながるだろう。

また、HFCVD 法膜では光電子分光測定でホウ素 1*s* スペクトルの観測が困難であった。膜中のホウ素量が少ないことが原因である。今後 BL10 でホウ素 1*s* の状態を観測するためには、ホウ素量を増やした試料を用いることが有効であろう。

謝辞

SLS で実験を進めるにあたり、PF スタッフに手続きでお世話になりました。また、実験では SLS の吉村氏、瀬戸山氏、岡島氏に多大なる技術支援を受けました。ここに感謝致します。

参考文献

[1] E.A. Ekimov *et al.*, Nature **428,** 42 (2004).
[2] A. Kawano *et al.*, Phys. Rev., B **82,** 085318 (2010).
[3] Z. L. Wang *et al.*, Diamond Relat. Mater. **15,** 659 (2006) .

*ymuraoka@cc.okayama-u.ac.jp

7C/2011G182

XAFS analysis of Ni-Zr alloys after thermal and chemical treatment

Ai NOZAKI[1], Takashi KAMEGAWA[1], Tetsutaro OHMICHI[1], Hiromi YAMASHITA*[1]
[1]Divisions of Materials and Manufacturing Science, Graduate School of Engineering, Osaka University, 2-1 Yamadaoka, Suita, Osaka 565-0871, Japan

Introduction

Amorphous materials have no long-range order at the atomic length scale and show different properties as compared to typical crystalline materials. Among of them, amorphous alloys are in thermodynamically non-equilibrium, crystallized by heating and used as catalysts and catalyst precursors. Investigations on the relationships between their catalytic performances and structural changes during the crystallization process of amorphous alloys are quite interesting research topics. To active catalysts, skeletal metal catalysts were also prepared by acid or base treatment of alloys.

In this study, porous Ni catalysts were prepared from Ni-Zr alloys via heating at various temperatures and following HF treatment for extraction of Zr moieties. XAFS analyses were performed to clarify the effect of heating on the catalytic performances of thus obtained porous Ni catalysts.

Experimental

Ribbon-shaped $Ni_{40}Zr_{60}$ amorphous alloy (amor-NiZr) was prepared by the rapid quenching method using a single steel roll. The heat treatments of amor-NiZr were carried out in a temperature range from 373 to 773 K under vacuum for 2 h. For extraction of Zr moieties, obtained samples were treated by aqueous HF solution (1.0 mol/L) for 5 min, and then thoroughly washed by ion-exchanged water. The catalytic performances of samples were tested by hydrogenation reaction of 1-octene to octane as a model reaction.

XAFS spectra at Ni K-edge were measured in the transmission mode at 298 K. Obtained data were examined using the analysis program (Rigaku REX2000).

Results and Discussion

The structures of untreated and heated samples at each temperature were investigated by XRD measurements. The untreated and heated samples below 573 K only showed a similar broad peak (halo). Overlapped diffraction peaks, (i.e., a broad peak (halo) and peaks assigned to crystalline $NiZr_2$,) as well as sharp peaks due to the formation of crystalline $NiZr_2$ and NiZr were observed after heating at 673 K and 773 K, respectively.

The SEM images and EDX data clearly showed the formation of porous structure and successful extraction of Zr moieties through the HF treatment of untreated and heated samples.

In the hydrogenation reaction of 1-octene to octane, amount of formed octane per surface area of each sample was increased with increasing the heating temperature of amor-NiZr up to 573 K. At higher heating temperatures,

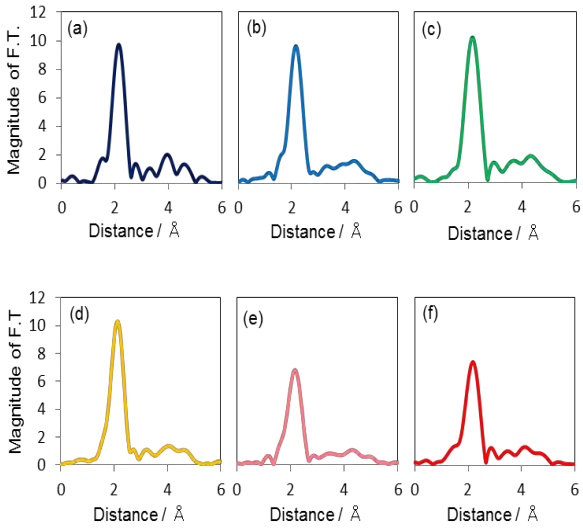

Fig. 1 Fourier transforms of EXAFS spectra of porous Ni catalysts prepared with an HF solution from Ni-Zr alloys (a) as-quenched, (b) heated at 373 K, (c) 473 K, (d) 573 K, (e) 673 K, (f) 773 K.

the decreases in the amount of formed octane was observed due to the crystallization and the aggregation of Ni moieties. Porous Ni catalyst prepared from heated amor-NiZr at 573 K exhibited higher catalytic performances, while the clear structural differences of heated amor-NiZr below 573 K were hardly detected by XRD measurements. XAFS analyses were thus carried out to clarify the structural differences at the atomic length scale.

Figure 1 shows the Fourier transforms of EXAFS spectra of porous Ni catalysts. The intensity of peak attributed to the Ni-Ni bond at around 2 Å (without phase-shift correction) was slightly increased with increasing the heating temperature of amor-NiZr up to 573 K. The intensity of this peak became weak after crystallization at higher temperature. These small changes below 573 K attributed to the short range structural rearrangement in amorphous structure.

This structural rearrangement by heating, i.e., the formation of intermediate crystalline states of amorphous Ni-Zr alloys, lead to the higher catalytic performances of porous Ni catalyst prepared from heated amor-NiZr at 573 K. The state of amorphous Ni-Zr alloys strongly affect to the catalytic performances of porous Ni catalyst.

* yamashita@mat.eng.osaka-u.ac.jp

7C, 9C, 12C/2011G195

Electro Luminescence 特性を持つ Tb ドープ繊維状アルミナナノ粒子ゾルの XAFS 解析

XAFS Analysis of Electro Luminescent Tb Doped Alumina Nanofiber Sol

阪東恭子[1*], 鈴木洋平[2], 井原和昭[2], 永井直文[2], 高島　浩[1], 小平哲也[1], 伯田幸也[1], 水上富士夫[1]

[1]産業技術総合研究所、〒305-8565 つくば市東 1-1-1

[2]川研ファインケミカル、〒350-1151 埼玉県川越市今福 2835 番地

1 はじめに

無機 Electroluminescence (EL) 材料は、化学的な安定性が高い長寿命なデバイスを低価格で構成することが可能であるが、有機 EL に比べ、成形性に乏しく、膜成形が困難であった。これに対して、永井らは、繊維状のアルミナ前駆体ナノ粒子(ベーマイトナノファイバー)からなるゾルから、自己組織化により、均一で透明な自立膜を作成することに成功した[1]。更にこのゾルに Tb を分散させて成膜した自立膜では、交流電圧を印加することで、膜全体を緑色に面発光する EL 性能を発現させることに成功した（永井ら、セラミクス協会 第２４回秋季シンポジウム, 札幌,2011 年 9 月 9 日）。更に輝度を向上させるためには、EL 発光の活性点の構造を正確に捉え、発光点構造形成に関わるメカニズムを解明し、活性構造が発現する条件を明確にとらえることが不可欠となってくる。Tb ドープアルミナ自立膜では、成膜後の加熱処理温度により発光効率が大きく変わることが見出されており、最も発光効率の高い構造を見出すこと、また、その生成過程を明らかにすることは、今後の材料設計に重要な指針を与えるものと期待される。本研究では、各種前処理を行った Tb ドープアルミナ自立膜の Tb L_{III}-edge XAFS を測定し、Tb 周りの構造について検討した。

2 実験

繊維状アルミナナノ粒子ゾルは、文献に従い調整した[1]。Tb は硝酸塩を用いて、アルミナナノ粒子ゾルに Al に対し、Tb が 5 mol%になるように添加し、膜成形した。この自立膜を焼成温度 773, 1073, 1173, 1273 K で 6 時間焼成したものを、EL 性能の評価したのち、粉砕しペレット状に成形して、室温大気下で XAFS 測定を行った。XAFS 測定は Si(111)モノクロメータを用いた BL7C, 9C, 12C を利用し、ステップスキャニングで測定した。データの解析には REX2000(理学)を用い、解析パラメーターは feff(ワシントン大学)を利用した。

3 結果および考察

Tb ドープアルミナナノ粒子ゾルの自立膜の EL 性能評価を行ったところ、膜形成後の焼成処理温度で EL 性能が変化することが分かった。４種類の焼成温度の中で、1073 K で処理したものが最も高い輝度を示すことが分かった。この時各サンプルについて測定した Tb L_{III}-edge XANES を比較すると、エッジ位置、ホワイトライン強度ともにほとんど差が見られず、Tb は３価で存在することが確認できた。更に EXAFS（$k^3\chi(k)$のフーリエ変換）を図１に示す。焼成温度の上昇とともに、Tb-O に帰属されるメインピークの強度は減少し、カーブフィット解析を行うと、配位数、Tb-O 距離共に減少していることが分かった。今後、Tb 周りの配位構造の変化とアルミナ側の構造変化を対応させた解析を行い、より詳細な情報を得ることを目指す予定である。

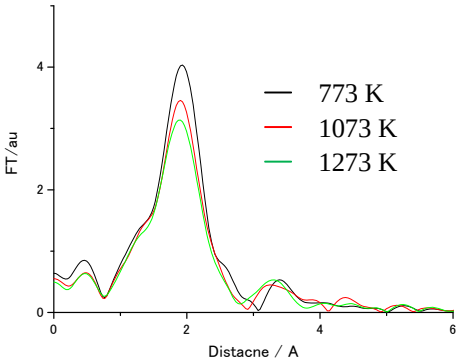

図１：各焼成温度で処理した Tb ドープアルミナナノ粒子ゾルの Tb L_{III}-edge EXAFS のフーリエ変換

謝辞

本研究は、NEDO ナノテク・先端部材実用化研究開発／形状制御されたアルミナナノ粒子ゾルの実生産にための基盤技術の確立と用途開発の支援を受けて実施された。

参考文献

[1] N. Nagai, F. Mizukami, *J. Mater. Chem.*, **21**, 14884-14889 (2011)..

* kk.bando@aist.go.jp

15C/2011G-247

SiC 溶液成長における貫通転位挙動
Evolution of Threading Dislocation during SiC Solution Growth

原田俊太*, 山本祐治, 関和明, 堀尾篤史, 三橋貴仁, 宇治原徹
名古屋大学工学研究科、〒464-8603 名古屋市千種区不老町

1 はじめに

低損失、高耐圧の SiC パワーデバイス実現の『カギ』を握るのが、SiC 単結晶の高品質化である。現在、市販されている昇華法により作製された SiC 単結晶には、高密度の転位欠陥が含まれている[1]。SiC 結晶中の転位は、電流のリーク源となり、デバイス特性、信頼性の大幅な低下をもたらす事が知られている[2]。溶液成長法は、液相を介した熱平衡に近い成長法であり、SiC の高品質化を実現できる成長法として期待されている。これまでの研究で、SiC 溶液成長では、マイクロパイプの閉塞や、基底面内転位 (BPD) が継承しないことが報告されている[3, 4]。

しかし、貫通らせん転位 (TSD) や、貫通刃状転位 (TED) など、貫通転位に関しては、溶液成長中の挙動は明らかとなっていない。そこで、本研究では、溶液成長における貫通転位の挙動を明らかにし、溶液成長法による、高品質 SiC 結晶成長のための指針を得ることを目的としている。

2 実験

SiC 結晶成長は、Top Seeded Solution Growth (TSSG) 法によって行った。カーボンるつぼ中で Si を溶解し、温度勾配下で保持し、そこに種結晶を張り付けたディップ軸を挿入する。高温部分でるつぼのカーボンが Si 溶媒中に溶出し、温度の低い種結晶付近で結晶が成長する。種結晶には 4H-SiC を使用した。欠陥の評価は、KEK-PF BL-15C および、Spring8 BL19B2 において、放射光 X 線トポグラフィー法により行った。使用した X 線の波長は 0.15 nm、$(11\bar{2}8)$の反射を用いて原子核乾板に結像した。

3 結果および考察

Fig. 1 に種結晶および成長結晶の X 線トポグラフィー像と成長結晶のノマルスキー像を示す。Fig. 1(a) において、A や B のような点状のコントラストは TSD を示している。成長後（Fig. 1(b)）、大部分の TSD は A'のように成長後にも結晶中に引き継がれるが、一部の TSD は B'のように線状の異なるコントラストに変換する。成長結晶の表面（Fig. 1(c)）をみると、変換した部分（B"）には、A"のようなスパイラルヒロックは観察されず、TSD が基底面上の異なる欠陥に変換したことが明らかとなった。変換した欠陥はステップフロー方向に伸びていることから、TSD はステップフローによって変換した事が予想される。このような TSD の変換を、エンハンスすることができれば、溶液成長法によって TSD の密度を低減させることが可能となるであろう。

謝辞

放射光 X 線トポグラフィー実験は、KEK-PF BL-15C（共同利用番号 2011G247）および、SPring8 BL19B2（被災量子ビーム施設ユーザー支援課題 2011A1950）において実施した。測定に際して、ご協力をいただいた、AiST の山口博隆氏、KEK の平野馨一氏、SPring8 の梶原堅太郎氏、松本拓也氏に感謝いたします。

参考文献

[1] P. G. Neudeck, *Mater. Sci. Forum* **338-342** (2000) 1161.
[2] A. Grekov *et al.*, *Microelectron. Reliab.* **48** (2008) 1664.
[3] R. Yakimova *et al.*, *Inst. Phys. Conf. Ser.* **142** (1996) 101.
[4] S. Kozawa *et al.*, *Mater. Sci. Forum* **679-680** (2011) 855.

* harada@numse.nagoya-u.ac.jp

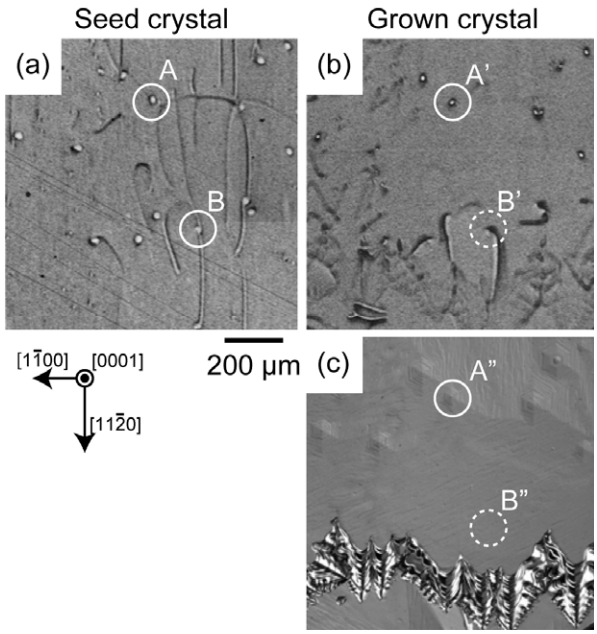

Fig. 1 種結晶および成長結晶の X 線トポグラフィー像 (a), (b) と、成長結晶のノマルスキー像 (c)。

6A, 15A/2011G508

Synthesis and Structural Analysis of Metal Particles in Ionic Liquids

Masafumi HARADA*[1], Masako YAMADA[1], and Kenji SAIJO[2]
[1]Department of Clothing Environmental Science, Faculty of Human Life and Environment, Nara Women's University, Nara 630-8506, Japan
[2]Department of Polymer Chemistry, Graduate School of Engineering, Kyoto University, Kyoto 615-8510, Japan

Introduction

Room-temperature ionic liquids (RTILs) are regarded as an interesting class of tunable reaction solvents with essentially low volatility, wide electrochemical window, non-flammability and high thermal stability [1]. Recently we have synthesized Ag particles by the photoreduction of silver perchlorate ($AgClO_4$) in water-in-[OMIm][BF_4] microemulsions in the presence of Tween 20, and elucidated the formation mechanisms of Ag particles [2, 3]. In this study we have investigated the size and polydispersity of Pd particles synthesized by the decomposition of organometallic Pd precursors in the mixture of nonionic surfactant and RTILs, such as Tween 20 (or Triton X-100) and OMImCl (or DMImCl), by means of *in-situ* SAXS measurements.

Experimental

Colloidal dispersions of Pd particles were synthesized by the decomposition of palladium acetylacetonate, $Pd(acac)_2$, in the mixture of Tween 20 (or Triton X-100) and 1-octyl-3-methylimidazolium chloride (OMImCl) (or 1-dodecyl-3-methylimidazolium chloride (DMImCl)). For example, 0.5 mL of Tween 20 was added to 2 mL of OMImCl, followed by the addition of 11 mg $Pd(acac)_2$ and mixed vigorously. In this case, the weight fraction (wt%) of Tween20 ($W_{Tween20}$) and $Pd(acac)_2$ ($W_{Pd(acac)2}$) was 21.35 and 0.42, respectively. OMImCl to Tween20 molar ratio (R) was 19.5. Subsequently, the mixture solution was poured into a cell (optical path length 1 mm), and the sample was stepwise heated to 333, 353, 373, 393, 413, 433, and 453 K. The in-situ SAXS measurements were performed at each temperature at BL-6A or 15A. The scattering data was detected by a CCD camera with an X-ray image intensifier or PILATUS.

Results and Discussion

Fig. 1 shows the SAXS profiles of the colloidal dispersions of Pd particles at various temperatures (up to 453 K) in the presence of Tween 20 mixed with OMImCl or DMImCl. These SAXS profiles show that all the samples have a broad peak (centered around 2.6-2.7 nm^{-1} for OMImCl [2] and 2.1-2.3 nm^{-1} for DMImCl) observed in a q range larger than 1.5 nm^{-1} and a second inner peak in a q range ($0.3 < q < 1.4$ nm^{-1}). The former is characteristic of the interference peak due to the existence of ordering for ILs, and the latter is related to an

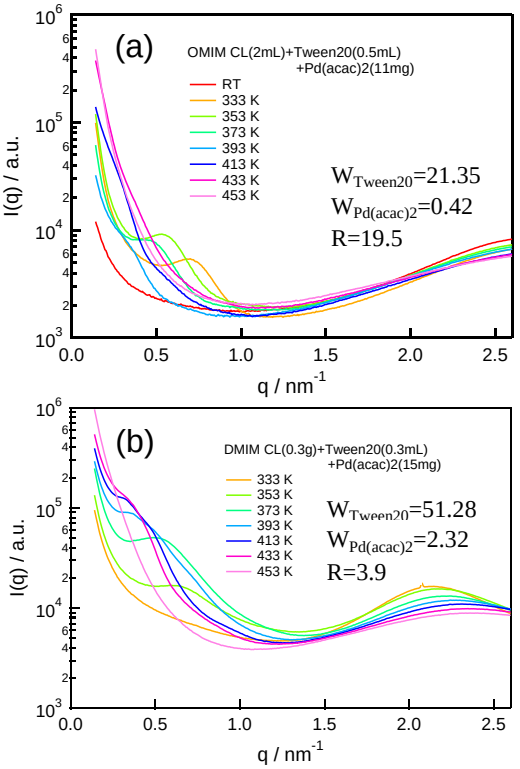

Fig. 1. SAXS profiles of the Pd colloidal solutions synthesized during raising the reaction temperature in the mixture of (a) Tween20/OMImCl and (b) Tween20/DMImCl.

interference due to the interaction between two neighboring Pd particles. Initially, the scattering profile has no second peak. The intensity of the second peak increases and its position shifts to lower q with increasing temperature. This indicates the growth of Pd particles in size during the temperature raising. From their Guinier plots, the average diameter of the aggregates, which consisted of ionic precursors of $Pd(acac)_2$ and Pd particles, is estimated to be about 30-40 nm. During the Pd particle formation process, aggregation of Pd atoms rapidly occurs in the micelles of Tween 20 in OMImCl rather than in DMImCl, indicating the dependence of the rate of particle formation on the alkyl chain lengths of ILs.

References

[1] J. Dupont, J. D. Scholten, *Chem. Soc. Rev.* **2010**, *39*, 1780. [2] M. Harada et al., *J. Colloid Interface Sci.* **2009**, *339*, 373. [3] M. Harada et al., *J. Colloid Interface Sci.* **2010**, *343*, 537.

*harada@cc.nara-wu.ac.jp

9C/2011G510

Coordination structures of transition-metal ions in ionic liquids.

Masayasu IIDA,[1] Shinobu TAKEMURA,[1] Mayu WATANABE,[1] and Masafumi HARADA*[2]
[1] Department of Chemistry, Faculty of Natural Science, Nara Women's University, Nara 630-8506, Japan
[2] Department of Clothing Environmental Science, Faculty of Human Life and Environment, Nara Women's University, Nara 630-8506, Japan

Introduction

Ionic liquids are nowadays attracting considerable attention owing to their potential use in a wide range of applications. Particularly, they have successfully been employed in the preparation of inorganic materials. We have been studying the preparations of alkylpolyaminium protic ionic liquids (= PILs) and of ionic liquids of silver(I) complexes (= AgILs) [1, 2] and the interactions of transition metal ions in the ILs. In this study, we have prepared a series of the PILs containing transition-metal ions and measured EXAFS for the coordination structures around the transition-metal ions.

Experimental

The PILs were obtained by the neutralizations of hexylethylenediamine (= Hexen) with HTFSA (= bis(trifluoromethanesulfonyl)amide acid) or HTFA(= trifluoroacetic acid) and of hexylamine (= Hexam) with HTFSA. These PILs are hereafter abbreviated as HHexen(TFSA), HHexen(TFA), and HHexam(TFSA), respectively. HHexen(TFSA) and HHexen(TFA) ILs significantly dissolve many kinds of metal salts while HHexam(TFSA) does only copper(II) salts. We studied the interactions of metal(II) ions in the PILs with an addition of metal compounds such as chlorides, bromides, and bis-TFSA complexes of Mn^{2+}, Co^{2+}, Ni^{2+}, and Cu^{2+}, and tetraammine complex of Cu^{2+}.

EXAFS measurements were performed at room temperature in a transmission mode at BL-9C. The solid samples were mixed with boron nitride to make a tablet specimen. The PILs and other liquids were sealed into polyethylene bags for measurements; the metal concentrations were 0.04-0.15 mol kg^{-1}. In order to extract the backscattering amplitude and phase shift functions for the curve-fitting, the reference compounds (MnO, $[Ni(en)_3]SO_4$, $[Cu(en)_3]SO_4$) were used in this experiment. The structural parameters for the respective metal(II) samples were determined referred to those for the corresponding metal(II) reference compounds.

Results and Discussion

Figure 1 shows typical Fourier transformed EXAFS spectra for the solid and concentrated solutions of copper(II) salts. For all the samples except $Cu(TFSA)_2$ solid, the peak around 0.23 nm assigned to the bond of copper(II)-N appears with the same height.

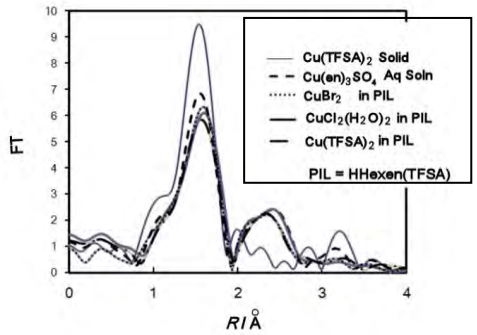

Figure 1. Fourier transformed $|F(r)|$ of the $k^3\chi(k)$ curves for copper(II) ions. (uncorrected for the phase shift)

The en complex shows a characteristic peak due to a weak second shell contribution of carbon as well as a single monatomic first shell of nitrogen.[3] The relative magnitude of the second peak to the first one is useful to monitor the extent of the interaction of the copper(II) ion with the en chelate in the HHexen(TFSA) PIL system in comparing with $[Cu(en)_3]SO_4$. The spectra showed that copper(II) ions strongly coordinate to the en-chelate ring in the HHexen cation rather than the TFSA anion; the coordination mode around the copper(II) ion is close to that in 0.05 mol kg^{-1} $[Cu(en)_3]SO_4$ aqueous solution. The selective interaction occurs against the electrostatic disadvantage and is almost independent on the kinds of copper(II) salts. On the other hand, in the HHexam(TFSA) PIL (not described here), copper(II) ions prefer the TFSA anion rather than the hexylaminium cation. The other metal ions (Mn^{2+}, Co^{2+}, Ni^{2+}) also prefer the HHexen cation over the TFSA anion in the PIL; the selectivity to the HHexen cation is the largest for copper(II) ion. These selective interactions of the metal ions with the PILs and analogous liquids are consistent with the results obtained by paramagnetic NMR relaxation methods.

References

[1] M. Iida, C. Baba, M. Inoue, H. Yoshida, E. Taguchi, and H. Furusho, *Chem. -Eur. J.*, **2008**, *14*, 5047-5056.
[2] M. Iida, S. Kawakami, E. Syouno, H. Er, and E. Taguchi, *J. Colloid Interf. Sci.*, **2011**, *356*, 630-638.
[3] Y. Inada, K. Ozutsumi, S. Funahashi, S. Soyama, T. Kawashima, M. Tanaka, *Inorg. Chem.*, **1993**, *32*, 3010-3014.

* harada@cc.nara-wu.ac.jp

6C,15B/2011G530

Three-dimensional atomic images of GeSbTe phase-change materials

Shinya Hosokawa,[1,*] Naohisa Happo,[2] Shinya Senba,[3] and Kouichi Hayashi[4]
[1]Kumamoto University, Kumamoto 860-8555, Japan
[2]Hiroshima City University, Hiroshima 731-3194, Japan
[3]Ube National College of Technology, Ube 755-8555, Japan
[4]Tohoku University, Sendai 980-8577, Japan

1 Introduction

GeTe is one of the laser-induced crystalline-amorphous phase change materials. Although its phase change speed is much slower than e.g., $Ge_2Sb_2Te_5$ (GST) used as the raw material for the commercially available DVD-RAM disks, GeTe is considered as a useful material for investigating the fundamental mechanism of the phase change.

X-ray fluorescence holography (XFH) is a powerful method that provides three-dimensional (3D) atomic images around a specified element which has a large spacial range of up to a few nm [1]. We utilized this technique to investigate the local structure around the Ge atoms in GST single-crystal thin film [2], and the results seem to support the umbrella flip model for the phase change mechanism proposed by Kolobov *et al.* [3]

In order to precisely investigate the mechanism of the phase change, we have measured Ge $K\alpha$ XFH on GeTe single-crystal thin film at room temperature. In this paper, we report the spacial fluctuations of each neighboring atom in the GeTe single crystal.

2 Experiment

GeTe single-crystal thin film sample was grown on a BaF_2 (111) substrate using a molecular beam epitaxy technique. The XFH experiments were performed at BL6C and BL15B of the PF-KEK. Incident x-rays were irradiated onto the (111) surface of the sample. The hologram patterns were collected in inverse mode at room temperature at seven different incident x-ray energies of 11.2–14.2 keV in steps of 0.5 keV. The Ge $K\alpha$ (9.885 keV) fluorescent x-rays were collected by an avalanche photodiode via a cylindrical graphite energy-analyzer [1]. Using Barton's algorithm [4], the three-dimensional (3D) atomic images were reconstructed by imposing holograms at different incident x-ray energies.

3 Results and Discussion

Crystal structure of GeTe is shown in Fig. 1, and the obtained 3D atomic image of GeTe around the central Ge atoms is given in Fig. 2. The images of the nearest-neighboring Te atoms are clearly seen in the obtained 3D image. The Te images are, however, not a normal spherical shape, but ellipsoid with angular directions. The second neighboring Ge atoms are hardly visible. Thus it can be concluded that the distortion of lattice is mainly occur at the central Ge sites, and the fluctuation of the Ge sites has the angular directions of the $GeTe_3$ pyramid. This conclusion may support the umbrella flip motion of the Ge atoms in the dynamical sense.

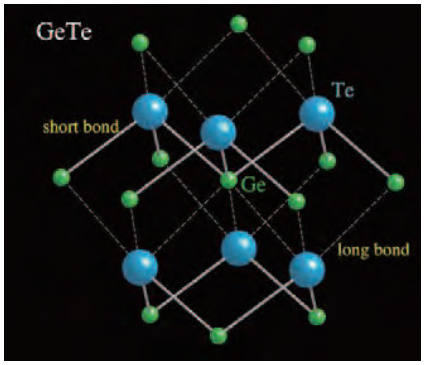

Fig. 1: Crystal structure of GeTe.

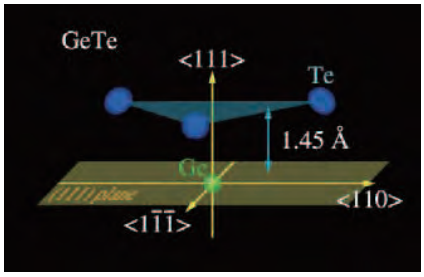

Fig. 2: 3D atomic image obtained from Ge $K\alpha$ XFH of GeTe.

Acknowledgement

We acknowledge Professor S. Sasaki for the support of the present XFH experiments at BL6C.

References

[1] K. Hayashi *et al.*, J. Phys.: Condens. Matter **24** (2012) 093201.
[2] S. Hosokawa *et al.*, Appl. Phys. Lett. **90** (2007) 131913.
[3] A. V. Kolobov *et al.*, Nature Mater. **3** (2004) 703.
[4] J. J. Barton, Phys. Rev. Lett. **67** (1991) 3106.

* hosokawa@sci.kumamoto-u.ac.jp

6C, 15B/ 2011G530, 2011G601

Middle range local structure analysis of semiconductor $ZnSnAs_2$ thin film by X-ray fluorescence holography

Akiko SUZUKI[1], Keitaro YAMAGAMI[1], Naohisa HAPPO[*2], Kouichi HAYASHI[3], Shinya HOSOKAWA[4], Wen HU[5], Motohiro SUZUKI[6], Naotaka UCHITOMI[1]
[1]Department of Electrical Engineering, Nagaoka University of techonology, Niigata 940-2188, Japan
[2]Graduate School of Information Sciences, Hiroshima City University, Hiroshima 731-3194, Japan
[3]Tohoku University, Sendai 980-8577, Japan
[4] Kumamoto University, Kumamoto 860-8555, Japan
[5]Quantum Beam Science Directorate, JAEA, Sayo, Hyogo 679-5148, Japan
[6]SPring-8/JASRI, Sayo, Hyogo 679-5198, Japan

1 Introduction

The continued research into semiconductors exhibiting room-temperature ferromagnetic for spintronics application has led to the exploration of transition metal oxides and ternary compounds for preparing diluted magnetic semiconductors. The $ZnSnAs_2$:Mn thin film, which is grown by a molecular beam epitaxy, is a II-IV-V_2 compound semiconductor with the ferromagnetism at T_c = 333 K [1]. The film is lattice-matched to the InP substrate ,which is the III-V compound semiconductor. Thus, the $ZnSnAs_2$:Mn is one of the promising candidates for the next generation spintronics materials. Erwin and Žutić reported that the Mn atoms can substitute for both Zn and Sn atoms in the cation sites [2]. Figure 1 shows two possible crystal structural models of $ZnSnAs_2$. However, we have not known which of them is dominant in the film sample. In order to understand the true crystal structure of the $ZnSnAs_2$, we performed the X-ray fluorescence holography experiment, which is a powerful tool for the local structure analysis [3].

2 Experiment

We observed the holograms at synchrotron radiation facilities of Photon Factory and SPring-8. The obtained 3D atomic images around Mn and Zn within 3 nm in a radius. (This large analytical range is called the “middle range”).

3 Results and discussion

Figure 2 shows the reconstructed atomic images around Zn in $ZnSnAs_2$. Moreover, we calculated holograms for the chalcopyrite model structure, and reconstructed the atomic images, as shown in Fig. 3. The cation plane atomic image at z = 0.0 Å of the theoretical holograms shows the chalcopyrite site pattern in Fig. 3 (a). However, such a pattern cannot be seen in the experimental atomic image in Fig. 2(a). Thus, it suggests that the sphalerite structure is dominat in the film sample. Moreover, in Fig.2 (b), the As images at z = 1.5 Å are rarely observed compared with the cation plane, revealing strong distortions at the As plane. The As plane plays an role of a buffer layer for relaxing the cation layer where Zn and Sn are randomly substituted for the cation sites.

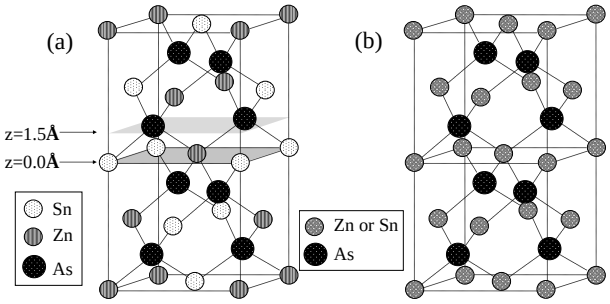

Fig. 1 Structural models of $ZnSnAs_2$.(a) Chalcopyrite model. (b) Sphalerite model.

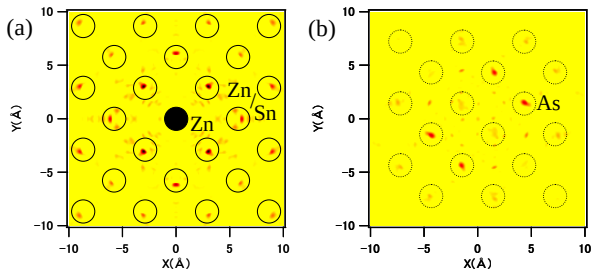

Fig. 2 Experimental atomic images around Zn in $ZnSnAs_2$. (a) z = 0.0Å. (b) z = 1.5 Å.

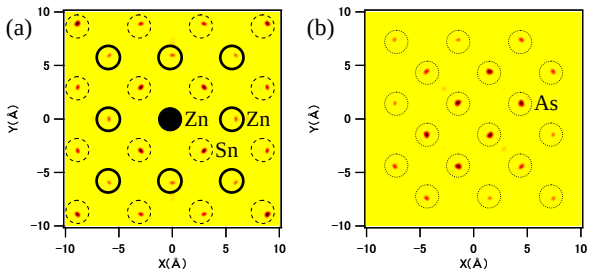

Fig. 3 Theoretical atomic images around Zn in $ZnSnAs_2$. (a) z = 0.0Å. (b) z = 1.5 Å.

References

[1] J. T. Asubar, *et. al*., J. Crystal Growth **311** (2009) 929.
[2] S. C. Erwin, *et. al*., Nature Mater. **3** (2004) 410.
[3] K. Hayashi, Advances in Imaging and Electron Physics **140** (2006) 119.
* happo@hiroshima-cu.ac.jp

7A/2011G539

NEXAFS Investigation of Order in Vertically Aligned Carbon Nanotubes formed by Surface Decomposition of SiC

Takahiro Maruyama[1,*] Yuki Ishiguro[1], Kenta Amemiya[2], Hideshi Ishii[3] and Toshiaki Ohta[3]
[1]Department of Materials Science and Engineering, Meijo University, Nagoya 468-8502, Japan
[2]Photon Factory, Tsukuba 305-0801, Japan
[3]SR Center, Ritsumeikan University, Kusatsu 525-8577, Japan

1 Introduction

Carbon nanotube (CNT) growth by surface decomposition of SiC can produce high-density, vertically aligned CNTs with fairly uniform tube diameters simply by heating SiC in a vacuum. Previous TEM studies showed that, compared to those grown by CVD method, the alignment of CNTs formed by the surface decomposition of SiC was fairly high [1]. However, the quantitative characterization has never been attempted.

In this study, we carried out NEXAFS measurements to evaluate the degree of vertical alignment of CNTs grown by the surface decomposition of SiC.

2 Experiment

The CNTs were prepared by heating an n-type 6H-SiC(000-1) C-face (CREE) in a vacuum electric furnace. Most of the CNTs were 2-5 walled and the diameters were between 3 and 6 nm. The average length of the CNTs was about 400 nm.

C K-edge NEXAFS spectra were obtained for both the total electron yield (TEY) and the partial electron yield (PEY) modes under ultrahigh vacuum (UHV) at BL2 in the SR Center, Ritsumeikan University.

3 Results and Discussion

Fig. 1 shows TEY C K-edge NEXAFS spectra for the CNTs grown by the surface decomposition of SiC. The spectra were measured at different incident angles and all spectra were pre- and post-edge normalized. The C K-edge NEXAFS spectra of the CNTs were quite similar to those of graphite [2], which were characterized by a sharp C-C π* transition near 286 eV and a sharp σ* bound exciton near 293 eV. Fig. 1 shows that the intensity of the π* resonance increased with the temperature, while, for the σ* resonances, there does not appear to be a systematic variation in intensity with the incidence angle.

Fig. 2 shows the variation in intensity of the π* and σ* resonances with the angle of incidence from the TEY NEXAFS spectra. The π* and σ* intensities were determined by subtracting an arctan function from the pre- and post- edge normalized spectra to simulate the edge jump followed by fitting the π* and σ* peaks with a Gaussian function. It is clear in the TEY spectra that, as the incidence angle increased, the π* intensity was enhanced, while the σ* intensity decreases. This tendency confirms that the CNTs are formed perpendicular to the substrate surface. Taking into account that the π* intensity

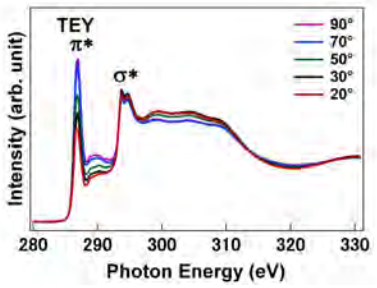

Fig. 1 TEY C K-edge NEXAFS spectra of the CNTs grown by the surface decomposition of SiC obtained at different incidence angles.

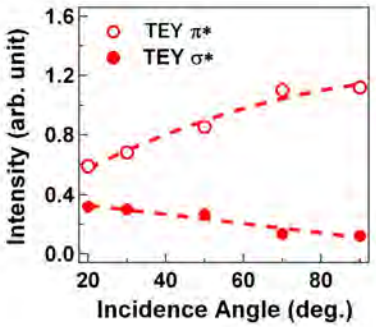

Fig. 2 Intensities of the π* and σ* resonances in the TEY NEXAFS spectra at different angles of incidence.

for the vertical CNTs show sine-squared dependence, we estimated the orientation parameter to be 0.38. This value is larger than those reported for vertically aligned CNTs grown by CVD, 0.08-0.145. These results clearly indicate that the order of vertical alignment of CNTs grown by the surface decomposition of SiC is fairly high.

Acknowledgement

A part of this work was supported by the JSPS, a grant-in-Aid for Scientific Research (c) 21510119 and the Nanotechnology Support Project (the Synchrotron Radiation Research Group).

References

[1] M. Kusunoki et al. Appl. Phys. Lett. **77** (2000) 531.
[2] S. Banerjee et al. J. Phys. Chem. B **109** (2005) 8489.
*takamaru@meijo-u.ac.jp

7A/2011G539

In situ NEXAFS Study on Carbon Nanotube Formation Process by Surface Decomposition of SiC

Takahiro Maruyama[1,*] Yuki Ishiguro[1], Satoshi Sakakibara[1], and Kenta Amemiya[2]
[1]Department of Materials Science and Engineering, Meijo University, Nagoya 468-8502, Japan
[2]Photon Factory, Tsukuba 305-0801, Japan

1 Introduction

Carbon nanotube (CNT) growth by surface decomposition of SiC is a unique growth technique, because zigzag-type CNTs are selectively formed only by heating SiC crystals in a vacuum without any catalysts. At the initial stage of CNT formation, nanosized hemispherical structures composed of carbon atoms are formed on SiC surface [1]. These "carbon nanocaps" determined the structure of CNTs, such as the number of walls, diameter and chirality [2]. Therefore, clarifying the formation process of carbon nanocaps would lead to control of the CNT structure. In this study, we carried out *in situ* NEXAFS measurements at high temperature to investigate the formation process of carbon nanocaps.

2 Experiment

After HF etching, 6H-SiC(000-1) substrates were placed in a high vacuum chamber. Then, the samples were gradually heated to an intended temperature, followed by annealing under a H_2 ambient for 30 min. The sample temperature was monitored with a pyrometer, and the H_2 pressure was kept between $1\text{-}0.5\times10^{-4}$ Pa. After exhausting the H_2 gas, C K edge NEXAFS spectra were measured at BL-7A in Auger electron yield mode, keeping the sample at the heating temperature. For all temperature, the NEXAFS measurements were carried out with two different incident angles, θ, i. e. 30º and 90º, to investigate the orientation of the C-C bond.

3 Results and Discussion

Fig. 1(a) shows NEXAFS difference spectra of SiC(000-1) at 960ºC, where the spectral component of SiC was subtracted. By the subtraction of SiC component, π* resonance peak of C-C bond was clearly observed for the two incident angles. This indicates that the sublimation of Si atoms occurred and the formation of C-C bond began to start at this temperature. The relative intensity of π* resonance peak at normal incidence was weaker than that measured at θ =30º, suggesting that the C-C bond was inclined from the surface normal. NEXAFS spectra measured at 1380ºC are shown in Fig. 1(b). Both π* resonance peak and σ*bound exciton peak were clearly observed for the two incident angles. It should be noted that, in contrast to the spectra at 960ºC, the π* resonance peak at normal incidence was stronger than that for θ =30º at 1380 ºC. This indicates that the orientation of C-C bond changed as temperature rose. Taking into account the results of the QM/MD calculation

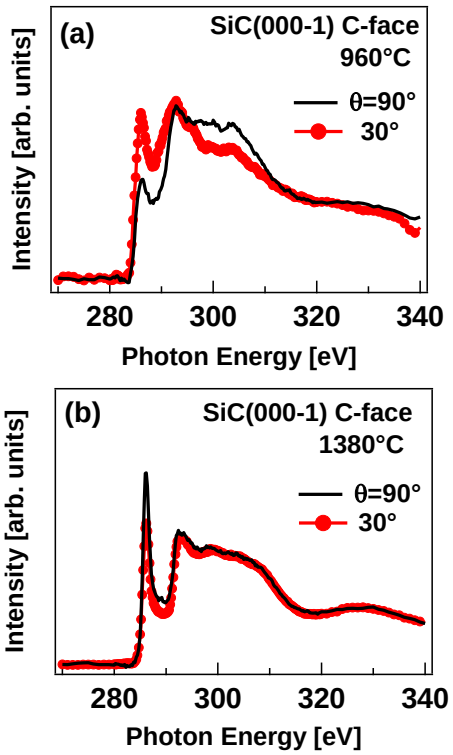

Fig. 1: *In situ* NEXAFS spectra for &H-SiC(000-1) at 960 and 1380 ºC.

[3], we consider that the graphene flakes formed on the surface were curved by the dangling-bonds on SiC(000-1) face, leading to the orientation change of the C-C bond and that this induced the formation of carbon nanocaps.

Acknowledgement

A part of this work was supported by the Japan Society for the Promotion of Science (JSPS), a grant-in-Aid for Scientific Research (c) 21510119. The NEXAFS measurements were performed under the approval of Photon Factory Program Advisory Committee (Proposal No. 2011G539).

References

[1] M. Kusunoki et al. Appl. Phys. Lett. **77** (2000) 531.
[2] T. Maruyama et al. Chem. Phys. Lett. **423** (2006) 317.
[3] Z. Wang et al. J. Phys. C111, **12960** (2007).
*takamaru@meijo-u.ac.jp

BL4B2/2011G544

添加剤との Co-crystal 化によるアシクロビルの物性の改善
Improvement of physicochemical character for Acyclovir by co-crystallization with additives.

米持悦生 [1*], 寺田勝英 [1], 藤井孝太郎 [2], 植草秀裕 [2]
[1] 東邦大学大学院薬学研究科、〒274-8510 船橋市三山 2-2-1
[2] 東京工業大学大学院理工学研究科　〒152-8550 東京都目黒区大岡山 2-12-1

1 はじめに

アシクロビルは最も重要な抗ウイルス薬の一つとして、内服、静注、外用と様々な投与形態で用いられているが、難溶解性に起因する課題を持っている。例えば、アシクロビルの経口固形製剤におけるバイオアベイラビリティーの低さについて、水への溶解性の低さとの関係性が指摘されている。また、局所皮膚適用製剤については、アシクロビル軟膏の経皮吸収性の低さと軟膏基剤中における薬物の熱力学的活動度の低さとの関係性が指摘されている。これらの課題は、アシクロビルの溶解性を改善することにより解決できると考えられるが、アシクロビルの溶解性改善は難しく、現在でも溶解性改善を目的とした様々な研究が報告されている。

固体医薬品における溶解性改善の手法としては、塩形成や結晶多形等、様々な手法がこれまでに研究されてきているが、近年では薬物の物性改善手法として、薬物と 1 種以上の化合物で複合体を形成する Cocrystal という技術が注目されている。Cocrystal は塩形成と異なり薬物をイオン化することなく利用できるため適用範囲が広く、さらに、原薬の相手化合物の候補として安全性の高い医薬品添加物を利用できるというメリットがある。そこで、本研究では、医薬品添加物を用いてアシクロビルの Cocrystal 化を試みた。本研究では、アシクロビルと医薬品添加物の相互作用を利用することで、医薬品添加物との間での Cocrystal 形成を試み、アシクロビルの溶解性と経皮吸収性を改善することを目的とした。

2 実験

(1) Cocrystal のスクリーニングとキャラクタリゼーション：様々な医薬品添加物を用いて、溶媒法及び粉砕法により行った。Cocrystal の可能性がある結晶複合体について、PXRD、TG/DTA、IR、DSC、HPLC によりキャラクタリゼーションを行った。

(2) Cocrystal 結晶構造解析：放射光粉末 X 線回折測定データから結晶構造解析ソフトウェア DASH を用いて Simulated Annealing 法による実空間法により結晶構造解析を行った。得られた初期構造はソフトウェア GSAS を用いてリートベルト法により精密化を行った。

(3) Cocrystal の溶解性評価：Cocrystal 化によるアシクロビルの溶解性改善効果を確認するために、得られた cocrystal について、精製水、pH 6.8 リン酸緩衝液、エタノールに対する飽和溶解度を測定した。また、pH 6.8 リン酸緩衝液を用いて静止円盤法による溶出試験を実施し、初期溶出速度を確認した。

3 結果および考察

(1) Cocrystal のスクリーニングとキャラクタリゼーション：スクリーニングの結果、アシクロビルと酒石酸の組み合わせで Cocrystal が形成されることを見出した（この Cocrystal は以下 ACV-TA cocrystal と略す）。アシクロビル（無水物 1 型及び 2 型、2/3 水和物、2 水和物）、酒石酸、ACV-TA cocrystal 及び ACV-CA 非晶質の PXRD パターンを図 1 に示した。ACV-TA cocrystal 特有の PXRD パターンはアシクロビルや酒石酸と区別できるものであった。ACV-CA 非晶質においては 2θ が 5° から 25° の範囲でハローパターンとなった。さらに、物性の詳細を TG/DTA、IR、DSC、HPLC により評価した結果、ACV-TA cocrystal については、溶媒和結晶ではなく、アシクロビルのプリン骨格上の窒素原子と酒石酸のカルボニル基やヒドロキシル基と水素結合をすることで、1:1 のモル比で Cocrystal を形成していることが確認された。

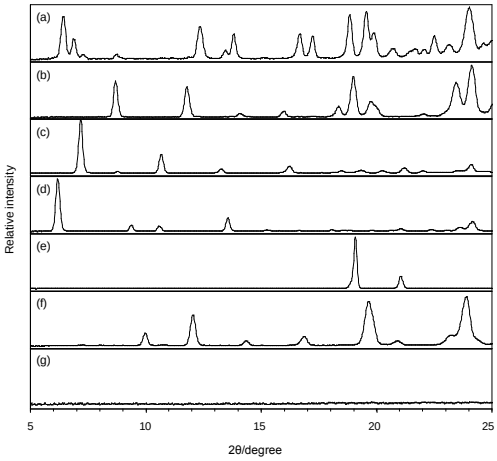

図 1 ：PXRD patterns of acyclovir (anhydorous form 1 (a), anhydrous form 2 (b), two-thirds hydrate (c), dihydrate (d)), tartaric acid (e), ACV-TA cocrystals (f), ACV-CA amorphous (g).

(2)　Cocrystal 結晶構造解析：ACV-TA cocrystal の結晶構造を図.2 に示した。キャラクタリゼーションで確認されたように、ACV-TA cocrystal におけるアシクロビルと酒石酸のモル比は 1:1 であった。また、アシクロビルの結晶構造中で形成されていたプリン骨格のスタッキング構造に酒石酸が入り込むことにより、結晶のパッキングが崩れている可能性が示唆されたため、Cocrystal 化による溶解性改善効果が期待された。

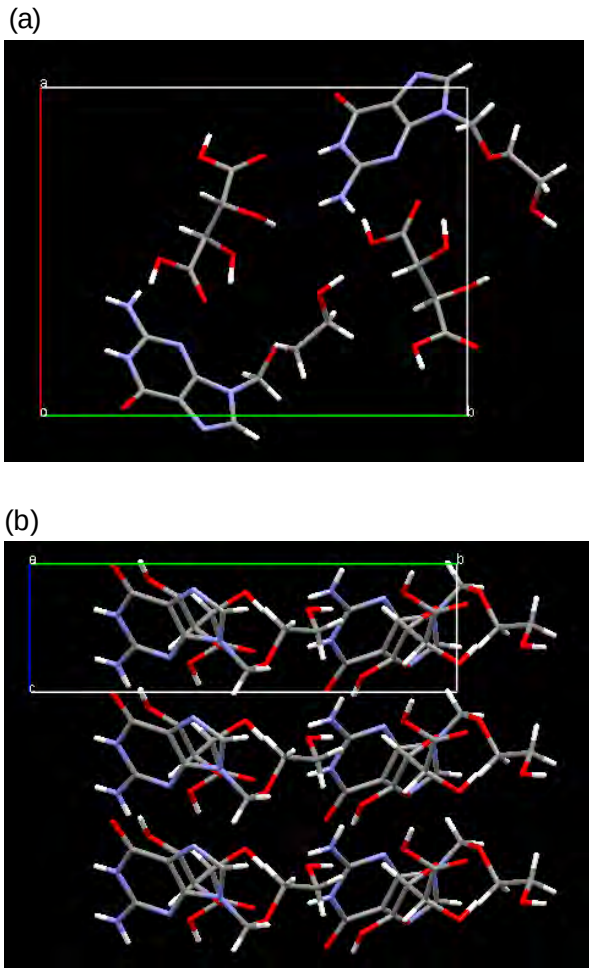

図 2. Packing diagram along the ab plane for ACV-TA cocrystal (a) and the bc plane for ACV-TA cocrystal (b).

(3)　Cocrystal の溶出試験：アシクロビル無水物 2 型、アシクロビル - 酒石酸物理的混合物（ACV-TA-PM）、ACV-TA cocrystal の各溶媒に対する飽和溶解度を図 3 に示した。また、アシクロビル結晶多形、ACV-TA-PM、ACV-TA cocrystal の溶出プロファイルを図 4 に示した。ACV-TA cocrystal は、溶解度及び初期溶出速度ともに、アシクロビル結晶多形及び ACV-TA-PM と比較し、顕著に改善した。

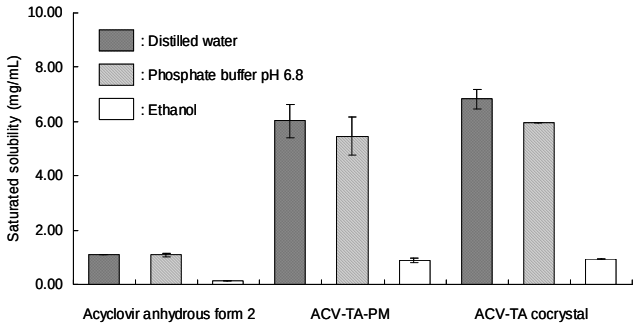

図 3. Dissolution profiles of acyclovir polymorph forms, ACV-TA-PM and ACV-TA cocrystals in phosphate buffer (error bars show SD, n=3).

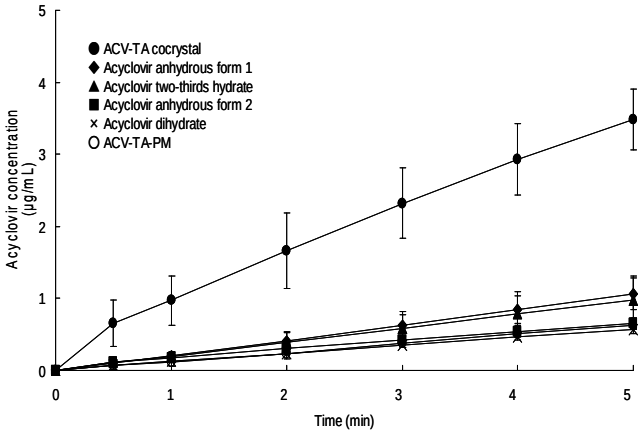

図 4. Dissolution profiles of acyclovir polymorph forms, ACV-TA-PM and ACV-TA cocrystals in phosphate buffer (error bars show SD, n=3).

4　まとめ

本研究において、アシクロビルは医薬品添加物と相互作用させることで、Cocrystal 化が可能であることを見出した。さらに、アシクロビルは Cocrystal 化により溶解性が顕著に向上したことで、経口固形製剤における有用性の向上が期待できた。[1] 本研究で見出したアシクロビルの Cocrystal 化による溶解性の改善は、臨床現場におけるアシクロビルの有用性をさらに高められる可能性を秘めた技術であると言える。

参考文献

[1] T. Masuda *et al.*, Int. J. Pharm., **422** (2012) 160.

* yone@phar.toho-u.ac.jp

AR-NE1/2011G545

$NaCoF_3$の室温高圧ポストペロブスカイト転移
Postperovskite transition in $NaCoF_3$ at room temperature under high pressure

遊佐　斉[1*], 亀掛川卓美[2]
[1]物質・材料研究機構　〒305-0044 つくば市並木 1-1
[2]物質構造科学研究所　〒305-0801 つくば市大穂 1-1

1 はじめに

2004 年、ペロブスカイト構造より高密度の $CaIrO_3$ 構造（いわゆるポストペロブスカイト）が $MgSiO_3$ において発見されたことは、地球科学の分野において大きな反響となるだけではなく、物質・材料科学の分野においても、ABX_3 型化合物における $CaIrO_3$ 構造の普遍性を再認識するきっかけともなった。それと同時に、$CaIrO_3$ 構造に対する理解も進み、ペロブスカイト構造からの歪みの帰結として $CaIrO_3$ 構造が存在すること、BX_6 八面体が崩壊せずに維持されること、また、その構造の類似性ゆえ密度増が高々2%程度にとどまることなどが明らかなった。その一方で、変位型の転移機構が優勢であるにもかかわらず、室温高圧下でポストペロブスカイト相転移が容易に誘起されないという疑問点も生じている。この点を検証するために、我々は酸化物に比べ圧縮されやすいフッ化物ペロブスカイト($Na\mathit{B}F_3$: *B*=Co, Ni, Fe)について、相転移実験を系統的におこなっている。本報告では、$NaCoF_3$ についての室温高圧その場観察実験について報告する[1]。

2 実験

高圧下粉末 X 線その場観察実験に用いた試料は、川井型高圧装置において 15GPa, 1273K で合成した $NaCoF_3$ ペロブスカイト相($GdFeO_3$ 型)である。実験は、ダイヤモンドアンビルセル(DAC)を用い、メタノール・エタノール・水混合溶液を圧力媒体とし、室温にておこなった。AR-NE1 にて 30keV の単色 X 線により、イメージングプレート(IP)により回折 X 線を検出した。解析は GSAS による多相プロファイルフィットによりおこなった。なお、圧力スケールには試料中に混合した金の回折線を用いた。

3 結果および考察

その場観察 X 線実験の結果、約 12GPa 付近からポストペロブスカイトへの相転移が観察され始めたが、約 20GPa にいたっても完全にポストペロブスカイト単相にはならなかった(図１)。しかしながら、1 気圧に減圧しても構造を維持していた。これらの点は、高温においてのみ相転移が進み、かつ減圧時にアモルファス化する酸化物ポストペロブスカイトと対照的である。格子定数から計算される BX_6 八面体の回転角は、圧力に対して大きく変化している(図２)。このことは、フッ化物ペロブスカイトが単に圧縮されやすいだけではなく、その異方的な圧縮挙動がポストペロブスカイト転移機構に大きく関係していることを示している。

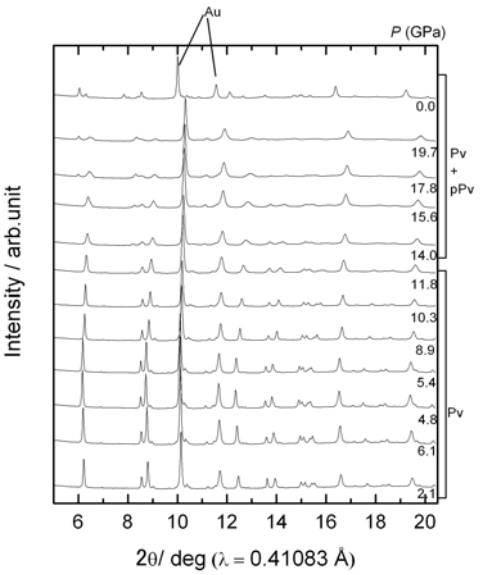

図１：室温加圧による X 線回折パターンの代表的変化。 Pv は $GdFeO_3$型、pPv は $CaIrO_3$型を示す。

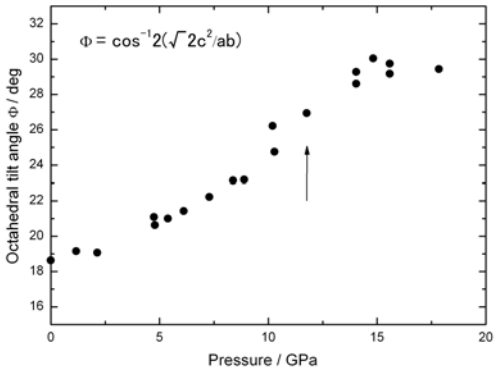

図２：格子定数から計算した pV(*Pnma*)における $NaCoF_6$ ペロブスカイトにおける CoF_6 八面体の回転角。矢印は pPv への転移開始圧力。

謝辞

実験に用いた試料は、学習院大学白子雄一博士により合成されました。ここに感謝致します。

参考文献

[1] H. Yusa *et al*., Inorg. Chem., **51** (2012), in press.

*yusa.hitoshi@nims.go.jp

14A/2011G549

Space Group Determination of the Magnetically Induced Ferroelectric Phase of Multiferroic YMn_2O_5

Terutoshi Sakakura[1], Takahiro Nakano[1], Hiroyuki Kimura[1], Yoshihisa Ishikawa[1], Yukio Noda[1*]
[1]Institute of Multidisciplinary Research for Advanced Materials, Tohoku University, 2-1-1 Katahira, Aoba-ku, Sendai 980-8577

1 Introduction

Multiferroic YMn_2O_5 belongs to a centric space group *Pbam* and shows paraelectric properties at RT, and the spontaneous polarization grows along a b-axis about 40K by cooling [1]. Although the atomic displacement pattern, which might originate the spontaneous polarization, is one of the most significant and interesting topics of structural science of YMn_2O_5, even the space group symmetry in the ferroelectric phase is not determined yet without ambiguity. In our previous study at PF4C and SPring-8 BL02 using a four-circle diffractometer, super lattice reflections indicating the formation of twice as large unit cell along the *c*-direction referred to the paraelectric phase were observed. However, since the contributions of the displacements to diffracted intensities are so small and easily contaminated by false intensities of multiple diffractions, space group determination was not fully succeeded at that time. This time, applying psi-rotation method and changing photon energy to avoid simultaneous reflections, we tried space group determination again.

2 Experimental

Single crystals of YMn_2O_5 were grown by the flux method and grinded into sphere of 245 μm in diameter and used for X-ray diffraction measurement at BL14A. Psi-scan simulation software MCD++ was prepared and optimum four-circle angles setting to avoid simultaneous reflection condition were calculated for every reflection. All the diffracted intensities were measured at the calculated angles using the four-circle diffractometer installing avalanche photodiode (APD) detector whose count loss is less than 1% up to 10^7 cps. Compressed cold helium gas was directly flowed onto the specimen to cool the sample. Temperature dependencies of diffracted intensities of extinction-reflections in paraelectic phase and superlattice reflections were measured around ferroelectric transition temperature. Since the diffracted intensities of these reflections are more than 10^6 times less than that of the strongest one, complete avoidance of multiple reflections are not easy.

Figure 1 shows peak profiles of (3 0 1) reflections above and below the transition temperature and exhibits that contamination in 1.0 Å is much less than in 0.723 Å. Therefore, testing with various wavelengths is crucially important to judge the observed peak is real one or spurious one.

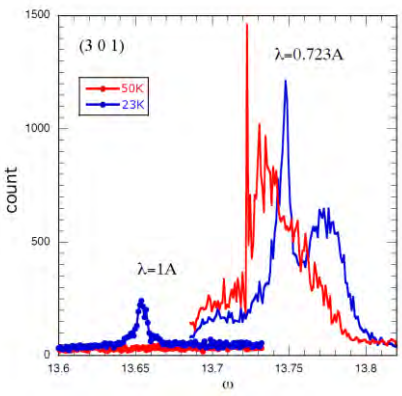

Figure 1: Peak profiles of (3 0 1) reflections above and below *Tc* for different incident X-ray wavelengths λ=1Å and λ=0.723Å. ; 23K in blue, 50K in red.

3 Results and Discussions

Figure 2 shows a part of the results. A superlattice reflection (0 0 4.5) and an extinction-reflection (3 0 1) in paraelectric phase are shown, and temperature dependency of these two are synchronize below the transition temperature. From these, the space group of ferroelectric phase should be $Pb2_1m$ which removed the *a*-glide plane from *Pbam*. An extinction reflection due to *b*-glide planes vertical to ***a*** (0 5 5) is also observed with this wavelength but shows no temperature dependency, thus, this is ascribed to simultaneous reflections.

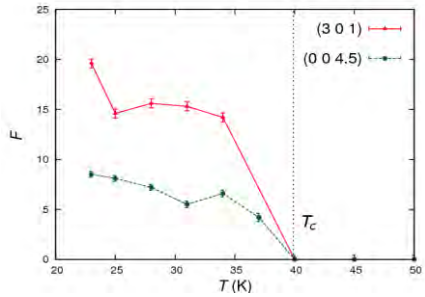

Figure 2: Temperature dependency of diffracted intensities; superlattice reflection (0 0 4.5), and extinction-reflection at RT due to *a*-glide planes vertical to ***b*** (3 0 1). Relatively lower energy of 0.85 angstrom X-ray was used.

References
[1] M.Fukunaga, et.al, JPSJ **79**, 054705 (2010)
* ynoda@tagen.tohoku.ac.jp

18C/2011G555

X-ray diffraction study of CeT_2Al_{10} (T=Fe, Ru, Os) at high pressures

Yukihiro Kawamura[1*], Kazuki Matsui[1], Takayuki Kuwayama[1], Takuma Kawaai[1], Satoshi Yamaguchi[1], Yusuke Nishijima[1], Junichi Hayashi[1], Keiki Takeda[1], Chihiro Sekine[1], Takashi Nishioka[2]

[1]Muroran Institute of Technology, Muroran, Hokkaido 050-8585, Japan

[2]Graduate School of Integrated Arts and Sciences, Kochi University, Kochi 780-8520, Japan

1 Introduction

CeT_2Al_{10} (T=Fe, Ru, Os) crystallizes in the orthorhombic $YbFe_2Al_{10}$-type (space group *Cmcm* No. 63) crystal structure [1]. These compounds exhibit a long range ordering with unusually high transition temperature (T_0) and Kondo semiconducting behavior [2-4]. The long range ordering suddenly disappears under high pressures (at 2 GPa (T = Os) and 4 GPa (T = Ru)). In order to investigate a structural change around the pressures the order disappears, we performed synchrotron X-ray diffraction study at room temperature under high pressure.

2 Experiment

Single crystals of CeT_2Al_{10} (T=Fe, Ru, Os) were grown by using Al self-flux method. The single crystals of CeT_2Al_{10} were crushed into a fine powder. The X-ray diffraction measurements under high pressures were conducted using synchrotron radiation. An imaging plate was used as a detector. The pressure was applied by diamond anvil-type pressure cell. A 4:1 mixture of methanol/ethanol was used as a pressure-transmitting medium. The applied pressure was determined from a pressure shift in the fluorescence spectrum of ruby.

3 Results and Discussion

No additional peak is observed up to 10 GPa on CeT_2Al_{10} (T = Fe, Ru, Os), indicating no structural change. Figure 1 shows the lattice parameters of CeT_2Al_{10} normalized at ambient pressure. All lattice parameters decrease monotonically with increasing pressure. The monotonic decrease of lattice parameters indicates that reduction of a long range ordering at 2 GPa on $CeOs_2Al_{10}$ and that at 4 GPa on $CeRu_2Al_{10}$ are not attributed to a structural distortion.

While the decrease ratio of lattice parameters along a-axis and c-axis are almost the same, that along b-axis is the smallest in every compound. The high-energy syncrotron x-ray powder diffraction experiments of $LaRu_2Al_{10}$ clarified the charge density distribution [5]. The charge density around Ru site and Al5 site are connected along b-axis. We propose that the hardness of the lattice parameter along b-axis is attributed to this charge density connecting Ru and Al5 site.

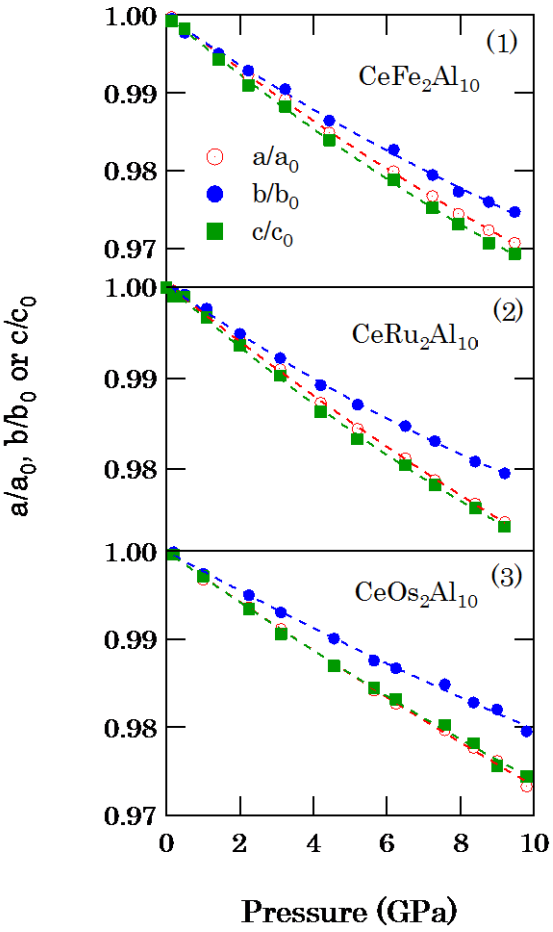

Fig. 1: The lattice parameters normalized at ambient pressure a/a_0(red, open circle), b/b_0(blue, closed circle), c/c_0(green, closed square) on $CeFe_2Al_{10}$ (1), $CeRu_2Al_{10}$ (2) and $CeOs_2Al_{10}$ (3).

Acknowledgement

The authors gratefully acknowledge the support from Muroran Institute of Technology (a grant for the Kidorui (Rare Earth) Program).

References

[1] V. M. T. Thiede *et al.*, J. Mater. Chem. **8** (1998) 125.
[2] Y. Muro *et al.*, J. Phys. Soc. Jpn. **78** (2009) 083707.
[3] A. M. Strydom : Physica B **404** (2009) 2981.
[4] T. Nishioka *et al.*, J. Phys. Soc. Jpn **78** (2009) 123705.
[5] H. Tanida *et al.*, Phys Rev B **84** (2011) 115128.

* y_kawamura@mmm.muroran-it.ac.jp

6A/2011G589

Lamellar-to-Onion and Onion-to-lamellar Transition Processes with Varying Temperature under Shear Flow in a Nonionic Surfactant/Water System

Daijiro SATO, Youhei KAWABATA, and Tadashi KATO*
Department of Chemistry, Tokyo Metropolitan University
1-1 Minami-Osawa, Hachioji, Tokyo 192-0397, Japan

Introduction

In the past 20 years, much attention has been paid to the effects of shear flow on the structure of the lamellar phase. Among them, the most striking result may be the transition from the lamellar phase to the "onion phase" where all the space is filled by multilamellar vesicles alone [1]. Recently, we have reported the lamellar-to-onion transition with *increasing* temperature under a constant shear rate in the lamellar phase of a nonionic surfactant $C_{16}E_7$/water system (C_nE_m is an abbreviation of $C_nH_{2n+1}(OC_2H_4)_mOH$) by using simultaneous measurements of shear stress/small-angle light scattering and shear stress/small angle X-ray scattering (rheo-SAXS) [2, 3]. We have also found reentrant lamellar-onion (lamellar → onion →lamellar) transition with increasing temperature for a $C_{14}E_5$/water system [4]. In the present study, we have performed rheo-SAXS experiments near the the lower transition temperature to compare the transition processes of the lamellar-to-onion transition with increasing temperature and onion-to-lamellar transition with decreasing temperature.

Experimental

A rheometer AR550 (TA Instruments) is modified for rheo-SAXS experiments. Details of the cell have been reported previously [2]. Measurements were performed on the beamline 6A. The scattered beam was recorded using the CCD area detector covering the scattering vector range from 0.15 to 2.5 nm^{-1}.

Results

Figure 1 shows temperature dependences of the diffraction-peak intensity in each direction and shear stress at the shear rate of 3 s^{-1} in heating (upper panel) and cooling (lower panel) processes in a $C_{14}E_5$/water system (50 wt%). In the heating process, the most lamellae are oriented with the layer normal along the velocity gradient direction at 32 °C. As the temperature exceeds 34 °C, the peak intensity in the velocity gradient direction abruptly increases and takes a maximum at 35°C, just before the increase in the shear stress. As the temperature increases by 0.5 K, the intensity in the gradient direction rapidly decreases and instead, the intensity in the neutral direction increases. As the temperature increases further, the intensities in all the directions become equal, corresponding to the formation of onions. These results are similar to the results for the $C_{16}E_7$/water system [3].

In the cooling process, the temperature dependences

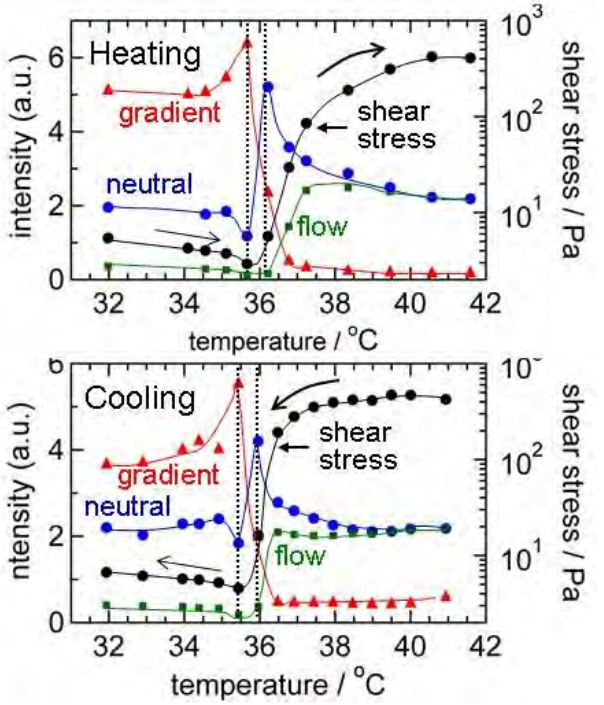

Fig. 1 Temperature dependences of the diffraction-peak intensity for each direction and shear stress at the shear rate of 3 s^{-1} in heating (upper panel) and cooling (lower panel) processes in a $C_{14}E_5$/water system (50 wt%).

in the peak intensity and the shear stress are very similar to those in the heating process although the slight hysteresis (~0.3 K) is observed. This suggests that the onion-to-lamellar transition process is a reverse process of the lamellar-to-onion transition process and that the intermediate structures are not transient but characteristic to temperature.

References

[1] D. Roux, in "Nonequilibrium Dynamics, Metastability and Flow" ed. by M. E. Cates, M. R. Evans, and P. Osborne, Institute of Physics Publishing, Bristol (2000).
[2] Y. Kosaka, M. Ito, Y. Kawabata, and T. Kato, *Langmuir*, **26**, 3835 (2010).
[3] M. Ito, Y. Kosaka, Y. Kawabata, and T. Kato, *Langmuir*, **27**, 7400 (2011).
[4] D. Sato, Y. Kawabata, and T. Kato, *Photon Factory Activity Report 2010*, #28, Part B, 154 (2011).

* kato-tadashi@tmu.ac.jp

3A/2011G610, 2010PF-17, 2010PF-31,

Fe 置換した $La_{0.5}Sr_{1.5}MnO_4$ における X 線誘起相転移の研究
X-ray Photo-induced Phase Transition in Fe-doped Layered Manganite

八巻佑樹 [1,2*], 山﨑裕一 [2], 中尾裕則 [2], 村上洋一 [2], 金子良夫 [3,4], 十倉好紀 [3,4,5]
[1] 東北大学大学院理学研究科、〒980-8578 宮城県仙台市青葉区荒巻字青葉 6-3
[2] 高エネルギー加速器研究機構　構造物性研究センター、〒305-0801 つくば市大穂 1-1
[3] ERATO Multiferroics Project、〒113-8656 東京都文京区本郷 7-3-1
[4] 理化学研究所　強相関量子科学研究グループ、〒351-0198 埼玉県和光市広沢 2-1
[5] 東京大学大学院工学系研究科、〒113-8656 東京都文京区本郷 7-3-1

1 はじめに

光誘起相転移は、高速に物質の状態を変化できることから、応用上の観点からも盛んに研究されている。我々は Mn サイトに不純物を置換した $La_{0.5}Sr_{1.5}MnO_4$ において、電荷・軌道秩序相と強磁性相との間の双方向の X 線光誘起相転移を観測することに成功した。

2 実験

本研究では $La_{0.5}Sr_{1.5}Mn_{0.97}Fe_{0.03}O_4$ の単結晶を用いて、電荷・軌道秩序とともに生じる格子歪みを反映した(1/4 7/4 0)反射の散乱強度の測定を行った。入射 X 線のエネルギーは 6.5 keV で、BL-3A の 4 軸回折計を用いて実験を行った。また X 線照射下での交流磁化率の測定は、図 2 に示すようなコイルとロックインアンプ(LA)を用いて行った。

3 結果および考察

図 1 は 10 K と 70 K での格子歪みを反映した散乱強度の X 線照射時間依存性を示している。10 K における測定では、電荷・軌道秩序転移温度である 140 K よりも十分に高い温度から 10 K まで X 線を照射しない状態で温度を下げた後に測定を行っている。X 線の照射とともに散乱強度が減少し始め（図中の on の領域）、X 線を当てていない状態（図中の off）では散乱強度は変化していない。この結果から散乱強度の減少は X 線の照射によって生じていることが分かる。一方で 10 K において強度が変化しなくなった状態から X 線を照射しないで 70 K に温度を上げて測定を行ったところ、10 K の場合とは逆に X 線の照射によって散乱強度が増加した。こちらも X 線を当てていない状態では強度が変化しないことから、X 線の照射によるものだと分かる。これらの結果から、X 線の照射によって 10 K では電荷・軌道秩序が抑制され、70 K ではより秩序化していると考えられる。

図 2 は 10 K、70 K における交流磁化率の変化量の X 線照射時間依存性である。変化量は、それぞれの照射時間における交流磁化率の値から初期値を引くことで求めている。これによって X 線を照射することで交流磁化率が、10 K では増加し、70 K では減少しているのが分かる。この系はもともと低温で CE タイプと呼ばれる反強磁性磁気秩序を示し、交流磁化率の増加・減少は強磁性成分の増加・減少に対応しているため、10 K では反強磁性/電荷・軌道秩序相から強磁性/電荷・軌道無秩序相への転移が、70 K ではその逆の転移が X 線の照射によって起こっていると考えられる。

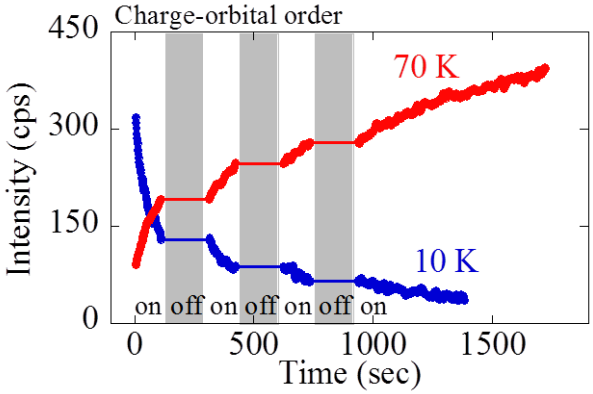

図 1：$La_{0.5}Sr_{1.5}Mn_{0.97}Fe_{0.03}O_4$ における 10 K、70 K での格子歪みを反映した散乱強度の X 線照射時間依存性。

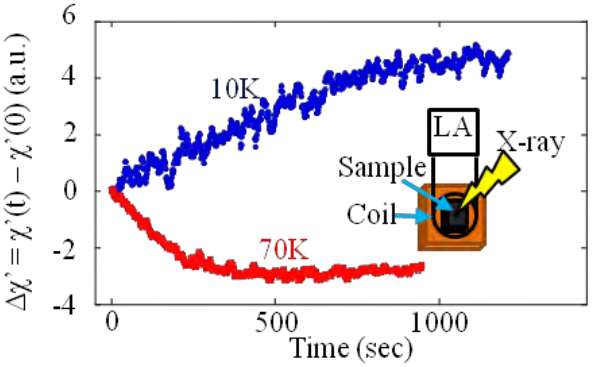

図 2：$La_{0.5}Sr_{1.5}Mn_{0.97}Fe_{0.03}O_4$ における 10 K、70 K での交流磁化率の X 線照射時間依存性と交流磁化率の測定における実験配置の概念図(inset)。

* yamaki@post.kek.jp

9C, 10C/2011G612

SAXS Studies on Deformation of the BCC Lattice for Spherical Microdomains Formed in an Elastomeric Block Copolymer Film Along Several Cycles of Uniaxial Stretching (Loading and Unloading)

Madoka UOZUMI, Sono SASAKI, Shinichi SAKURAI*
Department of Bio-based Materials Science, Graduate School of Science and Technology, Kyoto Institute of Technology, Matsugasaki, Sakyo-ku, Kyoto 606-8585, Japan

In block copolymers comprising rubbery and glassy chains with the glassy minor component, spherical microdomains are formed due to microphase separation, which are dispersed in the rubbery matrix. Such a microphase-separated structure imparts elastomeric properties to the material since the glassy spherical microdomains play the role of a crosslinker. Meanwhile, they can be melt-processed above the glass transition temperature of the glassy component. Thus, they are referred to as a thermoplastic elastomer. The microphase-separated structures in block copolymers have been studied for many decades and much has been uncovered, such as that spherical microdomains regularly order in the body-centered cubic (bcc) lattice. We recently reported that the bcc lattice achieved enhanced packing regularity in the direction parallel to the uniaxial stretching. In order to reveal structure-property relationship for this system, we conducted two-dimensional small-angle X-ray scattering (2d-SAXS) along several cycles of uniaxial stretching (loading and unloading processes).

The material used is a polystyrene-block-poly(ethylene-co-but-1-ene)-block-polystyrene (SEBS8) triblock copolymer, having the volume fraction of (PS) polystyrene of 0.084, Mn = 6.7×10^4, and Mw/Mn = 1.04 where Mn and Mw are the number- and weight-average molecular weight, respectively. It should be also noted that the glass transition temperatures (Tg), for PS and PEB (poly(ethylene-co-but-1-ene)) are 100 °C and −58 °C, respectively, indicating that the PS domains play a role of physical crosslinking in the rubbery PEB matrix.

The SAXS measurements were performed at SAXS beamline BL-10C in the Photon Factory of the High Energy Accelerator Research Organization, Tsukuba, Japan. The wavelength of the X-rays was tuned to 0.1488 nm. RAXIS-VII (Rigaku) was used as the area detector. The measured two-dimensional SAXS pattern was converted to the one-dimensional profile by conducting sector averaging in the direction parallel or perpendicular to the stretching direction.

Based on the position of the first-order peak, the domain spacing d was evaluated, and shown in the plot against the stretching ratio α in Figure 1. Note that the solid red lines and curves indicate the Affine deformation. It is surprisingly very nice that the data points fall down on the curves very well for the first stretching process. This means that the bcc lattice of the hard (spherical) domains (microscopic strain) are exactly deformed in the same magnitude of the macroscopic strain loaded externally. On the other hand, we found huge deviation for the first unloading process where the mechanical strain was gradually released from uniaxially-stretched sample. However, further close examination reveals that the slope of the behavior for $d_{//}$ vs. α is coincident with the Affine approximation. The deviation is considered to be due to the offset value of α at which the $d_{//}$ value becomes unchanged in the unloading (relaxing) process. Note here that the offset value of α should be referred to as the remaining strain. For the second loading (stretching) process, one can find a bit of the remaining strain, and the slope of the behavior for $d_{//}$ vs. α is coincident with the Affine approximation. Furthermore, almost identical behavior was detected for the second unloading process as compared to that observed for the first unloading process. For the third cycle of the loading-and-unloading process, almost similar behavior was found as compared to that for the second cycle.

*shin@kit.jp

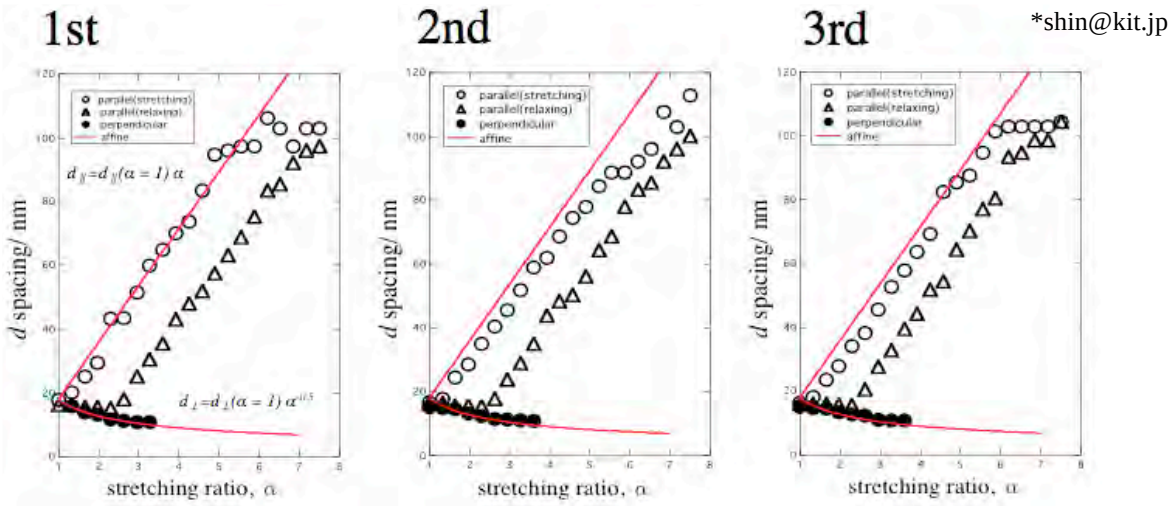

Figure 1. Changes in the domain spacing d with the stretching ratio α, along the cycles of uniaxial stretching (loading and unloading process). $d_{//}$ and $d_{//}$ stand for the $d_{\perp}$ values parallel and perpendicular to the stretching direction, respectively.

6A, 9C/2011G613

水平方向の温度勾配下で結晶化させた ポリエチレングリコールの結晶ラメラの自発配向

Spontaneous Orientation of Crystalline Lamellae upon the Directional Crystallization of Poly(ethyleneglycol) under a Temperature Gradient

木村 剛, 佐々木 園, 櫻井 伸一
京工繊大院バイオベースマテリアル、〒606-8585 京都市左京区松ヶ崎御所海道町

1 はじめに

温度勾配は温度が場所によって連続的かつ直線的に変化する外場の一種であり、結晶性高分子を温度勾配下で結晶化させると、温度勾配に沿って連続的に結晶化温度の異なる系が成立する。このような系では、等温結晶化とは異なった結晶成長過程や高次構造を有することが期待できる。そこで、当研究室が開発した水平方向に精度よく温度勾配を付与することができる装置[1]を用いて、ポリエチレングリコール(PEG)を温度勾配下で結晶化させ、その結晶成長過程の偏光顕微鏡観察を行った。完全に結晶化させた後、結晶ラメラ構造の解析を小角 X 線散乱(SAXS)法によって行った。

2 実験

用いた試料は分子量 2.0×10^4 (和光純薬)の PEG であり、DSC 測定で求めた融点は 63.5°Cである。この試料を 3.0 mm の間隙中に詰め、この間に直線的な温度勾配を与えた(試料の厚さは 1.0 mm)。まず最初に、左右の温度を融点より十分に高い温度にして試料を完全に融解させた。その後、瞬時に高温側が 60°C、低温側が 40°Cになるように試料の左右の温度を再設定し、この状態を 90 分間保持した。この間、偏光顕微鏡観察を行った。最後に、氷水中で急冷した。結晶ラメラの配向状態の解析は高エネルギー加速器研究機構の BL-6A と 9C で２次元小角 X 線散乱測定(2d-SAXS)によって行った。具体的には、温度勾配方向に X 線ビーム(ビームの直径は 0.50 mm)の入射位置を 0.12 mm ずつずらせながら室温で測定を行った。

3 結果および考察

Fig.1 は低温側から、(a) 0.48 mm, (b) 2.04mm の位置に X 線ビームを入射して測定した結果である。これらの位置での熱処理（結晶化）温度はそれぞれ、(a) 43.3°C, (b) 54.3°C に対応する。q は散乱ベクトルの大きさであり、$q = (4\pi/\lambda)\sin(\theta/2)$で定義される。λ は X 線の波長、θ は散乱角である。Fig.1(a)(b)で子午線方向付近の１つの方向に散乱が集中していることがわかる。この散乱は結晶ラメラの長周期に起因しているので、結晶ラメラが温度勾配方向に配向しているといえる。結晶ラメラの配向傾向を議論するため Fig.1 の結果から配向度と配向角を求めた(Fig.2)。Fig.2 の曲線はビームの広がりを考慮して求めた真の配向係数である。Fig.2 から、結晶化温度が 50°C以下では、結晶化温度が高温側になるにつれて結晶ラメラがより高度に配向すること、及び、結晶ラメラは温度勾配に対して完全に平行ではないことがわかった。一方、結晶化温度が 50°C以上では、結晶ラメラが高度に配向しており、配向角はほぼ 90°であること、すなわち結晶ラメラが温度勾配に対して平行に配向していることが明らかになった。Fig.3 は温度勾配を付与してからの経過時間 (a) 120 秒後, (b) 470 秒後, (c) 5400 秒後での偏光顕微鏡(クロスニコル)観察結果である。Fig.3(a) からわかるように、低温側(40°C) で核形成が起こり、放射状に結晶成長するが、温度勾配方向と垂直な方向への成長はやがて互いに衝突する。これに対して温度勾配に平行方向に成長しているラメラはそのまま成長を遂げることができる。そのため、高温側では温度勾配方向の成長が選択的に支配的になることがわかる。(Fig.3(b)と(c))。このような成長を模式的に図示したものが Fig.3(d)である。矢印は結晶ラメラの成長方向を示している。

参考文献

[1] 保田皓是, 山根宗昭, 山西弘樹, 山田康博, 櫻井伸一, 材料, *60*, 57 (2011)

*shin@kit.jp

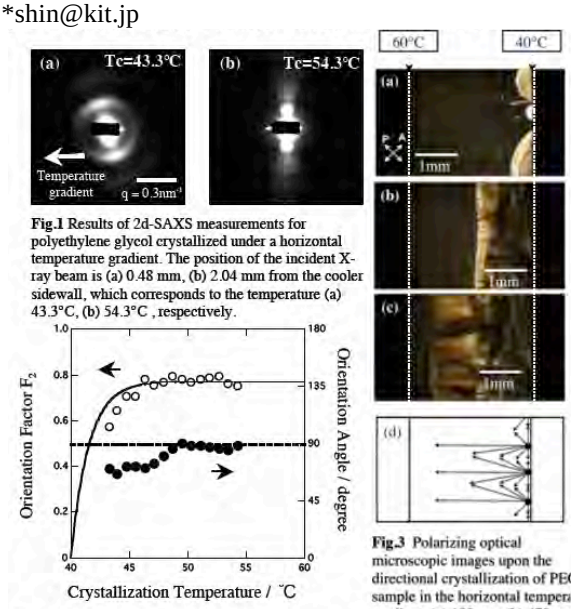

Fig.1 Results of 2d-SAXS measurements for polyethylene glycol crystallized under a horizontal temperature gradient. The position of the incident X-ray beam is (a) 0.48 mm, (b) 2.04 mm from the cooler sidewall, which corresponds to the temperature (a) 43.3°C, (b) 54.3°C , respectively.

Fig.2 Orientation factor F_2 (○), and the orientation angle (●) as a function of the crystallization temperature. The solid curve indicates the true value of F_2, which is obtained by deconvolution of the observed values.

Fig.3 Polarizing optical microscopic images upon the directional crystallization of PEG sample in the horizontal temperature gradient (a) 120 sec, (b) 470 sec, (c) 5400 sec elapsed. (d) Schematic diagram for the growth of crystalline lamellae . Arrows indicate growth direction of the crystalline lamellae.

NW10A/2011G617

Local Structure in fast-ionic conductive AgI-As_2Te_3 Glasses

Takeshi USUKI*[1], Rie IIZAWA[1], Yoshinori ABIKO[1], Toshio NASU[2]
[1]Depertment of Material and Biological Chemistry, Yamagata Uni., Yamagata 990-8560, Japan
[2]Faculty of Science, Art and Education, Yamagata Uni., Yamagata 990-8560, Japan

Introduction

Many kinds of studies for ionic conducting glasses, especially for AgI-doped glass systems, have been carried out from academic and practical points of view [1,2]. Recently, it was demonstrated that the $(AgI)_x(As_2Te_3)_{100-x}$ glass powders have surprisingly been obtained up to 80 mol% AgI content by the mechanical milling method. Furthermore the progression of amorphization and the appearance of fast ionic conduction in $(AgI)_x(As_2Te_3)_{100-x}$ system have been investigated. This paper will present preliminary results of XAFS experiments on AgI-As_2Te_3 glasses.

Experimental procedure

$(AgI)_x(As_2Te_3)_{100-x}$ (x = 20, 40, 50, 60, 70 and 80) samples were prepared at room temperature by means of the mechanical milling method (milling time = 0, 0.5, 1, 2, 10, 20 and 40 hours) using a planetary ball mill equipment.

EXAFS studies for amorphous samples were carried out for Ag, Te and I K-edges at NW10A station, KEK. The intensity of the incident beam, I_0, and that of the transmitted beam, I, were measured using ionization chambers. The measurement temperature was set to be 20K.

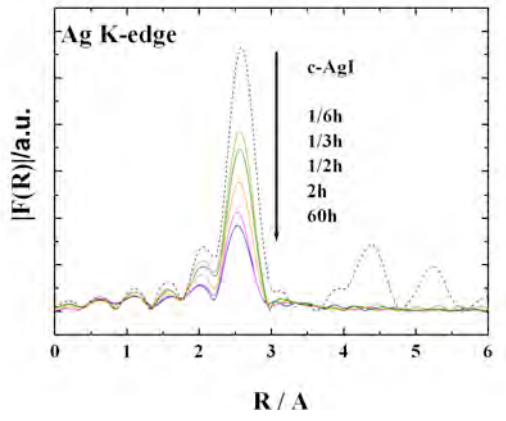

Fig. 1 Magnitude of Fourier transformation of the EXAFS oscillation function at the Ag K-edge for $(AgI)_{80}(As_2Te_3)_{20}$ glass.

Results

Figure 1 provides the magnitude of the Fourier transformation, $|F(R)|$, of the EXAFS oscillation function at Ag K-edge for the $(AgI)_{40}(As_2Te_3)_{60}$ samples at the different milling stages. The position of a main peak in $|F(R)|$ shifts slightly to shorter R with increasing milling steps. The intensity of this peak significantly decreases, implying the decrement of the coordination number of iodine atoms around the mobile Ag ions. These tendencies are reasonably confirmed by the result for I K-edge EXAFS data.

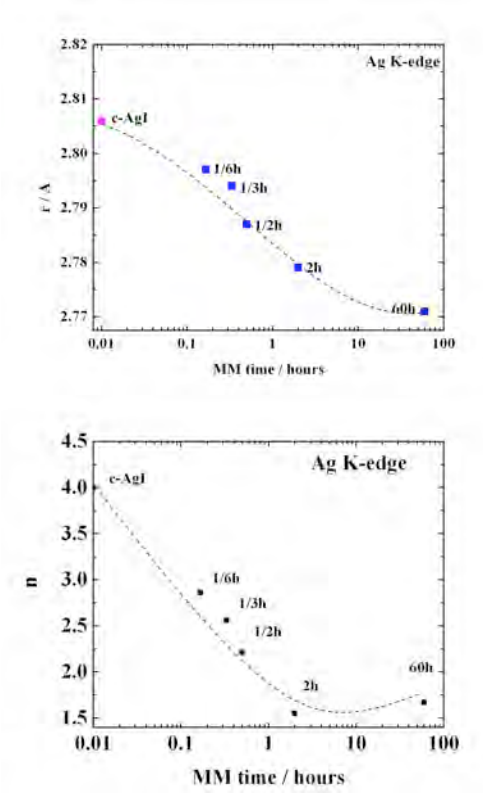

Fig. 2 Milling time dependence of the interatomic distance and the coordination number of Ag-I pairs in $(AgI)_{80}(As_2Te_3)_{20}$.

The milling time dependences of the interatomic distance, $r_{Ag\text{-}I}$, and the coordination number, $n_{Ag\text{-}I}$, of Ag-I pairs are illustrated in Fig. 2. The $r_{Ag\text{-}I}$ and $n_{Ag\text{-}I}$ decrease clearly with increasing milling time. The apparent decrease of coordination number of Ag-I pairs corresponds to the disordering of Ag ions in the glass (or distortion of AgI units in the glass matrix), which might be strongly related to the appearance of fast ion conduction in the present glass system.

References

[1] M. Sekine, Y. Suzuki, H. Ueno, Y. Onodera, T. Usuki, T. Nasu, S. Wei: J. Non-Cryst. Solids **353** (2007) 2069.
[2] T. Usuki, K. Nakajima, T. Furukawa, Y. Onodera, T. Nasu, M. Sakurai, S. Kohara: Solid State Ionics **177** (2006) 2581.

* usuki@sci.kj.yamagata-u.ac.jp

27A/2011G-638

Swift heavy ion irradiation effect on structural properties for epitaxial $Ba(Fe_{0.5}Mn_{0.5})O_{3-\delta}$ thin films

Toshiyuki MATSUI[1*], Akihiro IWASE[1], Hiroyuki YAMAMOTO[2], Norie HIRAO[2] and Yuji BABA[2]
[1]Osaka Prefecture University, Sakai, Osaka 599-8531, Japan
[2]Japan Atomic Energy Agency (JAEA), Tokai, Ibaraki 319-1195, Japan

1 Introduction

We have ever studied novel magneto-dielectric Ba-based perovskite oxides without using toxicant heavy elements [1, 2]. We have revealed so far that single crystalline $Ba(Fe_{0.5}Mn_{0.5})O_{3-\delta}$ (BFMO) thin films synthesized on (001)$SrTiO_3$(STO) are ferromagnetic insulators at room temperature. It has also been reported that the amount of oxygen deficiencies of the BFMO thin films plays a dominant role in determining these natures of the films. Hence, the precise control of the oxygen amount in the films should be indispensable to design such a class of materials. However, the previous experiments have shown that it is quite difficult to control the total oxygen amount in the films quantitatively. Here, it should be noticed that the swift heavy ion irradiation possibly becomes a potential method for the quantitative control of the oxygen vacancies of oxides through the high density electronic excitation. In the present report, we discuss the changes in the structural and magnetic properties of BFMO films due to the irradiation with the 200 MeV Xe^{14+} ion.

2 Experiment

BFMO thin films with a thickness of 60 nm were synthesized on (001)STO single crystal substrates by a PLD technique. The deposition was performed in a vacuum at the pressure of $1.0x10^{-5}$ Pa. The oxygen gas was introduced into the film during the subsequent cooling at the pressure of 10 mTorr. The sample without introducing oxygen (named as 0 mTorr film) was also synthesized for reference. Then, four samples were irradiated with 200 MeV Xe^{14+} ions by using a high energy ion accelerator at JAEA-Tokai. The irradiation was performed at room temperature and the ion fluences were $1x10^{10}$, $3x10^{10}$, $1x10^{11}$ and $3x10^{11}$ /cm^2 for the four samples. Structural characterizations of the films were investigated by x-ray diffraction (XRD). The magnetic properties were measured by SQUID magnetometer. The valence state of the Fe and Mn ions was evaluated by XPS analysis by using soft X-ray radiation at KEK-PF.

3 Results and Discussion

The (001) epitaxial grown BFMO thin film with a pseudo tetragonal perovskite crystal structure were successfully synthesized. Figure 1 shows the XRD narrow-scanned spectra for the sample before and after 200 MeV Xe ion irradiation to the fluence of $3x10^{11}$ /cm^2. For comparison, these figures also show the spectra for the 0 mTorr film. The (00L) BFMO diffraction peaks for the irradiated sample, however, apparently sift toward the low-angle side, suggesting that the lattice of the BFMO films are expanded by the ion irradiation. As can be seen in the figure, the XRD spectrum for the 0 mTorr sample also exhibits a similar tendency.

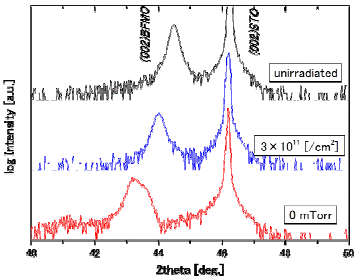

Fig. 1: XRD scans for the BFMO films.

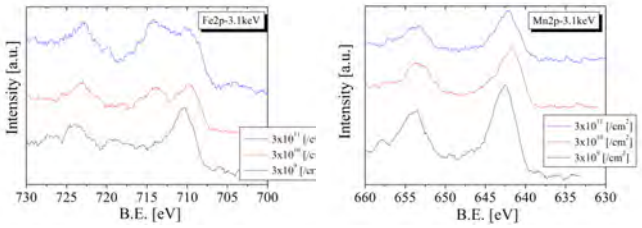

Fig. 2: $2p_{2/3}$ and $2p_{1/2}$ core level XPS spectra for Mn and Fe ions for the irradiated BFMO films.

Figures 2 show $2p_{2/3}$ and $2p_{1/2}$ core level XPS spectra for Mn and Fe ions. AS is clearly in the figure, the peak of the Fe spectra significantly shifted toward the higher energy side with increasing in the ion irradiation fluence, while the peak position of the Mn little changed. This tendency is quite similar to our previous work for the BFMO thin films having oxygen deficiencies. Hence, it can be speculated that the swift heavy ion irradiation effectively displaces the oxygen atoms and increase the amount of oxygen deficiency in the films.

References

The swift heavy ion irradiation experiments were carried out at JAEA-Tokai. The authors are grateful to Dr. N. Ishikawa for his kind assistance.

References

[1] T. Matsui, R. Sato and H. Tsuda, J. Appl. Phys. **103** (2008) 07E304.
[2] K. Katsube, T. Matsui, *et al.*, J. Appl. Phys. **105** (2009) 07D904.

t-matsui@21c.osakafu-uac.jp

8A, 8B/2011G643, 2011PF-12

有機化合物を対象とした構造解析用圧力セルの開発
Development of Pressure-cell for Structure Analysis of Organic Compounds

小林賢介 [1*], 熊井玲児 [1,2,3], 村上洋一 [1]
[1]KEK 物構研構造物性研究センター、〒305-0801 つくば市大穂 1-1
[2]産業技術総合研究所、〒305-0801 つくば市大穂 1-1
[3]科学技術振興機構 CREST、〒102-0076 東京都千代田区五番町 7

1 はじめに

圧力によって物性に変調を与え、新奇物性の探索及び物性発現機構の解明を行う研究手法は、有機・無機を問わず様々な物質に対して行われている。特に有機分子から構成される有機化合物の場合、比較的低圧力(~1 GPa)によって劇的な物性の変化を示す物質も存在する[1]。圧力印加による効果は、基本的に格子定数の圧縮であるので、物性変調の起源を解明するには、結晶構造の変化を調べることが重要となる。しかし、有機化合物のように単位胞内の原子数が多い物質の場合、圧力下の結晶構造を調べることは容易ではない。そこで我々は、有機物における構造物性研究を推進するため、高輝度な放射光 X 線と大型 IP を生かした単結晶構造解析用圧力セルの開発を行った。

2 実験

単結晶構造解析用圧力セルとしては、過去に長谷川らによって報告されたものが存在する[2]。Be をシリンダー材料として用いたこのセルは、低温で 1.5 GPa まで加圧できるが、Be 由来のデバイリングが存在するため単位胞内の全ての原子の座標を決定するフル構造解析の精度向上の妨げとなっていた。今回、このセルをベースとして、シリンダー材料を PBI へ変更したセルを用いてタウリン単結晶の構造解析を 18 keV の X 線を用いて室温で行った。試料は圧力媒体 Daphne7373 で満たしたテフロンカプセル内に封入し、印加圧力は試料室内に封入した NaCl の格子定数より決定した。

3 結果および考察

新たに開発した PBI セルと従来の Be セルの IP 写真を図 1 に示す。PBI セルでは従来セルに存在した明確なデバイリングは存在せず、常圧下と同様の手法で解析が可能であった。構造解析の結果、R 値は 0.024 となり、Be セルの 0.043 から大幅に向上した。解析精度の向上は、バックグラウンドがなだらかになった事で、測定可能な反射点数の増加と積分強度の見積りが正確になった事が原因と考えられる。PBI セルを用いた場合、低角に比較的高いバックグラウンドが存在するが、高角では Be セルとほぼ同じ程度にまで低下しており、有機結晶で重要となる高角反射を充分測定可能であることが分かった。

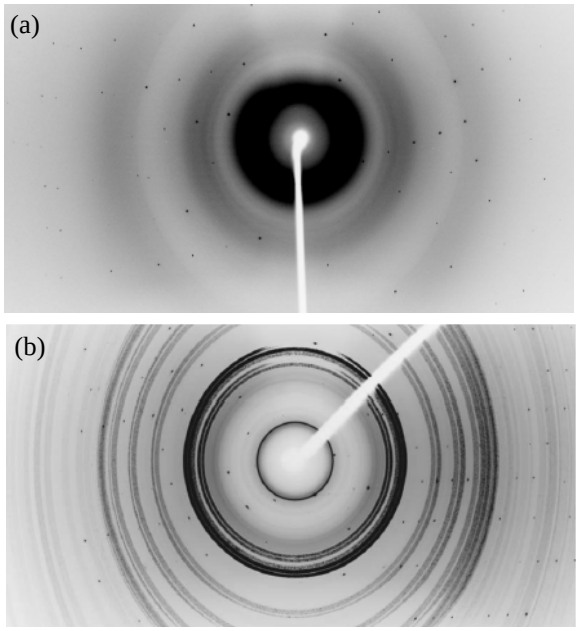

図 1 ：0.4 GPa 下におけるタウリン単結晶の IP 写真. (a)PBI セル. (b)Be セル.

4 まとめ

高圧下での構造解析には DAC がよく用いられているが、単位胞内の原子数が多い有機化合物の場合は、高角まで測定可能($2\theta_{MAX}$ ~120°)なピストンシリンダー型圧力セルでなければ単結晶構造解析は困難である。今回新たに開発した圧力セルは、今後有機化合物における圧力誘起相転移の構造物性研究を推進する上で非常に強力なツールとなる事が期待される。

参考文献

[1] K. Murata *et al.*, J. Phys. Soc. Jpn. **75** (2006) 051015.
[2] T. Hasegawa *et al.*, Rev. Sci. Instrum. **76** (2005) 073903.

* kensuke.kobayashi@kek.jp

7A/2011G657

Magnetic and electronic structures of Fe and Mn co-doped SnO_2

Jun Okabayashi[1,*] Shin Kono[1,2], and Kiyoshi Nomura[2]
[1]Research Center for Spectrochemistry, The University of Tokyo 113-0033, Japan
[2]Department of Applied Chemistry, The University of Tokyo 113-8656, Japan

1 Introduction

Since the discovery of Co-ion doped TiO_2 diluted magnetic oxides (DMO), room-temperature ferromagnetism in DMOs has opened up a new research field for spintronic applications combining the functionalities of transparency and chemical sensitivity in host oxide materials such as TiO_2, ZnO, and SnO_2. In the doped DMOs, magnetic interaction between the diluted transition metal (TM) ions mediated by oxygen vacancies is also attractive from the perspective of fundamental physics. The physical origin for room-temperature ferromagnetism in DMOs is still debated, although magnetic polaron formation and defect-induced exchange interaction are proposed. Thus, in order to investigate the mechanism for room temperature ferromagnetism, the electronic structures have to be determined explicitly. We aim to discuss not only the synthesis of dilutely Fe–Mn co-doped SnO_2 nanoparticles but also the electronic and magnetic properties [1].

2 Experiment

Fe and Mn co-doped SnO_2 samples were synthesized by a sol-gel method. 0.1 M of $SnCl_2 \cdot H_2O$, and 0.01 M of Fe and Mn salts were dissolved by using citric acid and HCl. Each solution was mixed together with ethylene glycol for the nominal compositions. These solutions were condensed at 80 °C, calcinated at 250 °C for 2 hours, and annealed at 550 °C for 0.5 hours. After milling samples, the samples were finally annealed at 550 °C for 3 hours. The magnetization was measured by vibrating sample magnetization (VSM) at room temperature, XAS was performed at KEK-PF BL-7A (Research Centre for Spectroschemistry, The University of Tokyo).

3 Results and Discussion

X-ray diffraction (XRD) patterns of all samples corresponded to the rutile-type crystalline structure of SnO_2. No other phases were observed within the detectable limit in XRD patterns.

VSM revealed the hysteresis loop at room temperature. Largest saturation magnetization was observed at 1 % Fe and 1 % Mn co-doped case. Here, we note that pure SnO_2 is a diamagnetic material and that the only Fe or Mn doped SnO_2 showed no clear hysteresis loop at room temperature. It suggests that the co-doping of Fe and Mn in SnO_2 was effective for the ferromagnetic ordering as compared with single doping.

The valence states of Mn were determined by XAS. Figure 1 shows the X-ray absorption spectra of the Mn L-edge region in Fe–Mn co-doped SnO_2. Spectra of Mn^{4+} in MnO_2, Mn^{3+} in Mn_2O_3 and Mn_3O_4, and Mn^{2+} in MnO are shown too as references. The shape of the peak at higher photon energy depends on the higher valence states of Mn ions. The line shapes of the references are similar to those in a previous report. The spectrum of Fe–Mn co-doped SnO_2 remains unchanged for all concentrations. Therefore, we confirm that Mn^{2+}/Mn^{3+} mixed valence states are dominant in Fe–Mn co-doped SnO_2. Furthermore, we note that the Fe L-edge cannot be detected by the XAS since the Fe L-edge regions overlap with the $M_{4,5}$-edge absorption peaks.

The electronic and magnetic properties of Fe ions are also discussed using Mössbauer spectrometry. The isomer shift values revealed the Fe^{3+} states for Fe and Mn co-doped SnO_2.

Although the model of defect-induced ferromagnetism is proposed for the single-ion doping [2], the enhancement of magnetization in co-doping cannot be explained within that model. The double-exchange-like mechanism through the carrier kinetics between Fe^{3+} (d^5) and Mn^{3+} (d^4) electrons accompanying the self-carrier doping must be considered.

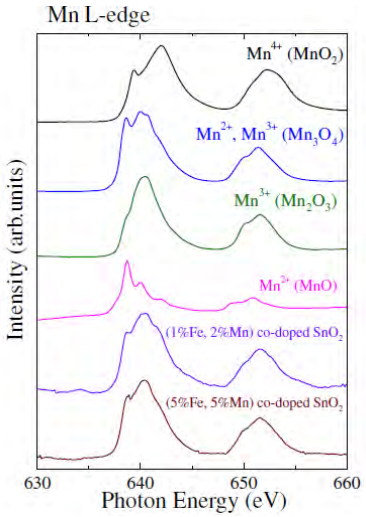

Fig. 1: X-ray absorption spectra of Fe–Mn co-doped SnO_2. As references, spectra of MnO_2, Mn_3O_4, Mn_2O_3, and MnO are also shown.

References

[1] J. Okabayashi *et al*., Jpn. J. Appl. Phys. **51** (2012) 023003.
[2] J.M.D. Coey *et al*., Nat. Mater. **4** (2005) 173.

* jun@chem.s.u-tokyo.ac.jp

9A/2011G659

Local Structure Analysis on Functional Element doped Hydroxyapatite for use as a Drug Delivery System and Imaging Beads Materials

Mitsutaka Sato[1*], Yuki Nishio[2], Toshiki Shirai[2], Chiya Numako[3], and Atsushi Nakahira[1,2]
[1]Kansai center for Industrial Materials Research, Tohoku University, Sakai, Osaka 599-8531, Japan
[2]Osaka Prefecture University, Sakai, Osaka 599-8531, Japan
[3]Chiba University, Chiba 2613-8522, Japan

1 Introduction

Calcium phosphate has been well understood as bioactive and biodegradable materials. Especially, hydroxyapatite ($Ca_{10}(PO_4)_6(OH)_2$, HAp) is chief inorganic component of hard tissue and exhibits excellent bone conductivity and biocompatibility[1]. Therefore, HAp has been widely used as alternates of hard tissue and surface modification film of artificial implants to connect them with remaining bone rapidly. Since HAp also has non toxicity and excellent ion exchange ability, many kinds of studies for some functional elements doped HAp such as Mn, Si, Zn, Fe and Mg have been reported so far[2]. Those doped HAp will be a good candidate for not only alternates of hard tissue but also drug delivery system (DDS) and heavy-metal removable materials[3]. In this study, we prepared Fe doped HAp as a novel magnetic bead to control its action using magnetic field and investigated the effects of preparation condition on the crystal phase, morphology and other properties.

2 Experimental Procedure

0.1 mol/l calcium nitrate ($Ca(NO_3)_2$), ammonium phosphate dibasic ($(NH_4)_2HPO_4$) and iron chloride ($FeCl_3$) aqueous solutions were used as starting materials. After adjusting the pH of solutions, phosphate solutions were gently dropped to mixed solution of calcium and iron to become the ratio of Ca to P equals to 1.67. The ratio of Fe was changed in the range from 0 to 20 mol% against the amount of Ca. After mixing up each other, obtained solution was aged at room temperature for 1 h, and then, it was filtered and dried at 323 K for 24 h. The local structure of samples was investigated by XAFS spectra for Ca-K and Fe-K edge. Both of Ca-K and Fe-K edge XAFS data were corrected by transmission and fluorescence mode using Si (111) double crystal monochrometer at BL-9A in the Photon Factory. The analysis of XANES data was conducted using the commercial software "REX2000" (Rigaku Co. Ltd., Japan).

3 Results and discussion

Figure 1 shows Ca-K edge XANES spectra of Fe doped HAp powders prepared at the ratio of Ca to P of 1.67 and the ratio of Fe from 0 to 20 mol%. The local structure of near Ca atom was evaluated by XAFS to circumstantially examine the state of doped Fe to HAp. The Ca-K edge spectra of all samples were very close to the peak position of commercial HAp. This result indicated that the local structure of near Ca atom in samples were similar to HAp.

Figure 2 shows Fe-K edge XANES spectra of Fe doped HAp powders. For the Fe-K edge XANES measurement, α-Fe_2O_3, γ-Fe_2O_3, Fe_3O_4 and α-FeOOH were used as references. The Fe-K edge spectra of samples changed by increasing the ratio of Fe, and the Fe-K edge spectra of samples prepared in low Fe ratio region were close to α-FeOOH and those prepared in high Fe ratio region were close to lapped spectra of α-Fe_2O_3 and α-FeOOH. This result indicated that the doping amount of Fe into HAp structure is less than 1 mol% against the Ca, and most amount of doped Fe exists as α-FeOOH and α-Fe_2O_3 at the surface and/or boundary of powders.

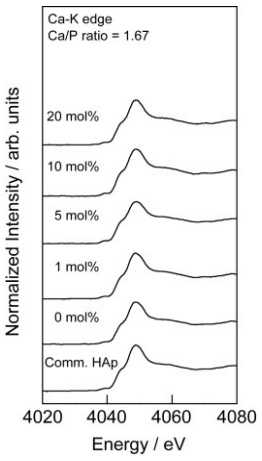

Fig.1 Ca-K edge XANES spectra of Fe doped HAp powders.

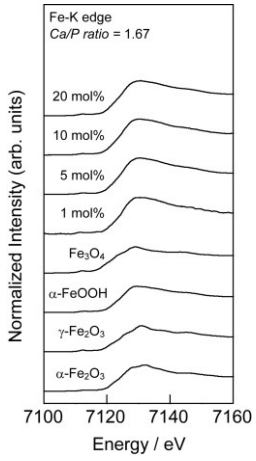

Fig.2 Fe-K edge XANES spectra of Fe doped HAp powders.

References

[1] M. Sato, R. Tu, T. Goto: Mater. Trans., **48** (2007) 3149-3153.
[2] K. Nakata, T. Kubo, C. Numako, T. Onoki, A. Nakahira: Mater. Trans, **50** (2009) 1046-1049.
[3] A. Nakahira, S. Nakamura and M. Horimoto: IEEE Trans. Mag., **43** (2007) 2465-2467.

* m-sato@imr.tohoku.ac.jp

11B/2011G690, 16A/2009S2-008

$LaCo_{1-x}Rh_xO_3$ の X 線吸収分光による研究
X-ray absorption study of $LaCo_{1-x}Rh_xO_3$

須田山貴亮 [1*], 岡本淳 [1], 山崎裕一 [1], 中尾裕則 [1], 村上洋一 [1],
浅井晋一郎 [2], 古田倫靖 [2], 岡崎竜二 [2], 安井幸夫 [2], 寺崎一郎 [2]
[1]KEK 物構研 PF/CMRC、〒305-0801 茨城県つくば市大穂 1-1
[2]名古屋大学理学研究科、〒464-8602 愛知県名古屋市千種区不老町

1 はじめに

$LaCoO_3$ は Co^{3+}でペロブスカイト構造を有し、金属絶縁体転移、スピンクロスオーバー現象等の興味深い物性を示すことでよく知られており盛んに研究されている物質である[1]。この物質の Co を Rh で置換した物質である $LaCo_{1-x}Rh_xO_3$ は、エンド物質は両方とも非磁性にも関わらずに低温において強磁性が出現することが報告された[1]。

以前、我々は Rh の濃度が x = 0.0, 0.2, 0.5 の試料について X 線吸収分光実験を行い、Rh、Co の価数、スピン状態の情報を得た。Rh 置換に伴い、Rh、Co の価数はそれぞれ 3 価のまま変わらず、Co のスピン状態だけが変化するということを報告した[2]。x = 0.0, 0.2, 0.5 の濃度依存性を見ると Co の L_3吸収端において低スピン状態を主に反映しているピークが Rh 濃度の増加につれて抑制されているのではないかという結果を得た。しかしながら、細かいな組成依存性が分からず、スピン転移がどのように連続的に起こっているのかはっきりした結論が得られなかった。本研究では、我々は、細かい Rh の組成依存性を系統的に調べることにより Co のスピン状態の変化がどのように起こるのかについての研究を行った。

2 実験

高エネルギー加速器研究機構のフォトンファクトリーにて多結晶試料$LaCo_{1-x}Rh_xO_3$のX線吸収分光実験を行った。測定方法は蛍光収量法を用い、検出器としてPhotodiodeを使用した。測定はすべて室温で行った。BL-11BでRhについては*L*吸収端(2*p*→4*d*)、BL-16AにてCoについては*L*吸収端(2*p*→3*d*)、酸素についてはK吸収端(1*s*→2*p*)を用いた。

3 結果および考察

図 1 は Co L 吸収端における $LaCo_{1-x}Rh_xO_3$ の X 線吸収スペクトルの Rh 濃度依存性である。蛍光収量法であるため、自己吸収の効果があり L_3 と L_2 の比については言及できないが、明確な変化が L_3 と L_2 それぞれで観測することが出来た。スペクトルの形状から Co はどの濃度であっても 3 価を保つことが確認された。また、L_3のおよそ 781.5 eV にある高エネルギー側のショルダー構造は低スピン状態の時に顕著に現れるピークであり、Rh の濃度が増えるに従い抑制されていることが分かる。これは以前に報告した結果と一致する [2] 。今回、新たに L_2吸収端について明瞭な変化を観測した。L_2 吸収端の Co 3 価のスペクトルはクラスター計算や $LaCoO_3$ の温度変化の先行研究によれば 2 つのピークで構成されており、およそ 794.8 eV の低エネルギー側のピークは主に Co^{3+}低スピン状態の場合に、およそ 795 eV の高エネルギー側のピークは Co^{3+}高スピン状態の場合にそれぞれ強度が大きくなる振る舞いを示すことが知られている。今回の実験結果から、Co^{3+}低スピン状態と Co^{3+}高スピン状態の比が Rh 濃度により変化し、高スピン状態が安定化するような傾向があることが実験から得られた。

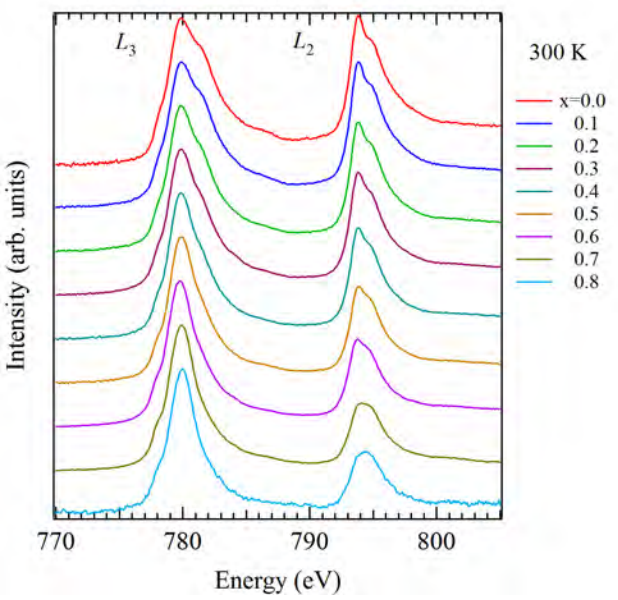

図 1 ：X 線吸収分光による $LaCo_{1-x}Rh_xO_3$ (x = 0 ~ 0.8) の室温における Co *L* 吸収端のスペクトル。

参考文献
[1] S. Asai *et al.*, JPSJ **80** (2011) 104705.
[2] T. Sudayama *et al.*, 日本物理学会　第 67 回年次大会　25aYD-7.
[3] M. Abbate *et al.*, PRB **47** (1993) 16124-16130.

* Takaaki.sudayama@kek.jp

7A/ 2011P102

Direct evidence for orientations in the amorphous functional polymer thin films deposited on Si surface

Kiyotaka Asakura[1], Takahiro Wada[1], Hiromitsu Uehara[1], Hiroko Ariga[1], Satoru Takakusagi[1] , Kenta Amemiya[2] , Norimasa Yokoyama[3], and Daisuke Yokoyama[4]

[1]Catalysis Research Center, Hokkaido University, Sapporo 001-0021, Japan
[2]Photon Factory, Institute of Materials Structure Science, Tsukuba 305-0801, Japan
[3]Research and Development Center, Hodogaya Chemical Co., Tsukuba, 305-0841, Japan
[4] Graduate School of Science and Engineering, Yamagata University, Yonezawa, 992-8510, Japan

1 Introduction

Vacuum-deposited organic amorphous thin layers are used for organic light emitting diodes (OLED) which have a feature of flat surface in a nanometer order, flexibility in the choice of the underlying materials, easily controlled thickness, homogeneous structure and a simple high-purity fabrication process. Although the orientation and overlapping of two molecular π plains are important for the electric conductivity, they are usually neglected only because the materials are in the amorphous film.

Recently Yokoyama et al. reported that some of amorphous films had an orientation and the electric conductivities depended strongly on the orientations.[1] In this paper we have investigated that the polarization C and N K-edge NEXAFS.

2 Experiment

The samples were vacuum-deposited on the Si (100) (n-type) with thickness of 100 nm. The samples were following planar tripheyl amines or pyridine/bipyridines linked with biphenyl bonds.

The measurement was carried out in BL7A. The x-ray was monochromatized by the grazing incidence monochromator with varied line spacing grating(VLSG)(300 /mm) and the higher harmonics were rejected by a Si total reflection mirror. The entrance and exit slit sizes were 100 μm. The spectrum was measured in a sample current mode. The current was in the 0.1 nA order. The measurement energy range was 395-440 eV for N K-edge and 270 -320 eV for C K-edge. The energy step in the NEXAFS region was 0.1 eV (upto 292 eV for C and 395 eV for N) and 0.5 eV afterwards. The measurement angles which were defined as angles between the incidence direction and the sample surface were 90º, 60º, 45º and 15º. The 90 º meant the electric vector was parallel to the surface while 15 º meant the vertical component to the surface was the main one. Total time per scan requires less than 10 min for each direction and total exposure time to X-ray was less than 2 hours.

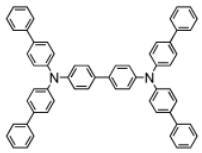

Fig.1 TPD15

3 Results and Discussion

Fig.2 shows the N and C K-edge NEXAFS of TPD15 (see Fig.1). It shows the clear polarization dependence in N K-edge. The strong peak appearing at the edge region can be assigned to 1s to π* transition which directed perpendicular to the molecular plane.

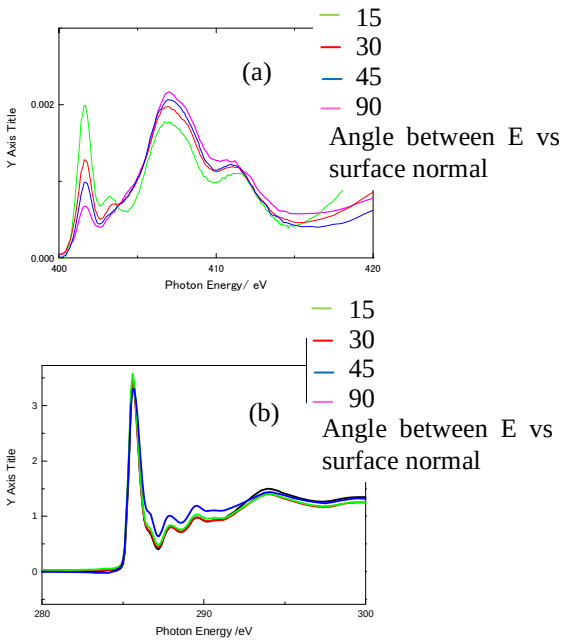

Fig.2 N (a) and C(b) K-edges NEXAFS of TPD15

It suggests that the TPD15 molecule lies parallel to the surface. However, the appearance of 1s to π* transition with the normal incidence indicated the orientation of the molecule was not perfect. No polarization dependence in K-edge indicates that N-C(phenyl group) was rotated and the aromatic planes have no common directions.

The work directly demonstrates that the amorphous layer of organic films can have a horizontal orientation to the surface.

[1] D. Yokoyama, A. Sakaguchi, M. Suzuki, C. Adachi, Organic Electronics 2009, 10, 127 ; D. Yokoyama, A. Sakaguchi, M. Suzuki, C. Adachi, Applied Physics Letters 2009, 95, 243303.

askr@cat.hokudai.ac.jp

11A, 16A/ 2011PF-02, 2011G597, 2009S2-008

共鳴軟 X 線小角散乱による(Fe,Co)Si の磁気散乱観測
Small Angle Resonant Soft X-ray Magnetic Scattering in (Fe,Co)Si

山崎裕一、中尾裕則、須田山貴亮、岡本淳、村上洋一、久保田正人[A]、
于秀珍[B]、柴田基洋[C]、金澤直也[C]、小野瀬佳文[C]、十倉好紀[B, C, D, E]
KEK 物構研 PF/CMRC, JAEA[A], RIKEN-CERG[B], 東大工[C],RIKEN-CMRG[D],ERATO-MF[E]

1 はじめに

B20 型結晶構造を有する(Fe,Co)Si は、ゼロ磁場においてヘリカル磁性体であるが、磁場中の A 相と呼ばれる温度・磁場領域ではスピンが渦上に配列したスキルミオン格子（図 a）を形成することが、中性子小角散乱[1]やローレンツ電子顕微鏡[2]によって観測されている。本研究では、 (Fe,Co)Si において磁気散乱の観測を目的に研究を行った。軟 X 線散乱法は、元素選択性や、スペクトル解析による電子状態の解析、MCD の総和則によるスピンと軌道モーメントの観測、円偏光軟 X 線を利用したスピンヘリシティの検出などの利点が挙げられる。

2 実験

本研究では磁気変調波長が 90 nm に達する $Fe_{0.5}Co_{0.5}Si$ を、イオンミリング法によって軟 X 線が透過する sub-μm 程度まで薄く加工して実験を行った。小角領域の共鳴軟 X 線散乱を測定する装置を開発し、Fe と Co の L 吸収端において共鳴軟 X 線散乱実験を行った。装置にはヘルムホルツコイルを取り付け X 線入射方向に磁場を印加できるようにし、回折光は CCD カメラを用いて観測した。

3 結果および考察

図 b には CCD カメラで観測した Fe の L3 吸収端における共鳴軟 X 線磁気散乱を示している。2 つの回折光は $Fe_{0.5}Co_{0.5}Si$ のゼロ磁場で観測されているヘリカル磁気構造からの反射に対応している。同じように Co の L 吸収端においても磁気散乱を観測しており、元素ごとに磁気散乱を観測できたことになる。図 c には Fe の L 端における共鳴軟 X 線磁気散乱のエネルギー依存性を示している。L3 吸収端ではピークが観測されているのに対して、L2 吸収端では磁気散乱がほとんど観測されていない。磁場をかけた状態で測定した XMCD スペクトに関しても同じように L2 吸収端ではほとんど観測されなかった。磁気散乱強度は XMCD スペクトルに 2 乗に比例することからコンシステントな結果といえる。XMCD の総和則から、これらの結果は軌道モーメントが凍結していないことを示唆している。

このヘリカル磁気構造に磁場を印加したところ、磁場方向に変調ベクトルが揃い、さらに磁場を印加すると、磁場と垂直方向に変調ベクトルが向くような変調ベクトルのフロップが観測された。このフロップ相はバルク試料に比べ低温まで拡がっていることを確認した。これは、サンプルを薄くした効果によるものと考えられる。

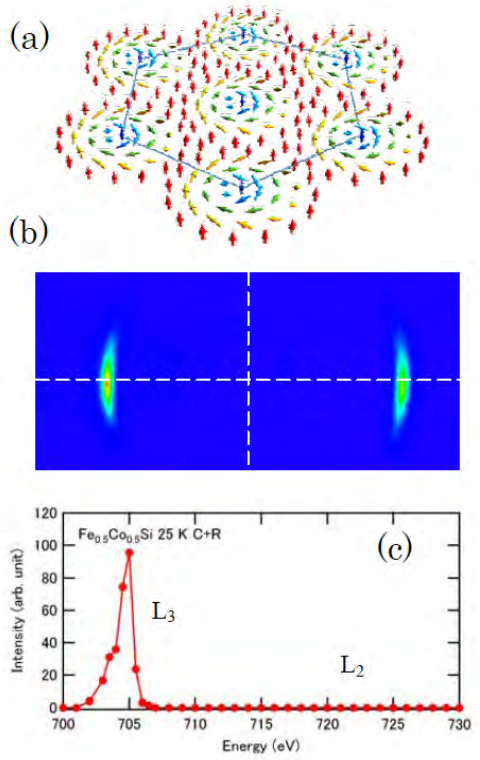

(a) スカーミオン格子。(b) Fe L_2 吸収端における軟 X 線磁気散乱と(c)そのエネルギー依存性

参考文献

[1] W. Münzer et al., Phys. Rev. B 81, 041203(R) (2010)

[2] X. Z. Yu et al., Nature 465, 901 (2010)

* yuichi.yamasaki@kek.jp

4B-2/2011PF-17

機能性ペロブスカイトセラミックスにおける精密粉末 X 線構造解析のための最適測定条件の検討

The optimized investigating condition for precise X-ray powder diffraction analysis in functional perovskite ceramics

籠宮 功*, 神保 圭吾, 西 智広, 柿本 健一
[1]名古屋工業大学　〒466-8555 名古屋市昭和区御器所町

1 はじめに

最近の機能性セラミックスの研究分野において、これまで注目されていなかった、より小さい格子歪みあるいはイオン変位がその機能性向上と密接な相関があることが分かってきている。この小さい変位を明らかにする上で、測定 X 線強度の SN 比および角度分解能の高い測定が可能な BL-4B-2 ビームラインの使用がきわめて有効である。ただし、小さい変位を明らかにする上で、BL-4B-2 を最大限に活かす詳しい実験・解析条件を検討する必要がある。またマシンタイムを考慮した効率の面で問題が生じる懸念がある。BL-4B-2 について本優先ビームラインを利用することで、ペロブスカイト型機能性セラミックスの小さいイオン変位を精度良く明らかにする効率的な実験条件を明確にする。これより、BL-4B-2 が今後の機能性材料研究分野での回折実験において、効率性と有効性を両立できる測定条件を提示したい。

2 実験

注目するペロブスカイト機能性セラミックスについて、放射光 X 線回折およびその精密構造解析を行い、結晶学的な立場から機能性（圧電性・導電性）を明らかにするための予備実験を行う。具体的には、機能性ペロブスカイト試料を円盤型試料ホルダーに充填セットして、波長 1.2 オングストローム、測定角度 0～155 °の範囲で、2θ スキャンを行い、回折データを収集した。このときの入射スリット幅は、横 10 mm、縦　1mm である。以上の実験を通じて，機能性セラミックスを中心とした無機系材料の精密な構造評価を実現し、速やかに成果をあげるために、KEK-PF BL-4B-2 ビームラインにおける測定条件を最適化、さらに測定時間の効率化の検討を行った。

3 結果および考察

本実験で得られた XRPD パターンの一例として、単純ペロブスカイト $La_{0.4}Sr_{0.6}CoO_3$ の測定結果を Fig. 1 に示す。2θについて、0.005 度のステップスキャンを行った。ステップごとの検出時間は、シンチレーションカウンターの数え落としの効果を最小限にするよう、各試料でカウント数が 1 万カウント以上、2 万カウント以下になるように調整した。調整した結果、具体的なステップごとの検出時間は、それぞれ 0.5 秒となった。なおステップごとの照射時間 0.5 秒の場合トータルの測定時間は、約 3 時間 30 分であった。

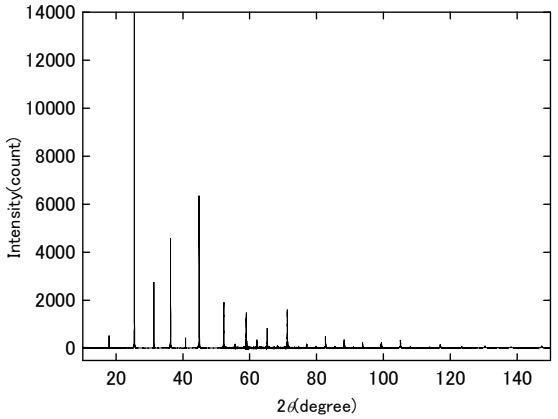

Fig. 1: 4B-2 を用いた $La_{0.4}Sr_{0.6}CoO_3$ の回折パターン

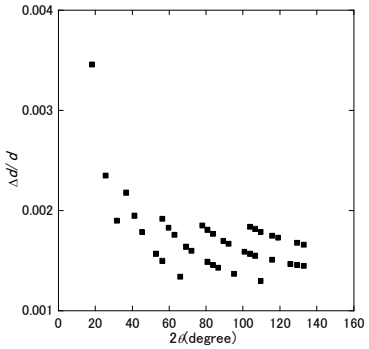

Fig. 2: $La_{0.4}Sr_{0.6}CoO_3$ 回折パターンより得られた$\Delta d/d$

このとき、各角度においてブラッグ反射の半値幅から求められる$\Delta d/d$ を Fig.2 に示す。2θ の全範囲で、高い分解能を有していることを確認した。これより、４B-2 を用いる際、ペロブスカイトの小さい変位に伴うピークのスプリットの存在が、$\Delta d/d$ =10^{-3} の分解能のオーダーで捉えうることを知見として得た。

謝辞

本研究は、PF スタッフの方々、4B-2 の管理者のご協力のもと行ったものです。ここに感謝を申し上げます。

BL-2C/2011S2-003

High-resolution soft-X-ray photoemission study on $SrTi_{0.99}Sc_{0.01}O_3$ thin film

Teppei Okumura[1], Tohru Higuchi[1*], Enju Sakai[2] and Hiroshi Kumigashira[2]
[1] Department of Applied Physics, Tokyo University of Science, Tokyo 162-8601, Japan
[2] Photon Factory, Tsukuba 305-0801, Japan

1 Introduction

Undoped $SrTiO_3$ is one of dielectric materials with cubic perovskite structure. The $SrTiO_3$ transfers from the insulator to metal or semiconductor by small carrier doping. The doping can be achieved by alternating of the three sublattices, namely, those of Sr^{2+}, Ti^{4+}, and O^{2-}. The Sc^{3+}-doped $SrTiO_3$ single crystal exhibits proton conductivity as well as hole conductivity in the temperature region of 200~400 °C. The proton conduction of Sc-doped $SrTiO_3$ is useful for electrochemical applications of solid state oxide fuel cell and hydrogen sensor in the energy source industry.

In this study, the electronic structure of Sc-doped $SrTiO_3$ ($SrTi_{0.99}Sc_{0.01}O_3$) thin film has been probed by high-resolution photoemission spectroscopy (HRPES) and X-ray absorption spectroscopy (XAS). As a reference, the electrical conductivity was also measured. Understanding the detailed structural and electrical properties of the thin film is one of the important subjects in term of electrochemical application. However, the details of the thin film have not been clarified thus far. In this paper, the authors would like to propose that the $SrTi_{0.99}Sc_{0.01}O_3$ thin film becomes *p*-type oxide semiconductor in comparison with undoped $SrTiO_3$ and Nb-doped $SrTiO_3$ single crystals.

2 Experiment

The $SrTi_{0.99}Sc_{0.01}O_3$ thin films were prepared on 0.1 wt.% Nb-doped $SrTiO_3$ (100) single crystals by RF magnetron sputtering using ceramic target. The RF power, deposition pressure and substrate temperature were fixed at 40 W, ~3.0×10^{-3} Torr and 500 °C, respectively. The film thickness was approximately 100 nm. The prepared thin film was examined using X-ray diffraction and atomic-force microscope. The detailed structural properties have been reported in Ref. [1]. The electrical conductivities were measured by A.C impedance method. The XAS and HRPES spectra were measured using a soft-X-ray spectrometer installed at an undulator beamline BL-19B and BL-2C (in Photon Factory) at the High Energy Accelerator Organization in Tsukuba, Japan. The energy resolutions of XAS at $h\nu$=400~500 eV and HRPES at $h\nu$=800 eV were 50 meV and 120 meV, respectively. The energy axis was calibrated by measuring the HRPES spectrum of the 4*f* core level of Au film.

3 Results and Discussion

Figure 1(a) shows the Ti 2*p* XAS spectra of the $SrTi_{0.99}Sc_{0.01}O_3$ thin film and $SrTiO_3$ single crystal. Each XAS spectrum was measured on different beam line.

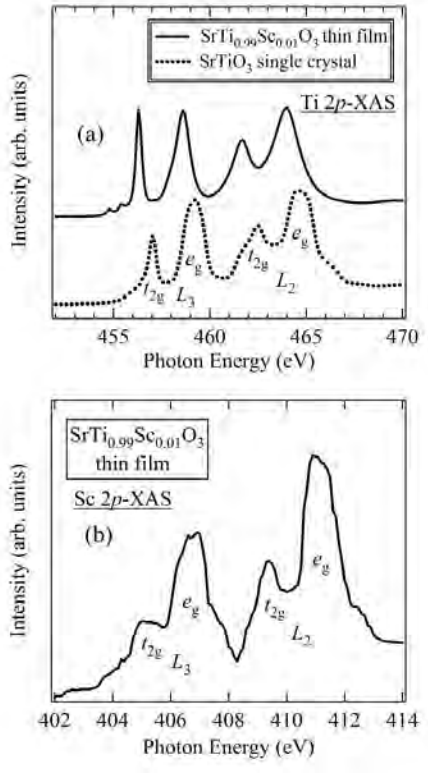

Fig. 1 (a) Ti 2*p* XAS spectra of the $SrTi_{0.99}Sc_{0.01}O_3$ thin film and $SrTiO_3$ single crystal. (b) Sc 2*p* XAS spectrum of the $SrTi_{0.99}Sc_{0.01}O_3$ thin film.

The Ti 2*p* XAS spectra correspond to the transition from the Ti 2*p* core level to the unoccupied Ti 3*d* state. The spectra consist of two parts derived from the spin orbit split of L_3 ($2p_{3/2}$) and L_2 ($2p_{1/2}$) states. They are further split into the t_{2g} and e_g states by the octahedral ligand field. Comparing with the $SrTiO_3$ single crystal, the peak of the thin film shifts to the lower energy side. This corresponds to the rigid band shift. Furthermore, the intensity of the t_{2g} peak for L_3 state is higher in the $SrTi_{0.99}Sc_{0.01}O_3$ thin film. This may indicate that the Sc^{3+} ions are substituted into Ti^{4+} site in $SrTiO_3$.

Figure 1(b) shows the Sc 2*p* XAS spectrum of the $SrTi_{0.99}Sc_{0.01}O_3$ thin film. The Sc 2*p* XAS spectrum corresponds to the transition from the Sc 2*p* core level to the unoccupied Sc 3*d* state. The spectrum splits into the t_{2g}- and e_g-subbbands of L_3 ($2p_{3/2}$) and L_2 ($2p_{1/2}$) by the octahedral ligand field. The existence of the peak structure indicates that the Sc^{3+} ions are substituted for Ti^{4+} site in the $SrTi_{0.99}Sc_{0.01}O_3$ thin films.

Figure 2 shows the HRPES spectrum in the valence band region of the $SrTi_{0.99}Sc_{0.01}O_3$ thin film. The spectral shape is in a good agreement with the PES spectra of Nb-doped $SrTiO_3$ single crystal. The valence band has two structures of A and B. It is known that the peak A corresponds to the nonbonding state and the peak B corresponds to the bonding state that is well mixed with Ti 3*d* state. On the other hand, the Fermi level (E_F) of the thin film locates at ~1.2 eV from the top of the valence band. The E_F locates at ~2.6 eV from the top of the valence band in the case of $SrTi_{0.98}Sc_{0.02}O_3$ single crystal. The E_F of the thin film locates at the valence band side. Furthermore, the additional structures within the band gap, which are commonly observed at oxide surfaces with defects or disorders, are hardly visible in the present spectra, indicating that a well-defined surface is obtained. These results indicate that the band bending effect of the single crystal is suppressed by postannealing in O_2 atmosphere. From Figs. 1 and 2, the E_F of the $SrTi_{0.99}Sc_{0.01}O_3$ thin film corresponds to that of *p*-type oxide semiconductor.

The energy band-DOS curves in the valence band, which are obtained by two authors of Matheiss *et al*. [3] and Toussaint *et al*. [4], are also shown as histogram lines. The DOS curves of solid lines are obtained by convoluting the original DOS with Gaussian broadening functions widths of 0.1 eV. Matheiss *et al*. calculated the DOS using the APW and Slater-Coster linear combination of atomic orbital interpolation method. Toussaint *et al*. calculated the DOS using the tight-binding method with a Green function.

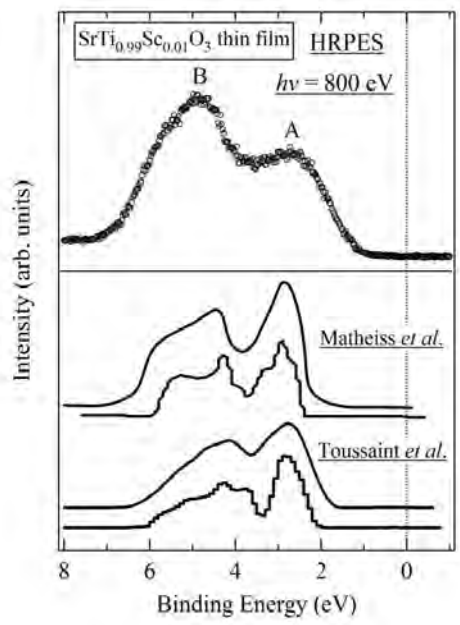

Fig. 3 (a) Valence band of the $SrTi_{0.99}Sc_{0.01}O_3$ thin film measured by HRPES, which is shown as open circles. (b) The band-DOS curves calculated by two authors, Matheiss *et al*.[3] and Toussaint *et al*. [4], which are also shown as solid lines.

The influence of electron correlation is not calculated in the two DOS. The spectral shape and bandwidth of HRPES spectrum are in good agreement with two band DOS curves. However, the ratio of the peak intensity of the HRPES spectrum is different from that of two DOS curves. This is considered to be due to the change of the Ti-O hybridization effect in the valence band.

4 Conclusion

The authors have studied the electronic structure of the $SrTi_{0.99}Sc_{0.01}O_3$ thin film using XAS and HRPES. The Ti 2*p* and Sc 2*p* XAS spectra exhibit that Sc^{3+} ions are substituted into Ti^{4+} site. The electrical conductivity exhibits the thermal activation-type behavior. The E_F of the $SrTi_{0.99}Sc_{0.01}O_3$ thin film locates to the valence band side. The energy separation between E_F and the top of valence band corresponds to the E_a, which is estimated from the Arrhenius plot of conductivity. The valence band consists of the O 2*p* state hybridized with the Ti 3*d* state. The hybridization effect between the O 2*p* and Ti 3*d* states in the valence band is weaker in the thin film. These results indicate that the $SrTi_{0.99}Sc_{0.01}O_3$ thin film become *p*-type oxide semiconductor with the large E_a.

Acknowledgement

The present work was supported by the Grant-In-Aid for Science Research C (No. 22560670) from the Ministry of Education, Culture, Sports, and Technology in Japan.

References

[1] T. Okumura, Y. Kobayashi, F. Ihara, and T. Higuchi; Trans. Mater. Res. Soc. Jpn. **37** (2012) 85.
[2] T. Okumura, T. Inoue, Y. Tasaki, E. Sakai, H. Kumigashira and T. Higuchi, J. Phys. Soc. Jpn. (2012) to be published.
[3] L. F. Matheiss, Phys. Rev. B **6** (1972) 4718.
[4] G. Toussaint, M. O. Selme, and P. Pecheur, Phys. Rev. B **36** (1987) 6135.

* higuchi@rs.kagu.tus.ac.jp

1A/2012S1-001

3 元ブロック共重合体ラメラ相のずり流動誘起構造転移
Shear-induced structural transition of triblock copolymer lamellar phase

藤井修治
長岡技術科学大学、〒940-2188 新潟県長岡市上富岡待ち 1603-1

1 はじめに

ブロック共重合体系リオトロピックラメラ相が示すずり誘起型構造転移にはラメラの配向転移が知られているが、溶媒組成を変化させるとラメラ/オニオン転移も発現する．これまで、これら二つの転移現象は独立の研究課題として扱われてきたが、ラメラ相が流動下で発現する多様な非平衡構造転移を理解するには、それぞれの構造転移がどのような経路を辿り達成されるのか統一的に議論する必要がある．．

本研究ではその出発点として両親媒性ブロック共重合体のラメラ相を用い、粘度測定、流動小角光散乱測定（Rheo-SALS）、流動複屈折測定を行うことにより動的相図を作成することを目的とした．

2 結果および考察

Pluronic P123/ブタノール/水 三成分系ラメラ相について、ブタノールと水の混合比を変えると、I：混合比 0.320 以下では高ずり速度域においてラメラの *c* 配向から *a* 配向への配向転移（L_α- *c* /L_α-*a*）に起因する複屈折の増大とニュートニアン挙動が、II：0.325 以上ではオニオン相形成（L_α- *c* /Onion）に起因する複屈折の減少とシアシックニング挙動が観察された．さらに高ずり速度域ではオニオン破壊（Onion/L_α-*c*）によるラメラ再形成に起因すると考えられる流動複屈折の増大と、L_α- *c* / L_α-*a* 配向転移に起因するシアシニングからニュートニアン挙動への変化も見られた．これらの構造転移は、図 1 下図に示した例のように、Rheo-SAXS パターンを基に決定した。これらの結果を基に動的相図を作成した．図より、ラメラ配向転移はオニオン形成・破壊の臨界ずり速度よりも高ずり速度域で生じることがわかる．このことはラメラ配向転移やオニオン相形成を支配する固有のダイナミクスがそれぞれ異なる時間スケールにあることを示唆する．また Rheo-SALS よりオニオン破壊前にはずり速度の増加と共にオニオンサイズが減少し破壊するのではなく、オニオンサイズはずり速度の関数として極小値を迎えた後に徐々に増大してから破壊されることもわかった．今後、このオニオン形成・破壊のキネティクスを詳細に調べる予定である．

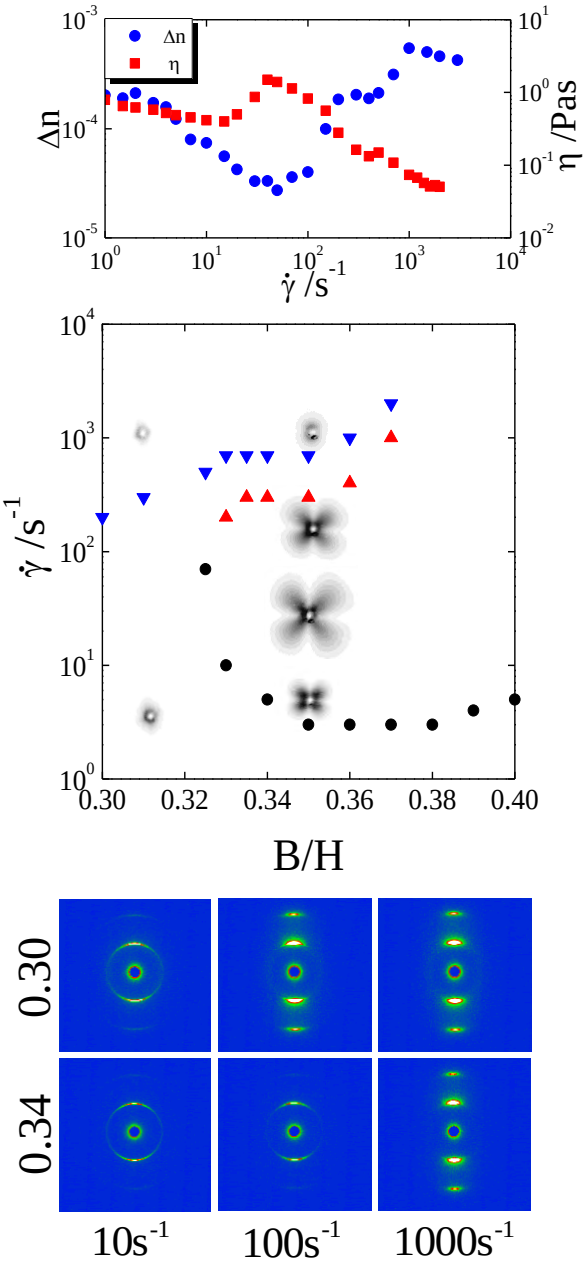

図 1 ：上図：B/H＝0.35 における複屈折と粘度のずり速度依存性．中図：上図を基に作成したずり誘起構造転移の動的相図．下図：BH=0.3 と 0.34 での Rheo-SAXS パターン．

2012G080

Local structure analysis of nanocrystalline $Fe_{83.3}Si_4B_8P_4Cu_{0.7}$ alloy studies by XAFS

Akimi Oono[1].Takafumi Miyanaga[1*].and Takeshi Kubota[2]
[1]Department of Advanced Physics, Hirosaki University Hirosaki Aomori 036-8561,Japan
[2]NJRISE, Hirosaki University, Aomori 030-0813, Japan

1 Introduction

The FeSiBPCu nanocrystalline alloy has a feature of the high saturation magnetic flux density and a super-low core loss as a soft magnetism material. It is expected as a material of a transformer or a motor core in the future, and drastic reduction of the amount of discharge of carbon dioxide can be realized from the character of a super-low core loss. As a just preparation of the sample, the structure is amorphous like. A primary phase transition occurs at the 675K where the part of amorphous Fe crystallizes first and a secondary phase transition at 800K shows that the sample changes to crystalline completely. The intermediate state annealed between these temperatures shows high magnetic density and low core loss. The local structure is expected to be nanocrystalline state, however, detail mechanism for the formation of nanocrystalline is not clear. EXAFS is powerful tool for investigation of the local structure with element selectively. In this paper, *K*-edge XAFS analyses of Fe, Si, P, and Cu were performed for the sample prepared with various annealing conditions.

2 Experiment

The ribbon sample of $Fe_{83.3}Si_4B_8P_4Cu_{0.7}$ of produced by the arc melting in Ar and was solidified rapidly in the atmosphere using single-roller melt-spinning. They were annealed at 693K, 713K, 733K, 793K, and 823K for 60 min with a heating rate of 40K/min. The annealing time is 60 min and the speed of heating is 40K /min. The *K*-edge XAFS of Fe (BL12C, Trans), Si (BL11B, SSD), P (BL11B, SSD), and Cu (BL12C, 19SSD) were performed at Photon Factory, KEK, Japan.

3 Results and Discussion

The Fourier transform (FT) of the EXAFS of Fe *K*-edge is shown in Fig. 1. FT of the as-spun sample shows amorphous. By annealing at 693K the peak intensities increases compared with an as-spun sample and become close to bcc Fe structure. This indicates that the circumference of Fe crystallized by the annealing at 693K and it shows no more change with further annealing. Figure 2 shows FT for P *K*-edge. The peak intensities once decreases by annealing at 693K, and increases greatly by annealing at 793K. The results suggest that the local structure is distorted after the first annealing (693K) and crystallize higher annealing (793K) than Fe. Figure 3 shows FT for Cu *K*-edge. FT for an as-spun sample shows the amorphous like and change to crystalline, which behaviour is similar Fe. In addition, by annealing at more than 793K, behaviour in peak strength and the peak position shows that like P. Therefore, it can be supposed that there is two phase transitions for Cu.

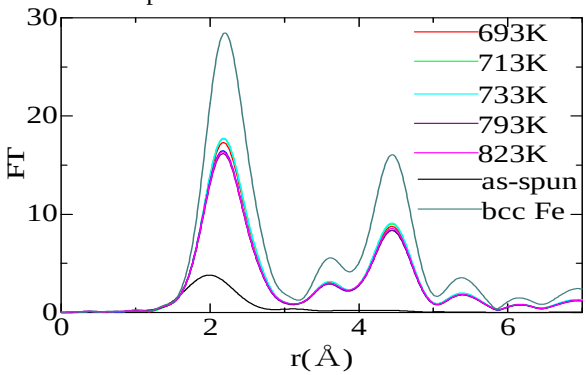

Fig. 1 FT of Fe *K*-edge EXAFS

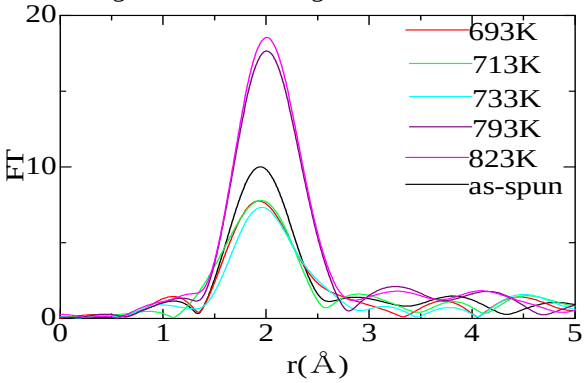

Fig. 2 FT of P *K*-edge EXAFS

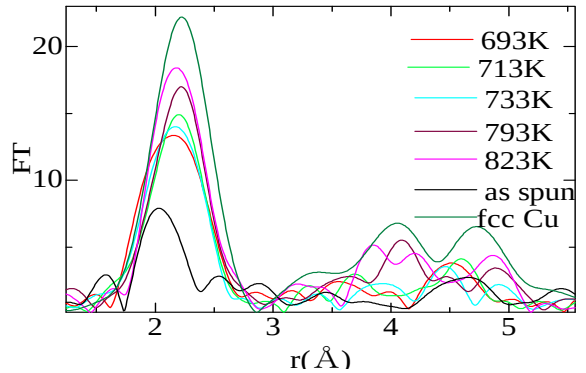

Fig. 3 FT of Cu *K*-edge EXAFS

References

[1]F.Kong A.Wang X.Fan H.Men B.Shen G.Xie A.Makino A.Inoue, J. Appl. Phys. 109 07A303 (2011).
[2]A.Makino, T.Kubota, K.Yubuta, A.Inoue, A.Urata, H.Matsumoto. S.Yoshida. J. Appl. Phys. 109 07A302 (2011).

* takaf@cc.hirosaki-u.ac.jp

4C/2012G128

エピタキシャル成長した $CoFe_2O_4$ 薄膜における逆サイト欠陥の評価
Evaluation of anti-site defects in epitaxial films of $CoFe_2O_4$

柳原英人 [1*], 新関智彦 [1], 内海優史 [1], 鈴木和也 [1],井浦真 [1],喜多英治 [1], 中尾裕則 [2]
[1]筑波大学数理物質系物理工学域、〒305-8573 つくば市天王台 1-1-1
[2]高エネルギー加速器研究機構物質構造科学研究所 〒305-0801 つくば市大穂 1-1

1 はじめに

薄膜形状においてその磁化の容易軸が反磁場に打ち勝ち、膜面垂直方向を向くようないわゆる垂直磁化膜は、今日ではハードディスクドライブ（HDD）の記録層や、スピントロニクスに不可欠な磁気特性である。その起源は薄膜と基板などの界面における対称性の低下に起因した界面磁気異方性、そしてバルクの結晶構造に起因した結晶磁気異方性に分類されることが多い。また、基板との格子不整合によってその界面部分に導入される結晶ひずみも磁気弾性結合を通じて磁気異方性の原因となる。

強い磁気異方性を示す磁性材料の多くは、大きなスピン軌道相互作用にその原因を持つ。一般的には、Pt や Pd、Rh などの白金族元素を含む化合物や合金、あるいは人工格子が垂直磁化材料としてよく知られているが、希少金属に関する供給不安のため貴金属を含まない垂直磁化膜が望まれる。

我々は、立方晶である Co フェライトが MgO(001)上にエピタキシャル成長した時に現れる強い垂直磁気異方性について調べている。Co フェライト薄膜の垂直磁気異方性の起源は、基板との格子不整合であると言われているが、実際に格子ひずみや、Co 原子の配向の有無、サイト欠陥などの膜構造の詳細について包括的に検討した研究例はない。エピタキシャル Co フェライト薄膜の磁性は、応用上大きな可能性を秘めているもののその物理については再考の余地がある。そこで今回は、Co イオンがどの結晶位置に存在しているか吸収端を用いた回折実験を用いて評価することを試みた。

2 実験

試料は、MgO(001)単結晶基板上に成膜した。Co と Fe の組成比は、化学量論比(1:2)よりも Fe が多い 1:3 となるように設計した。測定は、A サイト＋O の構造因子のみからなる逆格子点、そして O のみの逆格子点の回折強度について、Co や Fe の K 端をまたぐようなエネルギー分散の測定を行った。

測定は、室温大気中の条件で PF-4C で行った。また Fe および Co の吸収端（K 端）の校正のため、それぞれ箔状試料の吸収測定を行った。

3 結果および考察

図 1 に A-サイト＋O の構造因子からなるスピネルの(220)反射に関するエネルギー依存性を示す。

Fe の吸収が見られることから A サイトには Fe が存在していることがわかる。一方 Co の吸収は見られず、Co の K 端より数十 eV 高いエネルギーに強度の変化が現れた。このことは A サイトはほとんど Fe によって専有されていることを示唆している。C 今後、Co や Fe といった構成元素の蛍光の影響を考慮して、より定量的な解析を行なう必要がある。

図 1 ： K 端での(220)反射強度のエネルギー依存性

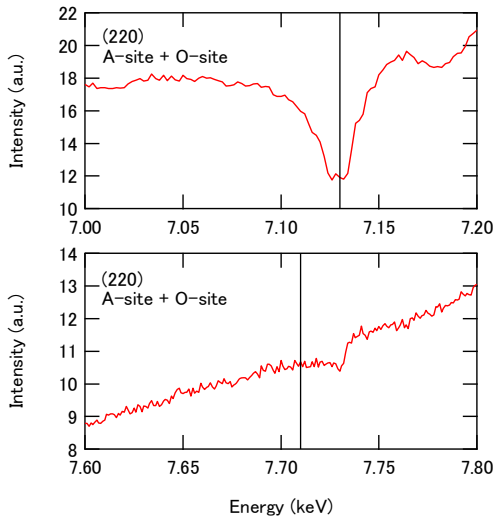

4 まとめ

Co フェライト薄膜における Co イオンが専有する結晶位置を評価するため、エネルギーをパラメータとして逆格子点の回折強度を調べた。その結果、A サイトはほぼ Fe によって専有されているような結果が得られたことから、Co は B サイトに位置しているものと考えられる。

謝辞

本研究は、文部科学省元素戦略プロジェクト「複合界面制御による白金族元素フリー機能性磁性材料の開発」の一環として行われた。

16A/2010S2-001

Ga^+-induced changes in magnetic anisotropy of Pt/Co/Pt thin films studied by X-ray magnetic circular dichroism

Kenta AMEMIYA[1,*], Masako SAKAMAKI[1], Piotr MAZALSKI[2], Iosif SVEKLO[2], Zbigniew KURANT[2], Andrzej MAZIEWSKI[2], Maciej Oscar LIEDKE[3], Juergen FASSBENDER[3], Andrzej WAWRO[4] and Lech Tomasz BACZEWSKI[4]

[1]Photon Factory & Condensed Matter Research Center, Tsukuba 305-0801, Japan
[2]Department of Physics, University of Bialystok, Białystok 15-424, Poland
[3]Helmholtz-Zentrum Dresden-Rossendorf, Dresden 01328, Germany
[4]Institute of Physics, Polish Academy of Sciences, Warszawa 02-668, Poland

1 Introduction

Plenty of efforts have been made to realize perpendicular magnetic anisotropy (PMA) in thin films and multilayers, in view of the application to high-density magnetic recording media. Among them, the control of magnetic anisotropy by ion irradiation has attracted much interest in this decade, due to a possibility of nanostructure patterning by using a focused ion beam. In fact, a Ga^+-induced spin reorientation transition to perpendicular magnetization from an in-plane magnetized Pt/Co/Pt thin film has been reported at medium ion fluences in the 10^{14} ions/cm^2 region [1]. Although the film exhibits in-plane magnetization at higher doses, it has very recently revealed that PMA appears again at much higher ion fluences in the 10^{15} ions/cm^2 regions [2].

In the present study, we performed X-ray magnetic circular dichroism (XMCD) experiments to clarify the origin of the Ga^+ irradiation-induced changes in magnetic anisotropy of a Pt/Co/Pt thin film in a wide range of the ion fluence.

2 Experiment

Co L-edge XMCD spectra were taken at room temperature in the total-electron-yield mode at the soft X-ray undulator beamline, BL-16A. The XMCD measurements were performed in an applied magnetic field of 1.2 T in the normal and grazing incidence configurations, in which the angle between the X-ray beam and sample normal is 0 and 55°, respectively.

3 Results and Discussion

The XMCD spectra are shown in Fig. 1, and the magnetic moments are estimated by the sum-rule analysis, which are summarized in Fig. 2. A larger orbital magnetic moment of Co in the out-of-plane direction compared with that in the in-plane direction is observed at the first PMA region with medium ion fluences. This is consistent with the recent study, in which the appearance of PMA is accompanied with larger out-of-plane orbital moment and a large lattice distortion as revealed by extended X-ray absorption fine structure (EXAFS) measurements [3]. On the other hand, no significant difference in the orbital moments is found in the second PMA region with higher ion fluences, suggesting a different origin for the appearance of PMA. An EXAFS experiment at the high Ga^+ fluence region is being planned in order to clarify the lattice distortion and the degree of Co-Pt mixing, and to understand the origin of PMA.

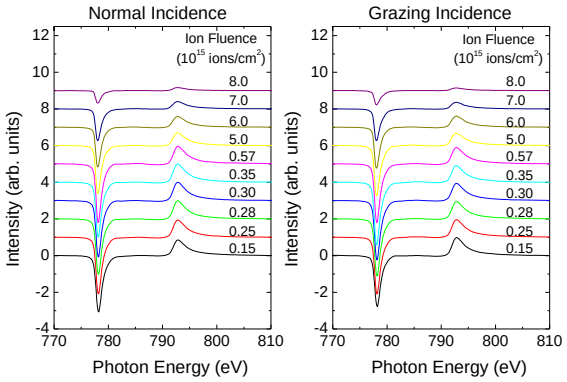

Fig. 1: Co L-edge XMCD spectra for a Pt/Co/Pt film with different ion influences.

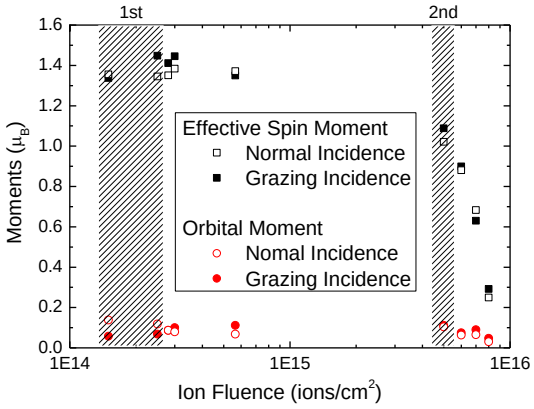

Fig. 2: Effective spin and orbital moments. Shaded areas correspond to the PMA regions.

References

[1] J. Jaworowicz *et al.*, Appl. Phys. Lett., **95** (2009) 022502.
[2] A. Maziewski *et al.*, Phys. Rev. B **85**, (2012) 054427.
[3] M. Sakamaki *et al.*, Phys. Rev. B, in press.

* kenta.amemiya@kek.jp

4B2/2009G092,2011G683

Crystal structure analysis of $Li_2MP_2O_7$ (M =Fe, Mn)

Shinichi NISHIMURA* and Atsuo YAMADA
Department of Chemical Sytem Engineering, School of Engineering,
The University of Tokyo, Tokyo 113-8656, Japan

1 Introduction

Cathode materials of lithium-ion battery (LIB) have many issues of safety and performance improvements. Development of new cathode materials can solve such stagnant of LIB performance. Lithium transition-metal phosphates are the most prominent material group for cathode active materials for lithium ion battery. Recently Adam *et al.* discovered a new material $Li_2MnP_2O_7$, which have a completely new crystal structure[1]. This class of material $Li_2MP_2O_7$ is expected for the cathode material as its ideal Li/M ratio of 2 , which means availability of larger battery capacity. Following the Adam's work, we started to synthesize $Li_2FeP_2O_7$ and tried to characterize the structure and battery performances.

2 Experiment

Powder XRD experiment were performed by using a two-axis diffractometer with multiple-detector system installed at the beam-line 4B2 of Photon Factory (PF), High Energy Accelerator Organization (KEK) in Tsukuba[2]. The diffraction patterns were collected in asymmetric reflection geometry where the incident angle was fixed at 3°. The recorded pattern of each detectors were merged by an Igor Pro macro system developed by Ida[3]. Rietveld refinement of the powder diffraction patterns were conducted by TOPAS-Academic (Ver. 4.1).

3 Results and Discussion

Fig.1 shows Rietveld refinement patterns of $Li_2MnP_2O_7$ and $Li_2FeP_2O_7$. The both patterns were successfully refined with $P2_1/c$ space group and a structural model, which is based on Adam's model[1]. The good ness of fit (S) and reliability indices were converged to reasonable values (see Fig.1) by including a small amount of impurities (< 2wt% in total). These structures are essentially isomorphic, while the peak intensity ratios are significantly different. Origin of such differences are originated from the significant disordering of cation position. Detailed Rietveld and Fourier analysis suggests that an anti-site type defect between a specific crystallographic site of Li and Fe is the most reasonable model for describing the cation disorder. Surprisingly the crystal structure of $Li_2FeP_2O_7$ have never been reported. Thus our report was the first synthesis and structure determination of $Li_2FeP_2O_7$[4].

Recently we found that the $Li_2MnP_2O_7$ is electrochemically active, although the previous studies showed negligible performance at the conventional voltage

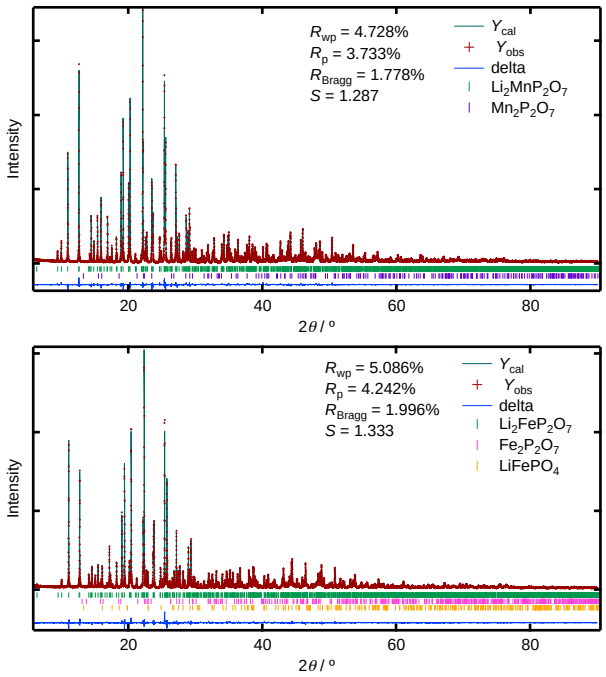

Fig. 1: Rietveld refinement patterns of $Li_2MnP_2O_7$(top) and $Li_2FeP_2O_7$(bottem).

range of 2.0 - 4.5 V. The average redox potential was 4.45 V vs. Li, which is the highest value among manganese phosphate materials. This activity was achieved by careful optimization of the material. Details of electrochemical data and structural analysis will be reported elsewhere[5].

Acknowledgement

Part of this work was financially supported by Mitsubishi Motors Co. and Funding Program for World-Leading Innovative R&D on Science & Technology and Cabinet Office, Government of Japan.

References

[1] L. Adam *et al.*, J. Solid State Chem. **181(11)**, (2009) 3110.
[2] T. Toraya *et al.*, J. Synchrotron Rad. **3(2)** (1996) 75.
[3] T. Ida *et al.*, J. Appl. Cryst. **38**, (2005) 795.
[4] S. Nishimura *et al.*, J. Am. Chem. Soc. **132(39)**, (2010) 13596.
[5] M. Tamaru *et al.*, submitted.

* nishimura@chemsys.t.u-tokyo.ac.jp

5A, 17A, NW12A, NE3A/2009G208, 2011G020, BL26B2/2011A1904

Crystal structure of the C-terminal globular domain of oligosaccharyltransferase from *Archaeoglobus fulgidus*

Shunsuke Matsumoto[1], Mayumi Igura[1], James Nyirenda[1], Masaki Matsumoto[1], Satoru Yuzawa[1], Nobuo Noda[2], Fuyuhiko Inagaki[2], and Daisuke Kohda[1]
[1]Kyushu University, Fukuoka 812-8582, Japan
[2]Hokkaido University, Sapporo 060-0812, Japan

1 Introduction

Asparagine-linked glycosylation (N-glycosylation) of proteins is widespread not only in eukaryotes, but also in archaea and some eubacteria. Oligosaccharyltransferase (OST) creates the oligosaccharide-asparagine bond by transferring glycan from a lipid-linked oligosaccharide (LLO) to asparagine residues in the N-glycosylation sequon, Asn-X-Ser/Thr (X ≠ Pro). OST is a multi-subunit membrane protein complex in higher eukaryotes, and a single-subunit membrane protein in lower eukaryotes, archaea and eubacteria. The catalytic subunit of the OST enzyme has a common evolutionary origin, but is referred to as STT3 in eukaryotes, AglB in archaea, and PglB in eubacteria. The STT3/AglB/PglB proteins consist of an N-terminal multi-span transmembrane region and a soluble C-terminal, globular domain. The STT3 proteins share more than 40% sequence identity, but exhibit limited sequence identity with the AglB and PglB proteins, typically less than 20%. Thus, a meaningful multiple sequence alignment across the three domains of life was almost impossible without referencing three-dimensional structures.

We previously determined the crystal structures of the C-terminal globular domains of *Pyrococcus furiosus* AglB [1] and *Campylobacter jejuni* PglB [2]. The structures facilitated the multiple sequence alignment in the C-terminal globular domain region, and unexpectedly led to the identification of a new, short motif within a characteristic, kinked helix. A comprehensive phylogenetic analysis revealed two conserved amino acid motif within the kinked helix, named DK and MI motifs, and suggested the existence of a third motif at the spatially equivalent position [2].

2 Experiment

Crystals grew from a hanging drop with a 1:1 volume ratio (total volume, 2 μl) of the protein stock solution (20 mg/ml, 20 mM Tris buffer, pH 8.0) and the reservoir solution (0.1 M MES buffer, pH 6.5, 12.5% polyethylene glycol 3350) at 293 K. Crystals were soaked in the reservoir solution containing 20% ethylene glycol for cryoprotection, and were cryo-cooled in liquid nitrogen.

The crystals belonged to the space group $P4_12_12$ with unit cell parameters, a = 47.05 Å, c = 159.82 Å, and diffracted to a resolution of 1.75 Å at beamlines 5A, PF and BL44XU, SPring8. The structure was refined to R/R_{free} of 0.223/0.254 using Se SAD phase. The atomic coordinates have been deposited in the Protein Data Bank, with the accession code 3VGP.

3 Results and Discussion

We determined the structure of the C-terminal globular domain of *Archaeoglobus fulgidus* AglB (*Af*AglB-S1), which possesses the third motif [3]. The crystal structure revealed that the kinked helix contained an unexpected inserted loop structure. A revised sequence alignment based on this finding identified that the third motif was actually a variant type of the DK motif. When taken together with the fact that the DK/MI motifs are involved in the formation of a binding pocket that recognizes the +2 Ser/Thr residue in the N-glycosylation sequons, this study defines the classification of OST: one group consisting of eukaryotes and most archaea possesses the DK-type Ser/Thr pocket, and the other group consisting of eubacteria and the remaining archaea possesses the MI-type Ser/Thr pocket. This classification provides a useful framework for future OST studies.

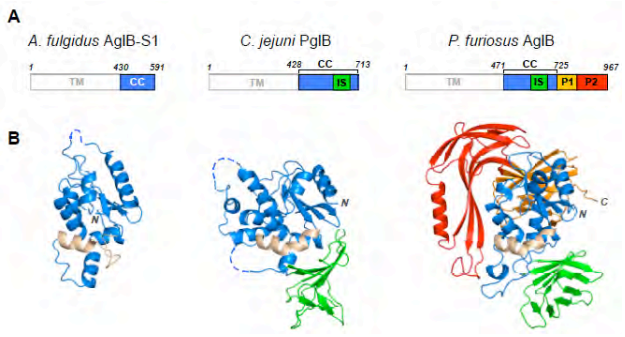

Fig. 1: Comparison of the structures of *Archaeoglobus fulgidus* AglB (this study), *Campylobacter jejuni* PglB, and *Pyrococcus furiosus* AglB. (**A**) Domain organization of the three AglB/PglB proteins. (**B**) Overall structures of the C-terminal globular domains. The characteristic kinked helix bearing the DK/MI motifs is highlighted in light brown.

References

[1] M. Igura *et al.*, EMBO J **27** (2008) 234.
[2] N. Maita *et al.*, J. Biol. Chem. **285** (2010) 4941.
[3] S. Matsumoto *et al.*, Biochemistry **51** (2012) 4157.

* kohda@bioreg.kyushu-u.ac.jp

1A, 5A, 17A, NW12A /2009G524

Structural approach to inhibitor design for African trypanosome glycerol kinase

Balogun Emmanuel Oluwadare[1], Tomoo Shiba[1], Daniel Inaoka Ken[1]
Kimitoshi Sakamoto[1], Kiyoshi Kita[1], Shigeharu Harada*[2]
[1]Department of Biomedical Chemistry, Graduate School of Medicine, The University of Tokyo, Tokyo 113-0033, Japan
[2]Department of Applied Biology, Graduate School of Science and Technology, Kyoto Institute of Technology, Kyoto 606-8585, Japan

Introduction

Human African Trypanosomiasis is caused by *Trypanosoma brucei gambiense* (Tbg) and *T. b. rhodesiense*. It is a threat to 60 million human lives. Currently available treatments have become unsatisfactory, hence the need for development of new chemotherapies. Although glycerol kinase (GK) of the parasites is a validated promising target of chemotherapy, an effective and selective parasite GK inhibitor is yet to be available. In this study we are utilizing structure-based approach to develop trypanosome GK-specific inhibitor(s). The enzyme was overexpressed in *Escherichia coli*, purified to homogeneity, and crystallized [1]. Crystals of unliganded (apo) and ligand-bound forms were obtained with precipitant solutions that was composed of 10 % sorbitol, 12 % isopropanol, and 0.1 M HEPES pH 7.0; and 11 % hexane-1,6-diol, 25 % PEG 400 in 0.1 M HEPES pH 7.5; respectively.

Results and discussion

Complete X-ray diffraction data sets were collected to 2.90, 2.40, 2.70, 1.90, and 2.0 Å resolutions respectively for Apo, glycerol, glycerol 3-phosphate, ADP, and ATP forms of TbgGK. While the Apo form crystals formed in space groups $P2_12_12_1$, the liganded belonged to $P2_1$. The structure of TbgGK revealed that the enzyme is a homodimer (Fig. 1), which is formed by a somewhat strong association of two monomer chains A and B where the dimer interface is made up of an anti-parallel β-sheet (β15) and three α-helices (α12, α14, and α19) that are contributed by each of the monomers. Contact surface area of each monomer is about 5700 Å^2, representing about 30 % of total surface area for each of them; Nature of interactions that forms the dimer interface is largely hydrophobic interactions. Each monomer of the enzyme is made up of two functional domains I and II, (Fig. 1). Domain I is made up of N-terminal residues 1-262, while domain II is composed of residues 269-512. They are linked by a hexapeptide loop made up of NMCFEK, which formed a turn between α11 and β12 of the respective domains on the monomer surface. In between these domains is the located a clearly carved out active site cleft/grove (Fig. 1). Each domain is made up of the secondary structure signature of the sugar kinase/Hsp70/actin super family that is the typical core ββ βαβαβ structure. In total, each monomer is composed of 18 β-strands and 19 α-helices, with lengths ranging from 3-7 and 6-26 residues respectively.

Our findings have revealed some unique structural characteristics of TbgGK, which we have utilized for *in silico* screening (Fig. 2A). An encouraging number of inhibitors with novel scaffold, which have IC_{50} in the nanomolar range have been identified. Shown in Figs 2B-2C are best docking poses of some of the inhibitors (Inh-1, Inh-2, and Inh-3, respectively), which may lead to design of potent drug candidates against the disease.

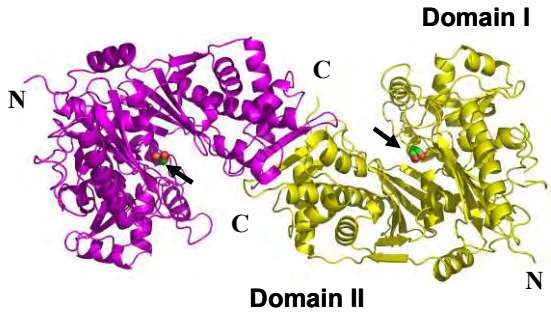

Fig. 1

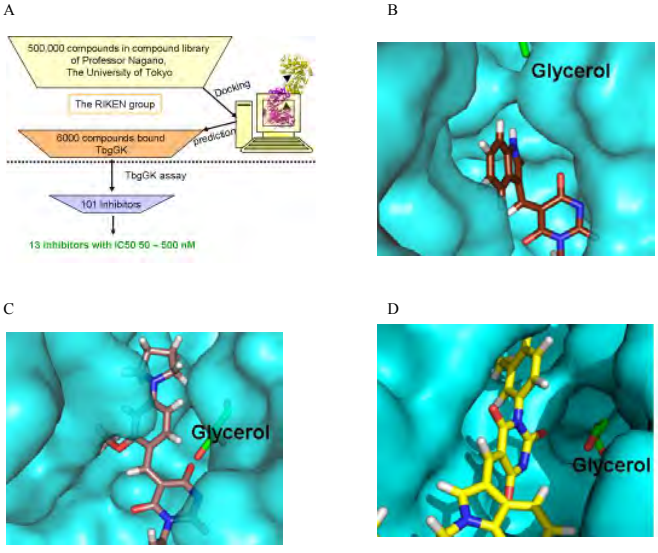

Fig. 2

[1] EO. Balogun *et al*., Acta Cryst. F 66, 304 (2010).

* harada@kit.ac.jp

NW2A/ 2009G636

A superposed kagome-lattice Crystallization of a Keplerate-type polyoxometalate

Masaki Saito and Tomoji Ozeki*
Department of Chemistry and Materials Science, Tokyo Institute of Technology, 2-12-1-H-63 O-okayama, Meguro-ku, Tokyo 152-8551, Japan.

1 Introduction

A frequently occurring packing mechanism for an ionic crystal is to arrange larger ions into a close-packed array and smaller ones into the interstices between the larger ones. In this context, it seems reasonable that the exceedingly large Keplerate-type spherical polyoxometalates, the $[Mo^{VI}_{72}Mo^{V}_{60}O_{372}(CH_3COO)_{30}(H_2O)_{72}]^{42-}$ anion (hereafter, abbreviated as $\{Mo_{132}\}$), prefer to crystallize into cubic or trigonal space group types where the huge spherical anions (approximate diameter of 30 Å) adopt strict or slightly distorted cubic close packing arrays. However, the $\{Mo_{132}\}$ anion, which consists of 12 pentagonal $[Mo^{VI}_6O_{21}(H_2O)_6]^{6-}$ and 30 $[Mo^{V}_2O_4(CH_3COO)]^+$ moieties (Figure 1), is not completely isotropic but approximates to the I_h symmetry. It is incompatible with the site symmetry of the spheres in any type of close packings. Therefore, introduction of intermolecular interactions specific to the local structures of $\{Mo_{132}\}$ could lead to a different and less dense arrangement of the anions. By using Sr^{2+} as counter cations, we succeeded in crystallizing $\{Mo_{132}\}$into an unprecedented superposed kagome-lattice structure with huge channels.[1]

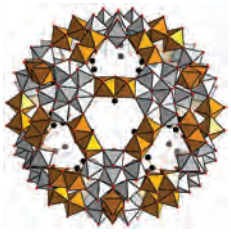

Fig. 1: Structure of $\{Mo_{132}\}$.

2 Experiment

A 15.0 mL aqueous solution dissolving 0.50 g of $(NH_4)_{42}\{Mo_{132}\}\cdot ca.300H_2O\cdot ca.10CH_3COONH_4$ was mixed with a 15.0 mL aqueous solution containing 1.26 g of $SrCl_2\cdot 6H_2O$. The mixed solution was heated to 65 °C for 1.5 h and kept at 40 °C for two weeks. After the solution cooled down to the room temperature, dark red hexagonal prismatic crystals of $Sr_{18.5}(NH_4)_5[Mo^{VI}_{72}Mo^{V}_{60}O_{372}(CH_3COO)_{30}(H_2O)_{72}]\cdot mH_2O$ (**1**) were precipitated. Single crystal X-ray diffraction experiment was carried out at the NW2A beamline of PF-AR.

3 Results and Discussion

Compound **1** crystallizes in the space group $P6_3/mmc$. The $\{Mo_{132}\}$ anions are located at the 2/*m* sites to make a superposed kagome-lattice. The $\{Mo_{132}\}$ anions are connected so as to sandwich hydrated Sr^{2+} cations with their Mo_9O_9 pores. Each connection is supported by two additional Sr^{2+} cations that are directly bound to the terminal O atoms of the two $\{Mo_{132}\}$ anions. At the connections parallel to the crystallographic *a*, *b* or *a*+*b* axes (perpendicular to the *c* axis, Figure 4a), two O–Sr–O linkages stem from the Mo atoms that belong to the Mo_9O_9 pores but belong to different $[Mo^{VI}_6O_{21}(H_2O)_6]^{6-}$ moieties. The two Mo_9O_9 pores are almost parallel to each other with the dihedral angle of 11.16(1)° and the distance between two $\{Mo_{132}\}$ is 30.765 Å. Due to the I_h symmetry, $\{Mo_{132}\}$ can accommodate up to only four Mo_9O_9 pores on a great circle. Therefore, this type of interaction leads to a kagome-lattice sheet of $\{Mo_{132}\}$ spanning parallel to the crystallographic *ab* plane. Six $\{Mo_{132}\}$ surrounding the large space at the origin of the unit cell point their $[Mo^{V}_2O_4(CH_3COO)]^+$ moieties to the space and they cannot establish similar interactions with another $\{Mo_{132}\}$ in this cavity. As a result, the cavity is left unoccupied by $\{Mo_{132}\}$ and presumably filled with disordered water molecules.

The kagome-lattice sheets are superposed to form a three-dimensional framework as shown in Figure 2. The sheets are connected by a similar interaction between two $\{Mo_{132}\}$ through their Mo_9O_9 pores. The dihedral angle of the two Mo_9O_9 pores is as large as 39.55(1)°. Thus the two O–Sr–O linkages supporting this connection stem from two Mo atoms that belong to the same $[Mo^{VI}_6O_{21}(H_2O)_6]^{6-}$ moiety but are not in the Mo_9O_9 at the rim of the pore. As a result, the kagome-lattice sheets are arranged so that the cavities of one sheet fall exactly above those of the sheet below, leading to a channel running through the crystal along the *c* axis.

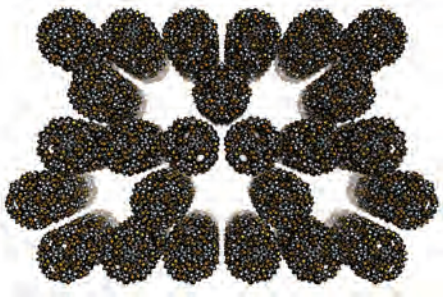

Fig. 2: Superposed kagome lattice of $\{Mo_{132}\}$.

References

[1] M. Saito, T. Ozeki, Dalton Trans. (2012) in press, DOI: 10.1039/C2DT30582H.

* tozeki@cms.titech.ac.jp

8A/2009S2-008

鉄ニクタイド超伝導体における微視的結晶構造と転移温度との関係
The Relation between Crystal Parameters and T_c in Iron Pnictide Superconductors

竹森章 [1*],宮坂茂樹 [1], 田島節子 [1],
中尾朗子 [2], 中尾裕則 [2], 熊井玲児 [2], 村上洋一 [2]
[1]阪大院理、〒560-0043 豊中市待兼山町 1-1
[2]KEK 物構研 PF/CMRC　〒305-0801 つくば市大穂 1-1

1　はじめに

2006 年に東工大の細野らによって LaFePO が T_c = 4K で超伝導転移を示すことが報告された[1]。さらにこの物質の P サイトを同じ 15 族の As で置換することにより T_c は 26K まで上昇し[2]、世界中で精力的に研究が行われるようになった。La サイトをイオン半径の小さい Sm で置換することにより T_c は最終的に 55K まで上昇し、鉄系超伝導体は銅酸化物高温超伝導体に次ぐ高い転移温度を有するようになった。

*R*FePO（*R*: 希土類元素）と *R*FeAsO の間で T_c は最高 50K 以上異なっており、これは T_c が Fe 周りの微視的結晶構造と強く相関しているためと考えられている。例えば C. H. Lee らによる報告では、Fe 原子に対して最近接の As 原子が正四面体配位をとるとき（即ち As-Fe-As の結合角 α が 109.47° に近づくとき）に T_c が最も高くなる、という経験則が主張されている[3]。一方理論的立場からは、数ある結晶構造パラメータの中でも Fe 2 次元面からのニクトゲン *Pn* の高さ h_{Pn} が大きくなるほど T_c が上昇する可能性が主張されており[4]、実際の系においても一致が見られる。

今回の実験では $PrFeP_{1-x}As_xO_{0.9}F_{0.1}$ の組成において x を 0 から 1.0 まで連続的に変化させ、結晶構造が T_c と輸送現象に及ぼす変化を系統的に調べることで、鉄系に働く超伝導メカニズムを解明することを目的とした。

2　実験

原料の PrAs, PrP, Fe_2O_3, Fe, FeF_2 を秤量・混合し、それを石英管封管中で焼成することで $PrFeP_{1-x}As_xO_{0.9}F_{0.1}$ の多結晶体を合成した。得られた試料について粉末 X 線回折、磁化率、電気抵抗率、ホール係数などの測定を行った。加えて PF BL-8A において室温における放射光 X 線回折実験を行い、各元素のサイトポジションの決定を行った。

3　結果および考察

$PrFeP_{1-x}As_xO_{0.9}F_{0.1}$ は室温において正方晶 *P*4/*nmm* の結晶構造をとった。 図 1 に(a)格子定数 *a*, *c*、(b)ニクトゲンの高さ h_{Pn}, *Pn*-Fe-*Pn* 結合角 α、(c)T_c の組成依存性を示す。x の増加とともに *a*, *c* 軸長および h_{Pn} は線形に上昇し、α は減少した。T_c は x の増加とともに連続的に上昇しており、T_c と結晶構造が P/As の固溶系においても過去の報告と同様の相関関係があることが明らかになった。

一方で角度分解型光電子分光（ARPES）や磁場侵入長の温度依存性の測定結果から、FeP 系化合物と FeAs 系化合物との間で超伝導ギャップの対称性が異なることが報告されている。本研究においても電気抵抗率やホール係数の温度依存性が P 側から As 側にかけて極めて非線形な As 濃度 x 依存性を示したことから、結晶構造の変化に起因して磁気揺らぎの増大などの変化がもたらされていることが示唆された。

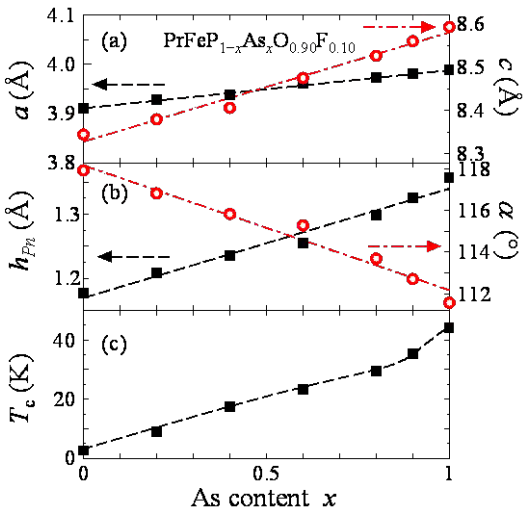

図 1 ：結晶構造パラメータと T_c の組成依存性

4　まとめ

$PrFeP_{1-x}As_xO_{0.9}F_{0.1}$ において P/As 固溶効果を調べ、結晶構造と T_c との相関を明らかにした。またそれに由来して非線形に変化する物理的パラメータの存在も示唆された。

参考文献

[1] Y. Kamihara, *et al.*, J. Am. Chem. Soc. **128** (2006) 10012.
[2] Y. Kamihara, *et al.*, J. Am. Chem. Soc. **130** (2008) 3296.
[3] C. H. Lee, *et al.*, J. Phys. Sci. Jpn. **77** (2008) 083704.
[4] K. Kuroki, *et al.*, Phys. Rev. B **79** (2009) 224511.

* takemroi@tsurugi.phys.sci.osaka-u.ac.jp

BL-10A/2010G015

The effects of pressure on crystal structure of δ-AlOOH up to 9.0 GPa

Takahiro KURIBAYASHI[1*], Asami Sano-Furukawa[2] , Toshiro Nagase[3]
[1]Department of Earth Science, Graduate School of Science, Tohoku Univ., Sendai 980-8578, Japan
[2]JAEA, Tokai, Ibaraki 305-, Japan
[3]The Tohoku University Museum, Tohoku Univ., Sendai 980-8578, Japan

Introduction

δ-AlOOH is a high-pressure polymorph of AlOOH. δ-AlOOH was synthesized by Suzuki et al. (2000) [1] at 1600ºC and 21 GPa conditions using a Kawai type multi-anvil apparatus. According to some previous studies [2-3], δ-AlOOH is stable under wide PT conditions such as 18-130 GPa and <2300K, and is recognized as an important phase in the view of the carriers and reservoirs of hydrogen in the Earth′s deep interior.

Crystal structure of δ-AlOOH is a distorted rutile type structure with space group $P2_1nm$ and has hydrogen bonding in its structure. It is considered that hydrogen bonding would be influenced on its thermal stability.

The previous powder X-ray diffraction study [4] implied the pressure induced phase transition of δ-AlOOH around 10 GPa, but it is not clear. Also Ab-initio calculations [5-6] suggested that the space group of δ-AlOOH would be changed from $P2_1nm$ to $Pnnm$ by re-arrangements of hydrogen under high-pressure conditions. Hydrogen bonding, therefore, is the key to understand the mechanism of the pressure-induced phase transition.

We reported that some results of a high-pressure single crystal X-ray diffraction study on a δ-AlOOH at ambient, 0.6, 1.2, 4.0, 4.2, 6.2, 7.0, 8.7 and 9.0 GPa in order to investigate the effects of pressure on δ-AlOOH.

Experimental Procedure

The sample used for this study was synthesized at 18 GPa and 900-1000ºC kept by 1 hour using a Kawai-type multi-anvil apparatus installed in Tohoku University. A single crystal of δ-AlOOH (50×50×30 μm^3 in size) was mounted in a modified Merrille-Bassett type diamond anvil cell. He gas was used for the pressure medium and a GIN6 stainless plate used for a gasket. Pressure was determined by the EOS of δ-AlOOH [4]. X-ray diffraction intensities were measured using an automated four-circle X-ray diffractometer installed at the beam line BL-10A, Photon Factory, High Energy Accelerator Research Organization. The wavelength (λ=0.6513Å) of synchrotron radiation was calibrated by the unit cell volume of the NIST ruby standard crystal at ambient temperature. Unit cell parameters of δ-AlOOH at each pressure point were determined from 15-34 centered reflections in the 2θ range between 11.9° and 34.9°. X-ray reflection intensity data sets were collected up to (sin $\theta/\lambda < 0.99$ $Å^{-1}$, $2\theta_{max}=80°$) at 0.6, 4.2, 6.2 and 8.7 GPa. The $h0l$ and $0kl$ series reflections were used for the determination of space group.

Results

The unit cell parameters of δ-AlOOH at each pressure point were summarized in Table 1. No discontinuity was observed up to 9.0 GPa in the volume compression curve of δ-AlOOH (Fig 1). On the other hand, a new additional systematic absence ($k+l=2n+1$, in $0kl$ series) was observed in the X-ray diffraction reflection intensities up to 8.7 GPa. This observation suggested that the pressure induced phase transition of δ-AlOOH was occurred around 8.7 GPa and was a high-ordered transition. The candidate of the space group of the after transition phase was $Pnnm$ or $Pnn2$ based on the extinction rule.

Table 1. The lattice parameters of δ-AlOOH at each pressure point up to 9.0 GPa

P (GPa)	*a*	*b*	*c*	*V*
0.0001	4.7147(5)	4.2250(4)	2.8318(2)	56.408(9)
0.6	4.709(6)	4.216(1)	2.830(2)	56.18(8)
1.2	4.700(2)	4.211(1)	2.828(1)	55.97(3)
4.0	4.673(1)	4.177(1)	2.816(1)	54.96(3)
4.2	4.671(2)	4.175(1)	2.816(1)	54.91(3)
6.2	4.654(2)	4.153(1)	2.808(1)	54.27(3)
7.0	4.647(2)	4.145(1)	2.805(1)	54.03(3)
8.7	4.637(2)	4.129(1)	2.799(1)	53.60(4)
9.0	4.632(2)	4.129(1)	2.797(1)	53.49(3)

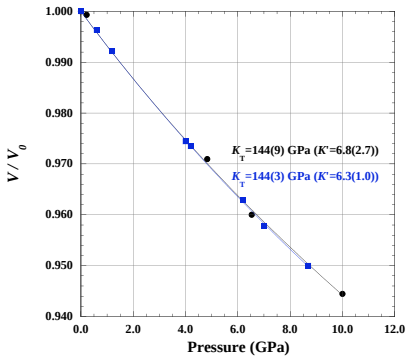

Figure 1. The compression curve of δ-AlOOH up to 9 GPa.

References

[1] Suzuki *et al.* (2000) *Phys. Chem. Mineral*, **27**, 689-693. [2] Ohtani *et al.* (2001) *Geophys. Res. Lett.*, **28**, 3991-3993. [3] Sano *et al.* (2008) *Geophys. Res. Lett.*, **35**, L03303. [4] Sano-Furukawa et al. (2009) *Amer. Mineral.*, 94, 1255-1261. [5] Tsuchiya *et al.* (2002) *Geophys. Res. Lett.*, **29**, 1909. [6] J. Tsuchiya and T. Tsuchiya (2002) *Phys. Rev. B.*, **83**, 054115.

* t-kuri@m.tohoku.ac.jp

NW12A/2010G062

The Structural flexibility of the shank1 PDZ domain is important for its Binding to different ligands

Soo Hyun Eom*

School of Life Science, Gwangju Institute of Science and Technology, Gwangju 500-712, Korea

Introduction

The PDZ domain of the shank protein interacts with numerous cell membrane receptors and cytosolic proteins via the loosely defined binding motif X-(Ser/Thr)-X-Φ-COOH (Φ represents hydrophobic residues) at the carboxyl terminus of its target protein. We have determined the crystal structure of the shank1 PDZ in complex with the βPIX C-terminal pentapeptide (642–646, DETNL) at 2.3 A resolution and modeled shank1 PDZ binding to selected pentapeptide ligands. The resulting structures revealed a large hydrophobic pocket within the PDZ domain that can accommodate a variety of ligand residues at the P(0) position. A H-bond between His735 and Ser/Thr at the P(-2) position is invariant throughout the model structures. In addition, we identified multiple PDZ domain residues that are able to form H-bonds and salt bridges with an incoming target protein. Overall, our study provides a new level of understanding of the specificity and structural plasticity of the shank PDZ domain

Experiment

Pentapeptide DETNL, which has the same amino acid sequence as the bPIX C-terminus, was synthesized by Anygen Co.(Korea). The Shank1 PDZ:bPIX complex was then prepared by mixing 10 mg/ml of the protein with the peptide stock at a 1:3 M ratio. Crystals of the shank1 PDZ: βPIX complex were grown by vapor diffusion using 1λ of ~0.8 mM complex and an equal volume of reservoir solution containing 100 mM sodium acetate (pH 5.5–6.0),

0.8 M lithium sulfate and 0.7 M ammonium sulfate. Successful flash freezing was achieved using Paratone N oil (Hampton Research). A diffraction dataset with Bragg spacings of 2.3 A was collected at beam line NW AR12 at the Photon Factory (Tsukuba,Japan) using the X ray beam at a single wavelength (1.000 A).The data set was indexed and processed using the program HKL2000

Results

Comparison of shank1 PDZ–interacting peptides and switch residues in a shank1 PDZ–peptide complex model.

Interaction mode of the receptor tyrosine kinase C terminal pentapeptide (AFTRF) (A), the somatostatin receptor type 2 C-terminal pentapeptide (LQTSI) (B), the Na^+/H^+ exchanger 3 C-terminal pentapeptide (ESTHM) (C), and the CaV1.3 L-type calcium channel C-terminal pentapeptide (CITTL) (D) with the rat shank1 PDZ. The bound peptides and the key PDZ residues involved in the interactions are shown in stick models. The PDZ domains are drawn as ribbon diagrams. H-bonds are represented as red dotted lines. The amino acid sequences of the bound peptides are written in red

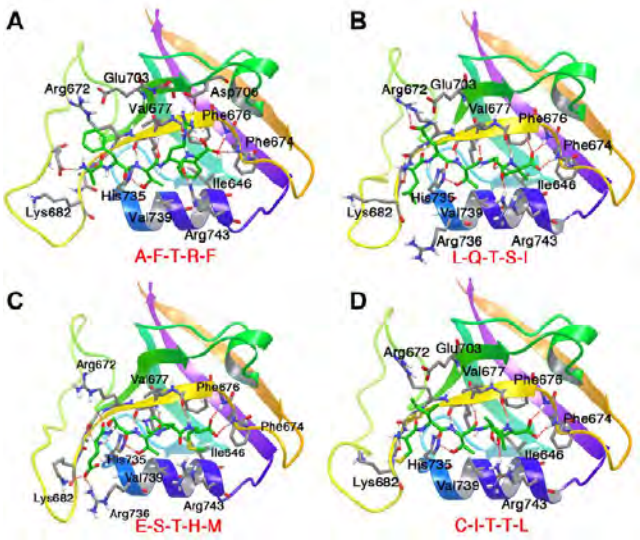

References

[1] H. Zitzer, H.H. Honck, D. Bachner, D. Richter, H.J. Kreienkamp, Somatostatin receptor interacting protein defines a novel family of multidomain proteins present in human and rodent brain, J. Biol. Chem. 274 (1999) 32997–33001.

* eom@gist.ac.kr

4B1/2010G142

地球圏外物質の結晶学的研究
Crystallographic studies of extraterrestrial materials.

萩谷健治[1*], 大隅一政[2], 三河内岳[3], M.E.Zolensky[4], 佐竹渉[3]
[1]兵庫県立大学大学院生命理学研究科、〒678-1297 上郡町光都 3-2-1
[2]高輝度光科学研究センター、〒679-5198 佐用町光都 1-1-1
[3]東京大学大学院理学系研究科、〒113-0033 文京区本郷 7-3-1
[4]NASA Johnson Space Center, 2101 NASA Parkway Houston, Texas 77058, USA

1 はじめに

人類が手にすることのできる地球圏外物質（彗星塵、宇宙塵、小惑星回収試料、隕石、月試料等）は、太陽系の誕生からその後に起こった惑星物質進化の過程を記録していると考えられる極めて重要な試料である。このキャラクタリゼーションのために、化学組成や同位体組成などの化学的側面からの研究が数多く行われている。しかしながら、この他に物質の同定に必須とされる結晶学的情報を得るためのX線回折法による研究は、微小領域からの回折データの収集が容易ではないことからほとんど行われていないのが実情である。そこで本課題では、これら地球圏外物質について放射光を用いた微小領域X線回折による研究を行った。ここでは、アポロ月試料60016 薄片に含まれる鉄酸化物試料についての解析結果を報告する。

2 実験

実験は BL-4B1 に設置された微小領域回折計を用いて行った[1]。放射光白色 X 線はビームラインに備えられたピンホールにより直径 100μm に制限され回折計に導かれる。さらに試料直前に設置したマイクロピンホールにより試料位置で直径 1.6μm に絞られている。このマイクロビームに対し、アポロ月試料 60016 薄片中に存在する鉄酸化物試料の位置を光学顕微鏡下で調整した。回折像を円筒形のイメージングプレート（富士フィルム）上に 30 分間露光して撮影した。得られた回折像は非常に複雑であり（図 1）、これは複数のドメインからの回折像が重なっていることを示している。この写真から透過反射 283 点、背面反射 417 点、合計 700 点の回折点が得られた。

3 解析および結果

複数のドメインからの回折像が重なっているため、回折点の指数付けにはこれらを各ドメインのものに分ける必要がある。そこで同じ晶帯に属すると考えられる回折点の組をいくつか見出し、これを基に分離することを試みた。例えば晶帯の交差する位置に回折点がある場合、それらの回折点は同じドメインからのものであると判断した。このようにして、ある一つのドメインからのものと考えられる回折点の組を選び出した。試料の鉄酸化物としてはヘマタイト(α-Fe_2O_3)とマグネタイト(Fe_3O_4)が予測されていた。そこで選択した回折点について、それぞれの格子定数を用いて指数付けを試みた。ヘマタイトの格子定数では満足できる結果が得られなかったが、マグネタイトと仮定した結果、189 点に指数付けできた。この他の回折点についても、晶帯に着目するという同様の方法で同一のドメインからの回折点の組を選別し、指数付けを行った。これを繰り返すことにより、最終的に 4 つのマグネタイトのドメインを見出し、全部で 562 の回折点に指数付けできた。これらの回折点位置は、試料をマグネタイトと仮定した計算結果と良く一致した。残り 138 点は比較的回折強度が弱く、また 3 点以上の回折点が同一の晶帯上に存在するような関係のものも見出せなかった。これらのことから、残りの回折点は非常に細かい多数のドメインからのものであると考えられる。

解析結果の妥当性について、回折点位置だけでなく、回折強度に基づき評価した。すなわち比較的シャープで且つ回折強度も強い 2 つのドメインからの回折点について積分強度を測定し、計算値との比較を行った。その結果、重みつきの R 因子はそれぞれ Rw = 0.079, 0.119 となり、積分強度からもこの鉄酸化物はマグネタイトであることが確認された。還元的な環境で形成された月試料からマグネタイトが見つかったのは初めてであり、この存在理由についての考察を現在行っているところである。

参考文献

[1] K. Ohsumi *et al.*, Rev. Sci. Instrum. **66**-2 (1995) 1448

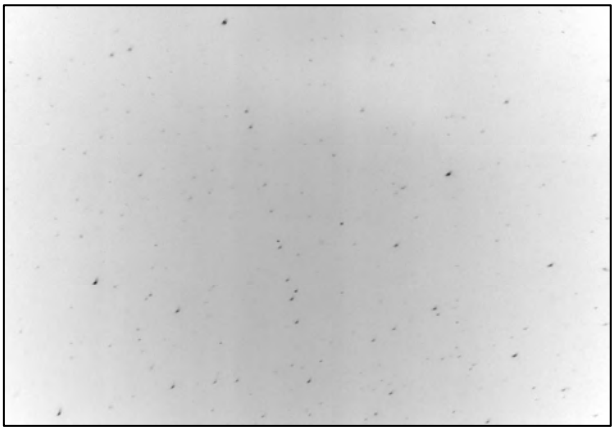

図 1　得られた X 線回折像（背面反射の領域）

* hagiya@sci.u-hyogo.ac.jp

4B2/ 2010G144

水酸アパタイトおよび炭酸水酸アパタイトの結晶構造と電子密度分布
Crystal structure and electron density distributions of hydroxyapatite and carbonated hydroxyapatite

久保直幸[1], 八島正知[2], 米原幸彦[1], 藤森宏高[3], 井奥洪二[4], 上高原理暢[5],朴運炅[5]
[1]東京工業大学大学院 総合理工学研究科〒226-8502 神奈川県横浜市緑区長津田町 4259
[2]東京工業大学大学院 理工学研究科〒152-8550 東京都目黒区大岡山 2-12-1
[3]山口大学大学院 理工学研究科〒755-8611 山口県宇部市常盤台 2-16-1
[4]慶応義塾大学大学院 経済学研究科〒223-8521 神奈川県 横浜市港北区日吉 4-1-1
[5]東北大学大学院 環境科学研究科〒980-8579　宮城県仙台市青葉区荒巻字青葉 6-6-20

1 はじめに

水酸アパタイト($Ca_{10}(PO_4)_6(OH)_2$：HAp)と炭酸水酸アパタイト(CO_3HAp)は骨と歯の主要無機化合物であり、生体親和性から人工骨や人工歯根として活発な臨床的応用研究が行われている。またプロトン伝導性を示し、CO_3HAp のプロトン伝導度は HAp より高い。化学結合は HAp と CO_3HAp の特性を理解するのに重要であり、電子密度解析は化学結合を議論するのに大切な役割を果たす。しかし、電子密度を研究した報告は少ない(著者ら *J. Phys. Chem.* C, **115**, 25077-25087 (2011))。また燃料電池が動作する高温で結晶構造を研究することは大事である。そのため本研究では高角度分解能放射光粉末回折データにより化学量論組成(Ca/P=5/3)の HAp と炭酸を 5.1wt%含む AB 型 CO_3HAp の高温における結晶構造および電子密度分布を研究した。

2 実験

化学両論組成の水酸アパタイトと炭酸を 5.1wt%含んだ炭酸水酸アパタイトを用い PF の BL-4B2 に設置された多連装粉末回折計により放射光粉末回折測定を行った。測定した温度は水酸アパタイトでは 673 K と 923 K, 炭酸水酸アパタイトでは 673 K であった。得られたデータを，リートベルト法(RIETAN-FP)、最大エントロピー法(MEM, PRIMA)により解析した。また、得られた結晶学パラメーターを初期値に用いて密度汎関数理論(DFT)計算により原子位置を最適化し、価電子密度分布を調べた。

3 結果および考察

放射光粉末回折データのリートベルト解析は化学量論組成の HAp と AB 型 CO_3HAp は 673 K で六方晶系 $P6_3/m$ を示した(Fig.1)。 673 K で HAp の信頼度因子は、R_{wp}=6.06%, R_I=4.40%, R_F=3.75% および GOF=1.530 であった。格子定数は a=9.47907(2), c=6.91842(1)であった。923K での信頼度因子は、R_{wp}=6.38%, R_I=4.90%, R_F=5.48%および GOF=1.454 であった。格子定数は a=9.51486(5) Å, c=6.94378(3) Å であった。CO_3HAp の 673 K での信頼度因子は、R_{wp}=7.49%, R_I=3.67%, R_F=2.76%および GOF=1.271 であった。格子定数は a=9.4764(4) Å, c=6.91565(19) Å であった。MEM 電子密度図は、HAp と CO_3HAp の両方において P-O は共有結合性を持ち、Ca-O 結合がよりイオン性であることが分かった。CO_3HAp においては CO_3 の O の存在による電子密度分布の広がりを確認した。これらの結果は DFT 価電子密度分布と定性的に一致した。また HAp において 673 K に比べて 923K の電子密度分布の方が大きく広がることを確認した(Fig. 2)。

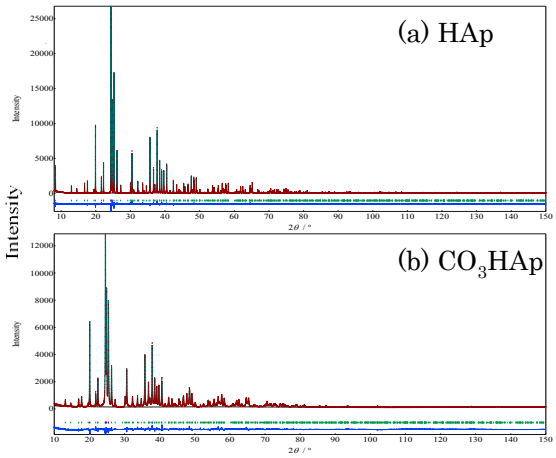

Fig.1 Rietveld patterns for synchrotron X-ray diffraction data of (a) HAp and (b) CO_3HAp at 673 K.

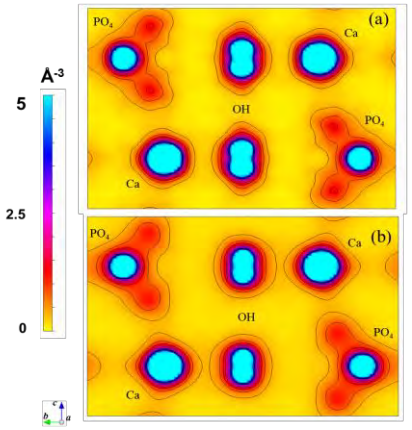

Fig.2 Electron density distributions on the (010) plane of HAp with black contours in the range from 0.0 to 5.0 $Å^{-3}$(0.4 $Å^{-3}$ step) at (a) 673 K and (b) 923 K.

* yashima＋@＋cms.titech.ac.jp

9C / 2010G173

$CoMn_2O_4$ の SiO_2 包含による Jahn-Teller 歪みの抑制と局所構造解析

宮坂俊樹，坂井直樹，祝黎明，黒川瑛宣，竹内宏賢，矢野真也，矢納拓弥，小沼一紀，
近藤貴哉，三池和成，一柳優子*
横浜国立大学，〒240-8501，神奈川県横浜市保土ヶ谷区常盤台 79-5

１．はじめに

当研究室では、これまでに 3d 遷移金属を含む酸化物やフェライトのナノ微粒子を作製し、その磁気特性、結晶構造等を報告してきた[1]。これらの研究成果から Cu ferrite を amorphous SiO_2 包含することで Jahn-Teller 歪みの抑制を可能にし、その抑制の結果、磁気特性が向上するという報告もある[2]。

M Mn_2O_4(*M* は 3d 遷移金属)は、正スピネル構造をとり、Mn^{3+}の影響により B サイトで Jahn-Teller 歪みを引き起こし、高温から徐冷することで立方晶から正方晶へと結晶構造が歪むことが知られている。また傾斜反強磁性を示すため、今回は、$CoMn_2O_4$ ナノ微粒子を SiO_2 包含することで、焼成温度や SiO_2 の濃度による Jahn-Teller 効果を抑制することを試み、その局所構造を解析することを目的とした。

２．実験

$CoMn_2O_4$ ナノ微粒子は、$CoCl_2 \cdot 6H_2O$、$MnCl_2 \cdot 4H_2O$、$Na_2SiO_3 \cdot 9H_2O$ を mol 比 1 : 2 : x (x = 2, 3, 4, 6)の割合で SiO_2 の濃度を調整し湿式混合法で作製した。pH 調整のために NaOH や HCl を用いた。得られた沈殿物を洗浄した後、約 350 K の恒温槽にて乾燥させ、さらに空気雰囲気中で 873 K から 1273 K の範囲で焼成した。その後、作製した微粒子に対して粉末 X 線回折(XRD)にて物質同定を行い、高エネルギー加速器研究機構の Photon Factory の BL-9C にて X 線吸収微細構造(XAFS)測定を行い、吸収端近傍(X-Ray Absorption Near Edge Structure, XANES)より各金属イオンの酸化数、吸収端から数 keV の範囲 (Extend X-ray Absorption Fine Structure, EXAFS) より、吸収端元素からの原子間距離や配位数、局所構造についての情報を得た。

３．結果および考察

XRD の結果より 1273 K 焼成では x =2, 3, 4 で正方晶 $CoMn_2O_4$ の生成を確認でき、1073 K 焼成では x が増えるに従って不純物のピークが弱くなり、x =6 では立方晶の $CoMn_2O_4$ を単相で作製できたことを確認した。XRD ピークの形状より粒径を見積もった結果、4.1 nm から 23 nm 程度の粒径をもつことが分かった。

XANES スペクトルからは、標準試料との比較により Co が 2 価、3 価共に存在すること、Mn がほぼ 3 価であることが確認できた。Fig. 1 に標準試料と作製した試料の Mn K 殻吸収端の XANES スペクトルを示す。EXAFS スペクトルの波形変化より、正方晶から立方晶への構造変化が確認できた。Mn K 吸収端での立方晶と正方晶 $CoMn_2O_4$ の EXAFS スペクトルを Fig. 2 に示す。

XRD、XAFS の結果から、SiO_2 濃度の増加は、包含している微粒子への圧力を強くし、B サイトの Jahn-Teller 歪みを抑制したと考えられる。

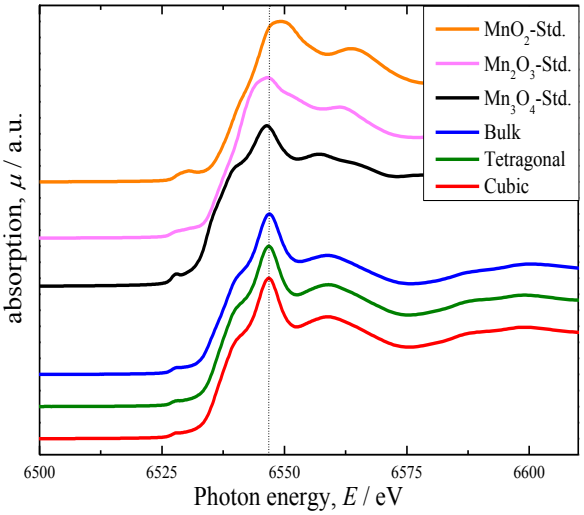

Fig. 1 Mn K 殻吸収端 XANES スペクトル

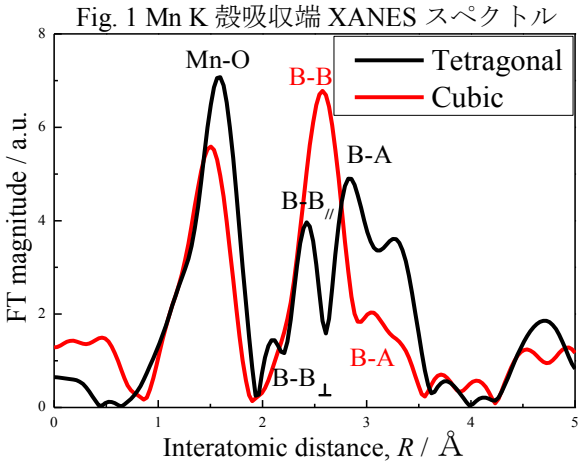

Fig. 2 Mn K-edge の EXAFS 振動のフーリエ変換

４．結論

SiO_2 の濃度および焼成温度を制御することで Jahn-Teller 歪みを抑制し、立方晶の $CoMn_2O_4$ ナノ微粒子を作製することに成功した。また、XAFS 測定の結果からは、結晶構造が正方晶から立方晶への変化により原子間距離が等距離秩序化したことが確認できた。これにより、磁気特性の向上も期待できる。

参考文献

[1] Y.Ichiyanagi et al. Phys. Stat. Sol. (c)1,(2004)
[2] S.Kimura, Y.Ichiyanagi et al. Thermochimica Acta. 532(2012)119-122

*yuko@ynu.ac.jp

3A/2010G190

A look inside epitaxial cobalt nanoparticles with a 3D reciprocal space imaging

Sergey M. SUTURIN [1]*, Vladimir V. FEDOROV [1], Alexander M. KOROVIN [1], Nikolai S. SOKOLOV [1], Gleb A. VALKOVSKIY [1] and Masao TABUCHI [2]
[1]Ioffe Physical-Technical Institute, St. Petersburg 194021, Russia
[2] Synchrotron Radiation Research Center, Nagoya University, Nagoya, Japan

1 Introduction

In recent years intense research efforts have been devoted to the heterostructures with ferro- and antiferromagnetic layers. Particular effects observed in these systems are of great importance as being related to the design of modern high density magnetic media [1]. Cobalt nanoparticles on Si produced by growth of Co on nonmagnetic CaF_2 (used as a buffer) or antiferromagnetic MnF_2, provide a suitable framework to study properties of magnetically ordered nanosystems. The current work presents an extensive diffraction study of such a system with Co epitaxially grown on CaF_2 / Si.

2 Experiment

Cobalt nanoparticles were grown at 600°C on CaF_2 / Si by molecular beam epitaxy (MBE) at Ioffe institute. A 0.1 nm low temperature Co seeding layer was used to ensure nucleation of regular arrays of nanoparticle with high crystalline quality. Nanoparticles with three major orientations of cobalt lattice (111, 110 and 001) were produced by appropriate choice of Si substrate face and CaF_2 growth parameters.

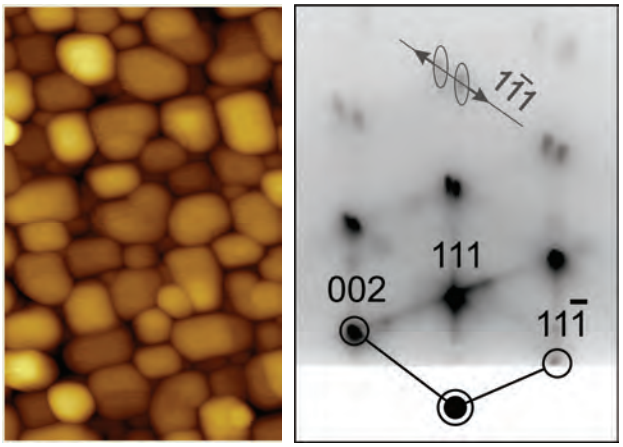

Fig. 1: AFM image of Co(001) nanoparticles (left). Image size 1000 nm × 600 nm × 80 nm. RHEED pattern from Co(111) nanoparticles (right) showing streaking and Bragg reflection splitting in the (1-10) zone.

The structures have been pre-characterized by atomic force microscopy and electron diffraction prior to the synchrotron studies (Fig. 1). Interestingly, RHEED patterns exhibit bright (111) and (11-1) streaks showing up as lines normal to the sample surface and inclined by 70.5° correspondingly. Presence of the other two streaks: (1-11) and (-111) is expected due to the symmetry reasons. These streaks indeed appear in RHEED images causing Bragg reflections to split when the sample is rocked. In order to study streaking and reflection shape in general the samples were investigated by GIXD at BL3A beamline at Photon Factory using λ=1.033 Å radiation. The measurements were partly carried out with a Hamamatsu 2D CCD detector. Finally GIASXS measurements have been carried out at the same beamline to study particle faceting.

3 3D mapping by GIXD

The electron and X-ray diffraction studies confirm that on either face of CaF_2 cobalt grows in fcc phase with its lattice cooriented with the underlying fluorite layer. Interestingly bright and long {111} streaks have been observed passing through Bragg reflections of Co by recording 3D intensity maps around several Bragg reflections of cobalt (Fig. 2 top).

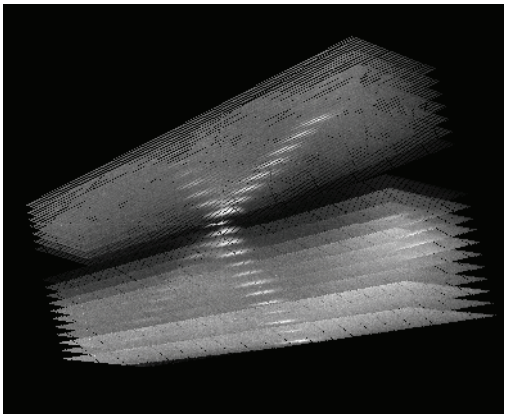

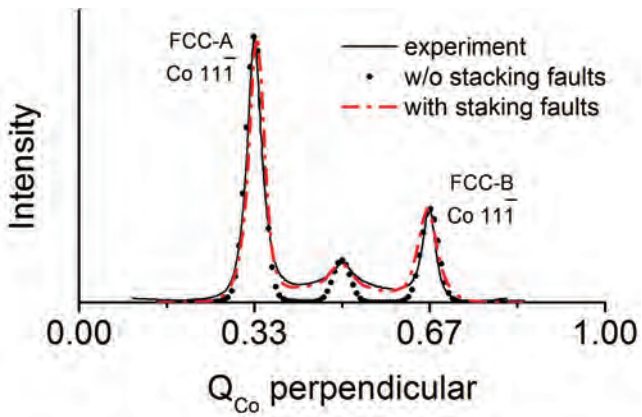

Fig. 2: GIXD data obtained from Co(111) nanoparticles. 3D intensity distribution around Co(111) reflection

showing {111} streaks (top). Experimental and simulated intensity profiles along the Co [111] streaks (bottom).

Intensity profiles along the streaks have been recorded and then modeled assuming that islands are facetted with {111} planes (Fig. 2 bottom). It was shown that although faceting does produce streaks, the intensity along these streaks drops much faster ($\sim q^{-2}$) compared to the experiment. The other hypothesis checked was that the streaks are due to the stacking faults. The latter may naturally occur in cobalt that is stable as hcp at normal conditions and grows as fcc at elevated temperatures. The length of the stacking fault related streaks is defined by the correlation length in the faulted structure. A calculation was carried out suggesting three types of stacking order existing within a cobalt island. The calculation involved random insertion of stacking faults and averaging over few thousands of islands. A reasonable fit was achieved for a fault density of ~0.06 $Å^{-1}$ (Fig. 2 bottom). Although the presented data show data for Co (111) islands, similar 3D intensity distribution maps have been also measured for Co (001) and Co(110) islands to show presence of {111} streaks with similar intensity profiles.

3 GISAXS studies

Since the stacking fault streaks mask any existing facet streaks, information about faceting can hardly be extracted from the Bragg reflection shape. For this reason Co nanoparticles were further examined with GISAXS that is not influenced by lattice defects and at the same time is sensitive to the particle shape. GISAXS patterns from Co(111) islands (Fig. 3) clearly show streaks perpendicular to Co(111) planes. In case when cobalt was grown on CaF_2 (110) surface, streaks from (001) facets were also present.

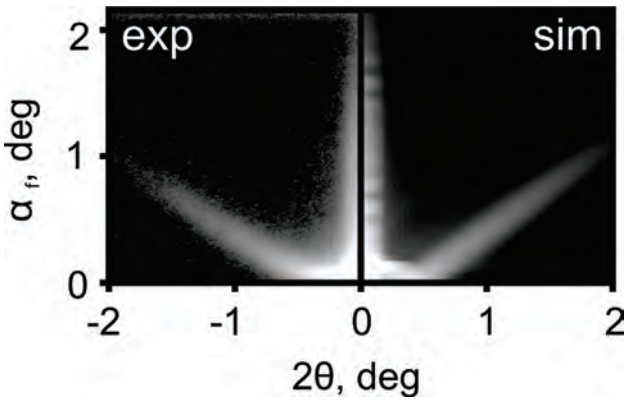

Fig. 3: Comparison of experimental (left) and simulated (right) GISAXS patterns from Co(001) islands.

The intensity was found to drop fast along the streaks following the q^{-n} behavior where n ranged between 2.4 and 3.6. This is faster than expected from a parallelepiped (q^{-2}) and slower than for a polyhedron (q^{-4}). The GISAXS patterns were then analyzed using the "simulation annealing" algorithm implemented in the IsGISAXS software [2]. A reasonable fit was achieved for a model in which Co(001) islands were assumed to be truncated pyramids. The obtained island parameters appeared to be in good agreement with the AFM results allowing a better evaluation of the island aspect ratio.

Conclusion

Epitaxial Co islands of three different substrate induced orientations were extensively studied from inside - to reveal an unstrained fcc lattice with the presence of {111} stacking faults, and from outside - to show that the islands are facetted with {111} and {001} crystal planes. The usage of 3D Bragg reflection imaging combined with GISAXS proved effective to separate different contributions to streaking. Various parameters were obtained from fitting the XRD and GISAXS data. These are statistically averaged over a large sample area that is of particular importance when it comes to understanding magnetic properties of the samples with Co nanoparticles. Simultaneous study of all three cobalt orientations (111, 001 and 110) made it possible to get a more comprehensive understanding of the particle shapes, size distributions and crystal structure. The summarized data obtained for Co on CaF_2 is believed to be useful in predicting the properties of Co nanoparticles on antiferromagnetic MnF_2.

Acknowledgement

The study was carried at PF out along the proposal 2010G190. The work was partly supported by Joint Research Center "Material science and characterization in advanced technology" under financial assistance of the Ministry of Education and Science of the Russian Federation. The authors wish to acknowledge the BL3A beamline staff for the help in conducting the synchrotron experiments.

References

[1] Bae Seongtae,.et al., Spin Valves in Spintronics Applications: Materials, Device Applications, and Electrical, VDM Verlag Dr. Mller, ISBN: 978-3639234794

[2] G. Renaud, R. Lazzari, and F. Leroy, Surf. Science. Reports **64** (2009) 255.

* suturin@mail.ioffe.ru

9A/2010G512

Local structure of Ti in tektite by XAFS spectroscopy

Ling Wang[1], Akira YOSHIASA[1], Maki OKUBE[2] and Tomotaka NAKATANI[1]
[1]Faculty of Science, Kumamoto Univ., Kumamoto 860-8555, Japan
[2] Tokyo Institute of Technology, Nagatsuta, Yokohama 226-8502, Japan.

Introduction

The tektite is formed at meteoroid impact stage. Tektites are natural silicate glasses, which can be found at the strewn fields over wide areas. Terrestrial impact theory is widely accepted as its formation. Tektites are among the "driest" rocks, with an average water content of 0.005%. This is very unusual, as most if not all of the craters where tektites may have formed were underwater before impact. It suggests that the tektites were formed under extreme temperature and pressure not normally found on the surface of the Earth. Glass structure (i.e., cation coordination number) is affected by the pressure and temperature conditions existing during the glass formation process. n this study, we will show that the local structure of Ti in tektite should indicate information about the impact event and the following process.

Experimental

The samples we studied comprised six tektites that comes from different strewn field: Hainanite, Indochinite, Philippinite and Australite from Australian strewn field; Bediasite from North American strewn field and Moldavite from European strewn field. We choosed the green and brownish moldavites, black and grey Bediasites, the core and rim of Hainanites. The standards used for XAFS measurement are titanium oxides, such as TiO2 anatase and TiO2 rutile. The XAFS measurement of Ti K-edge was preformed with a Si (111) double crystal monochromator at the beam line BL-9C of the Photon Factory. Analyses of XAFS data were performed by using XAFS93 programs. Details of analysis were given in reference [1].

Results and Discussion

The Titanium XANES spectra in tektites are shown in Fig. 1. These spectra are divided into three groups according to the pre-edge and shape: Group I: Indochinite, Bediasite-Black, Moldavite-Brownish; Group II: Hainanite-Core, Hainanite-Rim, Australite, Philippinite and Group III: Moldavite-Green. In group I, the percentage of pre-edge is 59%-49%, and at the end of threshold, the density is around 86%. In group II, the percentage of pre-edge is 49%-47%, and at the end of threshold, the density is around 90%. The intensity of pre-edge in Moldavite-Green is about 14%, and at the end of threshold, the density is highest.

In order to obtain the detail local structure information, we figured out the parameter fitting with analytical EXAFS formula [1]. The precursor of tektite is primarily of terrestrial origin, different types of local structure and composition in these tektites are almost same (Table 1), so the chemical fraction of the parent rocks is not important, should be indicating the different physical conditions at impact events. There are some difference in the bonding structure of Ti atoms and arrangements of neighbour atoms. So the local structure of Ti maybe closely related with the temperature, pressure, quenching rate, and size of meteorite and falling melts. The 4-fold, 5-fold and 6-fold titanium is formed under diverse atmosphere [1].

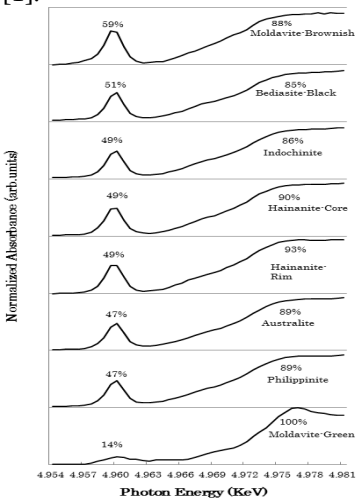

Fig.1. Figure 2 XANES spectra near the Ti K-edge for tektites

Table 1. The structure parameter determined by XAFS.

Sample	σ^2(Å)	CN	Ti-O (Å)	R (%)
Indochinite	0.009(1)	4	1.812(5)	4.3
Moldavite-B	0.020(1)	4	1.817(4)	6.3
Bediasite-B	0.004(1)	4	1.835(3)	0.7
Hainanite-C	0.005(1)	4,5	1.868(4)	0.3
Hainanite-R	0.006(1)	5	1.888(6)	0.1
Australite	0.002(1)	5	1.892(4)	3.5
Bediasite-G	0.015(1)	5	1.896(9)	0.1
Philippinite	0.003(1)	5,6	1.921(5)	2.7
Moldavite-G	0.003(1)	6	2.001(4)	3.5

* yoshiasa@sci.kumamoto-u.ac.jp

[1] Wang et al. J. Synchrotron Rad. (2011). 18, 885–890

BL-17A/2010G-566

Using InCl Vapor to Ion Exchange Indium into Zeolite Na-X. Single Crystal Structure of $|In_{34}Na_{50}|[Si_{100}Al_{92}O_{384}]$-FAU Containing In^{+} and In_5^{7+}

Dipak Sen and Nam Ho Heo*
Laboratory of Structural Chemistry, Department of Applied Chemistry, College of Engineering, Kyungpook National University, Daegu 702-701, Korea

Introduction

Indium zeolites are important industrial catalysts with high activity and selectivity for several catalytic reactions [1,2]. Some of the difficulties intrinsic to aqueous methods of ion exchange can be overcome by vapor phase ion exchange (VPIE). Because the vapor pressure of InCl is appreciable, 13 Torr, at a moderate temperature, 673 K, it was hoped that In^{+} could be introduced into zeolites in their dehydrated as-synthesized Na^{+} forms by VPIE. This work was done with one step reaction in mind,

$$Na–Z + InCl(g) \rightarrow NaCl(s) + In–Z. \quad (1)$$

Experiment

A single crystal, of sodium zeolite X ($|Na_{92}(H_2O)_x|[Si_{100}Al_{92}O_{384}]$-FAU**,** $Na_{92}–X\cdot xH_2O$ [3] a colorless octahedron about 0.15 mm in cross-section, was selected and loaded into a fine Pyrex capillary near 0.04 g InCl (Sigma-Aldrich, 99.999%). The crystal was then dehydrated at 673 K at 1 x 10^{-6} Torr for two days. After complete dehydration, the reaction vessel containing the remaining dry InCl not in physical contact with the crystal in its capillary was sealed off under vacuum and baked at 673 K for two days, exposing the crystal to 13 Torr of InCl(*g*). The crystal, now gray and opaque, was sealed off under vacuum in its capillary by torch. Finally, X-ray diffraction data for the resulting crystal were collected at 294(1) K at the BL-17A beam line of the Photon Factory, KEK, Japan.

Results and Discussion

$In_{14}^{+}(In_5^{7+})_4Na_{50}^{+}–X$ (approximate formula, see Table 1) was prepared by the reaction of fully dehydrated $Na_{92}^{+}–X$ with 13 Torr of InCl(*g*) at T = 673 K. Its structure was determined using single-crystal crystallography with synchrotron X-radiation and was refined in the space group $Fd\bar{3}$ (a = 24.996(1) Å) with all 1566 unique data; the final error index R_1 is 0.076. Thus, InCl(*g*) reacted with about 46% of the Na^{+} ions in the zeolite, to give In_5^{7+} (centered tetrahedral, In–In = 2.684(7) Å) and In^{+} cations. In_5^{7+} centers exactly half of the sodalite cavities, strongly suggesting alternating occupancy; each terminal atom (at site I') bonds to three framework oxygen atoms of a double 6-ring (In–O = 2.248(6) Å and O–In–O = 102.2(2)°). The In^{+} ions occupy four crystallographically distinct cationic sites: 5.8(3) per unit cell are in the sodalite cavities (site I'), 2.7(7) are near single 6-rings in the supercage (site II), 2.6(4) are near triple 4-rings in the supercage (site III'), and 3.1(5) are at second III' site. About half of the Na^{+} ions complete the filling of the single 6-rings; the remainders are at 12-ring sites. Most of In^{n+} ions are easily approachable by guest molecules through th e zeolite's 12- ring channel system.

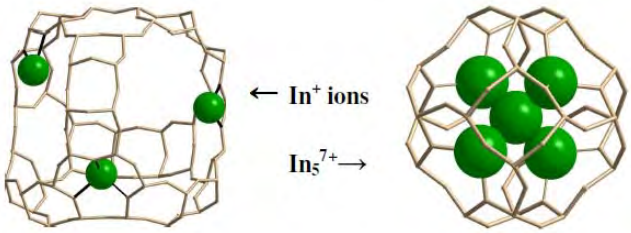

Figure 1. Distribution of In^{n+} ions in the supercage and sodalite cavity.

Table 1. Assignment of Oxidation States and Charge Budget

Sites	Atoms	Occ.[a]	r,[b] Å	NC[c]	Charge	ΣCharges
I′	In11	16.0(3)	0.93	4	+2[d]	32.0
	In12	5.8(3)	1.12	3	+1	5.8
II	In2	2.7(7)	1.16	3	+1	2.7
	Na2	22(3)	0.99	3	+1	22
III′	In31	2.6(4)	1.14	2	+1	2.6
	In32	3.1(5)	1.25	2	+1	3.1
	Na31	16(2)	1.2	2	+1	16
	Na32	7.6(17)	1.14	2	+1	7.6
U	InU	4.00(7)		4	–1[f]	–4.0
	Σ In	34.2[e]				87.8(42)[f]
	Σ Na	45.6[e]				

[a]Occupancy given as the number of ions per unit cell. [b]Radii of In and Na species obtained by subtracting 1.32 Å from the shortest In–O and Na–O bond lengths. [c]Coordination numbers. [d]Formal charges of the component atoms of In_5^{7+}. [e]Number per unit cell. [f]This value, 87.8(42)+, differs from the negative charge of the zeolite framework per unit cell, 92– (known only to the nearest integer), by one esd. To achieve charge balance with ∑Na = 50, the occupancies at Na2 and Na3 have each been increased by ca. 0.8 σ.

References

[1] Y. Traa, B. Burger, and J. Weitkamp, *Microporous Mesoporous Mater.* **30** 3 (1999).
[2] J. R. Mowry, R. F. Anderson, and J. A. Johnson, *Oil Gas J.* **83** 1288 (1985).
[3] V. N. Bogomolov, and V. P. Petranovskii, *Zeolites* **6** 418 (1986).

* nhheo@knu.ac.kr

12C, NW10A/2010G592

EXAFS analysis of Pt doped SnO_2 Catalyst for Micro gas sensor

Naoyoshi Murata[*1,2], Takuya Suzuki[1], Makoto Kobayashi[1], and Kiyotaka Asakura[3]
[1]Corporate R&D Headquarters, Fuji Electric Co., Ltd, Tokyo 191-8502, Japan
[2] Department of Quantum Science and Engineering, Graduate School of Engineering, Hokkaido University, Sapporo, 001-0021, Japan.
[3]Catalysis Research Center, Hokkaido University, Sapporo 001-0021, Japan

1 Introduction

SnO_2 has been widely utilized as gas sensors due to its conductivity which changes according to partial pressure of oxygen or reducing gases. For the sensors used especially in house, cordless type models are required since these days social needs to utilize town gas safely rises high to achieve safe and secure life. To realize sensors which have 5 years of lifetime, high reliability and low electricity consumption are required. In addition, high selectivity for methane, which is a main ingredient in natural gas, is required. Recently a thin film of a catalyst supporting Pt on SnO_2 is paid attention to realize battery-powered sensors with low electricity consumption. Clear understanding device material is of great importance to make sensors fit for practical use.

Recently, addition of Pt increases the SnO_2 sensor sensitivity for methane. Metallic Pt is a good catalyst for many reactions including the CO and hydrocarbon oxidation reaction. In the catalysts, Pt metal clusters are speculated as an active structure. Pt clusters deposited on the SnO_2 was often assumed and the spill-over reaction created from Pt cluster to SnO_2 might play important role. In this work we carried out the local structure analysis of Pt on the SnO_2 film by EXAFS to elucidate the reaction mechanism. What we found was quite unexpected, i.e., Pt was atomically dispersed in SnO_2 thin layer.

2 Experimental

Pt and SnO_2 targets were both sputtered on a Si wafer. Pt and SnO_2 ratio was controlled by the loading ratio in the targets and finally the concentration of Pt in the film was determined by the ICP by dissolving the film using hydrochloric acid.

3 Results and Discussion

Figure 1 shows Pt L_{III}-edge EXAFS oscillations ($\chi(k)$) and their Fourier transform of Pt-SnO_2 samples together with reference samples. Pt L_{III}-edge EXAFS of Pt-SnO_2 was quite different from those of Pt foil and PtO_2. The peaks corresponding to the Pt-O and Pt-Sn appeared at 1-2 Å and 2.5-4 Å The peak shape at 2.5-4 Å was similar to that of SnO_2, indicating the Pt was incorporated in the SnO_2 lattice.

Figure 2 shows the Sn K-edge EXAFS oscillations and their Fourier transforms. The SnO_2 structures were maintained in Pt-SnO_2. The first peak was corresponding to Sn-O while characteristic double peak appeared in Sn-Sn interactions in rutile SnO_2.

Moreover, XRD patterns of Pt-SnO_2 thin film on Si substrate gave a rutile structure.

No Pt clusters were observed during the reaction.

We concluded that the active site structure was not Pt clusters but Pt placed at the SnO_2 lattice. This result was quite surprising but it is informative to lead to a rational design of the high-performance gas sensor system.

Acknowledgement

This research was carried out with support from the "Next Generation High Reliability Gas Sensor Technical Development" project of the New Energy and Industrial Technology Development Organization (NEDO). All XAFS measurements were conducted in Photon Factory, KEK as PAC nos. 2010G592. The authors wish to express their gratitude to all parties concerned.

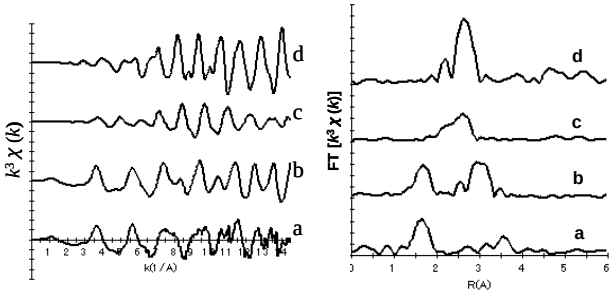

Figure 1: EXAFS oscillation by Pt L_{III}-edge (left figure) and Fourier Transform (Right figure) of Pt-SnO2
a:Pt-SnO2 **b:**PtO2 **c:**PtSn alloy **d:**Pt-foil

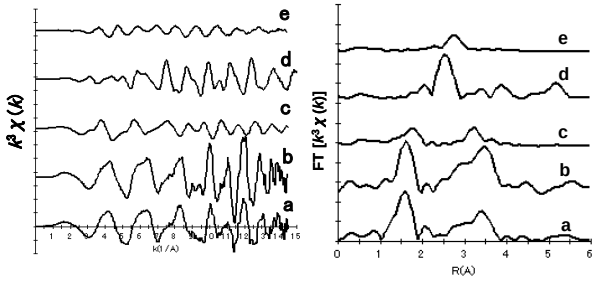

Figure 2: EXAFS oscillation by Sn K-edge (left figure) and FOURIER Transform (Right figure) of Pt-SnO2
a:Pt-SnO2 **b:**SnO2 **c:**SnO **d:**PtSn alloy **e:**Sn-foil

murata-naoyoshi@fujielectric.co.jp

10A/2010G608

Effective potential for Ca-O bonds in CaGeO3 perovskite.

Akira YOSHIASA[1], Akihiko NAKATSUKA[2], Ai KOGANEMARU[1], Maki OKUBE[3], Tomotaka NAKATANI[1], Tatsuya HIRATOKO[1], HiroshiARIMA[4] and Kazumasa SUGIYAMA[4]
[1]Faculty of Science, Kumamoto Univ., Kumamoto 860-8555, Japan
[2] Graduate School of Science and Engineering, Yamaguchi University, Ube 755-8611, Japan
[3] Tokyo Institute of Technology, Nagatsuta, Yokohama 226-8502, Japan.
[4] Institute for Materials Research, Tohoku University, Sendai 980-8577, Japan

Introduction

High-pressure modification of silicate minerals such as perovskite- and garnet-type MgSiO3 could be the dominant phases in the Earth's mantle, so detailed knowledge of their structures and thermal properties is of great importance for understanding the state of the deep mantle. It is known that phase boundary between perovskite- and garnet-type phases has the negative Clausius-Clapeyron's curve, which has great meaning geophysically. Metagermanates are useful as structural analogues of silicate minerals at high pressures because of thermal stability of high pressure phases. CaGeO3 perovskite and garnet structures are isotypic with MgSiO3 perovskite and garnet, respectively. In this study, we have determined the precise local structure around Ca in perovskite- and garnet-type CaGeO3 polymorphs. The analysis of temperature-dependent Debye-Waller factor allows us to evaluate the interatomic force constants. Unique thermal vibration in perovskite-type phase has been introduced.

Experimental

The perovskite- and garnet-type CaGeO3 crystals were synthesized in a cubic anvil type high-pressure apparatus under 10GPa 1250K and 3GPa 1300K, respectively. Single-crystal X-ray diffraction measurements were carried out with a four-circle diffractometer at the BL-10A beam line of the Photon Factory, Tsukuba, Japan, using monochromatized synchrotron X-ray (λ = 0.70006 Å) radiation. Structute refinements were performed using full matrix least squires program RFINE2 (Table 1).

Results and Discussion

Figure 1 shows the temperature dependence of Debye-Waller factor (mean square displacement), u, for atoms in perovskite- and garnet-type CaGeO3. The Debye-Waller factor u includes the effects of static and dynamic disorders. The static disorder is the configuration disorder, while the dynamic disorder arises from the thermal vibration of atoms. The contribution of the thermal vibration can be estimated under the assumption of classical statistical dynamics by the temperature dependence. A steep slope in the figures represents a weak bonding. The magnitude of MSD for Ca atom in perovskite-type phase is extraordinary larger than those for other atoms in perovskite and garnet phases: the one particle potential for Ca in perovskite is significantly braoder than those for other atoms. The potential coefficients the Ca-O bond in CaGeO3 perovskite are 4.6 eV/Å2 and -4.4 eV/Å3, respectively. The effective pair potential for Ca-O bond in perovskite is broader than those in other CaGeO3 polymorphs. This is one reason for the Clausius-Clapeyron's curve for perovskite-garnet phase boundary having a negative slope. In the expression, dP/dT= $\triangle$S/ $\triangle$V, the dS becomes negative because denser high pressure phase perovskite has larger thermal vibration amplitude.

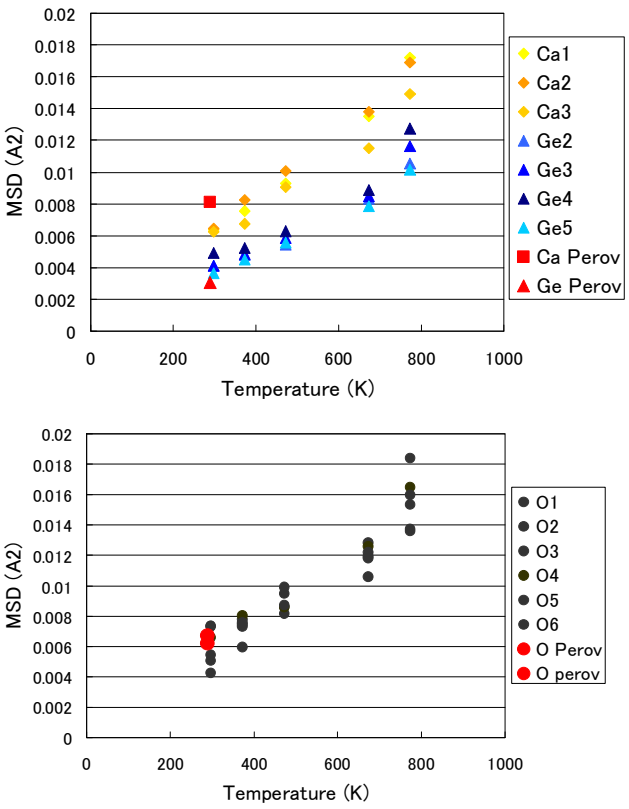

Fig.1. Mean square displacement (MSD) for CaGeO3 garnet and perovskite.

* yoshiasa@sci.kumamoto-u.ac.jp

BL-17A and AR-NW12A / 10G711

Association of a novel domain in the active site of the archaic hyperthermophilic maltogenic amylase from Staphylothermus marinus.

Tae-Yang Jung[1,2], Dan Li[2], Jong-Tae Park[3], Se-Mi Yoon[1], Phuong Lan Tran[4], [1]Byung-Ha Oh[1], Štefan Janeček[5,6], Sung Goo Park[2], Eui-Jeon Woo[2,7‡], Kwan-Hwa Park[4‡]

[1]Biological Science Dept. KAIST, Daejeon 305-701, Korea

[2]Medical Proteomics Research Center, Korea Research Institute of Bioscience and Biotechnology, Daejeon 305-333, Korea

[2]Department of Food Sci. and Eng., Changchun University, Changchun 130022, P. R. China

[3]Department of Food Sci. and Tech., Chungnam National Univeristy, Daejeon, Korea

[4]Department of Food Service Management and Nutrition, Sangmyung University, Seoul 110-743, Korea

[5]Institute of Molecular Biology, Slovak Academy of Sciences, SK-84551 Bratislava, Slovakia

[6]Department of Biotechnology, Faculty of Natural Sciences, University of SS. Cyril and Methodius, SK-91701 Trnava, Slovakia

[7]Department of Analytical Bioscience, University of Science and Technology, Daejeon 305-333, Korea

1 Introduction

Staphylothermus marinus maltogenic amylase (SMMA) is a novel extreme thermophile maltogenic amylase with an optimal temperature of 100 °C, which hydrolyzes α(1–4)-glycosyl linkages in cyclodextrins and in linear malto-oligosaccharides [1]. This dual enzyme activity is differs from the classic α-amylases in the glycoside hydrolase 13 (GH13) family [2]. This enzyme has a long N-terminal extension that is conserved among archaic hyperthermophilic amylases but is not found in other hydrolyzing enzymes from the glycoside hydrolase 13 family. The three dimensional structure of SMMA will provides a a molecular basis for the functional properties that are unique to hyperthermophile maltogenic amylases from archaea and that distinguish SMMA from moderate thermophilic or mesophilic bacterial enzymes.

2 Experiment

SMMA crystallization trials were conducted using the sitting drop method at 18 °C. We mixed 1.5 □1 of a 14 mg/ml SMMA solution with an equal volume of crystallization reservoir solution containing 12% polyethylene glycol (PEG) 4000, 2% isopropyl alcohol, 0.1 M ADA, pH 6.5, and 0.1 M Li2SO4. Before data collection, rhombus-type crystals were cryocooled to 95Kusing a cryoprotectant consisting of mother liquor supplemented with 25% glycerol. The crystal diffracted to a resolution of 2.28 Å, and the data were collected with a 1° rotation and a total of 340 frames. Diffraction data were processed and scaled using HKL2000 [3].

3 Results and Discussion

The crystal structure revealed that SMMA comprises four domains: the N, catalytic, and C domains, which are observed in most CD-hydrolyzing enzymes, and an additional novel N-terminal domain, the N'-domain, which was first observed in this study (Fig. 1a). Initially, the structure was determined and refined to a 2.28 Å resolution using molecular replacement, with the catalytic and C domains of neopullulanase from *B. stearothermophilus* (Protein Data Bank entry 1J0H) as the template structure. SMMA forms a homodimer via an interaction between the adjacent, novel N'-domains, which have a 2-fold axis perpendicular to the arc shape of the β-strands' interface (Fig. 1a). Each monomer is primarily associated through hydrophobic interactions at the center of the region of aa 5–19 (Ile5 and 19 from one molecule against Ile9 from the other). This interaction is supplemented by salt bridges (Arg181/Asp422 and Arg50/Glu198) at both ends of the strands, which yield a 2140.7 $Å^2$ interface. Most CD-hydrolyzing enzymes form dimers with the N-domain intertwined. However, the SMMA dimer configuration is different from previously reported CD-hydrolyzing enzymes, in that the dimer is arranged with adjacent monomers and an interface unrelated to the active sites. The active site pockets in bacterial CD-hydrolyzing enzymes are generated by the N-domain from the other subunit and yield a groove that is slightly extended between the catalytic domain and the N-domain. In comparison, the SMMA active site pocket is generated by the N'- domain of the same subunit. In the SMMA N'- domain, Phe95, Phe96, and Tyr99 are along the loop, and numerous aromatic residues, such as Tyr43, Phe46, and Phe77, lie on the β -sandwich fold surfaces (Fig 1b). This result suggests that extremophilic archaea that live at high temperatures may have adopted a novel configuration that combines all of the substrate binding components within a monomeric subunit.

a.

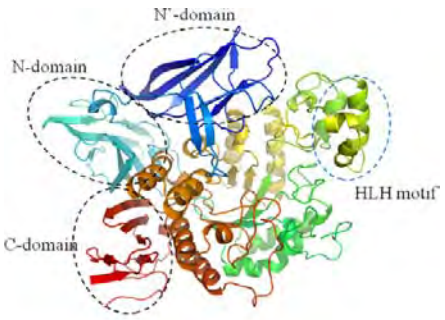

b.

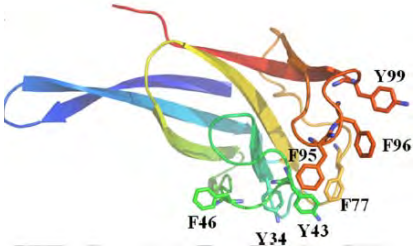

Fig. 1: The overall and N'-domain structure of SMMA. a, a schematic overview of an SMMA monomer that shows the conserved N, catalytic, and C domains in CD-hydrolyzing enzymes with a novel N'-domain. The monomer is colored in a spectrum; the N terminus is in *blue*, and the C terminus is in *red*. b, aromatic residues located near the loop protruding from the N'-domain. The domain has been colored in a spectrum; the N terminus is in *blue*, and the C terminus is in *orange*.

Acknowledgement

We thank the beamline staff at Photon Factory, KEK, Japan, for data collection and technical assistance.

References

[1] Li, D.,*et al*., New. Biotechnol **27** (2010) 300-307.
[2] Auh, J.H.,et *al*, J. Agric. Food Chem. 54(2006) 2314–9
[3] Otwinowski, Z., and Minor, M., *Enzymol.***276**(1997), 307–26

BL32XU/2011A1877, 2009G592

Crystallographic analysis of a BphA4 mutant

Miki Senda[1], Ayaka Harada[2], Akito Nishizawa[3], Shigenobu Kimura[3] and Toshiya Senda*[2]
[1]JBIC, 2-4-7 Aomi, Koto-ku, Tokyo 135-0064, Japan
[2] BIRC, AIST, 2-4-7 Aomi, Koto-ku, Tokyo 135-0064, Japan
[3]VBL, Ibaraki University, Hitachi, 316-8511, Japan

1 Introduction

We have studied an electron transfer system of a multi-component dioxygenase, BphA, derived from *Acidovorax* sp. strain KKS102. BphA4, which is an FAD-containing NADH-dependent ferredoxin reductase, receives two electrons from NADH and delivers one electron each to ferredoxins (BphA3). In the present study, we tried a perfect conversion of co-factor specificity of BphA4 from NADH to NADPH. In order to change its co-factor specificity, target residues for mutation were selected on the basis of the crystal structure of the wild type (WT) BphA4-NAD^+ complex [1]. This structure showed that Glu175, Thr176, Gln177, Ser182 and Arg183 interacted with a ribose moiety of NAD^+. Of the five residues, three consecutive residues, Gln175, Thr176 and Gln177, are nearby located to 2'-OH of NAD^+. Therefore, these residues were selected as targets of mutation, and random mutagenesis was applied for them. As a result, mutant E175C/T176R/Q177G, hereafter CRG, showed high specificity to NADPH. In order to elucidate the molecular mechanism of $NADP^+$ binding, mutant CRG was crystallographically analyzed. Here we report a preliminary X-ray crystallographic analysis of the BphA4 CRG mutant.

2 Experiment

A mutant gene of BphA4 was prepared by the PCR mutagenesis method. Mutant CRG was expressed in *Escherichia coli* and was purified as described previously [2]. Crystallization and soaking experiments were performed under anaerobic conditions in order to avoid the oxidation of reduced FAD in BphA4 [3]. The BphA4 CRG mutant was crystallized by the sitting-drop vapour diffusion method. Yellow crystals appeared in 2.0 M sodium formate, 0.1 M sodium acetate pH 5.2. Obtained crystals were soaked in an artificial mother liquor (2.5 M sodium formate, 0.1 M sodium acetate pH 5.2) containing 10 mM NAD(P)H for 2 hours, and then crystals were transferred into a cryoprotectant solution (27.5%(v/v) glycerol, 0.1 M sodium acetate pH 5.2) for 20 seconds. The crystals were then frozen using liquid nitrogen.

3 Results and Discussion

Diffraction data of BphA4 CRG mutant crystals were collected at BL32XU of SPring-8 (Table 1). The diffraction data were processed and scaled using the program XDS and XSCALE, respectively. The crystals belonged to space group $P6_122$, which is the same as that of BphA4 WT crystals. The crystal structures were determined by the molecular replacement method by MOLREP using the structure of BphA4 WT as a search model. Crystallographic refinement is in progress.

Table 1 Crystallographic summary

Crystal form	E175C/T176R/ Q177G	E175C/T176R/ Q177G
Soaking condition	10 mM NADH, 2hr	10 mM NADPH, 2hr
X-ray source	SPring-8	SPring-8
Beamline	BL32XU	BL32XU
Oscillation angle (°)	0.5	0.5
Exposure time (s)	1	1
Wavelength (Å)	0.97934	0.97934
Temperature (K)	95	95
Space group	$P6_122$	$P6_122$
Unit-cell parameters (Å)	a=b=98.2, c=171.3	a=b=98.2, c=171.0
Resolution (Å)	50.0-1.70 (1.79-1.70)	50.0-1.75 (1.84-1.75)
Unique reflections	101,249 (14,531)	93,099 (12,974)
Completeness (%)	99.6 (99.9)	100.0 (100.0)
Redundancy	5.6 (5.7)	11.5 (11.4)
Average $I/\sigma(I)$	14.1 (3.3)	22.9 (4.2)
Rmerge (%)	0.075 (0.553)	0.067 (0.610)

Values in parentheses are for the outermost resolution shell.

References
[1] M. Senda *et al*., *J. Mol. Biol*. **373**, 382-400 (2007).
[2] T. Yamada *et al*., *Protein Pept. Letters*, **7**, 277-280 (2000).
[3] M. Senda *et al*., *Acta Crystallog. Sect F*, **63**, 311-314 (2007).
*toshiya-senda@aist.go.jp

4B2/ 2011G185

$YBaCo_4O_7$系材料の高温における結晶構造解析

Crystal structure analysis of $YBaCo_4O_7$–based materials at high temperatures

原武大樹[1],チンイジン[1],尾本和樹[1],藤井孝太郎[2],八島正知[1,2,*]
[1]東京工業大学大学院総合理工学研究科材料物理科学専攻
〒152-8551 東京都目黒区大岡山 2-12-1-W4-17
[2]東京工業大学大学院理工学研究科物質科学専攻
〒152-8551 東京都目黒区大岡山 2-12-1-W4-17

1. 概要

電子-酸素イオン混合伝導性セラミックスは燃料電池の空気極や酸素透過膜への応用が期待されている。混合伝導セラミックスは高温状態で動作するため、高温における結晶構造を明らかにすることは、次世代の材料開発に向けた重要な知見になる。本研究では、混合伝導性セラミックスとして有望な $YBaCo_4O_7$ および Co 席を Zn で置換した $YBaCo_{2.5}Zn_{1.5}O_7$ の 800°C における結晶構造を高分解能 X 線粉末回折データより明らかにした。

2. 実験

$YBaCo_4O_7$ および $YBaCo_{2.5}Zn_{1.5}O_7$ 試料を、1100°C で 24 時間焼成する固相反応法により合成した。高分解能 X 線回折測定は、高エネルギー加速器研究機構(KEK)の PF BL-4B$_2$ において行った。測定は空気中 800°C で行った。得られた X 線回折データについてリートベルト法による構造解析を行い、結晶構造を精密化した。

3. 結果および考察

800°C における $YBaCo_4O_7$ および $YBaCo_{2.5}Zn_{1.5}O_7$ の結晶構造を、空間群 $P6_3mc$ に基づいて精密化した（図 1）。最終的なリートベルト解析の信頼度因子 R_{wp} はそれぞれ 17.71% ($YBaCo_4O_7$)、および 11.35%($YBaCo_{2.5}Zn_{1.5}O_7$)であった。両物質は室温から 800°C へ温度変化させても原子位置の大きな変化はなく、対称性 $P6_3mc$ を保った。また、格子定数は温度に対してほぼ直線的に増加した。800°C における格子定数と格子体積はそれぞれ $YBaCo_4O_7$ について $a = b = 6.33749(3)$ Å, $c = 10.33480(4)$ Å, $V = 359.474(3)$ Å^3 、$YBaCo_{2.5}Zn_{1.5}O_7$ について $a = b = 6.35225(1)$ Å, $c = 10.34950$ (2) Å, $V = 361.6641$ (12) Å^3 となり、$YBaCo_4O_7$ のほうが大きい格子となっていた。これは Zn^{2+}のイオン半径(0.74 Å)が Co^{3+}(0.63 Å)より大きいことが原因であると考えられる。

$YBCo_4O_7$、$YBaCo_{2.5}Zn_{1.5}O_7$ 両物質の結晶構造において、Co,Zn は二つの異なる結晶学席に存在し、O は三つの異なる席に存在している(図 2)。結晶構造には c 軸に垂直な二種類の酸素層が存在し、6c 席の O1 と 2a 席の O2 から成る層と 6c 席の O3 のみから成る層が存在しているとみなせる。Co1,Zn1 は O2 一つ、O3 三つと配位しており、Co2,Zn2 は O1 二つ、O2 一つ、O3 一つと配位している。Co1,Zn1 の存在する層では 6 配位の Y と 4 配位の Co1,Zn1 が頂点を共有して層を作っており、Co2,Zn2 のみから成る層では 4 配位の Co2,Zn2 がそれぞれ頂点を共有して層を作っているとみなせる。Ba は O1, O3 とそれぞれ六つと配位している。電子密度解析を行えば、構造と電子-イオン伝導性の関係について更に理解が進むと期待される。

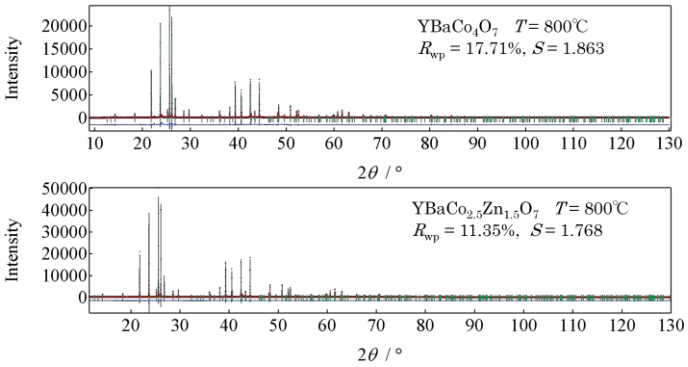

図 1. 800℃で測定した $YBaCo_4O_7$ および $YBaCo_{2.5}Zn_{1.5}O_7$ の放射光 X 線回折データのリートベルト解析図形

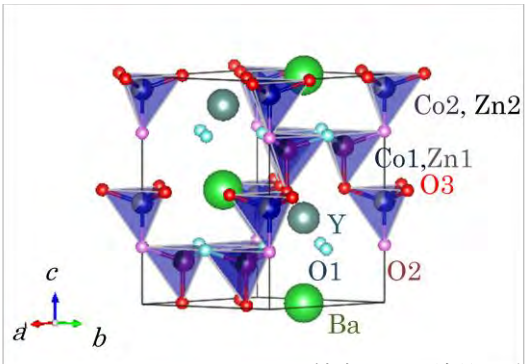

図 2. $YBaCo_{2.5}Zn_{1.5}O_7$ の精密化した結晶構造(800℃)

* yashima@cms.titech.ac.jp

4B2/2011G185

放射光 X 線回折による Ca*Ln*AlO$_4$(*Ln*=希土類)の結晶構造解析
Crystal structure analysis of Ca*Ln*AlO$_4$ (*Ln* = rare earth) by synchrotron x-ray diffraction

尾本和樹 [1*], 八島正知 [1,2]
[1] 東京工業大学大学院　大学院総合理工学研究科、〒152-8551 東京都目黒区大岡山 2-12-1
[2] 東京工業大学大学院　大学院理工学研究科、〒152-8551 東京都目黒区大岡山 2-12-1

1 はじめに

K_2NiF_4 型構造を有する Ca*Ln*AlO$_4$(*Ln*=希土類)は基板材料や電極材料として応用が期待されている。これまで Ca*Ln*AlO$_4$ の結晶構造に関する報告は室温におけるものに限られており, 高温での結晶構造について詳細に研究した例はない。本研究は温度可変放射光 X 線回折測定により, Ca*Ln*AlO$_4$ の結晶構造の温度依存性を研究した。

2 実験

Ca*Ln*AlO$_4$(*Ln*=希土類)試料を固相反応法により作製した。出発原料は $CaCO_3$ (99.9%)、 $SrCO_3$ (99.9%), Al_2O_3 (99.9%), Ln_2O_3 (Ln=希土類, 99.9%)を使用した。出発原料をエタノール中で湿式混合粉砕後, 得られた混合粉を一軸プレス成形し, 1400℃で 3h 焼成した。。結晶構造およびその温度変化は高エネルギー加速器研究機構(KEK)の Photon Factory、BL-4B2 に設置されている多連装高分解能粉末回折計を用いた温度可変放射光 X 線回折測定により評価した。得られたデータをプログラム RIETAN-FP を用いた Rietveld 法で結晶構造パラメータを精密化した。

3 結果および考察

Ca*Ln*AlO$_4$(*Ln*=Y, Pr, Sm, Er, Yb) の放射光 X 線回折データを正方晶系 *I*4/*mmm* の K_2NiF_4 型構造に基づいてリートベルト解析を行った。600℃で測定した CaSmAlO$_4$ の放射光 X 線回折データのリートベルト解析における信頼度因子は R_{wp} = 15.01%, R_I = 11.5%, R_F = 5.91%, GOF = 1.49 であり、良いフィットが得られた(図 1)。その他のデータについても同様な結果が得られた。精密化した CaSmAlO$_4$ の格子定数は *a* = 3.68891(1) Å, *c* = 12.15420(2) Å であった。精密化された結晶構造を Fig.2 に示す。K_2NiF_4 型構造はペロブスカイトユニットと岩塩ユニットが交互に重なって構成される。Fig.3 は単位格子体積の希土類のイオン半径依存性である。Ca*Ln*AlO$_4$(*Ln*=Y, Pr, Sm, Er, Yb)の単位格子体積は *Ln* サイトに置換する希土類のイオン半径が増加すると共に増加する。Ca*Ln*AlO$_4$(*Ln*=Y, Pr, Sm, Er, Yb)の高温中性子回折データのリートベルト解析の結果、室温～1200℃までの間に構造相転移は観測されなかった。また、格子定数は温度増加とともに単調に増加する。

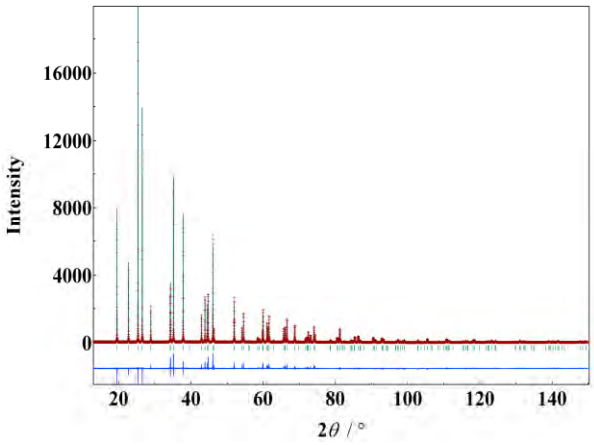

Fig. 1 Rietveld pattern for synchrotron X-ray diffraction data of CaSmAlO$_4$ measured at 600°C.

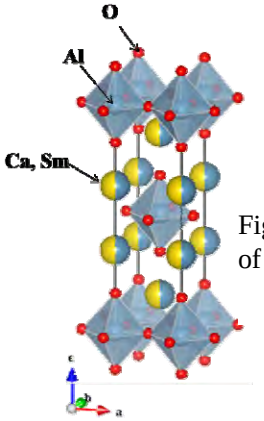

Fig. 2 Refined crystal structure of CaSmAlO$_4$ at 600°C..

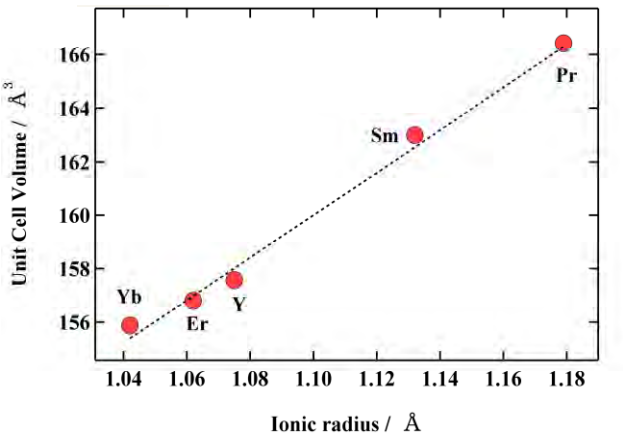

Fig. 3 Unit cell volume of Ca*Ln*AlO$_4$ (*Ln*=rare earth) at 26.5°C.

10A/2011G528

Structure of TiO_2 rutile synthesized under strong gravity field

Akira YOSHIASA[1], Rabaya BAGUM [1], Kazumasa SUGIYAMA[2], Yuta OGATA[1],Tomotaka NAKATANI[1], Maki OKUBE[3] and Tsutomu MASHIMO[1]

[1] Graduate School of Sciences, Kumamoto Univ. Kumamoto 860-8555, Japan

[2] Institute of Material Science, Tohoku *University*, *Sendai 226-8503, Japan*

[3] Tokyo Institute of Technology, Nagatsuta, Yokohama 226-8503, Japan.

Introduction

Materials research using strong gravitational field (1-10 x10^5 G, 1G =9.8 m/s^2) is still an unexploited area, even though materials science research utilizing microgravity fields is now active. To study sedimentation of atoms or crystal instability in solids under strong gravitational fields, we developed a high temperature ultracentrifuge apparatus that can generate a long duration acceleration field in excess of 10^6 G at elevated temperatures [1]. Titanium oxide-based materials attracted great interest and have been under intensive investigation due to their interesting optical, dielectric, catalytic, thermal and mechanical properties. Ultracentrifuge experiments were performed on single crystals of TiO2 rutile in the solid-state phase to examine changes in structure to produce new gravitationally induced phases at comparatively lower temperatures, below the melting point of the initial material. The crystal structure was investigated by X-ray diffraction analysis.

Experimental

We created this structure by applying a strong gravitational field (0.4×106 G) along the c-axis direction during heat treatment at 400°C.The rotor could be heated by radiation from a hot carbon, hollow cylinder that is heated by a high frequency heating system. Compositions of the single crystals were determined by EPMA.

Single-crystal X-ray diffraction measurements were carried out with a four-circle diffractometer at the BL-10A beam line of the Photon Factory, Tsukuba, Japan, using monochromatized synchrotron X-ray (λ = 0.70006 Å) radiation. Structute refinements were performed using full matrix least squires program RFINE2 (Table 1). Our refinement yields full occupancies for all sites.

Results and Discussion

A portion of crystallographic data for samples is summarized in Tables 1. Ambient rutile-type TiO2 consists of edge-sharing TiO6 octahedral groups. The Ti ions form a tetragonal lattice which are expanded along a, when we apply gravity along with c-axis direction and the octahedra are distorted small. The small changes in the crystal structure induce drastic changes in electronic properties. The anisotropy (c/a ratio) of the tetragonal phase changed, as the TiO6 octahedral unit in the structure became more anisotropic. The ratio of the shared and unshared edges has decreased than standard sample. These changes occurred well below the melting point of rutile, indicating that strong gravity method can control structures with developing properties. Strong gravitational fields has practical means of producing new phase materials. This is totally different from usual rutile. We open a new area in strong gravity-induced material science research.

Table 1. TiO_2 Experimental data

This study

Crystal data	Starting sample	Gravity sample
Space group	$P4_2/mnm$	$P4_2/mnm$
a(Å)	4.5973(4)	4.6189(4)
c(Å)	2.9538(4)	2.9357 (4)
c/a	0.643(3)	0.635(3)
V (Å^3)	62.42(3)	62.635(3)
Z	2	2
Wavelength (Å)	0.71069	0.70006

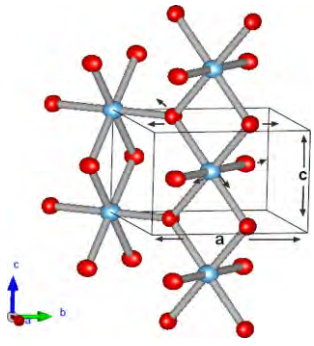

Figure 5. Crystal structure of gravity sample with indicating gravity effect.

References

[1] Rabaya Bagum, Akira Yoshiasa, Satoru Okayasu, Yusuke Iguchi, Masao Ono, Maki Okube, Tsutomu Mashimo, JOURNAL OF APPLIED PHYSICS (2010) 108 053517 7pp

* yoshiasa@sci.kumamoto-u.ac.jp

7C/2011G611

Local structure of Ca in natural glasses and tektite

Tsubasa TOBASE[1], Ling WANG[1], Akira YOSHIASA[1], Maki OKUBE[2], Hiroshi ISOBE[1] and Tomotaka NAKATANI[1]

[1]Faculty of Science, Kumamoto Univ., Kumamoto 860-8555, Japan

[2] Tokyo Institute of Technology, Nagatsuta, Yokohama 226-8502, Japan.

Introduction

In nature, several kinds of glasses are formed by various geological actives. Tektites and impact glasses are produced by impact event; volcanic actives formed volcanic glass; and plate boundary active produced fault rocks. These natural glasses experienced different extreme environments, which should lead changing of local structure. Titanium, iron, and aluminum local structures are studied on natural glasses and tektites (ex. Wang et al., 2011). Only calcium aluminosilicate glasses were investigated. Few Ca K-edge XANES structure on natural glasses and tektites have been reported although this technique probes information on Ca environment.

Experimental

The specimens of tektites are from different strewn fields, they are tektite (hainanite, indochinite, philippinite, australite, bediasite and moldavite), impact glass (impactite, suevite, and kofelsite), volcanic glass (perlite, obsidian, pitch stone, rhyolitic glass, Kilauea volcanic glasses), and fault rock (pseudotachylite). In order to analysis the local structure of calcium in natural glasses, we used the XAFS methods. The XAFS measurement of calcium local structure was preformed with a Si (111) double crystal monochromator at the beam line BL-7C of the Photon Factory. Spectra near calcium K-edge were collected in transmission and fluorescence mode at the room temperature. Details of analysis were given in reference [1].

Results and Discussion

Fig.1A shows XANES spectra of impact glasses. XANES spectra of two impact glass- impactite and köfelsite composed of pre-edge at 4039.132eV with intensity of 8.5%, a shoulder at 4045.17 with intensity of 67.5% and 67.8%, and white line at 4049.208eV. The pre-edge of impact glasses is lower than tektites, this may cause of high distortion around Ca atom in tektites. The shoulder of tektite is a bit higher and broader than impact glasses. In addition, a slight difference in the trend of post-edge details became apparent in the calcium K-edge XANES spectra of impact glasses, with a possible splitting a contribution. In Fig.2B, pre-edge and shoulder in natural glass possess more lower intensities than tektites and impact glass, and around 4.0-8.0%, 60.1-68.0%.

The difference in the post-edge features in impact glasses and natural glasses suggests a modification in calcium environment, being possible that calcium ions partially substitute for other ions in eight-coordinated site. Glass relaxation of impact glasses and volcanic glasses trends to lower than tektites. Different relaxation processes are caused by the environment when impact glasses are formed. Temperature and annealing time are most important condition for relaxation.

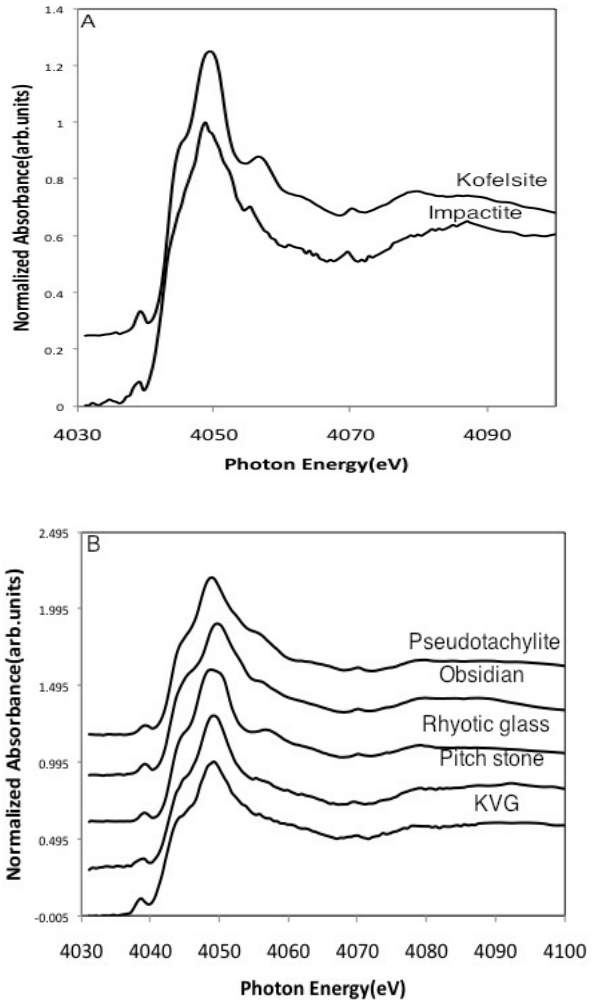

Fig.1. XANE spectra near Ca K-edge for impact glasses and natural glasses

* yoshiasa@sci.kumamoto-u.ac.jp

[1] Wang et al. J. Synchrotron Rad. (2011). 18, 885–890

15B/2011G675
1105037PF

X線断層写真を用いた格子欠陥の三次元再構成

Three-dimensional reconstruction of defect images using limited projection topographs

水野　薫 [1*], 岡本博之 [2]
[1] 島根大学総合理工学部　　〒690-8504 松江市西川津町 1060
[2] 金沢大学医薬保健研究域　〒920-0942 金沢市小立野 5-11-80

1 はじめに

ダイヤモンドは物質中で最も硬く，熱伝導率が高いなどの特性を持つため，高精度の切削工具やヒートシンク材料などで利用され始めている。しかし，これまでは育成条件が高圧，高温のような極限条件であったため大型結晶の合成法が確立されておらず，天然産ダイヤモンドに頼るところが多かった。近年，合成技術の発達により増産が可能となり，人工ダイヤモンドの比率が増してきている 。[1]

しかしながら，結晶の強度や特性を左右する欠陥と育成条件の関係については，未だ未解明な部分も多く，さらなる良質な結晶を育成する際の障害となっている。また結晶中に欠陥が存在することは理想的な結晶から予想される物性と，実測で得られる結果の間にずれが生じることを意味する。つまり，実際の結晶においては，本来期待されうる強度や熱伝導特性を示さず，使用上の制約となることがある。そのような経緯から，できるだけ欠陥の少ない結晶を育成する技術が求められている。そのためには，結晶の育成過程における，格子欠陥の生成や消滅の機構について，詳細な研究を行うことが必要と考えられている。

そこで，将来的に有望な材料である人工合成ダイヤモンドについて，X線３次元トポグラフ法を用いて観察し，格子欠陥の３次元的な配置とその種類の同定を試みた。また，その結果から結晶の育成過程における条件のゆらぎなどの検討も試みた。

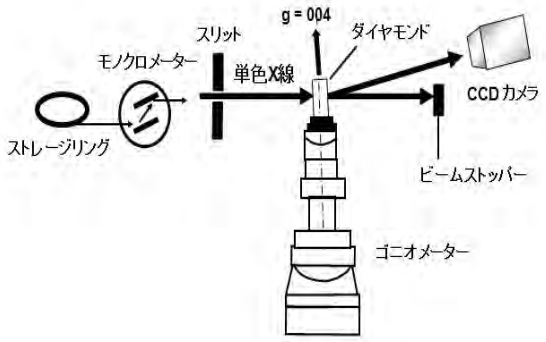

図 1. 三次元トポグラフカメラ

2 実験

今回の実験では，結晶中に存在する欠陥の分布と形状を確認することが重要で有るため，３次元トポグラフ法を用いた。[2, 3]

実験は九州シンクロトロン光研究センターの県有ビームラインBL09とKEK-PFのBL-15Bを用いて行った。その際の，実験配置の概略を，図１に示す。スリットを用いて単色X線ビーム(波長0.0815nm)の上下幅を絞り横長のリボン状ビームにして結晶に入射し，特定の回折面を用いて回折させて撮影を行った。この撮影方法はセクショントポグラフ法と同様であり，結晶の照射部分の断層像が得られる。この撮影を，厳密に回折条件を保ったまま，試料を鉛直方向に移動しながら繰り返す。得られた数百枚の断層写真を，パーソナルコンピュータ上で画像処理ソフトを用いて３次元像に構築した。

試料にはHPHT法合成した人工ダイヤモンド単結晶（住友電工製スミクリスタル，タイプⅠb）を用いた。サイズは2×2×1.5mm^{3}程度で，その外形は図２のような面方位をもつっている。

3 結果および考察

図３は BL09 において(004)を回折面とし，構築した三次元トポグラフ像を，(110)面に平行に切断した像である。図の上下の辺は(001)面に相当する。まず，図中に実線①，②で示すような２種類の面状欠陥が観察された。実線②は（001）面に対して約 64° をなすため，この面状欠陥は（33-2）面上に存在して

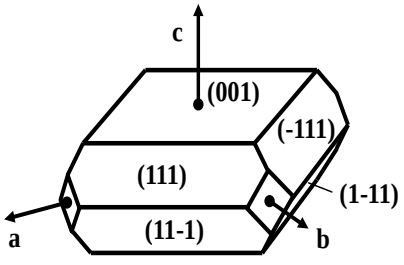

図 2. 合成ダイヤモンド試料の方位

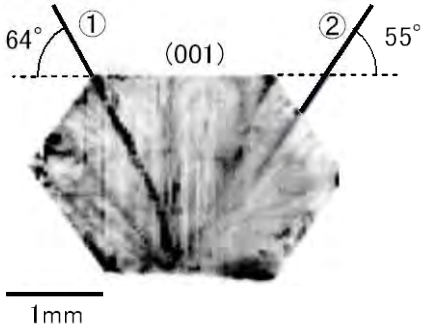

図 3. (004)を回折面として再構成した三次元トポグラフの(110)面の断面

いると考えられる。実線①は（001）面に対して約55°をなすため，欠陥は（111）面上に存在していると思われる。この結果から，まず②の欠陥について調べるため，(004)回折面の３次元トポグラフ像を(22-3)面で切断し観察した。すると，図４のような，いびつな欠陥像を観察できた。その欠陥像は図４下部の種結晶部から，上部の(001)と(111)のエッジ部に向かって延びていた。さらに水平方向に，ステップ状の模様も観察できた。これらのことから，②の面状欠陥は結晶の成長過程において条件が揺らいだことによる，成長痕ではないかと考えられる。スッテプ状に見える部分において，成長速度の変化が生じ，溶媒金属がインクルージョンとして含まれた可能性が有ると考える。

次に，①の面状欠陥は面心立方構造の最密面である(111)面上に存在するため，積層欠陥の可能性を疑った。そこで，{111}面で３次元トポグラフ像を撮影し，欠陥像の回折面依存性を検討した。回折面を（1-11）とした３次元トポグラフを撮影し，（111）面で切断し観察すると図５に示すような面欠陥であることが分かった。しかし回折面を（111）とした３次元トポグラフ像から，図５と同じ位置で切断し観察すると，このような面欠陥像は見られなかった（図６）。他の{111}回折面についても同様に，回折面に平行に存在する面欠陥は観察されずに，それ以外の欠陥は観察できた。これらの結果から，この面欠陥は積層欠陥であると考えられる。

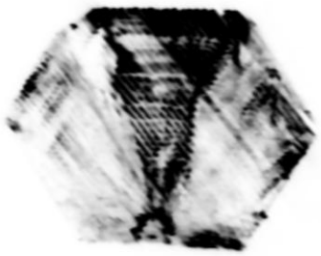

図 4. (004)を回折面として再構成した三次元トポグラフの(22-3)面の断面

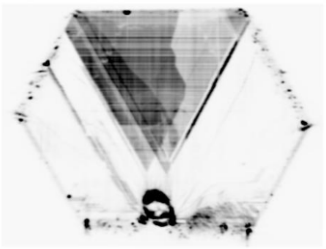

図 5. (-111)を回折面として再構成した三次元トポグラフの(1-11)面の断面

図 6. (1-11)を回折面として再構成した三次元トポグラフの(1-11)面の断面

4 まとめ

人工合成ダイヤモンドについて，X線３次元トポグラフ法を用いた観察を行い，格子欠陥の３次元的な配置とその種類の同定を試みた。その結果，結晶の成長過程での成長条件のゆらぎにより生じた成長痕と積層欠陥と思われる面状欠陥を同定できた。

謝辞

九州シンクロトロン光研究センターにおける実験に際して石地耕太朗博士および川戸清爾博士にご協力いただいた。ここに感謝致します。

参考文献

[1] 角谷均, 日本結晶成長学会誌 **38** (2011)281.
[2] S.kawado and J. Aoyama: Appl. Phys. Let. **34**(1979) 428.
[3] Kajiwara et al., Phys. Stat. Sol. **204**(2007)2682.

* mizuno@riko.shimane-u.ac.jp

3A/2011G691, 2011A1942

X-ray diffraction analysis of Hayabusa-returned samples

Tomoki Nakamura*, Aiko Nakato, and Takahide Misu
Faculty of Science, Tohoku University
Aramaki, Aoba, Sendai, Miyagi 980-8578, Japan

Hayabusa spacecraft successfully captured dust particles on the Muses C Regio of asteroid 24153 Itokawa. Hayabusa touchdowned Itokawa twice and the particles at the first touchdown site were stored in the room B of the sample catcher and those at the second touchdown site were stored in the room A. Room-A particles were investigated first in early 2011 (Nakamura et al. 2011) and room-B particles were analyzed later. In this report, we describe the results of mineralogical analysis of room-B particles.

We used Synchrotron X-ray diffraction method at photon factory beamline 3A and at Spring-8 beamline 39XU by applying ultra-high inteisity of X-ray to identify crystals species in the Itokawa dust particles. Unfortunately the particles are very small, but we have to draw maximum information from the particles. For this purpose, synchrotron radiation X-ray is the most powerful tool, because it enables us to identify crystal species in such a small partilce without any destructive treatment. We can perform a variety of destructive analyses, as shown later, after non-destructive X-ray analysis.

Synchrotron-radiation X-ray diffraction analysis indicates that mineralogy of the room-A dust particles is identical to most primitive solar system materials, chondrites, and dissimilar to terrestrial rocks (Nakamura et al. 2011). The analysis of individual particles indicates that most abundant mineral is highly crystalline olivine and next abundant minerals are low- and high-Ca pyroxene. Plagioclase is also abundant, but crystallinity differs between particles. Plagioclase crystallization temperatures based on triclinicity are obtained to be 600 - 800 °C (Nakamura et al. 2011). Room-B particles have mineralogies and mineral chemistries similar to those of room-A particles (Figs. 1 and 2). The similarity suggests that Muses-C regio has relatively homogeneous mineralogy that represent average mineral signatures of asteroid Itokawa.

Acknowledgement

We thank Drs. Nakao and Yamazaki for technical support during X-ray diffraction analysis and SPring-8 for providing us an alternative machine time during shutdown of KEK due to damages of the Great East Japan Earthquake.

References

[1] T. Nakamura *et al.*, Science **333** (2011) 1113-1116.

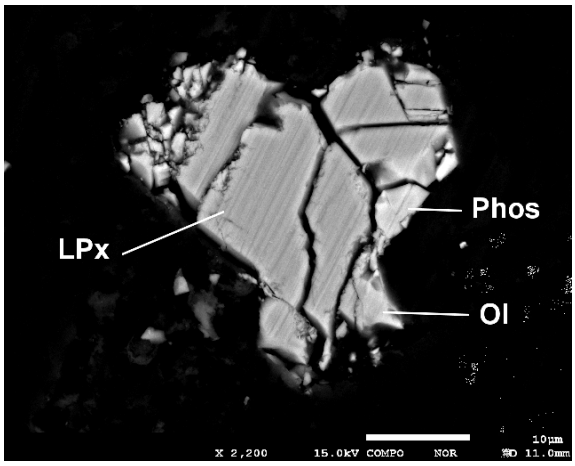

Fig. 1: Back-scattered electron image of room-B particle RB-QD04-0025, consisting of low-Ca pyroxene “LPx”, phosphate merrillite “Phos”, and olivine “Ol”..

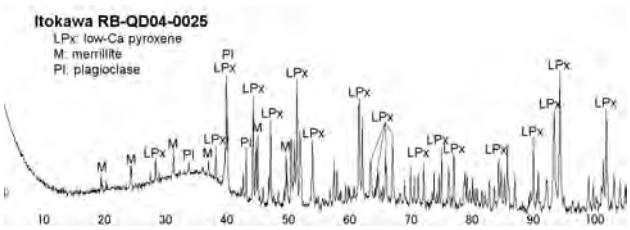

Fig.2: A diffraction pattern of RB-QD04-0025.

* tomoki@m.tohoku.ac.jp

13A, NE1A/2008G534

金とナトリウムの高圧反応
High-pressure Reaction between Au and Na

竹村謙一 [1*], 藤久裕司 [2]
[1] 物質・材料研究機構　〒305-0044 つくば市並木 1-1
[2] 産総研計測フロンティア　〒305-8565 つくば市東 1-1-1 中央第 5

1 はじめに

金は多くの金属と金属間化合物を作るが[1]、それらは通常、高温下で合成される。今回、金とナトリウムを室温で加圧すると Na-Au 金属間化合物が生成することを見いだした。また加圧によって組成変化を伴う構造相転移がおきることを観測した[2]。

2 実験

高圧実験にはダイヤモンドアンビルセルを用いた。Re ガスケットに金粉末（純度 99.9%、粒径 0.7 μm）を少量入れ、アルゴン雰囲気のグローブボックス中でナトリウム（純度 99.95%）を封入した。圧力はルビー蛍光法で決定した[3]。PF BL-13A（旧）および AR-NE1A において室温高圧粉末 X 線回折実験を行った。

3 結果および考察

わずかの圧力（P< 1 GPa）で金はナトリウムと反応し、金属間化合物を作ることがわかった。表 1 に高圧下で生成する Na-Au 金属間化合物の安定圧力領域、組成および構造をまとめる。金は常に多量のナトリウムで取り囲まれているため、加圧による組成変化と構造相転移が並行して起きる。観測された相を低圧側から順に I 相～IV 相と名付ける。

表 1: 高圧下で生成する Na-Au 金属間化合物.

Phase	P (GPa)	Formula	Type	Space group
I	0-0.8	Na_2Au	$CuAl_2$	*I*4/*mcm*
II	0.8-3.6	Na_3Au	Cu_3As or Cu_3P	*P*-3*c*1 or $P6_3cm$
III	3.6-54	Na_3Au	BiF_3	*Fm*-3*m*
IV	54-	?	?	?

I 相は既知の Na_2Au （$CuAl_2$ 型、正方晶、*Z*=4、*I*4/*mcm*）である。$CuAl_2$ 型は金属間化合物に多く見られる。この相は常圧で Na と Au を加熱すると生成するが、室温でもわずかの加圧で合成できることが新しい。一方、約 0.8 GPa 以上に存在する II 相は初めて見つかった相である。リートベルト解析と DFT 計算を行った結果、構造は三方晶、*Z*=6 で組成は Na_3Au、空間群は *P*-3*c*1（Cu_3As 型）または $P6_3cm$（Cu_3P 型）と決定された。二つの空間群で示される構造はたいへんよく似ており、R-因子も同程度の値なので、どちらであるかを決定することはできない。I 相にくらべ II 相では格子中の Na の数が 1 個ふえている。なお Na_3Au という組成比の化合物は常圧では存在しない。約 3.6 GPa 以上で安定な III 相は立方晶、*Z*=4、空間群 *Fm*-3*m*（BiF_3 型）で II 相と同じく Na_3Au の組成を持つ。この構造は、K と Ag を室温加圧することによって得られる K_3Ag と同型である[4]。III 相は広い圧力範囲で安定であり、約 56 GPa で IV 相へ転移する。IV 相はアモルファスと結晶の中間的な非常にブロードな回折パターンを与え、構造に大きな乱れがあることがわかる。現在のところこの相の組成や構造はわからない。IV 相は最高圧 60 GPa まで安定であった。減圧するといずれの相もヒステリシスを伴いながら可逆的に変化するが、I 相は常圧付近まで安定で、Na と Au に分解することはなかった。

今回の結果から、他のアルカリ金属も高圧下で金と多彩な金属間化合物を作ることが予想される。

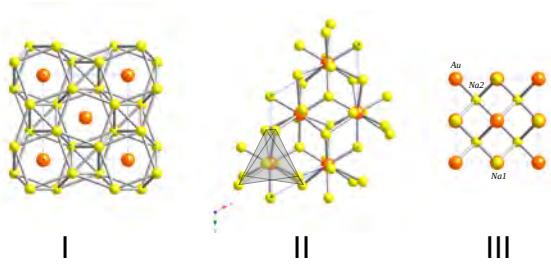

図 1 ：Na-Au 金属間化合物 I 相～III 相の結晶構造. 黄色は Na、オレンジが Au. II 相は二つの可能性のうち Cu_3As 型を示した.

参考文献
[1] M. Jansen, Chem. Soc. Rev. **37**, 1826 (2008).
[2] K. Takemura and H. Fujihisa, Phys. Rev. B **84**, 014117 (2011).
[3] C.-S. Zha, H.-k. Mao, and R.J. Hemley, Proc. Natl. Acad. Sci. USA **97**, 13494 (2000).
[4] T. Atou, M. Hasegawa, L.J. Parker, and J.V. Badding, J. Am. Chem. Soc. **118**, 12104 (1996).

* takemura.kenichi@nims.go.jp

NE1A/2009G070

Mg_2Si 熱電材料の高圧 X 線回折
High-pressure X-ray diffraction study of Mg_2Si thermoelectric material

森嘉久 [1*]
[1]岡山理科大学理学部，〒700-0005　岡山市北区理大町 1-1

1 はじめに

Mg_2Si は，中温領域の 650 K 付近にピークを持つ N型半導体の熱電材料で，その構成元素が人体に無害で且つその埋蔵量が豊富にあるので，近年活発に開発が進んでいる．しかし良質の Mg_2Si を合成することは容易ではない．なぜなら試料合成は Mg と Si を化学量論比に配合して Mg_2Si の融点(1358K)近傍に加熱して合成を行うが，その融点の 5K 上には Mg の沸点（1363K）あるため，Mg 蒸発による組成ずれが生じてしまう．そのため試薬として購入できる Mg_2Si（純度 2N5）にも少しの未反応物などが存在しており，その試料を出発原料として高温高圧合成しても，得られる合成物にまでその影響がもたらされてきた．近年，高純度の Mg_2Si 試料がユニオンマテリアル社から購入することが可能となり，その試料を出発原料として高温高圧合成法により高い熱電特性を有する材料の合成研究を進めている．本研究課題では，まずその高純度 Mg_2Si の基礎物性を明らかにするため高圧 XRD 実験を行い，その体積弾性率や圧力誘起構造相転移などを調べた．

2 実験

高圧 XRD 実験は PF-AR の NE1A ビームラインで，アンビルの先端が 0.6 mm ϕ のダイヤモンドアンビルセルを用いて実験した．高純度試料の Mg_2Si を微粉末にした後，インコネルガスケットの試料室内に圧力測定用のルビーボールとともに封入した．圧力媒体にはメタノール：エタノール：水=16:3:1 のアルコール媒体を使用し，実験はそのアルコール媒体が固化するまでの圧力領域で行った．波長は 0.04128 nm で，露光時間は 5 分であった．

3 結果および考察

高圧 XRD の結果を Fig. 1.に示す．0.00 GPa のプロファイルには Mg_2Si 以外の回折線はほとんどなく，高純度の試料であることが分かる．4.00 GPa におけるプロファイルから，6.1, 7.7, 8.3, 2.3 度に高圧相からの回折線が確認できた．さらに昇圧すると，高圧相からの回折線強度が増加するとともに，Mg_2Si からの回折線強度は減少した．Fi.g.2 に体積の圧力依存性を示す．体積弾性率は Birch-Murnaghan の式により B_0=53.1 GPa，B_0'=3.76 と求められた．

4 まとめ

Mg_2Si 高圧 XRD 実験により，圧力誘起構造相転移が 4.00 GPa で生じることが明らかとなった．また，Mg_2Si の体積弾性率は，Birch-Murnaghan の式により B_0=53.1 GPa，B_0'=3.76 と求められた．

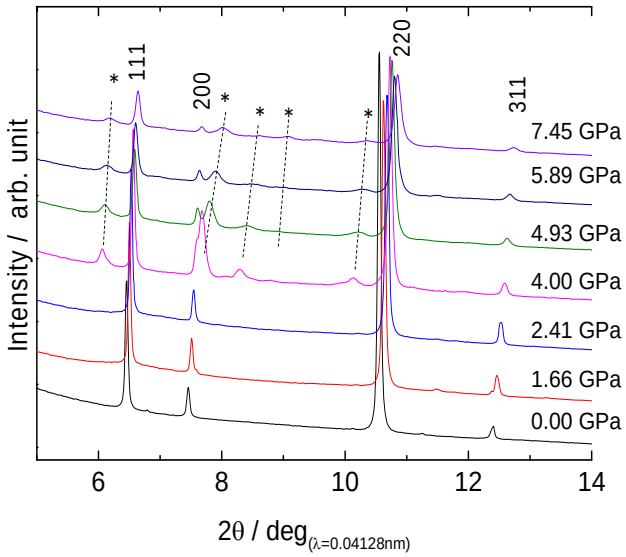

Fig.1. X-ray diffraction profiles of Mg_2Si up to 7.45 GPa. Pressure-induced phase transition occurred at 4.00 GPa. Some diffraction peaks of the high-pressure phase are denoted by dotted line and asterisk (*).

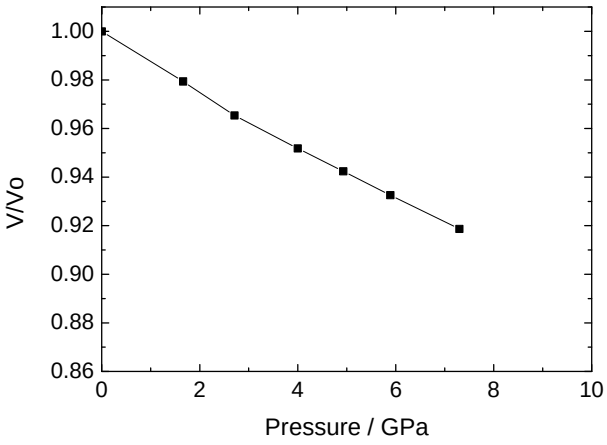

Fig.2. Volume change of Mg_2Si as a function of pressure. Bulk modulus was determined by Birch-Murnaghan equation to be 53.1 GPa.

* mori@das.ous.ac.jp

NE7A/2009G507

Structural Phase Transition in $CaGeO_3$

Shigeaki Ono[1,*]

[1] Institute for Research on Earth Evolution (IFREE), Japan Agency for Marine-Earth Science and Technology (JAMSTEC), Yokosuka 237-0061, Japan

1 Introduction

The phase transformation and physical properties of the garnet and the perovskite structures at high P-T conditions have attracted attention to understand the dynamics of the Earth's interior because major compositions ($MgSiO_3$ or $CaSiO_3$) have these structures in the Earth's mantle. It is known that some ABO_3 compounds are excellent analogues of $MgSiO_3$ or CaSiO3. Calcium germinate ($CaGeO_3$) exhibits a sequence of phase transitions from a pyroxenoid to a tetragonal garnet phase, and subsequently to an orthorhombic perovskite phase. The phase boundaries in $CaGeO_3$ have been also used as a pressure calibration point at high temperatures in high-pressure experiments, such as for SiO_2 and Mg_2SiO_4. Therefore, the precise phase boundary of $CaGeO_3$ needs to be determined.

2 Experiment

The starting material was $CaGeO_3$ wollastonite, synthesized from a starting mixture composed of finely powdered $CaCO_3$ and GeO_2. High-pressure X-ray diffraction experiments were performed using a multi-anvil high-pressure apparatus. The cubic anvil assembly was compressed using a "Max III" high-pressure apparatus, and was combined with a synchrotron radiation source located at the KEK in Japan. The diffracted X-rays were detected using a germanium solid-state detector at an angle of $2\theta = 6.0°$. A cylindrical graphite heater was inserted into the octahedral pressure medium and enclosed within a ZrO_2 sleeve for thermal insulation [1]. The powdered sample and platinum, which was used as pressure calibrant, were loaded directly into the graphite heater, which also served as a sample capsule. The pressure was determined from the unit cell volume of platinum using the equation of state for platinum. After reaching the required temperature, we performed in situ measurements using the synchrotron X-rays. The duration of heating was 0.5-2.0 hours. Determination of the stable phase in each experimental run was carried out by observing the X-ray diffraction pattern of the sample. To check the identification of each phase in the in situ experiments, the recovered samples were also examined using micro Raman spectroscopy.

3 Results and Discussion

We performed approximately 30 experimental runs, and the boundary determined in this study is in general agreement with that reported in previous high-pressure experiments. However, the value of our dP/dT slope was 2-3 times more negative than that in previous experiments. The calculated value of the dP/dT slope using calorimetry data in previous study is consistent with our value of dP/dT [1]. It is likely that the discrepancy between previous and our high-pressure experiments dues to the kinetics of the structural phase transition. In previous in situ experiments, the P-T condition was changed several times during each run while observing the transition from the garnet to the perovskite structure. It is known that a metastable overshoot (ΔP or ΔT) is required to provide a sufficiently large energy driving force to overcome a nucleation and/or growth barrier for the transition. To avoid any influence of the kinetic effect, we used the same heating cycle as that used in conventional quench experiments.

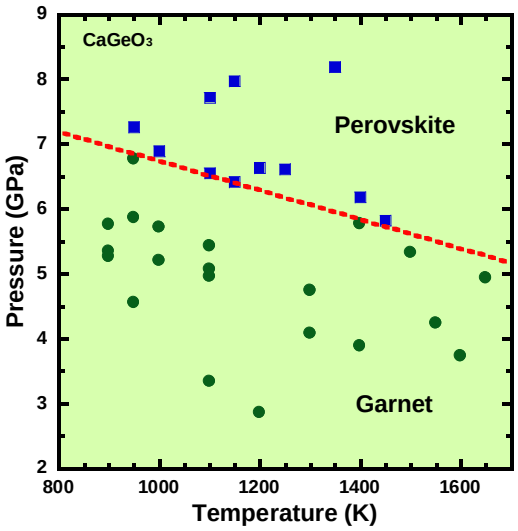

Fig. 1: Experimental results and phase boundary of the garnet-perovskite transition in $CaGeO_3$. The solid circles and squares denote the conditions where the garnet and perovskite phases were stable, respectively. The dashed line shows the inferred phase boundary between the garnet and perovskite phases.

Acknowledgement

We thank the PF staffs for their help in carrying out the experiments.

References

[1] S. Ono *et al.*, (2011) Phys. Chem. Minerals **38** (2011) 735-740.

* sono@jamstec.go.jp

8B/2009G529, 2011G511

Anisotropic strain effects on $LaMnO_{3+\delta}$ nanoparticles embedded in mesoporous silica

Takayuki Tajiri[1,*], Seiya Saisho[2], Yuki Komorida[2], Masaki Mito[2], and Hiroyuki Deguchi[2]
[1]Faculty of Science, Fukuoka University, Fukuoka 814-0180, Japan
[2]Fuculty of Engineering, Kyushu Institute of Technology, Kitakyushu 804-8550, Japan

1 Introduction

The influence of anisotropic strain, which causes distortion of particle shape, on the physical properties of nanoparticles is of particular interest. The changes in the surface state and crystal structure due to anisotropic stress are different from those due to hydrostatic pressure. These changes due to anisotropic stress lead to changes in physical properties of the material, especially in the case of nanometer-sized materials. $LaMnO_{3+\delta}$ (LMO) nanoparticles with diameters of about 8 nm embedded in SBA-15 showed novel size effects such as coexistence of two non-interacting magnetic components [1]. In this study, we attempted to apply anisotropic stress to LMO nanoparticles embedded in one-dimensional pores of mesoporous silica SBA-15 by applying pressure to SBA-15/nanoparticle composites [2]. The LMO nanoparticles were subjected to anisotropic stress by the silica walls separating the one-dimensional pores.

2 Experiment

The average particle size of the LMO nanoparticles at ambient pressure was about 10 nm. Powder X-ray diffraction (XRD) measurements for the LMO nanoparticles were performed under high pressure at room temperature. SBA-15 containing the LMO nanoparticles was pressurized using a diamond anvil cell. The ac magnetic susceptibility of the LMO nanoparticles under high pressure was measured using a SQUID magnetometer. A piston-cylinder type of pressure cell made of CuBe was used to generate pressure.

3 Results and Discussion

Powder XRD patterns showed that the LMO nanoparticles maintained the rhombohedral structure (space group: $R\bar{3}c$) up to 15.3 kbar. Both the evaluated lattice parameters *a* and *c* decreased up to 7.7 kbar and did not exhibit any noticeable change above that pressure, as shown in inset of Fig. 1. The pressure dependence of the lattice parameters indicates that the LMO lattice was compressed in an anisotropic manner; the compression ratio in the direction of *c* axis was about 2.5 times greater than that in the direction of *a*-axis. In contrast, the $La_{0.7}Sr_{0.3}MnO_3$ bulk crystals with the rhombohedral symmetry exhibited linear isotropic compression of the lattice under hydrostatic pressure [3]. Figure 1 shows the pressure dependence of the lattice strain in the LMO nanoparticles. The lattice strain in LMO nanoparticles was estimated from the slope of the straight line in the Williamson-Hall plot. The lattice strain increased monotonically up to 7.7 kbar. Above 7.7 kbar, the lattice strain was saturated. The pressure dependence of the lattice strain was qualitatively similar to that of the lattice constants.

As pressure increased, both the magnetic transition temperatures, T_C and T_N, for the LMO nanoparticles increased monotonically and saturated above 4.2 kbar. All of magnetic transition temperatures, lattice constants, and strain saturated in similar pressure ranges. These results indicated that the increase in the magnetic transition temperatures was related to the changes in the crystal structure. It was considered that the anisotropic compression of the crystal structure facilitated an increase in the Mn-O-Mn bond angle in the LMO nanoparticles. As a result, the change in the crystal structure under anisotropic stress induced enhancement of the exchange interaction, resulting in the increase in the magnetic transition temperatures.

These experimental results indicated that successful application of anisotropic stress. It was considered that the LMO nanoparticles in the one-dimensional pores of SBA-15 were subjected to anisotropic strain, so that the distortion of the particle shape, the changes in the crystal structure, and the changes in magnetic and electronic states of the nanoparticles were induced.

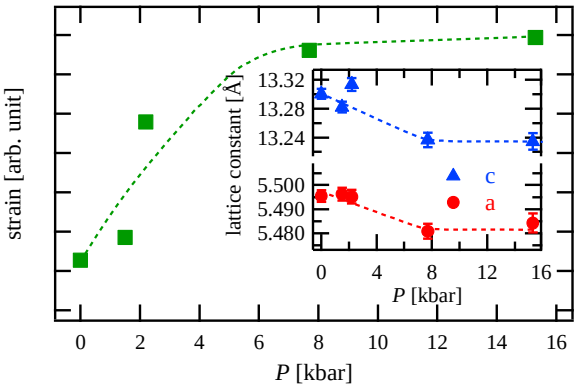

Fig. 1: Pressure dependence of lattice strain in LMO nanoparticles in SBA-15. Inset shows pressure dependence of lattice constants a and c for LMO nanoparticles.

References
[1] T. Tajiri *et al.*, J. Phys. Soc. Jpn. **75**, 113704 (2006).
[2] T. Tajiri *et al.*, J. Appl. Phys. **110**, 044307 (2011).
[3] D. P. Kozlenko *et al.*, J. Phys. Condens. Matter **16**, 6755 (2004).

* tajiri@fukuoka-u.ac.jp

AR-NE5C/2009G541

In-situ Synchrotron X-ray Powder Diffraction of Antigorite at High Pressure and Temperature

Tohru WATANABE*[1], Satoru URAKAWA[2], Takumi KIKEGAWA[3]
[1]Univ. Toyama, Gofuku, Toyama 930-8555, Japan
[2]Okayama Univ., Kita-ku, Okayama 700-8530, Japan
[3]KEK-PF, Tsukuba, Ibaraki 305-0801, Japan

Introduction

Antigorite plays key roles in subduction zone processes including transport of water and seismogenesis. The equation of state (EoS) of antigorite is critical for understanding of its stability field and for interpretation of seismological observations. Although a few compression tests have been conducted at room temperature [1], EoS is still poorly understood at high temperatures. We have conducted in-situ synchrotron X-ray powder diffraction experiments to understand EoS of antigorite.

Experimental

The sample is a natural antigorite collected from Inner Mongolia, China. The chemistry is shown in Table 1. The dark part in a BSE image has distinctly higher Al content than the bright part (Fig.1).

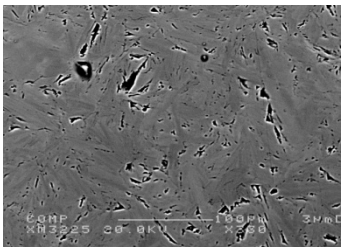

Fig.1 BSE image of the sample

Table 1: Chemistry of antigorite sample (wt%)

	Dark	Bright
SiO_2	45.00	45.16
Al_2O_3	0.26	0.07
FeO	0.47	0.45
MgO	40.29	40.53
CaO	0.00	0.01
Total	86.04	86.24

Selected-Area Electron Diffraction reveals that most of antigorite grains has m-value of 15 (the number of tetrahedra within a wave). There are also grains with m=16 and 17. The sample was finely ground and mixed with NaCl, and loaded in a multi-anvil type high-pressure apparatus (MAX80).

X-ray powder diffraction experiments were done by the energy dispersive method with 2θ=5º. The exposure time was around 1000 seconds. Experiments were conducted at pressures of 0.5~6 GPa and temperatures of 200~500 ºC. The pressure was estimated from the compression of NaCl.

Results

A typical diffraction spectrum is shown in Fig.2. Diffraction peaks of antigorite are indexed with the aid of reported indices [2].

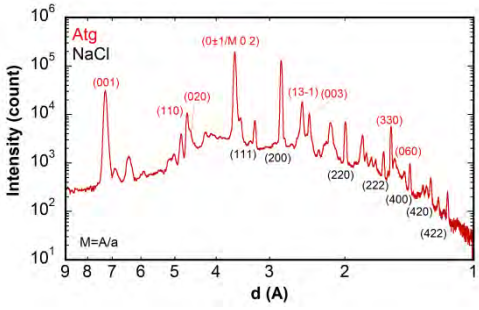

Fig.2 Diffraction spectrum at P= 0.007 GPa, T=27ºC

The identification of peaks (13-2) and (220) is essential for precise determination of lattice parameters. However, it is difficult to resolve these two peaks with the resolution of ~0.003 A (Fig.3). They can be resolved by using a powder X-ray diffractometer (Rigaku, SmartLab) employing the angle dispersive method. The resolution is ~0.0005 A (Fig.3). It is thus difficult to refine lattice parameters of antigorite by using the energy dispersive method. We are planning to apply a more precise method.

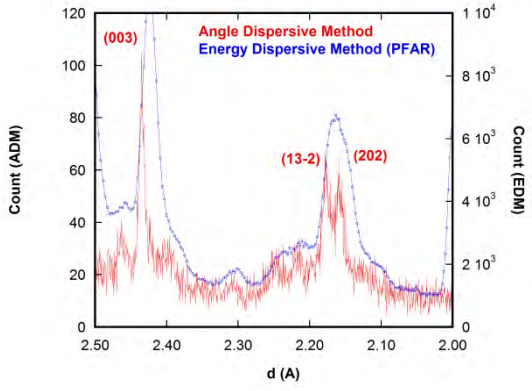

Fig.3 Angle dispersive method and energy dispersive method

References

[1] F. Nestola et al., Contrib. Mineral. Petrol. 160, 33 (2010)
[2] S.Uehara and H. Shirozu, Mineral. J. 12, 299 (1985).

* twatnabe@sci.u-toyama.ac.jp

NE1A/ 2010G060

Formation of the perovskite solid solution in the system of $CaSiO_3$-$MnSiO_3$ at high pressure and high temperature

Lin LI and Takaya NAGAI*
Hokkaido Univ., Sapporo, Hokkaido 060-0810, Japan

Introduction

According to the earth modeling PREM, the lower mantle continues from 660 km down to the core–mantle boundary, located at approximately 2900 km depth. It is making up 82% the volume and 65% the mass of the earth. High pressure and high temperature experiments indicate that the most probable mineral phases in lower mantle conditions were mainly: $(Mg,Fe)SiO_3$ – perovskite (Mg-Pv, ~70vol%), (Mg,Fe)O-magnesiowüstite (Mw, ~20vol%), $CaSiO_3$-perovskite (Ca-Pv, ~5%). $CaSiO_3$ is believed to be the third important major phase in the lower mantle, for further understanding of the deep earth, it is necessary to pay more attention on Ca-Pv. An important note about $CaSiO_3$-perovskite is stable in the pressure range of the Earth's mantle. While $(Mg,Fe)SiO_3$-perovskite transfers to mineral of post-perovskite structure, the structure of $CaSiO_3$-perovskite will keep just only some change from the lattice parameter. Another interesting point should be note on the Ca-Pv, is the low solubility of Ca in $(Mg,Fe)SiO_3$-perovskite, Fe in $CaSiO_3$-perovskite. Recently, our team has found that $MnSiO_3$ has the perovskite structure [1], and it seems stable under the lower mantle temperature pressure conditions. Except those chemically pure minerals, solid solutions seem to be more common in the lower mantle as $(Mg,Fe)SiO_3$-perovskite. To obtain a more realistic picture of the lower mantle, therefore, it is necessary to consider the minerals as solid solutions, existing in nature. From the foregoing knowledge, both of $CaSiO_3$ and $MnSiO_3$ have perovskite structure at lower mantle condition; it is interesting to study the phase relation of the two perovskite.

Experimental

In $CaSiO_3$- $MnSiO_3$ binary system, gels with 10%, 25%, 50%, 75% of $CaSiO_3$ contents were synthesized by conventional sol-gel method. Then we heated them at 1023 K for 3 hours under the controlled oxygen fugacity in order to keep Mn^{2+}. We finally made starting materials with desired chemical compositions.

High pressure conditions were generated using diamond anvil cells (DAC) with 200 or 300 μm culets diamond anvils. Sample was sandwiched between NaCl pellets and loaded into the DAC. NaCl works not only as a pressure transmitting materials but also as a thermal insulator. Small amount of gold powder was added to the sample as internal pressure marker. The diameter of a sample chamber in a pre-indented Re gasket is 80-100 μm. Samples in a DAC are heated from both sides with an YLF or YAG laser. The synthesis conditions were at pressures of 35-50 GPa and at temperatures of 1500-1800K, keeping the heating duration in between 40-120 min. Monochromatic synchrotron X-ray diffraction experiments were performed at AR-NE1A of Photon Factory KEK. X-ray diffraction patterns were measured by an angle dispersive method using an imaging plate (IP). Two dimensional IP data were integrated along Debye-Scherrer rings and converted to one dimensional data by the software IPAnalyzer [2]. Chemical analysis was conducted for recovered samples by FE-SEM with the EDS detector in Hokkaido Universty.

Results and Discussion

The symmetry of the perovskite is cubic when the $MnSiO_3$ content in the solid solution varies from 0% to 50%, and the perovskite has the orthorhombic structure when the $MnSiO_3$ content varies from 75% to 100%. The author's present experiments on the $CaSiO_3$-$MnSiO_3$ system give out an exciting result, which shows that this system almost bears complete solid solubility in the entire composition range with the perovskite structure. Because of the large cationic size of Ca^{2+}, and the quite stringent cubic perovskite structure of $CaSiO_3$, $(Mg,Fe)SiO_3$ cannot be the ideal candidate for substitution by Ca^{2+}. But for $MnSiO_3$ side, this orthorhombic perovskite just very little modified from the cubic may cause the possibility to form the solid solution with $CaSiO_3$ cubic perovskite.

References

[1] K. Fujino et al., Am. Mineralogist, 93, 653 (2008).
[2] Y. Seto et al., Review High Press. Sci. & Tech., 20, 269 (2010).

* nagai@mail.sci.hokudai.ac.jp

NE7A/2010G136

高圧下でのカンラン石の流動特性への水の影響
Influence of water on olivine rheology under high-pressure

大内智博[1*]，西原遊[2]，川添貴章[1]，西真之[1]
[1]愛媛大学地球深部ダイナミクス研究センター、　〒790-8577 愛媛県松山市文京町 2-5
[2]愛媛大学上級研究員センター、〒790-8577 愛媛県松山市文京町 3

1 はじめに

かんらん石は上部マントルの主要構成鉱物であり、上部マントルのダイナミクスを支配する。そのため、高温下におけるかんらん石の変形実験が数多くなされてきた。過去の研究によれば、転位クリープと拡散クリープが上部マントルにおける、かんらん石の主要な変形メカニズムであるとされてきた（例えば Karato et al., 1986）。一方、粒界すべりを伴う機構（即ち超塑性）も上部マントルにおいて重要な役割を果たす可能性があることが多数指摘されている（例えば[1]）。現在のところ、超塑性は地球の一部分（氷河：[2]；下部地殻・上部マントルのせん断集中帯: [3]；下部マントル： [4]）において支配的な変形メカニズムであると考えられている。

これまでに、系における部分溶融メルトや流体の存在によってかんらん石多結晶体のクリープ強度が低下することが報告されている。かんらん石－玄武岩メルト系においては、転位クリープ及び拡散クリープそれぞれの領域においてクリープ強度が低下する[5]。部分溶融メルトの量が多い場合には（> 4 vol.%）、粒界すべり支配の変形メカニズムが卓越する[1]。かんらん石－水系においても粒界すべり支配の変形メカニズムが卓越することが報告されている[6]。かんらん石－流体間の二面角は圧力の上昇とともに減少することが知られており[7]、このことは全界面における粒界の割合が圧力の上昇とともに減少することを意味する。そのため、かんらん石多結晶体のクリープ強度低下における流体の効果が高圧においてより効果的であることが期待される。しかし、部分溶融系におけるこれまでの変形実験は低圧（< 0.6 GPa）に限定されており、実際の上部マントルの圧力条件において、超塑性が卓越するかどうかについては検討されてこなかった。

2 実験

本研究では、上部マントル条件下（P = 1.3−5.7 GPa, T = 1270−1490 K）における、含水メルトを含むかんらん岩のレオロジー的物性を理解することを目的として、含水メルト（< 2.5 vol.%）を含むダナイト（かんらん石＋4 vol.%斜方輝石＋4 vol.%単斜輝石）の“放射光その場観察”変形実験を行った。実験は、PF-AR の NE7A に設置されている D-DIA 型高圧変形装置（D-CAP）および単色 X 線を用いて行った。

3 結果および考察

歪速度が定常クリープ強度の約 2 乗に比例することや、定常クリープ強度が転位クリープ流動則から予想される強度よりも顕著に低いことが観察された。さらには、33－55%の歪を加えたにも拘わらず、結晶の伸張や結晶方位定向配列の発達が殆ど観察されなかった。これらの特徴から、今回の実験条件における変形メカニズムにおいて粒界すべりが重要な役割を果たしていた（すなわち超塑性）ことが考えられる。

また、かんらん岩にメルト相が加わることにより、かんらん岩の変形強度が低下することは低圧条件（0.3 GPa）においては知られていた[5]ものの、本研究の高圧条件下においては、より顕著なかんらん岩の強度低下が観察された。

4 まとめ

天然におけるかんらん石の超塑性は、せん断集中帯のような低温・高応力の条件において卓越し、せん断集中帯への流体の進入によって引き起こされるものと予想される。

謝辞

東北大学理学部の白石令博士、鈴木昭夫准教授、大谷栄治教授及び KEK の亀卦川卓美講師には多くのご支援を頂いた。以上の結果は、Earth and Planetary Science Letter 誌において掲載予定である。

参考文献

[1] G. Hirth and D. L. Kohlstedt, J. Geophys. Res. **100** (1995) 15441.
[2] D. L. Goldsby and D. L. Kohlstedt, J. Geophys. Res. **106** (1995) 11017.
[3] J. H. Behrmann and D. Mainprice, Tectonophysics **140** (1987) 297.
[4] S. Karato, S. Zhang, H.-R. Wenk, Science **270** (1995) 458.
[5] S. Mei, W. Bai, T. Hiraga, D. L. Kohlstedt, Earth Planet. Sci. Lett. **201** (2002) 491.
[6] R. D. McDonnell, C. J. Peach, H. L. M. van Roermund, C. J. Spiers, J. Geophys. Res. **105** (2000) 13535.
[7] K. Mibe, T. Fujii, A. Yasuda, Nature **401** (1999) 259.

* ohuchi@sci.ehime-u.ac.jp

NE1A/2010G141

超高圧高温下におけるキセノンと金属およびケイ酸塩との反応
Reaction of Xenon with Metals and Silicates under High Pressure and Temperature

八木健彦*, 浜根大輔, 岡田卓
Takehiko YAGI, Daisuke HAMANE, Taku OKADA
東大物性研究所、〒277-8581 柏市柏の葉 5-1-5
Institute for Solid State Physics, University of Tokyo

1 はじめに

地球大気中のキセノンガス存在度は、太陽系の存在度から期待される量に比して 1 桁近く少ないことから、地球内部に何らかの化合物の形で存在する可能性があると考えられている。本研究では、ダイヤモンドアンビル装置を用いて、地球の核やマントルを構成する金属やケイ酸塩鉱物とキセノンガスを超高圧下まで加圧し、レーザーで試料を高温まで加熱した後室温に下げ、圧力を保持したままX線回折実験を行うことにより、何らかの化合物が生成したか否か、あるいは金属や鉱物中にキセノンが取り込まれた兆候があるか否か、を検証した。

2 実験

金属試料としては地球核の主要成分と考えられている鉄およびニッケル、それにケイ酸塩鉱物としてはマントルの主要成分であるオリビンを用いて実験を行った。ダイヤモンドアンビルの試料室内にまず、NaCl の薄板を断熱材兼ダイヤと試料の反応を防ぐために敷き、その上に試料を載せて、1 気圧低温下で液化したキセノンを満たした。所定の圧力まで室温で加圧しX線回折実験を行った後、ファイバーレーザーで 1600K から 2600K 程度まで加熱し、室温に戻して再びX線回折実験を行い、加熱前後における変化の様子を観察した。

3 結果および考察

キセノンは約 120GPa で金属化し高圧下の鉄と同じ hcp metal となることから、コアの主成分である鉄と反応する可能性は高いと考えられ、コアの圧力に対応する約 155GPa までの実験を行った。しかしこの圧力で 2600K まで加熱しても、化合物の生成を示唆する新しい回折ピークは全く観測されず、かつ鉄の体積も全く変化しなかった。このことからコア条件下でも、鉄とキセノンは全く反応しないことが明らかにされた。常圧下において、同形の金属が合金を作るには両者の原子半径が 15%以上違わない必要があることがヒューム・ロザリー則として知られているが、155GPa という超高圧下でもそれが当てはまることが明らかにされた。この結果はすでに論文として公表された[1]。鉄と共に地球の核に存在すると考えられるニッケルについても実験を行ったが、鉄と同様に、反応を示す結果は一切得られなかった。

図 1 はマントルの最も主要な構成鉱物であるオリビンを出発試料にして、19GPa 及び 28GPa で加熱後得られたX線回折パターンである。オリビンはこれらの条件下で各々、Wadsleyite および perovskite + periclase に転移・分解するが、図から明らかなようにいずれもキセノンとの反応を示唆する新たな回折線は見られず、それぞれの体積も純粋な相のそれと有意な違いは見られなかった。

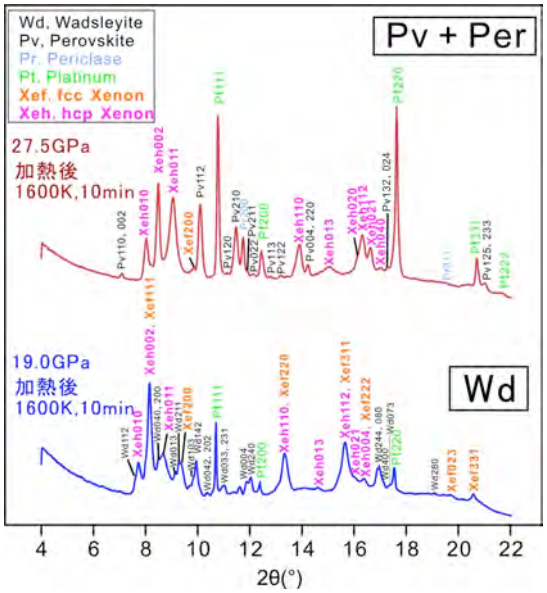

図 1．Xe とケイ酸塩を高圧下で加熱した後のX線回折パターン

4 まとめ

これらの実験結果から、キセノンは地球の核やマントルを構成する物質と反応するとは考えにくく、大気中のキセノン欠損を説明するには、何らか別のメカニズムが必要とされることが明らかになった。

謝辞

NE1A での実験にあたっては、PF の亀卦川卓美氏に大変お世話になった。記して感謝する。

参考文献

[1] D. Nishio-Hamane *et al.*, Geophys. Res. Lett., **37**, L04302 (2010).

* yagitakehiko@76.alumni.u-tokyo.ac.jp

NE7A/2010G182

Viscosity of CO_2-bearing silicate melts at high pressure

Akio Suzuki[1,*]
[1]Tohoku University, Sendai 980-8578, Japan

1 Introduction

Viscosity is an important property of magma (silicate melt), because it controls the transportation of magma in the planetary interior. Traditionally, viscosity at high pressure was measured in quenching experiments. At the beginning a metallic sphere was places at the top of a sample chamber. The falling velocity was determined from the falling distance during the molten period of sample. Kanzaki et al. [1] developed the *in situ* falling sphere technique, in which the movement of a metallic sphere in a sample chamber was recorded in X-ray radiography image. We have used this technique to determine the pressure, temperature and compositional dependence of the viscosity of silicate melts. The main goal of our study is to determine the effect of dissolving carbon dioxide on the viscosity of silicate melts at high pressure. It has been known that volatiles are dissolved in natural magmas and affects the physical properties. However, very few studies have been performed to investigate the effect of carbon dioxide on the viscosity of silicate melts at mantle pressures. In the present study, the viscosity of carbon-dioxide bearing $CaMgSi_2O_6$ and $NaAlSi_2O_6$ composition melts have been determined up to 4 GPa.

2 Experiment

We installed an X-ray radiography system at the NE7A station at High Energy Accelerator Research Organization (KEK) in Tsukuba, Japan. A charge—coupled device (CCD) camera with a YAG:Ce fluorescence screen was used to obtain the X-ray absorption contrast image. High-pressure was generated using a Kawai type multi-anvil apparatus, which was driven by a DIA type guide block in the MAX-III system.

The pressure was determined by using an equation of state for MgO. A pure-Ge solid sate detector was used to collect the X-ray diffraction data of the pressure standard by energy-dispersive method. Experimental setup has been described in detail elsewhere [2]. The starting mixture was synthesized from reagents at 1 atm. A powder mixture of oxides and carbonates were fused and quenched to make a glass. Carbonate powder was finally added as a source of carbon dioxide.

3 Results and Discussion

Structural study has suggested that the $CaMgSi_2O_6$ composition melt is depolymerized. The viscosity of pure $CaMgSi_2O_6$ melt increases with increasing pressure. By the addition of 1.0 wt % of carbon dioxide produces about 50% decrease under pressure. $NaAlSi_2O_6$ composition melt has polymerized structure. In our previous study [2], we observed the decrease of viscosity of the pure $NaAlSi_2O_6$ melt with elevating pressure. In this study, we measured the viscosity of $NaAlSi_2O_6$ + 1.0 wt% CO_2 melt. The viscosity of CO_2-bearing $NaAlSi_2O_6$ melt decreases by about one order of magnitude. Our results suggest that the viscosity of the polymerized silicate and aluminosilicate melts are relatively reduced by the addition of CO_2, because CO_2 depolymerizes the SiO_4 and AlO_4 networks.

References

[1] M. Kanzaki, K. Kurita, T. Fujii, T. Kato, O. Shimomura, S. Akimoto, *in High Pressure Research in mineral physics*, M. H. Manghnani and Y. Syono, Eds. (TERRAPUB/AGU, 1987), pp.195-200.

[2] A. Suzuki, E. Ohtani, H. Terasaki, K. Nishida, H. Hayashi, T. Sakamaki, Y. Shibazaki, T. Kikegawa, *Phys. Chem. Miner.* **38**, 59 (2011).

* a-suzuki@m.tohoku.ac.jp

18C/2010G508

A stabilizing mechanism of carbon dioxide hydrate under low-temperature and high-pressure

Hisako Hirai[1,*], Satoshi Nakano[2]
Yoshitaka Yamamoto[3], Takehiko Yagi[4], Takumi Kikegawa[5]
[1] Geodynamics Research Center, Ehime University, Matsuyama, 790-8577, Japan
[2] National Institute for Material Science, Tsukuba, Ibaraki 305-0044, Japan
[3] AIST, Methane Hydrate research Center, Tsukuba, Ibaraki 305-8569, Japan
[4] Institute for Solid State Physics, Tokyo University, Chiba 277-8581, Japan
[5] Institute of Materials Structure Science, KEK,Tsukuba 305-0801, Japan

1 Introduction

CO_2 hydrate consists of cages formed by hydrogen-bonded host water molecules with guest CO_2 molecules in the cages [1]. CO_2 hydrate takes sI structure similar to many other gas hydrates, but it exhibits characteristic behaviors different from those of other gas hydrates. For most gas hydrates, the slopes of the phase boundaries between gas hydrates and gas + water are positive in temperature versus pressure field. On the other hand, for CO_2 hydrate the phase boundary turned from a positive slope to a negative one at an inflection point (294K,328 MPa) [1]. Recently, the authors determined phase changes of CO_2 hydrate in a region from 80 to 300 K and from 0.2 to 3.0 GPa [2]. However, it has not been known why the sI structure of CO_2 hydrate survives at such conditions. In this study, high-pressure and low-temperature experiments were performed to clarify a stabilizing mechanism under low-temperature and high-pressure.

2 Experiment

A clamp-type diamond anvil cell (DAC) and a helium-refrigeration cryostat were used. Pressure measurements were made by using the ruby fluorescence method. Temperature measurements were made with Si-diode thermometer and chromel-alumel thermocouples. The initial materials were prepared using a conventional ice-gas interface method, of which conditions were 271 K and 2.0 MPa. The occupancies for large and small cages of the initial samples were estimated to be 98% and 94%, respectively, by Rietveld analysis. X-ray diffractometry (XRD) was performed using synchrotron radiation at BL-18C at the Photon Factory, KEK. A monochromatized beam with a wavelength of 0.06198 nm was used.

3 Results

Changes in the lattice parameter with temperature were measured at a few fixed pressures of approximately 0.2 GPa and 0.4 GPa (Fig.1a and 1b). A peculiar behavior was observed as follows. With decreasing temperature, the lattice parameters decreased, which is normal behavior. However, at approximately 210 K, the lattice parameter abruptly increased, and after that the lattice parameter reduced again with decreasing temperature. Fig.1c and 1d show XRD patterns before and after the expansions of the lattice. Before the expansion, only sI, as a matter of course, existed, whereas ice Ih appeared and continued to exist after the expansion at both pressures. It is noteworthy that dry ice was never observed with these expansions. This means that sI was not simply decomposed, but only H_2O molecules was released to form ice Ih. The release of ice Ih indicates an increasing degree of guest occupancy.

The lattice expansion accompanied by a release of ice Ih was observed at 210 K. Release of H_2O molecules indicates increasing cage occupancies, i.e. becoming a denser structure. Transforming into a denser structure by releasing H_2O molecules is an effective way to sustain the cages structure, therefore this can be recognized as a stabilizing mechanism under high pressure and low temperature.

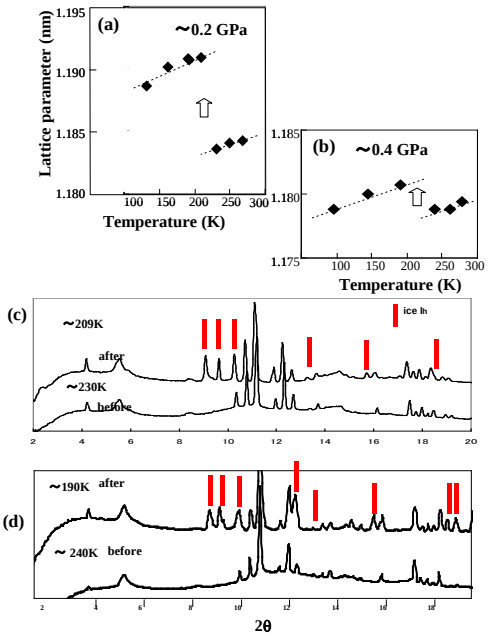

Fig.2 a and b: Variations of lattice parameter, c and d: XRD patterns before and after the lattice expansion.

References

[1] S. Nakano et al., J. Chem. Eng. Data 43, 807 (1998).
[2] H. Hirai et al., J. Chem. Phys. **133** (2010) 124511.
Corresponding author: hhirai@sci.ehime-u.ac.jp

18C /2010G516

錯体水素化物 $LiNH_2$ の圧力誘起相転移
Pressure-induced phase transitions of complex-hydride $LiNH_2$

山脇 浩 [1*], 藤久 裕司 [1], 後藤 義人 [1] 中野 智志 [2]
[1](独)産業技術総合研究所、〒305-8565 つくば市東 1-1-1
[2](独)物質・材料研究機構、〒305-0044 つくば市並木 1-1

1 はじめに

近年、錯体水素化物は水素貯蔵物質として注目を集める一方、Li 系の錯体水素化物においては高い Li イオン伝導性も発現することが見出されてきた。なかでも $LiBH_4$–$LiNH_2$ 複合体では室温から融解温度までの温度範囲で高い Li イオン伝導率が報告されている[1]。Li イオン固体電解質開発の有用な指針を得るために、我々は Li 系錯体水素化物の温度−圧力により出現する様々な結晶相の構造と　そのイオン伝導度の相関関係を明らかにすることを目標にしている。$LiBH_4$–$LiNH_2$ 複合体と対比するために、今回、$LiNH_2$ 単体の相図や構造を調べた。$LiNH_2$ は常温常圧で正方晶($I\bar{4}$)の α 相であり、646 K で融解する。ラマン測定により室温, 8〜14 GPa で β 相への転移が報告されている[2]が、構造は未定であった。高圧下での構造変化に関する情報を得るため、高圧粉末 X 線回折、赤外測定、ラマン測定を行い、相転移や高圧相の構造について明らかにした。

2 実験

試料は市販の $LiNH_2$(Aldrich, >95%)を用いた。圧力発生にはダイヤモンドアンビル・セル（キュレット径 0.3–0.5 mm）を用い、ガスケット(Re or spring steel)に穴をあけて試料部とした。サンプリングは dry Air (露点 -40℃)をフローさせたグローブボックス中で行った。圧力はルビー蛍光法で求めた。粉末 X 線回折測定は、KEK PF, BL-18C において、20 keV の X 線を用いて室温下で圧力媒体無しで測定した。赤外測定は顕微赤外分光器 (Jasco VIR-9500 and IRT-30)を使用し室温で KBr 圧媒体を用いて行った。ラマン測定は、セルをヒーター加熱しながら行った。波長 488nm の Ar レーザーを使用し、液体窒素冷却 CCD 検出器付きの分光器(SPEX 1877)によりラマンスペクトルを得た。

3 結果および考察

$LiNH_2$ の室温での赤外測定からは、11 GPa で 1550 cm^{-1} 付近の N-H 変角振動ピークの低波数側に shoulder peak が一旦現れて、その後 13 GPa で消失するなどの挙動が観測された。粉末 X 線回折測定でも、12 GPa 付近で α 相、β 相のピークの他に新たなピークが現れ、β 相への転移前に中間相が存在することが明らかになった（図 1）。高圧 β 相に関しては、X 線回折データをもとにリートベルト解析と DFT 計算を行い、その構造は斜方晶(*Iba*2)と求まった（図 2）。α 相中では Li に対する配位数が加圧による原子間の接近と共に 2 から 4 へ増加し、β 相でも 4 配位となっていることがわかった。さらに、N-H 結合距離が β 相への転移時に一旦伸びていることがわかった。これは、振動分光において、β 相の出現と共に N-H 伸縮振動数が低波数側に不連続なとびを示すことと良く対応している。

高温高圧下でのラマン測定によると、α 相は 500 K まで室温とほぼ同じ 11 GPa 付近の圧力で転移した。11 GPa 以下の広い温度範囲で $LiNH_2$ は α 相として存在することが明らかになった。

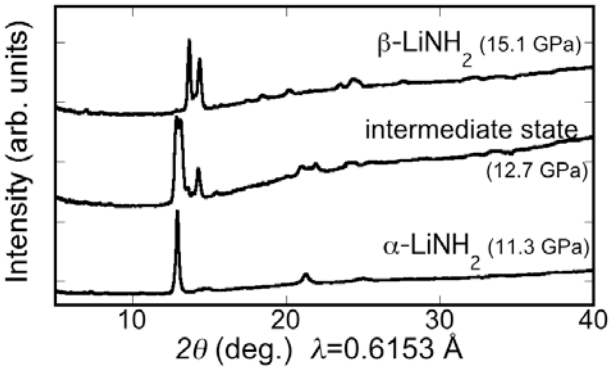

図 1： $LiNH_2$ 各相の粉末X線パターン。

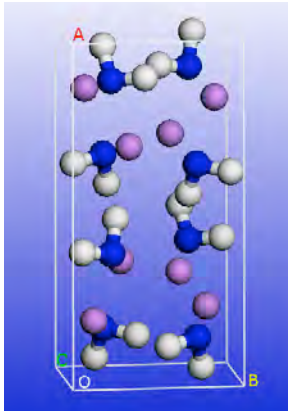

図 2： 高圧 β 相の結晶構造。

謝辞

本研究は文部科学省の科研費(22550185)の助成を得た。

参考文献

[1] M. Matuo *et al.*, J. Am. Chem. Soc. **131** (2009) 16389.
[2] R.S. Chellappa *et al.*, J. Phys. Chem. B **111** (2007) 10785.

* h.yamawaki@aist.go.jp

PF BL-18C/2010G519,
SPring-8 BL10XU/2011A1943

準静水圧環境での $Ba_{24}Ge_{100}$ の低温高圧 X 線回折実験
High-Pressure/Low-Temperature X-Ray Diffraction Experiment for $Ba_{24}Ge_{100}$ under Quasi-Hydrostatic Pressure Condition

中野智志 [1*], 今枝佑太 [2], 中本琢磨 [2], 船橋健太 [2], 久米徹二 [2]
[1] 物質・材料研究機構　〒305-0044 つくば市並木 1-1
[2] 岐阜大院環境エネルギーシステム　〒501-1193 岐阜市柳戸 1-1

1 はじめに

構造 I'型 Si 系クラスレート $Ba_{24}Si_{100}$ と $Ba_{24}Ge_{100}$ は、同構造ながら物性やその高圧挙動などに相違点がある[1-3]。$Ba_{24}Si_{100}$ は Tc = 1.4 K の超伝導体であるが、体積が約 11%大きい $Ba_{24}Ge_{100}$ は Tc = 0.24 K と低い。また、$Ba_{24}Ge_{100}$ は温度 T_{s1}＝225 K から T_{s2}＝175 K で $Ba_{24}Si_{100}$ にない低抵抗相から高抵抗相への相転移を起こし、格子定数や磁化率の温度依存性に anomaly が現れる。また、高圧下の Tc 変化も、$Ba_{24}Si_{100}$ は低下、$Ba_{24}Ge_{100}$ は上昇と逆の傾向がある。これらの違いは、$Ba_{24}Ge_{100}$ では、Ba イオンのうち open cage に入っている Ba(3)が、低温下で非対称的なラットリング振動をするためとされている。

上記の実験的検証のため、低温高圧下における $Ba_{24}Ge_{100}$ の構造変化を精密に解析することを目的として、静水圧性の高いヘリウム圧力媒体を用いて高圧粉末X線回折測定を行った。

2 実験

$Ba_{24}Ge_{100}$ は、元素の定比混合物を加熱する直接合成法で得た。高圧セルには Cu-Be 製クランプ型 DAC を用い、ガスケットには Cu-Be 板（100 μm^t）を用いた。試料空間に微粉砕した試料を入れ、さらにヘリウム圧力媒体を 180MPa で導入した。これを KEK-PF BL-18C および SPring-8 BL10XU に持ち込み、クライオスタット中で He ガス駆動によりセルを加圧し、低温高圧下での粉末X線回折測定を行った。実験は常圧ー3.0 GPa、室温ー5 K の範囲で行った。

3 結果および考察

5 K においても 250 K とほぼ同等のシャープな回折図形を得ることができ、低温高圧下におけるヘリウムの静水圧効果が確認された。電気抵抗の変化から転移が示唆されている温度 T_{s1} および T_{s2} の前後にで、$Ba_{24}Ge_{100}$ の回折図形に大きな変化はなかった。

回折パターンのリートベルト解析から、Ba(3)のラットリング挙動と温度・圧力の関係を調べた。解析では、Ba(3)の存在位置を Ba(3_1): 12*d* (1/8, y, z) 以外にもう 1 か所 Ba(3_2): 12 *d*(x, y, z) を仮定し、それらの x 座標の差Δx = x(Ba3_1) - x(Ba3_2)が Ba(3)のラットリングを表現するとして評価した。Fig.1 にこのΔx の温度依存性を示す。0.8 GPa では 100 K 付近でΔx が大きくなった。この結果は低温での Ba(3)のラットリング挙動に対応しており、低温で相転移が現れること、超伝導転移温度 Tc が低く押さえられること等の物性に反映していると考えられる。圧力が 1.5 GPa に上昇すると、このΔx の増大は抑制されて低温側にシフトする。そして 2.1 GPa 以上では、もはやΔx の増大は見られない。これらは、圧力上昇により低温での相転移が抑制され、Tc が上昇する $Ba_{24}Ge_{100}$ の特徴的な物性に対応している。

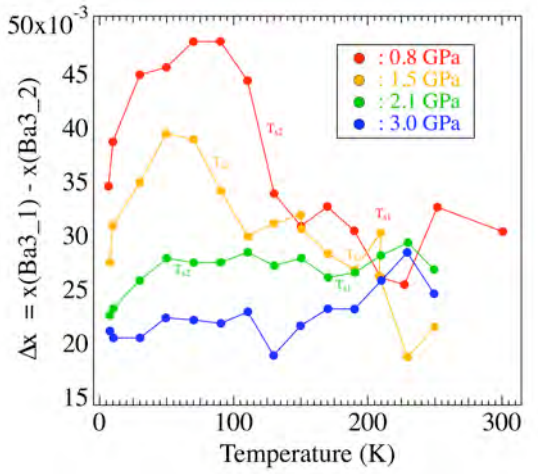

Fig.1 The x-coordinate difference of two Ba(3) positions in $Ba_{24}Ge_{100}$ calculated by Rietveld

謝辞

本研究の一部は文科省科研費特定領域研究「配列ナノ空間を利用した新物質科学–ユビキタス元素戦略」の助成を得て行われました（20045019, 22013021）。試料を提供してくださった谷垣勝巳教授，熊代良太郎准教授（東北大院理）に深く謝意を表します。本実験は，高エネルギー加速器研究機構物質構造科学研究所放射光共同利用実験（2010G519）および SPring-8 量子ビーム施設震災優先枠（2011A1943）を利用して行われました。

参考文献

[1] T. Rachi *et al.*: PRB **72**, 144504 (2005).
[2] F. M. Grosche *et al.*: PRL **87**, 247003 (2001).
[3] W. Carrillo -Cabrera, *et al.*: J. Solid State Chem., **178**, 715 (2005).

* nakano.satoshi@nims.go.jp

18C/2008G012, 2010G609

Pressure-induced changes in hydrogen bonds in hydrous materials

Hiroyuki Kagi[1,*], Riko Iizuka[1], Kazuki Komatsu[1], Yu Yamaguchi[1] and Shin-ichi Machida[2]
[1]Graduate School of Science, The University of Tokyo, Tokyo 113-0033, Japan
[2]Geodynamic Research Center, Ehime University, Ehime 790-8577, Japan

1 Introduction

Water and hydrogen play important roles on dynamics and mineral properties of deep earth and planets. Pressure-induced changes in structure of hydrous materials including hydrous minerals are one of the fundamental research targets to the understanding properties of hydrogen in the deep earth and planets. We report our recent research activities on X-ray diffraction measurements at high pressure conducted at the beamline-18C, Photon Factory.

2 Experimental procedures

We are going to introduce a couple of representative experimental results on $Ca(OH)_2$ and ice at high pressure using diamond anvil cells. Angular-dispersive synchrotron XRD patterns of the powder samples were obtained at high pressure at the BL-18C, High Energy Accelerator Research Organization (KEK). X-ray diffraction patterns of ices were observed at low temperatures down to 100 K. A monochromatized incident X-ray with energy of 20 or 30 keV (ca. 0.6 or 0.4 Å in wavelength) was used. The beam was collimated to a diameter of 30–60 μm. The diffracted X-ray patterns were recorded on an imaging plate (IP) detector. Profile fitting was conducted using a symmetric pseudo-Voigt function with the software PDIndexer [1].

3 Pressure responses of $Ca(OH)_2$ and H–D isotope effects on pressure-induced phase transitions [2]

The pressure responses of $Ca(OH)_2$ and the isotope effect on the phase transition were investigated at room temperature from powder X-ray diffraction and single-crystal Raman and IR spectra using diamond anvil cells under quasi-hydrostatic conditions in a helium pressure-transmitting medium. Phase transformation and subsequent peak broadening (partial amorphization) observed from the Raman and IR spectra of $Ca(OH)_2$ occurred at lower pressures than those of $Ca(OD)_2$. In contrast, no isotope effect was found on the volume and axial compressions observed from powder X-ray diffraction patterns. X-ray diffraction lines attributable to the high-pressure phase remained up to 28.5 GPa, suggesting no total amorphization in a helium pressure medium within the examined pressure region. These results suggest that the H–D isotope effect is engendered in the local environment surrounding H(D) atoms. Moreover, the ratio of sample to methanol–ethanol pressure medium (i.e., packing density) in the sample chamber had a significant effect on the increase in the half widths of the diffraction lines, even at pressures below the hydrostatic limit of the pressure medium.

In conclusion, we have confirmed that a reversible pressure-induced phase transition occurs in $Ca(OH)_2$ at around 6 GPa at room temperature. XRD peaks of the high-P phase were observed even at 28 GPa, whereas all the Raman and IR spectroscopic peaks disappeared at pressures greater than about 20 GPa under quasi-hydrostatic conditions. The H–D isotope effect was observed on the pressures of transformation to the high-P phase and partial amorphization; the transition pressure of $Ca(OH)_2$ is lower than that of $Ca(OD)_2$. In contrast, no isotope effect was found on the volume and axial compression of $Ca(OH)_2$. The present results suggest that the pressure responses accompanying the isotope effect are closely related to hydrogen bond interactions.

4 Uptake of salt components in high-pressure ices [3]

Recently, uptake of salt components, for instance LiCl and NaCl, into ice VII, a high-pressure phase of ice, have been reported (eg., Klotz et al., 2009) in contrast to the incompatible nature of salts into the crystal structure of normal ice (ice Ih).

We have determined precisely the lattice volumes of high-pressure phases of ices (see Fig. 1 for the P-T conditions). The obtained experimental results showed several percents of volume excess in ice VII which was grown from MgCl solution. The results suggest that substantial amount of $MgCl_2$ was contained in ice VII. The result is the first report on the uptake of divalent metal ion salt into a high-pressure phase of ice. The details will be reported in an original paper in preparation.

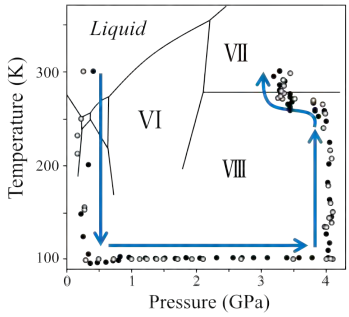

Fig. 1 *P-T* path of experiments on the phase diagram of H_2O.

References

[1] Y. Seto et al. Rev. High Press. Science Tech., 20 (2010) 269.
[2] R. Iizuka et al. Physics and Chemistry of Minerals, 38 (2012) 777.
[3] Y. Yamaguchi et al., (to be submitted).
* kagi@eqchems.s.u-tokyo.ac.jp

18C/2010G620

低温高圧X線回折による $FeSe_{1-x}S_x$ の結晶構造

Crystal Structure of $FeSe_{1-x}S_x$ at Low Temperature under Pressure

冨田崇弘[1*], 高橋博樹[1], 水口佳一[2], 高野義彦[2], 松林和幸[3], 上床美也[3]

[1] 日本大学文理学部、〒156-8550 世田谷区桜上水 3-25-40
[2] 物質・材料研究機構　〒305-0047 つくば市千現 1-2-1
[3] 東京大学物性研究所　〒277-8581 柏市柏の葉 5-5-1

1 はじめに

鉄系超伝導の中で最も単純な結晶構造を持つ FeSe 系は、超伝導転移温度 T_c が圧力によって敏感に変化し、常圧で T_c = 8 K から 6 GPa で最大 37 K に達することが報告されている。[1] また、Se の一部をより小さな元素の硫黄 S で置換することで化学的圧力を印加させて T_c を上昇させることがで、$FeSe_{0.8}S_{0.2}$ (T_c = 11 K)で最適組成となる。[2]これは、FeSe が *Cmmm* と斜方晶であるのに対して、S ドープにより低温での結晶構造が *P4/nmm* と変化する事で対称性が良くなり超伝導の転移温度が高くなるとも考えられている。今回我々は低温で *P4/nmm* を持つ S ドープに注目して、その高圧下での超伝導転移温度と結晶構造の関係について研究を行った。

2 実験

今回、我々は固相反応法により合成された多結晶試料 $FeSe_{1-x}S_x$ ($0.1 \leqq x \leqq 0.3$)を用いて、ピストンシリンダー型圧力セルとキュービックアンビルを利用して 8 GPa まで静圧下で電気抵抗測定を行い、圧力温度相図を作成した。各組成で 5~6 GPa で T_c が最大まで上昇するが FeSe の最大 T_c には達しない。(図 1) しかし、低圧領域($0 \leqq P \leqq 2$ GPa)で T_c の圧力変化が、磁化と電気抵抗測定から一端下降し上昇する現象が観測されており、FeSe では見られない圧力異常が現れた。この低圧力領域での構造を確認するため、放射光科学研究施設(PF)で冷凍機を用い DAC による高圧X線回折実験を行った。

3 結果および考察

$FeSe_{0.8}S_{0.2}$ の T_c は、FeSe には及ばなかったがこれは、S ドーピングにより超伝導レイヤーが乱されたことが原因であると考えられる。また、今回行った実験から低圧力側に超伝導転移のU字型変化が見られた。このような超伝導転移の振る舞いは、今まで他の超伝導物質では確認されていない。この振る舞いは超伝導転移温度が圧力パラメータに対して 2 つ以上のコントロールパラメータが存在していると考えられる。図 1 に今回X線回折実験を低温で行い得られた Fe 面からの距離「アニオン Se(S)の高さ」と T_c と関係を示す。この圧力相図を確認すると、このU 字型の T_c と「アニオン Se(S)の高さ」に相関があることが分かった。特に、アニオンの高さ（$c \times z$）は、c 軸の格子定数と単位格子で考えた Se の z 位置から決定されており、この 2 つのコントロールパラメータが今回見られた超伝導転移温度の圧力異常の原因であると考えられる。

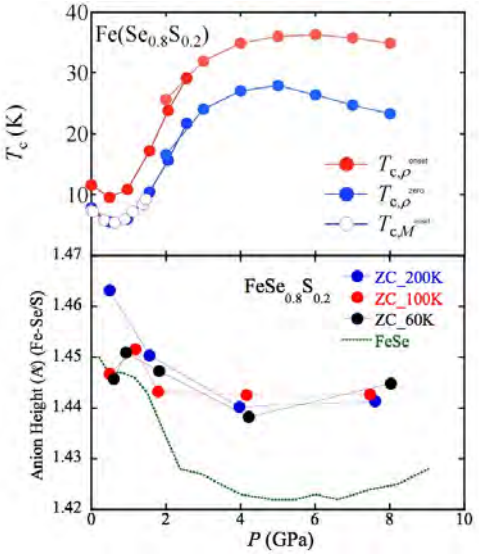

図 1 ：$FeSe_{1-x}S_x$ 圧力温度相図

4 まとめ

$FeSe_{1-x}S_x$ の高圧中の結晶構造から Se(S)の役割について研究を行った。この結果、従来の Fe-As-Fe ボンド角では説明がつかない実験結果が得られ、Fe 面からの距離「アニオン Se(S)の高さ」が良く超伝導転移の振る舞いを再現している事が分かった。

謝辞

中野正志博士には、放射光での X 線使用に関してご指導頂きました。ここに深く感謝致します。

参考文献

[1] Y. Mizuguchi, F. Tomioka, S. Tsuda, T. Yamaguchi, and Y. Takano, Appl. Phys. Lett. 93 (2008) 152505.
[2] Y. Mizuguchi, F. Tomioka, S. Tuda, T. Yamaguchi, and Y. Takano, J. Phys. Soc. Jpn. **78** (2009) 074712.

* tomita@phys.chs.nihon-u.ac.jp

NE5/2010G668

Ag ドープした Mg_2Si 熱電材料の高温高圧 X 線回折
High-temperature and high-pressure X-ray diffraction study of Ag-doped Mg_2Si thermoelectric material

森嘉久 [1*]
[1]岡山理科大学理学部，〒700-0005　岡山市北区理大町 1-1

1 はじめに

現在，環境問題の解決策の一つとして排熱エネルギーの積極利用が求められており，その熱電材料の研究が盛んに行われている．熱電材料はその利用する温度により材料が異なり，低温領域の Bi-Te 系（～500 K）や中高温領域の Pb-Te 系（～800 K）などが実用素子として使用されているが，これらを構成する元素は，人体に有害化が危惧される元素や稀少元素で構成されている材料が多い．そこで，人体に無害で埋蔵量が豊富な次世代用高効率熱電変換材料の開発が進められており，Si と Mg を主成分とした Mg_2Si 熱電変換材料の研究が積極的に進められている．この Mg_2Si は，中温領域の 650 K 付近にピークを持つN型半導体の熱電材料である．近年この材料を用いてモジュールが作成されるなど活発に開発が進んでいるが，高性能の熱電変換モジュールを製作するには，一対のP型半導体とN型半導体の材料が必要で，P型化への課題が残っている．その課題克服のため 2 価の Mg を 1 価の Ag と置換することによるP型化の研究がおこなわれている．そこで本研究課題では，高温高圧状態で Mg_2Si における Ag 置換の可能性を明らかにするために，高温高圧 XRD 実験を行った．

2 実験

高温高圧 XRD 実験は NE5C ビームラインの MAX80 装置を使用した．試料は試薬の Mg_2Si（純度 2N5）粉末と Ag 粉末，Si 粉末を用い，$(Mg_{0.95}Ag_{0.05})_2Si$ になるよう Ag や Si の量を仕込んだ試料を準備した．その試料を内径 2.5 mmφの BN カプセルに封入し，熱電対を挟んで対称位置には NaCl と MgO の混合粉末を同様の BN カプセルに封入し圧力の評価を行った．

実験は，常温常圧の状態からまず圧力を 1 GPa まで昇圧し，温度を徐々に上げながら 973 K まで昇温した後，常温常圧に戻すプロセスで，随時X線回折実験を行った．

3 結果および考察

XRD の結果を Figure に示す．常温常圧の状態(Figure (a))では，出発試料の Mg_2Si(*), Ag, Si と Mg_2Si の不純物として混入されていた Mg の回折線がある．1 GPa まで加圧の後(Figure (b))，温度を上昇していくと(Figure (c)-(f))，773 K辺りで Ag と Mg の回折線が消失し，それに代わって AgMg が合成されることが分かった．この温度は Mg の融点(923K)や Ag の融点(1235K)よりも低く，固体状態での反応もしくは圧力誘起による固液反応と考えられる．この反応は不純物の Mg と置換目的で仕込んだ Ag が反応したのみとも考えられるが，その後の温度上昇により Si の回折線強度が減少することや MgO の回折線が得られること，出発試料の Mg_2Si と回収試料の格子定数を比較すると，わずかながら格子定数が増加しているなどを考慮すれば，一部で Mg と Ag の置換が行われ，$(Mg_{1-x}Ag_x)_2Si$ が合成されている可能性がある．また 973K まで昇温すると，50keV 辺りのバックグランドが上昇し，Mg などが液体状態になることが分かった．

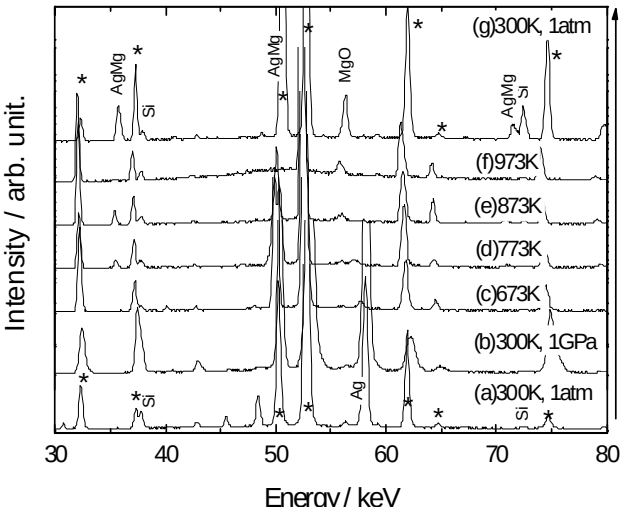

Figure X-ray diffraction profiles of Ag-doped Mg_2Si up to 973K at 1GPa. Starting material includes Mg_2Si, Si, Ag and Mg. The diffraction lines of Mg_2Si are denoted by asterisk (*).

4 まとめ

高圧 XRD 実験により，Mg_2Si に Ag を仕込んだ試料を 1GPa の高圧状態にすれば，773K で反応が進み，一部 Ag 置換された Mg_2Si 熱電材料が合成される可能性が示唆された．

* mori@das.ous.ac.jp

NE5C, 18C/2010P102, 2011G681

High-pressure synthesis and phase transformation of $LiNbO_3$-type oxides

Kie TANAKA[1], Yoshiyuki INAGUMA[1]*, Daisuke MORI[1], Akihisa AIMI[1], Hiroshi KOJITANI[1], Masaki AKAOGI[1], Tetsuhiro KATSUMATA[2], Hiroyuki SAITOH[3], Satoshi NAKANO[4], Takumi KIKEGAWA[5]

[1]Gakushuin Univ., Mejiro, Toshima-ku, Tokyo 171-8588, Japan
[2]Tokai Univ., Kitakaname, Hiratsuka, Kanagawa, 259-01292, Japan
[3]Japan Atomic Energy Agency (JAEA), 1-1-1 Kouto, Sayo-cho, Sayo-gun, Hyogo, 679-5148, Japan
[4]National Institute for Materials Science, Namiki, Tsukuba, Ibaraki 305-0044, Japan
[5]KEK-PF, Tsukuba, Ibaraki 305-0801, Japan

1 Introduction

$LiNbO_3$ (LN)-type structure have a common framework with perovskite (Pv)-type ones in terms of MO_6 (M : metal) octahedra linking all vertices, but a small number of LN-type oxides have been reported compared to Pv-type oxides. On the other hand, in the field of earth science, LN-type phase is considered as unquenchable high pressure Pv-type phase, and several LN-phases have been reported as meta-stable quenched phases [1, 2]. It is anticipated that novel functional LN-type oxides will be synthesized under high-pressure the same as perovskite-type oxides. Recently we have synthesized novel LN-type oxides such as a polar $ZnSnO_3$ [3], a magnetic semiconductor $PbNiO_3$ [4] in addition to known LN-type $MnMO_3$ (M = Ti, Sn) showing the dielectric-magnetic coupling [5] by a solid-state reaction under high-pressure at elevated temperature and investigated their structure, and physical properties. Among them, it has been reported that Pv-type $PbNiO_3$ synthesised under high-pressure keeps its structure under ambient pressure and the Pv-phase transforms into the LN-phase by a heat treatment under ambient pressure [3, 4]. However, details of mechanism of phase transformation have not been clarified.

We have performed synchrotron X-ray diffraction (XRD) measurements to observe the behaviour of LN-type $PbNiO_3$ under high pressure at room and/or high temperature. It was found that LN-type $PbNiO_3$ transforms into Pv-type $PbNiO_3$ under about 8 GPa at room temperature [6]. In this report, the variation of lattice parameters as a function of pressure for LN-type $PbNiO_3$ is primarily presented.

2 Experimental procedure

Pv-type $PbNiO_3$ were synthesized at high-pressure and high-temperature using a cubic-anvil-type apparatus NAMO2001 at Gakushuin University. LN-type $PbNiO_3$ was prepared by a heat treatment of Pv-type $PbNiO_3$. *In-situ* powder XRD experiments of LN-type $PbNiO_3$ under high-pressure at room temperature were performed with a diamond-anvil cell (DAC) and imaging plate at BL18C (PF). MeOH – EtOH mixed liquid was used as a pressure-transmitting medium. The reaction at high-pressure and high-temperature was monitored by an *in-situ* energy dispersive XRD experiment using a multianvil-type high pressure apparatus MAX80 installed in BL NE5C (PF-AR).

3 Results and Discussion

Figure 1 shows the variation of the relative lattice parameters for a and c for LN-type $PbNiO_3$ with a pressure at room temperature. As shown in Fig. 1, both of the lattice parameters decrease linearly with a pressure. In addition, the larger variation in c parameter than that of a parameter was observed. The anisotropic variation is probably attributed to the displacement of Pb ions along c-axis with a pressure.

The analysis of *in-situ* XRD results at high-pressure and high-temperature on the formation of LN-type $ZnSnO_3$ is now in progress, which will be reported in the near future.

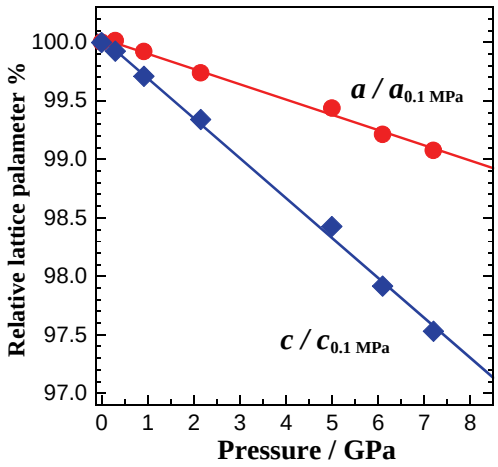

Fig. 1 Variation of relative lattice parameters of a and c versus a pressure for $PbNiO_3$ at room temperature.

References

[1] K. Leinenweber et al., Phys. Chem. Miner. **18**, 244 (1991).
[2] A. Navrotsky, Chem. Mater. **10**, 2787 (1998).
[3] Y. Inaguma et al., J. Am Chem. Soc. **130**, 6704 (2008).
[4] Y. Inaguma et al., J Am. Chem. Soc. **133**, 16920 (2011).
[5] A. Aimi et al., Inorg. Chem., **50**, 6392 (2011).
[6] K. Tanaka et al., PF Activity Report 2010 #28, Part B p. 240.

*yoshiyuki.inaguma@gakushuin.ac.jp

5C, 7A/2011-G065

圧力下における無水、含水 $KAlSi_3O_8$ 融体の構造
Structure of hydrous and anhydrous $KAlSi_3O_8$ melts under pressures

山田 明寛 [1*], 井上徹 [1], 亀卦川卓美 [2]
[1] 愛媛大学地球深部ダイナミクス研究センター、〒790-8577 松山市文京町 2-5
[2] 高エネルギー加速器研究機構 物質構造科学研究所　〒305-0801 つくば市大穂 1-1

1. はじめに

長石に分類される鉱物(例えば、曹長石 $NaAlSi_3O_8$, カリ長石 $KAlSi_3O_8$, 灰長石 $CaAl_2Si_2O_8$)は地球表層に存在する岩石に普遍的に見られる鉱物である。それらは地殻を起源として、地球のプレートテクトニクスを通して地球内部にもたらされ、少なくとも地球内部の浅い部分では主要な構成鉱物として存在していると予想されている。一方、地球浅部には多くの含水鉱物及び間隙水の存在が示唆されており、鉱物の脱水等による鉱物-水の反応によるいわゆる脱水融解は、地球内部でのマグマ発生において、主要なモデルの一つとして考えられている。鉱物の脱水融解によって生じたマグマには少なからず水成分が含まれている事が予想され、水を含むマグマの構造を圧力下の「その場」で調べる事は、実際に地球内部で生成されているマグマの特性を知る上で重要な知見が得るために必要不可欠である。特にマグマ中の Al^{3+}は、複雑な編目構造を形成するネットワーク形成イオンに分類され、その圧力によって引き起こされる配位数変化や Al-O-Al 結合角変化などの構造変化はマグマ全体での物性(密度、粘性)を支配しうる情報と考えられる。

我々は、上述の長石について、まず、含水曹長石組成マグマの構造について、高温高圧 X 線回折実験を用いて調べてきた。その結果、およそ 3 GPa 付近において水を含むマグマにおいてのみ、Al^{3+}の著しく配位数変化が促進されることを明らかにした。そこで、本研究では、更に同様の長石系である $KAlSi_3O_8$ 組成のマグマについて、同様に Al^{3+}の構造変化が見られるか調べるため、実験を行っている。本レポートでは、現在までに得られた構造データ(構造因子)、およびそれから得られる情報について報告する。

2. 実験手法

実験試料は、無水のもので K_2CO_3、Al_2O_3、SiO_2 をモル比で 1:1:6 となるよう混合した酸化物粉末を 1000℃、9 時間で脱 CO_2 処理したものを用いた。また、含水の試料では、あらかじめ K_2O-SiO_2 ガラスを合成し、$Al(OH)_3$ を $KAlSi_3O_8$-H_2O 組成となるよう混合したものを用いた。高温高圧 X 線構造解析は PF-AR の NE5C ビームラインで行った。高圧発生装置は当ビームライン設置の MAX80、DIA 型プレスを使用し、加圧方式は 6-6 型加圧方式[1]を採用した。第一段アンビルは 27 mm を用いて、実際に試料を圧縮する第二段アンビルには背面面積 18×18 mm^2 のアンビルで、先端(Truncated Edge Length; TEL)は 4-6 mm をターゲット実験条件により使い分けた。試料、ヒーターを設置したボロンエポキシ製圧力伝達媒体のサイズは TEL に応じて 7-9 mm のものを用意した。ヒーターは円筒形グラファイト、試料容器は無水試料ではグラファイト、含水試料では白金と単結晶ダイヤモンド管の複合容器[2]を使用した。液体の回折測定は、回折線より判断した融点よりおよそ 50℃上で行った。使用した X 線は白色(20-140 keV)で、幅広い波数領域での回折データを得るため、回折角 3-30° の範囲で測定を行い、それぞれの回折パターンの強度を規格化し、構造因子、S(Q)を求めた。

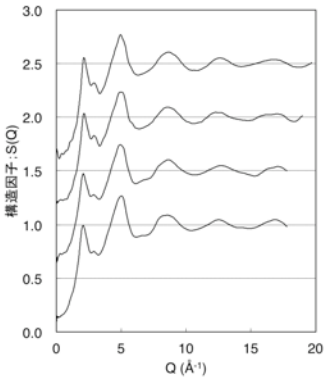

図 1　含水 $KAlSi_3O_8$ メルトの構造因子(下から 2.5, 3.2, 4.4, 5.1 GPa のデータ)

3. 実験結果

図 1 に含水 KAlSi3O8 メルトの構造因子を示す。回折角最大 30° までの測定を行う事によって、最高 20 $Å^{-1}$ までのデータ収集に成功した。珪酸塩などのネットワーク形成液体の大きな特徴として、約 1-2 $Å^{-1}$ に他ピークに比べ比較的鋭いピークが見られる (First Sharp Diffraction Peak; FSDP)。このピーク位置から、液体の中距離構造の周期を見積もる事ができる。この FSDP の位置を無水のそれと比較した結果、含水のものは、特に低圧領域において高 Q 側に位置していた。Q は実空間の距離の逆数なので、高い Q は実空間にしてより短い距離を意味している。つまり、水を含むメルトはより短い周期構造を持つ事を示唆している。これは以前の研究によって示唆されていた通り、水の効果によって…-Si-O-Si-…や…-Al-O-Al-…などのネットワーク構造が分断され手いる事を意味している。

4. 謝辞

本研究は高エネルギー加速器研究機構の補助に加え、基盤研究 A(代表:井上徹)、若手研究 B(代表: 山田明寛)および、新学術領域「中性子地球科学」(代表: 八木健彦)によるサポートのもと行われています。

* a-yamada@sci.ehime-u.ac.jp

1A/2012S1-001

高温高圧下における新規シリサイドの探索
New Silicide Search at High Pressures and High Temperatures

今井　基晴 [1*]
[1](独)物質・材料研究機構、〒305-0047 茨城県つくば市千現 1-2-1

1 はじめに

近年、欧州ではローズ（RoHS）指令により Pb、Hg、Cd 等の毒性の強い元素の使用は制限されていることから、資源埋蔵量が多く、毒性の少ない低環境負荷型の元素から構成される物質が次世代の材料として注目されている。地殻中の元素存在度を大きい順に 10 元素表すと、Si、Al、Fe、Ca、Mg、Na、K、Ti、Mn、Mo となる。そこで、資源・環境の視点から新たな機能材料として、地殻存在度第 1 位である Si の化合物シリサイドが注目されている[1]。現在では Mg_2Si、β-$FeSi_2$、Si クラスレートが熱電材料として、$BaSi_2$、 Si クラスレートが太陽電池材料として注目されている。この様な状況を鑑みると、新シリサイドを発見しその物性を明らかにすることは新機能材料探索として意義深い。今まで高温・高圧下において、大気圧下での安定相とは異なる結晶構造を持つシリサイドが合成されてきた。例えば、$BaSi_2$ では、室温・大気圧で安定である $BaSi_2$ 相 $BaSi_2$ から $EuGe_2$ 相 $BaSi_2$、$SrSi_2$ 相 $BaSi_2$ が高温・高圧下で合成される。出発物質である $BaSi_2$ 相 $BaSi_2$ はエネルギーギャップ約 1.1eV を持つ半導体であるが、高温・高圧合成された $SrSi_2$ 相 $BaSi_2$ はナローギャップ半導体であり、$EuGe_2$ 相 $BaSi_2$ は超伝導を示す金属である。この様に高温・高圧下で合成された物質は出発物質とは異なる物性を示す。

我々は、高温・高圧環境を利用して Mg-Si 系新化合物の探索を行っている。Mg は地殻存在度第 5 位である。大気圧下で報告されているバルクとして存在している Mg-Si 系化合物は、Mg_2Si のみである。先に述べたように、Mg_2Si は熱電材料として注目されている。本研究では高温・高圧下において Mg_2Si がどのような振る舞いを示すか、X 線回折法によって調べる。

2 実験

高温高圧下でのその場観察は、高エネルギー加速器研究機構 PF-ARNE5C ビームラインでマルチアンビル型高圧発生装置 MAX80 を用いて行った。X 線回折はエネルギー分散法で行った。試料は BN カプセルに充填した。温度はアルメルークロメル熱電対を用いて、圧力は NaCl の格子定数から見積もった。室温で約 5.0GPa まで加圧した後、加熱・冷却を行い、この過程で X 線回折によるその場観察を行った。

3 結果

図 1 に Si リッチ Mg_2Si の約 5GPa の加熱過程での X 線回折パターンを示す。室温・5GPa では Mg_2Si の相転移は観測されなかった。5GPa で加熱をしていくと新しい相からの回折パターンが 770K から観測された。この相転移は 970K で完了した。この高温・高圧相は 1370K で直接熔融した。高温・高圧相の結晶構造について現在検討中である。

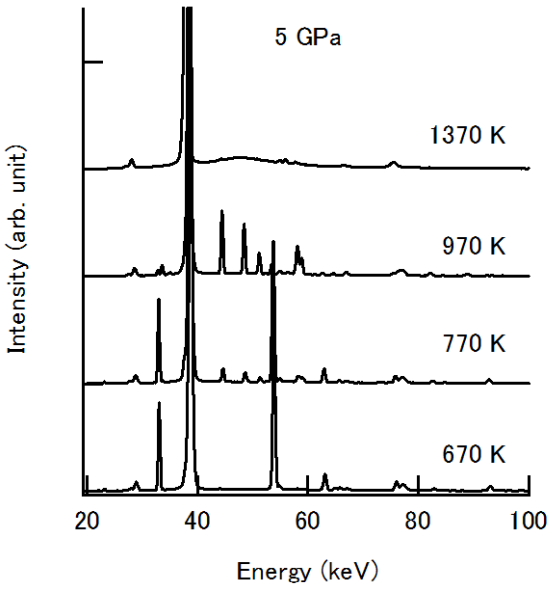

図 1 ：5GPa での Si リッチ Mg_2Si の回折パターン

参考文献
[1] 今井基晴、環境エネルギー材料ハンドブック、8.2 節（オーム社、2011）
[2] M. Imai, T. Kikegawa, Chem. Mat. **15** (2003) 2543.
[3] M. Imai, T. Hirano: J. Alloys Compds **224** (1995)111.
[4] M. Imai, K. Hirata, T. Hirano: Physica C **245** (1995) 12.

* IMAI.Motoharu@nims.go.jp

NE5C /2011G100

PVT data collection for EoS analyses of antigorite and phase A under high pressure and high temperature

Toru INOUE *[1], Cuiping YANG[1], Hideki SUENAMI[1], Akihiro YAMADA [1], , Kohei HAYASHI[1], Takumi KIKEGAWA[2]
[1]Geodynamics Research Center, Matsuyama, Ehime 790-8577, Japan
[2]High Energy Accelerator Research Organization, Tsukuba, Ibaraki 305-0801, Japan

Introduction

Serpentine is an important hydrous phase in the hydrous peridotite layer of the descending slab, and one of the high pressure polymorph of serpentine, antigorite, should be the most important hydrous phase to discuss the transportation of water into the Earth's interior. In addition, antigorite dehydrates to form forsterite (Fo) - enstatite (En) - H_2O below ~6 GPa at around ~600℃, while above ~ 6 GPa, phase A is formed as a dehydration product of antigorite. Thus phase A is a hydrous phase in the upper mantle condition, and should be an important hydrous phases to further transport water into the Earth's deep mantle [1]. The density is an important physical parameter, but the equations of state (EoS) of antigorite and phase A have not been adequately clarified yet under high pressure and high temperature conditions.

We are trying to determine the EoS of antigorite and phase A precisely to clarify the density of hydrous subducted slab under high pressure temperature. In 2011, we could have only one term beam time, because we could not conduct experiment in the period of more than first half of the year.

Experimental

Natural antigorite was used as a starting material, and phase A was synthesized in advance by the mixture of MgO, $Mg(OH)_2$ and SiO_2 in the adequate proportion using the multi-anvil apparatus in Ehime University. We tried to use h-BN and NaCl sleeves to release the deviatric stress. Temperature was measured by W-Re thermocouple, and pressure was calculated by equation of state of NaCl proposed by [2]. Experiments were conducted up to ~10 GPa in the truncated edge length of 4 mm on WC anvil. The diffraction data of sample and pressure standard were collected alternatively for 150 seconds each at intervals of 100℃ with decreasing temperature to release the deviatric stress.

Results and discussion

The data collected P-T conditions of antigorite and phase A were shown in Fig. 1 and Fig.2, respectively. The derived P-V-T data show slightly strange but interesting phenomena, so we are trying to continue further analysis. In the next annual report, we will report the further detailed result of EoS of antigorite and phase A.

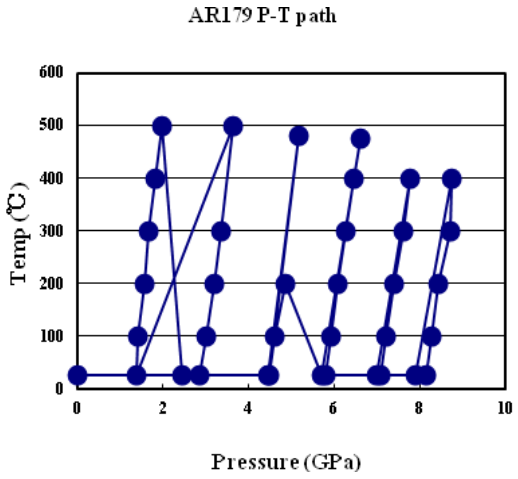

Fig.1 The data collected P-T condition of antigorite using NaCl sleeve.

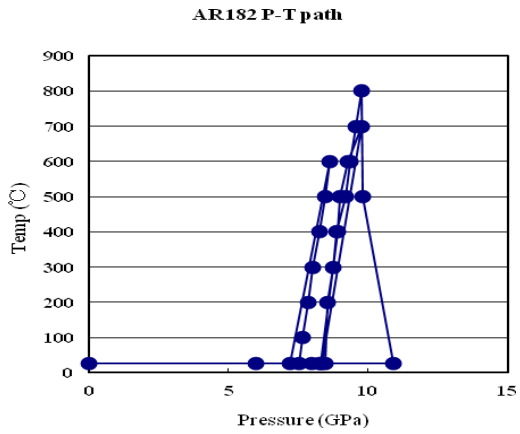

Fig.2 The data collected P-T condition of phase A using NaCl sleeve.

References

[1] T. Inoue et al., J. Mineral. Petrol. Sci. **104**, 105 (2009)
[2] D.L. Decker, J. Appl. Phys., **42**, 3239 (1971)
* inoue@sci.ehime-u.ac.jp

NE5C/2011G139, 18C/2011G095

High-temperature and high-pressure phase diagram of $RhSb_3$

Kazuki MATSUI, Hirotaka KATOU, Masatoshi KANAZAWA, Junichi HAYASHI,
Keiki TAKEDA, Chihiro SEKINE
Muroran Institute of Technology, Muroran, Hokkaido 050-8585, Japan

Introduction

The skutterudite compounds have been actively studied as potentially useful thermoelectric materials. The compounds have also attracted many researchers' interest as strongly correlated electron systems. The binary unfilled skutterudite compounds with a body centered cubic (space group *Im*3) have a general formula TX_3 or T_4X_{12} (T=Co, Rh and Ir, X=P, As and Sb, site 24*g*), where the symbol represents a vacancy (site 2*a*). While earlier studies have indicated that the unfilled skutterudite compounds are quite stable under high pressure, a pressure induced structural change at room temperature of unfilled skutterudite compounds has been reported recently [1-3]. These behaviors could be interpreted as a pressure-induced self-insertion reaction, in which antimony atoms from the compound framework partially fill the voids (site 2*a*) at room temperature. Furthermore, similar behaviors have also been reported under high temperature and high pressure [1, 4]. In this study, we have tried to observe structural changes of the unfilled skutterudite compound $RhSb_3$ in-situ at high temperature and high pressure.

Experimental

In-situ x-ray diffraction patterns were taken by an energy-dispersive method using the synchrotron radiation. High pressure was applied using a 6-6 compression system and the multi-anvil high-pressure apparatus (MAX80) installed at the beam line AR NE5C. We used Tr. 27mm WC anvil for first stage anvil and Tr. 4mm WC anvil for second stage anvil. The boron epoxy was used for pressure medium. Pressure was determined by the lattice constant of NaCl internal pressure marker. High quality polycrystalline samples of $RhSb_3$, used as stating materials, were synthesized at 2GPa and 550°C, using a cubic-anvil high-pressure apparatus.

Results and discussion

Figure 1 shows x-ray diffraction patterns of $RhSb_3$ at 6GPa and room temperature (a) and 640°C (b). The peaks of $RhSb_3$ appear doubled (indicated by arrows) and displaced toward lower energy at 640°C. This suggests that the self-insertion reaction occurs. Peaks for an impurity phase ($RhSb_2$) also observed between 67 and 75keV, indicated by cross symbol at 640°C. The temperature dependence of peak positions of $RhSb_3$ show a significant shift toward lower energy around 500°C at 6GPa. Similar behavior was also observed around 400°C under 8GPa [4]. From these results, the high-temperature and high-pressure phase diagram of unfilled skutterudite $RhSb_3$ was obtained as shown in Figure 2.

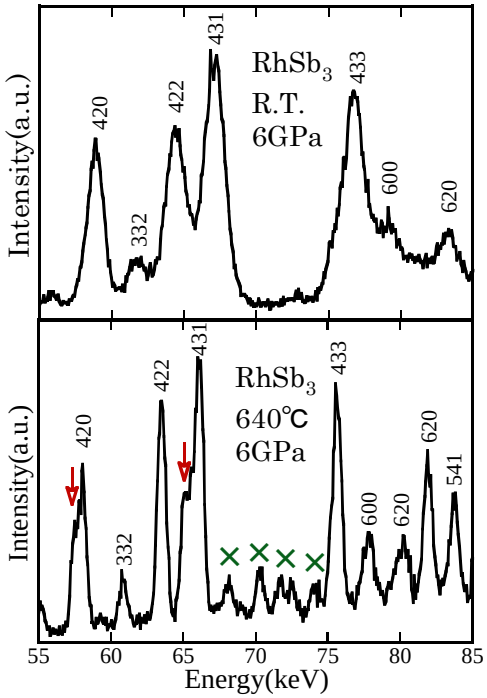

Fig.1. X-ray diffraction patterns of $RhSb_3$ at 6GPa and room temperature (a) and 640°C.

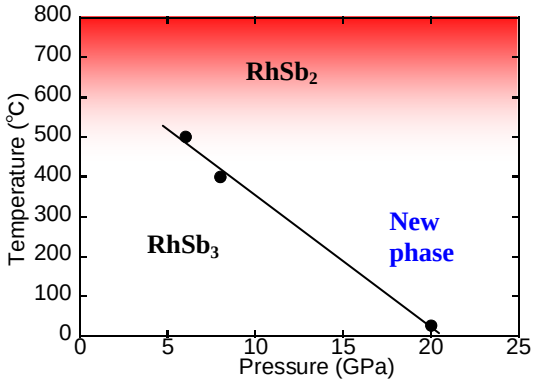

Fig. 2. High-temperature and high-pressure phase diagram of $RhSb_3$

Reference

[1] A. C. Kraemer *et al.*, Phys. Rev. B, **75** (2007) 024105.
[2] K. Matsui *et al.*, PF activity report (2009) 196.

[3] K. Matsui *et al*., PF activity report (2010) 224.
[4] C. Sekine *et al*., PF activity report (2010) 222.
*s1724073@mmm.muroran-it.ac.jp

18C/2011G244

放射光 X 線回折法による高圧下リン酸亜鉛系極圧添加剤の構造解析
Structural Analysis of Zinc Orthophosphate under High Pressure by Synchrotron X-Ray Diffraction

平山朋子 [1*], 細野優人 [2], 竹原弘耕 [2], 松岡 敬 [1]
[1] 同志社大学 理工学部 〒610-0394 京田辺市多々羅都谷 1-3
[2] 同志社大学大学院 理工学研究科 〒610-0394 京田辺市多々羅都谷 1-3

1 はじめに

エンジンの高性能化，運転条件の過酷化，あるいは排出ガス対策装置の装着などに伴い，エンジン油に対する摩耗防止性，酸化防止性，腐食防止性といった要求は年々厳しくなってきている．それらの要求に応えるため，エンジン油には様々な添加剤が使用される．特に，ジチオリン酸亜鉛（ZDDP）は今まで発明された中でほぼ間違いなく最も良好な添加剤である．60 年以上前に導入されてから使い続けられ，今もなおほとんどのエンジン油に使用されている．

ZDDP は極圧添加剤に分類され，非常に優良な耐摩耗特性を持っているが環境汚染を引き起こす．環境に優しい添加剤の構築には耐摩耗特性をもたらす基本的メカニズムの把握が必要である．ZDDP は高圧を発生する二面間の摩擦を通して分解し，ポリリン酸亜鉛を含むトライボフィルムと呼ばれる耐摩耗膜を形成する．ZDDP の耐摩耗特性はこのトライボフィルムに起因するとされているが，トライボフィルム形成の化学的メカニズムは明らかになっていない．近年，Mosey らは分子動力学シミュレーションにより，リン酸亜鉛に静水圧をかけたとき，圧力増加とともに短鎖のリン酸亜鉛が徐々に繋がって長鎖のポリリン酸亜鉛となることを示した．また，Dassenoy らはラマン分光法を用いてリン酸亜鉛鎖の長さに関する考察を行った．

このような研究の高まりから，リン酸亜鉛の圧力に対する影響を明らかにすることが求められている．そこで本研究では，ラマン分光法および X 線回折法を用いて，短鎖であるオルトリン酸亜鉛（$Zn_3(PO_4)_2$）の高圧下における分子挙動を把握することを目的とする．

2 試料

本研究では，ジョンソン・マッセイの Alfa Aesar 社製のオルトリン酸亜鉛 $Zn_3(PO_4)_2$（Zinc phosphate（ortho），Puratronic®，99.995%（metal basis））および和光純薬工業株式会社製のピロリン酸亜鉛 $Zn_2P_2O_7$（二リン酸亜鉛）（Zinc Pyrophosphate（Zinc Diphosphate））を使用した．

3 実験方法

本実験は，KEK 内の PF のビームライン BL18C に設置されている超高圧粉末回折計（角度分散型，高圧相の結晶構造および高圧相転移の探査などに用いられている）に DAC を設置し行った．本装置の光学系を図 5 に示す．モノクロメータにより波長が一定となった X 線がコリメータを通過し平行光線となり，試料に入射し回折が起こる．その回折 X 線の回折角，回折強度の検出にはイメージング・プレートを用いた．本実験では，波長 λ=0.6174 Å の X 線を用いた．コリメータ直径は 40 μm とした．

4 実験結果

実験で得られた回折プロファイルを図 1 に示す．これより，①オルトリン酸亜鉛は圧力増加とともに非晶質化が進行する，②オルトリン酸亜鉛は圧力増加と圧力減少のサイクルにおいて不可逆の構造変化をする．また，最大圧力が高い方が，初期構造を回復しにくい，③オルトリン酸亜鉛は圧力増加とともに原子間距離が縮まる，④オルトリン酸亜鉛が重合するためには摩擦が必要である，⑤オルトリン酸亜鉛は 7.25 GPa と 10.58 GPa の間で相変態する，等の結論が得られた．

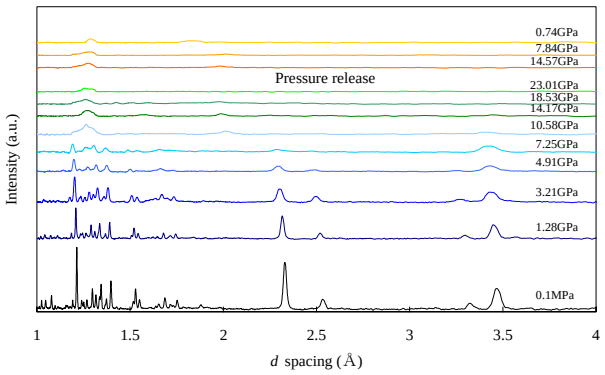

図 1 ：高圧下オルトリン酸亜鉛の回折プロファイル

謝辞

実験の実施に際して，様々なアドバイスおよびサポートを頂いた高エネルギー加速器研究機構 亀卦川卓美先生に心よりの謝意を表す．

* thirayam@mail.doshisha.ac.jp

NE-5C/2011G245

放射光 X 線回折法による高圧・高温環境下 DLC 被膜の構造解析
Structural Analysis of Diamond-Like Carbon under High Pressure and High Temperature by Synchrotron X-Ray Diffraction

平山朋子 [1*], 江口友梨 [2], 山下健志 [2], 松岡 敬 [1]
[1] 同志社大学 理工学部 〒610-0394 京田辺市多々羅都谷 1-3
[2] 同志社大学大学院 理工学研究科 〒610-0394 京田辺市多々羅都谷 1-3

1 はじめに

DLC（Diamond-like Carbon）は，sp^2 結合で構成されるダイヤモンド構造や sp^3 結合で構成されるグラファイト構造の 2 種類の炭素結合からなる準安定な硬質アモルファス炭素である．一般的に，DLC は sp^2 結合や sp^3 結合，水素原子の比率でその性質が変化するが，硬度，摩擦特性および表面平滑性などの優れたトライボロジー特性を示すことから，エンジン摺動部，切削工具，金型，軸受，磁気記録媒体などの幅広い工業分野で応用がなされている．

しかし，トライボロジー環境下で使用される DLC 膜は，摺動面において生じる繰り返しの摩擦や摺動時に作用する負荷により摺動面全体が高温，高圧にさらされる．それ故に，トライボロジー環境下での DLC 膜の構造は温度，圧力により変化し，それに伴い摩擦特性も変化すると予測される．そのため，高温，高圧下 DLC 膜の構造変化は重要であり，その DLC 膜の構造変化を定量評価することは高温，高圧下で使用される DLC 膜の設計の指針を与え，また，低摩擦の基礎的構造を明確にする一助となると考えられる．現在のところ，温度変化による DLC 膜の構造変化は研究報告されているが，圧力変化による DLC 膜の構造変化を実際に測定した報告は見当たらない．そこで本研究では，放射光 X 線回折法を用いて，高温，高圧下 DLC 膜の構造解析を行うこととした．

2 試料および実験系

本研究では，高エネルギー加速器研究所機構（KEK）内の Photon Factory Advanced Ring（PF-AR）ビームライン NE5C に設置されている一段圧縮加圧方式のキュービックアンビル型高温高圧発生装置 MAX80 を用いた．本実験では，サンプルセルの寸法を 16×16×16 mm^3，アンビル先端サイズを 12×12 mm^2 とした．DLC はテフロン容器内に封入し，圧力媒体には非晶質ボロンをエポキシ樹脂で固めたものを用いた．また，圧力マーカーには NaCl プレートを用いた．スリット系に関しては，上流側は 0.1×0.5 mm^2，コリメータ径は 0.3 mm，下流側は 0.1×0.2~2.0 mm^2（X 線強度に応じて変更）とし，加熱なし試料および加熱あり試料の 2 種類を対象として，室温環境下で分析を行った．

3 実験結果

各回折角度において，DLC 膜の散乱 X 線プロファイルはブロードなピークとなった．これは DLC 膜のようなアモルファス構造に見られる典型的な散乱プロファイルである．また，圧力が増加するにつれて X 線散乱強度のピーク位置が高エネルギー側にシフトすることが確認できた．これは圧力によって原子間距離が徐々に縮まっているためであると考えられる．得られた回折プロファイルより，二体分布関数を算出した．その結果，r=1.46Å と r=2.50Å 付近に大きなピークが，また，r=3.22Å と r=3.70Å 付近に小さなピークが現れた．r=1.46Å 付近のピークは原子間の結合距離である sp^3 結合の r=1.54Å と sp^2 結合の r=1.42Å を反映し，r=2.50Å は sp^2 結合の 6 員環構造の 2 近傍距離である r=2.46Å を反映していると推察できる．圧力の増加に伴うこのピーク高さの変化を図 1 に示す．これより，圧力が増加するにつれて，DLC が徐々に sp^3 化することが分かった．

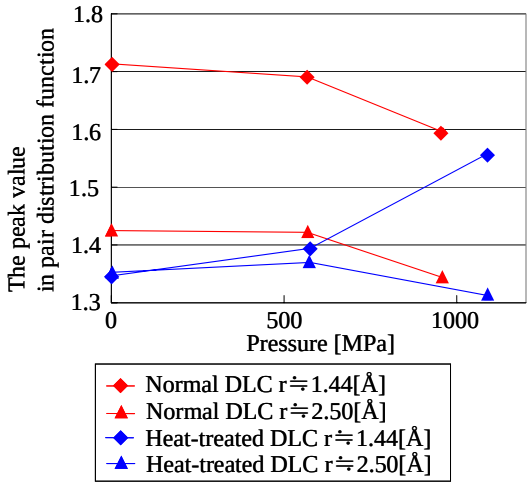

図 1 ：圧力変化に伴う DLC の二体分布関数におけるピーク高さの変化

謝辞

実験の実施に際して，様々なアドバイスおよびサポートを頂いた高エネルギー加速器研究機構 亀卦川卓美先生に心よりの謝意を表す．

* thirayam@mail.doshisha.ac.jp

NE1/2011G580

高温高圧下での窒化炭素の合成と相図研究
Synthesis and phase-boundary of a new carbon-nitride-related material

寒川匡哉*, 財部健一
岡山理科大学

1 はじめに

高密度低圧縮性窒化炭素の合成探索を試みている。高密度低圧縮性窒化炭素は Liu と Cohen により理論予測され、ポストダイヤモンド低圧縮性材料として関心が持たれている。今回、大気圧窒素プラズマ法により合成した $C_3N_4H_xO_y$ ナノ粒子を出発物質としてレーザー加熱ダイヤモンドアンビルセル（LHDAC）による高温高圧実験を行った結果、圧力 40 GPa、温度 1200-2000 K の条件で、世界で初めて新規窒化炭素化合物 $C_2N_2(CH_2)$が再現性よく合成できることを見出した。また、内部座標を含めた結晶構造[1,2]と圧縮率が決定できた。

$C_2N_2(CH_2)$は、斜方晶系で空間群 *Cmc*2_1、格子定数 *a*=7.625 Å, *b*=4.490 Å, *c*=4.047 である。C を中心とした 4 面体 C（N_3C）（3 本の C-N の単結合と 1 本の C-C 単結合）を構成単位としており、この 4 面体が頂点共有し 3 次元的構造を作っている。この 4 面体の C-N 結合距離は 1.444~1.503 Å で、β-C_3N_4 の C-N 結合距離 1.447~1.456 Å に近く、更に C-C 結合距離 1.480 Å はダイヤモンドの 1.540 Å より短い。頂点共有されている C は、4 本の結合の内 2 本が 4 面体を構成し、残りの 2 本は H と結合し終端している。$C_2N_2(CH_2)$の体積弾性率は B_0 = 258 ± 3.4 GPa であり、ダイヤモンドの体積弾性率の 60 %程度に留まることが分かった。その理由は、β-C_3N_4 やダイヤモンドには無い 4 面体 C（N_3C）の回転自由度があることに由来することを明らかにした。

本レポートでは、温度圧力条件を変化させた LHDAC 実験により合成した試料の XRD 測定を行い、$C_2N_2(CH_2)$の生成条件の検討を行った結果について纏める。

2 実験方法

LHDAC 実験の合成条件は 40 GPa,~3000 K 以下である。ガスケットには Re を使用し、試料室サイズは~150 μm とした。レーザー加熱時間は 15 min.とした。各温度圧力下で LHDAC 実験後に合成試料を回収し、大気圧下において XRD 測定を行った。

3 結果と考察

Fig. 1 に圧力 30 GPa において各種温度条件下で合成した試料の大気圧下での XRD 測定結果を示す。温度 1700-2000 K の条件で熱処理すると、$C_2N_2(CH_2)$が再現性よく合成されることを確認した。Au の回折線（●）は、出発試料 $C_3N_4H_xO_y$ ナノ粒子に混入したレーザー吸収体である。更に、温度>2000 K の条件で熱処理すると、ダイヤモンド（■）が合成されることがわかった。同様の実験を圧力 20 GPa においても実施した。結果、$C_2N_2(CH_2)$の合成は確認されず、温度 1500 K 以上においてダイヤモンドが合成されることが分かった。

以上より、出発試料として $C_3N_4H_xO_y$ を用いると、圧力 30 GPa 以上において $C_2N_2(CH_2)$が初めて合成され、30 GPa 以下では $C_2N_2(CH_2)$は合成されずダイヤモンドが合成されることが明らかとなった。

$C_2N_2(CH_2)$の物性を調べるにはミリオーダーサイズの試料が望ましい。ＬＨＤＡＣ合成では極微小である。そこで、現在はマルチアンビル型高圧発生装置を用いたミリサイズ試料の合成を試みている。

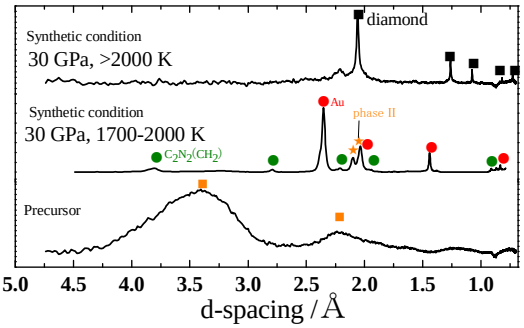

Fig. 1. XRD profiles of the recovered sample outside the DAC after heating at the pressure of 30 GPa and the various temperatures.

Acknowledgement

本研究は東大物性研究所の八木健彦研究室(現愛媛大学)との共同利用研究である。研究に際し、ご指導・ご助言を頂きました八木健彦教授ならびに岡田卓氏に深く感謝の意を表します。

参考文献

[1] M. Sougawa et al., Jpn. J. Appl. Phys. **50**, 095503 (2011).
[2] M. Sougawa et al., J. Phys.: Conf. Ser. **215**, 12137 (2010).

18C/2011G-620

I および VIII 型 Si クラスレートの圧力誘起構造相転移
Pressure Induced Phase Transition of Type I and VIII Si Clathrates

久米徹二[1*], 今枝佑太[1], 中野智志[2], 佐々木重雄[1], 清水宏晏[1], 岸本堅剛[3], 小柳剛[3]
[1]岐阜大工、〒501-1193 岐阜市柳戸 1-1
[2]物質・材料研究機構　〒305-0044 つくば市並木 1-1
[3]山口大院　〒755-8611 宇部市常盤台 2-16-1

1 はじめに

半導体クラスレートの多くは 14 族（一部 13 族に置換）のホスト原子によって形成された多面体ケージで構成される。各ケージはアルカリ、アルカリ土類、またはハロゲン原子をゲスト原子として内包する。I 型、II 型などの代表的なクラスレート構造は、２種類以上のケージにより構成されるが、VIII 型クラスレートの場合、1 種類のケージで構成される。$Sr_8Al_xGa_{16-x}Si_{30}$ は Al と Ga の組成比によって I 型と VIII 型を作り分けることが可能であり、Ga リッチ(5 < x < 7)では I 型構造、Al リッチ(8<x<15)では、VIII 型構造になる。これまでに、I 型については、高圧力下での構造安定性に関する研究が数多く行われてきたが VIII 型に関しては全く行われていない。本研究課題では I および VIII 型のケージの種類による構造安定性の違いを明らかにするとともに、I 型 VIII 型間の相転移の可能性を探ることを目的とし、高圧 XRD 測定を行った[1,2]。

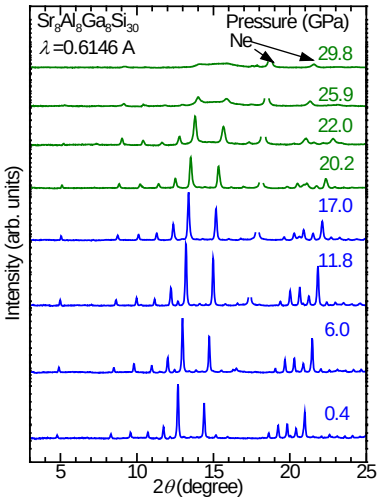

図１：VIII 型クラスレートの高圧 XRD パターン。

2 実験

Si 系クラスレート $Sr_8Al_7Ga_9Si_{30}$（I 型）と $Sr_8Al_8Ga_8Si_{30}$（VIII 型）を試料として使用し、高圧力発生装置としてダイヤモンドアンビルセル（DAC）を用いた。圧力媒体として He または Ne を、粉末状試料とともに DAC の試料室へ封入し、高圧下粉末 XRD 実験を PF-BL18 にて行った。試料の圧力はルビー蛍光法を用いた。

3 結果および考察

図 1 に高圧力下で得られた VIII 型クラスレートの粉末 XRD パターンを示す。圧力約 20 GPa 付近から全体に回折ピークが弱くなり、30 GPa 付近でほぼ消失し非晶質化を示唆する。しかしながら、1 気圧に戻すと、回折線が復活するため、これは可逆的な変化であることが分かった。図 2 は単位胞体積の圧力依存性である。20 GPa 付近で回折パターンに大きな変化がないにもかかわらず、体積が大きく減少していることが分かる。この様な現象は、従来 I 型クラスレートで観測されており、クラスレート化合物に共通する現象であることが分かった。また、ほぼ同じ組成の I 型クラスレートの結果と比べると、相転移圧力が VIII 型の方が高く、安定性に優れていることが初めて明らかになった。

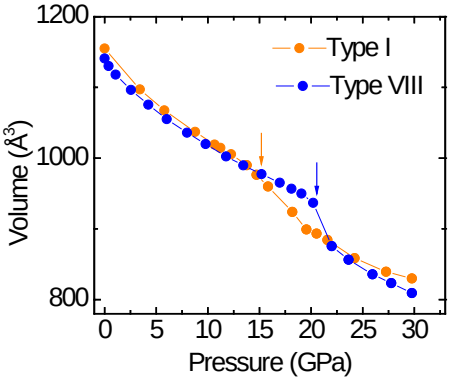

図２：I 型および VIII 型クラスレートの単位胞体積の圧力依存性。

4 まとめ

本課題により、初めて構造 VIII 型クラスレートの構造安定性が詳しく調べられた。I 型に比べ相転移圧力は高く、圧力に対する構造安定性に優れていることが明らかになった。組成がほぼ同一であることを考えると、この違いは構成する多面体ケージの形状に由来するものと理解できる。

参考文献

[1] H. Shimizu, Y. Takeuchi, T. Kume, S. Sasaki, K. Kishimoto, N. Ikeda, T. Koyanagi, J. Alloys Compds. **487** (2009) 47.
[2] Y. Imaeda, T. Kume, S. Sasaki, H. Shimizu, K. Kishimoto, N. Ikeda, T. Koyanagi, J. Phys.: Conf. Ser. (in press).

*kume@gifu-u.ac.jp

AR-NE5C/2011G652

Compressional behavior of hydrous SiO_2 glass

Satoru Urakawa[1,*], Ikumi Yokota[1], Kenji Mibe[2], and Takumi Kikegawa[3]

[1]Department of Earth Sciences, Okayama University, Okayama 700-8530, Japan
[2]Earthquake Research Institute, University of Tokyo, Tokyo 113-0032, Japan
[3]Photon Factory, KEK, Ibaraki 305-0801, Japan

1 Introduction

Water changes the properties of silicate melts such as viscosity, density, and sound velocity, when it is dissolved into melts. It is important to study how water dissolves in silicate melts, and many studies have been performed. Here, we focus our attention on the water-bearing vitreous silica and we have studied the structure of hydrous SiO_2 glass by the X-ray diffraction analysis using synchrotron radiation under pressure.

2 Experiment

Hydrous SiO_2 glass was synthesized using the internally heated gas pressure vessel installed at ISEI, Okayama University. Crystalline SiO_2 enclosed in Pt capsule with 3.6 wt% D_2O had been fused at 200 MPa and 1500 C for 3h, then it was quenched into glass. Unfortunately, part of deuterium was substituted by hydrogen by exchange reaction with the gas in the pressure vessel through Pt capsule. Raman spectroscopy showed the quenched hydrous glass contained Si-OH(D) as well as $H(D)_2O$ molecules.

Compression of hydrous SiO_2 glass was performed using the MAX80 system at AR-NE5C up to about 7 GPa. X-ray diffraction profiles were collected by energy dispersive method.

3 Results and Discussion

Interference function $Qi(Q)$ for hydrous SiO_2 glass at 0.1 MPa is almost the same as that of dry SiO_2 glass, except for the FSDP. The position of the FSDP of hydrous glass is at the higher Q side than that of dry one, indicating shrinkage of the intermediate range order by addition of water.

$Qi(Q)$ of hydrous glass changed gradually with pressure up to 7 GPa at 300 K (Fig. 1). Pressure variations in $Qi(Q)$ is the same as those of dry SiO_2 glass [1]. MD simulations showed that the Si-Si correlation changes with pressure and accounts for the variations of $Qi(Q)$. The radial distribution function $D(r)$ also shows the decrease of Si-Si distance with pressure without any change in Si-O and Si-Si distances. The FSDP of hydrous SiO_2 glass shift toward higher Q with pressure (Fig. 1), as shown in dry one [2]. Thus, in the hydrous SiO_2 glass, the network topology of SiO_4 tetrahedra changes with pressure.

Although hydrous SiO_2 glass takes a similar short range structure to dry one, comprising a SiO_4 tetrahedron, the medium range order of hydrous glass is smaller than dry glass. Unfortunately, we could not find how water works in structure changes of the hydrous SiO_2 glass under pressure. Compressional behavior of hydrous SiO_2 glass agrees with dry glass; the intermediate range order shrinks with increasing pressure.

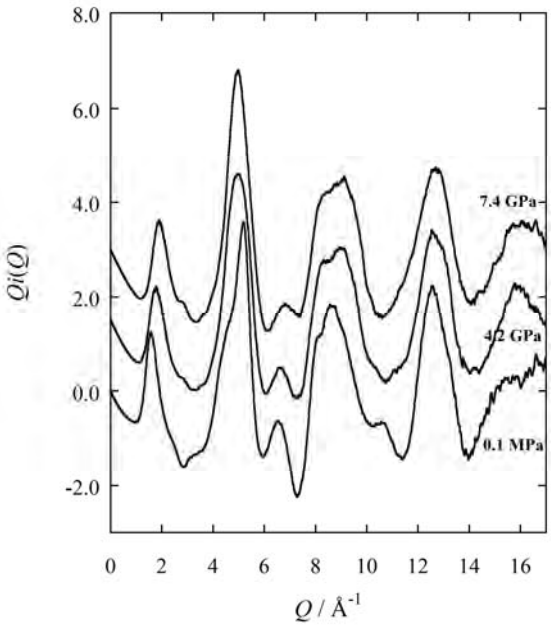

Fig. 1: Variation of interference function $Qi(Q)$ for hydrous SiO_2 glass during compression.

Acknowledgements

We are grateful to Prof. Kanzaki for synthesis of hydrous SiO_2 glass. This study was partly supported by the Earthquake Research Institute cooperative research program.

References

[1] Y. Inamura *et al*., Phys. Rev. Lett. **93** (2004) 015501.
[2] T. Sato and N. Funamori, Phys. Rev. B. **82** (2010) 184102.

* urakawa@cc.okayama-u.ac.jp

6A/2000G139

Contribution of asparagine residues to the stabilization of an antigen-antibody complex, HyHEL-10-hen egg white lysozyme.

Akiko YOKOTA[1], Kouhei TSUMOTO[1], Mitsunori SHIROISHI[1], Takeshi NAKANISHI[1], Hidemasa KONDO[2] and Izumi KUMAGAI*[1]

[1] Department of Biomolecular Engineering, Graduate School of Engineering, Tohoku University, Aoba-yama 6-6-11, Aoba-ku, Sendai 980-8579, Japan

[2] Research Institute of Genome-based Biofactory, National Institute of Advanced Industrial Science and Technology (AIST), 2-17-2-1 Tsukisamu-Higashi, Toyohira-ku, Sapporo 062-8517, Japan

Introduction

Many germ line antibodies have asparagine residues at specific sites to achieve specific antigen recognition. To study the role of asparagine residues in the stabilization of antigen-antibody complexes, we examined the interaction between hen egg white lysozyme (HEL) and anti-HEL antibody HyHEL-10 variable domain fragment (Fv). We introduced Ala and Asp substitutions into the Fv side chains of L-Asn-32, and L-Asn-92, which interact directly with residues in HEL via hydrogen bonding in the wild-type Fv-HEL complex, and we investigated the interactions between these mutant antibodies and HEL by thermodynamic analysis and x-ray structural analysis [1].

Experimental Procedures

Fv fragment-HEL complexes for the HyHEL-10 mutants LN32D and LN92D were crystallized under conditions similar to those used for the wild-type Fv-HEL complex [2]. The best crystals were grown in 0.1 M Hepes buffer, pH 7.6–7.8, 9–11% (w/v) polyethylene glycol 6000, 7–9% (w/v) 2-methyl-2,4-pentanediol, and 15% glycerol as a cryoprotectant. For the LN32A-HEL and LN92A-HEL complexes, however, the samples of mutant Fv fragments were too poor to crystallize.

Diffraction data were collected using synchrotron x-ray source at beamline BL6A of the Photon Factory and processed by the interactive data processing package DPS/MOSFLM/CCP4. Integration and scaling were carried out using the MOSFLM software and SCALA software, respectively. The final file of structural factors was obtained by using TRUNCATE and MTZ2VARIOUS in the CCP4 program suite. The mutant Fv-HEL complexes were determined by a molecular replacement method and refined with the program CNS and O.

Results and Discussion

For the overall structures of LN32D-HEL and LN92D-HEL, the relative orientation of Fv (VL and VH) and HEL were notably altered by the mutations, resulting in the local conformational changes around the mutated site and interfacial regions from the wild-type Fv-HEL (Figure 1). The structural changes observed in LN32D-HEL and LN92D-HEL were about the same, except for the existence (in LN92D-HEL) or nonexistence (in LN32D-HEL) of the hydrogen bond between N-δ2 of L-Asn-32 and O of HEL-Gly-16.

Isothermal titration calorimetric analysis showed that in LN92D-HEL interaction, a small loss in binding enthalpy led to a minor decrease in the affinity compared with the wild-type-HEL interaction (Table 1). By comparison, for LN32A- and LN32D-HEL interaction, there was a large decrease in binding enthalpy gain and in binding entropy loss, which notably decreased the binding Gibbs energy.

These results suggest that hydrogen bonds buried at the interfacial area, such as L-Asn-32, had large enthalpic advantage, despite entropic loss, and were crucial to the strength of the interaction. Deletion of these strong hydrogen bonds could not be compensated for by other structural changes. Consequently, asparagine might be an appropriate residue for the antigen recognition through providing the two functional groups for strong hydrogen bond formation, and their contribution to the antigen-antibody interaction can be attributed to their limited flexibility and accessibility at the complex interface.

Table 1: Thermodynamic parameters of the interaction

Mutant	K_a	G	H	$-T\,S$
	$x\ 10^7 M^{-1}$	$kJ\ mol^{-1}$	$kJ\ mol^{-1}$	$kJ\ mol^{-1}$
Wild type	82.1	-51.7	-99.7	48.0
LN32A	0.17	-36.1	-74.0	37.9
LN32D	0.93	-40.3	-47.2	6.9
LN92D	14.0	-47.2	-94.6	47.4

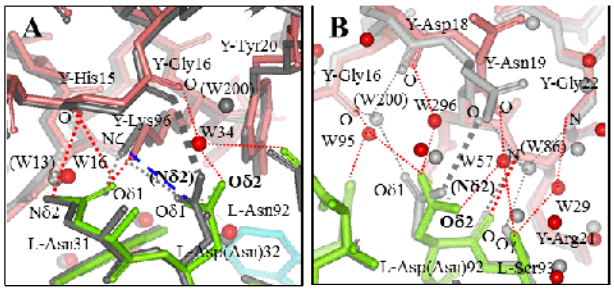

Figure 1. Comparison of local structures at the mutation site between mutant Fv-HEL (VL, green; VH, blue; HEL, pink; water, red) and wild-type Fv-HEL (grey) complexes. A, LN32D-HEL; B, LN92D-HEL

References

[1] A. Yokota et al., J. Biol. Chem. 285, 7686 (2010).
[2] H. Kondo et al., J. Biol. Chem. 274, 27623 (1999)
*kmiz@kuma.che.tohoku.ac.jp

5A, 17A, NW12A/2006-G164

Investigation of the Reaction Mechanism of Orotidine-5'-Monophosphate Decarboxylase

Masahiro Fujihashi[1], Shingo Kuroda[1], Lakshmi P. Kotra[2], Emil F. Pai[3] and Kunio Miki[1]
[1]Graduate School of Science, Kyoto University, Sakyo-ku, 606-8502, Japan
[2]Center for Molecular Design and Preformulations and Division of Cell & Molecular Biology, Toronto General Research Institute/University Health Network, Toronto, ON, Canada M5G 1L7
[3]Departments of Biochemistry, Medical Biophysics, and Molecular Genetics, University of Toronto, Toronto, ON, Canada M5G 1L7

1 Introduction

Orotidine-5'-monophosphate decarboxylase (ODCase) converts orotidine-5'-monophosphate (OMP) into uridine-5'-monophosphate (UMP), the final step of *de novo* pyrimidine biosynthesis. This enzyme is known as one of the most proficient enzymes known. The $t_{1/2}$ of the decarboxylation in water is estimated at about 78 million years. On the contrary, the enzyme completes the reaction within milliseconds. The reaction acceleration ratio is 17 orders of magnitude.

Despite the intensive structural, enzymological, computational and chemical investigations, there is still no general agreement regarding the overall mechanism of this enzyme. More than hundred crystal structures from various organisms have been determined so far. They all represent a dimer of TIM-barrel fold subunits. The active site is deeply buried and located at the dimer interface. A characteristic Lys-Asp-Lys-Asp network is found in all determined structures and the motif is considered to play a dominant role in decarboxylation.

We have long been investigated crystallographic and enzymological analyses of this enzyme in order to elucidate the molecular mechanism of this enzyme. Here, we report the importance of the substrate distortion in catalysis.

2 Experiment

Our investigations were performed using ODCase from *Methanothermobacter thermoautotrophicus (Mt*ODcase). Purified *Mt*ODCase (10 mg/ml) was mixed with 5-10 mM of ligands and the mixture was crystallized using the crystallization solution composed of 1.1-1.36 M sodium citrate and 5% (v/v) dioxane at pH 6-8.5. Crystals were dipped in a cryo-protectant buffer consisting of 1.2 M sodium citrate, 15% glycerol and 0.1 M MES-Na at pH 6.5 and flash-frozen in a nitrogen stream at 95 - 100 K. The data collections were performed using beamlines 5A, 17A and NW12A. The crystals diffracted X-rays around 1.5 Å resolution and belonged to the space group $C222_1$ with the cell parameters of a = 53 Å, b = 103 Å and c = 74 Å. Phasing was performed by the fourier synthesis using a previously determined structure of *Mt*ODCase.

3 Results and Discussion

The left panel of the figure shows the omit electron density map superposed on the atomic model of wild-type *Mt*ODCase with 6-cyano-UMP. The cyano substituent on the C6 position of the pyrimidine ring is apparently distorted from the pyrimidine plane. The distortion is also found in 6-cyano-UMP bound to the mutant of the active site lysine (Lys72Ala mutant, right panel). Similar distortions are found in various structures. These structural features suggest that the active site aspartate (Asp70) located close to the C6 substituent of the pyrimidine ring play a dominant role for the distortion and the catalysis

References

M. Fujihashi *et al*., J. Mol. Biol **387** (2009) 1199.

* mfuji@kuchem.kyoto-u.ac.jp

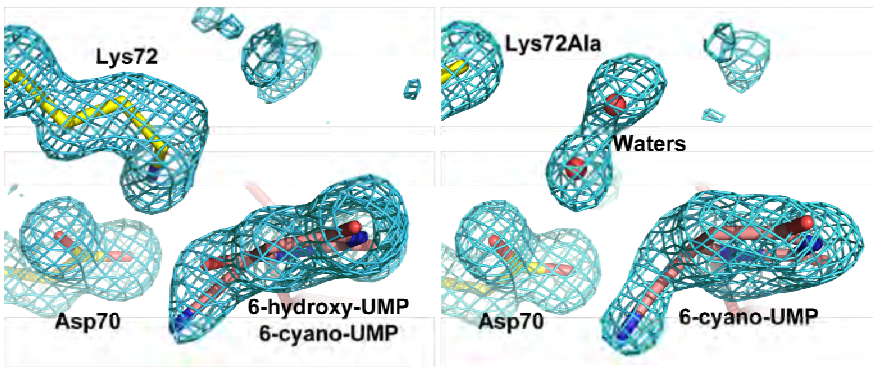

Left: 6-cyano-UMP bound to wild-type *Mt*ODCase. Since ODCase slowly converts 6-cyano-UMP into 6-hydroxy-UMP, both cyano and hydroxy substituents at C6 of pyrimidine ring can be seen in the omit electron density map. The cyano group is apparently distorted from the pyrimidine plane.

Right: 6-cyano-UMP bound to K72A mutant *Mt*ODCase. The cyano group is also distorted in this complex.

BL-5A, NW-12A, NE-3A/2006G165, 2011G129

Structural and mutational analyses of *Bacillus megaterium* glucose 1-dehydrogenase IV

Taiki Nishioka[1], Yoshiaki Yasutake[2,*], Yoshiaki Nishiya[3], and Tomohiro Tamura[1,2]
[1]Graduate School of Agriculture, Hokkaido University 060-8589, Japan
[2]Bioproduction Research Institute, National Institute of Advanced Industrial Science and Technology (AIST), Sapporo 062-8517, Japan
[3] Tsuruga Institute of Biotechnology, Toyobo Co., Ltd., Tsuruga 914-0047, Japan

1 Introduction

NAD(P)$^+$-dependent glucose 1-dehydrogenase isozymes from *Bacillus megaterium* (BmGlcDHs) catalyze the oxidation of β-D-glucose to D-glucono-1,5-lactone, using NAD(P)$^+$ as a cofactor. BmGlcDH is a member of the short-chain dehydrogenase/reductase (SDR) superfamily, and has been used clinically to examine blood glucose levels [1]. Two other types of GlcDHs have been used for blood glucose detection. One is a pyrroloquinoline-quinone-containing GlcDH (PQQ-GlcDH), which is a homodimer with a subunit weight of approximately 50 kDa. Another one is an FAD-containing enzyme (FAD-GlcDH) that has been isolated from 2 organisms, namely, *Aspergillus oryzae* (*A. oryzae*) and *Burkholderia cepacia* (*B. cepacia*). The *B. cepacia* FAD-GlcDH is known to be self-sufficient and relatively more thermostable than the PQQ-GlcDHs. In contrast to these 2 types of GlcDHs, BmGlcDH requires the addition of NAD$^+$ to the assay mixture. However, it is currently applied for the clinical assay, because of its relatively narrow substrate specificity toward D-glucose. Here, we describe for the first time the X-ray structures of the substrate-free, NADH-bound, and D-glucose-bound forms of BmGlcDH-IV. These structures reveal that the C-terminal carboxyl group derived from a neighboring subunit directly interacts with D-glucose. Based on the structures, we have performed site-directed mutagenesis of BmGlcDH-IV, and have obtained a useful mutant that showed the improvement of D-glucose specificity with retaining similar thermostability to the wild-type enzyme.

2 Experiment

The recombinant BmGlcDH-IV and its mutants were obtained using *Escherichia coli* as an expression host. His-tagged BmGlcDH-IV was purified by Ni-affinity chromatography. All crystals were obtained by the hanging-drop vapor-diffusion method at 20°C. The structures were solved by molecular replacement with GlcDH from *B. megaterium* IWG3 [2] as a search model.

3 Results and Discussion

The structures of BmGlcDH-IV in ligand-free form, in complex with NADH, and in complex with D-glucose were determined to a resolution of 2.0 Å. The homotetramer having a *222*-point-group symmetry was generated from the dimer in the asymmetric unit with the crystallographic 2-fold symmetry. Clear electron density showed that the trapped D-glucose is in the β form with the C1-hydroxyl group in the equatorial configuration. These results are consistent with previous reports that BmGlcDH acts on β-D-glucose, but not on α-D-glucose. It is interesting to note that the C-terminal carboxyl group (Gly261) derived from a neighboring subunit is inserted into the active-site pocket and directly interacts via hydrogen bonds with C4- and C6-hydroxyl groups in the bound β-D-glucose (Fig. 1). The side-chain amino group of Lys199 is also located near the C-terminal carboxyl groups at a distance of less than 3.0 Å. These elaborate inter-atomic interactions probably play a critical role in stabilizing the conformation of the active-site and the bound β-D-glucose. A site-directed mutagenic study showed that destabilization of the BmGlcDH-IV C-terminal region by substitution with more bulky and hydrophobic amino acid residues greatly affects the activity of the enzyme, as well as its thermostability and substrate specificity. Of the five mutants created, the G259A variant exhibited the narrowest substrate specificity relative to the wild-type enzyme, while retaining comparable catalytic activity with D-glucose, and similar thermostability to the wild-type enzyme.

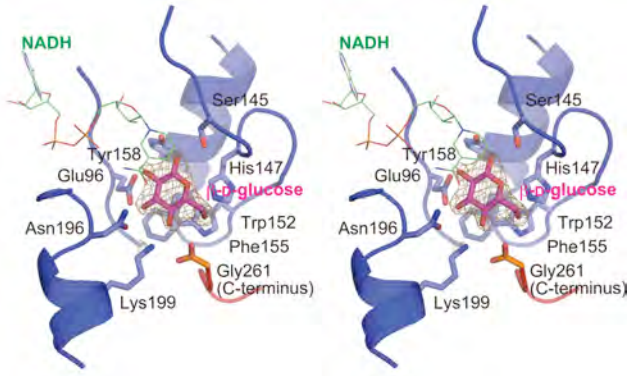

Fig. 1: Stereo view active site of BmGlcDH-IV. Fo-Fc omit map for the bound substrate is also shown.

References

[1] Jörnvall, H., Persson, B., Krook, M., Atrian, S., Gonzàlez-Duarte, R., Jeffery, J. & Ghosh, D. (1995) *Biochemistry* **34**, 6003–6013.
[2] Yamamoto, K., Kurisu, G., Kusunoki, M., Tabata, S., Urabe, I. & Osaki, S. (2001) *J. Biochem.* **129**, 303–312.

* y-yasutake@aist.go.jp

17A, NW12A/2007G025

Crystal structures of the inhibitor-bound quaternary complexes of 1-deoxy-D-xylulose 5-phosphate reductoisomerase from *Plasmodium falciparum*

Tomonobu UMEDA, Yoshio KUSAKABE, Yuki ODANAKA, Satoko MATSUBAYASHI, Yasuyuki KITAGAWA, and Nobutada TANAKA*
School of Pharmacy, Showa University,
1-5-8 Hatanodai, Shinagawa-ku, Tokyo 142-8555, Japan

Introduction

Malaria is one of the world's most serious parasitic diseases. There are estimated 300-500 million cases and more than a million deaths from malaria each year. Human malaria is caused by infection with intracellular parasites of the genus *Plasmodium*. *P. falciparum* is the most lethal among the four species of *Plasmodium* that infect humans. The emergence of strains of malarial parasite resistant to conventional drug therapy has stimulated searches for antimalarials with novel modes of action. The non-mevalonate pathway of isoprenoid biosynthesis present in *P. falciparum* is known to be an effective target of antimalarial drugs. The second enzyme of the non-mevalonate pathway, 1-deoxy-D-xylulose 5-phosphate reductoisomerase (DXR, EC 1.1.1.267), catalyzes the NADPH and divalent cation (Mg^{2+} or Mn^{2+})-dependent transformation of 1-deoxy-D-xylulose 5-phosphate into 2-*C*-mthyl-D-erythritol 4-phosphate. Here we report the crystal structures of *P. falciparum* DXR (PfDXR) complexed with inhibitors.

Experimental

Crystallization

Expression and purification of PfDXR were carried out as described previously [1]. To obtain the quaternary (PfDXR-NADPH-Mg^{2+}-inhibitor) complex crystals, the protein solution (10 mg/ml PfDXR, 50 mM Tris-HCl pH 7.8 and 2 mM DTT) was mixed with inhibitor solution (50 mM Tris-HCl pH 7.8, 2 mM DTT, 6 mM NADPH, 4 mM $MgCl_2$, and 4 mM fosmidomycin or FR900098) at a volume ratio of 1:1. Crystallization was carried out by the hanging-drop method, in which 2 μl of the protein-inhibitor complex solution was mixed with the same volume of reservoir solution (0.1 M Tris-HCl pH 8.0, 20 (w/v)% PEG8000, and 0.3 M Calcium acetate) and incubated at 293 K. Rod-shaped crystals with typical dimensions of about 0.02 x 0.02 x 0.1 mm^3 could be grown in 1 week.

X-ray data collection and structure determination

Data collections were performed by the rotation method at 100 K using an ADSC Q210r CCD detector with synchrotron radiation (λ = 1.000 Å on beamline NW12A of the PF-AR). The current best diffraction data for fosmidomycin and FR900098 complexes were collected up to 1.90 and 2.15 Å resolutions, respectively.

The initial phase determination for the fosmidomycin complex was carried out by the molecular replacement method using the coordinate set of the inhibitor-free ternary complex of PfDXR as a search model. Then the refined fosmidomycin complex model was used for the template of structure refinement of the FR900098 complex by D-Fourier method.

Results and Discussion

The overall structure of PfDXR is essentially similar to those of DXRs from other species [2]. The subunit of PfDXR consists of two large domains, linker region, and a C-terminal domain. One of the large domains is responsible for NADPH binding, and the other provides the groups necessary for catalysis. A comparison of the crystal structure of the inhibitor-free PfDXR and those of the inhibitor-bound PfDXR showed that the large cleft between the NADPH-binding and catalytic domains were closed upon inhibitor binding. Disordered loop region in the inhibitor-free form is well defined in the inhibitor-bound quaternary complexes. Fosmidomycin and FR900098 bind to PfDXR in a similar manner where each of the inhibitor is buried in the active site and is shielded from the solvent environment. We expect present structures to be a quite useful guide for design of more effective antimalarial compounds.

References

[1] T. Umeda *et al.*, Acta Crystallogr. F**66**, 330 (2010).
[2] T. Umdea *et al.*, Sci. Rep. **1**, MS#9 (2011).

*ntanaka@pharm.showa-u.ac.jp

17A, NW12A, NE3A / 2007G080, 2009G100

Structural and functional studies of Assimilatory Nitrite Reductase

Shogo Nakano, Misa Takahashi, Atsushi Sakamoto, Hiromichi Morikawa, and Katsuo Katayanagi*

Department of Mathematical and Life Sciences, Graduate School of Science, Hiroshima University, Higashi-Hiroshima 739-8526, Japan

1 Introduction

Nitrogen is an essential element required for the synthesis of physiological substrates, including nucleic acids and proteins. Higher plants acquire nitrogen, primarily as NO_3^-, from the soil. The NO_3^- is preserved in the vacuoles before being sequentially reduced to NH_4^+ by two enzymes: assimilatory nitrate reductase and assimilatory nitrite reductase (aNiR). The produced NH_4^+ is used by glutamine synthetase and glutamate synthetase in amino acid synthesis. These processes are known as nitrogen assimilation. In comparison with dissimilatory nitrite reductase (dNiR) for the alternative inorganic nitrogen metabolic pathway, the molecular mechanism of the reduction for aNiR has hardly been shown yet.

2 Structure-function relationship of assimilatory nitrite reductases from the leaf and root of tobacco based on the high resolution structure [1, 2]

Tobacco expresses four isomers of assimilatory nitrite reductase (aNiR), leaf-type (Nii1 and Nii3) and root-type (Nii2 and Nii4). The high resolution crystal structures of Nii3 and Nii4, determined at 1.25 and 2.3 Å resolutions respectively, revealed that both proteins had very similar structures. Although these structures are almost identical to spinach aNiR that were previously obtained at 2.8 Å resolution by Knaff & Allen's group, the Nii3 structure provided detailed geometries for the [4Fe-4S] cluster and the siroheme prosthetic groups. We have generated two types of Nii3 variants: one set focuses on residue Met175 (Nii3-M175G, Nii3-M175E and Nii3-M175K), a residue that is located on the substrate entrance pathway; the second set targets residue Gln448 (Nii3-Q448K), a residue near the prosthetic groups. Comparison of the structures and kinetics of the Nii3 wild-type (Nii3-WT) and the Met175 variants showed that the hydrophobic side-chain of Met175 facilitated enzyme efficiency (k_{cat}/K_m). The Nii4-WT has Lys449 at the equivalent position of Gln448 in Nii3-WT. The enzyme activity assay revealed that the turnover number (k_{cat}) and Michaelis constant (K_m) of Nii4-WT were lower than those of Nii3-WT. By combining detailed crystal structures with enzyme kinetics, we have proposed that Nii3 is the low-affinity and Nii4 is the high-affinity aNiR.

3 The reductive reaction mechanism of tobacco nitrite reductase derived from a combination of crystal structures and ultraviolet-visible microspectroscopy [3]

A reaction mechanism for Nii3, an aNiR from tobacco, is proposed based on high resolution X-ray structures and UV-Vis microspectroscopy of Nii3-ligand complexes. Analysis of UV-Vis spectral changes in Nii3 crystals with increasing X-ray exposure showed prosthetic group reductions. In Nii3-NO_2^- structures, X-ray irradiation enhanced the progress of the reduction reaction, and cleavage of the N-O bond was observed when X-ray doses were increased. Crystal structures of Nii3 with other bound ligands, such as Nii3-NO and Nii3-NH_2OH, were also determined. Further, by combining information from these Nii3 ligand-bound structures, including that of Nii3-NO_2^-, with UV-Vis data obtained at different X-ray doses, a reaction mechanism for aNiR was constructed.

4 X-ray crystal structure of a mutant assimilatory nitrite reductase that shows sulfite reductase-like activity [4]

aNiR reduces nitrite to ammonium, whereas assimilatory sulfite reductase reduces sulfite to hydrogen sulfide. Although aNiR can also reduce sulfite, its activity is much lower when nitrite is reduced as the substrate. To increase the sulfite reduction activity of aNiR, we performed a N226K mutation of Nii3, a representative aNiR. The resulting Nii3-N226K variant could bind non-native targets, SO_3^{2-} and HCO_3^-, in addition to its native target, NO_2^-. We have determined the high-resolution structure of Nii3-N226K in its apo-state and in complex with SO_3^{2-}, NO_2^- and HCO_3^-. A comparison of all ligand bound structures for Nii3-N226K revealed that structural changes in active site depend on the size of the substrate.

Acknowledgement

Authors are grateful to all the beamline stuffs and scientists for assistance with the experiments.

References

[1] Nakano,S., Takahashi,M., Sakamoto,A., Morikawa,H. & Katayanagi,K. *Protein Sci*. **21**, 383-395. (2012).
[2] Nakano,S. PhD thesis, *Hiroshima University* (2012).
[3] Nakano,S., Takahashi,M., Sakamoto,A., Morikawa,H. & Katayanagi,K. *Proteins: Struct. Funct. Bioinform.*, in press. (2012). DOI 10.1002/prot.24094
[4] Nakano,S., Takahashi,M., Sakamoto,A., Morikawa,H. & Katayanagi,K. *Chemistry & Biodiversity*. in press. (2012). DOI: 10.1002/cbdv.201100442

* kkata@sci.hiroshima-u.ac.jp

5A, NW12A, NE3A /2007G212, 2008G524

High Resolution X-ray Structure Analysis of HIV-1 Protease in Complex with Potent Inhibitors

Motoyasu ADACHI, Shigeki ARAI, Taro TAMADA* and Ryota KUROKI
JAEA-QuBS, Shirakata-Shirane 2-4, Tokai, Ibaraki 319-1195, Japan

Introduction

Currently, the development of the HIV-1 protease inhibitors is regarded as a major success of structure-based drug design, and the inhibitors of HIV-1 protease are important compounds to establish highly active antiretroviral therapy for AIDS. Despite this remarkable success, adverse effects linked to the use of the HIV-1 protease inhibitors and the emergence of HIV-1 mutants resistant to current drug remains critical factors in clinical failure in antiviral therapy. The mutant HIV-protease (L10F/V32I/M46I/I47V/Q58E/I84V) derived from A17 strain (A17-HIVPR) resistant to Lopinavir and Ritonavir [1] was prepared and crystallized to compare the complex structure with that of wild-type. Besides Lopinavir and Ritonavir, other potent inhibitors (KNI-764[2] and KNI-1657[3]) containing allophenylnorstatine with hydroxyl-methylcarbonyl(HMC) isostere were used to analyze interaction with the drug resistant mutant.

Crystallization and Data Collection

The WT- and A17-HIVPRs were prepared as reported previously[4]. After the inhibitors were dissolved into dimethylsulfoxide at a concentration of 11.5 mM, 2-fold molar excess amount of inhibitors were added to a 2.0 mg/mL protein solution. The protein solution was mixed with the reservoir solution containing 126 mM phosphate buffer (pH 5.0), 63 mM sodium citrate and either 0-30% saturated ammonium sulfate or 20-30% PEG4000 as precipitant. Crystallization was performed using hanging drop vapor diffusion method at 293 K. For data collection, crystals were soaked into the reservoir solution containing 25-45% (w/v) glycerol, then flash-frozen under a N_2 gas cryo-stream (100 K). Collected images were processed using the HKL2000 program suite, and the data collection and the refinement statistics are summarized in Table 1.

Refinement and Structure

The structure models were built using the program XtalView and were refined using the program SHELX97 (Table 1). Electron density maps belonging to the inhibitors bound to the WT- and A17-HIVPRs were clearly observed. Any significant differences of overall structure between the WT- and A17-HIVPRs were not observed. Although most of the positions of catalytically important hydrogen atoms were not determined at the resolution range employed here, accurate information regarding to the interaction between the bound inhibitor and protein obtained from high resolution X-ray structure analysis provides us important information for designing new drug candidates.

References

[1] Mo H., et al., Antiviral Res. 59, 173-180 (2003).
[2] Mimoto T., et al., J. Med. Chem. 42, 1789-1802 (1999).
[3] Hidaka K., et al., J. Med. Chem. 52, 7604-7617 (2009).
[4] Adachi M., et al., Proc. Natl. Acad. Sci. USA, 106, 4641-4646 (2009).

*tamada.taro@ jaea.go.jp

Table 1 Data collection and refinement statistics

HIV-1 protease	WT-HIVPR	WT-HIVPR	A17-HIVPR	A17-HIVPR	A17-HIVPR
Inhibitor	Lopinavir	KNI-764	KNI-1657	Ritonavir	KNI-764
Beam line	BL5A	NW12A	NE3A	NE3A	NW12A
Data collection					
Space group	$P2_12_12$	$P2_12_12$	$P2_12_12_1$	$P2_12_12$	$P2_12_12_1$
Cell constants (Å) *a, b, c*	59.6, 85.6, 46.4	57.4, 85.9, 46.3	28.7, 66.3, 92.5	60.2, 86.0, 46.5	28.8, 65.6, 92.0
Resolution (Å)	1.10	0.93	0.98	1.00	0.95
Unique reflections	93297	148138	101279	129304	109216
Completeness	95.6	95.9	99.3	98.8	98.6
R_{merge} (%)	8.4	4.5	6.8	8.0	7.6
$I/\sigma I$	51.1	54.0	61.5	63.0	49.3
Average redundancy	9.2	7.7	9.2	12.1	5.7
Refinement					
Resolution range (Å)	48.9-1.10	47.7-0.93	31.2-0.98	49.3-1.00	37.7-0.95
R_{work} (%)	13.5	11.1	14.8	14.4	15.6
R_{free} (%)	16.9	13.1	17.0	16.8	19.6

NW12A,5A/2008G030/2006G132

Crystal structure of actin specific ADP-ribosyltransferase Ia with β TAD and actin

Tsuge H[1, 3, *], Nagahama M[2], Oda M[2], Utsunomiya H[1], Katunuma N[1], Nishizawa M[2], Sakurai J[2].
[1]Institute for Health Sciences and [2]Faculty of Pharmaceutical Sciences, Tokushima Bunri University, 180 Yamashiro-cho, Tokushima 770-8514, Japan
[3]Faculty of Life Sciences, Kyoto Sangyo University, Kamigamo-Motoyama, Kyoto 603-8555, Japan

1 Abstract

ADP-ribosylating toxins (ADPRTs) facilitate scission of the N-glycosyl bond between nicotinamide and the N-ribose of NAD and transfer the ADP-ribose moiety to target proteins. ADPRTs are classified into four families based on their respective targets. Type I ADPRTs target heteromeric GTP- binding proteins. They include cholera toxin (CT). Type II ADPRT diphtheria toxin (DT) modify elongation factor 2 (EF2). Type III ADPRTs (Clostridium botulinum C3 exoenzyme) ADP-ribosylate small GTP-binding proteins. Type IV ADPRTs ADP-ribosylate actin. These actin-specific ADPRTs include a family of binary toxins. C. perfringens iota-toxin consists of an enzymatic component (Ia) and a cell- membrane-binding component (Ib). Ia ADP- ribosylate G-actin, but not F-actin, at Arg-177; this activity severely reduces the ability of actin to undergo polymerization, leading to disruption of the cytoskeletal architecture and cell death.

During the last few years, it has been revealed much about the structure and mechanism of actin ADPRTs. Up to now, many actin ADPRT structures are available including Ia [ref.1]. In this study, we first revealed the complex structure of actin specific ADPRT with substrate actin.

2 Experiment

To obtain good diffraction-quality crystals of G-actin with Ia, we used ATP and latrunculin A, which is an inhibitor of actin polymerization. Moreover, to obtain stable complex crystals, we used the non- hydrolyzable NAD analog βTAD. Using these crystals, we collected diffraction data for the actin (with ATP and the polymerization-inhibiting drug latrunculin A)–Ia–βTAD complex at a resolution of 2.8 Å. The crystal space group was determined to be $P2_12_12_1$ (a =57.0, b=126.3, c=147.1Å) and to contain one actin and one Ia in an asymmetric unit. Crystals are highly nonisomorphous, and their structure was determined by molecular replacement by using MOLREP. Using the structure of Ia (1GIQ), we identified and fixed the Ia position, after which we searched for actin by using the structure of actin (1IJJ). The βTAD, ATP, and latrunculin A densities were clear, so these cofactors were built in. The model was then iteratively rebuilt and refined at a 2.8-Å resolution by using REFMAC. The final model was then refined to Rwork=22.3% (Rfree=29.6%) and consisted of Ia, actin, βTAD, ATP, latrunculin A, calcium, and 79 water molecules.

3 Results and Discussion

The structure indicates that Ia recognizes actin via five loops around βTAD: loop I (Tyr-60 – Tyr-62 in the N domain), loop II (active-site loop), loop III, loop IV (PN loop), and loop V (ADP-ribosylating turn–turn loop). We used site-directed mutagenesis to confirm that loop I on the N domain and loop II are essential for the ADP-ribosyltransferase activity. Furthermore, we revealed that Glu-378 on the EXE loop is in close proximity to Arg-177 in actin, and we proposed that the ADP- ribosylation of Arg-177 proceeds by an SN1 reaction via first an oxocarbenium ion intermediate and second a cationic intermediate by alleviating the strained conformation of the first oxocarbenium ion [ref.2].

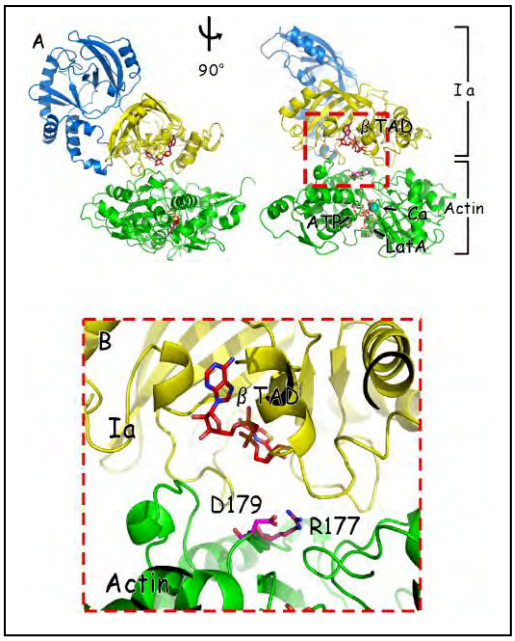

Fig. 1: (A)Ia consists of N-terminal(cyan) and C-terminal domain (yellow). Actin was drawn in green.(B)Close up of Arg177 and βTAD.

Acknowledgement

We thanks the PF staff for the data collection.

References

[1] H.Tsuge *et al.*, J.Mol.Biol. **325** (2003) 471-473
[2] H.Tsuge *et al.*, Proc.Natl.Acad.Sci. **105**(2008) 7399-7404

* tsuge@cc.kyoto-su.ac.jp

5A, 17A, NW12/2008G0149

Structure Determination of Enzymes Involved in the New Carbon Dioxide Fixation System

Akira Nakamura[1], Masahiro Fujihashi[1], Riku Aono[2], Takaaki Sato[2], Yosuke Nishiba[1], Shosuke Yoshida[2], Ayumu Yano[2], Haruyuki Atomi[2], Tadayuki Imanaka[3] and Kunio Miki[1*]

[1] Dept. of Chemsitry, Graduate School of Science, Kyoto University, Sakyo, Kyoto, 606-8502, Japan
[2] Dept. of Synthetic Chemistry and Biological Chemistry, Graduate School of Engineering, Kyoto University, Katsura, Nishikyo-ku, Kyoto 615-8510, Japan
[3] College of Life Sciences, Ritsumeikan University, Kusatsu, Shiga 525-8577, Japan

1 Introduction

Recently, a novel carbon dioxide fixation pathway is discovered in a thermophilic archaea, *Thermococcus kodakaraensis*. This pathway is composed of three enzymes and involved in AMP metabolism. Ribose-1,5-bisphosphate isomerase (R15P isomerase) is a novel enzyme involved in this pathway and isomerizes ribose-1,5-bisphosphate (R15P) into ribulose-1,5-bisphosphate (RuBP). We here report the crystal structure and molecular mechanism of this enzyme.

2 Experimental

We have determined three structures, unliganded wild-type enzyme (WT (unliganded)), wild-type complexed with its product RuBP (WT-RuBP) and the catalytically inactive mutant C133S in complexed with the substrate R15P (C133S-R15P). The unliganded crystals were obtained using PEG1000 as a precipitant. Crystals of WT-RuBP and C133S-R15P were obtained by co-crystallization method using the same precipitant solutions with WT (unliganded) crystals.

Diffraction datasets were taken at BL5A, BL17A and NW12A beamlines. Phasing was performed with a single anomalous dispersion (SAD) method using a seleno-methionine-labeled unliganded crystals. The WT (unliganded), WT-RuBP and C133S-R15P structures were determined at 2.50 Å, 2.60 Å and 2.85 Å resolution, respectively.

3 Results and Discussion

Six subunits are found in an asymmetric unit of the WT (unliganded) crystal. The oligomerization state is compatible with the gel-filtration analysis, suggesting the determined structure is the physiological state of this enzyme. The monomeric structure consists of two domains, N-terminal α-helical and C-terminal αβα-sandwich domains. A positively charged cavity is located between the two domains. The three-dimensional structure database search performed by DALI shows that the crystal structure of R15P isomerase resembles to those of PF1008 family proteins as deduced from the primary sequence.

The co-crystallized ligand molecule was bound at the cavity. The positive charge of the cavity is suitable to accommodate the ligand possessing two negatively charged phosphate groups. At the ligand binding-site of WT-RuBP, the conserved residues in PF1008 family, Cys133 and Asp202, are located around the ribulose moiety of the ligand. Mutations of these residues, C133S and D202N, result in non-detectable enzymatic activities. Based on these analyses, we prepared the crystal of C133S-R15P complex and determined the structure.

The Oγ of mutated C133S residue is located 3.3 Å from C2' of the ribose. This oxygen is also interacted with main chain nitrogen The carboxylate of Asp202 interacts with 2'-OH and O4' with 3.1 Å and 2.7 Å, respectively. The carboxylate is surrounded by several hydrophobic residues. These aspects suggest that the thiol of Cys133 and the carboxylate of Asp202 are deprotonated and protonated, respectively, in the enzyme-substrate complex.

The enzymatic reaction is assumed to be proceeded as following. Proton transfer from protonated Asp202 to O4' of the substrate is the first step. Then, proton abstraction from C2' and the cleavage of O4'-C1' bond result in the formation of *cis*-phosphoenolate intermediate. The intermediate is transformed to the product RuBP by the proton transfers from Cys133 to C1' and from O2' to Asp202.

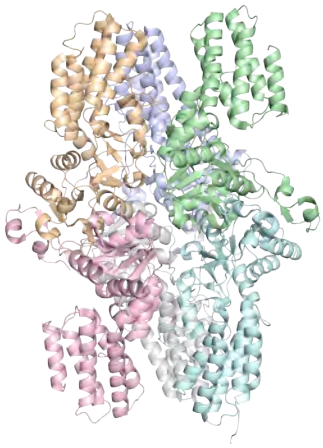

Figure. Overall structure of R15P isomerase hexamer

Reference

[1] A. Nakamura *et al*., J. Biol. Chem., **287,** 20784-20796 (2012).

* miki@kuchem.kyoto-u.ac.jp

10C/2008G520

Distribution of the αC Region of Fibrinogen Molecule

Kenji Kubota
Gunma University, Kiryu 376-8515, Japan

1 Introduction

Fibrinogen is a rod-shaped plasma protein that plays an essential role in the blood coagulation process. Fibrinogen is a dimer consisting of three peptide chains, Aα, Bβ and γ, and those peptides chains form unique functional domains that conduct in the coagulation process. Among them, the carboxyl terminal region of Aα peptide chain, αC region, has been taken much notice about its role in the lateral aggregation of protofibrils, which are the half-staggered double stranded axial association of fibrin converted from fibrinogen by the enzymatic action of thrombin. αC region contains b-sheet structure and is likely to form aggregates. Synthesized recombinant αC chains forms inclusion body easily, and forms amyloid structure in some case. It is useful to understand the spatial distribution of αC region in the fibrin polymerization process.

Fragment X is one kind of derivatives of fibrinogen by the enzyme plasmin, and the αC regions of intact fibrinogen molecule are cleaved. Therefore, fragment X is a useful material for the study on the functional roles of the αC regions. Additionally, it has been known the αC regions dissociate from the central region at acidic condition as pH 3. Then, scattering measurements of SAXS as well as light scattering will give important information about the spatial distribution.

2 Experiment

Bovine fibrinogen purchased from Sigma-Aldrich Co. was used. Fibrinogen dissolved in PBS was treated by plasmin (5 mU/1 mg fibrinogen) at 25°C. The reaction was stopped at the incubation time of 70 min by the addition AEBSF (protease inhibitor), and the digestion was passed through lysine-sepharose 4B column to remove plasmin. The elution was then analysed by GPC (HiLoad Sephadex 200) using tris-buffer with 0.3 M NaCl. Thus purified fragment X solution was stocked in the deep-freezer until use. By the SDS-PAGE results of those samples it was ascertained that the αC region was cleaved thoroughly and a decent amount of amino terminal region (Bβ1-49) was deleted additionally.

Measurements were carried out for the intact fibrinogen in PBS (pH 7.4), fragment X in tris-buffer (pH 7.4), and intact fibrinogen in 1 mM HCl (pH 3.0). SAXS measurements were achieved at KEK-PF (BL 10C) at Tsukuba. The obtained scattered intensity as a function of scattering vector Q was analysed by the cross-sectional Guinier plots to determine the average diameter of fibrinogen molecules. Dynamic light scattering measurements were also carried out to determine the Stokes diameter. Stokes diameter was obtained by the Stokes-Einstein equation from the characteristic decay time of the correlation function.

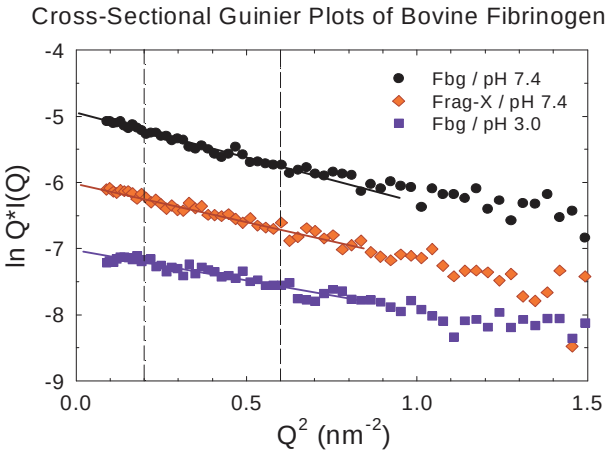

Fig. 1: Cross-sectional Guinier plots of bovine fibrinogen as a function of Q^2.

3 Results and Discussion

Cross-sectional diameter D_c of fragment X (4.2 nm) was significantly less than that of the intact fibrinogen (4.7 nm), and that of fibrinogen at pH 3.0 (4.0 nm) was further less than that of fragment X. On the other hand, Stokes diameter D_s of fragment X (15.8 nm) was significantly less than that of intact fibrinogen at pH 7.4 (22.8 nm). Stokes diameter of fibrinogen at pH 3.0 was a little larger than that at pH 7.4. When NaCl was added to the solution at pH 3.0 and the ionic strength was augmented up to 150 mM, a remarkable increase of diameter was observed (ca. 120 nm) suggesting the occurrence of aggregation.

The decrease of D_c as well as D_s in fragment X is attributable essentially to the deletion of the αC region, and this result suggests that the αC region snuggles up to the backbone of fibrinogen molecule. The decrease of D_c and increase of D_s at pH 3.0 means that the αC region dissociates from the central region of fibrinogen and is extended. Therefore, the contour of fibrinogen molecule becomes thinner. Cancellation between the elongation of molecular length and the decrease of cross-sectional diameter results in a slight increase of D_s.

In the fibrin polymerization, especially in the lateral aggregation of protofibrils, the αC regions dissociate from the central region and can interact with each other. At 150 mM NaCl the αC-αC interaction might result in the aggregates, where the electrostatic interaction is weakened. That interaction should be the origin of formation of aggregation in variant fibrinogen lacking N terminal region of Bβ chain, which might play the central role in the lateral aggregation.

Acknowledgments

The author thanks KEK-PF for the use of beam line.

17A/2008G555

Structural insights into the peroxidase activity and inactivation of human peroxiredoxin 4

Xi Wang[1], Likun Wang[1], Xi'e Wang, Fei Sun and Chih-chen Wang
National Laboratory of Biomacromolecules, Institute of Biophysics, Chinese Academy of Sciences, Beijing 100101, China
[1] These authors contributed equally to this work.

Abstract

Prx4 (peroxiredoxin 4) is the only peroxiredoxin located in the ER (endoplasmic reticulum) and a proposed scavenger for H_2O_2. In the present study, we solved crystal structures of human Prx4 in three different redox forms and characterized the reaction features of Prx4 with H_2O_2. Prx4 exhibits a toroid-shaped decamer constructed of five catalytic dimers. Structural analysis revealed conformational changes around helix α2 and the C-terminal reigon with a YF (Tyr-Phe) motif from the partner subunit, which are required for interchain disulfide formation between Cys87 and Cys208, a critical step of the catalysis. The structural explanation for the restricting role of the YF motif on the active site dynamics is provided in detail.

Crystal structure of reduced Prx4

In the presence of DTT Prx4 was crystallized into space group *C*2 with five chains in an asymmetric unit. The overall structure resembles a toroid-shaped decamer from two asymmetric units (**Fig 1A**). The toroid has a maximal diameter of ~120 Å and an inside diameter of ~60 Å. Each subunit exhibits a typical extended Trx fold (ββαβαβαβββαα) (**Fig 1B**). The peroxidatic Cys87 is located in the first turn of helix α2 and surrounded by three conserved residues, Pro80, Thr84 and Arg163. The resolving Cys208, located on a flexible loop between α5 and α6, is ~13.0 Å apart from Cys87 of the partner chain (**Fig 1B and C**). As the distance is obviously unfavorable for the disulfide formation, conformational changes are required for the resolving process.

Fig 1

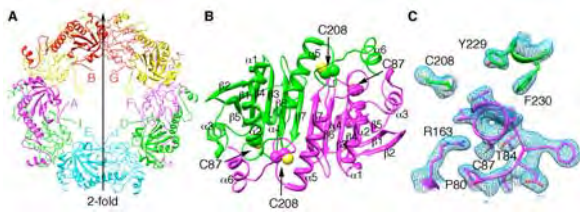

Locally unfolded conformation of oxidized Prx4

In the absence of DTT Prx4 was crystallized in a different unit cell, and the averaged 2Fo-Fc omit map of four chains in one asymmetric unit clearly showed that the region around Cys87 exists in mixed conformations (**Fig 2**). One is fully folded, quite similar to the reduced structure. The other is locally unfolded. Notably Cys87 shifted to the position that was occupied by the aromatic rings of the partner YF motif in the reduced structure, suggesting that the YF motif, which is absent in AhpC, has to move to allow the inter-chain disulfide formation between Cys87 and Cys208.

Fig 2

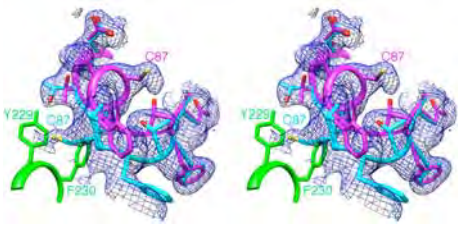

Oxidation of Cys87 by H_2O_2

Treatment with 1 mM H_2O_2 of reduced Prx4 crystal yielded a 2.4 Å structure. Cys87 are assigned in -SOH form in chain A and B, in -SO_2H form in chain C and D, and remains reduced in chain E (**Fig 3**). The B factors of helix α2 with Cys87 in -SO_2H form and its partner C-terminal region (chains C/G and D/F) are much lower than those in the -SOH and the reduced forms (**Fig 3**), showing much lower flexibility. The low flexibility of helix α2 in chain C and D as well as their partner C-terminal region would inevitably restrict conformational changes and thus gave Cys87 more chance to be over-oxidized. In this structure the crystal packing endowed subunits in the decamer with diverse flexibility around these regions leading to distinct oxidation states of Cys87, thus enabled us to address the necessity of conformation changes during the catalysis.

Fig 3.

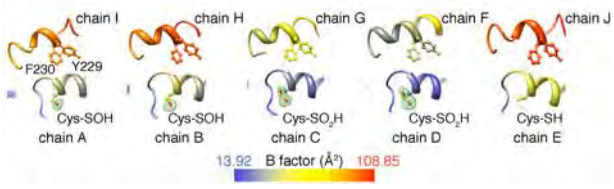

feisun@ibp.ac.cn
chihwang@sun5.ibp.ac.cn

6A/17A/NE3A/2008G555/2008G556

Structural insights into the substrate specificity of human granzyme H – the functional roles of a novel RKR motif

Li Wang[1], Kai Zhang[2], Lianfeng Wu[1], Shengwu Liu[1], Honglian Zhang[1], Qiangjun Zhou[2], Liang Tong[3], Fei Sun[2]*+, Zusen Fan[1]*++

[1]CAS Key Laboratory of Infection and Immunity

[2]National Laboratory of Biomacromolecules, Institute of Biophysics, Chinese Academy of Sciences, Beijing 100101, China

[3]Department of Biological Sciences, Columbia University, New York, New York 10027, USA.

*These authors contributed equally to this work.

1 Introduction

Human granzyme H (GzmH), a chymotrypsin-like serine protease, is constitutively expressed in NK cells, suggesting its critical role in NK cells-mediated immune responses. It has been shown that GzmH is capable of inducing tumor cell death via caspase-dependent apoptosis with DNA fragmentation through cleavage of ICAD to release CAD. Increasing reports have established the pivotal viral clearance role of GzmH. GzmH can directly hydrolyze important viral proteins, such as the adenovirus DNA-binding protein for viral DNA replication and the adenovirus 100K assembly protein for virus assembly. Degradation of 100K also unleashes its inhibitory effect on pro-apoptotic GzmB, suggesting the cooperative action of Gzms to thwart viruses. Recently, GzmH has been shown to cleave HBx, an important factor required for the HBV replication, to facilitate the eradiation of HBV. GzmH also degrades a multifunctional phosphoprotein La to inhibit hepatitis C virus (HCV)-internal ribosome entry site-mediated translational activity. Nevertheless, substrate specificity determinants of GzmH remain largely unknown. For lacking of mouse homolog, a GzmH knockout mouse model for anti-viral and anti-tumor investigation in vivo is not available. Chemical inhibition of human GzmH is an important alternative for studying the physiological roles of this enzyme. However, currently available inhibitors for GzmH are not specific, which hinder further research for GzmH functions.

2 Experiment

Crystals were generated in 2-μl hanging drops containing equal amounts of protein (8-10 mg/mL) and mother liquor equilibrated over 200 μL of reservoir solution at 16°C. D102N-GzmH was crystallized in a buffer containing 0.2 M Li2SO4, 0.1 M Bicine (pH 8.5), 25% (w/v) PEG3350 after one week incubation. For the generation of D102N-GzmH-decapeptide and DNH-inhibitor complexes, crystals of D102N-GzmH were soaked in the above mother liquor supplemented with either 10 mM decapeptide for 2 days or 2 mM inhibitor for 18 h. For data collection, crystals were dehydrated in a solution containing 0.2 M Li2SO4, 0.1 M Bicine (pH8.5), 30% (w/v) PEG3350 for 2 h and then fast frozen with liquid nitrogen. All data sets were collected at 100 K. Data for D102N-GzmH, D102N-GzmH-decapeptide, D102N-GzmH-inhibitor complexes were respectively collected at the beamline BL6A (λ=1.0Å), BL17A (λ=0.98Å), NE3A (λ=1.0Å) of Photon Factory (Japan). All diffraction data were indexed, integrated and scaled with the program HKL2000.

3 Results and Discussion

To provide structural insights into the substrate recognition mechanisms for GzmH, we solved the crystal structures of GzmH alone and in complex with a decapeptide substrate and an inhibitor to 2.2 Å, 2.4 Å and 2.7 Å, respectively. The Thr189, Gly216 and Gly226 specificity triad in the S1 pocket of GzmH defines its preference for bulky, aromatic residues (Tyr and Phe) at the P1 position. Notably, we discovered that an unusual RKR motif (Arg39-Lys40-Arg41), conserved only in GzmH, helps define the S3' and S4' pockets, indicating the preference for acidic residues at the P3' and P4' sites. Disruption of the RKR motif or the acidic P3' and P4' residues in the substrate abolished the proteolysis of GzmH. We designed a tetrapeptide chloromethylketone (CMK) inhibitor, Ac-PTSY-CMK, which can specifically and efficiently block the enzymatic and cytotoxic activity of GzmH, providing a useful tool for further studies on the function of GzmH.

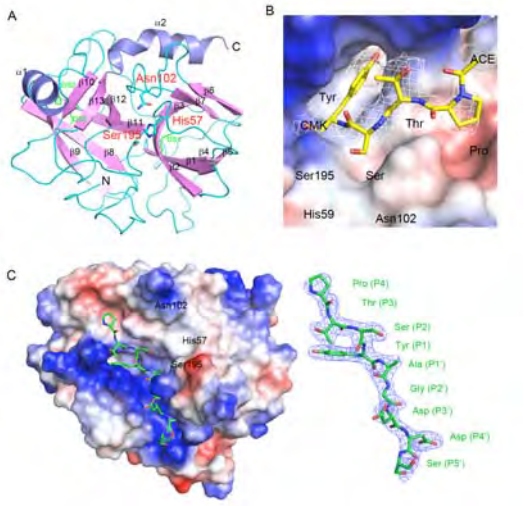

Fig. 1: Crystal structure of GzmH alone and complexes with a synthetic inhibitor and a decapeptide substrate.

*feisun@ibp.ac.cn; fanz@moon.ibp.ac.cn

17A,NE3A/2008G581

カイコ幼若ホルモン輸送メカニズムの解明
Structural mechanism of Juvenile hormone delivery in silkworm

鈴木倫太郎、藤本瑞、塩月孝博、土屋渉、門間充、多勢祥、宮澤光博、山崎俊正
独立行政法人 農業生物資源研究所、〒305-8602 つくば市観音台 2-1-2

1 はじめに

化学合成農薬は作物の安定的な生産に貢献してきましたが、一方でその過度な使用は環境汚染や人体への害などの問題を引き起こすことが危惧されています。昆虫制御剤(=農薬)開発の分野では、その解決策の一つとして、害虫だけを防除する農薬を開発し、人への有害性や環境への悪影響を回避することが求められています。昆虫幼若ホルモン(JH)は脱皮・変態、生殖など様々な生理現象に関与する昆虫に固有のホルモンで、その血中輸送を司る JH 結合タンパク質(JHBP)とともに、人に対して無害な新規昆虫制御剤の標的として注目されています。効果的な農薬開発を進めるため、カイコの JHBP と JH の立体構造解析を行い、ホルモンと輸送タンパク質の相互作用や JH 輸送の仕組みの解明に取り組みました。

2 実験

カイコの JHBP を大腸菌で大量発現させ、JH の複合体を作製し、結晶中と溶液中における複合体の立体構造を X 線結晶構造解析と多次元核磁気共鳴（NMR）解析によりそれぞれ決定しました。X 線結晶構造解析では、JHBP を結晶化し X 線回折データを Photon Factory の BL17A、BLNE3A で取得し、Se-メチオニン置換体を用いた単波長異常分散法を用いて構造決定しました。[1]

3 結果および考察

結晶と溶液構造は一致し、いずれの構造においても JH(赤色)は JHBP 内部の JH 結合ポケットに格納され、ポケットの扉(青色)が閉じることで完全に外界から隔離されていました(図 1A)。JH は標的細胞以外の部分に結合することなく、また、血液中に存在するホルモン分解酵素による分解からも保護されて、標的細胞まで無事に送り届けられることが明らかとなりました。JHBP が JH を取り込む仕組みを明らかにするために、JHBP 単体の立体構造を決定して複合体の構造との比較を行ったところ、JHBP 単体では、JH が結合ポケットに侵入しやすいように、扉(青色)が大きく開いた構造をとっていることが分かりました(図 1B)。

扉がどのような状況で開閉するのかを確かめるために、有機溶媒を加えた系で、JHBP の JH 結合能を確かめたところ、有機溶媒濃度がある程度高いところで、JHBP は JH を結合しなくなることがわかりました。このことから、JHBP と JH の複合体が標的細胞に到達すると、細胞膜近傍の誘電率の低下した疎水性の高い環境を感知して JH が複合体から解離することが明らかになりました。以上の結果を統合して、JHBP による血液中での JH 送達の分子構造メカニズムが解明できました。

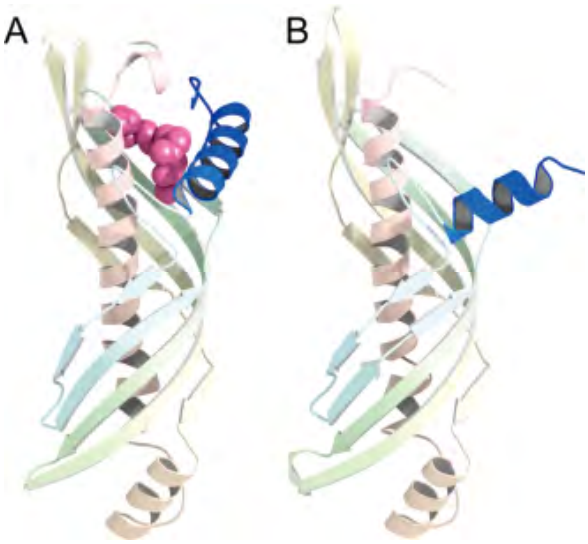

図 1 .(A)JHBP-JH 複合体と(B)JHBP 単体の結晶構造

4 まとめ

JHBP-JH 複合体の立体構造決定に成功したことにより、ホルモンとタンパク質の相互作用の仕組みが原子レベルで明らかとなりました。この立体構造情報を利用することで昆虫制御剤の精密な設計が可能になり、新たな農薬の開発が加速されるものと期待されます。また、本研究成果は昆虫の生活環の様々な局面で重要な役割を担っている JH のシグナル伝達について構造的知見を提供する初めての報告になります。[2]

謝辞

X 線データ測定においては PF スタッフの方々に大変お世話になりました。ここに感謝致します。

参考文献

[1] R. Suzuki, Z. Fujimoto, T. Shiotsuki, W. Tsuchiya, M. Momma, A. Tase, M. Miyazawa, and T. Yamazaki, *Sci. Rep.* **1** (2011) 133. DOI:10.1038/srep00133.

[2]http://www.natureasia.com/japan/srep/highlights/srep00133.php

* zui@nias.affrc.go.jp

17A/2008G628

ヒト NUDT5 の 予期せぬ基質認識と触媒反応機構
Unexpected substrate recognition and catalytic reaction mechanisms

有森貴夫 [1,2], 山縣ゆり子 [1*]
[1] 熊本大学大学院薬学教育部、〒862-0973 熊本市中央区大江本町 5-1
[2] 日本原子力研究開発機構量子ビーム応用研究部門　〒319-1195 東海村白方白根 2-4

1 はじめに

ヒト NUDT5 は，変異原性ヌクレオチドとして重要な 8-oxo-dGDP をはじめとする様々な酸化損傷ヌクレオシド二リン酸を加水分解し，DNA の突然変異の抑制に寄与している一方で，タンパク質の翻訳後修飾に関与する ADP-ribose などの ADP-sugar に対しても加水分解活性を示し，幅広く細胞内の浄化に貢献していると考えられている．NUDT5 の基質はいずれもヌクレオシド二リン酸を基本骨格としており，触媒反応により二つのリン酸基の間の結合が切断されるが，このピロリン酸部以外の化学構造には多様性があり，NUDT5 が如何にして様々な基質を認識し，加水分解するのかは不明であった．そこで我々は，X 線結晶構造解析と同位体ラベル化法による求核攻撃部位の特定を行い，NUDT5 の幅広い基質特異性獲得機構と加水分解反応機構を原子レベルで解明することに成功した[1].

2 実験

共結晶化法により NUDT5 と 8-oxo-dGDP（基質），8-oxo-dGMP（生成物），8-oxo-dADP（基質）の複合体結晶の取得に成功し，それぞれ 2.1，2.3，2.05 Å分解能で結晶構造を決定した．なお、回折データは PF と SPring-8 で収集した．また，^{18}O ラベル化水存在下で NUDT5 による 8-oxo-dGDP および ADP-ribose の加水分解反応を行い，その反応溶液の ^{31}P NMR スペクトルを測定することで，両基質が NUDT5 により加水分解される過程で水分子による求核攻撃を受けるリン原子を特定した（同位体ラベル化法）．

3 結果および考察

NUDT5/8-oxo-dGDP 複合体と，過去に報告された NUDT5/ADP-ribose 複合体[2]の結晶構造中に観測された基質の認識機構を比較したところ，両基質の構造が異なり，8-oxo-dGDP は Z 型，ADP-ribose は馬蹄型をとり、塩基部位の結合様式にも相違が見られただけでなく，さらに触媒反応を受けるピロリン酸部の α 位と β 位のリン酸基の結合位置が全く逆転していた（図１）．この結果から，NUDT5 によるこれらの基質の加水分解反応においては，基質および反応生成物の化学構造が類似しているにもかかわらず，求核攻撃を受けるリン原子が異なることが示唆された．そこで，同位体ラベル化法により触媒反応時の求核攻撃部位の特定を行い，8-oxo-dGDP と

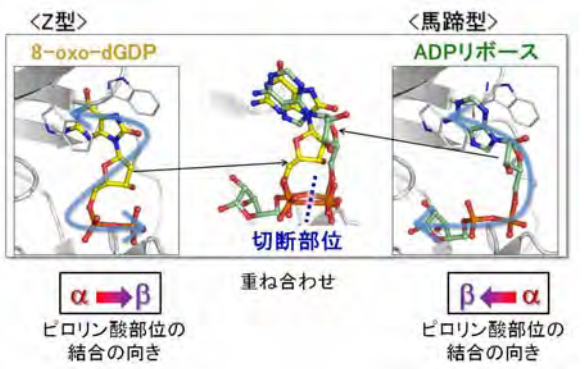

図１　8-oxo-dGDP と ADP-ribose の結合の比較

ADP-ribose では攻撃部位が異なる（8-oxo-dGDP は β 位，ADP-ribose は α 位のリンが攻撃を受ける）ことを証明した（図２）．これらの結果から，NUDT5 の幅広い基質特異性は，化学構造が異なる塩基部位のみならず，化学構造が同じで触媒反応を受けるピロリン酸部位まで結合様式を変化させることで獲得しているという我々が知る限り酵素で初めての知見が得られた．

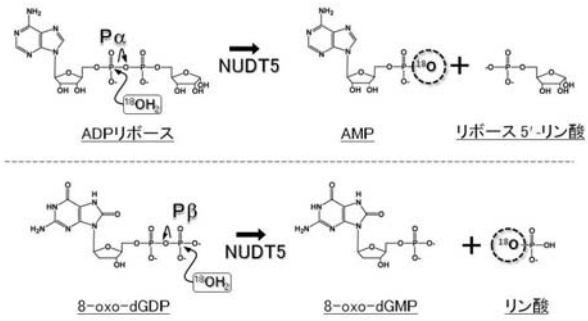

図２　求核攻撃を受けるリン原子の比較

謝辞

X 線回折実験を行うにあたり，ご協力頂きました PF ならびに Spring-8 のスタッフの方々に感謝申し上げます.

参考文献

[1] T. Arimori *et al*., Nucleic Acid Res. 39 (2011) 8972.
[2] M. Zha et al., J. Mol. Biol. 379 (2008) 568

*yamagata@gpo.kumamoto-u.ac.jp

5A, NW12A, BL41XU/2008G690/2009G637/2008S2-001

Crystal Structure of Arl1 in complex with Arfaptin-2 BAR domain

Kensuke Nakamura[1,2], Zhiqiu Man[3], Yong Xie[1,5], Ayako Hanai[3], Hisayoshi Makyio[1], Masato Kawasaki[1,2], Ryuichi Kato[1,2], Hye-Won Shin[3,4], Kazuhisa Nakayama[3], Soichi Wakatsuki [1,2,*]

[1]Structural Biology Research Center, Photon Factory, Tsukuba, Ibaraki 305-0801
[2]Graduate University for Advanced Studies, Tsukuba, Ibaraki 305-0801
[3]Graduate School of Pharmaceutical Sciences, Kyoto University, Sakyo-ku, Kyoto 606-8501
[4]Career-Path Promotion Unit for Young Life Scientists, Kyoto University, Sakyo-ku, Kyoto 606-8501
[5]Institute of Medicinal Plant, Chinese Academy of Medical Sciences & Peking Union Medical College, Haidian Distinct, Beijing, 100193, China

1 Introduction

We have recently shown that Arfaptin-2, which was originally identified as a binding partner for the Arf and Rac1 GTPases, binds to Arl1 through its BAR domain and is recruited onto Golgi membranes [1]. There, Arfaptin-2 induces membrane tubules. Here, we report the crystal structure of the Arfaptin-2 BAR homodimer in complex with two Arl1 molecules bound symmetrically to each side, leaving the concave face open for membrane association.

2 Experiment

In this study, Arl1 and Arfaptin-2 BAR domain was overexpressed in *Escherichia coli*, purified to homogeneity, and crystallized by the sitting- drop vapor diffusion method using PEG3350 as a precipitant [2].

3 Results and Discussion

The crystals of Arl1-Gpp(NH)p-Arfaptin-2 BAR domain were screened at BL5A, BL17A, NW12A and NE3A of PF/PF-AR at KEK and the final data set was collected at the BL41XU at SPring-8 (Table 1). The diffraction data were processed using the HKL2000 program. The crystal structure was determined by the MR method using the structures of Arl1 from PDBID:1UPT and Arfaptin-2 from PDBID:1I49 as search models.

The asymmetric unit of the crystal contained an Arfaptin-2 BAR homodimer flanked by two Arl1 molecules (Figure 1). The dimeric structure of Arfaptin-2 BAR in the complex closely resembles the previously reported structure of the free form (PDBID:1I49). Each Arfaptin-2 BAR monomer unit comprises an antiparallel three-helix bundle. The two Arl1 molecules bind symmetrically to each Arfaptin-2 BAR monomer, around the kinks of the two helices.

The N-terminal amphipathic helical region of Arl1 (residues 1–13), which was removed in our con- struct for crystallization, is expected to adopt the same orientation as the concave face of the Arfaptin-2 BAR dimer. Because the amphipathic helix, along with the N-terminal attached myristoyl moiety, participates in membrane anchoring of Arl1, the crystal structure indicates that the two Arl1 molecules facilitate the direct association of the concave face of the Arfaptin-2 dimer with membranes.

This is the first crystal structure to reveal the modulation of BAR domain by Small GTPase.

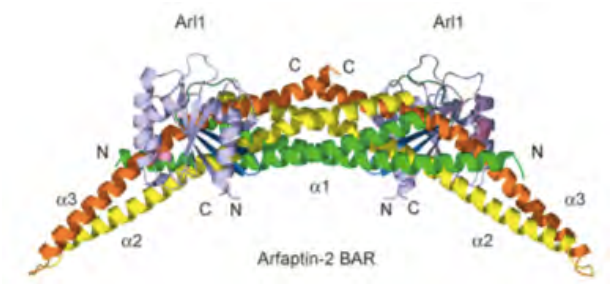

Fig. 1: The overall structure of Arl1 in complex with Arfaptin-2 BAR domain.

Table 1 Crystallographic summary

Crystal form	Arl1-Gpp(NH)p-Arfaptin-2 BAR
Crystal size (mm)	0.1x0.05x0.05
Xray source	SPring8
Beamline	BL41XU
Oscillation angle (°)	1
Exposure time	5
Wavelength (Å)	1.0000
Temperature (K)	95
Space group	P212121
a, *b*, *c* (Å)	62.7,111.1,119.8
Resolution (Å)	43.3-3.0(3.1-3.0)
R_{sym} or R_{merge}	9.4(46.2)
$I / \sigma I$	11.4(2.4)
Completeness (%)	96.5(93.4)
Redundancy	3.5(3.4)
R_{work} / R_{free}	26.2/33.3

References

[1] Z. Man, *et al.*, JBC (2011) **286** 11569 –11578
[2] K. Nakamura, *et al.*, JBC (2012) **287** in press
* soichi.wakatsuki@kek.jp

corresponding site of the other molecule. The structural superposition of BoNT/A – GT1b complex showed that the electron density overlapped onto the GT1b in the structure of BoNT/A, suggesting that the observed electron density corresponds to bound 3'-siallyllactose. However, we could not construct a model of 3'-sialyllactose, as the observed electron density was too small and ambiguous.

To confirm that the observed electron density was derived from 3'-sialyllactose, crystals of apo form OFD05HC was prepared under similar conditions in which MES buffer and magnesium sulfate were used, and the structure was determined at a resolution of 3.1 Å [2]. No electron density was observed around the GBS, although the structures of OFD05HC were quite similar (RMSD 0.29 and 0.62 Å over 418 Cα atoms for two molecules in an asymmetric unit, respectively). These results confirmed that the electron density observed in the complex structure was derived from 3'-sialyllactose. The side chains as well as the main chains around GBS of the apo and complex forms were superposed well, suggesting that no major structural changes occurred after binding with 3'-sialyllactose.

Acknowledgement

We thank the PF staff for help with data collection.

References

[1] N. Nuemket *et al.*, Biochem. Biophys. Res. Commun. **41** (2011) 433.
[2] N. Nuemket *et al.*, Acta Crystal. Sect. F Struct. Biol. Cryst. Commun. **66** (2010) 608.

* tanaka@sci.hokudai.ac.jp

5A/2009G-186

脂肪酸分解に関わる転写因子の構造解析
Structure analyses of a transcription factor involved in fatty acid degradation

藤橋雅宏*, 中谷大河, 三木邦夫
京都大学大学院理学研究科 〒606-8502 京都市左京区北白川追分町

1 はじめに

枯草菌由来の転写因子 $FadR_{Bs}$ は、脂肪酸分解に関わることが知られている。この因子は TetR superfamily に属し、脂肪酸のβ酸化に関わる遺伝子群で構成されるオペロンの転写を抑制しているが、dodecyl-CoA(脂肪鎖の炭素数 12)よりも長い脂肪鎖をもつ acyl-CoA と結合する事により、DNA との結合能を失う。脂肪酸のβ酸化に関わる遺伝子群の転写は、$FadR_{Bs}$ が acyl-CoA との結合により DNA から解離することで開始される。同様の働きを行う転写因子として、大腸菌の $FadR_{Es}$ 等も知られているが、$FadR_{Es}$ は脂肪酸の合成と分解の両方を制御するのに対し、$FadR_{Bs}$ は脂肪酸分解のみの制御を担っている。

本研究ではこの因子の転写制御機構を明らかにするために、DNA 結合能をもつ活性型と、acyl-CoA を結合し DNA との結合能を失った不活性型の構造解析を行った。

2 実験

$FadR_{Bs}$ の結晶は、活性型・不活性型とも、PEG3350 または PEG4000 を主な沈殿剤とした結晶化条件で得た。不活性型の調製は、炭素数 14 個の脂肪鎖をもつ stearoyl-CoA を $FadR_{Bs}$ に混合することで行った。X 線回折データは、BL5A で収集した。活性型の結晶は空間群 $P2_12_12_1$ に属し、格子定数は a = 56.2 Å, b = 66.1 Å, c = 99.0 Å であった。分解能は 2.15 Å であった。stearoyl-CoA を結合した不活性型の結晶も、空間群 $P2_12_12_1$ に属していたが、格子定数は a = 70.3 Å, b = 88.8 Å, c = 199.9 Å と大幅に異なるものであった。分解能は活性型とほぼ同じ 2.20 Å の回折データが得られた。

3 結果および考察

位相決定は類似配列をもつ転写因子の構造をモデル分子とした分子置換法によって得た。活性型 $FadR_{Bs}$ 結晶の非対称単位には、転写制御因子の基本単位である二量体が存在した。不活性型 $FadR_{Bs}$ 結晶の非対称単位には、二量体が三分子存在していた。活性型の構造は R/R_{free} 因子 23.5%/28.5%まで、不活性型の構造は R/R_{free} 因子 23.3%/28.2%まで精密化した。

得られた $FadR_{Bs}$ の全体構造を下図左に示す。構造は N 末及び C 末の二つのドメインに分かれており、DNA との結合に関わるのは N 末領域である。$FadR_{Bs}$ を不活性型に変換する stearoyl-CoA は、C 末ドメインの内部に結合していた。活性型・不活性型の二つの構造を、C 末ドメインを基準に重ねると、N 末ドメインが開くような構造変化が見られる(下図右)。この構造変化が DNA への結合能を制御していると考えられる。現在、さらに詳しい情報を得るため、DNA 複合体の結晶構造解析を検討している。

*mfuji@kuchem.kyoto-u.ac.jp

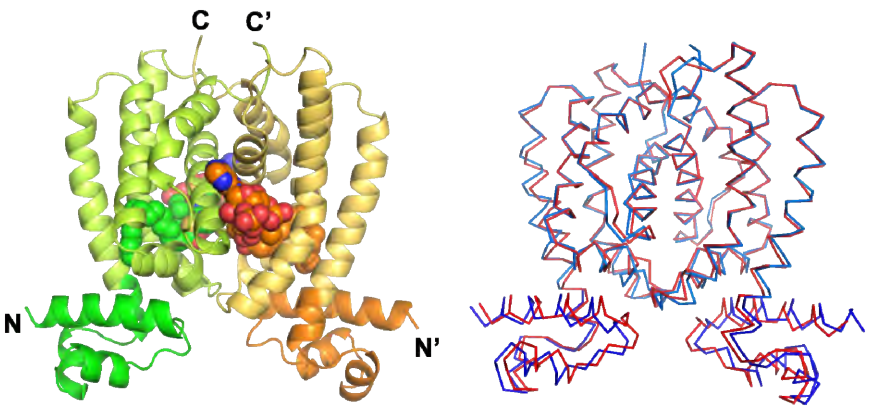

図左: $FadR_{Bs}$(活性型)の全体構造。二量体を構成するそれぞれのサブユニットを、緑、オレンジで示す。それぞれのサブユニット内の濃色・淡色は、N 末・C 末ドメインを示す。sphere model で示しているのは、$FadR_{Bs}$ に結合している stearoyl-CoA。
図右: DNA に結合可能な活性型(赤)、結合できない不活性型(青)構造の重ね合わせ。acyl-CoA が結合する事により、不活性型では N 末ドメインが両側に開くと考えられる。

17A, 5A, AR-NE3A, AR-NW12A/2009G501

Binding and Selectivity of the Marine Toxin Neodysiherbaine A, and its Synthetic Analogues, to GluK1 and GluK2 Kainate Receptors

Masaki Unno,[‖,†,‡,*] Ryuichi Sakai,[#] Makoto Sasaki,[|] and Masao Ikeda-Saito[†,‡,*]
‖ Frontier Research Center for Applied Atomic Sciences, Ibaraki University, Ibaraki 319-1106, Japan
†Institute of Multidisciplinary Research for Advanced Materials, Tohoku University, Sendai 980-8577, Japan
‡RIKEN SPring-8 Center, Harima Institute, Hyogo 679-5148, Japan,
#Graduate School of Fisheries Sciences, Hokkaido University, Hakodate 041-8611, Japan
|Graduate School of Life Sciences, Tohoku University, Katahira, Aoba, Sendai 980-8577, Japan

1 Introduction

Ionotropic glutamate receptors (iGluRs) are synaptic receptors that form L-glutamate-gated ion channels and play central roles in excitatory neurotransmission in the mammalian central nervous system. Pharmacologically, iGluRs are classified into three broad subfamilies: NMDA (*N*-methyl-D-aspartate), AMPA (α-amino-3-hydroxy-5-methyl-4-isoxazolepropionate), and kainate receptors (KARs). The iGluR subfamily is comprised of a total of eighteen proteins. Isoforms within each subfamily assemble into homo- or heteromeric oligomers in certain combination in order to form functional ion channels. Thus, functional synaptic receptors are highly diverse and inherently difficult to characterize.

Dysiherbaine (DH) and neodysiherbaine A (NDH), isolated from the marine sponge *Lendenfeldia chondrodes*, provide a particularly interesting example of such a molecule. DH and NDH have been shown to be potent convulsants in mice and have been characterized as potent agonists for KARs. DH has also been shown to bind selectively and to have unusually high affinity for both GluK1 (formerly known as GluR5) and GluK2 (GluR6) KAR isoforms, and can selectively activate subunits in some heteromeric receptor complexes. Thus, DH, NDH and their analogues may serve as interesting tools which characterize neuronal KARs in detail.

Structurally, DH and NDH contain a shared template, consisting of a *cis*-fused hexahydrofuro[3,2-*b*]pyran ring system with two functional groups at the C_8 and C_9 positions, in addition to a glutamate substructure. Since relatively small differences in the functional groups at C_8 were found to impart significant effects upon binding affinity and selectivity, as revealed by comparing the activity of DH and NDH, a series of NDH analogues including 8-deoxy-NDH, 9-deoxy-NDH, and 8,9-dideoxy-NDH (MSVIII-19), were synthesized. DH and NDH also bind strongly to GluK2, although 8-deoxy-NDH has a much lower affinity for GluK2 than those of DH and NDH. Furthermore, 9-deoxy-NDH and MSVIII-19 do not bind to GluK2. These binding profiles are rather unexpected considering the structural similarity of both ligands and receptors, where GluK1 and GluK2 have 74 % and 87 % identity overall in terms of ligand-binding core sequence identity, respectively. It has been shown that DH, NDH and 8-deoxy-NDH are full or efficient agonists for GluK1, while 9-deoxy-NDH is only a partial agonist. Most interest is that MSVIII-19 acts as a potential antagonist for GluK1. Furthermore, MSVIII-19 induced a coma-like sleeping state in mice when administrated intracerebroventricularly, rather than induce convulsions. Previously antagonists have been proposed to stabilize an "open" rather than "closed" state of the receptor-ligand complex. These drastic changes in the mode of activity and isoform selectivity, as a result of only a relatively small change in the functional group observed in NDH analogues, are intriguing issues to explore further.

2 Experiment

See PF Activity Report 2009 #27 Part B or [1].

3 Results and Discussion

We determined the structure of the human GluK1-S1S2 (hGluK1-S1S2) in complex with DH, NDH, MSVIII-19, 8-deoxy-NDH, and 9-deoxy-NDH, and obtained the structures at 1.5 Å resolution. In addition, we also obtained the structure of hGluK1-S1S2 complex with L-glutamate at 1.65 Å resolution. Finally, we determined the crystal structure of the human GluK2-S1S2 (hGluK2-S1S2) in complex with NDH. We found that differences in three amino acids (Thr503, Ser706, and Ser726 in GluK1 and Ala487, Asn690, and Thr710 in GluK2) in the ligand-binding pocket generate differences in the binding modes of NDH to GluK1 and GluK2. Furthermore, deletion of the C_9 hydroxy group in NDH alters the ligand conformation such that it is no longer suited for binding to the GluK1 ligand-binding pocket. In GluK2, NDH pushes and rotates the side chain of Asn690 (substituted for Ser706 in GluK1), and disrupts an interdomain hydrogen bond with Glu409. The present data supports the idea that receptor selectivities of DH analogues resulted from the differences in the binding modes of the ligands in GluK1/2 and the steric repulsion of Asn690 in GluK2. All ligands, regardless of agonist efficacy, induced full domain closure. Consequently, ligand efficacy and domain closure did not directly coincide with DH analogues and the kainate receptors.

References

[1] M. Unno *et al.*, *J. Mol. Biol.* **413** (2011) 667-683.

*unno19@mx.ibaraki.ac.jp

5A, 17A, NW12A, NE3A/2009G512, 2011G504, 2011A1873

X-ray structure of L-ribose isomerase from *Acinetobacter* sp.

Hiromi Yoshida[1*], Misa Teraoka[1], Akihide Yoshihara[2], Ken Izumori[2], Shigehiro Kamitori[1]
[1]Life Science Research Center and Faculty of Medicine, Kagawa University, Miki-cho, Kita-gun, Kagawa 761-0793, Japan
[2]Rare Sugar Research Center, Kagawa University, Miki-cho, Kita-gun, Kagawa 761-0795, Japan

1 Introduction

Acinetobacter sp. L-ribose isomerase (L-RI) catalyzes a reversible isomerization between L-ribose and L-ribulose. It has been reported as a new enzyme by Shimonishi and Izumori [1], since there was no sequence similarity to known amino acid sequences of available data bases. In previous study, we have succeeded in overexpression, purification and crystallization of recombinant his-tagged L-RI [2]. Here we determined the crystal structure of his-tagged L-RI by using selenomethionine-substituted L-RI.

2 Experiment

The expression and purification of *Acinetobacter* sp. his-tagged L-RI has already been reported [2]. The selenomethionine-substituted his-tagged L-RI (SeMet L-RI) was also prepared in the same manner as his-tagged L-RI but using *E. coli* B834 cells grown in LeMaster broth. By the hanging-drop vapor-diffusion method, crystals of SeMet L-RI were grown in a droplet mixing 2 µl of protein solution (11.5 mg ml^{-1} in 5 mM Tris-HCl, pH 7.5) and 2 µl of reservoir solution (0.2 M NaCl, 20 % (v/v) PEG 400 and 0.1 M HEPES pH 7.5) against 450 µl of the reservoir solution at 293 K. For his-tagged L-RI, the reservoir solution containing additional 10 mM hexaamine cobalt chloride was used. A crystal of SeMet L-RI mounted in a cryoloop was soaked in crystallization solution containing 30 % (v/v) glycerol and flash-cooled in liquid nitrogen at 100 K. His-tagged L-RI crystal was directly flash-cooled without cryoprotectant. X-ray diffraction data were collected on the PF-AR NW12A beam line in the KEK and on the BL26B1 in SPring-8. Diffraction data were processed using the programs HKL2000 and the CCP4 program suite.

After an initial phase of SeMet L-RI determination by MAD method using the program SOLVE, an initial model was built using the program RESOLVE. Further model building was performed with the programs Coot in CCP4 program suite, and X-fit in the XtalView program system, and the structure was refined using the programs Refmac5 and CNS.

3 Results and Discussion

The structure of L-RI is shown in Fig. 1 (a). L-RI has six α-helices and ten β-strands. The metal ion (Mn^{2+}) bound in the active site is located at a cupin-type beta-barrel, coordinated by Glu124 in β5, His117 and His119 in a loop between β4 and β5, His199 in a loop between β8 and β9. The structure of L-RI is similar in structure to that of L-lyxose isomerase from the pathogenic *E. coli* O157:H7 (3MPB). The sequence identity, the r.m.s. deviation for Cα atoms and Z-score of a DALI search between them were 18 %, 2.8 Å and 15.9, respectively.

There are two and one molecules in an asymmetric unit in SeMet L-RI and his-tagged L-RI structures, respectively. Each of them forms tetramer by symmetry operation and that was also suggested by PISA (Fig. 1 (b)), as was reported that L-RI is tetrameric enzyme [1].

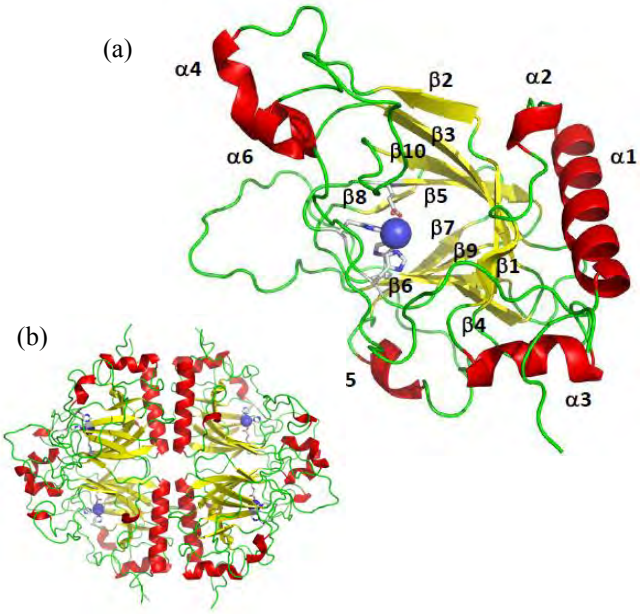

Fig. 1: (a) Monomeric structure and (b) predicted tetrameric structure of his-tagged L-RI.

Acknowledgement

This research was performed with the approval of the Photon Factory Advisory Committee and the National Laboratory for High Energy Physics (2009G512 and 2011G504), and SPring-8 (Priority Program for Disaster-Affected Quantum Beam Facilities 2011A1873), Japan.

References

[1] T. Shimonishi & K. Izumori. J. Ferment. Bioeng. **81** (1996) 493-497.
[2] H. Yoshida *et al.*, Acta Crystallogr. F**67** (2011) 1281-1284.

* h.yoshi@med.kagawa-u.ac.jp

5A, NW-12A, NE-3A/2009G517

Crystal structures of *Burkholderia thailandensis* nucleoside kinase: insights into catalytic mechanism and nucleoside selectivity

Yoshiaki Yasutake[1,*], Hiroko Ota[2], Emisa Hino[2], Shin-ichi Sakasegawa[2] and Tomohiro Tamura[1, 3]
[1]Bioproduction Research Institute, National Institute of Advanced Industrial Science and Technology (AIST), Sapporo 062-8517, Japan
[2]Asahi Kasei Pharma Corporation, Shizuoka 410-2321, Japan
[3]Graduate School of Agriculture, Hokkaido University 060-8589, Japan

1 Introduction

Mizoribine (MZR) is a purine nucleoside analogue, and is currently used as an immunosuppressant after renal transplantation, for lupus nephritis, rheumatoid arthritis, and primary nephritic syndrome. MZR is rapidly absorbed and phosphorylated to mizoribine 5′-monophosphate (MZR-P) intracellularly by adenosine (ADO) kinase. MZR-P acts as a competitive inhibitor of inosine 5′-monophosphate dehydrogenase (IMPDH) and guanosine monophosphate synthetase, which are crucial for *de novo* nucleic acid biosynthesis. Because proliferation of T and B cells highly depends on the *de novo* DNA synthesis pathway, MZR-P exhibits immunosuppressive activity. However, MZR dosage should be determined by measuring MZR levels in serum to avoid negative effects.

Nucleoside kinase from *Burkholderia thailandensis* (BthNK; UniProt code, Q2SZE4) belongs to the phosphofructokinase B (Pfk-B) family and catalyzes the phosphorylation of MZR by using ATP as a phosphoryl donor [1]. Among various bacterial ribokinase and ADO kinase homologues tested, BthNK is the only enzyme that effectively converts MZR to MZR-P, and is currently applied to a clinical assay for blood MZR level. To understand the catalytic and MZR binding mechanism, we have undertaken the crystallographic studies on BthNK.

2 Experiment

The expression of BthNK in *Escherichia coli* inhibited cell growth, probably due to the harmful influence of BthNK on the nucleotide metabolism of *E. coli*. Thus, *R. erythropolis* was used as a heterologous expression host [1]. His-tagged BthNK was purified by Ni-affinity chromatography. All crystals were obtained by the hanging-drop vapor-diffusion method at 20°C. The structures were solved by Br-SAD method. The detail experimental procedures were previously described [2].

3 Results and Discussion

The crystal structures of BthNK was determined in ligand-free form, and in complex with inosine, inosine-ADP, MZR-ADP, AMP-Mg-AMP at 2.1-1.55 Å resolution. The structures revealed that typical homodimeric architecture of Pfk-B enzymes in three distinct conformational states: asymmetric dimer with one subunit in an open conformation and the other in a closed conformation (ligand-free form), closed conformation (binary complex with inosine), and fully closed conformation (other ternary and quaternary complexes) (Fig. 1). The previously unreported fully closed structures suggest the possibility that Mg^{2+} might directly interact with the β- and γ-phosphate of ATP to maintain the neutralization of the negative charge throughout the catalytic reaction (Fig. 2). The nucleoside complex structures also indicated that the base moiety of the bound nucleoside is partly exposed to the solvent, enabling the recognition of a wide range of nucleoside bases. Gly170 is responsible for the solvent accessibility of the base moiety and is assumed to be a key residue for the broad nucleoside recognition of BthNK. Site-directed mutagenesis study also supported the importance of Gly170 for broad nucleoside specificity of BthNK.

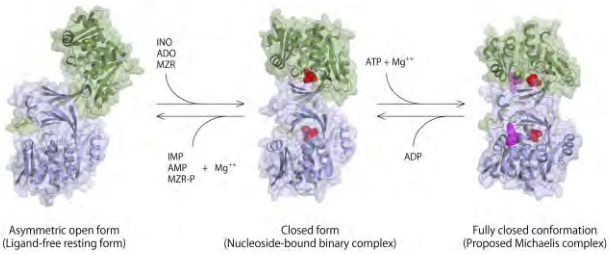

Fig. 1: Three distinct conformational states of BthNK.

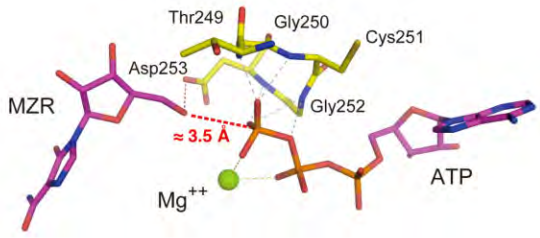

Fig. 2: Putative ES complex model of BthNK.

References

[1] Ota, H., Sakasegawa, S., Yasuda, Y., Imamura, S. & Tamura, T. (2008). *FEBS J.* **275**, 5865–5872.
[2] Yasutake, Y., Ota H., Hino, E., Sakasegawa, S. & Tamura T. (2011). *Acta Crystallogr.* **D67**, 945–956.

* y-yasutake@aist.go.jp

15A/2009G561 及び Spring-8 BL45XU/2011A1920

平滑筋フィラメント格子構造定量解析の試み

Quantitative analysis of lattice like structure of smooth muscles

渡辺　賢 [1*], 石田行知 [2], 木村雅子 [3],竹森　重 [3], 湯本正寿 [3]

[1] 首都大学東京・人間健康科学研究科、〒116-8551 荒川区東尾久７－２－１０

[2] 文京学院大学・保険医療技術学部　〒356-8533 埼玉県ふじみ野市亀久保 1196

[3] 東京慈恵会医科大学・分子生理学講座　〒105-8461　東京都港区西新橋 3-25-8

1 はじめに

内臓器官の「うごき」を司る平滑筋細胞の収縮弛緩は、太いフィラメント（重合したミオシン）と、細いフィラメント（重合したアクチンに制御タンパク質が結合したもの）の滑り合いの程度によって調節されるのみならず、ミオシンやアクチンの重合・脱重合に伴う細胞内分布の量的・空間的変化―リモデリング―によっても調節されている。この様な筋収縮タンパク質フィラメントのダイナミックな振る舞いは、特に血管攣縮・気管支喘息などの病的平滑筋収縮に関与することが指摘されており、主にリモデリングにかかわる細胞内情報伝達機構に関心が集まっている。しかし、リモデリングによる平滑筋細胞内の筋フィラメント構造変化の実態は未だ不明である。その一つの理由として、平滑筋細胞では収縮フィラメント構造が散在しており、標本固定等の操作によりフィラメント構造そのものの変化が起こる可能性があるため、電子顕微鏡観察や生化学的手法による詳細な解析が困難であることが挙げられる。一方 X 線回折法は、筋フィラメント構造を「生きたまま」経時的に観察できる手法ではあるが、脊椎動物の平滑筋から得られる X 線回折像は極めて微弱であり定量的な解析が困難であると考えられてきた。

本研究代表者らは平滑筋収縮フィラメント構造変化そのものを探ることを目的として、シンクロトロン放射光の輝度の強い X 線の利用によりモルモット盲腸紐標本から経時的に X 線小角散乱像を得ることに成功した。そして、平滑筋細胞の筋収縮フィラメント構造動態観察を、主に子午反射強度変化を指標にして行ってきた。最近、盲腸紐標本に放射光を照射した際に得られる小角散乱像のうち幅広の赤道反射が、従来いわれてきた 11-12 nm 周期の細いフィラメント格子様配列のみではなく、13.5 nm 付近、22 nm 付近にピークを持つ 2 種類の未知の反射も存在するという結果を得た。この事実は、平滑筋組織に細いフィラメントもしくは別のフィラメント由来の未知の格子構造が存在することを示唆する。しかし、その格子構造の実態は現在のところ全く不明であり、その解明には収縮・弛緩・硬直サイクルによる構造変化を詳細に検討する必要がある。

これを受けて本申請課題では、モルモット盲腸紐の細胞膜を化学的に破壊したスキンド標本を用いて、収縮・弛緩・硬直に伴う赤道反射の変化を定量的に解析することを具体的な研究目的とした。

2 実験

１）筋標本作成　実験当日又は前日に代表者の所属機関でモルモットから盲腸紐を摘出し、放射光実験施設へ搬入した。搬入後直ちに β-escin 処理により筋の細胞膜を破壊してスキンド標本を作製、その後、標本を回折用チャンバーに取り付け、人工細胞内液灌流下に標本の力学応答を測定し、平滑筋の活動状態を安定化した

２）X 線回折実験　a)標本をチャンバーに固定し、30℃の実験条件で人工細胞内液を灌流した状態でイメージングプレートに X 線回折像を記録した。 更に、 溶液条件を ATP を除去した硬直条件、又、Ca^{2+}を添加して収縮を起こす条件、に変え、X 線回折像の変化を見積もった。Radiation damage を防ぐため、電動ステージ上に標本チャンバーを固定し、照射位置を移動させた。

全ての記録画像は施設内の BAS-2500 で読み取り、電子メディアに保存し、研究代表者または共同研究者の所属機関で解析し、赤道反射ピークの位置と大きさの経時変化を定量的に算出した。。同時に測定した力学応答から、収縮及び硬直条件における、構造―力学応答関係を検討した。

3 結果および考察

盲腸紐標本を Ca^{2+}で収縮させた際に、赤道反射強度の増強が観察された。一方、硬直条件では赤道反射強度の減弱が観察され、弛緩条件に戻すことにより、一部回復した。現在までの解析の結果、14nm と 20nm にピークを持つ赤道反射の強度比の低下が硬直条件によく対応しており、筋フィラメント格子様構造が、筋硬直条件では撹乱していることが示唆された。

謝辞

被災量子ビーム施設ユーザー支援課題 2011A1920（受理番号：18847）として、本研究の一部の実験を Spring-8BL-45 小角散乱ステーションにて、実施致しました。関係各位のご厚意に厚く御礼申し上げます。

5A,17A/2009G577,2011A1875

Sensing actin dynamics: Structural basis for G-actin-sensitive nuclear import of MAL

Hidemi Hirano[1,2] and Yoshiyuki Matsuura[*1,2]
[1]Division of Biological Science and [2]Structural Biology Research Center, Graduate School of Science, Nagoya University, Furo-cho, Chikusa-ku, Nagoya, Japan

1 Introduction

The coordination of cytoskeletal actin dynamics with gene expression reprogramming is emerging as a crucial mechanism to control diverse cellular processes, including cell migration, differentiation and neuronal circuit assembly. The actin-binding transcriptional coactivator MAL (also known as MRTF-A/MKL1/BSAC) senses G-actin concentration and transduces Rho GTPase signals to serum response factor (SRF) [1]. MAL rapidly shuttles between the cytoplasm and the nucleus in unstimulated cells but Rho-induced depletion of G-actin leads to MAL nuclear accumulation and activation of transcription of SRF:MAL-target genes. MAL is implicated in human diseases: MAL was originally discovered as a gene fusion in patients with acute megakaryocytic leukemia, and defective regulation of MAL contributes to cancer cell migration and invasion.

MAL has a multi-domain structure containing an N-terminal actin-binding RPEL domain, a central SRF-binding domain, and a C-terminal transcription activation domain. The N-terminal domain has three tandem repeats (each containing the RPxxxEL sequence motif) in the amino acid sequence. The N-terminal domain is necessary and sufficient for Rho-regulated nuclear accumulation in mouse fibroblast [2]. Herein we report a crystal structure of MAL N-terminal domain in complex with nuclear import receptor (Impα). We also determined a crystal structure of MAL N-terminal domain in complex with five molecules of G-actin. The structures reveal how nuclear import machinery interacts with MAL in a way that responds to changes in G-actin concentrations [3].

2 Experiment

Crystals of MAL-Impα complex and MAL-actin complex were grown by hanging drop vapour diffusion method. X-ray diffraction datasets were collected at Photon Factory and SPring-8 beamlines. The structures of MAL-Impα complex and MAL-actin complex were solved by molecular replacement at a resolution of 2.10 Å and 3.45 Å, respectively.

3 Results and Discussion

The structure of MAL-Impα complex was refined to R_{free} 20.80 % (R_{cryst} 16.60%). The structure shows that MAL has a classical bipartite nuclear localization signal (NLS) in the N-terminal 'RPEL' domain (Fig. 1a). The NLS residues of MAL adopts an extended conformation and bind along the surface groove of Impα, interacting with the major- and minor-NLS binding sites.

The MAL-actin complex was refined to R_{free} 27.33 % (R_{cryst} 22.44%). The structure shows that the N-terminal RPEL domain of MAL can bind to five molecules of G-actin (Fig. 1b). In this structure, the crank-shaped MAL meanders through five G-actins, and the NLS residues are surrounded by multiple actins. The folding of MAL in this pentavalent complex is entirely different from that in the MAL-Impα complex. The α-helical conformation of MAL NLS residues in complex with actins is distinct from the extended conformation of the NLS in the MAL-Impα complex, and so is incompatible with Impα-binding. Thus, the induced folding and occlusion of NLS by G-actins can explain why G-actins inhibit nuclear import of MAL.

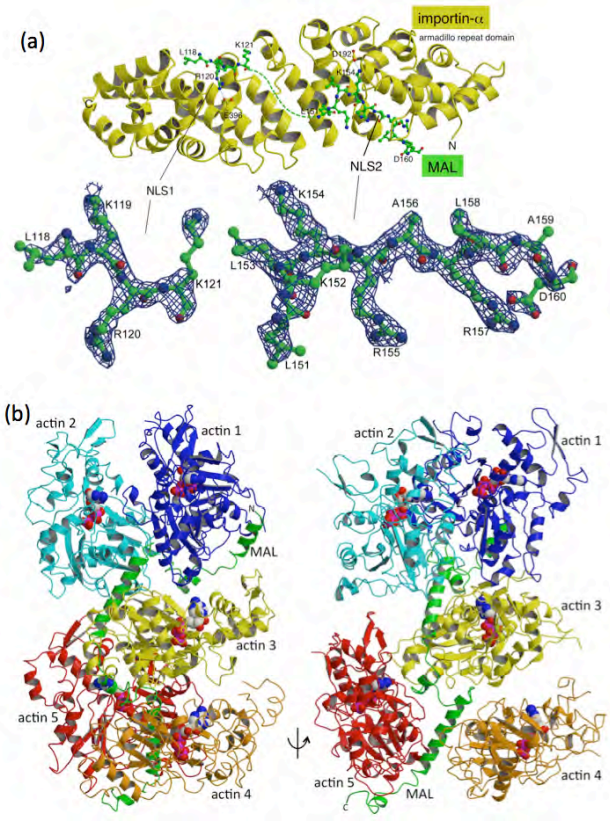

Fig. 1: Overview of the structures of the MAL complexes. (a) MAL-Impα complex. (b) MAL-actin complex.

References

[1] E. N. Olson and A. Nordheim, Nat. Rev. Mol. Cell Biol. **11** (2010) 353.
[2] S. Guettler *et al.*, Mol. Cell. Biol. **28** (2008) 732.
[3] H. Hirano and Y. Matsuura, Biochem. Biophys. Res. Commun. **414** (2011) 373.

* matsuura.yoshiyuki@d.mbox.nagoya-u.ac.jp

先端研究施設共用促進事業
フォトンファクトリーにおける産業利用促進
利用報告書

課 題 番 号： 2009I010
研究責任者： 辻　英一　キッセイ薬品工業株式会社　創薬研究部　創薬基盤研究所
利 用 施 設： 高エネルギー加速器研究機構　放射光科学研究施設　PF AR-NE3A
利 用 期 間： 2010 年　2 月～2010 年　3 月

ヒト由来核内受容体とリガンド複合体の結晶構造解析
Structural studies of human nuclear receptor and their ligand

辻　英一[1]、岡崎　浩輔[1]
Eiichi Tsuji[1], Kosuke Okazaki[2]

[1]キッセイ薬品工業株式会社

アブストラクト：
ヒト由来核内受容体とリガンド複合体の構造解析の為のデータを AR-NE3A を利用して取得した．その結果，リガンド相互作用部位に目的とするリガンドの電子密度を確認出来た．更なる構造精密化を行い，2.4Å 分解能で構造決定した．anti-target の構造と本実験で得られた構造を比較することより，選択性獲得の為のドラッグデザインの指針を得る事が出来た．

Abstract:
Nuclear receptor has a crucial role of hormonal balances or homeostasis within an organism. Here we report the structural studies of human nuclear receptor and their ligand. Data collection was done at PF AR-NE3A beam line and determines the structure at 2.4Å resolution. The obtained structure illustrates the selectivity of binding against anti-target.

キーワード：**蛋白質結晶構造解析，ドラッグデザイン**

１．はじめに：

背景：核内受容体はホルモンバランスなどを含め生体内の恒常性に深く関与している．その受容体と天然リガンドとの相互作用バランスが崩れることでガンや糖尿病などの疾病を引き起こす事が知られており，この受容体への agonist, antagonist の創製は疾病の治療に大きな役割を有している．

目的：ヒト由来の 270 残基からなる核内受容体と公知のアゴニストとの複合体結晶を調整した後，複合体結晶の回折データ収集及び構造解析を行い，リガンドと蛋白の相互作用を解析する．それにより，新規リガンド創製に関する化合物設計に関する情報を取得する．

目標:PF のビームラインを利用することにより，リガンドー蛋白質相互作用が解析可能なデータを取得し，リード化合物探索を推進したいと考えている．しかし，当該蛋白質と公知リガンドとの複合体結晶は未だ得られておらず，構造情報が無い．一方で，当研究グループは PF の利用経験が乏しく，どの程度の結晶であれば目的を達成できるようなデータが取得できるかを把握出来ていない．そこで，トライアルユースの機会を活用し，上記の課題を克服し，解析可能なデータの取得を目指したい．さらには，ビームラインの有効性、及びビームラインでの回折実験の効率性について確認したい．これらのデータは，出発母核構造の選定や，PF 利用の可否の判断等，今後の創薬プロジェクトの方向性を決める上で極めて重要な情報であり，早期に着手して明らかにしたい．

２．実験：

（１） 利用しようとする実験手法
PF の蛋白用 BL を使用し，一定波長による複合体結晶の回折データを取得する（注）．得られたデータをもとに，PDB(Protein Data Bank)に登録されている公知の座標を基にした分子置換法による構造解析を試みる．

（２） 試料
アミノ酸 270 残基からなるヒト由来の核内受容体及び公知化合物
（３） 大きさ
約 200 ~ 400 micron.
（４） 量及び濃度
蛋白質は 4.5mg/ml の濃度である．リガンドは 10mM の濃度である．
（５） 測定
結晶は振動法で測定し，温度は吹き付け低温の－173℃の窒素気流下で実施する．
（６） 要求スペック
分解能は 2.5Å 以上で，高角の redundancy は 5.0 以上を目指す．また，(I)/sigma(I)も全分解能レンジにおいて 10.0 以上を目指す．
（注）リガンドの電子密度を解釈する上で，当該蛋白質とリガンド複合体の結晶の目標とする分解能は 2.5Å 以上と想定しているが，その為には結晶はどの程度の大きさが必要で，どの程度の露光時間が必要であるかを検証したい．また，適切な実験条件が見つかった場合，全データセットを取得し，その解析結果から in vitro assay で既に確認されている活性の強さ，及び anti-target に対しての高選択性獲得の理由を考察し，初期母核構造選定の為のエビデンスを獲得したい．

３．結果および考察：

●データ測定
（１）Crystal 1
露光時間：2.0sec
アッテネータ：Al (700 micron)
結晶の大きさ：400 micron
検出器までの距離：315 mm
振動角度：0.5º
振動範囲：180º
最大分解能：2.46Å
格子定数：a=103.537, b=62.566, c=266.974 (Å), β= 89.977 (º)
空間群：*C*2
HKL2000 による統計値：
Total reflections: 54505
Completeness: 0.964 (0.963) overall (highest shell)
R-factor (square) = 0.109 (50 – 6.65Å)
R-factor (square) = 0.292 (2.49 – 2.46Å)
(I)/sigma (I) = 5.1 (50 – 6.65Å)
Average redundancy = 1.8

（２）Crystal 2
露光時間：1.0sec
アッテネータ：Al (700 micron)
結晶の大きさ：200 micron
検出器までの距離：315mm
最大分解能：2.83Å
当初の目的分解能に到達しなかったので，全フレームは測定していない．
● 構造解析
Crystal 1 のデータを基に，構造解析を行った．分子置換は Phaser[(1)]，構造精密化は REFMAC[(2)] を用いた．
結果
Resolution range: 31.28 – 2.46 Å (54468 reflections)
R/ R-free = 0.233 / 0.267
RMSD bond length (Å): 0.004
RMSD bond angle (º): 0.347
B-factor:

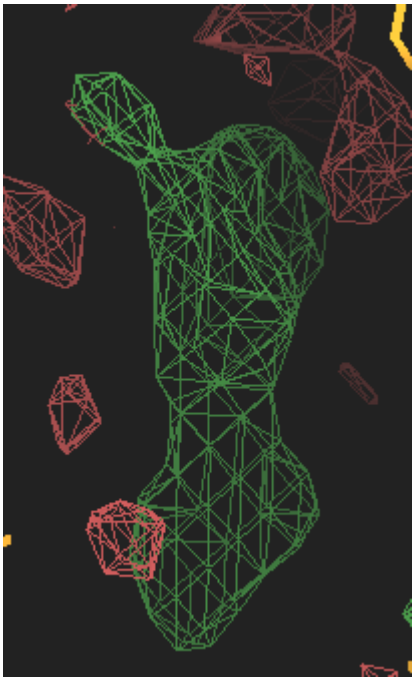

図１：リガンドの電子密度（*Fo*-*Fc* map ; 3.0 σ）

図１に示すようにリガンドの電子密度を捕らえることができ，当初の目的は達成した．また，ある特定の置換基が，anti-target 比較してかさ高さが違うアミノ酸側鎖部分と Van der Waals 相互作用をしている事が確認できた．これが原因で，本化合物は anti-target との選択性を獲得していることが推測できた．
一方，同じバッチから拾った Crystal 2（200 micron）は，予定の分解能には届かなかった．露光時間を長く設定しても，目的とする分解能には到達しなかった．
● 操作性
AR-NE3A の GUI は非常に使い易く，短時間ではあったが，効率的に実験ができた．今回は結晶も少なかったので，マニュアルマウントであったが，次回はサンプルチェンジャーも試用してみたい．

４．まとめ：

我々は本実験で得られた解析結果を，Structure-Based Drug Design による新規リガンド探索の基礎データとして活用した．創薬プロジェクトとしては初期段階の為，事業化，製品化については現時点では未定であるが，選択性獲得の為の基礎データを得ることができた．テーマの初期段階においては，様々な基本構造の違うリガンドと蛋白質複合体の構造を解析する必要がある．出発母核としてどの構造が適切であるかを選定する為には複合体の構造情報は極めて重要であり，本実験により得られた構造データは合成研究者もしくは計算化学研究者へのフィードバックを行った．今後も，PF の継続利用により高品質のデータを取得し，ドラッグデザインのスピードを加速させていきたい．

参考文献

(1) McCoy AJ, Grosse-Kunstleve RW, Adams PD, Winn MD, Storoni LC, Read RJ. J. Appl. Cryst. (2007). 40, 658-674.
(2) G.N. Murshudov, A.A.Vagin and E.J.Dodson, Acta Cryst. D53, (1997), 240-255.

成果発表状況：

学会及び論文発表：該当なし．
特許：該当なし．

NW12A/2010G001

Coprinopsis cinerea 由来セロビオヒドロラーゼ CcCel6A の結晶構造解析
Crystal structure of a cellobiohydrolase, CcCel6A, from *Coprinopsis cinerea*

殿塚隆史*, 田村瑞, 宮崎剛亜, 田中祐太郎, 西河淳, 吉田誠
東京農工大学大学院農学府　〒183-8509 府中市幸町 3-5-8

1 はじめに

糖質加水分解酵素ファミリー（GH）6 に属するセルラーゼは、植物バイオマスの利用に有用な酵素である。GH6 に属する酵素には、エンドグルカナーゼ（EC 3.2.1.4）とセロビオヒドロラーゼ（EC 3.2.1.91）が存在する。このうち、セロビオヒドロラーゼは、セルロースやセロオリゴ糖を非還元末端側から加水分解し、セロビオースを生成させる酵素として知られている。GH6 に属するセロビオヒドロラーゼの立体構造は、糸状菌由来のものしか報告されていなかったが、私達は、担子菌由来の酵素として初めて *Coprinopsis cinerea* よりセロビオヒドロラーゼ CcCel6C の立体構造を報告した[1]。*C. cinerea* は 5 種類の GH6 に属するセルラーゼを生産しており、これらの酵素の構造機能相関に興味が持たれる。今回は、*C. cinerea* 由来の GH6 に属する別のセロビオヒドロラーゼである CcCel6A の触媒ドメインの立体構造を決定したので報告する[2]。

2 実験

CcCel6A の触媒ドメイン（以下単に CcCel6A とする）は、His タグ融合タンパク質として大腸菌で発現させた。精製は Ni-NTA アガロースを用いたアフィニティークロマトグラフィーによった。結晶化は、100 mM HEPES/KOH（pH 7.0 - 7.5）、20 - 25 % ポリエチレングリコール 8000、50 - 200 mM 酢酸マグネシウムをリザーバーとし、CcCel6A とリザーバーを 1:1 で混合した溶液をドロップとした、ハンギングドロップ蒸気拡散法によった。リガンドとの複合体の構造決定のため、結晶をセロビオースおよび *p*-nitrophenyl β-D-cellotrioside（以下 *p*NPG3）の溶液に 5 分間浸した結晶を、回折データ収集に供した。回折データは PF-AR NW12A ビームラインで収集した。データのプロセスは、HKL2000 を用い、構造は、CCP4 の Molrep により、PDB 番号 1BVW を鋳型とした分子置換法によって決定した。構造の精密化は Refmac と Coot によった。

3 結果および考察

CcCel6A のリガンドなしの構造、および CcCel6A-セロビオース、CcCel6A-*p*NPG3 の各複合体の立体構造を決定した。GH6 のセロビオヒドロラーゼの特徴は、活性部位がトンネルの中に存在し、活性部位のトンネルを形成しているループは、オープン型から、リガンドの結合によってクローズ型へ構造変化を起こし、その結果トンネルの幅が狭くなることである。リガンドの結合していない CcCel6A は、オープン型の構造であった。これに対し、CcCel6A-セロビオース、CcCel6A-*p*NPG3 の各複合体ではクローズ型の構造であることが分かった。

特に興味深いのは、CcCel6A-*p*NPG3 である。糖質加水分解酵素は、基質が加水分解される際、加水分解される箇所より非還元末端側の基質と結合している酵素の部位をマイナスサブサイト、還元末端側の基質と結合している酵素の部位をプラスサブサイトと呼ぶ。GH6 のセロビオヒドロラーゼは、活性部位がトンネル構造であることから、基質は、まずプラスサブサイトに結合した後、トンネル中をスライドしマイナスサブサイトに達した後、加水分解を受けると推定される。*p*NPG3 は CcCel6A によって分解されることのない、いわゆる阻害剤である。今回、*p*NPG3 はプラスサブサイトにのみ結合した構造として決定され、マイナスサブサイトには見られないことが判明した（図 1）。このことは、*p*NPG3 はマイナスサブサイトに結合した後、活性部位のトンネル中をスライドすることができず、いわば、酵素反応の途中の状態を反映している構造であると考えられる。

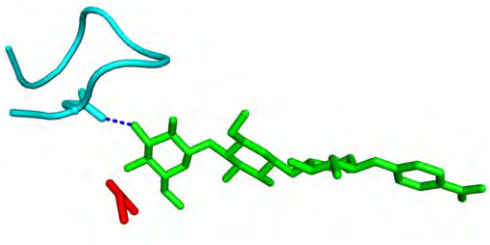

図 1 ：CcCel6A-*p*NPG3 の活性部位付近の構造
水色：トンネルを形成するループと Asp164、緑：*p*NPG3、赤：触媒酸残基（Asp210）、青：水素結合

4 まとめ

本研究では CcCel6A の構造を決定した。特に、CcCel6A-*p*NPG3 において、*p*NPG3 はプラスサブサイトにのみ結合した構造として決定された。

参考文献

[1] Y. Liu *et al.*, FEBS J. **277** (2010) 1532.
[2] M. Tamura *et al.*, FEBS J. **279** (2012) 1871.

* tonozuka@cc.tuat.ac.jp

SPring-8 BL26B2/2011A1881, 2010G001

Coprinopsis cinerea 由来セロビオヒドロラーゼ CcCel6C の構造変化
The structural change in a cellobiohydrolase, CcCel6C, from *Coprinopsis cinerea*

殿塚隆史*, 田村瑞, 宮崎剛亜, 田中祐太郎, 西河淳, 吉田誠
東京農工大学大学院農学府　〒183-8509 府中市幸町 3-5-8

1 はじめに

糖質加水分解酵素ファミリーGH6 に属するセロビオヒドロラーゼは、セルロースの分解に重要な役割を担っている。GH6 のセロビオヒドロラーゼは、活性中心がトンネルの中に存在し、基質が結合することでトンネルを形成するループがオープン型からクローズ型へ構造変化を起こすことが知られている。

私達は、担子菌由来の酵素として初めて *Coprinopsis cinerea* より GH6 に属するセロビオヒドロラーゼ CcCel6C のオープン型の立体構造を報告した[1]。CcCel6C のオープン型の構造を、GH6 に属する他の構造既知のセロビオヒドロラーゼと比較すると、活性中心を形成するトンネルの幅が広いことが判明している。今回、CcCel6C の変異型酵素を構築し、クローズ型の構造を決定した[2]。

2 実験

CcCel6C の活性中心のループの構造変化に最も重要なアミノ酸残基と推定されるアミノ酸残基に変異を導入した酵素、CcCel6C D102A を構築した。Ni-NTA アガロースを用いたアフィニティークロマトグラフィーにより精製し、ハンギングドロップ蒸気拡散法により野生型 CcCel6C とほぼ同様の条件（100 mM HEPES-KOH, pH7.0, 20% PEG）で結晶を得た。回折データは、震災による PF 共同利用実験停止に伴う SPring-8 の課題 2011A1881 により、BL26B2 ビームラインで行った。データのプロセスは HKL2000 を用い、構造は CCP4 の Molrep により、PDB 番号 3A64 を鋳型とした分子置換法によって決定した。構造の精密化は Refmac と Coot によった。

3 結果および考察

CcCel6C D102A の構造を分解能 1.6 Å で決定した。CcCel6C D102A の結晶は空間群 $P2_12_12_1$ であり、野生型 CcCel6C の $P1$ 結晶とは、全く異なる格子定数であった。両者の立体構造を比較したところ、野生型 CcCel6C はオープン型の構造であるのに対し、CcCel6C D102A はクローズ型の構造であることが判明した。

CcCel6C のオープン型からクローズ型へのコンフォメーション変化は、基本的には、私達が最近構造を決定した *C. cinerea* 由来の別のセロビオヒドロラーゼである CcCel6A の、オープン型からクローズ型へのコンフォメーション変化と類似していた。すなわち、活性中心が存在するトンネルを形成するループについて、その構造が変化し、トンネルの幅が狭くなることは同様であった。しかしながら、特筆すべき点は、CcCel6C の構造変化は、CcCel6A や、これまでに立体構造が報告されている糸状菌の GH6 セロビオヒドロラーゼと比較し、はるかに大きな変化であることがあげられる。構造変化を比較するため、Asp115CA、Ser236CA、Asn236CA の 3 つの原子について、これらの 3 点によって作られる角度の変化（図 1）を計算したところ 10.3° であった。これに対し、立体構造が報告されている他の GH6 セロビオヒドロラーゼでは、相当する角度の変化は、0.5～5.3° であった。

図 1 ： CcCel6C の構造変化
緑：CcCel6C 野生型（オープン型）、赤：CcCel6C D102A（クローズ型）、3 つの原子によって作られる角度の変化を示した。

4 まとめ

本研究において、CcCel6C のオープン型とクローズ型の構造は、これまでに立体構造が報告されている GH6 セロビオヒドロラーゼと比較し、はるかに大きな変化であることを明らかにした。*C. cinerea* において、CcCel6A は結晶性セルロースの分解の最も主要な酵素であるのに対し、CcCel6C は、*C. cinerea* において構成的に発現し、その生理学的な役割は異なることが示唆されている。本研究で示された GH6 セロビオヒドロラーゼの構造変化と、酵素の生理学的な役割の関係がより詳細に研究されることが望まれる。

参考文献

[1] Y. Liu *et al*., FEBS J. **277** (2010) 1532.
[2] M. Tamura *et al*., FEBS J. **279** (2012) 1871.

* tonozuka@cc.tuat.ac.jp

PF-BL5A, NSRRC-13B1&13C1/2010G085, SPring-8 BL44XU

Structural determination of GST of the silkworm, *Bombyx mori*.

Kohji Yamamoto[1], Akifumi Higashiura[2], Atsushi Nakagawa[2], Mamoru Suzuki*[2]

[1]Faculty of Agriculture, Kyushu University Graduate School, Fukuoka 812-8581, Japan
[2]Institute for Protein Research, Osaka University, Suita, 565-0871, Japan

1 Introduction

Glutathione S-transferases (GSTs, EC 2.5.1.18) are detoxifying enzymes widely distributed in vertebrates, plants, insects, yeasts and aerobic bacteria. GSTs catalyze the conjugation of reduced glutathione (GSH) to hydrophobic substrates, for example, hormones, herbicides and insecticides [1]. Based on classification system, there have been seven classes of mammalian GSTs, alpha, mu, pi, omega, sigma, theta, and zeta [2]. In case of dipteran insects, six different GST classes, named delta, epsilon, omega, sigma, theta, and zeta [3], have been identified. We have characterized GSTs of the domesticated silkworm, *Bombyx mori*, a lepidopteran model insect [4,5]. In this study, we focus on a Sigma-class GST of the silkworm, *B. mori* (bmGSTS). The physiological function of bmGSTS still remains unclear. A cDNA encoding this enzyme was sequenced and overproduced as a recombinant protein in *Escherichia coli* cells. To examine its biochemical and structural properties, it is important to obtain information regarding the three-dimensional crystalline structure of bmGSTS and the structure–function relationships in its catalytic reaction.

2 Experiment

(1) Crystallization and data collection
A cDNA encoding bmGSTS was inserted into expression vactor, pET-11b, and transformed into BL21 (DE3) *E. coli* cells. Recombinant bmGSTS was purified and concentrated to approximately 10 mg/ml. Crystallization was carried out with the sitting-drop vapor diffusion method at 20 °C Data on crystal structure, obtained using NSRRC BL13B1&13C1 and PF-BL5A and SPring-8 BL44XU with crystals soaked in cryoprotectant solution containing 30% (v/v) glycerol, and cooled to 100 K in a nitrogen gas stream, were collected. The diffraction data were processed using the HKL2000 package.

(2) Structure determination
The crystal structure of bmGSTu was determined by the molecular replacement method using the program MOLREP. The structure was refined using the program REFMAC5 with diffraction data. The stereo chemical quality of the final model was evaluated by the program Coot, and the program PROCHECK.

3 Results and Discussion

The bmGSTS protein was crystallized in space group $P6_522$. The bmGSTS crystal structure was determined at 1.9 Å. By soaking method, the crystal for GSH-bmGSTS complex was prepared. The GSH-bmGSTS complex structure was determined at 1.7 Å.

Acknowledgement

We thanks the PF and NSRRC staff for the data collection.

References

[1]Armstrong, R.N., 1997. Structure, catalytic mechanism, and evolution of the glutathione transferases. *Chem. Res. Toxicol.* 10, 2 – 18.
[2]Mannervik, B., Board, P.G., Hayes, J.D., Listowsky, I., Pearson, W.R., 2005. Nomenclature for mammalian soluble glutathione transferases. *Methods Enzymol.* 401, 1–8.
[3]Ranson, H., Hemingway, J., 2005. Mosquito glutathione transferases. Methods Enzymol. 401, 226–241.
[4]Yamamoto, K., Zhang, P., Miake, F., Kashige, N., Aso, Y., Banno, Y., Fujii, H., 2005. Cloning, expression and characterization of theta-class glutathione S-transferase from the silkworm, Bombyx mori. *Comp. Biochem. Physiol. B* 141, 340–346.
[5]Yamamoto, K., Zhang, P., Banno, Y., Fujii, H., 2006. Identification of a sigma-class glutathione S-transferase from the silkworm, Bombyx mori. *J. Appl. Entomol.* 130, 515–522.
* mamoru.suzuki@protein.osaka-u.ac.jp

5A,NW12A/2010G088

Specificity and efficiency in activity of anti-HIV actinohivin for sugar binding

Masaru TSUNODA[1*], Kaoru SUZUKI[2], Atsushi TAKAHASHI[1], Jiandong JIANG[3], Md. Mominul Hoque[1], Haruo TANAKA[1] and Akio TAKENAKA[1,3]

[1]Faculty of Pharmacy, [2]Faculty of Science and Engineering, [3]Graduate School of Science and Engineering, Iwaki Meisei University, 5-5-1 Chuodai iino, Iwaki, Fukushima 970-8551, Japan

Introduction

HIV/AIDS is a major health concern, a global pandemic which remains a relatively uncontrolled infectious disease. Over 20 kinds of inhibitors targeting the HIV enzymes (e.g. reverse transcriptase, integrase and protease) are currently used as medicines to disturb the HIV lifecycle after HIV entry into cells. These antiretroviral drugs have recently been evaluated further for their dual effects as treatments and in preventing HIV infections. In addition, some proteins which are able to bind the surface glycoprotein of HIV are now expected to prevent HIV entry into cells.

This effect on entry inhibition is also applicable to help suppress the spread of infection. Structurally, trimeric gp120 protruded from the HIV surface binds to human CD^{4+} cell to initiate entry. Each gp120 is highly glycosylated to cover the surface with highmannose type glycans (HMTG). As candidates for suppressing gp120-binding to susceptible cells, several carbohydrate-binding proteins (lectins) have been isolated and characterized. We succeeded in discovering a new lectin, actinohivin (hereafter designated AH) from an actinomycete, *Longispora albida*. This lectin possesses a potent, specific anti-HIV activity to inhibits the entry of various HIV-1 and HIV-2 strains into susceptible cells, as well as T-cell-tropic and macrophage-tropic syncytium formation. Therefore, we have at first determined the crystal structure of the *apo* form[1] and then that in complex with Man-α(1,2)-Man (hereafter MB) of HMTG by X-ray analyses.

Experimental

Crystallization

AH for crystallization was prepared several times. Acetonitrile-treated, lyophilized AH was dissolved in water and its concentration was adjusted to 20mg/ml. An MB solution (in water) was adjusted to the same concentration. The two solutions were mixed at equal volume to prepare a protein solution for crystallization. Crystallization screening of AH in complex with MB was carried out by the hanging-drop vapor-diffusion method at 298 K. In each well, a droplet of protein solution (2.0μl) mixed with the same volume of the reservoir solution was equilibrated to the reservoir solution (700μl). Commercially available crystallization kits were applied for the reservoir solution at the initial trial. From several conditions under which crystalline precipitates appeared, a suitable one was further optimized.

X-ray data collection

As crystals were obtained from a solution containing 50% (v/v) MPD, it was regarded that they were already cryo-protected. A crystal suitable for X-ray experiment was picked up and mounted into a Cryo-Loo. X-ray experiments were performed at 100 K using the synchrotron radiation with wavelength of 1.00 Å in Photon Factory. Diffraction images were recorded on an ADSC 210r CCD detector. In total 180 frames of the patterns were taken at 1º oscillation steps with 1 second exposure per frame. Raw data images were indexed and intensities around Bragg spots were integrated to a resolution of 1.90 Å, and then scaled and merged using the computer program Mosflm of the CCP4 suite. Intensities were further converted to structure-factor amplitudes with TRUNCATE from the CCP4 suite.

Results and Discussion

The numbers of observed reflections were 68064 in a resolution range 27.84~1.90 Å and an R_{merge} value was reasonably low at 11.2% for 10409 unique reflections with the completeness of 99.9%. The unit cell is composed according to the space group $P22_12_1$ with the cell dimensions of a = 27.8, b = 66.8 and c = 67.1 Å. These habits are quite different from those of the previous crystal ($P2_13$, a=56.2 Å). The previous crystal has a 3-fold symmetry, around the axis AH is disordered by rotating 120°. However the present crystal has no such a 3-fold symmetry. Therefore it is expected there is no such disorder of AH molecule. A calculated Matthews coefficient (V_M) and the solvent content (2.49 $Å^3$/Da and 50.60%, respectively) suggest that the asymmetric unit contains one AH molecule. This crystal could reveal not only the detailed interaction geometries, but also other effects on both structures of AH and the bound MB.

Reference

[1] H. Tanaka, et al. *Proc. Natl. Acad. Sci. USA*, 106, 15633-15638. (2009)

*masaru@iwakimu.ac.jp

1A, 5A, 17A, NE3A, NW12A/2010G-107/ 2011A1891

好気性超好熱性古細菌のマルチコンポーネント酸化還元酵素の構造解析
Crystallography of multi-component oxidoreductases from Archaea

伏信進矢*, 宋賢珍, イェンチェン, 若木高善
東京大学大学院農学生命科学研究科、〒113-8657 東京都文京区弥生 1-1-1

1 はじめに

好気性超好熱性古細菌 *Sulfolobus tokodaii* は pH 2-3、75-80℃の条件で至適に生育する好酸性超好熱性古細菌であり、半リン酸化 Entner-Douderoff (ED)経路と呼ばれる非常に変わった解糖系を持つ。また、好気性生物であるため、解糖系・TCA サイクル・呼吸鎖によりエネルギーを生産している。その中央代謝経路において、解糖系と TCA サイクルの両方で重要な段階に関わるマルチコンポーネント酸化還元酵素として、ピルビン酸／ケトグルタル酸：フェレドキシン酸化還元酵素（PKOR）がある[1]。通常の生物でピルビン酸、2-オキソグルタル酸などの 2-オキソ酸の酸化的脱炭酸反応を触媒するのは、$NAD(P)^+$ を電子受容体とする分子量数百万におよぶ巨大酵素複合体で、補酵素としてチアミン二リン酸(TPP)、リポ酸、FAD を持つが、それに対して、古細菌では TPP と鉄硫黄クラスターを持つ分子量 10 万程度の比較的単純な酵素が同様の反応を触媒する。同じファミリーに属する酵素の立体構造としては、嫌気性細菌 *Desulfovibrio africanus* の酵素の構造しか知られておらず、好気性細菌である *S. tokodaii* の PKOR はこれと配列相同性が非常に低い。我々は PKOR の結晶構造の決定を目的の一つとしている。

一方、*S. tokodaii* を含む好熱菌（古細菌およびバクテリア）の糖新生経路において、２段階の連続する反応を触媒する二機能酵素 FBP アルドラーゼ／ホスファターゼ(FBPA/P)が発見された[2]。我々は以前この酵素のホスファターゼ型の構造を決定しており[3]、今回はこのアルドラーゼ型の構造を決定した。

超好熱性古細菌 *Thermoproteus tenax* は変形 Embden-Meyerhof 経路と変形 ED 経路の２種類の解糖系を持ち、前者の鍵となる段階で、ATP ではなくピロリン酸を利用してフルクトース６−リン酸のリン酸化を触媒する酵素が、ピロリン酸依存性ホスホフルクトキナーゼ（TPFP）である。我々は、TPFP の特殊な基質特異性を解明するために構造決定を行った。

2 実験

今年度の前半は東日本大震災の発生による KEK の停止にともない、SPring-8 量子ビーム施設震災優先枠で実験を行った（2011 年 6 月 24 日 BL38B1：３シフト）。後半は通常どおりに KEK-PF で実験を行った。

3 結果および考察

FBPA/P のアルドラーゼ型の結晶構造を決定し、その分子機構を解明することに成功した[4]。詳細は、PF Activity Report 2011 “Highlights”に記載している。

PKOR は native 結晶が得られて中程度（約 3.0Å）の分解能のデータが測定できる段階まで来ており、現在最大で 2.5Å 分解能のデータセットが得られている。しかし、セレノメチオニン置換体の結晶の再現性が悪く、十分に大きな結晶がまだ得られていないため、位相決定には至っていない。

TPFP は構造決定に成功し（図１）、FBP や F6P、ピロリン酸や Mg^{2+}などのリガンドの存在下での構造が 1.8Å 程度の高分解能で得られている。

図１：TPFP の全体構造

謝辞

実験をサポートして下さった KEK および PF のみなさんに感謝いたします。震災枠での実験をサポートして下さった馬場清喜先生、熊坂崇先生をはじめとする SPring-8、JASRI のみなさんにも感謝いたします。

参考文献

[1] Q. Zhang *et al.*, J. Biochem **120** (1996) 587.
[2] R. F. Say and G. Fuchs, Nature **464** (2010) 1077.
[3] H. Nishimasu *et al.*, Structure **12** (2004) 949.
[4] S. Fushinobu *et al.*, Nature **478** (2011) 538.

* asfushi@mail.ecc.u-tokyo.ac.jp

NE3A/2010G125

Crystallographic Analysis of Prokaryotic V-type ATPase

Nobutaka Numoto[1], Akiko Kita[1], Kazuki Takeda[2] and Kunio Miki[2,*]
[1]Research Reactor Institute, Kyoto University, Kumatori, Osaka 590-0494, Japan
[2]Graduate School of Science, Kyoto University, Sakyo-ku, Kyoto 606-8502, Japan

1 Introduction

V-type ATPases (V-ATPases) synthesize or hydrolyze ATP through the rotary catalytic mechanism in a similar manner to well-known F-type ATPases (F-ATPases), and both enzymes belong to the rotary ATPase/synthase superfamily. V-ATPases occur in the membranes of acidic organelles, such as lysosomes and endosomes in eukaryotic cells, maintaining acidic pH by pumping protons coupled with ATP hydrolysis. In prokaryotic cells, V-ATPases exist in the plasma membrane and are primarily responsible for ATP synthesis. V-ATPases consist of cytosolic component (V_1-ATPase) and membrane embedded component. V_1-ATPase shows ATPase activity and its structural composition is A_3B_3DF.

Although V_1-ATPase is almost homologous to F_1-ATPase ($\alpha_3\beta_3\gamma\delta\varepsilon$) from the viewpoint of overall structures and catalytic mechanisms, detailed analyses of the rotation kinetics of V_1-ATPase have revealed divergence in the torque and rotation steps between V_1- and F_1-ATPases. Our structural study of whole V_1-ATPase from *Thermus thermophilus* at 4.5 Å resolution [1] strongly suggests that V_1-ATPase and F_1-ATPase utilize different rotation mechanisms due to different manners in inter-subunit interactions and in tertiary structural transitions of the catalytic subunits. To elucidate more abundant structural basis on the rotation mechanism of V_1-ATPase and a common essence of the two rotary ATPases, we have addressed a crystallographic analysis of prokaryotic V_1-ATPase at higher resolution.

2 Experimental

Purified V_1-ATPase was crystallized under high magnetic forces fields (gradient magnetic fields) from a superconducting magnet system designed for the protein crystallization. The protein solution containing 30 mg/ml of V_1-ATPase and final concentrations of 10 mM of Mg-ADP and 1 mM AlFx were prepared for the crystallization experiments. To compare the structures, crystallization was also preformed without the magnetic forces fields. All crystallization experiments were performed using the vapour-diffusion method with a reservoir solution containing 1.6-1.8 M ammonium sulphate, and typical dimensions of the obtained crystals were $0.3\times0.3\times0.2$ mm^3. X-ray diffraction experiments were performed at the NE3A beamline using an ADSC Q270 detector. The wavelength, beam size, camera length, oscillation range, and exposure time were 1.0000 Å, 100 $\times$100 μm^2 (with no attenuator), 457.9 mm, 0.5 degree, and 5.0 sec, respectively.

3 Results

The crystals grown in the high magnetic forces fields and the reference condition diffracted up to 6.0 Å resolution. The diffraction data were processed using programs HKL2000 and CCP4i, and the data collection statistics are given in Table 1. Slight improvements in the values of overall *R* and crystal mosaicity were observed for the crystal obtained in the high magnetic forces fields. These facts suggest that crystals grown in the high magnetic forces fields could exhibit an enhanced crystal quality and could be useful for the data collection at higher resolution.

Electron densities for the bound nucleotides were clearly observed in the difference Fourier map at two of three catalytic sites of V_1-ATPase. Further analyses are in progress.

Table 1: Data collection statistics

Crystal	Magnetic forces fields	Reference
Wavelength (Å)	1.0000	1.0000
Oscillation range (deg.)	0.5	0.5
Exposure time (sec)	5.0	5.0
Space group	*P*321	*P*321
Cell *a*/*c* (Å)	379.6 / 147.2	381.0 / 147.3
Resolution (Å)	50-6.00 (6.21-6.00)	50-6.00 (6.21-6.00)
No. of observed	340,862	342,312
No. of unique	30,813	31,049
Redundancy	11.1 (10.7)	11.0 (10.6)
Completeness (%)	99.8 (100)	99.9 (100)
$I/\sigma(I)$	34.8 (2.5)	24.2 (1.5)
Mosaicity	0.35-0.57	0.41-0.61
R_{sym} (%)	8.7 (>100)	9.8 (>100)

Values in parentheses are for the outermost resolution shell.

References

[1] N. Numoto *et al*., EMBO Rep., **10,** 1228 (2009).

* miki@kuchem.kyoto-u.ac.jp

NW12/2010G518

Crystal structure of Atg7 in complex with Atg8

Seung Beom HONG and Hyun Kyu SONG*
School of Life Sciences and Biotechnology, Korea University, Anam-Dong
Seongbuk-Gu, Seoul 136-701, South Korea

Introduction

Autophagosome formation is a very essential event during macroautophagic process for disassembling and recycling cellular components via lysosome in response to various signals. Two ubiqutin-like molecules, Atg12 and Atg8 play crucial roles for creation of this double-membrane vesicle sharing a common E1-like enzyme, Atg7. The N-terminal domain of Atg7 (Atg7N) reveals a unique protein fold and interacts with both autophagic E2-enzymes, Atg10 and Atg3. The C-terminal domain of Atg7 (Atg7C) in complex with Atg8 shows the mode of dimerization and mechanism of recognition of Atg8. Notably, the catalytic cysteine residue in Atg7 is positioned close to the C-terminal glycine of Atg8, its target for thioester formation, potentially eliminating the need for large conformational rearrangements characteristic of other E1s.[1]

Methods

Purified Atg7C (C507S mutant) and Atg8 were mixed in a molar ratio of 1:2 at 4 °C for 30 min and reloaded onto a gel-filtration column for purification of the complex. Samples were concentrated to approximately 10~14 mg/ml and crystallized by hanging drop vapor diffusion at 22 °C, after mixing of an equal volume of reservoir solution containing 0.1 M HEPES (pH 7.5), 7~10% (w/v) PEG3,350 and 20 mM proline. Atg7N was concentrated to 16 mg/ml, and crystals were also obtained by hanging-drop vapor diffusion at 22 °C with a reservoir solution containing 0.1 M Na-HEPES (pH 8.0), 1.5M Li_2SO_4 and 0.1M spermidine tetrahydrochloride. Crystals were flash-frozen with reservoir solution containing 20% (v/v) glycerol in a nitrogen stream at 100 K. All of the eight possible selenium sites in the asymmetric unit of Atg7C–Atg8 crystal, and two of three possible sites in Atg7N, were located using three-wavelength MAD data sets. Initial phases were calculated, and initial models for Atg7C–Atg8 and Atg7N were built automatically using the PHENIX package program with up to 90% of Atg7C–Atg8 and only 20% of the Atg7N polypeptide chain. Models were rebuilt manually using COOT and O. Refinement was also carried out using the PHENIX package program.

Results

The crystal structure of Atg7C−Atg8 complex reveals a compact dimer with approximate dimensions of 85 Å × 72 Å × 50 Å (Fig 1a). Each subunit (residues Asp294–Glu620) consists of 11 α-helices, four 3_{10}-helices, eight β-strands and connecting loops, and includes the adenylation region, a zinc-binding site and a catalytic cysteine residue (Cys507) for thioester bond formation. The binding surface for Atg8 can be divided into two parts: one region for binding the core of the domain and another for recognition of its C-terminal tail, including Gly116, the target of adenylation. The C-terminal helices of Atg7, in particular α17, are crucial for coordination of the core of Atg8. Primarily hydrophobic residues form the binding interface between Atg7C and Atg8, with some contribution from polar residues and hydrogen bonds**.** The buried surface area of the Atg7C−Atg8 complex is approximately 2,300 $Å^2$.

The isolated Atg7N covering 1–294 amino acids is monomeric and has an elongated shape with approximate dimensions of 64 Å × 38 Å × 34 Å (Fig 1b). It consists of six α-helices, three 3_{10}-helices, 16 β-strands and connecting loops organized in two structural subdomains. Using a SEC-MALS assay, we revealed that Atg7N forms 1:1 complex with E2s (Atg3 and Atg10). Therefore, Atg7N is defined as an 'autophagic E2-binding domain'.

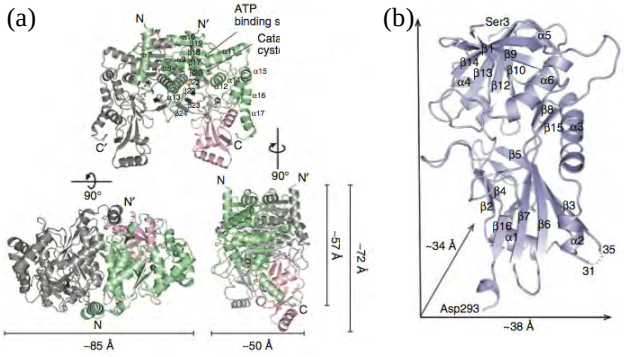

Figure 1. Structure of yeast Atg7. (a) Ribbon diagram of the structure of the Atg7C−Atg8 complex showing 2:2 stoichiometry. In one Atg7C−Atg8 pair, Atg7C is colored green and Atg8 is pink; the other pair is colored gray for clarity. (b) Ribbon diagram showing the structure of Atg7N (blue). The secondary structural elements are labeled and the N- and C-terminal residues of Atg7N are indicated. The region absent in the electron density map (residues 32–34) is indicated as a dotted line.

Reference

[1] S.B. Hong et al., Nature Struct. Mol. Biol. 18, 1323 (2011)

* hksong@korea.ac.kr

NW12A/2010G520

結核菌由来 Rv2613c タンパク質の Ser147Gln 変異体における結晶学的諸性質
Preliminary crystallographic analysis of Ser147Gln mutant of Rv2613c protein from *Mycobacterium tuberculosis* H37Rv

森茂太郎 [1*], 和知野純一 [1], 荒川宜親 [2], 柴山恵吾 [1]
[1] 国立感染症研究所・細菌第二部、〒208-0011 武蔵村山市学園 4-7-1
[2] 名古屋大学大学院・医学系研究科、〒466-8550 名古屋市昭和区鶴舞町 65 番地

1 はじめに

これまでに、結核菌由来 Rv2613c タンパク質について詳細な機能解析を行い、本タンパク質が基質である diadenosine polyphosphate（Ap_nA）に対して加リン酸分解活性を示すヌクレオチド加リン酸分解酵素であることを明らかにした[1]。また、X 線結晶構造解析を行い、本酵素の詳細な立体構造を決定した[2,3]。その結果、Rv2613c は α/β 構造を有するとともに、特徴的な 4 量体構造を形成していることが明らかとなった。この 4 量体構造は、他の Ap_nA を基質として利用する加リン酸分解酵素や加水分解酵素には見られない Rv2613c のみの特徴であった。さらに、変異体を作製してその機能を解析した結果、この 4 量体構造が Rv2613c の基質結合部位形成に関与していることが示された[3]。

Rv2613c の立体構造と Ap_nA 加水分解酵素の立体構造を比較検討した結果、活性中心部位の構造そのものは類似しているものの、活性中心部位に存在している 3 つのアミノ酸残基（Rv2613c では Asn-139 残基、Gly-146 残基、及び Ser-147 残基に相当）の種類が Rv2613c と Ap_nA 加水分解酵素とでは異なっていることが明らかとなった。そこで、これら 3 つのアミノ酸残基をそれぞれ置換した変異体を作成してその機能を解析した結果、Asn-139 残基は活性発現に必須であり、Gly-146 残基、並びに Ser-147 残基も活性発現に関与していることが示された。また、Gly-146 残基は Rv2613c において加リン酸分解反応を規定している重要な残基であることも示唆された。さらに速度論的解析を行った結果、Gly-146 残基と Ser-147 残基をそれぞれ置換した変異体の K_m 値はいずれも野生型の K_m 値とほぼ同じであるのに対して、変異体の V_{max} 値はいずれも野生型の V_{max} 値よりも著しく低下していることが示された。従って、Gly-146 残基と Ser-147 残基は、基質結合よりも触媒反応に関与していることが示唆された[3]。

そこで、さらに詳細に Ser-147 残基と活性との関連性を明らかにするために、Ser-147 残基を Gln 残基に置換した変異体（Ser147Gln）を作成し、機能と構造の解析を試みた。

2 実験

Ser147Gln 変異体を市販のキットを用いて作製し、大腸菌内で大量発現させた後、SDS-PAGE 上で単一バンドになるまで精製を行った。精製した Ser147Gln 変異体を用いて、蒸気拡散法により結晶化を行った。結晶化条件は、市販の結晶化スクリーニングキットを用いて決定した。

3 結果および考察

決定した結晶化条件（0.1M カコジル酸ナトリウム, pH 6.3、0.2 M 硫酸リチウム、及び 28.5%ポリエチレングリコール 400）は野生型の結晶化条件[2]とほぼ同じであった。20℃において約 2 週間で最大辺の長さが約 0.3 mm の X 線測定に適した結晶が得られた。この結晶を用いて BL-NW12A で測定を行い、回折データの収集を行った。HKL2000 を用いて回折データの解析を行った結果、本結晶は Ser147Gln 変異体の立体構造決定に適した結晶であることが示された（Table 1）。現在は、野生型の構造をテンプレートに用いた分子置換法により、Ser147Gln 変異体の立体構造の決定を進めている。

Table 1 Ser147Gln 変異体の結晶学的諸性質
（括弧内の値は最終分解能シェルに対する値）

X 線源	Photon Factory
ビームライン	BL-NW12A
振り角(°)	1
露光時間 (s)	2
波長 (Å)	1.0000
温度 (K)	100
空間群	*C*2
格子定数 (Å)	*a* = 101.0, *b* = 63.6, *c* = 79.0
(°)	*β* = 111.0
分解能範囲 (Å)	50.0 – 2.80 (2.85 – 2.80)
独立した反射数	11269 (518)
平均冗長度	7.0 (3.4)
完全性 (%)	96.1 (87.4)
平均 $I/\sigma(I)$	21.3 (4.9)
R_{merge} [#]	0.074 (0.190)

[#] $R_{merge} = \sum_{hkl}\sum_i | I_i(hkl) - \langle I(hkl)\rangle | / \sum_{hkl}\sum_i I_i(hkl)$.

参考文献
[1] S. Mori *et al.*, Protein. Expr. Purif. **69** (2010) 99-105.
[2] S. Mori *et al.*, Acta Crystallogr. **F66** (2010) 279-281.
[3] S. Mori *et al.*, J. Mol. Biol. **410** (2011) 93-104.

* mshige@nih.go.jp

5A, 6A, NW12A, NE3A/2010G530, 2008G587, 2007G052, 2011A1893

Structural elucidation for the metal storage function of *Helicobacter pylori* neutrophil-activating protein

Hideshi YOKOYAMA*, Osamu TSURUTA, Naoya AKAO and Satoshi FUJII
School of Pharmaceutical Sciences, University of Shizuoka, Shizuoka 422-8526, Japan

1 Introduction

Helicobacter pylori causes severe diseases such as chronic gastritis, peptic ulcers, and stomach cancers. *H. pylori* neutrophil-activating protein (HP-NAP) promotes adhesion of neutrophils to endothelial cells, and induces the production of reactive oxygen radicals. The crystal structure of HP-NAP from *H. pylori* strain 26695 (HP-NAP 26695) was first determined at 2.5 Å resolution [1]. HP-NAP is a ferritin-like iron storage protein, and is a dodecameric protein consisting of 17 kDa monomers with a central cavity where iron ions bind. HP-NAP can bind up to 500 atoms of iron per dodecamer in vitro. Ferritin binds metals such as Cd^{2+}, Zn^{2+}, Tb^{3+}, or Ca^{2+} in addition to Fe^{2+}. Due to the structural similarity between HP-NAP and ferritin, HP-NAP may bind metals other than irons, although, to our knowledge, there are no such reports. In order to understand the metal-storing function of HP-NAP, we determined the crystal structures of HP-NAP from strain YS39 (HP-NAP YS39) in the apo and metal-bound forms such as Fe^{3+}, Zn^{2+} and Cd^{2+} [2, 3]. HP-NAP YS39 was clinically isolated in Japan, and differs from HP-NAP 26695 at three residues (E46G, V59A and I73L).

2 Experiment

HP-NAP YS39 was expressed in *E. coli*, and purified using nickel affinity chromatography. Crystallization was carried out with the sitting-drop or hanging-drop vapor-diffusion method at 20°C. The protein solution of HP-NAP in 50 mM Tris-HCl and 0.1 M L-arginine (pH 8.8) was mixed with an equal volume of a reservoir solution to form the droplet. Crystals of the apo form were prepared using a reservoir solution containing 20% ethylene glycol. To obtain Zn^{2+}-bound crystals, the crystals were soaked into a solution containing 20% ethylene glycol and 20 mM $ZnSO_4$ for 15 min. To obtain Fe^{3+}-bound crystals, a reservoir solution consisting of 20% ethylene glycol and 10 mM iron(II) sulphate was used. To obtain Cd^{2+}-bound crystals, a reservoir solution containing 50 mM $CdSO_4$, 1.0 M sodium acetate, and 0.1 M HEPES-NaOH (pH 7.5) was used. For all crystallization conditions, crystals of cubic or rectangular form appeared and grew to an approximate size of 0.2 mm on a side.

Crystals were transferred into a solution of 30% glycerol in the mother liquor, and were flash-frozen in a stream of N_2 at 95 K. X-ray diffraction data were collected at beamlines BL5A, BL6A, NW12A, and NE3A, and were processed and scaled with HKL2000. The structures were solved by the molecular replacement method with MOLREP in the CCP4 suite. Crystallographic refinements and structural adjustments were performed with REFMAC5 and COOT, respectively.

3 Results and Discussion

The structures of HP-NAP YS39 were determined at 2.2-2.5 Å resolution. A total of 12 protomers form a dodecamer like a spherical shell about 90 Å in diameter with crystallographic point group 23. The internal cavity of the dodecamer is about 50 Å in diameter. The overall structures of HP-NAP YS39 determined here are similar to that of HP-NAP 26695.

In a Zn^{2+} or Cd^{2+}-bound form, two zinc or two cadmium ions and their bridged water molecule were located at the ferroxidase center (FOC). The two zinc ions are coordinated in a tetrahedral manner to the conserved residues among HP-NAP and Dps proteins. The two cadmium ions are coordinated in a trigonal-bipyramidal and distorted octahedral manner. In both structures, the second ion is more weakly coordinated than the first. In a Fe^{3+}-bound form, however, only one iron ion was located at almost the same position as the first (Zn1 or Cd1). It is possible that the di-iron sites are occupied only by Fe^{2+}, which is rapidly oxidized to Fe^{3+}. Therefore, in crystals of YS39 Fe following long exposure to oxygen, there is no second ion in the FOC. In the FOC of YS39 Zn, two zinc ions are separated by a distance of 3.3 Å, and two cadmium ions are separated by 4.2 Å, longer than the di-zinc distance of YS39 Zn. In YS39 Fe or YS39 Zn, another ferric or zinc ion is found inside of the negatively-charged three-fold-related pore, indicating that the pore is suitable for metal ions to pass through.

Between the apo and metal-bound structures, a major difference was observed. In comparison with the apo form, the side chains of Asp52 and Glu56 move toward the first metal ion (Fe1, Zn1, or Cd1) in metal-bound forms. Conversely, the Trp26 side chain flips out of the FOC. After the conformational change of Trp26, the side chains of Asp52 and Glu56 can be chelated by the first metal ion.

In conclusion, both zinc and cadmium ions can bind to the FOC, indicating that HP-NAP can store zinc and cadmium ions in addition to iron ions.

References

[1] G. Zanotti et al., J. Mol. Biol. **323**, 125-130 (2002).
[2] O. Tsuruta et al., Acta Crystallog. **F68** (2012) 134.
[3] H. Yokoyama et al., Biochem. Biophys. Res. Commun. **422** (2012) 745.

* h-yokoya@u-shizuoka-ken.ac.jp

11B, 4A/2010G542

Artificial oxidation treatment induces Ca accumulation in the peripheral part of human hair as determined by X-ray imaging

Atsushi ITO*[1], Takafumi INOUE[2], Tomomitsu KAWAI[2], Kouji TAKEHARA[2], Yoshiaki TAKI[1], Ryohei Takahashi[1], Kunio SHINOHARA[3]
[1]School of Engineering, Tokai Univ., Hiratsuka, Kanagawa 259-1292, Japan
[2]Kanebo Cosmetics Inc., Odawara, Kanagawa 250-0002, Japan
[3]Adv. Res. Inst. for Sci. and Eng., Waseda Univ., Shinjuku, 169-8555 Tokyo

Introduction

Possible correlation between Ca content in human hair and the incidence of human breast cancer has been proposed as one of the important applications of X-ray elemental analysis [1]. However, Ca content was also demonstrated to increase with the treatment of an oxidative colorant [2]. Therefore, the contribution of oxidative damage to the increase of Ca content in human hair should be evaluated in more detail. We have measured the distribution of a cysteic acid, a major component of oxidation product of cystine in normal human hair, with a submicron resolution by using soft X-ray contact spectromicroscopy at the S-K absorption edge [3]. Further we demonstrated a correlation between oxidative damage and Ca content by comparing the distributions of Ca and cysteic acid in human untreated hair and routinely bleached hair at a beauty parlor [4].

In the present study, we further confirmed that the oxidative damage induces Ca accumulation in human hair by the treatment with a controlled bleaching condition in the laboratory.

Materials and Methods

For the mapping of cysteic acid and Ca, X-ray contact microscopy with an electronic zooming tube with a resolution of about 0.5 μm was employed at the S-K edge for cysteic acid and at the Ca-K edge for Ca at BL-11B. Another analysis of Ca distribution has been carried out by X-ray fluorescence imaging at BL-4A with higher sensitivity than X-ray contact microscopy with an absorption contrast.

Hair specimens were prepared from normal women. For the artificial bleaching in the laboratory, they were soaked twice in a bleach solution containing 1.2% ammonia and 3.5% hydrogen peroxide for 30 min. Ca soaking was performed with 10 mM $CaCl_2$ for 2 days with a change of the solution. At the position of around 1 cm from hair roots, they were cut at the thickness of ca. 20 μm, and then placed on a SiN membrane with 100 nm thickness. The opposite side of the membrane was coated with Au as a photocathode of the zooming tube.

Results and Discussion

Fig. 1 shows X-ray absorption images of cystine, cysteic acid and Ca. Images in the upper row (a) and the lower row (b) are for untreated hair and for bleached hair, respectively. As expected, cysteic acid was increased by the bleach treatment. In accordance with the increase of cysteic acid, Ca content was also found to increase as shown in Fig. 1 and 2. It should be noted that the accumulation was evident particularly in the peripheral area of the hair, which indicates that the bleach treatment damages mainly the cuticle part followed by Ca accumulation. The present results confirmed that Ca accumulation is significantly induced by oxidative damage such as bleach treatment.

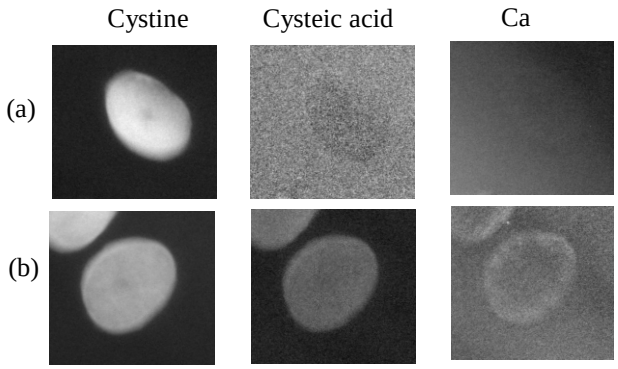

Fig. 1. Cystine, cysteic acid and Ca distributions in human hair. (a) untreated hair with Ca soaking; (b) artificial breached hair with Ca soaking.

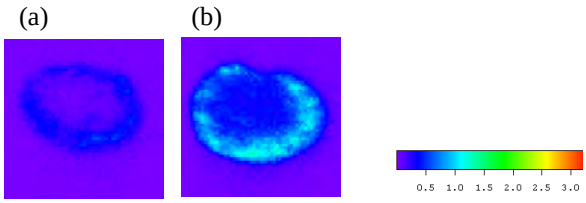

Fig. 2. Ca distribution in Ca-soaked human hair. (a): untreated hair; (b): artificial bleached hair.

References

[1] J. Chikawa et al., J. X-ray Sci. Tech., **15**, 109 (2007).
[2] K. E. Smart et al., J. Cosmet. Sci., **60**, 337 (2009).
[3] T. Inoue et al., J. X-ray Sci. Tech., **19**, 313 (2011).
[4] A. Ito et al., Adv. X-ray Chem. Anal., Japan, **43**, 161 (2012). (in Japanese)

* aeito@keyaki.cc.u-tokai.ac.jp

NW12A/2010G543, BL41XU/2011A1894

High-pressure-induced water penetration into IPMDH and pressure adaptation of proteins of deep-sea bacteria

Takayuki NAGAE[1], Takashi KAWAMURA[2], Leonard CHAVAS[3], Ken NIWA[1], Masashi HASEGAWA[1], Chiaki KATO[4], Nobuhisa WATANABE*[1, 2]
[1]Graduate School of Engineering, [2]Synchrotron radiation Research center, Nagoya University, Nagoya, Aichi 464-8603, Japan, [3]KEK-PF, Tsukuba, Ibaraki 305-0801, Japan, [4]Japan Agency for Marine-Earth Science and Technology (JAMSTEC), Yokosuka, Kanagawa 237-0061, Japan

Introduction

Several organisms have been found at greater ocean depths such as the Mariana Trench, and their proteins are known to be adapted to high-pressure environments. For example, 3-isopropylmalate dehydrogenase (IPMDH) from a deep-sea bacterium *Shewanella benthica* DB21MT-2 (SbIPMDH) is more tolerant towards high-pressure stress than the same enzyme from a land bacterium *S. oneidensis* MR-1 (SoIPMDH). To elucidate the mechanism of pressure adaptation of the protein, we have initiated structural studies on these IPMDHs by the high-pressure protein crystallography (HPPX) method.

Experiment

The high-pressure environment used in this study was generated by a diamond-anvil cell (DAC). While performing HPPX measurements, several difficulties have been noticed. For example, (i) since the pressure medium is liquid, crystals in the DAC are mobile and moving during measurements of the X-ray diffraction. (ii) Recording highly complete data is difficult for crystals belonging to lower symmetry space groups owing to the restricted aperture angle of the DAC, which is often less than 90 degrees.

To prevent the motion of crystals during measurements, the crystals were placed into the sample chamber with a few cigarette-filter fibres tied into a loose knot (Fig. 1). Since the space group of the SoIPMDH–IPM crystals is *C*2, we placed three or four crystals into the pressure cell at one time to collect high-completeness data sets at a given pressure. The different crystals were tiled with different orientations from each other using the knotted fibres (Fig. 1).

Results and Discussion

Structures of SoIPMDH at pressures ranging from 0.1 to 650 MPa were determined at about 2 Å resolution. In the 580 and 650 MPa structures, an additional cleft is generated on the surface of the protein. Three water molecules W697, W698 and W699 appeared inside or near the cleft (Fig. 2). These three waters were not observed in the structures at lower pressures ranging from 0.1 to 410 MPa. The water penetration of W697 into the cleft is supported by hydrogen bonding to Ser266 Oγ. On the other hand, the corresponding residue in deep-sea bacterium SbIPMDH is Ala266. A possible explanation of the different piezo-sensitivity of SbIPMDH could be that a water molecule at the same position as W697 cannot be stabilized in the case of SbIPMDH.

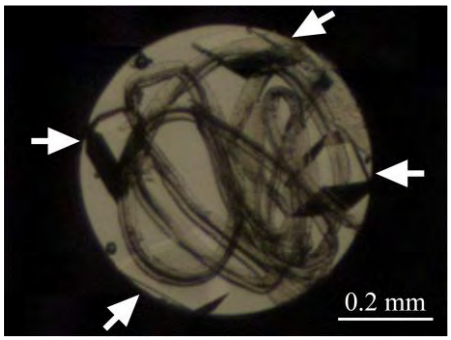

Fig. 1: Photograph of the sample chamber. Four SoIPMDH–IPM crystals (indicated by arrows) are tiled with different orientations from each other and fixed in position using the knotted cigarette-filter fibres.

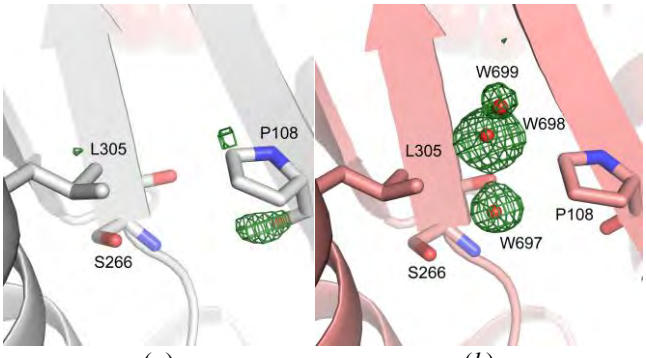

(*a*) (*b*)

Fig. 2: Generation of a new cleft on the surface of SoIPMDH with water penetration. (*a*) and (*b*) fo-fc map around P108, S266 and L305 is shown as a green mesh contoured at 3.0 sigma under 0.1 and 580 MPa, respectively. Three positive peaks are observed at 580 MPa in *b*, and were assigned as three water molecules, W697, W698 and W699 (represented by red balls).

References

T. Nagae *et al*., Acta Cryst. D**68** (2012) 300.

* nobuhisa@nagoya-u.jp

17A/2010G576

Crimean– Congo hemorrhagic fever virus nucleoprotein reveals endonuclease activity in bunyaviruses

Yu Guo[*,†,§,‖], Wenming Wang[†,§,‖], Wei Ji[†,§], Maping Deng[‡], Yuna Sun[¶], Honggang Zhou[†,§], Cheng Yang[†,§], Fei Deng[‡], Hualin Wang[‡], Zhihong Hu[‡,$], Zhiyong Lou[*,**] and Zihe Rao[*,†,§,¶,**]

[*] Laboratory of Structural Biology and MOE Laboratory of Protein Science, School of Medicine and Life Sciences, Tsinghua University, Beijing, 100084, China

[†] College of Life Sciences and Pharmacy, Nankai University, Tianjin 300071, China.

[‡] State Key Laboratory of Virology, Wuhan Institute of Virology, Chinese Academy of Sciences, Wuhan 430071, China

[§] High-throughput Molecular Drug Discovery Center, Tianjin Joint Academy of Biomedicine and Technology, Tianjin 300457, P.R.China

[¶] National Laboratory of Macromolecules, Institute of Biophysics, Chinese Academy of Science, Beijing, 100101, China

[‖] These authors contribute equally to this work

** To whom correspondence may be addressed: E-mail: raozh@xtal.tsinghua.edu.cn, louzy@xtal.tsinghua.edu.cn

1 Introduction

Crimean-Congo hemorrhagic fever virus (CCHFV), a virus with high mortality in humans, is a member of the genus *Nairovirus* in the family *Bunyaviridae*, and is a causative agent of severe hemorrhagic fever (HF). It is classified as a biosafety level 4 pathogen and a potential bioterrorism agent due to its aerosol infectivity and its ability to cause HF outbreaks with high case fatality (~30%) (1). However, little is known about the structural features and function of nucleoproteins (NPs) in *Bunyaviridae*, especially in CCHFV. Here we report a 2.3-Å resolution crystal structure of the CCHFV NP. The protein has a racket-shaped overall structure with distinct "head" and "stalk" domains and differ significantly with NPs reported so far from other negative-sense single-stranded RNA viruses. Furthermore, CCHFV NP shows a distinct metal-dependent DNA-specific endonuclease activity. Single residue mutations in the predicted active site resulted in a significant reduction in the observed endonuclease activity. Our results represent a new folding mechanism and function for a nucleoprotein of negative strand RNA virus NP, extend our structural insight into bunyavirus NPs, and provide a potential target for antiviral drug development to treat CCHFV infection.

2 Experiment

Diffraction data of the native crystal of CCHFV NP was first collected to 3.0 Å at 100 K using a MAResearch M165 CCD detector on beamline 1W2A at the Beijing Synchrotron Radiation Facility (BSRF). Anomalous diffraction data for selenomethionine derivatives were collected to 2.3 Å at 100 K using an ADSC Q315 CCD detector on beamline BL17 at the Photon Factory (Japan). All data sets were indexed, integrated and scaled using the HKL2000 package. The orthorhombic crystal form belongs to space group $P2_12_12_1$ with cell parameters a= 58.3 Å, b= 67.9 Å, and c= 131.5 Å.

Heavy atom searching, initial phase calculation and density modification were performed with PHENIX. The resulting electron density map was displayed with COOT and an initial model was built in manually. Several rounds of simulated annealing, restrained individual atomic displacement parameter refinement, energy minimization and individual B-factor refinement were carried out with PHENIX. Solvent molecules were located from stereochemically reasonable peaks in the σA-weighted 2*Fo*−*Fc* difference *Fourier* electron density map (1.2 σ). Model geometry was verified using the program PROCHECK. All structure figures were drawn with the program PyMOL. The coordinates and structure factors have been deposited with the RCSB under accession codes: 3U3I. The authors declare no competing financial interest.

3 Results and Discussion

The correct assembly of viral genomic RNA by nucleocapsid protein is crucial for single stranded virus assembly and maturation, and is also a significant process to protect viral RNA from host cell degradation. Additionally, recent structural work on LASV NP has extended our knowledge of virally encoded NP proteins beyond the packaging of viral genomic RNA (15, 16, 19), while the exact function of the N-terminal domain is still under discussion. Our finding that, despite the structural similarity between the head domain of CCHFV NP and the N-terminal domain of LASV NP, they may not function equivalently. CCHFV NP shows weak binding with RNA, and did not show any cap-snatching affinity *in vitro*. However, CCHFV reveals a novel endonuclease function which is not previously described for any member of this virus family.

The crystal structure of CCHFV NP reported in this work extends our knowledge of nucleocapsid protein of Bunyaviruses. The structure of CCHFV NP features a

racket-shaped overall structure, composed by a head domain which resembles the topology found in LASV NP but has a distinct nuclease function instead of cap binding. CCHFV NP potential surface displays several positive regions while unexpectedly show very weak binding activity with RNA *in vitro*. These data provide the new insight into the biological role of NP in Bunyavirus replication and provide valuable information for the development of intervention strategies designed to lessen the pathogenic burden of this important group of viral infections.

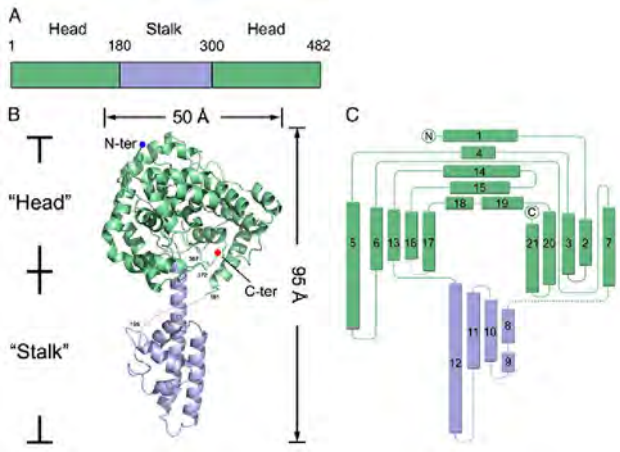

Fig. 1: Structure of CCHFV NP.

(A) Schematic diagram of domain organization of CCHFV NP in primary sequence. Stalk and head domain are colored as light blue and green, respectively.

(B) Overall structure in cartoon representation, missing residues are linked by dotted lines, and (C) in topology diagram. Head and stalk domains are colored in green and light blue, respectively.

Acknowledgement

We thank the staff at Beijing Synchrotron Radiation Facility and Photon Factory for their help with data collection; we also thank Prof. Hong-bing Shu from Wuhan University who supplied the plasmids for INF induction reporter assays. This work was supported by the National Natural Science Foundation of China, the Ministry of Science and Technology 973, the Special Program for Key Basic Research of the Ministry of the Science and Technology, and the Knowledge Innovation Program of the Chinese Academy of Sciences.

References

1. Varough M. Deyde MLK, Pierre E. Rollin,Thomas G. Ksiazek, and Stuart T. Nichol (2006) Crimean-Congo Hemorrhagic Fever Virus Genomics and Global Diversity. *JOURNAL OF VIROLOGY* 80(17):8834-8842.

5A, 17A, NW12A, NE3A/2010G582, 2011A1873

X-ray structure of hemagglutinin subcomponent HA70 from *Clostridium botulinum* in complexes with sialylated oligosaccharides

Satoshi Yamashita[1], Hiromi Yoshida[1], Takashi Tonozuka[2], Atsushi Nishikawa[2] and Shigehiro Kamitori[1,*]

[1] Life Science Research Center and Faculty of Medicine, Kagawa University
1750-1 Ikenobe, Miki-cho, Kita-gun, Kagawa 761-0793, Japan

[2] Department of Applied Biological Science, Tokyo University of Agriculture and Technology
3-5-8, Saiwai-cho, Tokyo 183-8509, Japan

1 Introduction

Clostridium botulinum produces the botulinum neurotoxin (NTX) which is one of the most potent toxins. The NTX exists as seven different serotypes A through G, and most NTXs form large complexes as progenitor toxins (PTXs) in association with nontoxic nonhemagglutinin (NTNHA) and/or several different hemagglutinin (HA) subcomponents. Type A-D and G toxins produce PTXs consisting of one NTX, one NTNHA, and three HA subcomponents, designated HA70, HA33, and HA17 based on molecular mass. HA70 is further proteolytically cleaved to HA22-23 and HA53 fragments. The mechanism of carbohydrate recognition by HA subcomponents is very important to elucidate the infection process of botulism. We determined four X-ray structures of HA70 from type C toxin (HA70/C) in complexes with sialylated oligosaccharides; α2-3-sialyllactose (3SiaLac), α2-3-sialyllactosamine (3SiaLacNAc), α2-6-sialyllactose (6SiaLac) and α2-6-sialyllactosamine (6SiaLacNAc).

2 Experiment

HA70/C was expressed as a maltose-binding fusion protein in *Escherichia coli* JM109 cells, and purified by affinity chromatography using amylose resin. Crystals of HA70/C were grown in a droplet containing 1.0 μl of protein solution (18 mg/ml in PBS) and 1.0 μl of reservoir solution (12 % (v/v) 2-methyl-2,4-pentendiol, 20 mM $CaCl_2$, 100 mM sodium acetate (pH4.6)) against 500 μl of the reservoir solution, by the hanging drop method, at 293 K. Crystals of the complexes with the oligosaccharide were obtained by adding 0.4 μl of 0.4 M oligosaccharide solution to the droplets of crystals for 40 hours at 293K. Data was collected on a PF-AR NE3A (KEK, Japan) and a BL26B1 (SPring-8, Japan). The initial phases were determined by molecular replacement, and the structure was refined by the programs Refmac5 and CNS. The bound oligosaccharide ligands could be found in the (Fo-Fc) maps.

3 Results and Discussion

The X-ray structures of the complexes of HA70/C with 3SiaLac, 3SiaLacNAc, 6SiaLac and 6SiaLacNAc were successfully determined [1]. There is one molecule of HA70/C in an asymmetric unit, and a crystallographic 3-fold symmetry generates a homo-trimer of HA70/C with a triangular shape. The carbohydrate-binding sites are in the vicinity of vertices of the triangle (Fig. 1A). Both 3SiaLac (3SiaLacNAc) and 6SiaLac (6SiaLacNAc) were found to bind to HA70/C, and each ligand was recognized by many hydrogen bonds in a similar manner, suggesting that HA70/C can recognize both α2-3- and α2-6-sialylated oligosaccharides (Fig. 1B).

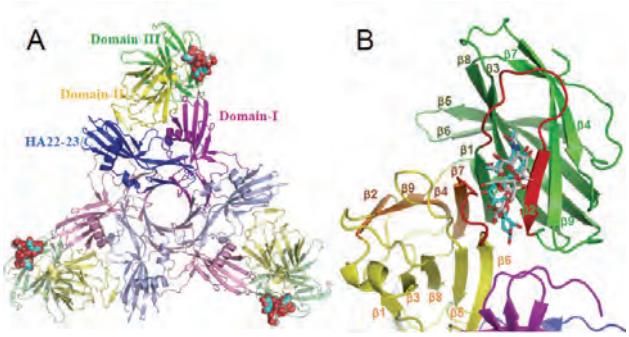

Fig. 1: Structure of HA70/C with the bound ligands. (A) Homo-trimer of HA70/C with the bound ligand in the space-filling mode with gray carbon (3SiaLac) and cyan carbon (6SiaLac). HA22-23/C, and domain-I, -II, and -III of HA55/C are in blue, magenta, yellow and green, respectively. (B) A close-up view of the carbohydrate-binding site with the bound ligand shown as a stick model.

Acknowledgement

This research was performed with the approval of the Photon Factory Advisory Committee and the National Laboratory for High Energy Physics (2009G512, 2010G001, 2010G582), and Priority Program for Disaster-Affected Quantum Beam Facilities of SPring-8 (2011A1873).

References

[1] S. Yamashita *et al.*, FEBS Letters (2012) in press. http://dx.doi.org/10.1016/j.febslet.2012.05.055

* kamitori@med.kagawa-u.ac.jp

NW12A, 5A, 17A/2010G585

Crystal structures of the bacterial A1408G-mutant A site with and without geneticin

近藤次郎 [1*]
[1] 上智大学理工学部、〒102-8554 東京都千代田区紀尾井町 7-1

1 はじめに

アミノグリコシド系抗生物質は細菌リボソームの活性部位 A サイトに存在する RNA 分子スイッチに作用して、デコーディングの正確性を低下させることで殺菌効果を示す。これに対して細菌は、RNA 分子スイッチをわずか 1 塩基のみ変異させる（16S rRNA の 1408 番目の A を G に変異させる）ことで抗生物質に対する耐性を獲得する（図１）。しかし、正確なタンパク質合成を可能にする分子スイッチを変異させることは、一方では細菌にとって自身の生命維持を脅かすリスクの高い行為でもある。

本研究では、細菌の薬剤耐性獲得メカニズムを分子レベルで明らかにするために、耐性型分子スイッチの X 線結晶解析を行った[1]。

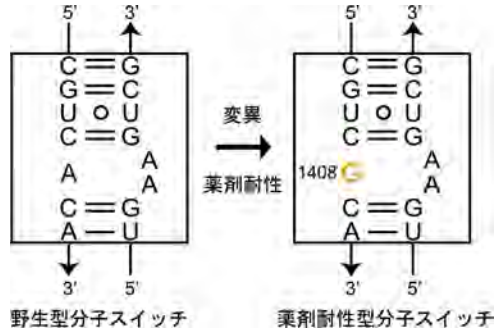

図１：薬剤耐性型 RNA 分子スイッチ

2 実験

A1408G 変異をもつ薬剤耐性型分子スイッチの配列を導入した RNA を化学合成し、結晶化に用いた。耐性型分子スイッチに対して親和性の高い抗生物質 geneticin を含む条件と含まない条件で結晶化を行った。それぞれ空間群 $P2_12_12$ と $P2_12_12_1$ の結晶が得られ、最大分解能 2.1 Å と 1.6 Å の X 線回折データを測定した。プログラム Phenix を用いて分子置換法と多波長異常分散法で初期位相を決定し、プログラム CNS を用いて原子パラメーターを精密化した。

3 結果および考察

16S rRNA に A1408G 変異を持つ薬剤耐性菌は、ring I の 6'位にアミノ基（NH_3^+）をもつ抗生物質に対して高い耐性を示すが、ヒドロキシ基（OH）をもつ抗生物質（geneticin など）に対してはわずかな耐性しか示さない。X 線結晶解析と分子モデリングの結果、6'-OH をもつ ring I は耐性型分子スイッチの G1408 と擬塩基対を形成できるが、6'-NH_3^+をもつ ring I はこの擬塩基対を形成できないことがわかった（図２）。

また、耐性型分子スイッチの ON 状態と OFF 状態の構造を野生型分子スイッチのそれらの構造と比較したところ、ほとんど違いがないことがわかった（図３）。つまり、16S rRNA の 1408 番目が A から G に変異しても分子スイッチは正常に作動するので、細菌は薬剤耐性を獲得しつつ生命を維持できると考えられる。

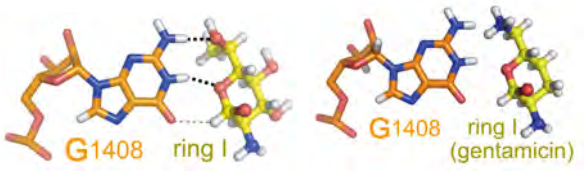

図２．Ring I と G1408 の間の擬塩基対
（左）6'-OH を持つ ring I は擬塩基対を形成できる
（右）6'-NH_3^+を持つ ring I は擬塩基対を形成できない

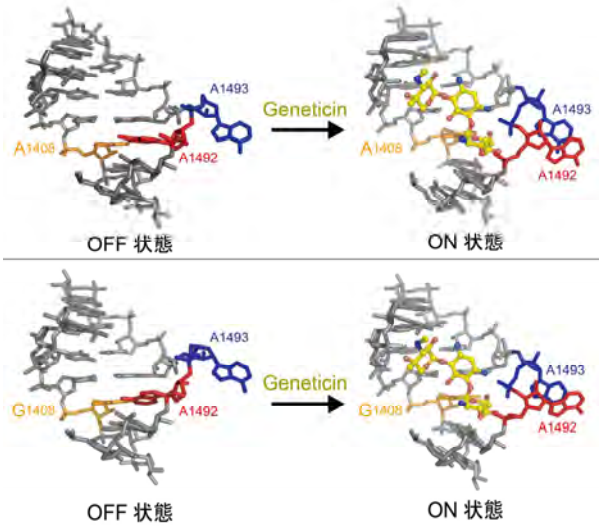

図３．野生型（上）および薬剤耐性型（下）分子スイッチの ON/OFF 状態の構造

4 まとめ

細菌は最適な原子種を選択して分子スイッチを自ら変異させることで、自身の生命を維持しながら巧妙に薬剤耐性を獲得することがわかった。

参考文献

[1] J. Kondo, Angew. Chem. Int. Ed. **51** (2012) 465-468.

* j.kondo@sophia.ac.jp

5A/6A/NW12A/2010G597

硫化カルボニル分解酵素の構造化学的研究
Structural studies on carbonyl sulfide hydrolase from *Thiobacillus thioparus* THI115

野口恵一[1*], 高橋翔平[2], 小川貴弘[3],大滝証[2], 尾高雅文[2], 養王田正文[2], 片山葉子[3]
[1]東京農工大学機器分析施設, [2]大学院工学研究院 〒184-8588 東京都小金井市中町 2-24-16,
[3]大学院農学研究院　〒183-8509 東京都府中市幸町 3-5-8

1 はじめに

硫化カルボニル (COS) は大気中に最も多く存在する硫黄化合物であり、自然界の生命活動だけでなく、化石燃料の燃焼等を通じ人為的にも発生している。COS は対流圏ではほとんど分解されず、成層圏で分解されエアロゾルの起源物質のひとつとなるため、地球の気候変動に影響を及ぼしている。最近、我々は、土壌細菌 *Thiobacillus thioparus* THI115 から COS を二酸化炭素と硫化水素に加水分解 (COS + H_2O → CO_2 + H_2S) する硫化カルボニル加水分解酵素 (COSase) を同定・単離し、その生化学的な解析を行った。アミノ酸配列の相同性検索の結果より、COSase は植物や真正細菌の持つ炭酸脱水酵素である β-炭酸脱水酵素 (β-CA) ファミリーに属することが予想されたが、二酸化炭素と炭酸水素イオンの相互変換活性 (CA 活性) は示さず、 COS 分解のみを触媒する酵素であった。そこで本研究では、COSase の基質認識機構、反応機構を明らかにすることを目的に、*T. thioparus* THI115 由来 COSase 天然型、および、基質類似化合物複合体の結晶構造解析を行った。

2 実験

X線回折測定は高エネルギー加速器研究機構放射光科学研究施設の BL-5A、BL-6A、NW12A ビームラインで行い、天然型は分解能 1.25 Å、基質類似化合物複合体は分解能 1.45 Å の回折強度データを収集した。*Mycobacterium tuberculosis* 由来 β-CA Rv1284 の構造 (PDB ID:1YLK) をプローブとして、分子置換法プログラム Molrep を用いて初期構造を得た。構造精密化には SHELXL-97 を使用し、天然型 (PDB ID: 3VQJ) は R = 0.135 (Rfree = 0.170)、SCN^- との複合体 (PDB ID: 3VRK) は R = 0.159 (Rfree = 0.204) の構造モデルを得た。

3 結果および考察

天然型と SCN^- 複合体の構造は同形であり、非対称単位はサブユニット 1 分子を含んでいた。結晶中において、COSase は互いに垂直な 3 本の結晶学的 2 回軸で関係づけられるサブユニットとの間で四量体を形成していた。四量体は、二量体が二量化した構造と考えられ、基本となる二量体構造は、これまでに結晶解析された β-CA に共通した二量体構造と類似していた。サブユニット構造は、5 本の β ストランドからなる β シートの両面に 4 本の α ヘリックスが接したコア部と、コア部から突出した 2 本の α ヘリックスから構成される α / β 構造であった。

触媒部位には亜鉛イオンが存在し、亜鉛イオンに対し Cys44 と Cys100 の S 原子、His97 の N 原子、水分子が正四面体型に配位していた。この触媒部位の構造はこれまでに結晶解析された β-CA で共通して見出されていた構造とほぼ同一のものであった。基質ポケットは主に疎水性アミノ酸で形成されており、その大きさ、形状はともに基質である COS とよく一致していた。触媒部位からタンパク質表面までの基質経路について検討したところ、コア部から突出したヘリックス部分が触媒部位を覆うように存在するため、COSase は β-CA に比べ基質経路となるトンネルが狭いことが判った。COSase が CA 活性を示さない原因として、トンネルのサイズが関係している可能性が示唆された。

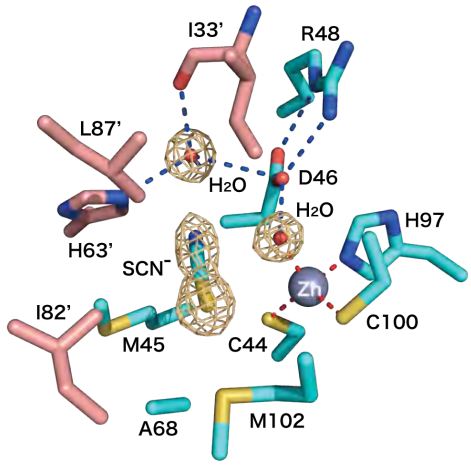

The catalytic site of COSase complex with thiocyanate.

* knoguchi@cc.tuat.ac.jp

27B/2010G602

X 線マイクロビーム暴露細胞からのバイスタンダー効果によるグリオーマ細胞遊走の誘導

Induction of migration on glioma cells by bystander effect of cells exposed to x-ray microbeams

前澤　博[1*], 宇佐美徳子[2], 小林克己[2]
[1]徳島大学大学院ヘルスバイオサイエンス研究部, 〒770-8509 徳島市蔵本町 3-15-21
[2]物質構造科学研究所, 〒305-0801 つくば市大穂 1-1

1 はじめに

陽子やヘリウム核のマイクロビームを用いた細胞死，突然変異あるいは形質転換誘発研究などにより，粒子線による低線量，低線量率および照射部位の依存性が研究された。Kobayashi らによって生物試料用の X 線マイクロビーム照射システムが開発され（KEK-PF BL27B）[1~3]，これは放射線影響研究のために世界で利用できる唯一のものである。Maeda らは線量および照射野が可変である特徴を利用し，1Gy 以下の領域で起こる hypersensitivity が細胞の全体照射では核照射よりも低下し，細胞死に細胞質が関与する機構を示唆した[4]。Tomita らは正常ヒト繊維芽細胞でバイスタンダー効果による致死を見いだした[5]。

細胞の運動能力は損傷治癒やがんの転移などと関係する。遊走や浸潤の活性は放射線量や細胞種に依存することが報告されている。しかし，小線量被ばく時のように集団内の少数細胞のみが細胞核あるいは細胞質の照射を受けた場合のバイスタンダー効果による非照射細胞の遊走や浸潤の活性変化については知られていない。

本稿では，マイクロビーム X 線で少数の細胞核が照射された時の非照射グリオーマ細胞の遊走について報告する。

2 実験

細胞培養：細胞はダルベッコ改変イーグル培地に 10%のウシ胎児血清を添加した培地で培養した（37℃，5%炭酸ガス培養器内）。

照射試料の調整：細胞は照射用ディッシュのポリプロピレン膜（5μm 厚）又はマイラー膜上に 2~3x10^5 個をプレーティングし 12〜16 時間培養した。照射前に細胞核はヘキスト 33258（1μM）で染色した。

マイクロビーム X 線の照射: PF BL27B の Si 二結晶分光器とスリットでエネルギー5.35 keV、サイズ 10 μm x 10 μm のビームを作製し照射に用いた。ビームの照射線量率はおよそ 7.7x10^{-3} C/kg (30 R)/sec であった。照射用ディッシュをビームラインの蛍光顕微鏡にセットし，細胞核蛍光画像を取得し選択した細胞核を任意の線量で照射した。

細胞遊走：遊走は改変 Boyden チェンバーを用い測定した。トランスウェル膜上面に 10,000 個の細胞をプレーティングし膜を通過した細胞数を測定した。

3 結果と考察

選択されたグリオーマ A172*mtp53* の細胞核を照射後に 24 時間培養し，その後細胞集団（ディッシュ上の全細胞）の遊走を調べた。表 1 に示すように実験間で照射効果が安定していない。線量 0.129 C/kg(500 R)の場合，細胞核 40 個の照射で遊走への影響があるようにみえるが不確実性が高い。また線量 0.0258 C/kg で 200 個の照射の場合，遊走の変化を認めた。細胞核照射された細胞から遊走誘導因子が放出されている可能性があり，またバイスタンダー効果がみえるには一定数の細胞の照射が必要であるが，さらに実験が必要である。

表 1: 照射細胞核数と遊走

実験	遊走細胞数の比 (sham 照射の場合を 1)
	0.129 C/kg 照射, 照射核数 40
1	2.3
2	1.4
3	1.1

実験結果が不安定な一因として，照射実験の開始時と終了時とでビーム位置が異なっていたことがあり，標的細胞核が正確に照射されなかった可能性が想定される。コンタミによる試料消失も限局されたデータの一因である。

参考文献

[1]K.Kobayashi et al., Nuci. Instrum. Methods **A467-8** (2001) 1329.
[2]N.Usami et.al., Radiat.Prot.Dosimetry, **122** (2006) 307.
[3]K.Kobayashi et al., J. Biomed Nanotechnol. **2** (2006) 116.
[4]M.Maeda et. al., J.Radiat.Res. **49** (2008) 171.
[5]M.Tomita et al.,Radiat Res. **173** (2010) 380.
* hmaezawa@medsci.tokushima-u.ac.jp

BL17A/2010G616

Crystal structure analysis of mouse SMP30

Ayaka Harada[1], Shingo Aizawa[1,2], Miki Senda[3], Naoki Maruyama[2], Akito Ishigami[2], Toshiya Senda*[1]

[1] BIRC, AIST, 2-4-7 Aomi, Koto-ku, Tokyo 135-0064, Japan
[2] TMIG, 35-2 Sakaemachi, Itabashi-ku, Tokyo 173-0015, Japan
[3] JBIC, 2-4-7 Aomi, Koto-ku, Tokyo 135-0064, Japan

1 Introduction

Senescence Marker Protein 30 (SMP30) was originally identified as an ageing marker protein whose expression decreases in an androgen-independent manner in rat liver and kidney cells [1]. Since proteins showing ageing change are typically influenced by hormones, they show different trends of increase or decrease between males and females. However, SMP30 is reduced with ageing in both males and females in the same manner and is not affected by hormones. While SMP30 is involved in biosynthesis of vitamin C in mouse cells, human cells cannot synthesize vitamin C due to mutational inactivation of L-glonolacton-oxygenase, which is the last enzyme of vitamin C biosynthesis. Therefore, human SMP30 (hSMP30) might have a function distinct from vitamin C synthesis. Details of the physiological function of SMP30 in human cells remain elusive.

We aim to elucidate the physiological function of SMP30 and have studied human and mouse SMP30s by comparative biochemistry. Here we report a preliminary crystallographic study of mouse SMP30 (mSMP30).

2 Methods

mSMP30, which shows 88% sequence identity with hSMP30, was crystallized by the sitting-drop vapor diffusion method. 1, 5-Anhydro-D-glucitol was used as a substrate analogue. Crystals of mSMP30 in complex with the substrate analogue were prepared by the soaking method. Diffraction data of mSMP30 crystals were collected at BL-17A of PF at KEK (Table 1). The diffraction data were processed using the program XDS. The crystal structure of mSMP30 was determined by the molecular replacement method with the program MOLREP in CCP4. Since the crystal structure of hSMP30 was already determined [2], it was used as a search model. The crystal structure of mSMP30 was refined using the program Phenix.refine.

3 Results

Mouse SMP30 has the β-propeller structure, which is composed of six β-sheets each of which is formed with four β-strands (Figure 1). At the center of the β-propeller structure, a strong electron density was found. This density was likely to represent a metal ion that was coordinated by three amino residues: Glu18, Asn154, Asp204.

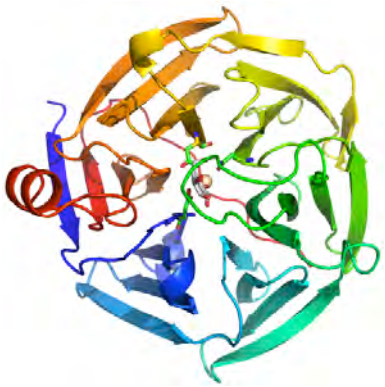

Figure 1 Overall structure of mouse SMP30

Table1 Crystallographic summary

Crystal Form	Substrate free form	Analogue binding form
Beamline	BL17A	BL-17A
Program	XDS	XDS
Wavelength (Å)	0.98	0.98
Oscillation angle (°)	0.5	0.5
Exposure time (s)	4	4
Space group	$P3_121$	$P3_121$
Unit cell parameters		
a	102.68	102.59
c	147.82	149.71
Resolution (Å)	76.2-1.95 (2.06-1.95)	76.4-1.7 (1.79-1.70)
R_{merge} (%)	0.048 (0.424)	0.04 (0.471)
I/σ(I)	22.71 (4.73)	27.18 (4.8)
Completeness (%)	100 (100)	99.9 (100)
No. of unique reflections	127,069 (19,296)	193,833 (27,838)
Redundancy	5.6 (5.7)	5.6 (5.6)
Mosaicity	0.1	0.1

Values in parentheses are for the outermost resolution shell.

4 References

(1) Fujita *et al.*, *Biochim. Biophys. Acta* **1116**, 122-128 (1992).
(2) Chakraborti and Bahnson, *Biochemistry* **49**, 3436-3444 (2010).

* toshiya-senda@aist.go.jp

6A/2010G641

Time course of the ordered phase formation in lipid bilayers caused by sphingomyelin hydrolysis

Masanao Kinoshita[1,*] and Satoru Kato[2]
[1]Department of Chemistry, Graduate School of Science, Osaka University, Toyonaka, Osaka, 560-0043, Japan
[2]Department of Physics, School of Science & Technology, Kwanseigakuin University, Sanda, Hyogo, 669-1337, Japan

1 Introduction

Sphingomyelin (SM) is a representative sphingolipid, distributed widely in plasma membranes. SM is known to form an ordered domain together with cholesterol (chol) and the SM/chol-rich domain has been extensively studied as a model for the biological raft [1]. SM/ceramide (Cer) mixed bilayer also forms an ordered domain similar to that in the SM/chol mixed bilayer [2].

Considering that Cer is produced by hydrolysis of SM in biological systems, Cer generation may preferentially occur in the SM-rich raft domain and involved in the raft formation. Although there are some reports on the physicochemical properties of the Cer-rich domains, the process/time course of the ordered phase formation still remains unknown. In this work, we tried to feed Cer molecules into SM bilayers as in biological systems; Cer molecules were generated in situ by hydrolysis of membrane-constituting SM. Cer formation was monitored by ordering in chain packing.

2 Experiments

SM derived from chicken egg and SMase were purchased from Avanti Polar Lipid and Sigma Aldrich, respectively. Other chemicals were purchased from Wako pure chemicals. The powder SMase was dissolved in the 5 mM HEPES buffer (20 mM $MgCl_2$ and 20 mM $CaCl_2$). The powder SM was dispersed in the buffer and incubated at 60ºC for 30 min with intermittent voltexing. We prepared ULVs by extruding sample through the membrane filter (Φ200 nm) for 29 times. Then the sample dispersion was centrifuged for 3-4 hours at 20,000G to obtain ULVs concentrated enough for wide angel x-ray (WAXD) measurements (~10 wt%). The sample was enclosed in the sample cell immediately after the addition of the SMase solution and the sample cell was put into the temperature controller kept at 43ºC.

The WAXD measurements were carried out at BL-6A with the imaging plate detector. The wave length was 0.15 nm and the camera length was estimated to be 19 cm by using cholesterol.

3 Results and Discussion

Fig. 1a shows a broad peak centered at 2.31 nm^{-1}, which is a typical WAXD pattern of SM bilayers in the fluid phase. The SM-ULV/SMase mixture after incubation at 43ºC for 5 min shows two peaks centered at 2.37 nm^{-1} and 2.46 nm^{-1} (arrowhead and arrow in Fig. 1b) overlapped by the broad peak. Considering that the main transition temperatures of the Cer-rich ordered domains are higher than that of pure SM bilayers (DSC data not shown), these peaks suggest the formation of the Cer-rich domains in the gel phase. Increase in the incubation time enhances the peak areas, suggesting the growth of the Cer-rich domains (Fig. 1b-f). After 8 hours about 70% of all domains transformed into the Cer-rich domains, judging from the area of the broad peak. Thus, we succeeded in detecting the dynamical change in bilayer structures induced by in situ introduction of Cer molecules as degradation products of SM.

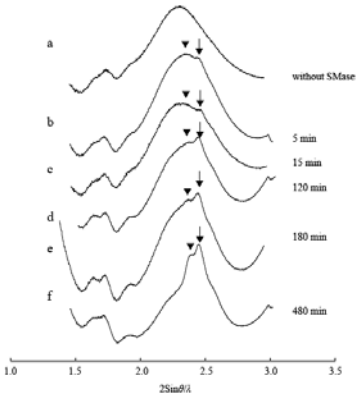

Fig. 1: WAXD patterns of SM-ULVs in the absence and presence of SMase (3 units) at 43ºC. The incubation time at 43ºC after the addition of SMase was directly indicated in the figure.

Acknowledgements

We thank professor Nomura for his help in setting up the x-ray experiment.

References

[1] J. R. Silvius, Biochim. Biophys. Acta **1610** (2003) 174.
[2] J. Sot *et al.*, Biophys. J., **90** (2006) 903.
[3] B. Boulgaropoulos *et al.*, Biophys. J. **99** (2010) 499.

* kinoshi@chem.sci.osaka-u.ac.jp

1A, 5A, NW12A/2010G662

芳香環二酸化酵素における触媒反応の分子基盤
Structural basis of the catalytic cycle of Rieske nonheme iron oxygenases

芦川雄二[1], 梅田隆志[1], 藤本瑞[2], 野尻秀昭[1*]
[1]東京大学生物生産工学研究センター　〒113-8657 東京都文京区弥生 1-1-1
[2]農業生物資源研究所　〒305-8602 茨城県つくば市観音台 2-1-2

1 はじめに

Rieske nonheme iron oxygenase (RO)は芳香環への *cis* の立体配置での二水酸化反応を触媒し、ダイオキシンや PCB を含む、種々の芳香族化合物の微生物分解の初発酵素である。RO は、酸化反応を触媒する oxygenase (Oxy)と電子伝達タンパク質［reductase (Red)のみ、あるいは Red と ferredoxin (Fd)］から構成されるマルチコンポーネント型酵素である。現在まで、多くの RO の Oxy コンポーネントの結晶構造が報告されており[1]、基質特異性や酸化反応の位置・立体選択性の決定メカニズムについては多くの知見が存在する。一方で、RO の反応機構、すなわち、酸素の活性化や基質の結合がどのような順序で行われているかについては報告が乏しく、未だ結論が得られていない状況であった。本研究では、RO の一種である carbazole 1,9a-dioxygenase (CARDO)を材料に、Oxy と基質や酸素との複合体結晶を取得し、RO の反応機構を詳らかにする事を目的とした。

2 実験

これまでに、CARDO の Oxy:Fd 複合体に基質である carbazole (CAR)を soaking し基質複合体の結晶構造を得ており[2]、本研究では更に、Oxy:Fd 複合体を還元処理した後に CAR を soaking したもの(Oxy:Fd$^{red\text{-}CAR}$)、還元処理した後に酸素を導入したもの (Oxy:Fd^{O2})、還元処理した後に CAR と酸素を導入したもの (Oxy:Fd$^{CAR\text{-}O2}$)の結晶構造をそれぞれ 1.95 Å、1.85 Å、2.0 Å の分解能で取得した。

3 結果および考察

図 1 に示すように、Oxy:Fd$^{red\text{-}CAR}$ では、還元処理をしていない Oxy:Fd:CAR 三者複合体 (Oxy;Fd^{CAR})と比較して、nonheme iron に配位している Asp333 が 0.5 Å 程度 CAR から離れる方向にシフトするということが明らかとなった。また、Oxy:Fd^{O2} では、二つの酸素原子と nonheme iron が三角形を形成する、side-on の形で酸素が存在していた。二つの酸素原子間の距離は 1.45 Å であったことから、酸素はペルオキシド体として存在することが示唆された。結晶化条件の pH (約 5.5)を鑑みると、Fe(III)-hydroperoxo として存在している可能性が考えられた (図 2)。Oxy:Fd$^{CAR\text{-}O2}$ では、CAR の 1 位、9a 位の炭素原子と peroxide のそれぞれの酸素分子の距離はいずれも 2.9 Å であったため、Oxy が CAR の 1 位と 9a 位に対する二水酸化を触媒することの構造的裏付けをとる事が出来た (図 2)。

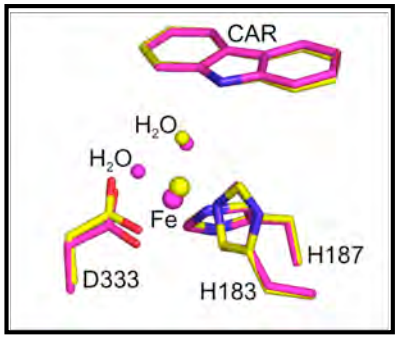

図 1 ：還元による Asp333 の移動
赤：Oxy:Fd$^{red\text{-}CAR}$、黄：Oxy:Fd^{CAR}

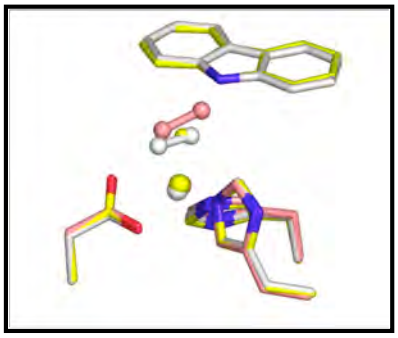

図 2：活性中心への酸素の結合
黄：Oxy:Fd^{CAR}、白：Oxy:Fd$^{CAR\text{-}O2}$、ピンク：Oxy:Fd^{O2}

4 まとめ

以上のことから、Oxy が Fd から電子を受け取ると、基質である CAR が結合し、それに伴い Asp333 の移動が起こる。この移動により作られたスペースに酸素が結合し、peroxide 体となる。その後、酸素原子間の結合が開裂し、CAR への二水酸化反応が起こるという一連の反応機構が提唱された[3]。

参考文献

[1] DJ. Ferraro *et al.*, BBRC **338** (2005) 175-90.
[2] Y. Ashikawa *et al.*, Structure **12** (2006) 1170-89.
[3] Y. Ashikawa *et al.*, BMC Struc. Biol. in press.

*anojiri@mail.ecc.u-tokyo.ac.jp

NW12A/2010G698

X-ray crystallographic analysis of Inhibitor-free Structure of L-(2*S*,3*S*)-Butanediol Dehydrogenase

Tomohito Shimegi[1], Takashi Ohtsuki[1], Masami Kusunoki[1], Sadaharu Ui[1,*]
[1]Graduate School of Medicine and Engineering, Univ. of Yamanashi, Takeda, Kofu, Yamanashi 400-8511, Japan

1. Introduction

2,3-Butanediol (BD) is known as a by-product of sugar metabolism in microorganisms. There are three types of stereoisomer of BD (D-, L-, and meso-forms). Since the ratio of BD stereoisomers depends on the organisms and the culture conditions of the fermentation process, various 2,3-butanediol dehydrogenases (BDHs) catalyzing the NAD-dependent redox reaction between acetoin (AC) and BD were identified from many microorganisms. Of these BDHs, meso-BDH from *Klebsiella pneumoniae* IAM 1063, specific for meso-BD and D-AC, and L-BDH from *Brevibacterium saccharolyticum* C-1012, specific for L-BD and L-AC belong to the short-chain dehydrogenase/

reductase (SDR) family, based on their amino acid sequence. These two enzymes share a 50% homology of their amino acid sequence. Therefore, it is very interesting to ascertain exactly how the homologous BDHs distinguish diastereomers.

We previously determined the crystal structures of meso-BDH and L-BDH in complex with NAD^+ and inhibitor mercaptoethanol[1-2]. In order to verify the influence of the inhibitor upon the conformation around the substrate binding pocket, we have tried to analyze crystal structure of L-BDH with NAD^+ only .

2. Results and Discussion

Crystals of L-BDH in complex with NAD^+ were prepared by the sitting drop vapor diffusion method in 50 mM MES buffer (pH 6.0), 30% PEG4000, 20% glycerol at 20°C. X-ray diffraction data collections were performed at Photon Factory BL-NW12A at 95 K. 370,634 measured reflection were reduced to 80,761 unique reflections with an overall R_{merge} of 8.0 %. Crystals belong to the space group $P2_1$ with unit cell dimensions a = 69.8 Å, b = 102.9 Å, c = 119.1 Å, β = 97.4°. This represented 95.5 % completeness and 3.5 redundancy at 2.38 Å. There are two molecules of L-BDH tetramers in the asymmetric unit. The structure of L-BDH in complex with NAD^+ was solved by the molecular replacement method using MOLREP. L-BDH in complex with NAD^+ and mercaptoethanol(PDB code:3A28) was used as a search model. Structure refinement was carried out with the program REFMAC5. Subsequently the molecular model was manually rebuilt using the maps with coefficients of sigma weighted $2F_O$-F_C and F_O-F_C maps with the program Coot of version 0.6.2. The final *R*-value was 18.7 % (R_{free} = 25.2) for the resolution range of 33 – 2.38 Å.

The eight subunits (A-H) in the asymmetric unit can be superimposed with an averaged pairwise RMSD of 0.27 Å for α-carbons. Therefore, the structure of subunit A is taken as the representative of the eight subunits.

The superposition around the substrate binding region of subunit A of the enzyme between with and without the inhibitor is shown in Fig. 1. Except side chains of Trp192 and Phe148 deviating slightly, there is little difference of side chain conformations of the residues around the substrate binding region upon binding of the inhibitor. Based on the determination of the inhibitor-free structure of L-BDH, we will be able to discuss substrate specificity and kinetic of the enzyme using crystal structures of mutated L-BDHs in complex with the inhibitor and free enzymes.

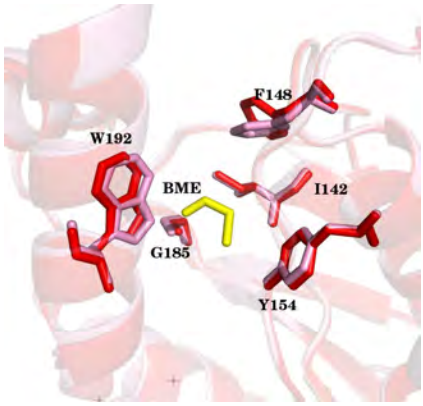

Fig. 1: The superposition around substrate binding region of L-BDH with(red) and without(pink) mercaprtoethanol.

References

[1] M. Otagiri *et al.*, J. Biochem. **129**, 205-208 (2001).
[2] M. Otagiri *et al.*, FEBS lett. **584**, 219-223 (2010).

* ui@yamanashi.ac.jp

5A, NW12A/2011G002, 2011G502 (PF); 26B1/2011A1902 (JASRI)

New insight into the substrate binding of dye-linked L-proline dehydrogenase

Haruhiko Sakuraba*[1], Kazunari Yoneda[2], Toshihisa Ohshima[3]
[1] Department of Applied Biological Science, Faculty of Agriculture, Kagawa University, 2393 Ikenobe, Miki-cho, Kita-gun, Kagawa761-0795, Japan
[2]Department of Bioscience, School of Agriculture, Tokai University, Kumamoto, Japan
[3]Institute of Genetic Resources, Faculty of Agriculture, Kyushu University, Fukuoka, Japan

Introduction

Dye-linked L-proline dehydrogenase (LPDH) catalyzes the oxidation of L-proline to Δ^1-pyrroline-5-carboxylate with reduction of 2,6-dichloroindophenol. The enzyme is supposed to function as the mediator of electron transfer from an L-proline into the electron transfer system. Two different types of LPDH, PDH1 and PDH2, have been identified in the anaerobic hyperthermophile *Pyrococcus horikoshii*. PDH1 is a heterooctameric complex (α4β4) that also contains FAD, FMN, Fe and ATP, while PDH2 is a heterotetrameric complex (αβγδ) composed of an L-proline dehydrogenase, an NADH dehydrogenase, a ferredoxin-like protein and a protein of unknown function. We have previously solved the three-dimensional structure of the PDH1 [1], which we found to be a unique diflavin dehydrogenase containing a novel electron transfer system. Here we report the crystal structure of a third type of LPDH (ApeLPDH), found in the aerobic hyperthermophilic archaeon *Aeropyrum pernix*, whose structure (homodimer) is much simpler than those of previously studied LPDH. This is the first description of an LPDH structure with L-proline bound, and it provides new insight into the substrate binding of LPDH.

Materials and Methods

Selenium multiple-wavelength anomalous dispersion data for selenomethionyl ApeLPDH and single-wavelength (1.0 Å) data for a deletion mutant lacking C-terminal Leu428 (ΔL428) were collected on the beamline 5A and NW12A at the Photon Factory. The data were processed using HKL2000 and the CCP4 program suite.

Results and Discussion

The overall fold of the ApeLPDH subunit showed similarity to that of the PDH1 β-subunit, which is responsible for catalyzing L-proline dehydrogenation. However, the situation at the subunit-subunit interface of the ApeLPDH was totally different from that in PDH1 [2]. The presence of additional surface elements in the ApeLPDH contributes to a unique dimer association. In addition, the C-terminal Leu428, which is provided by a tail extending from the FAD-binding domain, shielded the active site, and an L-proline molecule was entrapped within the active site cavity (Figure 1). Because L-proline was not present during crystal growth, this molecule might have originated in the *E. coli* cells and was then retained throughout the protein purification.

The Km of a ΔL428 for L-proline was about 800 times larger than the Km of the wild-type enzyme, though the kcat values did not differ much between the two enzymes. In the ΔL428 structure, we found no L-proline molecule in the active site. Moreover, we superimposed FAD-binding domain of the ApeLPDH onto the equivalent residues of ΔL428, and found that substrate-binding domain of ApeLPDH was rotated about 10° relative to the corresponding domain of ΔL428. This indicates that L-proline incorporation leads to a rotation of the substrate-binding domain. Therefore, the ApeLPDH structure assumes a closed conformation and the ΔL428 structure assumes an open one. The C-terminal chain of the ΔL428 was about 13° rotated clockwise compared with the corresponding residues of ApeLPDH, and this results in the active site cavity being solvent-accessible (Figure 2). These results strongly suggest that the function of the C-terminal Leu428 is to provide a solvent-inaccessible environment for the enzyme reaction, as well as to hold the substrate properly within the active site.

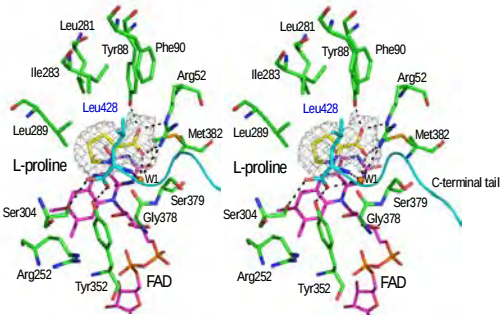

Figure1 Stereographic close-up of the L-proline-binding site in ApeLPDH

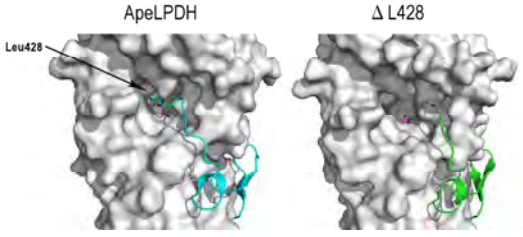

Figure 2 Close-up views of the active site and C-terminal region

References

[1] H. Tsuge *et al.*, *J. Biol. Chem.* **280,** 31045 (2005).
[2] H. Sakuraba *et al.*, *J. Biol. Chem.* **287,** 20070 (2012).

* sakuraba@ag.kagawa-u.ac.jp

1A, 5A, 17A, NW12A/2011G-023

L 型糖を基質とする代謝酵素の立体構造解析
Structural study of an enzyme catalyzing L-glucose

深野和紘[1]、清水哲[2]、佐々木康幸[1]、高谷直樹[2]、中村顕[2]、矢嶋俊介[1*]
[1]東京農業大学バイオサイエンス学科、〒156-8502 世田谷区桜丘 1-1-1
[2]筑波大学生命環境系、〒305-8572 つくば市天王台 1-1-1

1 はじめに

酵素には「基質特異性」と「反応特異性」がある。そのために生物には「ホモキラリティ」という現象がみられる。「ホモキラリティ」とは、生物が鏡像異性体のうちの一方を偏って利用する性質である。鏡像異性体の物理学的性質はほぼ等しいが、「形」は明らかに異なる。ゆえに、酵素は鏡像異性体を区別し、生物は利用しやすい一方のみを効率良く選択するように進化してきたと考えられている。例えば、酵素を構成するアミノ酸は L 体が、栄養源となるグルコースは D 体が利用される。

生物においてグルコースは D 体だけが利用されることは 1940 年に Rudney H.によって示されてから、現在に至るまでの常識である。事実、解糖を始めとした既知の異化経路に働くグルコース代謝酵素は専ら D-グルコースのみを基質として利用する。その一方で、L-グルコースの異化経路は知られておらず、L-グルコースを結合するための「形」も知られていない。

以上の点から、L-グルコースは生物の栄養源にはならないと考えられてきた。しかし近年、筑波大学・中村のチームにより L-グルコースを資化する微生物が複数単離された。そしてそのうち *Paracoccus* sp. 43P 株において、L-グルコース代謝経路の全貌が明らかになった。本代謝経路は、計 6 つの酵素から構成され、大きく 3 つの段階からなる。第一段階は L-グルコースの酸化であり、LgdA により L-グルコースが L-グルコノラクトンへと酸化され、自然酸化によりさらに L-グルコン酸へと変換される。そこで、LgdA の反応機構、基質特異性解明をめざし、立体構造解析を行った。

2 実験

Paracoccus sp.43P 株由来 L-グルコース脱水素酵素(LgdA)遺伝子を含むプラスミド pET21a(+)-*lgd*A を発現プラスミドとして用いた。*lgd*A 遺伝子領域の C 末端には、6 x His-tag が融合している。初期位相決定のために、 Se-Met 置換結晶を作成した。Se-Met 置換体の構造は、Se-Peak で集められた SAD データ由来の実験位相を用いて解かれた。実験位相情報から高い品質の電子密度が得られた。そして、Phenix AutoSol を用いて、自動的に構造構築が行われた。

自動で構築されなかったアミノ酸は、Coot を用いて、当てはめた。Native LgdA の apo 構造は、Se-Met 置換体の構造を用いて、1.75 Å の分解能をもって、Molrep を用いて、分子置換法により解を得た。基質および補酵素 NAD^+との複合体構造はソーキング法により取得した。初期構造は分子置換法を用いた。

3 結果および考察

構築された構造は最終的に、R/R_{free} がそれぞれ、16.3%/19.3%になるまで、Refmac5 を用いて精密化した。この構造は、４本のポリペプチド、1346 の水分子、そして１つの PEG 分子を含んでいる。LgdA は結晶中でほぼ完全な 222 対象を持つ四量体構造をとっていた。四量体内で最も大きな接触は、四量体の中心部に存在する、拡張されたβシート同士の接触である。サブユニット A-B と C-D のそれぞれで、２つのサブユニットの８ストランドβシートが隣り合って１６ストランドβシート構造をとっていた。四量体の中央でこの拡張βシートが２つ向かい合って接触していた。このβシートは顕著な右手ひねりをもっており、全体としてほぼ 180° 回っていた。今回、apo 型酵素の他に、ソーキング法により、基質と補酵素 NAD^+との３者複合体構造の取得にも成功した。L-グルコースと NAD^+との複合体構造において、４量体のすべての分子が NAD^+を結合していた。いずれもニコチンアミド基の環構造およびアミド基の電子密度が明瞭に観察できた。一方で基質は、４つのサブユニットのうち３つにおいて結合が観察された。

4 まとめ

今回、L-グルコースを代謝する酵素の立体構造を明らかにした。今後は、変異体などの解析を行い、より詳細な反応機構の解明を目指す。

謝辞

データ測定にあたり PF スタッフの方々に深く感謝致します。

* yshun@nodai.ac.jp

17A/2012S1-001

The structural basis for the 2D assembly of a β-neurexin 1/neuroligin 1 complex

Hiroki Tanaka[1], Terukazu Nogi[1, 2], and Junichi Takagi[1*]
[1]Osaka Univ. Yamadaoka 3-2, Suita, Osaka 565-0871, Japan
[2]Yokohama City Univ. Suehiro-cho 1-7-29, Tsurumi-ku, Yokohama, Kanagawa 230-0045, Japan

Introduction

Neurexins (Nrxs) and Neuroligins (NLs) are synaptic cell adhesion proteins that are thought to be involved in presynaptic and postsynaptic differentiation. Ectodomains of presynaptic Nrxs and postsynaptic NLs interact and assemble with each other across the synaptic cleft. This triggers the further assembly and rearrangement of several synapse-associated molecules through protein-protein interactions in the cytoplasmic region, resulting in the functional specialization of asymmetrical synapse [1]. The molecular mechanism of cell-cell adhesion mediated by Nrxs and NLs has been revealed through the X-ray structure, while it remains unclear if and how the trans-cellular complex can promote recruitment of cytoplasmic binding partners.

Here we report the crystal structure of Nrx1β and NL1 [2]. This structure exhibits the unique structural feature; the complexes assemble laterally into a "layer", that the spatial distribution is compatible with the trans-synaptic complex on adhered neurons.

Experimental Procedure

Recombinant NL1 ectodomain was produced as a fusion protein of the C-terminal segment of human growth hormone (hGH) in mammalian cell line CHOlec3.2.8.1 [3]. Nrx1β was overexpressed in E.coli as a fusion protein of glutathione S-transferase (GST). NL1 and Nrx1β were purified using affinity chromatography with Ni-NTA and immobilized glutathione respectively. Both proteins were treated with TEV protease to cleave fusion proteins and forther purified by ion-exchange chromatography. Equal molar mixture of both purified proteins was concentrated to approximately 10mg/ml for crystallization.

Unexpectedly, we observed the formation of crystalline precipitant immediately after addition of 2mM Ca^{2+} into the mixture. Finally, we obtained the crystal for X-ray diffraction analysis by hanging drop vapor diffusion. The crystal was grown under condition of 5 mM $CaCl_2$ in 10 mM Tris-Cl (pH 8.0) and 0.1 M NaCl at 293K, followed by the treatment of 10 mM Tris-Cl (pH 8.0), 0.1 M NaCl, and 20 % PEG400 for dehydration and cryoprotection.

Diffraction data were collected using synchrotron radiation beamline BL-17A of Photon Factory. The data were processed using the *HKL*-2000 program package [4]. Phase determination was accomplished by molecular replacement method using MOLREP [5]. The structure model was built using COOT [6] with cycles of model refinement with REFMAC5 [7]. This model structure was validated using the program MOLPROBITY [8].

Results and Discussion

The Nrx1β/NL1 complex comprises a heterotetramer in which two Nrx1β protomers bind to distal ends of NL1 homodimer. Additionally, the heterotetrameric complexes are regularly assembled into a plane in the crystal, forming a highly unique sheet-like structure (Figure 1). In this sheet, heterotetramers oriented in the same direction are aligned along the crystallographic *a*- and *c*-axis, and the most C-terminal tails of Nrx1β and NL1 are all pointing toward opposite membrane. This sheet mimics the situation that Nrx1β encounters and assembles with NL1 at the synaptic cleft. In fact, electron microscopic analysis revealed the 2D sheet-like structure at the site of cell-cell contact [2]. These findings indicate a mechanism in which Nrx1β and NL1 spontaneously assemble into the 2D sheet under physiological condition in the intact cell.

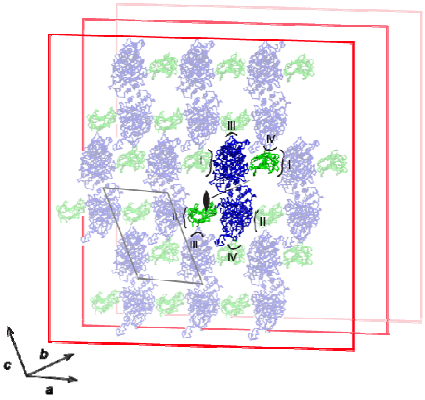

Figure 1 The 2D-assembled structure of Nrx1β/NL1 complex.

References

[1] T. C. Südhof, Nature **455** (2008) 903.
[2] H. Tanaka *et al.*, Cell Rep. **1** (2012) *in Press*.
[3] P. Stanley, Mol. Cell. Biol. **9**, (1989) 377.
[4] Z. Otwinowski and W. Minor Methods Enzymol. **276** (1997) 307.
[5] A. Vagin and A. Teplyakov Acta Crystallogr. **D66** (2010) 22.
[6] P. Emsley and K. Cowtan Acta Crystallogr. **D60** (2004) 2126.
[7] G. N. Murshudov *et al.*, Acta Crystallogr. **D53** (1997) 240.
[8] B. Vincent *et al.*, Acta Crystallogr. **D66** (2010) 12.
* takagi@protein.osaka-u.ac.jp

6A/2011G055

Conformation of YB-1 protein at moderate and high ionic strength studied by SAXS technique

Alexander Timchenko[1, 2], Sergey Guryanov[1], Lev Ovchinnikov[1], Gennady Semisotnov[1], Masaji Shinjo[2], Hiroshi Kihara[2*]

[1] Institute of Protein Research, Pushchino, Russia, 142290;
[2]Department of Physics, Kansai Medical University, Hirakata, Osaka 573-1136, Japan

Introduction

Amyloid structures were discovered as protein deposits associated with several neurodegenerative diseases. Recent studies have shown that various proteins, even not related to any known amyloid disease, can aggregate into fibrils under the native fold- destabilizing condition [1] and that normal proteins become toxic in this case. YB-1 is a multifunctional RNA and DNA-binding nucleocytoplasmic protein. It was shown that purified YB-1 in solution, as well as YB-1 in association with RNA at a high YB-1/mRNA ratio, formed multimers up to 800 kDa [2]. Recently we reported that YB-1 is capable of forming elongated fibril structures under high ionic strength conditions (2M LiCl) [3]. It was suggested that these fibrils were amyloid-like. It is interesting to understand the initial steps of this process of oligomerization. Here we present SAXS patterns of YB-1 at moderate ionic strength and at high one (1M KCl).

Experimental

The full length YB-1 (M=36kD) was purified as described earlier [2]. The buffer with moderate ionic strength was 500 mM K-phosphate pH 7.4 and protein concentration was 8.8 mg/ml. The buffer with high ionic strength was 20 mM K-phosphate 1M KCl pH 7.4 and protein concentration was 3.8 mg/ml. Synchrotron X-ray measurements were done on a small-angle camera BL-15A (Photon Factory, Tsukuba) using CCD-detector. The range of scattering vectors Q=0.008-0.2 $Å^{-1}$.

Results

SAXS patterns in the Guinier coordinates (log I versus Q^2) for YB-1 in 0.5 M K-phosphate and in 1 M KCl are presented in Fig. 1. One can see the non-linear character of scattering curves for the protein indicating substantial association of protein molecules. The values of molecular mass (M_w) and a radius of gyration (R_g) of particles estimated from the initial part of scattering curves are given in the legend to Fig. 1. These estimates show the association of the protein in both cases. The analysis of aggregate shape from SAXS data in coordinates log I versus log Q has shown that YB-1 aggregate in 0.5M K-phosphate is strongly elongated consisting of three monomers. The dimensions of this aggregate are given in the legends to Fig. 1. At high ionic strength very large compact aggregates are formed. Thus, one can speculate that at moderate ionic strength the strongly elongated particles consisting of three monomers might be the blocks forming amyloid-like fibrils. At high ionic strength both fibrils (2M LiCl) and compact aggregates (1M KCl) can be formed depending on ion characters.

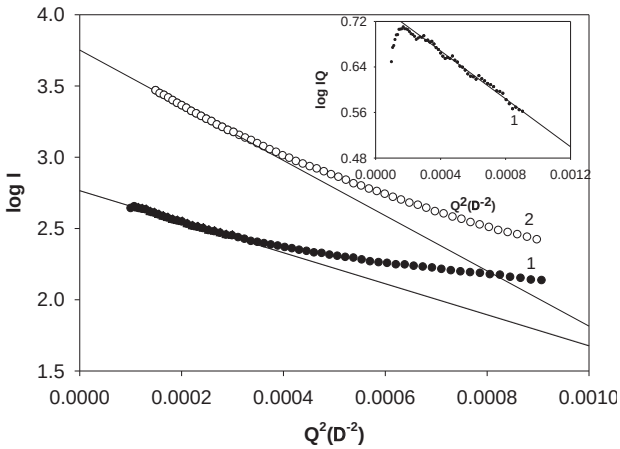

Fig.1 The Guinier plots for YB-1. 1 – at moderate ionic strengh; 2 – at high ionic strength. The corresponding values of molecular mass and radius of gyration evaluated from the initial part of scattering patterns are (M_w= 94 kDa, 1030 kDa; R_g= 60 Å, 116 Å, respectively). *Insert*: Log IQ versus Q^2 plot for the evaluation of R_c value of cross-section. The corresponding R_c value estimated from the slope is 31 Å and, as consequence, the value of length of particle is 285 Å for 1.

References

1) Bychkova & Ptitsyn , *FEBS Lett.*, **359**, 6, 1995
2) Evdokimova V.M. *et al*., *J. Biol. Chem*., **270**, 7, 1995.
3) Selivanova O.M. *et al*., *Bichemistry(Moscow)*, **75**, 1, 2010

*** E-mail: kiharah @aol.com**

5A/2011G075

Structure of free tRNA^{Gly}(CCC) from *Pyrococcus horikoshii*

Yukari Miyamoto, Emico Uchikawa & Michiko Konno*
[1] Department of Chemistry and Biochemistry, Graduate School of Humanities and Sciences, Ochanomizu University, 2-1-1 Otsuka, Bunkyo-Ku, Tokyo 112-8610, Japan

1 Introduction

Gly-tRNA synthetase (GlyRS) belongs to Class IIa as the same as Pro-tRNA synthetase, Thr-tRNA synthetase and His-tRNA synthetase (ProRS, ThrRS and HisRS) which have the anticodon binding domain consisting of mixed α/β domain in the C-terminal. Three bases XGU, XGG and XCC (X stands for A, G, U or C) of the anticodon of tRNA^{Thr}, tRNA^{Pro} and tRNA^{Gly}, respectively are anticipated to be bound on three corresponding regions of the anticodon binding domain with the same topology. However, in the structure of "tRNA^{Thr}(CGU) bound" ThrRS [1], the bases of G35 and U36 arrange at neighborhood in parallel to each other with hydrogen bond, whereas in the structure of the "tRNA^{Pro}(CGG) bound" ProRS [2] in which the 3'-CCA end is far away from the active site in ProRS, G35 locates the similar position with G35 of the former but G36 is at the different position from U36. In order to clarify the three binding regions of the anticodon bases of tRNA^{Gly}, we determined the crystal structure of free tRNA^{Gly}(CCC) from *Pyrococcus horikoshii* at 3.0 Å resolution and constructed the model of tRNA^{Gly} bound GlyRS from *Thermus thermophilus* [3]. We discuss that the conformation change of tRNA^{Gly} occurs in the process of bound GlyRS on the basis of comparison of structures between free tRNA and tRNA bound aaRS.

2 Experiment

Crystallization was carried at 20°C by vapour diffusion in sitting drops. The droplet produced by merging 0.7 μL of 10mg/mL GlyRS and tRNA^{Gly} with molar ratio of 1:1 and 0.7 μL of the reservoir solution was equilibrated against the reservoir solution containing 100 mM imidazole pH 8.0, 200 mM $Ca(OAc)_2$, 10% PEG8000. The intensity data of needle-like shaped crystals were collected in Photon Factory beam-line 5A and Spring-8 BL32XU, and dataset processed using HKL2000 suite gave R merge of 7.4 % at 3.0 Å. The lattice unit size revealed that crystal is not complex but free tRNA^{Gly}. The crystal is tetragonal system and belongs to space group $I4_122$. The lattice constants are a=b=162.8 Å, c=49.91 Å and Z=16. The reasonable solution was obtained using Ec tRNA^{Asp} (PDB code 1C0A) as search model by molecular replacement method (PHASER of CCP4). The repeats of model buildings and refinements using COOT program and the REFMAC5 program gave R_{factor} of 0.25 (R_{free} of 0.28).

3 Results and Discussion

The stick model of Ph tRNA^{Gly} is shown in Fig.1. The 3' single-stranded ACCA end has the base stacking on the next base and forms a regular helical conformation. The regular helical structure is also observed in the ACCA end of free Sc tRNA^{Asp}(GUC) from *Saccaromyces serevisiae* [4]. Comparison of structures of free tRNA^{Gly}, free Sc tRNA^{Asp}(GUC) and free Sc tRNA^{Phe}(GAA) [5] with structures of tRNA^{Asp} bound AspRS [6] and tRNA^{Thr} bound ThrRS indicates that the L shape of free tRNA has open conformation (the angle between helical axis of the acceptor stem and the anticodon stem is larger) whereas that of tRNA bound aaRS has close conformation. In the anticodon loop of Ph tRNA^{Gly}(CCC), the bases of C35C36A37A38 have stacking form but the base of C34 deviates and the base of U33 directs outside. On the other hands, in free tRNA^{Asp} and free tRNA^{Phe}, the 34-38th bases have stacking form. The bend is observed between the 33th and 34th backbone in all free tRNAs. The docking model of Ph tRNA^{Gly}(CCC) on Th GlyRS shows the 3'CCA terminal and the anticodon bases are apart away from the active site and the binding region of GlyRS, respectively if tRNA does not change conformation from open to close form. The attaching of the inside of tRNA^{Gly} to GlyRS maybe induces the conformation change of tRNA.

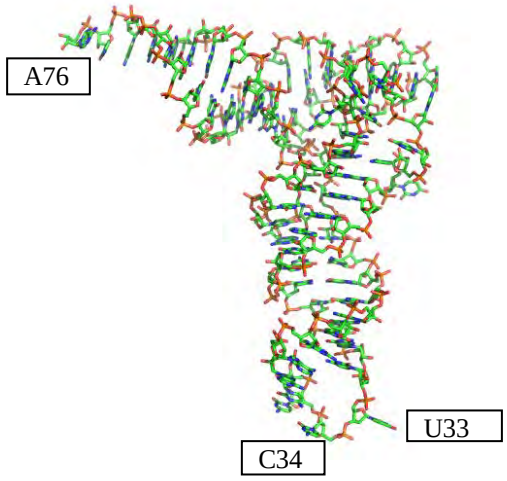

Fig. 1: Model of Ph tRNA^{Gly}

References
[1] R. Sankaranarayanan, *et al. Cell* **97**, 371-381, 1999.
[2] S. Cusack, *et al. Structure* **6**,101-108, 1998.
[3] D. T. Logon, *et al.* EMBO *J.* **14**, 4156-4167, 1995.
[4] D. Moras, *et al. Nature* **288,** 18-25, 1980.
[5] B. Hingerty, *et al. J. Mol. Science* **124**, 523-534, 1978.
[6] S. Eiler, *et al. EMBO J.* **18**, 6532-6541, 1999.
* konno.michiko@ocha.ac.jp

1A, 5A, 17A, NE3A, NW12A/2011G-080/ 2011A1908

バイオマス分解に適したβ-グルコシダーゼの結晶構造解析
Crystallography of beta-glucosidses suitable for biomass degradation

伏信進矢[1*], 鈴木健太郎[1], 城俊徳[1], 若木高善[1],
炭谷順一[2], 川口剛司[2], 矢追克郎[3], 宮崎健太郎[3]

[1]東京大学大学院農学生命科学研究科、〒113-8657 東京都文京区弥生 1-1-1
[2]大阪府立大学大学院生命環境科学研究科、〒599-8531 大阪府堺市中区学園町 1 - 1
[3]産総研 生物プロセス研究部門、〒305- 8566 茨城県つくば市東 1-1-1

1 はじめに

木質などのセルロース系バイオマスからのバイオエタノール生産は、バイオマス（植物細胞壁の多糖）を分解して単糖（またはオリゴ糖）を得る糖化過程と、そこから酵母を用いてエタノールを得る発酵過程からなる。酵素（セルラーゼ）によるセルロースの糖化においては、現在、トリコデルマ属などの糸状菌由来の酵素製剤が主に用いられているが、各種のセルラーゼ成分のうち、β-グルコシダーゼによるセロビオースからグルコースへの分解活性が低く、ボトルネックになりやすい。実際、市販されているセルラーゼ製剤の多くでβ-グルコシダーゼ活性が増強されている。本研究では、セロビオースに対する活性が非常に高く、セルラーゼ製剤への添加に盛んに用いられている糸状菌由来のβ-グルコシダーゼ(AaBGL)と、高濃度のグルコースの存在下においても活性が阻害されない、メタゲノム由来のグルコース耐性β-グルコシダーゼの立体構造を決定することを目的とした

2 実験

今年度の前半は東日本大震災の発生による KEK の停止にともない、SPring-8 量子ビーム施設震災優先枠で実験を行った（2011 年 7 月 20 日 BL26B1：3 シフト）。後半は通常どおりに KEK-PF で実験を行った。

3 結果および考察

AaBGL の結晶構造を決定し（図１）、基質フリー以外にも、各種の阻害剤との複合体の構造を得ることに成功した。AaBGL1 は分子の片面に多数の N-リンク糖鎖の修飾が起こっており、安定性に寄与すると推定された。さらに、活性中心では芳香環を持つ残基が集中しており、これが基質を強く結合して高い活性が発揮されていると考えられた。

メタゲノム由来のβ-グルコシダーゼからは、Td-2F2 と我々が呼んでいる遺伝子産物の構造決定に成功した（図２）。グルコース、D-フコースなどの存在下で、超高分解能(1.1Å)の構造が得られている。Td-2F2 は基質グルコースの C6 ヒドロキシル基の近傍のループ部分が特徴的な構造をとっていることが明らかになり、これがこの酵素の広い基質特異性とグルコース耐性に関わっていると考えられた。

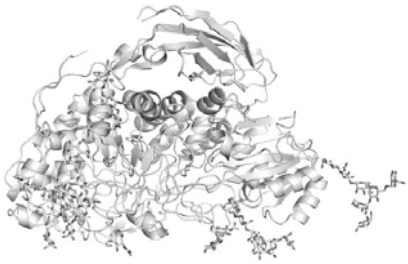

図１：AaBGL の全体構造

図２：Td-2F2 の全体構造

謝辞

実験をサポートして下さった KEK および PF のみなさんに感謝いたします。震災枠での実験をサポートして下さった馬場清喜先生、熊坂崇先生をはじめとする SPring-8、JASRI のみなさんにも感謝いたします。

* asfushi@mail.ecc.u-tokyo.ac.jp

17A, NW12A/2011G087

Crystal structure of Swi5-Sfr1C complex from fission yeast

Naoyuki Kuwabara[1*], Hiroshi Hashimoto[2], Mamoru Sato[2] and Toshiyuki Shimizu[1]
[1]Grad. Sch. of Pharm. Sci., Univ. of Tokyo, 7-3-1 Hongo, Bunkyo-ku, Tokyo 113-0033, Japan
[2]Grad. Sch. of Nanobio., Yokohama City Univ., 1-7-29 Suehiro-cho, Tsuruku, Yokohama, Kanagawa 230-0045, Japan

1 Introduction

Homologous recombination (HR) plays a central role not only in genetic diversity but also in preserving genomic integrity, and thus defects in HR may result in cancer susceptibility. RecA-family DNA recombinases are key players in HR. In eukaryotes, there are two known classes of recombinases, Rad51 and Dmc1; the former functions generally in both mitotic and meiotic HR and HR-mediated DNA repair, and the latter acts specifically in meiosis. The Swi5-Sfr1 complex from the fission yeast *Schizosaccharomyces pombe* is a second class of auxiliary proteins. The complex binds directly and stimulates both Rad51- and Dmc1-mediated strand-exchange reactions. However, the mechanistic insight remains unclear.

Here we present the crystal structures of Swi5 and its complex with the C-terminal domain of Sfr1 (Sfr1C), which is more conserved among various species than the N-terminal domain.

2 Experiment

Diffraction data were collected at 100 K on beamline BL-17A at the Photon Factory (PF), Tsukuba, Japan using an ADSC Quantum 270 detector and on beamline NW12A at the Photon Factory Advanced Ring (PF-AR) using an ADSC Quantum 210r detector. Diffraction images were indexed, integrated and scaled using the *HKL*-2000 package

The structure of the Swi5-Sfr1C complex was solved by single-wavelength anomalous diffraction using the SeMet-labeled Swi5-Sfr1C complex crystal. Experimental phases were calculated with SHELX. Refinment and model building were performed using the programs Refmac5 and Coot, respectively.

3 Results and Discussion

The three-dimensional structure of the Swi5-Sfr1C complex shows an elongated shape (Fig.1). Swi5 and Sfr1 form a parallel coiled-coil heterodimer. In the complex, the long continuous α helix observed in the Swi5 structure alone is interrupted. The Swi5 and Sfr1C subunits of the heterodimer are firmly joined by two leucine zippers and a bundle structure at the bottom. The first leucine zipper, formed by $\alpha1^{swi5}$ and $\alpha1^{sfr1}$, shows a typical arrangement. The second leucine zipper, composed of $\alpha2^{swi5}$ and $\alpha2^{sfr1}$. Remarkably, the structure of the Swi5-Sfr1C complex is sharply kinked (130°) beginning just after the first leucine zipper at $Lys30^{swi5}$ and $Lys212^{sfr1}$. Beyond this kink, the structure is held together by the second leucine zipper. The kinked region is stabilized by several interactions. These interactions maintain the relative orientation between the two leucine zippers.

We demonstrated that the Swi5-Sfr1C possesses the function of a recombination activator of Rad51. These results of the present study, including structural features, and biochemical analyses strongly suggest that the elongated and sharply kinked Swi5-Sfr1 is wedged into the Rad51 filament to fix it in an active ATP-bound form. The docking model also shows that Swi5-Sfr1 fits well in the continuous groove created by the in-silico-reconstituted Rad51 filament (Fig.2).

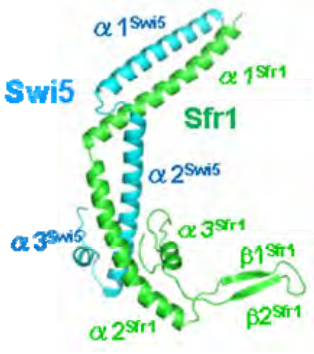

Fig. 1: Crystal structure of Swi5-Sfr1C

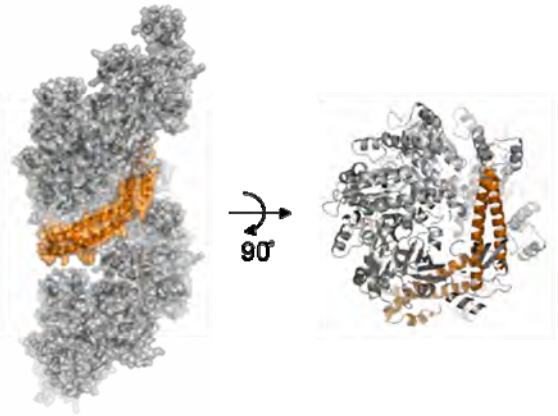

Fig. 2. Rad51 (gray) and Swi5-Sfr1C (orange) ternary complex model

References

[1] N. Kuwabara *et al.*, Acta Crystallogr. Sect. F **66** (2010) 1124.
[2] N. Kuwabara *et al.*, Structure. **20** (2012) 440.

* kuwanao@mol.f.u-tokyo.ac.jp

1A, 17A/2011G097

Crystal structure of the GAPDH-CP12 complex from *Synechococcus elongatus*

Hiroyoshi Matsumura[1*], Akihoro Kai[1], Tsuyoshi Inoue[1]
[1]Department of Applied Chemistry, Graduate School of Engineering, Osaka University

1 はじめに

植物は、カルビンサイクルと呼ばれる二酸化炭素固定経路の酵素群によって、大気中から二酸化炭素を吸収し、糖に変換して成長する。本研究で対象としている２種類の酵素（Phosphoribulokinase; PRK, $NADP^+$-glyceraldehyde-3-phosphate dehydrogenase; GAPDH）は、カルビンサイクルで機能する酵素であり、その酵素の活性は、光強度に応答して調節されることで知られる。具体的には、①暗所で酸化されたチオレドキシンによってこれら分子の分子内でジスルフィド結合が形成され、それによって酵素が不活性化する、また、②同じく酸化されたチオレドキシンがリンカータンパク質 CP12 を酸化し、さらに NAD(H)がトリガーとなって GAPDH-CP12-PRK 超分子複合体を形成し、それによって GAPDH, PRK が不活性化されるという調節が知られている。特に、②の調節メカニズムは最近その生理学的重要性が指摘されており、注目が集まってきているがその分子メカニズムは全く未知であった。

さらにタンパク質科学として興味深いことに、CP12 は、単独では立体構造をとらないタンパク質、すなわち、Intrinsically Disordered Protein （IDP）である。そして、CP12 は、GAPDH と結合しないと PRK と結合できない。つまり、元来特定の立体構造をとらない CP12 は、GAPDH と結合することで部分的に折り畳まれ、その折り畳みがあって初めて PRK と結合できると予想される。このような、IDP の段階的折り畳みメカニズムと GAPDH、PRK の阻害メカニズムを解明するため、本研究では、X線構造解析法による、GADPH-CP12-NAD 複合体の構造解析に取り組んだ。

2 実験

BL1A, 17A にて GAPDH-CP12-NAD の三者複合体の結晶の X 線回折実験を行った結果、2.5Å 分解能の回折強度データを収集した。ここで初めて位相を決定することができ、最終的に 2.2 Å 分解能での構造解析に成功した。

3 結果および考察

GAPDH-CP12-NAD 複合体の立体構造を 2.2 Å 分解能で決定した[1]（図 1）。CP12 の C 末端部分（Thr53-Asp75）のみが GAPDH と結合して立体構造を形成し、その他の部分は特定の立体構造を持たないことが分かった。さらに、CP12 はジスルフィド結合を分子内に有し、同時に NAD とも結合していたことから、GAPDH との結合に CP12 の酸化と NAD が必須である理由が明らかとなった．また、GAPDH の基質結合部位は CP12 によってふさがれており、GAPDH が CP12 の結合によって不活性化する原因が明らかとなった。

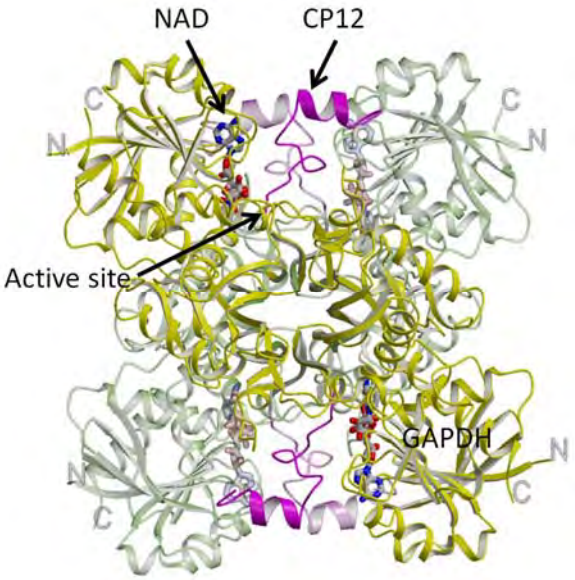

図１：GAPDH-CP12 複合体の立体構造

4 まとめ

本研究によって CP12 による GAPDH 活性の阻害メカニズムが示された。

謝辞

ビームラインサイエンティストの方々には回折強度データの収集に当たり大変御世話になりました。この場をお借りし深く感謝いたします。

参考文献

[1] H. Matsumura, *et al*., *Structure* **19,** (2011) 1846.
* matsumura@chem.eng.osaka-u.ac.jp

1A/5A/17A/2011G108

Structural analysis of temperature stabilization mechanisms using BPTI variants

Mohammad Monirul Islam, Keiichi Noguchi[1], Masafumi Yohda, Yutaka Kuroda

Department of Biotechnology and Life Sciences, and [1]Instrumentation Analysis Center, Tokyo University of Agriculture and Technology, Tokyo 184-8588, Japan.

1 Introduction

Enhancing protein stability is an important aspect of protein engineering, attracting considerable interest both from academic and pharmaceutical/biotechnological perspectives. However, most examples of significant stabilization result from a subtle interplay between the effects of multiple mutations, which is difficult to rationalize, because the effects are intertwined.

Analysis of proteins stabilized by one or two mutations may provide direct insight into stabilization mechanisms, since all effects necessarily result from these mutations. Here, we use BPTI-[5,55], which is a small globular 58 residue protein and is widely used as a model system in protein folding and biophysical studies. In order to shed light into stabilization mechanisms of proteins, we analyzed the thermodynamics and high resolution structure of nine BPTI-[5,55] variants with amino acid substitution at positions 14 and 38[1].

2 Experiments

All BPTI variants were over-expressed in E-coli using the pMMHA expression vector, purified by reverse phase HPLC, and lyophilized. The melting temperatures were measured by monitoring the temperature dependence of the secondary structure content using a Jasco J820 CD spectrophotometer. The X-ray diffraction data were recorded from single crystals at the Photon Factory (Tsukuba, Japan), and the structures were determined by molecular replacement.

3 Results and Discussion

We measured the melting temperatures of nine BPTI-[5,55] variants with G, A, and V at residues 14 and 38 (Table 1). We observed a remarkable twelve-degree thermal stability increase introduced by the A14G substitution, which appeared to be enthalpy driven. High resolution structure of BPTI-[5,55], determined at 1.2 Å resolution, indicated that the enthalpy stabilization is attributable to three structural factors (Fig.1, [3]). First, the A14G mutation displaced the 14-17 loop toward the 36-39 loop by up to 0.7Å improving the local packing, and therefore potentially contributing to enthalpy stabilization through an increase in van der Waals interactions. Second, it removed a potential side-chain steric clash between residues 14 and 36. Last, the A14G mutation also allowed the formation of additional hydrogen bonds between the protein and water molecules in the vicinity of the substitution sites. In contrast, the A38V substitution stabilized BPTI-[5,55] by 4 degree, in terms of entropy, probably by restricting the conformational freedom of the polypeptide chain in the denatured state.

The present observations is one of the first unambiguous analyses of the subtle interplay, taking place at the sub-Angstrom level, between the side-chain and backbone structures producing a major effect on protein stability. They suggest that computational and experimental tools that optimize packing densities by assessing both local backbone deformations and side-chain clashes would have a far-reaching impact on biotechnological industries.

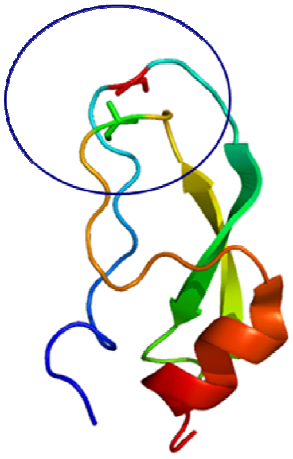

Ribbon model of BPTI-[5,55]. Residues 14 and 38 that were systematically mutated to G, A, V are encircled.

R14/R38	T_m(K)
A/G	310.8
A/A	312.5
A/V	316.7
V/G	313.1
V/A	316.2
V/V	324.4
G/G	322.6
G/A	325.6
G/V	326.9

Table 1: Melting temperatures of 9 variants with the indicated residues at position 14 and 38.

References

[1] Islam, M.M., et al., *PROTEINS,* **77**(4): 962 -970 (2009).

[2] Islam, M.M., et al., *Proc Natl Acad Sci U S A*, **105**(40):15334-9 (2008).

[3] The coordinates of BPTI-[5,55] A14GA38V have been deposited in the Protein Data Bank under the PDB entry code 2ZVX.

5A, 17A, NW12A , NE3A / 2011G112, 2011G122, 2011G1561

哺乳動物キサンチン酸化還元酵素の構造解析
Structural Analysis of Mammalian Xanthine Oxidoreductase.

岡本研*, 松村智裕,草野輝男
日本医科大学生化学（代謝・栄養）、〒113-8605 東京都文京区千駄木 1-1-5

複合金属酵素（鉄とモリブデンを含む）であるキサンチン酸化還元酵素 (xanthine oxidoreductase = XOR) は 2 量体からなる分子量 30 万の巨大タンパク質であり、プリンが分解過程でキサンチンを代謝して尿酸に変換する機能を持つ。体内で過剰に産生された尿酸は痛風の原因物質であるため XOR の阻害剤は痛風、高尿酸血症の治療薬として医学的に重要な化合物である。また XOR は電子受容体として酸素と反応することもあり、生成される活性酸素種による組織障害を予防する意味でも阻害剤の開発、につながる反応機構解明は重要である。

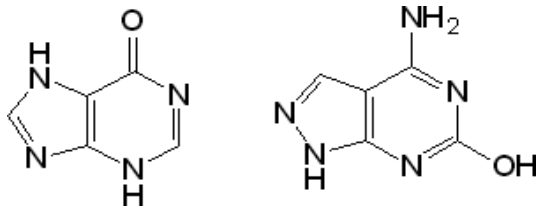

図 1. XOR の基質であるヒポキサンチン（左）基質アナログである 4-amino, 6-hydroxy pyrazolo pyrimidine（右）

我々は PF,AR のビームラインを使用し、還元状態での尿酸結合型酵素の結晶構造を決定することで、天然基質であるキサンチンの水酸化機構を決定した。本課題においてはキサンチンのアナログである 4-amino, 6-hydroxy pyrazolo pyrimidine（図 1）結合型ウシ酵素を還元状態で観察することで、もう一つの生体内基質であるヒポキサンチンの水酸化機構を解明する（図 2）。現在のところ 2.8Å 分解能でのデータ収集が完了しており、今後は結晶化条件、還元の手順などを改良することで、分解能の改善を行う。

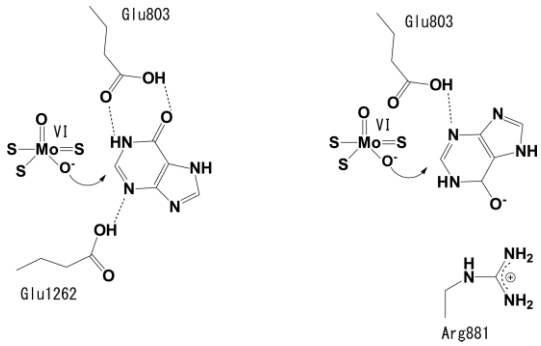

図 2. 基質ヒポキサンチンの結合モードと反応機構
2 個の異なったモデルが提唱されている。

XOR と酸素分子との反応は補酵素 FAD で行われる。哺乳動物 XOR は FAD 近傍の構造変化を生じ、脱水素酵素活性から酸化酵素活性に変換する。この反応機構は PF,AR におけるデータ収集の結果判明した。本課題においては FAD 近傍に存在し、生物種間で保存されているラット N350 をトレオニンに変換した酵素を発現し、結晶構造の決定を目指す。現在は 2.1Å 解像度でデータ収集を終えており、精密化を行なっている(図 3)。今後は基質 NADH 結合型の構造決定を行う予定である。変異酵素の生化学的解析結果とあわせて FAD 周囲の環境に与える影響と活性酸素生成機構の解明を目指す。

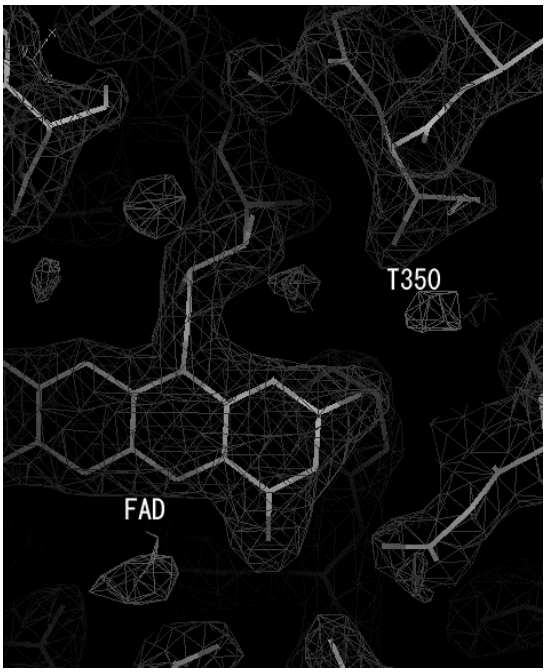

図 3. ラット N350T 変異酵素の結晶構造と 2Fo-Fc map

参考文献
[1] Okamoto K, Kawaguchi Y, Eger BT, Pai EF and Nishino T
J. Am. Chem. Soc. **132** (2010)

* okamoto@nms.ac.jp

10C/2011G114

Local structure of random-coiled poly(*L*-glutamic acid) in added salt solutions

Shigeru Shimizu , Hiroli Ikake, Yoshio Muroga
College of Science and Technology, Nihon University, Tokyo 101-8308, Japan

1 Introduction

Some of polypeptides exhibit the conformational transition, helix-to-coil transition, in aqueous solution. For example, poly(*L*-glutamic acid)(PLGA) shows the transition between the helical-state and random-coiled state by changing pH of solution. However, it is unclarified how the local structure of PLGA depends on added salt speices in aqueous solution.

2 Experiment

Sodium salt of poly(*L*-glutamic acid)(PLGA-Na) of Mw = 9.8×10^4 was purchased from Sigma-Aldrich Chemical Co. Sample solutions were prepared by adjusting the deree of ionisation α of PLGA to 0.8. Polymer concentration C_p was 0.01 g/mL and C_s of added salts concentration, LiCl, NaCl, KCl and CsCl were 0.1M.

SAXS measurements were performed using the small-angle X-ray scattering spectrometer installed at BL10C beam port Photon Factory of High Energy Accelerator Research Organization, Tsukuba, Japan. Scattered X-ray was recorded by an imaging plate system of R-AXIS VII from RIGAKU Co. Two-dimensional scattering data were circle-averaged about the beam center and data was registered over the modulus of the scattering vector q ranging from 0.1 to 4 nm ^{1}, where q is defined by $(4\pi/\lambda)\sin(\theta/2)$ and λ is the wavelength and θ is scattering angle. The details of the apparatus and the measurement are described elsewhere [1]. Since the size of X-ray beam at the sample position was so small compared with sample-to-detector distance that the system could be regarded as point-focusing system. The excess scattering intensity of the sample over the solvent was determined after transmission corrections for both solution and solvent.

3 Results and Discussion

The scattered intensity monotonically decreases with increasing q. Therefore, in the case of PLGA in added salt aqueous solutions of C_s=0.1M, the intermolecular interactions could be neglected. The mean-square radius of cross-section of PLGA chain $< R_{cs}^2 >$ was evaluated from cross-section plot. It was shown that $< R_{cs}^2 >^{1/2}$ was almost fixed at 0.4±0.05nm independently of added salt species. Fig. 1 shows the Kratky plot, $I_{thin}(q)q^2$ vs q, where $I_{thin}(q)$ is scattered intensity of a hypothetical chain with no cross-section. The solid line in Fig. 1 are theoretical scattering function $P(q)$ [2] [3] computed with excluded-volume effect assuming the contour length of the chain L_c = 199.0 nm estimated from molecular weight, M = 9.8×10^4 and the persistence length L_p = 0.3 0.54±0.05 nm, taking into account $< R_{cs}^2 >^{1/2}$.

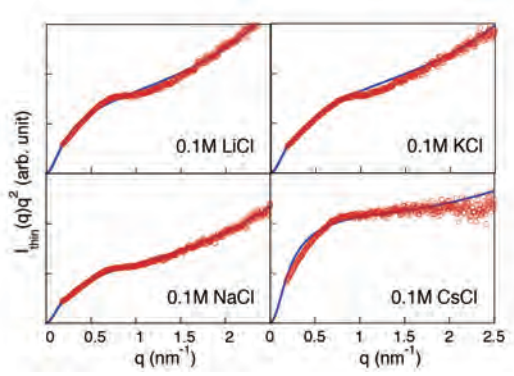

Fig. 1: Kratky plot of PLGA in several added salt solutions. Solid line shows the theoretical scattering function fot worm-like chain.

It is seen that the observed data is well mimicked by the theoretical curve. he persistence length of PLGA chain Lp thus evaluated is 0.54 nm for PLGA in LiCl, 0.54nm for PLGA in NaCl, 0.48 nm for PLGA in KCl, and 0.30 nm for PLGA in CsCl. The magnitude of L_p is comparable with an unpertubed effective bond-length of 0.8 nm [4]. These results might suggest that ionic radii of counter-ion condensed around PLGA chain affects the flexibility of the chain. That is, the chain flexibility was stiffer in the order of ionic radii of counter-ions, i.e., $Cs^+ < K^+ < Na^+ \leq Li^+$.

References

[1] N. Igarashi *et al.*, J. Phys. Conf. Ser. **272** (2011) 012026.
[2] P. Sharp *et al.*, Biopolymers **6** (1968) 1201.
[3] C. Schmid *et al.*, Biopolymers **10** (1971) 883.
[4] R. B. Hawkins *et al.* Macromolecules **5** (1972) 294.

* shimizu.shigeru@nihon-u.ac.jp

BL5A, BL17A, NW12A, NE3A/2011G115

ヒトα_1-酸性糖蛋白質 A 体と薬物の複合体結晶構造
Crystal structures of the A variant of human α_1-acid glycoprotein and drug complexes

中村照也*，丸山徹，山縣ゆり子
熊本大学大学院生命科学研究部
〒862-0973 熊本市中央区大江本町 5-1

1 研究背景

α_1-酸性糖蛋白質 (AGP) は，疎水性化合物の輸送蛋白質群であるリポカリンファミリーに属し，183 のアミノ酸残基から構成され 5 本の N 結合型糖鎖を有する血清蛋白質である．AGP は，臨床で用いられている実に多くの薬物と結合し，さらに，生体反応の急性期 (ストレス，炎症，腫瘍等) に血中および組織中で著しく増加するという特徴を持つ．よって，AGP は炎症・疾患時の薬物結合の主要因子の 1 つといえ，薬物の体内動態，薬理発現を考える上で，AGP の薬物結合機構の解明は重要である．

AGP には，2 つのバリアント (F1*S 体と A 体) が存在し，これらのアミノ酸配列は 88%という高い相同性を示すが，F1*S 体と A 体の薬物に対する結合特異性は大きく異なり，薬物結合の選択性がみられる．その一例として，A 体は，主に三環系抗うつ薬としての共通骨格を持つアミトリプチリンなどに対して高い親和性を有する．一方，F1*S 体は，A 体とは異なり，実に様々な骨格の化合物に対して高い親和性を示すという幅広い薬物結合性を有する．この様に，炎症・疾患時の発現量の変動に加え，バリアント間での結合選択性がみられる AGP の薬物結合を理解するには，バリアントそれぞれの薬物結合機構を解明することが必要不可欠である．

今回は，AGP A 体と 3 種の薬物 (アミトリプチリン，クロルプロマジン，ジソピラミド) との複合体の結晶構造を決定し，AGP の薬物結合選択性の構造学的知見を得たので報告する [1].

2 実験

A 体とアミトリプチリン複合体結晶，クロルプロマジン複合体結晶は BL5A において，ジソピラミド複合体結晶は BL17A において X 線回折実験を行った．アミトリプチリンおよびジソピラミド複合体結晶は空間群 *C*2 に属し，クロルプロマジン複合体結晶は空間群 $P2_12_12_1$ に属していた．これら複合体の構造解析は，既に精密化を完了していたアポ A 体の構造をサーチモデルとした分子置換法により行い，最終的に 2.15~2.20 Å 分解能の結晶構造を得た．なお F1*S 体のアポ体の結晶構造は，Skerra のグループにより決定されている[2].

3 結果および考察

アミトリプチリンとジソピラミドは，A 体に特異的に結合する薬物であり，アミトリプチリンとジソピラミドの芳香環部位は，A 体の薬物結合部位の底に結合し，Phe49 や Phe112 をはじめとする数多くの残基との相互作用により認識されていた (図)．また，薬物結合部位に位置する Ser114 は F1*S 体では Phe に置換されており，これら 2 つの薬物が A 体で見られた結合様式で F1*S 体に結合すると，F1*S 体の Phe114 と立体障害を引き起こすことから，アミトリプチリンとジソピラミドは，A 体に特異的に結合することが構造からも示された．一方，クロルプロマジンは，上述した薬物結合部位に結合していたものの，その芳香環部位は，アミトリプチリンとジソピラミドの芳香環に対して垂直に入り込んでおり，異なった結合様式で結合していた (図)．この構造からクロルプロマジンの F1*S 体での結合様式を予測すると，アミトリプチリンやジソピラミドで見られたような立体障害は見られず，クロルプロマジンが A 体と同様に F1*S 体にも結合することが説明できる．このように，A 体の薬物複合体構造から，AGP バリアント間の薬物選択性の構造学的知見を得た．

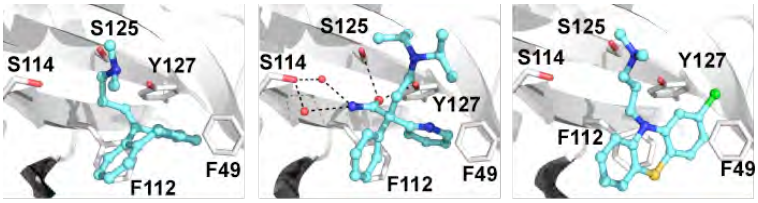

図：A 体における薬物結合様式 (左から，アミトリプチリン，ジソピラミド，クロルプロマジン)

謝辞

本課題は，崇城大学薬学部 小田切優樹教授，熊本大学大学院生命科学研究部 薬物動態制御学・医療薬剤学分野との共同研究で行いました．X 線回折実験を行うにあたり，ご協力頂きました PF スタッフの方々に感謝申し上げます．

参考文献

[1] K. Nishi, T. Ono, T. Nakamura, N. Fukunaga, M. Izumi, H. Watanabe, A. Suenaga, T. Maruyama, Y. Yamagata, S. Curry, M. Otagiri, J. Biol. Chem. **286** (2011) 14427-14434.
[2] D. L. Schonfeld, R. B. Ravelli, U. Mueller, A. Skerra, J. Mol. Biol. **384** (2008) 393-405.

* tnaka@gpo.kumamoto-u.ac.jp

6A/2011G118

透析法によるカードランゲルの X 線小角散乱
Small-Angle X-Ray Scattering of Curdlan Gels Prepared by Diffusion Method

槇 靖幸 [1*], 岡村英希 [1], 佐藤浩行 [1], 須永茉里 [1], 土橋敏明 [1]
[1] 群馬大学大学院工学研究科、〒376-8515 桐生市天神町 1-5-1

1 はじめに

微生物由来 β1,3-グルカンであるカードランは、水に不溶であるが、アルカリ水溶液には可溶である。水酸化ナトリウム水溶液を溶媒とするカードラン濃厚溶液を透析膜に入れ、塩化カルシウム水溶液中で透析するとゲルが生成し、得られた円柱形のゲルを軸に垂直に切り、断面を観察すると、半透明のゲルの中に白濁したリング状の構造があることが示される。また、ゲルは異方的な構造を持ち、クロスニコル下で観察すると、十字の暗い縞を持つ複屈折パターンを示した。これは、円柱形ゲルの円周方向、または動径方向に分子が配向することを意味する。透析によるカードランゲルでは、透析膜を介して流入した Ca^{2+}イオンが溶液中のカードラン分子を架橋することによりゲル化すると考えられる。ゲル化を律速するものが Ca^{2+}の拡散であることは、ゲル化過程の実験と理論との比較により明らかにされた。最近、ゲル化過程のより詳細な解析により、カードランのゲル化には、透析中の Ca^{2+}の流入と、OH^-の流出による pH の下降の両方の効果が関与していることが示唆され、これにより、ゲルの外側の相は Ca^{2+}架橋性ゲル、内側の相は pH 変化による水素結合性ゲル、その境界部分に白濁相が生じ、そこでは二種類のゲルが共存している、という描像が提案された。

本研究では、X 線小角散乱を用いて、透析によるカードラン異方性ゲルの構造を調べた。最初に、Ca^{2+}中の透析によるカードランゲルの分子配向を調べた。次に、透析中の pH 低下によるカードランのゲル化に関連して、水または酸性水溶液中の透析によりカードランゲルを調製し、分子配向の挙動を調べた。最後に、Ca^{2+}中の透析によるカードランゲルと pH 低下によるカードランゲルのミクロ構造の違いをみるため、それぞれのゲルの X 線小角散乱プロフィールを比較した。

2 実験

和光純薬より入手した分子量 $M_v = 5.9\times10^5$ のカードラン試料は精製されずに用いられた。カードランの異方性ゲルの調製は、カードランを 0.3M 水酸化ナトリウム水溶液に溶解したものを透析膜に入れ、透析外液に浸漬することにより、円柱形ゲルを得た。カードラン濃度は 3-5wt%、透析外液として 8.0g/dL 塩化カルシウム水溶液、pH0.9 の塩酸水溶液、Milli-Q 水を用いた。

ゲルの X 線小角散乱の測定のため、円柱形ゲルを、軸に垂直に厚さ約 1mm の円盤状に切り出した。X 線小角散乱(SAXS)実験は、高エネルギー加速器研究機構(PF, BL-15A/6A)において行われた。円盤状ゲル試料の中心からの距離 x に X 線照射したときの散乱パターンを二次元検出器で取得した。

3 結果および考察

Fig.1 に、Ca^{2+}中の透析によるカードランゲルの中心(x/R = 0)および周辺付近(x/R = 0.8)における SAXS パターンを示す。ここで R はゲルの半径である。ゲルの中心はほぼ等方的な散乱パターンであった。これに対し、周辺付近では異方的な散乱パターンで、円周方向、すなわち Ca^{2+}の拡散に垂直な分子配向を示唆した。水中での透析では、複屈折を持たない等方性ゲルが生成した。一方、酸性水溶液中の透析では異方性ゲルが生成した。SAXS パターンは、Fig.1 と定性的に同様で、ゲル円周方向への分子配向が示された。

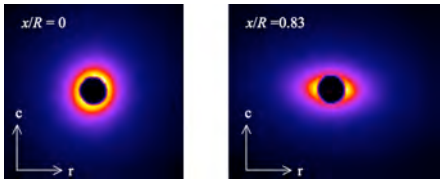

Figure 1. SAXS patterns for the Ca-Curdlan gel

Fig.2 はゲルの中心における散乱プロフィールの Kratky プロットの比較である。Ca^{2+}中の透析ゲルでは q=0.03Å^{-1} 付近で明確なピークが見られたが、水, 塩酸水溶液中の透析ゲルでは明らかなピークは見られなかった。Ca^{2+}架橋性のカードランゲルの白濁相の内側では pH 変化によるゲル形成が生じているという描像が提案されているが、散乱プロフィールは pH 変化のみで形成されるゲルと傾向が異なった。

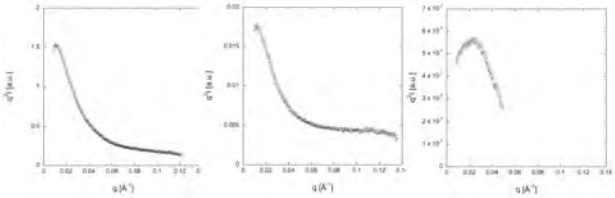

Figure 2. Kratky plots of the SAXS intensities for the Curdlan gels prepared by the dialysis in water (left), HCl aq (center), and $CaCl_2$ aq (right).

BL-5A, NE-3A, NW-12A/2011G124, 125

Crystal structures of beta-glucan recognition protein from *Plodia interpunctella*

Mayumi KANAGAWA[1], Tadashi SATOH[1], Akemi IKEDA[1], Yoshiyuki ADACHI[2], Naohito OHNO[2], Yoshiki YAMAGUCHI[1*]

[1]RIKEN Advanced Science Institute, Wako, Saitama 351-0198, Japan, [2]Laboratory for Immunopharmacology of Microbial Products, School of Pharmacy, Tokyo University of Pharmacy and Life Sciences, 1432-1 Horinouchi, Hachioji, Tokyo 192-0392, Japan

Introduction

Beta-glucan recognition protein (beta-GRP), a pattern recognition receptor of an innate immune system, evokes Toll pathway by binding to beta-glucan in pathogens. Beta-GRP binds to triple helical beta-glucan but not to denatured beta-glucan or shorter beta-1,3-linked glucose oligomers. However, details of the structural basis of the biological activity of beta-glucan have not been elucidated. Here we report how the triplex beta-glucan is recognized by beta-GRP [1].

Experimental Procedure

The $(His)_6$-MBP-TRX-fused *Plodia* beta-GRP N-terminal domain was purified with a Ni-Sepharose column and then digested with TEV protease. The MBP-TRX tag was removed by chromatography through a Ni Sepharose column. The protein was further purified by size exclusion chromatography. Beta-GRP-N crystals were obtained by the sitting drop vapor diffusion method with ligand laminarihexaose or without ligand and data sets were collected at PF BL5A, PF-AR NW12A and NE3A beamlines. The crystal structures were solved by molecular replacement method using a program Molrep. The refined structures of beta-GRP-N with ligand and without ligand have a crystallographic *R*-factor of 22.2% (R_{free} = 26.9%) in the 20.00-2.20 Å resolution range and 20.7% (R_{free} = 23.8%) in the 20.00-1.58 Å, respectively.

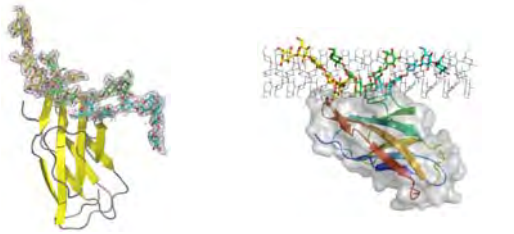

Fig. 1 Crystal structure of beta-GRP-N with ligand (left) and a structural model for binding between with beta-GRP-N and triplex beta-glucan (right).

Results and Discussion

The *Plodia* beta-GRP-N has an immunoglobulin-like beta-sandwich fold composed of two antiparallel beta-sheets containing three or five beta-strands (Fig. 1). There is little structural difference between liganded and unliganded forms of beta-GRP-Ns. Surprisingly, the laminarihexaoses are arranged in a right handed helical structure and fits well with beta-1,3-glucan triple helix structure derived from x-ray-fiber diffraction. Ligand binding of beta-GRP-N is attained through convex beta-sheet and a characteristic long loop. Six glucose residues from three laminarihexaose chains are involved in binding to beta-GRP-N, and eight amino acid residues show extensive polar and non-polar interactions. Our crystallographic data provide a structural basis for the unique recognition by such receptor of the triple helical structure of beta-1,3-glucan.

Reference

[1] M. Kanagawa et al., *J. Biol. Chem.*, **286**(33):29158-29165, (2011).

*yyoshiki@riken.jp

10C, 2011G136(PF), BL45XU,2011A1928(Spring8)

Complex Formation by the 20S proteasome and Its Activators in an Aqueous Solution

Masaaki SUGIYAMA*[1], Hirokazu Yagi[2] and Koichi Kato[2,3]
[1]Research Reactor Institute, Kyoto University, Kumatori, Osaka 590-0494, Japan
[2]Graduate School of Pharmaceutical Sciences, Nagoya City University, Nagoya 467-8603, Japan
[3]Okazaki Institute for Integrative Bioscience and Institute for Molecular Science, National Institutes of Natural Sciences, Okazaki 444-8787, Japan

Introduction

It is interesting of the formation mechanism and the functions of proteasomal systems consisting of several proteins, of which combinations depend upon their functions. The main component in the system is the 20S proteasome (PRS) with the molecular mass of ~700kDa known as a protein degradation machinery in cells. PRS has a hollow cylindrical shape constructed with four rings α-β-β-α rings, each of which consists of seven kinds of subunits. The function of this huge protease complex is regulated through the attachment of other protein complexes termed proteasome activators (PAs): PAs identify proteins which are degraded by PRS. For example, proteasome activator 28 (PA28) with the molecular mass of ~200 kDa has a truncated cone shape consisting of highly homologous α- and β-subunits. It is considered that PA28 connects to both basal planes of PRS and this protease complex (PRS + two PA28; PRS2PA28) contributes to the processing of antigenic proteins into peptides for presentation via the MHC class I pathway. Therefore, PA28, PRS and PRS2PA28 are very important in our immune system.

For a better understanding of the assembly mechanisms in this proteasomal system, it is necessary to reveal the state of PA28, PRS and PRS2PA28 in an aqueous solution. Therefore, we have started to characterize the state of components in the proteasome system. In our previous study, it was clarifies that two PA28s are in dissociation equilibrium. In this study, we examined the formation of PRS2PA28 in a solution of PA28 mixtured with PRS by utilizing small-angle scattering.

.

Experimental

The PA28 α-subunit lacking the loop segment (residue Val69 to Lys97) was generated using standard PCR and genetic-engineering techniques. A mutated α-subunit and a wild-type β-subunit were subcloned into the expression vectors pET21d and pET23a, respectively. Each subunit was separately expressed using *Escherichia coli* (BL-21) and purified by ammonium sulfate precipitation, hydroxyapatite chromatography, and ion-exchange chromatography. The hetero-oligomer of PA28 was constructed by mixing the two subunits and purified by gel filtration chromatography. PA28 was concentrated to 5.0 mg/mL in a buffer solution composed of the following: 50 mM Tris-HCl (pH 7.5), 1 mM dithiothreitol,

Cells of PRS were grown to an absorbance of 600 nm at 2.0 in YPD medium at 27C. The grown cells were harvested and suspended in 50mM Tris-HCl buffer (pH 7.5) containing 100 mM NaCl and 10\% glycerol, then lysed by mixing with glass beads.The extract was centrifuged at 26,740 g for 30 min at 4 C, then the supernatant was subjected to the affinity chromatography using anti-FLAG M2-agarose beads (Sigma). Anti-FLAG M2-agarose beads, to which the 26S proteasome had been bound, were incubated with 50mM Tris-HCl buffer (pH 7.5) containing 500mM NaCl, 10% glycerol and 10% Triton X-100 for 30 min at 25C to dissociate the 19S components from the 26S proteasome. After washing the column, PRS was eluted with 3×FLAG peptide and the concentration was tuned to be 3.8 mg/mL in same buffer.

In order to examine the formation of PRS2PA28 in a aqueous solution, both prepared samples were mixed with the molar ratio of [PA28]:[PRS]=2.6:1.The concentration of the mixture sample was also tuned to be 4.1 mg/mL.

Results and discussion

Figure 1 shows Guinier plot of the mixture of Pa28 and PRS. From this data, the gyration radius was found to be 87Å. The calculated gyration radius of PRS2PA28from PDB data is 86Å. Therefore, our data clearly show that the PA28 and PRS spontaneously form the complex in an aqueous solution.

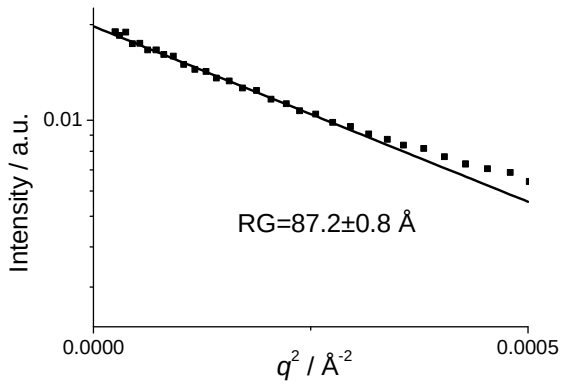

Figure 1. Guinier plot of the mixture of Pa28 and PRS. The straight line indicates the result of the least square fitting with Guinier formula.

* sugiyama@rri.kyoto-u.ac.jp

9A,12C,27B/2011G143, 2009G077

Oxidation states change of Ce in the mixtures of manganese oxides and *Pseudomonas fluorescens*

Toshihiko Ohnuki[1,*], Mingyu Jiang[1,2], Kazuya Tanaka[1,3]
Xiaobin Xia[3], Ke Yang[3], Jianhua He[3]
[1]Japan Atomic Energy Agency, Tokai, Ibaraki 319-1195, Japan
[2]Kyushu University, Hakozaki, Fukuoka 305-0801, Japan
[3]SSRF, Pudong-District, Shanghai 201204, China

1 Introduction

Many heavy elements (HEs) containing lanthanides and actinides exist in several oxidation states in the environments. Various physical-, chemical-, and biological-processes alter the speciation of HEs. Hence, the presence of multiple species and their complex chemistry make it difficult to predict their migration behavior in the environment.

HEs are sorbed by inorganic and organic materials in the environments during the migration. Manganese oxides are ubiquitous, and are known to oxidize redox sensitive HEs; i.e. Ce(III) [1, 2]. Several microorganisms are known to exhibit a high capacity to sorb HEs. Such binding to bacterial surfaces might well affect the movement of HEs in the environment. Unfortunately, we have limited knowledge of the role of microorganisms in the migration.

In this study, we have investigated the association of Ce(III) with the mixture of a common soil bacterium, *Pseudomonas fluorescens*, and manganese oxides. This microorganism is widespread in the terrestrial environment.

2 Experiment

The cells of *P. fluorescens* (ATCC 55241) were grown in the nutrient solution until log phase. Manganese oxides of MnO_2 and Mn_2O_3 were abiotically formed. The sorption experiments of a 0.1 or 0.01 mM $Ce(III)(NO_3)_3$ solution by the mixtures of *P. fluorescens* and manganese oxides were performed under atmospheric condition. The mixtures containing 1, 5, or 10 mg cells and 5 mg manganese oxides were immersed with a 0.01 mM $Ce(NO_3)_3$ solution at pH between 3 and 8.

The concentration of Ce in solution was measured by ICP-AES. The K_d, the ratio of Ce in solution and on the mixture was obtained by the concentration of Ce in the solution. The spatial distributions of elements in the mixtures were measured after the exposure to the Ce solution using micro beam at BL15U1 of SSRF. Ce L_{III}-edge (5723 eV) XANES spectra and Mn K-edge (6539 eV: δ-MnO2) were measured at BL15U1 of SSRF and at BL-9A, BL-12C, and BL-27B of PF.

3 Results and Discussion

The K_d of Ce increased with increasing pH of the solution. The lower Kd was obtained at higher Ce concentration. The XANES spectra of Ce sorbed by the mixture at 0.1 mM Ce solution (Fig. 1) showed that most of Ce was present as Ce(IV) at pH 5.72 and some fraction of Ce was present Ce(III) at pH 4.06 and 3.28. Ohta et al. showed oxidation of Ce(III) to Ce(IV) at pH between 3 and 7 [3]. Our results indicate that microorganism inhibits the oxidation of Ce(III) in acidic solution.

The spatial distribution of Ce and Mn (Fig. 2) showed that high intensity of Ce was detected at the position of Mn, indicating that most of Ce was present with manganese oxides.

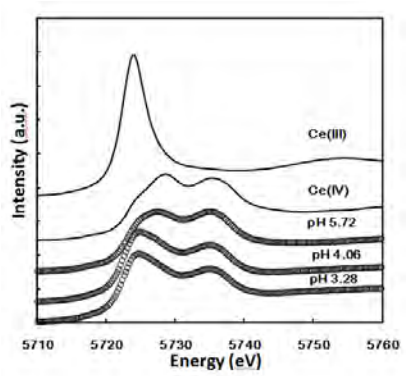

Fig. 1 XANES spectra of Ce sorbed at different pH by the mixtures of manganese oxides and *P. fluorescens*.

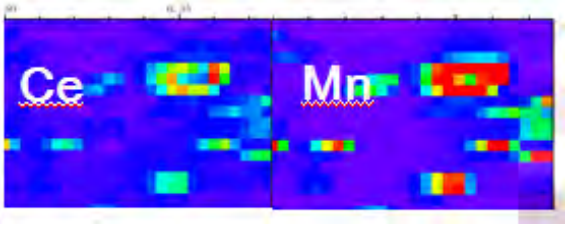

Fig. 2 Spatial distribution of Ce and Mn in the mixture.

Acknowledgement

The μ-XANES and spatial distributions of elements were measured at Shanghai Synchrotron Radiation Facility (SSRF) as alternative use of PF damaged by earthquake. We thank all staff of SSRF for their cooperation and hospitality.

References

[1] T. Ohnuki, *et al*., Chem. Geol. **253** (2008) 23.
[2] K. Tanaka, *et al*., GCA **74** (2010) 5463.
[3] A. Ohta, *et al*., GCA **65** (1999) 695.
* ohnuki.toshihiko@jaea.go.jp

10C/2011G145

MPD 存在下でのロイコシジンの多量体化の解明
Elucidation of the oligomerization of leukocidin in the presence of the MPD

郷田秀一郎*, 田中伸弥
長崎大学大学院工学研究科、〒852-8521 長崎市文教町 1-14

1 はじめに

孔形成毒素とは、タンパク質が細胞表面を認識して結合し、多量体化を経て細胞を破壊するタンパク質の一群であり、多くのタンパク質がその一群として報告されている。なかでもα-ヘモリジンはその多量体を形成した際の立体構造が報告されており、孔形成時の膜孔形成部位が明確となっている [1)]。孔形成毒素の一つにロイコシジンがあり、白血球を標的細胞とし、F 鎖と S 鎖からなるヘテロ多量体を形成することによって白血球を破壊することが報告されている。田中らは、α-ヘモリジンの膜孔形成複合体の結晶構造解析を報告し、沈殿剤として用いた 2-Methyl-2,4-pentandiol（MPD）が多量体化に重要な役割を果たしていると報告している [2)]。そこで、本研究では、ロイコシジンンの膜孔形成多量体構造解明及び、多量体化における構造変化を明らかとするため、MPD 存在下でのロイコシジンの四次構造変化を X 線小角散乱法によって測定した。

2 実験

X 線小角散乱測定は BL-10C にて行った。カメラ長は~80 cm、検出器には PSPC を用いた。すでに MPD 存在下での多量体化が報告されていることから、10%から 60%まで 10%おきに MPD 濃度を変化させて測定を行った。試料には、Panton-Valentin 型ロイコシジンの F 鎖及び S 鎖を用いた。

3 結果および考察

図 1 に各 MPD 濃度での Guinier プロット(a)及び Kratky プロット(b)を示した。Guinier プロットでは MPD 濃度 60%溶液中で大きな変化が見られ Rg 値の急激な上昇が見られた。Rg 値は MPD 濃度が 10 から 50%では約 30 Å であったのに対して 60%では、約 70 Å と急激に上昇しており、多量体化を確認することができた。

Kratky プロットでは、MPD 濃度 10 から 40%では明確ではないものの単量体に由来すると考えられるピークを含む曲線が観察されたが、濃度 50%では、ランダムコイル様の散乱曲線となり、60%で多量体のピークが観察された。このことは多量体化の過程で、立体構造が大きく崩壊していることを意味していた。

4 まとめ

α－ヘモリジンの MPD 存在下での結晶構造解析の結果は、MPD がタンパク質中の膜との相互作用によって構造変化する部位に入り込むことによって多量体化を推進することを示唆している。本測定より、10%から 40%MPD 溶液中で大きな構造変化は見られなかったが、50%において大きな立体構造変化を伴って構造が崩壊し、60%では多量体を形成していることを示していた。

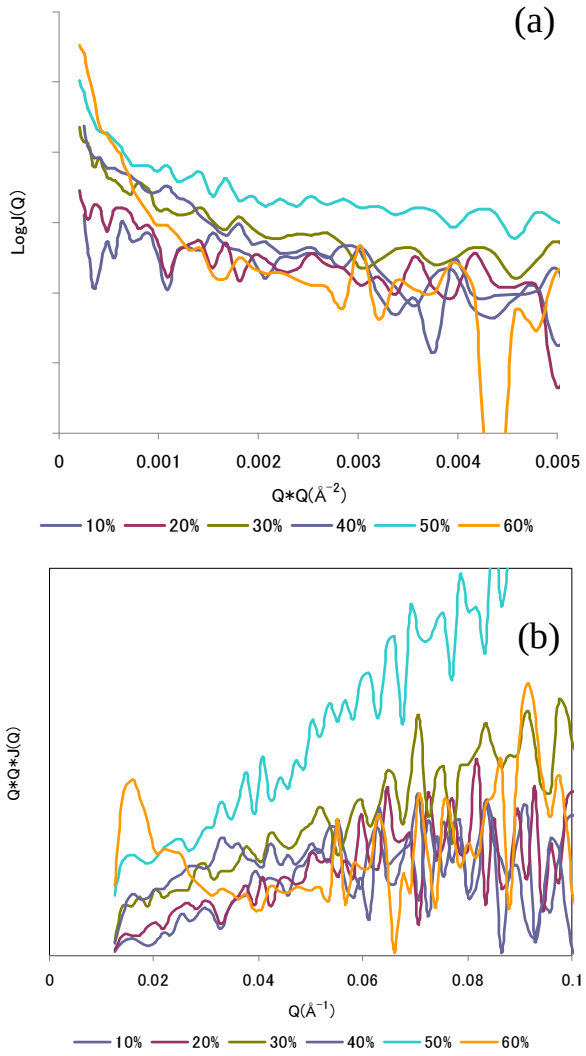

図 1 ：種々の MPD 濃度溶液中でのロイコシジンの Guinier(a)及び Kratky(b)プロット

参考文献
[1] L. Song *et al.*, *Science* **274** (1996) 1859-1866.
[2] Y. Tanaka *et al.*, Protein Sci. **20** (2011) 448-456.
* sgoda@nagasaki-u.ac.jp

5A, NW12A, NE3A / 2011G148

Crystallographic study of innate immune receptor RP105/MD-1

Umeharu Ohto[1,*] and Toshiyuki Shimizu[1]
[1] Graduate School of Pharmaceutical Sciences,
University of Tokyo, Hongo, Bunkyo-ku, Tokyo 113-0033, Japan.

1 Introduction

The Toll-like receptor 4 (TLR4)/MD-2 heterodimer senses lipopolysaccharide (LPS). Radioprotective 105 (RP105), a TLR-related molecule, is similar to TLR4 in that the extracellular leucine-rich repeats associate with MD-1, the MD-2-like molecule. MD-2 has a unique hydrophobic cavity that directly binds to lipid A, the active center of LPS. LPS-bound MD-2 opens the secondary interface with TLR4, leading to dimerization of TLR4/MD-2. MD-1 also has a hydrophobic cavity that accommodates lipid IVa, a precursor of lipid A, suggesting a role for the RP105/MD-1 heterodimer in sensing LPS or related microbial products. Little is known, however, about the structure of the RP105/MD-1 heterodimer or its oligomer. Here, we have determined the crystal structures of mouse and human RP105/MD-1 complexes at 1.9 and 2.8 Å resolutions, respectively [1].

2 Experiment

The extracellular domains of human RP105 (residues 21–626) and mouse RP105 (residues 21–626) were inserted into the expression vector pMT/BiP/V5-His of the Drosophila Expression System. Human MD-1 (residues 20–162) and mouse MD-1 (residues 20–162), fused to a C-terminal thrombin cleavage site located upstream of Protein A tags, were also inserted into the vector. Drosophila S2 cells were cotransfected with the RP105, MD-1, and pCoHygro vectors, and stably transfected cells were selected. Protein from culture supernatant was purified by IgG Sepharose affinity chromatography, Protein A tag cleavage by thrombin, saccharide trimming by endo Hf, Hitrap SP cation exchange, and finally, Superdex 200 gel filtration chromatography. Crystallization experiments were performed using the sitting-drop and hanging drop vapor-diffusion methods at 20°C. Crystals of mouse RP105/MD-1 were obtained with a reservoir solution containing 19% (w/v) PEG8000 and 100 mM Tris HCl (pH 9.0). Crystals of the human RP105/MD-1 were obtained with a reservoir solution containing 20% (w/v) PEG2000MME and 100 mM Tris HCl (pH 9.0). All diffraction datasets were collected on beamline NE3A at the Photon Factory (Tsukuba, Japan) under cryogenic conditions at 95 K. Phasing was performed using the autoSHARP (1) program and improved with the solvent flattening method using DM in the CCP4 suite..

3 Results and Discussion

RP105 is a curved solenoid that is characteristic of LRR-containing TLR family members. MD-1 resides on one side of the RP105 concave surface. Despite some differences in organization, the overall structure is very similar to that of the 1:1 TLR4/MD-2 complex. The crystallographic asymmetric unit contains two copies of the 1:1 RP105/MD-1 complex facing each other and forming a 2:2 RP105/MD-1 complex. Gel filtration and small-angle X-ray scattering analyses of RP105/MD-1 confirmed that both mouse and human RP105/MD-1 were dimeric in solution. The dimeric structure of RP105/MD-1 contrasts with those of reported 'm'-shaped TLR dimers such as the LPS-binding 2:2 TLR4/MD-2 complex [2], where the N-termini of the TLRs extend to opposite ends and their C-termini interact in the middle. As a result, two TLR4 molecules face each other in the C-terminal domain of the 2:2 TLR4/MD-2 complex. In contrast, the 'm'-shaped 2:2 RP105/MD-1 complex is structured such that the C-termini of RP105 extend to opposite ends and the N-termini interact in the middle. Because of this inverse arrangement, the C-terminal domains of RP105 in the 2:2 RP105/MD-1 complex are separated by approximately 100 Å.

Our structural study suggests that RP105/MD-1 is involved in lipid signaling as well as LPS signaling. Further studies of the relationship between RP105/MD-1 and lipid molecules would provide a new regulatory mechanism of activation for members of the TLR family.

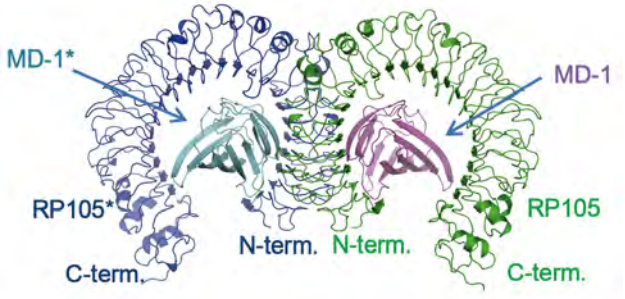

Fig. 1: Overall structure of RP105/MD-1 complex.

References

[1] Ohto, U., Miyake, K., and Shimizu, T. (2011). *J. Mol. Biol.* **413**, 815-825.
[2] Park et al. (2009) *Nature* **458**, 1191-1195.

* umeji@mol.f.u-tokyo.ac.jp

17A/2011G155

乳酸菌由来 FMN-bp ホモログの結晶構造解析

高木 利佳子, 前田 琢久磨, 中西 猛, 北村 昌也*

大阪市立大学大学院 工学研究科 化学生物系専攻 〒558-8585 大阪市住吉区杉本 3-3-138

1 はじめに

硫酸還元菌由来 FMN 結合タンパク質 (FMN-bp)は *in vivo* 機能未知の小さなフラビンタンパク質である。二量体を形成しており、FMN はその界面に挟み込むように存在している。これまで我々は、FMN-bp の構造と FMN 結合能の相関を調べることにより、アポタンパク質と FMN における結合反応機構の解明を行ってきた。本研究において、我々は新たに FMN-bp のホモログと比較することにより詳細な解析を行うことを目標として、硫酸還元菌由来 FMN-bp のアミノ酸配列と 39%一致している乳酸菌 (*Lactococcus lactis* IL1403) 由来 FMN-bp ホモログに着目した。しかし、大腸菌発現系を用いて組換え体を調製したところ、乳酸菌由来 FMN-bp ホモログは FMN を結合しておらず、*in vitro* においてもホロタンパク質として再構成されないことがわかった。そこで、この FMN-bp ホモログが FMN 結合能を持たない構造的要因を明らかにするために、X 線結晶構造解析を行った。

2 実験

まず、大腸菌発現系を用いて N 末端に His-tag を付加した組換え FMN-bp ホモログを作製し、アフィニティークロマトグラフィーにより精製した。次に、得られた FMN-bp ホモログを 10 mM Tris-HCl (pH 8.0) に対して透析した後、Amicon Ultra (Millipore) を用いて終濃度 29 mg/mL になるまで濃縮した。また、SDS-PAGE により、得られた FMN-bp ホモログの純度を確認した。

FMN-bp ホモログの結晶化には、シッティング・ドロップ蒸気拡散法を用いた。X 線回折実験に用いた結晶は、200 mM 硫酸リチウム、50 mM Tris-HCl (pH 8.3)、22.5 % (w/v) PEG 4000 溶液を沈殿剤とし、100 mM 塩化ストロンチウムを添加剤として加えることによって得た。

FMN-bp ホモログの X 線回折実験は Photon Factory (PF) のビームライン 17A にて行った。得られた回折データを、まず HKL2000 および SCALA (CCP4 program suite) を用いて処理した。次に MOLREP を用いて分子置換法により構造を決定した。また、得られた初期モデルについて、CNS を用いた Rigid Body Refinement および Simulated Annealing を行った。さらに、COOT および Refmac5 (CCP4 program suite) を用いて最終的な精密化を行った。

3 結果および考察

X 線回折実験の結果、分解能 2.0 Å、R_{merge} = 0.063、Completeness = 98.7%、Multiplicity = 6.8、$I/\sigma(I)$ = 19.3 のデータが得られた。また、FMN-bp ホモログ結晶の空間群は C_2 であり、a = 94.9 Å、b = 41.3 Å、c = 72.6 Å、β = 102.7°であった。

乳酸菌由来 FMN-bp ホモログ結晶において、非対称単位中に 2 つの単量体が存在し、ホモ二量体を形成していた。FMN-bp ホモログの全体構造を硫酸還元菌由来 FMN-bp と Cα で重ね合わせて図 1 に示した。全体の RMSD は 0.98 Åであり、FMN-bp ホモログの全体構造は FMN-bp とよく類似していることがわかった。しかし、A 鎖、および B 鎖をそれぞれ重ね合わせた時の RMSD に差が見られたことから、単量体同士の相対的位置が FMN-bp とは異なることが示唆された。

また、硫酸還元菌由来 FMN-bp の FMN 結合領域[1, 2]とそれに対応する領域を Cα で重ね合わせたところ、主鎖の構造は極めてよく類似していることがわかった。しかし、FMN との結合に重要な Trp106 が Phe109 に、FMN のリン酸基と水素結合を形成していた Thr54 が Leu55 にそれぞれ置換されていた。このようなアミノ酸残基の置換は FMN-bp ホモログが FMN 結合能を持たない主な原因となり得ると考えた。

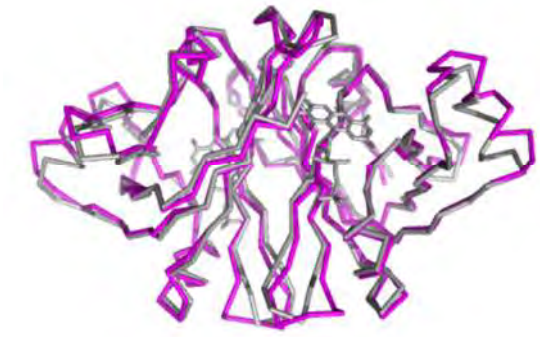

図 1：乳酸菌由来 FMN-bp ホモログおよび硫酸還元菌由来 FMN-bp の全体構造
FMN-bp ホモログをマゼンタ、FMN-bp (PDB ID : 1FLM) を灰色のリボンモデルで示した。また、FMN-bp 由来の FMN をスティックモデルで示した。

参考文献

[1] K. Suto *et al.,* Acta Crystallogr. **D56,** (2000) 368.
[2] M. Kitamura *et al.,* J. Biochem. **141,** (2007) 459.

* kitamura@bioa.eng.osaka-cu.ac.jp

15A/2011G188

Structural study of hNck2 SH3 domain protein by X-ray solution scattering III. Structure of hNck2 SH3 domain at pH 2.

Yoshitaka Matsumura[1], Masaji Shinjo[1], Tsutomu Matsui[2], Kaoru Ichimura[1] Jianxing Song[3] and Hiroshi Kihara[4*]

[1]Department of Physics, Kansai Medical University, 18-89 Uyama-Higashi Hirakata, Osaka 573-1136, Japan
[2]Stanford Synchrotron Radiation Lightsource, SLAC National Accelerator Laboratory, Stanford University, 14 2575 Sand Hill Rd, MS69, Menlo Park, CA, 94025 USA
[3]Department of Biochemistry, Yong Loo Lin School of Medicine and Department of Biological Sciences, Faculty of Science, National University of Singapore, Singapore 119260, Singapore
[4]SR center, Ritsumeikan University, 1-1-1 Noji-Higashi Kusatsu, Shiga, 525-8577, Japan

Introduction

In the series of reports, we have shown that hNck2 SH3 domain protein takes native β-structured state at pH 6 at low concentration of the protein, but takes dimer at the concentration higher than 1 mg/mL [1], and at low pH, the protein takes mainly monomer even at 3 mg/mL [2]. In this report, we show the acid-induced conformation is not compact. As this state has α-helix, in 12%, it is not randomly coiled, suggesting this state is similar to C state which Yamada *et al* proposed [3].

Experimental

X-ray scattering experiments were done at the beamline of 6A with the same set-up with [2]. Concentration of hNck2 SH3 domain was 3 to 4 mg/mL. At these concentration, the protein forms dimer at pH 6. Experiments were done at 12℃.

Results and Discussion

In Fig. 1, CD values at 222 nm are shown as a function of pH. At low pH, CD decreased drastically, showing the increase of α-helix. At pH 2, content of α-helix is 12 %.

Fig. 2 shows the normalized Kratky plots of hNck2 SH3 domain at various pH. As clearly seen in the figure, there appeared no peaks at acidic pH. This indicates that the protein at this condition was not compact globule state. *Rg* values at acidic pH were even a little higher than those at neutral pH [2]. This also suggests the protein takes non-compact, α-helix-rich, but probably more elongated structure at acidic pH. Results of the structural analysis will be presented in the next report [4].

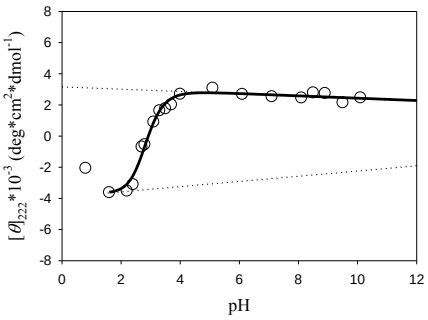

Fig. 1 $[\theta]_{222}$ dependence of pH induced-α-helix forming transition of hNck2 SH3 domain at 12℃.

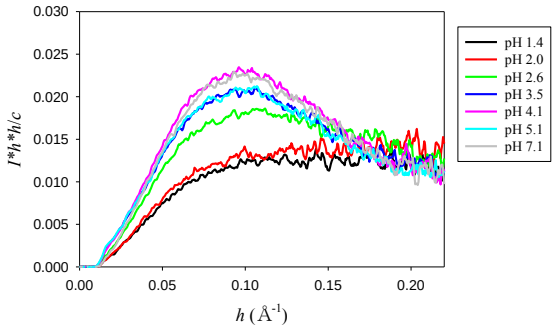

Fig. 2 Normalized Kratky plots of hNck2 SH3 domain at various pH.

References

[1] Matsumura *et al*. (2012) This proceedings, I.
[2] Matsumura *et a*l. (2012) This proceedings, II.
[3] Yamada *et al*. (2005) J. Mol. Biol. 350, 338-348.
[4] Shinjo *et al*. (2012) This proceedings, IV.

* kiharah@aol.com

6A,/2011G188

Structural study of hNck2 SH3 domain protein by X-ray solution scattering IV. Structural analysis of hNck2 SH3 domain at pH 2 and pH 8: non-native α-helix-rich monomer and native dimer

Masaji Shinjo[1*], Yoshitaka Matsumura[1], Kaoru Ichimura[1], Jianxing Song[2], Hiroshi Kihara[3]
1 Department of Physics, Kansai Medical University, 18-89 Uyama-Higashi Hirakata, Osaka 573-1136, Japan
2 Department of Biochemistry, Yong Loo Lin School of Medicine and Department of Biological Sciences, Faculty of Science, National University of Singapore,Singapore 119260, Singapore
3 SR Center, Ritsumeikan University, 1-1-1 Noji-Higashi Kusatsu, Shiga, 525-8577, Japan

Introduction

hNck2 SH3 domain is a protein which takes β-structure at the native state. Liu and Song reported [1] that the protein forms non-native α-helix-rich structure below pH 2 based on NMR spectroscopy.

We have shown in the series of reports that hNck2 SH3 domain protein takes native β-structured state at pH 6 and takes dimer at the concentration higher than 1 mg/mL [2], and at low pH, the protein takes mainly monomer even at 3 mg/mL [3]. This acid-stable monomer is rich in α-helix and non-compact [4].

In the present report, we show proposed structure of the protein at pH 2 and pH 8 from DAMMIN analysis [5].

Experimental and Calculation

X-ray solution scattering experiments were done at BL 6A. Details of the experimental procedures are shown elsewhere [3]. Protein concentration was 3 mg/mL. At this concentration, protein takes monomer at pH 2 and dimer at pH 8 from $I(0)$ analysis of the X-ray solution scattering data [3].

Structural calculations were done for the scattering data at pH 2 and pH 8 by using DAMMIN program [5].

Results

Scattering patterns of hNck2 SH3 domain protein at pH 2 and pH 8 are shown in Figure 1.

Figure 2 shows calculated structures at pH 2 and pH 8. At pH 2, an elongated structure was obtained. As the Kratky plot of this state did not show a peak, but a plateau shape, the structure at pH 2 is not compact. As the state is richer in α-helix than the native state, the hNck2 SH3 domain protein takes non-compact, but non-random coiled, i.e. C-state which Yamada suggested for equine beta-lactoglobulin [6]

At pH 8, the protein takes ellipsoidal structure. The volume of the structure at pH 8 is found to be almost twice as large as that at pH 2, which also supports the structure below pH 2 is monomer and the structure above pH 4 is dimer.

References

[1] Liu & Song (2008) Biophys. J. 95, 4803-4812.
[2] Matsumura *et al*. (2012) This proceedings, I.
[3] Matsumura *et al*. (2012) This proceedings, II.
[4] Matsumura *et al*. (2012) This proceedings, III.
[5] Svergun (1999) Biophys. J. 76, 2879-2886.
[6] Yamada *et al*. (2005) J.Mol.Biol. 350, 338–348.

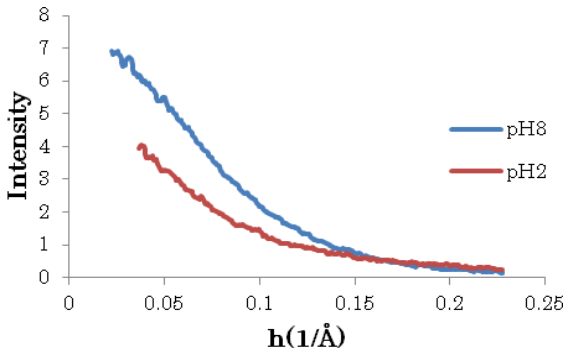

Figure 1. Scattering intensity of hNck2 SH3 domain at pH 2 and pH 8. Non-linear small angle region were cut for DAMMIN calculation.

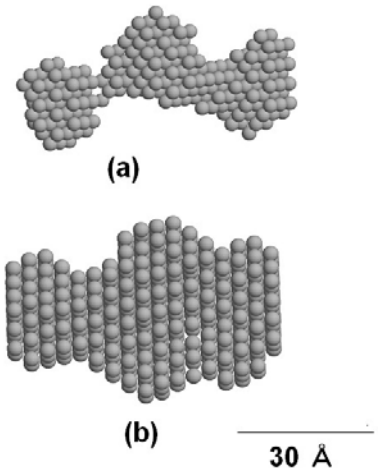

Figure 2. Calculated structure of hNck2 SH3 domain by DAMMIN program. (a) pH 2 (b) pH 8

* shinjom@makino.kmu.ac.jp

15A/2011G188

Structural study of hNck2 SH3 domain protein by X-ray solution scattering II. pH-dependent structural change.

Yoshitaka Matsumura[1], Masaji Shinjo[1], Tsutomu Matsui[2], Kaoru Ichimura[1] Jianxing Song[3] and Hiroshi Kihara[4*]

[1]Department of Physics, Kansai Medical University, 18-89 Uyama-Higashi Hirakata, Osaka 573-1136, Japan
[2]Stanford Synchrotron Radiation Lightsource, SLAC National Accelerator Laboratory, Stanford University, 14 2575 Sand Hill Rd, MS69, Menlo Park, CA, 94025 USA
[3]Department of Biochemistry, Yong Loo Lin School of Medicine and Department of Biological Sciences, Faculty of Science, National University of Singapore, Singapore 119260, Singapore
[4]SR center, Ritsumeikan University, 1-1-1 Noji-Higashi Kusatsu, Shiga, 525-8577, Japan

Introduction

hNck2 SH3 domain protein takes β-structured protein at neutral pH. However, Liu and Song found it takes α-helix-rich conforamation at acidic pH by means of NMR spectroscopy and CD [1].

We have started the study on pH-dependent structural change of hNck2 SH3 domain protein by X-ray solution scattering, and reported in three reports. The first report (the present one) shows pH-dependent monomer-dimer transition, the second one reports conformational study at pH 2, and the third one report gross structures at pH 2 and pH 8.

Experimental

X-ray scattering experiments were done at the beamline of 6A, keeping the sample-to-detector-distance at c.a. 1.3 m with a CCD-based X-ray detector (Hamamatsu Photonics, C7300). The obtained data were corrected for image distortion, non-uniformity of sensitivity, and the contrast reduction on X-ray image intensifier.

Concentration of hNck2 SH3 domain was 3 to 4 mg/mL. At these concentration, the protein forms dimer at pH 6 [2]. All experiments were done at 12℃.

Results and Discussion

Figure 1 shows X-ray scattering patterns of hNck2 SH3 domain at various pH. Figure 2 shows plots of $I(0)/c$ against pH. This shows $I(0)/c$ above pH 4 is nearly constant, and that below pH 2 is much less. As hNck2 SH3 domain takes dimer at pH 6 [2], the protein is mainly monomer at acidic pH, and dimer above pH 4. *Rg* values were shown in Fig. 3. Discussions will be developed in the next report [3].

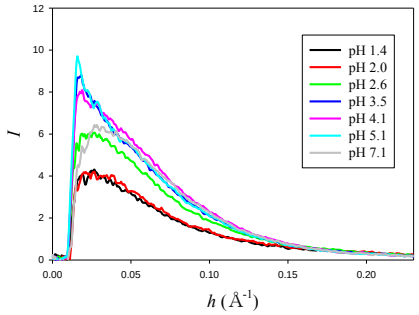

Fig. 1. Scattering patterns of hNck2 SH3 domain at various pH.

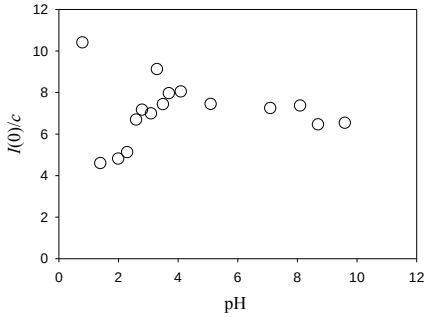

Fig. 2. $I(0)/c$ plots against pH.

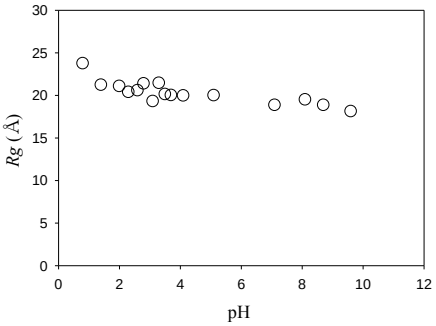

Fig. 3. *Rg* dependence of pH of hNck2 SH3 domain.

* kiharah@aol.com

References

[1] Liu & Song (2008) Biophys. J. 95, 4803-4812.
[2] Matsumura *et al*. (2012) This proceedings, I.
[3] Matsumura *et al*. (2012) This proceedings, III.

15A/2011G188

Structural study of hNck2 SH3 domain protein by X-ray solution scattering I. Concentration dependence at pH 6.

Yoshitaka Matsumura[1], Tsutomu Matsui[2], Kaoru Ichimura[1] Jianxing Song[3] and Hiroshi Kihara[4]*

[1]Department of Physics, Kansai Medical University, 18-89 Uyama-Higashi Hirakata, Osaka 573-1136, Japan
[2]Stanford Synchrotron Radiation Lightsource, SLAC National Accelerator Laboratory, Stanford University, 14 2575 Sand Hill Rd, MS69, Menlo Park, CA, 94025 USA
[3]Department of Biochemistry, Yong Loo Lin School of Medicine and Department of Biological Sciences, Faculty of Science, National University of Singapore, Singapore 119260, Singapore
[4]SR center, Ritsumeikan University, 1-1-1 Noji-Higashi Kusatsu, Shiga, 525-8577, Japan

Introduction

hNck2 SH3 domain protein takes β-structured conformation at neutral pH. However, Liu and Song found it takes α-helix-rich conformation at acidic pH by means of NMR spectroscopy and CD [1].

We have started the series of conformational study of this protein by means of X-ray solution scattering, and report in four reports; the first report (the present one) shows protein concentration dependent monomer-dimer transition at neutral pH, the second one reports pH-dependent monomer-dimer transition, the third one reports conformational study at pH 2, and the fourth one reports gross structures at pH 2 and pH 8.

Experimental

X-ray scattering experiments were done at the beamline of Bio-SAXS in Stanford Synchrotron Radiation Light Source (SSRL). Experiments were done at pH 6 at 12℃ for protein concentration dependent study.

Results and Discussion

Fig. 1 shows dependence of *Rg* of hNck2 SH3 domain on protein concentration. *Rg* value was 15.0 Å when the protein was 0.139 mg/mL, whereas *Rg* was nearly constant (20.8 Å) above 0.35 mg/mL. The former *Rg* value is in good agreement with that of the native state of src SH3 domain (14.6 Å) [2], whereas the latter *Rg* values are significantly bigger.

I(0) values were also obtained from Guinier analysis of the same experiments, and normalized *I*(0) values, *I*(0)/c, were plotted against the protein concentration (Fig. 2). As seen in the figure, *I*(0)/c value above 1 mg/mL is found to be c.a. twice as big as that at 0.139 mg/mL, indicating that hNck2 SH3 domain structure changed from monomer to dimer.

Fig. 3 shows normalized Kratky plots of hNck2 SH3 domain at various protein concentration. It is clear that all Kratky plots show obvious one peak, indicating that hNck2 SH3 domain was compact globule state at any concentrations both at monomeric and dimeric states.

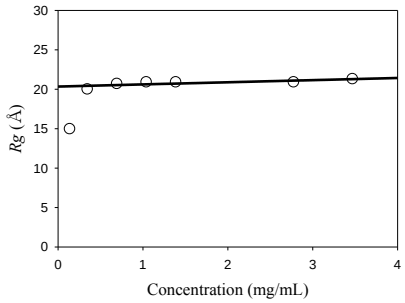

Fig. 1. *Rg* dependence of hNck2 SH3 domain concentration.

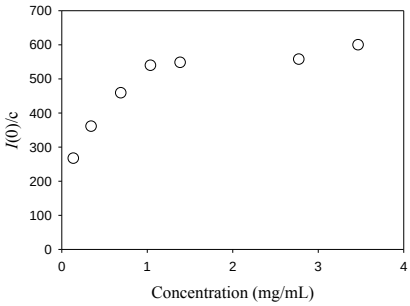

Fig. 2. *I*(0)/*c* plots against hNck2 SH3 domain concentration.

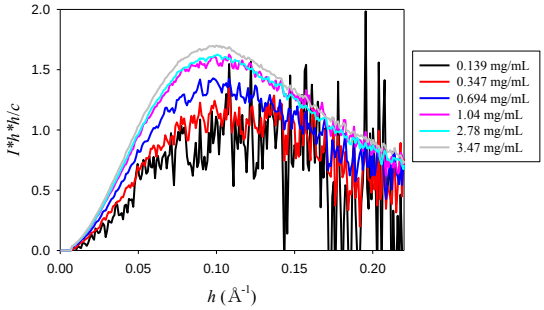

Fig. 3. Normalized Kratky plots of hNck2 SH3 domain.

Acknowledgement

We are grateful to SSRL for giving the beam time in order to do X-ray solution scattering experiments.

References

[1] Liu & Song (2008) Biophys. J. 95, 4803-4812.
[2] Li *et al*. (2007) Biochemistry. 46, 5072-5082.
* kiharah@aol.com

5A,17A,NE3A,NW12A/2011G193

バチライシン生合成酵素の結晶構造解析
Crystal structure analysis of bacilysin biosynthesis enzymes

津田岳夫*, 小島修一
学習院大学理学部生命科学科、〒171-8588 豊島区目白 1-5-1

1 はじめに

枯草菌が生産する抗生物質で、「バチライシン」と呼ばれるジペプチドがある（図 1）。バチライシン生合成には、*ywf* 遺伝子クラスター上に存在する 7 つの蛋白質が関与することが知られている。まず、YwfB, C, D, G, H 酵素によって、プレフェン酸を前駆体として非蛋白質性 L-アミノ酸であるアンチカプシンが合成される。合成されたアンチカプシンは、YwfE タンパク質によって ATP 依存的に L-アラニンと連結されることでバチライシンが産生される。

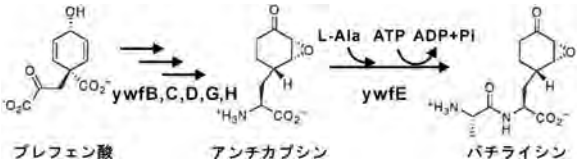

図 1 ：バチライシン合成経路。

同じくプレフェン酸を前駆体として生合成されるものは、フェニルアラニンやチロシンという芳香族アミノ酸がある。一方、アンチカプシンは芳香環ではなくシクロヘキサン骨格からなる。抗菌活性を有するエポキシ基が、どのように生合成されるかも謎である。さらに、最近発見された L-アミノ酸リガーゼの研究は D-アミノ酸リガーゼに比べ進んでいない。

本研究では、バチライシン合成酵素群の X 線結晶構造解析を行い、これら特徴的な反応機構の解明を目指している。今回は、酸化還元酵素である YwfD と L-アミノ酸リガーゼである YwfE の 2 つに着目して、リガンド共存下で結晶を得て、PF の放射光を利用してデータ収集を行った。

2 実験

YwfD、 E 蛋白質は、大腸菌で発現し、各種クロマトグラフィーにて高純度に精製された。結晶化初期スクリーニングは、QIAGEN 社のキットを用いてハンギングドロップ蒸気拡散法で行い、それを基にして更なる条件の最適化を進めた。得られた結晶を抗凍結処理し、PF にて回折データを収集した。YwfE に関しては Se-Met 置換体結晶を用いた SAD 法によるデータも収集した。

3 結果および考察

YwfE に関しては、1.9Å分解能で ADP-Mg が結合した状態の構造を決定した[1] 。全体構造は 3 つのドメインから構成され、ATP-grasp ファミリーに属した。D-アミノ酸リガーゼ等にはない、C2-domain が存在していた。ADP と 2 つの Mg^{2+}は 3 つのドメインに囲まれた領域に存在しており、このファミリーで保存されたアミノ酸によって認識されていた。

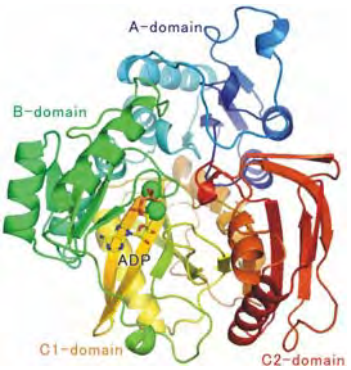

図 2 ：YwfE の全体構造。
ADP は B(緑)と C1(黄色)ドメインの間に存在している。C2(赤)ドメインは直接 ADP などと結合していないようだ。2 つの Mg^{2+}は緑色の球で示す。

基質となる L-アミノ酸が結合した状態を現す結晶は得られていないが、今回の構造を基にして反応を推測することが可能となった。

一方、YwfD については 1.5Å分解能のデータセットが得られ、現在、構造解析を進めている。

4 まとめ

今回、我々はバチライシン合成に関わる酵素のうち、L-アミノ酸リガーゼ YwfE の構造を決定した。YwfE は ATP-grasp ファミリーに保存されたアミノ酸残基を用いて ADP を認識していることが明らかになった。C2-domain は間接的に基質認識に関わっているようだ。今後、他の酵素の構造決定を進める。

謝辞

PF スタッフの皆様のご支援に深く感謝いたします。

参考文献

[1] T. Tsuda, T. Suzuki & S. Kojima. Acta Cryst. **F68** (2012) 203-306.

* takeo.tsuda@gakushuin.ac.jp

Crystal structures of MNV-1 RdRp-complexes

Intekhab Alam, Ji-Hye Lee, and Kyung Hyun Kim*
Department of Biotechnology and Bioinformatics, Korea University

Introduction

Norovirus (NV) is the leading cause of acute, nonbacterial gastroenteritis. Murine norovirus-1 (MNV-1) which can be grown in macrophage cell line RAW 264.7 serves as a surrogate model system for studying human norovirus (HuNoV) biology. MNV-1 RNA dependent RNA polymerase (RdRp) which is the main enzyme responsible for virus replication requires a protein primer VPg (Virion protein genome linked). The understanding of NV biology is important for the development of drug and vaccine against caliciviruses. In this study we have solved the crystal structureS of MNV-1 RdRp in complex with some inhibitors as 5-fluorouracil (5FU), ribavirin, and 2-thiouridine (2TU) [1, 2]. In order to gain further insight in NV replication attempts are made to solve the crystal structure of MNV-1 RdRp in complex with its protein primer VPg. Such structures will be helpful for better understanding of NV biology and will aid in designing some novel inhibitors against them.

Experiment

MNV-1 RdRp proteins were overexpressed in *E. coli,* and purified by affinity and size-exclusion chromatography. The final concentrations of RdRps were 5 mg/ml. Crystals were screened by hanging drop vapour diffusion method using commercial kits (Emerald biosystems, Bainbridge Island, USA). 1.5 µl of protein was mixed with 0.5 µl of buffer and two different temperatures 4˚C and 22˚C were tested for the initial screening. Crystals were observed at 4˚C in 1.26 M $(NH_4)_2SO_4$ and 0.1 M cacodylate (pH 6.5) and they were further refined with respect to salt and pH, to give diffraction quality cubic crystals in 1 M $(NH_4)_2SO_4$ and 0.1 M cacodylate (pH 6.5). For ribavirin and 2TU concentrated RdRp was incubated separately with 20 mM 2TU or ribavirin at 4˚C overnight and crystals were screened by sitting drop method using commercial kits (Emerald biosystems, Bainbridge Island, U.S.A). Good quality crystals for ribavirin were observed in 2-3 days after incubation at room temperature in 1.26 M $(NH_4)_2SO_4$, 0.1 M CHES (pH 9.5) and 0.2 M NaCl, which was further refined by hanging drop method with varying pH range (9.0-10.0) and $(NH_4)_2SO_4$ concentrations (0.8-1.4 M). For 2TU diffraction quality crystals were found in 2.0 M $(NH_4)_2SO_4$, 0.1 M cacodylate pH 6.5 and 0.2 M sodium chloride. To obtain crystals in complex with 5FU, crystals were soaked in 10 mM 5FU for 30-60 min prior to data collection. Diffraction data were collected with the crystals flash-cooled at 100 K in a stream of liquid N_2 using a synchrotron radiation source, BL-17A at Photon factory, Japan. Crystals diffracted to resolutions of 2.2-2.5 Å for the native and ligand complexed data. The native and ligand complexed crystals were of space group C2 and contained three monomers in the asymmetric unit.

Results

The MNV-1 RdRp structure was solved using CCP4 for molecular replacement, employing HuNoV RdRp structure (PDB ID 1SH2) with all its side chains retained as a search model. Molecular replacement gave a single prominent solution after the rotation and translation functions were employed. Difference Fourier maps with coefficients $2|F_o|-|F_c|$ and $|F_o|-|F_c|$ were used to model 5FU, 2TU and ribavirin interacting with amino acid residues at the active site. The overall structure with the ligand binding site is shown in figure 1.

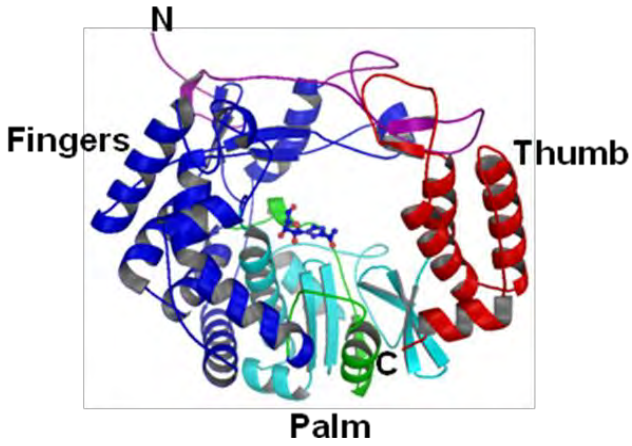

Fig.1 The overall structure of MNV-1 RdRp with palm (green and cyan), fingers (blue) and thumb (red) domains. N terminal is shown in pink while C is also in red. Ribavirin is represented as a ball and stick model (blue) in the active site.

Acknowledgement

This work was supported by a grant of the Korea Healthcare Technology R&D Project, Ministry of Health, Welfare and Family Affairs, Korea (A085119 and A080742).

References

[1]. Lee, J. H *et al*., Journal of General Virology **92** (2011) 1607-1616.
[2]. I. Alam *et al*., Virology **426** (2012) 143-151.

* khkim@korea.ac.kr

SPring-8 BL-26B1/2011G248 & Photon Factory BL-5A/2011A1917

単量体 Azami Green の安定緑色蛍光の構造基盤解明のための X 線結晶構造解析

Structure of mAG, a monomeric mutant of the green fluorescent protein Azami-Green, reveals the structural basis of its stable green emission

永田宏次*, 海老沢樹, 田之倉優
東京大学大学院農学生命科学研究科　〒113-8657 東京都文京区弥生 1-1-1

1 はじめに

mMC (monomeric Midoriishi Cyan) はミドリイシサンゴの一種 (*Acropara* sp.) から単離されたシアン色の蛍光タンパク質である Midoriishi Cyan を単量体化したものであり、Midoriishi Cyan と同様にシアン色の蛍光をもつ。mMC は代表的なシアン色蛍光タンパク質である amFP486 と 62%のアミノ酸配列相同性を持つが、両者の蛍光特性には違いがあり、mMC (励起ピーク: 469 nm, 蛍光ピーク: 496 nm) は amFP486 (励起ピーク: 453 nm, 蛍光ピーク: 486 nm) よりもやや長波長側に励起・蛍光ピークがある。このため、mMC は一般的な緑色蛍光タンパク質と amFP486 の中間の蛍光特性を持つ。本研究では、mMC の X 線結晶構造解析を行い、mMC と amFP486 の発色団付近の構造を比較することで、両者の蛍光特性の差を生じさせる構造的要因を解明することを目的としている。

2 実験

大腸菌を宿主として mMC を大量発現、精製し、シッティングドロップ蒸気拡散法により結晶化を行った。得られた mMC の結晶について、前期は SPring-8 BL-26B1 にて、結晶の質の評価を中心に回折実験を行い、後期は前期の結果を参考にして Photon Factory BL-5A で回折データを収集した。取得した回折データを用いて、分子置換法により mMC の 2.2 Å 分解能結晶構造を決定した。mMC と amFP486 の立体構造比較から、両者の蛍光特性の違いを生じさせるアミノ酸残基を推定した。また、mMC の点変異体発現系を作製した。現在、これらの点変異体の蛍光特性解析を進めており、今後、結晶構造解析を行う予定である。

3 結果および考察

大腸菌を宿主として mMC を大量発現し、精製、結晶化した。SPring-8 BL-26B1 および Photon Factory BL-5A での X 線回折データを用いた結晶構造解析により 2.2 Å 分解能の mMC の立体構造を決定した。mMC 結晶は、空間群 $P6_5$、格子定数 $a = b = 124.5$ Å, $c = 161.3$ Å で、非対称単位中に 4 分子の mMC が存在していた（図 1）。$R_{work} = 19.4\%$, $R_{free} = 23.9\%$まで構造精密化した。

mMC は他の蛍光タンパク質と同様の β バレル構造を有していた（図 1）。色素団は、β バレルの内側に存在し、Gln-Tyr-Gly の 3 アミノ酸残基の翻訳後修飾により形成されることが示された。色素団と周囲のアミノ酸残基の観察から、mMC と amFP486 の蛍光特性の違いを生じさせる構造要因として、両分子の色素団に共通の Tyr 側鎖と相互作用している異なるアミノ酸残基［mMC の Gln166（親水性で長い側鎖）と amFP486 の Ala165（疎水性で短い側鎖）］が候補に挙がった。現在、変異体解析により、この位置のアミノ酸残基側鎖が mMC の蛍光特性に与える影響について検証を進めている。

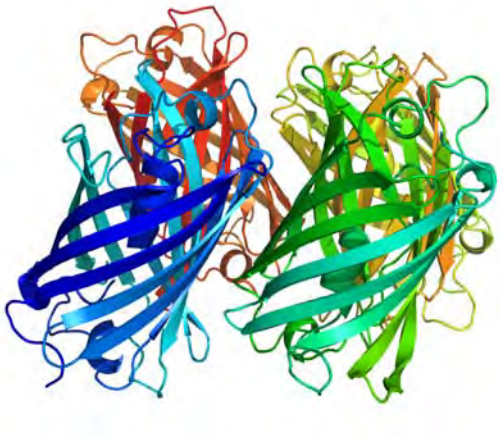

図 1 ：mMC の結晶構造

4 まとめ

mMC の 2.2 Å 分解能結晶構造を決定し、mMC と amFP486 との蛍光特性が異なる原因を特定中である。

謝辞

SPring-8 BL26B1 および Photon Factory BL-5A のスタッフの皆様に心より感謝申し上げます。

* aknagata@mail.ecc.u-tokyo.ac.jp

5A, 17A, NW12A, NE3A/ 2011G502, 2011G002

Crystal structure of UDP-galactose 4-epimerase-like L-threonine dehydrogenase

Kazunari Yoneda*[1], Haruhiko Sakuraba[2], Tomohiro Araki[1], Toshihisa Ohshima[3]
[1]Department of Bioscience, School of Agriculture, Tokai University, Aso, Kumamoto, Japan
[2]Department of Applied Biological Science, Faculty of Agriculture, Kagawa University, 2393 Ikenobe, Miki-cho, Kita-gun, Kagawa761-0795, Japan
[3]Institute of Genetic Resources, Faculty of Agriculture, Kyushu University, Fukuoka, Japan

Introduction

L-Threonine dehydrogenase (L-ThrDH) catalyzes NAD^+-dependent dehydrogenation at the β-carbon (C3) position of L-threonine. The primary structure of L-ThrDH was initially determined using the enzyme from *Escherichia coli*; it revealed that the enzyme belongs to the medium-chain alcohol dehydrogenase family. Recently, a novel L-ThrDH that shows no sequence similarity to the *E. coli* enzymes were identified in a psychrophilic bacterium *Flavobacterium frigidimaris* KUC-1. This enzyme exhibits notable sequence identity with UDP-galactose 4-epimerase (GalE) homologues which, belongs to the short-chain dehydrogenase-reductase family. We have previously solved the first three-dimensional structure of the GalE-like L-ThrDH from *F. frigidimaris* [1]. However, the catalytic mechanism of GalE-like L-ThrDH is unknown. To clarify the structural basis of the catalytic mechanism, we solved the four crystal structures of archaeal GalE-like L-ThrDH in the presence of NAD^+, a pyruvate (inhibitor) and two substrates were determined. This is the first description of the molecular basis for the substrate recognition of a GalE-like L-ThrDH.

Materials and Methods

Single-wavelength (1.0 Å) data for *Thermoplasma volcanium* L-ThrDH-NAD^+, L-ThrDH in complex with NAD^+ and pyruvate, Y137F inactive mutant in complex with NAD^+ and L-threonine, and Y137F in complex with NAD^+ and L-3-hydroxynorvaline were collected on the beamline 5A, 17A, NW12A and NE3A at the Photon Factory. The data were processed using HKL2000 and the CCP4 program suite.

Results and Discussion

Given the structure of pyruvate, we sought to predict the structure of the L-threonine molecule within the active site of *T. volcanium* L-ThrDH (Fig. 1A) [2]. Based on the structure of pyruvate, we tried the modeling of L-threonine binding into the active site of *T. volcanium* L-ThrDH. However, we could not postulate a single binding mode of L-threonine molecule. On the other hand, using the inactive *T. volcanium* L-ThrDH Y137F mutant, which trapped the substrate within the active site, we were able to determine the substrate-bound structures of the enzyme in complex with L-threonine or L-3-hydroxynorvaline (Fig. 1B, 1C).

Within the structures of the *T. volcanium* L-ThrDH Y137F/NAD^+/L-threonine and L-3-hydroxynorvaline, we observed that the Oη of Tyr^{137}, lies within hydrogen-bonding distance (2.4-2.6 Å) of the β-hydroxyl group of the L-threonine or L-3-hydroxynorvaline (Fig. 1D). This means that Tyr^{137} could serve directly as the active-site base. Taken together, this finding suggest the catalytic mechanism underlying the *T. volcanium* L-ThrDH reaction likely proceed through the following steps: 1) abstraction of the β-hydroxyl hydrogen of L-threonine via direct proton transfer driven by Tyr^{137}; and 2) transfer of a hydrogen from the β-carbon (C3) of the L-threonine to C4 of the NAD^+ (*si*-face), forming L-2-amino-3-oxobutyrate and NADH (Fig. 2).

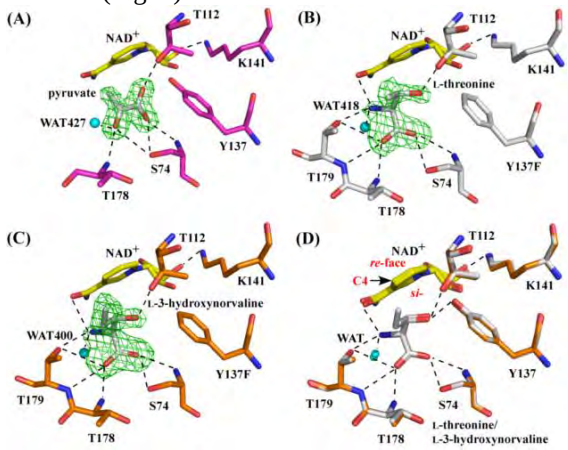

Figure1 *A*, The NAD^+/pyruvate-bound wild-type enzyme (*magenta*). *B*, The NAD^+/L-threonine-bound Y137F mutant enzyme (*white*). *C*, The NAD^+/L-3-hydroxynorvaline-bound Y137F mutant enzyme (*gold*). *D*, Superposition of the active site pocket of the NAD^+/L-threonine-bound Y137F mutant with that of the NAD^+/L-3-hydroxynorvaline-bound Y137F mutant.

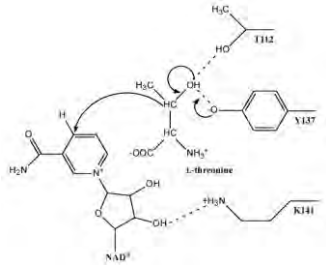

Figure 2 Proposed catalytic mechanism of *T. volcanium* L-ThrDH.

References

[1] K. Yoneda *et al.*, FEBS J. **277** (2010) 5124.
[2] K. Yoneda *et al.*, J. Biol. Chem. **287** (2012) 12966.

* kyoneda@agri.u-tokai.ac.jp

AR-NE3A, AR-NW12A/2011G518

Refined Crystal Structures of Human Ca^{2+}/Zn^{2+}- binding S100A3 Protein Characterized by Two Disulphide Bridges

Masaki Unno[1,2*], Hidenari Takahara[1,3], Claus W. Heizmann[4] and Kenji Kizawa[5]
[1]Frontier Research Center for Applied Atomic Sciences, Ibaraki University, Ibaraki 319-1106, Japan
[2]Graduate School of Science and Engineering, Ibaraki University, Ibaraki, 310-8512, Japan
[3]Laboratory of Biochemistry & Molecular Biology, Department of Applied Biological Resource Sciences, Ibaraki University, Ibaraki 300-0393 Japan,
[4]Department of Pediatrics, Division of Clinical Chemistry and Biochemistry, University of Zürich, Steinwiesstrasse, Zürich, Switzerland
[5]Skin Science Research Group, Innovative Beauty Science Laboratory, Kanebo Cosmetics Inc., Kanagawa 250-0002 Japan

1 Introduction

The S100 protein family constitutes the largest subgroup of the EF-hand type of Ca^{2+}-binding protein family. Among more than 20 members of this protein family, S100A3 has the highest cysteine content (10 out of 101 amino acids) and an exceptionally high affinity for Zn^{2+} ion (K_d = 1.5-11 μM). This Ca^{2+} and Zn^{2+}-binding protein is highly expressed in differentiating cuticular cells in the human hair follicle and organized into the mature cuticles. We previously reported that natural occurring S100A3 protein was post-translationally citrullinated in hair follicles. Peptidylcitrulline residues brought by peptidylarginine deiminases (PAD) have been considered to decrease the net positive charge of peptidylarginine residues in the substrate protein, thereby changing its structure owing to alterations of the intra- and inter-molecular ionic interaction. This irreversible post-translational modification has recently been implicated in several physiological and pathological processes and also associated with human diseases including cutaneous disorders. Among the five known human PADs (types I-IV and VI), type III isozyme (PAD3), which is dominantly expressed in hair follicles, converts a symmetric pair of Arg51 residues on dimeric S100A3 to citrullines in the presence of Ca^{2+}. This specific citrullination of S100A3 causes assembly of a Ca^{2+}-bound homotetramer and the Ca^{2+}-ions could transfer to PAD enzymes in turn. S100A3 is postulated to act as Ca^{2+}-modulating protein during its dimer-tetramer transition within the hair cuticular cells.

Although characterization of the Zn^{2+}- and Cu^{2+}-binding sites was initially hampered due to the absence of a conserved motif, recent analyses of the crystal and solution structures have revealed their unequivocal locations. Regarding the high affinity Zn^{2+}-binding site in S100A3, a structural model of a dinuclear thiolate-bridged Zn^{2+}-cluster coordination in the C-terminal cysteine-rich domain was proposed based on spectrophotometry. A putative single Zn^{2+}-binding site was also reported to be partially preformed in the helix IV terminal region based on the previously reported crystal structure of metal-free S100A3 dimer (PDB code 1KSO). However, the exact location of the Zn^{2+}-binding site was not determined.

2 Experiment

Purified proteins were concentrated by centrifugal filtration for crystallization. To attempt disulphide bond refolding within Ca^{2+}/Zn^{2+} bound forms (PR-treatment), $CaCl_2$ and $ZnSO_4$ were added to the protein solution to 2 equimolar with S100A3 monomer. Crystallization was carried out using the hanging-drop vapour diffusion method at 20°C. Crystals suitable for high-resolution structure determination for were obtained using 2.4 M $(NH_4)_2SO_4$ as a reservoir solution within a few days.

3 Results and Discussion

We identified two previously undocumented disulphide bridges: one is between Cys30 in the N-terminal *pseudo*-EF-hand and Cys68 in the C-terminal EF-hand (SS1), and another attaches Cys99 located in the C-terminal coil structure to Cys81 in helix IV (SS2). Mutational disruption of SS1 (C30A+C68A) abolished the Ca^{2+}-binding property of S100A3 and retarded citrullination of Arg51 by peptidylarginine deiminase type III (PAD3), while SS2 disruption inversely increased both Ca^{2+}-affinity and PAD3 reactivity *in vitro*. Similar backbone structures of WT, R51A and C30A+C68A indicated that neither Arg51 conversion by PAD3 nor SS1 alter the overall dimer conformation. SS1 renders the hinge region flexible and the helix III reorientation, those are essential for its Ca^{2+}-binding properties, whereas SS2 structurally shelters Arg51 in the metal-free form. A model of the tetrahedral coordination of a Zn^{2+} ion by $(Cys)_3His_1$ residues that is compatible with SS2 formation in S100A3 is proposed.

References

[1] M. Unno *et al.*, *J. Mol. Biol.* **408** (2011) 477-490.

*unno19@mx.ibaraki.ac.jp

NW12, NE3A, 5A/2011G524

Crystal structures of enzymes and transporters involved in amino acid metabolism

Takeo TOMITA, Yuko KANEMARU, Fumihito HASEBE, Makoto NISHIYAMA*
Biotechnology Research Center, the University of Tokyo, Yayoi, Bunkyo-ku, Tokyo 113-8657, Japan

Introduction

Lysine is produced industrially by *Corynebacterium glutamicum* mutants. *C. glutamicum* mutants with (*S*)-2-aminoethyl-L-cysteine (AEC) resistance were isolated, and their derivatives are used for industrial production of lysine.

Our recent crystallographic studies have proven that most of the mutations conferring AEC resistance are located at the regulatory domain of aspartate kinase (AK) from *C. glutamicum*. Although lysine is synthesized through diaminopimelate (DAP) pathway in most bacteria, it is synthesized through α-aminoadipate pathway in *Thermus thermophilus*. Lysine biosynthesis is regulated by two different stages in *T. thermophilus*: 1) feedback inhibition of homocitrate synthase (HCS), 2) transcriptional repression of genes involved in the biosynthesis. Interestingly, the growth of *T. thermophilus* was inhibited at 50 μM AEC, which contrasts with the cases for other bacteria, such as *E. coli* and *C. glutamicum*, which grow even in the presence of 500 μM AEC. This result indicates that *T. thermophilus* has hyper-sensitivity to AEC. Our previous study revealed that AEC inhibits HCS of *T. thermophilus* at μM levels. This suggested that the growth inhibition by AEC of *T. thermophilus* might be due to the inhibition of HCS. However, growth of a *T. thermophilus* mutant possessing HCS with H72L replacement, which gave complete AEC resistance to HCS, was also inhibited by AEC with sensitivity the same as that of wild-type strain. This result suggests that AEC acts on a target other than HCS to inhibit the growth of *T. thermophilus*. Analysis of the mutant strain with AEC resistance followed by its isolation revealed that two amino acids transporters were necessary for AEC resistance of the mutant. To clarify the mechanism of substrate recognition of the transporter, we performed crystallographic analysis of periplasmic substate-binding protein (PSBP) (TTC0807) complexed with AEC, Lys, Orn, and Arg.

Materials and Methods

Preparation of crystals and structure determination – Crystallization of TTC0807/AEC, TTC0807/Lys, TTC0807/Orn, TTC0807/Arg were performed by the hanging drop vapor diffusion method. The reserviour solutions for obtaining each complex are shown below.

TTC0807/AEC complex: 0.2 M sodium sulfate, 20% PEG 4000, 10 mM AEC. TTC0807/Lys complex: 0.2 M ammonium sulfate, 20% PEG 4000, 10 mM lysine. TTC0807/Orn complex: 0.2 M sodium sulfate, 20% PEG 4000, 10 mM ornithine. TTC0807/Arg complex: 0.2 M ammonium sulfate, 20% PEG 4000, 10 mM arginine

The structure of TTC0807/AEC complex was determined by molecular replacement method using the structure of StLAO-BP (PDB code, 1LST).

Results and Discussion

Overall structure of TTC0807 – TTC0807 was consisted from domain I and domain II. Structrure of TTC0807 was similar with that of StLAO-BP, while the hinge between the domains were replaced to a β-sheet β8-β12 (Fig. 1).

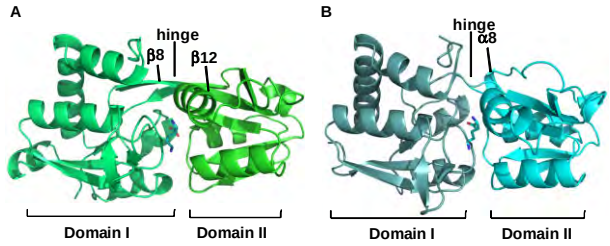

Fig. 1 Crystal structure of TTC0807/AEC complex (A) and StLAO-BP (B).

Substrate binding pocket of TTC0807 – The bound substrates were recognized by similar manner, while conformations of Glu19 in those complexes were altered to accommodate the different substrates.

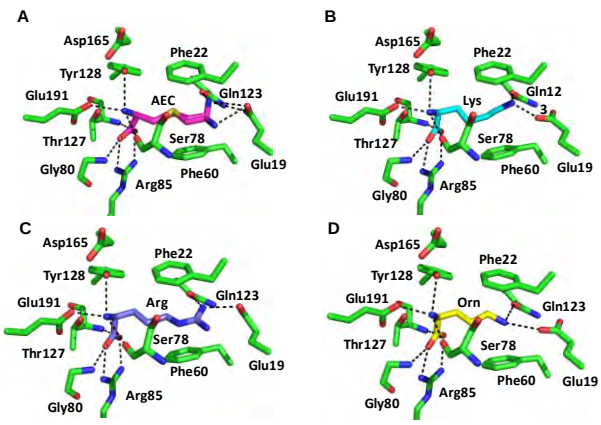

Fig. 2 Substrate binding pocket of TTC0807 complexed with AEC (A), lysine (B), arginine (C), and ornithine (D).

* umanis@mail.ecc.u-tokyo.ac.jp

NW12, NE3, 5A /2011G525

Crystal structures of the enzymes involved in novel lysine biosynthetic pathway using amino acid carrier protein

Takeo TOMITA[1], Ayako YOSHIDA[1], Kento TAKAHASHI[1], Makoto NISHIYAMA*[1]
[1]The Univ. of Tokyo, Yayoi, Bunkyo-ku, Tokyo 113-8657, Japan

Introduction

Bacteria and plants were thought to biosynthesize lysine via the diaminopimelate pathway, while fungi biosynthesize lysine from α-aminoadipate (AAA). We preriously found that although it is a bacterium, *Thermus thermophilus* synthesized lysine via AAA. The enzymes involved in the first half of the pathway in *T. thermophilus* are similar to those involved in the leucine biosynthetic pathway or tricarboxylic acid cycle. However, the latter half of the pathway is totally different from the corresponding part of fungal biosynthetic pathway. Since our discovery of lysine biosynthesis through AAA, evidence has mounted that many microorganisms synthesize lysine by a similar pathway, indicating that this pathway is one of origins of lysine biosynthesis. To date, we have characterized the enzymes involved in this unique lysine biosynthetic pathway. To clarify the structure-function relationships of these enzymes, we performed crystallographic analyses of enzymes and proteins involved in lysine biosynthetic pathway. Here, we describe the recently determined crystal structures of TK0278 and Saci_0600.

Materials and Methods

Data collection and processing.

The X-ray diffraction data of native proteins were collected using the beamline, NW12, NE3 and 5A at PF. The image sets were integrated and scaled using HKL2000.

Results and Discussion

TK0278

The genes coding the enzymes involved in lysine biosynthetic pathway *via* AAA are found in several bacteria and Archea. Hyperthermophilic archea, *T. kodakarensis* also has the gene cluster of AAA pathway. However, it has no genes encoding arginine biosynthetic enzymes which have similarity with AAA lysine biosynthetic enzymes. In the genome of *T. kodakarensis*, there is one copy (*TK0278*) of *lysX* homolog, encoding the first characteristic enzyme in the latter part from AAA of the pathway. We suppose that TK0278 can catalyzes two reactions involved in lysine and arginine (ornithine) biosynthesis, that is, TK0278 can ligate AAA and glutamate to C-terminal glutamate residue of LysW homolog (TK0279) in ATP-dependent manner. *In vitro* assay, we confirmed that TK0278 catalyzes the both reactions and are involved in both lysine and arginine biosynthesis. To elucidate structural basis of the bifunctionality of TK0278, we crystalized TK0278 with TK0279 (LysW), AMP-PNP, and AAA or glutamate. So far, we determined the crystal structure of TK0278 with AMP-PNP. It forms a tetramer (Fig. 1). The structure provides candidate of the residue involved in both AAA and glutamate bindings, which lies at the substrate-binding site.

Fig. 1 Overall structure of TK0278

Saci_0600

The forth reaction of lysine biosynthesis in *Thermus thermophilus* is catalyzed by homoisocitrate dehydrogenase (HICDH). On the genome of *Sulfolobus acidocaldarius*, Saci_0600 is annotated as a homologous enzyme, isopropylmalate dehydrogenase (IPMDH) in leucine biosynthesis and Saci_2375 is annotated as isocitrate dehydrogenase (ICDH) in tricarboxylic acid cycle, while HICDH gene is not found. Saci_0600 possesses IPMDH activity. To elucidate the mechanism of substrate recognition, we determined the crystal structure of Saci_0600 complexed with 3-isopropylmalate (3-IPM) at 2.2 Å resolution. Saci_0600 formed tetrameric structure. Saci_0600 has compact loop structure in its active site while IPMDH from *Thiobacillus ferroxidans* has extended loop structure. Saci_0600 recognizes the γ-moiety of 3-IPM by hydrophobic region consist of Ala78, Ala79, Val82, and Val83 (Fig. 2).

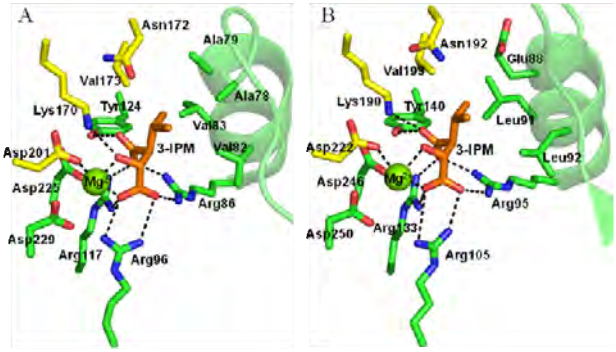

Fig. 2 Comparison of active sites between Saci_0600 complexed with 3-IPM/Mg^{2+} (A) and IPMDH from *Thiobacillus ferrooxidans* complexed with 3-IPM/Mg^{2+} (B)

* umanis@mail.ecc.u-tokyo.ac.jp

1A, 5A, 17A, NW12A/2011G-529

細菌におけるメナキノン合成経路酵素の立体構造解析
Structural study of an enzyme of menaquinone synthesis in bacteria

福岡大祐、秋山友了、佐々木康幸、矢嶋俊介*
東京農業大学バイオサイエンス学科、〒156-8502 世田谷区桜丘 1-1-1

1 はじめに

人を含め哺乳類においてビタミン K は、血液凝固因子の活性化を担う重要な化合物である。しかし、哺乳類はビタミン K を自ら合成できないため、植物（ビタミン K1）や腸内細菌（ビタミン K2）から得ている。細菌においてメナキノン（ビタミン K2）はシキミ酸経路で合成されたナフトキノン骨格とイソプレノイド鎖からなる化合物である。大腸菌や枯草菌において合成経路が詳しく研究されてきた。

近年、放線菌にはその経路に存在するいくつかの対応する遺伝子が存在せず、コリスミ酸から新規経路を経て、メナキノンが合成されることが明らかとなった。また、データベース解析から放線菌の他 *Helicobacter pyroli, Campylobacter jejuni* などの病原性菌もこの新規経路を持つ一方、乳酸菌は既知経路を使用していることが明らかとなり、この経路があらたなドラッグターゲットとして注目を集めている。

この経路の特徴として、コリスミ酸に続く化合物として通常の代謝物としては知られていないフタロシンが合成される。フタロシンはある種の放線菌の二次代謝産物として発見され、誘導体には制癌作用があることが認められている。経路第一段階目の酵素がフタロシン合成の一部をになっていると考えられているが、まだ詳細は不明である。そこで、この経路を有する好熱性放線菌である *Acidothermus cellulolyticus* 11B 由来酵素の立体構造を明らかにし、フタロシンを合成する反応機構を明らかにすることを目指している。

2 実験

データベース情報を元に *A. cellulolyticus* 11B におけるメナキノン合成経路の初発酵素である *Acel*_0261 遺伝子をクローニングし、大腸菌発現系 pET22b(＋)ベクターに導入した。サンプルの結晶化は全てハンギングドロップ蒸気拡散法で行ない、4 ℃で静置した。回折強度データの処理は HKL2000 でおこなった。

立体構造の構築は、PDB ID: 2NXO をサーチモデルとした分子置換法により MOLREP を用いて行ない初期構造を求めた。変異体の構造解析は、得られた立体構造をサーチモデルとした分子置換法により解を求めた。

3 結果および考察

得られた結晶について 2.3 Å 分解能で回折データを収集した。空間群は $P2_1$ に属しており、非対称単位にモノマーが 2 分子存在していた。XtalView でのモデル構築と Refmac5 を用いた精密化を行なった。N 末端および C 末端の各 1 残基を除いてすべてモデリングができた。分子の中心に大きな電子密度が観察され、基質あるいは反応物かと期待された。しかしながら、現在想定されている反応における化合物構造とは一致せず、化合物は未同定である。しかし、その空間が活性部位と考えられたため、酵素に変異を導入し構造解析を行うこととした。結晶化、構造解析を行うことができた変異体については、野生型と同じ空間群であったが格子常数がことなり、非対称単位に 1 分子が含まれていた。全体構造は野生型と同一であった。

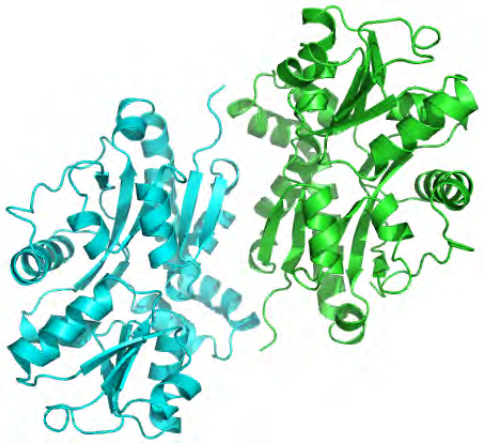

図 1 ：Acel_0261 の立体構造

4 まとめ

今回、*A. cellulolyticus* 由来のメナキノン合成経路初発酵素の立体構造を明らかにした。今後は、変異体などの解析を行い反応機構の解明を目指す。

謝辞

データ測定にあたり PF スタッフの方々に深く感謝致します。

* yshun@nodai.ac.jp

BL-27B/2011G572

Chromosomal Aberrations via Bystander Effect in Normal Human Fibroblasts Irradiated with Monochromatic X-ray Microbeams

Masao SUZUKI[1]*, Narongchai AUTSAVAPROMPORN[1], Noriko USAMI[2], Toshie IIZUKA[2], Takeshi MURAKAMI[1] and Katsumi KOBAYASHI[2]
[1]Res.Ctr.Charged Particle Therap., Natl. Inst. Radiol. Sci., Chiba 263-8555, Japan
[2]KEK-PF, Tsukuba, Ibaraki 305-0801, Japan

1 Introduction

The traditional dogma of radiobiological effects recently has been challenged by the observation of bystander effect, which is that similar effects can also be induced in non directly irradiated cells neighboring on irradiated cells. Most studies for bystander effect have been carried out using microbeam/broadbeam irradiations with high linear energy transfer (LET) particle radiations and only limited data is available to understand bystander effects induced by low-LET electromagnetic radiations, such as X or gamma rays. In this study we have been examining bystander cellular effects and demonstrated the bystander lethal effect by the targeted cell nucleus irradiations last year [1]. This year, we examined chromosomal aberrations to understand mechanism(s) of inducing bystander effect in chromosome/DNA levels.

2 Experiment

Monochromatic 5.35-keV X-ray microbeams with 20μm x 20μm size were produced with the cell irradiation system at BL27B. Irradiations were carried out with 40R in each point using the 256 cross-stripe method described previously [2]. Thirty minutes before irradiation, half of the dishes were treated with 18-α-glycyrrhetinic acid (AGA), which is a specific inhibitor of gap-junction mediated cell-cell communication. At the irradiation period, cultures were confluent and allowed direct intercellular communication via the gap junction. We examined micronucleus (MN) formation as the indicators for chromosomal aberrations. The MN formation was detected using the cytokinesis block technique. Briefly, after irradiation cells were subcultured and allowed to grow in the presence of 2 μg/ml cyctochalasin B for 72 h incubation at 37°C. Then the cells were fixed in ethanol and stained with Hoechst 33342 solution. At least 500 cells were examined for each data point under a fluorescence microscope and only micronuclei in binucleated cells were scored as a damaged cell.

3 Results and Discussion

Figure 1 shows MN formation induced by X-ray microbeams, comparing to neon-ion microbeams at the Takasaki Ion Accelerators for Advanced radiation Application of the Japan Atomic Energy Agency. The MN formation by neon-ion microbeams in the absence of AGA was higher than that in the presence of AGA, while we observed no significant difference between the absence and absence of AGA by X-ray microbeams. The percent of the binucleated cells with MN was 3-6% in the absence of AGA, whereas still exist in 2-4% level in the presence of AGA with any of the radiation sources. We estimate that only 0.04% of total cells on the dish was irradiated directly with the microbeams by our 256 cross-stripe method [2]. If MN formation could occur only in directly irradiated cells, the percent of MN formation could never go above 0.04%, assuming no bystander effects. However, the present results showed beyond our expectation. There is clear evidence that bystander effect occurred in the induction of chromosomal aberrations. The difference in our data between X-ray- and neon-ion microbeams suggests that two different mechanisms play a critical role in inducing bystander effect, such as gap-junction mediated cell-cell communication in the absence of AGA and secreted factor(s) to culture medium from the irradiated cells in the presence of AGA. And the bystander effect via secreted factor(s) only induces by low-LET X rays.

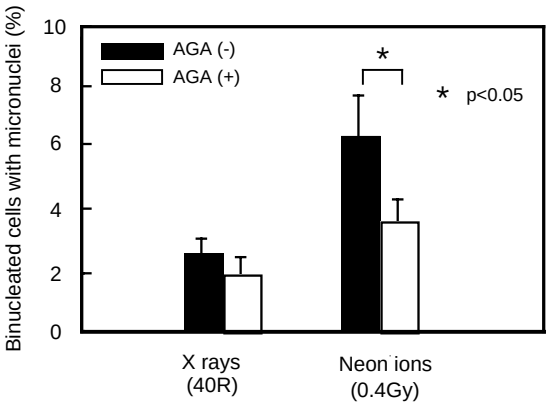

Fig.1: The MN formation irradiated with X-ray and neon-ion microbeams. The results were the means and standard deviations from the 3 independent beam times.

Acknowledgements

This study was supported in part by grants from the Japan Society of the Promotion of Sciences (23・01513) and the Quantum Beam Technology Program from the Japan Science and Technology Agency.

References

[1] M. Suzuki et al., Photon Factory Activity Report 2008 #26 Part B., 210 (2009).
[2] M. Suzuki et al., Photon Factory Activity Report 2010 #28 Part B., 288 (2011).

* m_suzuki@nirs.go.jp

1A, 5A, 17A/2011G600

X-ray crystallographic analysis of the (Runx1–CBFβ)$_2$–Ets1–DNA complex assembled on the enhancer of T cell receptor α chain gene

Masaaki SHIINA, Keisuke HAMADA, Taiko BUNGO, Mariko SHIMAMURA, Kazuhiro OGATA*
Dept. of Biochemistry, Yokohama City University School of Medicine, 3-9 Fukuura, Kanazawa-ku, Yokohama 236-0004, Japan

Introduction

Gene-specific transcription is involved in almost every cellular function, and an understanding of its regulation mechanism will give impact on the large area of biological researches. Gene-specific transcription is initially regulated through assembly of transcription factor (TF)–DNA complex formed on gene enhancers. To understand the mechanism by which TF–DNA-complex formation is regulated, we studied the T cell-specific TF–DNA complex formed on the *T cell antigen receptor* (*TCR) α chain* enhancer. This complex is known to contain multiple TFs such as Runx1, Ets1, CBFβ, CREB, etc., which synergistically bind to the *TCRα* enhancer, activating the target gene. Although each TF has been individually studied well, it remains unclear how they behave in the complex at the structural level. For example, a component of the complex, Ets1, is individually studied well: Ets1 activity is negatively regulated by the regulatory region (the exon VII) flanking its DNA binding domain (so called the ETS domain) and phosphorylations of the exon VII suppress a DNA binding activity of Ets1 more significantly. However, how Ets1 would behave in TF–DNA complexes are almost unknown. Here, we performed crystallographic analysis for the (Runx1–CBFβ)$_2$–Ets1–DNA complex.

Experiment

Bacterially expressed TFs, Ets1, Runx1 and CBFβ were purified and mixed with various lengths of double-stranded DNA containing *TCRα* enhancer in the following molar ratio: Runx1/CBFβ/Ets1/DNA = 2/2/1/1. The complex formation was checked by electrophoretic mobility shift assay and SDS-polyacrylamide gel electrophoresis. Then the complex solution was subjected to initial crystallization screening using Natrix, a crystallization reagents kit for nucleic acids (Hampton Research). The (Runx1–CBFβ)$_2$–Ets1–DNA complex was crystallized and soaked in cryoprotectant solutions, followed by flush-cooling in a stream of cold nitrogen gas at 100 K. Diffraction images were collected with synchrotron radiation at NW12A and BL-17A in Photon Factory and processed using HKL2000.

Results and Discussion

The crystals belong to the monoclinic space group *C*2, with unit cell dimensions of a = 330.0, b = 89.4 and c = 146.7. Due to a long a-axis, we had to reduce the angular width of the oscillation. The crystals were relatively resistant to a damage by X-rays and diffracted to 3.8 Å. Selection of the cryoprotectant agents was critical for diffraction quality.

We are currently trying to improve resolution and diffraction quality of the crystals. In parallel, we perform functional analyses of this complex using site-directed mutagenesis based on the obtained preliminary crystal structure.

Table 1: Data-collection statistics of (Runx1–CBFβ)$_2$–Ets1–DNA complex

Beam-line	BL17A
Wavelength	0.98
Resolution (Å)	50.0-3.8
Space group	*C*2
Unit-cell parameters (Å)	
a	330.0
b	89.4
c	146.7
β	115.7°
No. of reflections	
Observed	138731
Unique	37854
Completeness (%)	99.6 (97.1)[#]
I/σ (I)	12.5 (1.8)[#]
R_{merge} (%)	11.4

[#] Numbers in parentheses refer to data for high resolution outer shell 3.87-3.80 Å

* ogata@med.yokohama-cu.ac.jp

6A/2011G602

骨格筋の筋節伸展がミオシン頭部固有の状態に及ぼす効果

Effects of sarcomere length on the intrinsic distribution of myosin headsaround the shaft of thick filament

竹森　重[1*], 木村雅子[2], 山口眞紀[1], 中原直哉[1], 横溝駿矢[3], 渡邉　賢[4]
[1] 東京慈恵会医科大学・医学部・分子生理学、〒105-8461 東京都港区西新橋 3-25-8
[2] 女子栄養大学・統合生理学　〒350-0288 埼玉県坂戸市千代田 3-9-21
[3] 東海大学大学院・体育学研究科　〒259-1292 神奈川県平塚市北金目 4-1-1
[4] 首都大学東京・健康福祉学部・作業療法学科/大学院人間健康科学研究科
〒116-8551 東京都荒川区東尾久 7-2-10

1 はじめに

横紋筋は収縮性相互作用をする二つのタンパク質のうち、ミオシンを太いフィラメントに、アクチンを細いフィラメントに集積し、相互作用を制御するタンパク質のトロポニン、トロポミオシンとともに筋節という規則周期構造を作っている。この規則構造の中で両フィラメントが交互嵌合して稼働する。

この筋節構造は相互作用を効率的にするだけでなく、収縮と弛緩を自原性に調節する上でも重要であることが示唆されている[1,2]。この自原性調節機能のうち、筋節の伸展が弛緩から収縮への遷移を助ける作用を持つことはストレッチアクティベーションと呼ばれ[3]、心臓ではフランク-スターリングの法則と呼ばれる自原性収縮力調節を実現するものとして着目されている。

このストレッチアクティベーションの機構として、筋節伸展がコネクチン/タイチンと呼ばれる弾性タンパクフィラメントのひずみを通じて太いフィラメントからのミオシン頭部の突出状態を変え、これによって収縮・弛緩状態を自源性に調節するという仮説を立て、この仮説を検証する X 線回折実験を進めている。

2 実験

BL6A の小角カメラでイメージングプレートを使って直径 300 ミクロンほどの筋標本からの 2 次元回折像を記録した。微小な標本を X 線ビームの上に載せる位置調整にはイメージインテンシファイア付の CCD カメラを用いている。

標本はウサギ腸腰筋とラット心筋のスキンドファイバーである。アクチンとの相互作用によるミオシン頭部の突出状態変化を除外するためには、ゲルゾリン処理によってウサギ腸腰筋のスキンドファイバーの細いフィラメントを除去し、太いフィラメントだけにした標本を用いた。

ハッチ内の空調装置と循環恒温槽からの外部循環で温度管理（20 度または 5 度）した実験セルホルダに、あらかじめ調整して持参した筋標本をセットして実験を行った。

太いフィラメントが作る格子の間隔、ミオシン頭部の突出状態に対する筋節長の効果を主に解析した。

3 結果および考察

筋節を伸ばすと、コネクチン/タイチンの硬さに依らず太いフィラメントの格子間隔は狭まった。細いフィラメントを除去すると、太いフィラメントの間隔は狭まったが、この狭まった間隔を基準にすると、筋節長を伸ばした時の筋節に対する効果は細いフィラメントがあるときと同様であった。

ミオシン頭部の突出状態については、細いフィラメントがなくても筋収縮の可逆抑制薬ブタンジオンモノオキシム（BDM）はミオシン頭部を太いフィラメントのバックボーンのまわりに規則正しくらせん配列させる効果を持った。BDM と類似した構造を持つが収縮に対する特異作用を持たない小分子量ポリエチレングリコール(PEG3350)は、高濃度で太いフィラメントの格子間隔を狭めながら筋節構造の規則周期性を高めたが、ミオシン頭部のらせん配置に対する特異作用を持たなかった。両者の作用で高まった規則周期筋節構造の中で、ミオシン頭部の突出が筋節の伸展に伴って乱れていくことが観測された。

以上の結果は、筋節伸展がミオシン頭部の配置を介して、筋節構造がその収縮・弛緩状態を自原性に調節するとする仮説を支持するものである。

参考文献

[1] M. Yamaguchi. Jikeikai Med. J. **45** (1998) 115-125.
[2] H. Iwamoto, K. Inoue and N. Yagi. Proc. Biol. Sci. **273** (2006) 677-685.
[3] M. Endo. Nature New Biology. **237** (1972) 211-213.

* sml@jikei.ac.jp

5A/2011G606

超濃厚・超低塩濃度水溶液中でのリゾチームのコロイド結晶化・結晶化とそれらの結晶構造解析

Colloidal crystallization, crystallization and structure analysis of highly concentrated lysozyme molecules in very dilute electrolyte solution

鈴木良尚 [1*], 山田悠介 [2]

[1]徳島大学ソシオテクノサイエンス研究部、〒770-8506 徳島市南常三島町 2-1

[2]KEK-PF　〒305-0801 つくば市大穂 1-1

1 はじめに

ほとんどのタンパク質結晶は沈殿剤を使って結晶化されているが、多くの“柔らかい”タンパク質が結晶化できていない。これは、主に構造が大きく揺らいだまま無理やり引力によりひきつけたことによる不規則な凝集体形成ものと考えられる。

もし、タンパク質結晶を通常の引力結晶ではなく、斥力的な相互作用を利用したコロイド結晶にすることができるのであれば、これらの柔らかいタンパク質の結晶化の可能性は増加すると考えられる。

筆者らはこの研究に先立ち 2010P104 において、沈殿剤を用いなくてもニワトリ卵白リゾチームが針状の結晶を生成し、更にそれらが結晶性の回折スポットを生じることを発見している。本研究では、2010P104 において得られた結晶と同条件で育成した単結晶の回折スポットから、コロイド結晶化の有無を確認することを試みた。

2 実験

本研究では、モデルタンパク質としてニワトリ卵白リゾチーム（生化学工業、6 回再結晶）を、更なる精製なしに用いた。0.6 g のリゾチームを 15 mL の超純水（抵抗率> 18.2 MΩcm）に溶解し、遠心濃縮を 3 回行って脱塩し、最終濃度が 300 mgmL^{-1} 程度になるようにすると 25℃で結晶化した。その結晶スラリーから、0.1 – 0.2 mm のナイロンループを用いて比較的大きな結晶を掬い上げて、~ 90 mgmL^{-1} リゾチーム, ~ 40 mgmL^{-1} グリセロールの水溶液で洗い、フラッシュクーリングを行って、KEK-PF BL-5A におけるシンクロトロン放射光を使って振動写真を撮影した。

3 結果および考察

撮影に使用した結晶の写真を図 1 に示す。

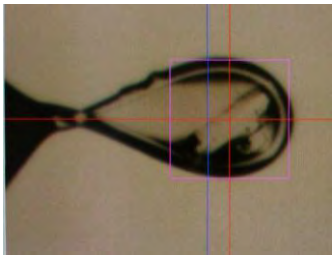

図 1: 構造解析に用いたリゾチーム結晶。ピンクの枠の一辺は 0.2 mm。

実際には、波長 1.00 Å の放射光を用いて、1° 振り、1 秒露光、1.7 Å までの分解能で 0 ~ 180° までの撮影を行った。その結果、図 2 に示したようにきれいな単結晶からの回折斑点を得ることができた[1]。

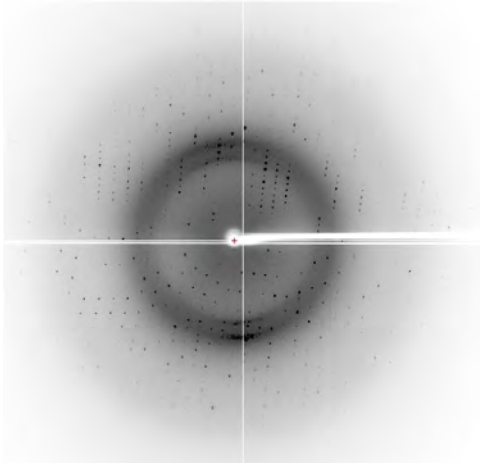

図 2: 波長 1.00 Å の放射光で、1° 振り、1 sec 露光の振動写真。

HKL2000 を使用した予備的な解析により、この結晶が a = 30.49 Å, b = 57.99 Å, c = 67.28 Å の格子定数の斜方晶系結晶であることが判明した。実は、この格子定数は、既に報告されている沈殿剤使用の斜方晶系リゾチーム結晶とほぼ変わらず、コロイド結晶ではない可能性が高い。しかし、既出の結晶では、Na^+もしくは Cl^-イオンを結晶格子内に含むものが多く、脱塩した本研究の結晶では、それらのイオンが存在しえないという点が大きく異なる。

今後、更なる詳細な構造精密化を行い、より詳細な結晶構造の差異の議論を行う予定である。

参考文献

[1] 鈴木良尚，津下英明，沈殿剤フリーのタンパク質結晶化法の開発，日本物理学会 2012 年年会 25aCK-10.

* suzuki@chem.tokushima-u.ac.jp

NW14A/2011G-608

Open-close dynamics of single protein molecule observed by diffracted X-ray tracking synchronized with pulse laser

Kouhei Ichiyanagi[1,2], Hiroshi Sekiguchi[2,3], Shunsuke Nozawa[4], Tokushi Sato[4], Ayana Tomita[4], Manabu Hoshino[4], Shin-ichi Adachi[4], Yuji C. Sasaki[1,2*],
[1]Graduate School of Frontier Sciences, the Univ. Tokyo, Kashiwa 277-8561, Japan
[2]JST-CREST Sasaski team, Kashiwa 277-8561, Japan
[3]JASRI SPring-8, Sayou-cho 679-5198, Japan
[4]Photon Factory, Tsukuba 305-0801, Japan

1 Introduction

Diffracted X-ray Tracking (DXT) measurement technique is a powerful tool to observe *in-situ* intermolecular motions of single protein. Understanding the rotational and tilting motions in channel and membrane protein molecules are a fundamental life scientific quest and basic research need in biological science. Sasaki et al., developed DXT technique using diffraction spot tracking from gold nanocrystals combined with the X-ray synchrotron source [1]. This technique can offer the milli-radian resolution of the rotational and tilting motion. We tracked θ and χ motions of the diffraction spot from gold nanocrystals attached on the cysteine group with the protein using the wide-energy band of X-ray (Fig.1). In reaction process between ATPase and protein, changing some rotation or tilt motions may occur inside protein with changing the conformation. In order to in-situ observing the intermolecular motion change under photo-dissociated ATPase reaction with the channel protein, we developed and constructed the DXT system synchronized with UV/VIS pulse laser at the NW14A beamline, the PF-AR. We demonstrated the open-close motion of group II chaperonine reacted with photo-dissociated ATPase.

2 Experiment

DXT measurement system was synchronized with 355 nm third harmonic generation of a nanosecond Q-switched Nd:YAG laser (Continuum, co. Inc., Powerlite 8000 plus, USA) for photo-dissociation of caged-ATP. The X-ray energy bandwidth and peak position were ΔE/E=15 % and 18 keV. The DXT movie can be measured by the CCD which is coupled with the image intensifier (C4880-10 and V7739P, Hamamatsu photonics, K.K, Japan). We took 90 diffraction images at the 36 ms/frames. The laser pulse was irradiated at the 31 frame.

3 Results and Discussion

A gold nanocrystal was attached on the top of chaperonin protein using Au-S bonding. The gold nanocrystal size was 20-40 nm. Fig.2 shows the mean square displacement of diffraction spot from gold nanocrystals attached on with the group II chaperonin before laser irradiation and after laser irradiation. The open-close motion is mainly associated with the c motion. In this work, the χ motion increased with producing the photo-dissociated ATPase after UV laser pulse irradiation.

We succeeded to observe the open-close dynamics in the group II chaperonin reacted with the ATPase.

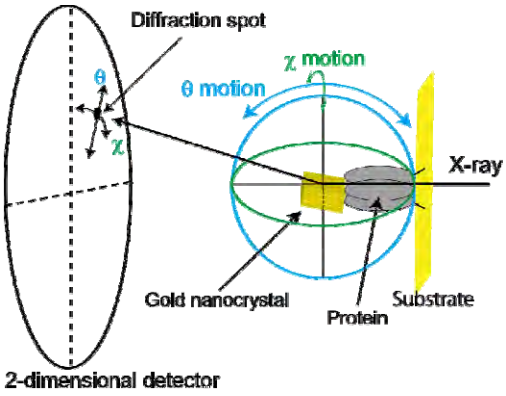

Fig. 1: The principle of diffraction X-ray tracking.

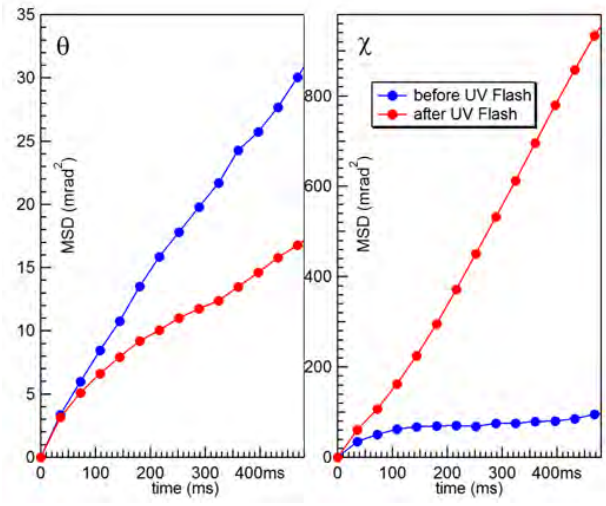

Fig. 2: Mean square displacement of θ and χ motions in the group II chaperonin before laser irradiation (blue line) and after laser irradiation (red line).

Acknowledgement

We thank the beamline staffs for supporting the DXT measurement.

References

[1] Y.C. Sasaki et al., Phys. Rev. Lett, **87**, 248102 (2001).

* ycsasaki@k.u-tokyo.ac.jp

15A/6A, 2011G668

The Sructural Fluctuation of the Calmodulin Evaluated by Small-Angle X-ray Scattering

Yasunobu SUGIMOTO*[1], Takahiko SUGIMOTO[2],Hideki SHISHIDO[3],
Shinsaku MARUTA[3], Katsuzo WAKABAYASHI[2]
[1]Nagoya University Synchrotron Radiation Research Center, Nagoya, Aichi 464-8603, Japan
[2]Graduate School of Engineering Science, Osaka University, Toyonaka, Osaka 560-8531, Japan
[3]Faculty of Engineering, Soka University, Hachioji, Tokyo 192-8577, Japan

Introduction

Proteins are molecular machines which carry out many functions in the biological systems. The structure of the protein is characteristic of its own function, just as artificial machines, while it is influenced by the thermal vibration and random collision of water molecules in the living cell. Under such condition, the structural fluctuation of the protein may have important role for the mechanism of the protein. Small-angle X-ray scattering has been used to measure an averaged structure of the protein in the solution and it is not considered suitable to measure the dynamic properties. We have attempted the detection of the dynamic fluctuation occuring at overall of the molecule using small-angle X-ray scattering measurements and molecular dynamics simulations analysis.

Experiments

Myosin subfragment-1 (S1) of skeletal muscle and engineered calmodulin molecules were prepared for X-ray scattering measurements. The X-ray solution scattering experiments were done at the BL15A1 using the small-angle diffractometer at a camera length of ~2.4 m and ~1.2 m. All X-ray scattering data were collected with an X-ray image intensifier (XRII) and a CCD camera. The two-dimensional X-ray patterns were measured and the intensity data were integrated as a one-dimensional function of the scattering vector length. The protein concentration was varied in the range of 2 to 8 mg/ml. X-ray scattering was measured at the temperatures of 5°, 10°, 20° and 30°C to vary the degree of fluctuation in protein structure.

Results and Discussion

The scattering intensities of calmodulin in the specific angular region exhibited a tendency to change monotonously with an increase in temperature. In the scattering pattern of calmodulin, the intensities around S~0.01 A^{-1} ($S=2\sin\theta/\lambda$) at 20°C was smaller than those at 5°C. The difference between 30°C and 5°C was much distinguished. From the observations, the characteristic nature of structural fluctuations of proteins in solution may be evaluated by the measurements of small-angle X-ray scattering.

The crystal structure of the calmodulin have been solved in both of the calcium present state and absent state. The scattering intensities calculated from these atomic structures were used to explain the scattering profile of the fluctuated structure. The scattering intensities of the calmodulin were calculated in the Ca++-binding state (CaCaM) and absent of the Ca++ state (apoCaM). The scattering intensity of fluctuated structure was evaluated to change the ratio of these intensities and add them. The small intensity change were derived when the ratio of CaCaM and apoCaM was altered. This intensity change was very similar to the temperature dependent experimental results, such as the intensity difference were observed in the range of S < 0.02.

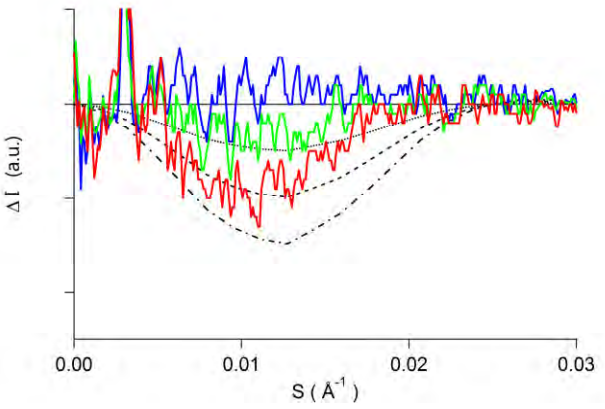

Figure 1. The intensity differences of the calmodlin scattering profile at various temperatures. The differences were calculated from the profile at 5°C. The calculated intensity differences from the two structures were also shown by the dotted line.

* y.sugimoto@nusr.nagoya-u.ac.jp

2011G-674, BL26B1/2011A-1882

好冷化変異体ウリカーゼの予備的 X 線結晶構造解析
Preliminary X-ray Crystallization of Psychrophilic Mutant of Uricase

日 幷隆雄[1*]，伊藤貴文[1]，西矢芳昭[2]
[1]福井県立大学生物資源学部、〒910-1195 福井県吉田郡永平寺町松岡兼定島 4-1-1
[2]摂南大学理工学部　〒572-8508 大阪府寝屋川市池田中町 17-8

1 はじめに

好冷性酵素は、一般に 15-20℃以下の温度領域で高い活性を示す酵素を指し、様々な分野での産業応用が期待される[1]。一般に、好冷性生物由来の酵素は不安定であり、これまで遺伝子工学的な手法による好冷性酵素の熱安定性化[2]や耐熱性酵素の低温適応化が検討されたが、50℃以上での高い熱安定性を持ち、且つ 20℃以下で十分高い活性を示す変異体酵素は得られていなかった。活性化エンタルピーが小さいという好冷性酵素の特徴は、遷移状態の安定化に寄与するタンパク質構造の柔軟性の増大としてしばしば説明され、それ故熱安定性が犠牲にされると解釈されてきた[3]が、耐熱性酵素と好冷性酵素の構造上の違いについて決定的な要素は未だ知られていない。また、酵素の不安定性と低温活性の間で厳密な直線的関係は成立せず[4]、高い安定性と低温活性の両立が可能かどうかは未解決であった。

我々は、*Bacillus* sp.由来尿酸酸化酵素(bUOD)のインターフェースループ II（277-300）に着目し、その結晶構造に基づいてアミノ酸２残基を選択的に改変することで、至適温度 45℃の野性型酵素に対して至適温度が 30℃に大きく低下した変異体酵素 W279L+P287G を得た[5]。本変異体は、野性型酵素と同様 65℃近傍まで熱安定性を保つことも CD 測定などから示された。その好冷化の分子基盤を明らかにするため、X 線結晶構造解析に取り組んでいる。今回は予備的測定の結果について報告する。

2 実験

結晶化は、ハンギングドロップ蒸気拡散法を用い、20℃で行った。リザーバーの初期溶液組成は、15%(w/v) PEG8000, 0.1 M Tris-HCl pH 8.0, 1 mM 9-methyluric acid, 0.04 M Na_2SO_4 とした。

X 線回折強度測定は SPring-8 ビームライン BL26B1 で行った。結晶は、10% PEG400 をリザーバー液に添加したクライオ溶液に浸した後、100K 窒素ガス雰囲気下で凍結させて測定に供した。

3 結果および考察

得られた 2.6Å分解能回折強度データセットの統計値を表 1 に示した。野性型酵素の構造(1j2g)を用いた分子置換法により初期位相を求めた。精密化は ccp4 を用い、精密化の結果 R = 0.19 R_{free} = 0.25 の構造モデルを得た。本モデルは野性型酵素と比較した場合、主鎖間の RMSD は 0.48 Åであり（図１）、顕著な構造変化はインターフェースループ II 間にのみ認められた。さらに高分解能データを得るため、結晶化温度など諸条件の検討を続行している。

表 1 ：回折強度データ収集の統計値

Space group	$P2_12_12$
Dimensions [Å]	a = 132.34, b = 142.24, c = 70.56
Resolution	2.6 Å
Total No. of reflections	202,023
No. of unique reflections	41,095
Completeness [%]	97.9 (98.9)
R_{merge}	0.104 (0.377)
$\langle I/\sigma \rangle$	17.3 (3.7)

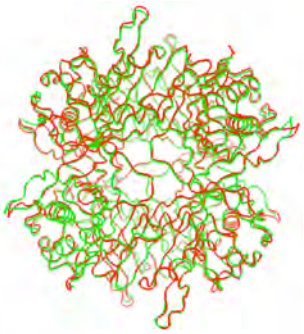

図１ ： W297L+P287G 変異体(緑)と野性型 (赤) との立体構造比較（主鎖 Cα原子リボンモデルの重ね合わせ）

謝辞

今回の測定の機会をご提供していただいた SPring8/JASRI スタッフの皆様に厚く御礼を申し上げます。また、震災による復旧作業で忙しいに関わらず、尽力していただいた PF スタッフにも心より感謝申し上げます。

参考文献

[1] Fller & Gerday (2003) *Nature Reviews*, **1**, 200-8; Yamagishi (2006) *Netsu Sokutei*, **33**, 2-9
[2] D'Amico *et al.* (2001) *J. Biol. Chem.*, **276**, 25791-6.
[3] D'Amico *et al.* (2003) *J. Biol. Chem.*, **278**, 7891-6; Cavicchioli *et al.* (2006) *Methods Microbiol.*, **35**, 395-436.
[4] Wintrode *et al.* (2000) *J. Biol. Chem.*, **275**, 31635-40.
[5] Nishiya & Hibi (2010) 日本農芸化学会大会講演要旨集, 167.

* hibi@fpu.ac.jp

BL17A, 5A/2011P005
BL38B1/2011A2031

ウイルススーパーファミリー１ヘリカーゼの結晶構造解析
Crystal Structure of the Superfamily 1 Helicase from *Tomato Mosaic Virus*

加藤悦子[1], 松村浩由[2]
[1](独)農業生物資源研究所、〒305-8602 つくば市観音台 2-1-2
[2]阪大・工・応用化学、〒565-0871　大阪府吹田市山田丘 2-1

1 はじめに

プラス鎖 RNA ウイルスに属するやトマトモザイクウイルス（ToMV）などは、一般に真核生物を宿主とするプラス鎖 RNA ウイルスが宿主細胞に進入し、脱外被を経てゲノム RNA が翻訳され、複製を司る複製タンパク質が合成される。複製タンパク質は複製鋳型となる自身のゲノム RNA を生体膜上にリクルートし、宿主因子と共に複製複合体を形成し、マイナス鎖 RNA を経てプラス鎖 RNA を複製する。ToMV のヘリカーゼドメインが複製に必要な宿主因子（低分子量 GTPase タンパク質 ARL8 や膜タンパク質 TOM1 など）との相互作用に重要であることが明らかになった。ToMV のヘリカーゼドメインは、アミノ酸配列から見出されたヘリカーゼモチーフの特徴からスーパーファミリー(SF)1 ヘリカーゼに属することが予想されたが、立体構造は解明されていなかった。本研究では ToMV のヘリカーゼドメインの立体構造を決定した。

2 実験

ヘリカーゼドメインと予測される領域を含む安定なタンパク質ドメイン(S666-Q1116：ToMV-Hel)を実験的に決定し、そのタンパク質の精製条件を決定した[1]。得られた ToMV-Hel について、沈殿化剤：0.1 M Sodium phosphate, pH6.5, 1.7 M ammonium sulfate を用いたハンギングドロップ法により 12℃で結晶化を行った[2]。位相決定は、SeMet 化 ToMV-Hel タンパク質を用いて SAD 法により行った。データ処理および構造の精密化は定法により行った。

3 結果および考察

ToMV-Hel は典型的な Rec-A 様α/βドメイン（ドメイン 1A および 2A からなるヘリカーゼコアドメイン(V802-Q1116)の他に、ToMV-Hel 特異的な N 末ドメイン (S666-V801) を持っていることが明らかになった（図）。3 個の硫酸イオンが 1A と 2A のドメインの間に存在する溝に位置していた。

ヘリカーゼドメインは、その立体構造や特徴的なモチーフの存在から SF1 から 6 に分類される。得られた構造について、類似の立体構造を DALLI server を用いて検索した結果、SF1 に属するタンパク質と相同性があることが分かった。SF1 ヘリカーゼは、立体構造に基づき、UvrD/Rep, Pif1-like, Upf1-like の 3 種類のグループに分類されている。これらは、ヘリカーゼドメインの各ドメイン中にアクセサリードメインと呼ばれる付加的なドメインを持つことを特徴として分類されている。

今回立体構造を決定した ToMV-Hel は、これら SF1 のタンパク質とは異なり、ヘリカーゼドメインの中にはアクセサリードメインをもたず、他のヘリカーゼタンパク質には見られない付加的な N 末ドメインをもっていた。これらのことから、ToMV-Hel はヘリカーゼ SF1 に属する新規なタンパク質ドメインを形成していることが分かった[3]。

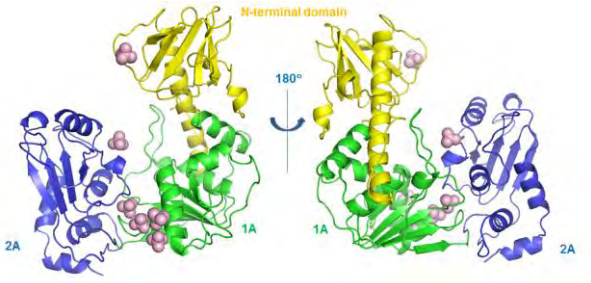

図：ToMV-Hel の立体構造
ヘリカーゼコアドメインを緑(1A)と青(2A)で、N 末ドメインを黄色で示した。

4 まとめ

ウイルスがコードする SF1 ヘリカーゼの構造を世界で初めて決定した。その構造はヘリカーゼコア構造と特徴的な N 末ドメインから構成されていた。今後、このドメインと相互作用する宿主因子およびそれらとの複合体について構造解析を目指したい。

謝辞

本研究は生研センター「新技術・新聞や創出のための基礎研究推進事業」により行われました。また、本研究は PF および Spring8 のスタッフの方々にサポートしていただきました。ここに感謝致します。

参考文献

[1] H. Xiang H. *et al.*, *Protein Expr Purif* **81** (2012) 89-95.
[2] H. Xiang H. *et al.*, *Acta Crystallogr Sect F Struct Biol Cryst Commun* **67**(Pt 12) (2011) 1649-52.
[3] M. Nishikiori *et al.*, *J. Virol.* **86** (2012) 7565-76.

* ekatoh@nias.affrc.go.jp

NW12, NE3, 5A/2012G019

Mechanism of diterpene cyclization in cyclooctatine biosynthesis

Takeo TOMITA, Ayuko Meguro, Seung-Young KIM, Taro OZAKI, Makoto NISHIYAMA, and Tomohisa KUZUYAMA*
Biotechnology Research Center, The University of Tokyo, Tokyo 113-8657, Japan

Introduction

Cyclooctatin is a potent inhibitor of lysophospholipase, which catalyzes the hydrolysis of the fatty acid ester bonds of lysophospholipids. This inhibitor was isolated from the broth of *Streptomyces melanosporofaciens* MI614-43F2 while screening for lead compounds for the development of anti-inflammatory drugs targeting lysophospholipase.

Cyclooctatin has a unique tricyclic diterpene skeleton characterized by a 5-8-5 fused ring system (Fig. 1A). In the biosynthesis of cyclooctatin, the biosynthetic gene product CotB1 synthesizes geranylgeranyl diphosphate (GGDP) from isopentenyl diphosphate and dimethylallyl diphosphate, and then CotB2 catalyzes the stereospecific cyclization of GGDP to give cycloocta-9-en-7-ol (Fig. 1B). Next, the cytochrome P450 enzymes, CotB3 and CotB4, catalyze the stereospecific hydroxylation to yield the final product, cyclooctatin. Although cyclization is a key reaction in cyclooctatin biosynthesis, mechanism of formation of stereo- and regio specific ring is uncleared since no 3D-structural information has been available to date. To clarify the cyclization mechanism of CotB2, we determined the crystal structure of apo-form of CotB, and the complex with a substarte analog, geranylgeranylthiodipho sphate (GGSPP).

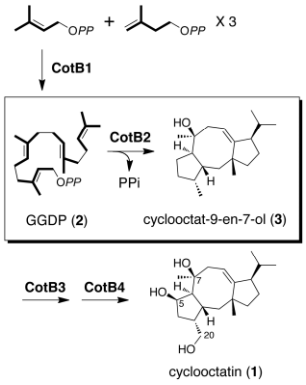

Fig. 1 Biosynthetic pathway of cyclooctatin

Materials and Methods

Crystallization - Crystal of apo CotB2 (apo type II) was obtained by the hanging-drop vapor-diffusion method. The reservoir solution contained 0.1 M HEPES-NaOH (pH7.0-8.5) and 2.2 M ammonium formate. Crystal of CotB2 complexed with GGSPP/Mg^{2+} (GGSPP/Mg^{2+} type I) is obtained with reservoir solution which contains 20 % PEG6000, 100 mM Bicine-NaOH (pH9.0), 5 mM $MgSO_4$, and 1 mM GGSPP.

Data collection and processing –The X-ray diffraction data were collected using the beamline NW-12, 5A at PF. The image sets were integrated and scaled using HKL2000.

Results and Discussion

Active site structure - The crystal structure of apo form of CotB2 was determined at 1.8 Å resolution by means of MR method with the model of apo form with 2.4 Å resolution as a search model. Apo CotB2 is composed of a terpene cyclase fold (Gly9-Asn292), forming 13 α-helices. The electron density of N-terminal and C-terminal residues of CotB2 (Met1-Ala8 and Lys293-Gln307) was not observed, indicating that this region is disordered in the crystal. In apo form, DDMD motif and NSE/DTE motif conserved among terpene cyclase family are located at the putative active site. In the GGSPP/Mg^{2+} form, GGSPP is bound at the pocket of the enzyme with a unique S-shaped conformation (Fig. 2B). Mg^{2+} ion was also bound near disphosphate group of GGSPP. Asn220, Ser224, and Glu228 from NSE/DTE motif binds with Mg^{2+}. The diphosphate group of GGSPP was recognized by Arg117 and bound with Mg^{2+}. Asp111 from DDMD motif forms Arg294 from 'basic motif' to close the active site. Newly defined Tyr295 forms diphosphate group of GGSPP. C20 carbon chain was surrounded by many aromatic and hydrophobic residues and several Asn residues. To elucidate the reaction mechanism, the mutational analysis of the residues which form active site is now on going.

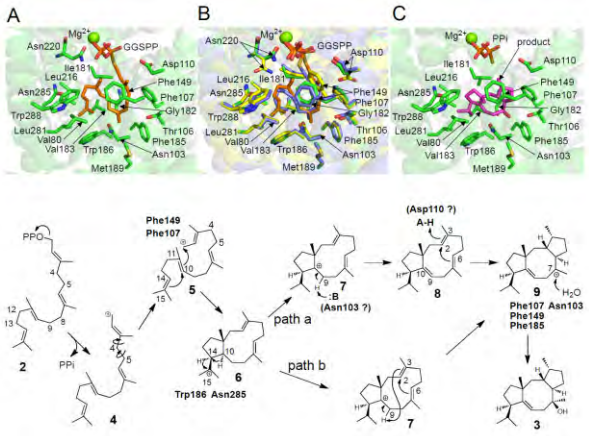

Fig. 2 Active site structures of CotB2. Apo form (A), GGSPP/Mg^{2+} bound form (B), and the model docked with the product (C). Proposed reaction mechanism (D).

1) T. Tomita *et al. in preparation*.

* utkuz@mail.ecc.u-tokyo.ac.jp

14C/2009P104

Examination of The specific spatial frequency of An analog image system for Diagnosis by Monochromatic X-ray

Chisato Kimura[1], Shinya Yoshino[1], Kazuyuki Hyodo[2]
[1]Teikyo University, Kaga, Itabashi-ku, Tokyo 173-8605, Japan
[2]KEK-PF, Tsukuba, Ibaraki 305-0801,Japan

1 Introduction

The degree of sharpness of an analog image system for diagnosis is estimated by the result of MTF measurement of a physical estimation of image quality method.

At the clinical spot, although the image is created based on the evaluation result of MTF, it was presupposed that the evaluation result of a visual evaluation (ROC analysis) was also important, and eventually the optimal picture for diagnosis is decided from both sides of a physical image evaluation method and a visual evaluation.

Spatial frequency which sharpness degree evaluation usually united with the resolution of man's eye since a MTF value changed with spatial frequency: It is carrying out by 2.0 Lp/mm.

This spatial frequency (2.0Lp/mm) is called "Specific spatial Frequency", and let it be a valuation basis in MTF of an analog image system for diagnosis.

This examination, it inquired for the purpose of setting up specific spatial frequency with spatial frequency higher than 2.0 Lp/mm in monochromatic X-ray from the MTF measurement result of the monochromatic X-ray of an analog image system reported at "28th PF symposium".

2 Equipment

i station : BL-14C
ii intensifying screen : HR-4 (FUJI FILM)
iii X-rays film : SuperHR-30s (FUJI FILM)
iv square wave chart
material : Pb
thickness : 0.05 mm
spatial frequency : 0.0,0.5,1.0,1.5,2.0,2.5,3.0, 4.0,5.0,6.0,8.0,10.0 Lp/mm
(Type1,KASEI OPTONIX)
v densitometer
diffusion : 301RS (FUJI FILM)
specular(microdensitometer) : PDM-7 (KONICA MINOLTA)

3 Method

i X-rays energy : 33 keV
ii distance : 110 cm
iii field : 40 mm × 40 mm
iv exposure
The quarter cassette was divided into two and the exposure time (10sec) from which spatial frequency :0.0Lp/mm (with no Pb) diffusedensity becomes about 1.50 was set up.
Two images were created in the X-ray film of one sheet.
By the same exposure time (10sec), two images were created also about spatial frequency:3.0, 4.0, 5.0,6.0,8.0,10.0 Lp/mm.
v density measurement
Density measurement was performed using the microdensitometer.
aperture width : 10 μ m
aperture height :100 μ m
stage movement speed : 0.05mm/sec
vi display
horizontal : spatial frequency
vertical : density
0.0Lp/mm : Fig.2a, 3.0～10.0Lp/mm : Fig.2b
vii calculation
The square wave MTF was computed from contrast (spatial frequency:0.0 Lp/mm standard).
The sine wave MTF (sine wave response function) was computed by having used the Coltman's correction formula for the square wave MTF.
viii display
horizontal : spatial frequency
vertical : MTF
ix visual evaluation of the square wave chart image
Observation distance (film～eyeball) : It was referred to as 30cm and the square wave chart image was observed.
x A setup of the specific spatial frequency
MTF value : The spatial frequency in the range of 0.600～0.400 was read from on the graph.

4 Result and Discussion

i The MTF value,monochromatic X-ray,it was set to 1.000～0.081and diagnostic X-ray:1.000～0.059, and fell from near spatial frequency:6.0Lp/mm (Table.1, Fig.1).
ii The specific spatial frequency, It was admitted that the MTF value in 2.0 Lp/mm became about 0.5 through about 0.6 (point estimate) and the diagnostic X-ray, and that of the direction of monochromatic X-ray was high through monochromatic X-ray.
iii In visual evaluation, it was judged that spatial frequency:3.0Lp/mm of a square wave chart image (Fig.3) could be decomposed (discernment).
iv In the specific spatial frequency in the diagnostic X-ray, if the spatial frequency in monochromatic X-ray is read in on a graph (Fig.1) in the MTF

value:0.600 ～ 0.400 based on the MTF value becoming about 0.5, it will be set to 2.5～3.5 Lp/mm.

v The spatial frequency : 2.5～3.5 Lp/mm resolution was set to about 0.20～0.14 mm by the following resolution formulas.

resolution : R mm

chart line width : d (2.5～3.5 Lp/mm)

$$R = \frac{1}{2d} \quad (\text{mm})$$

Spatial Frequency (Lp/mm)	Diagnostic X-ray MTF	Monochromatic X-ray MTF
0.0	1.000	1.000
0.5	0.906	
1.0	0.779	
1.5	0.656	
2.0	0.546	
2.5	0.452	
3.0	0.373	0.498
4.0	0.262	0.345
5.0	0.191	0.245
6.0	0.144	0.148
8.0	0.083	0.091
10.0	0.059	0.081

Table.1 MTF value

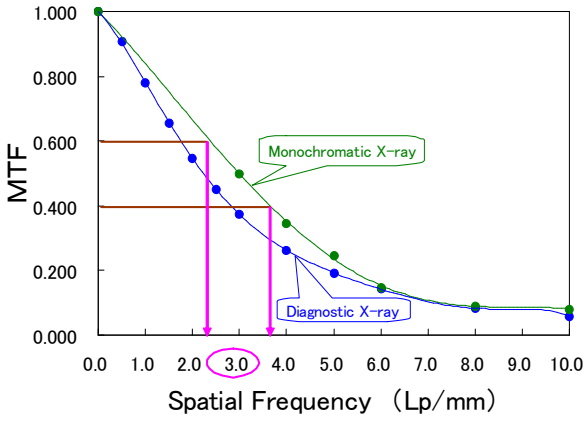

Fig.1 Graph of MTF

Fig.2a
Image of Square Wave Chart
Spatial Frequency：0.0Lp/mm

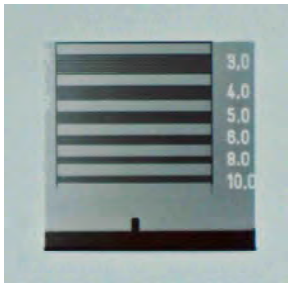

Fig.2b
Image of Square Wave Chart
Spatial Frequency：3.0～10.0Lp/mm

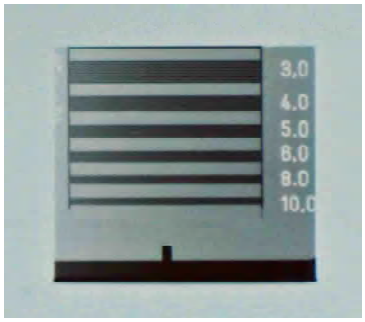

Fig.3
Image of Square Wave Chart
Spatial Frequency：3.0～10.0Lp/mm

5 Conclusion

Since the calculation result of resolution is a value lower than the resolution (0.2～0.3 mm) of an eye, the resolution of monochromatic X-ray can be said to be high compared with the resolution of an eye.

And, I think that the specific spatial frequency in monochromatic X-ray can be set as 3.0 Lp/ mm about.

Acknowledgement

In conducting this experiment, an understanding of you, the professors and the personnel of PF, is obtained and I express gratitude deeply.

Reference

T. Kozuka and K.Inamura, Textbook of Clinico-Radiological Technology 12 (2010) .

kchisa@med.teikyo-u.ac.jp

747-8F1A/2012S1-001

人工股関節周囲組織及び関節液に含まれる Co の XAFS 分析
XAFS analysis of Co contained in the surrounding tissues and synovial fluid of the artificial hip joint

宇尾基弘 [1*]
[1] 東京医科歯科大学　〒113-8549 文京区湯島 1-5-45

1 はじめに

コバルトークロム合金やチタン合金は人工股関節用の素材として幅広く利用されている。人工股関節は金属製の大腿骨側のステムと骨頭および骨盤側のカップから成っており、近年多く用いられている Metal on metal 型の人工関節では鏡面研磨したコバルトークロム合金の骨頭／カップの擦動により、高い耐久性と広い可動域を実現している。しかしながら微量の成分金属元素の溶出や摩耗粉の発生も懸念されている。特にコバルトは金属アレルギーの原因元素としても知られており、溶出による生体への影響が懸念される。本研究では人工股関節周囲の関節液や関節包に含まれる Co および Ti の状態を蛍光 XAFS 法により分析し、摩耗粉の発生状態や溶出可能性について検討を行った。

2 実験

試料は？？？？が疑われた患者より検査のため採取された関節液および人工股関節置換術を行った患者より切除された関節包組織を用いた。人工股関節はいずれも metal-on-metal 型で骨頭およびカップはコバルトークロム合金製であった。関節液は遠心分離し、沈殿物と上澄をそれぞれ測定に供した。関節包は薄切・乾燥後に蛍光 XAFS 測定は BL-9A において 19 素子 SSD を用いて行った。

3 結果および考察

図 1 に関節液の上澄および沈殿物（固形物）の Co K-edge XANES スペクトルを示す。沈殿物中には比較的高濃度に Co が存在しており、その状態は塩化コバルトなどに近いことから、この Co は摩耗粉などではなく、溶解して水和イオン状態になったものと考えられる。上澄中にも微量の同様の Co が検出された。沈殿物中に Co が多いのはタンパクや細胞成分などに Co イオンが吸着され、沈殿したものと推測された。他方の合金成分である Cr については検出されなかった。チタンについては沈殿物中に微量検出され、rutile(TiO_2)に近い状態と判断された。当該人工股関節ではチタン合金製のステム（大腿骨への固定部）が用いられており、それに由来するものと推測された。

また人工股関節置換が必要になった症例では関節包内面に黒色の沈着物が認められ、XANES 測定より、同沈着物が金属状態であり、Co-Cr 合金の摩耗粉であることが推測された。[1]

4 まとめ

以上より、人工股関節に多く用いられるコバルトークロム合金から、コバルトが関節液に溶出する可能性が示唆され、生体適合性の観点から更なる検討が必要と考えられた。

参考文献

[1] Uo M., Watari F., Asakura K., Katayama N., Onodera S., Tohyama H., Hamada K., Ohnuki S., Nano Biomedicine **1** (2009) 133.

Uo.abm@tmd.ac.jp

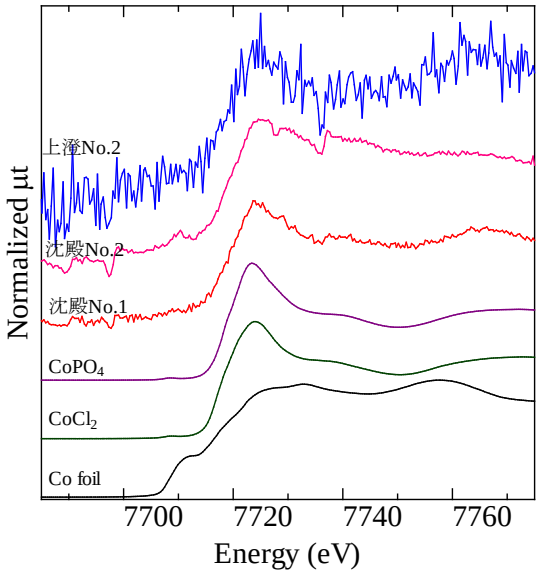

図 1　人工股関節関節液の Co K-edge XANES スペクトル

NE5A/2010G055

PRELIMINARY EXPERIMENTAL RESULTS WITH TRANSMISSION CT IMAGING SYSTEM FOR FLUORESCENT X-RAY CT

Tohoru TAKEDA[1], Hideaki KUROSAWA[2], Takafumi SATO[2], THET THET LWIN[1], Ryota SHIRAI[1], Takuya KUNII[1], Tetsuya YUASA [2], Kazuyuki HYODO[3]

[1]Kitasato University, Sagamihara, Kanagawa, Japan
[2]Yamagata University, Yonezawa, Yamagata, Japan
[3]High Energy Acceleration Research Organization, Tsukuba, Japan

1 Introduction

The fluorescent X-ray computed tomography (FXCT) has been developed to depict the cross sectional distribution of very low concentration of non-radioactive specific elements such as iodine, gadolinium, or aurum inside the biomedical objects for novel molecular imaging technique [1-5].

To image small animal, definition of imaging position is very important at in-vivo study because the pharmacological distribution of drug is changes rapidly. So the slice positioning of transmission CT images (TCT) can depict detailed morphological information which could not obtain from FXCT. In addition, to obtain the quantitative information with respect to specific element from FXCT image, TCT image are also applied. Attenuation correction of FXCT image is based on the distributions of linear attenuation coefficients which obtained from TCT images.

Here, we develop the TCT imaging system and to perform the reconstructed image of phantom to prove the efficiency of this imaging system.

2 Method and Material

We constructed the imaging system at the BL-NE 7A bending-magnet beam line (6.5GeV), KEK in Japan. The whit X-ray beam was monochromatized using monochromator Si (220) from 32 to 51 keV. The phantom flux rate in front of the object was approximately 9.3×10^7photons/s for a beam current of 40 mA. FXCT system consists of a Si double crystal monochromator, an X-ray slit system, a scanning table, fluorescent X-ray detector and CCD camera for TCT.

To confirm the efficiency, we performed an imaging experiment using physical phantom by using newly developed X-ray CCD camera (2 dimensional type). The projections are collected by rotating the object over 180 degree.

The phantom was a 10 mm in diameter acrylic cylinder containing 3mm paraxial channel filled with iodine (2.5 mg/ml, 5 mg/ml) and Gadolinium (5mg/ml, 10mg/ml). Exposure time for each data point was 150 msec. To examine the detection efficiency, monochromatic X-ray energy was changed from 32 to 51 keV. The K-edge energy of iodine and gadolinium are 33.2 keV and 50.2 keV, respectively.

3 Results and Discussion

Fig 1 showed the reconstructed image of the phantom obtained by this X-ray CCD camera. Four circles corresponding to the regions including the iodine and Gadolinium solution are successfully delineated at 37 keV X-ray energy. These CT image was obtained three dimensionally, and energy subtraction of each elements is also possible. These CT image was obtained within 1 min, so the positioning of object is also suitable.

Thus the new TCT imaging system will be useful for two-dimensional FSCT experiment.

Acknowledgement

This research was supported by a Special Coordination Funds from the Ministry of Education, Culture, Sports, Science and Technology, and was performed under proposal number (B) 21390339 approved by the High Energy Accelerator Research Organization.

References

[1]. Takeda T *et al*., Proc.SPIE **2708** (1996) 685.
[2]. Yuasa T *et al*., IEEE Trans.Nucl.Sci. **44 (**1997) 54.
[3]. Takeda T *et al*., Nucl.Instr.Meth. **467 (**2001) 1318.
[4]. Yu Q *et al*., J. Synchrotron Rad. **8** (2001) 1030.
[5]. Takeda T *et al*., Nucl. Instr. Meth. **A548 (**2005) 38.

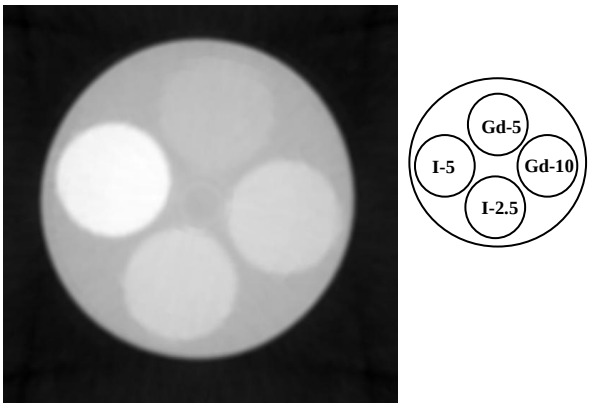

Fig 1. FXCT image of a 10 mm in diameter phantom with 4 holes. The 5 mg/ml iodine solution, 2.5 mg/ml iodine solution, 10 mg/Gd solution, 5 mg/Gd solution, projection time 150 msec, I= iodine, Gd= Gadolinium

14B/2010G140

X線屈折コントラスト法における密度分解能の定量的評価の研究

Quantitative investigation on density resolution in X-ray DEI

岡本博之[1*]，水野 薫[2]，森 浩一[3]

[1]金沢大学医薬保健研究域 〒920-0942 金沢市小立野 5-11-80
[2]島根大学総合理工学部 〒690-8504 松江市西川津町 1060
[3]茨木県立医療大学 〒300-0394 茨城県稲敷郡阿見町大字阿見 4669-2

1 はじめに

近年X線により物体を観察する方法として、位相変化を利用する方法が精力的に研究されている。物質のX線屈折率は1に近く、従来の装置では位相変化を観察することは困難であったが、放射光X線の利用と光学技術の進歩により、ようやく可能となった。この手法は、X 線の位相変化をコントラストの変化として検出する手法で、軽元素からなる吸収が少ない物質でも、位相変化は検出しやすいことから、たとえば軟組織等の観察用として医学診断への応用、軽金属についての物性測定への応用などが試みられている[1,2,3]。医療応用という立場からは、分解能の定量評価は患者の経年変化を追い、装置の性能を一定の水準に保つなどの目的から必須の項目と考えられている。このことから、医療応用を目指している屈折コントラスト法でも、分解能の定量評価は大変重要であると考える。しかし、現時点で分解能に関しての定量評価方法が確立されているとは言いがたい。そこで本研究は、定量的な測定が行いやすい、アナライザ結晶を用いるX線屈折コントラスト法について、コントラストに関する分解能を定量的に評価する方法を開発し、さらには将来の医学診断への応用につなげることを目的としている[4]。

2 実験

X線屈折コントラスト法とは、試料によるX線の屈折をアナライザ結晶のロッキングカーブを利用し、屈折角に応じたコントラストに変換する手法である。図1に示したような、くさび状物体を考えた時、X線透過方向への試料の屈折率の積分値を N とするならば、N をX線透過方向と垂直な方向（図1の x 方向）へ微分した値 $\mathrm{d}N/\mathrm{d}x$ により屈折角が決まる。これを仮に「密度変化」と呼ぶ。この、くさびが均質な材質で出来ているならば、N は屈折率と厚さの積であるので、X線透過方向への厚さの変化により屈折角 $\Delta\theta$ が決まる。つまり、くさびの傾斜角 α を使って表すならば、(1)式のような関係が得られる。ここで、屈折率を n=1-δ とした。

$$\frac{dN(x)}{dx} = \delta \tan\alpha = \Delta\theta(x) \qquad (1)$$

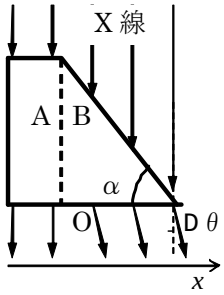

図1：くさび型の物体

このことを考慮し、我々は図2のような評価用試料（ファントム）を作製した。ファントムはX線入射方向に対して傾斜の無い A 部分と、端からの距離 h とともに傾斜角 α が変化する B 部分からなる。

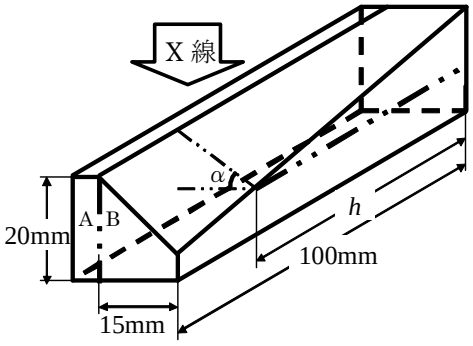

図2：作製したファントムの形状

まず、A 部分を透過したX線は、厚さが均一であるので屈折しない。一方、B 部分を透過したX線は、傾斜角 α に応じて屈折する。このファントムを透過したX線にアナライザを適用すると、A 部分と B 部分の境界で、屈折によるコントラストを生じるはずである。ここで、AB 境界部では A 部分と B 部分の厚みは等しいので、吸収によるコントラストの影響を除くことが出来る。また、α が小さいほど屈折による AB 間のコントラストは小さくなるので、判別不可能となる最小の α の値、つまり h の値を求めることにより、密度変化に関する分解能を得ることが可能と考える。この分解能は別な表現をすると、どれくらいの屈折角 $\Delta\theta$ まで、アナライザによりコントラストを付けて観察することが出来るかを表し

ている、とも言える。ここで、ファントムの形状から分解能と h の関係は(2)式のように表せる。

$$\Delta\theta(h) = \frac{\delta}{100}h \qquad (2)$$

我々はこのファントムをアクリル、アルミニウム、テフロン、ポリプロピレンの 4 種類の材質で作製し測定を行った。実験は KEK-PF の BL-14B を用いて行った。その際の、実験配置の概略を、図３に示す。

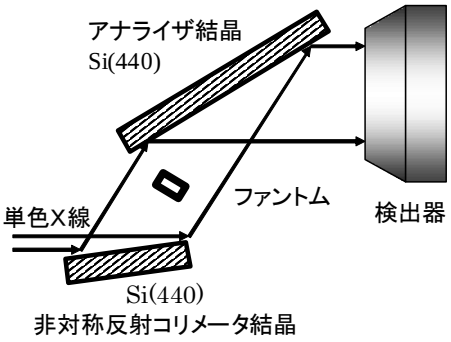

図３：実験に用いた光学系

モノクロメータによって単色化した31keVのX線を、表面が(440)面に対して10°傾いているSi結晶のコリメータにより非対称反射させ、ビーム幅を水平方向に約9倍広げ、スリットで10×10mm^{2}に成形した。コリメータからのX線はファントムを透過し、わずかに屈折を起こす。この屈折角の変化をアナライザで強度変化に変換しCCDカメラに記録した。このとき、アナライザはロッキングカーブのピーク値の半値になる角度に調整した。

3 結果および考察

図４は、アクリル製ファントムについて、h=0～45mmの間を撮影して得られた像である。黒矢印がファントムA部分とB部分の境界である。同様の撮影を他の材質についても行った。

図４：アクリルファントムの撮影結果

それぞれの結果について、h方向への強度分布曲線を作製し、AB間のコントラストが判別できる限界のhの値をもとめた。そして、(2)式を用いて分解能の計算を行った。なお、各材質についての δ はhの大きな領域で計測したコントラストから、ロッキングカーブを利用し屈折角$\Delta\theta$をもとめ、(1)式を用いて算出した。得られた結果を表１に示す。

表１：得られた分解能

材質	限界 h (mm)	分解能
ポリプロピレン	7.3	1.6×10^{-8}
アクリル	6.3	1.7×10^{-8}
テフロン	4.5	2.0×10^{-8}
アルミニウム	5.0	5.5×10^{-8}

まず、アクリル、ポリプロピレン、テフロン製のファントムを用いて得られた密度変化分解能は、ほぼ同じ値を示しており、結果に再現性がみられた。このことから、作製したファントムは分解能を正しく評価していると考えられる。しかし、アルミニウムで作製したファントムについては、他とは異なる値を示した。これはアルミニウムのX線に対する吸収係数が大きいため、X線がファントムに吸収され減衰したことが影響したと考えられる。本実験で使用したX線のエネルギーは31keVであるが、ビーム中にはモノクロメータで単色化する際に、わずかながら高調波である62keVのエネルギーのX線も含まれる。このことから、X線がファントムを通過する際、X線のエネルギー成分のうち、62keVの成分がより透過したため、コントラストが判別できるhが大きくなった、つまり分解能が低下したと考える。

さらに今回の実験において、各種材料により分解能の評価を行ったが、ポリプロピレンとテフロンでは密度が倍以上も異なるにも関わらず、読み取りの限界値は大きく異なっていない。今回作製したファントムでは、傾斜角 α が大きい位置での加工精度が高い。すなわち、読み取り限界のhは、より大きな位置である方が望ましいため、ファントムの材質の屈折率を、より１に近い物質で作製する必要が有ると考える。

謝辞

ファントムの作製にご協力いただきました、金沢大学技術支援センターの久保栄氏、松井大樹氏に深く感謝いたします。

参考文献

[1] J. Davis, D. Gao, TE. Gureyev, et al. : Nature, **373** (1995) 595.
[2] 安藤正海，杉山弘: 応用物理 **74**(4) (2005) 0446.
[3] K. Mizuno, Y. Furuya, K. Hirano, and H. Okamoto, phys. stat. sol. (a) **204**(2007) 2734.
[4] E. Foester, K. Goetz and P. Zaumseil, Krist. Tech. **15** (1989) 937.

NE7A, BL14C/2010G684

Visualization of renal collecting duct using synchrotron radiation micro-angiography with highly sensitive receiver

Shonosuke Matsushita[1,*], Kazuyuki Hyodo[2], Chiho Tokunaga[3], Hiroaki Sakamoto[3], Shizu Aikawa[3], Yoshiharu Enomoto[3], Fujio Sato[1], Shinya Kanemoto[3], Mio Noma[3], Yuji Hiramatsu[3], Yuzuru Sakakibara[3]

[1]Department of Health Science, Tsukuba University of Technology, Tsukuba 305-8521, Japan
[2]Photon Factory, Tsukuba 305-0801, Japan
[3]Department of Cardiovascular Surgery, Graduate School of Comprehensive Human Science, University of Tsukuba, Tsukuba 305-8575, Japan

1 Introduction

The kidneys are organs that serve several essential regulatory roles including urinary system and homeostatic functions such as the regulation of electrolytes, maintenance of acid-base balance, and regulation of blood pressure. Drip infusion pyelography is used to visualize the passage of contrast material to urinary system. However, in this system, renal pelvis is the first identified intrarenal structure, and collecting duct is not seen due to limitation of spatial and density resolution of conventional X-ray system. Since we have developed highly sensitive synchrotron radiation micro-angiography [1], we tried to visualize intrarenal duct using transvenous infusion of contrast material.

2 Experiment

Synchrotron radiation micro-angiography was performed at Photon Factory (PF and PF-AR) in KEK. Synchrotron radiation was obtained from a 6.5-GeV electron beam in PF-AR and 2.5-GeV in PF. Synchrotron radiation was converted to monochromatic x-rays by reflection on a silicon crystal. The energy of the monochromatic x-rays was 33.3 keV. After passing the subject, the x-rays were converted to visible light on a fluorescent screen made of cesium iodide. Receiver was used a highly sensitive HARP tube, which had been developed by Japan Broadcasting Corporation Science and Technical Research Laboratory [2]. It revealed at least 5 times sensitive in density resolution than conventional CCD angiographic system previously [1]. Contrast material (32% non-ionic iodine contained) was infused from right jugular vein of male Wistar rat at a rate of 1 ml/sec in 2 seconds. Several minutes later, the continuous images of kidney were captured with our system.

3 Results and Discussion

Whole shape of single kidney was imaged with many collecting ducts toward renal pelvis (Fig. 1) at PF-AR. In images at PF, enlarged shape of collecting duct was visualized (Fig. 2). In movie format, movement of contrast material in collecting duct was observed. Since contrast material is largely diluted in urine at level of collecting duct, it seems that the image of contrast material in collecting duct cannot be visualized without the use of highly sensitive receiver like HARP tube equipped with synchrotron radiation.

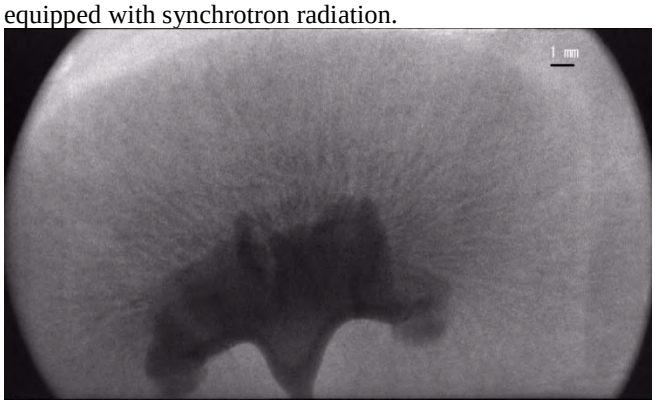

Fig. 1: Kidney showing collecting ducts at PF-AR.

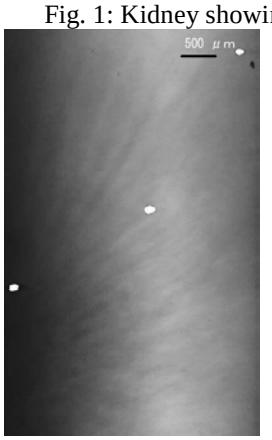

Fig. 2: Enlarged image of collecting ducts taken at PF.

4. Conclusion

The use of HARP tube enabled to visualize the shape of collecting tube of rat kidney. With this system, the size and flow of collecting ducts can be measured. It will be of help to understand the pathophysiology of collecting tube in various diseases from the aspect of flow visualization.

References

[1] Konishi *et al.,* Am J Roentgenol **197** (2011) W508
[2] Miyakawa *et al*., SPIE-IS&T **7536** (2010) 753604-1

* shomatsu@k.tsukuba-tech.ac.jp

NE7A/2010G695

Measurement of pulmonary arterial flow velocity in high flow pulmonary hypertension rat model using synchrotron radiation pulmonary micro-angiography

Chiho Tokunaga[1,*], Shonosuke Matsushita[1], Kazuyuki Hyodo[2], Hiroaki Sakamoto[1], Shizu Aikawa[1], Yoshiharu Enomoto[1], Fujio Sato[1], Shinya Kanemoto[1], Mio Noma[1], Yuji Hiramatsu[1], Yuzuru Sakakibara[1]

[1] Department of Cardiovascular Surgery, Graduate School of Comprehensive Human Science, University of Tsukuba, Tsukuba 305-8575, Japan
[2]Photon Factory, Tsukuba 305-0801, Japan

1 Introduction

Congenital heart disease with high pulmonary flow is frequently complicated by the development of irreversible pulmonary hypertension. The increased pulmonary flow and shear stress may trigger endothelial cell dysfunction and unfavorable vascular remodeling which increases vascular resistance, although the detailed mechanism is still unknown.

Visualization of the micro vasculature bed and the measurement of blood flow velocity in pulmonary hypertension rat would provide the insight for evaluating endothelial reactivity caused by shear stress derived from high pulmonary flow and help to understand the mechanism of vascular remodeling. In this study, we aimed to establish the method of the synchrotron radiation pulmonary micro-angiography and measure the pulmonary flow velocity in *in-vivo* pulmonary hypertension rat model.

2 Experiment

Synchrotron radiation pulmonary micro-angiography was performed at the Photon Factory of the High Energy Accelerator Research Organization （Tsukuba, Japan) using a 6.5GeV electron beam. The advantages of synchrotron radiation derived X-ray is high spatial resolution due to increased photon density and straightness of the waves. High density resolution is obtained from high-sensitivity HARP (high-gain Avalanche Rushing amorphous Photoconductor) detector camera provided by NHK Science and Technical Research Laboratories. Our preliminary study showed that the diameter of minimum identified pulmonary arteriole was 100 μm.

As a high flow pulmonary hypertension rat model, an arterio-venous fistula between abdominal aorta and inferior vena cava was created in male Wistar rat. After 8 weeks, pulmonary micro-angiography was performed by transvenous infusion via right jugular vein. The dynamic change of density at the right main pulmonary artery (RPA), superior branch to inferior lobe (A6) and pulmonary arterioles (PA) lying under the visceral pleura was measured by computer-imaging program ImageJ. The transit time of contrast medium at each three point was also measured and pulmonary blood flow was calculated. Sham operated rat was used as control.

3 Results and Discussion

The velocity of proximal pulmonary artery (between RPA and A6) in pulmonary hypertension rat was 111.5±23.5 mm/sec and 117.0±13.5 mm/sec in control. By contrast, the velocity of distal pulmonary artery (between A6 and PA) was significantly increased as 71.7±23.2 mm/sec compared with control as 9.4±2.6 mm/sec ($p<0.05$).

4. Conclusion

This result demonstrates the effectiveness of the synchrotron radiation pulmonary micro-angiography to visualize the microvasculature in *in-vivo* pulmonary hypertension rat model. The pulmonary flow velocity was also able to measure and higher flow velocity at distal arteries was revealed. This newly developed technology to visualize the microvasculature may help to investigate the mechanism of vascular remodeling associated with pulmonary hypertension.

References

[1] Miyakawa *et al*., SPIE-IS&T **7536** (2010) 753604-
[2] Matsushita *et al*., Euro J Radiol **68S** (2008) S84

* chiho-t@md.tsukuba.ac.jp

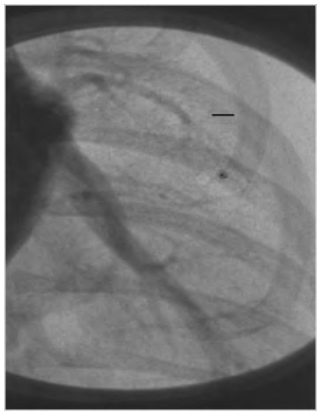

(Bar indicates 1 mm)

Fig. 1: Synchrotron radiation pulmonary micro-angiography with HARP receiver.

2011 R-27

ファントームを用いたX線イメージングにおける検出器特性予備評価実験

森　浩一[1*], 関根紀夫[2] ,大久保知幸[1],兵藤一行[3]
[1]茨城県立医療大学 〒300-0394　阿見町 阿見 4669-2
[2]首都大学東京 〒305-0801　荒川区 東尾久 116-8551
[3]物質構造科学研究所・放射光 〒305-0801　つくば市 大穂 1-1

1 はじめに

日本における最初の放射光X線の臨床医学利用は、心臓冠動脈の造影検査への適用であった[1]。この検査は、低濃度ヨード造影剤と単色エネルギーのX線を用いることで、軟組織である血管を鮮明に描写する手法である。単色エネルギーのX線は、元素の吸収端におけるX線吸収量の特異的な変化を画像コントラストに反映させるのに有利である。しかし、この手法は、被写体を通過したX線における吸収量の変化に基づく画像法であることから、低コントラスト被写体の描写には限界がある。これを解決する手法の１つとして、X線の位相量の変化に基づく低コントラスト被写体の可視化技術が提案された[2]。この手法によれば、従来法では描写が難しい軟組織を鮮明に描写できる[3]。

このような描写に優れた手法を臨床で応用するに当たり、被ばく量の軽減の観点からは、受像素子のピクセルサイズは 200μ m～数 10μ m程度になるであろう。この実験では、新たに用意した CMOS カメラについて、単色X線に対する動作特性（キャリブレーション、空間分解能、軟組織描写能等）を調べ、放射光X線を用いた位相イメージングに用いる電子受像素子としての性能を予備的に評価した。

2 実験

撮影には、Rad-icon 社製の CMOS カメラ（ピクセルサイズ: 48μ m，2048×1024, 2.7fps）を用いた。X線光学系には、非対称反射結晶（α＝5.3 度）、ラウエ型 Si アナライザーを用いた[3]。X線エネルギー30keV とし、試料なしにおいて、アナライザー結晶のロッキング曲線を測定した。また、ファントム試料の撮影を行った。ピクセルのキャリブレーションは、医療用X線管（60kV，25mA）で行った。

3 結果および考察

ファントム試料の画像を図 1 と図 2 に示した。撮影時間は、500msec であった。図１では、前方回折像・回折像ともに関節軟骨、十字靭帯、骨梁の鮮明画像を得た。関節軟骨や靭帯は、従来法では造影検査によりのみ画像が得られる組織である。図２では、輪郭線部がより鮮明に描写された。図１と２で得られた組織内、組織境界部の描写、組織の形状描写

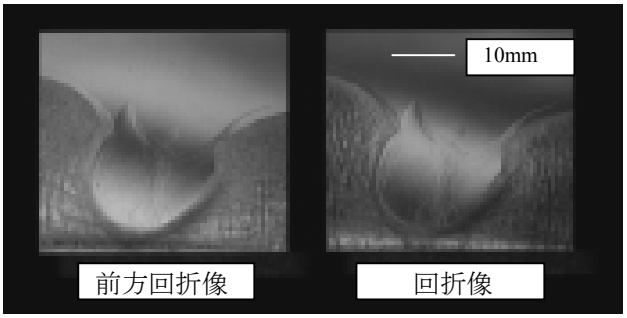

図１：骨（関節）ファントム画像（θ＝－1.2μ rad）

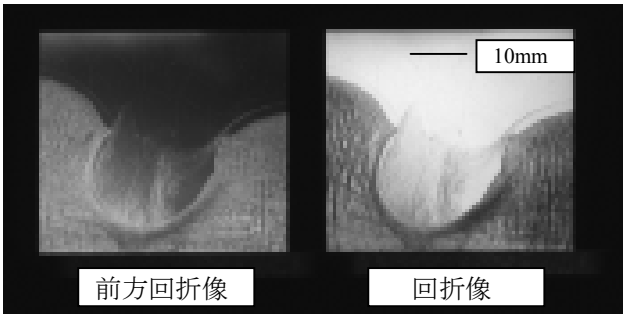

図２：骨（関節）ファントム画像（θ＝0μ rad）

（空間分解能）は、画像診断上、X線フィルムや Image-Plate による画像とほぼ同画質であった。今後は、感度や密度分解能を定量評価する必要がある。

4 まとめ

新型 CMOS カメラの単色X線（30keV）における描写特性を調べた。試料画像は、従来素子とほぼ同等の画質が得られた。この受像素子は、単色放射光X線を用いたイメージングに有用といえる。

参考文献

[1] K. Hyodo *et al*., JSR **5** (1998) 1123.
[2] V N Ingal *et al*., *J. Phys. D: Appl. Phys.* (1995) **28** 2314
[3] K. Mori , *et al*., J. Jpn.Health Sci. (2008) **10** 263.

12C/2008G177

活火山地域の河床堆積物に見られるマンガン濃集層の XAFS 分析
XAFS analysis of Mn-rich layers in fluvial deposits in active volcano area

勝田長貴 [1*],村上拓馬 [2]
[1]岐阜大学教育学部、〒501-1193 岐阜市柳戸 1-1
[2]金沢大学環日本海域環境研究センター、〒923-1224 能美市和気町オ 24

1 はじめに

浅間火山の火口南方の湧水を源とする河川には、方解石を主体とする縞状堆積物が生成されている。その縞構造は、明色の方解石の層と暗色の鉄に富む層の繰り返しからなり、これらの層の間にはマンガン濃集層が常に分布している。われわれは、この縞状堆積物の形成過程を解明し、その縞状堆積物に記録される環境指標を導き出すことを目指している。本研究では、この一環として、マンガン濃集層の存在形態を XAFS 法により分析した。

2 実験

XAFS 測定は BL12C にて蛍光法で行われた。入射 X 線は 6.490-6.630 (keV)の範囲を 0.5 (eV)の分解能で走査した。照射面積は縦横 1 (mm) × 1 (mm)とした。試料から放射された蛍光 X 線強度の測定は、19SSD を用いて、取り込み時間 2 (sec)で行われた。エネルギー軸の較正には、δ-MnO_2 のプレエッジ（6.5393 keV）を用いた。測定試料については、風乾させたトゥファ試料を BN とともにメノウ乳鉢で粉砕混合し、油圧式プレスで成形した試料を準備した。マンガンの酸化数 $f(Mn^{4+})$ (= $Mn^{4+}/(Mn^{2+}+Mn^{4+})$) は、Schulze et al.(1995)[1]に基づく。

3 結果および考察

本実験で用いた試料は、源泉から約 200 メートルの地点（NG3）と約 3 キロメートルの地点(NG5)で採取した河床堆積物である。これら試料の違いは、NG3 が軟泥状堆積物であるのに対し、NG5 の堆積物はコンクリート状に固結し、縞構造が発達している点である。図 1 に、これら 2 種類の堆積物の解析結果を示す。NG3 と NG5 のマンガンはともに Mn^{2+} の状態として存在する。これは、NG3 から NG5 にかけての河川水は、Mn^{2+}/Mn^{4+}境界に到達せず、マンガンに対して還元的な水質環境であることを意味する。一方、NG3 と NG5 のマンガンの存在形態については、XANES スペクトルの形状から互いに異なることがわかる。このうち、NG5 のマンガンについては、リファレンス試料のスペクトルとの比較から炭酸塩鉱物に含まれている。こうしたマンガンの存在状態の違いから、2 つの堆積場における水質の変化が示唆される。また、縞構造中の Mn 濃集層は、その場での環境変動による水質変化で生じたものと考えられる。

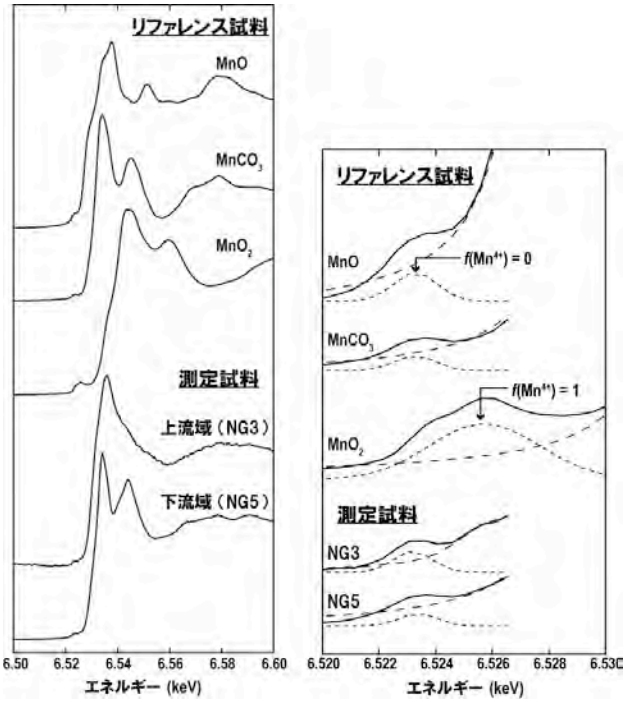

図 1 ： Mn K 吸収端（左図）とそのプレエッジピーク（右図）

謝辞

仁谷浩明氏には、試料準備法ならびに測定システムのセットアップ、測定中のトラブルの対処など、本実験にあたって多大な支援を受けました。ここに深く感謝いたします。

参考文献

[1] Schulze, D. G. et al., Soil Sci. Soc. Am. J. 59, 1540-1548 (1995).

*nkatsuta@gifu-u.ac.jp

先端研究施設共用促進事業
フォトンファクトリーにおける産業利用促進

課 題 番 号： 20091004
研究責任者： 人見尚、株式会社大林組　技術研究所
利 用 施 設： 高エネルギー加速器研究機構　放射光科学研究施設　BL-14B
利 用 期 間： 2009 年 10 月～2010 年 9 月

建設材料の欠陥や不良部位イメージングによる破壊メカニズムの解明

Solution of the destruction mechanism using imaging of the defect or the defective part of the construction materials

人見　尚
Takashi HITOMI

株式会社大林組技術研究所
Obayashi technical research institute

アブストラクト：
コンクリートの破壊メカニズムの解明を目的として，高分解能 X 線 CT を用いた欠陥・不良部位のイメージングを試みた。建設材料として，砂とセメントを混合したモルタルについて非破壊観察を行い，X 線 CT が建設材料の観察に適すると判断した。さらに不良部位であるモルタル中の 0.013mm 以上の幅のひび割れが観察可能であることを確認した。本観察法が破壊メカニズムの解明の有力なツールであることを確認した。

For the purpose of solution of the destruction mechanism of the concrete, the imaging of the defect or the defectiveness parts were tried with using high resolution X-ray computed tomography (X-ray CT). As construction material, nondestructive observation of mortar, which is mixture of sand and cement, was performed. With this result, X-ray CT was judged as suitable for the observation of the construction material. Furthermore, it was confirmed that the cracks of width more than 0.013mm that defect parts in mortar were observable. Than the above, this observational method confirmed that it was a convincing tool of the solution of the destruction mechanism.

キーワード：　X 線 CT，コンクリート，非破壊観察，ひび割れ，可視化

１．はじめに：

コンクリートは，粗骨材と呼ばれる粒径数十ミリ程度の岩石と，細骨材と呼ばれる粒径を 2㎜ 以下に調整した砂と，セメントと水を練り混ぜて作られる複合材料である。

コンクリートの劣化現象の一つに，ひび割れの発生がある。ひび割れの発生原因として，コンクリートが高脆性材料からなる複合材料であるため，引張り荷重の生じた部分でも弾性変形ができないことや，コンクリート作製時にセメントペーストと呼ばれるセメントと水の混合物が硬化に伴い収縮や発熱を起こし，部材の内外温度差による膨張割合の差によることが知られている。これらの解決はいまだ困難であり，ひび割れの補修や予防に，多くの労力が割かれ，多くの研究者がその対策に従事している。

コンクリートのひび割れの発生メカニズムに関しては，上述のような理解はなされているが，ミクロなスケールにおいて，粗骨材や細骨材，そしてセメントペーストのどこで，どのような条件で発生し，それが進展していくかに関しての研究的取り組みはいまだ始まったばかりである。これらを解明し，微細な組織の改良により，ひび割れの発生の予防は可能になると思われる。しかしこれまでは，セメントペーストや細骨材，

さらにそれらの界面といったミクロな領域を非破壊で直接観察する手段が無かった。

Photon Factory(以下，PF)では，市販の X 線 CT 装置に比べ，軽元素からなるコンクリートの観察に適したエネルギーの選択が可能で，高分解能な X 線 CT 観察が可能になっている。本研究では，コンクリート破壊メカニズムの理解のため，X 線 CT によるコンクリート材料観察の有効性評価のため，コンクリート材料の観察最適条件と破壊によって生じるひび割れの 3 次元的な観察を行った。

2．実験：

本研究では，PFにおけるX線CTがコンクリートの観察，特にひび割れの可視化に適するかの見極めを中心に実験を行った。第1回は，サンプル観察の最適条件の探索，第2回および第3回は，実際にひび割れを導入した供試体の観察を行い，不良部位すなわちひび割れの可視化が可能かを目的とした。

2.1　コンクリート直接観察の最適条件

（1）　目的

PF における X 線 CT 観察に最適な供試体サイズ，照射 X 線のエネルギーなどの最適条件を求める。

（2）　試験方法

1）供試体

供試体には，作製から 2 年が経過し水と結合材の比率(W/B)=50%で，砂とセメントを含む結合材の比率(S/B)=2.0 のモルタルを用いた。また一部確認用に砂を取り除いた同じ配合の普通ポルトランドセメント(OPC)のセメントペーストを用いた。供試体は 4 種類とし，OPC のモルタルとセメントペースト，一部をフライアッシュ(FA)に置換した低熱ポルトランドセメント(LPC+FA)および高シリカ含有フライアッシュセメント(HFSC)のモルタルである。表－1 に使用材料の一覧を示す。供試体の調合を表－2 に示す．供試体は、練混ぜ後、直径 5cm、高さ 10cm の円筒型枠に打設し、24 時間の封かん養生後、脱型し、観察まで水中養生を行った。観察用に直径 5mm で高さが 20mm 程度の円筒形に加工後，無水アルコールに浸漬し水和を停止させた後，炭酸化を防ぐために小瓶にシリカゲルとともに密封した。

表－1　使用材料

材料名	記号	品名	品質
セメント	OPC	普通ポルトランドセメント	密度 3.16g/cm^3
	LPC	低熱ポルトランドセメント	密度 3.16g/cm^3
混和材	SF	シリカフューム	密度 3.16g/cm^3, 比表面積 20000cm^2/g
	FA	フライアッシュ・JIS II 種	密度 3.16g/cm^3, 比表面積 20000cm^2/g
最骨材	S	陸砂・粒径 2.5mm 以下	密度 3.16g/cm^3, 比表面積 20000cm^2/g
混和剤	SP	高性能 AE 減水剤・SP-8SBMx2	ポリカルボン酸エーテル化合物ポリマー錯体

表－2　供試体の調合

供試体名称	W/B (%)	S/B	単位量(kg/m^3)						減水剤 (kg/m^3)
			W	OPC	LPC	SF	FA	S	
OPC	50	2.0	305	610				1220	0.5
LPC+FA			298		417		179	1192	1.2
HFSC			290	232		113	232	1159	0.3

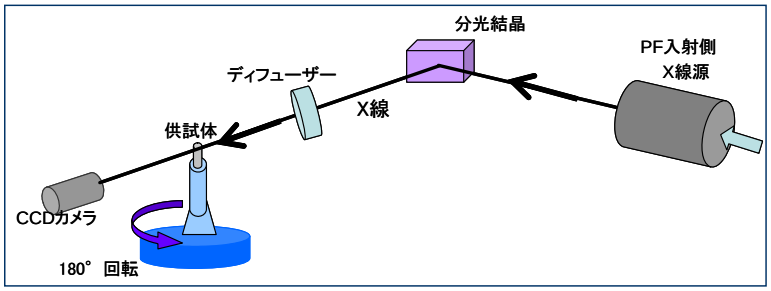

図－1　X 線 CT 装置の構成

2）X 線 CT

X 線 CT 撮影は，PF のビームライン BL-14B を用いた。図－1 に装置の構成を示す。PF のリングから引き込まれた X 線は，まず分光結晶に照射され，適切なエネルギーに調整される。さらに，照射範囲の X 線強度を揃えるためにディフューザーを透過させ，供試体に照射される。供

試体を透過したX線は像としてCCDで受光される。得られるデータは，角度を変えて撮影された透過像である。これらを再構成することで，供試体の断面図が得られる。コンクリート構成元素と空気のX線吸収係数の比較より，15～25keVがX線の照射エネルギーとして適していることがわかった[1)]。X線はエネルギーが小さいほど透過力が低下するため，本試験における照射エネルギーはおよそ25keV付近に設定した。再構成には，PFで作製されたソフトウエアCtCalc(画像における回転中心位置の算出)，CtCbp(Cbp法に基づく断面図再構成)，Raw2Bmp(画像の形式変換)を用いた。本試験で用いたCCDカメラは，Photonic Science社製のX-FDIで，水平方向は8.9mm，高さ方向は6.7mmの視野を有し，構成画素数は1384×1040である。断面図としては，9.0mm四方の領域となり，構成する画素の寸法は0.00645mmである。

（3） 試験結果

露光時間や投影数など，条件を変えた18回の観察を実施した。供試体，条件および結果の一部を表－3にまとめた。観察結果を元に断面図を求めた結果を図－2に示す。空気は黒色，材料部分はグレースケールで表示した。

観察番号1～11までは，最適な投影数を求めることを目的とした。360枚以下の投影数では，断面図は得られないことが分かった。観察番号4および8～11において，投影数を増やし，900枚の撮影で得られる断面図の画質が良好であることが分かった。また，露光時間は，1枚の投影像を撮影する間に供試体にX線を照射する時間のことを示すが，露光時間が長くなるほど，投影像のコントラストが向上することが分かった。しかし，露光時間を増やすと，受光側のCCDカメラ信号が飽和することや，供試体観察に必要な時間が増えることになり，今回は，3～4秒の露光時間が最適であることが分かった。

表－3 観察結果まとめ

試験番号	試験体仕様	投影数	露光時間(秒)	結果
1	OPC、φ5mm	45	5	輪郭のみ確認
7	OPC、φ5mm	180	4	結像せず(エネルギー低下)
9	OPC、φ5mm	360	2	金属性の明るい点を確認
12	OPC、φ5mm	900	3	空隙を確認
14	LPC，φ5mm	900	4	骨材の境界を確認
15	HFSC，φ5mm	900	4	骨材の境界を確認
16	OPC，φ5mm，ひび割れ	900	3	ひび割れを確認
17	HFSC，φ5mm，ひび割れ	900	4	骨材の境界，ひび割れを確認
18	LPC，ひび割れ(チューブ)	900	4	骨材の境界，ひび割れを確認

観察番号9～12までは，OPCのセメントペーストを観察対象とした。一番条件の良い観察番号12の断面図において，気泡が明瞭に観察できる結果となった。観察番号13～15においては，各種モルタルの撮影を行った。それぞれ骨材を明瞭に区別できることが分かった。しかし，観察番号9～12の結果も併せると，セメントペースト部分の詳細観察には不向きであること考えられた。観察番号16～18において，ひび割れを導入したモルタルの観察を行った。ひび割れは明瞭に観察することが可能であり，ひび割れ幅は画素数を数えることで求めることが可能である。観察番号18は熱収縮チューブを用い，側面を拘束した状態での撮影結果である。チューブは断面図には明瞭に現れず，また内部の断面図にも影響を及ぼさないことが分かった。

以上の結果より本測定法は建設材料の観察に適すると判断した。

2.2 コンクリートのひび割れ部の直接観察

（1） 目的

コンクリートの破壊は内部に微細なひび割れ

が発生し，それが伝播しひび割れ幅が増大していく過程をたどると考えられる。また，微細な

（２） 試験方法

１） 供試体

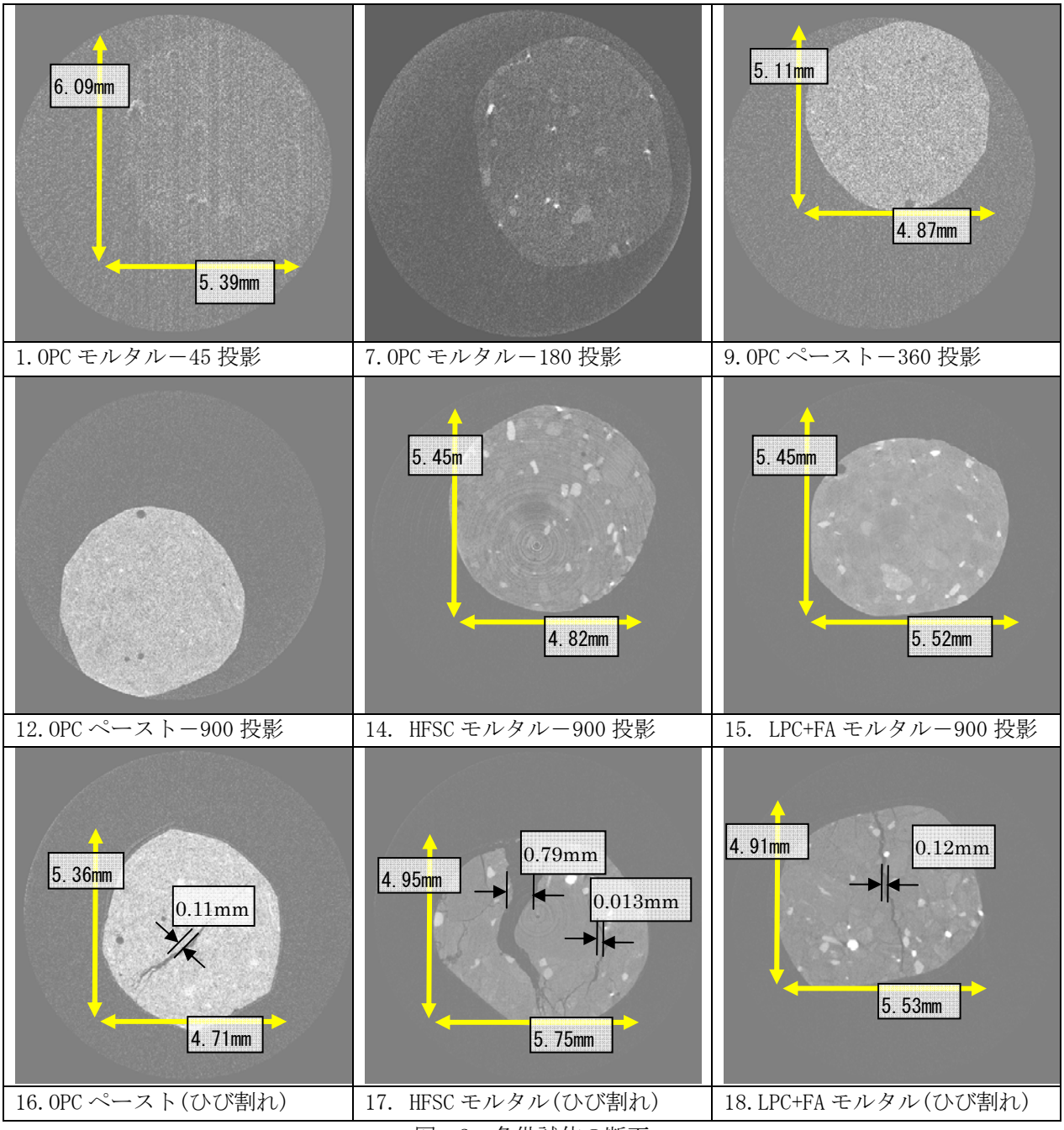

1. OPC モルタル－45 投影	7. OPC モルタル－180 投影	9. OPC ペースト－360 投影
12. OPC ペースト－900 投影	14. HFSC モルタル－900 投影	15. LPC+FA モルタル－900 投影
16. OPC ペースト(ひび割れ)	17. HFSC モルタル(ひび割れ)	18. LPC+FA モルタル(ひび割れ)

図－2 各供試体の断面

ひび割れの発生は，コンクリートに含まれる粗骨材や細骨材とセメントペースト部分の弾性係数などの物性値の違いにより，その界面より発生すると考えられている。本検討では，モルタル供試体内部の非破壊観察を行い，ひび割れを三次元的に把握できるかを確認し，さらにそのひび割れと細骨材との位置関係を求めることを目的とした。

供試体は，1 章で用いた配合のサンプルを用いた。供試体は，およそ直径 5mm の円筒形に加工後，熱収縮チューブで周囲を拘束し，万力を使い割裂する要領で円を横切るようにひび割れを導入した。ひび割れ幅の制御は行っていない。

２） 試験方法

X 線 CT 装置の構成は，前節と同様とした。照射エネルギーは，細骨材とセメントペースト部

分の区別のために，前節よりもエネルギーを落とし，22keV とした。露光時間は 3 秒，投影数は 900 とした。

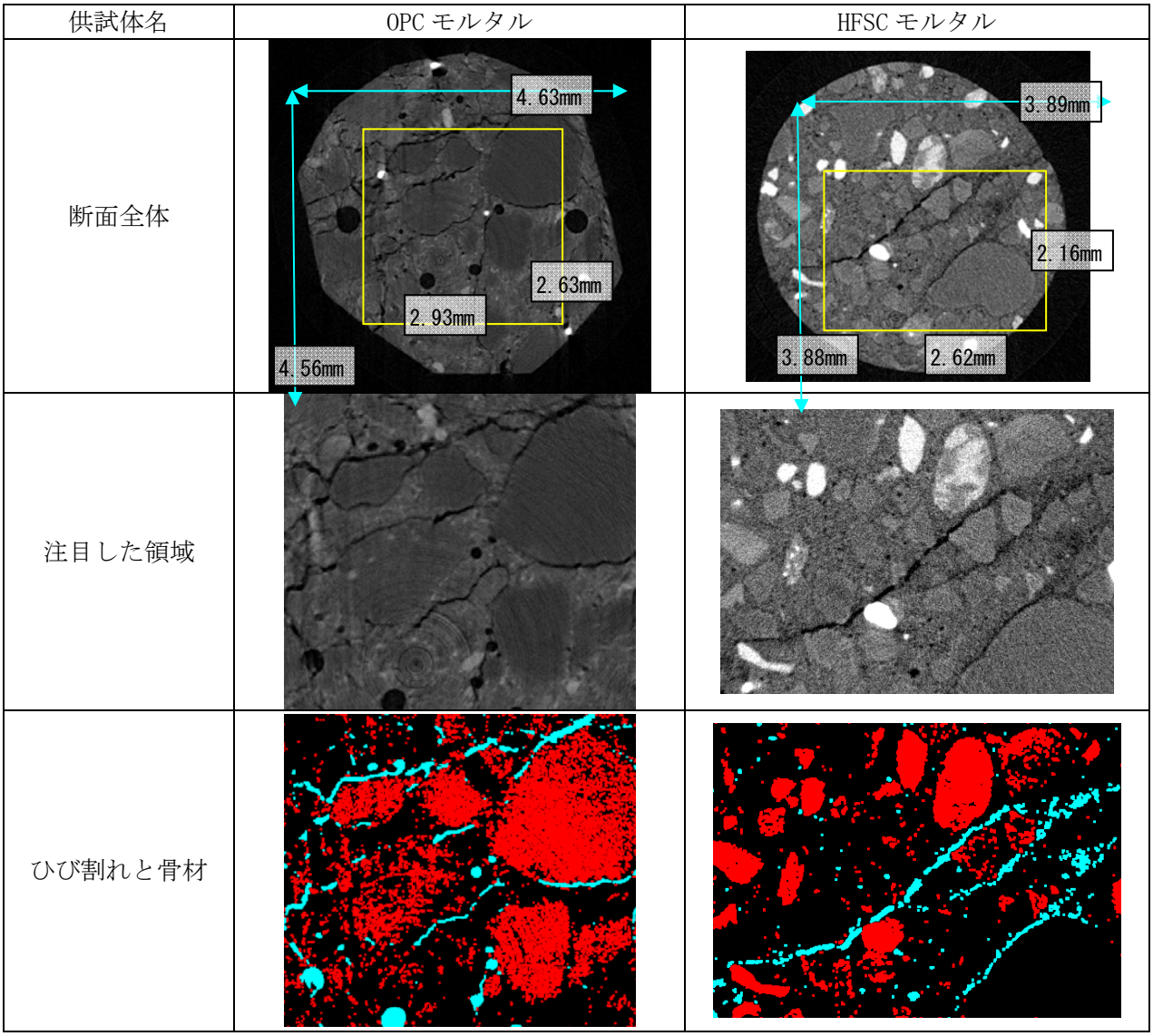

図－3　ひび割れおよび断面の可視化結果

3）　ひび割れおよび骨材の可視化方法

得られた透過像群を用い，PF で用意されたソフトウエア（CtCalc，CtCbp，Raw2Bmp）により断面図を求めた。断面全体では画像の規模が大きいため，供試体内部の長方形の領域を抽出し，その部分に関し，ひび割れ部分および骨材部分を二値化により抽出した。これらの処理には ImageJ を用いた。なお，二値化を行っても，画面全体には点状のノイズが残った。このノイズを消去するために，ひび割れおよび骨材の抽出後の結果の図にスムージング処理を施した。それぞれの図を合成して，ひび割れと細骨材の抽出画像を作成した。

（3）試験結果

観察結果のうち，普通ポルトランドセメント，および HFSC の結果を図－3 に示す。上段に断面の全体，中段に抽出した領域，下段にひび割れと細骨材をのみを抽出した画像を示す。周囲の空気やひび割れは黒色，未水和のセメントは白色で表示されている。細骨材は OPC では周囲より若干暗色の粒状の領域，HFSC では周囲の領域より若干明るい粒状の領域で表示されている。この細骨材の色調の違いは，OPC に比べ HFSC はケイ素を多く含み相対的にカルシウムの含有量が低いことに起因する。OPC モルタルの図－3 に

おいてひび割れは水色，骨材は赤色で示した。その他の部分は，セメント硬化体となる。いずれの供試体においても，ひび割れは細骨材とセメント硬化体との境界を通るように存在する傾向が見られた。図－4 にひび割れと細骨材の像を厚さ方向に 800 枚を集積することで得られる立体像を示す。いずれもひび割れは，骨材周囲を包むように存在する様子がみてとれる。本観察法により非破壊でひび割れを観察することが可能で，さらに，骨材などひび割れ発生と関係すると思われる材料を抽出しそれらの三次元的な位置関係を把握することが可能であり，コンクリートの破壊過程の観察には有用であることが分かった。

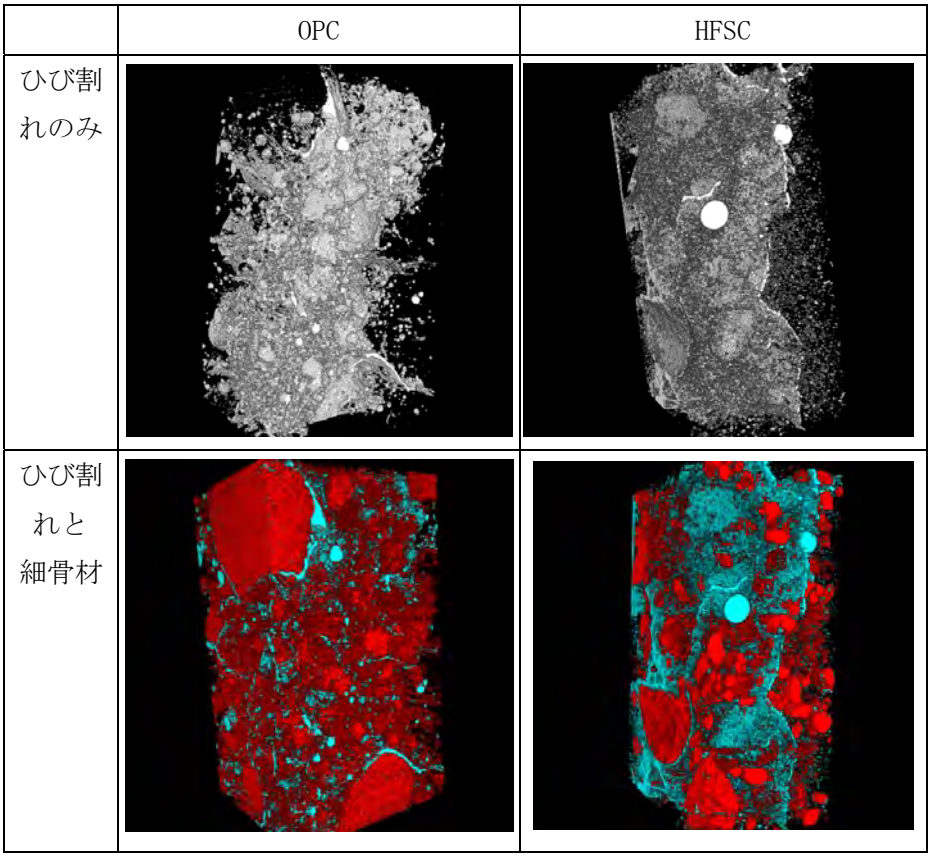

図－４　ひび割れ部と細骨材およびひび割れ部分の立体像

３．まとめ

PF における高分解能 X 線 CT を用い，コンクリートの構成材であるモルタルの観察に最適な条件を求め，コンクリート破壊メカニズムの解明に必要となるコンクリート中のひび割れの抽出を試みた。結果を以下にまとめる。

1. モルタルの観察には，照射エネルギーが 25keV の条件で，露光時間が 3～4 秒程度，投影数は 900 が最適である。
2. 供試体のサイズは，円筒形で直径 5mm 以下が最適であった。それ以上の直径では X 線が透過しない。
3. 観察可能なひび割れの最小幅は 0.0013mm であった。
4. 供試体の一部を抽出し，画像処理によってひび割れを抽出することが可能である。また，細骨材も抽出が可能である。
5. 抽出画像を用い，ひび割れの三次元分布を可視化することができた。さらに細骨材の位置関係の把握が可能である。

以上より，本観察法によりモルタル内部の非破壊観察が可能で，内部のひび割れを観察でき，コンクリートの破壊過程の観察には有用であることが分かった。

参考文献

1) 人見尚，三田芳幸，斉藤裕司，竹田宣典：SPring-8 における X 線 CT 像によるモルタル微細構造の観察，コンクリート工学年次論文集，Vol.26，pp645-650.2004

12C、 9A/2010G054

XAFS による As(V)共沈を用いた廃水処理における水酸化第二鉄構造の変化の把握
XAFS investigation for structure change of ferrihydrite during As(V) co-precipitation treatment in wastewater

所千晴[1*]、井澤彩[1]、渋谷駿太[1]、小田祐史[1]、沼子千弥[2]
[1]早稲田大学大学院創造理工学研究科、〒169-8555 新宿区大久保 3-4-1
[2]千葉大学大学院理学系研究科　〒263-8522 千葉市稲毛区弥生町 1-33

1 はじめに

鉱山からの酸性坑廃水のように、廃水量が比較的多く、排水基準をわずかに上回るような希薄なヒ素が含有されている場合には、水酸化第二鉄による共沈法を用いた処理法が広く行われている。しかし、水酸化第二鉄は一般に固液分離性が悪く、処理後に As(V)を含有した汚泥が大量に出ることから、その最終処分先の確保に問題を有している。

この汚泥量を減容化するためには、処理における薬剤添加量や pH 等のプロセス条件を最適化することが必要である。我々はかねてより、水酸化第二鉄による As(V)共沈の機構解明による処理法の最適化に取り組んでいる。これまでに収着等温線の作成や、ゼータ電位測定、XRD 分析等により、共沈機構は 2 次元的な As(V)の取り込み機構である表面錯体形成と、3 次元的な As(V)の取り込み機構である表面沈殿形成の 2 種類に大別できることを確認している[1]。それらの割合は初期 As/Fe 比によって決定され、As/Fe=0.3 を境目として、それより比が大きい場合には表面沈殿が共沈機構として優勢になることがわかっている。

本報では、その機構の詳細を、Fe K 端における EXAFS 解析によって検討した結果を報告する。

2 実験

As(V)源には $Na_2HAsO_4 \cdot 7H_2O$、Fe(III)源には $Fe(NO_3)_3 \cdot 9H_2O$ をそれぞれ用いた。As 濃度は 0.022 ～ 0.90 mmol/dm^3、Fe(III)濃度は 0.042 ～ 4.95 mmol/dm^3 の範囲で、初期 As/Fe モル比 0.13～11 になるように適宜濃度を調整した。本研究では、共沈実験と吸着実験とを厳密に区別している。共沈実験では、ビーカー内に As(V)および Fe(III)溶液を共存させ、KOH によって pH を上昇させることによって水酸化第二鉄を As(V)曝露下で沈殿させた。一方、吸着実験では、水酸化第二鉄の沈殿と As(V)の吸着を別々に生じさせた。すなわち、2 個のビーカーに対して、それぞれ As(V)溶液と Fe(III)溶液を別々に用意し、それぞれの溶液を pH5 または 7 に調整して水酸化第二鉄を沈殿させてから、両者を合わせて 1 つの溶液とした。

固液分離に際しては、微粒の水酸化第二鉄粒子も分離するために 3 kDa のメンブランフィルターを用いた。濾液の残留 As(V)濃度は ICP 発光分光分析装置によって分析した。濾紙上の沈殿物については、約－45℃、約 10 Pa で約 24 時間、凍結乾燥器で凍結乾燥させた。これを BN 粉末と混合し、錠剤成形機を用いて錠剤を作成して、XAFS 分析に供した。

その他の詳細な実験方法は文献[1、2]を参照されたい。

3 結果および考察

共沈処理で得られた沈殿の Fe K 端 EXAFS 信号を図 1 に、これをフーリエ変換し、同径構造関数にしたものを図 2 に示す。それぞれのスペクトルは pH5、Fe(III)濃度 10 mg dm^{-3}、As/Fe=0、0.125、0.25、0.5、1、2、5 の条件下において生成した沈殿と、非晶質ヒ酸鉄の沈殿のものである。

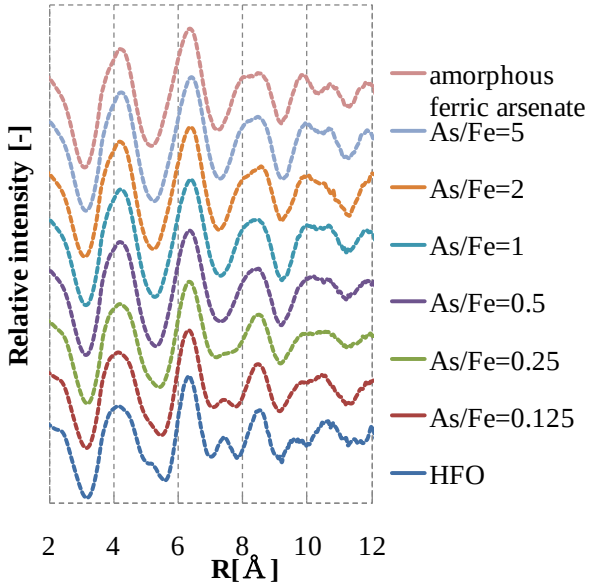

図 1　水酸化第二鉄による As(V)共沈物、水酸化第二鉄、非晶質ヒ酸鉄の Fe K 端における EXAFS

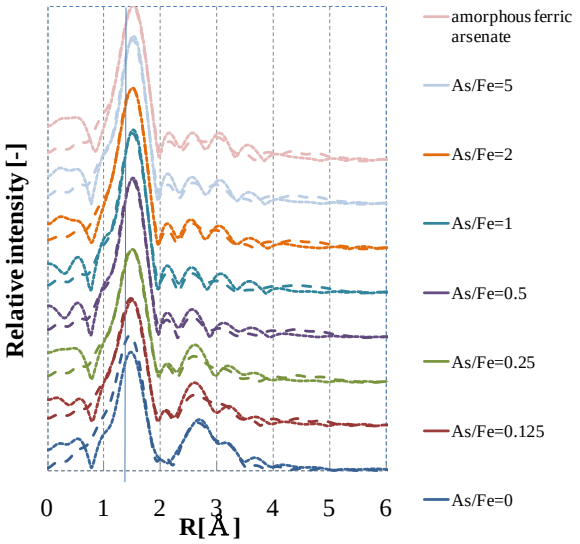

図 2　水酸化第二鉄による As(V)共沈物、水酸化第二鉄、非晶質ヒ酸鉄の Fe K 端における RDF

図 2 において、Fe-O のピークの次に見られる小さなピークは、水酸化第二鉄では認められず、As(V)共沈物および非晶質ヒ酸鉄のみに認められる。このピークは、As(V)の水酸化第二鉄への表面錯体形成によるピークであると予想される。As(V)の水酸化第二鉄への表面錯体構造には、単核単座錯体（Fe-Fe=2.8 Å）、二核二座錯体（Fe-Fe=2.8 Å）、単核二座錯体（Fe-Fe=2.5 Å）があり、ピークの位置はこれらの錯体における Fe-Fe 間距離に一致している。

水酸化第二鉄に見られる 3.0 Å 付近の大きなピークは、edge sharing linkage 構造に相当するが、このピークは、As(V)共沈物および非晶質ヒ酸鉄では、より近距離側にピークがシフトしている。このことから、As(V)はまず水酸化第二鉄の中の edge sharing linkage 構造の Fe へ取り込まれ、水酸化第二鉄のこの構造が崩れるものと考えられる。この構造の変化は、共沈構造が表面錯体かあるいは表面沈殿か、の区別による影響は見られない。

一方、このピークの更に外側に位置する 3.4-3.7 Å のピークは、水酸化第二鉄中の double-corner sharing linkage 構造に相当するが、このピークは、As/Fe≤0.25 ではシフトが見られないが、As/Fe≥0.5 では、より近距離側へのシフトが見られる。この As/Fe≥0.5 の領域は、他の実験結果より、表面錯体ではなく表面沈殿が優勢であると予想されることから、このピークシフトは表面沈殿に特有の現象であると予測される。すなわち、As/Fe が大きい場合には、As(V)は double-corner sharing linkage 構造中の Fe へ取り込まれ、その構造は表面沈殿構造、すなわち非晶質ヒ酸鉄へと変化すると考えられる。

4　まとめ

廃水中の希薄 As(V)の水酸化第二鉄による共沈処理を効率化すべく、種々の初期 As/Fe モル比に対して得られた共沈物中の構造を、Fe K 端における EXAFS 解析により詳細に明らかにした。As(V)が水酸化第二鉄中に取り込まれると、水酸化第二鉄には認められない Fe-Fe 間距離 2.8 Å 付近の小さいピークが認められ、これは単核単座錯体、二核二座錯体、単核二座錯体といった As(V)の表面錯体構造を示していると考えられた。一方、水酸化第二鉄中の Fe 構造としては、edge sharing linkage 構造に相当する Fe-Fe 間距離 3.0 Å 付近の比較的大きなピークと、double-corner sharing linkage 構造に相当する Fe-Fe 間距離 3.4-3.7 Å の小さなピークが認められたが、前者は、As(V)の取り込みによって近距離側へのシフトが認められた。したがって、希薄 As(V)は、まず edge sharing linkage 構造中の Fe へ取り込まれると考えられる。一方、後者は、As/Fe≥0.5 でのみ近距離へのシフトが認められた。初期 As/Fe モル比が 0.5 以上の領域では、表面錯体よりもむしろ表面沈殿が優勢であることを、我々は既に別の実験より確認している。このことから、表面沈殿が形成されるような高い As/Fe の領域では、As(V)は double-corner sharing linkage 構造中の Fe へ取り込まれ、水酸化第二鉄の構造を徐々に表面沈殿、すなわち非晶質ヒ酸鉄へと変化させることがわかった。

参考文献

[1] C. Tokoro *et al.*、 Environ. Sci. Technol. **44** (2010) 638.
[2] 所千晴ほか、 Journal of MMIJ. **127**(2011) 127.

* tokoro@waseda.jp

4C/2010G070

ゲルマニウム熱酸化膜中の残留秩序構造
Residual Order in the Thermally Oxidized Thin Film on Ge Substrates

志村考功*，下川大輔，松宮拓也，細井卓治，渡部平司
大阪大学大学院工学研究科 〒565-0871　吹田市山田丘 2-1

1 はじめに

近年、Si-LSI の微細化による性能向上の限界から歪み Si に次ぎ、Ge、GaAs 等の高移動度チャネルの導入が検討されている[1]。その中でも Ge は電子と正孔で Si より高い移動度を示すことや光電子集積デバイスへの応用も考えられることから特に勢力的に研究開発が行われている。

従来、Ge の熱酸化膜は化学的に不安定で、膜中や界面に多くの電気的欠陥が存在し、MOS デバイスのゲート絶縁膜には適用が困難であると考えられてきた。ところが最近では複数の研究機関から 10^{10} $cm^{-2}eV^{-1}$ 台の低い界面準位密度が示され、その良好な電気特性が報告されている[2,3]。しかしながら、その低い界面準位密度の起源やその劣化要因についての理解はほとんど進んでいない。

一方、我々は Si 熱酸化膜が単純なアモルファス構造ではなく秩序性を有していることを指摘し、その酸化機構や劣化過程について示してきた[4,5]。酸化した Si 基板の 111 ブラッグ反射から延びる CTR (Crystal Truncation Rod)散乱に沿って測定を行うと Si の指数で 1 1 0.45 付近に回折ピークを測定することができる。この回折ピークは酸化膜が厚い程強く、また、酸化膜の膜厚の逆数に対応する特徴的な強度変調を有している。これらの結果は Si 酸化膜が単純なアモルファス構造ではなく、Si 基板とエピタキシャルな関係をもつ周期構造を有していることを示している。詳細な検討からこの周期構造は酸化時に Si 基板のダイヤモンド構造の情報を完全に消失してしまうのではなく、基板の情報を引き継いだ構造であることがわかった。この残留秩序構造は疑アモルファス SiO_2 と結晶 Si との急峻な界面と構造の連続性を両立させるものであり、熱酸化 SiO_2/Si 界面の良好な電気特性の要因のひとつであると考えている。

そこで本研究では Ge の熱酸化膜中の秩序構造の有無を調べ、また、その変化を測定することにより酸化及び劣化過程の検討を行った。酸化膜中の秩序構造は酸化界面での原子レベルでの反応過程を直接反映したものであり、その酸化機構に関する多くの知見が得られるものと考えられる。

2 実験

熱酸化は、Dry O_2 雰囲気中、450°C、2-8 時間の範囲で行った。放射光 X 線回折実験はつくばの Photon Factory の BL4C で結晶分光型 4 軸回折計を用いて行った。Ge(001)基板の 111 ブラッグ反射から延びる CTR 散乱に沿って測定を行うことにより、酸化膜中の残留秩序構造からの回折ピークの有無を調べた。また、その回折ピークの強度分布測定から酸化膜の構造変化を調べた。

3 結果および考察

Fig. 1 に 450°C で 2 及び 8 時間酸化した試料の結果を示す。基板の 111 ブラッグ反射から延びる CTR 散乱の強度分布を示している。L=0.7 近傍で酸化前と比較して酸化時間が増加すると共にその強度が増加していることがわかる。これらの結果は Si 酸化膜中の残留秩序構造と同様の特徴であり、Ge 酸化膜中にも残留秩序構造が存在していることを示していると考えられる。

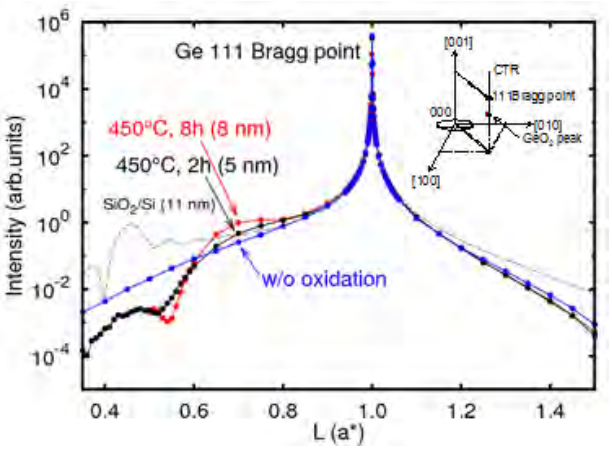

図 1 ：各種試料の 111 ブラッグ反射から延びる CTR 散乱の強度分布。

参考文献
[1] S. Takagi *et al.*, IEEE Trans. Electron. Devices **55** (2008) 21.
[2] H. Matsubara *et al.*, Appl. Phys. Lett. **93** (2008) 032104.
[3] C. H. Lee *et al.*, IEEE Electron Device Lett. **58** (2011) 1295.
[4] K. Tatsumura *et al.*, Phys. Rev. B **69**, (2004) 85212.
[5] T. Shimura *et al.*, J. Electrochem. Soc. **157** (2010) H977.

* shimura@mls.eng.osaka-u.ac.jp

15C/2010G070

Analysis of Lattice Distortion in Multicrystalline Silicon for Photovoltaic Cells by Synchrotron X-ray Diffraction

Takayoshi Shimura*, Takuya Matsumiya, Naoki Morimoto, Takuji Hosoi, and Heiji Watanabe
Graduate School of Engineering, Osaka University, Osaka 565-0871, Japan

1 Introduction

Photovoltaic (PV) cells promise to provide sustainable clean energy, since they directly convert solar energy into electricity. Approximately half of current PV cells are fabricated from cast multicrystalline silicon (mc-Si), because of its good balance between high conversion efficiency and low production cost. However, further improvements are required, such as a reduction of carrier recombination centers and thinning of the mc-Si wafers to reduce the cost of electricity.

The conversion efficiency of a mc-Si PV cell is usually a few percent lower than that of one based on monocrystalline Si, mainly due to the existence of grain boundaries (GBs). Many studies have been undertaken to clarify the electrical properties of GBs [1]. In these studies, electron backscattering diffraction (EBSD) was commonly used to map the grain orientation, with a typical accuracy of less than 1~2°. However, precise grain orientation maps are essential for an improved understanding of the electrical nature of the GBs.

Mc-Si contains residual lattice strain generated during inhomogeneous crystallization, which adversely affects the strength of the mc-Si wafers and can sometimes cause breakage during wafer slicing and device fabrication. The correlation between residual stress and electrical properties has been discussed [2, 3]. He et al. reported a correlation between residual stress, photoluminescence, and surface photovoltage [2], while Chen et al. claimed that the strain did not directly affect the electrical activity [3]. Therefore, imaging of the strain distribution in mc-Si is important for research and development aimed at reducing fabrication costs and improving conversion efficiency.

In this study, we demonstrate the use of synchrotron x-ray diffraction for the imaging of lattice distortion in mc-Si.

2 Experiment

The mc-Si materials used in this study were cut from high-purity large-grain mc-Si ingots, which were grown by a multistage solidification method [4]. Atomic absorption spectrophotometry revealed that most metallic impurities, except Fe, were below the detection limit. The Fe concentration was approximately 5×10^{12} cm^{-3}.

Monochromatic x-ray topographs were taken at BL15C of Photon Factory (PF) in Tsukuba, Japan. X-rays were monochromatized to 12.4 keV with a Si(111) double-crystal monochromator. The reflections in Bragg case were employed, and the diffracted x-rays were observed using an x-ray CCD detector with a pixel size of 6×6 μm^2. The sample images observed by the CCD detector were distorted, depending on the direction of the diffracted x-rays, and were manually corrected according to orientation maps obtained from EBSD measurements. For the strain measurements, a Si analyzer crystal was placed in front of the CCD detector to allow the observation of only x-rays diffracted in a certain direction, and to estimate the strain from the scattering angle.

3 Results and Discussion

Monochromatic x-ray topography is very sensitive to lattice distortion. In the monochromatic x-ray topography, the bending of the lattice was extracted from the rotation angle of the sample, and the strain was estimated from the rotation angle of the analyzer crystal. Figure 1 shows the the strain and bending maps, respectively.

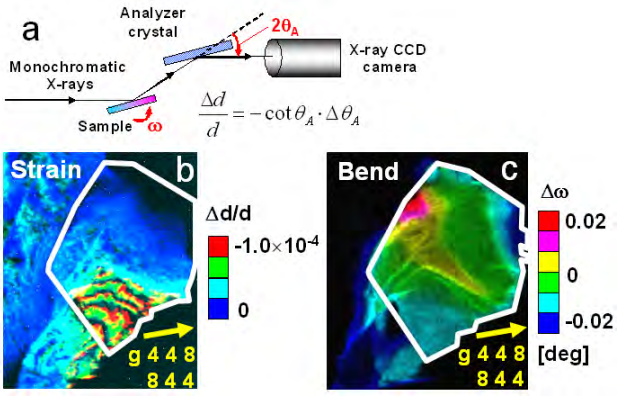

Fig. 1: (a) Experimental setup for monochromatic x-ray topography. (b) and (c) show the strain and bending maps, respectively.

Acknowledgement

We would like to thank Dr. J. Chen and Dr. T. Sekiguchi of NIMS for providing the mc-Si samples and helpful discussion.

References

[1] for example, J. Chen, T. Sekiguchi, D. Yang, F. Yin, K. Kido, and S. Tsurekawa, J. Appl. Phys. **96** (2004) 5490-5495.
[2] S. He, S. Danyluk, I. Tarasov, and S. Ostapenko, Appl. Phys. Lett. **89** (2006) 111909.
[3] J. Chen, B. Chen, T. Sekiguchi, M. Fukuzawa, and M. Yamada, Appl. Phys. Lett. **93** (2008) 112105.
[4] S. Nara, T. Sekiguchi, and J. Chen, Eur. Phys. J.: Appl. Phys. **27** (2004) 389-392.

* shimura@mls.eng.osaka-u.ac.jp

20A/2010G093

衛星表面材料の光電子放出電流の測定の検討
Mesurement of Photolectron Emission Current from Satellite Surface Materials

仁田 工美[1]、山納 康[2]、小林 信一[2]、三宅 弘晃[3]、伊藤 健二[4]
[1]宇宙航空研究開発機構、〒182-8522 調布市深大寺東町 7-44-1
[2]埼玉大学、〒338-8570 さいたま市桜区下大久保 255
[3]東京都市大学、〒158-8557 世田谷区 玉堤 1-28-1
[4]放射光科学研究施設、〒305-0801 つくば市大穂 1-1

1 はじめに

宇宙環境には様々なエネルギー・密度・粒子種のイオンや電子（プラズマ）が，固有の空間や特定の時間に存在し，宇宙機（人工衛星・探査機）にさまざまな影響を与える。宇宙環境において長期間安定して人工衛星，探査機を運用するためには，軌道上で生ずる帯電・放電に関する設計の妥当性を検証する事が不可欠である。宇宙機帯電を評価する基本は，宇宙機に流出入する各荷電粒子の電流を計算し，宇宙機表面に生じる電位差を計算することである。この電流の流入と流出は様々な原因により生ずる。

本研究では宇宙機の帯電を検討する上で重要な材料パラメータの一つである光電子電流についての検討を行った。衛星表面に用いられるあらゆる材料についての，光照射による光電子電流の値を測定し，照射された光の光子数に対する放出される光電子数の割合である量子効率を求め，この値を基に太陽光スペクトル照射時の光電子数に換算を行い，帯電解析時の入力値としたいと考えた。

リファレンス材料として金を用いた測定結果による装置の較正状況や太陽電池のカバーガラスなどの絶縁物の測定に伴う帯電の問題など得られた成果の概要について紹介する。

2 実験

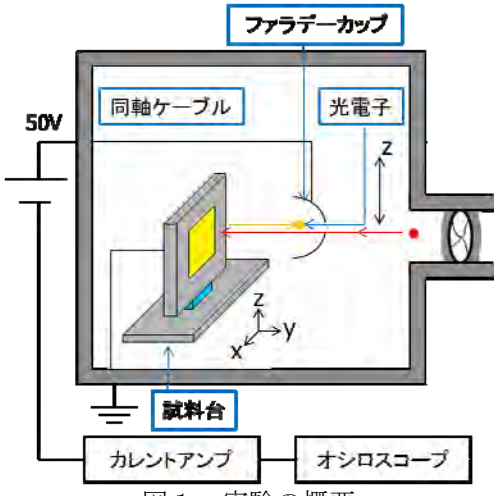

図１：実験の概要

図１に示すように。KEK ビームラインに真空チャンバーをゲートバルブ及び機械的なシャッターを介して設置し，チャンバー内には 3 軸制御可能な試料台と，光電子電流測定用のファラデーカップを装着した。放射波長範囲 50-240nm の波長の光を試料に照射し，光電子電流を測定し，照射された光の光子数に対する放出される光電子数の割合である量子効率を求めた。放出された電子の逆戻り，および装置内壁などで放出された電子の流入を避けるために，数 V 程度の負バイアスを試料台に印加した。放射光照射パターンは光を当て続ける連続光、シャッターで照射時間を 30ms にするパルス光の 2 通りで測定を行った。

3 結果および考察

量子効率の測定が妥当であったのかを検討するため，金の量子効率を用いて文献値と比較を行った。図２の横軸は光子エネルギー、縦軸は量子効率である。ここでエネルギー10eV（波長 120nm）では実験値 0.024、文献値 0.02 とほぼ一致し，10ev 以上の測定は妥当であった。しかし、10eV 以下では実験値が文献値と比べ 2 桁以上大きな値となっていた。照射光にはその半波長が 10%程度含まれていることから，長波長領域（120nm 以上）では，この影響が無

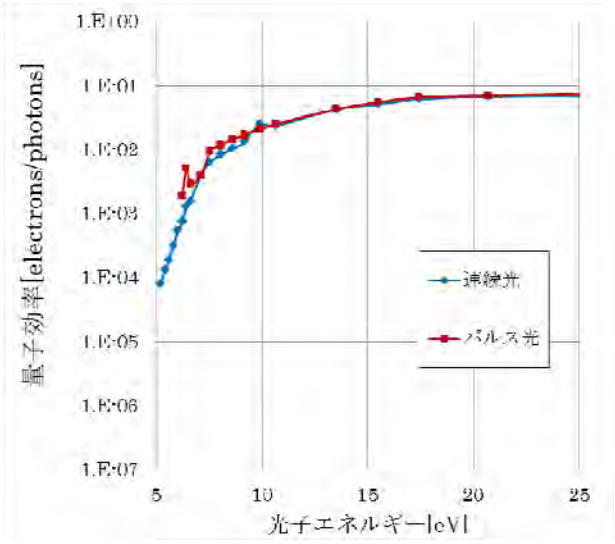

図２：金の量子効率

視できないことがわかった。長波長領域測定時には半波長の影響を防ぐフィルター等の設置が必要であると考えられる。

図２で示したように，連続光とパルス光での測定には差がないことがわかったため，パルス光を用いて，カバーガラスの光放出電流の測定を行った。その際，裏面の空隙により生じる静電容量の影響を検討するため，図 3 に示すようにカーボンテープをアルミ板との接着に用いた。図 4 に光放出電流値（測定単位 pA）を示す。テープが設置された場所と比較して，裏面に導電性のテープがない場合は，光電子電流値の値が二分の一以下となっていることがわかる。このことから、裏面の浮遊容量を小さくすることによって，放出した光電子が絶縁体に引き戻される作用を防ぐことができる可能性が高いことを示すことができた。

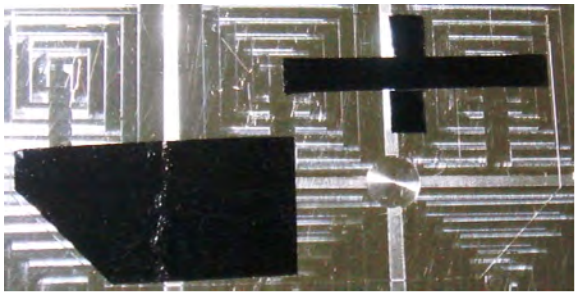

図３：カバーガラス裏面に導電性カーボンテープを装着した様子

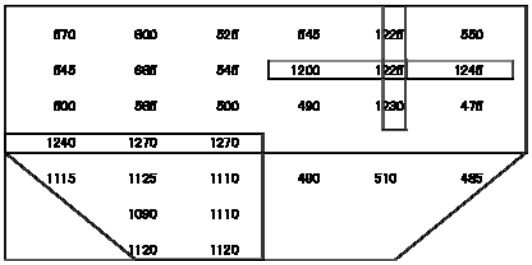

図４：カバーガラスからの光電子電流値［PA］

4 まとめ

衛星表面材料の光電子放出係数測定のための測定方法の検討を行い，以下の結果を得た。

1.今回の測定手法では，連続光とパルス光によって，金属の光電子電流値に違いは生じず、測定系の有効性が確かめられた。

2.絶縁物の測定では，試料裏面の浮遊容量を小さくすることが，試料表面への光電子の戻りを防ぎ，正確な測定を行うのに重要であることが分かった。

謝辞

本研究を行うにあたり、PF スタッフの方々並びに東京工業大学小田切助教，北島准教授には大変お世話になりました。ここに感謝致します。

参考文献

[1]Tateo Goka, “JAXA Space Environment Measurement: Overview & Plan,” 9th Spacecraft Charging Technology Conference, Aug. 2005, pp. 30-35.

[2]T. Muranaka et al., “Development of Multi-Utility Spacecraft Charging Analysis Tool (MUSCAT),” IEEE Transactions on Plasma Science Volume 36, Issue 5, Part 2, Oct. 2008 pp. 2336–2349.

[3]V. Viel and R. Reulet, “Irradiation Facilities and Test Space Technology Course, Space Environment: Prevention of risks related to spacecraft charging,” CEPADUES Editions, ISBN 2 85428 579 4, pp. 285-315, April 2002.

[4]K. Nitta, E. Miyazaki, and M. Takahashi, “Current Status and Future Plan for Material Property Measurements Related to Engineering Design Optimization Guidelines and Spacecraft Charging at JAXA,”11thISMSE, 2009

[5]B. Feuerbacher and B. Fitton, “Experimental Investigation of Photoemission from Satellite Surface Materials,” J. Appl. Phys., Vol. 43, No.4, pp. 1563-1572, April 1972.

[6]K. Ito, Y. Morioka, M. Ukai, and T. Hayashi, "A High-flux 3-M Normal Incidence Monochromator at Beamline 20A of the Photon Factory," Rev. Sci Instrum., Vol. 66, No.2, February 1995, pp. 2119-2121.

[7]B. Feuerbacher and B. Fitton, "Experimental Investigation of Photoemission from Satellite Surface Materials," J. Appl. Phys., Vol. 43, No. 4, April 1972, pp. 1563-350.

[8]J. G. Timsthy, “The solar spectrum between 300 and 1200 A”, Colord Assoc. Univ. press, 1977 , ed by O. R. White, Table 1.

[9]D. F. Heath and M. P. Thekaekara, “The solar spectrum between 1200 and 3000 A”, Colord Assoc. Univ. press, 1977 , ed by O. R. White, Table 2 .

* nitta.kumi@jaxa.jp

11D/2010G522

生物細胞の極紫外イメージングのための固定試料作製法の検討
Investigation of fixed-sample preparation method for EUV imaging of bio-cells

江島丈雄*、根市侑太郎、石田史彦、柳原美廣
東北大学多元物質科学研究所、〒980-8577 仙台市青葉区片平 2-1-1

1 はじめに

極紫外領域における直入射反射光学系の収差は、直入射反射光学系が凹面鏡と凸面鏡を持っているため、容易に補正が可能である。そのため直入射反射光学系は、収差補正による広い視野と使用波長の短さによる高い空間分解能を両立させることができる。視野と空間分解能が両立可能であることから、極紫外領域における直入射反射光学系は半導体産業における縮小露光装置や天体観察用の望遠鏡などに応用されている[1]。

一方で視野と空間分解能が両立した顕微鏡は、生物観察においても非常に有用な観察ツールとなる。例えば、脳における神経細胞はシナプスを介して神経細胞同士が回路を構成し、その回路に基づき複雑な機能を実現している、と考えられている。しかしその回路を実現するには実際に脳を観察して回路を明らかにする必要がある（コネクトーム計画）[2]。このような観察を行うためには、固定した脳に対し、シナプスを分解するだけの空間分解能(数 10nm)と脳を観察できるだけ少ない画像で解析できる視野（数 100×数 100μm^2）が必要となる。

既に開発された波長 13.5nm における露光機[3]や顕微鏡[4]は、この大脳皮質観察に必要な視野と空間分解能を十分に備えている。従来この波長域は、生物構成元素の吸収端から外れているため、観察には不向きであると考えられてきた。しかし、実際は生物構成元素の吸収断面積の差が大きいため、観察に必要な透過像のコントラストは十分に確保できると考えられる[5]。一方で、酸素による吸収が強いため、細胞程度の厚さの試料を透過できない、という問題が存在する[5]。

強すぎる酸素の吸収を減らす簡便な方法は、細胞中に含まれる水を除去し、その薄切を行うことである。この方法を採れば、試料全体の透過率が上がり、かつ炭素と窒素によるコントラストが確保できる。一方で、この波長域での生物細胞観察例が少なく、充分なコントラストを確保するための試料厚さ、固定方法、染色方法が分からない。今回は、水分量を減らす試料作製法として電子顕微鏡観察用の試料作製方法を採用し、その中で最適な試料厚さ、固定方法、染色方法を比較する。

2 固定細胞観察のための条件探索

2-1 最適試料厚さの決定

まず試料厚さと染色法の異なる試料を撮影し、コントラスト、透過率を評価し、最適な試料厚さを求めることにした。測定試料にはマウスの大脳皮質を用いた。2%パラホルムアルデヒド、2.5%グルタルアルデヒド、1%四酸化オスミウムによって固定し、Reynolds 法[6]によりブロック染色（以降、ブロック染色試料と呼ぶ）した。その後脱水・包埋後、ウルトラミクロトームにより 200 nm と 500 nm に薄切した。薄切した後、ブロック染色のままの試料と、更に Reynolds 法で再度染色[6]を行った試料（以降、電子染色試料と呼ぶ）の計 4 種類の試料を用意した。

用意した試料はそれぞれ我々の開発した透過型の軟 X 線顕微鏡 TXM[3] を用いて[4]、YAG レーザー 20shot（10 shot/sec）露光して得られた像を 5 枚撮像し、それらを平均して軟 X 線透過画像とした。得られた画像は、同様に撮影した I_0 像で規格化し、透過率像とした。その結果、オルガネラの判別が可能なコントラストを得ることができた。

得られた透過率像からオルガネラとして核を、透過率の基準として血管を選び、それぞれの透過率から核のコントラストを求めた。さらに、得られた透過率と試料厚から、それぞれの吸収係数 α を求め、試料厚によるコントラスト C と透過率 T の変化を計算で算出した。得られた試料の透過率 T とコントラスト C を図 1 に示す。得られた結果から、透過率を高くするとコントラストが下がり、透過率を低くとるとコントラストが上がることが分かる。また、染色法が異なってもおおよそ 400nm 前後の厚さで透過率とコントラストが均衡した。

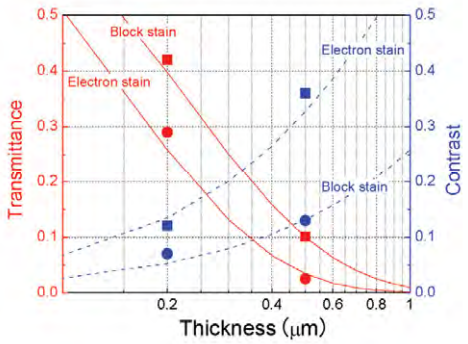

図 1：ブロック染色と電子染色したラット肝臓の 200nm 厚試料と 500nm 厚試料における生物核の透過率（赤実線）と血管に対するコントラスト（青破線）

2-2. 各オルガネラの透過率とコントラスト

2-1 節の結果に基づき厚さを 400 nm と固定し、２つの異なる準備法で作製したラットの肝細胞の主要なオルガネラの透過率、コントラストの比較を行った。作製したラットの肝細胞は、酢酸ウラニル染色法を用いて染色した試料[7]と、染色を避けるために、染色作用のある重金属を含む薬剤を使用せずに固定、包埋した試料[8]、の２つである。測定には、我々の開発した密着型顕微鏡を用いた。光源には Photon Factory BL11D ビームラインを用い、$\lambda/\Delta\lambda = 500$、露光時間 40 ~ 360 秒で、波長を変えて測定を行った。得られた透過像は露光時間で規格化した後、2-1 節と同様の手順により透過率像を得た。

それぞれの試料を観察した結果を図２に、すべての試料の透過率とコントラストを図３に示す。ウラニル染色試料では、非染色試料に比べて透過率のばらつきが小さくオルガネラ毎のコントラストの差の小さい２値画像のような像が得られた。一方、非染色試料ではオルガネラ毎に異なる透過率と異なるコントラストの像が得られた。

2-3. 細胞核における透過率の波長依存

2-2 節の結果から、オルガネラの相違より試料準備法の違いが像の質に与える影響が大きいと考え、比較するオルガネラを細胞核に絞って、各種の試料準備法の比較を行った。試料の作製法については、表中の reference を参照してほしい。

測定を行った試料を表 1 に示す。測定条件は 2-2 節と同じである。測定の結果、得られた細胞核の透過率を図 4 に示す。測定した試料のうち、サンプル D のエポキシ包埋を行って染色を行わなかった試料に関しては、オルガネラが区別できず、透過率を得ることができなかった。それ以外の試料は、すべて波長が長くなるにつれて、透過率が単調に減少した。これは、試料を構成する元素が測定した波長域で内殻準位を持たないことによる。酢酸ウラニルで染色した試料だけは、波長域 10nm 付近で透過率の減少の程度が増し、12~13nm で増減を繰り返し、ピーク構造を２つ示した。この構造は、染色に用いたウラン元素の内殻 $O_{4,5}$ 吸収端による構造と考えられる。

コントラストを求める際の比較対象とした血管の透過率は、ほぼ図 4 の細胞核と同じスペクトル形状を示した。その中で酢酸ウラニルだけは比較的高い透過率を示した。しかし細胞核で観察された U-$O_{4,5}$ 吸収端構造はほとんど観測されなかった。

3 評価関数による試料作製法の評価

実験結果に基づき最適な試料条件を決定するための評価関数を導入する。今、CCD 上に結像された物体が像として認識される場合を考えると、その物体像は背景像に対してコントラストがついていなければならない。これを背景の光子数に対する物体の光子数の差で表し、両者のコントラスト C とその平均光子数 $\overline{N}$ を用いて

$$2C\overline{N}$$

と近似する。今、検出される光子数が十分多いと仮定すると、物体像のノイズは光子数の揺らぎ σ_N によって表される。検出される光子はポアソン分布に従うので、その標準偏差 $\sqrt{\overline{N}}$ が光子数の揺らぎ σ_N を表す[27]。この時の SN 比は、

$$SN = \frac{2C\overline{N}}{\sqrt{\overline{N}}} = 2C\sqrt{\overline{N}}$$

と表される。平均光子数 $\overline{N}$ は、照明光強度、光学系のスループット、試料透過率 T、露光時間に依存するが、照明光強度、露光時間などを一定と仮定すると、平均光子数は試料の透過率に比例する。よって平均光子数を試料透過率 T に置き換えると、SN 比は

$$SN \propto C\sqrt{T}$$

となり、コントラスト C と透過率 T で表すことができる。以降これを評価関数と呼ぶ。

	Uranyl acetate stain	Lead citrate stain	Hema-toxylin stain	Non stain
Epoxy embedding	A [7]	B [6]	C [9]	D [10]
Acrylic embedding	×	×	×	E [8]

表 1： 測定したラットの肝細胞の包埋法、染色法一覧。試料厚さはすべて 400nm。

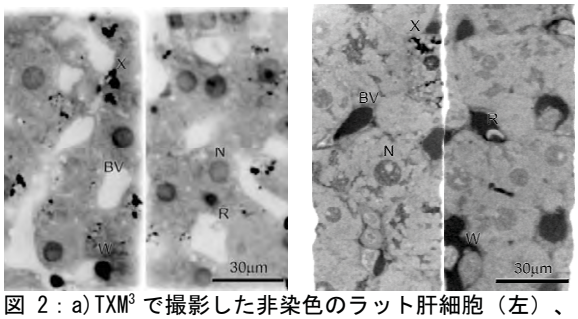

図 2：a)TXM[3] で撮影した非染色のラット肝細胞（左）、b)ウラニル染色したラット肝細胞（右）。N:核、BV:血管、W:洞様血管壁細胞、R:赤血球、X:不明

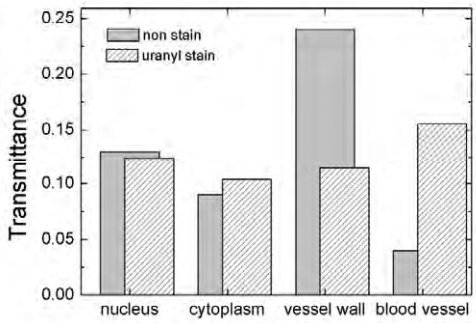

図 3：図 2 の軟 X 線像から求めた核、細胞質、血管壁細胞、血管の透過率。

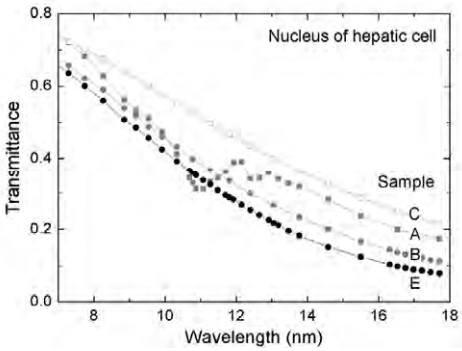

図4：各種試料における細胞核の透過率。

評価関数$C\sqrt{T}$を用いて最適な試料膜厚を評価する。図 1 に示した透過率と試料厚から、それぞれの染色法における生物核と血管の吸収係数aを求め、試料厚によるコントラストCと透過率Tの変化を計算した。以降、コントラストの基準はすべて血管の透過率である。得られた結果から評価関数を求めた結果を図 4 に示す。得られた曲線は、膜厚が増えるに従って SN 比が良くなり、最大値を示した後に減少する。それぞれの試料における SN 比が最大となる試料厚 d は、ブロック染色試料の場合が 300～700nm で、ブロック染色＋電子染色試料が 200～500nm であった。両染色法に共通する試料厚さとして 300～500nm が得られた。

同様に、試料厚さ 400nm に固定したウラニル染色とアクリル包埋をした２つのマウス肝臓試料について、それぞれのオルガネラにおける評価関数$C\sqrt{T}$を算出した。得られた結果を図５に示す。アクリル包埋試料はウラン染色試料よりも、各小器官において高い SN 比が得られた。これは、波長 13.5nm の軟 X 線にはウラン染色を行った試料よりも非染色試料の方が観察に適していることを意味している。

図６の評価関数の比較から、オルガネラの差よりも染色法の差の方が大きな違いがみられたことから、図４の細胞核における各染色法の評価関数の違いを図７にプロットした。得られた結果から、アクリル包埋のみで染色を行わなかった試料が波長 7 ～ 14.5nm の範囲で高い値を示した。また 14.5～18nm

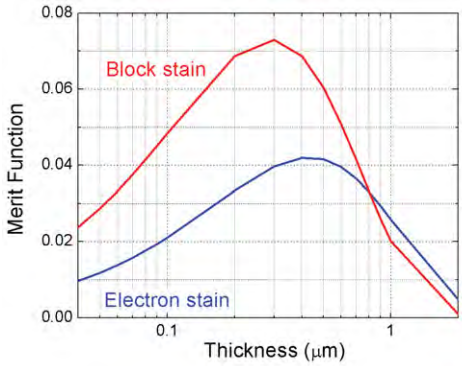

図5：図１から求めた各染色法の評価関数

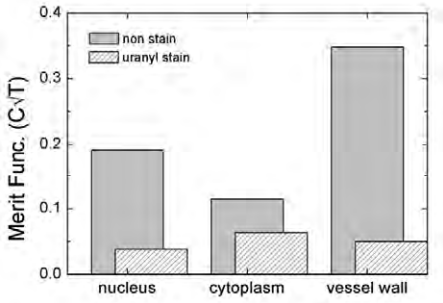

図6：図3から求めた波長13.5nmにおける評価関数

間では、Reynolds 法による鉛染色が良い値を示した。以上から、極紫外領域における透過像観察用の試料は、波長により最適な試料準備法が異なると考えられる。

4 考察

2 節の実験結果から、極紫外域において透過像により生物細胞を観察する際に、①最適な試料厚さは、透過型電子顕微鏡を用いて観察する場合の最適な厚さより６～７倍程度厚いこと、②乾燥・固定のみで染色しない試料を用いた観察が、より高いコントラストと、バックグランドに対してより多い光子数を与えること、が明らかとなった。

最適な試料厚さは、当初実験結果に基づき透過率とコントラストがほぼ等しい膜厚を選択した結果である。その後、3 節において導入した評価関数による評価結果から、この選択が、検出器に到達する光子数がバックグランドに対して十分大きくかつオルガネラ間のコントラストが最も大きくなる条件であることを示した。以上から、像の評価をする際の簡便な指標として、図 1 のように透過率とコントラストが同程度に寄与する画像を選べばよいことが考えられる。

非染色試料が②のような結果を得たのは、もともと生物を構成する元素の吸収が極紫外域で大きいことと、かつ観察した生物細胞内のオルガネラ間に大きな密度の差があるためである。一方で酢酸ウラニルなどの重金属で染色した場合の試料観察は、金属による吸収が大きく、かつ金属が特定のタンパク質を通してオルガネラと結びつくため、得られた画像は２値画像のような像となった。

また②の結果を得た際に導入した評価関数は、任意の２つの物体間の光子数とコントラストのみに注目し、それらの物体間の空間的スケールは任意であった。今回は比較的視認しやすい大きなオルガネラを選んで評価したため、そのオルガネラ間の距離は空間分解能よりもかなり大きい。従って得られた結果は、比較的大きなオルガネラ間の視認性のみに基づいている。今後、サンプル作製法に空間分解能程度の視認性を要求する場合には、物体間の距離を含んだ評価関数の方が望ましい。そのような試料では、むしろ今回はあまり評価の高くなかった染色試料の

方が、よい結果を与える可能性もある。このような評価関数には、例えば空間周波数に対するパワー値などを用いると良いだろう。

5 まとめ

従来軟 X 線顕微鏡の開発の動機は「水の窓」波長域における「生きた」生物細胞観察であったが、得られた結果は、波長 13.5nm で動作する軟 X 線顕微鏡が固定生物細胞観察に応用できることを示している。このような顕微鏡は、EUVL 技術の進展により、徐々に入手可能になると考えられるので、今後生物系への応用が期待される。今回の結果は、そのような観察には単純な電子顕微鏡用試料で観察するよりももっと情報量の多い試料作製法があることを示した。このような観察はコネクトーム計画のような、多くの細胞試料を広視野、高空間分解能で撮像しなければならない分野に最適な方法となるだろう。

謝辞

東北大学医学系研究科の河和善准教授、東京大学総括プロジェクト機構の水谷治央助教には試料を提供していただきました。また東北大学医学系研究科共通機器室の皆様には、試料作製についての多大なる御指導と御支援をして頂きました。ここに記して深く感謝申し上げます。

参考文献

[1] [1] D. Attwood, Soft X-rays and extreme ultraviolet radiation, (Cambridge University Press, Cambridge, 2000) Chap.4.
[2] O. Sporns, G. Tononi, and R. Kötter, PLoS Comput. Biol. 1, (2005) e42.
[3]P. P. Naulleau, K. A. Goldberg, E. Anderson, J. P. Cain, P. Denham, K. Jackson, A.-S. Morlens, S. Rekawa, and F. Salmassi, J. Vac. Sci. Technol. B 22(6), 2962-2965.
[4] T. Ejima, F. Ishida, H. Murata, M. Toyoda, T. Harada, T. Tsuru, T. Hatano, M. Yanagihara,M. Yamamoto, and H. Mizutani, Opt. Exp. 18, (2010) 7203-7209.
[5] http://henke.lbl.gov/cgi-bin/mldata.pl
[6] E. S. Reynolds, J. Cell Biol., 17 (1963) 325.
[7] 4%パラホルムアルデヒド、2.5%グルタルアルデヒド、1%四酸化オスミウムによって固定した後、1%酢酸ウラニルによりブロック染色する。その後エタノールにより脱水し、エポキシ樹脂に包埋後、ウルトラミクロトームにより 400nm に薄切した。
[8] 四酸化オスミウムによる固定を行った後、4%パラホルムアルデヒド、2.5%グルタルアルデヒドによって更に固定し、アクリル樹脂に包埋した。
[9] P. Mayer, Mitt Zool Stat Neapel, 10 (1981), 170-186.
[10] 4%パラホルムアルデヒド、2.5%グルタルアルデヒド、1%四酸化オスミウムによって固定した後、エタノールにより脱水し、エポキシ樹脂に包埋。ウルトラミクロトームにより 400nm に薄切した。

* ejima@tagen.tohoku.ac.jp

9A/2010G604

バイカル湖の湖底堆積層のヒ素の XAFS 分析
XAFS analysis of arsenic in Lake Baikal sediment

村上拓馬 [1*], 勝田長貴 [2]
[1] 金沢大学環日本海域環境研究センター、〒923-1224 能美市和気町オ 24
[2] 岐阜大学教育学部、〒501-1193 岐阜市柳戸 1-1

1 はじめに

バイカル湖はシベリア南東部に位置し、世界最大の淡水湖であり、その湖底堆積物にはアジア大陸内陸部で生じた環境変動の情報が詳細に記録されている。このうち、ウラン（U）に関しては、全球的な気候変動指標との相関性が高いことから、還元固定元素は環境変動指標と成り得ることが指摘されている。しかし、還元固定元素は、湖底に埋没後の続成作用による酸化還元状態の変化で、移動・集積する可能性があるため、この影響を評価することは古環境復元において重要である。

今回、我々は、新たな環境変動指標を見出すために、ウランと同じ還元固定元素の 1 つであるヒ素（As）に着目し、湖底表層から深度 39 cm にかけて XAFS 分析と定量分析を実施し、続成作用の影響を評価した。

2 実験

本研究で使用した堆積物中コア試料は、バイカル湖南部のセレンガデルタ沖で採取された BSS06-G2（全長 39 cm）である。このコアは採取後、酸化還元状態を維持するために、未開封のまま国内に移送し冷凍保存した。試料の分取作業については、大気による酸化を防ぐため、窒素雰囲気下のグローブボックス内にて、コアを深度方向に 1 cm 間隔で分取し、XAFS 分析用試料についてはシーラーを用いて酸素不透過性フィルムにより密封し、測定時まで冷凍保存した。なお、本実験では、11 試料（0-1、1-2、2-3、4-5、10-11、14-15、20-21、24-25、30-31、34-35、38-39 cm）を分析した。

XAFS 分析ついては BL9A にて蛍光法により行った。入射 X 線のエネルギー範囲を 11.830-11.930 (kev)、その分解能を 0.5 (eV)とした。照射面積は縦横 1 × 1 (mm^2)とした。得られた蛍光 X 線を 19 素子 Ge 半導体検出器により検出した。エネルギー軸の較正には、KH_2AsO_4 の K 吸収端のピーク（11.865 keV）を用いて行った。

定量分析については、Tessier の逐次抽出法[1]により抽出した As を ICP-MS を用いて定量した。本報告では、各抽出態の総量を全岩濃度として示す。

3 結果および考察

BSS06-G2 の As の XAFS スペクトルを図 1 に、As^{III} と As^{V} の K 吸収端ピークの解析から決定した $As^{III}/(As^{III}+As^{V})$ 比[2]と As 濃度の変動曲線を図 2 に示す。As は、表層（0-2 cm）で $As^{III}/(As^{III}+As^{V})$比が 0.2 未満であるのに対して、それ以深では 0.5 以上を示す。このことから、湖底堆積層は深度 2-3 cm の間で As^{V} が As^{III} に還元される環境となることが分かる。一方、As 濃度は、7-25 ppm の範囲で変動するが、$As^{III}/(As^{III}+As^{V})$比が増加する 2-3 cm 部分で大きく濃度変化しない。これは As が湖底に埋没後の続成作用により移動・集積していないことを意味する。したがって、バイカル湖湖底堆積物の As 含有量の変動は、堆積当時のバルク濃度を反映していることが示唆される。

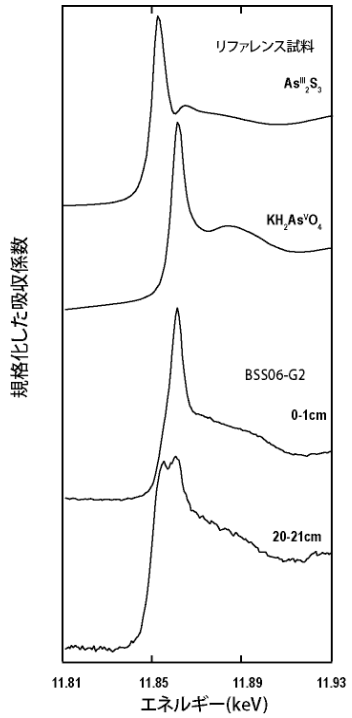

図 1 ：BSS06-G2 の As の XAFS スペクトル

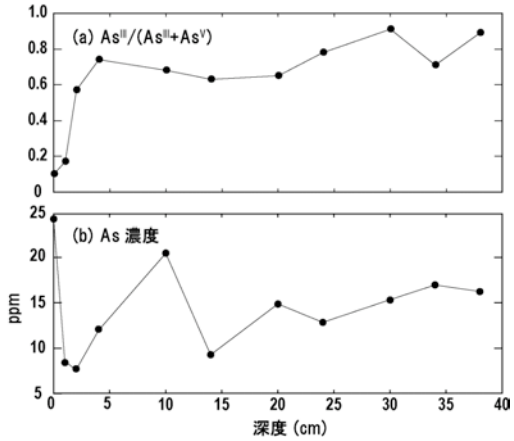

図 2：BSS06-G2 の As の(a)酸化数比と(b)濃度の深度分布

謝辞

阿部仁氏、丹羽尉博氏、仁谷浩明氏には、測定システムのセットアップ、測定中のトラブルの対処など、本実験にあたって多大な支援を受けました。ここに深く感謝致します。本研究は、財団法人日本科学協会の笹川科学研究助成ならびに住友財団 2010 年度環境研究助成による支援を受けて行われたものです。ここに感謝致します。

参考文献

[1] A. Tessier *et al.*, Anal. Chem. **51**, 844-851. (1979)
[2] Y. Takahashi *et al.*, Environ. Sci. Technol. **38**, 1038-1044. (2004)

* takuma@llrl.ku-unet.ocn.ne.jp

4B2/2011G015

Particle statistics in rotating-specimen powder diffractometry

Takashi IDA*
ACRC, Nagoya Inst. Tech., Asahigaoka, Tajimi, Gifu 507-0071, Japan

Introduction

Powder X-ray diffractometry has been utilized in identification, qualitative and quantitative analyses of minerals and synthesized materials, including natural resources, ceramics, metal, alloys, and pharmaceutical products. Discussions about the accuracy and reliability of powder diffraction analysis are practically getting more important, but theoretical difficulty about particle statistics, particularly for continuously rotating specimens, still remains. De Wolff has already suggested a theory about particle statistics for rotating specimens [1]. The effective numbers of diffracting crystallites for stationary and rotating specimens in reflection mode measurements have been expected to be proportional to cosecθ and cosec$^2\theta$, respectively, for the diffraction at the Bragg angle θ. However, it is difficult to justify the assumptions made by de Wolff, and the theory has not been justified by any experiments. The angular dependence of the particle statistics has been experimentally investigated in this study.

Experimental

A cylindrical sample holder was filled with standard LaB_6 powder (NIST SRM 660a), the volumetric median particle diameter of which has been estimated at 10 μm by a laser scattering analysis. The bulk penetration depth for the synchrotron X-ray at the wavelength of 0.1197 nm is estimated at μ^{-1} = 18 μm.

A high-resolution powder diffractometer at the beam-line BL-4B2 at KEK-PF was used for the diffraction measurements in flat-specimen reflection mode. The Ω -scan intensity profiles of 23 LaB_6 reflections were recorded on stepwise rotation of the powder specimen about the Ω–axis of the diffractometer. A couple of Ω-scan profiles measured for a stationary and (in-plane) rotating specimens were compared for each reflection.

Results

Figures 1 (a) and (b) show the dependence of the observed effective number of diffracting crystallites (N_{eff}) evaluated for the symmetric condition ($\Omega = \theta$), divided by the effective multiplicity of reflection (m_{eff}) evaluated by the analysis of Ω–scan diffraction intensity profile of the LaB_6 reflections measured for the stationary and rotating specimens, respectively. The observed dependences on 2θ are both fitted by a model profile:

$$N_{eff} / m_{eff} = (N_{eff} / m_{eff})_0 \text{ cosec } \theta.$$

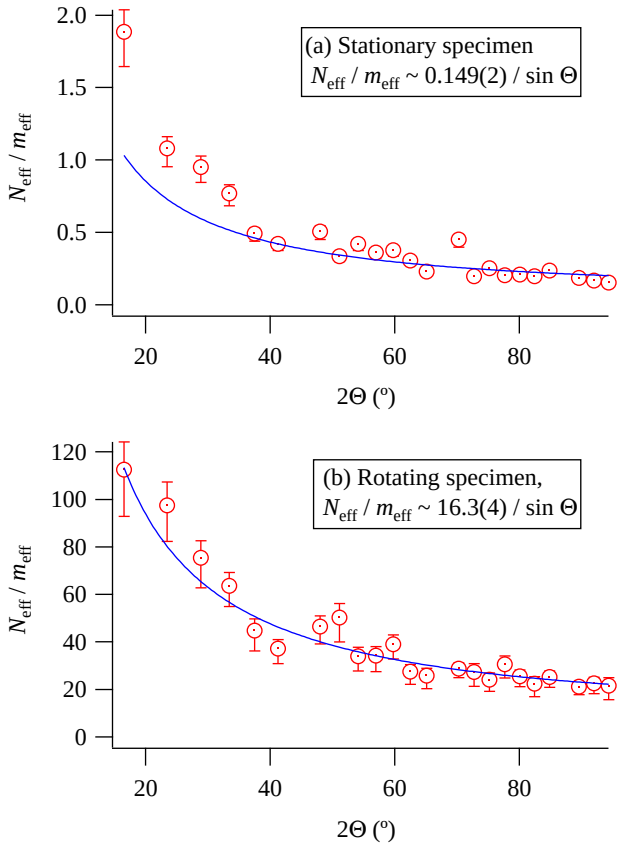

Fig. 1 2Θ-dependence of the effective number of diffracting crystallites divided by the effective number of multiplicity (N_{eff} / m_{eff}) evaluated by Ω–scan diffraction intensity measurements for (a) stationary and (b) rotating specimens of LaB_6 powder.

It has been confirmed that the effective number of diffracting crystallites appears to be increased by rotation by a factor of 100 over the observed angular range.

However, the experimental 2Θ-dependence of N_{eff} / m_{eff} for the rotating specimen (Fig. 1(b)) appears to be almost proportional to cosecΘ, rather than cosec^{2}Θ, contrary to the prediction from the theory of de Wolff.

Even though the experimental results do not necessarily mean that the assumption of de Wolff should thoroughly be rejected, it is concluded that we can practically apply the cosecΘ-dependence for maximum-likelihood analysis of powder diffraction data for rotating specimens.

References

[1] P.M. de Wolff, Appl.Sci.Res. B 7, 102 (1958).

* ida.takashi@nitech.ac.jp

11B/2011G174

Organochlorines in Surface Soil at Wire Burning and Metal Contribution by means of Quantitative X-ray Speciation

Takashi Fujimori[1,2,*], Hidetaka Takigami[1] and Masaki Takaoka[2]
[1]National Institute for Environmental Studies, 16-2 Onogawa, Tsukuba, 305-8506, Ibaraki, Japan
[2]Kyoto University, Katsura, Nisikyo-ku, 615-8540, Kyoto, Japan

1 Introduction

Toxic chlorinated aromatic compounds (aromatic-Cls) were known to be produced by various anthropogenic thermal processes. Recent studies found high concentration of aromatic-Cls in soil at wire burning sites (WBS) [1]. Workers recovered relative pure metals (especially copper) through the wire burning which was conducted by direct oil burning of various wires and cables from dismantled electronic-wastes on natural soil surface. Chlorine K-edge near-edge X-ray absorption fine structure (NEXAFS) enables us to detect the specific chemical form of Cl [2,3] and to estimate the amount of Cl present by using a spectrum jump [4] in the solid phase. In this study, we applied quantitative X-ray speciation of Cl to study the mechanisms of aromatic-Cl formation in surface soil at WBS in Southeast Asia.

2 Experiment

We collected environmental soil samples around Metro Manila, the Philippines (PHI), at August, 2010, and around Hanoi, Vietnam (VN), at January, 2011.

Powdered soil samples were mounted on carbon tape. We measured Cl K-edge NEXAFS spectrum of each sample between 2810 and 2860 eV detected by X-ray fluorescence using BL-11B in Photon Factory (Tsukuba, Japan). We used "difference between intensity at 2850.8 and baseline at pre edge" (denoted by "Δμt") of raw Cl K-edge NEXAFS spectrum to quantify total chlorine concentration (ppm) in a soil sample referred a calibration curve (1~1,400 ppm) by Leri et al. [4]. Δμt was thought to be useful indicator as Cl quantification below non-measurable range by ordinary XRF method. In this study, ratios of Cl chemical forms in soil sample were analyzed by linear combination fitting (LCF) by using inorganic chlorides, metal chlorides, and organic chlorides. Organic chlorides showed quite similar NEXAFS spectra depending on aliphatic and aromatic structures [2, 3]. So, we used representative chemicals such as 2,3-chlorophenol (aromatic) and polyvinyl chloride (aliphatic). To understand variability of LCF result, we examined 5 types of fitting range (2810~2830, ~2835, ~2840, ~2845, ~2850 eV). We calculated average and standard deviation of 5-types fitting results. Through combination concentration of total Cl by Δμt with ratio of chlorinated aromatic compound by LCF, concentration of aromatic-Cls was estimated.

3 Results and Discussion

We attempted to apply quantitative speciation by using Cl K-edge NEXAFS to estimate total Cl content, chemical form of Cl, aromatic-Cls concentration, and correlationship in relation to formation mechanism of aromatic-Cls in various soils at WBS. Quantitative speciation of Cl revealed aromatic-Cls concentration in environmental soil at WBS. Fig. 1 shows that blacken soil at WBS concentrated the highest aromatic-Cls. Compared with previous global measurements of natural aromatic-Cls concentrations [6], blacken and non-black soils at WBS had higher concentrations than a maximum value (360 mg/kg) among natural soils in 26 sampling sites denoted by Natural (World). We also explored the relationship between aromatic-Cls and chlorides of heavy metals. Heavy metals are well-known promoters of the thermochemical solid-phase formation of aromatic-Cls [5]. Although we need to study measurement accuracy of this analytical technique, Cl-connected compounds are able to be quantified with wide concentration range and we are possible to apply the quantitative speciation of chlorine to various environmental solid matrices.

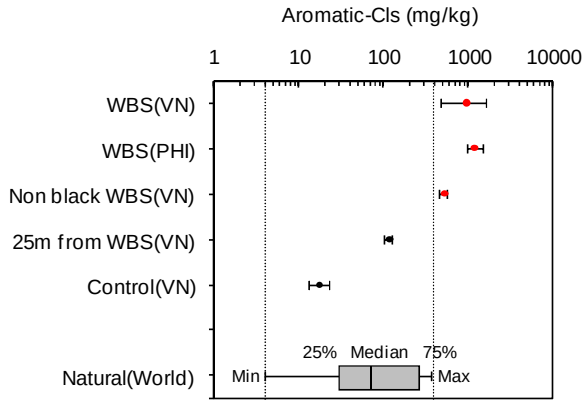

Fig. 1: Amount of aromatic-Cls by quantitative speciation of Cl K-edge NEXAFS.

References

[1] C. S. C. Wong *et al*., Environ. Pollut. **145** (2007) 434.
[2] S. C. B. Myneni, Science **295** (2002) 1039.
[3] T. Fujimori *et al*., Anal. Sci. **26** (2010) 1119.
[4] A. C. Leri *al*., Anal. Chem. **78** (2006) 5711.
[5] T. Fujimori *et al*., Environ. Sci. Technol. **43** (2009) 8053.
[6] G. Asplund and A. Grimvall, Environ. Sci. Technol. **25** (1991) 1346.

* fujimori.takashi.3e@kyoto-u.ac.jp

9A, 11B/2011G174

Relationship between PM emitted from MSWI plant and $PM_{2.5}$ in ambient air around plant about chemical states of sulfur and chlorine

Kenji Shiota*, Genya Imai, Kazuyuki Oshita and Masaki Takaoka
Kyoto University, Nisihkyo-ku Kyoto 615-8540, Japan

1 Introduction

It has been thought that municipal solid waste incinerator (MSWI) plant is one of the major stationary sources for particulate matter (PM) emission. However, PM emission from MSWI plants might be decreasing because of introduction of state-of-the-art flue gas treatment equipments for dioxins control, and there have been limited reports to measure amount of PM emission in recent year. It is important to understand present PM emission from MSWI and contribution of the emission to PM in air. This report aims to investigate relationship between PM from MSWI and $PM_{2.5}$ in ambient air around MSWI plant by analyzing chemical form of sulfur (S) and chlorine (Cl) in PM from MSWI by XAFS Spectroscopy.

2 Experiment

PM samples emitted from MSWI plant were collected in nine particle size fractions (from sub μm to about 10 μm) by an Andersen stack sampler (Tokyo dylec corp., AS-500) inserting into the flue gas ducts at the inlet of the stack [1]. $PM_{2.5}$ samples in the air around the plant were collected in one fraction under 2.5μm size particles ($PM_{2.5}$) by Low Volume Sampler (Tokyo dylec corp., FRM2000).

XAFS spectroscopy for sulfur (S) K-edge and chlorine (Cl) K-edge in the PM and $PM_{2.5}$ samples were carried out by CEY or TEY, and FY modes at 9A and 11B.

3 Results and Discussion

The XAFS spectra of S and Cl in the samples are shown in Fig. 1. According to S K-edge NEXAFS spectra, sulphate was predominant in both of PM from the plant and $PM_{2.5}$ in the ambient air. The spectra of PM from the plant had similar shapes in each particle size. The energy of whiteline peak top in the spectra of $PM_{2.5}$ in the air shifted lower than that of PM from the plant, so chemical states of $PM_{2.5}$ in the air were different from that of PM from the plant. It was inferred that sulphate in $PM_{2.5}$ in the ambient air is predominantly $(NH_4)_2SO_4$ and that in PM from the plant is predominantly $NaSO_4$ from results of ion chromatography and whiteline peak shift [2] [3].

Cl K-edge NEXAFS spectra showed that PM from the plant contained predominantly Cl as NaCl in each particle size. On the other hand, the spectrum of $PM_{2.5}$ in the ambient air had also absorption on about 2820 eV, lower energy than absorption of NaCl. Cl-K edge spectra in organic chlorine compounds have lower absorption energy than that of inorganic compounds [4], so that $PM_{2.5}$ in the ambient air might contain organic chlorine compounds.

In conclusion, chemical states of S and Cl in $PM_{2.5}$ in ambient air around MSWI plant were different from those in PM from MSWI plant, and this suggested that PM emission from MSWI plant do have little impact to $PM_{2.5}$ if contribution of secondary formed particles from gas phase is not considered.

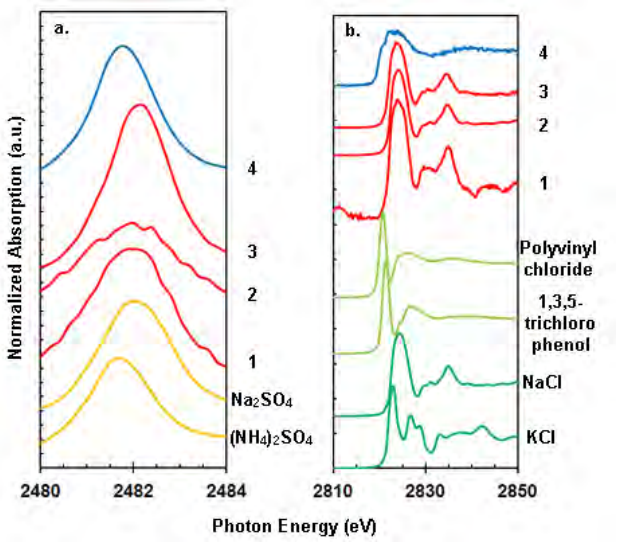

Fig. 1: NEXAFS spectra of PM from MSWI plant and $PM_{2.5}$ in ambient air around MSWI plant. a.:S K-edge, b.:Cl K-edge. 1~3 : PM from MSWI plant, 1: 1.0~2.0 μm, 2: 0.40~0.58 μm, 3: <0.40 μm. 4:$PM_{2.5}$ in ambient air around MSWI plant

Acknowledgement

This report was supported by the research grant 220002 from Osaka Bay Regional Offshore Environmental Improvement Center. We thanks T. Fujimori and the PF staffs for their support in Proposal No.2011G174.

References

[1] Shiota *et al.*, J. Japan Soc. Atmos. Environ. **46** (2011) 224 (in Janapese)
[2] Osan *et al.*, Atmospheric Environment **40** (2006) 4691
[3] Higashi *et al.*, Environ.Sci.Technol. **43** (2009) 7357
[4] Fujimori *et al.*, BUNSEKI KAGAKU **58** (2009) 221 (in Japanese)

* shiota.kenji.4x@kyoto-u.ac.jp

9A/2011G577

有機質肥料活用型溶液における植物への Fe 供給方法の開発
A study on developing Fe supply method to the plant in hydroponics with organic fertilizer

松井直樹[1]・村上拓馬[2]・勝田長貴[3]・高野雅夫[1*]
[1]名古屋大学大学院環境学研究科 〒464-8601 名古屋市千種区不老町
[2]金沢大学低レベル放射能実験施設　〒923-1224 石川県能美市和気町オ 24
[3]岐阜大学教育学部 〒501-1193 岐阜市柳戸 1-1

1 はじめに

化学肥料原料の枯渇が懸念され、また土壌中の肥料成分が地下水や河川に流出し、地下水や湖沼、内湾の汚染・汚濁が進行していることは、現在の農業が抱える大きな問題点である。有機質肥料活用型溶液栽培法[1]は、有機質肥料のみで栽培が行えるため化学肥料を使用する必要がなく、水耕栽培という閉鎖系で栽培を行うため肥料成分が流出することもない。しかし、本技術では植物の育成に必須となる Fe^{2+}が不足し、作物が鉄欠乏症を引き起こす問題がまだ解決されていない。Fe は溶液中に溶解している場合、主に Fe^{2+}の状態で存在するが、溶液中で酸素に触れると容易に酸化され Fe^{3+}となって沈殿してしまう。本技術では養液内を好気的に保っているため、Fe が溶出しにくく、また溶液中の Fe^{2+}も沈殿しやすい状況ができている。しかしながら、砂糖を精製した際に発生する廃糖蜜をカキやホタテの貝殻に混ぜた混合物を溶液に投入することで、好気的条件下でも Fe^{2+}の溶出が促進されることが経験的に知られている。ここでは、なんらかのキレート形成が起こっていると予想されるものの、その実態はまったく不明である。そこで、本研究では、カキやホタテの貝殻中の Fe、および廃糖蜜と混合した貝殻や Fe^{3+}試薬およびそこから溶出した Fe の X 線吸収微細構造（XAFS）分析を行い、Fe が溶出される前後での酸化数の変化ならびにその化学状態を明らかにすることを目的とする[2]。

2 実験

実験で用いた試料は、本技術で使用している肥料として、(1)カキの貝殻で作ったセルカ（ト部産業社製）と(2)それを粉末状にして廃糖蜜で固化した粒状セルカ、(3)粉末状のホタテの貝殻を廃糖蜜で固化したネオライム（ト部産業社製）である。廃糖蜜の還元作用を確認する試料としては、(4) Fe^{3+}試薬（FeOOH）と廃糖蜜の混合物（混合比 1:2、1:1、2:1）と(5)そこからの溶出した溶液を準備した。(5)は、0.1 g の Fe^{3+}試薬に 50 %に希釈した廃糖蜜溶液 8 ml を加え、蒸留水で 48 ml に調製する。その後 10 日間静置し、毎分 4000 回転の遠心分離を一分間行い、その上澄み液を測定試料とした。

XAFS 測定は BL9A にて蛍光法で行った。入射 X 線は 7.060-7.200 (kev)の範囲を 0.4 (eV)の分解能で走査した。照射面積は縦横 1 × 1 (mm^2)とした。試料から放射された蛍光 X 線強度の測定は、ライトル検出器を用いて、取り込み時間 2 (sec)で行われた。エネルギー軸の較正には、Fe 箔の K 吸収端（7.1112 keV）を用いて行った。Fe の酸化数の決定には、プレエッジピークの重心[3]により求めた。

3 結果および考察

こ Fe の吸収端プレエッジピークの結果を図 1 から 3 に示す。これらのスペクトルを解析した結果、Fe(II)と Fe(III)の割合は、セルカが 31.8 %と 68.2 %、粒状セルカが 49.0 %と 51.0 %、ネオライムが 74.8 %と 25.2 %となった。また、Fe^{3+}試薬（FeOOH）と廃糖蜜の混合物は、混合比によらずほぼ等しく、Fe(II)が約 10 %、Fe(III)が約 90 %であった。また、混合物からの溶出液は、Fe(II)が 57.2 %、Fe(III)が 42.8 %であった。

れ Fe^{3+}試薬（FeOOH）と廃糖蜜の混合物は、水に溶かさずに作成したものであり、その混合物から Fe(II)の存在が確認されたことは、廃糖蜜により Fe^{3+}試薬が還元されたことを意味する。さらには、セルカを廃糖蜜で固化した粒状セルカのほうが、セルカそのものに比べて、Fe(II)の割合が増加していることからも、廃糖蜜による還元作用が示唆される。さらには、Fe^{3+}試薬（FeOOH）と廃糖蜜の混合比を変えても、Fe の酸化数に変化が見られなかったことから、廃糖蜜による Fe の還元反応は物質表面でのみ生じていると見なされる。Fe^{3+}試薬（FeOOH）と廃糖蜜の混合物から溶出した溶液の XAFS 測定からは、廃糖蜜により溶出された Fe は、Fe(II)としてだけでなく Fe(III)の状態でも溶出されている可能性が示唆される。

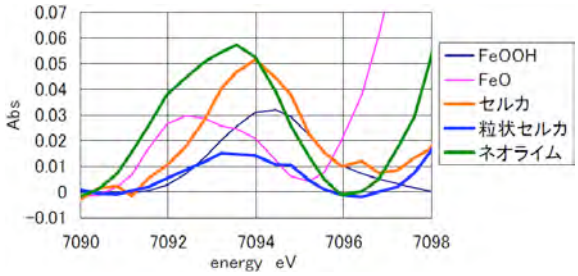

図 1. 有機石灰の Fe 吸収端プレエッジピーク：セルカ；粒状セルカ；ネオライム。

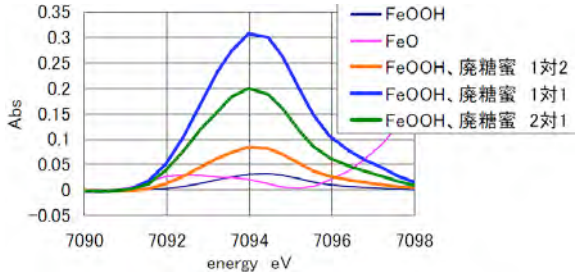

図 2. Fe^{3+}試薬（FeOOH）と廃糖蜜の混合物の Fe 吸収端プレエッジピーク

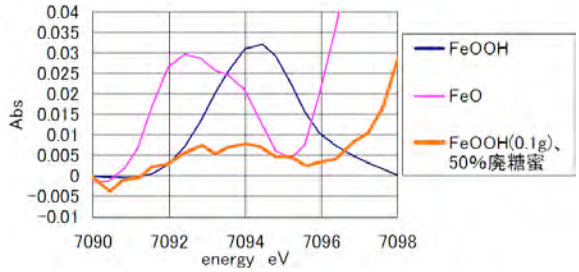

図 3. Fe^{3+}試薬（FeOOH）と廃糖蜜の混合物から溶出した溶液の Fe 吸収端プレエッジピーク

4 まとめ

以上の実験から、廃糖蜜による有機石灰中の Fe に対する還元作用とその溶出過程における Fe の存在状態を確認することができた。これにより、植物への Fe の供給において廃糖蜜が有効であることが示すことができた。

謝辞

仁谷浩明氏、阿部仁氏には、測定システムのセットアップ、測定中のトラブルの対処など、本実験にあたって多大な支援を受けました。ここに深く感謝いたします。

参考文献

[1] 篠原 信, 農業および園芸 **81** (2006) 753
[2] 松井直樹, 名古屋大学大学院環境学研究科修士論文 (2012) 19 p.
[3] Wilke, M. et al. Am. Mineral. 86, 714-730 (2001).

* masao@nagoya-u.jp

/

Construction of Simple Non-Evaporable Getter Assemblies Using St 707 Strips or St 172 Modules

Takashi Kikuchi[1], Kazuhiko Mase[1,*], and Fumio Watanabe[2]
[1]Photon Factory, Tsukuba 305-0801, Japan
[2]Vaclab Inc., Tsukuba 305-0035, Japan

1 Introduction

A non-evaporable getter (NEG) is an ideal pump for maintaining a clean ultra-high vacuum (UHV) [1,2]. Recently, we have constructed simple NEG assemblies using commercial St 707 strips [3], and they have been used to achieve a UHV in a vacuum ultraviolet soft-X-ray (VSX) beamline, BL-13A, at the Photon Factory (PF) [4]. In the present paper, we describe several simple NEG assemblies constructed of a commercial St 707 strip or a St 172 module, a conflat flange with an outer diameter of 203, 70, or 34 mm (CF203, CF70, and CF34, respectively), and a direct current heating mechanism [5]. We also report the measured pumping speeds of some of the NEG assemblies [5].

2 Results and Discussion

We have constructed NEG assemblies using the St 707 strips (Fig. 1) or the St 172 getter modules (Fig. 2). The pumping speeds of a CF70 NEG assembly made of a St 172 module (Fig. 2a), a CF70 NEG assembly made of a St 707 strip (Fig. 1b), and a CF152 NEG assembly made of St707 strips (Fig. 2 of ref. [3]) were measured for N_2 and H_2 at 20˚C with the orifice method (Fig. 3) [6]. The maximum pumping speeds for the three types of NEG assemblies were 4.8, 1.2, and 25 L s^{-1} (8.0, 3.6, and 82 L s^{-1}) for N_2 (H_2), respectively. These NEG assemblies are useful for laboratory UHV systems as well as VSX beamlines in synchrotron radiation facilities.

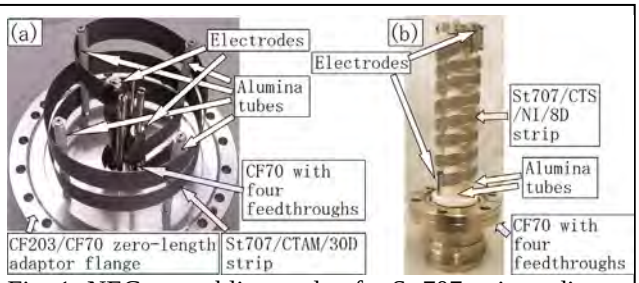

Fig. 1: NEG assemblies made of a St 707 strip, a direct heating mechanism, and (a) CF203 and (b) CF70 [5].

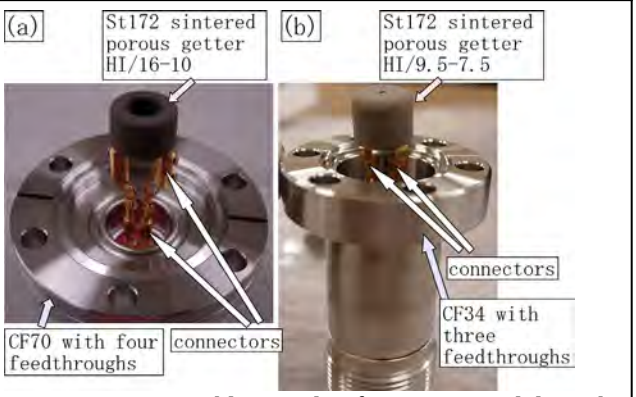

Fig. 2: NEG assemblies made of a St 172 module with (a) CF70 and (b) CF34 [5].

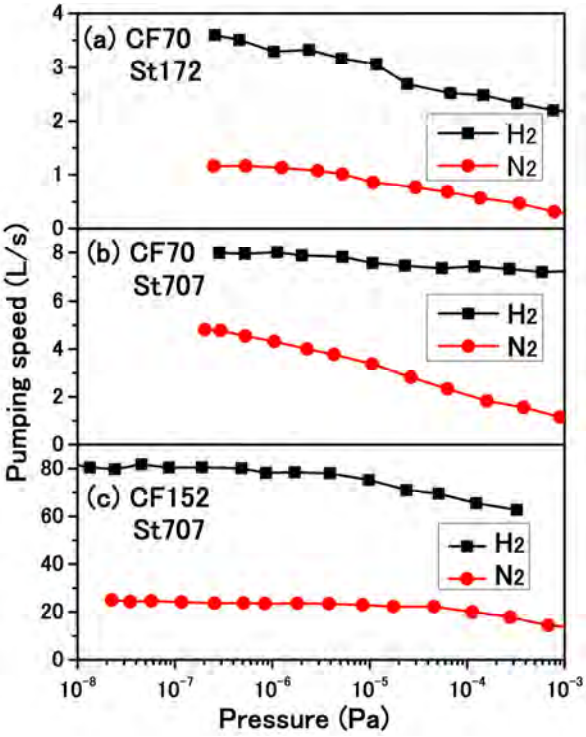

Fig. 3: Pumping speeds of (a) a CF70 NEG assembly made of a St 172 module (Fig. 2a), (b) a CF70 NEG assembly made of a St 707 strip (Fig. 1b), and (c) a CF152 NEG assembly made of a St 707 strip (Fig. 2 in ref. [3]) measured for N_2 and H_2 at 20˚C as a function of pressure [5].

References

[1] LEP Vacuum Group: Vacuum **41** (1990) 1882.
[2] C. Benvenuti and P. Chiggiato: J. Vac. Sci. Technol. A, **14** (1996) 3278.
[3] T. Kikuchi *et al.*, J. Vac. Soc. Jpn. **53** (2010) 533.
[4] A. Toyoshima, *et al.*, J. Vac. Soc. Jpn. **54** (2011) 580.
[5] T. Kikuchi, *et al.*, J. Vac. Soc. Jpn. **55** (2012) 21.
[6] M. H. Hablanian, J. Vac. Sci. Technol. A **5** (1987) 2552.

* mase@post.kek.jp

13A/

Performance of PF BL-13A, a Vacuum Ultraviolet and Soft X-ray Undulator Beamline for Studying Organic Thin Films Adsorbed on Surfaces

Akio Toyoshima[1], Takashi Kikuchi[1], Hirokazu Tanaka[1], Kazuhiko Mase[1,*], Kenta Amemiya[1], and Kenichi Ozawa[2]

[1]Photon Factory, Tsukuba 305-0801, Japan

[2] Tokyo Institute of Technology, Tokyo 152-8551, Japan

1 Introduction

A vacuum ultraviolet and soft X-ray undulator beamline, BL-13A, is mainly dedicated to the study of organic thin films adsorbed on well-defined surfaces, using angle-resolved photoelectron spectroscopy (ARPES), X-ray photoelectron spectroscopy (XPS), and X-ray absorption spectroscopy (XAS). Details of BL-13A have been described in previous papers [1,2]. In this paper, we report on the present status of the BL-13A and the apparatus for ARPES, XPS, and XAS.

2 Photon-energy resolution and photon intensity

The advantage of the BL-13A is that both high photon-energy resolution and high photon intensity can be achieved simultaneously [1,3]. In the initial stage, the measured photon intensity was one order of magnitude lower than the calculated value [2]. We attributed the reduced photon intensity to the small acceptance angles in the measurements (ca. 0.06 mrad (vertical) × 0.2 mrad (horizontal)) and contamination of the optics. To address this, we increased the acceptance angles to ca. 0.4 mrad (vertical) × 0.27 mrad (horizontal) using a new quadruple mask [4] and we removed the carbon contamination of the optics using oxygen activated by 0th-order synchrotron radiation [5]. To estimate the photon-energy resolution ($E/\Delta E$), we measured the photoionization spectra of rare gasses (He, Ar, and Ne) and nitrogen (N_2) in four different photon-energy regions at about 64.1 eV (He, Fig. 1), 244.4 eV (Ar, Fig. 2), 401.1 eV (N_2, Fig. 3), and 867.1 eV (Ne, Fig. 4). The measured photon-energy resolutions and photon intensities at the ring current of 450 mA are summarized in Fig. 5.

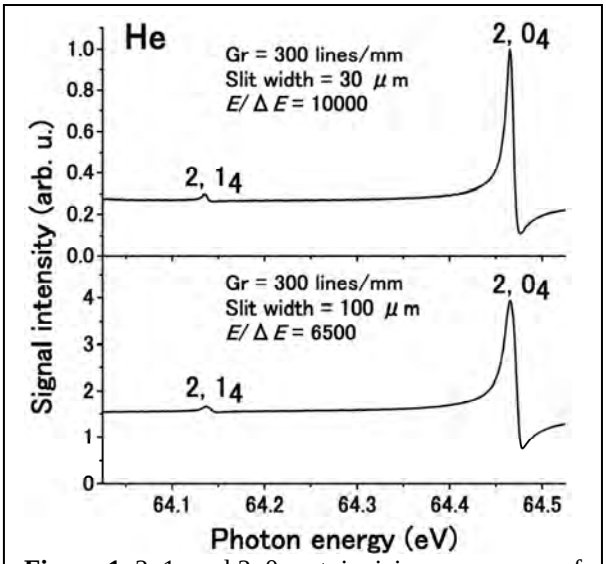

Figure 1. 2, 1_4 and 2, 0_4 autoionizing resonances of doubly-excited He.

3 Apparatus for the study of organic thin films on surfaces using ARPES, XPS, and XAS

Figure 6 shows the apparatus used for the study of organic thin films adsorbed on surfaces using ARPES, XPS, and XAS. The apparatus consists of the main ultrahigh vacuum (UHV) chamber equipped with an

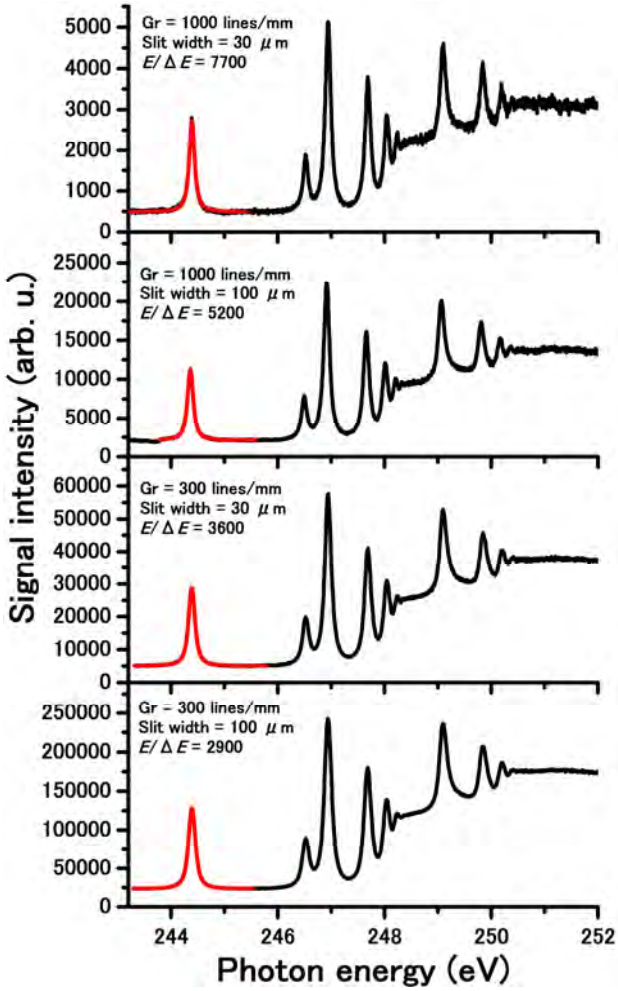

Figure 2. Photoionization spectrum of Ar taken in the region of $2p \rightarrow nl$ Rydberg transition.

electron-energy analyzer (Gamma Data/Scienta, SES200), a sample-preparation UHV chamber, and a UHV chamber for the evaporation of organic materials. The sample can be transferred among UHV chambers with a transfer rod. The sample-holder acceptors in the main and sample-preparation chambers are both equipped with a sample heating and cooling system. To estimate the overall electron-energy resolution, we measured a series of electron spectra in the Fermi region of an evaporated gold film at 5–9 K. The best overall electron-energy resolution was about 12 meV at a photon energy of 30 eV as shown in Fig. 7.

References

[1] K. Mase *et al.*, AIP Conf. Proc. **1234** (2010) 709.
[2] A. Toyoshima *et al.*, J. Vac. Soc. Jpn. **54** (2011) 580.
[3] K. Amemiya and T. Ohta, J. Synchrotron Rad. **11** (2004) 171.
[4] H. Tanaka *et al.*, J. Vac. Soc. Jpn. **54** (2011) 481.
[5] A. Toyoshima *et al.*, J. Synchrotron Rad., in press.

* mase@post.kek.jp

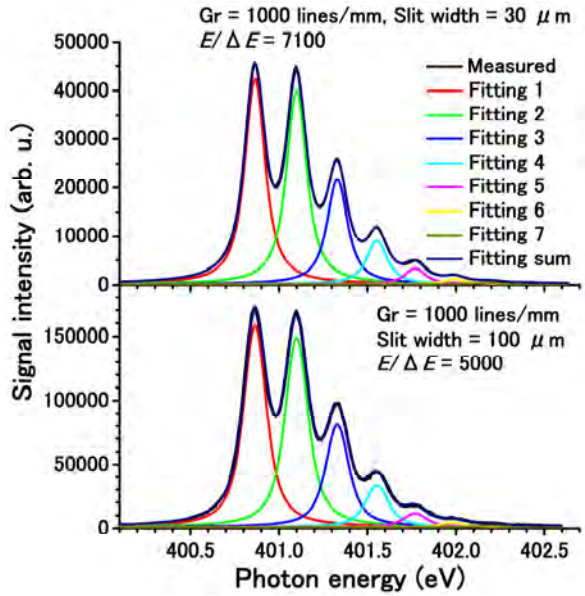

Figure 3. Photoionization spectrum of N_2 taken in the region of $1s \rightarrow \pi^*$ transition.

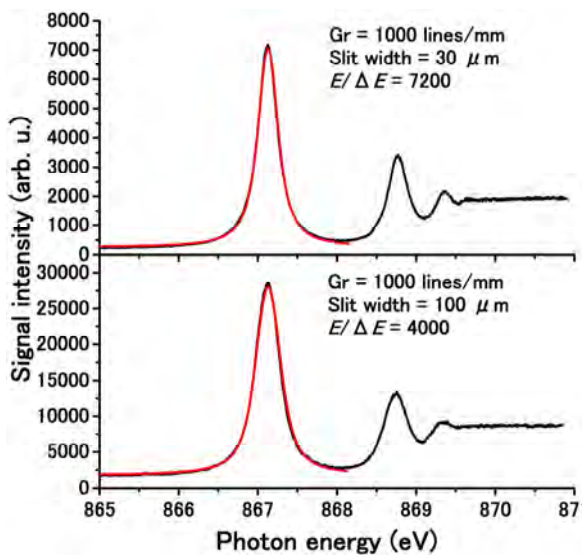

Figure 4. Photoionization spectrum of Ne taken in the region of $1s \rightarrow np$ transition.

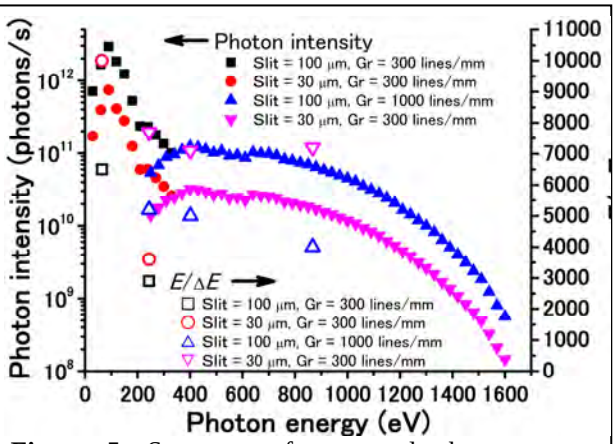

Figure 5. Summary of measured photon-energy resolutions ($E/\Delta E$) and photon intensities when the ring current is 450 mA.

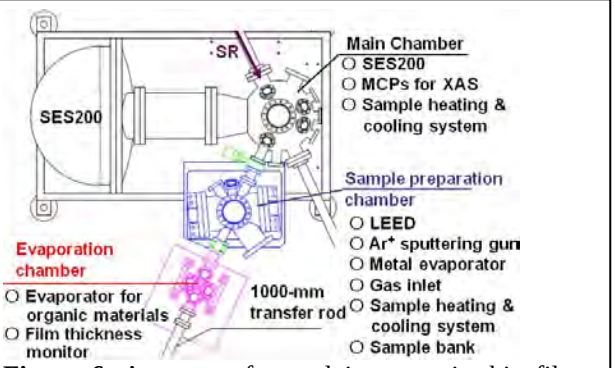

Figure 6. Apparatus for studying organic thin films adsorbed on well-defined surfaces using ARPES, XPS, and XAS.

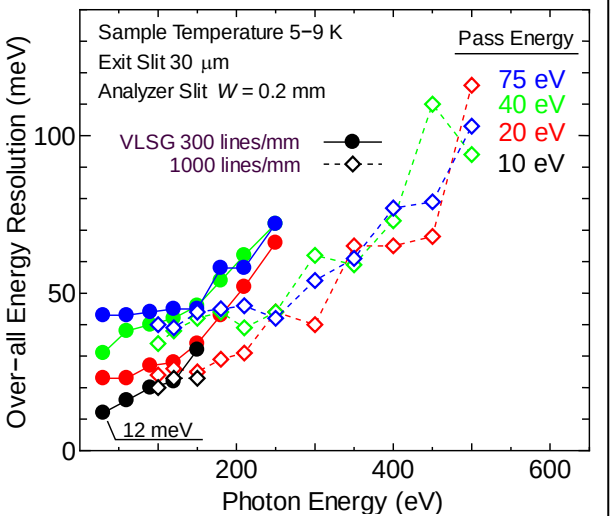

Figure 7. Overall electron-energy resolution as estimated with an electron-energy analyzer and an evaporated gold film at 5–9 K.

In Situ Removal of Carbon Contamination from Optics in a VSX Undulator Beamline, BL-13A, Using Oxygen Activated by 0th-Order Synchrotron Radiation

Akio Toyoshima[1], Takashi Kikuchi[1], Hirokazu Tanaka[1], Jun-ichi Adachi[1], Kazuhiko Mase[1,*], and Kenta Amemiya[1]
[1]Photon Factory, Tsukuba 305-0801, Japan

1 Introduction

When optics are irradiated with synchrotron radiation (SR) in the presence of residual hydrocarbon gases, they are contaminated with carbon [1]. The carbon contamination leads to a significant decrease in the reflectivity in the vacuum ultraviolet and soft X-ray (VSX) region. The photon flux loss in the carbon *K*-edge region is especially critical because it reduces the quality of experimental data, such as near-edge X-ray absorption fine structure (NEXAFS), resonant photoemission, and resonant soft X-ray emission spectra. *In situ* SR-activated oxygen cleaning seems to be most advantageous because optics can be cleaned by exposing them to oxygen at 10^{-2} Pa for 15 hours under 0th order SR irradiation [2]. In the present paper we report results of *in situ* SR-activated oxygen cleaning of optics in a VSX undulator beamline, BL-13A at Photon Factory [3].

2 Experiment

The VSX undulator beamline, BL-13A, has a Monk-Gillieson-type monochromator to cover a wide photon-energy range with a high energy resolution. The details of BL-13A have been described elsewhere [4,5]. Briefly, BL-13A consists of a focusing pre-mirror (M1), a plane mirror (M2), two varied-line-spacing plane gratings (VLSGs, 300 and 1000 lines/mm), an exit slit, and two focusing post-mirrors (M3, 2-m:2-m focusing; M3′, 2-m:6-m focusing). M1, M2, the VLSGs, M3, and M3′ are coated with a gold film with a thickness of 1000 Å or 500 Å. While the SR is vertically reflected by M1, M3, and M3′, it is horizontally reflected by M2 and the VLSGs. Dry oxygen with a purity of 99.9% was supplied by using variable leak valves attached to the beamline.

3 Results and Discussion

Figure 1 shows photon intensity spectra measured with the 300-lines/mm VLSG and M3 before and after *in situ* SR-activated oxygen cleaning. The exit slit was fixed at 30 μm. The photon intensity was measured by using a silicon photodiode (AXUV-100, International Radiation Detectors, Inc.). On the basis of the NEXAFS spectra of graphite [6], we ascribed the sharp dip at 285.1 eV to the C 1*s* → π^* transition of graphite-like carbon with a flat-on configuration on M1 and M3, and the sharp dip at 291.5 eV mainly to the C 1*s* → σ^* transition of graphite-like carbon with a flat-on configuration on M2 and the VLSG. The oxygen pressures in the M1, M2/VLSG, and M3/M3′ chambers were in the range 2×10^{-4} to 6×10^{-4} Pa, 5×10^{-3} to 1.5×10^{-2} Pa, and 1×10^{-5} to 4×10^{-5} Pa, respectively. M1, M2, the 300-lines/mm VLSG, and M3 were irradiated with 0th-order SR for 20 h. The averaged ring current was 450 mA. The photon intensity dips in the carbon *K*-edge region reduced to 2–5% after the cleaning. Since these absorption energies are different from those before the cleaning (285.1 and 291.5–291.9 eV), we ascribe them to the carbon contamination in the bulk of the gold film of the optics. The base pressure of the beamline recovered to 10^{-7}–10^{-8} Pa in one day without baking. The beamline can be used without additional commissioning. The interaction of oxygen molecules with photoelectrons emitted from the optics seems to play a dominant role in the removal of carbon contamination. Therefore, *in situ* SR-activated oxygen cleaning is suitable for optics in undulator beamlines where a high photon flux is easily achieved.

References

[1] K. Boller *et al.*, Nucl. Instrum. Methods Phys. Res. A **208** (1983) 273.
[2] W. K. Warburton and P. Pianetta, Nucl. Instrum. Methods Phys. Res. A **319** (1992) 240.
[3] A. Toyoshima *et al.*, J. Synchrotron Rad., in press.
[4] K. Mase *et al.*, AIP Conf. Proc. 1234 (2010) 709.
[5] A. Toyoshima *et al.*, J. Vac. Soc. Jpn. 54 (2011) 580.
[6] R. A Rosenberg *et al.*, Phys. Rev. B **33** (1986) 4034.

* mase@post.kek.jp

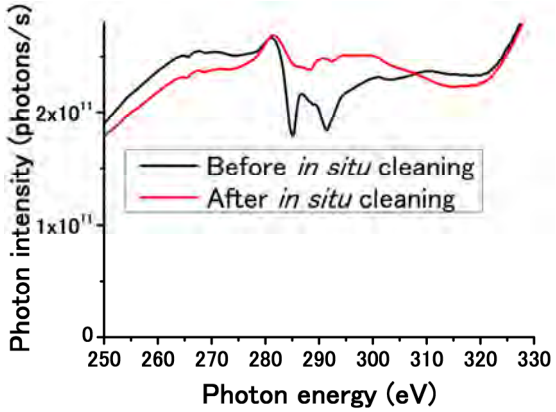

Fig. 1: Photon intensity spectra measured before and after the *in situ* SR-activated oxygen cleaning; the measurements were made with the 300-lines/mm VLSG and M3.

12A/1999G363, 2001G214, 2003G180

Speed Programmed Shuttering System for Laterally Graded Multilayer Fabrication

Tadashi Hatano*, Hiroo Umetsu, Shogo Kubota, Yasunobu Adachi, Tetsuo Harada and Masaki Yamamoto
IMRAM, Tohoku University, 2-1-1 Katahira, Aoba-ku, Sendai 980-8577, Japan

1. Introduction

Multilayers can reflect VUV lights in normal incidence geometry by constructive interference. For imaging application, multilayers should have specific period thickness distributions over the curved mirror substrates as a function of the local ray angles of incidence. Therefore a lateral thickness control is needed in imaging multilayer deposition. For X-ray beamline optics where the lateral gradient of the multilayer thickness is gentle, the source or substrate scan method is usefull [1, 2]. For a short radius of curvature mirror such as normal incidence VUV microscope optics, however, a more powefull thickness control method enabling a steep gradient larger than 3%/mm has been required. It is not easy without a mask technoque. A moving mask method was proposed by a group in Nikon [3]. That idea was developed into our speed programmed shuttering system [4]. An ion beam sputtering (IBS) deposition apparatus equipped with the shuttering system has been constructed and multilayer mirrors of various specifications have been fabricated successfully. A high throughput VUV multilayer microscope has been developed.

2. Design

The side view of the IBS deposition apparatus is illustrated in Fig. 1. Dual ultra high vacuum compatible ion guns of an electron cyclotron resonance type are equipped. Three targets can be mounted and switched

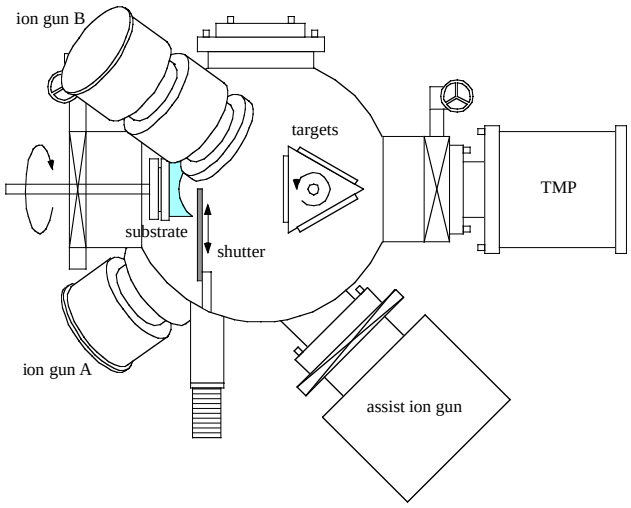

Fig. 1: Schimatic illustration of an IBS deposition apparatus with a speed programmed shuttering system.

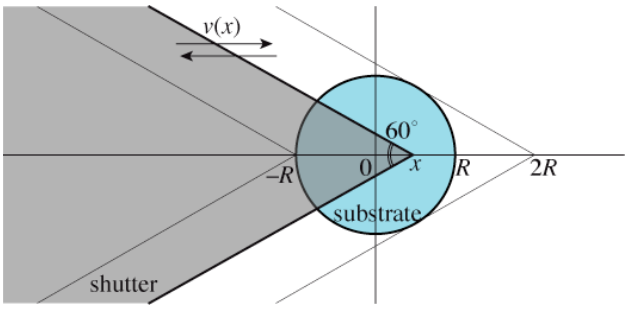

Fig. 2: Schematic illustration of the deposition shutter partially covering the spinning substrate.

during a deposition. The substrate spins at 60 rpm for the rotational thickness uniformity. In front of the spinning substrate the shutter moves along a speed function programmed to obtain a desired radial thickness distribution. The front view of the shutter is illustrated in Fig. 2. The x-axis in the figure is vertical in the actual apparatus. The deposition rate is higher at the center than at the edge while the designed thickness is usually thicker at the edge. That is a reason why the shutter shape is triangular. The angle of vertex is 60˚ or 90˚.

The shutter speed programming procedure is briefly described below when the shutter vertex is 60˚. The shutter covers the whole substrate at $x = 2R$, where x and R are the position of pointed end of the shutter and the radius of the substrate, respectively. For multilayer fabrication, the sputtering targets are switched at this position. The shutter opens from $x = 2R$ to $x = -R$ along a speed function $v(x)$. The whole substrate is exposed at $x = -R$. The shutter stays here for an interval T, and closes from $x = -R$ to $x = 2R$ along the same speed function. Through that sequence the deposition time has r-dependence, where r is a distance from the center of the substrate. The r-dependent deposition time is written as

$$T(r) = 2\int_{-R}^{2R} \frac{\Theta(x,r)}{2\pi}\frac{dx}{v(x)} + T\,,$$

where $\Theta(x, r)/2\pi$ means the exposed fraction at r when the shutter position is x [4]. Approximating $1/v(x)$ into a finite power series

$$\frac{1}{v(x)} = \sum_{n=0}^{N} c_n x^n\,,$$

the integral can be carried out into the form of

$$T(r) = \sum_{n=0}^{N} T_n r^n\,,$$

and the values of coefficients T_n's are

$$\begin{bmatrix} T_0 \\ T_1 \\ T_2 \\ T_3 \\ \vdots \end{bmatrix} = \begin{bmatrix} 1 & 2R & -R^2 & \frac{2}{3}R^3 & .. \\ 0 & \frac{4\sqrt{3}}{\pi} & 0 & 0 & .. \\ 0 & 0 & 2 & 0 & .. \\ 0 & 0 & 0 & \frac{4\sqrt{3}}{\pi} & .. \\ : & : & : & : & \end{bmatrix} \begin{bmatrix} T \\ c_0 \\ c_1 \\ c_2 \\ : \end{bmatrix}.$$

On the other hand, under the condition that the deposition rate distribution is $S(r)$ the r-dependent deposition time to achieve the designed thickness distribution $D(r)$ should be $D(r)/S(r)$. It determines $T(r)$. From a given $D(r)/S(r)$, T_n's, then c_n's and T are obtained. Only one thing that should be emphasized here is that the shutter speed programming procedure is analytical and clear. When the shutter vertex is 90˚, the matrix changes only with diagonal elements.

3. Multilayer Deposition and Evaluation

We fabricated a Mo/Si multilayer on a spherical substrate of 100 mm diameter and 300 mm radius of curvature without the shutter operation. The deposition rates $S(r)$'s of Mo and Si on this sample were measured by the normal incidence VUV reflectometry at BL-12A [5]. To use the multilayer as a high NA condenser mirror of a laser plasma source for 95 eV, we programmed $v(x)$'s and T's to deposit uniform thickness of $D(r)$ = 2.8 nm for Mo and $D(r)$ = 4.1 nm for Si. The shutter speed functions were obtained as shown in Fig. 3. Two curves are close to each other because the thickness to deposition rate ratios of Mo and Si were similar. We fabricated a 30 period multilayer of this design and measured the period thickness distribution by the reflectometry [5]. The results are plotted in Fig. 4. A thickness uniformity of *PV* 1.6% was achieved. With an improvement of the shutter speed program where a continuous function was divided into $x > 0$ and $x < 0$ regions making a jump at $x = 0$, the thickness error decreased to *PV* 0.9%.

A soft X-ray group in Tohoku University designed a transmission VUV microscope based on a laser produced plasma source. It contains four normal incidence multilayer mirrors of radii of curvature of +22.4 mm, –50 mm and –400 mm. We deposited 40 period Mo/Si multilayers on the mirror substrates. The measured thickness error among four mirrors was *PV* 1%, less than the multilayer bandpass $\Delta E/E$ = 4% [6]. The microscope works well with a high throughput at 92.5 eV [7]. It is concluded that a widely applicable multilayer deposition technique for normal incidence imaging optics has been developed using speed programmed shuttering system.

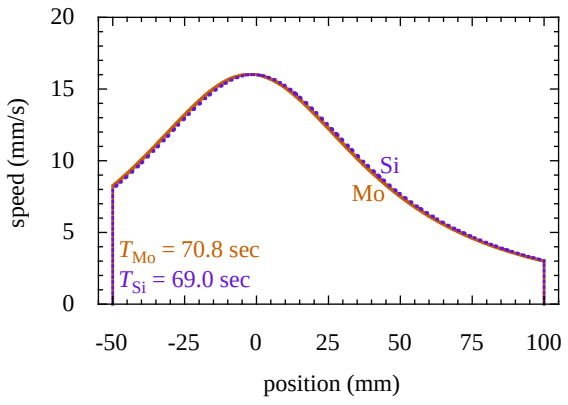

Fig. 3: Shutter speed functions programmed for a Mo/Si multilayer of uniform thickness on a 100 mm$^{\phi}$, 300 mm^{r} spherical substrate.

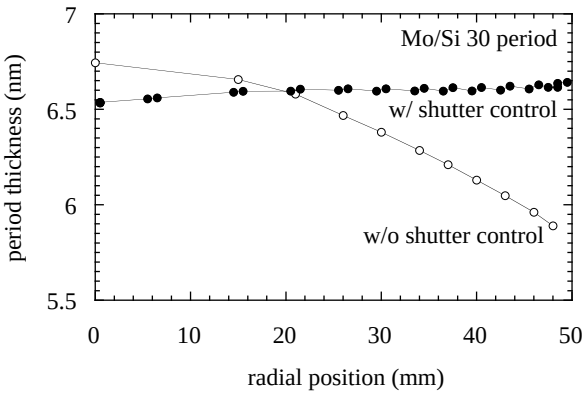

Fig. 4: Period thickness distribution of a Mo/Si multilayer measured by the normal incidence VUV reflectometry.

Acknowledgments

This work was supported in part by Grant-in-Aid for Basic Scientific Research, category C (2) No. 15560016, and also by Budget of "Research on Analyzing Technology of Materials and Devices by Photoelectron Micro-Spectroscopy" of Grant-in-Aid for Scientific Research, both of the Ministry of Education, Culture, Sports, Science, and Technology, Japan.

References

[1] Ch. Morawe, P. Pecci, J-Ch. Peffen, E. Ziegler, Rev. Sci. Instr. **70** (1999) 3227.
[2] Ch. Morawe, K. Friedrich, M. Osterhoff, J-C. Peffen, AIP Conf. Proc. **1234** (2010) 720.
[3] T. Oshino, N. Katakura, and K. Murakami, *JSPE Proc. 2nd US-Japan Workshop on Soft X-ray Optics, Yamanaka-ko Nov. 1996*, pp.528-540.
[4] T. Hatano, H. Umetsu and M. Yamamoto, *Precision Science and Technology for Perfect Surfaces, JSPE Publication Series No. 3* (JSPE, Tokyo, 1999) pp. 292-297.
[5] T. Hatano, S. Kubota, Y. Adachi, T. Tsuru and M. Yamamoto, AIP Proc. **705** (2004) 839.
[6] T. Hatano, T. Harada and M. Yamamoto, PF Act. Rep. 2007 A, **#25** (2009) 64.
[7] T. Ejima, F. Ishida, H. Murata, M. Toyoda, T. Harada, T. Tsuru, T. Hatano, M. Yanagihara, M. Yamamoto and H. Mizutani,Opt. Express **18** (2010) 7203.

* hatano@tagen.tohoku.ac.jp

14C1/2009G031

X 線 Talbot 干渉計と白色放射光による生きたブドウ虫の４D 位相 CT
4D Phase Tomography of Living Worm by X-ray Talbot Interferometry with White Synchrotron Radiation

百生敦 [1*], 矢代航 [2], Sebastien Harasse[2], 桑原宏萌 [2]
[1]東北大学多元研　〒980-8577 仙台市青葉区片平 2-1-1
[2]東京大学新領域　〒277-8561 千葉県柏市柏の葉 5-1-5

1 はじめに

透過格子を用いる X 線 Talbot 干渉計は、X 線位相ｲﾒｰｼﾞﾝｸﾞに使える新たなﾃﾞﾊﾞｲｽとして、近年注目が増している。柔軟で様々な撮影様式がとれることが特徴であり、特筆すべきは、実験室 X 線源でも現実的な撮影時間で使用可能であることである。一方、放射光を用いる応用としてもこれまで不可能であったいくつかの手法が可能となっている。本研究では、X 線 Talbot 干渉計が白色放射光に対しても機能することを活用し、４D 位相 CT、すなわち、位相 CT による高感度三次元画像の動画像取得を行った。時間分解能 2ms での微分位相像取得に基づき、時間分解能 0.5s の４D 位相 CT 像を、生きたﾌﾞﾄﾞｳ虫について取得することに成功した[1]。

2 実験

BL-14Cにおいて得られる白色放射光に対して、28.8keVのX線に最適となる配置でX線Talbot干渉計を構築した。これは、π/2位相格子（G1）と振幅格子（G2）から成り、共に5.3μmの周期を持つL&Sﾊﾟﾀｰﾝを持つ。被写体の背後にG1を配置し、その下流326mmの位置にG2を置き、さらにその背後に画像検出器を設置した。高速撮影を可能とするために、この画像検出器は、CMOSｶﾒﾗ(pco.1200hs, PCO AG)と20μm厚のP46蛍光ｽｸﾘｰﾝをﾚﾝｽﾞｶｯﾌﾟﾙしたものである。画素ｻｲｽﾞ12.7μmを持つ。ﾌﾚｰﾑﾚｰﾄは0.5kf/sとした。

位相CTでは、各投影方向について試料による位相ｼﾌﾄ像あるいは位相ｼﾌﾄ微分像を取得する必要がある。従来の位相CTによる静的撮影では縞走査法を使用していた。しかし、この方法では各投影方向において毎回格子を並進させて複数（例えば５枚）のﾓｱﾚ画像を撮影する必要があるため、高速撮影を目的とする本実験には望ましくない。そこで、ﾌｰﾘｴ変換法を採用した。これは、格子を傾けることにより生じる回転ﾓｱﾚをｷｬﾘｱﾌﾘﾝｼﾞとして使い、ﾌｰﾘｴﾌｨﾙﾀﾘﾝｸﾞにより微分位相像を得る方法である。一枚のﾓｱﾚ画像から一枚の微分位相像が得られるため、高速撮影に向いている。ただし、空間分解能はｷｬﾘｱﾌﾘﾝｼﾞの間隔によって決まるため、縞走査法に比べて空間分解能が劣ることは受け入れる必要がある。今回の実験では、ｷｬﾘｱﾌﾘﾝｼﾞ間隔を77.5μmとした。

試料としては、生きたﾌﾞﾄﾞｳ虫(larva of nokona regalis)を撮影した。ﾌﾟﾗｽﾁｯｸ管内に軽く接着し、1rpsで回転して動画像を取得し、４D位相CT像を再構成した。

3 結果および考察

図１に再構成した結果を示す。放射光照射から、0, 1, 2, 3, 4 秒経過した時点に相当する像である。これは、体内の気道を可視化したﾚﾝﾀﾞﾘﾝｸﾞ画像であるが、特に下段（頭部）に見られる鞘状の構造が縮むという動的変化が明瞭に見られる。

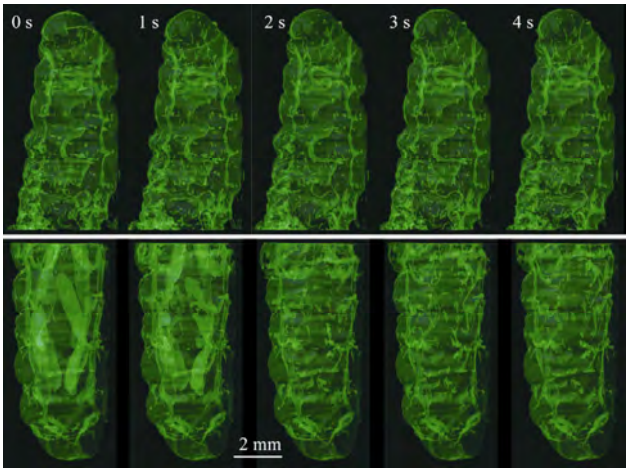

図１：ﾌﾞﾄﾞｳ虫の４D 位相 CT 像。上段：尾部、下段：頭部。放射光照射から 0, 1, 2, 3, 4 秒経過の様子。

4 まとめ

生きた幼虫の動的三次元画像（４D 位相 CT）に成功した。これまで静的観察が主であった位相 CT が動的観察のためのﾂｰﾙとして脱皮を迎えたと言える。生体以外にも各種材料の動的三次元観察にも適用を広げたい。

謝辞

本研究は、JST 先端計測のｻﾎﾟｰﾄにより推進した。

参考文献

[1] A. Momose *et al.*, Opt. Express **19** (2011) 8423.

* momose@tagen.tohoku.ac.jp

14C2/2009S2-006

Observation of gas diffusion layer of fuel cells by X-ray interferometric laminography

Akio YONEYAMA[*1], Satoshi Takeya[2], Kazuyuki HYODO[3], and Tohoru TAKEDA[4]
[1]Central Research Laboratory, Hitachi Ltd., Hatoyama, Saitama 350-0395, Japan
[2]National Institute of Advanced Industrial Science and Technology, Tsukuba 305-8565, Japan
[3]KEK-PF, Tsukuba, Ibaraki 305-0801, Japan
[4]Allied Health Sciences, Kitasato University, Sagamihara, Kanagawa 228-8555, Japan

1 Introduction

X-ray interferometric imaging, which detects phase shifts by X-ray interferometer, is a powerful tool for biomedical and material imaging. The phase shift cross-section of light elements in a hard X-ray region is about 1000 times bigger than the absorption cross-section; therefore, this imaging technique enables us to perform fine two- and three-dimensional observations of samples mainly composed of light elements without any supplemental methods. Many detailed observations of biological soft tissues such as kidney, liver, brain, organic material, and clathrate hydrates were performed using an imaging system fitted with a two-crystal X-ray interferometer [1]. For wider application of this imaging technique, we developed X-ray interferometric laminography making it possible to observe thin and flat objects nondestructively and applied it to the observation of a thin gas diffusion layer of fuel cells.

2 Experiment

Figure 1 shows the schematic view of our experimental set-up of interferometric laminography. The incident X-ray beam was divided, refracted, and recombined in turn by the 4-crystal wafers of the interferometer. Two generated interference beams were detected by two CCD-based X-ray imagers for the measurements and the feedback control of the interferometer.

The sample was placed in one interference path and rotated around an axis inclined by 45 degrees with respect to the path in the horizontal plane. At each rotational angle, phase map, which depicts spatial distribution of phase shift caused by the samples, was obtained by fringe scanning methods with three steps.

The three-dimensional image was reconstructed by algebraic reconstruction technique (ART), which is based on an iterative calculation of three-dimensional projection and back projection. To shorten the calculation time, a general purpose graphic processer unit (GPGPU) was used.

3 Results and Discussion

Figure 2 shows three-dimensional and sectional images of the layer. The interference images were obtained using a 35-keV X-ray with 5-s exposure. The sample was rotated through 360 degrees in 0.72 degree steps. Many fibers composing the layer were visualized clearly, and image quality was good enough to perform quantitative estimation of the length and the overlap structure of fibers. The spatial resolutions estimated from the slope of the line profile near the fiber were 30 μm and 50 μm in the horizontal and vertical directions, respectively. The density resolution calculated from the standard deviation of phase fluctuations was 3 mg/cm^3.

This result indicates that X-ray interferometric laminography is a powerful tool for the observation of thin and flat samples consisting of light elements.

References

[1] A. Yoneyama *et al.*, Nucl. Instr. and Meth. A 523, 217 (2004).

* akio.yoneyama.bu@hitachi.com

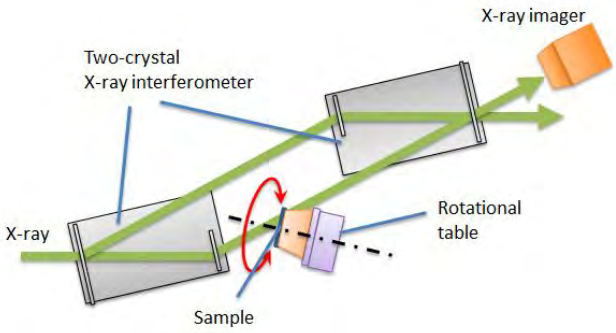

Fig. 1: Schematic view of X-ray interferometric laminography.

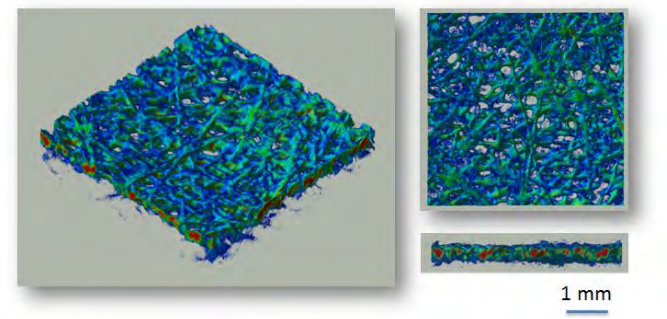

Fig. 2: Three-dimensional and sectional images of gas diffusion layer.

11B,16A/2009S2-008

共鳴軟 X 線散乱用シリコンドリフト検出器の開発

Silicon drift detector developed for resonant soft X-ray scattering measurements

中尾 裕則
KEK、物質構造科学研究所、放射光科学研究施設・構造物性研究センター
〒 305-0801 つくば市大穂 1-1

1 はじめに

強相関電子系では、電子の局在状態と遍歴状態の狭間で、通常の金属では見られない高温超伝導、巨大磁気抵抗効果といった特徴的な物性が頻繁に発現する。例えば、強相関電子系で発見された超伝導体は、スピン・電荷の秩序状態 (局在相) が抑制され消失する量子臨界点近傍に一般に位置していることが知られている。つまり、局在性と遍歴性の競合した電子状態の研究が、新奇物性発現メカニズムの解明の上で極めて重要となっている。ここで局在性と遍歴性を支配しているのが、原子間での電子軌道の混成状態であり、単純には電子軌道の混成が大きくなることで金属状態が出現すると考えられる。特に、局在性の強い電子 (遷移金属 3*d* 電子, 希土類 4*f* 電子) と遍歴性の強い電子 (酸素 2*p* など) の混成した電子が作り出す局在相での”軌道混成秩序状態”や、局在相から遍歴相への転移に伴う局在的電子・遍歴的電子のそれぞれの役割解明が望まれているものの、これらの電子を区別して観測することが難しいため、未解決の問題となってきた。そこで我々は、共鳴 X 線散乱 (RXS) 手法を用いることで軌道混成状態の定量的な解明を目指している。特に、この混成に寄与している電子軌道の吸収端エネルギーは、遷移金属 3*d* (0.4 -1.0 keV), 4*d* (1.0-4.0 keV), 希土類 4*f* (1.1 - 2.2 keV), 軽元素 (C,N,O,S,P) (0.5 - 2.5 keV) であり、軟 X 線を用いた RXS 実験により、これらの電子軌道を直接的に捉えることが可能となる。この共鳴軟 X 線散乱 (RSXS) 実験は、この数年で世界的に行われるようになったものの、微弱な信号を捉えるための回折計や検出器の整備は、我々が行ってきた硬 X 線領域での RXS 実験と比較すると相当遅れている。そこで物性変化に伴う微弱信号を捉えるために硬 X 線領域では当たり前だが軟 X 線回折装置では出来ていない 1 光子検出可能な検出器の整備を、今回目指した。

2 実験

1 光子検出、さらにはエネルギー分解の性能を持つ、軟 X 領域での X 線検出器としてすでにシリコンドリフト検出器 (SDD) が知られており、蛍光 X 線測定などでは利用が始まっている。しかしながら、共鳴軟 X 線散乱実験では、真空中に設置された 2θ 軸上に検出器を設置する必要があり、検出器全体が真空チャンバー内に設置できる必要がある。そこで今回、真空チャンバー内に設置可能な検出器の作製を試みた。さらに検出器の性能を、BL-11B, 16A にて確認した。

3 結果および考察

図 1 に、作製した SDD を真空チャンバー内に設置した様子を示す。RXS 実験で原理的に避けることのできない蛍光 X 線のバックグラウンドの寄与を軽減するため設置した 4 象限スリットの下流側に SDD を取り付けている。入射 X 線 (2400 eV) で $Y_2Nb_2O_7$ からの蛍光をこの配置にて測定した結果を、図 2 に示す。弾性散乱 (λ) だけでなく試料の構成元素に対応して、Nb, Y, O の蛍光が観測出来ているだけでなくコールドヘッドの Cu の蛍光が観測されていることがわかる。またこの時、エネルギー分解能は 100 eV 程度である。

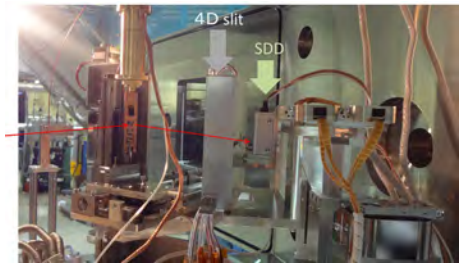

図 1: 軟 X 線用 2 軸回折計内に設置した SDD。赤矢印で入射 X 線と散乱 X 線の方向を示す。

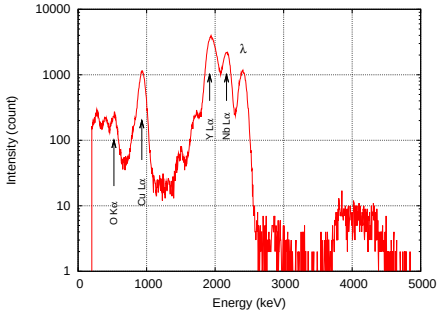

図 2: 入射 X 線 (2400 eV) で測定した $Y_2Nb_2O_7$ からの発光スペクトル。

4 まとめ

今回、共鳴軟 X 線散乱実験用シリコンドリフト検出器を開発し、ほぼ期待通りの性能を持つ検出器を作製することに成功した。本検出器は、これまで我々が実験に用いてきた検出器と比較して格段に感度良く信号検出ができており、今後の構造物性研究で活躍することが期待される。

* hironori.nakao@kek.jp

11A, 2C/2010G065

Blurred Image Correction in Soft X-ray Projection CT Microscopy - Comparison among radiation light sources -

Tatsuo SHIINA[1*], Moriaki KOYAMA[1], Hideyuki YOSHIMURA[2], Yasuhito KINJO[3], Atsushi ITO[4], Toshio HONDA[5], Keiji YADA[6], and Kunio SHINOHARA[7]

[1]Graduate School of Advanced Integration Science, Chiba Univ., Chiba-shi, Chiba, 263-8522, Japan
[2]School of science and Technology, Meiji Univ., Kawasaki-shi, Kanagawa, 214-8571, Japan
[3]Tokyo Metropolitan Industrial Technol. Res. Inst., Kita-ku, Tokyo 115-8586, Japan
[4]School of Engineering, Tokai Univ., Hiratsuka-shi, Kanagawa, 259-1292, Japan
[5]Honda Hikari Giken, Chiba-shi, Chiba, 260-0856, Japan
[6]Tohken Co., Ltd. Chofu-shi, Tokyo 182-0025 Japan
[7]Waseda Univ., Shinjuku-ku, Tokyo 169-8555, Japan

Introduction

Blur-correction of observed images on a soft X-ray projection CT microscope by iteration procedure has been continued [1]. Our study improves the precision of blur-correction and extends its application to biological specimens. In the recent study, our correction analysis was mainly carried out using a bending magnet line (BL11A), while more coherent beam would be more effective in the blur-correction of the observed images. Last year, we conducted the experiment at BL2C, which is an undulator beam line, in addition to BL11A. In this report, comparison of the blur-corrected images among several radiation light sources of soft and hard X-rays was discussed.

Results and Discussion

We used different radiation sources, BL11A, BL2C of Photon Factory, and BL20XU of SPring-8. BL11A is a bending magnet beam line ranging from 70 to 1900eV. BL2C is an undulator line covering photon energies of 250-1400eV. BL20XU is a hard X-ray undulator line at SPring-8. The observation of a biological sample such as chromosome is one of our targets. The projection microscope enlarges the image of the sample due to the layout of the zone plate, sample and CCD. The projection procedure easily magnifies the image, while it causes the blur image with Fresnel fringes.

The comparison of the blur-correction among the above three beams is conducted by using non-biological test samples. Figure 1 indicates the blur-correction of latex particles of 2.8μmϕ, which is observed at 700eV at BL11A. The adjacent particles were clearly reconstructed by the blur-correction. The particle size was matched with the nominal value. The spatial coherence of BL11A is not so high and the intensity distribution fluctuates temporally. The iteration procedure acted correctly to remove the fringes (blur). The undulator lines of BL2C and BL20XU are of high coherence and intensity. The Fresnel fringes were more clearly observed as shown in Fig.2 and 3. At BL2C with the energy of 500eV, a glass capillary of 5μmϕ could be reconstructed as its image contrast depended on the glass thickness. The edge of Au Mesh observed at 8 keV was clearly reconstructed at BL20XU. These blur-corrections were more rapidly converged than the BL11A data. It is because of the coherency of radiation source. Our study is focusing on the compensation of the missing fringe information.

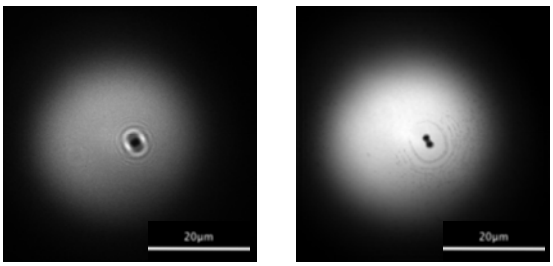

Fig.1 Blur and corrected images (latex particle of 2.8μmϕ) observed at the Photon Factory BL11A.

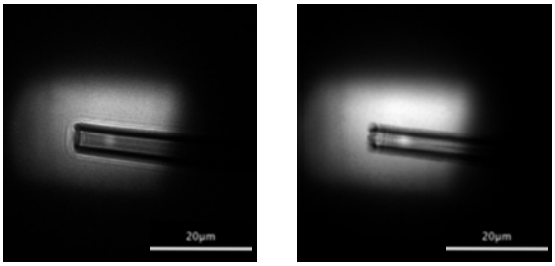

Fig.2 Blur and corrected images (glass capillary of 5μmϕ) observed at the Photon Factory BL2C (Undulator line).

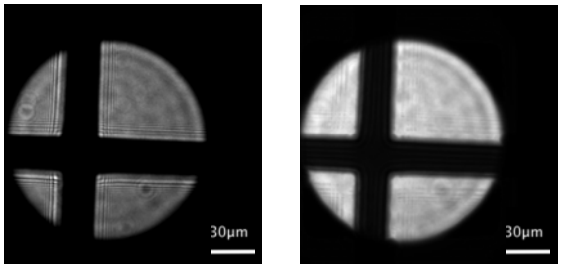

Fig.3 Blur and corrected images (Au Mesh) observed at the SPring-8 BL20XU.

References

[1] T. Shiina et al., Annual meeting of Japanese Society for Synchrotron Radiation Research, Proceedings, pp. 139, 2012.

* shiina@faculty.chiba-u.jp

14A/2010G102

硬 X 線偏光度検出器 PHENEX の性能試験

Performance test for hard X-ray polarimeter PHENEX

郡司修一[1*], 岸本祐二[2]

[1]山形大学理学部 〒990-8560 山形市小白川 1－4－1 2

[2]共通基盤研究施設 〒305-0801 つくば市大穂 1-1

1 はじめに

X 線天文学は、X 線のエネルギー、X 線の放出タイミング、X 線での画像イメージの 3 つのパラメーターの観測によって、様々な天体の物理を解き明かしてきた。しかし、X 線はもう一つ偏光という重要な情報を運んでくる。しかし、X 線の偏光情報を取得できる検出器の開発が困難である事から、ほとんど観測が行われてこなかったのが現状である。しかし、もし観測が実現すれば、パルサーやガンマ線バーストのエネルギー輻射メカニズムの解明、シンクロトロンネビュラの磁場構造、ブラックホール近傍の時空の歪みの検出などの興味深い現象を明らかにできると考えられている。そのため、我々は偏光を精度良く測定できる検出器の開発を行ってきた。我々が開発している検出器はコンプトン散乱の異方性を原理とした散乱型の検出器であり、30keV 程度から 200keV 程度に感度を有する硬 X 線偏光度検出器である。このエネルギーレンジであれば、天体からの硬 X 線は若干大気を通過するため、上空 40km 程度での観測が可能になる。そこで我々は観測用気球に搭載できる検出器の開発を行い、2006 年と 2009 年に気球実験を行った。このプロジェクトを PHENEX プロジェクトと呼ぶ。以下の写真は検出器を円筒状の気密箱に収めた荷姿の状態である。

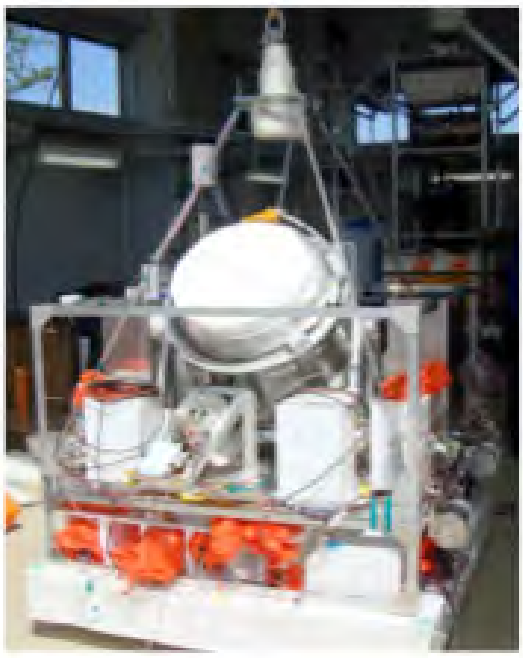

我々は当初 2010 年以降に再び気球実験を行うために、検出器のキャリブレーションを行うべく、Photon Factory の BL14A で実験を行うことを計画していた。しかし、以下の 2 つの理由から 2010～2012 年には気球実験が行えなかった。まず一つ目の理由は、2009 年から日本の気球放球場が北海道大樹町に移動した事である。この放球場では大きな検出器を安定して打ち上げられるというメリットがあるが、上空での風向きが安定していないために我々が希望する 6 時間程度の観測時間を稼ぐことができない。長い観測時間を稼ぐためには海外での気球実験が必要となるが、この時点でその準備は行えていなかった。もう一つの理由は 2011 年に起きた東日本大震災である。この震災により、検出器の開発スケジュールが若干遅れてしまった。そのため、検出器のキャリブレーション自体が必要なくなり、結局 2011 年度にはビーム実験を行わなかった。そのため、ここでは、2006 年～2010 年に行われたビーム実験の結果により得られた実験の進展を報告する。

2 実験の進展

まず我々は BL14A の偏光ビームを使って、我々が開発した偏光度検出器の偏光解析能力と検出効率を測定した。その結果、20%という検出効率を維持しつつ、53%という高い偏光解析能力を検出器が持っている事が明らかになった。この事により、我々が開発してきた偏光度検出器を小型衛星用に進化させる計画が進んでいる。

また散乱型の偏光度検出器がトランジェントな天体観測にも使用できることが分かり、超小型のガンマ線バースト偏光度検出器 GAP の開発に繋がった。GAP のキャリブレーションも BL14A で 2009 年に行う事ができ、2010 年 5 月に GAP は IKAROS 衛星に取り付けられて打ち上げられた。そして、現在 3 発のガンマ線バーストの偏光観測に成功した。3 発の中で一番強度の強いガンマ線バーストに関してはガンマ線バーストの継続時間の前半と後半で偏光方向が変化した事を明らかにした。この観測によりガンマ線バーストがパッチ状に光っている事が明らかになり、Astrophysical Journal Letter に論文が Publish された。

3 参考文献

[1]DETECTION OF GAMMA-RAY POLARIZATION IN PROMPT EMISSION OF GRB 100826A D.Yonetoku, T. Murakami, S. Gunji et al Ap.J. Vol.743 ppL30

3C/2010G147

Development of a new X-ray magnetic diffraction method using a long period of magnetic field reversal

Hiromi WATANABE, Kenta HIIRAGI and Masa-hisa ITO
Graduate School of Eng., Gunma Univ., Tenjin-cho 1-5-1, Kiryu, Gunma 376-8515, Japan

Introduction

X-ray magnetic diffraction (XMD) experiments on BL3C have been performed by using a short period, typically 10s, of magnetic field reversal to measure magnetic effect (flipping ratio) of diffraction intensities. This was because we have needed to compensate monotonic decrease of synchrotron radiation intensity. Recently the Photon Factory storage ring started top-up operation (April 2009), and the incident X-ray intensity has come to be almost constant. In this study we try a longer period of magnetic field reversal. This study will lead to the XMD experiment using a superconducting magnet that produces magnetic field of the order of ten tesla but needs long magnetic-field reversing time.

Experiments

First we modified the XMD measurement program that controls the experimental sequence for accepting various periods of magnetic field reversal. We made the XMD experiment of two samples. One was a pure Fe crystal and the other was a Fe_3Pt crystal. We measured the flipping ratio of diffraction intensities of (110) and (221) reflection plane for Fe and Fe_3Pt, respectively. The period of magnetic field reversal was 10s, 50s, 250s and 1000s.

Results and Discussion

The observed flipping ratios of Fe and Fe_3Pt are shown in Fig. 1 and Fig. 2, respectively. In these figures the flipping ratios of fluorescence intensities are also shown, which are expected to be much smaller in magnitude and much closer to zero than those of diffraction intensities. Miller indices of the diffracted X-rays are 220, 330, 440 and 550 for Fe, and 221 and 442 for Fe_3Pt. Fluorescence X-rays are FeK_α and FeK_β for Fe sample and FeK_α, FeK_β, PtL_α and PtL_β for Fe_3Pt sample. In Figs. 1 and 2 it is noted that the data points of 1000s deviate largely from the others. Especially the fluorescence data are shifted from zero, which infers variation of the incident X-ray intensity.

We tried to correct the spectrum data so as that the flipping ratio of fluorescence X-rays of $FeK_\alpha+K_\beta$ for Fe and PtL_α for Fe_3Pt is zero. The corrected flipping ratios of the diffraction data for Fe and Fe_3Pt are shown in Figs. 3 and 4, respectively. In Figs. 3 and 4 it is noted that the flipping ratios for 10s, 50s, 250s and 1000s agree within the statistical errors.

In conclusion, we have successfully performed the XMD experiment using a long period, 1000s, of magnetic field reversal by correcting the spectrum data so as that the flipping ratio of the fluorescence X-rays is zero. This result will lead to a new XMD experiment using a super-conducting magnet.

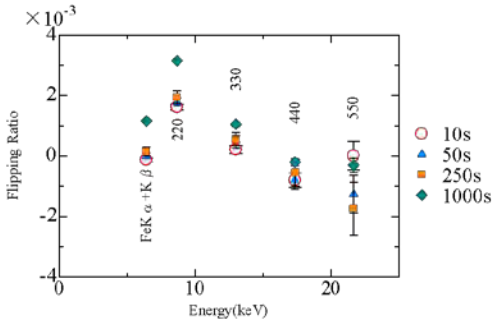

Fig. 1 Observed flipping ratio of Fe.

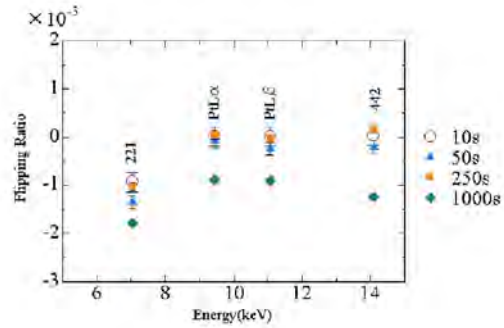

Fig. 2 Observed flipping ratio of Fe_3Pt.

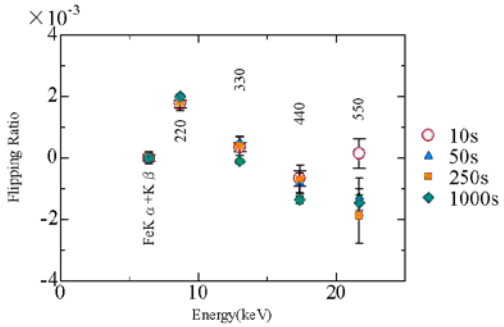

Fig. 3 Corrected flipping Ratio of Fe.

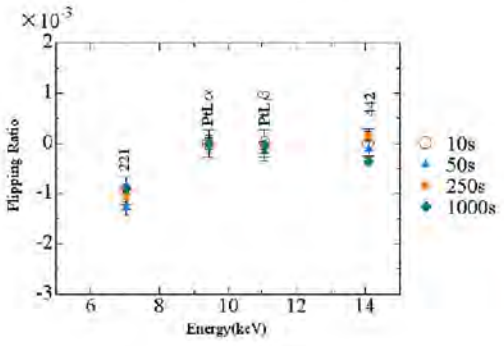

Fig. 4 Corrected flipping ratio of Fe_3Pt.

11D/2010G522

その場観察可能な密着型軟X線顕微鏡の開発
Development of contact SX microscope for in-situ observation of bio-cells

江島丈雄[1*]、根市侑太郎[1]、柳原美廣[1]
[1]東北大学多元物質科学研究所、〒980-8577 仙台市青葉区片平 2-1-1

1 はじめに

可視光学顕微鏡は、結像光学系の回折限界から、生物細胞中の 200 nm より小さな構造の観察は難しい。そのため可視領域で 200nm 以下の構造を観察するに、様々な間接的な観察手法が開発されてきた。例えば蛍光法は、特定のタンパク質を染色しオルガネラの種類とその位置をその発光色により特定することができる。また透明でコントラストの弱い細胞については、位相差を観察することにその形状を明らかにする微分干渉法が考えられてきた。また市販の可視光学顕微鏡ユニットの多くには、透過像、反射像、暗視野像、微分干渉像、蛍光像などの複数の観察手法が搭載されている。これらの観察手法を用いた観察により、可視領域では多くの生物細胞内のオルガネラ構造とその機能に対する知見の蓄積がある[1]。

軟X線は波長が可視光より 1 桁以上短く、この波長の短さを利用する軟X線顕微鏡は可視光学顕微鏡より一桁以上高い空間分解能を持つ。最近では、放射光光源を用いた Zone Plate 型顕微鏡(ZPM)により、数 10nm の空間分解能が達成されるようになった[2]。これらの顕微鏡を用いて「水の窓」や「炭素の窓」波長領域において生物細胞を観察すると、この波長域では水に対して透明で炭素、窒素による吸収が大きく、そのコントラストにより対象を観察するので、大きな構造は可視領域と同じ形状を示すものの、小さいオルガネラ構造は可視領域と軟 X 線領域で異なる形状を示すことが多い。先に述べたように、数多くの生物細胞試料は可視光学顕微鏡を用いて観察されてきたため、軟 X 線顕微鏡により構造の同定を行う場合でも、これらの可視光学顕微鏡観察の知見が利用できることが望ましい。

一方で、物質を構成する原子の内殻吸収端近傍では、物質の電子状態に応じて、吸収スペクトルが固有のピーク位置と固有のスペクトル形状を示す。水の窓領域の C, N, O 原子の K 殻吸収端近傍でも同様と考えられ、生物細胞内のオルガネラの吸収スペクトルが測定できれば、オルガネラ毎に異なる吸収スペクトルが得られるものと考えられる。そのためにはオルガネラのサイズに合わせてφ１μm以下の軟X線ビームをオルガネラに照射する必要があるが、そのようなマイクロビームを作り出すことは困難である。また、波長ごとの像から吸収スペクトルを得る方法も存在するが、ZPM 型の結像光学系は波長によりその焦点位置が変わるため[3]、同一試料に対する波長を変えた測定は手間が必要である。

我々は可視像と軟X線像の比較がし易くかつ波長を変えた測定が容易な軟 X 線顕微鏡として、これまで開発してきた軟X線用 2 次元検出器（SXV-IC）[4]を基に、新たに密着型の軟X線顕微鏡を開発した。開発した顕微鏡は、軟X線に対する結像光学系が省略されており、軟X線を用いる動機のひとつである高い空間分解能を備えていない。一方で、可視顕微鏡との共存が可能であること、観察波長に高い柔軟性を持つことから、これまでの知見に基づいた軟X線によるオルガネラ構造観察が可能である。本稿では、その詳細について述べる。

2 密着型軟X線顕微鏡の性能評価

開発した顕微鏡の概略を図１に示す。まず図の左側から試料に向かって軟X線を照射する。試料を透過して場所ごとに異なる強度の軟X線は、シンチレーターにより可視像に変換される。さらに変換された可視像はシンチレーターを透過して可視用の対物レンズにより拡大・結像され、CCD により画像として取得される。照射光を可視光にした場合もほぼ同様に像を読みだすことが可能である。

密着型顕微鏡では、測定する試料をシンチレーターに押し付けて、軟X線を照射してできた影を観察する。試料とシンチレーターが密着する程度により得られる像の鮮明度が異なるので、試料とシンチレーターは極力密着していることが望ましい。培養液中の生物細胞などの液体試料を計測するために新たに試料ホルダーを作製した。

図１に示すように、作製した試料ホルダーは測定する試料を SiN メンブレンとシンチレーターで挟む構造をしている。ステンレス板に接着したメンブレ

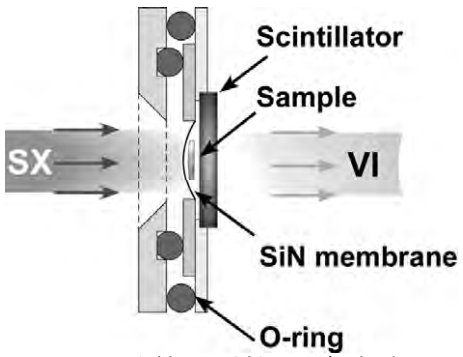

図１：作製した試料ホルダー概略

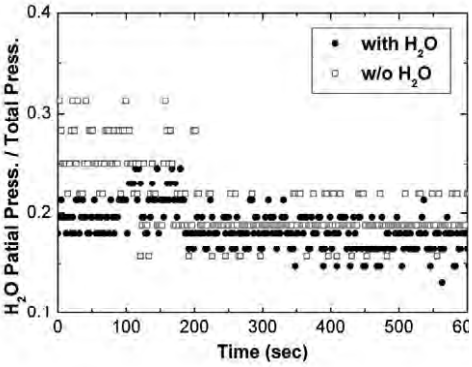

図２：試料ホルダーからのリーク量測定

ンとシンチレーターを O-リングを介して試料台に押し付け、試料となる液体が漏れないようにした。

試料ホルダーから溶液のリークの有無を確かめるために、試料ホルダー内に水を入れ真空槽内に置いて、真空槽内の水分子の分圧の変化を測定した。測定は、エントリーロックを備えた真空槽内に４重極質量分析計（CANNON-ANELVA, M-101QA-TDM）を取り付け、試料ホルダーを入れる前の水分子の分圧と、エントリーロックを通して試料ホルダーを入れた後の水分子の分圧を測定した。真空槽内の圧力は、試料ホルダーを入れる前が 2.3×10^{-6}Pa で、入れた後が 4.4×10^{-6}Pa であった。また測定後に試料ホルダー内に封入した水が残留していることを確認した。

測定した水分子の分圧の変化を、全圧に対する分圧の割合としてプロットしたグラフを図２に示す。横軸は、試料ホルダーの導入直後を 0 分として経過した時間を示す。グラフから、導入直後の圧力の安定しない時間帯を除くと、試料ホルダーの有無による全圧に対する水分子の圧力の変化は無視できる。

試料を透過してできた軟Ｘ線像は、シンチレーターにより可視像に変換され、変換された可視像を光学顕微鏡により読みだす。波長λ_{sx}の軟Ｘ線に対する顕微鏡の感度 $Q(\lambda_{sx})$は、シンチレーターの量子効率 $q(\lambda_{sx})$、対物レンズの開口数 NA、シンチレーターの発光波長λ_s に対する対物レンズの透過率 $T_{obj}(\lambda_s)$、光学窓の透過率 $T_w(\lambda_s)$、結像レンズの透過率 $T_l(\lambda_s)$、CCD の量子効率 $q_{CCD}(\lambda_s)$を用いて、

$$Q(\lambda_{sx}) = q(\lambda_{sx})\, T_{obj}(\lambda_s)\, T_w(\lambda_s)\, T_l(\lambda_s)\, q_{CCD}(\lambda_s) \times \\ \times \{1 - (1 - NA^2)^{1/2}\}$$

と与えられる。このうち、$q(\lambda_{sx})$以外のパラメータは既知で、かつ 対物レンズの透過率 $T_{obj}(\lambda_s)$、光学窓の透過率 $T_w(\lambda_s)$、結像レンズの透過率 $T_l(\lambda_s)$は十分に高く無視できる。またシンチレーターの発光波長に対する CCD の量子効率 $q_{CCD}(\lambda_s)$は 63%と分かっている[6]。従って、顕微鏡全体の量子効率はほぼシンチレーターの量子効率に依存と考えられる。

潮解性がなく、軟Ｘ線領域における量子効率の高いシンチレーターとして Ce:LYSO（株式会社オキサイド）を選び、両面を光学研磨して用いた。軟Ｘ線を照射して発光した光を無限遠補正の対物レンズ（20×、NA=0.4）（ユニオン光学）と結像レンズ（ユニオン光学）を用いて拡大し、CCD カメラ(浜松ホトニクス)により像を得た。顕微鏡の感度測定には Photon Factory BL11D ビームラインを用い、波長分解能 500、露光時間は 5～30 秒、波長は２～20nm で測定を行った。

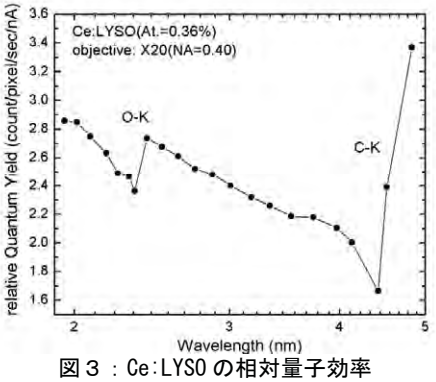

図３：Ce:LYSO の相対量子効率

得られた相対量子効率を図３に示す。得られた曲線の形状は、波長 2.3nm 付近で不連続なギャップ構造を示し、波長 3～3.7nm の範囲では大きなディップ構造を、波長 4.3nm 付近では再びギャップ構造を示した。さらに測定曲線は、7nm 付近で最大値を示したのち、20nm にかけて緩やかに減少した。このうち、波長 2.3nm で観察されたギャップは酸素の K 吸収端、波長 3～3.7nm で見られるディップ構造は Y の M 吸収端、波長 4.3nm のギャップ構造は炭素の K 吸収端と考えられる。このうち酸素と Y 原子はそれぞれシンチレーターに含まれるため、intrinsic な構造である。一方で、炭素は基板洗浄の際に用いた有機溶剤が表面に残ったため extrinsic な構造、と考えられる。また相対量子効率が波長 7nm 付近で最大値を示し、長波長側に向かってなだらかに減少していくのは、過去の測定結果と一致した[4]。

次に空間分解能を評価するため、水中のポリスチレン球（平均粒径 0.52μm）の観察を行った。測定は相対量子効率測定と同様に行い、観察波長範囲は 4.4 nm ～ 2.1 nm、波長分解能λ/Δλ=500、露光時間は 240 ～ 300 sec であった。540eV で撮像したポリスチレン球の像を図４(a)に示す。図の白い部分が水で、黒い点がポリスチレン球である。露光している間黒点が移動しなかったことから、ポリスチレン球はシンチレーターに付着しているものと考えられる。

図４(a)の黒点の強度プロファイルを作製し、平均処理した結果を図５(b)中の黒点で示す。また得られた強度プロファイルを Gaussian でフィッティングした結果が図 2(b)中の実線である。フィッティング結果から Gaussian の半値半幅は 0.72μm となった。この値は、対物レンズの開口数 0.4 とシンチレーターの発光波長 450nm を用いてレーリー条件から推定さ

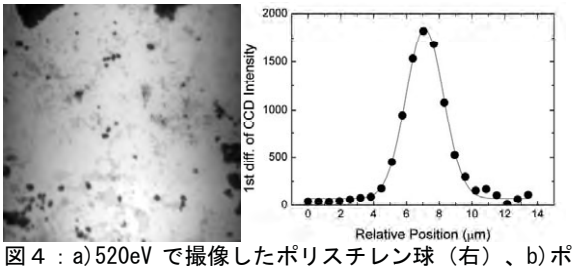

図４：a)520eV で撮像したポリスチレン球（右）、b)ポリスチレン球の強度プロファイルから求めた空間分解能（左）

れる対物レンズの回折限界における空間分解能の値 0.69μm とほぼ一致する。

3 測定例

作製した密着型顕微鏡を使用して、得られた像から吸収スペクトルを求めた例を示す。用いた試料は空間分解能評価に用いたポリスチレン球で、空間分解能評価と同じ測定条件で撮影を行った。光源を直接観察して光強度を求め、次に水中のポリスチレン球を観察したのち、それぞれの測定結果からバックグランドを差し引き、露光時間と光強度で規格化したポリスチレン球の透過率像を求めた。次に、試料に干渉がないと仮定して透過率像を求めた後、図４に示した黒い点の部分、白い部分の水について透過率を波長ごとに求めて、透過スペクトルを求めた。

得られた透過スペクトルを図 5 に示す。それぞれ低エネルギー側から C, N, O の K 殻吸収端であり、ポリスチレン球、水のどちらにも観測された。水で観測された C-K 吸収端の位置はポリスチレン球のエネルギー位置と異なっており、ポリスチレン球の C 吸収端はポリスチレン（polystyrene）の C-H 結合に由来すると考えられることから、水の C-K 吸収端は、SiN メンブレンないしはシンチレーターに付着した C と考えられる。N-K 吸収端は、どちらの物質に於いても同じエネルギー位置で観察されることから、試料ホルダーの窓材である SiN メンブレンの N 原子に由来すると考えられる。また O-K 吸収端も同じエネルギー位置に観察されることから、どちらも水に由来する酸素と考えられる。

4 まとめ

軟X線領域で高い量子効率を示す Ce:LYSO シンチレータを 2 次元検出器として用いた密着型軟 X 線顕微鏡を新たに作製した。作製した顕微鏡の相対量子効率を調べた結果、おおよそ 2nm から 5nm の波長領域で高い量子効率を示した。また、平均粒径 0.52μmの水中のポリスチレン球を用いて空間分解能を評価した結果、倍率 20（NA=0.4）の対物レンズを用いた場合で、0.72μm とほぼ回折限界の空間分解能を示した。最後に、波長ごとにポリスチレン球を撮像した透過像から透過率像を求め、さらに像の各部分について透過率を波長ごとにプロットした結果、ポリスチレン球と水の透過率スペクトルを得ることに

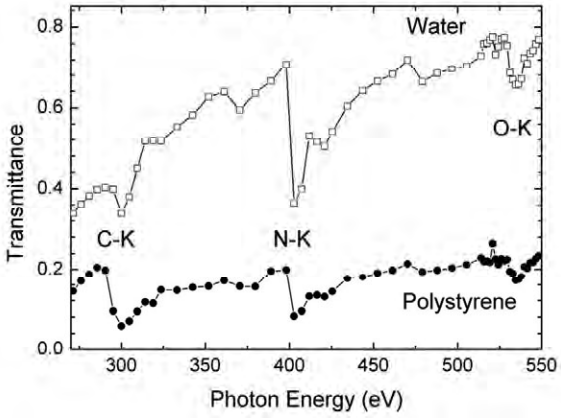

図５：ポリスチレン球の吸収スペクトル

成功した。以上の結果から、水中の生物細胞試料の各オルガネラに対して、透過率スペクトルないしは吸収スペクトルを求めることが可能となった、と考えられる。

謝辞

密着法全般に関して日本原子力研究機構の加道雅孝博士、石野雅彦博士に色々とご教示頂きました。また顕微鏡作製に当たっては、東北大学多元物質科学研究所技術室の朝倉和也氏、中村義浩氏、田中勇氏にたいへんお世話になりました。ここに記して感謝いたします。

参考文献

[1] B. Alberts *et al.*, Molecular Biology of The Cell, 5th (Garland Science, 2010, New York & Abingdom) Chap. 9.
[2] W. Chao, *et al.*, Nature 435, (2005) 1219.
[3] D. Attwood, Soft X-rays and extreme ultraviolet radiation, (Cambridge University Press, Cambridge, 2000) Chap.9.
[4] T. Ejima *et al.*, CP 1234, AIP(2010) pp. 811-814..

* ejima@tagen.tohoku.ac.jp

11B/2010G527

Development of a wideband multilayer grating with a new layer structure for a flat-field spectrometer attached to transmission electron microscopes in the 2-4 keV range (II)

Takashi Imazono,[1,*] Satoshi Kuramoto[2] and Masato Koike[1]
[1] Quantum Beam Sci. Directorate, Japan Atomic Energy Agency, Kizugawa, Kyoto 619-0215, Japan
[2] Device Department, Shimadzu Corp., Nakagyo-ku, Kyoto 604-8511, Japan

1 Introduction

Soft X-ray emission spectroscopy combined with transmission electron microscopy (TEM-SXES) is a helpful technique to understand both the physical property and chemical-bonding state of identified specimens in nanoscale. Original TEM-SXES instruments can detect soft x-ray emission (SXE) spectra in the 60-2000 eV range.[1] It is important to develop a SXES instrument to be able to cover a much wider energy range from 50 eV to 4000 eV. [2] It is because it is required to detect and analyze SXE spectra such as Li-*K* (55 eV), Pt-*M* (2.05 keV), In-*L* (2.84 keV) and Te-*L* (3.77 keV) emission bands in the fields of science, industry, etc. Unfortunately, it is difficult to observe 2-4 keV x-rays using a spectrograph equipped with a conventional grating with gold coating because such gratings are no longer practical due to Au-*M* resonant absorption. It is known that multilayer gratings are useful in higher energy region than ~2 keV. A conventional multilayer grating has high diffraction efficiency but narrow band in energy if it is used at a fixed angle of incidence. This indicates that the SXES instrument should employ some mechanisms for wavelength scanning to cover the required energy range. It is unsuitable as the spectrograph for TEM instruments. To overcome this problem, we have invented a new multilayer structure consisting of W and B_4C layers that enables to uniformly enhance the reflectivity in a few keV energy range at a fixed angle of incidence. [3]

We previously reported the diffraction efficiency of a multilayer grating in 2-4 keV, which the new layer structure was deposited on the gold-coated surface of a laminar-type varied-line-spacing (VLS) holographic master grating (M-MLG_N). [4] Here, we describe the diffraction efficiency of the identical multilayer-coated replica grating (R-MLG_N), and show that it works as the wideband multilayer grating along with M-MLG_N.

2 Experiment and Results

We prepared two replica gratings fabricated from the identical laminar-type VLS master grating having the radius of curvature of 11,200 mm, an average groove density of 2400 lines/mm, a 2.8 nm groove depth, and a 0.5 duty ratio, where all were produced holographically by Shimadzu Corp. The wideband multilayer was deposited on the gold-coated surface of one replica grating (R-MLG_N) by an ion-beam sputtering method. The other was left as just an Au-coated grating (R-AG) to compare the diffraction efficiencies. The layer structure

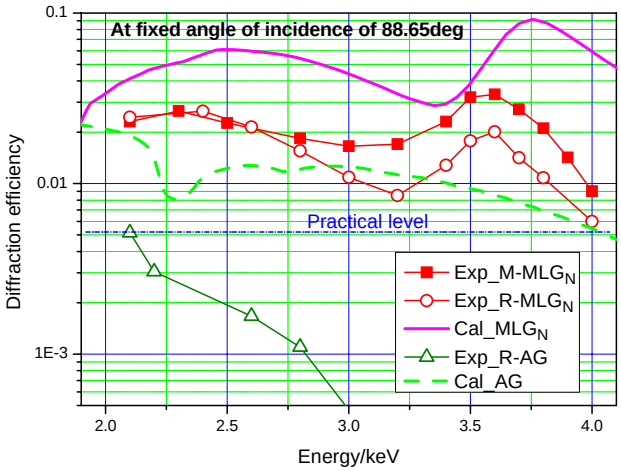

Figure 1 Experimental diffraction efficiencies of M-MLG_N, R-MLG_N, and R-AG at 88.65° in 2.1-4.0 keV. The calculated results are also shown.

on R-MLG_N was evaluated by an x-ray diffraction profile and confirmed to be as designed.

The experiments were carried out at BL-11B using an original evaluation apparatus for diffractometry and reflectometry. [4] Figure 1 shows the experimental diffraction efficiencies of M-MLG_N, R-MLG_N, and R-AG at a fixed angle of incidence of 88.65° in the energy region of 2.1-4.0 keV. Both M-MLG_N and R-MLG_N show wideband diffraction efficiencies and much higher than that of R-AG. They are also the higher efficiencies over the whole energy region than the practical level indicating as the efficiency at around the threshold of typical gold-coated gratings. The new multilayer scheme we have invented is obviously effective to uniformly enhance the diffraction efficiencies at fixed incident angle in 2-4 keV.

Acknowledgement

This study was conducted as part of a project of Collaborative Development of Innovative SEEDs (Practicability verification stage) by Japan Science and Technology Agency.

References

[1] M. Terauchi et al., J. Electr. Microsc. **59**, 251 (2010).
[2] T. Imazono et al., Appl. Opt. **51** 2351 (2012).
[3] T. Imazono et al., AIP CP, **1437**, 24 (2012).
[4] T. Imazono and M. Koike, PF Act. Rep. 2010 B, 318 (2011).

* imazono.takashi@jaea.go.jp

3C/2010G674

Differential phase microscope and micro-tomography with a Foucault knife-edge scanning filter

Norio Watanabe*, Junki Hashizume, Masahiro Goto, Masafumi Yamaguchi, Takayuki Tsujimura, Sadao Aoki
University of Tsukuba, Tsukuba, Ibaraki 305-8573, Japan

1 Introduction

In x-ray region, phase-contrast is much higher than absorption contrast. X-ray phase tomography is very attractive for the 3D observation of weakly absorbing material. In order to realize phase tomography, quantitative phase measurement is required. It was difficult by a conventional method like a Zernike phase-contrast microscope [1]. Nagayama showed that a quantitative differential phase image was obtained in electron microscopy by introducing a scanning knife-edge filter at a back focal plane of an objective lens [2]. We applied this method to an x-ray microscope with a zone plate [3]. In this report, x-ray differential phase imaging and phase tomography at 5.4 keV by using the synchronous operation between the scanning the knife-edge and the image accumulation are described.

2 Experiment

A Schematic of the differential phase microscope is shown in Fig. 1. An objective zone plate (NTT Advanced Technology Inc.) had the outermost zone width of 50 nm and the diameter of 330 μm. Monochromatic parallel x-rays of 5.4 keV were incident onto a specimen and the transmitted x-rays were focused on a CCD camera. The distance between the specimen and the CCD camera was 3.6 m and the magnification ratio was about 50. A gold wire of 250 μm in diameter was set as a knife-edge at the back focal plane of the zone plate. A differential phase image was calculated by $(I_R\text{-}I_L)/(I_R+I_L)$, where I_R and I_L were the images obtained by using the right- and left-scanning filter. A CT image was reconstructed from 360 projection images of different angles of view over the range of 360 degrees.

3 Results and Discussion

Polystyrene beads (diameter: 2.8 μm) in a glass capillary was observed. Figure 2 shows the bright field images. Figure 3 shows the Zernike phase-contrast images. The optical system was shown elsewhere [1]. Figure 4 shows the differential phase image and the reconstructed section phase image. The phase-contrast images in Fig. 3 have good contrast compared with the bright field images in Fig. 2. However, the glass capillary could not reconstruct in the CT image of Fig. 3. By using the differential phase microscope, the CT image could be successfully reconstructed as shown in Fig. 4(b).

Acknowledgement

This work was supported by a Grant-in-Aid for Scientific Research (C) (22611003) from the Ministry of Education, Culture, Sports, Science and Technology of Japan.

References

[1] S. Aoki et al., AIP Conf. Proc. 879 (2007) 1357.
[2] K. Nagayama, J. Phys. Soc. Jpn 73 (2004) 2725.
[3] N. Watanabe et al., AIP Conf. Proc. 1365 (2011) 313.

* watanabe@bk.tsukuba.ac.jp

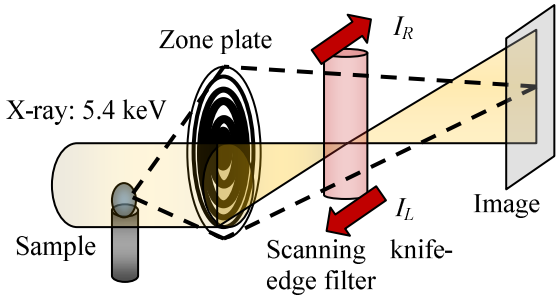

Fig. 1: Schematic of the differential phase microscope.

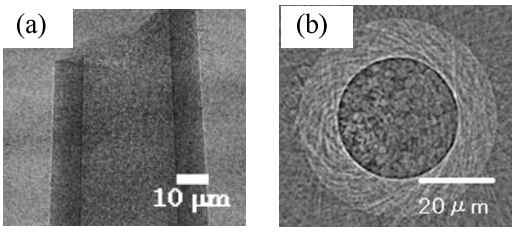

Fig. 2: (a) Bright field image and (b) the CT section image of polystyrene beads in a glass capillary.

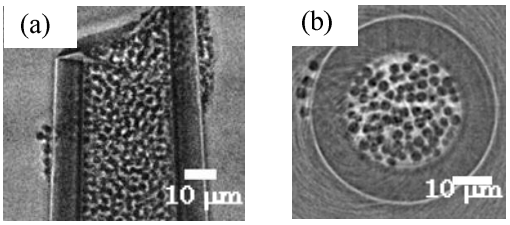

Fig. 3: (a) Phase-contrast image and (b) the CT section image of polystyrene beads in a glass capillary.

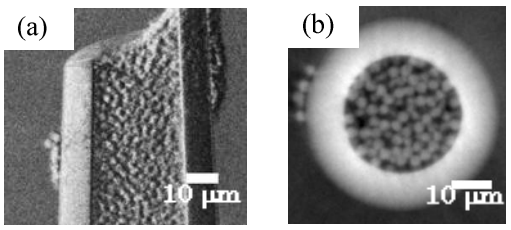

Fig. 4: (a) Differential phase image and (b) the CT section image of polystyrene beads in a glass capillary.

4A/2010R24/2011R01

蛍光X線深さ分析　－Confocal & Thin-Wire 法－
X-ray Fluorescence Depth Analysis –Confocal and Thin-wire methods

飯田厚夫
放射光科学研究施設、〒305-0801 つくば市大穂 1-1

1. はじめに

放射光マイクロビームやセミマイクロビームを使った蛍光X線元素マッピングは実用的な分析手法として定着している。元素マッピングによる空間分解能は面内ではビームサイズによって決まるが、深さ方向に不均一な厚い試料の場合には、得られる信号は深さ方向に（光軸方向に）積分されたものになる。厚さ方向の情報を得るためには、入射ビームに対して直交する検出器側に poly-capillary を備えて、入射側・出射側の焦点の一致した部分のみからの蛍光X線を検出し、試料を移動させることにより深さ分析機能（場合によっては３次元分析機能）を持たせた confocal システム（共焦点光学系）が近年開発されている[1]。この報告では留保ＢＴを使って BL4A においてテストした confocal システムの特性を紹介するとともに、より簡単な細い wire を使って深さ分析する手法についても説明する。

2. 実験及び結果

図１に示すように入射側 poly-capillary 集光系に対して、もう一つの出射側 poly-capillary を Si(Li)半導体検出器の前に置き、入射側と出射側の焦点を一致させると、その交点の情報のみ取り出すことができる。図２に示したのはカプトン膜を間に挟んだ２枚の金属薄膜（Cu、Co）をモデル試料に、深さ方向の分解能を調べたものである。Poly-capillary の集光性能はX線のエネルギーにも依存するが、使用した Poly-capillary は 8 keV 程度のエネルギーでそれぞれ 30 μm、40 μm 程度の分解能であるので、50μm 程度の深さ分解能が得られていることが分かる。図３はモエジマシダの根について２次元走査に深さ方向の走査を組み合わせて得られた Fe の蛍光X線信号から３次元像を求めたもので、実用的な分析が可能であることを示している。この方式は、発散した蛍光X線を集めるので効率が高く、また余分な光路からの散乱・蛍光X線を測定しないためにバックグラウンドも低い優れた方法である。この方法は勿論 XAFS 分析にも応用でき、３次元空間の特定の領域の分析が可能である。

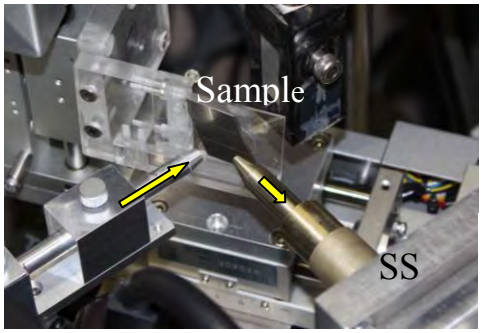

図１．Confocal system 配置

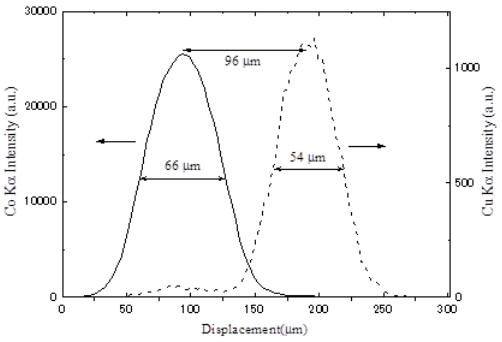

図２．Co/Kapton/Cu 膜の深さ分析

3. 考察

Confocal 法は優れているが、入射側焦点（集光点）と検出器側（出射側）焦点を一致させる必要があり、設定がやや煩雑である。出射側の poly-capillary の代りに細いワイアーを試料に近接させて置き試料を走査すると、検出器から見てワイアーが光路上の一点と交差した部分で蛍光X線強度が低下し、confocal システムと同じく深さ情報が得られる[2]。この方式は吸収を測定することになるので、confocal システムに比べて感度は低いが、濃度が高い試料に対しては有効で、分解能も 20 ミクロン以下が得られる。設定が極めて容易であることに特徴がある。

謝辞
シダ 試料を提供いただいた保倉明子先生（東京電機大学）に感謝いたします。

参考文献

[1]K.Janssens et al., Spectrochim. Acta B59(2004)1637
[2]A.Iida, X-Ray Spectrom. 40 (2011) 376 – 378
Atsuo.iida@kek.jp

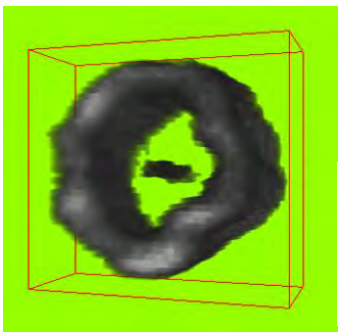

図３．モエジマシダ根における３次元鉄濃度分布。

14C1/2011G037

縞走査法に基づく高分解能高速位相 CT
High-Resolution High-Speed X-ray Phase Tomography Based on Phase Stepping

百生敦 [1*], 木林駿介 [2], Margie P. Olbinado[2], 太田崇士 [2], 矢代航 [2]
[1] 東北大学多元研　〒980-8577 仙台市青葉区片平 2-1-1
[2] 東京大学新領域　〒277-8561 千葉県柏市柏の葉 5-1-5

1 はじめに

透過格子を用いる X 線 Talbot 干渉計は、柔軟で様々な形態の X 線位相ｲﾒｰｼﾞﾝｸﾞに使えるﾃﾞﾊﾞｲｽとして、近年注目が増している。そのひとつの使い方として、白色放射光で動作させる４D 位相 CT がある[1]。位相 CT では、各投影方向で微分位相像を取得するｽﾃｯﾌﾟがある。微分位相像取得には縞走査法とﾌｰﾘｴ変換法があるが、高速撮影に有利なﾌｰﾘｴ変換法をこれまで採用していた。ただし、この場合の空間分解能は縞走査法を適用したときより劣るという問題がある。一方の縞走査法では格子の並進による複数の画像取得が求められるため、そもそも高速撮影には適さないとしていた。

本研究ではこれを再考し、振動を誘起しないｽｷｬﾝﾓｰﾄﾞを発案し、高速位相ＣＴに縞走査法のｺﾝｾﾌﾟﾄを適用した。ｽｷｬﾝ時間 5 秒で位相 CT 像を撮影することができた。ﾌｰﾘｴ変換法による高速位相ＣＴとの比較を行い、空間分解能が顕著に改善できることを確認した。

2 実験

BL-14Cにおいて得られる白色放射光に対して、28.8keVのX線に最適となる配置でX線Talbot干渉計を構築した。これは、π/2位相格子（G1）と振幅格子（G2）から成り、共に5.3μmの周期を持つL&Sﾊﾟﾀｰﾝを持つ。被写体の背後にG1を配置し、G2をその下流326mmに置き、さらにその背後に画像検出器を設置した。高速撮影を可能とするために、この画像検出器は、CMOSカメラ(pco.dimax, PCO AG)と20μm厚のP46蛍光ｽｸﾘｰﾝをﾚﾝｽﾞｶｯﾌﾟﾙしたものである。画素ｻｲｽﾞ11.2μmを持つ。ﾌﾚｰﾑﾚｰﾄは0.5kf/sとした。

単色X線を用いる位相CTなど、静的な試料を対象に測定する場合には、試料を所定角度回転して停止させ、その位置で格子をstep by stepで並進させて複数枚の画像を取得していた。これをこのまま高速化すると振動誘起の恐れもあるので、次のｽｷｬﾝ方式を考案した。

試料は一定ｽﾋﾟｰﾄﾞで連続回転しておく。格子も一定ｽﾋﾟｰﾄﾞで連続並進しておく。格子並進は、試料５回転で一周期異移動するようにｽﾋﾟｰﾄﾞ調整した。この状況で動画記録した各ﾌﾚｰﾑより、図１に示すように画像を抽出すれば、縞走査法の演算が各投影方向について行える。

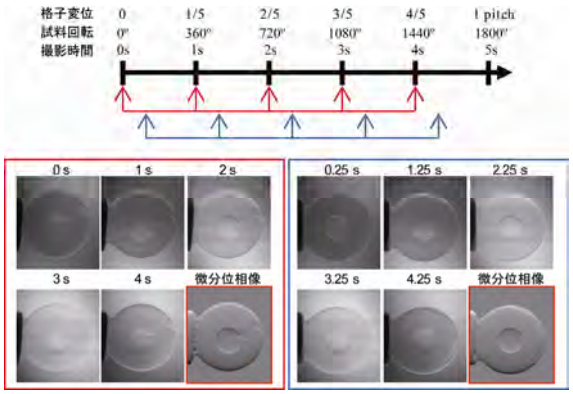

図１：本ｽｷｬﾝ方式による画像抽出ｽｷｰﾑ。

3 結果および考察

ﾌｰﾘｴ変換法と本手法による位相 CT 画像を同じ露光時間になるようにして比較した結果を図２に示す。空間分解能の明瞭な改善がみられ、図２(a)に見られるｱｰﾁﾌｧｸﾄも軽減することが分かった。

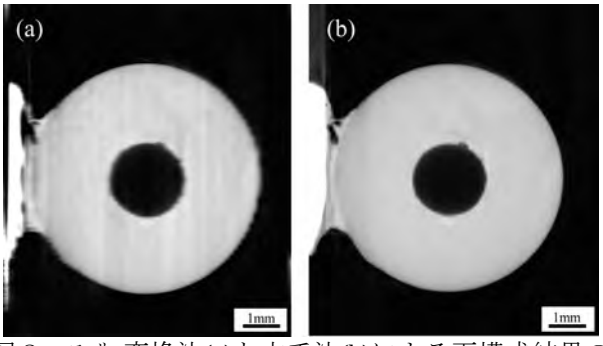

図２：ﾌｰﾘｴ変換法(a)と本手法(b)による再構成結果の比較。試料はﾌﾟﾗｽﾁｯｸ球（内部に空洞あり）。

4 まとめ

本研究より、空間分解能重視の場合の位相 CT 法が確立した。目的に応じてﾌｰﾘｴ変換法と本手法による位相 CT を使い分けることができる。

謝辞

本研究は、JST 先端計測のｻﾎﾟｰﾄにより推進した。

参考文献

[1] A. Momose *et al.*, Opt. Express **19** (2011) 8423.
* momose@tagen.tohoku.ac.jp

14C1/2011G037

白色放射光による X 線 Talbot-Lau 干渉計の動作
Operation of Talbot-Lau Interferometer with White Synchrotron Radiation

百生敦 [1*], Margie P. Olbinado[2], 木林駿介 [2], 太田崇士 [2], 矢代航 [2]
[1] 東北大学多元研　〒980-8577 仙台市青葉区片平 2-1-1
[2] 東京大学新領域　〒277-8561 千葉県柏市柏の葉 5-1-5

1 はじめに

透過格子を用いる X 線 Talbot 干渉計は、柔軟で様々な形態の X 線位相ｲﾒｰｼﾞﾝｸﾞに使えるﾃﾞﾊﾞｲｽとして、近年注目が増している。そのひとつの使い方として、白色放射光で動作させる４D 位相 CT がある[1]。放射光光源（電子ﾊﾞﾝﾁ）は水平方向に広がっており、空間的干渉性は鉛直方向にすぐれているため、X 線 Talbot 干渉計の格子（L&S ﾊﾟﾀｰﾝ）はﾊﾟﾀｰﾝが水平になるように配置する。このとき、位相 CT の試料回転軸も水平に配置する必要がある（図１(a)）。

この場合、柔らかい試料の観察を行うと、回転中に試料が重力のために変形するという問題があり、再構成像に致命的なｱｰﾁﾌｧｸﾄが発生しかねない。重力の影響を受けにくいように鉛直回転軸でｽｷｬﾝするためには、格子ﾊﾟﾀｰﾝを縦に配置する必要があるが、残念ながら PF の水平方向の空間的干渉性は不十分である。そこで、３枚格子からなる Talbot-Lau 干渉計の構築を考えた。

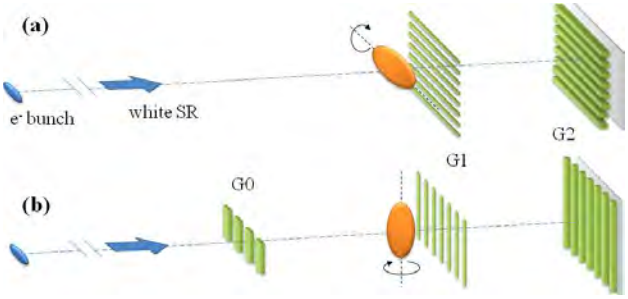

図１：PF での空間的干渉性に合わせた Talbot 干渉計(a)、及び、Talbot-Lau 干渉計(b)による位相 CT の構成。

2 実験

BL-14Cにおいて得られる白色放射光に対して、28.8keVのX線に最適となる配置でX線Talbot-Lau干渉計を構築した。これは、ﾏﾙﾁｽﾘｯﾄ（G0）、π/2位相格子（G1）と振幅格子（G2）から成る（図１(b)）。G0はｺﾋｰﾚﾝｽﾌｨﾙﾀｰの働きを持つ。すなわち、下流のTalbot干渉計（G1&G2）に対して、G0を成す各ｽﾘｯﾄを通るX線がそれぞれ形成するﾓｱﾚ像が合致すように設計してある。G0の周期は30μm、G1およびG2の周期はそれぞれ4.5μm と5.3μmである。G0-G1間は1.57m、G1-G2間は277mmとした。

3 結果および考察

格子を鉛直に立てて Talbot 干渉計を組むと、ﾓｱﾚ縞は検出できないのに対し、図１(b)の構成により、およそ 20%の鮮明度でﾓｱﾚ縞が発生した。図２(a)がその一例であり、図２(b)は縞走査法で計測した visibility 像であり、15%から 25%の範囲でｸﾞﾚｰｽｹｰﾙを与えている。図１(a)の Talbot 干渉計の構成では、全く同等の比較はできないものの、34%の visibility を得た結果がある。しかしながら、図２(c)に示すように、良好な微分位相像も得られており、十分に位相ｲﾒｰｼﾞﾝｸﾞが可能であることが分かった。

高速画像検出器でﾓｱﾚ動画像を観察する時、図示しないが、格子の振動の影響と思われるﾓｱﾚ縞の振動が見られる。これは Talbot 干渉計でも見られたが、Talbot-Lau 干渉計を構築した場合の方がより顕著であった。これは画質を劣化させる要因であるので、今後の改善が必要であろう。

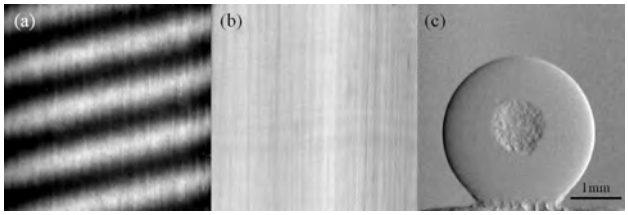

図２：Talbot-Lau 干渉計を構築して得られたﾓｱﾚ画像(a)、縞走査法で計測した visibility 像(b)および微分位相像(c)。試料はﾌﾟﾗｽﾁｯｸ球（内部に空洞あり）。

4 まとめ

本研究より、鉛直回転軸の４D 位相 CT が可能となった。今後、動的な試料について本構成を採用した実験を進める。

謝辞

本研究は、JST 先端計測のｻﾎﾟｰﾄにより推進した。

参考文献

[1] A. Momose *et al.*, Opt. Express **19** (2011) 8423.
* momose@tagen.tohoku.ac.jp

14C/2011G081

有機半導体放射線検出器の X 線応答特性評価
Evaluation on X-ray Detection Property of Organic Semiconductor Detector

高田英治[1*]、高田明成[1]、藤井一緒[1]、波戸芳仁[2]、中村尚司[3]
[1]富山高等専門学校　〒939-8630 富山市本郷町 13
[2]放射線科学センター　〒305-0801 つくば市大穂 1-1
[3]東北大学　〒980-8578 仙台市青葉区荒巻字青葉 6-3

1 はじめに

有機半導体光検出器（OPD）はその形状の可変性や低価格という長所を生かし、可視光発光素子、可視光受光素子において使用されており、その性能の向上は目覚ましいものがある。一方、OPD は生体と同様の元素で構成されており、OPD による放射線検出器が実現できれば、生体等価な検出器として被ばく管理等への適用が期待できる。そこで、著者らのグループでは有機半導体により構成される放射線検出器を自作し、X 線照射時の応答特性の評価を行っている。開発当初に試みたヘテロ型の構造と比べ、バルクヘテロ型の構造とすることで大幅な効率向上が実現できた。

2 実験

これまでの検討においては、Fig.1 に示すように n 型、p 型の有機半導体がそれぞれ 1 層をなすヘテロ型構造の OPD について検討を行ってきた。この構造で X 線照射時に電流が生成されることは確認できたが、感度が低いという問題点があった。そこで、Fig.2 に示すような n 型、p 型を混合した状態で塗布し製膜するバルクヘテロ型構造について検討を行った。実験は BC-14C において行い、単色 X 線の強度及びエネルギーを変化させて照射し、X 線誘起電流を微小電流計によって測定した。また、EGS5 によって OPD 中の各層へのエネルギー付与を計算し、実験結果と比較した。

3 結果および考察

図 3 に X 線エネルギーが 20keV の時の電流発生量を示す。バルクヘテロ型の構造を採用することで X 線誘起電流は 10 倍以上増加し、OPD の X 線に対する感度向上を実現できた。一方、実験から得られた電流発生量と X 線エネルギーの関係を、EGS5 による各層への X 線によるエネルギー付与を比較したところ、ピークの位置に違いがみられるなどの不一致が観測された。実験結果では 30keV 未満のインジウムの K 吸収端に近いエネルギーにおいて電流発生量にピークが観測されたのに対し、計算結果では有機層へのエネルギー付与においてそのようなピークは観測されなかった。実験による電流発生量は電荷収集プロセスも反映されていることから、今後は OPD 中での電荷の生成及び収集プロセスについて検討することが必要である。

4 まとめ

バルクヘテロ型構造とすることで、ヘテロ型構造よりも 10 倍以上の感度向上を実現できた。今後は電荷収集プロセスなど、OPD の放射線検出器としての動作について詳細な検討が必要である。

参考文献

[1] E. Takada et al., *J. Nucl. Eng. Sci.*, **35(8)** (2011) 547.

* takada@nc-toyama.ac.jp

Al (70 nm)
td-PTC (70 nm)
α-NPD (50 nm)
ITO (150 nm)
Glass Substrate (1 mm)

図 1 ：ヘテロ型 OPD の構造.

Al (70 nm)
PCBM:P3HT (600 nm, 1200nm)
PEDOT:PSS (40 nm)
ITO (150 nm)
Glass Substrate (1 mm)

図 2 ：バルクヘテロ型 OPD の構造.

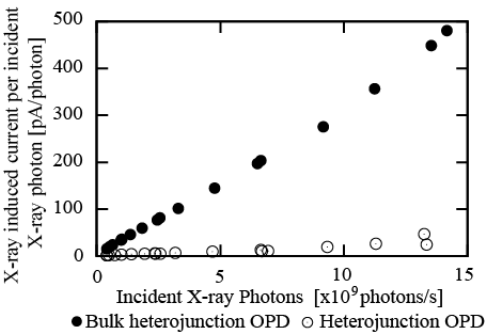

図 3 ： ヘテロ型 OPD，バルクヘテロ型 OPD の X 線誘起電流の比較

PF BL-14A, BL-14B, BL-14C1/2011G658

X-ray application of next-generation image sensors using SOI technology

Toshinobu MIYOSHI[1*]
[1]KEK-IPNS, Tsukuba, Ibaraki 305-0801, Japan

Introduction

The SOIPIX group is developing monolithic pixel sensors using SOI technology. The development project has started as an important subject in KEK Development and Technology Project (KEK-DTP). The sensors were evaluated with monochromatic X-rays at KEK-PF beamlines, PF BL-14A, BL-14B, and BL-14C1. This document describes a part of the experimental results.

Experimental Summary

The experiment was done in 3 beamlines in FY2011. The summary is shown in Table 1. In PF BL-14A, wide ranges of X-ray energy are available for various X-ray detector tests and therefore it was used for sensor gain and quantum efficiency (QE) measurement. In PF BL-14B, uniform beams in medium X-ray energy (10-17 keV) are available and thus it was used for demonstrations of the phase-contrast imaging and evaluation of the spatial resolution. In BL-14C1, uniform X-ray beams in high energy (25-40 keV) is available and so it was used for tests of the refraction-contrast and absorption-contrast imaging. The SOI sensors were compared with commercial X-ray CCD.

Table 1: Experiment summary

Beam line	Beam time [year/month]	Beam Energy [keV]	Subjects
14A	2011/11	17.5	Sensor gain, QE
14A	2012/2	6	Sensor gain, QE
14B	2011/10	16	Imaging
14C1	2011/11	33.1	Imaging

SOI image sensor chips and its performance

SOI image sensors were developed within multi-project wafer (MPW) runs every year in which various LSI designs were gathered in a common process mask [1]. Therefore, various SOI image sensors have been used in several beam times since 2009 [2]. In FY2011, we used the integration-type pixel detectors, INTPIX3e, DIPIX, and INTPIX4. Float-Zone (FZ-) SOI pixel sensors were also tested and compared with the existing Czochralski-(CZ-) SOI pixel sensors. The pixel size of those detectors is between 14 and 17 microns. In the DIPIX sensors, some chips were thinned to 50 microns to study behaviours at the full depletion condition. Focused X-ray beams were irradiated to the sensors in the beam line 14A. The beam spot was set to 400 by 400 microns using a X-Y slit. The number of photons was counted by NaI detectors and SOI sensors to evaluate the quantum efficiency of SOI sensors. The back bias voltage was applied up to 100 V and the quantum efficiency was evaluated. The results are shown in Fig. 1. It was found that the sensor was fully depleted at 30 V. The stability of the quantum efficiency at more than 40 V is less than 10%. The absolute value of the efficiency is about 6.5%. The SOI sensors have 5 metal layers for the CMOS circuit and the total thickness of them is about 5 microns. Therefore, the effective thickness is about 45 microns and the absorption ratio of the silicon is consistent of the quantum efficiency of the thin-SOI sensors. A large-area integration-type image sensor (the pixel size 17 μm and 832 x 512 pixels), INTPIX4, and INTPIX3e were demonstrated in X-ray imaging. The analysis is underway.

Future Plan

We developed a larger area INTPIX and fine pixel INTPIX in FY2011. We will evaluate them to apply X-ray imaging experiment and time-resolved X-ray study.

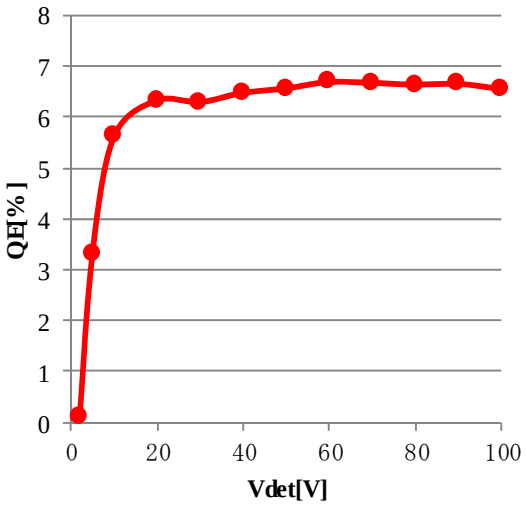

Fig.1 Dependence of quantum efficiency on back bias voltages of a 50 μm-thick SOI sensor with 17.5 keV monochromatic X-rays.

References

[1] T. Miyoshi et al., Nucl. Instr. And Meth. A, Vol. 636, Issue 1, Supplement 1, Pages S237-S241 (2011).
[2] T. Miyoshi et al., "Performance Study of Monolithic Pixel Detectors Fabricated with FD-SOI Technology", IEEE Nucl. Scien. Sympo. Conference Record, page 1704-1707, Valencia, Spain, Oct. 23-Oct.29 (2011).
* tmiyoshi@post.kek.jp

11D/2011G661

Energy Calibration in the Carbon Window Region at BL-11D

Tadashi Hatano*
IMRAM, Tohoku University, 2-1-1 Katahira, Aoba-ku, Sendai 980-8577, Japan

Recently BL-11D has been equipped with a new reflectometer to be a VUV and soft X-ray reflectometry beamline. To measure spectral reflectances here, however, the monochromator performance has not been enough. A brief description on the monochromator is given below.

The beamline BL-11D was constructed in 1996 for photoelectron spectroscopy. The monochromator is of a negative incidence-length varied deviation-angle type composed of a cylindrical mirror Mf, a plane mirror Mp and a spherical grating G. Two gratings G1 and G3 are mounted for soft X-ray and VUV regions, respectively. The photon energy scanning is made by changing the Mp and G angles. The designed G1 and Mp rotation angles as functions of photon energy are plotted in Fig. 1 by thick blue and red curves, respectively. The output photon energy was calibrated by photoelectron spectroscopy data in 300 – 700 eV and data points were fitted by fourth polynomials as plotted in Fig. 1 by dotted curves. The monochromator accepts only polynomial functions and has been actually operated along the dotted curves. Abnormal behaviours were found outside 300 – 700 eV. The C 1*s*-π^* absorption (285.5 eV) appeared at 299 eV for example. The situation is similar in VUV region covered by G3. It has been a serious problem that the monochromator did not work in the intermediate region 200 – 300 eV.

For reflectance measurements on our multilayer mirrors used in the carbon window region the monochromator has been tuned up at limited energy range of 250 – 300 eV.

The designed G1 and Mp rotation angles were fitted to fourth polynomials at 250 – 300 eV. The result are plotted in Fig. 1 by thin curves. This G1-Mp combination seems to work well through 200 – 350 eV. The spectral reflectance of a Cr/C multilayer was measured at various angles of incidence. The sample was deposited by ion beam sputtering. The period thickness, the C layer thickness to period thickness ratio and the period number are 3.06 nm, 0.32 and 200, respectively. Spectral reflectances calculated using optical constants from CXRO are plotted in Fig. 2. Above the C *K*-edge the ordinate is magnified by 10. Angles of incidence were chosen so that the interval of scattering vectors should be constant. The measured reflectances are plotted in Fig. 3. The good agreement between Figs. 2 and 3 shows a good spectral accuracy of the monochromator.

The author is grateful to Dr. T. Harada of LASTI, University of Hyogo for sample preparation.

* hatano@tagen.tohoku.ac.jp

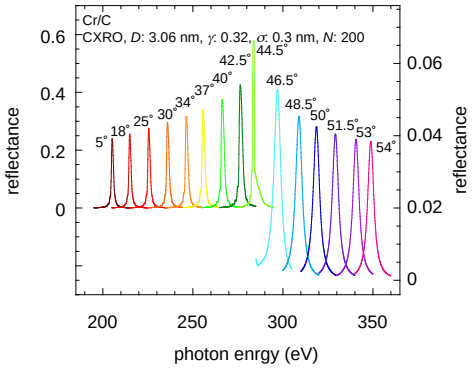

Fig. 2: Calculated spectral reflectances of a 3.06 nm period thickness Cr/C multilayer.

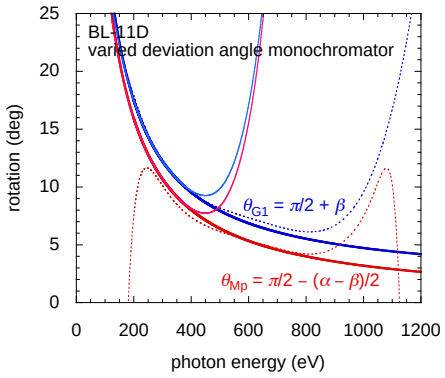

Fig. 1: Designed (thick), usually used (dotted) and the present (thin) rotation angles of G1 and Mp.

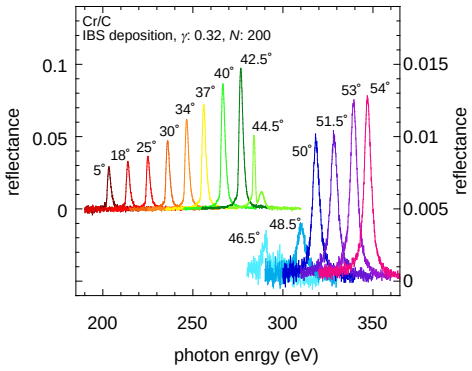

Fig. 3: Measured spectral reflectances of a Cr/C multilayer deposited by ion beam sputtering.

11A, 16A /2011G-678

超伝導検出器を用いた軟X線吸収分光ステーションの開発

X-ray absorption spectroscopy using superconducting detector in soft X-ray region

志岐成友[*1]、浮辺雅宏[1]、全伸幸[1]、小池正記[1]、
松林信行[1]、大久保雅隆[1]、北島義典[2]

[1]産業技術総合研究所、〒305-8567 つくば市梅園 1-1-1
[2]物質構造科学研究所　〒305-0801 つくば市大穂 1-1

1 はじめに

軽元素ドーパントや遷移金属の局所構造解析を実現するには、軟X線領域において高い感度と、高い元素選択能力を備えた、蛍光収量法によるX線吸収分光装置が必要である。高感度と高選択性を両立するため、100 画素超伝導トンネル接合(STJ)検出器アレイを備えたX線吸収分光装置を開発している[1]。

昨年度は、単一画素においてエネルギー分解能が12eV に達したこと、100 素子 STJ アレイ全体の分解能が 12-30eV であること、100 素子 STJ アレイを用いて吸収スペクトル測定が可能であること、を報告した[2]。2011 年度は、アレイ全域でエネルギー分解能を 20eV 以下とすること、BL-16A に於ける XMCD 測定の実現をめざし、装置の改良と制御ソフトウェアの開発を行った。

2 実験および結果

エネルギー分解能向上：軽元素の特性X線の選別には高いエネルギー分解能が必要である。図１は、BL-11A に於いて、STJ アレイとシリコンドリフト検出器(SDD)を用いて測定した六方晶窒化ホウ素の蛍光X線スペクトルである。STJ の測定結果は、81 画素の信号を積算したもので、B と N 以外に一般的に数%含まれることが多い O と、C による汚染が明確に確認できる。一方、SDD のスペクトルでは N と O が不完全に分離されるだけであり、C の信号は見えない。B のエネルギー位置に見えるピークは電荷収集が不完全なためにおこる N のゴースト信号である。STJ 検出器を用いると軽元素の分析能力が飛躍的に向上することがわかる。81 画素の信号を積算したスペクトルでエネルギー分解能は 16 eV FWHM で、単一画素のベストの性能(10 eV)に近づいている。

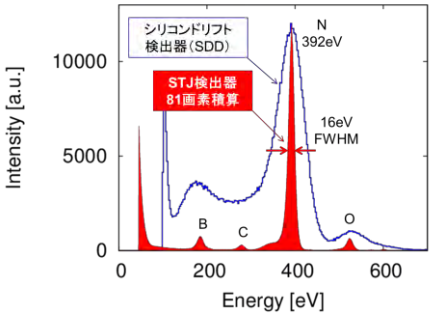

図１：STJ 検出器と SDD (Amptek X-123SDD, C1window) を用いて測定した窒化ホウ素の蛍光X線スペクトル。入射光のエネルギーは 600eV。

BL-16A の利用：BL-16A はアンジュレーターを光源としたビームラインで、高分解能・高感度で偏光を切り替えた分析が可能である。測定プログラムに BL-16A の回折格子の制御を組み込み、XMCD 測定が可能になった（図２左）。磁化した Fe-Co 薄膜を試料として STJ 検出器を用いた部分蛍光収量法による XMCD 測定を行った（図２右）。全電子収量法とほぼ同じ結果が得られた。

試料は液体ヘリウムにより冷却でき、現在、LaSrMnFeO に含まれる微量の鉄について、$L_{3,2}$吸収端における XMCD 測定に挑戦している。

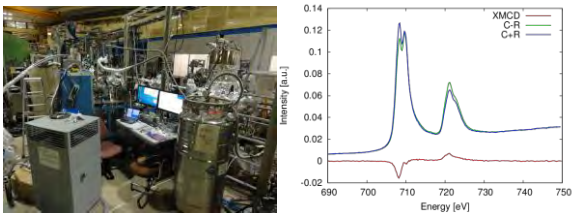

図２：BL-16A に装置を設置した様子（左）と STJ 検出器を用いた Fe-Co 薄膜の XMCD（右）。

装置公開：本装置は先端機器共用イノベーションプラットフォーム(IBEC)を通じて公開されている[3]。

3 まとめ

超伝導検出器を用いた、軟X線領域における蛍光収量法によるX線吸収分光装置を開発している。現在、BL-11A, BL-16A において 1 keV 以下の領域で、蛍光収量 XAFS, XMCD の測定が可能である。

謝辞

本研究は所属グループ各位の協力の元で実施されました。BL-16 での装置立ち上げに際し、永田康子先生に STARS への対応について情報提供・ご助言をいただきました。雨宮健太先生にはビームライン利用上のご配慮をいただき、Fe-Co 薄膜試料を提供していただきました。厚く御礼申し上げます。

参考文献

[1] S. Shiki, *et al.*, AIP Conf. Ser, 1185, 409 (2009).
[2] M. Ukibe, *et al.*, Jpn. J. Appl. Phys. **51**, 010115 (2012).
[3] http://open-innovation.jp/ibec/
* s-shiki@aist.go.jp

光源の現状 (Photon Factory News Vol.29 No.1 May 2011)

加速器第七研究系主幹　小林　幸則

光源リングの運転状況

PF リングにおける超伝導ウィグラーのトラブルについては前号で報告したが，結果的に再液化機のジュールトムソン（JT）弁のつまりによる不調のため，電磁石を液体ヘリウム温度に冷却することが困難となり，超伝導ウィグラービームライン（BL-14）は閉鎖となった。この JT 弁のつまりの対策は，春の停止期間中に行う予定であったが，大震災のため作業を延期した。2 月の運転は，PF リング，PF-AR ともに順調であった（図 1 ）。2 月 16 日に同時にビームダンプが発生しているが，これは ATF 地区での火災に伴って生じたビームダンプである。

東日本大震災被害状況

運転は 3 月 11 日の午前 9:00 まで行われ，停止期間に入った。地震は 3 月 11 日午後 2:46 に発生した。リングおよび基幹チャンネルは午前中の内にゲートバルブを締め，電磁石電源および高周波加速用高圧電源は OFF して長期停止モードに入っていた。リングトンネルおよび地下機械室にもほとんど人がいなかったので，怪我人が一人もでなかったことは幸いであった。

震災後の 3 月 17 日に照明を点灯して，目視による被害状況の調査を行った。光源棟，電源棟，入射路などを見て回ったところ，固定していなかった制御ラック等が転倒，移動等があったものの，電磁石および電磁石電源等の落下，転倒は見られなかった。しかし，PF リングにおいては壁電流モニターのベローズ管の破損（図 2），PF-AR においては，リングトンネルの建物のつなぎ目がずれたことに伴い，ベローズがゆがんでいる箇所が目視で確認できた。PF-AR の電磁石が一部湧き水が吹き出して汚れがあるのも見られたが，冷却水管が破裂したような箇所は無かった（図 3）。

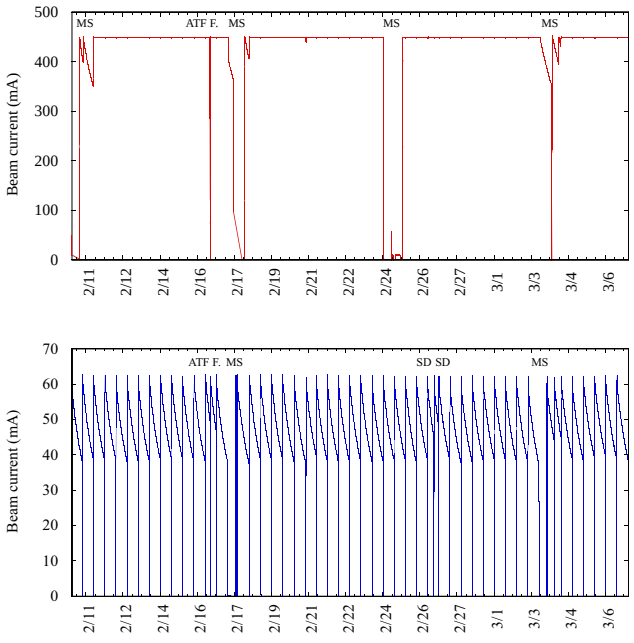

図 1　2011 年 2 月 10 日 ~3 月 7 日の PF リング（上図）および PF-AR（下図）における蓄積電流値。MS はメンテナンス・マシン調整日，SD は寿命急落，ATF F. は ATF で発生した火災時のビームダンプを示す。

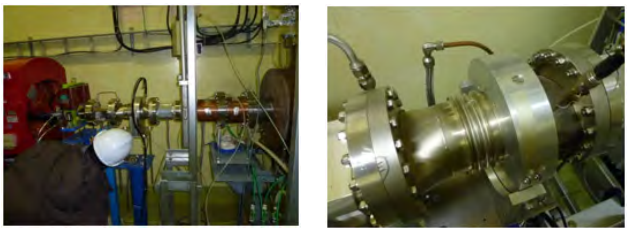

図 2　左：PF リング北 RF 下流側の破損箇所と右：破損したベローズ管（拡大）

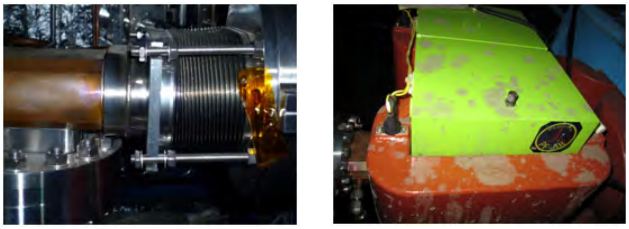

図 3　PF-AR の歪んだベローズおよび湧き水をかぶった電磁石

復旧計画案

PF リングと PF-AR は，それぞれ 5 月中旬および 6 月上旬の運転再開を目標にして，現在復旧作業を行っている。4 月 20 日現在，電力制限の中，真空度の確認，リーク箇所の調査，低電力での電源調査，クライストロンの真空立ち上げなどをこれまで行ってきた。図 4 に，震災後に測定

図 4　震災後に測定された PF リング一周の真空度

された PF リング一周の真空度を示す。北 RF 下流から南 RF 上流までリング西側半周が大気圧になっていることが分かったが，残り半周は真空に維持されていた。圧搾空気を供給し，ゲートバルブを制御したのち，リーク箇所の調査を行った。大きなリークは破損した壁電流モニターのベローズ 1 カ所で，その他超伝導ウィグラーダクトの下流部にスローリークが 1 カ所見つかった。現在，壁電流モニター箇所はダミー管と交換し，スローリークはバックシールで止めている。

PF-AR は幸いにも大きな破損は無かったようで，リング全周が真空に維持されていた。

4 月 5 日に，日本の放射光源加速器の関係者が集まり，被害状況の視察，および復旧への支援に関する打ち合わせを行った。まだ，電力や冷却水などの復旧の見通しが立たない事情により，被害状況は目視による調査の段階であったため，KEK から支援の具体案を提示はできなかったが，これを機会に相互の協力関係を構築することや，復旧・復興に関する情報を共有することで，今後に起こるであろう地震への対策ができるようにしようということになった。

人の動き

加速器第 7 研究系の坂中章悟さんが，4 月 1 日付けで教授に昇任されました。坂中さんには，光源第 2 グループのグループリーダーを継続していただくとともに，高周波加速システムに関する研究・開発および次世代放射光源 ERL の全体設計を行っていただく予定です。それから，東京大学物性研究所の中村典雄さんが，4 月 1 日付けで加速器第 7 研究系の教授に着任されました。中村さんには，光源第 1 グループに所属して頂き，軌道安定化に関する研究・開発を行っていただくとともに，次世代放射光源 ERL のビームダイナミックス研究において中心的な役割を担っていただけることを期待しています。

加速器第 7 研究系に所属していました佐藤康太郎さんと朴哲彦さんが，3 月 31 日付けで退職しました。佐藤さんは，シニアフェローとして加速器第 4 研究系（KEKB）に異動され，主に SuperKEKB の衝突点付近の開発・研究を行うことになりました。しかし，しばらくの間はコンパクト ERL の電子銃開発の方も兼務していただけるようお願いしています。朴さんは，シニアフェローとして引き続き

連の開発・研究を行っていただく予定です。

光源の現状 (Photon Factory News Vol.29 No.2 Aug 2011)

加速器第七研究系主幹　小林　幸則

光源リングの復旧作業

PF リングと PF-AR は，それぞれ 5 月 16 日および 6 月 1 日のビーム試験運転開始を目標にして，復旧作業を行った。PF リングでは，4 月 18 日の週に冷却水が復旧し，配管等からの水漏れが無いことを確かめた後，電磁石電源および RF における大電力健全性確認を行った。電力制限により電磁石電源は 1 台ずつ 10 分程度通電し，特に異常の無いことを確かめた。通電試験後に，四極電磁石の垂直レベル測量を行った。2009 年夏に行った測量データと比較すると最大で 0.3 mm 程度のずれであったので，ビーム試験はアライメントをせずに行うことにした。RF に関しては，1 台の高圧電源内部にガイシの破損があったため，当初健全性試験は 3 台で行ったが，破損の修理が 4 月中に行われたので健全性の確認はすべて連休前に終了した。クライストロンを含め特に問題はなかった。しかし，RF 空洞は大気にさらされたため，試験運転再開前にはある程度のエージングが必要で，真空作業との調整で連休明け 5 月 10 日から 5 月 13 日にかけて行うことになった。真空に関しては破損した壁電流モニターのベローズ部分をダミーダクトに交換し，またスローリークが見つかった超伝導ウィグラーダクトの下流部はバックシールで処置を行った。図 1 に 4 月 15 日時点と 5 月 12 日時点の PF リング 1 周の真空度のグラフを示す。リング半周部分が大気暴露されたため，ビーム試験運転では約一週間ほどの真空焼きだしが必要とされた。

PF-AR では，4 月 25 日の週に冷却水が復旧した。配管等に水漏れが無いかを調べたところ，特に心配していた電磁石用ブスバーには大きな漏れが無いことが分かった。さらに，大電力による健全性確認を連休明けに行ない，これも問題ないことを確認した。PF-AR でも電磁石の垂直レベル測量を行った。トンネル建て屋の接続部分 8 カ所で 2009 年夏の測量データと比較して 0.5 mm 程度のずれが生じているが，ビーム試験はアライメントをせずに行うことにした。

光源リング立ち上げ

5 月 14 日までに，PF リングでは電磁石通電，RF エージングが行われ，ほぼ再開の準備は整った。そして翌週の 5 月 16 日に予定通りビーム入射を開始した。午前中は入射器の調整が行われ，午後 2 時過ぎに 2.5 GeV 電子が入射器からビーム輸送路へやってきた。入射路のビーム通しは，スクリーンモニターを見ながら行われるが，坂の付近で垂直方向に大きくずれていることが分かり，補正電磁石を用いて大幅な修正を行った。地震の影響で坂の途中にある 4 極電磁石が垂直方向にずれたと推察される。何とか軌道修正を施してリング手前のスクリーンモニターでビームが到達していることを確認し，セプタム，キッカー電磁石を励磁して，リングへの入射を開始した。そして，4 時

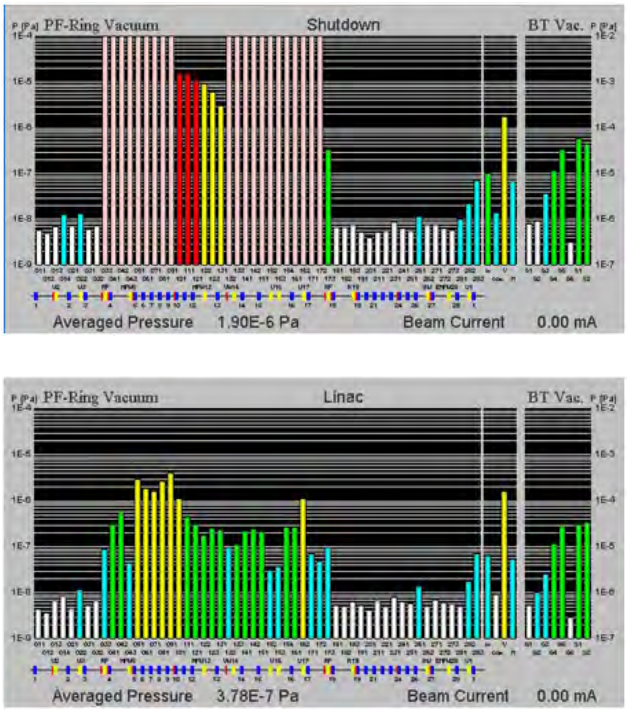

図 1　PF リング一周の真空度のグラフ。上図は 4 月 15 日時点，下図は 5 月 12 日時点での真空度を示している。北 RF ～南 RF の西側半周が大気暴露した。

50 分に 20 μA 蓄積に成功した。リングへの蓄積に成功した後は，入射パラメータの最適化や，リングの軌道調整を行いながら入射効率の改善を図った。真空度や RF 空洞の状態を確認して，徐々に電流を積み上げていき，夜までには 200 mA まで到達した。翌日には定格 450 mA の蓄積に成功した。PF リングはリングの半周が大気にさらされたため，真空度改善のための焼きだし運転を行いながら，挿入光源のギャップ変更動作を確認し，立ち上げから一週間後の 5 月 23 日にビームラインへの光導入を開始した。その日のうちにほぼすべてのビームラインで光を確認することができた。ビームラインでも各種調整が行われ，5 月 27 日 9:00 から光軸確認を行い，ビーム試験運転を開始した。なお，今年 1 月から不具合のあった超伝導ウィグラーも，6 月 9 日励磁に成功し，翌日 10 日には超伝導ウィグラービームライン BL-14 も無事再開となった。

PF-AR は，PF リングよりほぼ 2 週間遅れで復旧作業が行われた。RF 空洞エージングは 5 月 20 日より開始された。5 月 30 日にリングトンネル内をリミット管理にし，午前中に加速器の安全システムの検査を実施した。そして，予定通り 6 月 1 日に運転開始となった。入射器から PF-AR 用 3 GeV 電子が問題なく供給され，入射路も特に異常なところはなく，昼前には 10 mA の蓄積に成功した。一時リング 4 極電磁石電源 1 台が不調で運転が中断したが，電源の不調は制御基板の交換により解決した。その後は順調

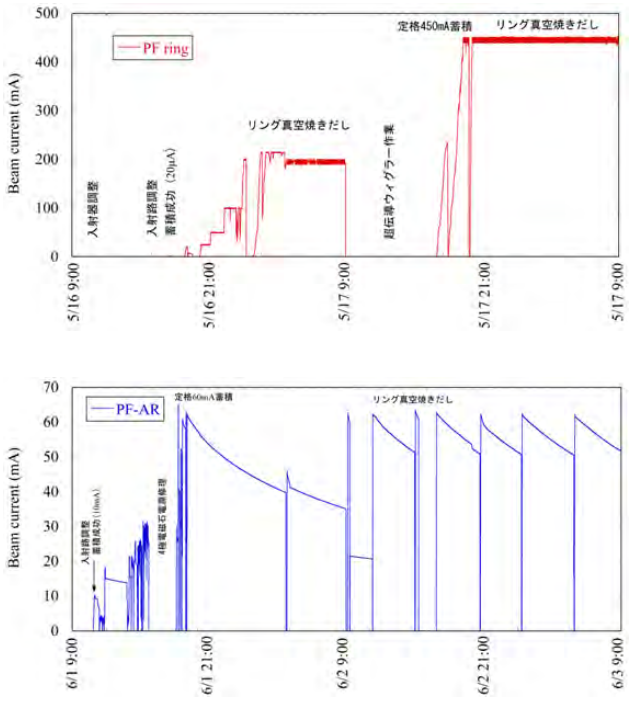

図 2　PF リングおよび PF-AR の立ち上げ 2 日間の蓄積電流値の推移を示す。

で，その日のうちに定格 60 mA の蓄積に成功し，予定通り真空焼きだしを行った。6 月 2 日から予定されていた各種の調整も順調に行われ，6 月 6 日 9:00 からビームライン光導入が開始された。5 mA からスタートして，光プロファイルの確認，放射線レベルの確認後，電流を上げて各種ビームライン調整を行った。ビームライン側も大きなトラブルもなく順調に進み，予定通り 6 月 10 日 9:00 から光軸確認を行い，初期電流値 60 mA でビーム試験運転を開始した。PF-AR は幸いにも大気暴露が無かったため，真空度の改善も早く，ビーム寿命もほぼ震災前の値に戻っている。図 2 に PF リングおよび PF-AR の立ち上げ 2 日間の蓄積電流値の推移を示す。

光源リングのビーム試験運転状況

ビームの試験運転は予想以上に順調立ち上がり，ほぼ全ビームラインに放射光を供給することができた。試験運転は多バンチモードで行われたが，秋からの単バンチモードを含めた本格的なユーザ運転に備えて，1 日ではあるがマシン調整日の 6 月 30 日に震災後初めて単バンチビームを蓄積するテスト運転を実施することになった。当日の朝 9:00 過ぎに 50 mA を蓄積すると，リングの 2 カ所 B09-B10 間，B23-B24 間で真空度が悪化した。直ちに入射を止め様子を見たが，徐々に真空度が改善してきたので，単バンチモードでの運転を続行した。しかしながら，夕方 B23-B24 区間で再び真空度が悪化し，しかもインターロックレベルの 10^{-5} Pa を上回ったため，ビームダンプが起こった。そこで多バンモードに切り替えて蓄積を試みたが 140 mA で再びビームダンプが発生した（図 3）。真空リークが疑われたため，ビーム試験運転を中断させてもらい，

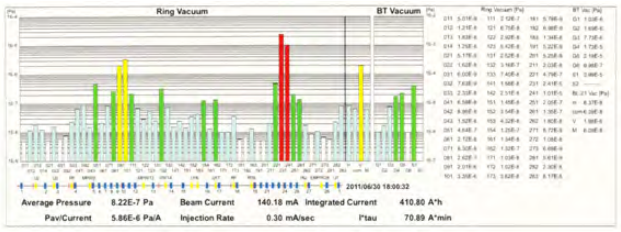

図 3　6 月 30 日 B23-B24 区間で真空悪化が発生してビームダンプが起こった時の，リングの真空度のグラフを示す。

翌日 7 月 1 日から 2 日にかけてリーク調査を行った。ベローズやその溶接部，アブソーバを丹念に調べたが，結局リーク箇所は特定できなかった。再び多バンチモードでの入射したところ，蓄積直後は真空悪化が起こったが，インターロックレベルには至らず徐々に改善が見られたので，運転を続行することになった。ただし，安全を見て蓄積電流値は定格 450 mA より 100 mA 少ない 350 mA として再開した。震災以前は単バンチビームを蓄積してもこのような急激な真空悪化は見られていないので，震災と何らかの関係はあると推察されるが，外部からの調査では特定できないため，運転停止後真空ダクト内を調査することにした。この時の結果については次項の本田氏の記事をご覧いただきたい。

PF-AR の方は，6 月 1 日から運転が開始され，小さなトラブルはあったものの，概ね順調にビーム試験運転が行われた。両リングともに 7 月 7 日 9:00 まで運転が行われ，停止期間に入った。図 4 に 6 月 7 日から 7 月 7 日までの一ヶ月の蓄積電流値の推移を示す。なお，毎火曜日は入射器ビーム調整に当てることとなり，その日はトップアップ運転を中断して，運転が行われている。

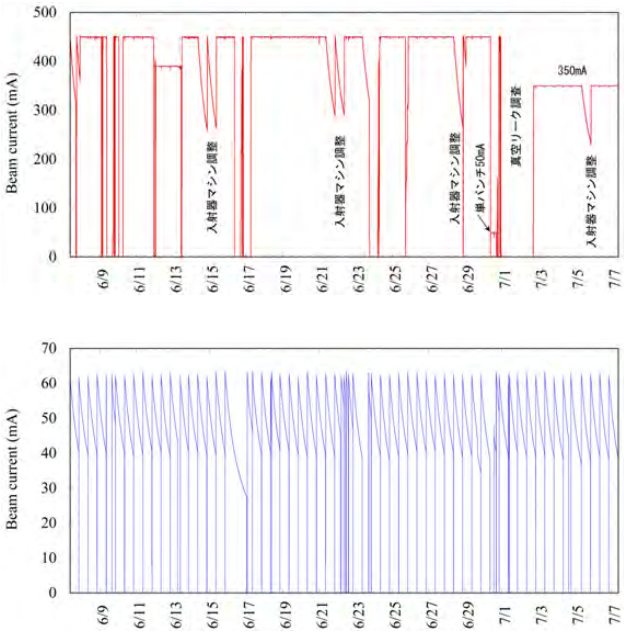

図 4　PF リングおよび PF-AR の 6 月 7 日から 7 月 7 日一ヶ月間の蓄積電流値の推移を示す。

光源の現状 (Photon Factory News Vol.29 No.3 Nov 2011)

加速器第七研究系主幹　小林　幸則

夏の停止期間中の作業

PF リング，PF-AR ともに 7 月 7 日 9:00 にビーム試験運転を無事終了した。PF リングでは，運転停止後すぐに，6 月 30 日に発生した単バンチビームでの B23-B24 付近の真空悪化の原因調査を行った（図 1)。真空チャンバー内の目視観察によって，図 2 に示すように RF シールド付きゲートバルブ付近が変色しており，さらにバルブの真空シールに使用している O リング（材質：エチレンプロピレンゴム）の変質が判明した（図 3)。真空悪化の原因はこのゲートバルブによるものと特定されるが，震災により何らかの歪みが生じ, 特に単バンチ運転では発熱しやすくなり，その発熱によって O リングからガス放出が起こったと推察される。PF リングでは，このタイプの RF シールド付きゲートバルブは他に 2 台使用しているが，この停止期間中に残り 2 台（B09-B10 間，VW#14 上流）の状態も調査することにした。その結果，やはりバルブ付近で変色が起こっていることから，これらのゲートバルブはすべてオールメタルの RF シールドゲートバルブに交換する方針とした。しかしながら，新規ゲートバルブの製作まで時間を要するので，状態の悪い B09-B10，B23-B24 間のゲートバルブは外してダミー管と交換し，比較的状態の良い VW#14 上流のバルブに関してはしばらく使用を継続することとした。

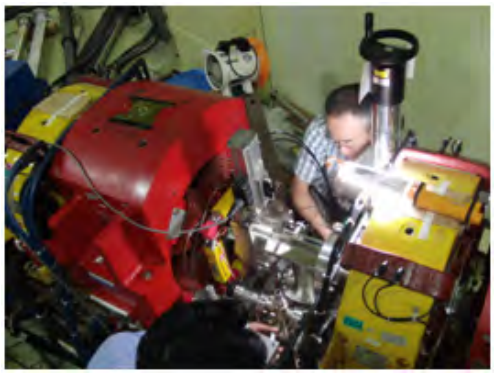

図 1　B23-B24 間真空チャンバー内調査。

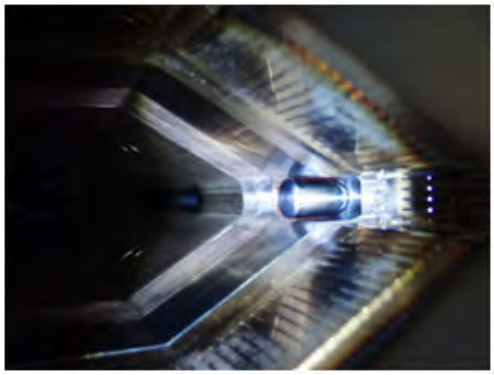

図 2　RF シールド付きゲートバルブ付近の真空チャンバー内部の様子。

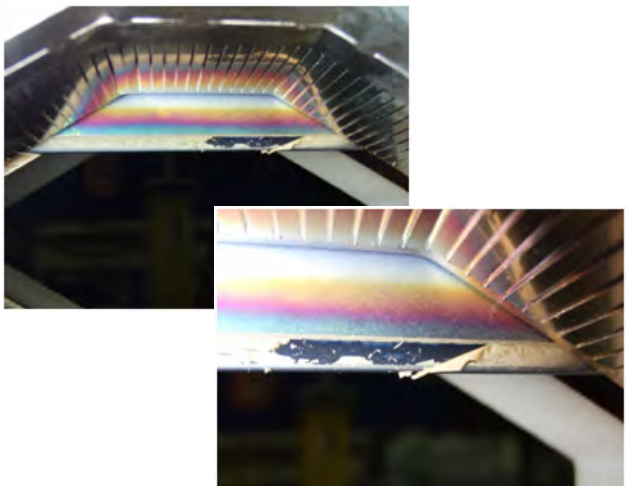

図 3　ゲートバルブ真空シール（O リング：エチレンプロピレンゴム）の変質。

今年の夏の停止期間中は，電源・真空などの各種コンポーネントや施設関連の保守・点検作業に加え，PF リングでは電磁石の水平測量・垂直再測量およびアライメント，PF-AR では水平測量・垂直再測量が追加で実施された。図 4 にリング垂直レベル測量の結果を，図 5 に水平測量の結果（PF リングのみ）を示す。横軸は電磁石が設置されているリング進行方向の位置であり，PF リングでは北直線部の中心を起点に，PF-AR では南直線部の中心を起点にしている。図 4 の垂直測量の結果は，変位を見やすくするため前回，前々回に実施された測量結果との差を表示している。図 5 の水平測量は，中心軌道からの変位を示している。震災後の 4 月の測量結果から，PF リングでは 150 m~200 m 付近すなわち入射点付近から北直線部にかけて，最大 0.5 mm ほど 2009 年 9 月に比べて沈んでいることが判明した。5 月の試験運転の際には，アライメントはせずにビームを回したが，夏の停止期間中に水平・垂直両方向のアライメントを実施した。急激な変位がでないように，なめらかにアライメントを行ない，図 4，5 に示すように水平方向はリング一周で± 0.2 mm 以内に，垂直方向は ± 0.3 mm 以内に補正することができた。一方，PF-AR では，4 月に実施した震災後の測量で，リングトンネルの接続部 8 カ所と北西棟付近において，0.5~0.7 mm 程度の変位が観測された。ところが，7 月の再測量では，図 4 の黒丸実線で示されているように，それらの変位がほとんど無くなるという結果になった。これまで PF-AR での測量は，夏の停止期間中にのみ実施されてきたため，接続部で観測された変位が震災の影響なのか季節変動なのか，現時点では区別がついていない。この区別は来年以降に行う測量データを待たねばならないが，今夏は PF-AR のアライメントを実施しないこととした。

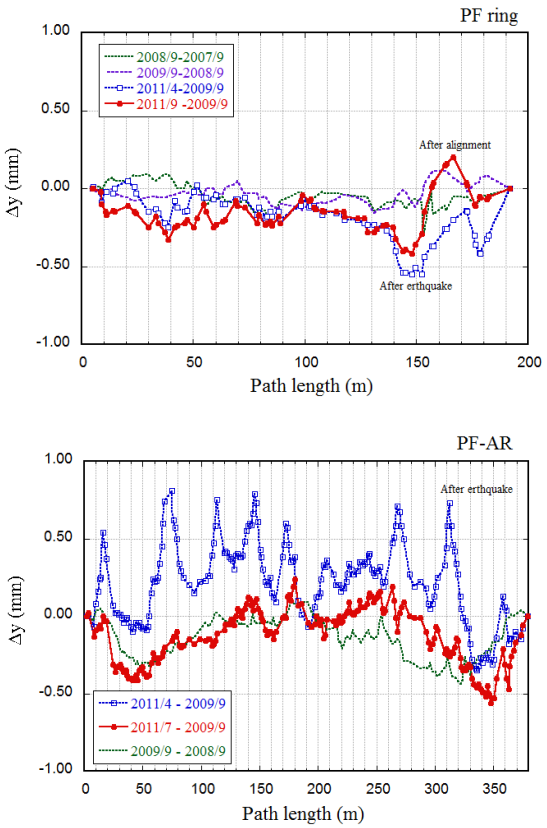

図 4　PF リングと PF-AR の垂直レベル測量の結果（変位）。PF リングでは 0 m 付近が BL-2，90 m 付近が BL-16，PF-AR では 100 m 付近が NW14，200 m 付近が NE1 に相当する。

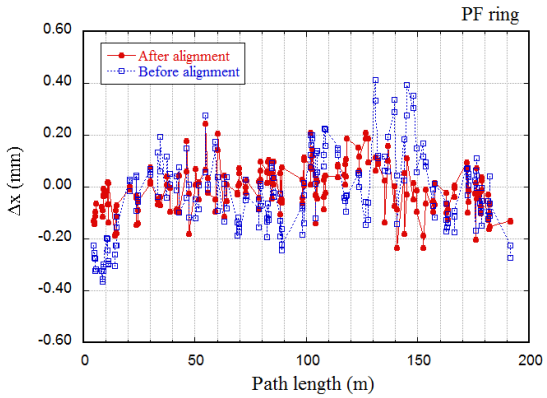

図 5　PF リングの水平測量の結果（横軸については Fig.4 の説明を参照）。

リング立ち上げ・運転状況

PF リングは 9 月 26 日 9:00 に立ち上げを行い，その後 1 週間で入射調整，真空焼きだし，光軸調整等を行ない，10 月 3 日 9:00 からユーザ運転を開始した。真空度の改善も順調で，10 月 14 日時点で蓄積電流値 450 mA においてビーム寿命約 18 時間となっている。10 月 2 日午後 2 時頃，AR 南実験棟において高圧ケーブル焼損事故が発生し消防車が来たことに伴い，入射器および PF リングの運転を一旦停止した。

PF-AR は 10 月 3 日 9:00 から立ち上げを開始した。停止期間中に真空作業が予定されていなかったため(実際には，U-NW2 上流のゲートバルブを交換する作業を行ったため，1 カ所であるが大気となった)，リング調整期間を 3 日間としていたが，この短い期間に入射調整，真空焼きだし，光軸調整等を実施して，10 月 6 日 9:00 からユーザ運転を開始した。両リングとも概ね順調にユーザ運転が再開された。図 6 に立ち上げ時からの蓄積電流値の経過を示す。

人の動き

高エネルギー加速器研究機構と東京大学物性研究所と人事交流により，篠江憲治さんが 9 月 1 日付けで加速器第 7 研究系の技師に着任されました。篠江さんには，光源第 2 グループに所属して頂き，ERL 主加速器超伝導空洞開発を中心に高周波加速空洞関連の仕事をして頂ける予定です。

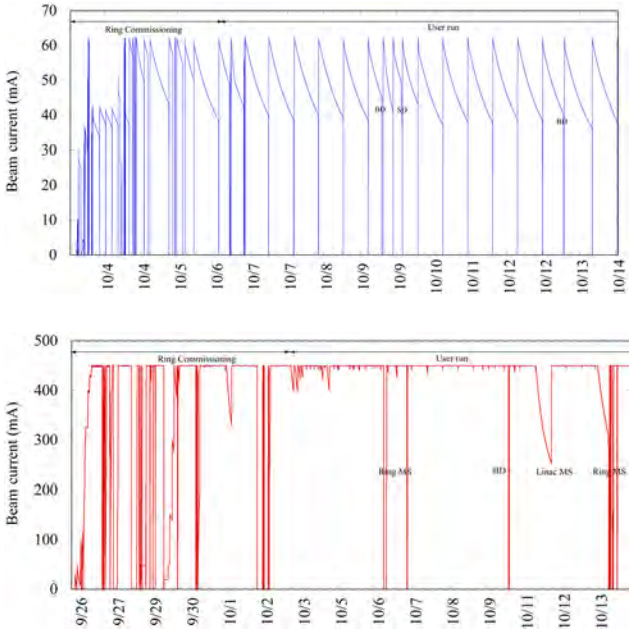

図 6　PF リング（上図）と PF-AR（下図）の蓄積電流値の推移。MS はマシン調整，BD はビームダンプ，SD は寿命急落である。

光源の現状 (Photon Factory News Vol.29 No.4 Feb 2012)

加速器第七研究系主幹　小林　幸則

光源リングの運転状況

PF リング，PF-AR ともに秋の運転は概ね順調だった。図 1 に典型的な運転として，11 月 7 日から 12 月 7 日までの蓄積電流値の推移を示す。PF リングでは 11 月 18 日から 11 月 24 日にかけては単バンチユーザ運転を行っている。単バンチモードは寿命が短いため，トップアップ運転は必須となっている。そのため，火曜日ごとに行われているリニアックマシン調整をこの週に限り中止して頂いた。また，12 月 1 日のマシン調整日に多バンチ 300 mA と単バンチ 50 mA を組み合わせたハイブリッドモードでのテスト運転をビームライン側と合同で行い，ビームライン側での問題点を洗い出して頂いた。特に，問題は無いようである。PF-AR では再入射を必要とする寿命急落が 11 月 11 日に 2 回，1 ～ 2 時間で回復する寿命急落が 11 月 12 日と 11 月 15 日に 3 回ずつ発生した（11 月 15 日には 2 分間隔で 2 回起きていた）。その 8 回のうち 5 回は SW12-13 間の FB ダンパ部の圧力のハネと同期していた。一度起きると頻発する傾向がある。カレント依存性も見えており，非回復型は 60 mA 付近で発生，回復型は 50mA 付近で発生している。放電条件やダストの種類やサイズの違いが考えられている。FB ダンパを改良型に交換する方向で検討している。さらに再入射を要する寿命急落が 11 月 22 日，11 月 25 日，11 月 29 日に 3 回あった。短時間で回復する急落も頻繁にあったが，そのうちの幾つかでは NW14-2 付近の圧力が変動していたこともあり，ギャップを 10 mm まで閉じたことによる（ダストではない）ビームロス率の上昇と思われる。

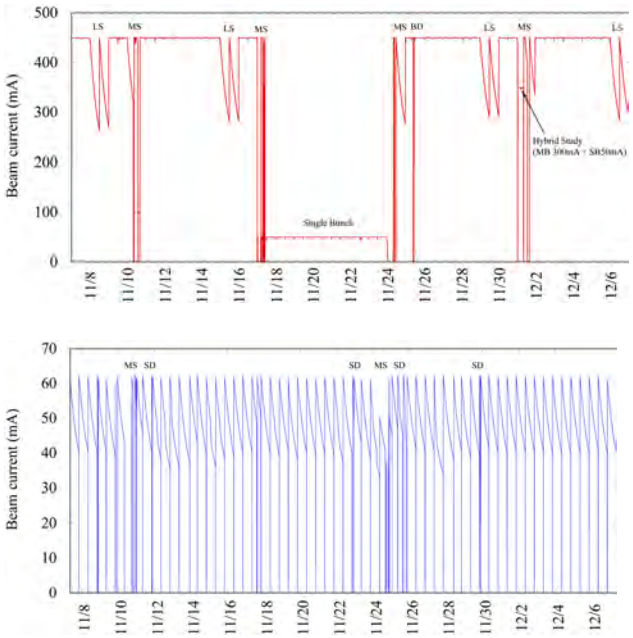

図 1　（上）PF リングと（下）PF-AR の蓄積電流値。MS はマシン調整，LS はリニアックマシン調整，BD はビームダンプ，SD は寿命急落を示している。

PF リング，PF-AR ともに，12 月 22 日 9：00 に運転を停止した。冬の停止期間中には，PF リングの超伝導ウィグラー上流のゲートバルブを取り外し，ダミー管と交換する作業を行った。このゲートバルブは震災後にハイブリッドモード運転での真空悪化が顕著になったので撤去した。1 月の立ち上げは，PF リングが 1 月 16 日に，PF-AR が 1 月 20 日に行われ，現在ユーザ運転が行われている。なお，1 月のマシン調整で，蓄積電流値を多バンチ 400 mA と単バンチ 50 mA で行ったが，顕著な真空悪化は見られなかったので，2 月 3 日から 2 月 7 日まで予定されているハイブリッドモードでのユーザ運転では，通常のマルチバンチ運転と同じ 450 mA で行う予定である。

PF リングにおける進行方向四極振動について

PF リングにマルチバンチ・大電流を蓄積した際には，進行方向のカップルドバンチビーム不安定が発生する。これを抑制するために，従来より広帯域進行方向キッカー，高速デジタル信号処理装置からなるフィードバックシステムを開発してきた。進行方向のフィードバックによって重心振動モード（シンクロトロン振動の二極振動成分）を完全に抑制することに成功し，2008 年秋からは常時ユーザー運転に供している。しかしながら，実際の不安定現象は二極振動だけではなく，バンチが進行方向に伸縮する四極振動が発生していることもこのとき判明した。これをフィードバックによって抑制するには新たなキッカーを設計・製作する必要があるうえ，強力なアンプも必要になるなど費用と時間の両面で容易に対処できなかった。そこで，主加速 RF 信号（約 500 MHz）にシンクロトロン周波数の 2 倍（約 43 kHz）で位相変調をかけることでバンチ長を伸ばし，全体としてビームを安定化する手法を併用してきた。この手法は四極不安定の安定化に有効である一方，ビームのエネルギー広がりが大きくなる欠点を持ち合わせている。したがって，リング内の分散がある場所ではビームサイズが大きくなり，結果としてビーム輝度の減少につながってしまう。とくに顕著に表れるのが BL3，BL17 など，分散のある場所にある挿入光源ビームラインである。

東日本大震災の後，6 月 30 日にはじめて単バンチ・大電流のビームを蓄積したところ，B23-B24 間の真空が悪化してビームダンプにつながる事態が発生した。この時点では原因究明に至らなかったものの，夏の停止期間の作業によって RF コンタクト付きのゲートバルブ付近が変色し，O リングが変質していることが判明した。このタイプのゲートバルブは PF リングでは全部で 3 カ所使用していたため，このうち 2 つはダミー管と交換し，残り 1 つは状態が比較的良いと思われたためそのままにする方針とした。

この状態で秋の運転を開始したところ，進行方向の四極振動の様子が従来とは変わっていることが判明した。四極振動が起き始めるビーム電流の閾値は 230 mA 程度であったものが 270 mA 程度まで上昇した（閾値は RF 空洞のパラメータにも依存しており，常に同じ電流で起き始めるわけではない）。また，蓄積電流値がさらに大きくなって 400 mA を越えたあたりでは，夏以前の運転では四極振動が起きたり起きなかったりを繰り返す奇妙な現象が起きていたのに対し，400 mA を越えても不安定が発生することが無くなり，ビームが安定になった（念のため付言するとビーム不安定の二極振動モードは起きているため，進行方向フィードバックによる抑制は不可欠である）。このため，ゲートバルブ部分が空洞構造となり，四極振動をひきおこすインピーダンス源になっていたものと推定した。

これで四極振動問題が全て解決したかと思ったのもつかの間，ビーム電流が 450 mA でトップアップ運転を継続している間は非常に安定であったのに対し，リニアックマシン調整にともなってトップアップを停止して蓄積モードで運転したところ，電流が 320 mA 付近まで減少したときに四極振動が起きはじめることが判明した（図 2）。この現象にはヒステリシスがあり，一度不安定が起きはじめると 450 mA でのトップアップ運転に戻しても四極振動が治まることは無かった。

フィードバックシステムの解析機能を使用して個々のバンチ振動の様子を測定したところ，バンチトレイン後半になるにしたがって振動が大きくなることが分かった。これまで PF はハーモニック数 312 に対し，連続した 250 バケットにビームを蓄積して，残り 62 バケットはイオン捕獲不安定を抑制するためのギャップとしていた（バンチトレイン 1 個）。バンチ列後半で不安定が成長するならば，バンチトレインの数を増やして，個々のトレインの長さを短くすれば不安定が抑制可能になると考えて，いくつかのフィルパターンを試行した。その結果，4 つのバンチトレイン（63 バンチ＋ 15 ギャップ）× 4 個，とすれば四極振動が起き始める電流値が下がることを確認できた（図 3）。これ以上分割しても効果は無く，むしろ不安定が起こりやすくなってしまった。当面のユーザーランは 4 バンチトレインで行うとともに，今後も原因究明のマシンスタディを継続する。

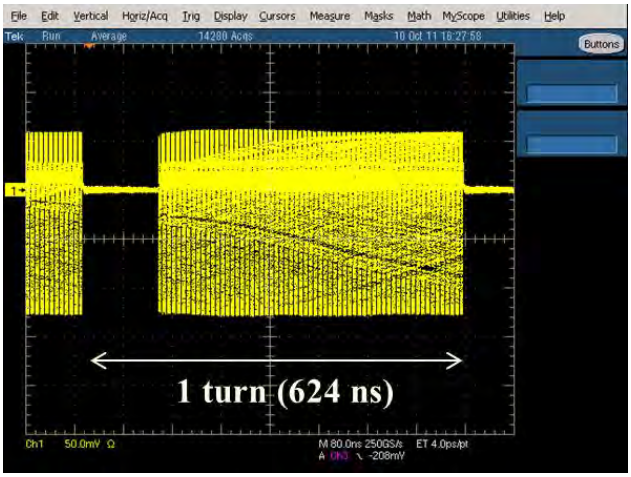

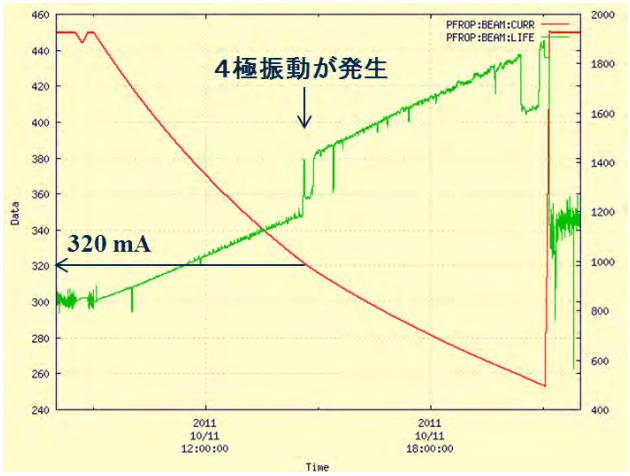

図 2　（上）250 バンチ＋ 62 ギャップのフィルパターン，（下）ビーム電流 320 mA 付近まで減少したときに四極不安定発生。バンチ体積が増えるためビーム寿命が増加する。

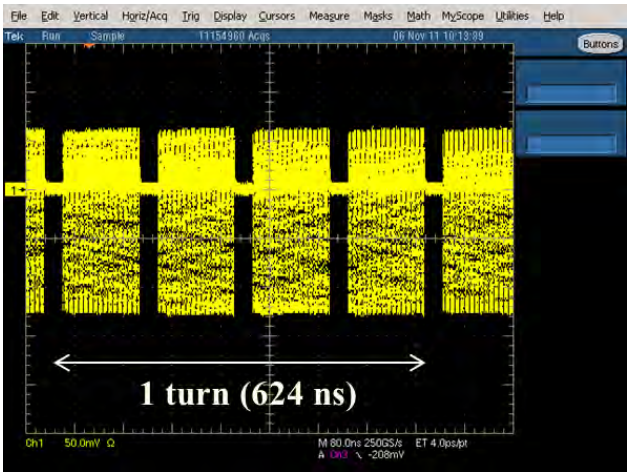

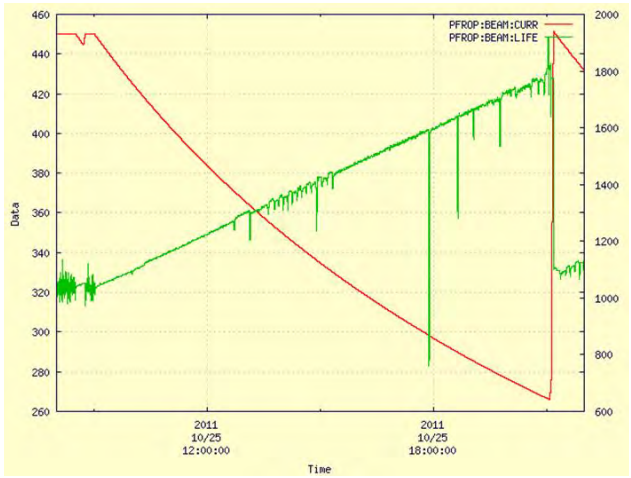

図 3　（上）（63 バンチ＋ 15 ギャップ）×4 個のフィルパターン，（下）ビーム電流 260 mA 付近になっても四極不安定は発生しない。（ビーム寿命がスパイク的に下がっているのは挿入光源のパラメータ変更にともなうもので，不安定とは無関係）